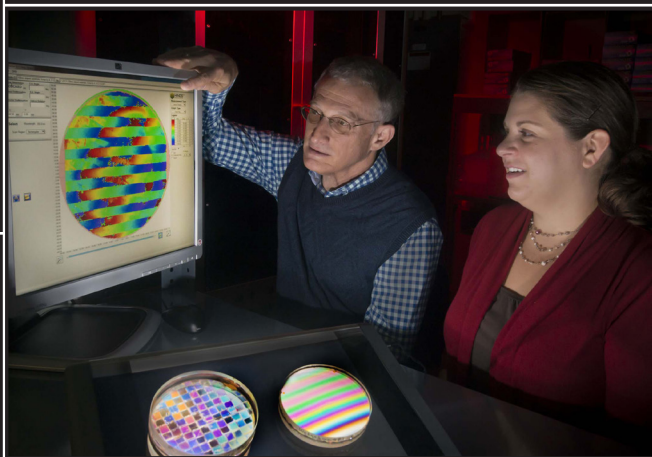
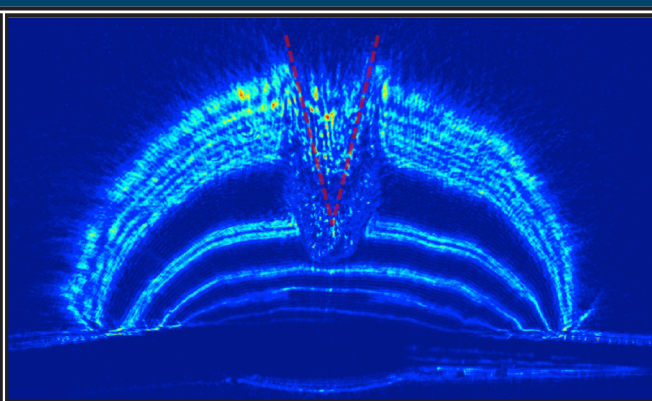


# LLE 2013 Annual Report



October 2012 – September 2013



## Cover Photos

Top left: OMEGA EP firing all four high-energy UV beams on a target shot along with a  $4\omega$  probe beam located inside the housing on the right. The green light comes from the frequency-doubled light remaining after frequency conversion of the primary beams from the infrared to the ultraviolet.

Bottom left: Photograph of the new high-precision neutron temporal diagnostic (NTD) being installed on OMEGA. The NTD measures the time history of the neutrons produced in OMEGA fusion-target experiments.

Top right: A channel formed in a plasma with a high-intensity OMEGA EP beam is imaged using the new OMEGA EP fourth-harmonic probe laser beam and an angular filter refractometer.

Center right: Steve Jacobs and Brittany Taylor examining a color-coded map of optical rotary power taken of a striped distributed polarization rotator. The device consists of a liquid crystal fluid confined between glass substrates.

Bottom right: Brighton High School student Erin Wang is shown preparing to disconnect the main gas line that feeds deuterium into a cryogenic calorimetry cell. The calorimeter measures the amount of heat flowing when the deuterium melts and freezes. In its 25th year, LLE's Summer Research Program for High School juniors has had 312 participants, 94 of whom have already attained advanced degrees.

---

Prepared for  
U.S. Department of Energy  
Albuquerque Service Center  
DOE/NA/1944-1149

Distribution Category  
October 2012–September 2013

Printed in the United States of America  
Available from

National Technical Information Services  
U.S. Department of Commerce  
5285 Port Royal Road  
Springfield, VA 22161  
[www.ntis.gov](http://www.ntis.gov)

This report was prepared as an account of work conducted by the Laboratory for Laser Energetics and sponsored by New York State Energy Research and Development Authority, the University of Rochester, the U.S. Department of Energy, and other agencies. Neither the above named sponsors, nor any of their employees, makes any warranty, expressed or implied, or assumes any legal liability or responsibility for the accuracy, completeness, or usefulness of any information, apparatus, product, or process disclosed, or represents that its use would not infringe privately owned rights. Reference herein to any specific commercial product, process, or service by trade name, mark, manufacturer, or otherwise, does not necessarily constitute or imply its endorsement, recommendation, or favoring by the United States Government or any agency thereof or any other sponsor. Results reported in the LLE Review should not be taken as necessarily final results as they represent active research. The views and opinions of authors expressed herein do not necessarily state or reflect those of any of the above sponsoring entities.

The work described in this volume includes current research at the Laboratory for Laser Energetics, which is supported by New York State Energy Research and Development Authority, the University of Rochester, the U.S. Department of Energy Office of Inertial Confinement Fusion under Cooperative Agreement No. DE-NA0001944, and other agencies.

For questions or comments, Laboratory for Laser Energetics,  
250 East River Road, Rochester, NY 14623-1299, (585) 275-5286.  
[www.lle.rochester.edu](http://www.lle.rochester.edu)

# LLE 2013 Annual Report

---

October 2012 – September 2013



Inertial Fusion Program and  
National Laser Users' Facility Program

---

# Contents

Executive Summary .....	v
A Polar-Drive Shock-Ignition Design for the National Ignition Facility.....	1
Polar-Drive Implosions on OMEGA and the National Ignition Facility .....	15
Cross-Beam Energy Transfer in Polar-Drive Implosions on OMEGA.....	27
Measured Hot-Electron Intensity Thresholds Quantified by a Two-Plasmon–Decay Resonant Common-Wave Gain in Various Experimental Configurations .....	33
Mitigation of Cross-Beam Energy Transfer: Implications of Two-State Optical Zooming on OMEGA .....	43
Measuring 8- to 250-ps Short Pulses Using a High-Speed Streak Camera on Kilojoule, Petawatt-Class Laser Systems.....	58
A Solid-State, Inductive-Adder, 10-kV Pulse Generator for Driving Large-Aperture Pockels Cells.....	64
Commissioning of a Multiple-Frequency–Modulation Smoothing by Spectral Dispersion Demonstration System on OMEGA EP.....	75
Simulations of the Propagation of Multiple-FM Smoothing by Spectral Dispersion on OMEGA EP .....	85
Fiber Front End with Multiple Phase Modulations and High-Bandwidth Pulse Shaping .....	98
Mitigation of Two-Plasmon Decay in Direct-Drive Inertial Confinement Fusion Through the Manipulation of Ion-Acoustic and Langmuir-Wave Damping.....	112
Hot-Electron Generation from Laser/Pre-Plasma Interactions in Cone-Guided Fast Ignition .....	127
Pulsed Laser Ablation of Dental Calculus in the Near Ultraviolet .....	136
Improving Cryogenic DT Implosion Performance on OMEGA .....	145
Polar-Drive Experiments with Shimmed Targets on OMEGA .....	156
Localized Time-Resolved Electron-Temperature Measurements Indicate Nonuniformly Driven Two-Plasmon–Decay Instability in Direct-Drive Implosions.....	161
Measurements of the Divergence of Fast Electrons in Laser-Irradiated Spherical Targets .....	167
Copper K-Shell Emission Cross Sections for Laser–Solid Experiments.....	173
Fracture Mechanics of Delamination Defects in Multilayer Dielectric Gratings.....	187

Demonstration of the Improved Rocket Efficiency in Direct-Drive Implosions  
by Using Different Ablator Materials ..... 199

Characterization of a High-Photon-Energy X-Ray Imager..... 205

Plasma-Ion-Assisted Coatings for 15-fs Laser Systems ..... 212

Spectral and Temporal Properties of Optical Signals with Multiple Sinusoidal  
Phase Modulations ..... 222

The Fifth Omega Laser Facility Users Group Workshop ..... 237

LLE’s Summer High School Research Program ..... 243

FY13 Laser Facility Report ..... 245

National Laser Users’ Facility and External Users’ Programs ..... 247

Publications and Conference Presentations ..... 323

---

## Executive Summary

The fiscal year ending September 2013 (FY13) included the first six months of the fourth five-year renewal of Cooperative Agreement DE-NA0001944 with the U.S. Department of Energy (DOE). A portion of the year was funded as an extension of the prior Cooperative Agreement DE-FC52-08NA2832 with DOE. This annual report summarizes work carried out under the Cooperative Agreement at the Laboratory for Laser Energetics (LLE) during the past fiscal year including work on the inertial confinement fusion (ICF) campaign; laser, optical materials, and advanced technology development; operation of the Omega Facility for the ICF and high-energy-density (HED) campaigns, the National Laser Users' Facility (NLUF), the Laboratory Basic Science (LBS) Program, and other external users; and programs focusing on the education of high school, undergraduate, and graduate students during the year.

### Inertial Confinement Fusion Research

One of LLE's principal missions is to conduct research in ICF with particular emphasis on supporting the goal of achieving ignition on the National Ignition Facility (NIF). This program uses the Omega Laser Facility and the full experimental, theoretical and engineering resources of the laboratory. During FY13, a total of 1984 target shots were taken at the Omega Laser Facility (comprised of the 60-beam OMEGA UV laser and the four-beam, high-energy petawatt OMEGA EP laser). More than 40% of the facility's target shots in FY13 were designated as ICF experiments or experiments in support of ICF. During the last five years of the current Cooperative Agreement, 8204 target shots were taken on the Omega Laser Facility in support of the National Nuclear Security Administration (NNSA) missions. The OMEGA and OMEGA EP lasers attained average experimental effectiveness of 96.6% and 93.7%, respectively, in FY13.

LLE plays a lead role in the validation of the performance of cryogenic target implosions, essential to all forms of ICF ignition. LLE is responsible for a number of critical elements within the Integrated Experimental Teams supporting the demonstration of indirect-drive ignition on the NIF and is the lead laboratory for the validation of the polar-drive (PD) approach

to ignition on the NIF. LLE has also developed, tested, and constructed a number of diagnostics that are being used at both the Omega Facility and the NIF. During this past year, progress in the inertial fusion research program continued in three principal areas: ICF experiments and experiments in support of ICF; theoretical analysis and design efforts aimed at improving direct-drive-ignition capsule designs (including polar-drive-ignition designs) and advanced ignition concepts such as shock ignition and fast ignition; and development of diagnostics for experiments on the NIF, OMEGA, and OMEGA EP.

#### 1. Inertial Confinement Fusion Experiments in FY13

Simulations of polar-drive-implosion experiments conducted on OMEGA are presented (p. 15). Good agreement is observed between the experimental measurements and *DRACO* simulations in terms of areal density and symmetry. The scaling of these experiments to the NIF and the role of laser-plasma interactions are discussed.

We report on a comparison of measured and simulated angular dependence of the unabsorbed light in OMEGA experiments (p. 27). The 3-D simulations show that cross-beam energy transfer explains the decreased laser absorption, which can be mitigated using smaller laser beams on target and tuning the wavelength of the laser beams organized in different rings.

We report (p. 33) on the measured hot-electron fraction generated by the two-plasmon-decay (TPD) instability in planar experiments using one to four linearly polarized beams, 18 beams with polarization smoothing, and, in spherical geometry, 60 beams with polarization smoothing. The overlapped intensity threshold for hot-electron generation is different for each experimental configuration. These measured thresholds are compared and shown to be consistent with convective gains calculated with a resonant common wave model.

The results from a series of cryogenic deuterium-tritium (DT) implosions are presented (p. 145). A flexible direct-drive target platform was used to implode cryogenic DT capsules on the OMEGA Laser System. The goal of these experiments

was to demonstrate hydrodynamically equivalent ignition performance, where the laser-drive intensity, implosion velocity, fuel adiabat, and in-flight aspect ratio (IFAR) were the same as those for a 1.5-MJ target designed to ignite on the NIF. The implosions spanned a broad region of design space to study target performance as a function of shell stability (adiabat) and implosion velocity. High implosion velocities are achieved with the higher-adiabat target designs that stabilize the hydro-instability growth at the ablation surface. For targets driven with higher-adiabat ( $\sim 4$ ) conditions, the measured areal density and primary neutron yields are  $>80\%$  to  $90\%$  and  $\geq 25\%$  of the 1-D code predictions, respectively. Comparable performance for targets with adiabats in the range of 2.0 to 2.5 is needed to demonstrate ignition hydrodynamic equivalence.

We report the results of polar-driven direct-drive experiments performed on the OMEGA Laser System (p. 156) using targets with a contoured shell thickness (shimmed). The objective of these experiments was to explore the efficacy of using a shimmed target to improve implosion symmetry. These experiments demonstrated that target shimming can improve the low-mode symmetry over beam pointing alone. Given the need to control the shape of PD implosions on the NIF, and the anticipated benefit of shimming to increase the ignition margin, these results indicate that further research into methods to shape the DT encapsulating shell, and possibly the DT layer itself, should be undertaken. The authors point out that even indirectly driven implosions may benefit from using shimmed capsules, emphasizing the importance of this method.

OMEGA experiments demonstrate that spectra and images near  $\omega_0/2$  (where  $\omega_0$  is the laser frequency) provide a powerful direct-drive, coronal plasma diagnostic for ICF (p. 161). Spatially and temporally resolved half-harmonic spectra and images of laser-driven implosions show evidence of local, multibeam-driven TPD instability. This instability always starts with the multibeam absolute instability that rapidly evolves into the convective regime extending between  $n_c/4 \leq n_e \leq n_c/5$ . The lower density is determined by Landau damping. Judging from the  $\omega_0/2$  spectra, this instability is never observed in its linear stage, consistent with expectations. When the target view included the target normal and the TPD threshold was exceeded, a sharp, red-shifted  $\omega_0/2$  spectral feature was observed that can serve as a convenient local electron temperature diagnostic. Time-resolved electron temperatures revealed locally increased electron temperatures in areas of enhanced overlapped irradiation intensities. Corroborating information was obtained from spatial images taken in the blue portion of the  $\omega_0/2$  spectrum.

We report on measurements of the divergence of fast electrons in laser-irradiated spherical targets (p. 167). In experiments using directly driven spherical targets on the OMEGA Laser System, the energy in fast electrons was found to reach  $\sim 1\%$  of the laser energy at an irradiance of  $\sim 1.1 \times 10^{15}$  W/cm<sup>2</sup>. The fraction of the fast electrons absorbed in the compressed fuel shell depends on their angular divergence. This divergence is deduced from a series of shots where Mo-coated shells of increasing diameter  $D$  were embedded within an outer CH shell. The intensity of the Mo-K $_{\alpha}$  line and the hard x-ray radiation were found to increase as  $\sim D^2$ , indicating a wide divergence of the fast electrons. Alternative interpretations of these results (electron scattering, radiation excitation of K $_{\alpha}$ , and an electric field caused by the return current) are shown to be unimportant.

Published measurements and models of the cross section for electrons causing K $_{\alpha}$  emission from copper are reviewed to find a suitable expression for analyzing K $_{\alpha}$  emission measurements in laser–solid experiments at peak intensities above  $10^{18}$  W/cm<sup>2</sup> (p. 173). There exist few measurements in the electron energy range currently of interest, 0.1 to 10 MeV, leaving a number of models that could be suitable. These models are summarized with a number of typographical errors corrected. Two different limiting forms for the cross section at relativistic energies are used, and existing measurements do not give a clear indication as to which is correct. Comparison with the limiting form of electron stopping power indicates (1) an alternative relativistic form and (2) that the density effect correction will be important in copper above 10 MeV. For data analysis relying on relative K $_{\alpha}$  emission caused by electrons with energy much greater than the K-shell binding energy, the existing uncertainty in cross sections is unimportant, but it will be a source of uncertainty when using absolute values and for electron energies up to about  $6\times$  the binding energy. K $_{\alpha}$  emission caused by photons and protons is also briefly reviewed.

The first experimental study of rocket efficiency where different ablators were used to vary the ratio of the atomic number over the atomic mass is presented (p. 199). Success of direct-drive implosions critically depends on the ability to create high ablation pressures ( $\sim 100$  Mbar) and to accelerate the imploding shell to ignition-relevant velocities ( $>3.7 \times 10^7$  cm/s) by using direct laser illumination. It is demonstrated that the implosion velocity of Be shells is increased by 20% compared to C and CH shells in direct-drive implosions. These measurements are consistent with the predicted increase in the hydrodynamic efficiency of 18% for Be and 7% for C compared to a CH ablator.

## 2. Theoretical Design and Analysis

Beginning on p. 1, the performance of a shock-ignition (SI) polar-drive design is estimated using 1-D and 2-D simulations for implementation on the NIF. This design was developed within the NIF Laser System specifications. The target implosion velocity is higher than for standard SI designs to account for laser power limitations on the NIF. The proposed capsule ignites in 1-D simulations on the NIF with an  $ITF_{1-D}$  (ignition threshold factor) of 4.1 using 700 kJ of input laser energy. The capsule is robust in 1-D to shock mistiming. Hot-electron energy coupling during the spike pulse is shown to have a positive effect on target margin at hot-electron temperatures up to 150 keV and hot-electron energy levels below 20% of the incident spike-pulse energy.

We review the physics and possible implementations of two-state optical zooming to mitigate cross-beam energy transfer on OMEGA (p. 43). Scattering of the incident laser energy is reduced using a smaller beam radius on target for the main drive pulse while maintaining the beam size for the picket pulses.

A generalization of the extended Zakharov model of TPD (p. 112) includes the evolution of the electron-distribution function in the quasi-linear approximation. This makes it possible to investigate anomalous absorption of laser light and hot-electron production caused by the TPD instability of multiple overlapping electromagnetic waves.

Particle-in-cell simulation results are reported (p. 127) pertaining to cone-in-shell integrated fast-ignition experiments at the Omega Laser Facility. These simulations provide further evidence of the detrimental effects of pre-plasma in the cone. Studies of hot-electron generation from laser/pre-plasma interactions and transport show that the generated hot electrons are dominated in number by low-energy electrons but in energy by multi-MeV electrons.

## 3. Diagnostics for ICF Experiments

We report on the reliability and accuracy improvement of streak-camera-based short-pulse measurements by homogenizing the slit illumination using an anamorphic diffuser and calibrating the space-charge broadening. These improvements apply to the measurement of OMEGA EP pulses with durations ranging from 8 to 250 ps (p. 58).

The characterization of a high-proton-energy x-ray imager is reported (p. 205). The Bragg angle, rocking curve, and reflection efficiency of a quartz crystal x-ray imager (Miller indices

234) were measured at a photon energy of 15.6909 keV, corresponding to the  $K_{\alpha 2}$  line of Zr, using the X15A beamline at the National Synchrotron Light Source at Brookhaven National Laboratory. Using one of the curved crystals, the Zr  $K_{\alpha 2}$  emission was imaged from a hot Zr plasma generated by LLE's 10-J Multi-Terawatt laser. Estimates of the reflectivity obtained by comparing the spatially integrated signal from the images to the direct x-ray emissivity of the source were, within experimental error, in agreement with values obtained at the X15A beamline.

## Lasers, Optical Materials, and Advanced Technology

The design of a new solid-state, high-voltage pulse generator for driving large-aperture Pockels cells is discussed beginning on p. 64. These generators are reliable replacements for the obsolete thyratron-based drivers used in the large-aperture ring amplifiers of the OMEGA and OMEGA EP front ends.

The performance of OMEGA EP seeded by optical pulses with high-frequency phase modulations is described (p. 75). This demonstration of multiple-frequency modulation smoothing by spectral dispersion includes angular dispersion by a diffraction grating, propagation, and amplification in a NIF preamplifier module and one OMEGA EP beamline, frequency conversion, beam smoothing after a distributed phase plate, and focusing. Laser operation is characterized under conditions relevant to an implementation of multi-FM beam smoothing on the NIF to support polar drive.

Modeling and simulation results describing the propagation of spatially dispersed frequency-modulated optical pulses are presented (p. 85). A comprehensive CEA-provided laser design and simulation code (Miró) was used to set a peak-power limit for multi-FM pickets, taking into account nonlinear propagation in the optical components and conversion of frequency modulation into amplitude modulation because of diffraction.

We describe the fiber front end laser system built to support the demonstration of multi-FM beam smoothing on OMEGA EP (p. 98). High-bandwidth pulse shaping, multi-FM phase modulation, spectral-amplitude compensation, chromatic dispersion compensation, and fail-safe systems have been implemented to provide seed pulses that meet all operational requirements.

We report on research on the fracture mechanics of delamination defects in multilayer dielectric coatings (p. 187). During the fabrication of multilayer-dielectric (MLD) thin-film coated optics, such as the diffraction gratings used in OMEGA EP's

pulse compressors, acid piranha cleaning can lead to the formation of chemically induced delamination defects. The causes of these defects are investigated, and a mechanism for the deformation and failure of the MLD coating in response to hydrogen peroxide in the cleaning solution is described. A fracture mechanics model was developed and used to calculate the crack path that maximizes the energy release rate, which was found to be consistent with the characteristic fracture pattern observed in MLD coating delamination defects.

A process is demonstrated for producing ultra-broadband coatings (for femtosecond pulse applications) with high reflectivity, high-laser-damage thresholds, and controlled dispersion (p. 212). Large-aperture deposition of high-laser-damage-threshold, low-dispersion optical coatings for 15-fs pulses was developed using plasma-ion-assisted electron-beam evaporation. Coatings are demonstrated over 10-in.-aperture substrates.

A study of the spectral and temporal properties of the optical signals generated by multiple sinusoidal temporal phase modulations (multi-FM) of a monochromatic source is presented (p. 222). Statistical analysis based on the central limit theorem shows that the signals' optical spectrum converges to a normal distribution as a number of modulations increases, making it possible to predict the frequency range containing a given fraction of the total energy with the associated cumulative density function. Analysis and simulation of frequency-modulation-to-amplitude-modulation conversion of arbitrary multi-FM signals are performed. These developments are of theoretical and practical importance for high-energy laser systems, where optical pulses are phase modulated in the front end to smooth out the on-target beam profile and prevent potentially catastrophic damage to optical components.

We present the results of experiments and models relating to dental calculus ablation in human teeth using 400-nm laser pulses (p. 136). This work was the result of a collaboration involving researchers from LLE, The Institute of Optics, the University of Toronto, and the University of California, San Francisco. Calculus-removal rates, microscopy, and spectroscopy after irradiation are consistent with tissue-specific ablation at 400 nm caused by absorption by bacterial porphyrins within calculus. A heuristic model for calculus ablation agrees well with observed data.

### FY13 Omega Facility Report

During FY13, the Omega Facility conducted 1408 target shots on OMEGA and 576 target shots on OMEGA EP for a

record total of 1984 target shots for the ICF, HED, NLUF, and LBS program and also provided several shot days for CEA and the University of Michigan's Center for Radiative Shock Hydrodynamics (CRASH) program (see Fig. 1).

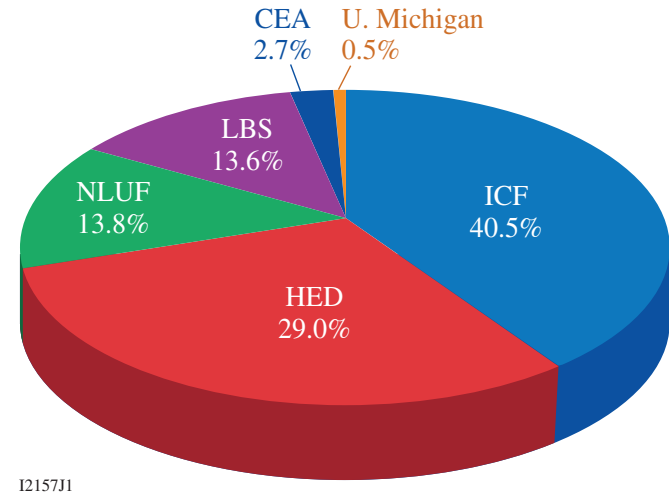


Figure 1  
Pie chart showing the distribution of Omega Facility target shots by program in FY13.

Nearly 70% of the shots were taken for the ICF and HED programs.

OMEGA averaged 11.5 target shots per operating day with availability and experimental effectiveness averages for FY13 of 93.9% and 96.6%, respectively. OMEGA EP was operated extensively in FY13 for a variety of internal and external users. A total of 576 target shots were taken into the OMEGA EP target chamber including 69 joint shots into the OMEGA target chamber. OMEGA EP averaged 6.7 target shots per operating day with availability and experimental effectiveness averages for FY13 of 93.8% and 93.7%, respectively. Highlights of achievements in FY13 are detailed starting on p. 245 and include the following:

- Joint cryo backlighting
- $4\omega$  probe diagnostics
- Replacement of neutron temporal diagnostics
- Tritium fill station cryo permeator
- Sydor framing camera
- Solid-state Pockels cell drivers

## National Laser Users' Facility and External Users' Programs

Under the facility governance plan that was implemented in FY08 to formalize the scheduling of the Omega Laser Facility, Omega Facility shots are allocated by campaign. Nearly 70% of the FY13 target shots were conducted for the ICF and HED campaigns.

The fundamental science campaigns accounted for ~27% of the target shots taken by the facility in FY13. Half of these were taken for the National Laser Users' Facility (NLUF) program and the remainder for the Laboratory Basic Science (LBS) program.

The Omega Facility is also being used for several campaigns by teams from the Commissariat à l'énergie atomique (CEA) of France and the Atomic Weapons Establishment (AWE) of the United Kingdom. These programs are conducted at the facility on the basis of special agreements put in place by DOE/NNSA and the participating institutions.

The facility users during FY13 included 11 collaborative teams participating in the NLUF program; 16 teams led by Lawrence Livermore National Laboratory (LLNL) and LLE scientists participating in the LBS program; many collaborative teams from LLE and the national laboratories conducting ICF experiments; investigators from LLNL and Los Alamos National Laboratory (LANL) carrying out HED experiments; and scientists and engineers from CEA, AWE, and the University of Michigan's CRASH program. In total, ~62% of the Omega facility target shots were conducted by teams led by external users.

### 1. FY13 NLUF Programs

FY13 was the first of the two-year period of performance for the NLUF projects approved for FY13–FY14 funding and Omega facility shots. Eleven NLUF projects (see Table 136.VII, p. 248) were allotted Omega facility shot time and conducted a total of 274 target shots. The work of the NLUF projects in FY13 is summarized beginning on p. 247. Particularly noteworthy in FY13 was the awarding of the Edward Teller Medal to R. D. Petrasso at the 2013 Inertial Fusion and Science and Applications Conference in September 2013. Much of the work for which Prof. Petrasso and his MIT group were recognized was carried out under the auspices of the NLUF program at the Omega facility.

### 2. FY13 LBS Programs

Sixteen LBS projects were allotted Omega facility shot time and conducted a total of 269 target shot on the facility in FY13

(see Table 136.IX, p. 265). This work is summarized beginning on p. 263 of this report.

In FY13, LLE issued a solicitation for LBS proposals to be conducted in FY14. A total of 38 proposals were submitted. An independent review committee reviewed the proposals and recommended that 17 proposals receive 28 shot days at the Omega facility in FY14. Table 136.VIII (p. 264) lists the successful FY14 proposals.

### 3. FY13 LLNL Omega Facility Programs

In FY13, LLNL teams led over 600 target shots on the Omega Facility: 166 for the ICF campaigns, 303 for the HED campaigns, and more than half of the LBS target shots.

The ICF campaign experiments included the following:

- A new platform for absolute equation-of-state (EOS) measurements
- VISAR (velocity interferometer system for any reflector) measurements of the EOS of boron carbide
- Shock-release isentropes measurements of ICF-relevant materials
- Thomson-scattering measurements from Au spheres
- Measuring the adiabatic index of polystyrene using counter-propagating shocks and x-ray Thomson scattering
- Angularly resolved x-ray Thomson-scattering measurements of shock-compressed aluminum
- Enhanced bremsstrahlung backlighters
- Hohlräum-drive spectroscopy
- Ablator opacity measurements
- Hohlräum wall-plasma emissivity measurements
- D–D and D–<sup>3</sup>He yield anomalies versus D:<sup>3</sup>He fuel ratio in indirect-drive exploding pushers
- Platform development for measuring charged-particle stopping in warm dense plasmas

High-energy-density experiments included the following:

- a. Material dynamics and strength:
  - Tantalum Rayleigh–Taylor experiments
  - Iron Rayleigh–Taylor experiments
  - Long-pulse silver backlighter development
  - Material recovery experiment
  - Diffraction studies on shocked tantalum
  - Classical Rayleigh–Taylor experiments

## b. Materials equation of state:

- Demonstration of single-shot EXAFS measurements on ramp-compressed Ta
- Sn melting and recrystallization
- Ta x-ray diffraction with ramp compression
- Development of a Soller-slit diagnostic for dynamic diffraction studies
- Radiographic EOS measurements of shocked foams
- High-energy x-ray diffraction development
- Lithium-hydride equation of state
- Ta equation of state

## c. Radiation transport and opacity:

- Heated wall radiation transport

## d. Hydrodynamics:

- Radiographic development for NIF hydrodynamic experiments
- Copper foam shock-breakout measurements
- Short-pulse, UV backlighting development for the NIF
- X-ray area backlighter development

## e. Burn physics:

- High-resolution measurements of velocity nonuniformities in boron carbide—an alternative ignition capsule ablator material
- Ablator physics tests of beryllium capsules

## f. X-ray source development:

- Solar cell electrostatic discharge
- X-ray source development with nanostructured materials

## 4. FY13 LANL Experimental Campaigns

In FY13, LANL executed 207 total target shots on the OMEGA laser. LANL experiments contributed to the ICF and HED campaigns.

The ICF campaigns included the following:

- Measurements of the x-ray ablative Richtmyer–Meshkov growth of isolated defects on beryllium ablaters
- Studies of the branching ratios and species separation (plasma kinetic effects) in DT fusion plasmas
- Development of neutron imaging and gamma-ray scintillator for the NIF
- Studies of the suppression of hohlraum laser–plasma interaction (LPI) with magnetic fields

The HED campaigns included the following:

- Studies of shear in a counter-propagating flow geometry driving turbulent mixing
- Backlit defect implosion experiments to study polar-drive symmetry control
- Measurement of spatial distribution of mix in gas-filled capsules
- Imaging x-ray Thomson-scattering platform development for dense plasmas and the EOS of warm dense matter
- Measurement of a supersonic radiation wave and foam aerogel EOS

## 5. FY13 CEA Experiments at the Omega Laser Facility

In FY13 CEA teams conducted 53 target shots on the OMEGA laser. The CEA experiments included the following:

- CEA vulnerability diagnostic development on OMEGA
- Neutron spectrometer [DEMIN (detector Micromegas for neutrons)] development on OMEGA
- Convergent ablation measurements using a gas-filled rugby hohlraum on OMEGA
- Laser-imprint mitigation using underdense foams

**OMEGA Laser Facility Users Group (OLUG)**

The fifth Omega Users Group (OLUG) Workshop was conducted at LLE in April 2013. More than 100 researchers from 25 universities met at the 2.5-day workshop to facilitate communications and exchanges among individual Omega users and between users and the LLE management; to present ongoing and proposed research; to encourage research opportunities and collaborations that could be undertaken at the Omega facility and other high-energy-density-physics facilities; to provide an opportunity for students, postdoctoral fellows, and young researchers to present their research in an informal setting; and to provide feedback to the LLE management from the users about ways to improve the facility and future experimental campaigns.

OLUG comprises 310 members from 35 universities and many centers and national laboratories. The interactions were wide ranging and lively as illustrated in the workshop report (p. 237). The first two mornings of the workshop included seven science and facility presentations. Since the facility is constantly evolving and improving, the facility talks proved particularly useful even to experienced users. The overview talks given by leading world authorities described the breadth

and excitement of HED science either being undertaken at the Omega facility or well within the capabilities of the facility with improvements or upgrades.

Fifty students and postdoctoral fellows participated in the workshop and 36 were supported by travel grants from NNSA. In total there were 68 contributed poster papers including eight presented by Omega facility operations staff.

An important function of the workshop was to develop a set of findings and recommendations to help set and define future priorities for development of the Omega Laser Facility. LLE uses these recommendations as a guide for making decisions about facility operations, priorities, and future directions. In addition, the status of these OLUG Findings and Recommendations were updated and reviewed at a satellite meeting during the 2013 APS-DPP Conference.

## Education

As the only major university participant in the National ICF Program, education continues as an important mission for LLE. The Laboratory's education programs cover the range from high school (p. 243) to graduate education.

### 1. High School Program

During the summer of 2013, 15 students from Rochester-area high schools participated in the LLE Summer High School Research Program. The goal of this program is to excite a group of high school students about careers in the areas of science and technology by exposing them to research in a state-of-the-art environment. Too often students are exposed to research only through classroom laboratories, which have prescribed procedures and predictable results. In LLE's summer program, the students experience many of the trials, tribulations, and rewards of scientific research. By participating in research in this "real" environment, students often become more excited about careers in science and technology.

The students spent most of their time working on their individual research projects with members of the LLE's technical staff. The projects were related to current research activities at the Laboratory and covered a broad range of interests including laser physics, computational modeling of implosion physics, experimental diagnostics development, spectroscopy, cryogenic deuterium properties, liquid crystal devices, tritium detection and capture, ballistic deflection transistors, positioning systems, and 3-D visual modeling (see Table 136.IV, p. 244).

Since its inception in 1989, 312 high school students have now participated in the program. This past year's students were selected from nearly 80 applicants. At the culminating "High School Student Summer Research Symposium" on 28 August 2013, the students presented the results of their research to an audience including parents, teachers, and LLE staff. At the symposium LLE presented its 17th annual William D. Ryan Inspirational Teacher Award. This year's recipient of the award was Mrs. Eugenie Foster, a mathematics teacher from Brighton High School. Teachers are nominated by alumni of the summer program. Mrs. Foster was nominated by Mitch Perry, Julia Tucker, and Jack Valinsky, participants in the 2010 program. They credited Mrs. Foster with developing a discrete math course to showcase mathematical topics outside of the core curriculum for students who "have that extra thirst which only mathematics can quench." They also credit Mrs. Foster with developing an Intro to College Math course "to reach out to students who do not perceive themselves pursuing math-related fields in college or those to whom math does not come easily."

### 2. Undergraduate Student Program

Forty undergraduate students participated in work or research projects at LLE this past year. Student projects include operational maintenance of the Omega Laser Facility; work in laser development, materials, and optical thin-film coating laboratories; computer programming; image processing; and diagnostics development. This is a unique opportunity for students, many of whom will go on to pursue a higher degree in the area in which they gained experience at the Laboratory.

### 3. Graduate Student Programs

Graduate students are using the Omega Laser Facility as well as other LLE facilities for fusion and HED physics research and technology development activities. These students are making significant contributions to LLE's research program. Twenty-six faculty members from five University academic departments collaborate with LLE scientists and engineers. Presently, 60 graduate students are involved in research projects at LLE, and LLE directly sponsors 37 students pursuing Ph.D. degrees via the NNSA-supported Frank Horton Fellowship Program in Laser Energetics. Their research includes theoretical and experimental plasma physics, HED physics, x-ray and atomic physics, nuclear fusion, ultrafast optoelectronics, high-power-laser development and applications, nonlinear optics, optical materials and optical fabrication technology, and target fabrication. In addition, LLE directly funds research programs within the MIT Plasma Science and

Fusion Center, the State University of New York (SUNY) at Geneseo, and the University of Wisconsin. These programs involve a total of approximately 6 graduate students, 25 to 30 undergraduate students, and 10 faculty members.

Over 310 graduate students have now conducted their graduate research work at LLE since its graduate research program began. In addition, 120 graduate students and post-graduate

fellows from other universities have conducted research at the LLE laser facilities as part of the NLUF program. Over 60 graduate students and undergraduate students were involved in research on the Omega Laser Facility as members of participating NLUF teams in FY13. Table 136.X (p. 308) lists the authors, dissertation titles, and originating university of the Ph.D. theses from LLE and NLUF research in FY13.

**Robert L. McCrory**

Director, Laboratory for Laser Energetics  
Vice President, University of Rochester

---

# A Polar-Drive Shock-Ignition Design for the National Ignition Facility

## Introduction

In direct-drive inertial confinement fusion (ICF),<sup>1</sup> a small spherical capsule filled with a deuterium–tritium (DT) mix is imploded by irradiating the capsule symmetrically with high-intensity lasers to achieve a high-density, high-temperature state where fusion reactions may readily occur. The capsule shell is accelerated by the ablation pressure of the laser-heated plasma at the outer edge of the shell to high velocity ( $v_{\text{imp}} > 3.5 \times 10^7$  cm/s, where  $v_{\text{imp}}$  is the implosion velocity), compressing the capsule to a high density. As the capsule implodes, the back pressure from the compressed plasma in the center of the capsule slows the implosion until the shell stagnates. At stagnation, the fill gas has been compressed and heated via shocks and adiabatic compression, forming a low-density central hot spot surrounded by a dense shell tamper consisting of DT fuel. If sufficient hot-spot temperature ( $\geq 10$  keV) and shell areal density ( $\rho R \equiv \int_0^\infty \rho dr \geq 0.3$  g/cm<sup>2</sup>) are achieved, energetic alpha particles created by the hot-spot fusion reactions are stopped in the cold dense shell, heating it quickly, and initiating ignition, which causes the fusion reaction rate to rise dramatically, burning a substantial portion of the DT fuel.

Shock ignition (SI)<sup>2</sup> is a relatively new concept in which the compression phase and ignition phase are separated.<sup>3</sup> Practically, this separation is achieved by dividing the laser pulse into two parts: a main-drive or compression pulse, and a spike or ignition pulse timed at the end of the main pulse. The main-drive pulse is typically of lower power than in hot-spot direct drive since the main pulse serves solely to compress the shell to the required areal density for ignition and not to heat the hot spot. This lower drive power corresponds to a lower implosion velocity, typically less than  $3.0 \times 10^7$  cm/s. At the end of the main pulse, an intense spike pulse launches a strong shock through the imploding shell material to heat the hot spot quickly to ignition temperatures.

By separating the compression from the hot-spot heating, SI somewhat resembles the fast-ignition concept.<sup>4</sup> However, SI requires a spherically symmetric laser illumination of much more moderate laser intensity (typically several times

$10^{15}$  W/cm<sup>2</sup>) than is required for fast ignition ( $> 10^{19}$  W/cm<sup>2</sup>), such that the SI heating pulse can be generated with the same laser system as the main-drive pulse. In contrast, fast ignition requires chirped-pulse amplification to generate pulses of high intensity. Furthermore, SI heating is accomplished via shock heating, which is well understood and easily modeled, as opposed to fast ignition, which delivers energy via the generation and transport of relativistic fast electrons, which is difficult to model theoretically or computationally.

Achieving ignition through SI is not without its uncertainties. For SI to be viable, laser-generated strong shocks of the order of 300 Mbar must be demonstrated experimentally in a spherical geometry. Furthermore, at these intensities, laser–plasma interactions (LPI’s) become significant and can greatly influence the coupling of laser energy to the imploding capsule, affecting the strong-shock formation and potentially preheating the cold fuel prior to full capsule compression. An experimental understanding of LPI in this intensity regime, therefore, is very important in predicting the success of SI implosions.

It should be noted that a concept similar to SI was proposed a few decades ago by Shcherbakov.<sup>5</sup> The concept proposed at that time, however, called for much lower initial compression velocities  $v_{\text{imp}} \simeq 2.0 \times 10^6$  cm/s (the final velocity after the shock pulse is quoted as  $v_{\text{imp}} \simeq 1.5 \times 10^7$  cm/s). The laser drive needed to compress and shock the capsule in that design was not specified, and only the absorbed laser energy  $E \simeq 30$  kJ was cited. An article by the same author two decades later<sup>6</sup> indicates laser-drive parameters of  $P \simeq 10$  TW,  $I \simeq 10^{13}$  W/cm<sup>2</sup>, and  $\Delta t_{\text{pulse}} \simeq$  tens of nanoseconds, with shock laser parameters of  $P \simeq 10$  PW,  $I \simeq 10^{16}$  W/cm<sup>2</sup>, and  $\Delta t_{\text{pulse}} \simeq$  a few hundreds of picoseconds. This work, therefore, seems to indicate very different regimes of both laser operation and capsule design relative to the conceptual paper of Betti *et al.*<sup>2</sup> even though the concept is essentially the same.

Research in SI<sup>7–30</sup> has garnered much interest both experimentally and theoretically in the international fusion community over the past several years. Theoretical models,<sup>7–10</sup> scaling

laws,<sup>7,11–16</sup> and computational target designs in one dimension (1-D)<sup>11,13,14,17,18</sup> and multiple dimensions<sup>13–15,18–20</sup> have investigated the feasibility of SI on a variety of target platforms. These studies have validated the claims of Betti *et al.*<sup>2</sup> that the addition of a strong shock reduces the energy required for ignition, allowing for higher gain at a given input laser energy. Strong-shock propagation experiments in planar<sup>21</sup> and spherical geometry<sup>22</sup> have validated computation modeling of shocks driven at intensities up to  $1.5 \times 10^{15}$  W/cm<sup>2</sup>. Full-implosion experiments<sup>23</sup> have been performed on OMEGA<sup>24</sup> showing increased neutron yield, areal density, and yield-over-clean (defined as the ratio of the experimental yield to 1-D simulated predictions) relative to similar no-spike experiments. Particle-in-cell LPI simulations of OMEGA experiments<sup>25</sup> and full-scale ignition designs<sup>26</sup> have reported hot-electron generation in the temperature regime up to 40 keV at SI-relevant laser intensities with total reflectivities (Raman and Brillouin scattering) from 10% to 35% of the incident laser energy. Spherical LPI experiments<sup>27,28</sup> performed on OMEGA at SI-relevant intensities and plasma conditions have resulted in similar findings. Planar LPI experiments<sup>29</sup> have also been performed in France. The hot-electron temperatures reported in these simulations and experiments appear favorable for SI in light of computational investigations of hot-electron coupling during spike propagation,<sup>30</sup> which report enhanced strong-shock pressures and higher ignition margin as a result of hot-electron energy coupling at electron temperatures up to 100 keV. All of these studies indicate that the SI method is a viable path to achieve ignition and gain in ICF.

Most of the theoretical research published to date has been limited to either conceptual designs or designs for proposed laser facilities or facilities still under construction. This article proposes a design for experiments on the currently operational National Ignition Facility (NIF).<sup>31</sup> These proposed experiments conform to the NIF system specifications and could be fielded in the polar-drive configuration on the NIF within the next several years, requiring only minor system modifications. Such modifications include the design and manufacture of specifically tailored phase plates;<sup>32,33</sup> implementation of multifrequency-modulation smoothing by spectral dispersion (multi-FM SSD)<sup>34,35</sup> in NIF beamlines; design and introduction of polarization plates for polarization smoothing; and the development of a polar-drive target insertion cryostat.

This article is organized as follows: A theoretical model for calculating target robustness is outlined; a 1-D target design for the NIF is developed and implosion robustness to 1-D physics and system uncertainties is detailed; and a polar-drive

beam configuration for the NIF is outlined and robustness to two-dimensional (2-D) drive and capsule nonuniformities is explored. The capsule is found to robustly ignite under all anticipated sources of 1-D uncertainty and 2-D perturbations.

### Characterizing Robustness

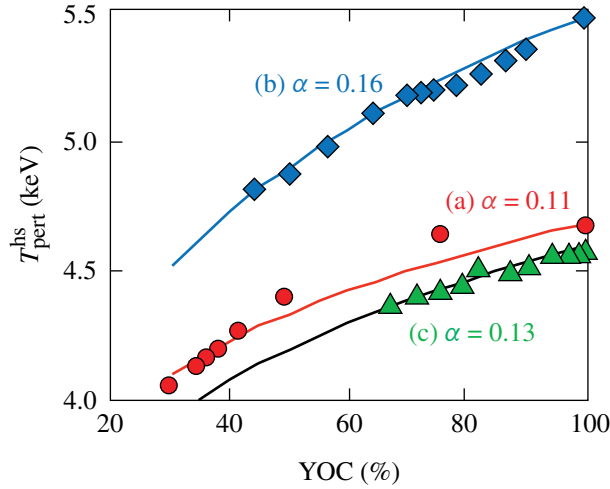
In ICF target design, it is important to characterize design performance. Often in the ICF community, 1-D target gain has been used as a metric to preferentially guide target design. One-dimensional gain in an igniting target, however, is largely a function of the assembled fuel areal density (see Ref. 1, p. 40) and, as a metric for target design, does not provide a reference for how close the target implosion is to the ignition threshold. It is therefore important to define a metric for the margin of error, in a 1-D sense, to quantify the robustness of the proposed shock-ignition design for the NIF. In this article, target designs will be characterized using the ignition threshold factor (ITF).<sup>36–38</sup> By the definition of ITF as described in Spears *et al.*,<sup>38</sup> an ITF of 1 corresponds to an ~50% chance of ignition with the DT target in simulations.

In this article, the ITF is calculated in 1-D simulations using the methodology of Chang *et al.*<sup>37</sup> Essentially, the fusion reactivity rate  $\langle\sigma\nu\rangle$  of the DT fuel is artificially reduced by a variable parameter in the simulation

$$\langle\sigma\nu\rangle_{\text{mod}} = \xi\langle\sigma\nu\rangle \quad (1)$$

until the target yield degrades to a gain of 1, where the fusion output energy equals the input laser energy. Here  $\langle\sigma\nu\rangle_{\text{mod}}$  is the modified fusion reactivity rate, and  $\xi$  is the fractional input parameter. This is analogous to multiplying the neutron yield obtained in the absence of alpha-particle heating by the same factor. One may characterize this input parameter  $\xi$  as a clean-volume fraction, defined as the fraction of the 1-D hot-spot volume  $\xi = V_{3\text{-D}}^{\text{hs}}/V_{1\text{-D}}^{\text{hs}}$ , where  $V_{3\text{-D}}^{\text{hs}}$  is the clean hot-spot volume in three dimensions (3-D) varied as an input parameter and  $V_{1\text{-D}}^{\text{hs}}$  is the 1-D hot-spot volume.

In simple models of clean volume fraction, the yield-over-clean (YOC), which is defined as the 3-D yield divided by the 1-D yield ( $\text{YOC} \equiv Y_{3\text{-D}}/Y_{1\text{-D}}$ ), is typically equated to the clean-volume fraction. These models, however, ignore the effect of shell perturbations on the hot-spot temperature. Two-dimensional DRACO<sup>39</sup> simulations of three igniting targets, described in Fig. 3 of Ref. 37 with varying levels of input nonuniformity, are used to evaluate the functional dependence of the hot-spot ion temperature on the YOC. In Fig. 133.1, the neutron-averaged ion temperature is plotted for these three



TC10412JR

Figure 133.1

Relation of the hot-spot temperature ( $T_{\text{pert}}^{\text{hs}}$ ) to the yield-over-clean (YOC), as calculated by 2-D DRACO simulations for the three targets discussed in Fig. 3 of Ref. 37. Power-law fits to each of these are shown as solid lines with power-law exponents varying from 0.11 to 0.16.

targets [labeled (a), (b), and (c), as in Ref. 37] versus the no-burn YOC. The perturbed, hot-spot ion temperature for each of these designs is shown to scale roughly as a weak power-law function of the YOC:

$$T_{\text{pert}}^{\text{hs}}(\text{YOC}) = T_{1\text{-D}}^{\text{hs}} \cdot \text{YOC}^{\alpha}, \quad (2)$$

as shown by the continuous lines of Fig. 133.1. The power-law exponent  $\alpha$  was found to vary from 0.11 to 0.16 in the different designs. Here, we will assume an average value of 0.13 for  $\alpha$ .

We employ a simple model of the hot spot, which assumes a single temperature over the hot-spot volume

$$\text{YOC} = \frac{Y_{3\text{-D}}}{Y_{1\text{-D}}} = \xi \left( \frac{T_{3\text{-D}}^{\text{hs}}}{T_{1\text{-D}}^{\text{hs}}} \right)^{\beta}, \quad (3)$$

where  $T_{3\text{-D}}^{\text{hs}}$  is the perturbed hot-spot ion temperature and  $T_{1\text{-D}}^{\text{hs}}$  is the 1-D hot-spot ion temperature. The fusion reactivity in the hot spot is assumed to scale as a power law<sup>40</sup> in the temperature over the temperatures of interest, with  $\beta = 2$ .

Using the formula for the  $\chi$  parameter from Eq. (12) of Ref. 37,

$$\chi = \left[ \rho R (\text{g/cm}^2) \right]^{0.8} (T/4.7 \text{ keV})^{1.7} (\text{YOC})^{0.5}, \quad (4)$$

the scalings for areal density  $\rho R$  and hot-spot ion temperature from Eqs. (19) and (52), respectively, of Ref. 41,

$$\rho R_{\text{shell}} \sim E_{\text{kin}}^{0.33} \quad (5)$$

and

$$T_{\text{hs}} \sim E_{\text{kin}}^{0.07}, \quad (6)$$

and defining the ITF as the ratio of the kinetic energy  $E_{\text{kin}}$  of the imploding shell to the minimum energy required to ignite the same shell, one obtains a scaling relation between  $\chi$  and the ITF,

$$\text{ITF} \sim \chi^{2.6}. \quad (7)$$

Substituting Eqs. (2)–(4) into Eq. (7) yields

$$\text{ITF} \sim \xi^{1.5}. \quad (8)$$

When a series of 1-D simulations with alpha-energy transport are performed, varying the clean-volume fraction  $\xi$ , one finds a critical value of  $\xi$ , below which ignition is quenched. We will term this the minimum clean-volume fraction required for ignition  $\xi_{\text{min}}^{\text{ign}}$ , which corresponds to an ITF of 1. Using  $\xi_{\text{min}}^{\text{ign}}$ , one can rewrite Eq. (8) for the 1-D ITF as

$$\text{ITF}_{1\text{-D}} \simeq \left( \xi_{\text{min}}^{\text{ign}} \right)^{-1.5}. \quad (9)$$

In this article, we will use Eq. (9) to determine the 1-D robustness of our target design.

### One-Dimensional Target Design and Robustness Studies

This section outlines the NIF SI target design in 1-D and details the robustness of the target to various sources of physics and system uncertainties. In designing a shock-ignition target for the NIF, the most-constraining system limitation is the total system's peak laser power. The early SI design at 290 kJ proposed by Betti *et al.*<sup>2</sup> used a laser spike with a peak laser power of 540 TW. Scaling this target to NIF's total energy of  $\sim 1.5$  MJ, the required laser power reaches  $\sim 1600$  TW, prohibitively high for the NIF, which recently achieved<sup>42</sup> a peak power of 520 TW. Indeed, Betti's design at 290 kJ already exceeds the demonstrated NIF peak power. Therefore, some modifications to the conceptual design must be made for experiments on the NIF. The first is to scale only to sub-MJ laser energy to allow for more headroom in power space. The second is to raise the capsule's implosion velocity by making the shell thinner. This recovers the stagnation pressure and temperature that is lost

when simply reducing the laser power to conform to the NIF’s power ceiling. Additional robustness is achieved by allowing that the laser pulse may be split, such that half of the NIF beams drive the target compression and are focused at the original target radius, while the other half drive the spike shock using more tightly focused beams to improve energy coupling to the target late in time. All 1-D simulations in this article were performed using the radiation–hydrodynamics code *LILAC*<sup>43</sup> with the *SESAME*<sup>44</sup> equation of state and a flux-limited Spitzer heat conductivity<sup>45</sup> with a flux-limiter value of 0.06.

The target design chosen is shown in Fig. 133.2. The capsule has a 1080- $\mu\text{m}$  radius with a 161- $\mu\text{m}$  solid-DT fuel layer surrounded by a 31- $\mu\text{m}$  outer plastic ablator layer. The ablator thickness is chosen such that the ablator material is fully ablated by the end of the laser pulse to mitigate deceleration-phase mixing of the plastic with the DT fuel. The total energy delivered by the laser is 689 kJ, divided into two pulses, as shown in Fig. 133.3. The main pulse shown by the solid line contains a total of 544 kJ and has a laser profile characterized as a super-Gaussian intensity profile  $I(r) = \exp\left[-(r/r_0)^\sigma\right]$  with a  $1/e$  radius  $r_0 = 677 \mu\text{m}$  and super-Gaussian exponent  $\sigma = 2.5$ . The spike pulse (dashed line) contains a total of 145 kJ with a peak power of 215 TW, also in a super-Gaussian spot of  $r_0 = 258 \mu\text{m}$  and  $\sigma = 2.5$ .

As seen in Fig. 133.3, the laser pulse design has two “picket” pulses at the beginning, followed by a low-intensity foot with a slow rise to the main compression drive, and ultimately concluding with a spike pulse at the end of the main compression.

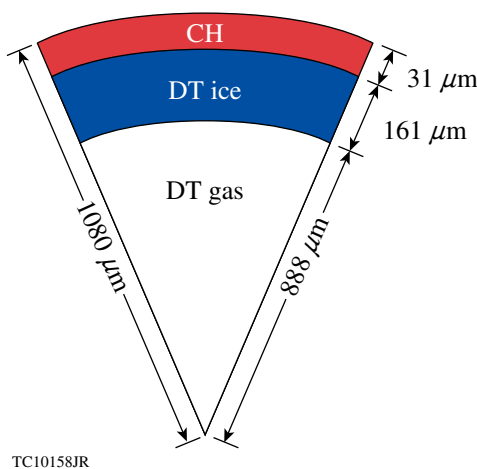


Figure 133.2  
Capsule dimensions for the NIF shock-ignition (SI) design.

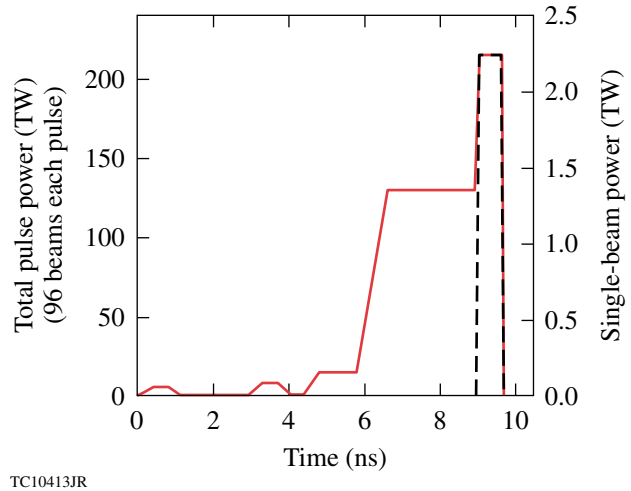


Figure 133.3  
Laser pulse history for the main drive beams (solid red) and spike beams (dashed black) comprising the 1-D SI laser pulse design.

The picket pulses serve two purposes: The first is to raise the ablation velocity<sup>46–49</sup>  $v_{\text{abl}} = \dot{m}/\rho_{\text{abl}}$  (where  $v_{\text{abl}}$  is the ablation velocity,  $\dot{m}$  is the mass ablation rate, and  $\rho_{\text{abl}}$  is the density at the ablation front) to reduce the growth of the Rayleigh–Taylor (RT) instability,<sup>50,51</sup> which is a major obstacle to ICF. This ablative stabilization of the RT instability has been demonstrated theoretically<sup>52–54</sup> and experimentally.<sup>55</sup> The second purpose of the picket pulses is to facilitate simplified shock tuning and adiabat control.<sup>56</sup>

The ramp times of the pickets and foot of the main drive are chosen as 400-ps linear ramps to account for a 350-ps spatiotemporal skew in the NIF beamlines that is introduced by the diffraction grating required for 1-D multi-FM SSD.<sup>57</sup> Shorter, more-intense pickets would more efficiently reduce laser imprint<sup>58–65</sup> and provide increased adiabat shaping<sup>48</sup> for multidimensional stability, but such pickets are not currently possible on the NIF. The flattop of each picket pulse is also 400 ps, chosen to facilitate better SSD smoothing.<sup>57,66</sup> This allows for a longer time when the laser pickets are at their highest power and while the beams fill the full aperture of the phase plates. The ramp time from the main drive to the spike pulse is, by design, 100 ps; however, 1-D simulations indicate that increasing the rise time to 400 ps (fixing the center of the rise in time) still gives full 1-D gain with the same  $\text{ITF}_{1\text{-D}}$ ; i.e., no margin is lost.

The compression pulse launches four distinct shocks: one by each picket, one by the foot, and one by the ramp to main compression drive. As in previous designs with multiple

shocks,<sup>48,49,56</sup> the shocks are tuned such that the shocks merge approximately at the rear surface of the solid DT fuel layer. The first picket pulse has a peak 96-beam (single-beam powers in parentheses) power of 6 TW (0.063 TW) and is followed by a second picket, which starts at 2.9 ns and has a peak power of 8 TW (0.083 TW). The foot of the main compression pulse is 15 TW (0.16 TW) beginning at 4.4 ns. Following the foot, the laser pulse rises beginning at  $t = 5.8$  ns over 800 ps to a main compression power of 130 TW (1.35 TW). Finally, at  $t = 8.95$  ns, the spike pulse begins, rising over 100 ps to 215 TW (2.24 TW). At the same time, the shock beams are turned on using the pulse history shown by the dashed curve, which also peaks at 215 TW (2.24 TW), giving a total system 192-beam peak power of 430 TW—17% below the recently demonstrated achieved peak power<sup>42</sup> of 520 TW on the NIF. Since both the peak power and individual pulse energies of this design are significantly below the demonstrated capabilities of the NIF, this design offers substantial system headroom for capsule tuning to match experimental and simulated absorption, shell velocity, and spike shock pressure, as well as 2-D polar-drive symmetry.

The result is a mass-averaged in-flight fuel adiabat at the end of the compression drive of  $\langle\alpha\rangle_{\text{fuel}} = 1.8$  with a minimum adiabat at the inner edge of the dense shell of  $\alpha_{\text{in}} = 1.2$ . The adiabat here is characterized using the “DT-standard” adiabat,<sup>40</sup> which is given by  $\alpha_{\text{DT-standard}} = P/(2.18 \rho^{5/3})$ , where  $P$  is in Mbar and  $\rho$  in  $\text{g/cm}^3$ . The implosion velocity is  $v_{\text{imp}} = 3.05 \times 10^7$  cm/s, which is substantially faster than Betti’s target of Ref. 2. The target achieves a 1-D gain of 58 with a peak areal density  $\rho R = 1.6$  g/cm<sup>2</sup>. The in-flight aspect ratio (defined as  $\text{IFAR} \equiv R/\Delta R$ , where  $R$  is the shell radius and  $\Delta R$  is the shell thickness), calculated when the shell radius is two-thirds of the initial target radius, is 22. Target robustness is excellent with an  $\text{ITF}_{1\text{-D}} = 4.1$ . These 1-D performance parameters are summarized in Table 133.I.

The effect of the spike shock on target robustness was studied in 1-D by varying the spike laser intensity to alter the applied

Table 133.I: One-dimensional performance characteristics of the NIF shock-ignition design.

Gain	58
$\rho R$ (g/cm <sup>2</sup> )	1.6
$v_{\text{imp}}$ ( $\mu\text{m/ns}$ )	305
$\text{IFAR}_{2/3}$	22
Average adiabat	1.8
$\text{ITF}_{1\text{-D}}$	4.1

pressure of the spike shock. Figure 133.4 plots the calculated  $\text{ITF}_{1\text{-D}}$  as a function of the initial shock pressure near the ablation surface. The nominal shock pressure of the original design is 300 Mbar. The lowest pressure in Fig. 133.4 corresponds to the case where the spike shock is removed entirely. In this case, the pressure reported (160 Mbar) is the ablation pressure. Figure 133.4 shows that this target is predicted to ignite in 1-D even without the spike shock, but with a much lower  $\text{ITF}_{1\text{-D}}$  of 1.3. It also shows clearly that additional ignition margin is predicted when the spike pulse is present.

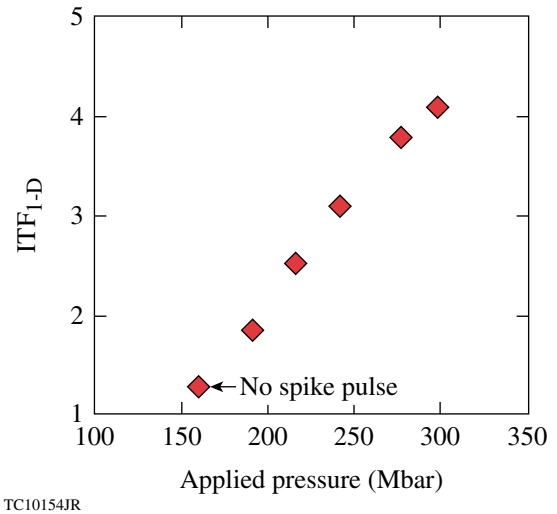
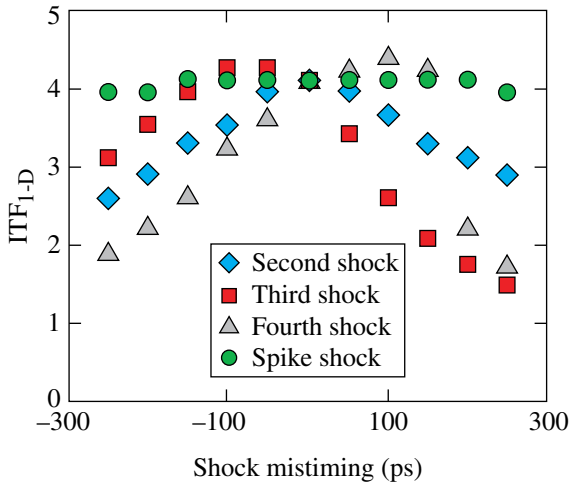


Figure 133.4  
Plot of the  $\text{ITF}_{1\text{-D}}$  versus the applied pressure in the spike shock. The lowest pressure point corresponds to the ablation pressure with no spike pulse. ITF: ignition threshold factor.

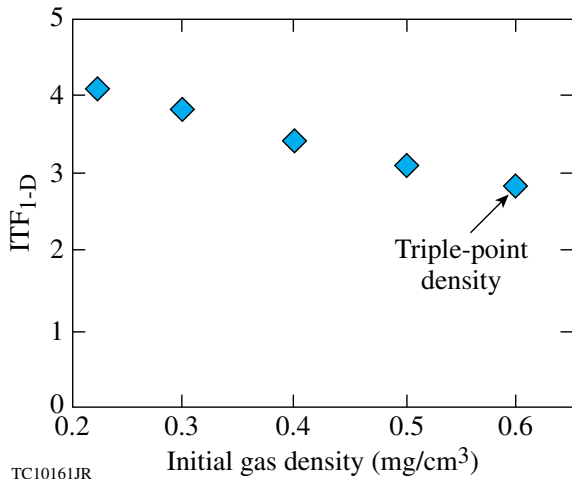
A series of 1-D simulations examined the robustness of the design to systematic mistiming of shocks. Figure 133.5 shows the calculated  $\text{ITF}_{1\text{-D}}$  as a function of shock mistiming for the second shock (launched by the second picket), the third shock (launched by the foot of the main pulse), the fourth shock (launched by the ramp to the main compression drive), and the spike-pulse shock. As can be seen from the plots, the design ignites for all mistimings studied and has large timing windows within which a high margin is maintained. For reference, systematic shock mistiming on the NIF is estimated<sup>67</sup> to be 10 ps.

It is anticipated that such a target would be shot on the NIF at a temperature of 17.8 K, two degrees below the triple point of the DT fuel mixture with an initial gas density of 0.225 mg/cm<sup>3</sup>. Figure 133.6 illustrates how changing the initial gas density affects the  $\text{ITF}_{1\text{-D}}$  in simulations. These data demonstrate the advantage of shooting at a lower temperature and gas density since the  $\text{ITF}_{1\text{-D}}$  drops noticeably as the temperature



TC10414JR

Figure 133.5  
Plot of the  $ITF_{1-D}$  versus shock mistiming for the 1-D capsule design.



TC10161JR

Figure 133.6  
 $ITF_{1-D}$  plotted versus the initial gas density in the target.

and gas density increase. It should be noted that the target is still predicted to ignite in 1-D at a gas density near the triple point ( $T = 19.8$  K,  $\rho_{\text{gas}} = 0.62$  mg/cm<sup>3</sup>) with an  $ITF_{1-D}$  of 2.8.

Since laser-plasma interactions can have a significant impact on ICF implosions, it is important to quantify the laser intensity, plasma temperature, and density scale lengths in the hot corona. Temporally and spatially averaged conditions at the quarter-critical surface are reported in Table 133.II during both the main compression pulse and the spike pulse. The laser intensities reported in this table are “nominal” in the sense that

Table 133.II: Average laser intensity  $\langle I_{14} \rangle$  at the quarter-critical radius (units of  $10^{14}$  W/cm<sup>2</sup>); average density gradient scale length  $\langle L_n \rangle$  ( $\mu\text{m}$ ); electron temperature  $T_e$  (keV); and the two-plasmon-decay hot-electron threshold  $F_{\text{TPD}}$ , calculated by Eq. (10). Values are reported during both the main-drive and spike pulses.

	Main drive	Spike
$\langle I_{14} \rangle$	8	34
$\langle L_n \rangle$ ( $\mu\text{m}$ )	350	450
$T_e$ (keV)	3.5	8.5
$F_{\text{TPD}}$	3.5	7.8

they are averaged over the quarter-critical surface. Since the laser spots of the spike beams are much smaller ( $1/e$  radius of  $258 \mu\text{m}$ ) compared to the average quarter-critical radius ( $\sim 1000 \mu\text{m}$ ), there will be hot spots of higher laser intensity in some locations.

From these plasma conditions, one can evaluate a two-plasmon-decay (TPD) threshold parameter  $F_{\text{TPD}}$  during both pulses using the formula<sup>68</sup>

$$F_{\text{TPD}} = \frac{I_{14} L_n}{230 T_e}, \quad (10)$$

where  $I_{14}$  is the laser intensity in units of  $10^{14}$  W/cm<sup>2</sup>,  $L_n$  is the density gradient scale length in microns, and  $T_e$  is the electron temperature in keV. For values of  $F_{\text{TPD}}$  greater than 1, hot-electron heating from TPD has been reported in OMEGA experiments.<sup>69,70</sup> The threshold parameter is predicted to be above 1 during both the main-drive and spike pulses, indicating a likelihood of hot-electron generation and preheating during both the compression and shock phases of the implosion. TPD thresholds for NIF targets have not yet been characterized, but thresholds for OMEGA targets have been shown to be dependent on beam geometry.<sup>71</sup> Hot-electron generation during the main-drive pulse caused by TPD may be an issue for this target. If so, one mitigation strategy that has been proposed is the use of higher-Z ablaters, e.g., silicon or glass.<sup>70,72</sup>

Given the high intensity of the spike pulse, and in light of recent shock-ignition-relevant experiments on OMEGA, it is predicted that during the spike pulse, stimulated Raman scattering (SRS), rather than TPD, will likely be the dominant factor in hot-electron generation.<sup>28,73,74</sup> The SRS hot-electron temperature in those experiments was shown to be  $\sim 40$  keV with a conversion efficiency of up to  $\sim 16\%$  of the incident spike laser energy.

With this in mind, 1-D simulations of hot-electron energy coupling were performed in *LILAC* using a multigroup diffusion model of suprathermal electron energy transport. Various electron temperatures and coupling efficiencies were studied. The results, plotted in Fig. 133.7, show that this SI design is robust to energy coupling from hot electrons with Maxwellian temperatures of up to 150 keV and coupling efficiencies of up to 30%, similar to the results of Ref. 30. Furthermore, an analysis of *LILAC* simulations at hot-electron temperatures above 100 keV suggests a competition between increased shock coupling as a result of the lower-energy hot electrons stopping at the ablation front and volumetric heating of the cold fuel caused by higher-energy hot electrons streaming through the target, increasing the shell adiabat and lowering compressibility. These two effects oppose one another: one to improve target performance, the other to degrade performance. A more-rigorous model of suprathermal electrons is required to more-accurately quantify the effects of hot-electron transport at temperatures above 150 keV.

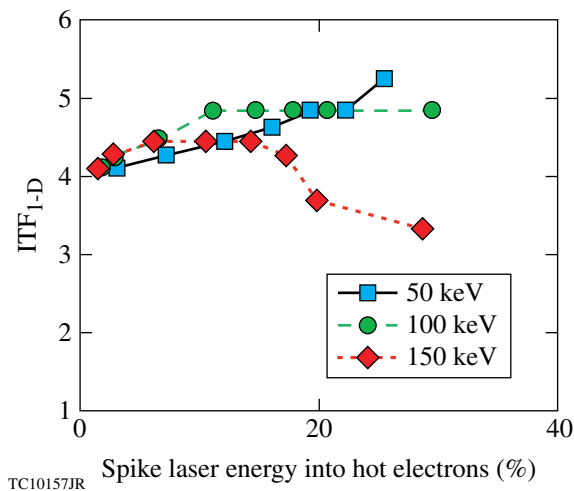


Figure 133.7  
ITF<sub>1-D</sub> plotted with various levels of hot-electron energy coupling during the spike pulse. Energy coupling is varied for different hot-electron temperatures and generation efficiency as a percentage of the spike laser energy.

### Two-Dimensional Polar-Drive Configuration and Nonuniformity Studies

Because of the current indirect-drive laser configuration on the NIF, in which the laser beams are clustered near the poles for entry into a vertically oriented hohlraum, it is necessary to devise a scheme that will directly drive a capsule uniformly to preserve shell integrity and hot-spot confinement. Simply pointing all the NIF beams with equal power toward the center of the capsule will result in higher intensities at the poles than at the equator. As such, the equator of the target would be driven

at a slower velocity than the poles, resulting in an unacceptable target asymmetry. In polar drive (PD), beams from the poles and mid-latitudes of the target chamber are deliberately pointed toward the equator of the target to correct for the lower drive intensity there. Hot-spot polar-drive targets have shown promise in both simulations<sup>75–78</sup> and experiments.<sup>79,80</sup> While other schemes have been devised in which no repointing is deemed necessary<sup>18</sup> or in which an equatorial ring is used to redirect laser energy toward the equator,<sup>80,81</sup> they are not investigated in this article.

As mentioned earlier, substantial margin can be regained for SI designs on the NIF by using two separate laser pulses—one to drive the compression and one to shock the capsule. For SI-specific purposes, two separate PD beam-configuration types have been proposed. NIF beams are bundled into groups of four termed “quads.” The first and simplest PD scheme to implement on the NIF is one where half of the NIF’s 48 quads drive the capsule compression and the other half drive the ignitor shock. The other scheme divides the beams within a single quad, using two beams from each of the 48 NIF quads for the compression and the remaining two beams for the shock. Here, we will use the term “full-quad” for the first scheme and “split-quad” for the second. It should be noted that the split-quad scheme requires modifications to the front end of the NIF Laser System to allow different laser pulses to propagate through separate beamlines within a single quad;<sup>82</sup> therefore, the full-quad scheme is more likely to be used in the near term. However, since much work has been done on PD designs of standard hot-spot capsules for the NIF using 48-quad beam pointings,<sup>75–77</sup> this article focuses mainly on polar-drive SI using 48 split quads as compression beams to capitalize on lessons learned in a similar beam geometry. Initial results from full-quad, polar-drive SI are also presented.

Modeling the laser deposition computationally in either scheme requires a fully 3-D ray trace. All 2-D PD simulations in this article were performed using the arbitrary Lagrangian–Eulerian radiation–hydrodynamics code *DRACO*.<sup>39,76</sup> In designing a PD pointing scheme for a specific target, one may use different laser spot shapes and sizes, as well as vary the pulse power from quad to quad until the desired shell uniformity is achieved. The NIF is currently capable of providing separate laser pulse shapes to each quad, and phase plates can be designed to produce specified laser spot shapes and sizes.

A specific split-quad beam-pointing scheme was developed for the compression beams wherein the 48 half-quads, which can be divided into five separate “rings” of beams with the

same port angle, were repointed toward five separate latitudes on the target surface. The beam repointings are summarized in Table 133.III. In this table, the beam port angle describes the location at which the beams enter the target chamber, relative to pole, and the repointing angle on target represents the polar-angle position of the center of the beam on the target surface. All the beams located at the 23.5° and 30° port angles are repointed to the target surface at 24.5° and 44°, respectively, both toward the target equator, and are referred to as Ring 1 and Ring 2 in Table 133.III. Half of the 44.5° quads (Ring 3) are repointed slightly toward the pole to the 44° target angle, and the other half (Ring 4) to the 82° position. Finally, the 50° quads (Ring 5) are all pointed to 82° on target.

Table 133.III: Split-quad polar-drive (PD) beam-repointing angles for the main-drive beams given by beam port location.

	Beam port angle (°)	Repointing angle on target (°)
Ring 1	23.5	24.5
Ring 2	30.0	44.0
Ring 3	44.5	44.0
Ring 4	44.5	82.0
Ring 5	50.0	82.0

In addition, laser-spot profiles for the drive beams were altered from the 1-D spot shapes to better distribute laser absorption and achieve better capsule uniformity and performance. The first alteration is to use a lower super-Gaussian order, reducing it from  $\sigma = 2.5$  in the 1-D design to  $\sigma = 2.2$ . This removes much of the short-wavelength nonuniformity in the absorption. Next, a secondary elliptical spot is superimposed over the circular spots of Rings 4 and 5. This secondary ellipse has an amplitude of 30% relative to the circular spot, an ellipticity of 2.5 with its major axis oriented in the same plane as the target’s equator, a super-Gaussian order  $\sigma = 2.2$ , and is offset relative to the center of the circular spot by 30% of the initial target radius toward the target’s equator. The addition of this secondary ellipse directs more energy toward the equator. Finally, this spot redesign also uses a spot masking that effectively redistributes back onto target laser energy that would otherwise be lost over the target horizon as a result of the beam repointing. This is done at time  $t = 0$  for all beams; however, the beam profile is modified only slightly in the polar and mid-latitude beams because of their more-moderate repointing angles. The resulting beam profiles are shown in Fig. 133.8.

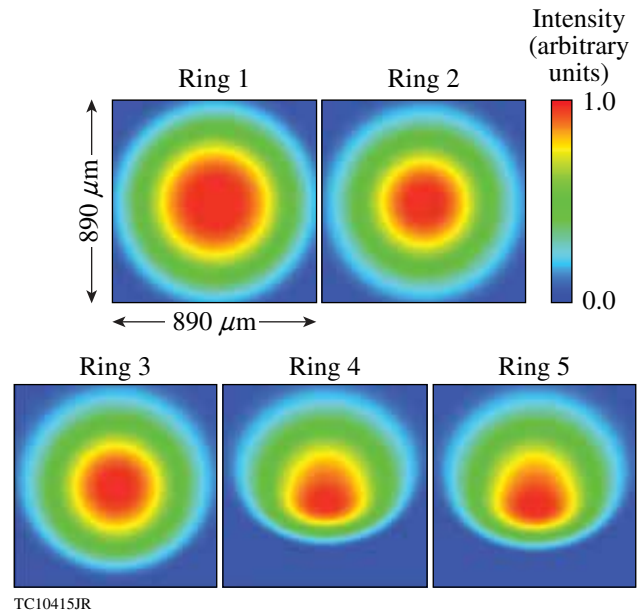


Figure 133.8

Laser-spot profiles for the split-quad polar-drive (PD) design. Laser intensity is plotted in arbitrary units with respect to position. Each box is approximately 890 μm square.

Finally, the beam powers of each ring are optimized to produce a more-uniform implosion. The beam power versus time for each ring is plotted in Fig. 133.9, along with the 1-D design pulse (black dashed line). The beams from Ring 1 are grouped together using a single laser pulse shape and are labeled the “polar.” The Ring-2 and Ring-3 beams share a second pulse shape and are labeled the “mid-latitude” beams. The Ring-4 and Ring-5 beams comprise the final grouping (“equatorial”

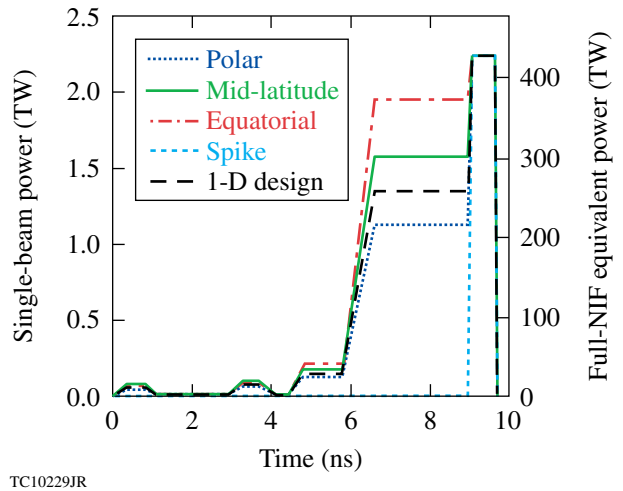


Figure 133.9

Laser pulse shapes for the split-quad PD design for each grouping of beams.

beams), all using a third pulse shape. Initial polar-drive SI simulations indicated that the final capsule symmetry is much more dependent on the compression-beam geometry than the spike-beam geometry. As such, in this design, no repointing of the shock beams in the remaining 48 half-quads was done to minimize refractive losses. The spike-beam profiles, therefore, are circular with the same super-Gaussian order  $\sigma = 2.2$  as the main-drive beams. Since symmetry is largely unaffected by the spike beams, each ignitor beam has a pulse shape exactly as in 1-D for all rings, as is shown in Fig. 133.9.

This 2-D PD design uses a total of 760 kJ of laser energy. Additional input laser energy compared to the 689 kJ of the 1-D design is required to offset the enhanced refractive losses of the repointed beams caused by their higher impact parameters as well as the loss in ablative drive efficiency in those same beams as a result of the ray turning points and the position of peak absorption lying farther away from the ablation front. The maximum laser energy in any single beam is 7.4 kJ. For reference, the NIF is rated at 1.8 MJ (9.4 kJ per beam) and has already demonstrated this energy level. The simulated target density and temperature profiles at peak compression, shortly before the onset of ignition, are shown in Fig. 133.10. This target achieves a 2-D simulated gain of 52.

Recently, comparisons between OMEGA experimental data and 1-D simulations have indicated the need for implementing a numerical model of nonlocal heat transport combined with a

model of cross-beam energy transfer (CBET)<sup>83</sup> due to stimulated Brillouin scattering. While nonlocal effects and CBET are anticipated to affect laser coupling and symmetry in this target to some extent, both the nonlocal transport<sup>84</sup> and CBET<sup>85</sup> models developed recently for *DRACO* in 2-D were being tested at the time of this publication. Therefore, these simulations all use flux-limited Spitzer heat transport with a flux-limiter value of 0.06 with no cross-beam model. Given that this target design is well below the energy and power limits of the NIF, it may be possible to recover lost energy coupling caused by CBET by increasing laser power and energy. Symmetry can likewise be recovered by tuning in future simulations with the added physics packages and through experiment.

Several robustness studies were performed on this PD design to evaluate the additional contributions to compression nonuniformity caused by both capsule asymmetries and laser system uncertainties. Unless otherwise specified, these simulations were performed in a half-sphere geometry and include all even perturbation modes from  $\ell = 2$  to  $\ell = 50$  with a minimum grid resolution of 12 cells per smallest-wavelength mode in the transverse direction. Capsule asymmetry studies include outer-surface roughness of the plastic ablator, inner-shell-surface roughness from DT ice layering, as well as target offset due to mispositioning of the target relative to the center of beam convergence. Modeled laser system uncertainties include random beam-mispointing errors, beam-to-beam mistiming of the laser pulse, power imbalance between beams, and laser speckle and imprint from the phase plates, including beam smoothing using multi-FM SSD. Each of the capsule nonuniformity sources has been characterized experimentally in NIF-scale or OMEGA-scale capsules, and laser system uncertainty<sup>68</sup> on the NIF is well quantified.

Robustness to capsule nonuniformities was found to exceed NIF specifications and achieved values. Each of the following sources of nonuniformity was added to the PD capsule design individually and varied in magnitude to assess the capsule's sensitivity to the perturbation source: capsule outer-surface roughness, inner-surface DT-ice roughness, target offset from target chamber center (TCC), beam-to-beam mispointing and mistiming, and laser power balance between beams. Note that root-mean-square (rms) values in laser parameters are not systematic variations from the design specifications, but rather indicate statistical deviations of individual beams from the intended design.

Outer-surface roughness on NIF-scale capsules has been quantified as 115-nm rms with a spectrum approximated by the

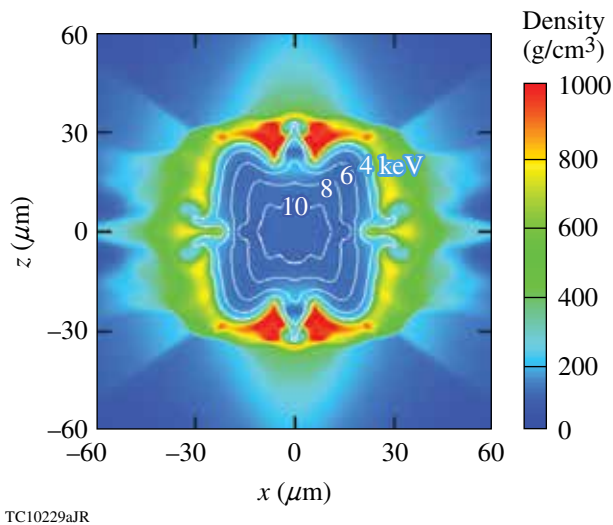


Figure 133.10  
Simulated density contour plot of the 2-D split-quad PD design at the onset of ignition. Temperature contours are plotted with white lines. The target gain is 52.

formula given in Eq. (2) of Ref. 86. Simulations of this polar-drive SI design with this outer-surface roughness spectrum indicate that the target can withstand outer-surface roughness up to  $5\times$  this NIF specification, or up to 575-nm rms, and still achieve ignition. The NIF specification for the inner DT-ice surface roughness is  $1\text{-}\mu\text{m}$  rms, and cryogenic DT-layered OMEGA capsules have routinely demonstrated this level of uniformity.<sup>87</sup> These simulations indicate that the SI design tolerates over  $5\text{-}\mu\text{m}$ -rms inner-surface ice roughness. Target offset was modeled in a full-sphere geometry, resolving modes  $\ell = 1$  to  $\ell = 50$ . This capsule ignited with a target offset of up to  $25\ \mu\text{m}$ — $2.5\times$  greater than the NIF specification of  $10\ \mu\text{m}$ . Figure 133.11 shows the predicted density and temperature profiles for this  $25\text{-}\mu\text{m}$ -offset implosion. One can see that the hot spot has been pushed away from the capsule’s original position, and that the hot-spot displacement is in the same direction as the initial target offset from TCC. This is expected as a result of the increased laser intensity on the side of the capsule closer to TCC. With a  $25\text{-}\mu\text{m}$  offset, the gain of this target is 56.

Robustness to laser system uncertainties likewise exceed NIF specifications with ignition indicated for beam-mispointing errors up to  $100\text{-}\mu\text{m}$  rms and beam-to-beam mistiming up to  $100\text{-ps}$  rms [for comparison, the NIF specifications are  $50\text{-}\mu\text{m}$  mispointing and  $30\text{-ps}$  mistiming (see Ref. 67)]. The NIF has demonstrated 8% rms quad-to-quad power imbalance,

corresponding to a 2% rms illumination nonuniformity on target (see Ref. 67). In a split-quad beam configuration, care should be taken when pairing beams within a quad, given that the power output of beams within a quad varies significantly. This variation is systematic, however, due to a design variation in the thickness of the frequency-conversion crystals and can be minimized in a split-quad configuration by consistently choosing the same beams in each of the drive quads. Therefore, effectively for this target design, the NIF-specified power imbalance between half-quads is  $\sim 11\%$  rms, a factor of  $\sqrt{2}$  higher due to the fact that half of the NIF beams are used. Simulations indicate that the SI target will ignite with power imbalance up to 15% rms between half-quads.

A full nonuniformity simulation including all of these sources of nonuniformity at the NIF specifications was performed. This simulation included expected levels of laser imprint on the NIF caused by phase-plate speckle with the multi-FM-SSD smoothing parameters used in Ref. 77. This simulation, which was performed on a full sphere and resolved modes from  $\ell = 1$  to  $\ell = 100$ , indicated a target gain of 38.

As mentioned earlier, SI with a full-quad PD beam configuration is more likely to be fielded on the NIF in the near term. Therefore, a full-quad PD beam configuration for the same capsule design has been developed. As in Ref. 88, all four quads from the  $30^\circ$  beams (Ring 1) and half of the quads from the  $44.5^\circ$  and  $50^\circ$  beams (Rings 2 and 3, respectively) are used for the main compression drive, while the other quads are used for the ignitor shock pulse. The main-drive beams are repointed as outlined in Table 133.IV. Each of these three rings of beams has a separate laser pulse-shape history. The pulse shapes for each ring are detailed in Fig. 133.12, with the 1-D design pulse shown for reference by the dashed line. Ring 1 comprises the polar beams, Ring 2 the mid-latitude beams, and Ring 3 the equatorial beams. As with the split-quad design, no repointing was considered for the shock beams, and the pulse shape is the same as the 1-D design. Simulations of this target design indicate a gain of 51. A density and temperature plot at the onset of ignition (Fig. 133.13) shows that the target exhibits

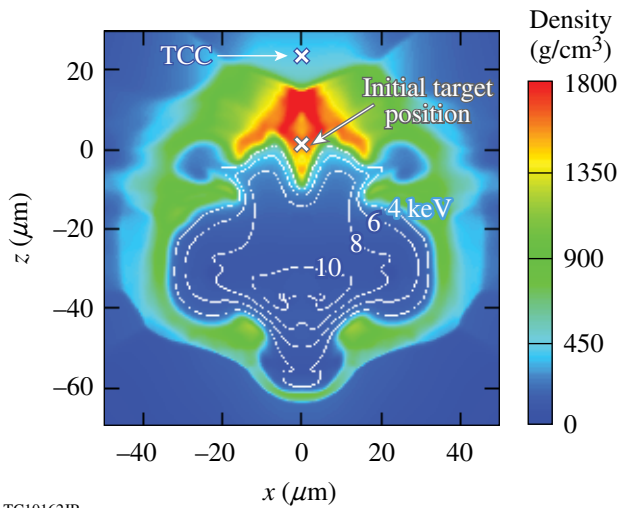


Figure 133.11 Simulated density contour plot of the 2-D split-quad PD design with an initial  $25\text{-}\mu\text{m}$  target offset. The plot is shown at the onset of ignition. Temperature contours are plotted with white lines. For reference, the position of the target chamber center (TCC) and the initial target position are indicated. The target gain is 56.

Table 133.IV: Full-quad PD beam-repointing angles for the main-drive beams given by beam port location.

Beam port angle ( $^\circ$ )	Repointing angle on target ( $^\circ$ )
30.0	25.0
44.5	59.0
50.0	85.0

similar shell integrity compared to the split-quad design shown in Fig. 133.10.

Further optimization and robustness studies on this full-quad design are underway. Beam configurations that offer different repointings of beams within a single quad, as in Ref. 88, are also being considered to improve drive symmetry. Simulations with the nonlocal heat transport and CBET models must be performed, and an accounting for laser backscatter caused by LPI should be included. In addition, hot-electron

preheat effects must be modeled in the 2-D simulations. It is also anticipated that 3-D effects will be somewhat larger in the full-quad design than in the split-quad design because of the smaller number of azimuthal beam ports used during compression, and, as such, 3-D PD simulations must be performed in the future.

**Conclusion**

A polar-drive SI design for the National Ignition Facility has been developed within the NIF Laser System specifications. The target implosion velocity is higher than for standard SI designs to account for laser power limitations on the NIF. The proposed target ignites in 1-D simulations with an  $ITF_{1-D}$  of 4.1 using 700 kJ of input laser energy. Excellent robustness in 1-D to shock mistiming and initial gas density is predicted. Hot-electron energy coupling during the spike pulse is shown to have a positive effect on target margin at hot-electron temperatures up to 150 keV and below 20% of the incident spike laser energy.

Two-dimensional PD simulations including a 3-D laser ray-trace modeling of NIF beams and using either a split-quad or a full-quad beam configuration predict good shell uniformity and ignition with gains above 50 using 750 kJ of laser energy. PD target robustness has been shown to be excellent with respect to individual nonuniformity sources. Simulations of the split-quad PD design including all anticipated levels of system uncertainty and capsule and laser nonuniformity predict a gain of 38.

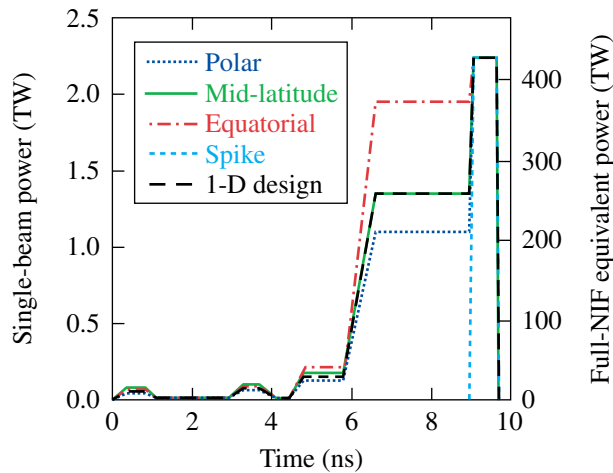
This target may be imploded on the NIF using the proposed full-quad PD beam configuration in a relatively short time frame, requiring only minor modifications to the NIF system. These modifications include the incorporation of 1-D multi-FM SSD beam smoothing, the manufacture of specially tailored laser phase plates, the introduction of polarization plates for polarization smoothing, and the development of a PD target insertion cryostat.

**ACKNOWLEDGMENT**

The authors thank L. J. Perkins, A. J. Schmitt, X. Ribeyre, and S. Atzeni for many enlightening discussions. This work was supported by the U.S. Department of Energy Office of Inertial Confinement Fusion under Cooperative Agreement Nos. DE-FC52-08NA28302 and DE-FC02-04ER54789, the University of Rochester, and the New York State Energy Research and Development Authority. The support of DOE does not constitute an endorsement by DOE of the views expressed in this article.

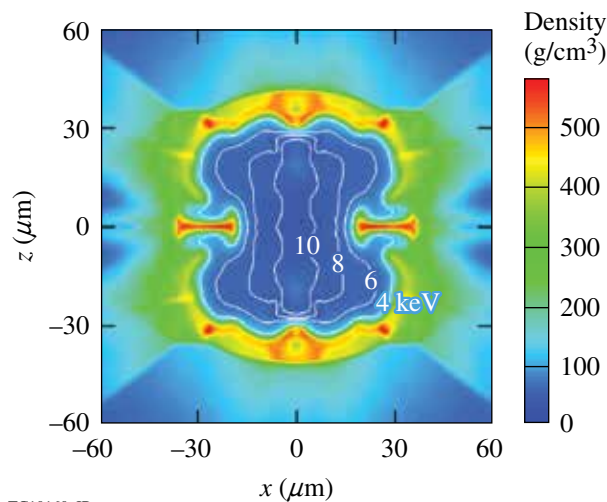
**REFERENCES**

1. S. Atzeni and J. Meyer-ter-Vehn, *The Physics of Inertial Fusion: Beam Plasma Interaction, Hydrodynamics, Hot Dense Matter*, International Series of Monographs on Physics (Clarendon Press, Oxford, 2004).



TC10160JR

Figure 133.12  
Laser pulse shapes for the full-quad PD design for each grouping of beams.



TC10160aJR

Figure 133.13  
Simulated density contour plot of the 2-D full-quad PD design at the onset of ignition. Temperature contours are plotted with white lines. The target gain is 51.

2. R. Betti, C. D. Zhou, K. S. Anderson, L. J. Perkins, W. Theobald, and A. A. Solodov, *Phys. Rev. Lett.* **98**, 155001 (2007).
3. N. G. Basov, S. Yu. Gus'kov, and L. P. Feokistov, *J. Sov. Laser Res.* **13**, 396 (1992).
4. M. Tabak *et al.*, *Phys. Plasmas* **1**, 1626 (1994).
5. V. A. Shcherbakov, *Sov. J. Plasma Phys.* **9**, 240 (1983).
6. V. A. Shcherbakov, presented at the XXXII Conference on Plasma Physics and CF, Zvenigorod, Moscow, 14–18 February 2005.
7. M. Lafon, X. Ribeyre, and G. Schurtz, *Phys. Plasmas* **17**, 052704 (2010).
8. G. Schurtz, X. Ribeyre, and M. Lafon, *J. Phys.: Conf. Ser.* **244**, 022013 (2010).
9. R. Nora and R. Betti, *Phys. Plasmas* **18**, 082710 (2011).
10. X. Ribeyre, V. T. Tikhonchuk, J. Breil, M. Lafon, and E. Le Bel, *Phys. Plasmas* **18**, 102702 (2011).
11. L. J. Perkins, R. Betti, K. N. LaFortune, and W. H. Williams, *Phys. Rev. Lett.* **103**, 045004 (2009).
12. X. Ribeyre, M. Lafon, G. Schurtz, M. Olazabal-Loume, J. Breil, S. Galera, and S. Weber, *Plasma Phys. Control. Fusion* **51**, 124030 (2009).
13. A. J. Schmitt, J. W. Bates, S. P. Obenschain, S. T. Zalesak, D. E. Fyfe, and R. Betti, *Fusion Sci. Technol.* **56**, 377 (2009).
14. A. J. Schmitt *et al.*, *Phys. Plasmas* **17**, 042701 (2010).
15. J. W. Bates *et al.*, *High Energy Density Phys.* **6**, 128 (2010).
16. B. Canaud and M. Temporal, *New J. Phys.* **12**, 043037 (2010).
17. S. Atzeni *et al.*, *Nucl. Fusion* **49**, 055008 (2009).
18. X. Ribeyre *et al.*, *Plasma Phys. Control. Fusion* **51**, 015013 (2009).
19. M. Temporal *et al.*, *Plasma Phys. Control. Fusion* **53**, 124008 (2011).
20. S. Atzeni, A. Schiavi, and A. Marocchino, *Plasma Phys. Control. Fusion* **53**, 035010 (2011).
21. M. Hohenberger, W. Theobald, S. X. Hu, K. S. Anderson, R. Betti, T. R. Boehly, A. Casner, D. E. Fratanduono, M. Lafon, D. D. Meyerhofer, R. Nora, X. Ribeyre, T. C. Sangster, G. Schurtz, W. Seka, C. Stoeckl, and B. Yaakobi, "Shock-Ignition Experiments with Planar Targets on OMEGA," submitted to *Physical Review Letters*.
22. R. Florido, R. C. Mancini, T. Nagayama, R. Tommasini, J. A. Delettrez, S. P. Regan, and B. Yaakobi, *Rev. Sci. Instrum.* **81**, 10E307 (2010).
23. W. Theobald, R. Betti, C. Stoeckl, K. S. Anderson, J. A. Delettrez, V. Yu. Glebov, V. N. Goncharov, F. J. Marshall, D. N. Maywar, R. L. McCrory, D. D. Meyerhofer, P. B. Radha, T. C. Sangster, W. Seka, D. Shvarts, V. A. Smalyuk, A. A. Solodov, B. Yaakobi, C. D. Zhou, J. A. Frenje, C. K. Li, F. H. Séguin, R. D. Petrasso, and L. J. Perkins, *Phys. Plasmas* **15**, 056306 (2008).
24. T. R. Boehly, D. L. Brown, R. S. Craxton, R. L. Keck, J. P. Knauer, J. H. Kelly, T. J. Kessler, S. A. Kumpan, S. J. Loucks, S. A. Letzring, F. J. Marshall, R. L. McCrory, S. F. B. Morse, W. Seka, J. M. Soures, and C. P. Verdon, *Opt. Commun.* **133**, 495 (1997).
25. O. Klimo *et al.*, *Phys. Plasmas* **18**, 082709 (2011).
26. O. Klimo *et al.*, *Plasma Phys. Control. Fusion* **52**, 055013 (2010).
27. W. Theobald, K. S. Anderson, R. Betti, R. S. Craxton, J. A. Delettrez, J. A. Frenje, V. Yu. Glebov, O. V. Gotchev, J. H. Kelly, C. K. Li, A. J. Mackinnon, F. J. Marshall, R. L. McCrory, D. D. Meyerhofer, J. F. Myatt, P. A. Norreys, P. M. Nilson, P. K. Patel, R. D. Petrasso, P. B. Radha, C. Ren, T. C. Sangster, W. Seka, V. A. Smalyuk, A. A. Solodov, R. B. Stephens, C. Stoeckl, and B. Yaakobi, *Plasma Phys. Control. Fusion* **51**, 124052 (2009).
28. W. Theobald, R. Nora, M. Lafon, A. Casner, X. Ribeyre, K. S. Anderson, R. Betti, J. A. Delettrez, J. A. Frenje, V. Yu. Glebov, O. V. Gotchev, M. Hohenberger, S. X. Hu, F. J. Marshall, D. D. Meyerhofer, T. C. Sangster, G. Schurtz, W. Seka, V. A. Smalyuk, C. Stoeckl, and B. Yaakobi, *Phys. Plasmas* **19**, 102706 (2012).
29. S. Depierreux, C. Goyon, K. Lewis, H. Bandulet, D. T. Michel, G. Loisel, V. Yahia, V. Tassin, C. Stenz, N. G. Borisenko, W. Nazarov, J. Limpouch, P. E. Masson Laborde, P. Loiseau, M. Casanova, Ph. Nicolaï, S. Hüller, D. Pesme, C. Riconda, V. T. Tikhonchuk, and C. Labaune, *Plasma Phys. Control. Fusion* **53**, 124034 (2011).
30. R. Betti, W. Theobald, C. D. Zhou, K. S. Anderson, P. W. McKenty, S. Skupsky, D. Shvarts, V. N. Goncharov, J. A. Delettrez, P. B. Radha, T. C. Sangster, C. Stoeckl, and D. D. Meyerhofer, *J. Phys.: Conf. Ser.* **112**, 022024 (2008).
31. G. H. Miller, E. I. Moses, and C. R. Wuest, *Opt. Eng.* **43**, 2841 (2004).
32. *LLE Review Quarterly Report* **33**, 1, Laboratory for Laser Energetics, University of Rochester, Rochester, NY, LLE Document No. DOE/DP/40200-65, NTIS Order No. DE88008065 (1987). (Copies may be obtained from the National Technical Information Service, Springfield, VA 22161.)
33. Y. Kato *et al.*, *Phys. Rev. Lett.* **53**, 1057 (1984).
34. *LLE Review Quarterly Report* **114**, 73, Laboratory for Laser Energetics, University of Rochester, Rochester, NY, LLE Document No. DOE/NA/28302-826, OSTI ID 93524 (2008).
35. S. Skupsky, R. W. Short, T. Kessler, R. S. Craxton, S. Letzring, and J. M. Soures, *J. Appl. Phys.* **66**, 3456 (1989).
36. D. S. Clark, S. W. Haan, and J. D. Salmonson, *Phys. Plasmas* **15**, 056305 (2008).
37. P. Y. Chang, R. Betti, B. K. Spears, K. S. Anderson, J. Edwards, M. Fatenejad, J. D. Lindl, R. L. McCrory, R. Nora, and D. Shvarts, *Phys. Rev. Lett.* **104**, 135002 (2010).
38. B. K. Spears *et al.*, *Phys. Plasmas* **19**, 056316 (2012).
39. P. B. Radha, V. N. Goncharov, T. J. B. Collins, J. A. Delettrez, Y. Elbaz, V. Yu. Glebov, R. L. Keck, D. E. Keller, J. P. Knauer, J. A. Marozas, F. J.

- Marshall, P. W. McKenty, D. D. Meyerhofer, S. P. Regan, T. C. Sangster, D. Shvarts, S. Skupsky, Y. Srebro, R. P. J. Town, and C. Stoeckl, *Phys. Plasmas* **12**, 032702 (2005).
40. R. Betti, K. Anderson, V. N. Goncharov, R. L. McCrory, D. D. Meyerhofer, S. Skupsky, and R. P. J. Town, *Phys. Plasmas* **9**, 2277 (2002).
  41. C. D. Zhou and R. Betti, *Phys. Plasmas* **14**, 072703 (2007).
  42. J. Kline, *Bull. Am. Phys. Soc.* **57**, 200 (2012).
  43. J. Delettrez and E. B. Goldman, Laboratory for Laser Energetics, University of Rochester, Rochester, NY, LLE Report No. 36 (1976).
  44. B. I. Bennett *et al.*, Los Alamos National Laboratory, Los Alamos, NM, Report LA-7130 (1978).
  45. R. C. Malone, R. L. McCrory, and R. L. Morse, *Phys. Rev. Lett.* **34**, 721 (1975).
  46. V. N. Goncharov, J. P. Knauer, P. W. McKenty, P. B. Radha, T. C. Sangster, S. Skupsky, R. Betti, R. L. McCrory, and D. D. Meyerhofer, *Phys. Plasmas* **10**, 1906 (2003).
  47. K. Anderson and R. Betti, *Phys. Plasmas* **10**, 4448 (2003).
  48. K. Anderson and R. Betti, *Phys. Plasmas* **11**, 5 (2004).
  49. R. Betti, K. Anderson, J. Knauer, T. J. B. Collins, R. L. McCrory, P. W. McKenty, and S. Skupsky, *Phys. Plasmas* **12**, 042703 (2005).
  50. Lord Rayleigh, in *Scientific Papers* (Cambridge University Press, Cambridge, England, 1900), Vol. II, pp. 200–207.
  51. G. Taylor, *Proc. R. Soc. London Ser. A* **201**, 192 (1950).
  52. S. E. Bodner, *Phys. Rev. Lett.* **33**, 761 (1974).
  53. H. Takabe *et al.*, *Phys. Fluids* **28**, 3676 (1985).
  54. R. Betti, V. N. Goncharov, R. L. McCrory, and C. P. Verdon, *Phys. Plasmas* **5**, 1446 (1998).
  55. J. P. Knauer, K. Anderson, R. Betti, T. J. B. Collins, V. N. Goncharov, P. W. McKenty, D. D. Meyerhofer, P. B. Radha, S. P. Regan, T. C. Sangster, V. A. Smalyuk, J. A. Frenje, C. K. Li, R. D. Petrasso, and F. H. Séguin, *Phys. Plasmas* **12**, 056306 (2005).
  56. V. N. Goncharov, T. C. Sangster, T. R. Boehly, S. X. Hu, I. V. Igumenshchev, F. J. Marshall, R. L. McCrory, D. D. Meyerhofer, P. B. Radha, W. Seka, S. Skupsky, C. Stoeckl, D. T. Casey, J. A. Frenje, and R. D. Petrasso, *Phys. Rev. Lett.* **104**, 165001 (2010).
  57. J. A. Marozas, J. D. Zuegel, and T. J. B. Collins, *Bull. Am. Phys. Soc.* **55**, 294 (2010).
  58. N. Metzler, A. L. Velikovich, and J. H. Gardner, *Phys. Plasmas* **6**, 3283 (1999).
  59. N. Metzler *et al.*, *Phys. Plasmas* **9**, 5050 (2002).
  60. N. Metzler *et al.*, *Phys. Plasmas* **10**, 1897 (2003).
  61. T. J. B. Collins and S. Skupsky, *Phys. Plasmas* **9**, 275 (2002).
  62. T. J. B. Collins, J. P. Knauer, R. Betti, T. R. Boehly, J. A. Delettrez, V. N. Goncharov, D. D. Meyerhofer, P. W. McKenty, S. Skupsky, and R. P. J. Town, *Phys. Plasmas* **11**, 1569 (2004).
  63. A. B. Iskakov *et al.*, *Phys. Rev. E* **61**, 842 (2000).
  64. E. Krouský *et al.*, *Laser Part. Beams* **18**, 87 (2000).
  65. V. A. Smalyuk, V. N. Goncharov, K. S. Anderson, R. Betti, R. S. Craxton, J. A. Delettrez, D. D. Meyerhofer, S. P. Regan, and T. C. Sangster, *Phys. Plasmas* **14**, 032702 (2007).
  66. J. A. Marozas, LLE, private communication (2012).
  67. C. J. Stolz, *Phil. Trans. R. Soc. Lond. A* **370**, 4115 (2012).
  68. A. Simon, R. W. Short, E. A. Williams, and T. Dewandre, *Phys. Fluids* **26**, 3107 (1983).
  69. W. Seka, D. H. Edgell, J. P. Knauer, J. F. Myatt, A. V. Maximov, R. W. Short, T. C. Sangster, C. Stoeckl, R. E. Bahr, R. S. Craxton, J. A. Delettrez, V. N. Goncharov, I. V. Igumenshchev, and D. Shvarts, *Phys. Plasmas* **15**, 056312 (2008).
  70. W. Seka, D. H. Edgell, J. F. Myatt, A. V. Maximov, R. W. Short, V. N. Goncharov, and H. A. Baldis, *Phys. Plasmas* **16**, 052701 (2009).
  71. D. T. Michel, A. V. Maximov, R. W. Short, S. X. Hu, J. F. Myatt, W. Seka, A. A. Solodov, B. Yaakobi, and D. H. Froula, *Phys. Rev. Lett.* **109**, 155007 (2012).
  72. J. F. Myatt, J. Zhang, V. N. Goncharov, A. V. Maximov, R. W. Short, D. F. DuBois, D. A. Russell, and H. X. Vu, *Bull. Am. Phys. Soc.* **57**, 299 (2012).
  73. C. Riconda *et al.*, *Phys. Plasmas* **18**, 092701 (2011).
  74. S. Weber *et al.*, *Phys. Rev. E* **85**, 016403 (2012).
  75. S. Skupsky, J. A. Marozas, R. S. Craxton, R. Betti, T. J. B. Collins, J. A. Delettrez, V. N. Goncharov, P. W. McKenty, P. B. Radha, T. R. Boehly, J. P. Knauer, F. J. Marshall, D. R. Harding, J. D. Kilkenny, D. D. Meyerhofer, T. C. Sangster, and R. L. McCrory, *Phys. Plasmas* **11**, 2763 (2004).
  76. J. A. Marozas, F. J. Marshall, R. S. Craxton, I. V. Igumenshchev, S. Skupsky, M. J. Bonino, T. J. B. Collins, R. Epstein, V. Yu. Glebov, D. Jacobs-Perkins, J. P. Knauer, R. L. McCrory, P. W. McKenty, D. D. Meyerhofer, S. G. Noyes, P. B. Radha, T. C. Sangster, W. Seka, and V. A. Smalyuk, *Phys. Plasmas* **13**, 056311 (2006).
  77. T. J. B. Collins, J. A. Marozas, K. S. Anderson, R. Betti, R. S. Craxton, J. A. Delettrez, V. N. Goncharov, D. R. Harding, F. J. Marshall, R. L. McCrory, D. D. Meyerhofer, P. W. McKenty, P. B. Radha, A. Shvydky, S. Skupsky, and J. D. Zuegel, *Phys. Plasmas* **19**, 056308 (2012).
  78. A. M. Cok, R. S. Craxton, and P. W. McKenty, *Phys. Plasmas* **15**, 082705 (2008).

79. F. J. Marshall, R. S. Craxton, M. J. Bonino, R. Epstein, V. Yu. Glebov, D. Jacobs-Perkins, J. P. Knauer, J. A. Marozas, P. W. McKenty, S. G. Noyes, P. B. Radha, W. Seka, S. Skupsky, and V. A. Smalyuk, *J. Phys. IV France* **133**, 153 (2006).
80. R. S. Craxton, F. J. Marshall, M. J. Bonino, R. Epstein, P. W. McKenty, S. Skupsky, J. A. Delettrez, I. V. Igumenshchev, D. W. Jacobs-Perkins, J. P. Knauer, J. A. Marozas, P. B. Radha, and W. Seka, *Phys. Plasmas* **12**, 056304 (2005).
81. R. S. Craxton and D. W. Jacobs-Perkins, *Phys. Rev. Lett.* **94**, 095002 (2005).
82. L. J. Perkins, LLNL, private communication (2011).
83. I. V. Igumenshchev, W. Seka, D. H. Edgell, D. T. Michel, D. H. Froula, V. N. Goncharov, R. S. Craxton, L. Divol, R. Epstein, R. Follett, J. H. Kelly, T. Z. Kosc, A. V. Maximov, R. L. McCrory, D. D. Meyerhofer, P. Michel, J. F. Myatt, T. C. Sangster, A. Shvydky, S. Skupsky, and C. Stoeckl, *Phys. Plasmas* **19**, 056314 (2012).
84. G. A. Moses, LANL, private communication (2012).
85. J. A. Marozas and T. J. B. Collins, *Bull. Am. Phys. Soc.* **57**, 344 (2012).
86. P. W. McKenty, V. N. Goncharov, R. P. J. Town, S. Skupsky, R. Betti, and R. L. McCrory, *Phys. Plasmas* **8**, 2315 (2001).
87. T. C. Sangster, R. Betti, R. S. Craxton, J. A. Delettrez, D. H. Edgell, L. M. Elasky, V. Yu. Glebov, V. N. Goncharov, D. R. Harding, D. Jacobs-Perkins, R. Janezic, R. L. Keck, J. P. Knauer, S. J. Loucks, L. D. Lund, F. J. Marshall, R. L. McCrory, P. W. McKenty, D. D. Meyerhofer, P. B. Radha, S. P. Regan, W. Seka, W. T. Shmayda, S. Skupsky, V. A. Smalyuk, J. M. Soures, C. Stoeckl, B. Yaakobi, J. A. Frenje, C. K. Li, R. D. Petrasso, F. H. Séguin, J. D. Moody, J. A. Atherton, B. D. MacGowan, J. D. Kilkenny, T. P. Bernat, and D. S. Montgomery, *Phys. Plasmas* **14**, 058101 (2007).
88. L. Tucker, *2010 Summer Research Program for High School Juniors at the University of Rochester's Laboratory for Laser Energetics*, University of Rochester, Rochester, NY, LLE Report No. 365, LLE Document No. DOE/NA/28302-1000 (2011).

# Polar-Drive Implosions on OMEGA and the National Ignition Facility

## Introduction

Polar drive (PD)<sup>1</sup> provides the capability to perform direct-drive-ignition experiments on laser facilities like the National Ignition Facility (NIF)<sup>2</sup> when cylindrically but not spherically configured for x-ray drive. Beams are absent near the equator in the x-ray drive configuration (Fig. 133.14). As a result, beams must be repointed to adequately irradiate the equator. This repointing of the beams results in oblique beams, which in turn result in laser energy deposition farther from the ablation surface, and consequently reduced kinetic energy of the imploding shell. Ignition designs<sup>3,4</sup> compensate for this reduced hydrodynamic efficiency (defined as the ratio of the maximum shell kinetic energy to the laser energy) by increasing the energy of the most-oblique beams. To achieve adequate uniformity locally near the equator, these designs use beam profiles that include a skewed ellipse for the most-oblique beams. The combination of beam pointing, higher energies for the equatorial beams, and the skewed elliptical beam profiles results in nonradial (or lateral) gradients of the deposited laser energy and the temperature in the corona. Departures from the model predictions of deposited laser energy and lateral heat flow can play an important role in determining the symmetry of the

implosion. The goal of OMEGA and early NIF experiments is to develop and validate ignition-relevant models of laser deposition and heat conduction.

Several aspects of PD are similar to symmetrically driven direct-drive implosions. In the latter, beams are located around the target with spherical symmetry and irradiate the capsule more normally. In these schemes, the implosion velocity  $V_{\text{imp}}$ , defined as the maximum shell velocity, and the adiabat  $\alpha_{\text{inn}}$ , defined as the ratio of the pressure to the Fermi-degenerate pressure averaged over the mass density that forms the high-density shell, are the most important parameters. The minimum energy for ignition  $E_{\text{min}}$  scales as<sup>5</sup>

$$E_{\text{min}} \text{ (kJ)} = 50.8 \alpha_{\text{min}}^{1.88} \left( \frac{V_{\text{imp}}}{3 \times 10^7 \text{ cm/s}} \right)^{-5.89} \left( \frac{P}{100 \text{ Mbar}} \right)^{-0.77},$$

where  $P$  is the ablation pressure. For both symmetric and polar drive, it is critical to achieve the designed implosion velocity while also setting the shell on the required adiabat. The implosion velocity and adiabat are primarily determined by one-dimensional (1-D) physics. The additional challenge in polar drive is multidimensional; it is necessary to adequately compensate for reduced energy coupling at the equator while achieving the required values of the adiabat and implosion velocity. Hydrodynamic simulations<sup>4</sup> suggest that this compensation is achievable. The parameter space of adiabat and implosion velocity over which ignition is possible, including multidimensional effects, is therefore the same between the two direct-drive schemes.

Short-wavelength nonuniformities result from the imprinting of single-beam nonuniformities on the target. Subsequent multidimensional growth caused by the Rayleigh–Taylor (RT) instability<sup>6</sup> influences the stability of the converging shell. Significant RT growth can degrade implosion performance. Since the number of  $e$  foldings of the most-dangerous mode to RT instability depends on the implosion velocity and details of the adiabat profile in the converging shell,<sup>7</sup> which is very

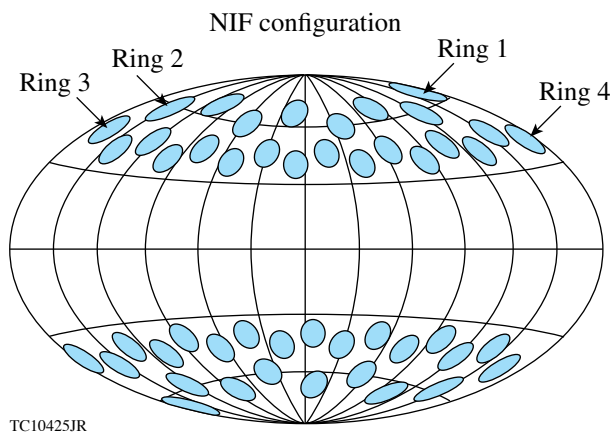


Figure 133.14  
The NIF beam-port configuration arranged in four rings.

similar between PD and symmetric drive, short-wavelength behavior is very similar between the two schemes. Therefore, symmetric-drive implosions on OMEGA<sup>8–10</sup> play an important role in validating models of laser imprint and RT growth that are also relevant for PD.

Polar drive differs from symmetric drive in the seeds that determine the low-mode asymmetry of the imploding shell and the hot spot. Beam geometry has a marginal influence on target symmetry and performance in symmetric drive. In PD, however, beam obliquity changes the angular and radial locations of the deposited laser energy. This influences the symmetry of the imploding shell. Seeds for long-wavelength nonuniformity are set throughout the laser pulse. Figure 133.15 shows the contours of laser energy deposited normalized to the volume as a function of radial location and polar angle for a NIF ignition design.<sup>4</sup> Two aspects are unique to polar drive. The conduction zone (the distance between the ablation surface and the peak in deposited energy) is larger near the equator than at the pole, leading to lower hydrodynamic efficiency near the equator. There are significant transverse gradients in the deposited energy primarily because of the unique beam profiles and the higher power in the equatorial beams. These lateral gradients are insignificant in the symmetric design. Modeling this lateral heat flow is critical for an accurate prediction of symmetry in polar drive.

Shock nonuniformity is another important determinant of shell asymmetry. Long-wavelength shock-front perturbations, determined primarily by polar variations in the laser deposition [Fig. 133.16(a)], seed the nonuniformities on the inner shell surface [Fig. 133.16(b)]. The shocks shown in Fig. 133.16 are from an OMEGA-scale design with deliberate repointing

and mistiming to illustrate the seeding of perturbations at the rear shell surface. These perturbations grow when subsequent shocks reach the surface. Inner shell perturbations also grow as a result of the feedthrough of perturbations being seeded at the ablation surface determined by polar variations in laser-energy deposition and heat conduction. Accurate predictions of symmetry rely on accurate modeling of laser deposition and heat conduction.

Laser–plasma interactions (LPI’s) can compromise target performance by reducing implosion velocity, altering symmetry, and preheating the cold shell. Incorporating LPI effects within fluid codes is challenging because of the different length and time scales over which plasmas and fluids evolve. Empirical guidance is critical to understanding the magnitude of the effects of LPI processes and in improving designs to mitigate their deleterious effects. The goal of the early NIF experiments is to understand issues relating to energetics, symmetry, and preheat in NIF-scale plasmas.

In the following sections, OMEGA PD experiments are discussed with emphasis on adiabat and symmetry. The implosion velocity has been discussed in previous work.<sup>11</sup> Next, limitations of OMEGA experiments and early experiments planned for the NIF are discussed, followed by the conclusions.

### OMEGA Experiments

The goal of OMEGA experiments is to predictably model target performance in polar drive. Twenty of the 60 OMEGA beams are omitted from the drive to emulate the 48-quad NIF x-ray-drive configuration [Fig. 133.17(a)].<sup>12</sup> The beams are then shifted toward the equator to directly drive the target more symmetrically. The 40 OMEGA beams can be considered to

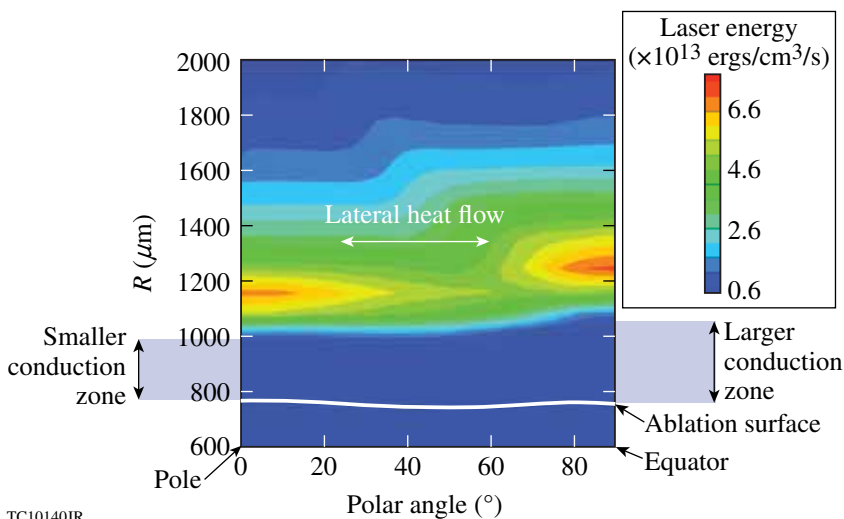


Figure 133.15

Density of laser energy deposited at the end of the laser pulse ( $t = 9.0$  ns) for a NIF ignition design versus polar angle. The white line shows the location of the ablation surface. The conduction zone is larger at the equator, leading to reduced hydrodynamic efficiency. A significant transverse gradient in the deposited laser energy leads to transverse heat flow in polar drive.

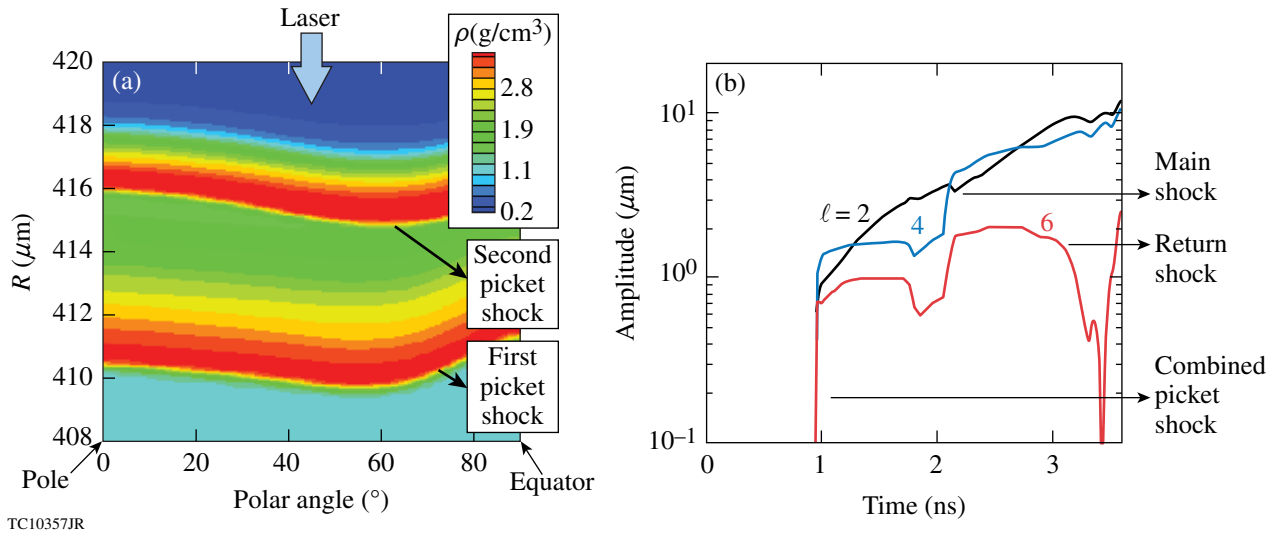


Figure 133.16

(a) Density contours at 650 ps showing nonuniform shocks from the first two pickets transiting the shell for an OMEGA PD design. (b) Perturbation amplitude at the rear shell surface is seeded by the shocks. Feedthrough from the ablation surface results in amplitude growth during acceleration and convergence (until 3 ns).

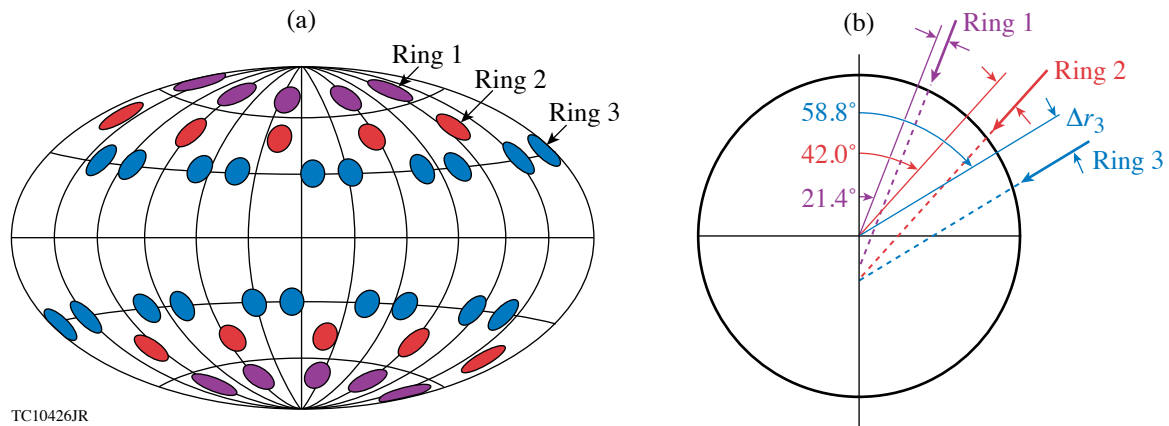


Figure 133.17

(a) The OMEGA beam port configuration with the equatorial beams omitted. There are three rings in each hemisphere. (b) Schematic showing the shifted beams for OMEGA PD geometry.

be arranged in three rings. Each ring is repointed only in polar angle by a distance  $\Delta r$  perpendicular to the beam axis (the azimuthal angles for OMEGA are already optimally pointed) [see Fig. 133.17(b)]. Each repointed configuration is characterized by three numbers  $\{\Delta r_1, \Delta r_2, \Delta r_3\}$ ; larger values of these numbers correspond to more-oblique beams. Room-temperature experiments on OMEGA employ a 24- to 27- $\mu\text{m}$ -thick plastic (CH) shell with 10 atm of deuterium ( $\text{D}_2$ ) fill [see Fig. 133.18(a)]. Since 40 of the 60 beams are used, the energy on target is limited to approximately 13.5 kJ. (In principle, nearly 16 kJ can be obtained for PD implosions—these highest-energy implosions are reserved for cryogenic capsules.) A variety of laser pulse

shapes, with different temporal histories, irradiate the target. A flat foot to a continuous rise<sup>12</sup> [Fig. 133.18(b)] and three pickets preceding a main pulse are used<sup>11,13</sup> [Fig. 133.18(c)]. The PD ignition design uses the latter pulse shape since nearly 1-D high areal densities have been demonstrated with this pulse shape in symmetric drive.<sup>14</sup> In the room-temperature CH designs, both of these pulse shapes set the shell at a minimum adiabat of approximately 3.5. The continuous pulse shape irradiates the target at a higher peak intensity of  $8 \times 10^{14} \text{ W/cm}^2$ , while the triple-picket pulse irradiates the target at  $4 \times 10^{14} \text{ W/cm}^2$  (these values are defined at the initial target radius). The advantage of the triple-picket pulse shape is the ability to achieve

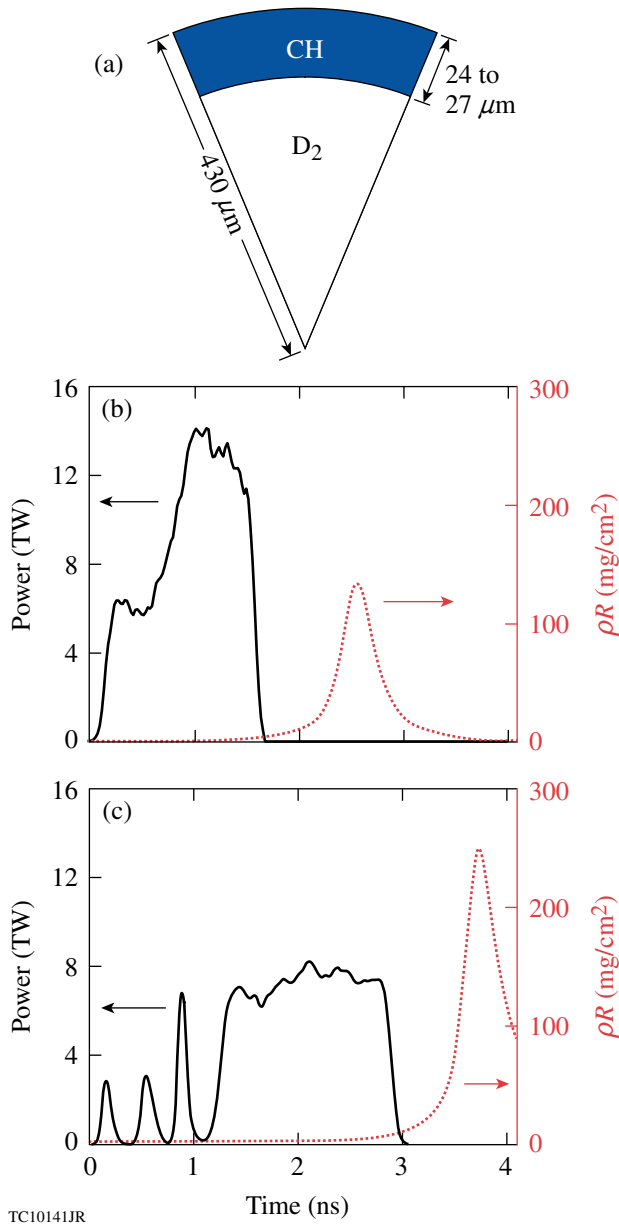


Figure 133.18  
 (a) Schematic of the target used in PD implosion experiments on OMEGA. [(b) and (c)] Laser pulse (left axis) and simulated areal density averaged over the polar angle (right axis) for (b) the continuous pulse shape and (c) the triple-picket pulse shape.

higher convergence as explained below. Full beam smoothing (1/3-THz three-color-cycle smoothing by spectral dispersion<sup>15</sup> and polarization smoothing<sup>16</sup>) is used. The implosion velocity of these capsules is approximately  $2 \times 10^7$  cm/s. Higher velocities can be obtained in cryogenic implosions where the lower-density deuterium–tritium (DT) layer permits thicker shells and technically feasible spacing between the pickets for less-massive targets.<sup>11</sup> Target performance is studied from

measurements of areal density ( $\rho R$ ) and x-ray images obtained by backlighting the converging shell using a subset of the beams omitted from the drive. Other measures of target performance such as yield, neutron rate history, and the related implosion velocity have been presented elsewhere.<sup>11</sup>

The predicted areal densities for the two pulse shapes discussed in this work differ quite significantly. The triple-picket pulse maintains the drive pressure until the shock is reflected from the center of the converging capsule, whereas the continuous pulse permits the shell to coast and decompress, reducing the areal density. Figure 133.19 shows the mass density and adiabat profile for the two pulse shapes at the end of the laser

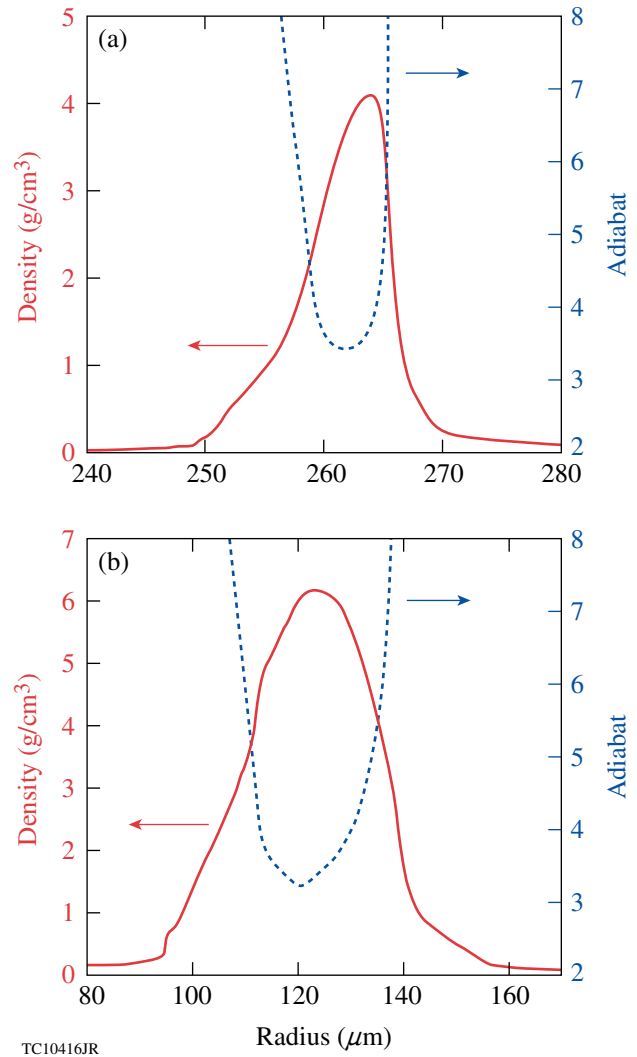
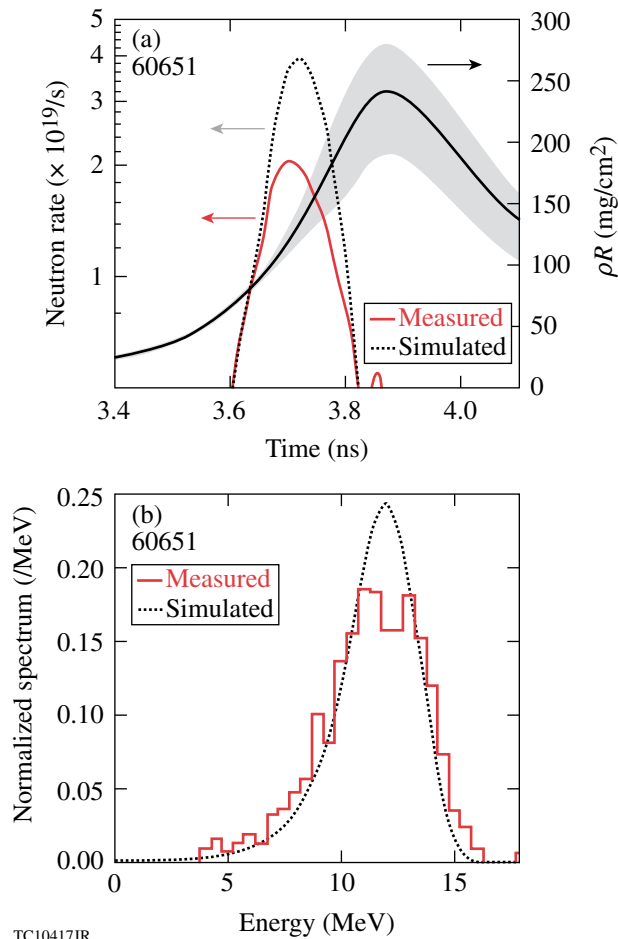


Figure 133.19  
 Mass-density profile at the end of the laser pulse (left axis) and adiabat profile in the converging shell (right axis) for (a) the continuous pulse shape and (b) the triple-picket pulse shape.

pulse; while the adiabat profiles are very similar, the shell has traveled a greater distance for the triple-picket pulse shape. At peak neutron production, the shell in the implosion driven with the triple-picket pulse is simulated to have higher convergence (the convergence ratio is  $CR \sim 19$  compared to  $CR \sim 13$  for the continuous laser pulse) and to have a higher density than the shell driven with the continuous pulse shape.

The areal density is inferred in implosion experiments through the energy loss of secondary protons<sup>17</sup> and is inferred only during neutron production. To compare the areal density from simulations with that inferred from observations, it is important to account for the observed neutron production history.<sup>8</sup> Figure 133.20(a) shows the measured and simulated rates

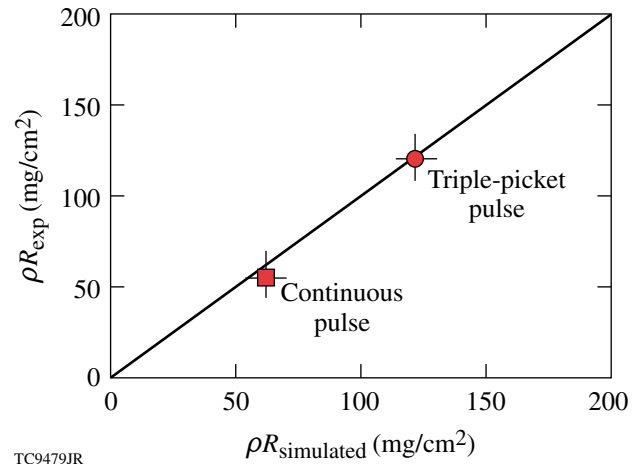


TC10417JR

Figure 133.20

(a) Simulated neutron rate (dotted line, left axis) overlaid on the measured neutron rate (red line, left axis), and the polar-angle averaged areal-density history (solid line, right axis). The shaded region indicates the minimum and maximum areal density in polar angle. (b) Measured (solid) and simulated (dotted) secondary proton spectrum.

for neutron history overlaid with the areal-density evolution for a PD implosion driven with a triple-picket pulse shape and beam repointing corresponding to  $\{90 \mu m, 150 \mu m, 150 \mu m\}$ . The simulations were performed with the hydrodynamic code *DRACO*<sup>18</sup> including a full 3-D laser ray trace,<sup>19</sup> collisional absorption as the only laser-energy deposition mechanism, a flux-limited heat-conduction model (with a flux limiter  $f = 0.06$ ) (Refs. 20 and 21), and multigroup diffusive radiation transport with astrophysical opacity tables. The experimental neutron rate history is measured using the neutron temporal diagnostic.<sup>22</sup> The *DRACO*-simulated profiles are post-processed with the particle-tracking code *IRIS*<sup>23</sup> using this measured rate history to calculate the emergent proton spectrum. Excellent agreement is obtained in the spectrum, as seen in Fig. 133.20(b), indicating that the adiabat is modeled well for this pulse shape. The areal density from the continuous pulse shape has been published previously.<sup>11</sup> The trend across pulse shapes is recovered experimentally as seen in Fig. 133.21. For an implosion with no coasting phase, the maximum areal density has been shown to depend primarily on the adiabat<sup>24</sup> as  $\rho R_{max} (mg/cm^2) = [2.6 \times 10^2 E_L^{1/3} (kJ)] / \alpha_{inn}^{0.6}$ , where  $E_L$  is the laser energy. Simulations reproduce the areal density for both pulse shapes, indicating that *DRACO* accurately models shock timing and the effect of coasting on compression. This result is consistent with independent PD shock-timing measurements using cone-in-shell geometries.<sup>13</sup>



TC9479JR

Figure 133.21

Inferred areal density compared to simulated values for the continuous and triple-picket pulse shapes. The vertical error bars represent the standard deviation of the four areal-density measurements around the target chamber center for each shot. The horizontal error bars represent the standard deviation of the inferred areal density in polar angle from the simulated spectra.

Backlit images indicate that simulations reproduce the gross features of the converging shell. Figure 133.22 shows the images obtained by backlighting the converging shell with an  $\sim 4.7$ -keV Ti backlighter for two different pointing configurations, corresponding to  $\{90 \mu\text{m}, 150 \mu\text{m}, 150 \mu\text{m}\}$  and  $\{30 \mu\text{m}, 150 \mu\text{m}, 150 \mu\text{m}\}$ , for the triple-picket pulse shape. *DRACO* simulations are post-processed with the code *Spect3D*,<sup>25</sup> which transports x rays through the *DRACO* profiles accounting for absorption using opacities generated by the PRISM group.<sup>25</sup> The plasma is assumed to be in local thermodynamic equilibrium (LTE), which is an excellent assumption for the densities (from solid up to  $\sim 150 \text{ g/cm}^3$ ) and temperatures (from  $\sim \text{eV}$  up to  $\sim \text{keV}$ ) characteristic in the compressing capsule. The detector resolution and the time window over which the images are integrated in the experiment are included in the postprocessing. The simulations reproduce the measured images very well. The images shown in Fig. 133.22 correspond to the latest time at

which the shell can be unambiguously viewed. At this time the shell has converged by approximately a factor of 5. Later in time the backlighter intensity is significantly lower than the self-emission from the compressed core, precluding an inference of the symmetry. For the first pointing configuration, the converging shell is prolate, for which one can correct by repointing Ring 1 closer to the pole. The second pointing configuration achieves a rounder core as seen in the images. The contour of maximum x-ray absorption (white line in Fig. 133.22) is decomposed into Legendre modes  $\ell$ . The normalized mode amplitudes (defined as the ratio of the mode amplitude to the radius of maximum absorption) for  $\ell = 2$  to 10 are in reasonable agreement between simulation and measurement. The typical error in the amplitude measurement is estimated to be of the order of 2% to 3%. The best observed uniformity with only repointing to correct for PD geometry has been obtained with the  $\{30 \mu\text{m}, 150 \mu\text{m}, 150 \mu\text{m}\}$  configuration.

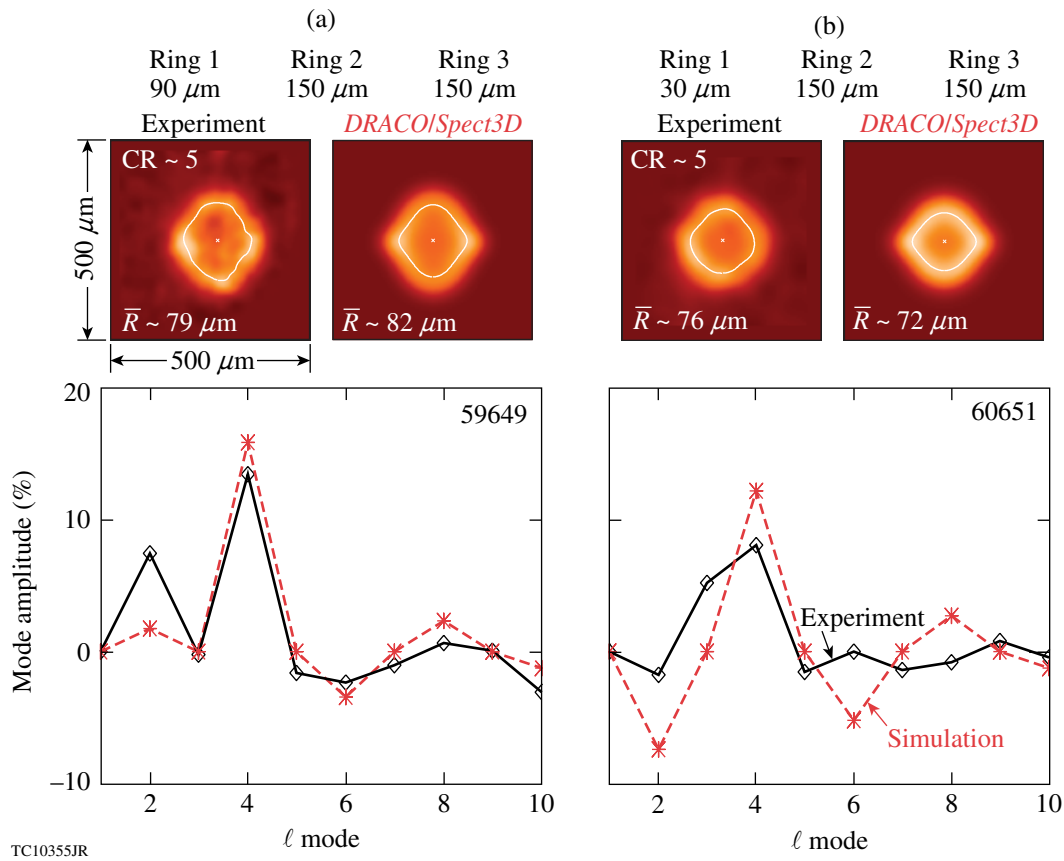


Figure 133.22

(a) Backlit image from the experiment together with the simulated image for the triple-picket pulse shape. The white lines indicate the contour of maximum absorption. The graphs show experimental and simulated normalized Legendre-mode amplitudes (the ratio of mode amplitude to average radius  $\bar{R}$ ) of the contour of maximum absorption. (b) Same as (a) but for a different pointing that reduces the amplitude of the  $\ell = 2$  Legendre mode.

Experimental and simulated backlit images for the two different pulse shapes for the same pointing configuration  $\{90 \mu\text{m}, 120 \mu\text{m}, 120 \mu\text{m}\}$  are compared for the continuous pulse shape [Fig. 133.23(a)] and the triple-picket pulse shape [Fig. 133.23(b)]. With this pointing configuration there is an observable difference in the shape of the core for the two pulse shapes, which is reproduced by simulation. Excellent agreement is obtained in the modal amplitudes of the shell perturbations.

Current high-convergence OMEGA PD implosions can only be driven at low intensities owing to the limited energy available from 40 beams combined with the fixed spot size produced by OMEGA's existing phase plates (860  $\mu\text{m}$  diameter corresponding to 95% of the energy enclosed).<sup>26</sup> Higher on-target intensities can be obtained with smaller targets and phase plates with smaller focal spots.<sup>11</sup> New phase plates have been obtained for the OMEGA laser, and experiments to study PD implosions at ignition-relevant intensities will begin in the near future.

NIF ignition targets have a radius that is nearly  $4\times$  the radius of OMEGA-scale targets. Consequently, the density scale lengths in the corona of NIF targets are larger by the same ratio. As discussed in the next section, laser-plasma interactions become increasingly important to target performance for larger scale lengths. Experiments at the NIF scale are critical to understanding the role of these interactions on target performance.

### Early NIF Experiments

The radial coronal density scale length in typical NIF ignition designs<sup>4</sup> is  $\sim 600 \mu\text{m}$ , compared to the OMEGA-scale density scale length of  $\sim 150 \mu\text{m}$ . The magnitude of LPI effects typically increases with scale length. LPI can influence shell adiabat,<sup>27</sup> energetics,<sup>28</sup> and symmetry.<sup>29</sup> Two-plasmon decay (TPD)<sup>30</sup> primarily determines the extent of fast-electron pre-heat in implosions. Energetic electrons, accelerated by plasma waves, deposit their energy in the cold shell, raising its adiabat,

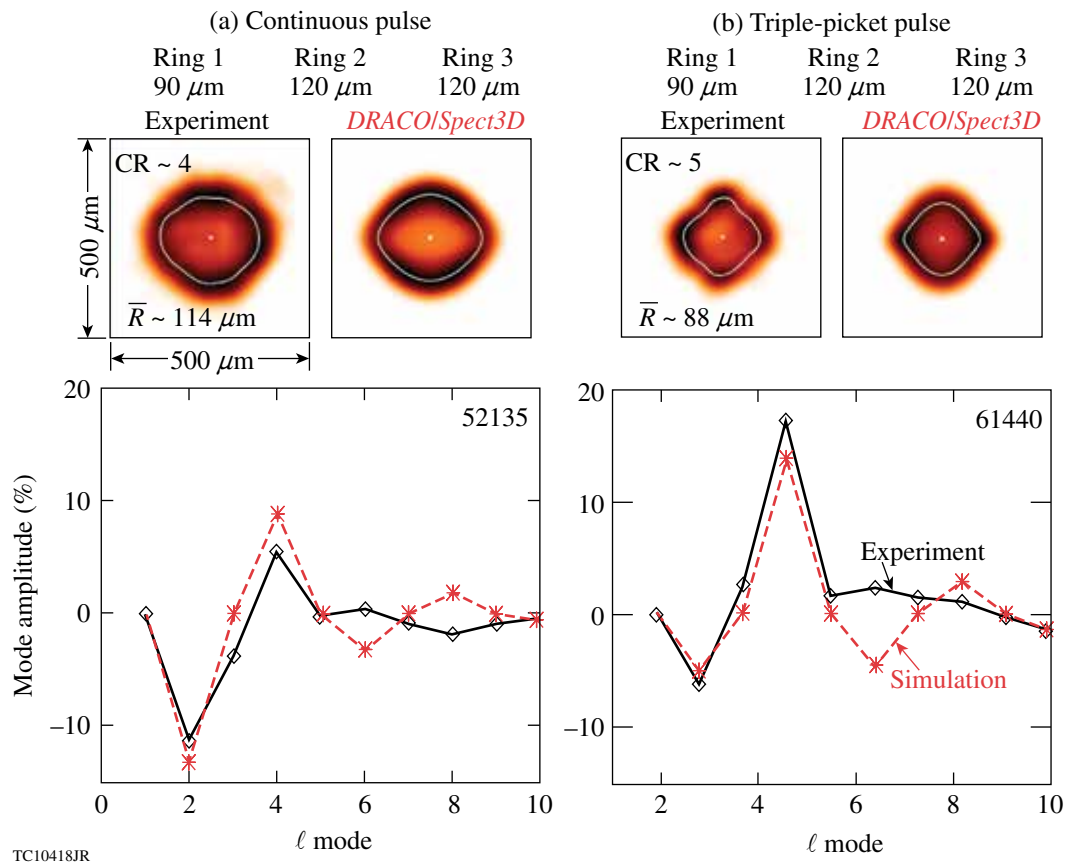


Figure 133.23

Experimental and simulated backlit images for the same pointing  $\{90 \mu\text{m}, 120 \mu\text{m}, 120 \mu\text{m}\}$  but for the two different pulse shapes: (a) the high-intensity continuous pulse shape and (b) low-intensity triple-picket pulse shape. The white line indicates the contour of maximum absorption. The graphs show normalized Legendre-mode amplitudes (the ratio of mode amplitude to average radius  $\bar{R}$ ) of the contour of maximum absorption.

making it more difficult to achieve the required compression. The extent of preheat is typically diagnosed by measuring energetic (“hard”) x rays ( $\geq 50$  keV) produced by fast electrons.<sup>31</sup> The threshold parameter for the TPD instability, defined as  $\eta = I_{n/4} (10^{14} \text{ W/cm}^2) L_{n/4} (\mu\text{m}) / 233 T_{n/4}^e (\text{keV})$  (Ref. 30), where  $I_{n/4}$ ,  $L_{n/4}$ , and  $T_{n/4}^e$  are the laser intensity, density scale length, and the electron temperature at the quarter-critical surface, respectively, has been shown to correlate with the observed hard x-ray signal in OMEGA symmetric-drive implosions.<sup>32</sup> However, the effect of this preheat on target performance in ignition-relevant OMEGA implosions is negligible.<sup>33</sup> The longer NIF scale lengths are suggestive of a higher threshold parameter and greater preheat from fast electrons; however, no clear physical mechanism links the threshold parameter to the observed hard x-ray signal. The threshold parameter has been defined in planar geometry for the absolute instability. TPD has also been shown to be convectively unstable<sup>34</sup> for the plasma conditions and profiles in direct-drive implosions, and this aspect is not included in the threshold parameter. Additionally, calculations of TPD indicate that this instability can become highly nonlinear and saturate.<sup>35</sup> Without detailed modeling of TPD, observations of hard x rays on the NIF are necessary to determine the extent of preheat.

In cross-beam energy transfer (CBET), incoming rays transfer their energy to outgoing rays through ion-acoustic waves.<sup>28</sup> This results in reduced laser-energy deposition and reduced hydrodynamic efficiency. The gain rate for CBET is  $L^{-1} \sim (I_1 I_2) / [\nu_a^2 \eta^2 + (1 - \eta^2)^2]$  (Ref. 28), where  $I_1$  and  $I_2$  are the intensities of the two beamlets,  $\nu_a$  is the damping rate of the ion-acoustic waves, and  $\eta = \mathbf{k}_a \cdot \mathbf{u} - \omega_a / k_a c_a$  (the resonance condition where  $\mathbf{k}_a$  is the ion-acoustic wave vector,  $\mathbf{u}$  the fluid velocity,  $\omega_a$  the ion-acoustic wave frequency, and  $c_a$  the ion-acoustic wave speed). Irradiating capsules with the relevant intensities ( $I_1$  and  $I_2$ ) is critical to understanding CBET effects. CBET reduces implosion velocity by  $\sim 10\%$  in symmetric-drive OMEGA-scale implosions.<sup>28</sup> PD implosions indicate a reduced implosion velocity although the exact mechanism is not yet understood.<sup>11</sup> As presented earlier, however, symmetry in PD implosions is reproduced well with simulations that do not include CBET. This may be caused by either the negligible effect of CBET on symmetry in OMEGA-scale implosions or the relatively early time when the converging shell is viewed. When velocity scale lengths are long, as in the NIF-scale coronal plasma, the resonance condition for CBET is satisfied over a larger volume. This likely results in a greater level of CBET. NIF experiments are again important in identifying the extent of CBET.

Room-temperature CH implosions are planned for initial NIF experiments [Fig. 133.24(a)]. The first set of experiments are planned at lower intensities where LPI effects such as TPD and CBET are less important, enabling one to validate models in *DRACO* that do not contain these LPI effects. Future experiments will probe higher-intensity implosions to develop and validate models in that regime and identify mitigating strategies if required. To obtain the scale of the initial set of implosions, consider the scaling law  $E \sim R_t^3$ , which retains the same laser energy density per target volume, where  $E$  is the laser energy and  $R_t$  is the target radius. Using OMEGA energies of 25 kJ

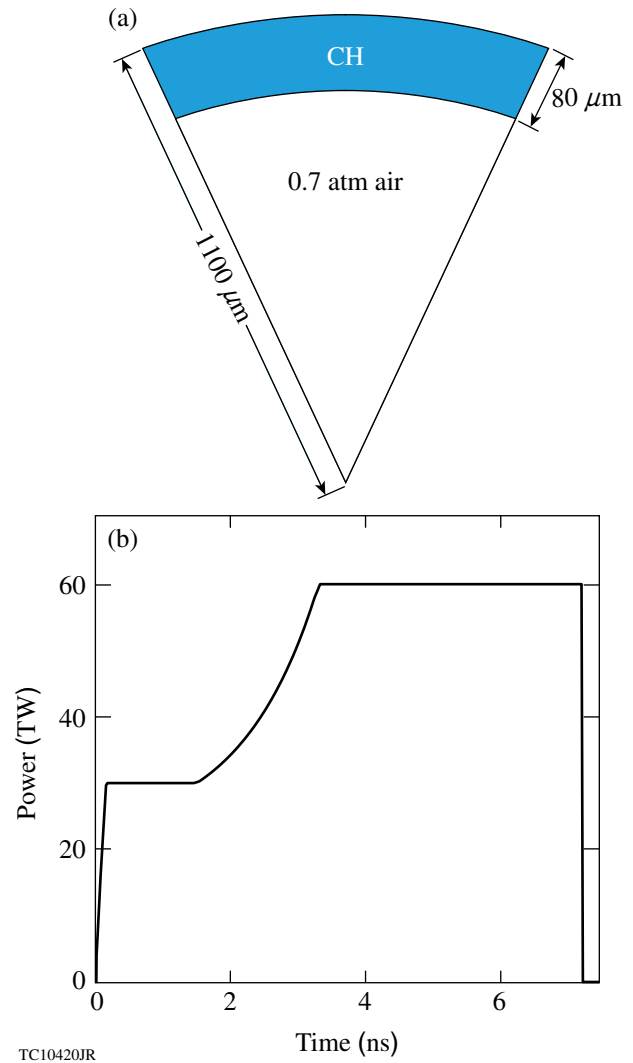


Figure 133.24

(a) Schematic of the target for early NIF experiments; (b) pulse shape from the 1-D design.

and the desired target radius of  $\sim 1100 \mu\text{m}$  (this is determined by the NIF phase plates<sup>36</sup>), these implosions must be driven with  $\sim 350 \text{ kJ}$ . Using  $P \sim R_t^2$  yields a peak power of  $P \sim 50 \text{ TW}$  and  $T \sim R_t$  yields a pulse length of  $T \sim 7.5 \text{ ns}$ . The laser pulse shape [Fig. 133.24(b)]—a low foot to a continuous rise, similar to the OMEGA pulse shape described earlier—sets the target at a low adiabat of  $\sim 3$ . These early experiments will use the existing NIF hardware including phase plates and single-beam smoothing. Beams are defocused<sup>37</sup> to achieve the optimal symmetry in the simulation. Beam phase fronts for the near field<sup>36</sup> are forward propagated using Fourier transforms to obtain the on-target beam shapes using the code *Waasikwa*.<sup>38</sup> The laser-related parameters of the design are shown in Table 133.V. In this reprinted configuration, some quads (a set of four beams form a quad) from the  $44.5^\circ$  cone are moved to  $46^\circ$ , while others are moved to  $69^\circ$ . Beams are repointed in azimuth to locations defined in Ref. 4. While this achieves excellent uniformity in the polar angle, it introduces an  $\sim 10\%$  peak-to-valley,  $\ell = 4$  variation in azimuth of the absorption because of the limited (four in each hemisphere) quads illuminating near a polar angle of  $69^\circ$ . This azimuthal variation can be reduced to 4% or lower with an  $\ell = 8$  variation instead by splitting the  $44.5^\circ$  quads with two of the beams pointed to  $46^\circ$  and the remaining two to  $69^\circ$ . This splitting of the quads is not used in this work but is being investigated for future designs.

The on-target intensity from each of the rings is shown in Fig. 133.25. Rings 1 and 2 primarily irradiate the target near the pole, whereas the re-shifted Rings 3a, 3b, and 4 irradiate more toward the equator. The overlapped on-target intensity is higher near the equator. This is necessary to compensate for the reduced hydrodynamic efficiency from the more-oblique beams. Shock breakout is nearly uniform with this configuration of beam pointing, laser defocus, and pulse shapes except near the equator (Fig. 133.26). This significantly reduces core temperatures by injecting a jet of shell material into the hot spot

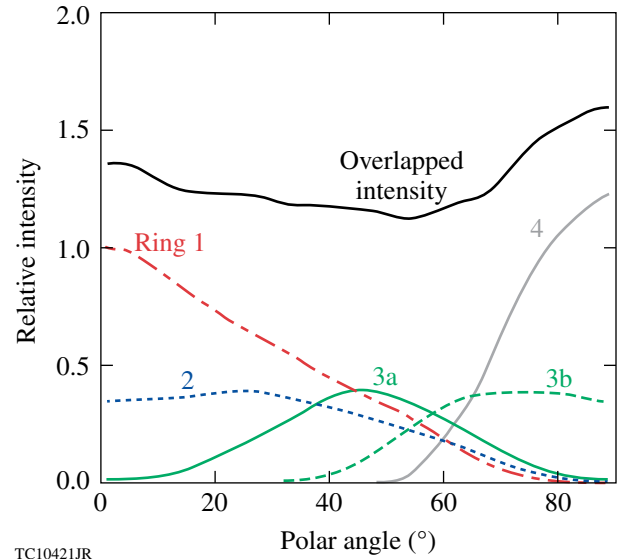


Figure 133.25

Intensity on target for the different rings at time  $t = 0$ . Rings 1 and 2 have peak irradiances near the pole. The shifting of Rings 3a, 3b, and 4 results in higher intensities toward the equator. The overlapped intensity is shown in black. Beams have been defocused and repointed (Table 133.V) to achieve this irradiation profile.

and radiatively cooling it. This can be corrected by designing an appropriate beam profile, as has been done for the ignition design, with the secondary ellipse on the equatorial beams.

For given pointing and defocus parameters, shell symmetry can be changed from spherical to prolate and oblate by changing the temporal pulse shapes, while maintaining the overall energy on target at  $\sim 350 \text{ kJ}$  (see Fig. 133.27). The foot portion of the pulse, which determines the shock strength, is held constant among the three cases. Therefore, adjustments to the shape of the imploded shell can be made by varying the peak-power portions of the pulse shapes.

Table 133.V: The repointing and beam defocus used for the NIF design presented in the text. The pointing shift is as defined in Fig. 133.17:  $\Delta r = R_t \times \sin(\theta_r - \theta)$ , where  $R_t$  is the target radius.

Rings	Original port angle ( $^\circ$ ) $\theta$	Repointed angle ( $^\circ$ ) $\theta_r$	Pointing shift ( $\Delta r$ ) ( $\mu\text{m}$ )	Number of quads (northern + southern)	Defocus distance (cm)
1	23.5	23.5	0	8	1.0
2	30.0	35.0	96	8	1.0
3a	44.5	46.0	29	8	1.5
3b	44.5	69.0	456	8	1.0
4	50.0	86.0	647	16	1.0

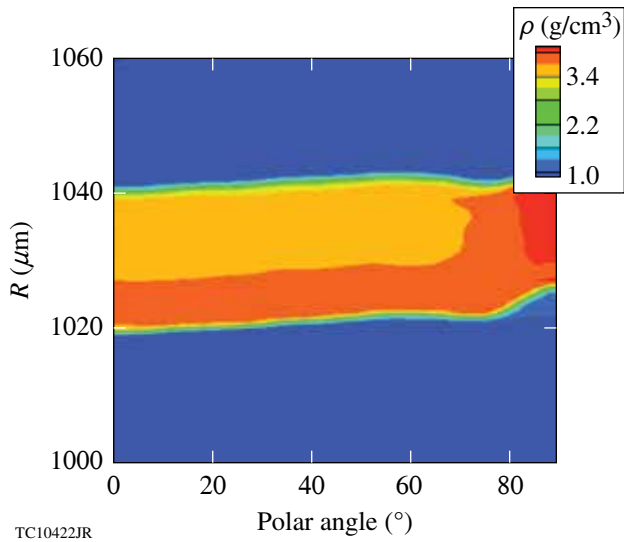


Figure 133.26  
Mass-density contour at shock breakout (1.5 ns) versus radius and polar angle. The shock is largely uniform except near the equator.

Symmetry in the early stages of the implosion will be diagnosed using gated x-ray framing camera images of self-emission.<sup>39</sup> Photon energies  $h\nu \geq 2$  keV from self-emission preferentially diagnose the imploding capsule outside the ablation surface.<sup>39</sup> For the three shell shapes, simulated images are shown in Fig. 133.27 at 7.2 ns—the latest time of observation corresponding to the end of the laser pulse. The *DRACO* simulations are post-processed with *Spect3D* including the pinhole diameter (100  $\mu\text{m}$ ), which is expected to be used in the initial experiments. Observable differences are predicted, as seen from Fig. 133.28, where the normalized amplitude of Legendre mode  $\ell = 2$  is plotted versus time. The shaded regions include results from three simulations for each shape, where other long-wavelength nonuniformities<sup>4</sup> such as beam mistiming (30-ps rms), beam mispointing (50- $\mu\text{m}$  rms), and energy imbalance (8% rms) are included in the simulation. The deliberate asymmetries imposed in the PD designs dominate over the other nonuniformity seeds.

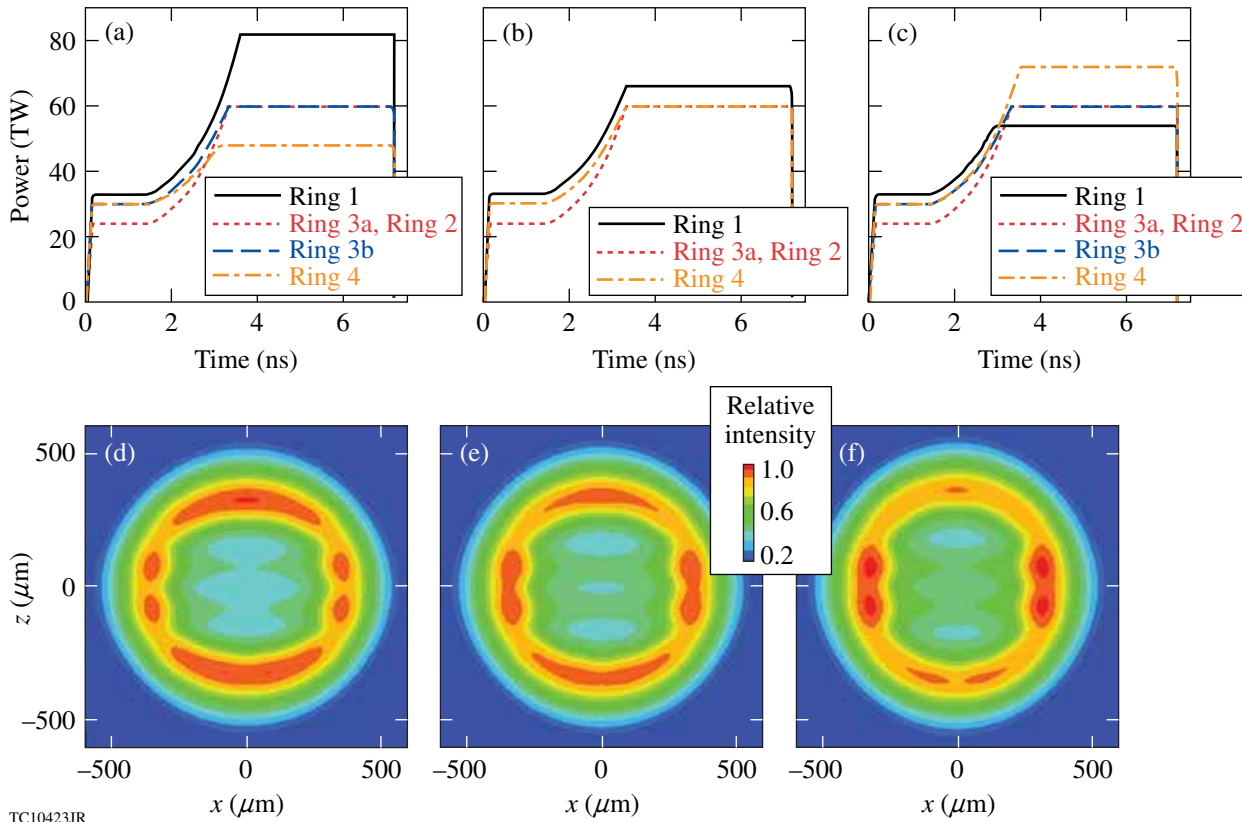


Figure 133.27  
[(a)–(c)] Variations in pulse shapes used to achieve different shapes of the converging shell: (a) prolate, (b) spherical, and (c) oblate. The peak power of the pulse is varied with the shock strengths kept the same. [(d)–(f)] Corresponding x-ray gated framing-camera images from self-emission for  $h\nu \geq 2$  keV.

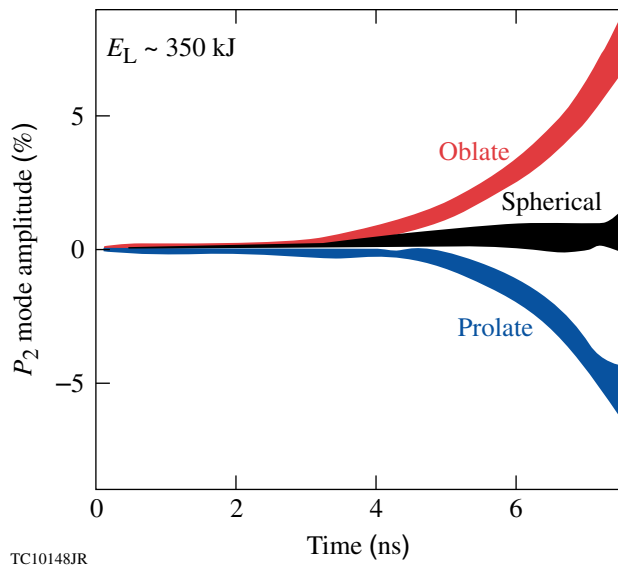


Figure 133.28

Relative amplitude (ratio of amplitude of Legendre mode  $\ell = 2$  to shell position) versus time for the three shapes in Fig. 133.27. The shaded areas correspond to uncertainties associated with errors in beam timing, pointing, and energy balance.

## Conclusions

The goal of OMEGA and NIF experiments is to validate physics models used to design PD ignition capsules and implement mitigating strategies for laser–plasma interactions. Laser-energy deposition and heat conduction are physics issues that need to be addressed at both OMEGA and NIF scales. In addition, it will be critical to understand issues related to preheat from energetic electrons produced by two-plasmon decay at the NIF scale. OMEGA PD experiments with emphasis on adiabat and symmetry were presented and observations compared with *DRACO* simulations. Two different pulse shapes were studied and it was found that areal density and symmetry are modeled well. Near-term PD experiments on OMEGA will be used to study PD target performance at ignition-relevant intensities. Initial NIF experiments are also discussed. The goal of these early experiments is to understand and address issues relating to the effect of two-plasmon decay on preheat and cross-beam energy transfer on implosion energetics and potentially symmetry.

## ACKNOWLEDGMENT

This work was supported by the U.S. Department of Energy Office of Inertial Confinement Fusion under Cooperative Agreement No. DE-FC52-08NA28302, the University of Rochester, and the New York State Energy Research and Development Authority. The support of DOE does not constitute an endorsement by DOE of the views expressed in this article.

## REFERENCES

1. S. Skupsky, J. A. Marozas, R. S. Craxton, R. Betti, T. J. B. Collins, J. A. Delettrez, V. N. Goncharov, P. W. McKenty, P. B. Radha, T. R. Boehly, J. P. Knauer, F. J. Marshall, D. R. Harding, J. D. Kilkenny, D. D. Meyerhofer, T. C. Sangster, and R. L. McCrory, *Phys. Plasmas* **11**, 2763 (2004).
2. E. Moses, presented at The Seventh International Conference on Inertial Fusion Sciences and Applications, Bourdeaux-Lac, France, 12–16 September 2011.
3. T. J. B. Collins, J. A. Marozas, K. S. Anderson, R. Betti, R. S. Craxton, J. A. Delettrez, V. N. Goncharov, D. R. Harding, F. J. Marshall, R. L. McCrory, D. D. Meyerhofer, P. W. McKenty, P. B. Radha, A. Shvydky, S. Skupsky, and J. D. Zuegel, *Phys. Plasmas* **19**, 056308 (2012).
4. T. J. B. Collins, J. A. Marozas, and P. W. McKenty, *Bull. Am. Phys. Soc.* **57**, 155 (2012).
5. M. C. Herrmann, M. Tabak, and J. D. Lindl, *Nucl. Fusion* **41**, 99 (2001).
6. Lord Rayleigh, *Proc. London Math Soc.* **XIV**, 170 (1883); G. Taylor, *Proc. R. Soc. London Ser. A* **201**, 192 (1950).
7. C. D. Zhou and R. Betti, *Phys. Plasmas* **14**, 072703 (2007).
8. P. B. Radha, C. Stoeckl, V. N. Goncharov, J. A. Delettrez, D. H. Edgell, J. A. Frenje, I. V. Igumenshchev, J. P. Knauer, J. A. Marozas, R. L. McCrory, D. D. Meyerhofer, R. D. Petrasso, S. P. Regan, T. C. Sangster, W. Seka, and S. Skupsky, *Phys. Plasmas* **18**, 012705 (2011).
9. T. C. Sangster, V. N. Goncharov, R. Betti, T. R. Boehly, R. Epstein, C. Forrest, V. Yu. Glebov, S. X. Hu, I. V. Igumenshchev, D. H. Froula, R. L. McCrory, D. D. Meyerhofer, P. B. Radha, W. Seka, W. T. Shmayda, S. Skupsky, C. Stoeckl, J. A. Frenje, D. T. Casey, and M. Gatu-Johnson, *Bull. Am. Phys. Soc.* **57**, 200 (2012).
10. *LLE Review Quarterly Report* **130**, 72, Laboratory for Laser Energetics, University of Rochester, Rochester, NY, LLE Document No. DOE/NA/28302-1058 (2012).
11. P. B. Radha, J. A. Marozas, F. J. Marshall, A. Shvydky, T. J. B. Collins, V. N. Goncharov, R. L. McCrory, P. W. McKenty, D. D. Meyerhofer, T. C. Sangster, and S. Skupsky, *Phys. Plasmas* **19**, 082704 (2012).
12. F. J. Marshall, P. W. McKenty, J. A. Delettrez, R. Epstein, J. P. Knauer, V. A. Smalyuk, J. A. Frenje, C. K. Li, R. D. Petrasso, F. H. Séguin, and R. C. Mancini, *Phys. Rev. Lett.* **102**, 185004 (2009).
13. P. B. Radha, F. J. Marshall, T. R. Boehly, T. J. B. Collins, R. S. Craxton, R. Epstein, V. N. Goncharov, J. A. Marozas, R. L. McCrory, P. W. McKenty, D. D. Meyerhofer, T. C. Sangster, A. Shvydky, S. Skupsky, J. A. Frenje, and R. D. Petrasso, “Polar Drive on OMEGA,” submitted to the *European Physical Journal*.
14. V. N. Goncharov, T. C. Sangster, T. R. Boehly, S. X. Hu, I. V. Igumenshchev, F. J. Marshall, R. L. McCrory, D. D. Meyerhofer, P. B. Radha, W. Seka, S. Skupsky, C. Stoeckl, D. T. Casey, J. A. Frenje, and R. D. Petrasso, *Phys. Rev. Lett.* **104**, 165001 (2010); P. B. Radha, J. A. Marozas, F. J. Marshall, A. Shvydky, T. J. B. Collins, V. N. Goncharov, R. L. McCrory, P. W. McKenty, D. D. Meyerhofer, T. C. Sangster, and S. Skupsky, *Phys. Plasmas* **19**, 082704 (2012).

15. S. Skupsky, R. W. Short, T. Kessler, R. S. Craxton, S. Letzring, and J. M. Soures, *J. Appl. Phys.* **66**, 3456 (1989).
16. T. R. Boehly, V. A. Smalyuk, D. D. Meyerhofer, J. P. Knauer, D. K. Bradley, R. S. Craxton, M. J. Guardalben, S. Skupsky, and T. J. Kessler, *J. Appl. Phys.* **85**, 3444 (1999).
17. F. H. Séguin, C. K. Li, J. A. Frenje, D. G. Hicks, K. M. Green, S. Kurebayashi, R. D. Petrasso, J. M. Soures, D. D. Meyerhofer, V. Yu. Glebov, P. B. Radha, C. Stoeckl, S. Roberts, C. Sorce, T. C. Sangster, M. D. Cable, K. Fletcher, and S. Padalino, *Phys. Plasmas* **9**, 2725 (2002).
18. P. B. Radha, V. N. Goncharov, T. J. B. Collins, J. A. Delettrez, Y. Elbaz, V. Yu. Glebov, R. L. Keck, D. E. Keller, J. P. Knauer, J. A. Marozas, F. J. Marshall, P. W. McKenty, D. D. Meyerhofer, S. P. Regan, T. C. Sangster, D. Shvarts, S. Skupsky, Y. Srebro, R. P. J. Town, and C. Stoeckl, *Phys. Plasmas* **12**, 032702 (2005).
19. J. A. Marozas, F. J. Marshall, R. S. Craxton, I. V. Igumenshchev, S. Skupsky, M. J. Bonino, T. J. B. Collins, R. Epstein, V. Yu. Glebov, D. Jacobs-Perkins, J. P. Knauer, R. L. McCrory, P. W. McKenty, D. D. Meyerhofer, S. G. Noyes, P. B. Radha, T. C. Sangster, W. Seka, and V. A. Smalyuk, *Phys. Plasmas* **13**, 056311 (2006).
20. R. C. Malone, R. L. McCrory, and R. L. Morse, *Phys. Rev. Lett.* **34**, 721 (1975).
21. J. Delettrez, *Can. J. Phys.* **64**, 932 (1986).
22. R. A. Lerche, D. W. Phillion, and G. L. Tietbohl, *Rev. Sci. Instrum.* **66**, 933 (1995).
23. P. B. Radha, J. A. Delettrez, R. Epstein, S. Skupsky, J. M. Soures, S. Cremer, and R. D. Petrasso, *Bull. Am. Phys. Soc.* **44**, 194 (1999).
24. R. Betti and C. Zhou, *Phys. Plasmas* **12**, 110702 (2005).
25. J. J. MacFarlane *et al.*, *High Energy Density Phys.* **3**, 181 (2007).
26. R. A. Forties and F. J. Marshall, *Rev. Sci. Instrum.* **76**, 073505 (2005).
27. J. D. Lindl, *Inertial Confinement Fusion: The Quest for Ignition and Energy Gain Using Indirect Drive* (Springer-Verlag, New York, 1998), p. 154.
28. I. V. Igumenshchev, D. H. Edgell, V. N. Goncharov, J. A. Delettrez, A. V. Maximov, J. F. Myatt, W. Seka, A. Shvydky, S. Skupsky, and C. Stoeckl, *Phys. Plasmas* **17**, 122708 (2010).
29. J. A. Marozas and T. J. B. Collins, *Bull. Am. Phys. Soc.* **57**, 344 (2012).
30. A. Simon, R. W. Short, E. A. Williams, and T. Dewandre, *Phys. Fluids* **26**, 3107 (1983).
31. C. Stoeckl, R. E. Bahr, B. Yaakobi, W. Seka, S. P. Regan, R. S. Craxton, J. A. Delettrez, R. W. Short, J. Myatt, A. V. Maximov, and H. Baldis, *Phys. Rev. Lett.* **90**, 235002 (2003).
32. P. B. Radha, J. P. Knauer, T. C. Sangster, V. N. Goncharov, I. V. Igumenshchev, R. Betti, R. Epstein, D. D. Meyerhofer, and S. Skupsky, *Bull. Am. Phys. Soc.* **52**, 143 (2007).
33. C. Stoeckl, P. B. Radha, R. E. Bahr, J. A. Delettrez, D. H. Edgell, V. Yu. Glebov, V. N. Goncharov, I. V. Igumenshchev, T. C. Sangster, W. Seka, J. A. Frenje, and R. D. Petrasso, *Bull. Am. Phys. Soc.* **56**, 241 (2011).
34. M. N. Rosenbluth, *Phys. Rev. Lett.* **29**, 565 (1972).
35. D. A. Russell and D. F. DuBois, *Phys. Rev. Lett.* **86**, 428 (2001).
36. L. Divol, LLNL, private communication (2012).
37. A. M. Cok, R. S. Craxton, and P. W. McKenty, *Phys. Plasmas* **15**, 082705 (2008).
38. J. A. Marozas, S. P. Regan, J. H. Kelly, D. D. Meyerhofer, W. Seka, and S. Skupsky, *J. Opt. Soc. Am. B* **19**, 7 (2002).
39. D. T. Michel, C. Sorce, R. Epstein, N. Whiting, I. V. Igumenshchev, R. Jungquist, and D. H. Froula, *Rev. Sci. Instrum.* **83**, 10E530 (2012).

---

# Cross-Beam Energy Transfer in Polar-Drive Implosions on OMEGA

In the direct-drive approach to inertial confinement fusion, laser beams directly illuminate a spherical target, depositing their energy in the coronal plasma. This energy is transported to higher densities where ablation occurs and material rapidly expands, driving the nuclear fuel toward the center of the capsule. Symmetric illumination is required to produce a spherically symmetric drive. Ideally, the target is illuminated by a sufficient number of beams, distributed symmetrically around the target, to provide an adequately uniform drive with sufficient pressure to achieve ignition.<sup>1</sup>

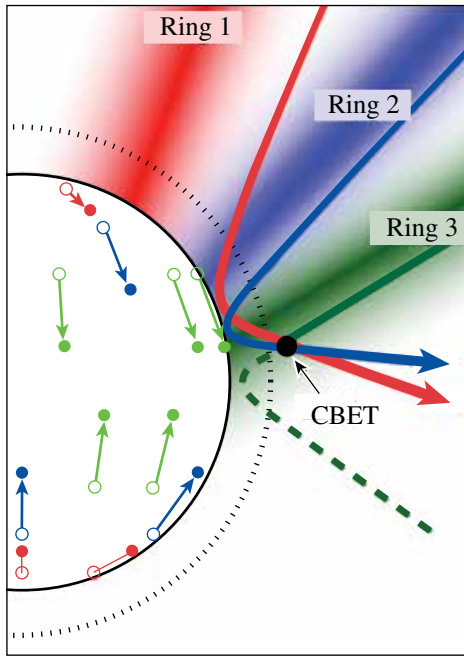
In the current x-ray drive configuration of the National Ignition Facility (NIF),<sup>2</sup> there are no laser beams near the equator of the target chamber and direct-drive experiments are performed in the polar-drive (PD) geometry.<sup>3</sup> PD creates a uniform implosion by combining and repointing the NIF beams toward the target equator, employing phase plates designed to create specific on-target spot sizes, pulse shaping, and shimming of the target layers.<sup>4</sup> The coupling of laser energy into the target can be decreased by cross-beam energy transfer (CBET)<sup>5–7</sup> between the lasers.

CBET occurs when laser light seeds stimulated Brillouin scattering (SBS) in a plasma by crossing two or more laser beams. This low-gain SBS can drive ion-acoustic waves and transfer a significant amount of energy from one of the crossing beams to the other. Hydrodynamic one-dimensional (1-D) modeling of symmetric 60-beam direct-drive implosions on OMEGA that do not include CBET physics overpredict the laser drive by 10% to 20% as indicated by discrepancies with the observed bang times and time-dependent scattered-light spectra.<sup>8–10</sup> Recently it was shown that decreasing the laser beams' radius with respect to the target radius reduces CBET and improves fusion yields.<sup>11</sup> The incorporation of CBET physics into the 1-D hydrodynamic modeling of symmetrically illuminated implosions produces good agreement with the observables, but the large scattering angles and three-dimensional (3-D) nature of the PD geometry has prevented previous CBET models from quantifying CBET in PD implosions.

CBET has been identified as a mechanism responsible for transferring significant amounts of energy between the NIF beams in indirect-drive hohlraum experiments.<sup>6</sup> Independently varying the wavelength of the NIF beams to control CBET is used to tune the implosion symmetry.<sup>12</sup> CBET in indirect-drive experiments occurs at relatively low densities and the angle between crossing beams is small, so the models that post-process the hydrodynamic simulations to calculate CBET can use a paraxial approximation.<sup>6,7,13</sup>

This article presents the first measurements of the effects of CBET in PD. The angular dependence of the unabsorbed light is measured to decrease from 1200 J/sr on the pole to 200 J/sr along the equator. These measurements and those of the unabsorbed light intensity and the spectra are reproduced by 3-D CBET modeling. These results indicate that CBET in PD reduces the absorbed energy by 10%. This reduction in absorption is consistent with the measurement of the bang time, which is ~180 ps later than predicted when CBET modeling is not included.<sup>14</sup> Calculations indicate that the drive symmetry is reduced by energy transferred from the center of beams pointed near the equator to the outer edge of the beams pointed near the pole. This drive symmetry can be recovered by shifting the relative wavelength of the beams in each cone but the overall reduction in absorption is not ameliorated. The model predicts that CBET can be mitigated by using smaller beam spots.

The CBET calculations in this polar-drive geometry were carried out by post-processing two-dimensional (2-D) hydrodynamic simulations using a 3-D CBET model. The time-varying coronal plasma parameters were calculated by the code *DRACO*,<sup>15</sup> where a Spitzer–Härm heat-transport model was used that limits the heat flow to a fraction ( $f = 0.06$ ) of the free-streaming flux.<sup>16</sup> The PD beam profiles in the CBET model are treated as the sum of many beamlets where the path and Doppler-shifted wavelength of each beamlet through the corona are determined by 3-D ray tracing (Fig. 133.29). This is a major difference between modeling CBET for polar drive and previous work modeling indirect-drive CBET, where the



E21825JR

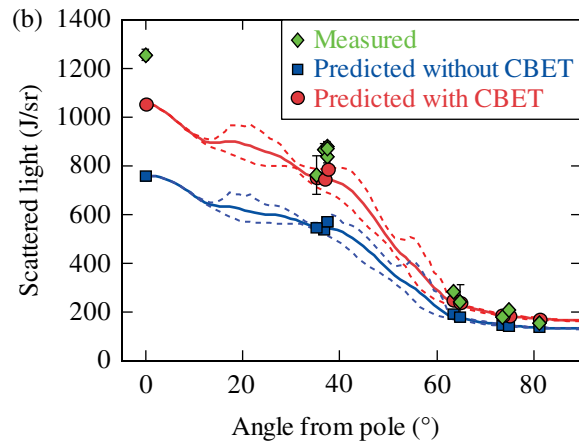
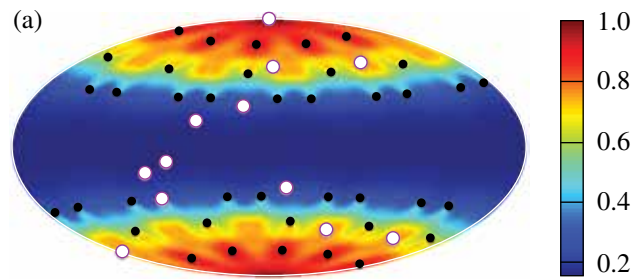
Figure 133.29 Pointing offsets for the beam rings for the polar-drive (PD) implosions on OMEGA used in this article: Ring 1 (red), Ring 2 (blue), and Ring 3 (green). Open circles show the pointing of each ring in symmetric drive (i.e., toward target chamber center); closed circles show the re-pointed PD geometry. The beamlets (rays) in the corona illustrate the effect of cross-beam energy transfer (CBET) on the laser illumination. The green Ring 3 beamlet directed toward the target equator is crossed by outgoing beamlets from Rings 1 and 2 before it reaches its nearest approach to the ablation surface, where it will be strongly absorbed. CBET scatters energy from this equatorial beamlet to the outgoing beamlets, reducing the energy deposition at the equator near the ablation surface.

refraction of the laser beams is ignored.<sup>13</sup> The CBET at crossings between beamlets for all PD beams is calculated from the SBS spatial gain length in the strong damping limit.<sup>9,17</sup>

The PD implosions used 40 ultraviolet ( $\lambda_0 = 351$  nm) OMEGA laser beams.<sup>18</sup> In the PD geometry, the beams are grouped into three rings with offset pointing toward the target equator as shown in Fig. 133.29. The laser beams were smoothed by polarization smoothing,<sup>18</sup> distributed phase plates,<sup>19</sup> and smoothing by spectral dispersion.<sup>20</sup> All beams used the same pulse shape and distributed phase plates with circular super-Gaussian ( $n = 4$ ) beam profiles, where 95% of the power is within a diameter of  $865 \mu\text{m}$ . The beams were incident on spherical CH capsules with  $27\text{-}\mu\text{m}$ -thick walls and a total diameter of  $866 \mu\text{m}$ . The targets were filled with 11.4 atm of  $\text{D}_2$ .

The angular dependence of the unabsorbed light was measured using 12 calorimeters located around the target chamber [Fig. 133.30(a)]. Four of these locations couple the unabsorbed light to a 1.25-m spectrometer with a Rochester Optical Streak System via optical fibers. This system has a spectral resolution of 0.05 nm and a temporal resolution of 90 ps.

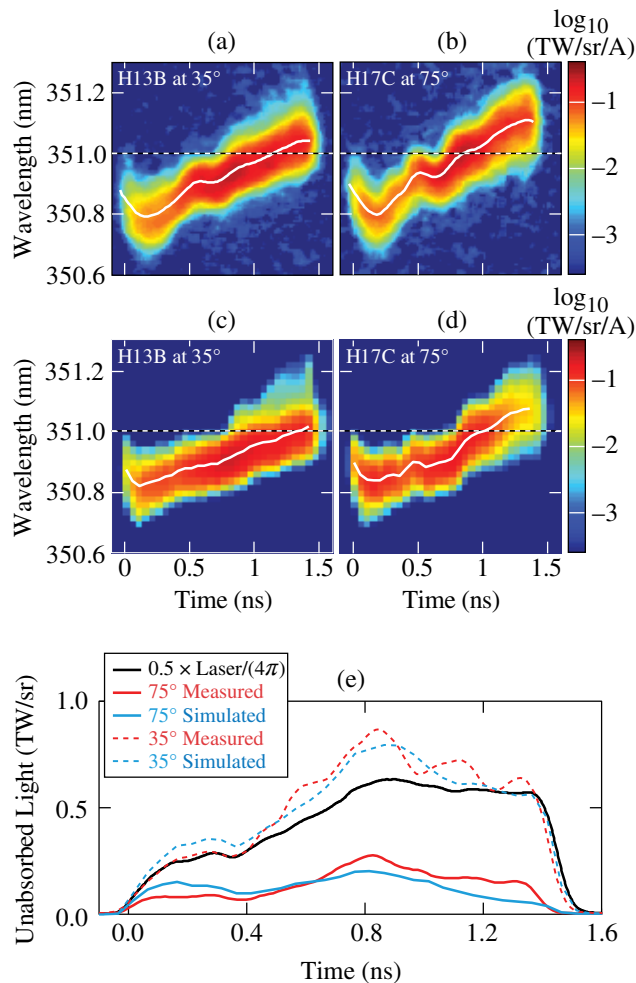
Figure 133.30(b) shows the time-integrated angular distribution of the light that is scattered (i.e., not absorbed) by the coronal plasma. A factor-of-6 more light is measured on the pole than the equator. This is in good agreement with calculations of the unabsorbed light when using the CBET model, and Fig. 133.30(b) shows that the unabsorbed light at all angles is significantly underestimated when the CBET model is not used.



E21281JR

Figure 133.30 (a) Aitoff projection of the calculated distribution of the normalized time-integrated scattered light over the inner surface of the OMEGA target chamber. White circles show the locations of the scattered-light calorimeters in the OMEGA chamber. Black dots represent the beam ports. (b) Time-integrated, unabsorbed-light radiant intensity as a function of angle from the PD symmetry axis as predicted without CBET modeling (blue squares), predicted with CBET modeling (red circles), and measured (green diamonds). The error bars on the measurements are the standard deviation of multiple measurements from nominally identical PD implosions. The solid lines show the model calculations of the mean value of the radiant intensity, while the dashed lines show the calculated minimum/maximum range around the target azimuthally.

Figure 133.31 shows that, in addition to the total integrated scattered power, the CBET model accurately predicts the time-varying spectrally resolved details of unabsorbed light from the PD implosions. The measured spectra from two polar angles [Figs. 133.31(a) and 133.31(b)] show the variation in wavelength and power of the unabsorbed light. This variation is the result of the time-varying optical path length of the light traveling through the coronal plasma. The initial blue shift in the spectra occurs as the light propagates through a rapidly increasing electron density when the plasma is formed.<sup>21</sup> The blue shift



E21538JR

Figure 133.31

Unabsorbed laser light spectra measured at (a) 35° and (b) 75° from the PD pole along with the respective simulated spectra [(c) and (d)]. (e) The time-varying radiant intensity of the measured (red curves) and simulated (blue curves) unabsorbed laser light. Shown for reference is the radiant intensity that would result if the total incident laser power (black curve) were spread evenly over  $4\pi$  steradian (divided by 2 for convenient scaling).

results partially from the outward movement of the plasma's critical-density surface (a moving-mirror Doppler shift) and partially from the outward buildup of the coronal plasma that reduces the optical path length of the laser light because plasma has a smaller index of refraction than vacuum. As the plasma scale length reaches a steady state, the plasma's critical-density surface implodes, red shifting the unabsorbed light.

Figures 133.31(c) and 133.31(d) show the time-varying spectral intensity calculated by the CBET model. The important features present in the measured spectra are reproduced, indicating the accuracy of the hydrodynamic modeling used to calculate coronal plasma conditions. The discrepancy in the magnitude of the initial blue shift in the spectra is similar to that observed for symmetric drive implosions when a flux-limited heat-transport model was used. A nonlocal electron-transport model was required to accurately model the initial blue-shifted unabsorbed light for symmetric implosions.<sup>9</sup> The flux-limited model predicts shorter density scale-lengths than the nonlocal model, resulting in a slower initial outward movement of the plasma's critical-density surface and less coronal plasma density along the laser light's optical paths. Both effects decrease the predicted initial blue shift of the unabsorbed light spectrum.

The time-varying radiant intensity (TW/sr) of the unabsorbed light shown in Fig. 133.31(e) is obtained by integrating the spectra over wavelength. The calculations are in good agreement with the measurements. The accuracy of the scattered-light predictions given by the CBET model allows one to draw conclusions about the effect of CBET on the drive energetics during a PD implosion and to suggest possible CBET mitigation strategies.

Calculations indicate that CBET reduces the absorption from 85% to 76% and that this reduction is disproportionately distributed among the rings. The closer the ring is pointed to the equator, the more it is affected by CBET. The absorption in Ring 1 (the most-polar ring) drops to 82%, while Ring 3 (the most-equatorial ring) has its absorption reduced to 72% by CBET. This is consistent with the measured bang time being ~180 ps later than predicted when CBET is not included in the hydrodynamics code.<sup>14</sup>

The location where CBET occurs in PD is illustrated in Fig. 133.32. For all three beam rings, CBET results in a net loss of energy from the center portion of the beam profiles. This central portion includes the beamlets with the smallest impact parameters that penetrate farthest into the coronal plasma. In

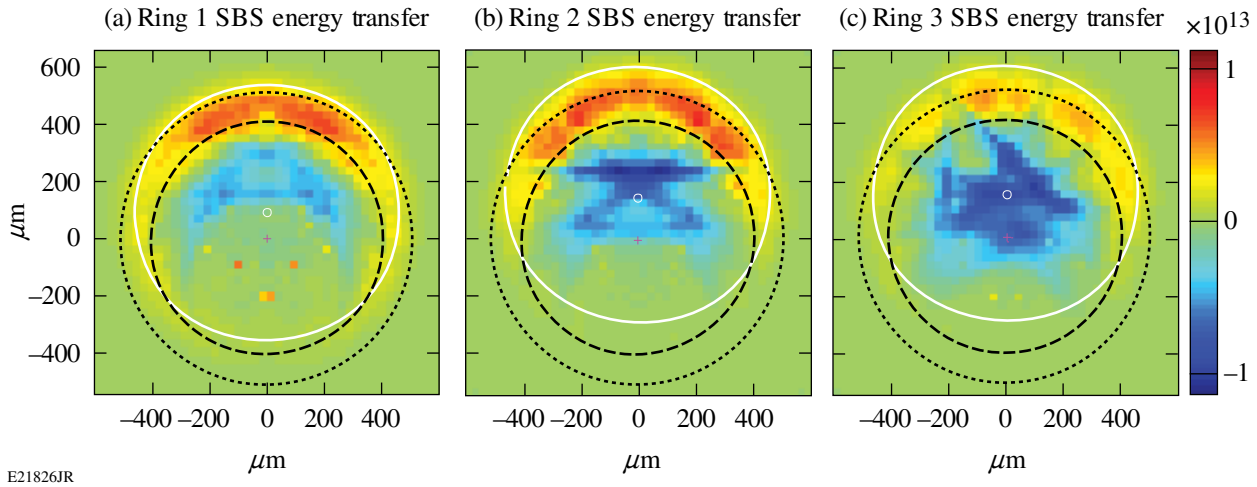


Figure 133.32

The normalized energy transferred for each OMEGA PD beam ring: (a) Ring 1, (b) Ring 2, and (c) Ring 3. The position of each pixel is the launch point of a beamlet, the sum of which represents the beam profile of one of the beams in an OMEGA PD beam ring. The magnitude of each pixel is the relative net energy transferred into (positive/red) or out of (negative/blue) a beamlet integrated along the path of each beamlet. The black curves show the position of the target’s critical surface (dashed) and quarter-critical surfaces (dotted) with respect to the launched position of the beamlets. The white curve is the 95% power contour of the laser-beam spot.

the absence of CBET, these beamlets deposit their energy closest to the ablation surface and would most efficiently drive the target. In contrast, beamlets with impact parameters outside the plasma’s critical-density radius gain a net amount of energy from CBET but are less efficiently absorbed. In effect, energy is transferred from the drive-efficient, small-impact-parameter beamlets to the less-efficient, higher-impact-parameter beamlets, resulting in reduced hydrodynamic efficiency.

The distribution of CBET over the beam profiles suggests a possible strategy to reducing its detrimental effect on driving the target: eliminating the high-impact-parameter beamlets that “steal” energy from the drive-efficient beamlets. The CBET model predicts that for the coronal plasma conditions in the OMEGA PD implosions, the overall absorption loss to CBET can be recovered using 30%-smaller beam radii. This improvement comes from a combination of reducing CBET and concentrating the beam energy into the more-efficient, low-impact-parameter beamlets. The effect of smaller spot sizes on implosion symmetry should be studied because PD implosions require some high-impact-parameter beamlets to direct energy toward the equator for symmetry.

Figure 133.33 illustrates the effect that varying the wavelength of the laser beams has on the energy absorbed from each ring. The predicted CBET among the rings is altered when laser

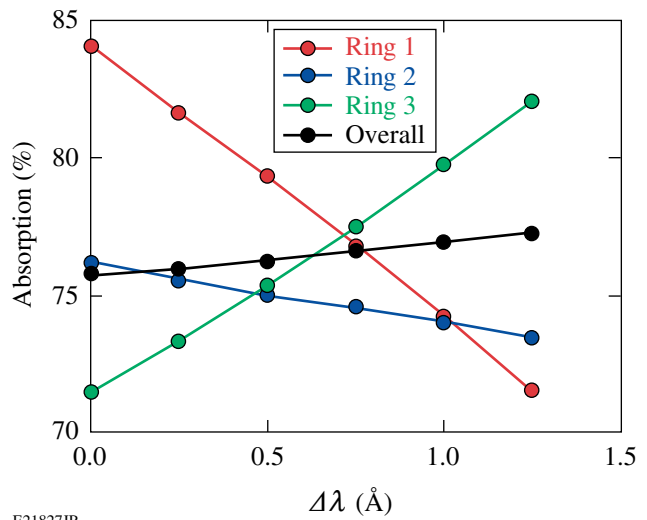


Figure 133.33

The absorption in each PD ring varies significantly when there is a difference in wavelength between the rings. Here  $\Delta\lambda$  is the separation in wavelength between the rings. For example if  $\Delta\lambda = 1 \text{ \AA}$ , the wavelength of Ring 3 is  $1 \text{ \AA}$  greater than Ring 2, which has a wavelength  $1 \text{ \AA}$  greater than Ring 1.

beams of different rings have different wavelengths. The flow of energy is biased toward the beams in the rings with the longer wavelengths. When the wavelengths of the beams in all rings are equal ( $\Delta\lambda = 0$ ), CBET between the beams in Rings 1 and 3

results in a net gain for the beams in Ring 1 and a net loss for Ring 3 beams. As the wavelength separation between the beams in different rings increases (with Ring 3's wavelength growing larger than Ring 1's), the net transfer between Rings 1 and 3 is reduced and eventually reverses until the beams in Ring 3 experience a net gain in energy from CBET with beams in Ring 1. At wavelength shifts greater than  $\sim 0.75 \text{ \AA}$ , the absorbed energy from beams in Ring 3 is greater than that from beams in Ring 1. The change in absorption for beams in Ring 2 is less pronounced. As  $\Delta\lambda$  increases, the beams in Ring 2 take more energy from beams in Ring 1, which is offset by losing energy to beams in Ring 3. The overall energy absorption is nearly constant as  $\Delta\lambda$  increases because gains by one ring are offset by losses in another. These results suggest that the power balance of the rings in a PD implosion can be controlled by independently setting the wavelengths of the rings with wavelength separations of the order of  $1 \text{ \AA}$  (Ref. 7). This makes it possible to control the symmetry of a PD implosion.

In summary, measurements of the angular dependence of the unabsorbed light during polar-drive implosions at the Omega Laser Facility have been recorded. The radiant intensity of the unabsorbed light decreases from 1200 J/sr on the pole to 200 J/sr along the equator. The measured unabsorbed light intensity and spectrum are in good agreement with predictions from a 3-D CBET model. The modeling shows that CBET reduces the overall laser absorption in PD by  $\sim 10\%$ . The ring of beams directed toward the PD equator is compromised most severely. The modeling provides insight into two possible CBET mitigation strategies. The location where the energy transfer occurs suggests that reducing the spot size will reduce the CBET losses. This is supported by modeling with small spot sizes where the laser absorption increased by  $\sim 10\%$ . The modeling shows that the flow of energy between the PD beam rings can be manipulated by varying the wavelength separation between the rings. This could be used to regulate the power balance between the rings and exert control over the implosion symmetry. These results will help guide upcoming polar-drive experiments on the NIF, where 1.5 MJ of laser energy will be used to implode  $\sim 2$ -mm-diam capsules with the ultimate goal of producing fusion.<sup>4</sup>

#### ACKNOWLEDGMENT

We acknowledge the OMEGA operations team whose efforts enabled us to perform these polar-drive experiments. This work was supported by the U.S. Department of Energy Office of Inertial Confinement Fusion under Cooperative Agreement No. DE-FC52-08NA28302, the University of Rochester, and the New York State Energy Research and Development Authority. The support of DOE does not constitute an endorsement by DOE of the views expressed in this article.

#### REFERENCES

1. J. Nuckolls, L. Wood, A. Thiessen, and G. Zimmerman, *Nature* **239**, 139 (1972); V. N. Goncharov, T. C. Sangster, T. R. Boehly, S. X. Hu, I. V. Igumenshchev, F. J. Marshall, R. L. McCrory, D. D. Meyerhofer, P. B. Radha, W. Seka, S. Skupsky, C. Stoeckl, D. T. Casey, J. A. Frenje, and R. D. Petrasso, *Phys. Rev. Lett.* **104**, 165001 (2010).
2. E. I. Moses, *Fusion Sci. Technol.* **44**, 11 (2003).
3. S. Skupsky, J. A. Marozas, R. S. Craxton, R. Betti, T. J. B. Collins, J. A. Delettrez, V. N. Goncharov, P. W. McKenty, P. B. Radha, T. R. Boehly, J. P. Knauer, F. J. Marshall, D. R. Harding, J. D. Kilkenny, D. D. Meyerhofer, T. C. Sangster, and R. L. McCrory, *Phys. Plasmas* **11**, 2763 (2004).
4. T. J. B. Collins, J. A. Marozas, K. S. Anderson, R. Betti, R. S. Craxton, J. A. Delettrez, V. N. Goncharov, D. R. Harding, F. J. Marshall, R. L. McCrory, D. D. Meyerhofer, P. W. McKenty, P. B. Radha, A. Shvydky, S. Skupsky, and J. D. Zuegel, *Phys. Plasmas* **19**, 056308 (2012).
5. C. J. Randall, J. R. Albritton, and J. J. Thomson, *Phys. Fluids* **24**, 1474 (1981).
6. P. Michel *et al.*, *Phys. Rev. Lett.* **102**, 025004 (2009).
7. P. Michel *et al.*, *Phys. Rev. E* **83**, 046409 (2011).
8. W. Seka, D. H. Edgell, J. P. Knauer, J. F. Myatt, A. V. Maximov, R. W. Short, T. C. Sangster, C. Stoeckl, R. E. Bahr, R. S. Craxton, J. A. Delettrez, V. N. Goncharov, I. V. Igumenshchev, and D. Shvarts, *Phys. Plasmas* **15**, 056312 (2008).
9. I. V. Igumenshchev, D. H. Edgell, V. N. Goncharov, J. A. Delettrez, A. V. Maximov, J. F. Myatt, W. Seka, A. Shvydky, S. Skupsky, and C. Stoeckl, *Phys. Plasmas* **17**, 122708 (2010).
10. I. V. Igumenshchev, W. Seka, D. H. Edgell, D. T. Michel, D. H. Froula, V. N. Goncharov, R. S. Craxton, L. Divol, R. Epstein, R. Follett, J. H. Kelly, T. Z. Kosc, A. V. Maximov, R. L. McCrory, D. D. Meyerhofer, P. Michel, J. F. Myatt, T. C. Sangster, A. Shvydky, S. Skupsky, and C. Stoeckl, *Phys. Plasmas* **19**, 056314 (2012).
11. D. H. Froula, I. V. Igumenshchev, D. T. Michel, D. H. Edgell, R. Follett, V. Yu. Glebov, V. N. Goncharov, J. Kwiatkowski, F. J. Marshall, P. B. Radha, W. Seka, C. Sorce, S. Stagnitto, C. Stoeckl, and T. C. Sangster, *Phys. Rev. Lett.* **108**, 125003 (2012).
12. S. H. Glenzer *et al.*, *Science* **327**, 1228 (2010).
13. P. Michel *et al.*, *Phys. Plasmas* **17**, 056305 (2010).
14. P. B. Radha, J. A. Marozas, F. J. Marshall, A. Shvydky, T. J. B. Collins, V. N. Goncharov, R. L. McCrory, P. W. McKenty, D. D. Meyerhofer, T. C. Sangster, and S. Skupsky, *Phys. Plasmas* **19**, 082704 (2012).
15. P. B. Radha, V. N. Goncharov, T. J. B. Collins, J. A. Delettrez, Y. Elbaz, V. Yu. Glebov, R. L. Keck, D. E. Keller, J. P. Knauer, J. A. Marozas, F. J. Marshall, P. W. McKenty, D. D. Meyerhofer, S. P. Regan, T. C. Sangster, D. Shvarts, S. Skupsky, Y. Srebro, R. P. J. Town, and C. Stoeckl, *Phys. Plasmas* **12**, 032702 (2005).

16. R. C. Malone, R. L. McCrory, and R. L. Morse, *Phys. Rev. Lett.* **34**, 721 (1975).
17. J. Myatt, A. V. Maximov, W. Seka, R. S. Craxton, and R. W. Short, *Phys. Plasmas* **11**, 3394 (2004).
18. T. R. Boehly, V. A. Smalyuk, D. D. Meyerhofer, J. P. Knauer, D. K. Bradley, R. S. Craxton, M. J. Guardalben, S. Skupsky, and T. J. Kessler, *J. Appl. Phys.* **85**, 3444 (1999).
19. Y. Lin, T. J. Kessler, and G. N. Lawrence, *Opt. Lett.* **20**, 764 (1995).
20. S. Skupsky, R. W. Short, T. Kessler, R. S. Craxton, S. Letzring, and J. M. Squires, *J. Appl. Phys.* **66**, 3456 (1989).

---

# Measured Hot-Electron Intensity Thresholds Quantified by a Two-Plasmon–Decay Resonant Common-Wave Gain in Various Experimental Configurations

## Introduction

In inertial confinement fusion (ICF), a spherical capsule is imploded using multiple laser beams to produce an energetic fusion reaction by compressing nuclear fuel to high densities and temperatures.<sup>1</sup> In the direct-drive scheme,<sup>2</sup> the capsule is uniformly illuminated by overlapping beams, and in the indirect-drive scheme,<sup>3</sup> the laser beams are first converted into x rays that then illuminate the capsule. In both schemes, the laser beams can drive the two-plasmon–decay (TPD) instability.<sup>4–8</sup> When TPD is driven strongly, an extended spectrum of large-amplitude electron plasma waves (EPW's) is generated that accelerates electrons to high energies ( $\sim 100$  keV) (Refs. 9–12). These electrons can deposit their energy in the fuel (preheat), reducing the compression efficiency and potentially inhibiting ICF ignition. Although no experiments have definitively measured the effects of preheat, hydrodynamic simulations that include an *ad hoc* hot-electron model indicate low-adiabat ignition designs can survive  $\sim 0.1\%$  of laser energy converted into hot electrons and coupled to the fusion fuel.<sup>13</sup>

The TPD instability results from the decay of an electromagnetic wave into two electron plasma waves.<sup>4,5</sup> Phase matching, energy conservation, and the dispersion relations of the waves limit the instability to a small region near the quarter-critical density surface. Stability calculations of a single linearly polarized electromagnetic wave show that the absolute threshold of the instability is proportional to  $I_s L_n / T_e$ , where  $I_s$  is the laser-beam intensity,  $L_n$  is the plasma density scale length, and  $T_e$  is the electron temperature of the plasma at the quarter-critical density.<sup>6</sup> More-recent particle-in-cell (PIC) simulations have shown the importance of convective mode in the nonlinear stage that also depends on  $I_s L_n / T_e$  (Ref. 14). Multibeam experiments have shown that hot-electron production scales with the overlapped vacuum laser-beam intensity ( $I_{\text{OVP}}$ ) (Ref. 15) independent of the number of beams used. This scaling is not expected if the laser beams drive TPD independently. To explain these results, a multibeam model was proposed where different laser beams share a common electron plasma wave.<sup>16,17</sup> Recent experiments at the Omega Laser Facility<sup>18,19</sup> showed that the overlapped intensity threshold for hot-electron

generation depends on the laser-beam and target geometries.<sup>20</sup> A model that calculates the homogeneous, multibeam, TPD growth rate shows that beams that share the same angle with respect to the common-wave vector can couple through the resonant common electron plasma wave and that this coupling occurs in the region in  $k$  space bisecting the laser beams.<sup>21</sup> In this common-wave region, the TPD growth rate depends on the geometry and the polarization of the laser beams.

This article reports on the measured hot-electron fraction generated by TPD in planar experiments using one to four linearly polarized beams, 18 beams with polarization smoothing, and, in spherical experiments, 60 beams with polarization smoothing. The overlapped intensity threshold for hot-electron generation is different for each experimental configuration. These measured thresholds are compared with convective gains calculated with the resonant common-wave model.

The following sections describe (1) the various experimental configurations; (2) the experimental results, where the overlapped intensity threshold for hot-electron generation is observed to be different for the various experimental configurations; and (3) the multibeam TPD resonant common-wave growth rate for linearly polarized beams and beams with polarization smoothing. Next, the common-wave gain is shown to be consistent with observed variations in the TPD thresholds, followed by the conclusions.

## Experimental Setup

The experiments discussed here were designed to measure the intensity thresholds for the production of hot electrons while varying different parameters in the common-wave gain. On OMEGA EP,<sup>19</sup> the hot-electron fraction was measured in planar geometry as a function of the laser energy for one-, two-, and four-beam configurations to study the variation of the hot-electron production with a maximum normalized growth rate that depends on the polarization and geometry of the laser beams. The four-beam results were compared to OMEGA planar experiments, where 18 beams distributed in three cones were used to study the variation in the hot-electron production

with the number of beams that contribute to the common-wave TPD. The planar experiments are compared to OMEGA experiments in spherical geometry to measure the variation in the hot-electron production with the plasma parameters.

## 1. Laser Setup

**a. OMEGA EP planar geometry.** In the OMEGA EP experiments, four vertically polarized 351-nm beams intersected the target at an angle of  $23^\circ$  with respect to the target normal [Fig. 133.34(a)]. The focal spots of the beams were spatially overlapped to within  $20\ \mu\text{m}$ . The beams used 2-ns flattop laser pulses that were co-timed to within 50 ps. Two sets of distributed phase plates (DPP's)<sup>22</sup> were used [860- $\mu\text{m}$  full width at half maximum (FWHM) for Beams 1 and 2 and 800- $\mu\text{m}$  FWHM for Beams 3 and 4] to produce an  $\sim 1$ -mm-diam, ninth-order super-Gaussian intensity profile. A maximum single-beam energy of 2.0 kJ (2.6 kJ) was used on Beams 1 and 2 (3 and 4), resulting in peak single-beam intensities  $I_{\text{max}} = 1.8 \times 10^{14}\ \text{W/cm}^2$  ( $I_{\text{max}} = 2.6 \times 10^{14}\ \text{W/cm}^2$ ). Experiments were performed using one beam; two beams in a horizontal configuration (Beams 1 and 4), vertical configuration (Beams 1 and 3), and diagonal configuration (Beams 1 and 2); and four beams [Fig. 133.34(a)].

**b. OMEGA planar geometry.** In the OMEGA planar experiments, 18 beams at a wavelength of 351 nm intersected the

target in three cones of six beams at angles of  $23^\circ$ ,  $48^\circ$ , and  $63^\circ$  with respect to the target normal [Fig. 133.34(b)]. The beams were spatially overlapped to within  $20\ \mu\text{m}$ . The beams used 2-ns flattop laser pulses that were co-timed to within 10 ps. All beams were smoothed by polarization smoothing (PS)<sup>23</sup> and DPP's (710- $\mu\text{m}$  FWHM) to produce an  $\sim 1$ -mm-diam, fourth-order super-Gaussian intensity profile. The single-beam energy ranged from 240 J to 380 J, providing a peak single-beam intensity ranging from  $3.4 \times 10^{13}\ \text{W/cm}^2$  to  $5.4 \times 10^{13}\ \text{W/cm}^2$ .

**c. OMEGA spherical geometry.** In the OMEGA spherical experiments, 60 laser beams at 351 nm smoothed by PS and DPP's (710- $\mu\text{m}$  FWHM) uniformly illuminated an 860- $\mu\text{m}$ -diam spherical target [Fig. 133.34(c)]. The beams were pointed with an accuracy of  $20\ \mu\text{m}$ . The beams used 1-ns flattop laser pulses that were co-timed to within 10 ps. The 60 laser beams used a total energy of 13 kJ to 29.5 kJ to produce a spherically symmetric illumination of the target. The peak single-beam intensity was varied from  $5 \times 10^{13}\ \text{W/cm}^2$  to  $1.2 \times 10^{14}\ \text{W/cm}^2$ .

## 2. Targets

**a. Planar geometry.** For the planar experiments on both OMEGA and OMEGA EP, the laser beams illuminated a 30- $\mu\text{m}$ -thick CH layer deposited on 30  $\mu\text{m}$  of Mo and backed with an additional 30  $\mu\text{m}$  of CH. Hydrodynamic simulations using the two-dimensional (2-D) code *DRACO*<sup>24</sup> indicated that

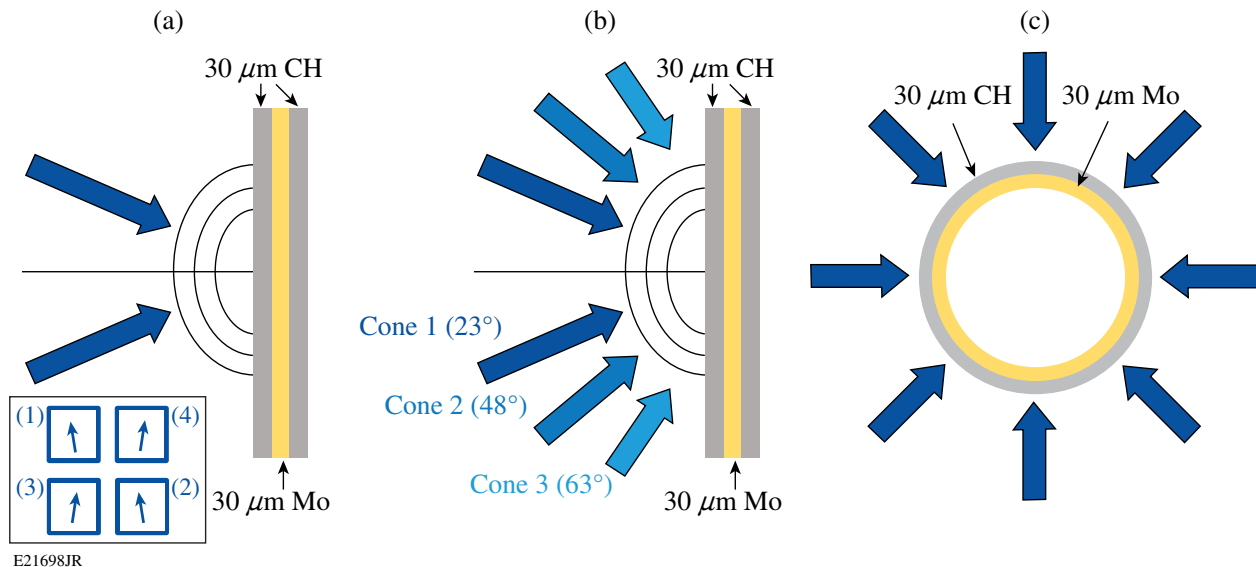


Figure 133.34

Schematic of the laser-beam configurations on (a) OMEGA EP, (b) OMEGA (planar geometry), and (c) OMEGA (spherical geometry). In OMEGA EP experiments, the polarizations of the beams are  $8^\circ$  from vertical [inset in (a)], and in OMEGA experiments, the beams used polarization smoothing.

the laser light interacted with the first layer, producing a CH plasma with density and temperature profiles that depended (for each configuration) only on the overlapped laser intensity. For the experimental conditions presented here, the hydrodynamic profiles near quarter-critical density reached steady state after about 1.5 ns. After this time, the calculated quantity  $I_{\text{ovr,q}}L_{\text{n,q}}/T_{\text{e,q}}$  varied by less than 10% at the quarter-critical density (the subscript “q” refers to quantities at the quarter-critical density surface).

For the OMEGA EP experiments, the overlapped laser intensity was increased from  $1.5 \times 10^{14}$  W/cm<sup>2</sup> to  $7 \times 10^{14}$  W/cm<sup>2</sup>, the density scale length ( $L_{\text{n,q}}$ ) increased from 260  $\mu\text{m}$  to 360  $\mu\text{m}$ , and the electron temperature ( $T_{\text{e,q}}$ ) increased from 1.5 keV to 2.5 keV; the ratio  $L_{\text{n,q}}/T_{\text{e,q}}$  was nearly constant over this intensity range ( $\approx 160$   $\mu\text{m}/\text{keV}$ ). The laser intensity at quarter-critical density was about half the vacuum intensity.

For the OMEGA planar experiments, the overlapped laser intensity was increased from  $4 \times 10^{14}$  W/cm<sup>2</sup> to  $6.5 \times 10^{14}$  W/cm<sup>2</sup>, the density scale length ( $L_{\text{n,q}}$ ) increased from 260  $\mu\text{m}$  to 320  $\mu\text{m}$ , and the electron temperature ( $T_{\text{e,q}}$ ) increased from 2 keV to 2.4 keV; the ratio  $L_{\text{n,q}}/T_{\text{e,q}}$  was nearly constant over this intensity range ( $\approx 135$   $\mu\text{m}/\text{keV}$ ). The overlapped laser intensity at quarter-critical density was about half the vacuum overlapped intensity.

**b. Spherical geometry.** In the spherical experiments, the laser beams illuminated an 800- $\mu\text{m}$ -diam, 30- $\mu\text{m}$ -thick Mo shell coated with 30  $\mu\text{m}$  of CH. Hydrodynamic simulations using the one-dimensional (1-D) code *LILAC*<sup>25</sup> showed that the laser light interacted only with the CH layer and the hydrodynamic profiles near quarter-critical density reached a steady state after about 0.5 ns. After this time, the calculated quantity  $I_{\text{ovr,q}}L_{\text{n,q}}/T_{\text{e,q}}$  varied by less than 10%, where  $I_{\text{ovr,q}} \equiv P_{\text{L,q}}/4\pi R_{\text{q}}^2$ ,  $P_{\text{L,q}}$  is the laser power at the quarter-critical-density surface, and  $R_{\text{q}}$  is the radius of the quarter-critical-density surface. When the overlapped laser intensity was increased from  $5 \times 10^{14}$  W/cm<sup>2</sup> to  $12 \times 10^{14}$  W/cm<sup>2</sup>, the density scale length ( $L_{\text{n,q}}$ ) increased from 120  $\mu\text{m}$  to 140  $\mu\text{m}$  and the electron temperature ( $T_{\text{e,q}}$ ) increased from 2.1 keV to 2.2 keV; the ratio  $L_{\text{n,q}}/T_{\text{e,q}}$  was nearly constant over this intensity range ( $\approx 60$   $\mu\text{m}/\text{keV}$ ). The overlapped laser intensity at quarter-critical density (570  $\mu\text{m}$ ) was about half the overlapped vacuum intensity.

### 3. Diagnostics

Two principal diagnostics were used to determine the amount of laser energy converted to hot electrons: an x-ray spectrometer

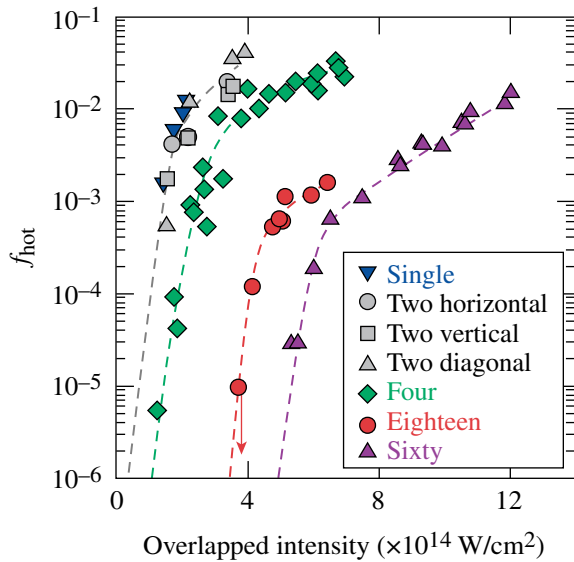
(XRS)<sup>26–28</sup> and a hard x-ray detector (HXRD).<sup>29</sup> Monte Carlo simulations using the code *EGSnrc*<sup>30</sup> were used to determine the total hot-electron energy ( $E_{\text{e}}$ ) given the measured hard x-ray temperature and the total energy in the  $\text{K}_{\alpha}$  emission.<sup>26</sup>

**a. X-ray spectrometer.** The XRS measures the energy emitted into the Mo  $\text{K}_{\alpha}$  emission line ( $E_{\text{K}_{\alpha}}$ ) using an absolutely calibrated planar LiF crystal spectrometer that views the target from the laser’s incident side at an angle of 63° from the target normal<sup>26</sup> on OMEGA EP, 37.4° from the target normal on OMEGA planar experiments, and along the target normal for spherical experiments. The Monte Carlo simulations show that electrons with energies less than 120 keV are stopped in the Mo. The 17.5-keV Mo  $\text{K}_{\alpha}$  line is sufficiently energetic so that photoexcitation from the 2.5-keV coronal plasma region does not contribute to the  $\text{K}_{\alpha}$ -emission measurement.

**b. Hard x-ray detector.** The hard x-ray detector consists of a three-channel filtered scintillator array that measures the x-ray radiation generated by the hot electrons in the Mo above  $\sim 40$  keV,  $\sim 60$  keV, and  $\sim 80$  keV (Ref. 29). The hard x-ray detector views the back of the target at an angle of 40° from the target normal on OMEGA EP and 42° from the target normal on OMEGA planar experiments. The hard x-ray temperature is estimated using the exponentially decreasing x-ray energies measured by the three channels. The relative error in the measurement of the slope ( $T_{\text{rad}}$ ) in the hard x-ray spectrum is 20%. Monte Carlo simulations indicate that the hard x-ray temperature is a good measure of the hot-electron temperature  $T_{\text{hot}}$  ( $T_{\text{rad}} \simeq T_{\text{hot}}$ ) (Ref. 26).

## Experimental Results

Figure 133.35 shows that for all configurations tested, the hot-electron fraction defined as the fraction of laser energy converted to hot electrons ( $f_{\text{hot}}$ ) increases exponentially with the overlapped vacuum laser-beam intensities and, at high intensities, the increase is much slower. The rapid increase in hot-electron production at low intensities is used to determine an intensity threshold defined as the overlapped intensity when the hot-electron fraction is equal to  $10^{-4}$  (near the detector threshold). For one and two linearly polarized beams in the horizontal, vertical, and diagonal configuration (OMEGA EP planar geometry), a similar evolution with the overlapped-laser-beam intensity is measured and a hot-electron-production threshold of  $I_{\text{th}} \sim 10^{14}$  W/cm<sup>2</sup> is inferred. For the four-beam configuration (OMEGA EP planar geometry), the threshold dependence on the overlapped intensity is increased by a factor of 2 and a threshold of  $I_{\text{th}} \sim 2 \times 10^{14}$  W/cm<sup>2</sup> is measured. A factor-of-2 further increase in the



E21699JR

Figure 133.35

Hot-electron fraction ( $f_{\text{hot}}$ ) as a function of vacuum overlapped laser intensity. Single, two, and four correspond to OMEGA EP planar experiments where the beams are linearly polarized; 18 (60) corresponds to OMEGA planar (spherical) experiments where the beams have polarization smoothing. The dashed lines are drawn to guide the eye. In each case, the overlapped intensity at quarter-critical density is about half the vacuum overlapped intensity. For the 18-beam configuration, at an overlapped intensity of  $4 \times 10^{14}$  W/cm<sup>2</sup>, the signal was lower than the diagnostic detection threshold (red arrow).

intensity threshold ( $I_{\text{th}} \sim 4.2 \times 10^{14}$  W/cm<sup>2</sup>) is observed for the 18-beam configuration (OMEGA planar geometry). In spherical geometry, the intensity threshold is  $\sim 3\times$  higher than for the four-beam configuration ( $I_{\text{th}} \sim 6 \times 10^{14}$  W/cm<sup>2</sup>). These data underline the fact that the hot-electron intensity threshold depends strongly on the experimental configuration.

The measured rapid growth of the hot-electron fraction with the laser intensity is consistent with the exponential growth expected for convective TPD. This suggests that nonlinear mechanisms that may occur at low intensities are not sufficient to saturate the growth of the electron plasma waves. At higher intensities, the increase in the hot-electron fraction with laser intensity is reduced, suggesting that the TPD growth is affected by a nonlinear saturation mechanism.

Time-resolved data obtained with HXRD show that the hot-electron production occurs toward the end of the laser pulse. The instantaneous hot-electron fraction at the end of the pulse is typically a factor of  $\sim 2$  higher than the value aver-

aged over the entire pulse.<sup>12</sup> These hot-electron measurements account for all electrons produced. In a fusion experiment, the hot-electron energy coupled to the core is expected to be significantly reduced by the divergence of the electrons angle and the variation in their energy.

### Common-Wave Modeling

In this section, the resonant-TPD growth rate is calculated for multiple laser beams. The growth rate is shown to depend on the beam geometry, the beam polarization, and the sum of the intensities of the beams that share the same angle with the common electron plasma wave vector. For multiple laser beams with polarization smoothing, the maximum normalized growth rate is shown to be constant and independent of the geometry of the beams.

The multibeam coupling is relevant to calculations of both absolute growth or the convective TPD amplification. To interpret the experimental results described above, the convective gain was derived following the Rosenbluth method,<sup>14,31</sup> which assumes that the common plasma wave propagates parallel to a linear density profile.

#### 1. Multiple Linearly Polarized Beams

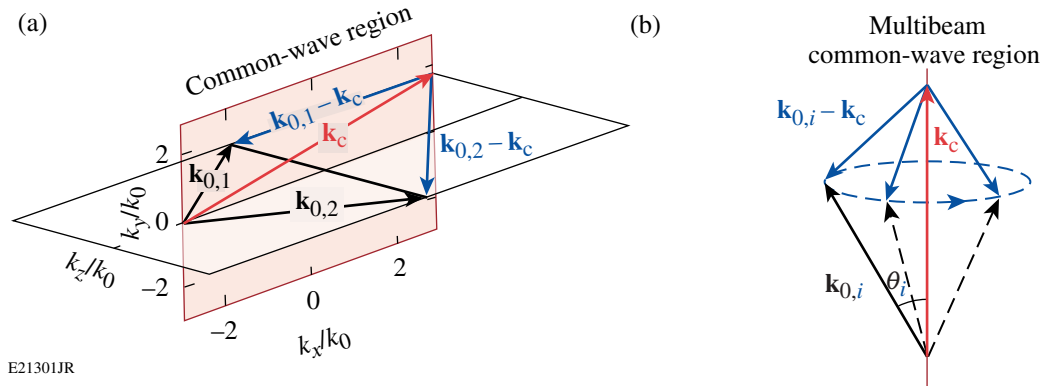
In the case of multiple laser beams driving a common electron plasma wave with frequency and wave vector ( $\omega_c, \mathbf{k}_c$ ), the dispersion relation for the common wave is  $\omega_c^2 = \omega_{pe}^2 + 3\mathbf{k}_c^2 v_{\text{th},e}^2$  and for the corresponding daughter waves

$$(\omega_c - \omega_0)^2 = \omega_{pe}^2 + 3|\mathbf{k}_c - \mathbf{k}_{0,i}|^2 v_{\text{th},e}^2,$$

where  $v_{\text{th},e}$  is the electron thermal velocity and  $\omega_0$  and  $\mathbf{k}_{0,i}$  (with a magnitude  $k_0$  independent of  $i$ ) are the frequency and the wave vector of beam  $i$ . A common-wave region is defined where a resonant process exists and is determined by satisfying the dispersion relations for all laser beams and electron plasma waves leading to

$$\theta_i = \text{const}, \text{ for } i = 1 \dots n, \quad (1)$$

where  $\theta_i$  is the angle between  $\mathbf{k}_{0,i}$  and  $\mathbf{k}_c$ . All laser beams that drive a resonant common electron plasma wave must share the same angle with the common wave. For a two-beam configuration, Fig. 133.36(a) shows that this condition defines a plane in  $k$  space bisecting the wave vectors of the two laser beams. For more than two symmetrically oriented laser beams, Fig. 133.36(b) shows that this condition restricts the resonant common waves to a line.



E21301JR

Figure 133.36

(a) The common-wave region for two beams is given by a plane that bisects the wave vectors ( $\mathbf{k}_{0,1}, \mathbf{k}_{0,2}$ ) of the laser beams (red plane). (b) A common electron plasma wave (EPW) can be driven only by multiple laser beams that share the same angle to the common-wave vector ( $\theta_i$ ) to satisfy the dispersion relation for each daughter EPW ( $|\mathbf{k}_{0,i} - \mathbf{k}_c| = \text{const}$ ).

The dispersion relation for the common wave is derived following the TPD linear theory for the conditions where the collision frequency is much smaller than the growth rate

$$D(\omega_c, \gamma, |\mathbf{k}_c|) = - \sum_i \frac{(\gamma_{0,i}^2)^{\text{SB}}}{D(\omega_c - \omega_0, \gamma, |\mathbf{k}_c - \mathbf{k}_{0,i}|)}, \quad (2)$$

where the superscript SB refers to single beam,  $\gamma$  is the temporal growth rate,

$$D(\omega, \gamma, |\mathbf{k}|) = \left\{ \left[ 1 - \omega_{\text{pe}}^2 / \omega^2 (1 + 3k^2 \lambda_{\text{De}}^2) \right] \omega / 2 + i\gamma \right\}$$

is the dispersion relation,  $\lambda_{\text{De}} = v_{\text{th},e} / \omega_{\text{pe}}$  is the Debye length, and  $\omega_{\text{pe}}$  is the electron plasma frequency. The single-beam growth rate is given by  $(\gamma_{0,i}^2)^{\text{SB}} = f_c (\gamma_{0,i}^2)_{\text{max}}^{\text{SB}} \cos^2 \alpha$ , where  $\alpha$  is the angle between the electric-field polarization vector and the common-wave vector and

$$f_c = \left[ (k_c^2 - |\mathbf{k}_c - \mathbf{k}_0|^2) / k_0 |\mathbf{k}_c - \mathbf{k}_0| \right]^2.$$

The maximum single-beam growth rate squared is

$$(\gamma_{0,\text{max}}^2)^{\text{SB}} = 2 / (cn_e m_e) (k_0 / 2)^2 I_i,$$

where  $c$  is the light velocity,  $m_e$  is the electron mass,  $n_c = m_e \omega_0^2 / 4\pi e^2$  is the critical density, and  $e$  is the electron charge.

To evaluate the maximum value of the growth rate, the minimum value of  $D(\omega, \gamma, |\mathbf{k}_c - \mathbf{k}_{0,i}|)$  is determined by ensuring that the dispersion relations for all daughter

waves are satisfied [i.e., Eq. (1) is satisfied]. It follows that  $D(\omega_c - \omega_0, \gamma, |\mathbf{k}_c - \mathbf{k}_{0,i}|) = \gamma = \text{const}$  and the temporal growth rate is given from Eq. (2) by

$$(\gamma_0^2)^{\text{MB}} = \sum_i (\gamma_{0,i}^2)^{\text{SB}}. \quad (3)$$

The common-wave growth rate is normalized to the maximum single-beam growth rate calculated for the overlapped intensity of the beams contributing to the common wave ( $I_\Sigma$ ):

$$(\Gamma_0^2)^{\text{MB}} = \frac{(\gamma_0^2)^{\text{MB}}}{(\gamma_0^2)_{\text{max}}^{\text{SB}, I_\Sigma}} = f_c \sum_i \cos^2(\alpha_i) \beta_i, \quad (4)$$

where  $\beta_i = I_i / I_\Sigma$ ,  $I_i$  is the intensity of the laser beam  $i$ , and  $\alpha_i$  is the angle between the electric-field polarization vector and the common-wave vector. To determine the dominant common electron plasma wave, a maximum normalized growth rate  $[(\Gamma_0^2)_{\text{max}}^{\text{MB}}]$  is calculated that depends only on the geometry and polarizations of the laser beams. The convective gain is given by

$$G_c = 6 \times 10^{-2} \frac{I_\Sigma L_n \lambda_0}{T_e} (\Gamma_0^2)_{\text{max}}^{\text{MB}}, \quad (5)$$

where  $I_\Sigma$  is in units of  $10^{14}$  W/cm<sup>2</sup>,  $L_n$  is in  $\mu\text{m}$ ,  $T_e$  is in keV, and  $\lambda_0$  is the laser wavelength in  $\mu\text{m}$ .

## 2. Multibeams with Polarization Smoothing

For more than two beams, the common-wave region defines a line [ $I_c$  displayed in Figs. 133.37(a) and 133.37(b)] and the growth rate for multiple beams is equal to the sum of the

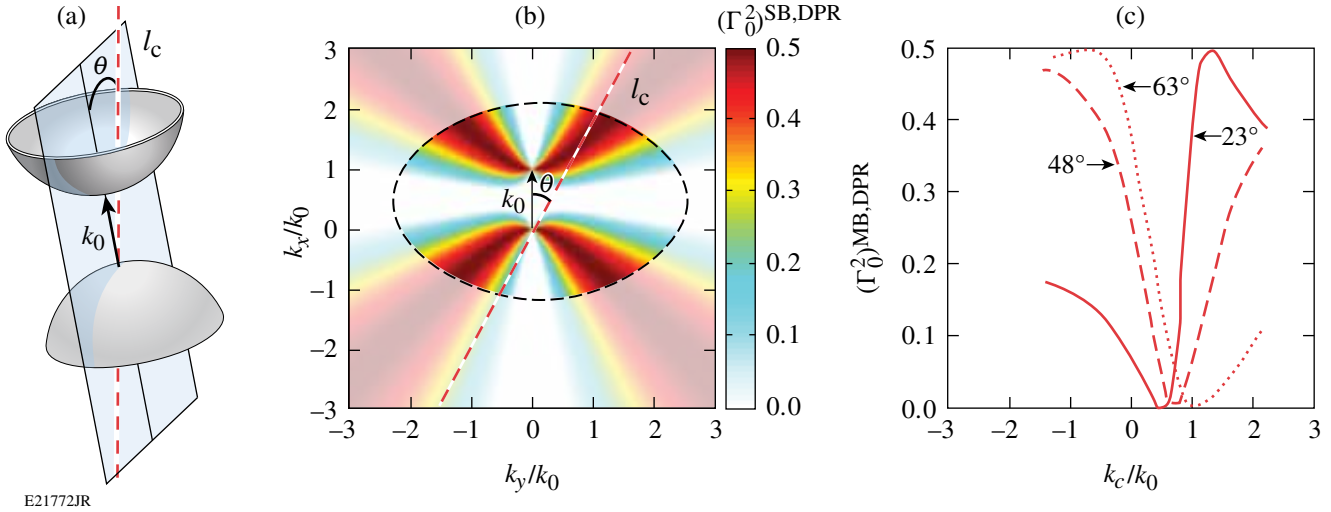


Figure 133.37

(a) A 3-D representation of the maximum growth rate for a single beam with polarization smoothing (gray hyperboloids). Multiple beams with polarization smoothing can couple through the common wave along the common-wave line ( $l_c$ , red dashed line) at an angle  $\theta$ . (b) Normalized single-beam with polarization smoothing growth rate in the plane ( $\mathbf{k}_0, l_c$ ). The Landau cutoff ( $k\lambda_{De} = 0.25$ , where  $k$  is the maximum value between  $k_c$  and  $|\mathbf{k}_c - \mathbf{k}_0|$ ) for  $T_e = 2$  keV is represented with a black dashed line. The normalized multibeam growth rate is equal to the single-beam growth rate along  $l_c$ . (c) Normalized multibeam growth rate calculated along the common-wave line for  $\theta = 23^\circ$  (solid red line),  $\theta = 48^\circ$  (dashed red line), and  $\theta = 63^\circ$  (dotted red line). The cutoff for small and large  $\mathbf{k}_c$  corresponds to the Landau cutoff calculated for  $T_e = 2$  keV.

growth rate for a single beam along this line [applying Eq. (3)]. Since the growth rate is azimuthally symmetric around  $\mathbf{k}_0$  for each beam (Appendix A) and Eq. (1) must be satisfied, the growth rate along  $l_c$  is equal for each beam. The growth rate for multiple beams is given by the single-beam growth rate times the number of beams ( $N_\Sigma$ ) that can drive the common wave  $\left[ (\gamma_0^2)^{\text{MB,PS}} = N_\Sigma (\gamma_0^2)^{\text{SB,PS}} \right]$ . The multibeam growth rate is normalized to the maximum single-beam growth rate  $\left[ (\gamma_0^2)_{\text{max}}^{\text{SB,I}_\Sigma} = N_\Sigma (\gamma_0^2)_{\text{max}}^{\text{SB,I}_s} \right]$ , resulting in a factor that depends only on the beam geometry

$$(\Gamma_0^2)^{\text{MB,PS}} = (\Gamma_0^2)^{\text{SB,PS}} = \frac{1}{2} f_c \sin^2 \theta. \quad (6)$$

To determine the maximum normalized growth rate, the common-wave line is plotted over the top of the single-beam growth rate calculated in the plane ( $\mathbf{k}_0, l_c$ ) [Fig. 133.37(b)]. The multibeam normalized growth rate along the common-wave line is plotted in Fig. 133.37(c) for three angles. For most conditions, the common-wave line crosses the maximum normalized single-beam growth rate: for small values of  $\theta$  [solid red curve in Fig. 133.37(c)], the common-wave line crosses the upper hyperbola and for large values of  $\theta$  [dotted red line in Fig. 133.37(c)], the common-wave line crosses the lower hyperbola. In these two cases, the maximum normalized

multibeam growth rate with PS is  $(\Gamma_0^2)_{\text{max}}^{\text{MB,PS}} = 0.5$ . When the common-wave line does not intersect the hyperbola, the maximum normalized multibeam growth rate is slightly reduced [dashed red line in Fig. 133.37(c)]. The range of angles where the common-wave line does not cross the hyperbolas is given by the Landau cutoff and is, in general, small. The common-wave gain for multibeams with PS is given by

$$G_c^{\text{PS}} = 3 \times 10^{-2} \frac{I_\Sigma L_n \lambda_0}{T_e} \quad (7)$$

and, contrary to the gain in the case of polarized beams, does not depend on the geometry of the beams except as noted above. These results are consistent with the initial experiments that demonstrate multibeam effects on hot-electron generation.<sup>15</sup>

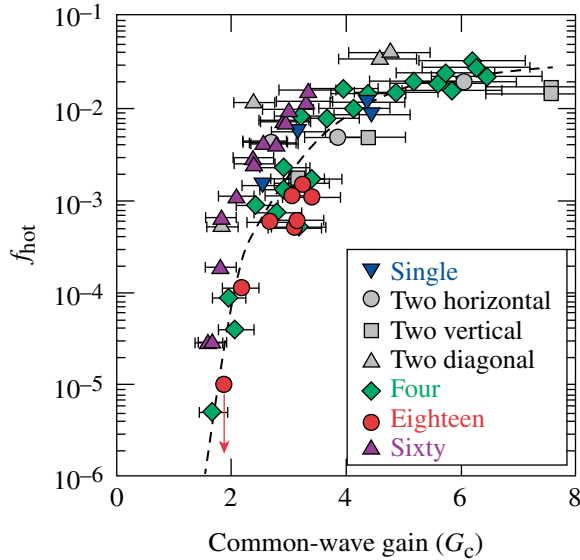
### Interpretation of Experimental Results

In this section, the experimental results are discussed in the context of the common-wave model, where each experimental configuration was designed to vary a different parameter in the gain  $\left[ (\Gamma_0^2)_{\text{max}}^{\text{MB}}, N_\Sigma/N_{\text{beam}}$ , and  $L_{n,q}/T_{e,q}$  (Table 133.VI) ]. Figure 133.38 shows that the common-wave gain reproduces the measured hot-electron intensity thresholds shown in Fig. 133.35. For all laser-beam configurations, a gain threshold of  $\sim 2$  is observed and a saturation is measured for  $G_c \gtrsim 3$ . This thresh-

Table 133.VI: List of parameters defining the common-wave gain that were varied during the experiments.  $N_\Sigma$  is the number of beams that share an equivalent angle with the common electron plasma wave [see Eq. (3)] with the largest growth rate,  $L_{n,q}/T_{e,q}$  is in units of  $\mu\text{m}/\text{keV}$ ;  $(I_{\Sigma,q})_{\text{th}}^{\text{MB}}$  is in units of  $10^{14} \text{ W}/\text{cm}^2$ .

Configuration	$N_{\text{beam}}$	$(\Gamma_0^2)_{\text{max}}^{\text{MB}}$	$N_\Sigma$	$L_{n,q}/T_{e,q}$	$(I_{\Sigma,q})_{\text{th}}^{\text{MB}}$
Single	1	1.0	1	175	0.5
Two vertical	2	1.0	2	175	0.5
Two horizontal	2	0.8	2	175	0.7
Two diagonal	2	0.6	2	175	0.9
Four	4	0.5	4	175	1.1
Eighteen	18	0.5	6	135	1.4
Sixty	60*	0.5	6	60	3.1

\*The number of beams that contribute in spherical geometry on OMEGA to the total overlapped intensity is  $\sim 20$ .



E21699JR2

Figure 133.38  
The hot-electron fraction is plotted as a function of the common-wave gain for each experimental configuration tested.

old is about  $5\times$  lower than required for significant convective amplification from thermal noise. This discrepancy could be attributed to enhanced Langmuir wave noise, modified density profiles,<sup>32</sup> or laser speckles.<sup>33</sup>

The experimental results can be used to calculate an intensity threshold for hot-electron production from Eq. (5), when the convective gain is equal to 2, given by

$$(I_{\Sigma,q})_{\text{th}}^{\text{MB}} = \frac{94}{(L_{n,q}/T_{e,q})(\Gamma_0^2)_{\text{max}}^{\text{MB}}} \quad (8)$$

The intensity threshold for the different configurations is computed in Table 133.VI.

### 1. Beam Geometry and Polarization

On OMEGA EP, the maximum normalized growth rate was varied between the different configurations by changing the beam geometry and polarization while the other parameters remained constant (Table 133.VI). For the one- and two-beam configurations, a similar hot-electron production as a function of intensity is observed (Fig. 133.35). This demonstrates that for the two-beam configuration, the TPD is driven by a multi-beam process. For the four-beam configuration, the observed factor-of-2 increase in the intensity threshold (Fig. 133.35) is explained by the factor-of-2 decrease in the maximum normalized growth rate (Eq. 4) (Ref. 21).

The spectrum in  $k$  space where the normalized growth rate is maximum is larger for the single-beam configuration than for the two-beam configuration, whereas the maximum normalized growth rate is similar. The fact that the hot-electron fraction produced by the one-beam and two-beam configurations is similar suggests that the  $k$ -space volume of the large EPW's plays a minor role in the generation of hot electrons and that the hot-electron production depends, to first order, on the maximum normalized growth rate.

### 2. Number of Contributing Beams

In the 18-beam configuration on OMEGA, only a third of the beams contribute to the common-wave process, and the intensity that contributes to the maximum growth rate is reduced by 50% from the total overlapped intensity at the quarter-critical density. This is the primary explanation for the experimentally observed increase in the overlapped intensity threshold

(Fig. 133.35), where the beams are arranged in three cones of six at three different angles. As a result of the common-wave condition [Eq. (1)], each cone drives a different common wave and the coupling that dominates the TPD growth is the one with the largest growth rate. Since the beams were smoothed by polarization smoothing in this experiment, the coupling with the largest growth rate corresponds to the cone that has the highest intensity at the quarter-critical density. *LILAC* simulations indicate that the beams in the  $23^\circ$  cone have the highest intensity at the quarter-critical density ( $I_{\Sigma,q}^{23^\circ} = 0.6 I_{\text{OVR},q}$ ,  $I_{\Sigma,q}^{48^\circ} = 0.3 I_{\text{OVR},q}$ , and  $I_{\Sigma,q}^{63^\circ} = 0.1 I_{\text{OVR},q}$ ). This result is consistent with the experiments reported in Ref. 8, where the hot-electron generation was shown to depend only on the intensity of the beams of a single cone.

### 3. Plasma Parameters

The difference in the 18-beam and 60-beam thresholds observed in Fig. 133.35 is primarily a result of the difference in the plasma parameters,  $L_{n,q}/T_{e,q}$  (Table 133.VI). For the spherical results, the maximum number of beams that are symmetrically oriented is six, arranged in a hexagon [a nine-beam coupling also exists but the large angle between the target normal and the beams ( $63^\circ$ ) significantly reduces their intensity at quarter-critical density]. As in the OMEGA planar experiments, the beams in the  $23^\circ$  cone produce the largest common-wave gain.

### Conclusions

These experimental results indicate that the hot-electron threshold depends on the hydrodynamic parameters at the quarter-critical density, the configuration of the laser beams, and the sum of the intensity of the beams that share the same angle with the common-wave vector. A TPD model where multiple laser beams can share a common electron plasma wave has been presented. The resonant common-wave process occurs only when the multiple laser beams share the same angle with the common EPW. This creates a common-wave region where a maximum growth rate defines the dominant EPW, independent of the plasma conditions. To compare with the experimental results, the maximum common-wave growth rate is used to calculate a convective gain.

The experiments were designed to measure the threshold for hot-electron production while varying the different parameters [ $N_\Sigma$ ,  $(\Gamma_0^2)_{\text{max}}^{\text{MB}}$ ,  $I_s$ ,  $L_n/T_e$ ] in the common-wave gain. A significant increase in the hot-electron intensity threshold was observed when the maximum normalized growth rate was reduced by using four beams compared to one or two beams. A further reduction was observed when the number of beams that

can contribute to the common wave was reduced by distributing 18 beams into three cones. The overlapped intensity threshold was observed to be different for the various experimental configurations and is explained by the common-wave TPD model.

The common-wave theory is consistent with the initial experiments that first demonstrated multibeam effects on hot-electron generation.<sup>15</sup> In these experiments, the hot-electron fraction was shown to be independent of the number of beams. The beams that were varied were from the same cone and therefore shared the same common plasma wave. These results can be applied to the indirect-drive experiments reported in Ref. 8 that showed the dependence of hot-electron generation on the intensity of the beams in a single cone.

### ACKNOWLEDGMENT

This work was supported by the U.S. Department of Energy Office of Inertial Confinement Fusion under Cooperative Agreement No. DE-FC52-08NA28302, the University of Rochester, and the New York State Energy Research and Development Authority. The support of DOE does not constitute an endorsement by DOE of the views expressed in this article.

### Appendix A: Single Beam with Polarization Smoothing

Polarization smoothing employs a birefringent crystal that separates the incident linearly polarized laser beam into two beams with orthogonal polarizations propagating at a slight angle ( $\sim 40 \mu\text{rad}$ ) with respect to each other. The angle is small compared to the  $f$  number (25 mrad) of the laser beam so that the  $k$ -vectors of the two beams can be treated equivalently. From the normalized common-wave growth rate [Eq. (4)] and the fact that the intensity is equivalent between the two polarizations ( $I_{\parallel} = I_{\perp} = I_{\Sigma}/2$ ), the normalized growth rate for a single beam with a PS is given by

$$\begin{aligned} (\Gamma_0^2)^{\text{SB,PS}} &= f_c \left[ \frac{I_{\parallel}}{I_{\Sigma}} \cos^2(\alpha_{\parallel}) + \frac{I_{\perp}}{I_{\Sigma}} \cos^2(\alpha_{\perp}) \right] \\ &= 0.5 f_c \sin^2(\theta), \end{aligned} \quad (\text{A1})$$

where  $\parallel$  ( $\perp$ ) refers to the parallel (perpendicular) polarized beam, and from Fig. 133.39, it is apparent that

$$\begin{aligned} \cos^2(\alpha_{\parallel}) + \cos^2(\alpha_{\perp}) &= \frac{(\mathbf{k}_c \cdot \mathbf{e}_{\parallel})^2 + (\mathbf{k}_c \cdot \mathbf{e}_{\perp})^2}{k_c^2} \\ &= \frac{\mathbf{k}_c^2}{k_c^2} = \sin^2 \theta, \end{aligned} \quad (\text{A2})$$

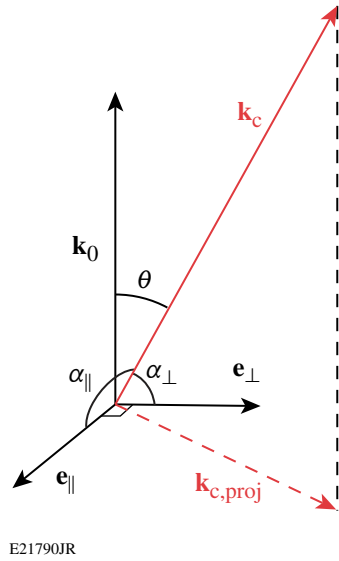


Figure 133.39  
The projection of the common-wave vector  $\mathbf{k}_c$  in the plane  $(\mathbf{e}_{\parallel}, \mathbf{e}_{\perp})$  for a single beam with a polarization smoothing (PS).

where  $\mathbf{e}_{\parallel}$  ( $\mathbf{e}_{\perp}$ ) is the polarization vector of the parallel (perpendicular) polarized beam and  $\mathbf{k}_{c,\text{proj}}$  is the projection of  $\mathbf{k}_c$  onto the plane  $(\mathbf{e}_{\parallel}, \mathbf{e}_{\perp})$ .

Equation (A1) shows that for a single beam with polarization smoothing, the growth rate in  $k$  space is symmetric around  $\mathbf{k}_0$  ( $f_c$  depends only on  $|\mathbf{k}_c|$ ,  $|\mathbf{k}_0|$ , and  $|\mathbf{k}_c - \mathbf{k}_0|$ ). When  $\mathbf{k}_c$  is in the plane  $(\mathbf{k}_0, \mathbf{e}_{\parallel})$ , the term  $\mathbf{k}_c \cdot \mathbf{e}_{\perp}$  cancels out and the normalized growth rate is simply equal to half the normalized growth rate for a beam with parallel polarization calculated in the polarization plane. Due to symmetry, the maximum growth rate is 0.5 and in  $k$  space defines two hyperboloids [Fig. 133.37(a)]. In each plane that contains  $\mathbf{k}_0$ , the growth rate is equal to half the growth rate calculated for a linearly polarized single beam calculated in the polarization plane [Fig. 133.37(b)].

## REFERENCES

1. J. Nuckolls *et al.*, *Nature* **239**, 139 (1972).
2. R. L. McCrory, D. D. Meyerhofer, R. Betti, R. S. Craxton, J. A. Delettrez, D. H. Edgell, V. Yu. Glebov, V. N. Goncharov, D. R. Harding, D. W. Jacobs-Perkins, J. P. Knauer, F. J. Marshall, P. W. McKenty, P. B. Radha, S. P. Regan, T. C. Sangster, W. Seka, R. W. Short, S. Skupsky, V. A. Smalyuk, J. M. Soures, C. Stoeckl, B. Yaakobi, D. Shvarts, J. A. Frenje, C. K. Li, R. D. Petrasso, and F. H. Séguin, *Phys. Plasmas* **15**, 055503 (2008).
3. J. D. Lindl *et al.*, *Phys. Plasmas* **11**, 339 (2004).
4. M. V. Goldman, *Ann. Phys.* **38**, 117 (1966).
5. C. S. Liu and M. N. Rosenbluth, *Phys. Fluids* **19**, 967 (1976).
6. A. Simon, R. W. Short, E. A. Williams, and T. Dewandre, *Phys. Fluids* **26**, 3107 (1983).
7. W. Seka, D. H. Edgell, J. F. Myatt, A. V. Maximov, R. W. Short, V. N. Goncharov, and H. A. Baldis, *Phys. Plasmas* **16**, 052701 (2009).
8. S. P. Regan, N. B. Meezan, L. J. Suter, D. J. Strozzi, W. L. Krueer, D. Meeker, S. H. Glenzer, W. Seka, C. Stoeckl, V. Yu. Glebov, T. C. Sangster, D. D. Meyerhofer, R. L. McCrory, E. A. Williams, O. S. Jones, D. A. Callahan, M. D. Rosen, O. L. Landen, C. Sorce, and B. J. MacGowan, *Phys. Plasmas* **17**, 020703 (2010).
9. D. W. Phillion *et al.*, *Phys. Rev. Lett.* **49**, 1405 (1982).
10. J. F. Myatt, J. Zhang, J. A. Delettrez, A. V. Maximov, R. W. Short, W. Seka, D. H. Edgell, D. F. DuBois, D. A. Russell, and H. X. Vu, *Phys. Plasmas* **19**, 022707 (2012).
11. R. Yan, C. Ren, J. Li, A. V. Maximov, W. B. Mori, Z. M. Sheng, and F. S. Tsung, *Phys. Rev. Lett.* **108**, 175002 (2012).
12. D. H. Froula, B. Yaakobi, S. X. Hu, P.-Y. Chang, R. S. Craxton, D. H. Edgell, R. Follett, D. T. Michel, J. F. Myatt, W. Seka, R. W. Short, A. Solodov, and C. Stoeckl, *Phys. Rev. Lett.* **108**, 165003 (2012).
13. *LLE Review Quarterly Report* **79**, 131, Laboratory for Laser Energetics, University of Rochester, Rochester, NY, LLE Document No. DOE/SF/19460-317, NTIS Order No. DE2002762802 (1999). (Copies may be obtained from the National Technical Information Service, Springfield, VA 22161.)
14. R. Yan, A. V. Maximov, C. Ren, and F. S. Tsung, *Phys. Rev. Lett.* **103**, 175002 (2009).
15. C. Stoeckl, R. E. Bahr, B. Yaakobi, W. Seka, S. P. Regan, R. S. Craxton, J. A. Delettrez, R. W. Short, J. Myatt, A. V. Maximov, and H. Baldis, *Phys. Rev. Lett.* **90**, 235002 (2003).
16. A. V. Maximov, J. Myatt, R. W. Short, W. Seka, and C. Stoeckl, *Bull. Am. Phys. Soc.* **52**, 195 (2007).
17. R. W. Short, *Bull. Am. Phys. Soc.* **53**, 245 (2008).
18. T. R. Boehly, D. L. Brown, R. S. Craxton, R. L. Keck, J. P. Knauer, J. H. Kelly, T. J. Kessler, S. A. Kumpan, S. J. Loucks, S. A. Letzring, F. J. Marshall, R. L. McCrory, S. F. B. Morse, W. Seka, J. M. Soures, and C. P. Verdon, *Opt. Commun.* **133**, 495 (1997).
19. J. H. Kelly, L. J. Waxer, V. Bagnoud, I. A. Begishev, J. Bromage, B. E. Kruschwitz, T. J. Kessler, S. J. Loucks, D. N. Maywar, R. L. McCrory, D. D. Meyerhofer, S. F. B. Morse, J. B. Oliver, A. L. Rigatti, A. W. Schmid, C. Stoeckl, S. Dalton, L. Folsbee, M. J. Guardalben, R. Jungquist, J. Puth, M. J. Shoup III, D. Weiner, and J. D. Zuegel, *J. Phys. IV France* **133**, 75 (2006).
20. D. H. Froula, D. T. Michel, I. V. Igumenshchev, S. X. Hu, B. Yaakobi, J. F. Myatt, D. H. Edgell, R. Follett, V. Yu. Glebov, V. N. Goncharov, T. J. Kessler, A. V. Maximov, P. B. Radha, T. C. Sangster, W. Seka, R. W. Short, A. A. Solodov, C. Sorce, and C. Stoeckl, *Plasma Phys. Control. Fusion* **54**, 124016 (2012).

21. D. T. Michel, A. V. Maximov, R. W. Short, S. X. Hu, J. F. Myatt, W. Seka, A. A. Solodov, B. Yaakobi, and D. H. Froula, *Phys. Rev. Lett.* **109**, 155007 (2012).
22. T. J. Kessler, Y. Lin, J. J. Armstrong, and B. Velazquez, in *Laser Coherence Control: Technology and Applications*, edited by H. T. Powell and T. J. Kessler (SPIE, Bellingham, WA, 1993), Vol. 1870, pp. 95–104.
23. T. R. Boehly, V. A. Smalyuk, D. D. Meyerhofer, J. P. Knauer, D. K. Bradley, R. S. Craxton, M. J. Guardalben, S. Skupsky, and T. J. Kessler, *J. Appl. Phys.* **85**, 3444 (1999).
24. P. B. Radha, T. J. B. Collins, J. A. Delettrez, Y. Elbaz, R. Epstein, V. Yu. Glebov, V. N. Goncharov, R. L. Keck, J. P. Knauer, J. A. Marozas, F. J. Marshall, R. L. McCrory, P. W. McKenty, D. D. Meyerhofer, S. P. Regan, T. C. Sangster, W. Seka, D. Shvarts, S. Skupsky, Y. Srebro, and C. Stoeckl, *Phys. Plasmas* **12**, 056307 (2005).
25. J. Delettrez, *Can. J. Phys.* **64**, 932 (1986).
26. B. Yaakobi, P.-Y. Chang, A. A. Solodov, C. Stoeckl, D. H. Edgell, R. S. Craxton, S. X. Hu, J. F. Myatt, F. J. Marshall, W. Seka, and D. H. Froula, *Phys. Plasmas* **19**, 012704 (2012).
27. B. Yaakobi, C. Stoeckl, T. Boehly, D. D. Meyerhofer, and W. Seka, *Phys. Plasmas* **7**, 3714 (2000).
28. B. Yaakobi, C. Stoeckl, W. Seka, J. A. Delettrez, T. C. Sangster, and D. D. Meyerhofer, *Phys. Plasmas* **12**, 062703 (2005).
29. C. Stoeckl, V. Yu. Glebov, D. D. Meyerhofer, W. Seka, B. Yaakobi, R. P. J. Town, and J. D. Zuegel, *Rev. Sci. Instrum.* **72**, 1197 (2001).
30. I. Kawrakow *et al.*, NRC, Ottawa, Canada, NRCC Report PIRS-701 (May 2011).
31. M. N. Rosenbluth, *Phys. Rev. Lett.* **29**, 565 (1972).
32. D. R. Nicholson and A. N. Kaufman, *Phys. Rev. Lett.* **33**, 1207 (1974).
33. G. Laval, R. Pellat, and D. Pesme, *Phys. Rev. Lett.* **36**, 192 (1976).

---

# Mitigation of Cross-Beam Energy Transfer: Implications of Two-State Optical Zooming on OMEGA

## Introduction

Two approaches to inertial confinement fusion (ICF)<sup>1</sup> employ megajoule-class laser systems<sup>2,3</sup> to compress a fusion capsule to thermonuclear burn conditions. For the indirect-drive approach,<sup>4</sup> the laser beams heat a radiation cavity, crossing in a low-density plasma on their path to the cavity wall; for the direct-drive approach,<sup>5,6</sup> the laser beams directly illuminate the fusion capsule and laser rays cross in higher-density coronal plasma. In both ignition schemes, crossing laser beams can excite ion-acoustic waves that facilitate the energy transfer away from regions of interest.<sup>7–11</sup>

For indirect-drive-ignition experiments, cross-beam energy transfer (CBET) removes significant energy from the beams directed near the equator of the capsule, compromising the symmetry of the implosion.<sup>10</sup> By changing the relative frequency between the laser beams, CBET has been mitigated and frequency shifts are now used to control the symmetry of the fusion capsule at the National Ignition Facility.<sup>12–14</sup>

Direct-drive implosions on the OMEGA laser<sup>15</sup> use three ~100-ps-long laser pulses (“pickets”) to launch shocks into the target, setting the implosion onto a low adiabat.<sup>6</sup> These picket pulses are followed by a high-intensity drive pulse that compresses the fuel. During the drive, experiments have shown that CBET can reduce the hydrodynamic coupling by linking the scattered-light spectra to a lack of energy penetrating to the critical surface.<sup>16,17</sup> Laser light in the edge of the laser beams propagating past the target beats with the incident laser light from the opposing beams and excites ion-acoustic waves. The enhanced ion-acoustic waves scatter light primarily from the central rays of the incident laser beams to the outgoing rays.

Studies have shown that reducing the diameter of the laser beams by 30% can restore 70% of the energy lost to CBET at the cost of reduced hydrodynamic stability.<sup>18</sup> Simulations indicate no deleterious effects on hydrodynamic stability when the laser-beam diameters are reduced after a significant thermal conduction zone has been generated (two-state zooming). Zooming is predicted to increase the hydrodynamic efficiency,

allowing OMEGA to drive more-stable implosions at higher velocities and ignition-relevant, one-dimensional (1-D) yields.<sup>19</sup>

Potential schemes to achieve zooming of the focal spot on target involve modifications to the spatial coherence of the laser that cause broadening in the far field of the beam.<sup>20</sup> Two primary options for implementing zooming on OMEGA were investigated: (1) time-dependent phase conversion and (2) increased deflection from two-dimensional (2-D) smoothing by spectral dispersion (SSD).<sup>21</sup> The most-practical method for implementing zooming on OMEGA appears to be time-dependent phase conversion. It is predicted to increase the absorption and allow for designs that include 9.5  $\mu\text{m}$  of carbon–deuterium (CD) polymer and 66- $\mu\text{m}$ -thick deuterium–tritium (DT) shells to be driven at  $\sim 3.2 \times 10^7$  cm/s and produce ignition-scalable 1-D yields of  $7.8 \times 10^{13}$ —a factor of ~2.5 larger yields than produced without zooming. Implementing time-dependent phase conversion on OMEGA will require zooming phase plates (ZPP’s) and co-propagating dual-driver lines.

## 1. Zooming Phase Plates

A new phase-plate design, referred to as a zooming phase plate (ZPP), in conjunction with a time-dependent near-field profile will produce a larger laser spot during the pickets and a smaller laser spot during the main drive. The ZPP would contain a radial transition where the central area produces a larger, low-order super-Gaussian focal spot, while the outer area produces a smaller, high-order super-Gaussian focal spot. This configuration requires a smaller-diameter beam during the pickets and a mid-section cutout of the near field during the drive pulse, as shown in Fig. 133.40(a). OMEGA operates near its maximum stored-energy capacity, requiring that the diameter of the laser beams during the drive fill the complete aperture [Fig. 133.40(b)]. The OMEGA-limited near-field profiles combined with the proposed ZPP’s produce laser spots with low-intensity wings.

## 2. Co-Propagating Dual-Driver Lines

To produce the required two-state near-field profile, a co-propagating dual-driver configuration is required. The picket

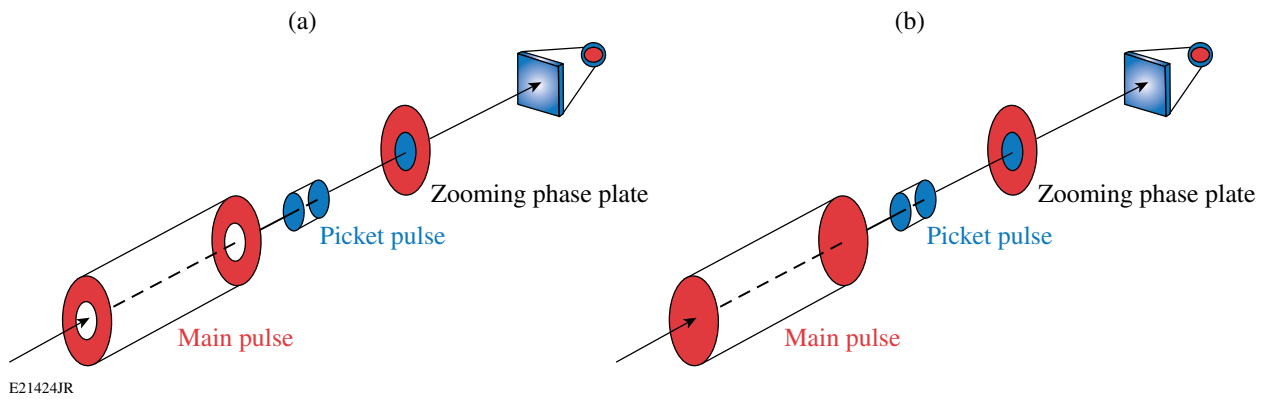


Figure 133.40

The (a) optimum and (b) OMEGA-limited near-field profiles for implementing radially varying ZPP's to produce large-diameter laser spots during the pickets (blue) and small-diameter spots during the drive pulse (red).

driver with SSD would pass through an apodizer, forming a beam of half the standard diameter. The second main-pulse driver would propagate without SSD through its own apodizer, forming a full-diameter beam [Fig. 133.40(b)].

Introducing a dual-driver configuration will provide the following:

- a 14-cm-diam beam during the pickets ( $1.5\text{-}\text{\AA} \times 3\text{-}\text{\AA}$  SSD) and a full-aperture, 28-cm-diam beam (no SSD) during the main drive;
- an  $\sim 10\%$  increase in on-target energy as a result of better frequency-conversion efficiency; and
- a proof-of-principle dynamic bandwidth reduction for the National Ignition Facility (NIF).

Implementing zooming using the proposed method presents two main concerns: (1) The small-diameter beams required during the pickets will increase intensity modulations in the imprint spectrum by a factor of 1.5 to 2. The impact of this increased imprint will be investigated but recent mitigation studies have demonstrated a factor-of-2 imprint reduction when using doped ablaters.<sup>22,23</sup> (2) Zooming increases the single-beam intensities ( $\sim 2\times$ ) during the drive. This may be above the backscatter intensity thresholds and lead to larger levels of hot electrons produced by two-plasmon decay.

This article is organized as follows: The target-physics implications of CBET and the initial results that are the foundation for a CBET mitigation scheme are described; a CBET mitigation scheme for direct-drive implosions, reviews of the physics considerations, and requirements for implementing this scheme on OMEGA are presented; proposed physics studies

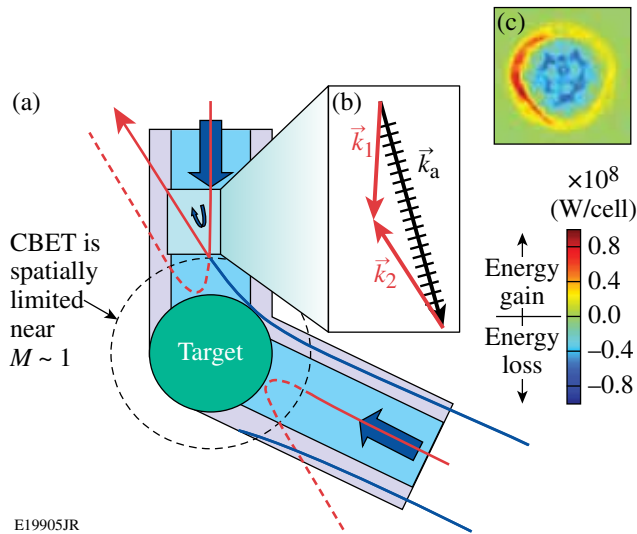
to be completed prior to implementing the scheme are summarized; implementation of zooming on OMEGA is discussed; and the findings are summarized. An appendix presents an alternative concept for zooming (increased deflection from 2-D SSD) and the related calculations used to assess its feasibility.

### Target Physics

#### 1. Implications of Cross-Beam Energy Transfer in Direct Drive

The direct-drive approach to inertial confinement fusion requires that the laser beams efficiently deposit their energy in the coronal plasma where the energy is transported through the conduction zone to the ablation surface, producing the pressure that drives the implosion. This ablation pressure ( $P_a$ ) determines the minimum laser energy required for ignition ( $E_{\min} \propto P_a^{-2}$ ) (Ref. 24). Reducing the diameter of the laser beams increases the ablation pressure because it increases the energy in the central portions of the laser beams that propagate most normal to the target surface and deposit their energy closest to the ablation surface. This is balanced by the required increase in the diameter of the laser beams to minimize the illumination nonuniformities on target.

CBET is a mechanism that reduces the ablation pressure in direct-drive implosions.<sup>11,16–18</sup> It reduces the incident energy in the central portion of the laser beams, making it possible for the incoming light to bypass the highest-absorption region near the critical surface (Fig. 133.41), significantly reducing the hydrodynamic efficiency.<sup>17</sup> Laser light in the edge of the laser beams ( $\vec{k}_2$ ) propagating past the target seeds stimulated Brillouin scattering (SBS) using light from the opposing laser beams ( $\vec{k}_1$ ) and drives ion-acoustic waves ( $\vec{k}_a$ ). The ion-acoustic waves scatter light primarily from the central rays of the incident laser beams to the lower-energy outgoing rays.



E19905JR

Figure 133.41

(a) Light rays propagating past the target (blue) interact with light rays in the central region of another beam (red). (b) The interacting light rays seed an ion-acoustic wave near the Mach-1 surface (dashed curves). The ion-acoustic wave scatters light before it can penetrate deep into the target. (c) A calculation of the total energy transferred (gain/lost) integrated along the path of a ray into and out of the target. The calculation shows that energy in the central rays propagating into the target is reduced by CBET, while the energy in the edges of the beam propagating away from the target is increased.<sup>25</sup>

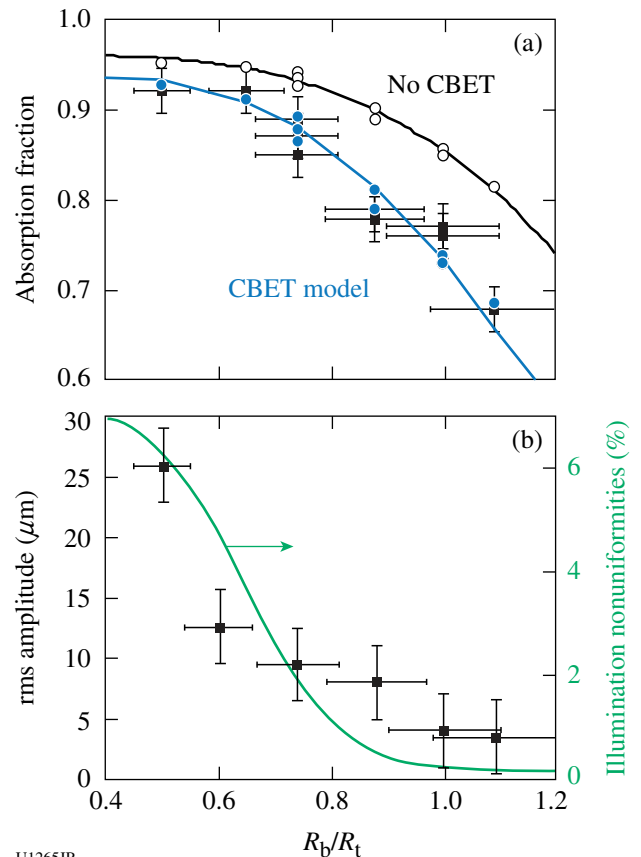
Simulations of direct-drive implosions using the 1-D radiation–hydrodynamics code *LILAC*<sup>26</sup> that include CBET modeling indicate that the ablation pressure is reduced by  $\sim 40\%$ , lowering the implosion velocity ( $v_{\text{imp}} \propto P_a$ ), the hot-spot pressure ( $P_{\text{hs}} \propto P_a^{1/3}$ ), the areal density ( $\rho R \propto \sqrt{P_a}$ ), and negatively impacting the stability of the implosion as inferred from the in-flight aspect ratio (IFAR  $\propto P_a^{-2/5}$ ) (Ref. 24). The loss in ablation pressure limits OMEGA cryogenic implosions, reducing the 1-D yield by nearly an order of magnitude.

The implosion velocity calculated for a 1.5-MJ, symmetric, direct-drive–ignition design<sup>6</sup> is reduced from  $4.0 \times 10^7$  to  $3.3 \times 10^7$  cm/s (Ref. 19). CBET significantly increases the minimum energy required for ignition and 1-D simulations suggest that the ignition margin cannot be recovered by increasing the on-target laser energy while maintaining a constant overlapped intensity. Increasing the laser energy to account for the lost ablation pressure requires an increased laser-beam radius that results in longer scale lengths and increased CBET. The increased energy does not recover the loss in hot-spot pressure, suggesting that the implosions must be driven at higher velocities, further reducing their hydrodynamic stability.

## 2. Mitigation of Cross-Beam Energy Transfer (Zooming)

Experiments have demonstrated that reducing the laser-beam diameters with respect to the target diameter can reduce CBET at the cost of increased illumination nonuniformities (Fig. 133.42).<sup>18</sup> To mitigate CBET and maintain sufficient illumination uniformity, a two-state zooming has been proposed.<sup>19</sup> During the critical time for seeding nonuniformities, the radii of the laser beams  $R_b$  are equal to the target radius  $R_t$  ( $R_b/R_t = 1$ ), minimizing the low-frequency laser imprint. Once a conduction zone is long enough to suitably smooth laser imprint, the diameters of the laser beams are reduced and CBET can be mitigated.

*LILAC* simulations show that implementing zooming by reducing the 95% encircled energy radii of the laser beams after the third picket from  $R_b = 430 \mu\text{m}$  ( $R_b/R_t = 1.0$ ) to  $R_b = 365 \mu\text{m}$



U1265JR

Figure 133.42

The measured (a) absorbed light (squares) and (b) rms deviation from the average shell radius (squares, left axis), along with the calculated illumination nonuniformities (right axis) are plotted as functions of the ratio between the laser-beam and target radii, where  $R_b$  is the 95% encircled energy radius. The calculated absorption is shown in (a) for simulations with (blue solid circles) and without CBET modeling (open circles) for an overlapped intensity of  $4.5 \times 10^{14}$  W/cm<sup>2</sup> (Ref. 17).

( $R_b/R_t = 0.85$ ) recovers 35% of the absorption lost to CBET and the implosion velocity for less-massive targets ( $10\ \mu\text{m}$  of CD +  $44\text{-}\mu\text{m}$ -thick DT shells) reaches values of  $3.7 \times 10^7\ \text{cm/s}$  [Fig. 133.43(a)]. Further reducing the radii of the laser beams to  $R_b = 300\ \mu\text{m}$  ( $R_b/R_t = 0.7$ ) recovers 70% of the energy lost to

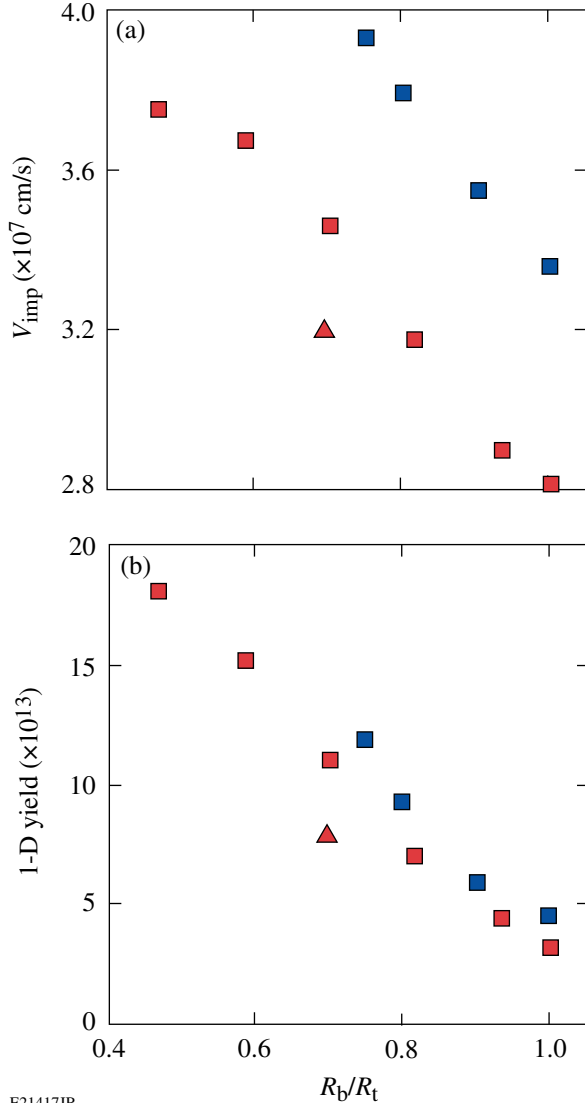
CBET. Figure 133.43 shows that this increased absorption leads to an increased implosion velocity and a factor-of-3 increase in the 1-D predicted neutron yield.

For these simulations (square symbols), the ZPP profiles are given by

$$I_i = P \frac{\exp\left[-\left(r/r_i\right)^{m_i}\right]}{\int \exp\left[-\left(r/r_i\right)^{m_i}\right] r dr},$$

where  $P$  is the laser power,  $i$  indicates the parameter during the pickets ( $i = p$ ) or main drive ( $i = d$ ),  $m_p = 4$ ,  $r_p = 353\ \mu\text{m}$  (corresponding to  $R_b/R_t = 1$ , where  $R_b$  is the 95% encircled-energy radius),  $m_d = 4$ , and  $r_d$  was varied from  $182\ \mu\text{m}$  ( $R_b/R_t = 0.5$ ) to  $353\ \mu\text{m}$  ( $R_b/R_t = 1$ ).

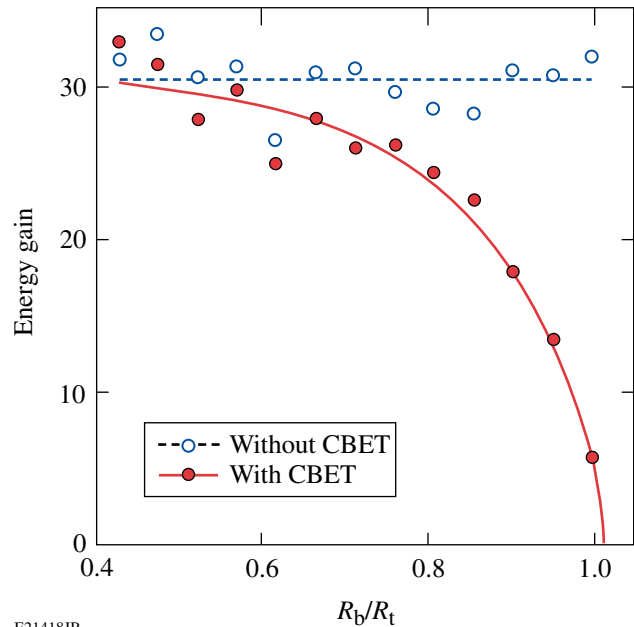
For the 1.5-MJ symmetric direct-drive-ignition design,<sup>6</sup> zooming can recover a significant portion of the ablation pressure lost to CBET.<sup>19</sup> Figure 133.44 shows that reducing the diameter of the laser beams by 30% is sufficient to recover 90% of the calculated 1-D gain when simulated without including CBET. For a fixed ignition margin ( $E_{\text{KE}}/E_{\text{min}} \propto \text{IFAR}^3 P_a^3$ ,



E21417JR

Figure 133.43

The calculated (a) implosion velocity and (b) 1-D yield are plotted as functions of the normalized laser-beam radius for the main drive pulse for two typical low-adiabat OMEGA cryogenic conditions. Low-mass targets ( $10\ \mu\text{m}$  of CD +  $44\text{-}\mu\text{m}$ -thick DT shells) (blue) and higher-mass targets ( $9.5\ \mu\text{m}$  of CD +  $66\text{-}\mu\text{m}$ -thick DT shells) (red) corresponding to OMEGA shots 66612 and 55722, respectively, with optimal zooming profiles (squares) are shown. The predictions using the proposed OMEGA zooming scheme (triangles) are shown. The total energy on target was  $\sim 25\ \text{kJ}$ , corresponding to an overlap intensity  $I_{\text{ovr}} = 8.8 \times 10^{14}\ \text{W/cm}^2$ .



E21418JR

Figure 133.44

The 1-D gain is calculated for a series of symmetric simulations where the ratio of the laser-beam radius to the target radius ( $R_t = 1.7\ \text{mm}$ ) is varied. The design parameters are taken from Ref. 6.

where IFAR is a measure of the target stability), this increased ablation pressure increases the stability of the implosions ( $\text{IFAR} \propto 1/P_a$ ), providing a more-robust design.

### Implications of Zooming on Direct-Drive Implosions

The following section presents the proposed zooming scheme, defines the zooming laser-spot profiles (consistent with OMEGA capabilities), and addresses both the hydrodynamic efficiency (1-D physics) and the hydrodynamic stability (2-D physics) of the OMEGA cryogenic direct-drive target design. Specifically, the hydrodynamic efficiency is increased by the reduced diameter of the laser beams (i.e., reduced CBET) and the increased energy in the normal rays (i.e., energy deposition closer to the ablation surface). The hydrodynamic efficiency may be reduced if the increased single-beam laser intensity exceeds the backscatter thresholds. The hydrodynamic stability is potentially affected by the reduced diameter of the laser beams during the main drive (low mode) and the reduced power spectrum during the pickets (high-frequency imprint).

#### 1. Proposed Focal-Zooming Scheme

**a. Time-dependent near field.** The basic construct for the time-dependent near-field profile involves a sub-aperture beam for the initial pickets with a full-size beam for the main pulse. The area of each beam depends on three considerations: beam intensity to prevent laser damage, controlled power spectrum to obtain irradiation uniformity, and the stored energy in the beamline.

Based on the maximum required picket power ( $\sim 0.12$  TW/beam) and the currently allowed intensity, the minimum sub-aperture beam diameter during the pickets is 14 cm. This sub-aperture beam is half of the nominal diameter and would limit the total energy on target to 75% of the maximum OMEGA energy if an annular main drive pulse were used. The proposed OMEGA zooming scheme will implement a full-aperture beam during the main drive [Fig. 133.40(b)].

**b. Zooming phase plates.** The proposed zooming approach is made possible by designing a ZPP containing a central region that produces a larger focal spot, while its outer annular region produces a smaller, high-order focal spot. During the picket pulses, a small-diameter beam propagates through the center region of the ZPP, producing a large focal spot. This configuration produces a small central focal spot on top of a lower-intensity larger profile defined by the center of the ZPP. The design methodology for this ZPP involves using a deeper surface relief in the central region, with a smaller one in the annular region of the phase plate. A slowly varying, continu-

ous surface relief is required to reduce the near-field irradiance modulation imposed on the optics at the end of the laser.

The laser profiles consistent with the OMEGA capabilities (“OMEGA ZPP”) are shown in Fig. 133.45. The laser profiles during the pickets are defined by the central 14-cm diameter of the ZPP. Their intensity profiles are given by

$$I_p = P \frac{\exp\left[-\left(r/r_p\right)^{m_p}\right]}{\int \exp\left[-\left(r/r_p\right)^{m_p}\right] r dr},$$

where  $m_p = 4$  and  $r_p = 365 \mu\text{m}$  (corresponding to a 95% encircled energy radius  $R_b = 430 \mu\text{m}$ ).

After the third picket, the OMEGA beams will use the full aperture (28-cm diameter). The outer ring of the ZPP will produce a high-order super-Gaussian profile. The profile during the drive will consist of the sum of the two profiles, where 3/4 of the total laser power will be within the higher-order profile and 1/4 in the lower-order profile,

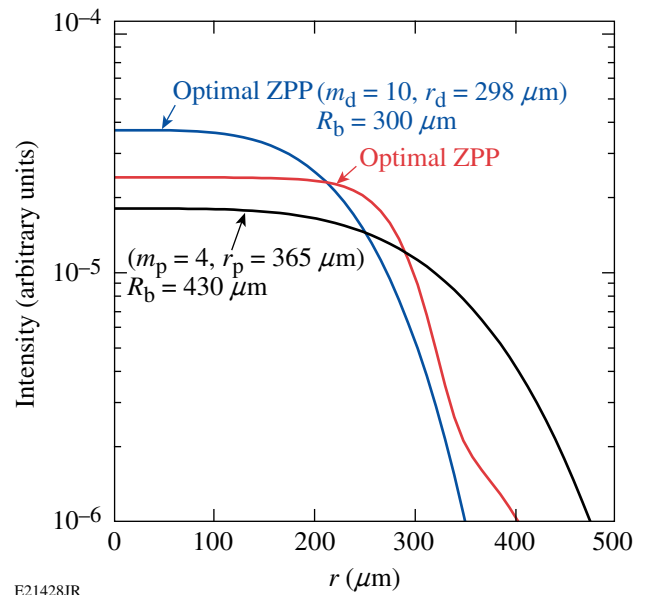


Figure 133.45

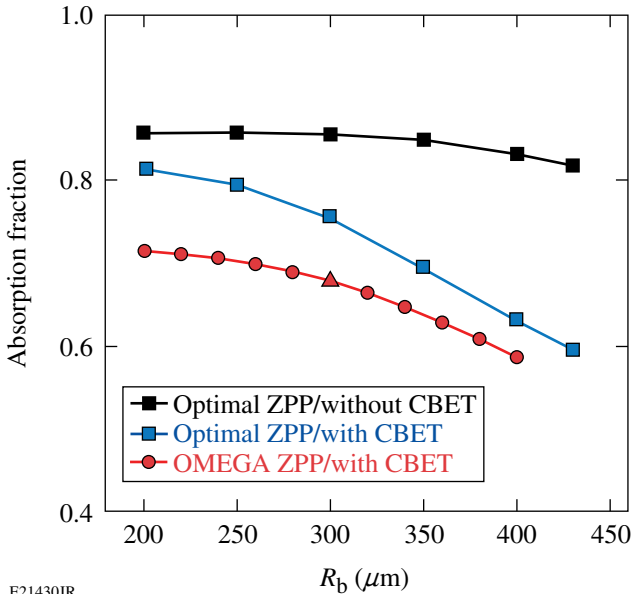
The proposed OMEGA ZPP profiles of the laser beams during the pickets (black curve) and during the main drive (red curve). The more-optimal ZPP profile  $R_b/R_t = 0.7$  (blue curve) is shown for  $R_b = 300 \mu\text{m}$ . The profiles are normalized to the laser power.

$$I_d = P \left\{ \frac{1}{4} \frac{\exp[-(r/r_p)^{m_p}]}{\int \exp[-(r/r_p)^{m_p}] r dr} + \frac{3}{4} \frac{\exp[-(r/r_d)^{m_d}]}{\int \exp[-(r/r_d)^{m_d}] r dr} \right\},$$

where  $m_d = 10$  and  $r_d = 298 \mu\text{m}$  (corresponding to a 95% encircled energy radius of  $R_b = 300 \mu\text{m}$ ). The lower-order profile is determined by the picket profile but is slightly modified as a result of turning SSD off (not included in this analysis). With the current rectangular SSD kernel ( $1.5 \text{ \AA} \times 3.0 \text{ \AA}$ ), the laser spots during the drive will be slightly elliptical unless compensated for by the ZPP. The ZPP's will be designed to account for the slight ellipticity introduced by the distributed polarization rotators (see Appendix A.1).

## 2. Hydrodynamic Efficiency (1-D Physics)

**a. Cross-beam energy transfer.** Figure 133.46 shows results from hydrodynamic simulations with (blue squares) and without CBET (black squares). For the nominal laser beam radii ( $R_b/R_t = 1$ ), CBET reduces the absorption from 82% to 60%. Using the more-optimal ZPP profiles and reducing their radii to  $R_b = 300 \mu\text{m}$  ( $R_b/R_t = 0.7$ ), the system recovers more than



E21430JR

Figure 133.46

A comparison of the absorption calculated when including CBET for the zooming configurations with the more-optimal ZPP (squares) and the OMEGA ZPP scheme (circles). The proposed OMEGA zooming profile is shown (triangle). For comparison, simulations without CBET using the more-optimal ZPP scheme are shown (black squares). The overlapped intensity is  $8 \times 10^{14} \text{ W/cm}^2$  in all simulations. Shot parameters correspond to OMEGA shot 55722.

70% of the absorbed energy lost to CBET. This is compared with hydrodynamic simulations that use the proposed OMEGA ZPP profiles. For the OMEGA ZPP profile (triangle), CBET is reduced and recovers 35% of the absorbed energy lost to CBET. The residual wings in the laser-beam profiles during the drive (Fig. 133.45) limit the ability of zooming to completely mitigate CBET. The OMEGA ZPP configuration increases the velocity of the thick-target design ( $9.5 \mu\text{m}$  of CD +  $66 \mu\text{m}$  of DT) from  $2.8 \times 10^7 \text{ cm/s}$  ( $R_b/R_t = 1$ ) to  $3.2 \times 10^7 \text{ cm/s}$  and the corresponding 1-D predicted neutron yield increases from  $3.4 \times 10^{13}$  to  $7.8 \times 10^{13}$  (Fig. 133.43). For a less-massive target ( $10 \mu\text{m}$  of CD + a  $44\text{-}\mu\text{m}$ -thick DT shell), the velocity for  $R_b/R_t = 0.7$  is  $4.1 \times 10^7 \text{ cm/s}$  when using the more-optimal beam profiles during the drive, compared to an estimated  $3.7 \times 10^7 \text{ cm/s}$  when using the OMEGA ZPP profiles.

**b. Laser-plasma interactions.** Reducing the radii of the beams during the drive increases the single-beam laser intensity. In typical cryogenic designs on OMEGA, where  $R_b/R_t = 1$ , the peak single-beam intensity is approximately

$$I_p(r=0) \cong \frac{8}{N} I_{\text{ovr}} \sim 1.2 \times 10^{14} \text{ W/cm}^2,$$

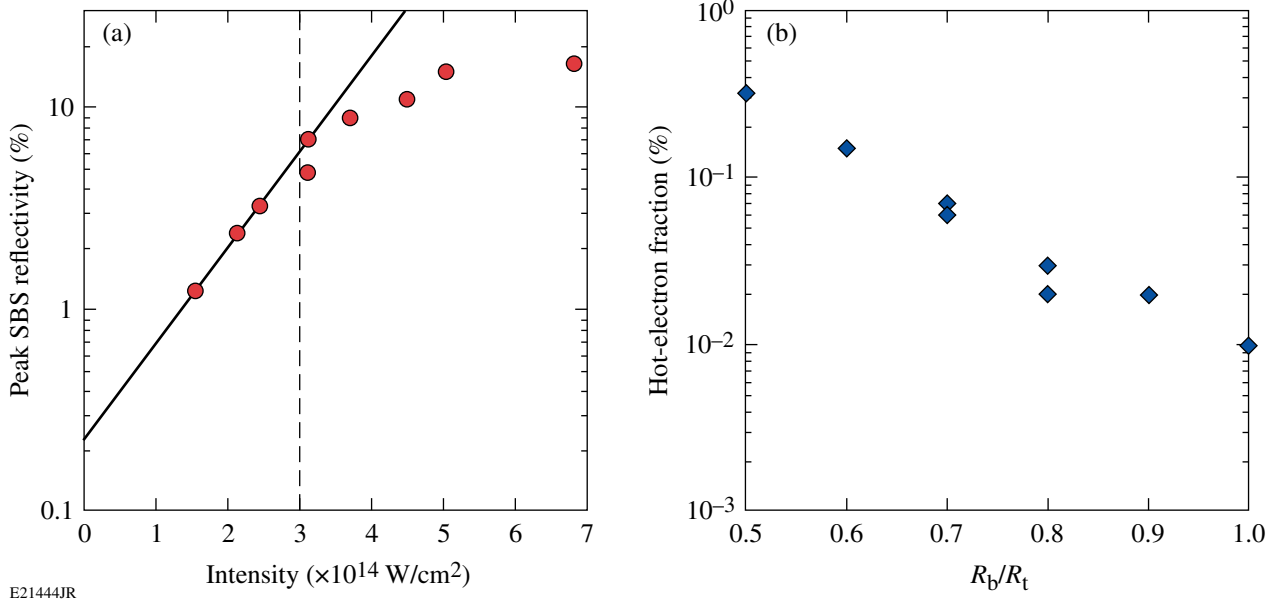
where  $N = 60$  is the number of beams,  $I_{\text{ovr}} = P_d/A_t = 8.8 \times 10^{14} \text{ W/cm}^2$ ,  $P_d = 20 \text{ TW}$  is the power in the drive, and  $A_t$  is the surface area of the target. The single-beam intensity is increased as the radii of the beams are reduced:

$$I_d(r=0) \cong 1.2 \times 10^{14} \left( \frac{R_t}{R_b} \right)^2 \text{ W/cm}^2.$$

For  $R_b = 300 \mu\text{m}$ , the corresponding single-beam intensity during the drive is  $\sim 2.5 \times 10^{14} \text{ W/cm}^2$ .

Figure 133.47(a) shows the measured peak SBS reflectivity threshold for OMEGA direct-drive plasmas. Exceeding the SBS intensity thresholds will backscatter laser light from the target, reducing the drive efficiency. These results suggest that the peak laser intensities must remain below  $3 \times 10^{14} \text{ W/cm}^2$  to keep SBS from becoming energetically significant, but this threshold depends on the exact plasma conditions.

Experiments on OMEGA show an increase in the hot-electron fraction when reducing the radii of the laser beams (see Ref. 18 for the experimental setup). Figure 133.47(b) shows that the fraction of laser energy converted to hot electrons increased by more than an order of magnitude when the radii of the laser beams were changed from  $430 \mu\text{m}$  to  $215 \mu\text{m}$ .



E21444JR

Figure 133.47

(a) The peak SBS reflectivity measured from OMEGA 860- $\mu$ m-diam CH implosion experiments is shown as a function of the peak single-beam laser intensity. The SBS reflectivity peaks during the intensity rise in the main drive pulse when the electron temperature is low. (b) The fraction of laser energy converted to hot electrons inferred from hard x-ray measurements is shown as a function of the radii of the laser beams normalized to the target radius ( $R_t = 430 \mu\text{m}$ ). The overlapped intensity was held nearly constant at  $4.5 \times 10^{14}$  W/cm $^2$ .

### 3. Hydrodynamic Stability (2-D Physics)

**a. Low-mode stability.** Two-dimensional *DRACO*<sup>27</sup> simulations were performed to investigate the level of perturbations induced by the lower illumination uniformity when the diameter of the laser beams were reduced at various times in the laser pulse. The simulations use a cryogenic, low-adiabat, triple-picket implosion design (OMEGA shot 55722, 9.5  $\mu\text{m}$  of CD + a 66- $\mu\text{m}$ -thick DT shell). The simulations that do not include CBET employ a thermal-transport model where the heat flux was limited to a fraction ( $f = 0.06$ ) of the free-streaming flux.<sup>28</sup> This is a reasonable approach since 1-D simulations indicate very little effect from CBET for these conditions (i.e.,  $R_b/R_t = 0.7$ ).

Figure 133.48 shows simulated shell densities at maximum compression. Improvements in target uniformity are clearly seen in Fig. 133.48(b), where two-state zooming was applied after the third picket in comparison with those simulations where zooming was not used [Fig. 133.48(a)]. Table 133.VII summarizes the performance of simulated targets depending on the transition time from large- to small-diameter beams. At peak neutron flux, the normalized areal-density perturbations ( $\Sigma_{\text{rms}}$ ) are shown and quantify the effect of the overlapped nonuniformities. These results indicate that the amplitude of perturbations is reduced by an order of magnitude when the

Table 133.VII: A summary of the effect of zooming on areal-density perturbations at peak neutron flux when zooming at different times from  $R_b/R_t = 1.0$  to  $R_b/R_t = 0.7$ .

Zooming	$R_b/R_t$	$\Sigma_{\text{rms}}$ (%)
Not applied	0.7	9
After first picket	1.0 to 0.7	7
After second picket	1.0 to 0.7	1.1
After third picket	1.0 to 0.7	1.1
At beginning of main pulse	1.0 to 0.7	1.1
Not applied	1.0	1.2

transition occurs after the second or third picket and that zooming between the third picket and the main pulse will maintain target uniformity while mitigating CBET.

**b. High-frequency imprint.** The proposed OMEGA zooming scheme requires that the near-field diameter be reduced by a factor of 2 to produce larger laser spots during the pickets. This reduced near-field diameter may impact the target performance by increasing the rms (root-mean-square) illumination nonuniformity. Figure 133.49 shows the ratio of the  $\ell$ -mode  $\sigma_{\text{rms}}$  amplitude spectrum for the OMEGA ZPP design during the pickets ( $D_{\text{ZPP}} = 14$  cm) to the standard OMEGA configuration ( $D = 28$  cm). The  $\ell$ -mode  $\sigma_{\text{rms}}$  is given by<sup>29</sup>

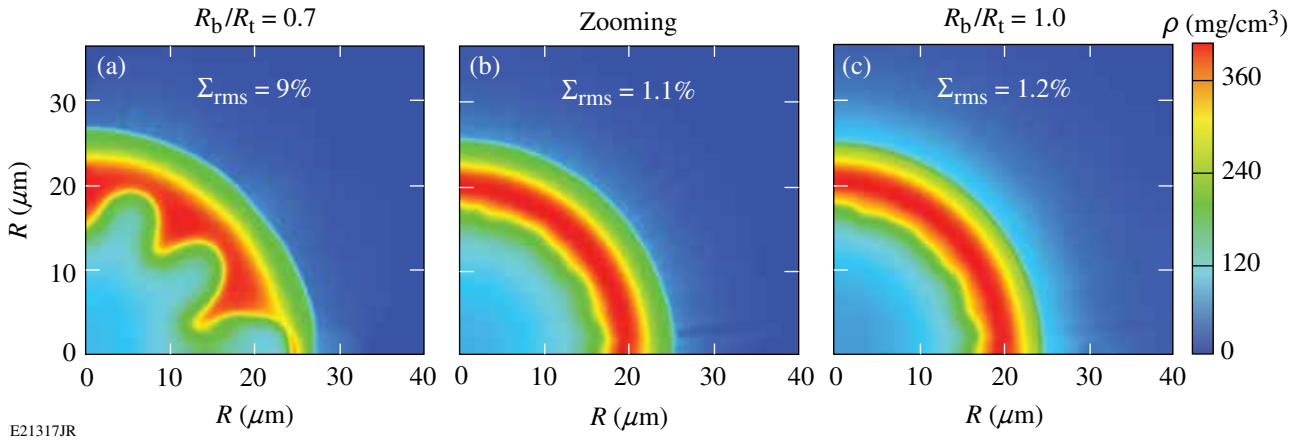


Figure 133.48

Simulated shell density at maximum compression in the case of using (a) small-diameter beams ( $R_b/R_t = 0.7$ ) for the entire laser pulse, (b) large-diameter beams ( $R_b/R_t = 1$ ) for pickets and small-diameter beams ( $R_b/R_t = 0.7$ ) for the main pulse, and (c) large-diameter beams for the entire pulse.

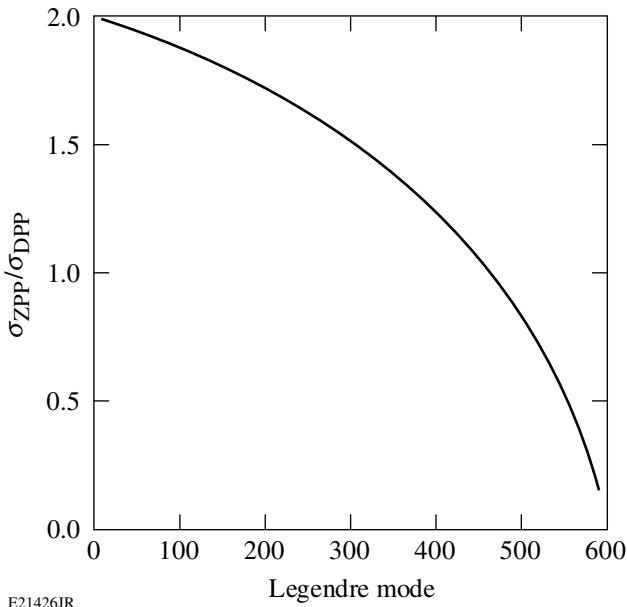


Figure 133.49

The ratio of rms (root-mean-square) illumination uniformity for the sub-aperture pickets (half-aperture) over the standard OMEGA full-aperture configuration is plotted against the Legendre mode for a target radius of 430  $\mu\text{m}$ .

$$\sigma_l^2 = \frac{16}{\pi \ell_{\max}} \frac{\ell}{\ell_{\max}} \times \left[ \cos^{-1} \left( \frac{\ell}{\ell_{\max}} \right) - \left( \frac{\ell}{\ell_{\max}} \right) \sqrt{1 - \left( \frac{\ell}{\ell_{\max}} \right)^2} \right],$$

where  $\ell_{\max} = Rk_{\max} = 2\pi R/F^\# \lambda$ ,  $R = 460 \mu\text{m}$  is the target radius,  $F^\# = FL/D$ ,  $FL = 190 \text{ cm}$ , and  $D$  is the diameter of the beam at the lens plane.

Over the range of modes that most significantly impacts target performance (10 to 300),  $\sigma_{\text{rms}}$  increases by a factor of nearly 2. In addition, the  $4\times$  reduction in beam area will result in fewer speckles to fill out the envelope and the focal spot will contain a lumpy pattern. An assessment of the impact of increased illumination uniformities will be performed but mitigation strategies have been demonstrated that reduce imprint by a factor of 2 when using doped ablaters.<sup>22,23</sup> Although a larger beam size during the pickets would fill out the power spectrum, the correspondingly larger central region of the ZPP would increase the energy in the tails of the beam profiles during the drive and would increase CBET.

Propagation of a beam with a half diameter through the current SSD system will produce 1.5 color cycles over the beam rather than the current three color cycles. Although the angular dispersion remains constant, the simultaneity of the colors in the spectrum is not guaranteed and a certain amount of modulation frequency may appear in the integrated focal spot on target, i.e., unwanted pulse shaping. If this is found to be a problem for the experiment, the SSD system will need to be modified.

#### 4. Target Physics Requirements for Zooming on OMEGA

The physics requirements for zooming are based on demonstrating implosion performance on OMEGA that is hydrodynamically equivalent to a 1.5-MJ ignition implosion on the National Ignition Facility (NIF). This requires a Lawson criteria<sup>30</sup>  $\left[ \chi \approx (\rho R)^{0.6} (0.24 Y_n / M_{\text{fuel}})^{0.3} \right]$  of  $\chi = 0.16$ , where  $\rho R$  is in  $\text{g/cm}^2$ ,  $Y_n$  is the yield in units of  $10^{16}$ , and  $M_{\text{fuel}}$  is the mass of the fuel in milligrams (mg) (Ref. 31). For the total laser energy available on OMEGA, this corresponds to a  $\rho R$  of

300 mg/cm<sup>2</sup> and a yield of  $4 \times 10^{13}$ . Currently, the best implosions on OMEGA produce a yield of  $2.1 \times 10^{13}$  and a  $\rho R$  of 160 mg/cm<sup>2</sup> corresponding to  $\chi = 0.09$  (Ref. 32). Mitigation of CBET will increase the ablation pressure, providing both a higher  $\rho R$  ( $\rho R \propto \sqrt{P_a}$ ) and a higher yield ( $Y \propto P_a$ ). The physics requirements for zooming on OMEGA are based on increasing the ablation pressure by reducing CBET without imposing deleterious effects through nonuniformities or laser–plasma interactions. The following section provides the physics basis for the OMEGA zooming design and presents the main logic used to determine the requirements summarized in Table 133.VIII.

Table 133.VIII: Target physics requirements for zooming on OMEGA.

	$R_b$ ( $\mu\text{m}$ )	Power spectrum	SG order	Peak power (TW/beam)
Pickets	430	See below*	4	0.12
Drive	365**	Best effort	2 to 20	0.35

\*See **Power Spectrum (Pickets)** below.

\*\*See **Drive-Beam Radius** below.

**a. Picket-beam radius.** The radii of the laser beams during the pickets are defined to maximize illumination uniformity and minimize the energy lost outside of the target. The proposed design assumes that the current SG4 distributed phase plate (DPP) profiles are optimized ( $m = 4$ ,  $r = 365 \mu\text{m}$ ). A further optimization study could be performed to characterize the effect of reducing the picket-beam radius on the illumination nonuniformities and the CBET during the drive; reducing the beam radius during the pickets will reduce the wings in the drive profile.

**b. Drive-beam radius.** The minimum drive-beam radius is governed by the acceptable low-frequency modulations and the acceptable laser–plasma interaction intensity thresholds. The maximum drive-beam radius is governed by the required reduction in CBET to regain hydrodynamically equivalent implosions on OMEGA. A minimum radius of  $R_b = 300 \mu\text{m}$  is proposed to ensure that the peak intensity remains below the intensity, where SBS scatters <5% of the incident laser light.

**c. Power spectrum (pickets).** The power spectrum between Legendre modes 10 and 300 has the largest impact on target performance. A study will be performed to assess the impact of the increased power spectrum over these modes, but mitigation strategies exist that can reduce the imprint by a factor of 2 (Refs. 22 and 23).

**d. Super-Gaussian order (pickets).** To maintain reasonable illumination uniformities during the pickets, a super-Gaussian order consistent with the current OMEGA SG4 design ( $m = 4$ ) is proposed.<sup>33,34</sup> With the OMEGA near-field limitations during the drive, increasing the super-Gaussian order may reduce CBET; a further study will be performed to optimize this gain with the loss of illumination uniformity.

**e. Super-Gaussian order (drive).** A series of 1-D LILAC simulations were performed to investigate the sensitivity of CBET to the super-Gaussian order of the laser beams during the main drive. In these simulations the profile of the laser beams during the pickets was given by a fourth-order super-Gaussian with 95% of the energy contained within the target diameter ( $2R_t = 860 \mu\text{m}$ ), and the super-Gaussian order during the main drive was varied between 2 and 20 [Fig. 133.50(a)] while maintaining 95% of the energy within  $R_b = 300 \mu\text{m}$ . Figure 133.50(b) shows a small effect on the laser-beam absorption. For a given laser power and spot size, high-order super-Gaussian beam profiles reduce the peak intensities limiting the risk of laser–plasma instabilities.

**f. Peak power (pickets).** The picket-pulse shapes (timing and peak powers) are used to set the adiabat, and it is not currently envisioned that the peak power in the pickets will exceed 0.12 TW. This peak power must be consistent with the diameter of the laser beams during the pickets to ensure the laser system remains below damage thresholds.

**g. Peak power (drive).** The current cryogenic target design uses 25 kJ of energy to produce a peak power of nearly 0.35 TW in the drive.

## 5. Proposed Physics Studies

Several physics issues are identified that require further study:

1. The fraction of laser energy converted to hot electrons will be measured and their impact on target performance assessed for laser beams with  $R_b = 300 \mu\text{m}$ , producing an overlapped intensity of  $8 \times 10^{14} \text{ W/cm}^2$  on a standard 430- $\mu\text{m}$ -radius target.
2. The impact of the increased power spectrum during the pickets on the OMEGA implosion performance will be studied and mitigation strategies developed to reduce the effects of imprint.
3. A study is required to optimize the picket-beam profiles. Because the drive pulse shares the central portion of the ZPP with the pickets, the picket profile defines the wings during the main pulse. Reducing the beam radius or increasing the super-Gaussian order during the pickets will further reduce CBET but may increase laser imprint.

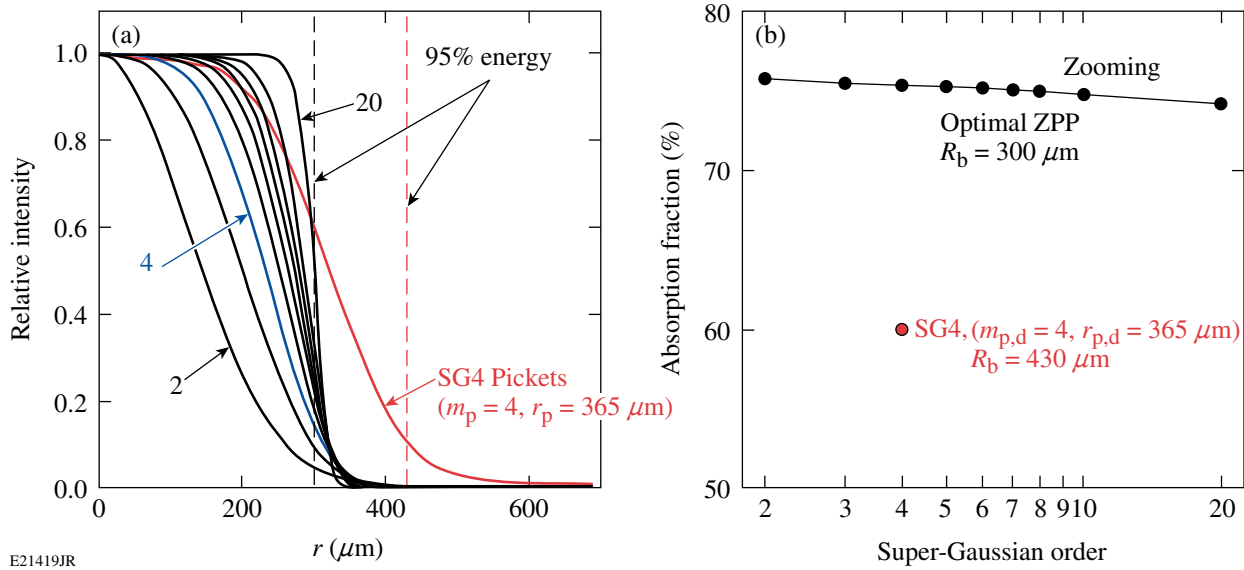


Figure 133.50

The profiles used in simulations to investigate the sensitivity of CBET to super-Gaussian order during the main drive. (a) The profiles in the main drive were varied by changing the super-Gaussian order between 2 and 20 while maintaining 95% of the energy within  $R_b = 300 \mu\text{m}$ . (b) The effect of super-Gaussian order over this range has a small effect on total absorption.

- The  $4\times$  reduction in the area of the laser beam during the pickets will result in fewer speckles to fill out the envelope and the focal spot could contain lumps. This effect on target performance will be assessed by simulating the implosion performance using the calculated ZPP phase.

### Implementation of Zooming on OMEGA

The proposed implementation of zooming on OMEGA requires a dynamic two-state near-field profile and a set of ZPP's. To generate the required two-state near-field profile, a dual-driver co-propagation configuration is proposed. The driver that will generate the pickets will contain the current rectangular SSD kernel and pass through an apodizer, forming a beam of half the standard diameter. A second driver will generate the drive pulse and propagate without SSD through its own apodizer, forming a full-diameter beam.

Implementation of focal-spot zooming on OMEGA will require the development of a new main-pulse driver (zooming driver) that can be combined and co-propagated with the current SSD driver after the SSD modulators (Fig. 133.51). By combining the drivers at the base of the periscope, the losses introduced by the combining optic can be offset by rebalancing the engineered losses that currently exist at the output of the regenerative amplifier. The driver combination would be located before the G4 grating(s). To compensate for the G4

grating(s), a G3 surrogate grating would be integrated into the zooming driver line to apply the required spatiotemporal shear to precompensate for the G4 grating.

An initial study of implementing zooming on OMEGA indicates no technical limitations. Introducing a dual-driver co-propagation configuration will provide (1) a 14-cm-diam beam during the pickets ( $1.5\text{-}\text{\AA} \times 3\text{-}\text{\AA}$  SSD) and a full-aperture, 28-cm-diam beam (no SSD) during the main drive; and (2) an  $\sim 10\%$  increase in on-target energy as a result of better frequency-conversion efficiency.

### Summary

To demonstrate hydrodynamic-equivalent ignition performance on OMEGA, CBET must be mitigated. For a nominal direct-drive configuration, CBET scatters  $\sim 20\%$  of the laser energy from the target, reducing the ablation pressure by 40%. This reduced ablation pressure impacts the direct-drive implosions by reducing the hot-spot pressure and the implosion velocity. This results in a lower yield and reduced stability of the implosion when maintaining a constant minimum energy. On OMEGA cryogenic implosions, the reduced ablation pressure results in an order-of-magnitude reduction in yield. Reducing the radii of the laser beams during the main drive, while maintaining the nominal radius of the laser beams during the pickets (two-state zooming),<sup>19</sup> is shown to significantly reduce

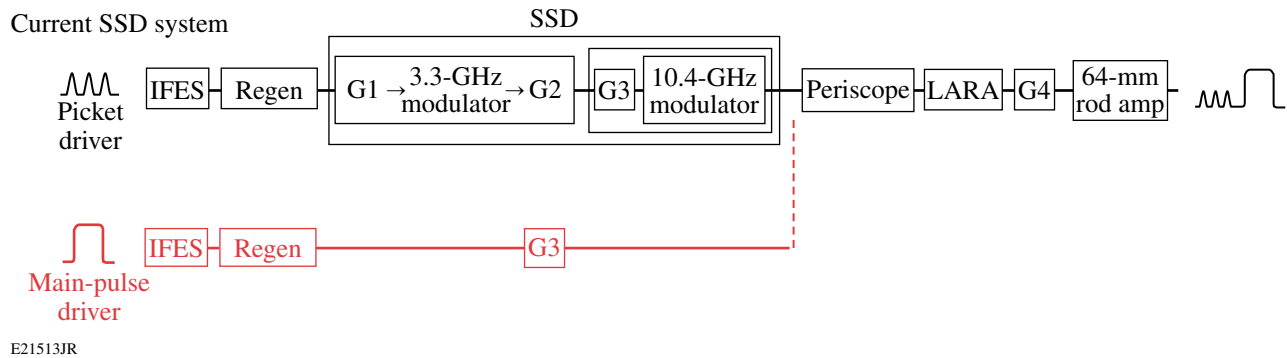


Figure 133.51

The current smoothing by spectral dispersion (SSD) driver line (black) and the proposed zooming drive line (red) are shown. IFES: integrated front-end source; Regen: regenerative amplifier; LARA: large-aperture ring amplifier.

CBET while maintaining high-quality implosions. A two-state zooming scheme is proposed for OMEGA that will recover 35% of the energy lost to CBET.

Implementing zooming on OMEGA will require a new set of phase plates and a dynamic near-field profile. The proposed dynamic near-field profile can be produced using a co-propagating dual-driver configuration. The initial driver line would produce the pickets and propagate through the central half-diameter of the laser system, while the second driver would produce the drive pulse and propagate through the full aperture of the laser system. The central 14-cm diameter of the radially varying phase plates would produce the nominal laser profile on target during the pickets and a smaller radius profile during the main drive.

Implementing zooming on OMEGA will provide a higher hydrodynamic efficiency that will allow targets to be driven faster with higher stability and is equivalent to an increased velocity corresponding to a 30% increase in the on-target laser energy.

#### ACKNOWLEDGMENT

This work was supported by the U.S. Department of Energy Office of Inertial Confinement Fusion under Cooperative Agreement No. DE-FC52-08NA28302, the University of Rochester, and the New York State Energy Research and Development Authority. The support of DOE does not constitute an endorsement by DOE of the views expressed in this article.

#### Appendix A: Alternate Concepts for Zooming on OMEGA

Additional focal-zooming schemes are available for consideration. The zooming effect from 2-D SSD is proportional to the bandwidth, the grating dispersion, and the focal length of the final lens. Increasing either the bandwidth or the grating dispersion on OMEGA would necessarily require opening

the spatial-filter apertures. Placing the final dispersion grating closer to the end of each beamline would allow greater angular dispersion without the risk of damaging the laser chain. Alternatively, the focal length of the final lens could be increased to achieve larger deflection at the focal plane. In this case the focal lens assemblies would be positioned within the hex tubes and the vacuum windows would be repositioned outside the surface of the target chamber rather than being re-entrant. Another option involves using a circular grating at the end of the system to provide both beam smoothing and focal-plane broadening.

#### 1. Zooming with Enhanced 2-D SSD Reduction

An alternative approach to zooming that takes advantage of the reduced deflection that occurs when SSD is turned off was investigated. This approach could achieve the optimum reduction of CBET (i.e., no wings in the profiles during the main drive) but requires that the SSD deflection be symmetric and significantly increased to achieve a change in the focal-spot radius of  $65 \mu\text{m}$  (from  $430 \mu\text{m}$  to  $365 \mu\text{m}$  for equivalent ZPP scheme performance). This initial study indicates that the small SSD dimension could be doubled to form a symmetric 2-D SSD kernel that would produce an  $\sim 35\text{-}\mu\text{m}$  change in the focal-spot radius, but it is unlikely that a further increase to accommodate the required deflection is feasible.

Currently, laser-beam smoothing on the OMEGA 60-beam system includes 2-D SSD and distributed polarization rotation (DPR). The 2-D angular deflection kernel is square and consists of SSD deflection in the first dimension with a 50/50 combination of SSD and DPR deflections in the second dimension. The magnitude of angular deflection from SSD is the product of the angular dispersion and the bandwidth. The angular deflection from the DPR is set by the wedge in the birefringent plate. The

resulting spatial shift in the focal plane is the product of the total angular deflection and the focal length of the lens.

To fully benefit from SSD broadening in two dimensions, the wedged DPR is removed, while the second dimension of SSD is doubled in magnitude. This could be achieved by either doubling the bandwidth or doubling the angular dispersion, or an optimized combination of both. The resulting focal spots would be nominally round either with or without 2-D SSD. Downward zooming would be achieved by turning off the bandwidth, and, therefore, the deflection kernel, in such a way that a smaller monochromatic focal spot would irradiate the target. In this scenario, a 2-D symmetric SSD kernel would be turned off after the pickets and before the main pulse.

**a. Ability for OMEGA to support a symmetric 2-D SSD kernel.** Removing the current DPR's and making the resultant rectangular far-field kernel square by increasing the deflection  $\Gamma$  in the narrow dimension were investigated to determine if a symmetric SSD kernel could be supported by the OMEGA system. Since the far-field deflection is the product of the frequency dispersion ( $\partial\theta/\partial\lambda$ ) and the total bandwidth  $\Delta\lambda$ , the deflection may be increased by increasing either the dispersion or the total bandwidth.

Prior to addressing changes to OMEGA that are required to support the symmetric kernel, the current state of SSD on OMEGA was assessed. The current implementation of three-color-cycle SSD consists of 1.5 Å of FM bandwidth at 3.3 GHz dispersed in the phase-matching direction of the frequency doubler and 3.0 Å of FM bandwidth at 10.4 GHz dispersed in the phase-matching direction of the tripler. The dispersion, measured at the 30-cm output aperture of OMEGA, is  $32 \mu\text{rad}/\text{Å}$  in both directions. In the absence of any aberrations, this results in a rectangular far field with a 2:1 aspect ratio [Fig. 133.52(a)]. The actual far-field pattern is a convolution of the theoretical rectangle with the aberrated, undispersed focal spot.

Figure 133.52(b) shows an estimated OMEGA IR far-field spot along with the limiting pinhole aperture in the OMEGA Laser System. Plasma blowoff from laser intensity on the pinhole edges ultimately limits how much dispersed bandwidth can be propagated through OMEGA. This is a statistical function of the deflection, temporal pulse shape, beamline aberration, pulse length, alignment tolerances, and pinhole geometry and cleanliness.

To assess OMEGA's ability to support a symmetric SSD kernel, the required system changes, implications for the

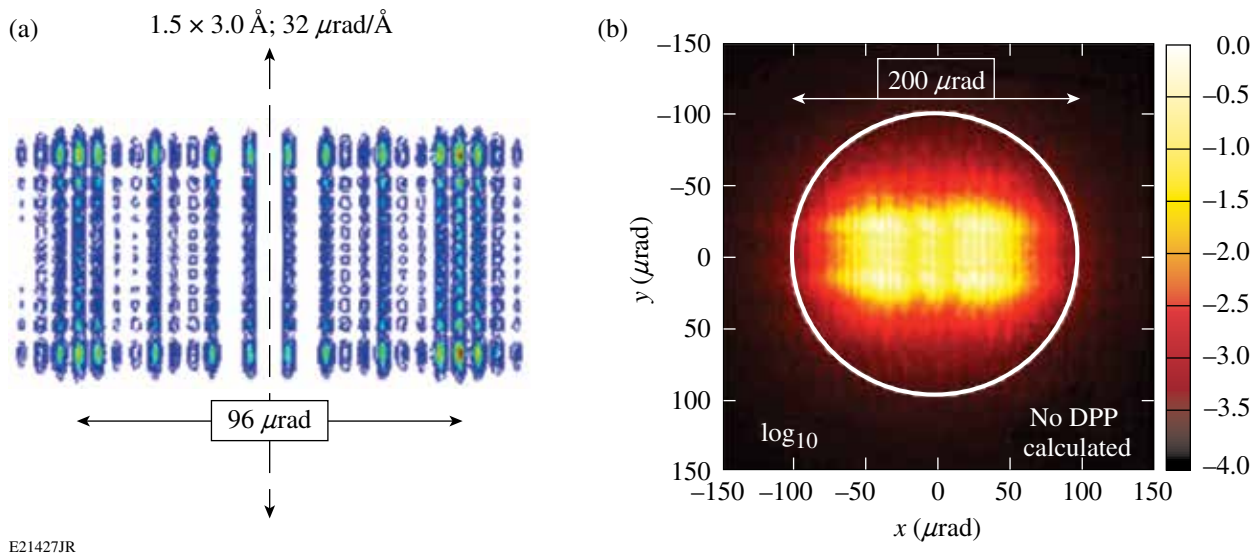


Figure 133.52

(a) The theoretically perfect rectangular far-field pattern. Note the Bessel-function structure in either direction. The narrow (vertical in figure) dimension is the 1.5-Å bandwidth, 3.3-GHz direction; the wide (horizontal in figure) dimension is the 3.0-Å bandwidth, 10.4-GHz direction. (b) Simulated IR  $\log_{10}$  far-field spot ( $4\times$  diffraction limit) at the 30-cm aperture. The white circle is the aperture of the limiting pinhole calculated at the end of the laser system.

OMEGA pinholes as a result of the focal-spot shape change, and the impact on the frequency-conversion efficiency and potential FM-to-AM effects of the increase in bandwidth and/or dispersion are investigated.

*System changes:* Achieving a symmetric focal spot requires increasing the far-field deflection of the 3.3-GHz axis. This can be achieved by increasing the bandwidth at 3.3 GHz or increasing the dispersion. Further increases in bandwidth would require testing of the 3.3-GHz modulator, which is currently near its power limit. It is possible that some increase in bandwidth can be realized, but this remains to be experimentally demonstrated. Increasing the dispersion in the 3.3-GHz direction requires that a single grating in the pulse-generation room be replaced with a new grating. The actual implementation of a new grating geometry would require substantial realignment of the 3.3-GHz SSD arm.

*Pinhole implications:* In the early days of three-color-cycle SSD on OMEGA, it became clear that the current pinhole configuration cannot tolerate any increase in the far-field deflection in the 10.4-GHz direction (wide direction). Any increase in the current OMEGA pinhole size is prohibited by the observed damage rate to the Stage-D, -E, and -F input spatial-filter lenses and the necessity of preventing catastrophic retroreflections in the beamlines. It is possible that the current pinholes could tolerate an increase in the far-field deflection in the narrow 3.3-GHz direction.

Several factors contribute to the position and size of the focal spot relative to the pinhole. These factors are statistical in nature, so while theoretical calculations can provide an estimate of the amount of deflection in the narrow direction that can be realized, the actual capability of OMEGA to support this change can be measured only via a series of laser shots. This experimental investigation will require a dedicated laser campaign that increases relative deflection while monitoring the transmitted near-field profile, transmitted temporal pulse shape, retroreflected energy, and pinhole-scattered light.

*Frequency conversion:* A deflection increase in the narrow 3.3-GHz direction has the potential to limit conversion efficiency and introduce FM-to-AM conversion because of the poor conversion efficiency of certain components of the FM spectrum. This loss of frequency conversion can occur regardless of which technique (increased dispersion or increased bandwidth) is used to increase deflection. Both options have been examined with respect to frequency-conversion implica-

tions using the code Miró,<sup>35</sup> and preliminary results indicate no preferred method from this standpoint. Implementation difficulty will most probably dictate the choice of technique.

**b. Effects of the current OMEGA kernel on the focal spot.**

To estimate the effect of 2-D dynamic bandwidth reduction, the best understanding of the current OMEGA SSD/DPR deflection kernel [Fig. 133.53(a)] was used. Figure 133.53(b) shows

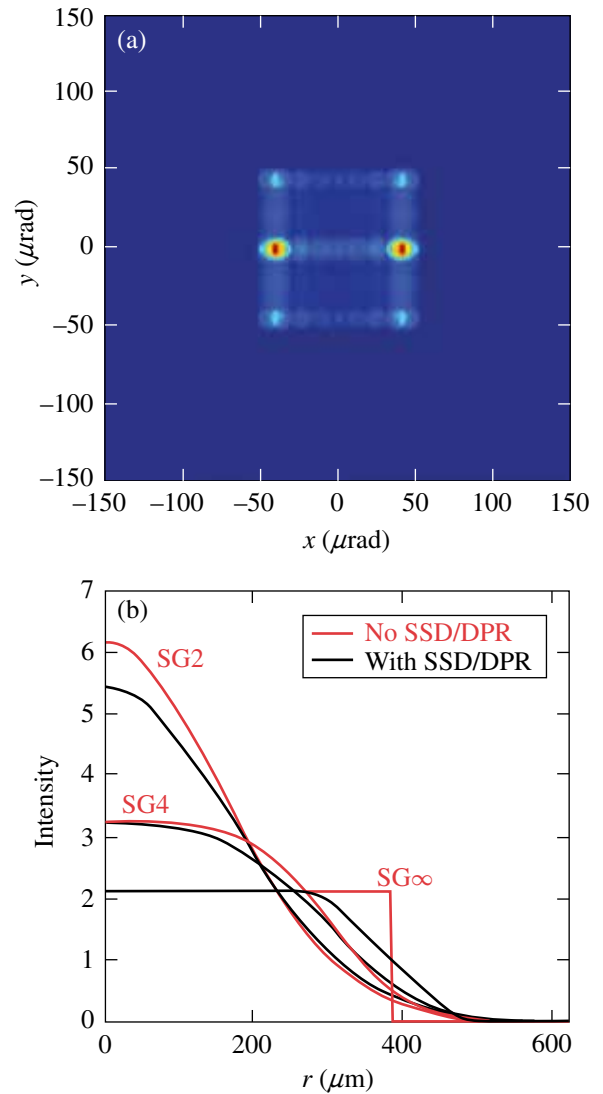


Figure 133.53 (a) The current OMEGA far-field SSD/DPR convolution kernel applied to a diffraction-limited (~12 μm at the target plane) beam (smoothed for presentation purposes). (b) The beam profiles when the current SSD/DPR kernel is applied (black) to the “no SSD/DPR” (red) profiles generated with super-Gaussian orders of 2, 4, and infinity. All beams have a “with SSD/DPR” diameter of 860 μm.

the effect of this kernel on various laser-beam far-field profiles. Table 133.IX summarizes these results with respect to zooming; the maximum effect occurs for an infinitely steep profile where the 95% encircled-energy radius is increased from 377  $\mu\text{m}$  to 430  $\mu\text{m}$ . To achieve the proposed zooming conditions (430  $\mu\text{m}$  to 300  $\mu\text{m}$ ), where 70% of the energy lost to CBET is recovered, the kernel would need to be increased by more than a factor of 2.5. This approach requires that the spatial-filter apertures on OMEGA be increased in size beyond the point considered appropriate for a noisy and aging laser system.

Table 133.IX: The 95% encircled-energy radius increase as a result of SSD/DPR versus order of super-Gaussian of “no SSD/DPR” beam. All beams have a “with SSD/DPR” diameter of 860  $\mu\text{m}$ .

Super-Gaussian order	$R_b$ increase ( $\mu\text{m}$ )
2	24.5
4	31.8
6	36.1
8	39.6
10	42.1
20	47.3
100	51.6
$\infty$	52.9

## 2. New DPR Options

To maintain a round focal spot throughout the laser pulse when implementing zooming with a symmetric 2-D SSD kernel, the wedged DPR’s must be removed from the current system. Polarization smoothing, using advanced DPR’s, could be maintained on OMEGA even with fully dispersive 2-D SSD. Several non-wedged DPR options are being developed for use in polar-drive experiments on the NIF. A  $4 \times 4$  checkerboard array of left-handed and right-handed glancing-angle deposition coatings are being developed at LLE to provide an improved power spectrum with smoothing. Alternatively, a  $2 \times 2$  checkerboard array of KD\*P half-wave plates and air is the baseline DPR for polar drive on the NIF.

## REFERENCES

1. J. Nuckolls *et al.*, Nature **239**, 139 (1972).
2. E. I. Moses and C. R. Wuest, Fusion Sci. Technol. **47**, 314 (2005).
3. C. Cavaller, Plasma Phys. Control. Fusion **47**, B389 (2005).
4. J. D. Lindl *et al.*, Phys. Plasmas **11**, 339 (2004).

5. R. L. McCrory, D. D. Meyerhofer, R. Betti, R. S. Craxton, J. A. Delettrez, D. H. Edgell, V. Yu. Glebov, V. N. Goncharov, D. R. Harding, D. W. Jacobs-Perkins, J. P. Knauer, F. J. Marshall, P. W. McKenty, P. B. Radha, S. P. Regan, T. C. Sangster, W. Seka, R. W. Short, S. Skupsky, V. A. Smalyuk, J. M. Soures, C. Stoeckl, B. Yaakobi, D. Shvarts, J. A. Frenje, C. K. Li, R. D. Petrasso, and F. H. Séguin, Phys. Plasmas **15**, 055503 (2008).
6. V. N. Goncharov, T. C. Sangster, T. R. Boehly, S. X. Hu, I. V. Igumenshchev, F. J. Marshall, R. L. McCrory, D. D. Meyerhofer, P. B. Radha, W. Seka, S. Skupsky, C. Stoeckl, D. T. Casey, J. A. Frenje, and R. D. Petrasso, Phys. Rev. Lett. **104**, 165001 (2010).
7. R. K. Kirkwood *et al.*, Phys. Rev. Lett. **76**, 2065 (1996).
8. W. Seka, H. A. Baldis, J. Fuchs, S. P. Regan, D. D. Meyerhofer, C. Stoeckl, B. Yaakobi, R. S. Craxton, and R. W. Short, Phys. Rev. Lett. **89**, 175002 (2002).
9. J. Myatt, A. V. Maximov, W. Seka, R. S. Craxton, and R. W. Short, Phys. Plasmas **11**, 3394 (2004).
10. P. Michel *et al.*, Phys. Rev. Lett. **102**, 025004 (2009).
11. I. V. Igumenshchev, W. Seka, D. H. Edgell, D. T. Michel, D. H. Froula, V. N. Goncharov, R. S. Craxton, L. Divol, R. Epstein, R. Follett, J. H. Kelly, T. Z. Kosc, A. V. Maximov, R. L. McCrory, D. D. Meyerhofer, P. Michel, J. F. Myatt, T. C. Sangster, A. Shvydky, S. Skupsky, and C. Stoeckl, Phys. Plasmas **19**, 056314 (2012).
12. P. Michel *et al.*, Phys. Rev. E **83**, 046409 (2011).
13. S. H. Glenzer *et al.*, Science **327**, 1228 (2010).
14. J. D. Moody *et al.*, Nat. Phys. **8**, 344 (2012).
15. T. R. Boehly, D. L. Brown, R. S. Craxton, R. L. Keck, J. P. Knauer, J. H. Kelly, T. J. Kessler, S. A. Kumpan, S. J. Loucks, S. A. Letzring, F. J. Marshall, R. L. McCrory, S. F. B. Morse, W. Seka, J. M. Soures, and C. P. Verdon, Opt. Commun. **133**, 495 (1997).
16. W. Seka, D. H. Edgell, J. P. Knauer, J. F. Myatt, A. V. Maximov, R. W. Short, T. C. Sangster, C. Stoeckl, R. E. Bahr, R. S. Craxton, J. A. Delettrez, V. N. Goncharov, I. V. Igumenshchev, and D. Shvarts, Phys. Plasmas **15**, 056312 (2008).
17. I. V. Igumenshchev, D. H. Edgell, V. N. Goncharov, J. A. Delettrez, A. V. Maximov, J. F. Myatt, W. Seka, A. Shvydky, S. Skupsky, and C. Stoeckl, Phys. Plasmas **17**, 122708 (2010).
18. D. H. Froula, I. V. Igumenshchev, D. T. Michel, D. H. Edgell, R. Follett, V. Yu. Glebov, V. N. Goncharov, J. Kwiatkowski, F. J. Marshall, P. B. Radha, W. Seka, C. Sorce, S. Stagmitto, C. Stoeckl, and T. C. Sangster, Phys. Rev. Lett. **108**, 125003 (2012).
19. I. V. Igumenshchev, D. H. Froula, D. H. Edgell, V. N. Goncharov, T. J. Kessler, F. J. Marshall, R. L. McCrory, P. W. McKenty, D. D. Meyerhofer, D. T. Michel, T. C. Sangster, W. Seka, and S. Skupsky, “Laser-Beam Zooming to Mitigate Crossed-Beam Energy Losses in Direct-Drive Implosions,” to be published in Physical Review Letters.
20. M. C. Myers *et al.*, Nucl. Fusion **44**, S247 (2004).

21. S. Skupsky, R. W. Short, T. Kessler, R. S. Craxton, S. Letzring, and J. M. Soures, *J. Appl. Phys.* **66**, 3456 (1989).
22. G. Fiksel, S. X. Hu, V. N. Goncharov, D. D. Meyerhofer, T. C. Sangster, V. A. Smalyuk, B. Yaakobi, M. J. Bonino, and R. Jungquist, *Phys. Plasmas* **19**, 062704 (2012).
23. S. X. Hu, G. Fiksel, V. N. Goncharov, S. Skupsky, D. D. Meyerhofer, and V. A. Smalyuk, *Phys. Rev. Lett.* **108**, 195003 (2012).
24. M. C. Herrmann, M. Tabak, and J. D. Lindl, *Phys. Plasmas* **8**, 2296 (2001).
25. "Cross-Beam Energy Transfer in Polar-Drive Implosions on OMEGA," published in this volume.
26. J. Delettrez, *Can. J. Phys.* **64**, 932 (1986).
27. P. B. Radha, T. J. B. Collins, J. A. Delettrez, Y. Elbaz, R. Epstein, V. Yu. Glebov, V. N. Goncharov, R. L. Keck, J. P. Knauer, J. A. Marozas, F. J. Marshall, R. L. McCrory, P. W. McKenty, D. D. Meyerhofer, S. P. Regan, T. C. Sangster, W. Seka, D. Shvarts, S. Skupsky, Y. Srebro, and C. Stoeckl, *Phys. Plasmas* **12**, 056307 (2005).
28. R. C. Malone, R. L. McCrory, and R. L. Morse, *Phys. Rev. Lett.* **34**, 721 (1975).
29. R. Epstein, *J. Appl. Phys.* **82**, 2123 (1997).
30. P. Y. Chang, R. Betti, B. K. Spears, K. S. Anderson, J. Edwards, M. Fatenejad, J. D. Lindl, R. L. McCrory, R. Nora, and D. Shvarts, *Phys. Rev. Lett.* **104**, 135002 (2010); R. Betti, P. Y. Chang, B. K. Spears, K. S. Anderson, J. Edwards, M. Fatenejad, J. D. Lindl, R. L. McCrory, R. Nora, and D. Shvarts, *Phys. Plasmas* **17**, 058102 (2010).
31. R. Betti, presented at the 24th IAEA Fusion Energy Conference, San Diego, CA, 8–13 October 2012.
32. T. C. Sangster, V. N. Goncharov, R. Betti, P. B. Radha, T. R. Boehly, D. T. Casey, T. J. B. Collins, R. S. Craxton, J. A. Delettrez, D. H. Edgell, R. Epstein, C. J. Forrest, J. A. Frenje, D. H. Froula, M. Gatu-Johnson, V. Yu. Glebov, D. R. Harding, M. Hohenberger, S. X. Hu, I. V. Igumenshchev, R. T. Janezic, J. H. Kelly, T. J. Kessler, C. Kingsley, T. Z. Kosc, J. P. Knauer, S. J. Loucks, J. A. Marozas, F. J. Marshall, A. V. Maximov, R. L. McCrory, P. W. McKenty, D. D. Meyerhofer, D. T. Michel, J. F. Myatt, R. D. Petrasso, S. P. Regan, W. Seka, W. T. Shmayda, R. W. Short, A. Shvydky, S. Skupsky, J. M. Soures, C. Stoeckl, W. Theobald, V. Versteeg, B. Yaakobi, and J. D. Zuegel, "Improving Cryogenic DT Implosion Performance on OMEGA," submitted to *Physics of Plasmas*.
33. F. J. Marshall, J. A. Delettrez, R. Epstein, R. Forties, R. L. Keck, J. H. Kelly, P. W. McKenty, S. P. Regan, and L. J. Waxer, *Phys. Plasmas* **11**, 251 (2004).
34. F. J. Marshall, J. A. Delettrez, R. Epstein, R. Forties, V. Yu. Glebov, J. H. Kelly, T. J. Kessler, J. P. Knauer, P. W. McKenty, S. P. Regan, V. A. Smalyuk, C. Stoeckl, J. A. Frenje, C. K. Li, R. D. Petrasso, and F. H. Séguin, *Bull. Am. Phys. Soc.* **48**, 56 (2003).
35. O. Morice, *Opt. Eng.* **42**, 1530 (2003).

---

# Measuring 8- to 250-ps Short Pulses Using a High-Speed Streak Camera on Kilojoule, Petawatt-Class Laser Systems

## Introduction

Optical streak cameras have been used as the primary diagnostic for a variety of laser and target experiments. OMEGA EP<sup>1</sup> uses a high-speed optical streak camera comprising a P820 streak tube<sup>2</sup> in a ROSS (Rochester Optical Streak System)<sup>3–5</sup> to measure the pulse shape for pulse durations ranging from 8 to 250 ps. A small percentage (0.7%) of the main laser beam (370 mm × 370 mm) is picked off by a full-size diagnostic mirror, demagnified to a size of 65 mm × 65 mm by a down-collimator inside the grating compressor chamber (GCC), and transported to the short-pulse diagnostic package (SPDP) residing outside the GCC. This diagnostic beam is further demagnified to 4 mm × 4 mm by three stages of down-collimators inside the SPDP (65 mm × 65 mm to 25 mm × 25 mm, to 12 mm × 12 mm, and, finally, to 4 mm × 4 mm). In the initial configuration, the 4-mm × 4-mm beam was focused onto the input slit of the ROSS by a cylindrical lens. The streak image of the line focus provides the temporal profile and the spatial profile in one direction of the laser beam. The focusing of a laser beam with aberration [approximately 0.5- $\lambda$  rms (root mean square),  $\lambda = 1053$  nm] by a cylindrical lens produces multiple local hot spots within the focal line. Because of shot-to-shot focal-spot pointing and structure variations, these hot spots move across the slit in both the space and time directions, leading to distorted pulse-shape measurements. Moreover, interactions among the photoelectrons transiting in the streak tube cause the electrons to repel each other (space-charge broadening).<sup>6</sup> This effect is particularly pronounced for shorter pulses, leading to an artificially broadened pulse measurement. The space-charge broadening is further exacerbated by the hot spots imaged onto the photocathode. The signal's sensitivity to far-field-based coupling and the space-charge broadening make it very challenging to operate a streak camera during short-pulse laser operations. The initial shot-to-shot streak measurements are found to exhibit a large signal variation (5:1 is typical), making it operationally impractical to accurately control space-charge-induced pulse broadening and to operate the streak camera within the traditionally defined dynamic range of less than 20% broadening.<sup>6</sup>

We report a beam-homogenizing method that uses an anamorphic diffuser to provide significantly more uniform illumination on the photocathode of a streak camera as compared with the conventional cylindrical-lens coupling approach, therefore increasing the signal-to-noise ratio and the ability to conduct a global space-charge-broadening calibration. A method to calibrate space-charge-induced pulse broadening of streak-camera measurements is described and validated by modeling and experiments.

## Anamorphic Diffuser for Uniform Photocathode Illumination

Figure 133.54(a) illustrates a typical streak image of a 230-ps laser pulse obtained with the cylindrical-lens-coupling approach. Figures 133.54(b) and 133.54(c) show the corresponding spatial and temporal profiles, respectively. The hot spots typically induce an undesired 5-to-1 spatial modulation. As shown in Fig. 133.54(c), the pulse shape is also somewhat distorted into a tilted top by the hot spots present during the first half of the pulse. The spatial-profile variation at different times also indicates that the streak image is sensitive to the far-field structure and pointing changes. A new coupling scheme is required to provide more-uniform streak images, higher signal-to-noise ratios, and less sensitivity to focal-spot structure and pointing changes.

An anamorphic-diffuser-based coupler has been developed to provide more-uniform streak images and to increase the signal-to-noise ratio. Figures 133.55(a) and 133.55(b) show the principle of the new coupling approach: it consists of an anamorphic diffuser followed by a spherical focusing lens. The divergence angles of the anamorphic diffuser are 10° and 0.4° along and across the ROSS slit (corresponding to the spatial and temporal directions), respectively. A 12-mm × 12-mm collimated beam is transmitted through the diffuser and diverges into a 10° × 0.4° solid angle. The focusing lens, having a 35-mm focal length, transfers the common angle from the diffuser to the same location on the focal plane, forming a focal line. All the rays with the same angle on the object plane contribute to

the energy collected at a particular location on the focal plane; therefore, any hot spot in the incoming beam will be averaged out at the image plane.

The spatial profile of this diffuser-based coupler was measured with a continuous-wave (cw) laser at a 675-nm wavelength. The profiles along the spatial and temporal directions

are shown in Figs. 133.55(c) and 133.55(d), respectively. The full-width-at-half-maximum (FWHM) spot sizes are  $270\ \mu\text{m}$  and  $6.1\ \text{mm}$  across and along the slit, respectively. The measured coupling efficiency through a  $100\text{-}\mu\text{m}$  slit was 20%.

The diffuser coupler was tested with a ROSS on a pulsed laser system. Figures 133.56(a)–133.56(c) show the measured

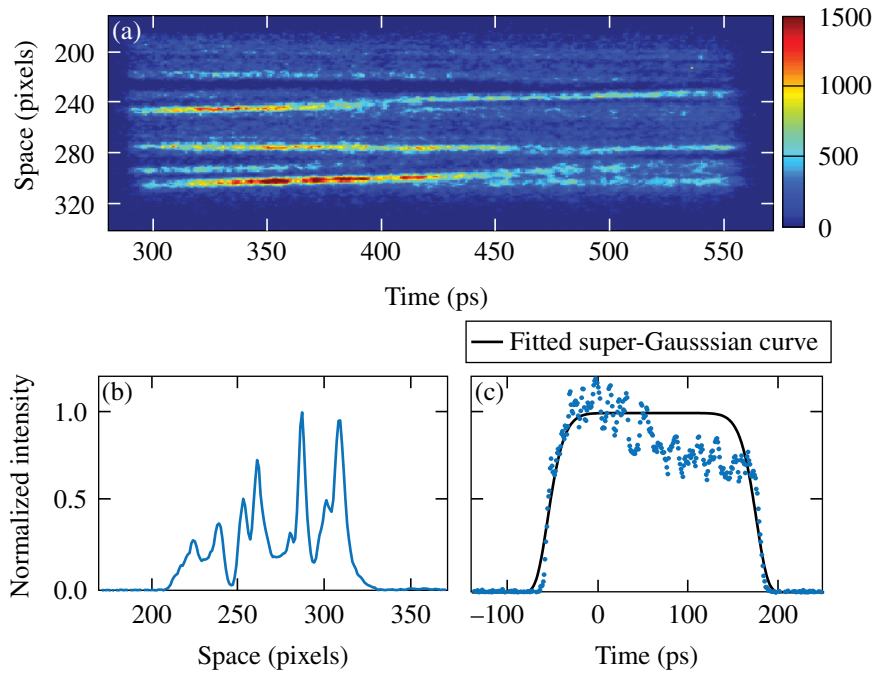


Figure 133.54  
(a) Streak image with a cylindrical lens coupling; (b) spatial profile showing modulation from the hot spots; (c) temporal profile distorted by the hot spots.

G9373JR

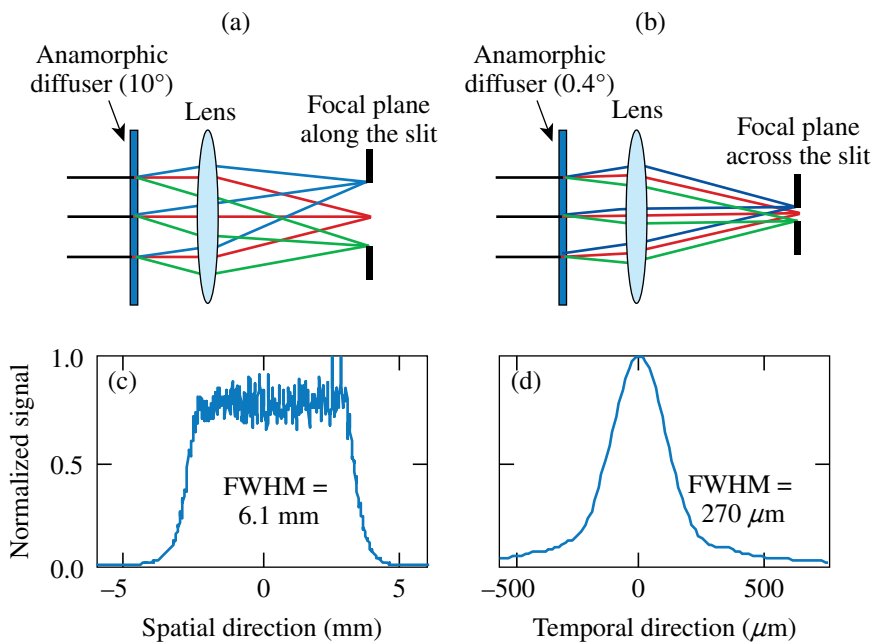


Figure 133.55  
[(a),(c)] A  $10^\circ$  divergence angle in the spatial direction achieved a 6.1-mm-long focal line along the slit. [(b),(d)] A  $0.4^\circ$  divergence angle in the temporal direction achieved a  $270\text{-}\mu\text{m}$ -wide focal line across the slit.

G9374JR

streak image and spatial and temporal profiles of a 180-ps (FWHM) laser pulse. Compared to the cylindrical-lens coupling results shown in Fig. 133.54, the anamorphic-diffuser-based coupling provides a more-uniform photocathode illumination; the spatial modulation is less than 2:1, down from 5:1 for the cylindrical-coupling approach. Figure 133.57 illustrates

that the temporal distortions induced by the hot spots in region of interest #2 (ROI2) [Fig. 133.57(a)] with the cylindrical lens coupling were eliminated through the more-uniform illumination [Fig. 133.57(b)] on the photocathode with the  $10^\circ \times 0.4^\circ$  diffuser [comparing Figs. 133.57(a), 133.57(c) and 133.57(b), 133.57(d)]. Therefore, consistent temporal profiles are achieved

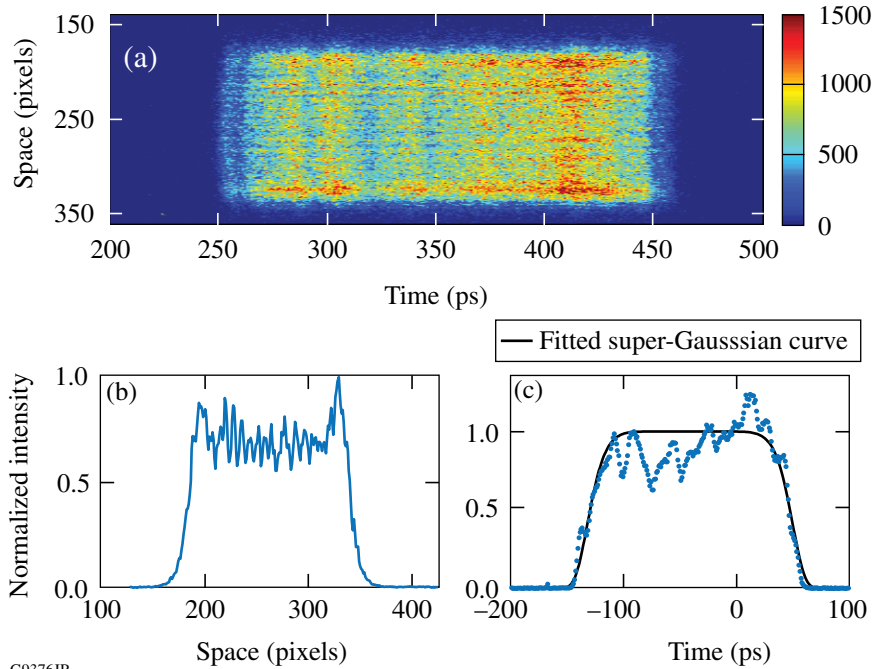


Figure 133.56  
(a) A streak image obtained with the  $10^\circ \times 0.4^\circ$  diffuser; (b) spatial profile; (c) temporal profile.

G9376JR

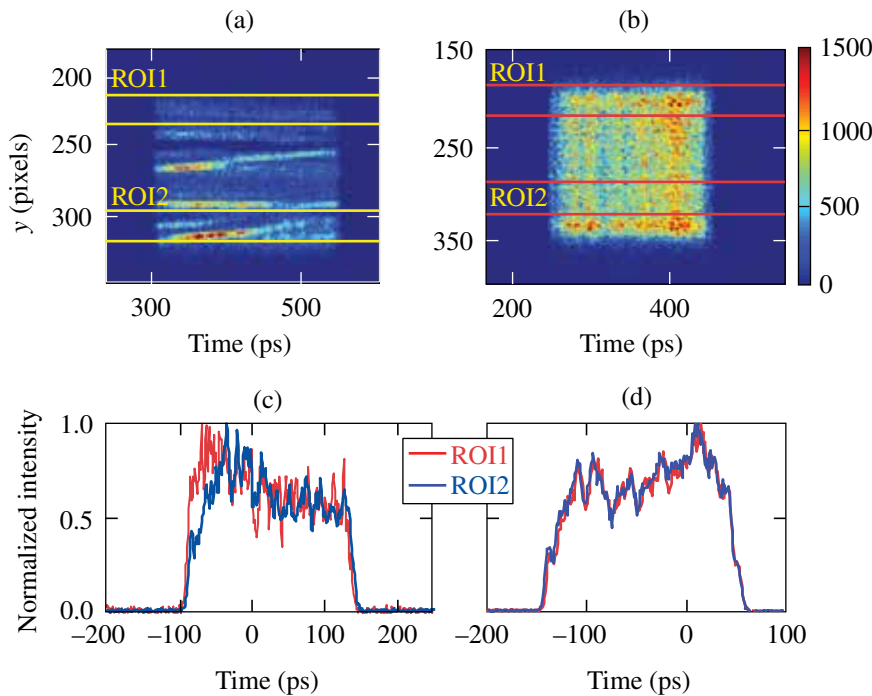


Figure 133.57  
[(a),(c)] Streak image and temporal profiles obtained through a cylindrical lens. Temporal profiles were distorted by the hot spots in ROI2. [(b),(d)] Streak image and temporal profiles obtained through a  $10^\circ \times 0.4^\circ$  diffuser. Temporal profiles are consistent across the spatial direction.

G9716JR

across the spatial direction. A higher signal-to-noise ratio can be achieved by averaging across the spatial direction without compromising the pulse-shape measurement.

The maximum optical-path difference (OPD) of the rays traveling from the diffuser to the focal plane was investigated in OSLO®, and induced pulse broadening was found to be less than 0.5 ps ( $140 \lambda$ ,  $\lambda = 1053 \text{ nm}$ ). The impulse response of the ROSS and diffuser-coupler system was measured with a subpicosecond pulse to verify that diffuser-induced pulse broadening was minimal. The measured impulse response width remained at 3 ps (FWHM, shown in Fig. 133.58), narrow enough to measure 10-ps pulses.

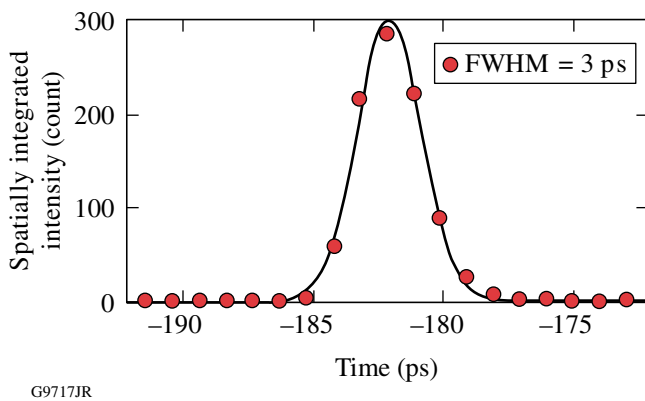


Figure 133.58 Impulse response of the streak camera using the  $10^\circ \times 0.4^\circ$  diffuser with a 3-ps FWHM.

### Characterization of Space-Charge–Broadening Effects

Maintaining the dynamic range of a streak camera requires that the input signal to the photocathode be controllable under a certain level and stable from shot to shot. However, the large 5-to-1, shot-to-shot streak signal variation makes it difficult to control the space-charge–induced broadening effect. Therefore, the traditionally defined dynamic range is operationally impractical to achieve; the pulse width broadens with an increasing total number of electrons per pulse.

The spatial averaging produced by the diffuser eliminates the local hot spots imaged to the photocathode and subsequently simplifies the space-charge mechanism so that pulse broadening depends on the total current in the tube, rather than on local variations in intensity. As a result, a global space-charge analysis can be used to determine the amount of broadening from the total signal, integrated in space and time.

A method to calibrate space-charge–induced pulse broadening has been developed and validated on OMEGA EP. The input energy to the slit of the ROSS was varied to obtain a series of broadened pulses for each stretcher position. The true pulse width was determined by a linear regression between the measured pulse width and the total pixel values in an analog-to-digital units (ADU’s) measured by the ultrafast ROSS charge-coupled device (CCD). The offset at zero ADU represents the true pulse width without space-charge broadening.

Rather than using a  $10^\circ \times 0.4^\circ$  diffuser that provided only 20% coupling efficiency, a  $10^\circ \times 0^\circ$  diffuser with 75% coupling efficiency was used to provide sufficient energy for a ROSS on OMEGA EP to characterize the space-charge effects on streak measurements of short pulses with various lengths and shapes. Characterization traces were measured for stretcher positions of 16 mm, 40 mm, and 80 mm (relative to the position corresponding to a best-compression pulse width of approximately 1 ps). With the full front-end spectrum, these stretcher positions produce approximately square pulses with FWHM’s of 23 ps, 58 ps, and 120 ps, respectively, as predicted by a system model. When the beamline amplifiers are fired, spectral gain narrowing produces approximately Gaussian pulses with widths of 10 ps, 25 ps, and 50 ps for these stretcher positions. Figure 133.59 demonstrates that the pulse width linearly increases with the total signal on the photocathode. In the absence of gain narrowing, for stretcher positions of 16 mm, 40 mm, and 80 mm, the regressed true pulse widths are 21.1 ps, 55.7 ps, and 113.7 ps, respectively. The corresponding 95%

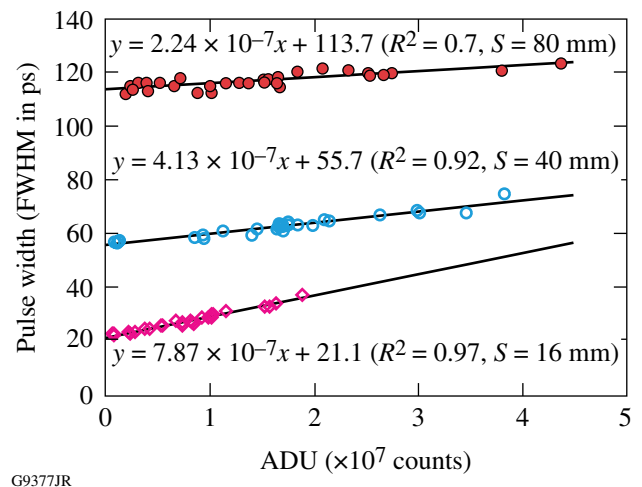
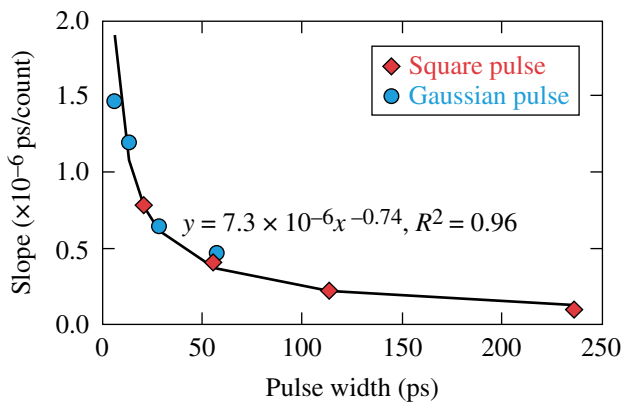


Figure 133.59 Space-charge–broadening calibration for stretcher positions of  $S = 16 \text{ mm}$ ,  $S = 40 \text{ mm}$ , and  $S = 80 \text{ mm}$ .

confidence intervals are [20.6 ps, 21.7 ps]; [54.8 ps, 56.7 ps]; and [112.7 ps, 114.7 ps]. The slopes obtained from linear regressions between the measured pulse width and photocathode signal at each stretcher position reveal that the magnitude of the space-charge–broadening effect depends on the stretcher position, i.e., the pulse width to be measured. The shorter the pulse to be measured, the larger the slope, and the more pronounced the space-charge–broadening effects.

Figure 133.60 shows the inverse relation between space-charge–induced pulse broadening (slope) and pulse width (offset) for both square and Gaussian pulses. For the limited number of measurements, the space-charge–broadening effect is comparable for these two pulse shapes, although the electron density at the edges of a Gaussian pulse is smaller than that of a square pulse. One would expect the effect on the former is less than that on the latter because a Gaussian pulse shape distorts to a super-Gaussian and to a square pulse shape with the increasing energy to the input slit.<sup>7</sup>



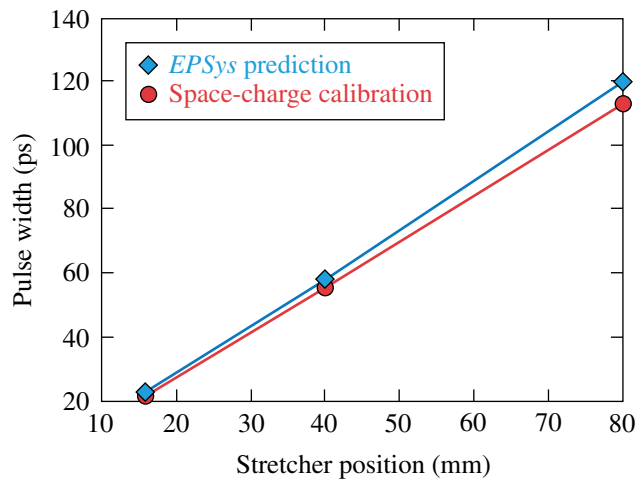
G9378JR

Figure 133.60  
Inverse relation between space-charge broadening and pulse width.

During laser operations, the slope of each calibration trace, in conjunction with the streak-image signal level and measured pulse width, can be used to determine the true pulse width, removing space-charge–broadening effects.

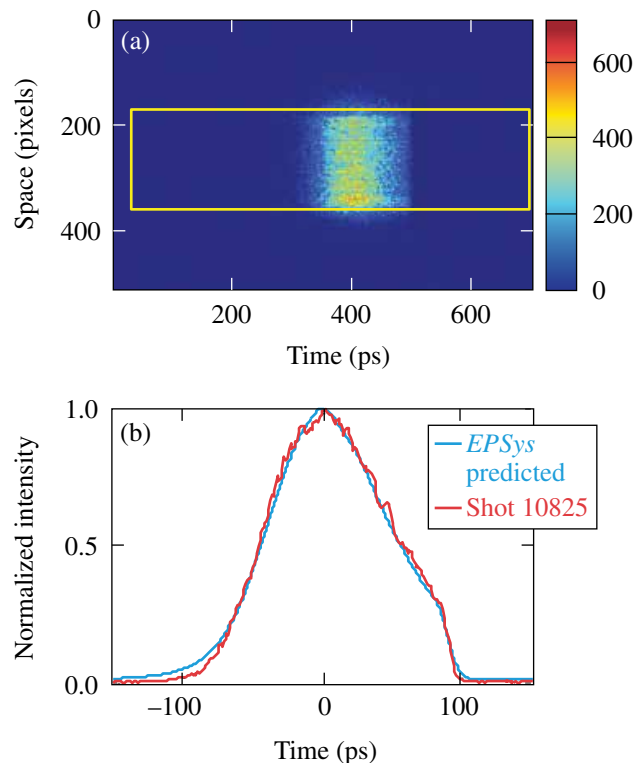
The inferred pulses are compared to the results from an *EPSys* model<sup>8</sup> that predicts the pulse shape from the measured spectrum, the stretcher and compressor angles, and the stretcher slant distance. The pulse widths determined using the two methods show a systematic error of 5% (Fig. 133.61). Figure 133.62(a) shows a uniform streak image obtained on a high-energy shot. Figure 133.62(b) illustrates that the measured pulse shape, at a low input energy level to minimize space-charge broadening, agrees with the *EPSys*-predicted pulse shape.

To validate the accuracy of the space-charge–broadening calibration method, a <10-ps inferred pulse from the streak-camera measurements was compared to the measurements from



G9718JR

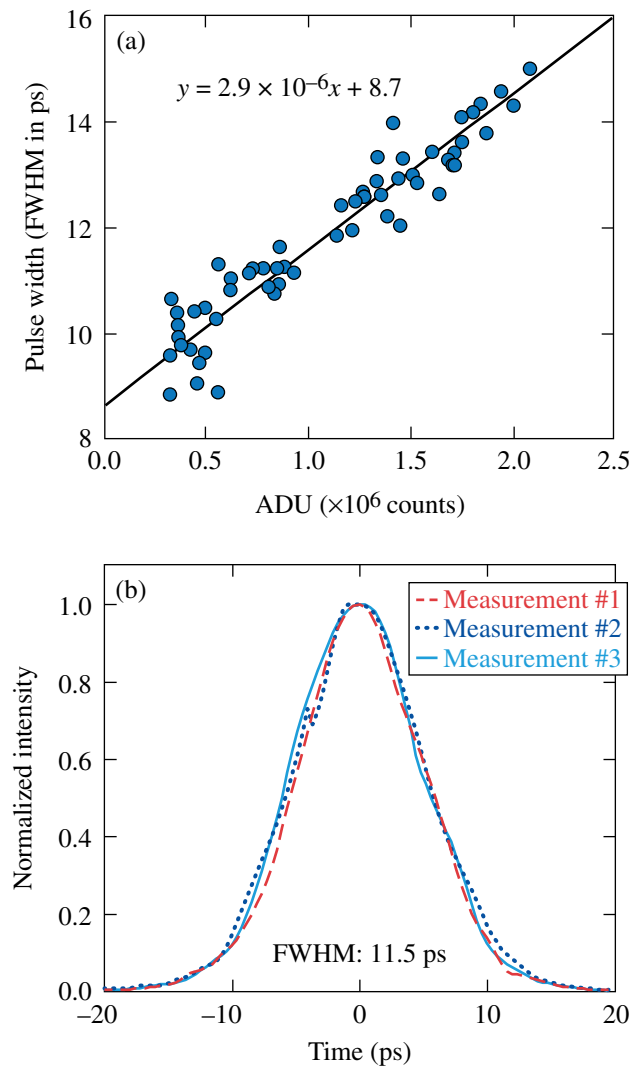
Figure 133.61  
Comparison of results from space-charge–broadening calibration and *EPSys* prediction.



G9485JR

Figure 133.62  
(a) Uniform streak image achieved on high-energy laser shots; (b) Measured pulse shape and model prediction.

a scanning autocorrelator (suitable for pulses ranging from 0.2 to 20 ps). Figure 133.63(a) shows the streak-camera data. The pulse width (FWHM), after a space-charge-broadening calibration was applied, was  $8.7 \text{ ps} \pm 0.5 \text{ ps}$ . Figure 133.63(b) shows three consecutive autocorrelation measurements with an averaged FWHM of 11.5 ps and a standard deviation of 0.1 ps. By applying a decorrelation factor of 1.36 (the ratio of the width of the autocorrelation of the pulse predicted by *EPsys* to the width of the pulse itself), the pulse width determined from the scanning autocorrelator was 8.5 ps, which agrees with the space-charge-broadening-calibrated measurement of 8.7 ps by the ultrafast ROSS.



G9550JR

Figure 133.63  
 (a) Space-charge-broadening-calibrated pulse measurement (FWHM = 8.7 ps). (b) Three autocorrelation measurements leading to a pulse FWHM of 8.5 ps using a decorrelation factor of 1.36 obtained by modeling.

## Conclusions

The insertion of an anamorphic-diffuser coupler provides more-uniform photocathode illumination, less sensitivity to focal-spot pointing and structure changes, and improved space-charge-broadening characterization, resulting in improved pulse-measurement accuracy. A linear regression method was developed to calibrate space-charge-broadening effects. By increasing the effective dynamic range and reducing the sensitivity to wavefront errors, the space-charge-broadening calibration method, in conjunction with the anamorphic diffuser coupler, allows one to more easily operate a streak camera and obtain more-accurate pulse measurements in the 8- to 250-ps range on OMEGA EP. This approach is well suited for other short-pulse laser systems.

## ACKNOWLEDGMENT

This work was supported by the U.S. Department of Energy Office of Inertial Confinement Fusion under Cooperative Agreement No. DE-FC52-08NA28302, the University of Rochester, and the New York State Energy Research and Development Authority. The support of DOE does not constitute an endorsement by DOE of the views expressed in this article. The authors thank M. Millecchia and A. Kalb for their support on the anamorphic-diffuser-based coupler testing.

## REFERENCES

1. J. H. Kelly, L. J. Waxer, V. Bagnoud, I. A. Begishev, J. Bromage, B. E. Kruschwitz, T. J. Kessler, S. J. Loucks, D. N. Maywar, R. L. McCrory, D. D. Meyerhofer, S. F. B. Morse, J. B. Oliver, A. L. Rigatti, A. W. Schmid, C. Stoeckl, S. Dalton, L. Folsbee, M. J. Guardalben, R. Jungquist, J. Puth, M. J. Shoup III, D. Weiner, and J. D. Zuegel, *J. Phys. IV France* **133**, 75 (2006).
2. PHOTONIS, 19106 Brive, France.
3. W. R. Donaldson, R. Boni, R. L. Keck, and P. A. Jaanimagi, *Rev. Sci. Instrum.* **73**, 2606 (2002).
4. R. A. Lerche, J. W. McDonald, R. L. Griffith, G. Vergel de Dios, D. S. Andrews, A. W. Huey, P. M. Bell, O. L. Landen, P. A. Jaanimagi, and R. Boni, *Rev. Sci. Instrum.* **75**, 4042 (2004).
5. Sydor Instruments, LLC, Rochester, NY 14624.
6. D. J. Bradley *et al.*, *Rev. Sci. Instrum.* **49**, 215 (1978).
7. X. Wang *et al.*, *Rev. Sci. Instrum.* **80**, 013902 (2009).
8. *Final Proposal for Renewal Award for Cooperative Agreement DE-FC52-92SF-19460*, Between the U.S. Department of Energy and the Laboratory for Laser Energetics of the University of Rochester, Part 1: Technical Program (Rochester, NY, 2007), p. 2.245.

# A Solid-State, Inductive-Adder, 10-kV Pulse Generator for Driving Large-Aperture Pockels Cells

## Introduction

Pockels cells use electro-optic crystals with electrodes to apply electric fields that modulate the birefringence of the crystals and serve as voltage-controlled wave plates in laser systems. When combined with polarizers, these devices operate as optical switches for laser applications that include picking individual pulses from pulse trains,  $Q$ -switching laser cavities, isolating the gain of multiple amplifier stages, and protecting stages early in a power-amplifier chain from backward-propagating beams caused by unwanted retroreflections. These applications are illustrated schematically in Fig. 133.64. In this figure, a ring laser amplifier, such as the large-aperture ring amplifier (LARA)<sup>1</sup> or a similar system using Nd:YLF crystals for the laser gain (CLARA),<sup>2</sup> is shown.

Highly deuterated potassium dihydrogen phosphate ( $KD_2PO_4$ , often abbreviated  $KD^*P$  or  $DKDP$ ) is a common crystal used in Pockels cells, especially in devices that apply the electric field in the direction of the light beam propagation when large apertures are required. An important property of a Pockels cell is the half-wave voltage  $V_\pi$ . It is defined as the potential producing a retardance within the Pockels cell that rotates linear polarized light  $90^\circ$  to change the transmission state through an accompanying polarizer from minimum to maximum. The half-wave voltage for  $KD^*P$  Pockels cells with longitudinal electrodes is approximately 8 kV, which is roughly independent of the aperture size. Voltage pulses up to 9 kV are needed to accommodate losses.

Figure 133.65 shows high-voltage pulse generation and delivery schemes used to drive Pockels cells. These cells form

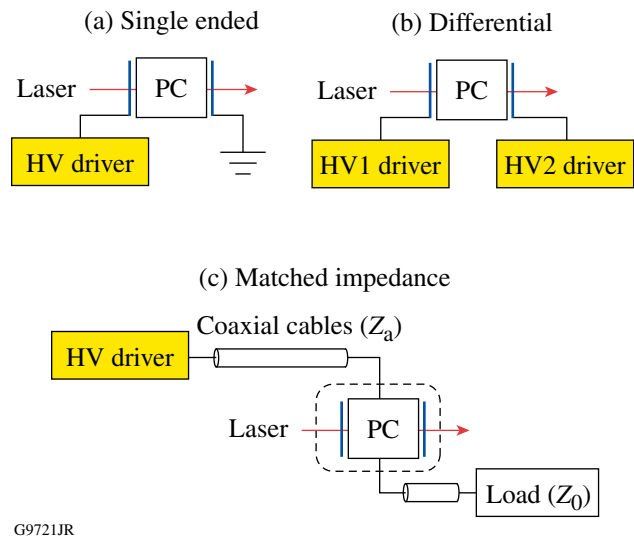


Figure 133.65 Pockels cell schemes. (a) A low-impedance, high-voltage (HV) half-wave driver is connected directly to the Pockels cell in the single-ended scheme. (b) Two low-impedance quarter-wave voltage drivers of opposite polarity are connected directly to the Pockels cell in the differential scheme. (c) In the matched-impedance scheme, a half-wave driver is connected to a Pockels cell, shunted with a resistance  $Z_0$ , via a coaxial line of characteristic impedance  $Z_0$ .

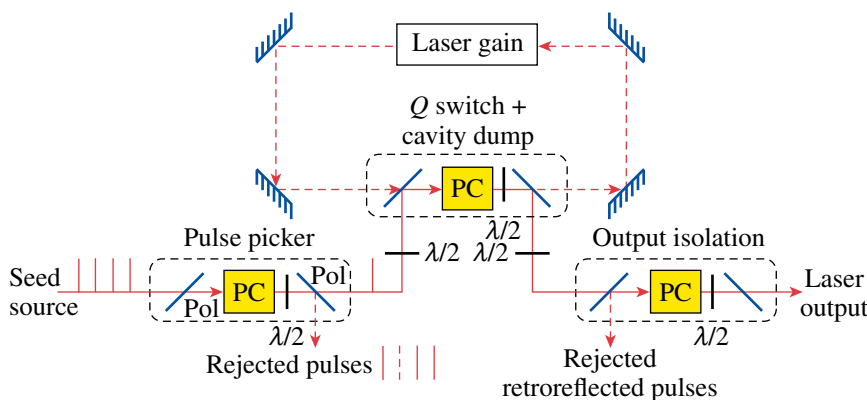


Figure 133.64 Applications of Pockels cells in laser systems. Pulse pickers use a Pockels cell (PC) between polarizers (Pol) in combination with a half-wave plate ( $\lambda/2$ ) to select an individual pulse from a repetitive seed source. Output isolation stages similarly gate through single pulses to reject pulses leaked from multipass amplifiers; in addition, they protect front-end systems from retroreflected light. Pockels cells are used to  $Q$ -switch and cavity-dump multipass laser cavities.

G9720JR

capacitive loads with capacitance ranging from a few picofarads for small cells to hundreds of picofarads for large-aperture cells. Drive schemes include single-ended<sup>3</sup> [Fig. 133.65(a)] and differential<sup>4</sup> [Fig. 133.65(b)] schemes with short-length connections that directly drive the electrodes to limit pulse distortion resulting from parasitic reactances. Also illustrated is a matched-impedance driver<sup>5</sup> [Fig. 133.65(c)] that delivers high-voltage pulses on shielded coaxial cable to a resistively shunted Pockels cell with resistance equal to the characteristic impedance of the coaxial line  $Z_0$ . Two advantages of the coaxial-cable matched-impedance driver scheme are limited radiated electromagnetic interference (EMI) and the option of physical separation of the pulse generator from the Pockels cell with minimal distortion of the driver pulse shape.

A commonly used matched-impedance Pockels cell driver employs a thyratron electron tube as a closing switch to connect a fixed-length charged transmission line (charge line) to the Pockels cell.<sup>5</sup> This design generates high-voltage pulses with nanosecond switching times required for many applications. The charge line produces a rectangular pulse at half of the line charge voltage and twice the transmission line's pulse propagation length. Thyratrons designed for this application can switch voltages and currents up to 25 kV and 1 kA, respectively, and one device per pulser is generally used. Unfortunately, these electron tubes degrade with operation. Currently, aging thyratron pulsers are no longer serviceable since manufacturers have discontinued production of suitable thyratron replacement tubes.

It is desirable to replace thyratron-based drivers with drivers based on solid-state devices to avoid matched-impedance drivers based on modern solid-state devices is desirable to avoid degradation over time, improve reliability, and address availability issues associated with electron tubes. Several fast-switching, high-voltage, high-current technologies exist including metal-oxide-semiconductor field-effect transistors (MOSFET's),<sup>6</sup> avalanche bipolar transistors,<sup>7</sup> dynistors,<sup>8</sup> and drift-step-recovery diodes.<sup>9</sup> A fundamental advantage of MOSFET's compared to the other devices is that they can be turned on and off using low-voltage gate drive signals, allowing them to act as both opening and closing switches, making it possible to adjust output-pulse lengths without changing charge-line hardware. Avalanche and dynistor devices act only as closing switches and require a hardware pulse-forming network, such as a charge line, to set the duration of the output pulse. High-voltage MOSFET's are economical and produce fast switching speeds of less than 5 ns. Fast-switching, high-voltage MOSFET's can switch 1.2 kV at currents in the tens of amperes for each device and can be configured in various

series- and parallel-connected networks to increase the total switching voltage and current capability.

The circuit topology used in this design—an inductive adder schematically illustrated in Fig. 133.66—is a circuit utilizing inductive coupling to achieve high-voltage pulse outputs from lower-voltage, ground-referenced pulse generators, or primary drivers. The output pulse is initiated when the switches in each primary driver simultaneously close and provide a current path from the charge-storage capacitors across the transformer's primary winding. The desired output level is obtained by series connecting, or adding, a sufficient number of individual transformer secondary windings. The pulse is terminated when the primary switches open and the primary current flow ceases. The lower-voltage primary driver units improve reliability and reduce switching device and charge-storage voltage requirements, as well as circuit layout stand-off requirements. The inductive-adder topology allows one to adjust both pulse amplitude and duration without changing the pulser's internal components.

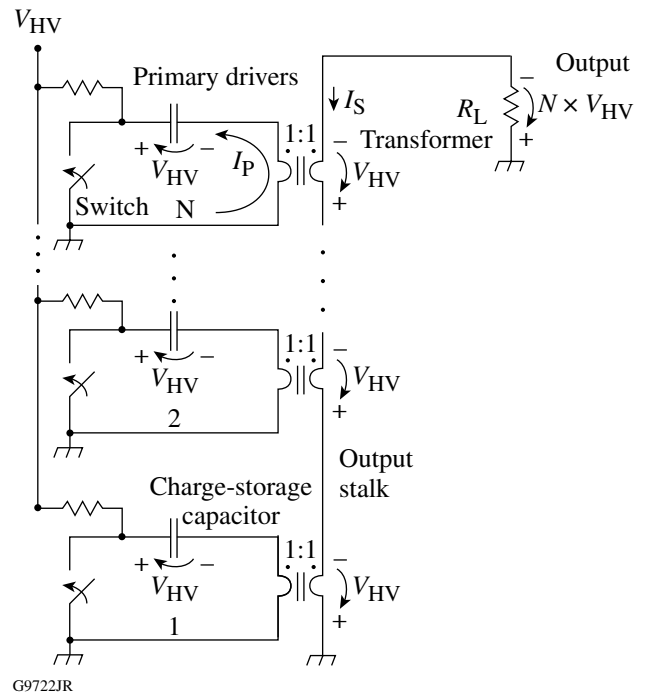


Figure 133.66 Inductive-adder schematic. When the switches simultaneously close within the  $N$  primary driver circuits, the charge-storage capacitance creates a current in the primary circuit of each coupled inductor (transformer). This current is inductively coupled to each transformer secondary and creates a voltage equal to the capacitor charge voltage. The secondary of each transformer is series connected to add the pulse voltage from each primary circuit and apply it to the load  $R_L$ .

Inductive-adder technology for driving Pockels cells has been demonstrated at voltages of tens of kilovolts and currents of hundreds of amperes with switching times less than 10 ns. Original designs were developed at Lawrence Livermore National Laboratory (LLNL) for fast pulse beam “kickers” in particle accelerators<sup>10</sup> and adapted at LLE to produce 20-kV pulses to switch the plasma-electrode Pockels cell (PEPC) in the OMEGA EP laser, where a closing and opening switch was required to produce the necessary double-pulse waveform.<sup>11</sup> Five solid-state switch-pulse PEPC driver (SS-SPD) units have been fielded at LLE since 2005 with performance and reliability far exceeding that of equivalent thyatron-based drivers.

A solid-state, high-voltage pulse generator based on inductive-adder technology for driving 50-Ω, KD\*P Pockels cells is reported. The design considerations, subsystem characteristics, and electrical and optical performance are presented, as well as considerations to optimize the design for other potential applications.

**Solid-State Pockels-Cell Driver Design**

The requirements for a matched-impedance, solid-state Pockels-cell driver (SSPD) are summarized in Table 133.X. The output voltage and output impedance specifications determine the transmission values and stability for large-aperture KD\*P Pockels cells<sup>12</sup> used in the half-wave applications illustrated in Fig. 133.64. The electrical pulse-timing values determine the

Table 133.X: Solid-state Pockels-cell driver requirements.

Specification	Requirement
Output Voltage	
Peak output	5 to 10 kV
Peak voltage stability	<±3%
Pre-/post-pulse voltage	<±3%
Flattop variation	<±4%
Output Impedance	50 Ω
Pulse Timing	
10% to 90% rise time	<10 ns
90% to 10% fall time	<10 ns
Pulse duration	9 to 100 ns
Pulse jitter	<200-ps rms
Maximum repetition rate	10 Hz
External Trigger	5-V Logic Edge
Output Voltage Monitor	10,000:1
Primary Power	110/220 VAC, 50/60 Hz

maximum usable laser pulse length in a multipass laser amplifier and the maximum repetition rate of laser pulse trains from which a single pulse can be isolated.

State-of-the-art, fast-switching, high-voltage (1200-V) power MOSFET’s, de-rated to 750 V, are utilized in the design of the primary drivers. A charge-storage voltage of 750 V requires an inductive-adder stack of at least 15 transformers to produce output-pulse voltages up to 10 kV, accounting for inductive coupling and driver losses. This circuit is shown schematically in Fig. 133.67. The 15 identical transformers and corresponding primary drive circuits are easily maintained, repaired, and inventoried as spares. An adjustable 750-V (dc) power supply charges all of the primary drive circuit charge-storage capacitors to the appropriate voltage for the desired pulse amplitude. The driver circuits are triggered simultaneously from a common trigger conditioning system initiated from an external 5-V logic trigger edge. Details of these subsystems and other features of the SSPD are provided below.

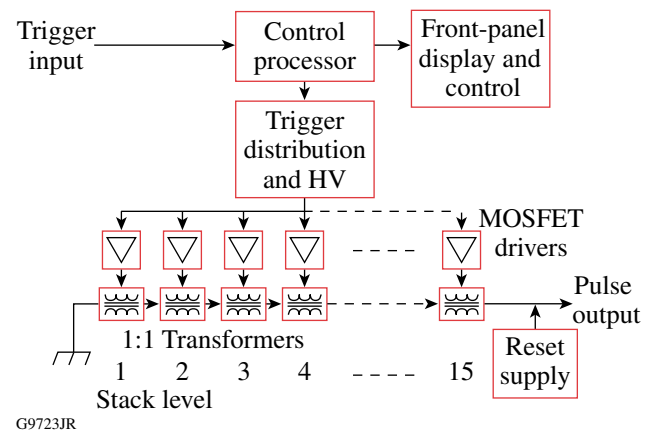
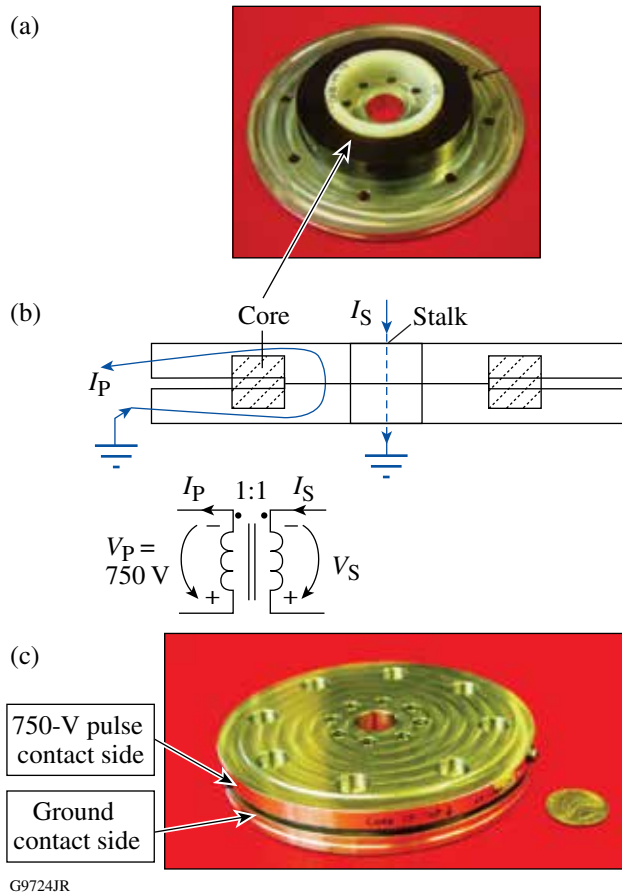


Figure 133.67 Schematic diagram of the solid-state Pockels-cell driver (SSPD). The pulser consists of 15 ground-referenced drivers, each driving a 1:1 transformer with secondaries series-connected to form the high-voltage output pulse.

**1. Pulse Transformer Design**

An inductive-adder transformer is illustrated in Fig. 133.68. The transformer uses a single-turn, solid primary winding machined from aluminum that completely surrounds a toroidal transformer core [Fig. 133.68(a)]. This configuration maximizes the inductive coupling between primary and secondary by minimizing the leakage inductance from uncoupled magnetic fields. Leakage inductance appears in series with the primary drive circuit, directly impacting high-frequency performance and resulting in increased pulse transition times and reduced pulse amplitude. The secondary circuit of the transformer



G9724JR

Figure 133.68

Inductive-adder transformer cell. [(a),(b)] The 750-V pulse contact side of the primary winding of a cell is isolated from the ground side of the next transformer above by standoffs seated on the ground contact side. (c) The standoffs are positioned in eight cut-outs (holes) in the 750-V side with sufficient air-gap clearance. The standoffs provide both isolation of the 750-V contact side and connection of successive transformers ground contact sides in the stack. Threaded rods extend through the center of the standoffs to hold the cells in the stack together. An isolated conductive rod extends through the center hole of each transformer to form the series-connected secondary circuit.

structure is created by passing an isolated metal rod through the center of the transformer structure [Fig. 133.68(b)]. This metal rod extends through the entire stack of transformer cores, thereby series-connecting the secondaries of each. This rod is termed the “stalk.”

A toroid core geometry was chosen to create an efficient magnetic coupling path between the primary and secondary that had minimal leakage inductance. The size of the core is selected to have sufficient cross-sectional area and magnetic path length (average circumference) to support the pulse voltage–time product without magnetic-flux saturation of the core material. If core flux saturation occurs, the single-turn primary

drops to a very low impedance, which results in catastrophic over-current failure of the primary drive circuits. A safety margin was applied to the design of the transformer core to ensure that the magnetic-flux density in the core is three times less than the saturation flux density for the longest pulse of the largest amplitude.

The first step in the design is to determine the core material and size for the 1:1 single-turn transformer. The core is constructed from a tape-wound, low-loss amorphous ferromagnetic alloy. The core material was selected for its large saturation flux density and low loss. This type of core provides high coupling over a wide bandwidth extending into the VHF (very high frequency) range. The core material chosen was Metglas 2601SA1 (Ref. 13), which is the same material used in the SS-SPD for the OMEGA EP PEPC pulser.<sup>11</sup> The material saturation flux density swing ( $\Delta B_{\text{sat}}$ ) is 3 teslas (T). The maximum operational flux density was set at 1 T to provide a 3× safety margin. The core effective cross-sectional area  $A_e$  to achieve this flux density is derived from the standard equations for flux density  $B$  (tesla), inductance  $L$  (henrys), and voltage of a toroid wound inductor:<sup>14</sup>

$$A_e = \frac{3 \cdot V \cdot \Delta t}{\Delta B_{\text{sat}} \cdot PF} (\text{m}^2), \quad (1)$$

where  $V$  is the maximum voltage across the primary circuit for the pulse duration  $\Delta t$  and  $PF$  is the core packing factor defined as the ratio of the ferromagnetic material cross-sectional area to the overall cross-sectional area of the core material. The value of 3 in the numerator relates to the safety margin.

With the values of  $V = 750\text{ V}$ ,  $\Delta t = 100\text{ ns}$ ,  $\Delta B_{\text{sat}} = 1\text{ T}$ , and  $PF = 0.65$ ,  $A_e = 1.15\text{ cm}^2$  is obtained. A toroid core with a  $1.27\text{-cm}^2$  cross section was chosen. Once the cross-sectional area is calculated, the circumference of the toroid must be determined. For a transformer, the inductance of a winding, with all others open-circuited, is termed the “magnetizing inductance.” This inductance is electrically in shunt with the drive or load circuitry of that winding. The magnetizing inductance must be large enough that the current through the inductor at the end of the maximum amplitude pulse will not create distortion by excessive loading. Ideally, a large inductance is desirable; however, a tradeoff must be made since a large inductance requires a small core diameter. A small core diameter decreases the driver circuit board’s component placement area if minimum current path length is required for low leakage inductance. The circumference was selected

as a compromise between magnetizing inductance value and driver circuit board's component physical layout. The chosen 3-in. outer diameter produces a magnetizing inductance of approximately 2  $\mu\text{H}$  as calculated using Eq. (2) (Ref. 14):

$$L = \frac{\mu_0 \mu_r N^2 A_e}{l_e} (\text{H}), \quad (2)$$

where the number of turns  $N = 1$ ,  $\mu_0 \mu_r$  is the core material's magnetic permeability, and the effective magnetic path length or the average circumference  $l_e$  is  $2\pi(r = 2.5\text{-in.}/2)$ . An inductance of 2  $\mu\text{H}$  produces a magnetizing current of about 13% of the total primary current at the end of the longest pulse operation.

Another characteristic of the ferromagnetic core material is the core magnetization current. This current is required to overcome the permanent magnetization of the core material since it will take on an amount of permanent magnetization. This is exhibited in the hysteresis loop of the  $B-H$  curves (magnetic field versus flux density).<sup>13</sup> An  $\sim 45\text{-A}$  magnetization current is required for the core material chosen in this design to overcome the magnetization hysteresis.

## 2. Primary Drive Circuit

A simplified schematic of the transformer and the associated primary drive circuit is illustrated in Fig. 133.69. The primary drive to each transformer of the inductive adder is produced by a low-impedance, pulsed-voltage source formed by a group of 12 parallel-connected MOSFET's and a bank of charge-storage capacitors. The pulsed-drive units are connected to the primary

winding along its circumference to minimize parasitic inductance. The primary driver is split into two identical printed wiring boards that plug into the transformer circumference from opposite sides for ease of assembly and maintenance. The number of parallel-connected MOSFET's for each primary driver is determined by the sum of the current required at the output plus the core magnetizing and magnetization currents. The total primary current is equally divided among the parallel-connected, synchronously triggered MOSFET's. The design uses a higher MOSFET count than what is minimally required to switch the output current level to provide a safety margin. In the SSPD design, the maximum MOSFET operational current is limited to 64% of the MOSFET pulsed maximum current as specified by the MOSFET manufacturer.<sup>6</sup>

The primary-driver board is illustrated in Fig. 133.70. This board contains the high-voltage-power MOSFET's as well as the MOSFET gate-driver integrated circuits and charge-storage capacitors. The MOSFET gate-driver integrated circuit is a low-voltage (24-V), 14-A peak switching current driver specifically designed to drive MOSFET gates with nanosecond switching times. Each MOSFET has its own gate driver to maximize switching speeds. The charge-storage capacitors charge to the potential of the primary pulse voltage, which is theoretically  $15\times$  less than the actual output-pulse voltage. The capacitors are effectively connected across the primary winding when the MOSFET turns on (low impedance from drain to source). The pulse output current flows from the discharging storage capacitors through the primary winding and is coupled to the secondary via the transformer. The charge-storage capacitor value is calculated to support the output current pulse requirement with less than a 1% droop in charge voltage over the maximum

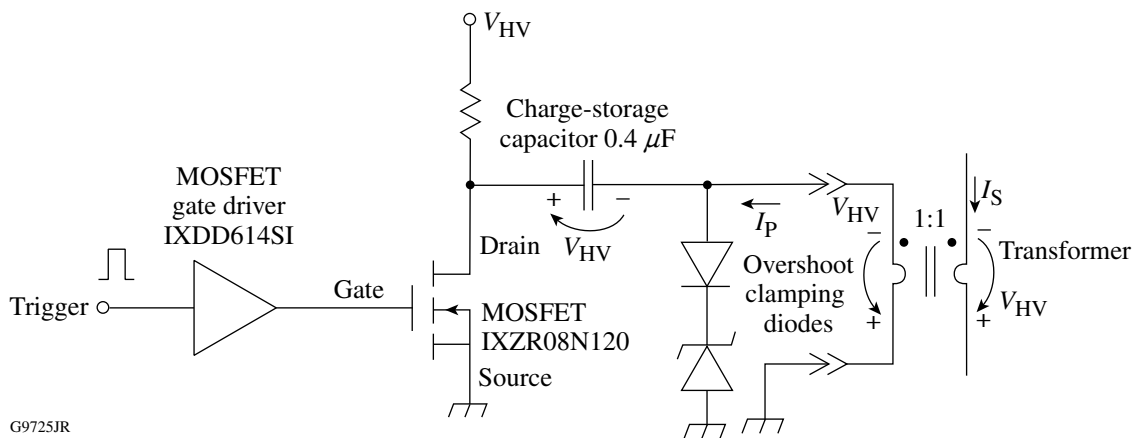


Figure 133.69  
Schematic of the transformer primary drive circuit.

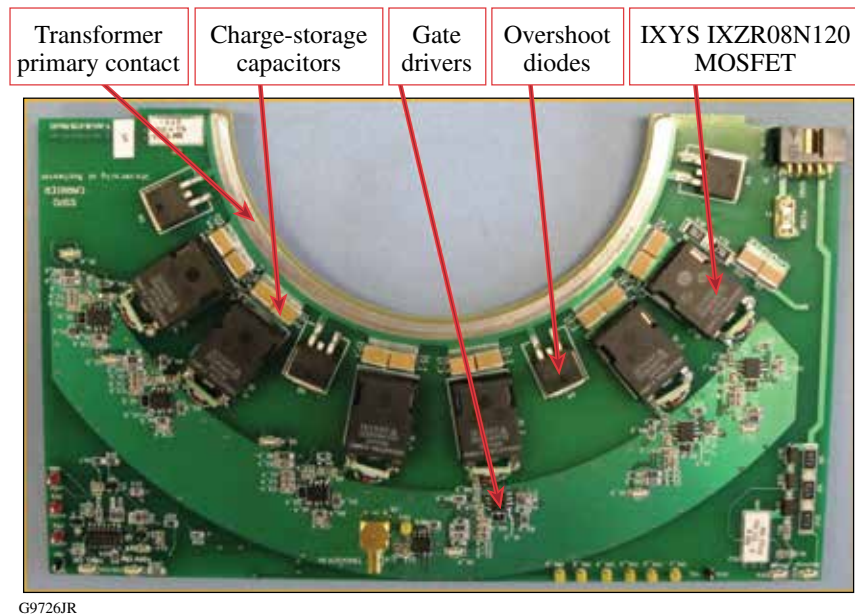


Figure 133.70

MOSFET driver board. The MOSFET driver board contains the circuitry to produce the pulsed voltage to the primary of the inductive-adder transformers. Each transformer has two driver boards that plug in and connect to the circumference of the primary winding. Each driver board contains six MOSFET's.

pulse duration. Overshoot clamping diodes are included in the driver circuit and connected across the transformer primary. The diodes clamp the inductive spike voltage produced by the magnetizing and leakage inductance when the MOSFET driver turns off (high impedance from drain to source). Clamping prevents the drain-to-source spike from exceeding the breakdown voltage of the MOSFET's while preventing output post-pulse ringing and overshoot.

To drive the 50- $\Omega$ -loaded LARA and CLARA Pockels cells, the maximum load current is 200 A with the maximum load voltage set at 10 kV. The total primary current is approximately 280 A, including the magnetization current and the magnetizing inductance current. IXYS-Colorado Semiconductor IXZR08N120 1200-V MOSFET's were chosen to provide sufficient voltage-breakdown headroom to prevent inductively generated overshoot in the transformer primary circuit waveforms from damaging them. These devices are also designed for ultralow internal capacitance and parasitic inductance to enhance switching speed. Twelve MOSFET devices are connected in parallel for each primary winding to limit the drain switching current to 23 A per device for the maximum duration and amplitude output pulse. The MOSFET pulsed drain current rating is significantly higher (40 A) (Ref. 6), but allowances are made for adverse load conditions, such as capacitive transients and arc-over short circuits.

When switching a MOSFET, the gate is biased positively with respect to the source to create a negative charge accumulation within the drain-source conduction layer. The gate is insulated from the other terminals of the device by the gate oxide layer above the conduction channel. The negative charge in the conduction layer creates a low-impedance channel for electron flow between the drain and source, thereby turning the MOSFET switch on. The insulated gate is mainly capacitive in nature with respect to the other terminals of the device. The gate capacitance is increased by the Miller switching capacitance effect between the gate and drain while they are changing potential.<sup>15</sup> Taking the Miller effect into account, the total gate input switching capacitance is of the order of 28 nF. The MOSFET gate driver's integrated circuit (IC) from the Clare Semiconductor division of IXYS (IXDD614SI) provides peak gate currents up to 14 A to charge and discharge the gate input switching capacitance. With 14 A, the charge rate for 28 nF across the gate switching transition of 2.5 V is 4.9 ns. This rate is fast enough to switch the MOSFET in the time required by the overall pulser performance specification.

The charge storage for the primary current pulse must be sufficient to restrict voltage droop over the pulse duration. For the SSPD design, the droop was limited to 7.5 V (1%) for a 100-ns pulse at full load current. The total charge-storage capacitance was calculated to be 4.8  $\mu$ F to meet this require-

ment. This is divided into 12 0.4- $\mu$ F capacitor blocks, one in the drain circuit of each of the 12 MOSFET's. Each capacitor block is formed from four individual 0.1- $\mu$ F, 1000-V ceramic multilayer capacitors.

Groups of overshoot clamping diodes are connected across the primary transformer winding to dissipate the energy within the leakage and magnetizing inductance after the MOSFET's are turned off. This limits ringing and overshoot on the trailing edge of the output pulse and protects the MOSFETs from overvoltage breakdown failure.

The charge storage, MOSFET's, and driver IC's are split into two boards that plug into the circumference of the transformer primary winding to minimize circuit path lengths, thereby minimizing the leakage inductance effects. Splitting the drivers onto two boards also simplifies transformer assembly and removal/repair of the driver boards. Each board contains diagnostic test points and light-emitting-diode (LED) fault indicators to facilitate diagnosis of board failures. Diagnostics are focused on isolating failures down to the component level for quick repair turnaround.

Fifteen identical driver/transformer units (30 driver boards and 15 transformers) are required in the pulser stack to sum the output level to that required in the output specifications defined in Table 133.X. The inductive-adder stack is illustrated in Fig. 133.71.

### 3. Output Stalk

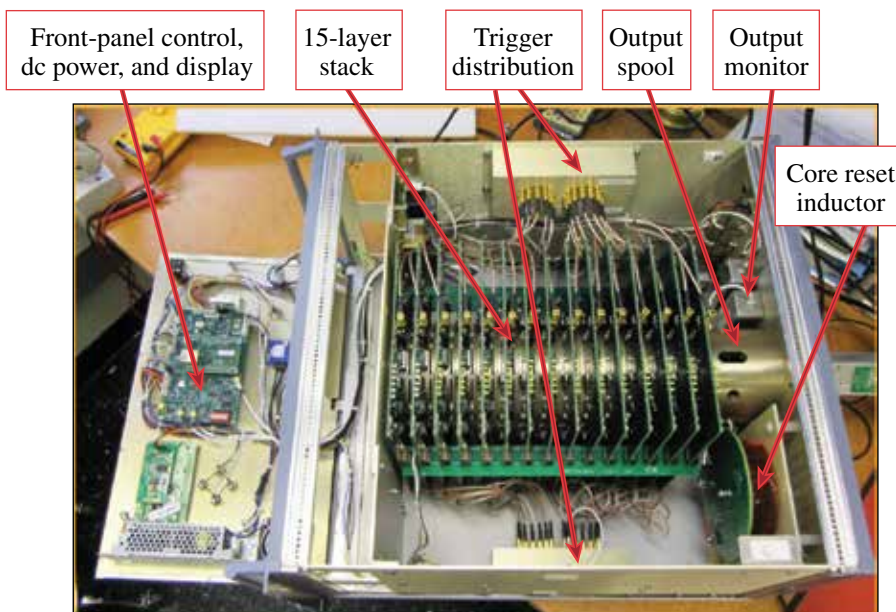
The series-connected secondary of the stacked transformers is a single conductive rod (the output stalk) that extends through the center of each transformer. One end is connected to ground and the other is connected to the 50- $\Omega$  output connector. Previous modeling studies have indicated that the stalk characteristic impedance should be set equal to the standard load impedance for optimal rise- and fall-time performance.<sup>16</sup> The stalk characteristic impedance is given by

$$Z_0 = \sqrt{\frac{L_{\text{stalk}} + L_{\text{leakage}}}{C_{\text{stalk}}}}, \quad (3)$$

where  $L_{\text{stalk}}$  is the inductance of the stalk per unit transformer length,  $L_{\text{leakage}}$  is the transformer leakage inductance for each individual transformer placed in series with the stalk inductance with the MOSFET switch on, and  $C_{\text{stalk}}$  is the capacitance of the stalk to ground per unit transformer length. For this design, the stalk diameter is adjusted to provide optimal matching to 50  $\Omega$ , the load impedance of the pulser.

### 4. Control

Overall control of the pulser is accomplished by utilizing an embedded microprocessor. The microprocessor controls operational conditions of the pulser and monitors safety and failure detection circuits. The processor is capable of remote control communications via an Ethernet connection; however,



G9727JR

Figure 133.71  
SSPD pulser stack with top cover removed and front panel open. All circuit boards are accessible without major disassembly of the enclosure.

this feature has not been implemented in the current design pending an operational need. The control assembly also conditions the incoming trigger to produce the desired output-pulse length. The externally supplied input trigger pulse edge is used to initiate an adjustable-width pulse generator, which is the source for internal synchronous triggers utilized by each of the 30 driver boards. The pulse length is adjustable in binary steps with a maximum length of 100 ns and a resolution of 0.5 ns. The front-panel interface is also implemented within the control assembly. This interface provides a menu-driven display with a simple push button panel for control of the pulser operation.

#### 5. Front-Panel Display

The front-panel display is an LCD-backlit display that provides pulser operational information. The display includes three pages of information containing control firmware revision status, pulse voltage setting and output level, pulse output length, pulse output state (on/off), and fault status.

#### 6. Trigger Distribution

Each of the 30 driver boards requires a synchronous trigger of the appropriate duration for the desired output pulse. To accommodate this, we use two 1-to-15 active trigger splitters whose trigger source is supplied by the trigger conditioning circuits on the control assembly board. Each splitter has a trigger driver integrated circuit and a resistive trigger splitter that can drive 15 driver board trigger inputs terminated in 50  $\Omega$ . The triggers are supplied to each transformer driver board via equal-length, 50- $\Omega$  shielded coaxial cables to maintain synchronization of all triggers on the stack.

#### 7. Reset-Current Circuit

The output pulse is a unipolar pulse, and over repeated pulses, the transformer cores will take on a permanent magnetization that will saturate the magnetic core material. To avoid core saturation, a direct current (dc) is connected into the output stalk of opposite polarity to the output current. The dc current is called the “core reset current.” The supply to produce this current must be isolated from the output pulse with a low-pass filter constructed from a large series inductor capable of withstanding the longest-duration and maximum-amplitude pulse output voltage.

#### 8. High-Voltage Power Supply Control

The high-voltage supply is the main charging supply for the charge-storage capacitors on the MOSFET primary circuit driver boards. This supply is adjustable from 0 to 750 V in accordance with the desired output-pulse voltage. This supply is set by the controller board in response to an operator’s

front-panel commands. The controller board monitors a scaled version of the supply output voltage to verify that the supply is operating correctly. The controller displays the monitor value as well as the set-point value on the front-panel display.

#### 9. Housekeeping Supply

The low-potential dc power for all of the circuit boards throughout the pulser is provided by the housekeeping power supply, which is 24 V dc. Lower voltages, like 12 V, 5 V, and 3.3 V, are regulated down on individual boards as required by the circuitry contained on each assembly. The controller board monitors the 24-V housekeeping supply and will issue a fault if the supply drops below a prescribed fault threshold value.

#### 10. Enclosure

The packaged SSPD prototype is shown in Fig. 133.72. The enclosure is a standard 19-in. rack-mount chassis that is six rack units (6 U = 10.5 in.) high and 20 in. deep. The enclosure is designed to facilitate assembly and for ease of pulser repair. All stack MOSFET driver boards are accessible through removable top and bottom covers, as shown in Fig. 133.71. The front panel hinges forward to allow access to the control board and dc supplies.



G9728JR

Figure 133.72  
Solid-state Pockels-cell driver package.

#### 11. SSPD Electrical Performance

Two SSPD prototype units were assembled and tested with nearly identical performance into a 50- $\Omega$  load network. Figure 133.73(a) illustrates electrical output for approximately 100-ns-long pulses at various output levels. The inset table summarizes the performance parameters at the approximate quarter- and half-wave voltages for KD\*P Pockels cells (5 kV and 10 kV, respectively). Figure 133.73(b) shows the measured

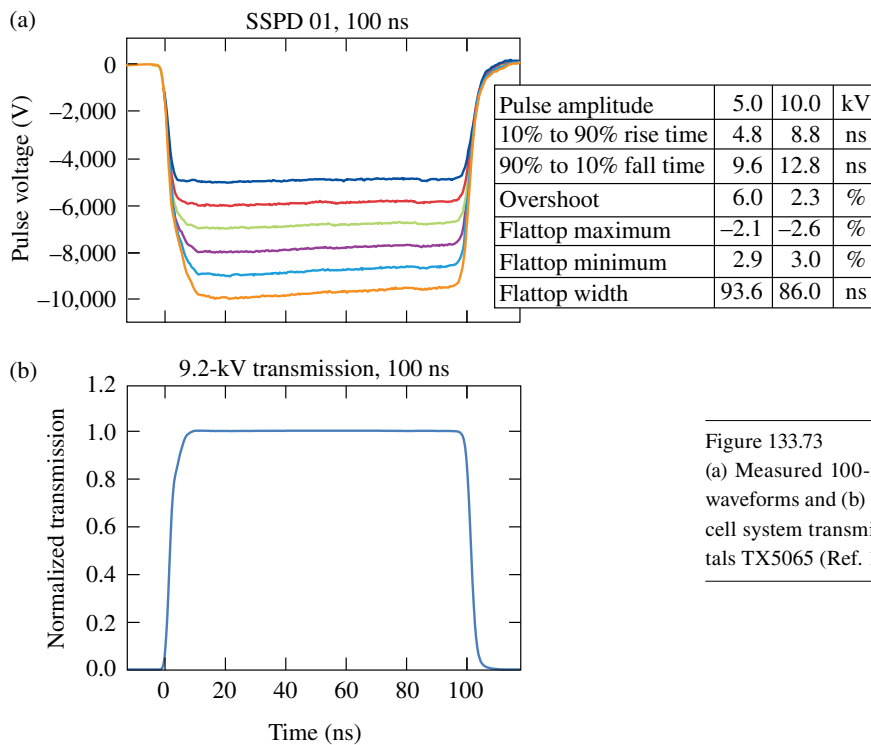


Figure 133.73  
 (a) Measured 100-ns output pulse electrical waveforms and (b) 100-ns measured Pockels-cell system transmission for Cleveland Crystals TX5065 (Ref. 12).

G9729JR

transmission of a Pockels cell [Cleveland Crystals TX5065 (Ref. 12)] driven by the SSPD. Similarly, Fig. 133.74 shows the measured electrical SSPD output and calculated optical performance for approximately 25-ns pulses.

A prototype SSPD pulser was connected to a 25-mm Pockels cell [Cleveland Crystals TX-2650 (Ref. 12)] operating as a cavity Q-switch in a CLARA and tested. Measured laser performance, including energy stability and pulse shape, matched performance produced by the thyatron pulser that was replaced by the prototype SSPD unit.

**Future Considerations**

Future enhancements can be explored to improve SSPD operation, including optimizing the transformer core size to improve output-pulse fidelity. Core selection can be further optimized to improve rise and fall time as well as reduce the magnetization current. The mechanical design of the transformer can also be improved to reduce the cost of manufacture as well as weight.

The number of parallel-connected MOSFET’s in each stack could be reduced by working each at higher pulsed currents. This may improve switching speed and reduce the driver size but may reduce the overcurrent safety margin. The same may be accomplished as future higher-performance MOSFET devices

are developed without impacting safety margin. Overall, a reduction in MOSFET count could reduce the total parts count and size of each driver board with potential reductions in the overall size and weight of the pulser enclosure.

As noted in Fig. 133.74, the trailing edge of the two largest-amplitude, 25-ns pulses has a tail that increases the rise time. Future work may expose the cause of this and determine a correction.

**Summary**

A solid-state, 50-Ω, 10-kV, 100-ns Pockels-cell driver has been designed and assembled as a replacement for aging thyatron switched drivers. The design is based on the inductive-adder approach developed at Lawrence Livermore National Laboratory. Performance tests in a CLARA produced results equivalent to the thyatron driver in the same application.

**ACKNOWLEDGMENT**

We acknowledge the efforts of the LLE Electronics Shop and Mechanical Engineering group in the design, assembly, and testing of the inductive-adder pulser. We also acknowledge the design consultation support provided by Ed Cook of LLNL. This work was supported by the U.S. Department of Energy Office of Inertial Confinement Fusion under Cooperative Agreement No. DEFC52-08NA28302, the University of Rochester, and the New York State Energy Research and Development Authority. The support of DOE does not constitute an endorsement by DOE of the views expressed in this article.

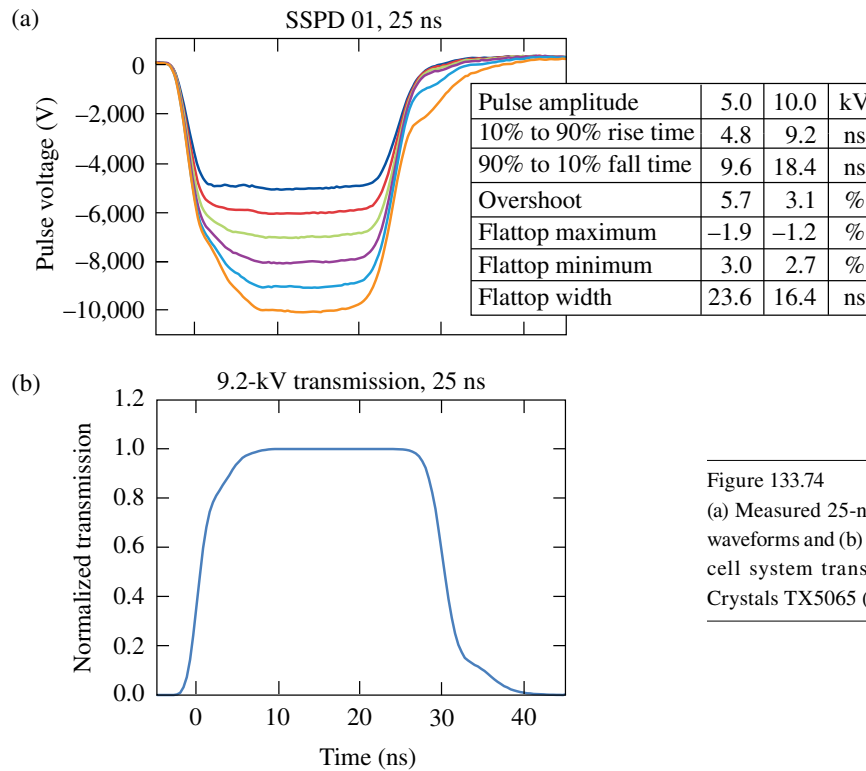


Figure 133.74

(a) Measured 25-ns output pulse electrical waveforms and (b) 25-ns measured Pockels-cell system transmission for Cleveland Crystals TX5065 (Ref. 12).

G9730JR

REFERENCES

1. A. Babushkin, J. H. Kelly, C. T. Cotton, M. A. Labuzeta, M. O. Miller, T. A. Safford, R. G. Roides, W. Seka, I. Will, M. D. Tracy, and D. L. Brown, in *Third International Conference on Solid State Lasers for Application to Inertial Confinement Fusion*, edited by W. H. Lowdermilk (SPIE, Bellingham, WA, 1999), Vol. 3492, pp. 939–943.
2. V. Bagnoud, M. J. Guardalben, J. Puth, J. D. Zuegel, T. Mooney, and P. Dumas, *Appl. Opt.* **44**, 282 (2005).
3. Series 5056D Self-Contained Q-Switch Driver Data Sheet, FastPulse Technology, Inc., Lasermetrics Division, Saddle Brook, NJ 07663 (see <http://www.fastpulse.com/pdf/5056D.pdf>).
4. “Pumped Diode Regen Cavity Switch,” E-DN-B-022, Laboratory for Laser Energetics, University of Rochester, Rochester, NY (19 October 2004).
5. Pulse Generators, Models 3148 and 3150, Operating Instructions and Service Manual, Bournlea Instruments, Ltd., Ipswich, England (1990).
6. IXZR08N120 and IXZR08N120A/B Z-MOS RF Power MOSFET Data Sheet, IXYS Colorado, Fort Collins, CO 80525 (see [http://www.directedenergy.com/index.php?page=shop.product\\_details&flypage=flypage.tpl&product\\_id=71&category\\_id=15&option=com\\_virtuemart&Itemid=34](http://www.directedenergy.com/index.php?page=shop.product_details&flypage=flypage.tpl&product_id=71&category_id=15&option=com_virtuemart&Itemid=34)).
7. FMMT415 and FMMT417 SOT23 NPN Silicon Planar Avalanche Transistor Data Sheets, Diodes Incorporated, Plano, TX 75024 (see <http://www.diodes.com/datasheets/FMMT415.pdf>).
8. V. N. Efanov *et al.*, in *11th IEEE Pulsed Power Conference, 1997* (IEEE, Piscataway, NJ, 2013), Vol. 2, pp. 988–991.
9. V. A. Kozlov *et al.*, in *Conference Record of the Twenty-Fifth International Power Modulator Symposium and 2002 High-Voltage Workshop*, edited by H. C. Kirbie, D. Goebel, and L. Gordon (IEEE, Piscataway, NJ, 2002), pp. 441–444.
10. E. G. Cook *et al.*, in *Proceedings of the Particle Accelerator Conference, 2005* (IEEE, Piscataway, NJ, 2005), pp. 637–641.
11. “OMEGA EP PEPC Inductive Adder Solid State Pulser Requirement Specification,” C-AP-R-001, Laboratory for Laser Energetics, University of Rochester, Rochester, NY (4 January 2005).
12. Large Aperture Pockels Cells Specifications, Cleveland Crystals, Inc. (CCI), Highland Hts, OH 44143 (see [www.clevelandcrystals.com/tx.htm](http://www.clevelandcrystals.com/tx.htm)).
13. Magnetic Alloy 2605SA1 Technical Bulletin, Metglas®, Inc., Conway, SC 29526 (see <http://metglas.com/assets/pdf/2605sa1.pdf>).
14. M. Plonus, *Applied Electromagnetics* (McGraw-Hill, New York, 1978).
15. J. Millman and C. C. Halkias, *Integrated Electronics: Analog and Digital Circuits and Systems*, McGraw-Hill Electrical and Electronic Engineering Series (McGraw-Hill, New York, 1972).
16. W. Zhang *et al.*, in *Proceedings of the 2007 IEEE Particle Accelerator Conference (PAC)* (IEEE, Piscataway, NJ, 2007), pp. 2553–2555.



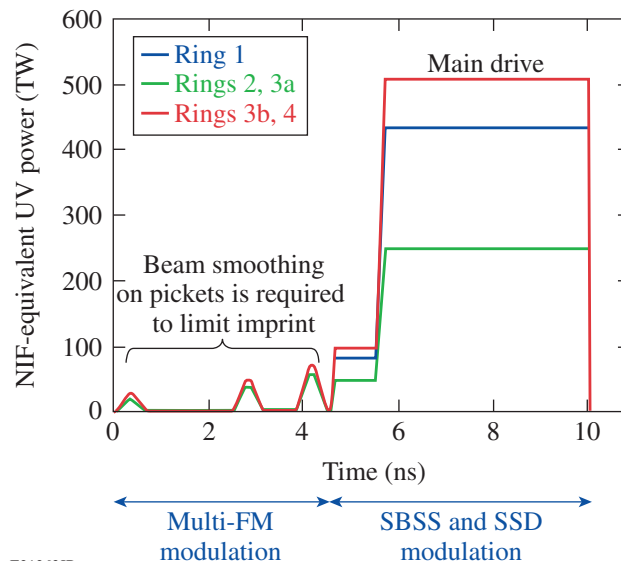
# Commissioning of a Multiple-Frequency–Modulation Smoothing by Spectral Dispersion Demonstration System on OMEGA EP

## Introduction

Smoothing by spectral dispersion (SSD) has become a critically important method for smoothing laser-imprinted nonuniformities in target implosions.<sup>1</sup> The spot shape on target is generally controlled using distributed phase plates (DPP's), which effectively control the low-order beam profile but introduce fine-scale speckle structures that require smoothing.<sup>2</sup> Recently, a new concept for a one-dimensional (1-D) SSD system was proposed that utilizes multiple frequencies for phase modulation (multi-FM SSD).<sup>3</sup> By carefully selecting modulation frequencies, resonant features that often limit the effectiveness of SSD systems can be eliminated. As a result, effective beam smoothing can be achieved with a 1-D system using a modest modulation bandwidth in a frequency-conversion scheme that utilizes a single tripler crystal. These features allow for the integration of multi-FM SSD into either the OMEGA EP Laser System<sup>4</sup> or the National Ignition Facility (NIF)<sup>5</sup> laser.

Polar-drive experiments on the NIF will require pulse shapes that incorporate multi-FM SSD.<sup>6</sup> Conceptual pulse shapes are illustrated in Fig. 134.1. The three different shapes correspond to three different latitudes of the beams entering the NIF target chamber, with Ring 1 corresponding to higher latitudes and Ring 3 being nearest the equator. Beam smoothing using multi-FM SSD is required only during the three pickets at the beginning of the pulse. During the main pulse, at which higher power levels are required and amplitude modulation becomes a correspondingly greater concern, only the standard NIF 1-D SSD and stimulated Brillouin scattering suppression (SBSS) would be applied. Therefore, dynamic application of the multi-FM SSD bandwidth must be accommodated in the system design.

To demonstrate multi-FM SSD on a laser system with an architecture similar to the NIF, a prototype system was developed and integrated into a long-pulse beamline of OMEGA EP. Simulations of amplitude modulation caused by free-space propagation of a frequency-modulated beam in the OMEGA EP beamline and the design and performance of the fiber front end supporting multi-FM experiments on OMEGA EP are



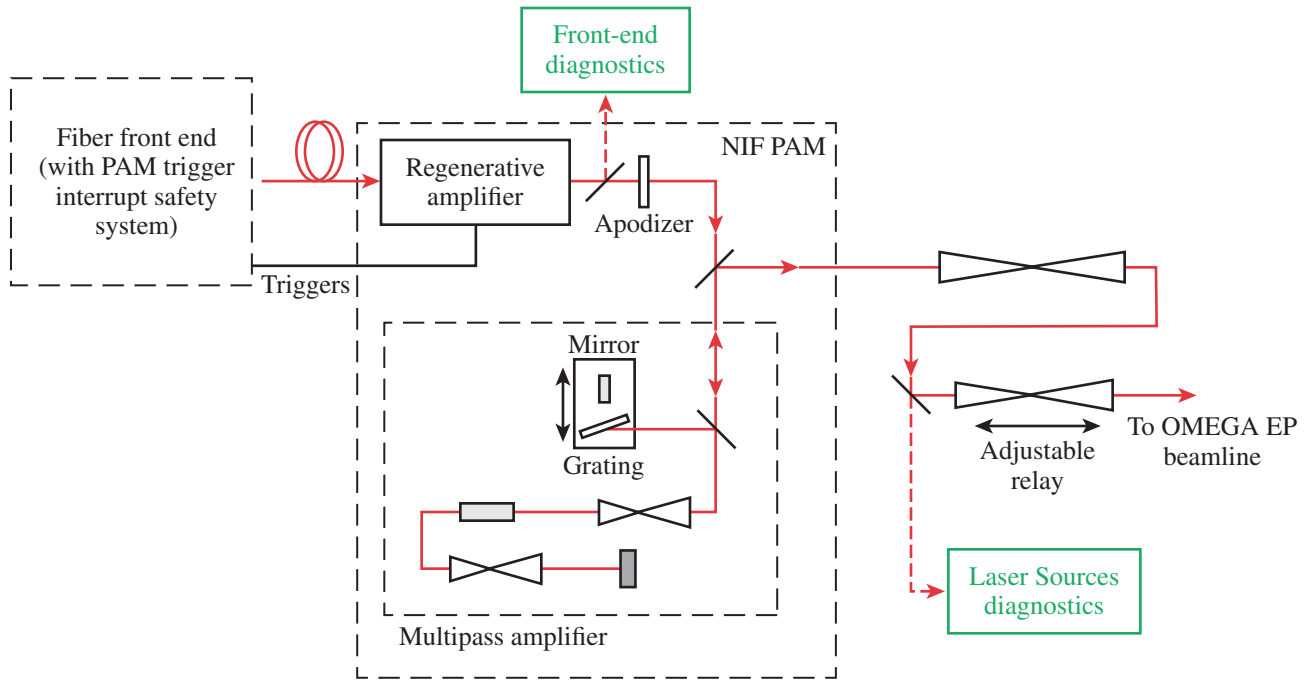
E21263JR

Figure 134.1  
Representative triple-picket pulse shapes for polar-drive experiments on the NIF. The three pulse shapes correspond to beams entering the target chamber at different latitudes. In all cases, multi-FM smoothing by spectral dispersion (multi-FM SSD) is applied for only the picket pulses. SBSS: stimulated Brillouin scattering suppression.

presented in *Simulations of the Propagation of Multiple-FM Smoothing by Spectral Dispersion on OMEGA EP* (p. 85) and *Fiber Front End with Multiple Phase Modulations and High-Bandwidth Pulse Shaping* (p. 98). This article describes the prototype system and presents results from the integration and commissioning on the OMEGA EP beamline. Particular attention is paid to the important issue of amplitude modulation in the high-power beam at critical points in the system.

## System Description

The prototype multi-FM SSD front end is illustrated in Fig. 134.2. A fiber front end comprises two separate channels—a main-pulse channel and a multi-FM picket channel.<sup>7</sup> (Details on the phase modulation for multi-FM and other system specifications can be found in Table 134.I.) The main-pulse channel is similar to the NIF front end, including phase modulation at 3 GHz for SBSS and 17 GHz for SSD, although the



G9742JR

Figure 134.2

Schematic layout of the multi-FM SSD prototype front end. Red lines indicate the optical path, black lines indicate electrical trigger signals, and green blocks indicate laser diagnostics. PAM: preamplifier module.

Table 134.I: Specifications of the multi-FM SSD demonstration system.

Parameter	Value
Modulation frequencies ( $f_1, f_2, f_3$ )	21.165, 22.837, 31.881 GHz
Modulation indices ( $\delta_1, \delta_2, \delta_3$ )	0.45, 1.04, 2.07 rad
Grating angular dispersion (in PAM), $d\theta/d\lambda$	381.4 $\mu\text{rad}/\text{\AA}$
Spectral bandwidth	7.3 $\text{\AA}$
Magnification, PAM to beamline	21.5
Temporal skew from pulse-front tilt	229 ps

17-GHz, 1-D SSD phase modulation was not utilized for high-energy shots.

The two channels are fiber optically combined and injected into a NIF preamplifier module (NIF PAM).<sup>8</sup> Pulses are initially amplified to the mJ level in a regenerative amplifier. The fiber front end also contains a system safety feature called the PAM trigger interrupt safety system (PTISS), which monitors

the seed pulses and prevents emission of an amplified pulse from the regenerative amplifier in the event of an unsafe condition.<sup>7</sup> Upon exiting the regenerative amplifier, the beam is passed through an apodizer that shapes the edges of the beam and precompensates for spatial-gain variations in the beamline amplifiers. After an image relay, the beam is injected into a multipass amplifier (MPA), where it undergoes amplification to ~500 mJ via four passes through a flash-lamp-pumped, 32-mm-diam  $\times$  300-mm-long Nd:glass rod amplifier. The beam is angularly multiplexed in the MPA and passes through a spatial filter with an array of four 5.16-mm-diam pinholes on each pass. After accounting for magnification into the OMEGA EP beamline, these pinhole sizes correspond to a full-angle acceptance of ~200  $\mu\text{rad}$  in the final OMEGA EP beam, making them the tightest pinholes in the system.

A diffraction grating inserted into the MPA after the second pass of the MPA disperses the SSD bandwidth. The 1700-lines/mm gold grating is aligned at the Littrow angle and mounted on a translation stage that also supports a flat mirror. This allows us to translate the mirror into place and operate the system without any angular dispersion of the SSD bandwidth. Note that because phase modulation is performed in a fiber system, there is no pre-shear diffraction grating as found

in most SSD systems. As a result, the dispersing diffraction grating also introduces a pulse-front tilt, or temporal shear, of 229 ps across the beam width.

After exiting the NIF PAM, the beam passes through a set of image relays and is injected into the OMEGA EP beamline. One of the image relays is adjustable to allow for fine control of the image plane's position.

Two sets of beam diagnostics are provided within the multi-FM front-end system. The front-end diagnostics characterize the output of the regenerative amplifier and comprise an energy diagnostic, a spectrometer (<5-GHz resolution), and fast photo-detection (45-GHz response) for measuring amplitude noise. The Laser Sources diagnostics, characterizing the beam at the output of the NIF PAM, contain energy diagnostics, cameras that image the near-field and far-field beam profiles, a streak camera that measures the pulse shape, and a setup for measuring the amplitude noise near an image plane of the diffraction grating.

The pulse exiting the Laser Sources Bay is injected into the OMEGA EP long-pulse beamline (illustrated in Fig. 134.3).

The OMEGA EP beamline is similar to a folded version of the NIF beamline. The beamline is an angularly multiplexed system in which a pulse undergoes two passes through the seven-disk booster amplifier and four passes through the eleven-disk main amplifier. The transport and cavity spatial filters (TSF and CSF, respectively) are each populated with 300- $\mu$ rad full-angle pinholes to filter high-frequency spatial modulations on the beam. After undergoing full amplification in the beamline, the pulse exits the TSF and propagates to the frequency-conversion crystals (FCC's), which convert the 1.053- $\mu$ m beam to the third harmonic. One critical difference from the NIF system is that the FCC's are physically separated from the final focusing optics by 8 m. The final focusing optics include a DPP, a focusing lens ( $f = 3.4$  m), a vacuum window, and a thin debris shield.

Finally, one important consideration for a frequency-converted system with SSD is that the  $1\omega$  beam at the input of the frequency conversion should have a minimal amplitude modulation (AM). Because propagation away from the dispersing grating in a SSD system will convert FM to AM, it is beneficial to accurately image the grating to the FCC plane. This was accomplished on OMEGA EP by translating the

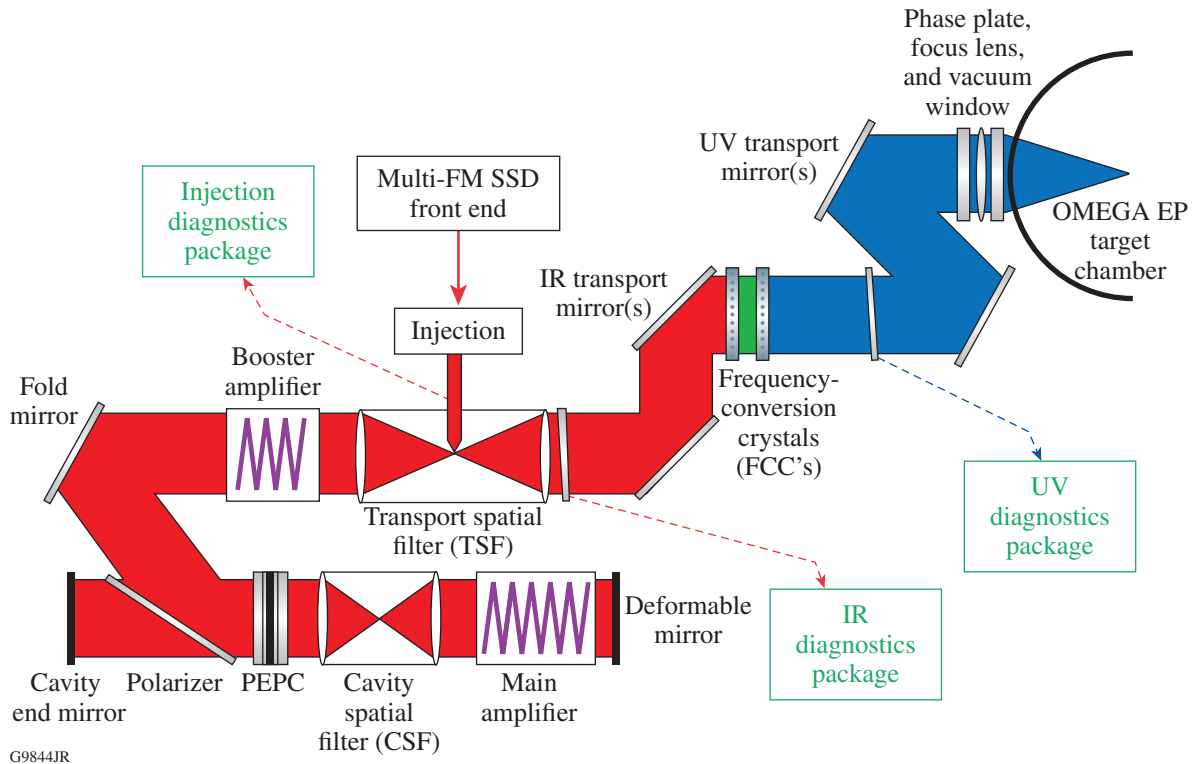


Figure 134.3  
Schematic layout of the OMEGA EP long-pulse beamline. PEPC: plasma-electrode Pockels cell.

adjustable image relay in the front end (see Fig. 134.2) to shift the grating image plane onto the FCC's.

Three different diagnostics packages monitor the beam properties at various points in the system. An injection diagnostic package measures the energy, pulse shape, and near-field beam profile of the beam prior to up-collimation into the beamline. At the output of the beamline, the infrared diagnostics package (IRDP) contains diagnostics that measure the energy, near-field and far-field beam profiles, pulse shape, and wavefront of the  $1\omega$  amplified beam. Finally, after the frequency conversion, the ultraviolet diagnostics package (UVDP) measures the energy in the first, second, and third harmonics, and the near field, far field, and pulse shape of the  $3\omega$  beam. The UVDP also has provisions for inserting a DPP to measure the focal spot at an equivalent target plane.

### Amplitude-Modulation Concerns

One of the key concerns with frequency modulation in a high-energy laser system is the generation of high peak intensities caused by AM. FM can be converted into AM by a number of mechanisms.<sup>9</sup> Ideally, a direct AM measurement in the planes of all the optics would ensure that AM is within tolerable levels; however, this measurement would be extremely difficult to make. A streak camera—the deployed pulse-shape diagnostic—does not have sufficient resolution to accurately measure noise at the multi-FM SSD frequencies. Therefore, for this demonstration, our approach was to measure the AM in the front end of the system and produce a budget for further AM in the beamline, based on simulations where possible and on conservative estimates where simulation was impossible. This budgeting process, which resulted in a limit to the peak power that could be safely produced on the system, is described in this section along with the results.

#### 1. Amplitude Modulation in the UV Optics

A model of multi-FM propagation in the final stages of the OMEGA EP system is presented in *Simulations of the Propagation of Multiple-FM Smoothing by Spectral Dispersion on OMEGA EP* (p. 85).<sup>10</sup> The model, implemented in the laser simulation code Miró,<sup>11</sup> simulated a pulse with multi-FM SSD, beginning from the final pinhole in the TSF and propagating to the final UV optics at the target-chamber port. The pulse was assumed to be free of AM and to cleanly propagate through this final pinhole, and the SSD diffraction grating was assumed to be well imaged to the FCC plane. Amplitude modulation caused by the frequency-conversion process and propagation away from the FCC's was simulated, and a spatiotemporal model of the pulse intensity was developed for each optic. From this data,

the  $B$ -integral ( $\Sigma B$ ) accumulated from the final pinhole through the remaining transmissive optics was calculated. To keep the accumulated  $\Sigma B$  below 2.0 rad, it was determined that the maximum  $3\omega$  power on target (in the absence of other sources of AM) should be limited to 1.6 TW. Note that the simulations were performed assuming a grating with a larger dispersion (1800 lines/mm) than was actually used for this commissioning. Using this result as a basis for setting a system performance limit was therefore a conservative approach.

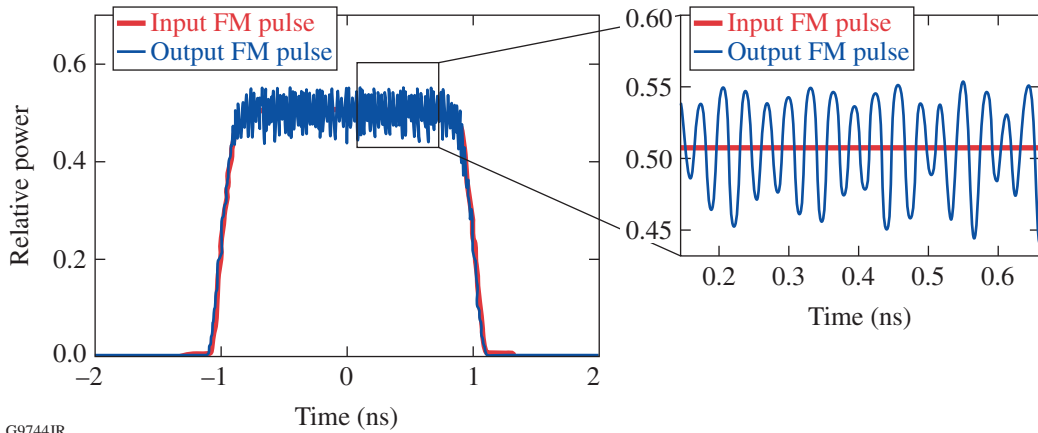
#### 2. Amplitude Modulation via Amplification in the OMEGA EP Beamline

Amplification of the broadband multi-FM pulse can lead to FM-to-AM conversion and therefore must be considered when apportioning a budget for AM in the laser chain. Specifically, we consider the effects of material dispersion, gain narrowing, and phase changes caused by the line shape of the gain medium, referred to as the Kramers–Kronig phase. Additional effects such as etaloning in the system's optics or spectral clipping on the pinholes were not considered because these effects are specific to the optics and alignment of the particular beamline. A broadband, 1-D model of the IR portion of OMEGA EP, including material dispersion of all of the optics, the gain spectrum of the Nd-doped, LHG-8 glass amplifiers, and the phase introduced by this gain spectrum, was developed. Because the multi-FM spectral width is comparable to that of the gain spectrum of the Nd:glass, one expects that gain narrowing and the associated phase effects may alter both the power spectrum and the spectral phase of the multi-FM pulse, thereby producing AM.

Figure 134.4 shows the results of the model described above for a noise-free multi-FM pulse that is injected into the beamline (red). The multi-FM spectrum was created using the parameters shown in Table 134.I. This simulation shows that one can expect some FM-to-AM conversion to take place in the amplifier chain, producing an output pulse with amplitude modulation (blue). Zooming in on the modulation pattern, it is clear that amplification of the FM pulse in the OMEGA EP laser chain will lead to about a 10% peak-to-mean modulation on the pulse as a result of the effects considered in the model. This amount of AM must be included in the modulation budget as will be discussed in the following section.

#### 3. Peak-Power Specification and AM Budget

A budget to allow for a reasonable level of AM accumulation in the OMEGA EP Laser System was developed to specify a peak power. The 1.6 TW determined from the Miró model of the final optics was used as a starting point, and allowances



G9744JR

Figure 134.4  
Result of a simulation of amplitude modulation in a 1ω pulse introduced by amplification in the OMEGA EP beamline.

were made for other sources of AM. The first of these was AM arising in the beamline (via dispersion, gain narrowing, and the Kramers–Kronig phase), as discussed in **Amplitude Modulation via Amplification in the OMEGA EP Beamline** (p. 78). The second was AM arising from “technical” sources of AM that cannot be predicted via simulation. These include AM arising from etalons, loss of spectrum from clipping on pinholes, etc. Finally, an allowance was made for residual AM in the front end. These sources of AM were assumed to contribute incoherently and were root sum squared to form an overall budget. Finally, a safety margin was applied to allow for both model uncertainties and energy instability in the system. A summary of the AM budget is shown in Table 134.II.

The result of the budgeting process is that the maximum UV on-target power for which OMEGA EP will utilize the multi-FM SSD system is 0.85 TW.

**System Integration and Commissioning**

1. Spectral Dispersion Concerns in the PAM Spatial Filters  
One of the key concerns in limiting AM in the SSD system is to ensure that the spectrum, which is dispersed in the far

field as a result of dispersion from the diffraction grating, cleanly passes through the pinholes of the system. The limiting pinholes in the system are in the multipass amplifier in the NIF PAM, i.e., the first pinholes after the diffraction grating. Therefore, the dispersion of the grating was selected to ensure that the beam can propagate through these pinholes without spectral clipping. To evaluate this, the far-field camera in the Laser Sources diagnostics (see Fig. 134.2) was used to image the dispersed spectrum at the output of the PAM and compared to the expected spectrum resulting from the multi-FM modulation. The result is shown in Fig. 134.5.

Inspection of the plot in Fig. 134.5(b) clearly shows that all the significant sidebands of the modulation spectrum can be observed in the output beam and therefore are not being clipped in the pinholes. In fact, under perfect alignment conditions, the pinhole cutoff frequency is given by

$$f_{\text{cutoff}} = \frac{c}{\lambda_0^2} \frac{\theta_{1/2}}{(d\theta/d\lambda)_{\text{grating}}}, \tag{1}$$

Table 134.II: Amplitude modulation budget and peak-power specification.

	Allowance	Resulting Peak Power
B-integral in UV optics (Miró model)	—	1.6 TW
AM in front end	15% peak to mean	—
AM introduced in beamline	10% peak to mean	—
Other “technical” sources of AM	20% peak to mean	—
Root-sum-square total	27%	1.17 TW
Safety margin	28%	<b>0.85 TW</b>

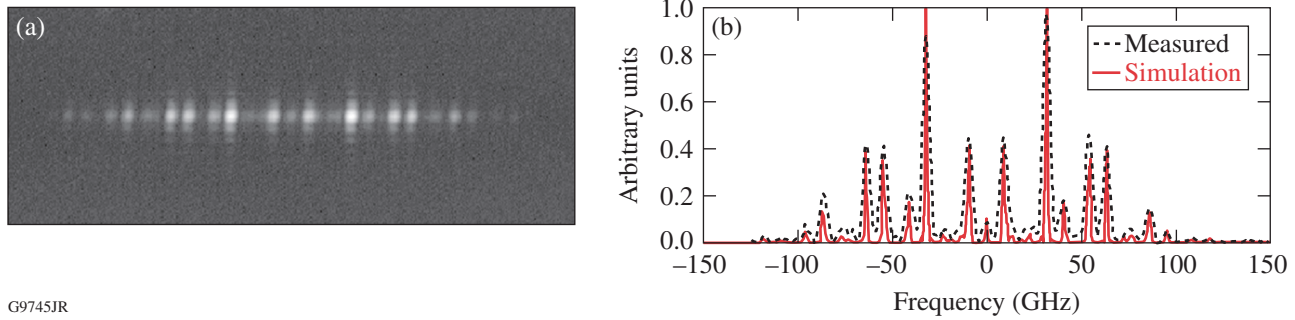


Figure 134.5

(a) Far-field image of the beam exiting the PAM with multi-FM SSD applied. (b) Lineout of the far-field image (black dashed line) with the calculated modulation spectrum superimposed (red solid line), with the far-field camera spatial scale converted to the spectral domain based on the grating dispersion and the magnification to the camera.

where  $\theta_{1/2}$  is the acceptance half-angle of the spatial filter (2.07 mrad for the spatial filter with a 1.249-m-focal-length lens and 2.58-mm-radius pinhole),  $(d\theta/d\lambda)_{\text{grating}}$  is the angular dispersion of the diffraction grating (given in Table 134.I), and  $\lambda_0$  is the central frequency of the seed source (1053.044 nm). The result is an ideal cutoff frequency of 146 GHz, significantly higher than the highest signal frequency shown in Fig. 134.5. In practice, the pinhole cutoff will be somewhat lower because of misalignment into the spatial filters and between the multiple passes through the MPA. Finally, noise measurements on the beam at the output of the MPA in the Laser Sources diagnostics have confirmed that the AM is below the 15% peak-to-mean allowance in Table 134.II (see Fig. 134.34).

## 2. Commissioning on OMEGA EP

The commissioning process on OMEGA EP proceeded by initially activating without dispersion of the modulation bandwidth, by removing the diffraction grating from the beam path in the NIF PAM and inserting the mirror (see Fig. 134.2). Each of the two channels (the multi-FM SSD channel and the main-pulse channel) was introduced individually. Initial shots were taken just within the Laser Sources Bay to confirm stability and acceptable beam quality and to develop configurations to produce the appropriate energies. Subsequent shots energy ramped the system first just to the beamline output. Finally, a UV energy ramp to the system limits was undertaken and the picket and main channels were combined. After full-system performance was demonstrated, the diffraction grating was inserted and the system was methodically ramped to full performance. Only the final results are presented herein.

Results from a UV shot near the 0.85-TW system limit using a triple-picket pulse applied to the multi-FM channel (no main pulse) are shown in Fig. 134.6: the near-field beam profiles at

the injection [Fig. 134.6(a)]; beamline output [Fig. 134.6(b)]; and the UV output [Fig. 134.6(c)]. The beam quality as shown is comparable to a typical performance on this beamline with the narrowband OMEGA EP front end. The UV pulse shape, calibrated to on-target power [shown in Fig. 134.6(d)], indicates that the shot did, in fact, achieve a peak power of >0.8 TW.

The far-field intensities measured on a multi-FM picket-only shot are plotted in Fig. 134.7. The measured focal spot at the beamline output, from the far-field camera in the IRDP, is shown in Fig. 134.7(a). A lineout of this image along with the simulated dispersion of the modulation spectrum is shown in Fig. 134.7(b). The same measurements at  $3\omega$  from the UV far-field camera are shown in Figs. 134.7(c) and 134.7(d). Note that the wavefront error accumulated in the beamline has broadened these focal spots, making the different sidebands of the  $1\omega$  spectrum difficult to distinguish in the IR far-field image. The width of the focal-spot lineout is consistent, however, with the width of the simulated spectrum, providing evidence that the spectrum is not clipped by propagation in the beamline.

The  $3\omega$  spectrum is by design very complex with a large number of closely spaced sidebands approximating a quasi-uniform modulation spectrum. As a consequence, the far field approximates a continuously blurred version of the narrowband far-field profile, with the blurring applied in one dimension. Note in Fig. 134.7(d) that the width of the far field is consistent with the width of the modulation spectrum, indicating that the full spectrum was frequency converted.

In addition to the triple-picket pulse shape shown in Fig. 134.6(d), a variety of other pulse shapes have been used with the multi-FM SSD source in the process of commissioning. The sample shown in Fig. 134.8 includes a narrow

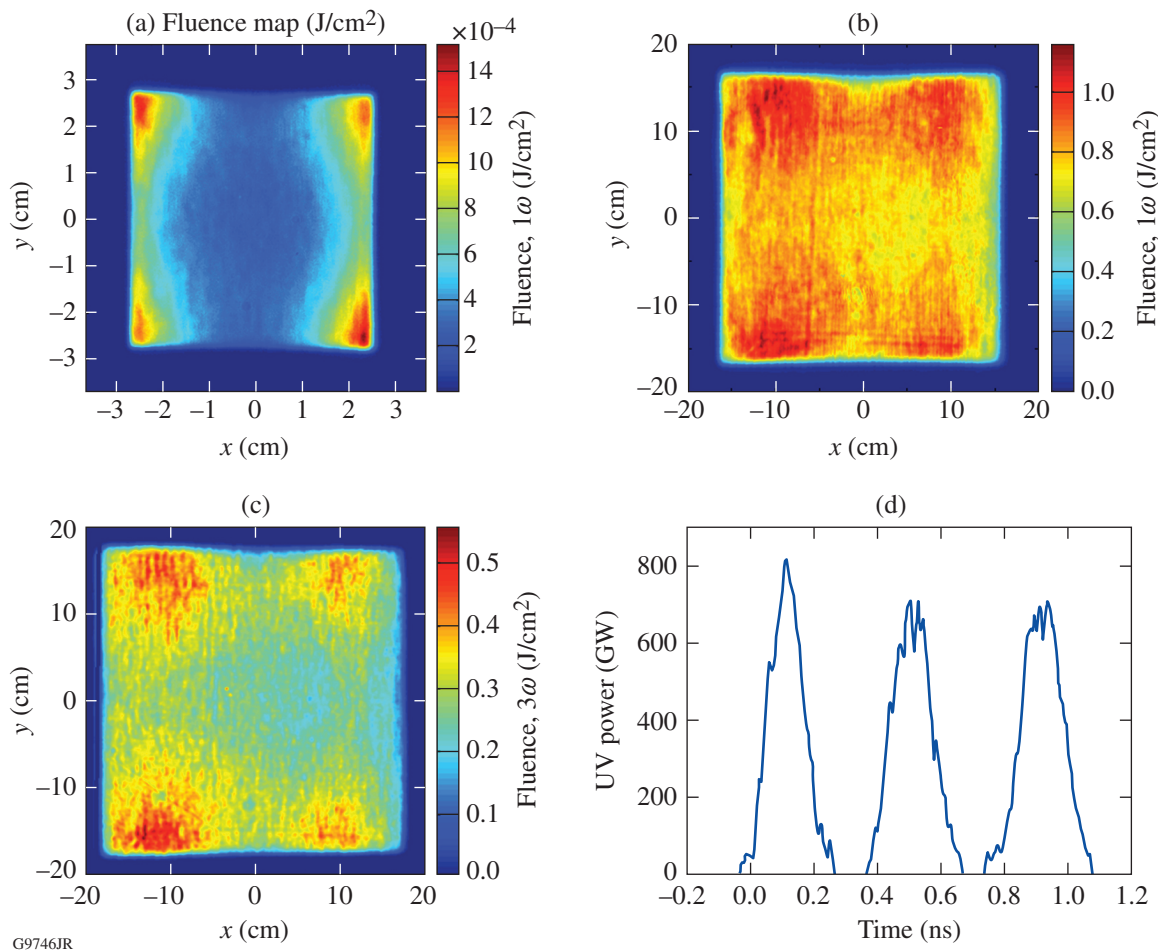


Figure 134.6

Beam profile at various points in the system for a triple-picket multi-FM SSD shot near the system performance limit. Beam profiles as measured by the near-field cameras in the (a) injection diagnostics, (b) IRDP, and (c) UVDP; (d) the UV pulse shape as measured by the streak camera in the UVDP.

150-ps picket [Fig. 134.8(a)], a series of three 650-ps pickets [Fig. 134.8(b)], and a 2-ns square pulse at the system power limit [Fig. 134.8(c)].

### 3. Demonstration of Beam-Smoothing Performance

Upon completion of the commissioning of the multi-FM SSD demonstration system on OMEGA EP, an experiment was performed to demonstrate the resulting beam smoothing. A DPP, designed to produce a super-Gaussian spot with a 1.1-mm diameter at the target plane, was mounted in the UV diagnostics path. In this configuration, the UV far-field camera measures the fluence distribution in an equivalent target plane. For this experiment, a single 650-ps picket pulse was used.

A baseline measurement was first made with the narrow-band main-pulse source (with only the 3-GHz SBSS band-

width applied). To eliminate any dispersion of even this low bandwidth, the PAM diffraction grating was not used and was replaced with the mirror. The resulting target-plane intensity distribution is shown in Fig. 134.9(a). Lineouts through the center of the beam in both the horizontal and vertical directions [shown in Fig. 134.9(b)] indicate a high speckle contrast.

A smoothed beam profile was measured using the identical pulse shape formed with the multi-FM picket seed source. The diffraction grating was reinserted into the beam path in the PAM to provide dispersion of the bandwidth. The smoothed target-plane intensity distribution is plotted in Fig. 134.9(c) and the corresponding lineouts in Fig. 134.9(d). The effect of SSD on the beam profile is clear, with the smoothing being more effective in the horizontal (dispersion) direction, as expected in a 1-D SSD system.

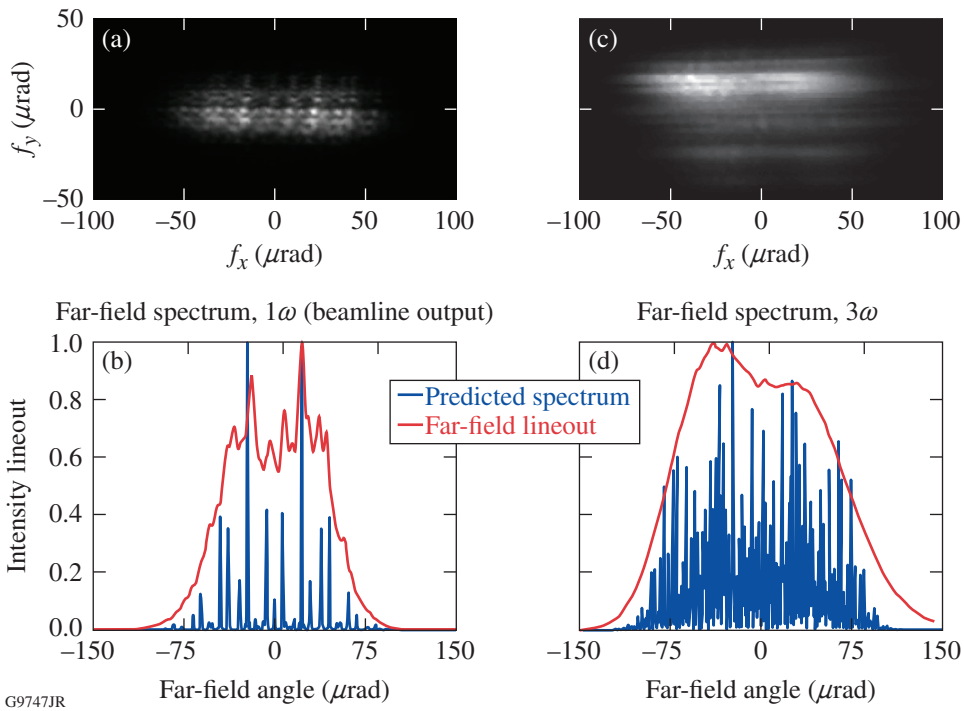


Figure 134.7

Far-field measurements at the [(a) and (b)] IRDP and [(c) and (d)] UVDP for a multi-FM picket shot. [(a) and (c)] The raw images are shown with the scale calibrated to the far-field angle in  $\mu\text{rad}$ . [(b) and (d)] The simulated optical spectra are plotted (in blue) along with lineouts from the camera images (red).

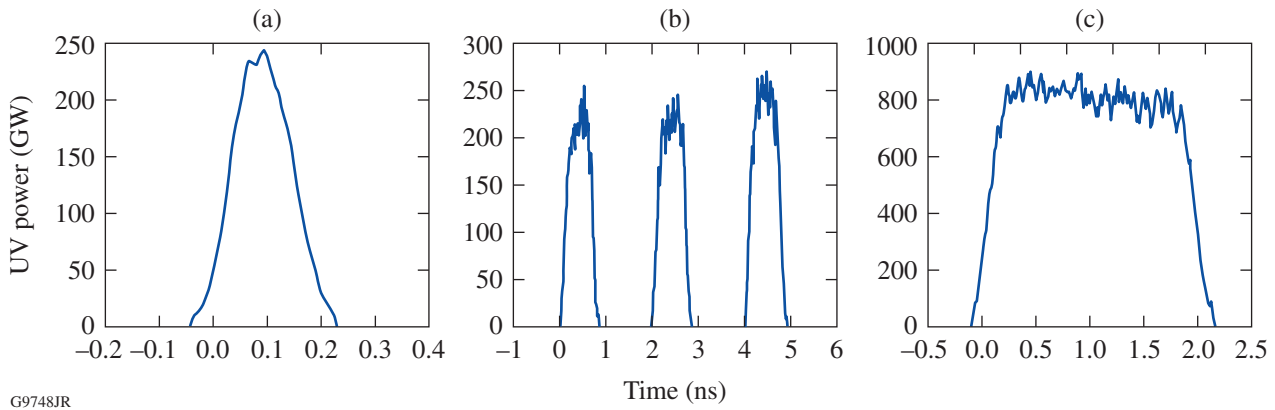


Figure 134.8

UV streak-camera measurements of a variety of multi-FM pulse shapes used during commissioning. (a) A single 150-ps full-width-at-half-maximum (FWHM) picket, (b) a sequence of three 650-ps FWHM pickets, and (c) a 2-ns square pulse.

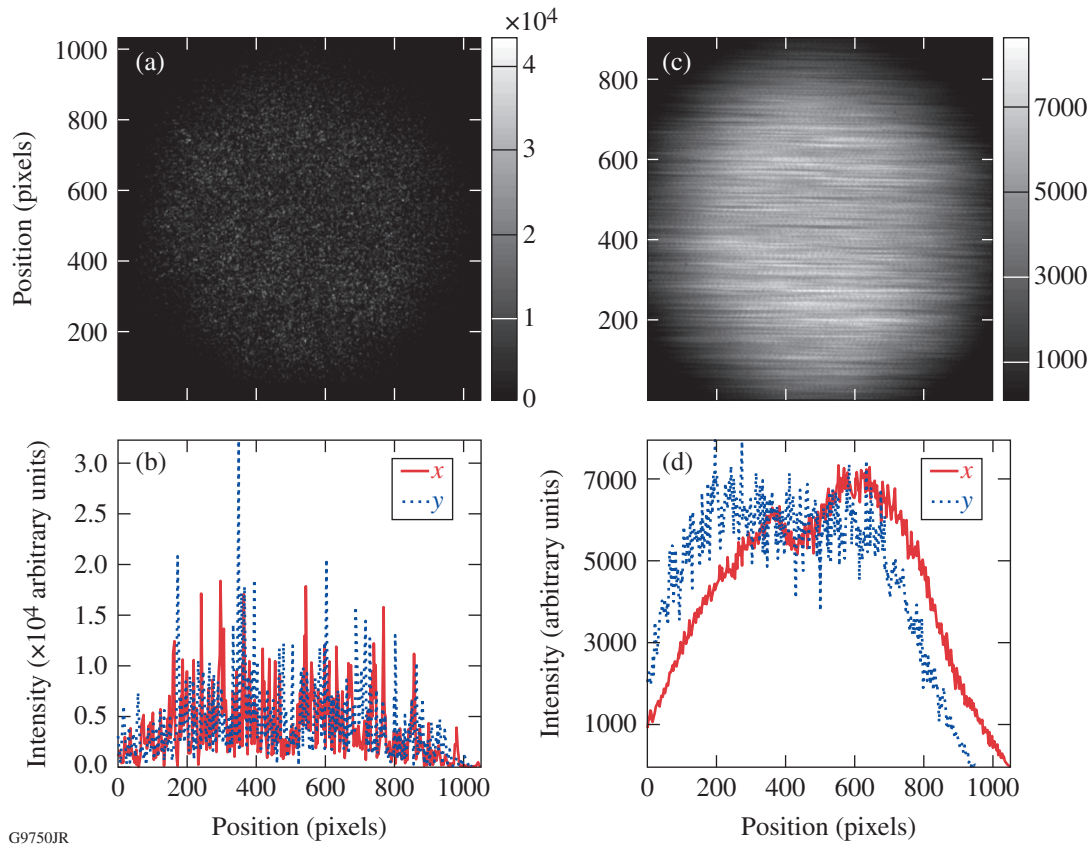


Figure 134.9

Equivalent-target-plane fluence measurements showing beam smoothing caused by multi-FM SSD applied to a 650-ps picket pulse. [(a) and (c)] Fluence profiles and [(b) and (d)] fluence lineouts in the horizontal and vertical directions are plotted for a narrowband main-channel pulse and a multi-FM SSD pulse, respectively.

### Conclusion

A prototype multi-FM SSD demonstration system has been successfully commissioned on a long-pulse beamline of the OMEGA EP Laser System. The system utilizes a fiber-based front end with a NIF PAM to deliver dispersed, phase-modulated pulses to the beamline, where the beam is amplified, converted to the third harmonic, and focused on the target after a DPP. A 0.85-TW limit for the peak power delivered to the target using the multi-FM SSD system was derived from a combination of simulating pulsed beam propagation through the UV optics, modeling the beamline gain processes, and budgeting for other potential sources of amplitude modulation. The multi-FM system was operated up to the system power limit using a variety of pulse shapes, and no evidence of spectral loss or beam degradation was observed on the available diagnostics. The beam-smoothing improvement obtained with the multi-FM SSD system was characterized using equivalent-target-plane fluence-profile measurements.

Since commissioning on OMEGA EP, the multi-FM system has been used in a number of target campaigns with the goal of validating the predicted effect on target physics. This work is ongoing, and the system will continue to provide useful data critical to future OMEGA EP experiments and potentially future polar-drive fusion experiments.

### ACKNOWLEDGMENT

This work was supported by the U.S. Department of Energy Office of Inertial Confinement Fusion under Cooperative Agreement No. DE-FC52-08NA28302, the University of Rochester, and the New York State Energy Research and Development Authority. The support of DOE does not constitute an endorsement by DOE of the views expressed in this article.

### REFERENCES

1. S. Skupsky, R. W. Short, T. Kessler, R. S. Craxton, S. Letzring, and J. M. Soures, *J. Appl. Phys.* **66**, 3456 (1989).
2. Y. Kato *et al.*, *Phys. Rev. Lett.* **53**, 1057 (1984).

3. *LLE Review Quarterly Report* **114**, 73, Laboratory for Laser Energetics, University of Rochester, Rochester, NY, LLE Document No. DOE/NA/28302-826, OSTI ID 93524 (2008).
4. J. H. Kelly, L. J. Waxer, V. Bagnoud, I. A. Begishev, J. Bromage, B. E. Kruschwitz, T. J. Kessler, S. J. Loucks, D. N. Maywar, R. L. McCrory, D. D. Meyerhofer, S. F. B. Morse, J. B. Oliver, A. L. Rigatti, A. W. Schmid, C. Stoeckl, S. Dalton, L. Folsbee, M. J. Guardalben, R. Jungquist, J. Puth, M. J. Shoup III, D. Weiner, and J. D. Zuegel, *J. Phys. IV France* **133**, 75 (2006).
5. G. H. Miller, E. I. Moses, and C. R. Wuest, *Opt. Eng.* **43**, 2841 (2004).
6. T. J. B. Collins, J. A. Marozas, K. S. Anderson, R. Betti, R. S. Craxton, J. A. Delettrez, V. N. Goncharov, D. R. Harding, F. J. Marshall, R. L. McCrory, D. D. Meyerhofer, P. W. McKenty, P. B. Radha, A. Shvydky, S. Skupsky, and J. D. Zuegel, *Phys. Plasmas* **19**, 056308 (2012).
7. “Fiber Front End with Multiple Phase Modulations and High-Bandwidth Pulse Shaping,” published in this volume.
8. M. Bowers *et al.*, in *Solid State Lasers XVI: Technology and Devices*, edited by H. J. Hoffman, R. K. Shori, and N. Hodgson (SPIE, Bellingham, WA, 2007), Vol. 6451, p. 64511M.
9. J. E. Rothenberg, D. F. Browning, and R. B. Wilcox, in *Third International Conference on Solid State Lasers for Application to Inertial Confinement Fusion*, edited by W. H. Lowdermilk (SPIE, Bellingham, WA, 1999), Vol. 3492, pp. 51–61.
10. “Simulations of the Propagation of Multiple-FM Smoothing by Spectral Dispersion on OMEGA EP,” published in this volume.
11. O. Morice, *Opt. Eng.* **42**, 1530 (2003).

# Simulations of the Propagation of Multiple-FM Smoothing by Spectral Dispersion on OMEGA EP

## Introduction

Smoothing by spectral dispersion<sup>1</sup> (SSD) is a technique that, when coupled with the use of a distributed phase plate (DPP), smoothes on-target laser illumination. The principle is shown in Fig. 134.10. Frequency modulation (FM) at a frequency  $\omega_M$  is applied to the laser beam. After transiting a diffraction grating, the beam is angularly deflected at  $\omega_M$  as its instantaneous frequency varies. In the far field of the beam, where the target is positioned, the focal spot is laterally deflected. If the deflection is sufficiently greater than the far-field feature size of a DPP located before the focusing lens, significant smoothing is obtained on a time-averaged basis.

The selection of the appropriate  $\omega_M$ , grating dispersion  $d\theta/d\lambda$ , asymptotic smoothing time  $\tau_{\text{asympt}}$ , and DPP feature size is subject to an optimization that depends on the target hydrodynamics and the particular Legendre modes to be reduced.<sup>2</sup> For the work described here, three simultaneous modulation frequencies were optimum,<sup>3</sup> therefore the “multi-FM” nomenclature.

The actual implementation of SSD puts the modulator(s) and the grating in the front end of the laser where the apertures and energies are small, thereby avoiding optical-damage issues and the high cost of large specialty optics such as gratings. This requires, however, the propagation of dispersed FM beams through the amplifier and frequency-conversion sections of the laser. Conversion of this dispersed FM to amplitude modulation (AM) becomes a concern, particularly in the high-energy/high-intensity sections of the laser. There are numerous mechanisms for the conversion of FM to AM,<sup>4</sup> particularly in fiber components. The conversion of FM to AM inherent in free-space propagation is the mechanism of exclusive concern in this article.

## FM-to-AM Conversion from Free-Space Propagation

### 1. Geometrical-Optics Model

Undispersed FM beams, by definition, have no AM. This condition is readily seen by examining the Bessel-function expansion of a single-tone FM signal,<sup>5</sup>  $E(t)$ :

$$E(t) = A \exp[i\omega_0 t + i\delta \sin(\omega_M t)]$$

$$= A \sum_{n=-\infty}^{+\infty} J_n(\delta) \exp[i(\omega_0 + n\omega_M)t], \quad (1)$$

where  $J_n$  is the  $n$ th-order Bessel function,  $\delta$  is the modulation depth,  $\omega_0$  is the optical frequency,  $\omega_M$  is the modulation (tone) frequency, and  $A$  is a constant. Taking the magnitude of Eq. (1) leads to  $|E(t)| = A$ . Note that this result depends critically on maintaining the phase relationship<sup>6</sup> of each sideband in the

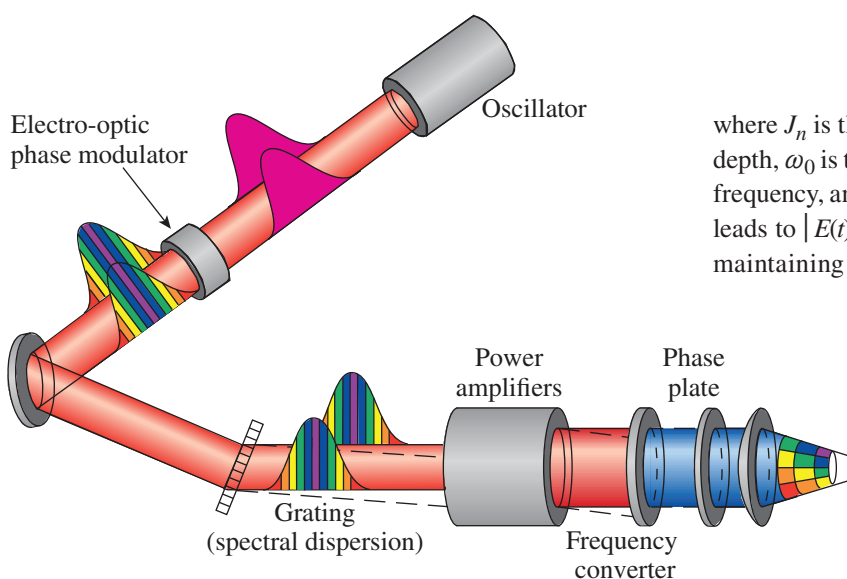


Figure 134.10 The smoothing by spectral dispersion (SSD) concept. Frequency modulation from one or more sequential electro-optic phase modulators is applied to the beam in the front end of the laser system prior to lateral magnification, amplification, and frequency conversion.

1723JR

Bessel-function expansion. This result may be readily extended to two-tone modulation:

$$\begin{aligned}
 E(t) &= A \exp\left[i\omega_0 t + i\delta_1 \sin(\omega_1 t) + i\delta_2 \sin(\omega_2 t)\right] \\
 &= A \sum_{n=-\infty}^{+\infty} \sum_{m=-\infty}^{+\infty} J_n(\delta_1) J_m(\delta_2) \\
 &\quad \times \exp\left[i(\omega_0 + n\omega_1 + m\omega_2)t\right] \quad (2)
 \end{aligned}$$

and so on for multitone modulation. The result is the same: as long as the sideband phases are maintained, there is no AM.

The effect of diffraction from the grating is to introduce a dephasing of the sidebands that depends on the sideband frequency, the dispersion of the grating, and the distance from the grating plane. Rewriting Eq. (1) with the grating dispersion in the  $y$  direction of a beam propagating in the  $z$  direction included yields

$$E(t) = A \sum_{n=-\infty}^{+\infty} J_n(\delta) \exp\left[i(\omega_0 + n\omega_M)t - i\mathbf{k}_n \cdot \mathbf{r}\right], \quad (3)$$

where  $\mathbf{k}_n \cdot \mathbf{r}$  is given by

$$\begin{aligned}
 \mathbf{k}_n \cdot \mathbf{r} &= \frac{\omega_0 + n\omega_M}{c} \left[ \sin(\theta_n) \mathbf{j} + \cos(\theta_n) \mathbf{k} \right] \cdot (y\mathbf{j} + z\mathbf{k}) \\
 &= \frac{\omega_0 + n\omega_M}{c} \left[ y \sin(\theta_n) + z \cos(\theta_n) \right] \quad (4)
 \end{aligned}$$

with the  $z$  direction taken along the propagation direction of the fundamental frequency ( $n = 0$ ,  $z = 0$  at the grating),  $\mathbf{j}$  and  $\mathbf{k}$  being the unit vectors in the  $y$  and  $z$  directions, the  $\mathbf{r}$  vector being the distance from the grating to a point on the beam at coordinates  $(y, z)$ , and  $\theta_n$  being the propagation angle of the  $n$ th sideband. The angle  $\theta_n$  is given by

$$\theta_n = \frac{d\theta}{d\omega} n\omega_M. \quad (5)$$

Equation (3) demonstrates that for any finite distance from the grating, the sideband  $n$  becomes dephased from the pure-FM phasing by the quantity  $\mathbf{k}_n \cdot \mathbf{r}$ .

In the case of two-tone modulation, Eq. (3) becomes

$$\begin{aligned}
 E(t) &= A \sum_{n=-\infty}^{+\infty} \sum_{m=-\infty}^{+\infty} J_n(\delta_1) J_m(\delta_2) \\
 &\quad \times \exp\left[i(\omega_0 + n\omega_1 + m\omega_2)t - \mathbf{k}_{n,m} \cdot \mathbf{r}\right], \quad (6)
 \end{aligned}$$

where  $\mathbf{k}_{n,m} \cdot \mathbf{r}$  is given by

$$\mathbf{k}_{n,m} \cdot \mathbf{r} = \frac{\omega_0 + n\omega_1 + m\omega_2}{c} \left[ y \sin(\theta_{n,m}) + z \cos(\theta_{n,m}) \right] \quad (7)$$

and  $\theta_{n,m}$  is given by

$$\theta_{n,m} = \frac{d\theta}{d\omega} (n\omega_1 + m\omega_2) \quad (8)$$

and so on for multitone modulation.

Because this dephasing is a function of  $\mathbf{r}$ , it leads to not only temporal AM but also spatial AM. Chuang<sup>7</sup> developed an analytic expression for the spatiotemporal AM from a single modulator in the geometrical-optics approximation. In the case of free-space propagation, the intensity  $I(y, z, t)$  in a plane at a distance  $z$  from the grating is given by<sup>7</sup>

$$I(y, z, t) = \frac{I_0}{\left\{ 1 + \frac{\delta\beta^2 z}{k_0} \sin\left[\omega_M t + \beta y_0(y, z, t)\right] \right\}}, \quad (9)$$

where  $I_0$  is the intensity at the grating plane (assumed to be at  $z = 0$ ) and  $y_0$  is the  $y$  location of the ray being traced at  $z = 0$ . Note that since the beam has not yet propagated any distance,  $I_0$  will have no SSD-induced time variation or  $y$ - (dispersion) direction variation. The quantity  $\beta$  is the grating-induced shear in radians per unit transverse length in the dispersion direction at the modulation frequency  $\omega_M$ . A straightforward calculation of the shear<sup>8</sup> yields

$$\beta = 2\pi \frac{d\theta}{d\lambda} \frac{\omega_M}{\omega_0}. \quad (10)$$

The result in Eq. (9) is valid where diffraction effects are negligible. Since some regions of  $I_0$  will have positive phase curvature (i.e., be focusing), there will exist a critical distance  $z_c$  at which the intensity goes to infinity (i.e., a caustic exists) in

the geometrical-optics approximation and Eq. (9) is no longer valid. This is trivially seen by inspecting the denominator in Eq. (9). At

$$z = z_r = \frac{k_0}{\delta\beta^2} \quad (11)$$

the denominator of Eq. (9) is equal to zero where the sine function is equal to  $-1$ . The distance  $z_r$  is termed the “critical distance.”

It is more physically intuitive to derive this result from a wavefront curvature standpoint. This is shown in Fig. 134.11. From Eq. (4) we may write the expression for the wavefront in terms of either the phase  $\phi$  or the optical path difference (OPD)  $z$  as:

$$\begin{aligned} \phi &= \delta \sin(\omega_M t + \beta y), \\ z &= \frac{\delta}{k_0} \sin(\omega_M t + \beta y). \end{aligned} \quad (12)$$

The critical distance  $z_r$  is calculated by applying the expression for the radius of curvature of an arc at the point  $\omega_M t + \beta y = -\pi/2$  where the wavefront is focusing:

$$z_r = \left. \frac{[1 + (dz/dy)^2]^{3/2}}{d^2 z / dy^2} \right|_{\omega_M t + \beta y = -\pi/2}. \quad (13)$$

Inserting the expression in Eq. (12) for the OPD  $z$  into Eq. (13) yields

$$\begin{aligned} z_r &= \frac{k_0 \left\{ 1 + \left[ \frac{\delta\beta}{k_0} \cos(\omega_M t + \beta y) \right]^2 \right\}^{3/2}}{-\delta\beta^2 \sin(\omega_M t + \beta y)} \bigg|_{\omega_M t + \beta y = -\pi/2} \\ &= \frac{k_0}{\delta\beta^2} \end{aligned} \quad (14)$$

for the critical distance. The critical distance  $z_r$  plays the same role as a focal length in geometrical optics. As such, the usual geometrical-optics formulae may be applied to it.

For distances  $z < z_r$ , the model in Eq. (9) can be used to visualize the spatiotemporal modulation related to the propagation of SSD. The case of a  $1.054\text{-}\mu\text{m}$ -wavelength,  $0.75\text{-ns} \times 10\text{-cm}$

FWHM (full width at half maximum) Gaussian pulse modulated at  $10\text{ GHz}$ ,  $\delta = 4\text{ rad}$  with  $60\text{-}\text{\AA}/\mu\text{rad}$  dispersion is shown in Fig. 134.12. Note that a similar plot of the intensity versus

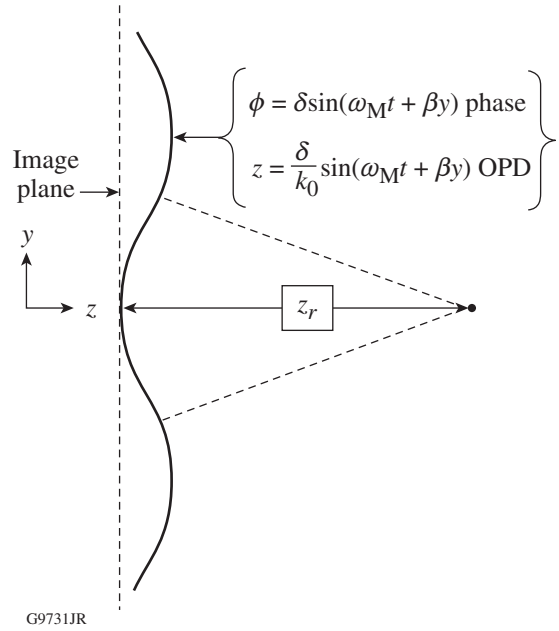


Figure 134.11 Schematic of the calculation of the critical distance  $z_r$ , from the local radius of curvature of the phase front. The usual formula for the curvature of an arc is applied to the expression for the optical path difference (OPD) at the location of positive phase curvature or  $\omega_M t + \beta y = -\pi/2$ .

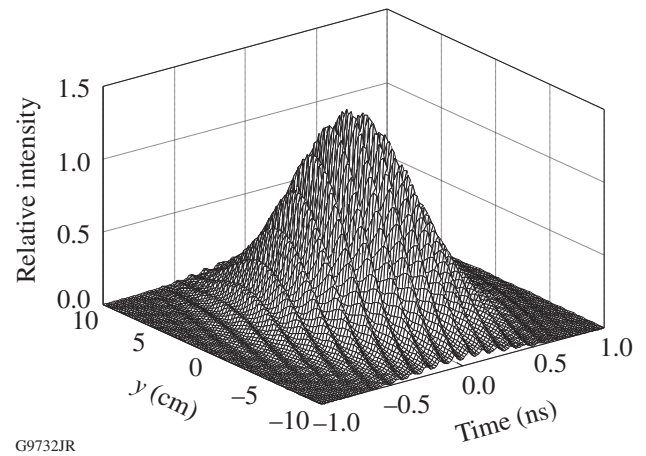


Figure 134.12 Relative intensity 2000 cm from the grating for a  $0.75\text{-ns} \times 10\text{-cm}$  FWHM Gaussian pulse phase modulated with  $\delta = 4\text{ rad}$  at  $10\text{ GHz}$  with  $60\text{-}\text{\AA}/\mu\text{rad}$  dispersion. This is a replot of Fig. 6-2 in Chuang’s thesis.<sup>7</sup>

$x, t$  rather than  $y, t$  would show no modulation. It is worth noting that for this particular example,  $z = 2000$  cm and  $z_r = 6800$  cm; therefore the geometrical-optics condition for validity is well satisfied. The ratio of  $z/z_r \sim 0.3$  is typical of the ranges of interest for large laser systems. Figure 134.13 displays lineouts in the temporal and spatial dispersion directions. The intensification relative to the unmodulated beam becomes of concern in those regions of a laser where the beam is close to the coating-damage, self-focusing, or stimulated-scattering limits.

From Eq. (9) an expression may be written for the normalized peak-to-valley amplitude modulation  $\alpha$ , assuming that the slowly varying envelope is removed:

$$\alpha(z) = \frac{I_{\max} - I_{\min}}{(I_{\max} + I_{\min})/2} = \frac{2\delta\beta^2 z}{k_0}. \quad (15)$$

From Eq. (15) it is seen that the normalized peak-to-valley modulation, in the geometrical-optics limit, is proportional to the propagation distance  $z$ , the modulation index  $\delta$ , and the square of the shear  $\beta$ .

## 2. Linear-Dispersive-Filter Model

Hocquet *et al.*<sup>9</sup> developed a similar metric termed a “distortion criterion” for temporal AM caused by SSD propagation away from a grating. Starting with the concept of free-space propagation as a linear dispersive filter,<sup>10</sup> the temporal Fourier transform of the electric field,  $E(z, \omega)$ , at a distance  $z$  from a grating is written as

$$E(z, \omega) = E_0(\omega) H(z, \omega), \quad (16)$$

where  $H(z, \omega)$  is a Fourier-domain transfer function. In the case of a grating, this transfer function is a phase-only filter. The phase can be expanded in a Taylor series in  $\omega$  of which the quadratic component  $\phi_2$ , the quadratic spectral phase, is the first term of interest for AM calculation. Assuming  $\phi_2$  is small, the transfer function is written as

$$H(z, \omega) = \left[ 1 - \frac{i}{2} \phi_2(z) \omega^2 \right]. \quad (17)$$

Substituting Eq. (17) into Eq. (16) and using Eq. (1) for  $E_0(\omega)$  and then inverse transforming and taking the magnitude of the resulting inverse transform yields

$$I(z, t) \approx 1 - \phi_2(z) \delta\omega_M^2 \cos(\omega_M t). \quad (18)$$

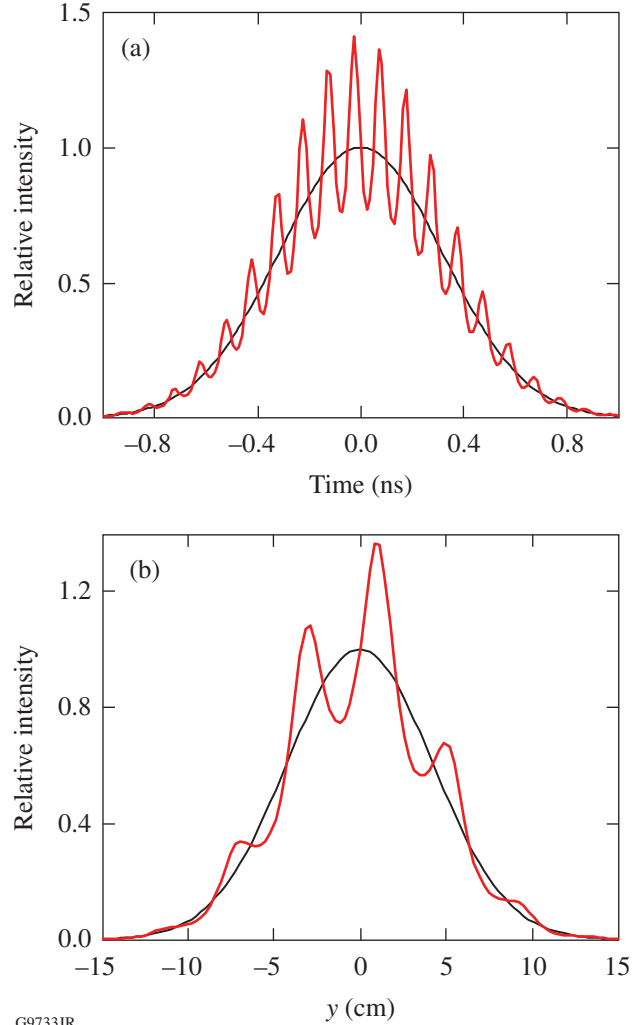


Figure 134.13

Lineouts (red line) in the temporal direction at  $(x, y) = (0, 0)$  and in the  $y$  (dispersion) direction at  $x = 0$  and  $t = 0$  of the relative intensity shown in Fig. 134.12. In both plots the unmodulated beam profile is also shown to illustrate the local intensification (black line).

Hocquet defines the “distortion criterion”  $\alpha$  as in Eq. (15). The values of  $I_{\max}$  and  $I_{\min}$  obtained by substituting  $\pm 1$  for the extrema of the cosine function in Eq. (18) lead to

$$\begin{aligned} \alpha(z) &= 2 \frac{1 + \phi_2(z) \delta\omega_M^2 - 1 + \phi_2(z) \delta\omega_M^2}{1 + \phi_2(z) \delta\omega_M^2 + 1 - \phi_2(z) \delta\omega_M^2} \\ &= 2\phi_2(z) \delta\omega_M^2. \end{aligned} \quad (19)$$

Substituting Chanteloup’s<sup>11</sup> expression for the quadratic part of the spectral phase  $\phi_2(z)$  at  $y = 0$ , the center of the beam, into Eq. (19) yields

$$\alpha(z) = \frac{2(2\pi)^2 c N^2}{\omega_0^3 \cos^2(\theta_0)} \delta\omega_M^2 z, \quad (20)$$

where a grating at Littrow angle  $\theta_0$  and a linear groove density of  $N$  per unit length have been assumed. Applying the expression for the dispersion of a grating at the Littrow angle

$$\left. \frac{d\theta}{d\lambda} \right|_{\theta=\theta_0} = \frac{N}{\cos(\theta_0)} \quad (21)$$

in Eq. (10) and substituting  $k_0 = \omega_0/c$ , Eq. (20) is seen to be identical to Eq. (15), which is Chuang's result.<sup>7</sup> The geometrical-optics and linear-dispersive-filter models, using completely different approaches, lead to the same result for the normalized peak-to-valley amplitude modulation. We choose to continue with Chuang's result since it provides a spatiotemporal description of the pulse intensification resulting from SSD propagation that may be readily compared to numerical models.

### 3. *B*-Integral Considerations

The so-called *B*- or "breakup" integral is an important measure of the transverse stability of a high-intensity beam. Physically, it is the integral of the local phase pushback in radians caused by propagation of the beam through media of thickness  $L$  with a positive  $\chi^3$ . By definition, it is

$$B \triangleq \frac{2\pi}{\lambda} \int_0^L \gamma I(x, y, z, t) dz, \quad (22)$$

where  $\gamma$  is a characteristic of the material.<sup>12</sup> In large laser systems, values of  $B$  in excess<sup>13</sup> of 2.0 to 2.2 rad between spatial filters can lead to catastrophic small-scale self-focusing of the beam. Laser-performance limits, particularly for temporally short pulses that do not experience significant gain saturation, are determined by the requirement to limit  $B$ . This is known as the "peak-power limit."

During laser design, the *B*-integral is calculated using the average local intensity; that is, transverse small-scale features that would be eliminated in a spatial-filtering operation are averaged out prior to computing  $B$ . In a system with SSD applied, the pinholes are carefully sized to ensure passage of the dispersed beam (at least to the Carson<sup>14</sup> limit =  $2\delta\omega_M$ ) through the system. The local intensification on any optical component induced by the propagation of SSD therefore needs to be carefully included in the calculation of the system's peak-power limit.

### Modeling

LLE's OMEGA EP laser is a multipass-architecture laser similar to that of the National Ignition Facility (NIF)<sup>15</sup> with important differences to optimize it for its primary mission of radiography of cryogenic implosions on the OMEGA laser<sup>16</sup> and separate flat-target experiments. The laser is shown schematically in Fig. 134.14. The multipass cavity formed by the end mirror and the deformable mirror is identical to that of the NIF. The input-output arm containing the booster amplifier is different, however, than that of the NIF. Because the beam-path distance to OMEGA EP's UV target chamber is significantly shorter than that to the NIF's (80 m versus ~140 m from the fold mirror to the target), the transport spatial filter is shorter. OMEGA EP's frequency-conversion crystals (FCC's) are located 8.1 m in front of the  $f/6.5$ , UV focus lens with a 3.4-m effective focal length. The most-damage-threatened component, the 4.0-cm-thick fused-silica vacuum window, is located 25 cm downstream of the focus lens in the converging beam. The distributed phase plate (DPP) is located 20 cm in front of the focus lens.

Unlike on the NIF, the 11-mm-/9-mm-thick, type-I/type-II, KDP/KD\*P frequency-conversion crystals are located on the floor upstream of the focus lens. The IR input polarization is vertical. The SSD dispersion direction is in the sensitive direction of the doubler (horizontal) at the FCC's.<sup>17</sup> The sign of the dispersion is chosen to compensate the frequency detuning<sup>18</sup> at the FCC's. A more-optimal choice, in terms of conversion efficiency, would have the dispersion direction in the sensitive direction of the tripler. The two UV transport mirrors immediately following the UV diagnostic beam splitter (DBS) are dichroic and strip residual  $1\omega$  and  $2\omega$  light from the beam so that only UV light is delivered to the focus lens.

Frequency conversion is an intensity-dependent nonlinear process that can increase amplitude modulation, particularly if operating in an unsaturated input intensity regime like the 11-mm-/9-mm-thick OMEGA EP FCC's. Since amplitude modulation from SSD propagation is minimized at the actual SSD grating and its image planes, the FCC's are located at a grating image plane. In the simulation, this is accomplished by translating the SSD grating in the front end of the system in the axial direction to make use of the large longitudinal magnification<sup>19</sup>  $M \sim 400$  ( $M = m^2$ , where  $m$  is the lateral magnification) of the system to shift the image. Magnification differs in the horizontal and vertical directions at least in part because of the large number of multipass tilted slabs.<sup>20</sup> Detailed ray-trace models of the system were used to set the SSD grating image on the FCC's.

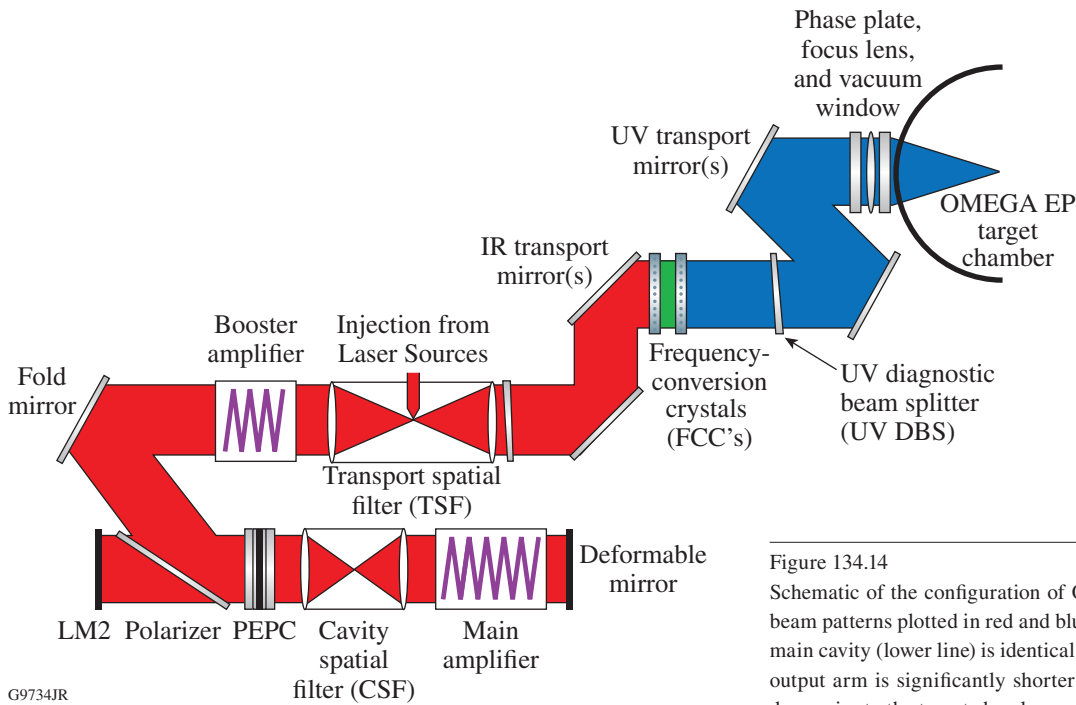


Figure 134.14 Schematic of the configuration of OMEGA EP with IR and UV beam patterns plotted in red and blue respectively. The multipass main cavity (lower line) is identical to that of the NIF. The input-output arm is significantly shorter and frequency conversion is done prior to the target chamber.

The multi-FM temporal pulse shape consists of one to three “pickets” in front of a main compression “drive” pulse. A typical shape is shown in Fig. 134.15. Multi-FM SSD is applied to only one or more of the pickets; the system is capable of applying 17-GHz, single-FM SSD modulation to the drive pulse.<sup>21</sup> Although the available 17-GHz, single-FM SSD was not applied to the drive pulse for the majority of the demonstration shots,  $\delta = 5.5$  of 3.0-GHz stimulated Brillouin scattering suppression (SBSS) modulation was applied to the drive pulse for all the demonstration shots. The bulk of the on-target smoothing benefit is obtained prior to the second picket.<sup>2</sup> The pickets themselves have a UV FWHM of 150 ps.

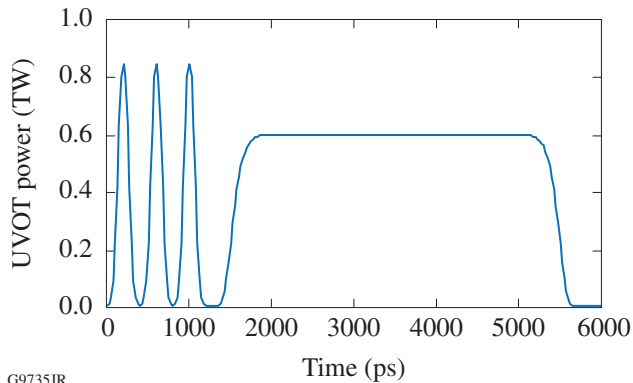


Figure 134.15 Unsheared UV on-target (UVOT) pulse shape. The three pickets are followed by a main drive pulse.

The pickets shown in Fig. 134.15 are temporally short (150-ps FWHM in the UV, ~175 ps in the IR) compared to the main pulse. Because of their short pulse width, as these pickets increase in energy, they represent a peak-power threat to the system rather than an optical coating damage-fluence threat. It is therefore necessary to calculate the maximum *B*-integral attained at any spatiotemporal point in the pulse to assess the threat to the system. In order to do that for the complicated actual case of three modulators and laser system components including frequency conversion, the propagation code Miró is used.

Miró is a comprehensive laser design and simulation code developed<sup>22,23</sup> at CEA/CESTA, France. Miró models typical high-peak-power laser components and operations such as (but not limited to) free-space propagation, amplifiers, frequency converters, and gratings. Consistent with the progressively increasing levels of sophistication in the typical design process of high-peak-power lasers, Miró offers increasing levels of modeling sophistication in the form of “modes” of calculation starting with basic one-dimensional (1-D) ray tracing up to full diffraction calculation that includes broad-spectrum propagation with group-velocity dispersion.

For these simulations of multi-FM SSD, Miró’s “broad spectrum” mode and “inhomogeneous wave” grid transformation are used to render the problem computationally tractable. (For

more details, refer to the Miró V5<sub>ε</sub> Reference Manual.<sup>24</sup>) To ensure that the SSD model was being set up correctly in Miró, the analytical case of Chuang in Fig. 134.13, was first simulated. The results are shown in Fig. 134.16. The close agreement between the Miró prediction and the analytical treatment of Chuang gives confidence that the Miró SSD model has been constructed correctly and can be confidently used to predict AM in the region where  $z < z_r$ .

Since the expected picket energies are low ( $\sim 100$  J) and the beam areas are large ( $\sim 1200$  cm<sup>2</sup>), the picket fluence

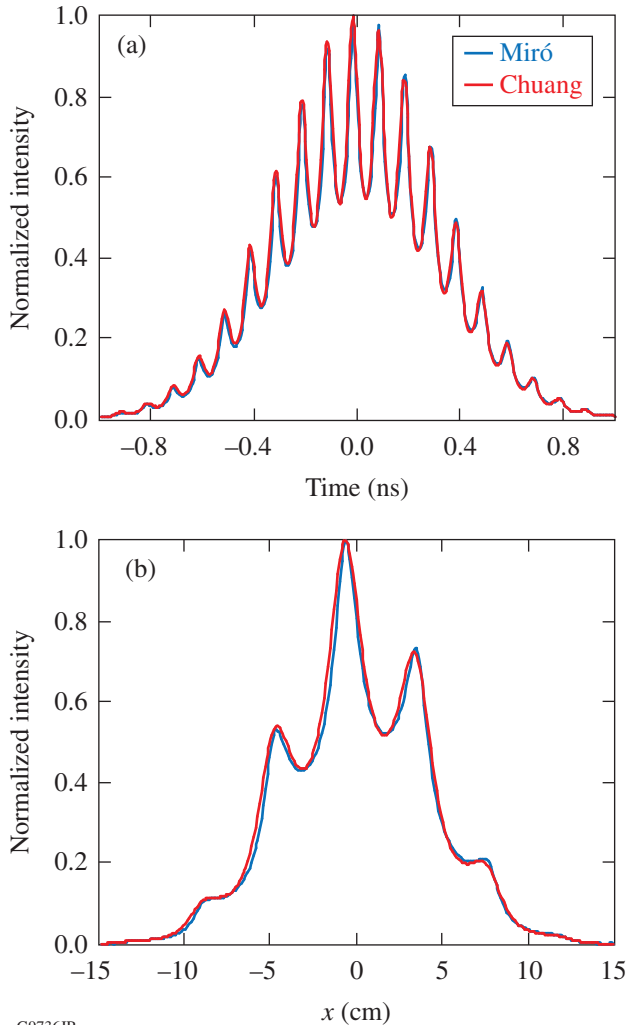


Figure 134.16

Lineouts of the relative intensity predicted by Miró (blue line) in the (a) temporal and (b) spatial directions for the case of Fig. 134.13 compared to the predictions of the Chuang model (red line) with  $\delta = 4$  rad at 10 GHz and  $60\text{-}\text{\AA}/\mu\text{rad}$  dispersion. This is at a distance from the grating of 2000 cm compared to  $z_r = 6800$  cm.

( $\sim 0.08$  J/cm<sup>2</sup>) is low compared to the equivalent (beam-normal) saturation fluence of the system ( $\sim 5.7$  J/cm<sup>2</sup>). The pickets are therefore in the small-signal-gain regime and their highest intensities are attained after the booster (final) amplifier, which has a small-signal gain of  $\sim 6$ . The highest  $B$ -integral, which is essentially an intensity/length product, is in the section of OMEGA EP downstream from the transport spatial filter to the target with the most-threatened component being the vacuum window on the target chamber. The relevant part of OMEGA EP is shown in Fig. 134.17.

The three modulation frequencies applied to the beam are detailed in Table 134.III. These modulation frequencies and their modulation depth have been chosen for optimal smoothing.<sup>25</sup> If the grating-induced beam shear across the nominal  $w = 35$ -cm beam width is given by

$$\Delta t = w \frac{2}{c} \tan(\theta), \quad (23)$$

where  $\theta$  is the angle of incidence on the grating (assumed to be at Littrow), then writing  $\tan(\theta)$  in terms of the dispersion  $d\theta/d\lambda$  yields

$$\Delta t = \frac{w\lambda}{c} \frac{d\theta}{d\lambda} = 360 \text{ ps} \quad (24)$$

for the temporal shear introduced by an 1800-lines/mm diffraction grating.

The phasing of the modulators in the Miró model is important to ensure that the *maximum* intensification is calculated. The 22.8- and 31.9-GHz modulators impart the most bandwidth to the beam and therefore the most local phase curvature. These modulators have a 9.1-GHz frequency difference, so near-maximum local wavefront curvatures can be expected in any pulse longer than  $\sim 110$  ps. For this reason the modulators are modeled as *co*-sinusoidal modulators with zero relative phase and  $t = 0$  is centered on the picket.

Table 134.III: FM parameters for the multi-FM SSD system on OMEGA EP.

Modulator	1	2	3
Frequency (GHz)	21.165	22.838	31.881
IR modulation depth (radians)	0.450	1.040	2.071
IR bandwidth ( $\text{\AA}$ )	0.7	1.8	4.9
IR dispersion ( $\mu\text{rad}/\text{\AA}$ )	29.3	29.3	29.3
$\beta$ ( $\text{m}^{-1}$ )	136.9	147.7	206.3
$z_r$ (m)	707.9	263.1	67.8

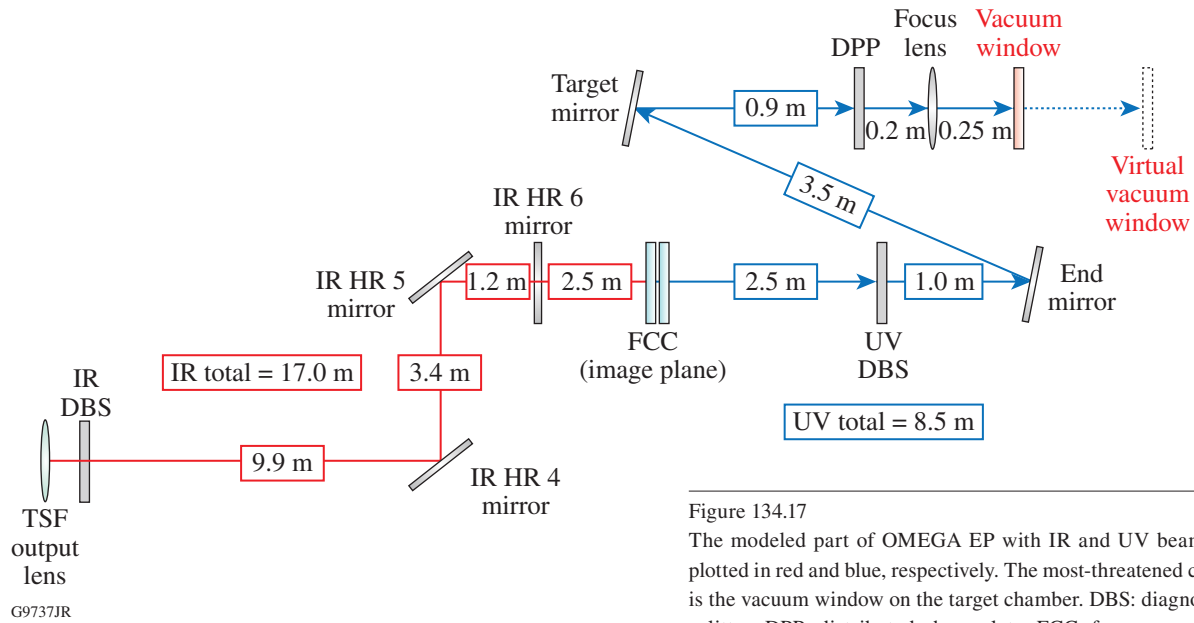


Figure 134.17

The modeled part of OMEGA EP with IR and UV beam patterns plotted in red and blue, respectively. The most-threatened component is the vacuum window on the target chamber. DBS: diagnostic beam splitter; DPP: distributed phase plate; FCC: frequency-conversion crystal; TSF: transport spatial filter; HR: high reflector.

To minimize amplification of AM in the frequency-conversion process, the SSD grating was carefully imaged onto the FCC's.<sup>26</sup> The component located the farthest from the image plane of the grating will experience the greatest intensification as a result of propagation. From Fig. 134.17 it is clearly seen that these components are the IR diagnostic beam splitter and the transport spatial filter's (TSF's) output lens upstream of the image plane and the vacuum window downstream of the image plane. The TSF output lens is  $\sim 17$  m from the image plane. When calculating the expected intensification, it is useful to first estimate how close the caustic is approached. To do that, the concept of critical distance  $z_r$  must be extended to a multifrequency-modulated beam. Recall from the discussion surrounding Fig. 134.11 that  $z_r$  is the radius of curvature of the wavefront caused by one modulation. At points in space and time where the frequency modulations are in phase, the resulting phase curvature is the sum of the individual phase curvatures. The thin-lens law<sup>27</sup> for two thin lenses in contact may be applied to add the phase curvatures where  $1/f$  is the power of a lens of focal length  $f$

$$\frac{1}{f_1} + \frac{1}{f_2} + \frac{1}{f_3} = \frac{1}{f_{\text{total}}} \quad (25)$$

to obtain

$$\frac{1}{z_{r,1}} + \frac{1}{z_{r,2}} + \frac{1}{z_{r,3}} = \frac{1}{z_{r,\text{total}}}, \quad (26)$$

where  $z_{r,i}$  is the critical distance corresponding to the  $i$ th modulation. Using Eq. (26) it is immediately found that  $z_{r,\text{total}}$  for this system is 50.1 m and the TSF output lens, 17 m from the image plane, is far from the caustic and in the region ( $z/z_r \sim 0.34$ ) where the Miró SSD model has been tested.

The vacuum window is in the UV section of OMEGA EP. The critical distance for the UV beam is required. Recall from Fig. 134.11 that

$$z_r = \frac{k_0}{\delta\beta^2} = \frac{k_{0,\text{IR}}}{\delta_{\text{IR}}\beta_{\text{IR}}^2} = \frac{k_{0,\text{UV}}/3}{(\delta_{\text{UV}}/3)\beta_{\text{UV}}^2} = \frac{k_{0,\text{UV}}}{\delta_{\text{UV}}\beta_{\text{UV}}^2} \quad (27)$$

because the propagation vector  $k_0$  triples after tripling to the UV ( $k_{0,\text{UV}} = 3k_{0,\text{IR}}$ ), the modulation index  $\delta$  is increased by a factor of 3 ( $\delta_{\text{UV}} = 3\delta_{\text{IR}}$ ), and the grating-induced shear in radians  $\beta$  at the modulation frequency is unchanged ( $\beta_{\text{UV}} = \beta_{\text{IR}}$ ). Equation (27) implies that for a single modulation,  $z_r$  is unchanged under frequency conversion. This is expected since the local wavefront radius of curvature is not expected to be changed by frequency conversion.<sup>28</sup> By Eq. (26) this also holds

for  $z_{total}$ . The vacuum window is located a physical distance of 8.5 m from the image plane and is therefore also far from the caustic and in the region where the Miró SSD model has been tested.

A screen shot of the Miró model used for these simulations is shown in Fig. 134.18 with the source shown in the lower left. The modeled beam was temporally 450 ps long and had an experimentally measured temporal profile. This is longer than the actual pickets propagated in the system and was chosen to ensure that multiple cycles of all three modulators were at the maximum intensity of the pulse shape. The spatial shape of the  $1\omega$  beam was a 20th-order, square super-Gaussian with 35-cm FWHM. The grid size for these simulations was  $16 \times 384 \times 1024 (x \times y \times u)$ , where  $y$  is the dispersion direction and  $u$  is the “inhomogeneous wave”<sup>29</sup> transformed grid coordinate.

The IR phase modulators and the reflection grating used in the model to disperse the beam are in the lower left. To reduce the model’s complexity and therefore computation time, the model’s phase modulation and SSD dispersion were applied at the 40-cm aperture (35-cm-sq beam). This required a model grating with 289.57 lines/mm used at its Littrow angle of  $8.78^\circ$  for  $\lambda = 1.054 \mu\text{m}$ . The distance in the model from the reflection grating to the cavity end mirror was adjusted to ensure the grating was imaged onto the mid-plane of the FCC’s.

Although the booster amplifier disks are included in the Miró model for future work, they are modeled as zero- $B$ -integral,

unity-gain optics to reduce computation time. The main laser cavity, including the cavity spatial filter (CSF), is modeled as a two-pass instead of the actual four-pass to model the imaging of the cavity while again reducing model computation time. All components in this early part of the laser have their nonlinear coefficient  $\gamma$  set to zero. All components from the TSF pinhole onward have their  $\gamma$ ’s specified to ensure  $B$  is accurately calculated. The  $\gamma$ ’s for the optical materials in OMEGA EP at their use wavelengths are detailed in Table 134.IV.

Three components have more than one wavelength on them simultaneously: the KDP doubler, the KD\*P tripler, and the fused-silica UV diagnostic beam splitter. The IR  $B$  contributed by the doubler consists of the  $B$  as a result of the IR beam itself and the cross-phase-modulation contribution caused by the  $2\omega$  beam on the IR beam. Similarly, its  $2\omega B$  contribution is the  $B$  attributed to the  $2\omega$  beam itself plus the cross-phase-modulation term contribution attributed to the IR beam. Where there are three wavelengths present as in both the tripler and the UV diagnostic beam splitter, the calculation is generalized for three waves. The actual calculation proceeds by finding the temporal maximum of the intensity and then calculating the  $B$  through the crystal by a split-step method.

The preceding calculates the *contribution* of the particular crystal to the  $B$ -integral. The  $B$ -integral at each harmonic does not start at a zero value and must be initialized.<sup>30</sup> For the doubler, the conservative assumption is made that the initially small divergence added to the fundamental frequency beam by nonlinear ripple growth ( $B$ ) is completely transferred to

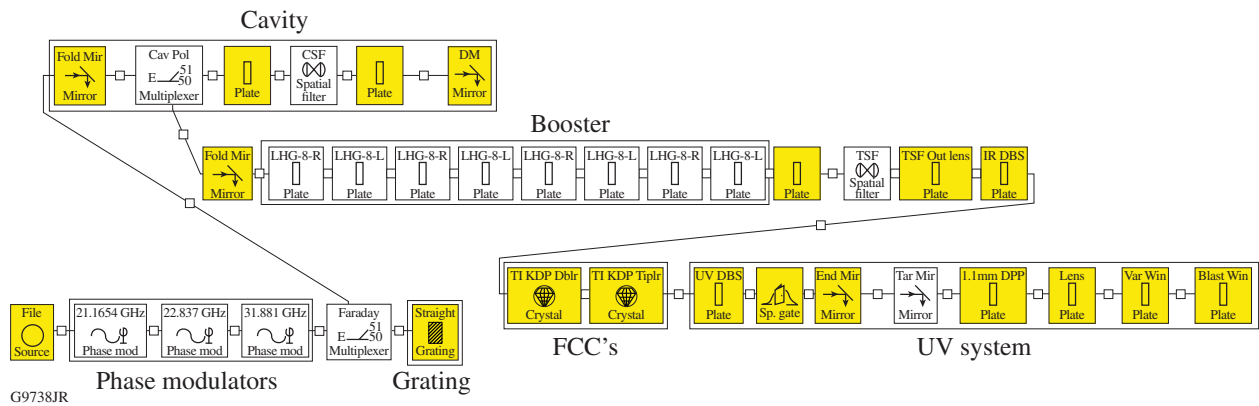


Figure 134.18 The OMEGA EP Miró model. The IR phase modulators are in the lower left. A reflection grating was used in the model to disperse the beam at the 40-cm aperture. Although the booster amplifier disks are included in this model, they are modeled as zero- $B$ -integral, unity-gain plates to reduce running time.

Table 134.IV: Nonlinear coefficients ( $\gamma$ ) for OMEGA EP components.

Component	Wavelength	Material	Thickness (cm)	$\gamma$ (cm <sup>2</sup> /GW)
TSF output lens	IR	fused silica	5.6	$2.7 \times 10^{-7}$
Diagnostic beam splitter	IR	fused silica	1.0	$2.7 \times 10^{-7}$
KDP doubler	IR and $2\omega$	KDP	1.1	$2.5 \times 10^{-7}$
KD*P tripler	IR, $2\omega$ , and UV	KD*P	0.9	$3.0 \times 10^{-7}$
Diagnostic beam splitter	IR, $2\omega$ , and UV	fused silica	1.0	$3.88 \times 10^{-7}$
Distributed phase plate	UV	fused silica	4.0	$3.88 \times 10^{-7}$
Focus lens	UV	fused silica	4.0	$4.00 \times 10^{-7(a)}$
Vacuum window	UV	fused silica	4.0	$4.86 \times 10^{-7(a)}$
Free space	IR or UV	air	various	$5.0 \times 10^{-10}$

<sup>(a)</sup>The component values have been increased to account for other effects.

the harmonic beam(s). By this assumption the initial  $B$  of the second harmonic ( $2\omega$ ) is simply set equal to the  $B$  of the fundamental beam.

The case of frequency tripling, which involves the mixing of two different frequencies, is more complicated. In this case Miró makes use of a phenomenological expression for the transmission  $T$  of a spatial filter<sup>31</sup> as a function of the  $B$ -integral  $B$ , and an experimentally determined “noise parameter”  $\varepsilon$ , for the system under consideration:<sup>32</sup>

$$T(B) = 1 - \frac{\varepsilon}{2} \left[ (1 + 2B^2) + \cosh(2B) \right]. \quad (28)$$

The loss  $L$  in transiting the spatial filter is from Eq. (27):

$$L(B) = \frac{\varepsilon}{2} \left[ (1 + 2B^2) + \cosh(2B) \right]. \quad (29)$$

Miró postulates that these losses, weighted by frequency (energy), are conserved in frequency conversion. This is roughly equivalent to postulating that the energy-weighted modulations on the beams to be mixed appear on the harmonic. Mathematically, the equation

$$\begin{aligned} & 3\omega \left[ 1 + 2B_{3\omega}^2 + \cosh(2B_{3\omega}) \right] \\ &= \sum_{n=1}^2 n\omega \left[ 1 + 2B_{n\omega}^2 + \cosh(2B_{n\omega}) \right] \end{aligned} \quad (30)$$

is solved numerically for  $B_{3\omega}$ , given  $B_{1\omega}$  and  $B_{2\omega}$ .

The focus lens is modeled as a 4-cm-thick plane-parallel plate of fused silica. The vacuum window is located 25 cm downstream of the 3.4-m effective-focal-length focusing lens in the converging beam. This portion of the UV system can be efficiently modeled by making use of the Talanov<sup>33</sup> transformation. To determine the beam modulation on the vacuum window, the beam is propagated the transformed distance  $z'$  with coordinates  $(x', y')$  given by

$$z' = \frac{z}{1 - z/f}, \quad (31)$$

$$(x', y') = \frac{(x, y)}{1 - z/f}. \quad (32)$$

This transformation yields the beam profile at the vacuum window by propagating the 40-cm aperture beam  $z' = 27$  cm instead of  $z = 25$  cm. Since only the resulting increase of the  $B$ -integral is of interest, rather than applying the transverse grid transformation in Eq. (32), the value of  $\gamma$  for the vacuum window was simply increased by the square of  $1/(1-z/f)$  to model the beam area's reduction and therefore intensity increase. This changed the value of  $\gamma$  from  $3.88 \times$  to  $4.52 \times 10^{-7}$  cm<sup>2</sup>/GW.

An additional complication of the model is the presence of the DPP 20 cm in front of the focusing lens. The DPP's spatial-phase modulation will itself be converted into spatial-amplitude modulation by propagation. The DPP's spatial phase will add and subtract from the SSD-induced phase in a complicated way. In the worst case, converging phase features from SSD and the DPP will increase the intensification. The DPP used for the OMEGA EP demonstration experi-

ments was designed at LLE<sup>34</sup> to produce a 1.1-mm-diam focal spot. Adequately resolving the phase features generated by this optic required very large spatial-grid resolutions ( $>1024 \times 1024$ ). Over the 47 cm of equivalent propagation distance from the DPP to the vacuum window, no caustics are generated. A simulation generated by propagating the design phase map of the DPP over the distances in question is shown in Fig. 134.19. In the absence of any other modulation, the peak intensity increase caused by modulation from the DPP on the focus lens and the vacuum window would be 3.2% and 7.6%, respectively. As a zero-order approximation to the effect of the DPP on  $B$ , the  $\gamma$ 's for the focus lens and the vacuum window were further increased by 3.2% and 7.6%, respectively, to  $4.00 \times 10^{-7} \text{ cm}^2/\text{GW}$  and  $4.86 \times 10^{-7} \text{ cm}^2/\text{GW}$ .

**Results**

The temporal shape used in the model is shown in Fig. 134.20, along with the modulators' waveform. This shape was taken from an early measurement of one of the IR pickets in the front end. The pickets generated for the OMEGA EP demonstration shot campaign were closer to Gaussian with a shorter (~150-ps) temporal width. The advantage of wider pickets for these simulations is to ensure that the peak temporal intensity extends over the time the modulators are co-phased. Since OMEGA EP operates in the small-signal regime for these pickets, it is an excellent representation of the picket at the TSF lens output.

The  $B$ -integral as a function of distance from the FCC's for the maximum power determined by a  $B$ -integral limit equals 2.0, as shown in Fig. 134.21. The UV  $B$ -integral starts at 0.5 rad

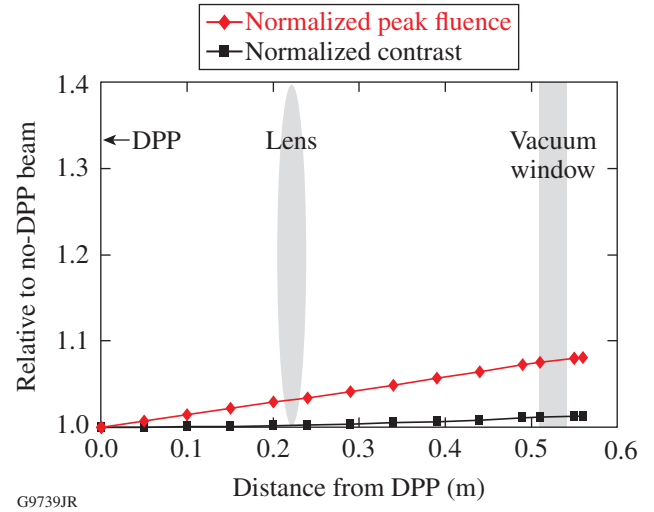


Figure 134.19 The normalized peak fluence and the normalized contrast caused by modulation from the 1.1-mm-spot DPP as a function of distance from the DPP.

at the FCC's largely because of the IR contribution from the TSF output lens and the IR DBS. This result was obtained by adjusting the peak input intensity until a  $B$ -integral of 2.0 was obtained. This was achieved at a peak UV power measured at the vacuum window of 1.6 TW, which represents an upper bound for the picket power.

This result is the  $B$ -integral due only to AM resulting from the propagation of multi-FM SSD in the OMEGA EP Laser System. Many other effects have been neglected in this analysis including, but not limited to, gain narrowing in the amplifiers, etaloning in beamline components, etc. Therefore, this result is *not* the ultimate peak-power limit of OMEGA EP with multi-

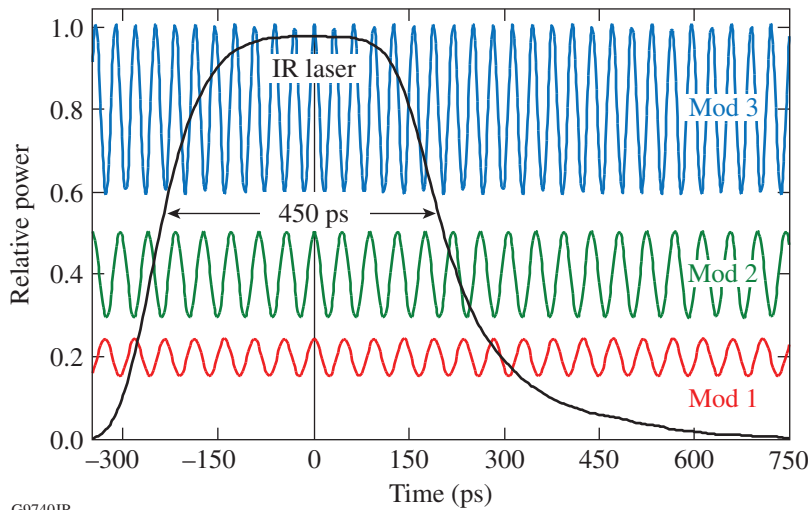
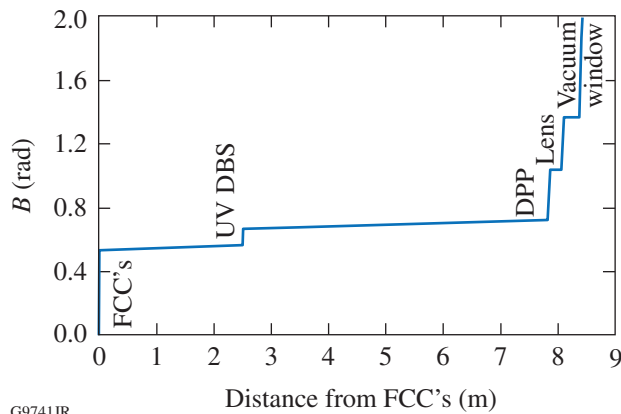


Figure 134.20 The IR pulse shape used in the modeling along with the modulator waveforms.



G9741JR

Figure 134.21

$B$ -integral as a function of distance from the FCC's for a 710-J, 444-ps pulse of 1.60-TW peak power. The  $B$ -integral at the output of the vacuum window for this pulse is 2.0 rad.

FM SSD applied. Indeed, there is significant uncertainty in this calculation simply caused by the knowledge of the  $\gamma$ 's of each of the materials.

### Conclusions and Additional Work

An estimate of the peak-power limit resulting from the addition of multi-FM SSD to the OMEGA EP Laser System has been calculated. A connection was made between the work of Chuang<sup>7</sup> and the work of Hocquet,<sup>9</sup> and it was shown that their predictions are the same. The advanced laser design code Miró was then applied to first computationally replicate the results of Chuang and then compute the OMEGA EP peak-power limit in the presence of multi-FM SSD. This peak-power limit then becomes one part of a budget that determines the actual on-target peak-power limit of the system.

The  $B$ -integral is a convenient metric to rapidly estimate the damage threat to a system from self-focusing. The actual threat to the final optic is most accurately assessed<sup>35</sup> by comprehensive modeling that includes the phase contributions of all the system optics to directly model the beam filamentation at the vacuum window. Further work would involve high-resolution simulations to compute these effects. The issue of the longitudinal magnification should be addressed by an actual measurement on the system of the AM as a function of transverse beam location in the dispersion direction. Additional amplitude modulation caused by gain narrowing in the amplifiers can be added to the existing Miró model.

### ACKNOWLEDGMENT

This work was supported by the U.S. Department of Energy Office of Inertial Confinement Fusion under Cooperative Agreement No. DE-FC52-08NA28302, the University of Rochester, and the New York State Energy Research and Development Authority. The support of DOE does not constitute an endorsement by DOE of the views expressed in this article.

### REFERENCES

1. S. Skupsky, R. W. Short, T. Kessler, R. S. Craxton, S. Letzring, and J. M. Soures, *J. Appl. Phys.* **66**, 3456 (1989); in *LLE Review Quarterly Report* **78**, 62, Laboratory for Laser Energetics, University of Rochester, Rochester, NY, LLE Document No. DOE/SF/19460-295 (1999).
2. T. J. B. Collins, J. A. Marozas, K. S. Anderson, R. Betti, R. S. Craxton, J. A. Delettrez, V. N. Goncharov, D. R. Harding, F. J. Marshall, R. L. McCrory, D. D. Meyerhofer, P. W. McKenty, P. B. Radha, A. Shvydky, S. Skupsky, and J. D. Zuegel, *Phys. Plasmas* **19**, 056308 (2012).
3. J. A. Marozas, T. J. B. Collins, and J. D. Zuegel, "Multiple-FM Smoothing by Spectral Dispersion—An Augmented Laser Speckle Smoothing Scheme," to be submitted to the *Journal of the Optical Society of America B*.
4. J. E. Rothenberg, D. F. Browning, and R. B. Wilcox, in *Third International Conference on Solid State Lasers for Application to Inertial Confinement Fusion*, edited by W. H. Lowdermilk (SPIE, Bellingham, WA, 1999), Vol. 3492, pp. 51–61.
5. A. B. Carlson, *Communication Systems: An Introduction to Signals and Noise in Electrical Communication*, McGraw-Hill Electrical and Electronic Engineering Series (McGraw-Hill, New York, 1968), p. 228.
6. The correct phasing of the sidebands is such that all of the odd-order lower sidebands are  $\pi$  out of phase. For a very illustrative phasor representation of why this particular phasing eliminates AM and leads to pure frequency modulation, see Ref. 5, pp. 228–232.
7. Y.-H. Chuang, "Amplification of Broad-Bandwidth Phase-Modulated Laser Counterpropagating Light Waves in Homogeneous Plasma," Ph.D. thesis, University of Rochester, 1991.
8. Note that this result is independent of a grating being upstream from the modulator used to pre-shear the pulse.
9. S. Hocquet *et al.*, *Appl. Opt.* **47**, 3338 (2008).
10. J. W. Goodman, *Introduction to Fourier Optics* (McGraw-Hill, New York, 1968), p. 53.
11. J.-C. Chanteloup *et al.*, *J. Opt. Soc. Am. B* **17**, 151 (2000).
12. D. C. Brown, in *High-Peak-Power Nd:Glass Laser Systems*, edited by D. L. MacAdam, Springer Series in Optical Sciences (Springer-Verlag, Berlin, 1981), Vol. 25, Chap. 1, p. 45.
13. J. Trenholme, *Laser Program Annual Report 1974*, Lawrence Livermore National Laboratory, Livermore, CA, Report UCRL-50021-74, 197 (1975).

14. J. R. Carson, Proc. IRE **10**, 57 (1922).
15. C. A. Haynam *et al.*, Appl. Opt. **46**, 3276 (2007). In particular, see Fig. 4 in this reference.
16. Non-Major System Acquisition, NNSA Division of Secondaries and Inertial Fusion, NA-113.1, U.S. Department of Energy National Nuclear Security Administration, Washington, DC (1 May 2003).
17. The dispersion direction is horizontal in laser sources, is vertical in the main laser chain, and is horizontal again at the frequency-conversion crystals.
18. M. D. Skeldon, R. S. Craxton, T. J. Kessler, W. Seka, R. W. Short, S. Skupsky, and J. M. Soures, IEEE J. Quantum Electron. **28**, 1389 (1992).
19. R. S. Longhurst, *Geometrical and Physical Optics*, 3rd ed. (Longman, London, 1973).
20. R. Korniski and J. K. Lawson, in *International Optical Design Conference*, 2002 OSA Technical Digest Series (Optical Society of America, Washington, DC, 2002), Paper ITuD5.
21. It does, however, have a modest FM modulation to suppress stimulated Brillouin scattering in the UV optics.
22. O. Morice, Opt. Eng. **42**, 1530 (2003).
23. LLE makes use of Miró through the kind permission of CEA/CESTA.
24. Ph. Donnat *et al.*, MIRÓ V5<sub>e</sub> Reference Manual (1998).
25. J. A. Marozas, J. D. Zuegel, and T. J. B. Collins, Bull. Am. Phys. Soc. **55**, 294 (2010).
26. Since there are two FCC's, the grating was imaged to the midplane between them.
27. R. S. Longhurst, *Geometrical and Physical Optics*, 3rd ed. (Longman, London, 1973), p. 14.
28. This assumes, of course, that the normal to the wavefront remains within the tuning acceptance angle of the crystals.
29. O. Morice, X. Ribeyre, and V. Rivoire, in *Third International Conference on Solid State Lasers for Application to Inertial Confinement Fusion*, edited by W. H. Lowdermilk (SPIE, Bellingham, WA, 1999), Vol. 3492, pp. 832–838.
30. Ph. Donnat *et al.*, MIRÓ V5<sub>e</sub> Reference Manual (1998), Chap. 3, Sec. 3.12.6, pp. 162–164.
31. J. Trenholme *et al.*, *Shiva Nova CP&D Interim Report, Laser Fusion Program*, Lawrence Livermore National Laboratory, Misc. 107, 2-3-2-324 (1977); for a fuller discussion of this expression and its derivation, see D. C. Brown, in *High-Peak-Power Nd:Glass Laser Systems*, edited by D. L. MacAdam, Springer Series in Optical Sciences (Springer-Verlag, New York, 1981), Vol. 25, Chap. 7, Sec. 7.5, p. 216.
32. Here the fraction of noise power in the two frequency ranges of large ripples and fast-growing ripples has been assumed to be equal.
33. V. I. Talanov, JETP Lett. **11**, 199 (1970); for a discussion of the applicability of this transformation, see J. B. Trenholme and E. J. Goodwin, *Laser Program Annual Report 1976*, Lawrence Livermore National Laboratory, Livermore, CA, Report UCRL-50021-76, 2-339–2-344 (1976).
34. *Final Proposal for Renewal Award for Cooperative Agreement DE-FC52-92SF-19460* Between the U.S. Department of Energy and the Laboratory for Laser Energetics of the University of Rochester, Part I: Technical Program (Rochester, NY, 2007).
35. P. J. Wegner *et al.*, in *Optical Engineering at the Lawrence Livermore National Laboratory II: The National Ignition Facility*, edited by M. A. Lane and C. R. Wuest (SPIE, Bellingham, WA, 2004), Vol. 5341, pp. 180–189.

---

# Fiber Front End with Multiple Phase Modulations and High-Bandwidth Pulse Shaping

## Introduction

Since their first demonstration, lasers have led to incredible progress in many scientific and technological fields. High-intensity lasers have allowed researchers to explore new regimes for the interaction of light with matter. One far-reaching potential application of lasers is inertial confinement fusion (ICF), where nuclear fusion reactions are initiated by heating and compressing a deuterium–tritium (DT) target with laser beams. Large-scale laser facilities are in operation or in construction with the goal of demonstrating ignition,<sup>1,2</sup> following decades of research.<sup>3</sup> One difficulty of ICF is to maintain a high degree of spherical symmetry when the target is compressed: a spatially nonuniform on-target illumination can seed Rayleigh–Taylor instabilities at the target surface and detrimentally impact the fuel compression.<sup>4</sup> Smoothing by spectral dispersion (SSD) is an approach to reduce the spatial nonuniformities of the illumination generated by high-energy laser beams.<sup>5</sup> SSD lowers the coherence of the beams by frequency modulating them (i.e., increasing the optical-frequency content), spatially dispersing them with a diffraction grating (i.e., introducing a relation between optical frequency and wave vector), and focusing them after a random phase plate (i.e., creating a broad range of wave vectors in the near field and a speckle distribution in the far field).<sup>6,7</sup> The time-integrated far-field fluence of individual beams is smoothed because the phase plate generates randomly distributed speckles with a frequency-dependent distribution; consequently, the frequency-modulated optical pulse leads to a time-varying speckle field that averages out. SSD is routinely used at facilities such as the National Ignition Facility (NIF)<sup>1</sup> and the OMEGA Laser System.<sup>8</sup> The required amount of smoothing and the architecture of the laser systems determine the implementation of SSD: the NIF uses one-dimensional (1-D) SSD with modulation at ~17 GHz and a single diffraction grating in the front end, while OMEGA uses two-dimensional (2-D) SSD with modulation along two axes at ~3 GHz and 10 GHz and multiple gratings.<sup>9</sup> Phase modulation is also required in large-scale, high-energy laser systems to prevent stimulated Brillouin scattering (SBS): a high-intensity monochromatic beam can create acoustic waves in a physical medium (e.g., a fused-silica lens) that will scatter the beam,

resulting in instability, losses, and optical damage.<sup>10</sup> Phase modulation generates sidebands that are individually below the threshold for SBS, suppressing its detrimental effect. This modulation is typically performed at a frequency of 3 GHz with a modulation index of ~5 rad on the NIF, resulting in approximately ten sidebands in an ~30-GHz bandwidth.

The NIF is currently configured for indirect drive, where the UV laser beams are incident on the internal sides of a gold hohlraum and generate x-ray radiation that compresses the target. SSD is performed at 17 GHz with a modulation index equal to a few radians. Simulations of direct drive, where the UV beams directly compress the target, on the NIF show that SSD must be implemented on the initial part of the pulse shape with three distinct modulation frequencies (multi-FM).<sup>11</sup> These modulations are approximately at 21.2 GHz, 22.8 GHz, and 31.9 GHz, i.e., at significantly higher frequencies than what is currently being used on existing laser systems for SSD and SBS suppression (SBSS). The main part of the pulse shape, which produces most of the on-target energy, uses SSD at 17 GHz and SBSS. With the parameters of Table 134.V, the multi-FM optical spectrum (98% of the energy in a 200-GHz bandwidth) is ~50% broader than the main-pulse spectrum (98% of the energy in a 133-GHz bandwidth). A fiber front-end prototype demonstrating the required technologies has been developed. It relies on high-bandwidth LiNbO<sub>3</sub> phase modulators and Mach–Zehnder modulators for phase modulation and pulse shaping, respectively. Large-scale laser systems operate close to the technological limits of optical components, and amplitude modulation caused by spectral distortion of frequency-modulated signals must be understood and controlled to avoid optical damage. Subsystems that compensate and characterize for frequency-modulation-to-amplitude-modulation (FM-to-AM) conversion have been developed. The front end has supported multiple shot campaigns on the OMEGA EP Laser System<sup>12</sup> to demonstrate the laser and beam-smoothing performance.<sup>13</sup>

In this article, we first describe the architecture of the fiber front end with an emphasis on the modulators used for phase modulation (SSD/SBSS) and amplitude modulation (pulse

Table 134.V: Characteristics of the phase modulations applied in the front end. All the frequencies were multiples of the reference frequency  $f_{\text{Ref}} = 37.998935$  MHz. The first two modulations were performed in the main channel; the three other modulations were performed in the picket channel.

Modulation	Frequency (GHz)	Multiple of $f_{\text{Ref}}$	Modulation Index (rad)
Stimulated Brillouin scattering suppression (SBSS)	$f_{\text{SBSS}} = 3.002$	79	5.5
Smoothing by spectral dispersion (SSD)	$f_{\text{SSD}} = 16.986$	447	2.6
Multi-FM 1	$f_1 = 21.165$	557	0.45
Multi-FM 2	$f_2 = 22.837$	601	1.04
Multi-FM 3	$f_3 = 31.881$	839	2.07

shaping) and the subsystems developed to reduce FM-to-AM conversion and safely operate the laser system. The experimental characterization of the fiber front-end performance is then presented, in particular, phase modulation, pulse shaping, and amplitude noise, followed by the conclusions.

## Front-End Architecture

### 1. Requirements

The front-end requirements for this demonstration on the OMEGA EP Laser System have been set based on simulations of polar-drive ignition on the NIF and the requirement that the new front end be integrated into the existing laser systems. The typical pulse shape in the ultraviolet (UV), i.e., after amplification in the full laser system and frequency conversion, is shown in Fig. 134.22. It is composed of two sections:

- Between 0 and 4.5 ns, three short pulses (named “pickets”) launch shocks into the target.<sup>14</sup> Each picket has a duration of a few hundred picoseconds and must be phase modulated at three noncommensurate microwave frequencies (multi-FM modulation) to provide optimal beam smoothing on target. The three modulation frequencies in this design are approximately 21.2 GHz, 22.8 GHz, and 31.9 GHz (Table 134.V).
- After 4.5 ns, a rectangular high-energy pulse preceded by a low-intensity step pulse between 4.5 ns and 6 ns is required. The step pulse launches an additional shock into the target before compression by the main high-energy pulse. The main pulse lasts for several nanoseconds but has rise/fall times that are in the hundreds-of-picoseconds range. This pulse must be phase modulated at 3 GHz for SBSS and at 17 GHz for SSD (Table 134.V).

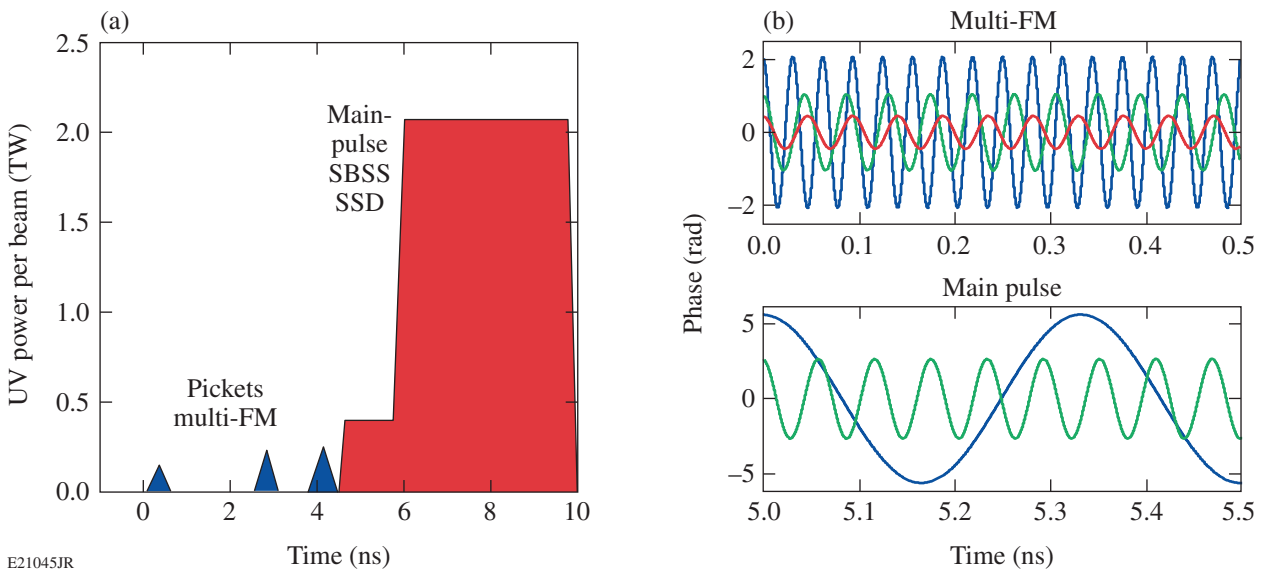


Figure 134.22

(a) Schematic of the pulse shape (power versus time) after frequency conversion at the end of the laser system, composed of three short, low-energy pickets and a main high-energy pulse. (b) Plots of the phase modulations required at the fundamental wavelength on the pickets ( $f_1, f_2, f_3$ ) and on the main pulse ( $f_{\text{SSD}}$  and  $f_{\text{SBSS}}$ ), with parameters given in Table 134.V. FM: frequency modulation; SBSS: stimulated Brillouin scattering suppression; SSD: smoothing by spectral dispersion.

The front end must operate at ~1053 nm, which is the peak of the gain for neodymium-doped phosphate glass. It is designed as a proof-of-concept of a system that could be used in the NIF Master Oscillator Room<sup>15,16</sup> and has been built around technologies that are either compatible with its environment and requirements or can be upgraded to suitable technologies for an actual deployment. It must contain fail-safe systems that will interrupt the amplification so that no high-energy pulse propagates in the laser system if such propagation could lead to damage. The output pulses must have low variations in energy and pulse shape, and have sufficient energy to seed the preamplifier module (PAM), a sequence of amplifiers used on the NIF to boost the energy before amplification in the main beamline.<sup>17</sup>

2. General Structure

The front end optically combines two distinct optical channels operating at wavelengths close to 1053 nm—one generating the main pulse and one generating the pickets (Fig. 134.23). The two channels have a symmetric architecture, combining programmable pulse shaping by LiNbO<sub>3</sub> Mach–Zehnder modulators driven by arbitrary waveform generators (AWG’s), phase modulation by LiNbO<sub>3</sub> phase modulators, and two stages of amplification to compensate for propagation and insertion losses. Fail-safe systems protecting the high-energy beamline and components operate in real-time and can interrupt the propagation of an improperly modulated pulse before amplification to high-energy levels. The two channels are combined by a fiber coupler with a fixed coupling ratio. The relative level of the two channels is adjusted via the gain of fiber amplifiers (there are two amplifiers in each channel and one amplifier in the combined section of the front end). Most pulse shapes

of interest require similar output levels for the two channels, which is facilitated by the symmetric structure. All components are fiber coupled up to the PAM.

Birefringent optical fibers maintain the polarization state throughout the system. Most components use polarization-maintaining (PM) fibers that support two orthogonal propagation modes. The fibers connecting components and chassis are polarizing (PZ) fibers that support only one propagation mode at 1053 nm: linearly polarized light launched along the guiding direction is nominally transmitted without loss but light polarized along the orthogonal direction is strongly attenuated. The absence of crosstalk in such fibers helps to reduce the FM-to-AM conversion caused by delayed self-interference when successive PM fibers are used.<sup>18</sup> An extinction ratio (ratio of the guided-mode transmission to the blocked-mode transmission) higher than 30 dB is nominally obtained with 4-m patchcords.

The phase-modulation drive voltages are synchronized to the reference frequency  $f_{Ref} = 37.998935$  MHz used throughout the OMEGA EP Laser System. The phase modulations at the required five microwave frequencies (Table 134.V) are obtained using commercial phase-locked oscillators, ensuring that the output frequency is an exact integer multiple of the reference frequency. A phase shifter on each phase-modulation drive allows for independent temporal tuning of the phase modulation relative to the optical pulse. The performance of on-target smoothing does not depend significantly on the relative phases of the three sinusoidal modulations.<sup>11</sup> Tuning of the relative phases is included because it could be used to control the amplitude of the power modulation caused by FM-to-AM conversion, although this has not been studied in detail. All

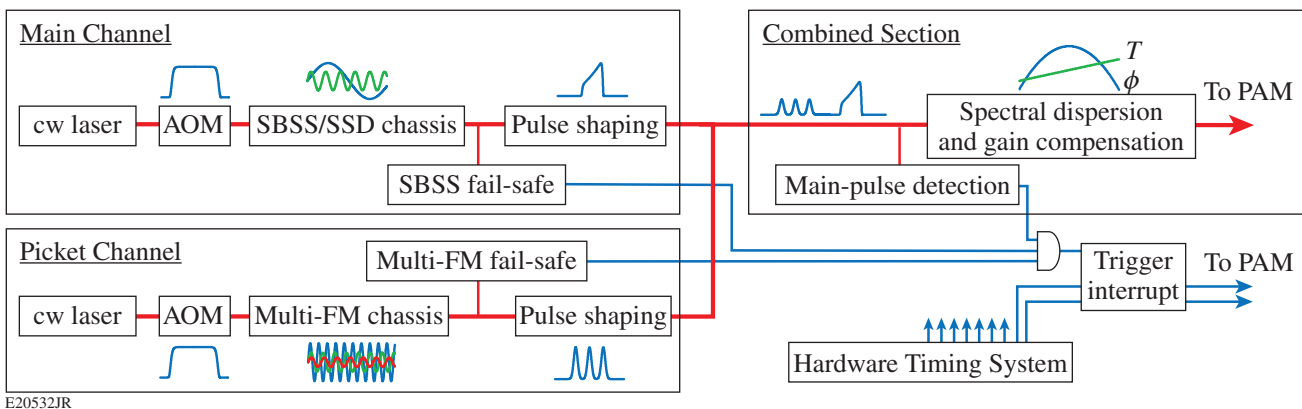


Figure 134.23 General layout of the front end. The picket and main channel are independently phase modulated and shaped after gating of a continuous-wave (cw) seed source by an acousto-optic modulator (AOM). Dispersion and amplitude compensations are performed after optical combination. Three fail-safe systems are used to ensure safe operation. Five fiber amplifiers (two in each independent section and one in the combined section) have not been represented. PAM: preamplifier module.

components in the front end are synchronized to the Hardware Timing System (HTS) used throughout the laser facility, which is also synchronized to  $f_{Ref}$ . The fiber front end operates at 300 Hz. All electronic components (including the fail-safe systems described in the following subsections) can operate at 960 Hz, the repetition rate of the NIF front end. The ytterbium-doped fiber amplifiers have not been tested at 960 Hz, which corresponds to operation close to the fluorescence lifetime of ytterbium, but similar amplifiers are operated in the NIF front end at that rate. The timing of the two channels relative to each other and to the laser facility is adjusted by controlling the delay of all the corresponding trigger signals from the HTS.

### 3. Main Channel

The main channel (Fig. 134.23) uses a cw (continuous-wave) laser operating at  $\sim 1053$  nm gated by an acousto-optic modulator (AOM) to a duration of 100 ns. The gated pulse is phase modulated by the custom three-section phase modulator shown in Fig. 134.24. The phase modulator has three consecutive sections of LiNbO<sub>3</sub> that can be independently driven. Each section is externally terminated to allow for the use of high-power drives that could damage an internal 50- $\Omega$  termination. A single device with three phase-modulation sections is advantageous compared to the cascaded sequence of three distinct phase modulators: the modulator is more compact and easier to mount, and the optical losses from input to output are lower than 5 dB. In the main channel, phase modulation is provided in only two of the three sections. In one section, phase modulation at 3 GHz is induced with a modulation index of 5.5 rad for SBSS. In the second section, phase modulation at 17 GHz with an index of 2.6 rad is performed for on-target beam smoothing. The resulting optical spectrum is plotted in Fig. 134.25(a).



Figure 134.24  
The three-section phase modulator, with distinct input and output ports for the three phase-modulating sections.

Pulse shaping is implemented in a custom two-section modulator comprised of two consecutive LiNbO<sub>3</sub> Mach-Zehnder modulators (MZM's). One of the MZM's is driven by a shaped voltage from the amplified output of a 10-GS/s AWG

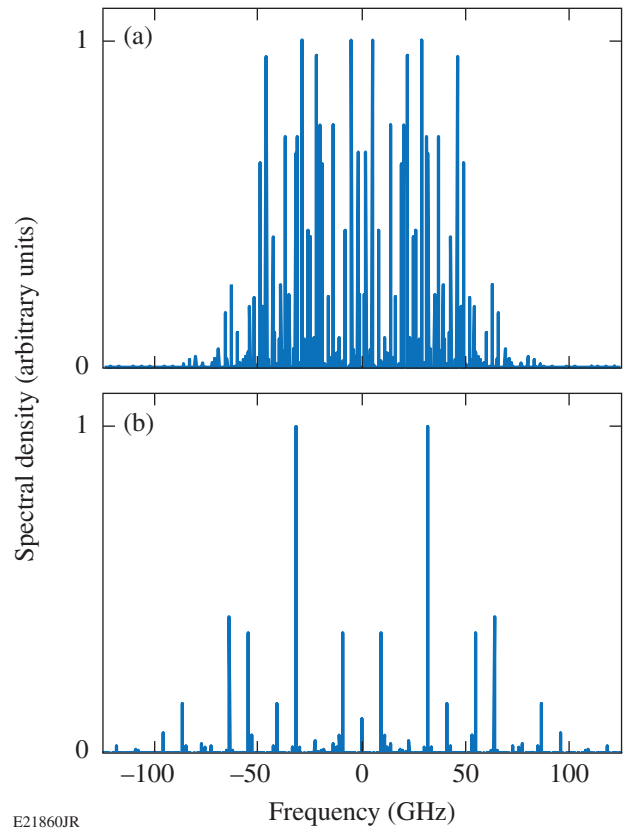


Figure 134.25  
(a) Optical spectrum of the pulse after phase modulation in the main channel; (b) optical spectrum of the pulse after phase modulation in the picket channel.

(Kentech AWG-10). This modulator is used for precise pulse shaping, ensuring that the channel output meets the requirements imposed by the target physics and the safety of the laser system. The other MZM is driven by an unshaped square pulse with programmable duration. This MZM acts as a gate on the shaped pulse: when the duration of the square pulse is set appropriately, the modulator does not shape the optical pulse but enhances the temporal contrast (ratio of the power at full transmission to the power at extinction). For example, with two MZM's having a nominal extinction ratio of  $\geq 20$  dB, the overall extinction ratio is  $\geq 40$  dB. High extinction ratios are particularly important when optically combining optical pulses from two distinct sources because leakage from one source can detrimentally interfere with the pulse from the other source.

A fraction of the main channel is sent to a fail-safe system to monitor the 3-GHz phase modulation and avoid optical damage from SBS.<sup>10</sup> The SBSS fail-safe is a unit provided by Lawrence Livermore National Laboratory.<sup>15</sup> The unit intentionally induces FM-to-AM conversion on the monitored signal with a spectral filter to convert the 3-GHz phase modulation into a

3-GHz amplitude modulation that can be measured with an AM detector. The unit monitors in real-time the phase-modulation amplitude and duration on the optical pulse, i.e., it ensures that the phase modulation is sufficient and applied during the total length of the  $\sim 100$ -ns pulse gated by the AOM. It also detects undesirable characteristics of the optical pulse, spurious amplitude modulation not intentionally generated by the fail-safe system, and sudden changes in the input energy that could prevent the fail-safe from adequately detecting a fault. Its output is a 5-V logic trigger that is high if the duration and amplitude of the phase modulation are nominal and low if at least one of the safe operating conditions is not met. This trigger is sent to the PAM Trigger Interrupt Safety System (PTISS) to prevent unsafe high-energy amplification if there is a fault.

#### 4. Picket Channel

The picket channel (Fig. 134.23) uses a set of optical components identical to the one deployed on the main channel. The three sections of the phase modulator are driven by the three distinct phase modulations at 21.2 GHz, 22.8 GHz, and 31.9 GHz with respective modulation indices of 0.45 rad, 1.04 rad, and 2.07 rad. The resulting optical spectrum is plotted in Fig. 134.25(b). Pulse shaping is performed by driving one section of a two-section MZM with the output of a Tektronix 7122 AWG operating at 24 GS/s amplified by a broadband amplifier. The other section is driven by a square pulse to increase the extinction ratio.

The pickets are nominally short optical pulses, i.e., with a spectrum relatively broad compared to the typical nanosecond pulses shot on high-energy laser systems, therefore reducing concern for SBS in the absence of phase modulation, but a fail-safe system was designed to prevent high-energy amplification in the absence of significant phase modulation on this channel. The fail-safe system measures the power in two spectral bands of the phase-modulated pulse, one on each side of the carrier frequency, to infer the amount of phase modulation. A diffraction grating disperses the optical pulse, and a focusing lens generates a Fourier plane in which spectral components are spatially separated and individually focused. Multimode optical fibers mounted on a V-groove array are used at the Fourier plane to couple light from the two bands of the optical spectrum to two amplified photodiodes. The system is designed to detect the optical power in two bands centered 127.6 GHz apart, i.e., on the sidebands of the carrier at twice the modulation frequency  $f_3$ . These two bands correspond to the spectrally dispersed light from the diffraction gratings on two fibers separated by  $500\ \mu\text{m}$  at the Fourier plane. Each  $105\text{-}\mu\text{m}$ -diam fiber integrates the optical power over 26.8 GHz. Thresholds for the

measured powers are set when the system operates at the default phase-modulation amplitudes so that the fail-safe trips when the modulation at  $f_3$  does not have sufficient amplitude, regardless of the presence of the modulation at  $f_1$  and  $f_2$ . This would detect malfunction of the entire phase-modulation unit for the picket channel and malfunction of the sub-unit responsible for phase modulation at the frequency  $f_3$ . A precise analysis of the different failure modes and their impact on SBS has not been conducted at this point, but operation with  $f_3$  operating at its nominal modulation index was thought to be safe for the system because the corresponding spectrum is spread over more than 100 GHz with each sideband broadened to several GHz because of the short picket duration. Simultaneous failure of the two sub-units responsible for phase modulation at  $f_1$  and  $f_2$  is highly unlikely because of the architecture of the phase-modulation unit; therefore, the detection of the frequency  $f_3$  indicates that at least one other modulation frequency is also present, further contributing to SBS reduction. The fail-safe 5-V logic output (high for the nominal modulation and low for insufficient bandwidth) is sent to the PTISS to prevent high-energy amplification in the latter case.

#### 5. Combined Section

The picket and main channels are combined with identical polarization states by a fiber coupler after timing and amplitude adjustments. Chromatic dispersion and nonuniform spectral gain are compensated identically after the combiner for economy of scale and minimized complexity. A rack-mounted device combining dispersion and amplitude compensation has been built (Fig. 134.26). Spectral distortion (i.e., phase and/or amplitude) of a phase-modulated pulse leads to amplitude modulation in the time domain. FM-to-AM conversion is detrimental to the operation of high-energy laser systems because amplitude modulation leads to higher peak power for a given pulse energy.<sup>19,20</sup> Amplitude modulations are also a concern when the propagation is nonlinear. The chromatic dispersion of optical fibers and other optical components at 1053 nm corresponds to a positive second-order dispersion ( $d^2\phi/d\omega^2 > 0$ , where  $\phi$  is the phase accumulated by propagation as a function of frequency). The total length of fiber for each channel (calculated from the output of the phase modulator to the last fiber amplifier) is  $\sim 130$  m. A frequency-dependent amplitude modulation arises from gain tilt in the ytterbium-doped fiber amplifiers and the Nd:glass regenerative amplifier. The fiber amplifiers are broadband, but their gain varies over the spectral range of interest, with a typical gain slope of 5% per 100 GHz (i.e., the difference between the gain at  $f_0 + 50$  GHz and  $f_0 - 50$  GHz normalized to the gain at  $f_0$  is 5%). The regenerative amplifier gain is approximately Gaussian with a

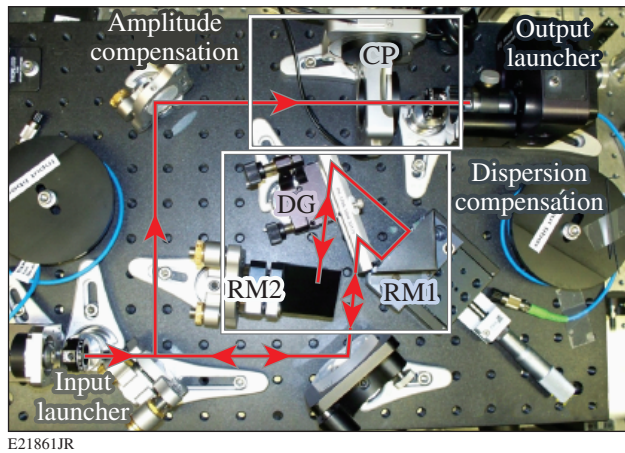


Figure 134.26

The amplitude/dispersion compensator. The dispersion compensator is composed of two roof mirrors, for horizontal (RM1) and vertical (RM2) beam displacement and inversion, and a transmission diffraction grating (DG). The amplitude compensator is composed of a calcite plate (CP) mounted on two rotation stages.

full width at half maximum (FWHM) of 400 GHz. The front end is configured to seed the regenerative amplifier on the long-wavelength slope of the Gaussian gain curve, for which the gain slope is approximately 40% per 100 GHz. The uncompensated gain slope over the fiber front end and regenerative amplifier would lead to large-amplitude modulation. Spectral distortions have been compensated with fiber-coupled free-space subsystems that were combined in a single enclosure to minimize losses: without any spectral amplitude modulation, the input-to-output loss is  $\sim 5$  dB.

Dispersion compensation ( $d^2\phi/d\omega^2 < 0$ ) is performed with a compact compressor using a single transmission grating in a four-pass configuration. The transmission grating is a 1700-l/mm fused-silica grating used in the Littrow configuration. The diffracted beam is sent back to the same grating after a lateral displacement and horizontal beam inversion by a roof mirror; it is then diffracted again by the grating, displaced vertically by another roof mirror, and sent back to the grating, first roof mirror, and grating. The dispersion is controlled by a translation stage on the first roof mirror modifying the distance between the first and second diffractions on the grating and identically between the third and fourth diffractions. The compensator was designed to overcompensate the dispersion of the front end because of its future use in a system mimicking the front end of the NIF. In that system, the front end is in a different room from the NIF PAM's, resulting in the shaped phase-modulated optical pulse traveling in several hundred meters of PZ fibers. This compensator is built for  $\sim 100$  m of

additional PZ fiber between the front end and the PAM, even if these two systems are physically separated by only a few meters in our system. Translation of the first roof mirror allows for an increase in the magnitude of the introduced negative second-order dispersion to compensate for longer fiber lengths.

The optical source is linearly polarized, allowing for spectral amplitude modulation using a Lyot-type filter implemented with a birefringent calcite plate.<sup>21</sup> The plate can be rotated relative to a vertical rotation axis (Axis 1) and relative to an axis perpendicular to its surface (Axis 2) to adjust the spectral modulation. At normal incidence, rotation around Axis 2 changes the relative ratio of the two polarization components traveling along the two axes of the plate, which controls the depth of the spectral modulation. Rotation around Axis 1 changes the retardance of the plate, which controls the location of the spectral modulation along the frequency axis. The calcite plate is followed by a zeroth-order half-wave plate and a PZ fiber acting as a polarizer. Calcite plates with thicknesses from 1 mm to 4 mm have been used during a testing phase, with similar results, and a 4-mm calcite plate has been installed for operation.

The pickets are nominally short pulses that can reach high peak powers if the system is configured for the generation of a high-energy main pulse but the latter pulse is absent—for example, because of an equipment failure, triggering issue, or operator error. A fail-safe system (“main-pulse detection fail-safe”) prevents amplification and subsequent damage when the main pulse is absent. This system uses photodetection and integration of the combined output to generate a signal representative of the front-end output energy, which must be higher than a user-set threshold for safe operation. The system output is a 5-V logic signal that is high when operation is safe and low otherwise. This signal is sent to the PTISS.

The three fail-safe systems (SBSS fail-safe operating on the main channel; picket-bandwidth fail-safe operating on the picket channel; and main-pulse detection fail-safe operating on the combined output) provide three logical signals to the PTISS. The latter system is fed with two triggers: the switch-out trigger to the Pockels cell in the regenerative amplifier and the slicer-on trigger for the Pockels cell located after the regenerative amplifier. In safe operation, the front end delivers a seed pulse to the regenerative amplifier; this pulse is amplified after multiple round-trips in the cavity; the amplified pulse is ejected by the Pockels cell located inside the amplifier; and the output pulse is gated by an external Pockels cell (the slicer) that is turned on to let the ejected pulse go through. In the absence

of trigger signals from the three fail-safe systems, the PTISS interrupts the two triggers. The pulse being amplified in the regenerative amplifier remains in the laser cavity and is not ejected by the intracavity Pockels cell. The slicer is not turned on, further decreasing the transmission.

## Front-End Performance

### 1. Pulse Shaping

Temporal characterization of the shaped optical pulses was performed with a 45-GHz, 120-GS/s Teledyne LeCroy Wave-master oscilloscope and a fiber-coupled 60-GHz Discovery Semiconductors DSC10 InGaAs photodetector. The impulse response of this diagnostic had a FWHM lower than 20 ps. Various algorithms and procedures were tested to correct the frequency-dependent response of the photodetection system (for example, isolating one frequency component and adjusting its spectral amplitude by the known spectral response at that particular frequency to compare its amplitude to a prediction made using known system parameters). It was decided to not use post-processing of the measured waveforms when reporting amplitude noise, although the reported noise values correspond to averages of the noise values over multiple waveforms, as described below. Most measurements have been performed in the front end at 300 Hz and after the regenerative amplifier since that amplifier has the largest amount of square-pulse distortion in our demonstration (the gain on the pulse is a decreasing function of the time because the leading edge of the pulse propagates in the amplifying medium before the trailing edge and experiences more gain). It also has the most-significant impact on the optical spectrum because of its relatively narrow amplification bandwidth and large gain slope. Finally, it operates at a repetition rate of 1 Hz, allowing for the acquisition of statistically meaningful sets of data: the rod amplifier in the PAM after the regenerative amplifier typically operates at one shot every 20 min, significantly impacting the experimental ability to collect multiple data sets for statistical analysis.

The impulse response of the picket and main pulse-shaping systems has been determined by setting one electrical sample of the corresponding AWG to full voltage and measuring the optical output as a function of time. The measured responses have a FWHM of 55 ps and 115 ps for the picket channel and main channel, respectively. The corresponding 10/90 rise and fall times, measured on the impulse responses, are similar to the FWHM for the two systems. These values correspond to the pulses shaped by the fiber front end. Because of the pulse-front tilt introduced by the SSD grating ( $\sim 230$  ps across the full beam), the on-target pulse duration is significantly longer. The choice of the faster AWG for the picket channel

stems from the technical requirements for pulse shaping in these two channels, although generating pickets shorter than  $\sim 100$  ps is not required.

A wide range of pulse shapes has been generated with the two channels, including single and multiple pickets, long square pulses, and shaped pulses. Figure 134.27(a) displays an example of a pulse shape with three pickets and a long shaped pulse measured at the output of the regenerative amplifier. Figures 134.27(b) and 134.27(c) show close-ups of the measured pulse shape with shaded areas, indicating the root-mean-square (rms) and peak-to-valley variations at each acquisition time, obtained by measuring 50 successive pulses. The rms and peak-to-valley energy variations over 50 measurements are 1.9% and

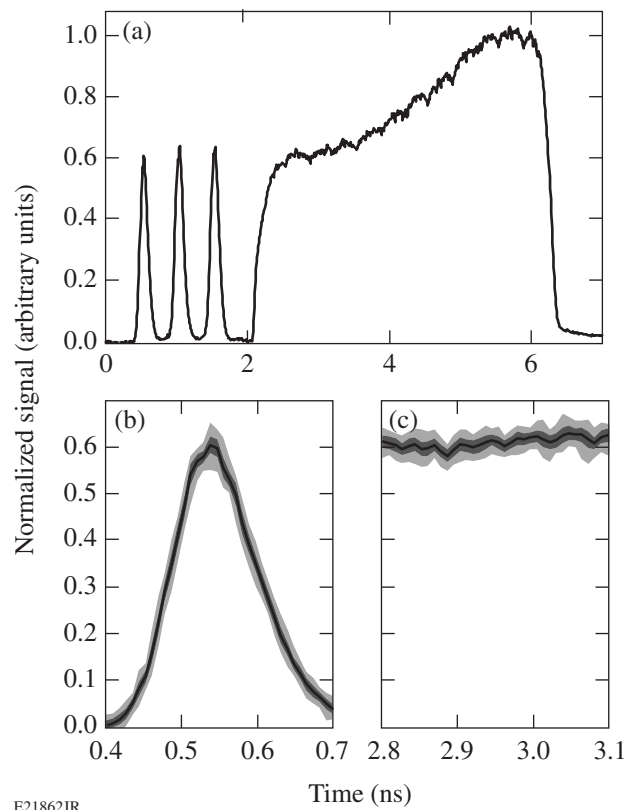


Figure 134.27

(a) Example of pulse shape  $P(t)$  measured at the output of the regenerative amplifier. The plotted pulse is an average of 50 successive measurements. [(b) and (c)] Close-ups of the first picket (time between 0.4 and 0.7 ns) and the main pulse (time between 2.8 and 3.1 ns). The black line corresponds to the average of 50 measurements; the dark-gray-shaded region corresponds to the power range  $[P(t) - \sigma(t), P(t) + \sigma(t)]$ , where  $\sigma(t)$  is the standard deviation of  $P$  at time  $t$  over the 50 measurements, and the light-gray-shaded region corresponds to the power range  $[M_-(t), M_+(t)]$ , where  $M_-(t)$  and  $M_+(t)$  correspond to the lowest and highest value of the power measured at time  $t$  over the 50 measurements.

9.8%, respectively, for one picket and 1.2% and 5.1%, respectively, for the main pulse. These are overestimates of the actual energy variations because of the oscilloscope analog-to-digital conversion noise, particularly for the picket with a FWHM of  $\sim 100$  ps for which the energy is obtained by summation over a small number of acquired samples. A 1-ns pulse generated by the picket channel in the same conditions has rms and peak-to-valley energy variations equal to 1.8% and 6.6%, respectively, while the energy variations calculated in a 1-ns window for the monochromatic laser chopped by the AOM before phase modulation are 0.5% and 2.0%. The energy statistics are in agreement with the energy statistics independently measured with an energy meter that indicates a rms variation lower than 2% after the regenerative amplifier seeded by either channel.

The jitter and timing drift between the two channels have been measured over 300 waveforms produced by the front end acquired in a short time window (1.5 min) or long time window (150 min) by estimating the location of the 50% points of the picket-channel trailing edge and main-channel leading edge. The relative timing between the two channels has a rms jitter of 15 ps and a monotonic drift of 20 ps over 2.5 h. The timing drift is attributed to drifts in the pulse-shaping electronics (e.g., triggers) and small temperature changes (although the front end operates in a temperature-controlled environment, each channel contains more than 100 m of optical fibers that are physically distinct). The timing of the picket channel and main channel relative to the oscilloscope time base has rms jitter values of 13 ps and 9 ps, respectively. These are overestimates of the jitter of the front end relative to the reference frequency, i.e., the remainder of the laser system, since they include the oscilloscope jitter. These values are within the required range for this demonstration. The jitter and the finite rise and fall times of the shaped pulses constrain the relative timing between the channels to values greater than 125 ps (delay between the 50% points of the picket-channel trailing edge and main-channel leading edge). Random amplitude modulation related to interference of the two optical pulses is observed for shorter separations.

## 2. Phase Modulation

Precise characterization of the phase modulators and resulting phase modulation is important. The modulators must first be characterized to ensure that they are suitable for this application, i.e., that they can be driven adequately at the five different microwave frequencies with the required modulation index. During operation, the phase-modulation index must be characterized to ensure that it matches the required specifications. A cw laser field at the optical frequency  $f_0$  phase modulated

at the frequency  $f_m$  with modulation index  $m$  has the temporal electric field

$$E(t) = E_0 \exp(2\pi i f_0 t) \exp[i m \sin(2\pi f_m t)]. \quad (1)$$

In the frequency domain, the field is given by

$$\tilde{E}(f) = \sum_n J_n(m) \delta(f - f_0 - n f_m), \quad (2)$$

where  $J_n$  is the Bessel function of the first kind of index  $n$ . The optical spectrum is composed of an infinite number of sidebands at the frequencies  $f_0 + n f_m$  with spectral density  $|J_n(m)|^2$ , but 98% of the energy is concentrated in a  $2m f_m$  bandwidth centered at  $f_0$  according to Carson's rule.

Fitting the measured spectrum with the calculated spectrum of a phase-modulated field, where  $m$  is the single parameter, makes use of all the measured data and is computationally efficient; this was chosen for modulation-index determination at frequencies corresponding to sidebands that can be resolved. The spectral modes corresponding to  $f_{\text{SSD}} = 17$  GHz,  $f_1 = 21.2$  GHz,  $f_2 = 22.8$  GHz, and  $f_3 = 31.9$  GHz are easily resolved with a commercial scanning grating monochromator. The modes corresponding to 3 GHz cannot be individually resolved because the response of the monochromator broadens the individual spectral modes, resulting in a smoothed spectrum. One experimental solution is to develop a dedicated diagnostic measuring the optical spectrum with a resolution suitable to resolve spectral modes separated by 3 GHz (typically sub-GHz); for example, using a scanning Fabry–Perot etalon. It was chosen to use numerical post-processing to estimate the modulation index in this case.

For modulator characterization, a microwave signal generator was used to generate drives with frequency ranging from 15 GHz to 40 GHz. The power of the drive was calibrated at each modulation frequency. The modulation index was determined for each of the three sections of the phase modulators. The corresponding  $V_\pi$  was calculated by scaling the phase-versus-voltage measurement, where the phase is related to the modulation index and the voltage is proportional to the square root of the power. The characterization of the  $V_\pi$  is shown in Fig. 134.28 for one of the modulators. The three sections behave similarly, and the  $V_\pi$  increases from  $\sim 5$  V to  $\sim 7$  V in the measurement range.  $V_\pi$  values lower than 7 V are acceptable since the voltages required to reach the requested modulation indices are within the range of medium-power solid-state microwave amplifiers. Similar performance was measured on three other phase modulators.

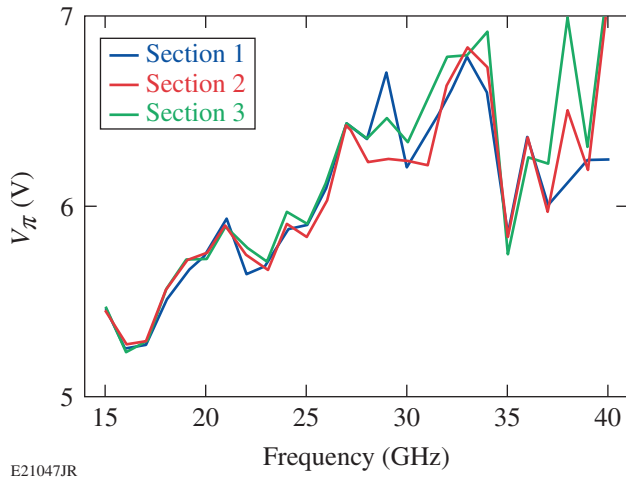


Figure 134.28  
Determination of  $V_\pi$  on the three sections of a phase modulator.

For operational characterization of the frequency modulation induced by one modulator, the other drive voltage(s) is (are) turned off, e.g., the drives at  $f_1$  and  $f_2$  are turned off when characterizing the modulation at  $f_3$ . An optical spectrum is measured and fitted to determine the modulation index. The drive voltage is increased or decreased via a continuous attenuator, and the measurement is repeated until the measured index matches the requested index within an acceptable uncertainty. Figure 134.29(a) shows the agreement between the measured spectral modes at frequency  $f_3$  with the modes obtained after fitting. Figure 134.29(b) shows the measured optical spectrum when the three drives to the picket-channel phase modulator are turned on. This spectrum agrees very well with the calculated spectrum. For operational characterization of the modulation

index at  $f_{\text{SBSS}}$ , which leads to spectral modes that cannot be distinguished with the available monochromator, an indirect approach was used. The archived spectrum of a cw source, e.g., the spectrum of the same source with all modulations turned off, was used as the instrument response to calculate the optical spectrum that should be measured for a given modulation index. Figure 134.30(a) shows that the bandwidth of the convolved spectrum increases monotonously with the modulation index and is within 1 GHz of the actual bandwidth for modulation indices between 5 and 6 rad. The drive for  $f_{\text{SSD}}$  is turned off and the modulated spectrum with  $f_{\text{SBSS}}$  turned on is measured. The modulation drive is precisely set by comparing the measured bandwidth to the bandwidth of the theoretical spectrum corresponding to 5.5 rad convolved with the measured response function. The theoretical spectrum, measured response function, and convolved spectrum are shown in Fig. 134.30(b). The excellent agreement between the measured and convolved spectrum, demonstrated in Fig. 134.30(c), and the monotonic relation between actual bandwidth and measured bandwidth, demonstrated in Fig. 134.30(a), allow us to conclude that the modulation index is adequately set.

### 3. Extinction of Mach–Zehnder Modulators

MZM extinction is a critical parameter of the pulse-shaping systems because interference between the co-polarized optical waveforms after combination of the picket and main channel can generate large amounts of amplitude modulation. The combined field from the two pulse-shaping channels is

$$p(t) = p_1(t) + b_1(t) + p_2(t) + b_2(t), \quad (3)$$

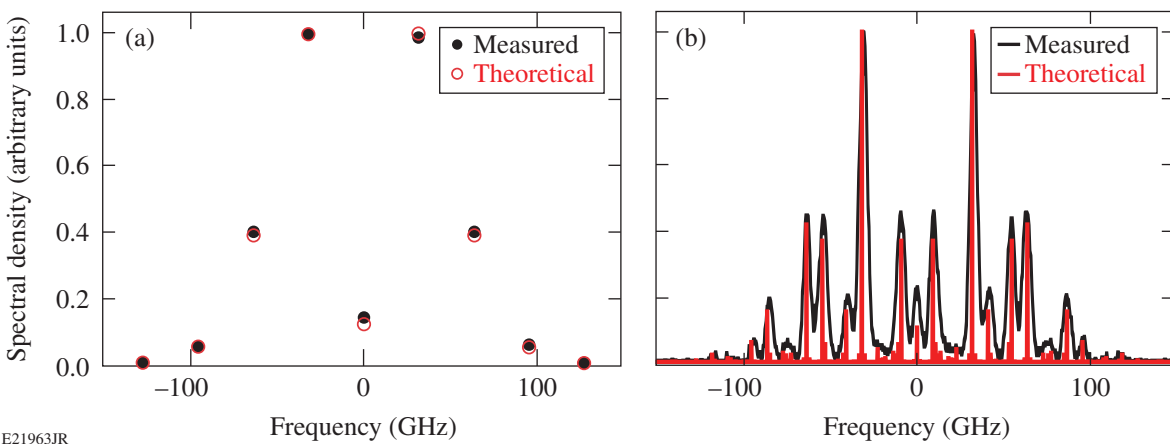
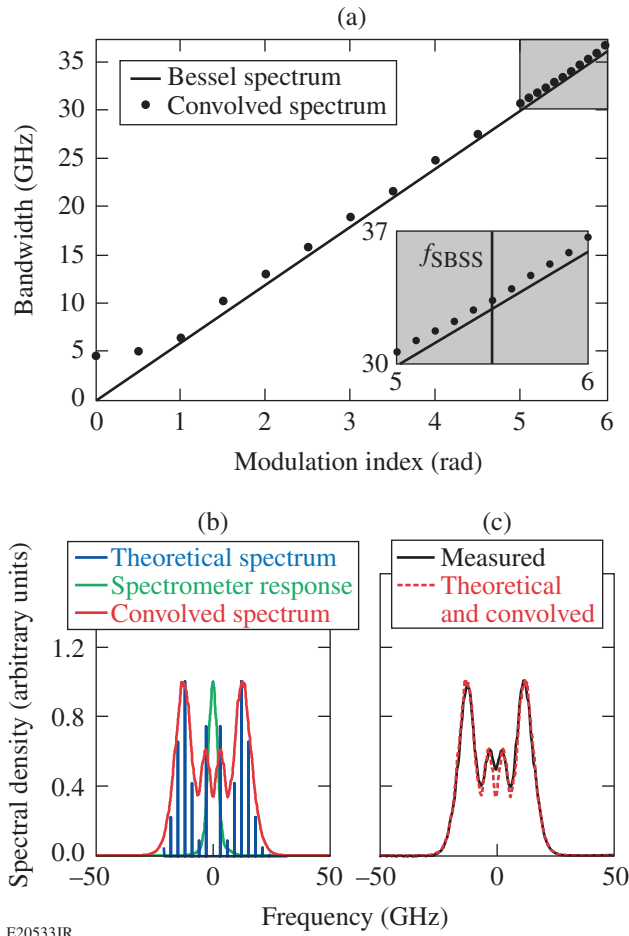


Figure 134.29  
(a) Example of a measured spectrum (solid black circles) and fit (open red circles) for the modulation frequency  $f_3$ ; (b) measured and theoretical optical spectra when the three multi-FM drives are turned on.



E20533JR

Figure 134.30

(a) Plot of the FWHM of the spectrum obtained by convolution of the measured monochromator response with the theoretical spectrum of a monochromatic source after phase modulation at  $f_{\text{SBSS}}$ . The inset shows a close-up of the range of modulation index between 5 and 6 rad. (b) Theoretical spectrum of a phase-modulated field at 3 GHz with a modulation index of 5.5 rad, measured response function of the spectrometer, and spectrum obtained by convolution of these two spectra. (c) Comparison of the measured spectrum with the convolved spectrum calculated with the nominal SBSS specifications.

where  $p_1$  and  $p_2$  are the fields of the two shaped pulses,  $b_1$  is the field leakage of channel 1, and  $b_2$  is the field leakage of channel 2.  $p_1$  and  $p_2$  are finite-duration pulses that are not overlapping because the two channels are timed to generate distinct pulse shapes;  $p_1$  and  $p_2$  are equal to zero during  $b_1$  and  $b_2$ , respectively. With these definitions, the power is

$$\begin{aligned}
 P(t) = & P_1(t) + P_2(t) \\
 & + 2\text{Re}\left[p_1(t)b_2^*(t)\right] + 2\text{Re}\left[p_2(t)b_1^*(t)\right] \\
 & + 2\text{Re}\left[b_1(t)b_2^*(t)\right] + B_1(t) + B_2(t), \quad (4)
 \end{aligned}$$

where  $P_1$  and  $P_2$  are the shaped pulses of interest,  $p_1b_2^*$  and  $p_2b_1^*$  are the interference of each shaped pulse with the background leakage from the other channel (the main source of noise), and the other terms correspond to the power and interference of the backgrounds (usually negligible). A channel with extinction ratio  $R$  leads to a modulation with peak-to-valley amplitude equal to  $4\sqrt{R}$  at times when the pulse generated by the other channel has a power equal to 1. This modulation can be highly detrimental: for  $R = 20$  dB, the resulting noise is 40%, and increasing  $R$  to 40 dB decreases the peak-to-valley noise to 4%, still negatively impacting the system performance. If the same monochromatic laser is used in the two channels, the self-interference will manifest itself as an energy variation from shot to shot, owing to the slow phase drift between the two channels. If two distinct lasers with an optical frequency difference  $\Delta f_{12}$  are used, the interference is a time-varying amplitude modulation of the optical pulse at the frequency  $\Delta f_{12}$ .

The two cascaded MZM's in each channel ensure that the intrinsic extinction ratio is higher than 40 dB, assuming that the corresponding voltage biases are adequately set. The pulse-shaping systems are calibrated for optimal biasing on each MZM. The front end is built with two distinct monochromatic lasers that are spectrally tuned to make the frequency of their interference easily measurable, i.e., distinct from all the microwave frequencies potentially present in the system (all the frequencies in Table 134.V and the sum and differences of all the frequencies present in a given channel), within the bandwidth of the photodetection system (lower than 45 GHz). The frequency of the offset must be small enough that the two channels essentially have the same central wavelength to avoid impacting amplification and frequency conversion to the UV and allow for identical dispersion compensation. The beams corresponding to the two channels are spatially offset in the far field after the SSD grating because of the angular dispersion. The beam corresponding to the broadest spectrum was chosen for alignment because of the more-stringent alignment requirement to avoid spectral clipping by pinholes in the far field. A frequency approximately equal to 5 GHz was chosen. The seed lasers are spectrally tuned by temperature-controlled fiber Bragg gratings with a spectral drift much smaller than 1 GHz over extended periods of time. The frequency offset is quite stable once set. Figure 134.31 shows examples of waveforms measured with proper biasing and with an intentional bias offset. The bias voltage of the two MZM's in each channel is optimized daily by measuring their transmission as a function of the voltage and determining the voltage for minimal transmission. Bias drift caused by charge accumulation is avoided by temporal alternation of the bias between the

optimal value in a time interval encompassing the shaped pulse and another value to set the time-averaged voltage to zero. No interference between channels has been observed with these pulse-shaping systems and procedures and no fail-safe system actively detecting the interference was implemented because of the reliability and stability of this approach, which is also used for pulse shaping on OMEGA<sup>8</sup> and OMEGA EP.<sup>12</sup>

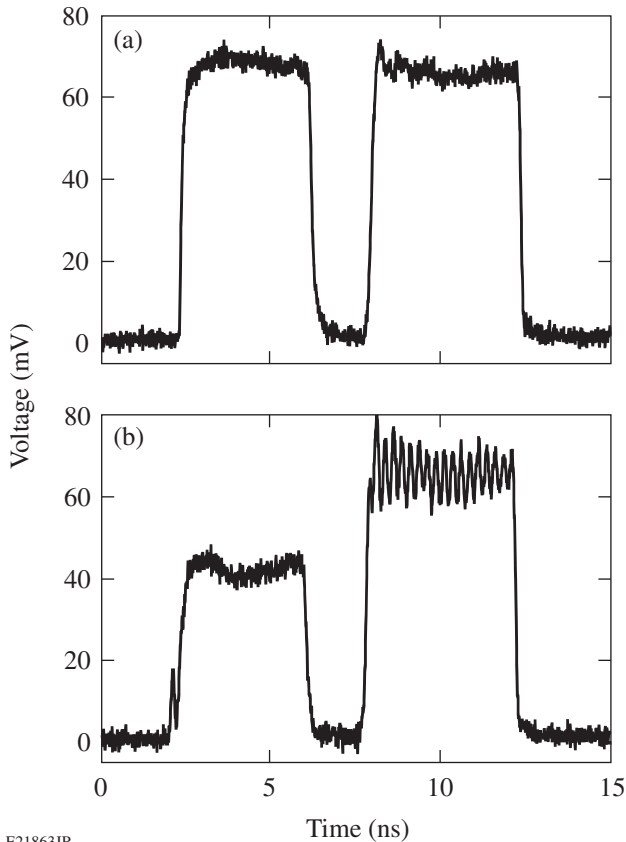


**Figure 134.31**  
Measurement of the pulse shape obtained by combining the picket channel (first pulse) and the main channel (second pulse) in (a) optimal biasing conditions and (b) when the bias of the gate MZM of the picket channel is purposely offset by  $\sim V_{\pi}/10$ . In the latter case, the amplitude of the first pulse is reduced because of the lower transmission, and AM at  $\sim 5$  GHz is present on the second pulse because of the increased background.

**4. Dispersion Compensation**

Dispersion compensation is optimized by first accounting for all sources of chromatic dispersion in the full laser system, from the fiber-coupled phase modulators to the end of the large Nd:glass amplifiers, with optical fibers in the front end being the largest contributor. The two channels in the front end are symmetric, and optimal compensation is expected to be reached for these two systems for the same setting of the dispersion

compensator. A 100-m PZ patchcord was initially installed between the front end and the NIF PAM, based on an estimate of the dispersion of the fiber in the front end and the single-grating compressor. Various lengths of PZ fiber were added between the output of the regenerative amplifier and the temporal diagnostic, and the resulting amplitude noise was estimated on a pulse from the picket channel with the three multi-FM modulations turned on (Fig. 134.32). Dispersive propagation has the same effect on the AM whether it occurs before or after the regenerative amplifier in the absence of nonlinearity in that amplifier. Once the optimal fiber length was determined, the corresponding patchcords were placed between the front end and the amplifier to optimize the the amplified signal propagating in the laser system. It is not known if the propagation in the regenerative amplifier is perfectly linear, but no significant difference in the measured AM was found when dispersion compensation was adjusted before or after the amplifier.

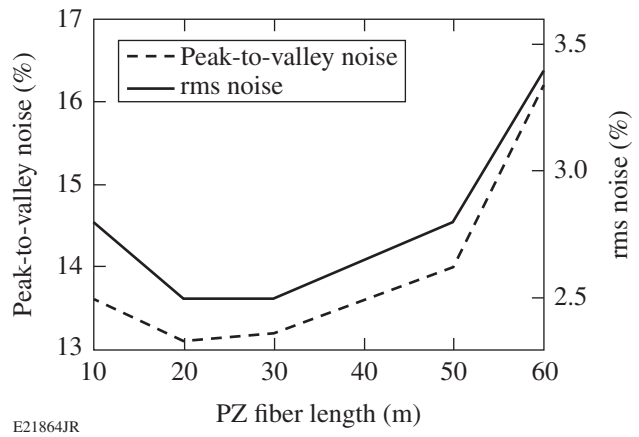
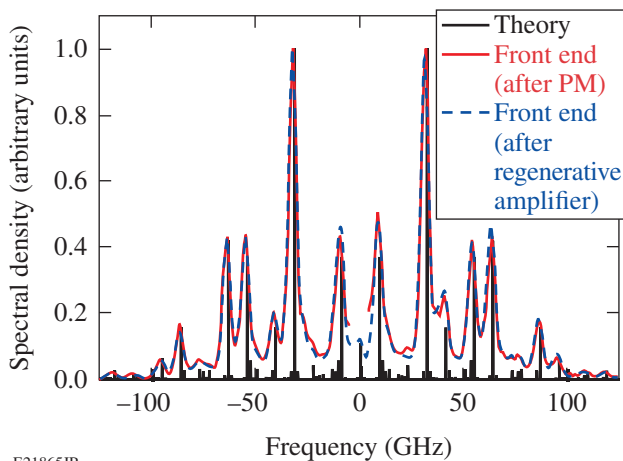


**Figure 134.32**  
Amplitude noise [dashed line: peak-to-valley noise; solid line: rms (root-mean-square) noise] measured as a function of the length of the polarizing (PZ) fiber added before photodetection.

**5. Amplitude Compensation**

Spectral amplitude compensation is performed by tuning the two angles of the birefringent calcite plate relative to the incident beam. Initial tests and setup used measurements obtained with a spectrometer: the spectrum at the output of the regenerative amplifier is monitored as the plate is tuned by an operator, and the match between the measured spectrum and the expected spectrum (e.g., the spectrum of the pulse with  $f_1, f_2,$  and  $f_3$  on) is used as feedback. Figure 134.33 compares the optical spectrum measured after the phase modulator and after the regenerative amplifier. These two optical spectra are indistinguishable and are in excellent agreement with the

theoretical spectrum. Although some amplitude modulation of the spectrum might still be present (beyond the measurement capability in the spectral domain), the time-domain amplitude-noise measurements presented in the next section indicate that the spectral gain tilt in the fiber amplifiers and the regenerative amplifier are adequately compensated. During operation, the amplitude noise measured in the time domain is used as the feedback mechanism. The rf spectrum of the measured waveform (e.g., a square pulse with all multi-FM frequencies turned on at the output of the regenerative amplifier) is calculated in real-time and an operator minimizes the observed rf tones. The amplitude noise on the waveform is then determined. The measured amplitude noise must be below 20% peak-to-valley, as required by a noise budget made for the entire OMEGA EP Laser System. Values of the order of 15% are typical for the peak-to-valley noise, corresponding to rms noise of the order of 3%. The amplitude compensator is stable enough for operation without active stabilization: the amplitude noise was observed over several days without significant increase.



E21865JR

Figure 134.33

Optical spectrum corresponding to a pulse with the three multi-FM frequencies calculated (solid black line), measured after the phase modulator (PM) (solid red line), and measured after the regenerative amplifier (dashed blue line). The measurements were performed with a grating spectrometer having a resolution of 5 GHz. The spectral density data between  $-5$  GHz and  $+5$  GHz after the phase modulator have been removed because the data in that range are corrupted by the cw leakage from the AOM integrated by the detector at the Fourier plane of the spectrometer.

## 6. Amplitude-Noise Measurements

Amplitude-noise measurements were routinely performed at the output of the regenerative amplifier in the PAM. Quantifying the amplitude noise is crucial for the operation of a large-scale laser system because AM increases the peak power

incident on the optical components for a given energy. A power increase can lead to higher nonlinearity experienced by the optical pulse and to optical damage. This amplifier operates at 1 Hz, allowing for the acquisition of a sufficient set of data for statistical analysis. Data similar to that presented in Fig. 134.27 are used: a set of 50 successive waveforms is measured, a temporal range where the pulse shape is not rapidly varying (i.e., avoiding the sharp leading and trailing edges) is isolated, the pulse shape over that range is normalized by a low-order fit, the rms and peak-to-valley variations of the normalized pulse are determined, and the global rms and peak-to-valley noise are obtained by averaging the values determined for each pulse. Using this procedure, the data of Fig. 134.27(a) for the main pulse lead to rms and peak-to-valley noise of 2.3% and 13.2%, respectively. Using the same procedure on a 1-ns pulse from the picket channel leads to similar values for the rms and peak-to-valley noise, 2.8% and 13.5%, respectively. The remaining noise can be attributed to measurement noise, imperfect amplitude and dispersion compensation, propagation effects in polarization-maintaining fibers, and etaloning in optical components. Amplitude noise caused by broadband analog-to-digital conversion by the oscilloscope is likely to be the largest contributor: direct measurement of a cw laser with the same photodetection led to rms and peak-to-valley amplitude noise of 1.6% and 9.6%, respectively, in a 3-ns time window. The measured noise is acceptable, considering the noise budget for the entire laser system, which requires less than a 20% peak-to-valley noise in the front end. Apart from the broadband noise from the photodetection system, the spectrum of the measured waveforms typically has low-density tones at the modulation frequencies. A parabolic spectral-amplitude modulation and high-order spectral phase modulations can lead to intermodulation components, i.e., sidebands of equal amplitude at the sum and difference of the modulation frequencies. The sum terms (e.g.,  $2f_3 \sim 63.8$  GHz and  $f_1 + f_3 \sim 53.1$  GHz for the picket channel) are beyond the photodetection bandwidth, but the difference terms (e.g.,  $f_3 - f_1 \sim 10.7$  GHz) correspond to a high value of the detection frequency response. No significant spectral components at the difference frequencies have been observed when the amplitude compensator is adequately set, giving confidence in the spectral-amplitude compensation and showing that the impact of high-order terms in the spectral phase is negligible. These aspects will be studied in detail in the future. These experiments confirm that AM compensation to an acceptable noise level can be obtained simultaneously on the two channels.

A diffraction grating mounted inside the PAM is required for SSD: the angular dispersion (frequency versus wave vector

in the near field) of a phase-modulated pulse leads to a time-varying speckle distribution in the far field of the focusing lens after frequency conversion and random spatial-phase modulation from a phase plate.<sup>6</sup> The current system has a 1700-l/mm diffraction grating mounted in the Littrow configuration. The groove density is a trade-off between smoothing, pulse-shape, and laser requirements. A larger angular dispersion leads to more smoothing in the far field, but it temporally broadens the pulse shape. Angular dispersion widens the far field of the optical pulse, which can disrupt the propagation of the amplified pulse in vacuum spatial filters that re-image the beam throughout the laser system. Pinholes in vacuum spatial filters are designed to spatially filter the high spatial frequencies of the beam as it propagates in the laser system, but they can lead to spectral clipping of the spectrum of angularly dispersed phase-modulated pulses, which adds amplitude modulation in the time domain.

The tightest pinhole in the entire laser system is located in the PAM. The full optical spectrum was observed in the far field after that pinhole,<sup>13</sup> but amplitude noise was measured at an image plane of the diffraction grating after this pinhole to confirm that no amplitude noise is added to the front-end pulses. A PZ fiber was used to probe the laser beam, which has an ~2-cm size in that plane. Figure 134.34 displays the amplitude noise as a function of the longitudinal distance relative to a reference position. The noise is expected to be minimal at the image plane and to increase before and after the image plane.<sup>20</sup> The minimum noise should be equal to the noise before angular dispersion. The measured rms and peak-to-valley noise at the output of the regenerative amplifier (i.e., before the diffraction

grating) were 2.8% and 14.2%, respectively, in good agreement with the minimum values observed at the image plane, 2.5% and 13.5%. The lower noise observed at the image plane is not fully understood, but it could be a result of a slight mismatch in the dispersion compensation: propagation away from the image plane is equivalent to second-order dispersion;<sup>20</sup> therefore a signal with a small amount of dispersion has lower amplitude noise when measured at a longitudinal distance slightly offset from the image plane.

## Conclusion

The front end demonstrates the use of high-bandwidth pulse shaping and phase modulation for high-energy laser systems. In particular, high-bandwidth, three-section phase modulators have been calibrated at microwave frequencies up to 40 GHz and routinely used at frequencies ranging from 3 to 32 GHz. The optical combination of optical pulses with different pulse shapes and phase modulations has made it possible to generate complex optical fields. Fail-safe systems have been used to detect the presence of adequate phase modulation and sufficient optical power at the output of the front end. A grating compressor and a Lyot filter have been used to decrease the FM-to-AM conversion caused by dispersive propagation and spectrally dependent amplifier gain. Pulse shape and noise measurements at frequencies up to 45 GHz have confirmed the accuracy of the compensation and adequacy of the system for seeding a high-energy laser system.

The front end has been used to generate seed pulses with a variety of shapes and phase modulations for the OMEGA EP Laser System to study the amplification, frequency-conversion, and beam-smoothing properties of these pulses.<sup>13</sup> The front end and associated technologies have made it possible to validate the multi-FM approach for beam smoothing and its application to a large-scale laser system. Implementation on a multibeam system will require significant multiplexing of the resources in the front end (particularly cw lasers, AWG's, and modulators) to minimize the associated space and cost. The 48 PAM's on the NIF might require seeding with optical pulses that have different shapes and central wavelength<sup>1,11</sup> requiring different front-end outputs, but building 48 front ends identical to the one described here would be prohibitive.

## ACKNOWLEDGMENT

The authors thank M. W. Bowers, D. F. Browning, and G. V. Erbert (Lawrence Livermore National Laboratory) for fruitful discussions and assistance with NIF-related equipment, and T. J. B. Collins, J. H. Kelly, B. E. Kruschwitz, J. A. Marozas, and A. Shvydky (LLE) for fruitful discussions. This work was supported by the U.S. Department of Energy Office of Inertial Confinement Fusion under Cooperative Agreement No. DE-FC52-08NA28302, the Univer-

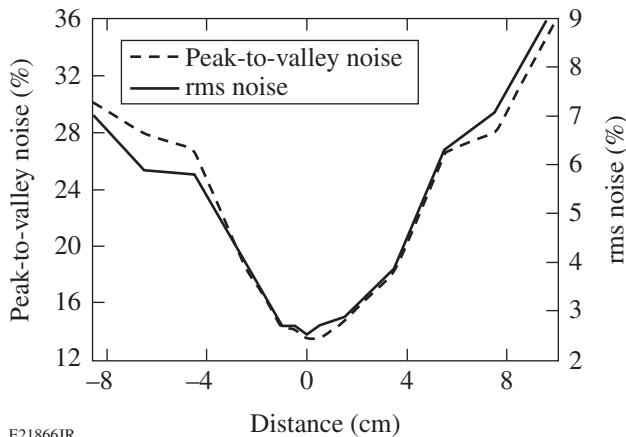


Figure 134.34

Amplitude noise (dashed line: peak-to-valley noise; solid line: rms noise) measured as a function of the longitudinal distance close to an image plane of the diffraction grating.

sity of Rochester, and the New York State Energy Research and Development Authority. The support of DOE does not constitute an endorsement by DOE of the views expressed in this article.

## REFERENCES

1. C. A. Haynam *et al.*, *Appl. Opt.* **46**, 3276 (2007).
2. N. Fleurot, C. Cavailler, and J. L. Bourgade, *Fusion Eng. Des.* **74**, 147 (2005).
3. J. D. Lindl, *Phys. Plasmas* **2**, 3933 (1995).
4. J. D. Kilkenny, S. G. Glendinning, S. W. Haan, B. A. Hammel, J. D. Lindl, D. Munro, B. A. Remington, S. V. Weber, J. P. Knauer, and C. P. Verdon, *Phys. Plasmas* **1**, 1379 (1994).
5. R. L. McCrory, D. D. Meyerhofer, R. Betti, R. S. Craxton, J. A. Delettrez, D. H. Edgell, V. Yu Glebov, V. N. Goncharov, D. R. Harding, D. W. Jacobs-Perkins, J. P. Knauer, F. J. Marshall, P. W. McKenty, P. B. Radha, S. P. Regan, T. C. Sangster, W. Seka, R. W. Short, S. Skupsky, V. A. Smalyuk, J. M. Soures, C. Stoeckl, B. Yaakobi, D. Shvarts, J. A. Frenje, C. K. Li, R. D. Petrasso, and F. H. Séguin, *Phys. Plasmas* **15**, 055503 (2008).
6. S. Skupsky, R. W. Short, T. Kessler, R. S. Craxton, S. Letzring, and J. M. Soures, *J. Appl. Phys.* **66**, 3456 (1989).
7. J. E. Rothenberg, *J. Opt. Soc. Am. B* **14**, 1664 (1997).
8. T. R. Boehly, D. L. Brown, R. S. Craxton, R. L. Keck, J. P. Knauer, J. H. Kelly, T. J. Kessler, S. A. Kumpan, S. J. Loucks, S. A. Letzring, F. J. Marshall, R. L. McCrory, S. F. B. Morse, W. Seka, J. M. Soures, and C. P. Verdon, *Opt. Commun.* **133**, 495 (1997).
9. S. Skupsky and R. S. Craxton, *Phys. Plasmas* **6**, 2157 (1999).
10. J. R. Murray *et al.*, *J. Opt. Soc. Am. B* **6**, 2402 (1989).
11. T. J. B. Collins, J. A. Marozas, K. S. Anderson, R. Betti, R. S. Craxton, J. A. Delettrez, V. N. Goncharov, D. R. Harding, F. J. Marshall, R. L. McCrory, D. D. Meyerhofer, P. W. McKenty, P. B. Radha, A. Shvydky, S. Skupsky, and J. D. Zuegel, *Phys. Plasmas* **19**, 056308 (2012).
12. D. N. Maywar, J. H. Kelly, L. J. Waxer, S. F. B. Morse, I. A. Begishev, J. Bromage, C. Dorrer, J. L. Edwards, L. Folsbee, M. J. Guardalben, S. D. Jacobs, R. Jungquist, T. J. Kessler, R. W. Kidder, B. E. Kruschwitz, S. J. Loucks, J. R. Marciante, R. L. McCrory, D. D. Meyerhofer, A. V. Okishev, J. B. Oliver, G. Pien, J. Qiao, J. Puth, A. L. Rigatti, A. W. Schmid, M. J. Shoup III, C. Stoeckl, K. A. Thorp, and J. D. Zuegel, *J. Phys. Conf. Ser.* **112**, 032007 (2008).
13. “Commissioning of a Multiple-Frequency-Modulation Smoothing by Spectral Dispersion Demonstration System on OMEGA EP,” published in this volume.
14. V. N. Goncharov, T. C. Sangster, T. R. Boehly, S. X. Hu, I. V. Igumenshchev, F. J. Marshall, R. L. McCrory, D. D. Meyerhofer, P. B. Radha, W. Seka, S. Skupsky, C. Stoeckl, D. T. Casey, J. A. Frenje, and R. D. Petrasso, *Phys. Rev. Lett.* **104**, 165001 (2010).
15. P. J. Wisoff *et al.*, in *Optical Engineering at the Lawrence Livermore National Laboratory II: The National Ignition Facility*, edited by M. A. Lane and C. R. Wuest (SPIE, Bellingham, WA, 2004), Vol. 5341, pp. 146–155.
16. M. Bowers *et al.*, in *Solid State Lasers XVI: Technology and Devices*, edited by H. J. Hoffman, R. K. Shori, and N. Hodgson (SPIE, Bellingham, WA, 2007), Vol. 6451, p. 64511M.
17. J. K. Crane *et al.*, in *Solid State Lasers for Application to Inertial Confinement Fusion: Second Annual International Conference*, edited by M. L. André (SPIE, Bellingham, WA, 1997), Vol. 3047, pp. 601–609.
18. D. Penninckx *et al.*, *J. Lightwave Technol.* **24**, 4197 (2006).
19. J. E. Rothenberg, D. F. Browning, and R. B. Wilcox, in the *Third International Conference on Solid State Lasers for Application to Inertial Confinement Fusion*, edited by W. H. Lowdermilk (SPIE, Bellingham, WA, 1999), Vol. 3492, pp. 51–61.
20. S. Hocquet *et al.*, *Appl. Opt.* **47**, 3338 (2008).
21. B. Lyot, *C. R. Acad. Sci. (Paris)* **197**, 1593 (1933).

# Mitigation of Two-Plasmon Decay in Direct-Drive Inertial Confinement Fusion Through the Manipulation of Ion-Acoustic- and Langmuir-Wave Damping

## Introduction

Two-plasmon decay<sup>1–6</sup> (TPD) is a three-wave-decay instability in which an electromagnetic (EM) wave parametrically decays into two longitudinal (Langmuir) waves. Experimentally, signatures of TPD have been observed in the ionosphere<sup>7</sup> and in laser-plasma interaction experiments.<sup>8,9</sup> In the context of laser fusion, TPD has been identified in both the indirect-<sup>10</sup> and direct-drive<sup>11</sup> approaches. In these schemes, TPD is undesirable because of the anomalous absorption of laser light at densities below the critical density and the potential to accelerate electrons to high energies.<sup>12–16</sup> High-energy electrons can preheat the target and severely degrade performance since efficient implosions require the fuel to remain on a low adiabat.

The linear stability of a single-plane EM wave subject to TPD has been studied for quite some time,<sup>1–6,17,18</sup> although not without controversy regarding its absolute/convective nature in inhomogeneous plasma.<sup>16,19,20</sup> In TPD, a photon decays into two plasmons, fulfilling the frequency- and wave-number-matching conditions,  $\omega_0 = \omega + \omega'$ ,  $\vec{k}_0 = \vec{k} + \vec{k}'$ , where  $\omega_0$  and  $\vec{k}_0$  ( $k_0 \equiv |\vec{k}_0| = \omega_0 / c \sqrt{1 - n_e/n_c}$ ) are the frequency and wave vector, respectively, of an EM wave in a plasma having an electron number density  $n_e$  relative to the critical density  $n_c [= m_e \omega_0^2 / (4\pi e^2)]$  at which EM waves are evanescent. Here,  $e$  and  $m_e$  are the electron charge and mass, respectively, and  $c$  is the speed of light. The quantities  $\omega$ ,  $\omega'$ ,  $\vec{k}$ , and  $\vec{k}'$  are the frequencies and wave vectors of the two decay Langmuir waves (LW's) (note that in the literature, the terms “Langmuir wave,” “plasma wave,” and “plasmon” are used interchangeably). The essential features are described by the temporal TPD growth rate  $\gamma$  (in the presence of LW damping rate  $\nu_e$ ):

$$\gamma = \gamma_0 - \nu_e = \frac{\vec{k} \cdot \vec{v}_{\text{osc}}}{4} \frac{[(\vec{k}_0 - \vec{k})^2 - k^2]}{k |\vec{k}_0 - \vec{k}|} - \nu_e, \quad (1)$$

where  $\vec{v}_{\text{osc}} = e\vec{E}_0 / \omega_0 m_e$  is the oscillation velocity of an electron in the electric field of the plane EM wave  $\vec{E}_0$ . The relation between  $k_{\parallel}$  and  $k_{\perp}$  (parallel and perpendicular components of  $\vec{k}$

with respect to  $\vec{k}_0$ ) corresponding to maximum growth defines a hyperbola in  $k$  space,  $\vec{k}_{\perp}^2 = k_{\parallel}(k_{\parallel} - k_0)$ . From Eq. (1) it can be seen that two-plasmon decay cannot be studied in one spatial dimension (since  $\vec{k}_0 \cdot \vec{v}_{\text{osc}} = 0$  for EM waves). For this reason most, if not all, numerical calculations to date have been performed in 2-D in the plane of maximum growth, i.e., the plane of polarization (such is the case here).

In experiments utilizing multiple overlapping laser beams, the instability is believed to be driven cooperatively by several beams<sup>21</sup> through the sharing of common TPD waves.<sup>22–24</sup> To retain this feature in two spatial dimensions, all calculations were performed with two EM waves arranged symmetrically about the density gradient with angles of  $\pm 23^\circ$  (as in previous work<sup>25–28</sup>).

Parametric instabilities occur when the pump amplitude exceeds a threshold that depends on collisional effects, Landau damping, and plasma inhomogeneity. The effect of collisional damping of LW's was not emphasized in earlier theoretical works. This was either for simplicity or motivated by the dominance of inhomogeneity in experiments. In this work, all three effects are included.

In several previous studies of the nonlinear saturation of electromagnetically driven parametric instabilities, the level of LW excitation was seen to depend on the ion-acoustic-wave (IAW) damping rate. This was reported in detail in simulations of the nonlinear stage of stimulated Raman scattering (SRS) in laser hot spots,<sup>29</sup> in regimes of low Landau damping of the Langmuir wave. It was found that the SRS reflectivity increased linearly with the IAW damping rate. In general, the development of Langmuir turbulence and collapse physics is known to depend on the ion-acoustic damping rate.<sup>30–32</sup> These earlier results suggest that TPD could be less severe in materials with high collisional damping of LW and weak collisional damping of IAW (experimental evidence suggests TPD suppression in mid-Z targets<sup>33,34</sup>). More importantly, there could be practical implications for directly driven inertial confinement fusion (ICF) since Betti<sup>35</sup> and Lafon<sup>36</sup> have shown that igniting targets

can be designed using mid-Z ablaters at the megajoule (MJ) scale. These could provide an alternate path to ignition should TPD preheat be too high in directly driven designs using plastic (CH) ablaters.<sup>37</sup>

The following sections describe the numerical “QZAK” model and explain in detail the approximations that have been made; the properties of linear stability; and the anomalous absorption of hot-electron production that is characteristic of the nonlinearly saturated state, emphasizing the sensitivity to plasma conditions, followed by a summary and discussion.

### Numerical Simulation of TPD Growth and Saturation in Inhomogeneous Collisional Plasma

Zakharov models<sup>38,39</sup> have been used extensively to study the evolution of Langmuir waves and their nonlinear coupling with ion-acoustic waves, particularly LW self-focusing and collapse. The Zakharov model describes both three- and four-wave interactions,<sup>40</sup> which have been used to study strong Langmuir turbulence<sup>41,42</sup> relevant to laboratory plasmas,<sup>43,44</sup> ionospheric modification experiments,<sup>30,31,45</sup> laser-plasma experiments,<sup>32,46,47</sup> and pulsar radio emissions.<sup>48</sup> The weak turbulence regime<sup>40</sup> assumes random phase interactions between the linear modes and does not accurately describe the results from Zakharov models<sup>49</sup> because of strong turbulence effects. The strong turbulence regime<sup>41,42</sup> involves phase-coherent interactions including self-focusing, cavitation, and collapse, which can coexist<sup>50</sup> with wave–wave processes such as the Langmuir decay instability (LDI).<sup>40,51</sup> The key approximation of the model is that of temporal enveloping. The fast variations ( $\partial/\partial t \sim \omega_{pe}$ ) of the LW electrostatic field are explicitly removed, and the slow variations ( $\partial/\partial t \ll \omega_{pe}$ ) are followed by the complex-valued function, or “envelope”  $\tilde{E}_1(\vec{x}, t)$ . For example, the physical LW electrostatic field  $\tilde{E}$  is given by  $\tilde{E} = 1/2 [\tilde{E}_1(\vec{x}, t) \exp(-i\omega_{pe}t) + \text{c.c.}]$ , which is centered at the reference plasma frequency  $\omega_{pe} = (4\pi n_0 e^2/m_e)^{1/2}$ .

In the extended quasi-linear Zakharov model of TPD,<sup>32,46</sup> multiple envelopes are defined by an expansion in harmonics of the reference electron plasma frequency  $\omega_{pe}$  (which is itself defined in terms of a reference density  $n_0$ ). This is useful since TPD is localized between a narrow range of densities in the neighborhood of  $n_c/4$ . Two envelopes and a low-frequency term are sufficient for the present analysis,<sup>52</sup> shown below for the plasma current:

$$\begin{aligned} \vec{J}(\vec{x}, t) = & \vec{J}_0(\vec{x}, t) + \frac{1}{2} \left[ \vec{J}_1(\vec{x}, t) \exp(-i\omega_{pe}t) \right. \\ & \left. + \vec{J}_2(\vec{x}, t) \exp(-i2\omega_{pe}t) + \text{c.c.} \right], \end{aligned} \quad (2)$$

where  $|\partial \vec{J}_1/\partial t| \ll \omega_{pe} |\vec{J}_1|$ , etc. The term proportional to  $\vec{J}_1$  is centered at the plasma frequency  $\omega_{pe}$  and therefore close to one half of the laser frequency. The longitudinal component of  $\vec{J}_1$  drives the first Zakharov equation (LW response), while the transverse component is responsible for the  $\omega_0/2$  radiation<sup>53–56</sup> (including SRS<sup>29</sup> and the mixed-polarization, high-frequency hybrid instability<sup>18</sup>). The term  $\vec{J}_2$ , near twice the plasma frequency  $2\omega_p$  and therefore close to the laser frequency  $\omega_0$  (with mismatch  $\Delta\omega \equiv \omega_0 - 2\omega_{pe} \ll 2\omega_p$ ), modifies the laser propagation and is the source of pump depletion. [The subscript “0” denoting the laser frequency  $\omega_0$  throughout is not to be confused with the subscript “0” in Eq. (2), where it denotes terms with a frequency far below the electron plasma frequency.] The plasma response to low-frequency terms is assumed to be quasi-neutral  $\delta n = \delta n_e \approx Z\delta n_i$ , where  $Z$  is the ion charge and  $\delta n_e$  and  $\delta n_i$  are the electron- and ion-density perturbations, respectively. Inhomogeneous plasmas with a weak density gradient are investigated by the addition of a static term describing density perturbations from the reference density (as described in Russell *et al.*<sup>46</sup>) and by a constant flow velocity  $\vec{u}_0$ .

The primary disadvantage of a fluid-moment model such as the Zakharov model<sup>32,46</sup> is the lack of nonlinear kinetic saturation mechanisms. Although often derived from the plasma fluid equations,<sup>57</sup> ZAK<sup>25,26,32,46</sup> and also the QZAK (described below) and RPIC numerical codes (described in Vu *et al.*<sup>25</sup>) can be shown to be direct consequences of the Vlasov equation by the use of a multiple time-scale analysis and the requirement that certain parameters remain “small,” e.g.,  $|\tilde{E}_1|^2 / (4\pi n_0 T_e) < 1$ ,  $\delta n_0 / n_{e0} < 1$ , and  $k\lambda_{De} < 1$  (Ref. 58), where

$$\lambda_{De} = \sqrt{T_e / (4\pi n_0 e^2)}$$

is the electron Debye length. The ZAK model of TPD<sup>25,26,32,46</sup> [which includes linear wave–particle interactions (Landau damping)] is improved upon by QZAK, which evolves the electron-distribution function in the quasi-linear approximation. RPIC is a time-enveloped particle-in-cell (PIC) code that improves on QZAK since it does not make the quasi-linear approximation.<sup>25</sup> When the proper conditions are met, the predictions of RPIC and QZAK should agree. Since PIC codes generally make no small-parameter assumptions, they can be used to check the validity of QZAK calculations. This was discussed in a recent paper by Vu *et al.*<sup>27</sup> using the code RPIC and also briefly in **Confirmation of the Sensitivity to**

**Ion-Acoustic Damping Using RPIC Calculations** (p. 122) (unlike typical PIC codes, RPIC assumes that a separation of time scales exists, which could in some sense be considered as an expansion parameter).

*The Extended Quasi-Linear Zakharov (QZAK) Model of TPD*

The harmonic decomposition in  $\omega_{pe}$  suggested by Eq. (2) leads to the following equation for EM waves having frequencies of  $2\omega_{pe}$  (i.e., near that of the laser pump):

$$\begin{aligned} & \left\{ -2i(2\omega_p)(\partial_t + \nu_{2,T}) + c^2 \nabla^2 + (2\omega_{pe})^2 \right. \\ & \left. \times \left[ 1 - (n_0 + \delta N + \delta n) / (4n_0) \right] \right\} \vec{E}_{2,T} \\ & = (e/m_e) [(\nabla \cdot \vec{E}_1) \vec{E}_1]_T. \end{aligned} \quad (3)$$

This equation describes the laser pump field, which is imposed as a boundary condition, together with other components resulting from nonlinearities. The relation of the laser electric field  $\vec{E}_0$  to the transverse component of the second-harmonic envelope is given by  $\vec{E}_0 = \vec{E}_{2,T} \exp(i\Delta\omega t)$ , where  $\Delta\omega$  represents the slight frequency mismatch that arises because  $n_0 (= 0.23 n_c)$  is slightly less than  $n_c/4$  (to allow for the density gradient). The subscript “*T*” denotes the transverse component, which is most easily expressed in Fourier space:  $\vec{E}_{2,T}(\vec{k}) = (\vec{I} - \vec{k}\vec{k}/k^2) \cdot \vec{E}_2(\vec{k})$ . The quantity  $\nu_{2,T}$  is the collisional damping rate of transverse waves  $\nu_{2,T} \approx (n_0/n_c) \nu_{ei}$  that gives rise to inverse-bremsstrahlung absorption,<sup>59</sup> where

$$\nu_{ei} \approx 3 \times 10^{-6} \log(\lambda) (n_e / 1 \text{ cm}^{-3}) Z / (T_e / 1 \text{ eV})^{3/2}$$

is the usual electron–ion collision frequency (in  $s^{-1}$ ), where  $\log(\lambda)$  is the Coulomb logarithm and  $T_e$  is the electron temperature. The term  $\delta N(\vec{x})$  is a small, nonevolving density perturbation describing the weakly inhomogeneous density,<sup>46</sup> while  $\delta n(\vec{x}, t)$  is the quasi-neutral piece that is driven by the ponderomotive pressure of the high-frequency fluctuations. The total low-frequency density is given by  $n_e(\vec{x}, t) = n_0 + \delta N(\vec{x}) + \delta n(\vec{x}, t)$  with the assumption that both  $\delta N/n_0 \ll 1$  and  $\delta n/n_0 \ll 1$ . In all calculations presented here,  $\delta N$  varies linearly in the  $x$  direction only (the “longitudinal” direction), while the initial density scale length  $L_n \equiv [d/dx \ln(n_0 + \delta N)]^{-1} = 330 \mu\text{m}$  (at box center) unless otherwise noted. The right-hand side of Eq. (3) describes the depletion of  $\vec{E}_{2,T}$  as a result of its decay into electrostatic waves  $\vec{E}_1$ .

In two-plasmon decay it is likely that the background particle-distribution functions are significantly changed during the nonlinear stage of the instability. High levels of LW’s or IAW’s can lead to important modifications of the electron and ion distribution functions; these modifications, in turn, affect the nonlinear levels of the wave excitation. A multiple time-scale analysis of the spatially averaged electron Vlasov equation, together with a quasi-neutral low-frequency response, leads to the same coupled envelope equations for the electrostatic response:

$$\begin{aligned} & \nabla \cdot \left[ 2i\omega_{pe} (D_t + \nu_e \cdot) + 3v_e^2 \nabla^2 - \omega_{pe}^2 (\delta n + \delta N) / n_0 \right] \vec{E}_1 \\ & = \left( \frac{e}{4m_e} \right) \nabla \cdot \left[ \nabla (\vec{E}_0 \cdot \vec{E}_1^*) - \vec{E}_0 \nabla \cdot \vec{E}_1^* \right] e^{-i\Delta\omega t} + S_E, \end{aligned} \quad (4)$$

(described by  $\vec{E}_1$ ) and for the low-frequency response

$$\left[ D_t^2 + 2\nu_i \cdot D_t - c_s^2 \nabla^2 \right] \delta n = \frac{Z}{16\pi m_i} \nabla^2 \left( |\vec{E}_1|^2 + \frac{1}{4} |\vec{E}_0|^2 \right), \quad (5)$$

as described previously<sup>32</sup> [with the exception of the terms representing inhomogeneity (discussed in more detail below)]. The important difference is that the linear response [i.e., the coefficients on the left-hand side of Eqs. (4) and (5)] varies over times that are long compared with the variation of the envelopes. In both Eqs. (4) and (5),  $D_t \equiv (\partial_t + \vec{u}_0 \cdot \nabla)$  is the convective derivative and the term  $S_E$  is the time-random-phase Čerenkov noise source<sup>60</sup> for Langmuir waves as described in Russell *et al.*<sup>46</sup> Noise enters the acoustic-wave equation only through the LW ponderomotive force. In Eq. (4),  $\nu_e = \nu_{coll} + \gamma_L$  is the sum of the collisional and Landau damping for LW’s (which evolves in time) and whose dispersion depends on the electron thermal velocity  $v_e = \sqrt{T_e/m_e}$ . The first term on the right-hand side is the longitudinal part of the nonlinear current  $\vec{J}_1$ , which drives density perturbations with frequencies close to  $\omega_{pe}$ . In Eq. (5),  $c_s = (ZT_e/m_i)^{1/2} (1 + \gamma_i T_i / ZT_e)$  is the speed of ion-acoustic waves that damp with the rate  $\nu_i$ , where  $\gamma_i \approx 3$ ,  $m_i$ , and  $T_i$  are the ion ratio of specific heats, mass, and temperature, respectively. The first term on the right-hand side describes the low-frequency ponderomotive forces of Langmuir and electromagnetic fluctuations.

As in the work of Sanbonmatsu *et al.*,<sup>61</sup> the slow temporal evolution of the spatially averaged electron distribution func-

tion  $\langle F_e \rangle$ , which is a function of velocity  $\vec{v}$  and time  $t$  only, is governed by a Fokker–Planck equation:

$$\begin{aligned} & \partial_t \langle F_e \rangle + \nu(\vec{v}) (\langle F_e \rangle - F_0) \\ &= \partial_{\vec{v}} \cdot \left[ \hat{D}(\vec{v}) \cdot \partial_{\vec{v}} \langle F_e \rangle \right] + \partial_{\vec{v}} \cdot (\delta \hat{D} \cdot \vec{v}) \langle F_e \rangle / v_e^2 \\ &+ \hat{\sigma}_{\text{IB}} \left[ \left| \vec{E}_1 \right|^2 \right] + \hat{\sigma}_{\text{IB}} \left[ \left| \vec{E}_2 \right|^2 \right]. \end{aligned} \quad (6)$$

The diffusion coefficient  $\hat{D}(\vec{v})$  is given by the usual quasi-linear form:

$$\hat{D}(\vec{v}) \approx D_{\text{QL}}(\vec{v}) = \frac{\pi e^2 |\Delta \vec{k}|}{2m_e^2 \Delta k_x \Delta k_y} \sum_{k: (\omega_{\text{pe}} - \vec{k} \cdot \vec{v} = 0)} \frac{\vec{k} \vec{k}}{|\vec{v}|} \left| \psi_1(\vec{k}) \right|^2, \quad (7)$$

where  $\psi_1(\vec{k})$  is the electrostatic potential  $\vec{E}_1(\vec{k}, t) = -i\vec{k}\psi_1(\vec{k}, t)$ . The quantity  $\Delta \vec{k}$  is the wave-vector spacing along the line in  $k$  space defined (for given  $\vec{v}$ ) by the constraint  $\omega_{\text{pe}} - \vec{k} \cdot \vec{v} = 0$ , while  $\Delta k_x$  and  $\Delta k_y$  are equal to  $2\pi/L_x$  and  $2\pi/L_y$ , respectively. The quantities  $L_x$  and  $L_y$  are the lengths of the simulation domain in the  $x$  and  $y$  directions. The second term on the left-hand side of Eq. (6) involving the term  $\nu(\vec{v}) \equiv s_x |v_x|/L_x + s_y |v_y|/L_y$ , with  $s_x, s_y$  taking the values of either 0 or 1, is the result of spatially averaging the advective term in the kinetic equation for the distribution function over the domain in which Eqs. (4) and (5) are solved:  $[0, L_x] \times [0, L_y]$  (Ref. 61). If the calculation is periodic in the  $y$  direction, for example, the corresponding contribution to this term vanishes (i.e.,  $s_y = 0$ ). It is assumed that the outgoing distribution of velocities at each spatial boundary is the same as the spatially averaged distribution function.<sup>27</sup> The term  $\delta \hat{D}$  entering into Eq. (6) has the same definition as  $\hat{D}$  in Eq. (7), but it is calculated with the initial LW noise spectrum to ensure that  $\langle F_0 \rangle$  is a steady-state solution to the undriven Eqs. (4)–(7) as described in Sanbonmatsu *et al.*<sup>61</sup> *Ad hoc* differential operators  $\hat{\sigma}_{\text{IB}} \left[ \left| \vec{E}_1 \right|^2 \right]$ ,  $\hat{\sigma}_{\text{IB}} \left[ \left| \vec{E}_2 \right|^2 \right]$ , which have been added to Eq. (6), are intended to correspond to the collisional absorption of LW and EM waves, described by the envelopes  $\vec{E}_1$  and  $\vec{E}_2$ , respectively, since they can become important for collisional plasmas. The form of these operators is left unspecified.

The distribution function  $\langle F_e \rangle(\vec{v}, t)$ , which evolves according to Eq. (6) starting from the initial condition  $\langle F_e \rangle(\vec{v}, t) = F_0$ , redefines the linear response of the plasma in time through the

linear susceptibilities that modify the frequencies (e.g.,  $c_s$  and  $v_e$ ) and damping rates ( $\gamma_L$ ) of the linear modes. In the current implementation of *QZAK*, only the electron Landau damping [entering into  $\nu_e$  of Eq. (4)] is evolved:

$$\gamma_L(\vec{k}, t) \approx \frac{\pi \omega_{\text{pe}}^2}{k^2} \int d\vec{v} \vec{k} \cdot \partial_{\vec{v}} \langle F_e \rangle(\vec{v}, t) \delta(\omega_{\text{pe}} - \vec{k} \cdot \vec{v}). \quad (8)$$

Equations (3)–(8) are solved in two spatial dimensions by a split-step method. Equation (3) is currently solved by neglecting collisional absorption, pump depletion, and nonlinear terms (i.e., trivially), while Eqs. (4) and (5) are advanced by a pseudospectral method.<sup>62,63</sup> All the linear propagation terms of Eqs. (4) and (5) are computed in Fourier space (Landau damping can be easily written in  $k$  space), while the nonlinear term in Eq. (4) is updated in real space. Both the transverse ( $y$  direction) and longitudinal ( $x$  direction) boundary conditions for the fields  $\vec{E}_1$  and  $\delta n$  are assumed to be periodic. Physically, the longitudinal direction should be open. In the longitudinal direction the LW's are strongly damped, however, in the low-density region due to Landau damping, and they are evanescent beyond the quarter-critical density, so there is actually negligible cross-communication and differences between periodic and outgoing boundary conditions should be negligible. Ion fluctuations are strongly damped at both longitudinal boundaries by the addition of a “beach” to ensure there is no recirculation.<sup>29</sup> This can be important for weakly damped IAW.

The distribution function  $\langle F_e \rangle$  is updated less frequently than the envelopes by evolving Eq. (6), neglecting the inverse bremsstrahlung operators, using an alternating-direction implicit (ADI) scheme.<sup>64</sup> At each update of Eq. (6), the Landau-damping term  $\gamma_L$  is updated according to Eq. (8). Although Eqs. (6)–(8) have been written here in the nonrelativistic approximation (for clarity), *QZAK* actually solves their relativistic generalization.

A major assumption used in the derivation of Eq. (6) was that the electron-distribution function is well approximated by its spatial average. It is not evident that this should be so, given that the plasma is (weakly) inhomogeneous. However, recent results using the time-enveloped particle-in-cell code RPIC indicate this to be a valid assumption.<sup>27</sup> This important simplification is very beneficial because it makes large-scale simulations of the nonlinear evolution of TPD using Eqs. (3)–(8) practical, particularly in three dimensions. Three-dimensional simulations are important

since it has been demonstrated that the TPD process is driven by the mutual interaction of multiple laser beams.<sup>21,23,24</sup>

The self-consistent set of equations [Eqs. (3)–(8)] reach, in many cases, a statistical steady state in which it is possible to associate a heat flux associated with suprathermal particles and an anomalous absorption because of all the dissipative processes. Solutions to the velocity-space diffusion equation [Eqs. (6) and (7)] allow one to estimate hot-electron production, which is important if connections are to be made with experiment<sup>16,24,65</sup> and other kinetic modeling.<sup>25,27,28,66–68</sup>

### Aspects of Linear Stability

Two-plasmon decay in a strictly linearly varying density profile was first found to be convectively unstable using an analysis based on the spatial envelope approximation.<sup>2</sup> Later, Simon *et al.*,<sup>6</sup> arguing that the spatial envelope approximation becomes invalid near the LW turning point, showed that two-plasmon decay of a plane EM wave propagating in the direction of the density gradient is absolutely unstable.<sup>3,6,17,69,70</sup> The correct threshold intensity was obtained by Simon *et al.*<sup>6</sup> and is given approximately by

$$I_{14} \approx 1.4 (T_e / 2 \text{ keV}) / (L_n / 330 \text{ } \mu\text{m}) \quad (9)$$

for conditions of current experiments,<sup>16</sup> where  $I_{14}$  is the laser intensity in units of  $10^{14}$  W/cm<sup>2</sup> and  $L_n$  is the density scale length. This threshold condition is plotted in Fig. 134.35. The TPD instability extends to wave numbers outside the region of absolute instability to include modes that have been determined to be convectively unstable,<sup>24,67</sup> with the convective “threshold” intensity a factor of a few times higher for a single-plane EM wave pump.<sup>67</sup> These works<sup>6,24,67</sup> neglected the damping of the decay plasma waves. As can be seen in Fig. 134.35, this is a good approximation since the damping threshold intensity is much smaller than the inhomogeneity threshold at the scale accessible by ~10- to 20-kJ lasers (e.g., OMEGA<sup>71</sup>/OMEGA EP<sup>72</sup>) indicated by the yellow shaded region.

In the opposite (homogeneous) limit, the damping threshold (also shown in Fig. 134.35) is simply given by  $\gamma_0 \gtrsim \nu_{ei}/2$  (cf., e.g., Goldman<sup>1,73</sup> or Kruer<sup>74</sup>) since collisional damping  $\nu_{coll} \sim \nu_{ei}/2$  greatly exceeds Landau damping  $\gamma_L$  for wave numbers  $k \lesssim 0.25 k_D$  in a Maxwellian plasma (i.e.,  $\nu_e \approx \nu_{ei}/2$ ), where  $\gamma_0$  is the temporal growth rate and  $k_D = 1/\lambda_{De}$  is the Debye wave number. A stability analysis of Eq. (4) performed for a single-plane EM wave and taking  $\delta N = 0$  can be shown to give

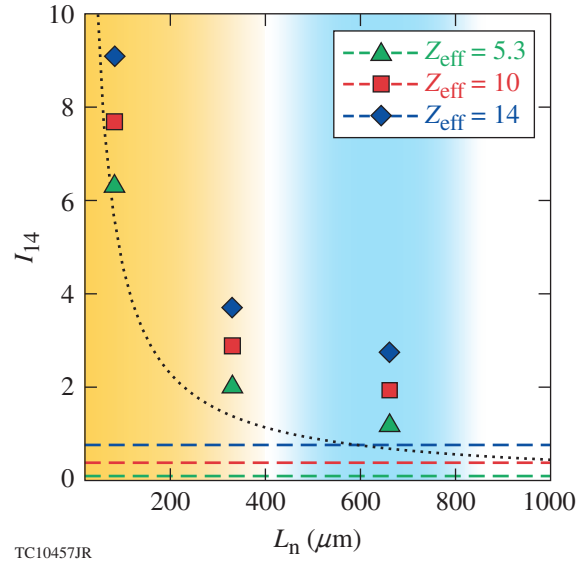


Figure 134.35

The markers show the numerically determined threshold for absolute two-plasmon-decay (TPD) instability of two plane electromagnetic (EM) waves incident at angles of  $\pm 23^\circ$  with respect to a density gradient of scale length  $L_n$  for different values of  $Z_{\text{eff}}$  [and, therefore, collisional Langmuir-wave (LW) damping]. The plotted intensity is the sum of the single-beam intensities. For comparison, the dotted line shows the approximate absolute threshold intensity, in the absence of LW damping, for a single, normally incident plane EM wave<sup>6</sup> as a function of density scale length. The collisional threshold in the absence of plasma inhomogeneity is shown by the horizontal dashed lines for various  $Z_{\text{eff}}$ . In all cases, the electron temperature is given by  $T_e = 2$  keV. The yellow-shaded region indicates scale lengths characteristic of OMEGA experiments, while the blue-shaded region indicates scale lengths for ignition-scale designs.

the expected growth rate [Eq. (1)] and can be simply generalized to the case of multiple EM plane-wave irradiation.<sup>22,24</sup> A similar analysis can be performed including a linear variation in density  $\delta N$ . This results in the same two coupled differential equations (in wave-number space) that have been shown by Simon *et al.* to lead to the approximate threshold condition of Eq. (9) [e.g., Eqs. (3) and (4) in Simon *et al.*<sup>6</sup>].

Equation (4) can be used to compute the properties of linear stability with the combined effect of a density gradient and LW collisional damping, which are described by the terms  $\delta N$  and  $\nu_e$  in Eq. (4), respectively, together with the effects of multibeam irradiation through the boundary conditions applied to Eq. (3). Figure 134.35 shows the numerically determined absolute threshold containing both LW dissipation and plasma inhomogeneity by solving Eq. (4) for two overlapped plane EM waves (see Fig. 134.36). A more-complete stability analysis must take into account the geometry and polarization of laser irradiation for a given experiment<sup>24</sup>—a three-dimensional

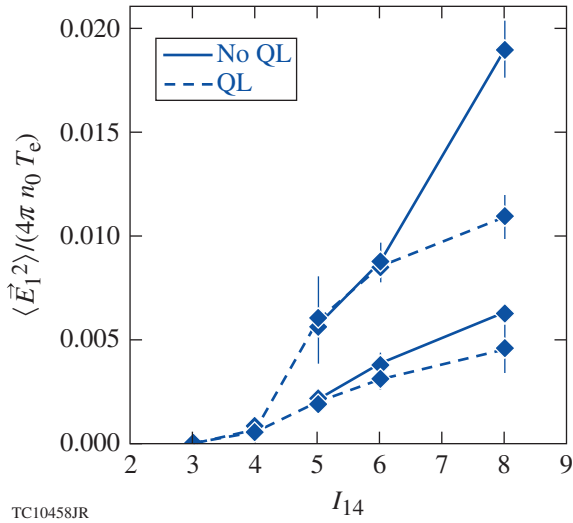


Figure 134.36  
 The electrostatic field intensity  $\langle |\vec{E}_1|^2 \rangle / (4\pi n_0 T_e)$  at nonlinear saturation as a function of laser intensity for a plasma with  $Z_{\text{eff}} = 14$ ,  $L_n = 330 \mu\text{m}$ , and  $T_e = 2 \text{ keV}$ . The dashed (solid) curves show the results with (without) quasi-linear (QL) evolution of the electron-distribution function. The upper and lower sets of two curves correspond to strong ( $\tilde{\nu}_i = 0.1$ ) and weak ( $\tilde{\nu}_i = 0.02$ ) IAW damping, respectively. The error bars indicate the root-mean-square (rms) deviation from the average value at saturation.

problem. Currently, this is being investigated using a new code (ZAK3D) that solves Eqs. (4) and (5) in three dimensions.<sup>75,76</sup>

For ignition-class lasers with  $\sim 1 \text{ MJ}$  of laser energy [e.g., the National Ignition Facility (NIF)<sup>77</sup>], the TPD threshold in direct-drive designs<sup>37</sup> is exceeded by a wider margin than in experiments on OMEGA/OMEGA EP, not because of a significant increase in laser intensity but because of the  $2\times$  to  $3\times$  increase in density scale length. As can be seen in Fig. 134.35, the inhomogeneity threshold is decreased by roughly a factor of 2 to 3. For such scale lengths, the collisional threshold can be made comparable to the inhomogeneity threshold by increasing the effective ionization state  $Z_{\text{eff}} \equiv \langle Z^2 \rangle / \langle Z \rangle$  of the ablator material to  $Z_{\text{eff}} \sim 14$  (e.g., silicon) (for multiple ion-species plasmas, the effective electron-ion collision frequency is obtained by replacing  $Z \rightarrow Z_{\text{eff}}$  in the usual expression for  $\nu_{ei}$ ). From the point of stability with respect to TPD, Fig. 134.35 suggests that increasing the  $Z_{\text{eff}}$  of the ablator is beneficial (for a fixed electron temperature), particularly if TPD is marginally unstable in CH, since satisfactory mid-Z ablators can be designed.<sup>35,36</sup>

All calculations presented in **Nonlinear Saturation** (p. 118) have assumed that the electromagnetic pump consisted of two plane EM waves incident at angles of  $\pm 23^\circ$  with respect to the direction of the density gradient (see Fig. 134.37). The plasma

parameters were chosen to be those of recent long-scale-length experiments in CH targets.<sup>16,65</sup> When  $Z_{\text{eff}}$  was varied, these hydrodynamic parameters were not changed: the electron temperature was  $T_e = 2 \text{ keV}$  with  $T_i = 1.5 \text{ keV}$  for ions. The density scale length was  $L_n = 330 \mu\text{m}$  with the simulation box length  $L_x$  set to include densities from  $0.19 n_c$  to  $0.27 n_c$ , i.e.  $L_x = (8/23) L_n$ . [A separate analysis based on radiation-hydrodynamic simulations has been used to calculate the dependence of plasma parameters (e.g., density scale length and electron temperature) at the quarter-critical surface for different ablator materials with similar irradiation conditions<sup>34</sup> but this will not be discussed here.] When simulating a multiple-ion-species plasma, Eq. (5) was used to simulate an “effective” IAW such that  $Z$  and  $m_i$  were replaced by their averages (over ion species) except in the collisional LW damping rate as mentioned previously. Values of  $Z_{\text{eff}} = 5.3, 10,$  and  $14$  were obtained by modeling CH,  $\text{SiO}_2$ , and Si plasmas, respectively. The IAW damping rate  $\nu_i$  is currently a fixed parameter that is initialized at the start of the calculation. This was equated with the expected Landau-damping rate of the least-damped IAW mode<sup>78,79</sup> for CH,  $\text{SiO}_2$ , and Si, except for the  $Z_{\text{eff}} = 10$  and  $14$  strong damping cases, where  $\tilde{\nu}_i$  was set to  $\tilde{\nu}_i = 0.1$ , where  $\tilde{\nu}_i \equiv \nu_i / \omega_s$  is the dimensionless IAW damping rate and  $\omega_s \simeq kc_s$  is the IAW frequency.

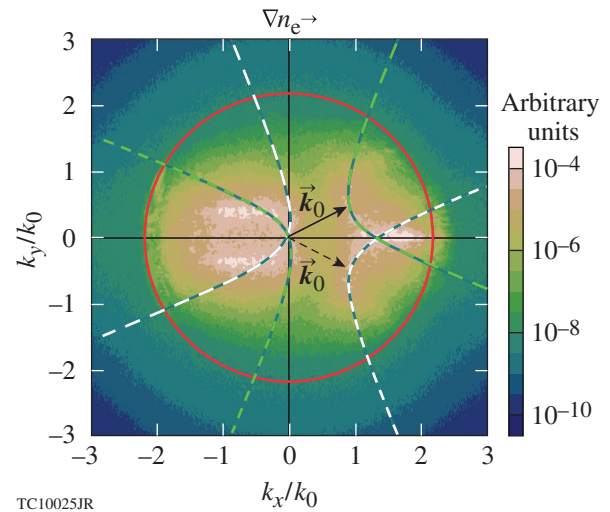


Figure 134.37  
 The time-averaged electrostatic field spectrum  $\langle |\vec{E}_1(\vec{k})|^2 \rangle_\tau$  (in arbitrary units) taken from a representative run at a time when nonlinear saturation has been attained. The instability is driven by two plane EM waves (black arrows) that are incident at an angle of  $\pm 23^\circ$  with respect to the direction of the density gradient ( $x$  direction) and are polarized in the simulation ( $x, y$ ) plane. The green (white) curves show the location of the maximum in growth rate as calculated by homogeneous theory [Eq. (1)]. The red circle indicates the location of the Landau cutoff ( $|\vec{k}| \lambda_{De} = 0.25$ ).

For non-negligible LW amplitudes, the *QZAK* model includes nonlinear coupling to ion fluctuations  $\delta n$ , which introduces a rich variety of nonlinear and turbulent phenomena. It also includes quasi-linear (kinetic) effects. Together, these effects will determine the long-time behavior of TPD relevant to experiment and the relative importance between absolute modes and convective modes in the nonlinear state.

## Nonlinear Saturation

### 1. Anomalous Absorption

#### (Heating of Near-Thermal Electrons)

Several diagnostics have been implemented to quantify the level of two-plasmon-decay instability and its dependence on plasma composition. Figure 134.37 shows the spatially averaged Langmuir-wave intensity  $\langle |\tilde{E}_1|^2 \rangle / 4\pi n_0 T_e$  as a function of laser intensity for  $Z_{\text{eff}} = 14$  at late time, when  $\langle |\tilde{E}_1|^2 \rangle$  is judged to be steady. In all cases, spatial averaging is carried out over the whole simulation box that spans initial densities from  $0.19 n_c$  to  $0.27 n_c$ . It is convenient to define the energy (per unit length in the ignorable coordinate  $z$ ) associated with electrostatic

$$W_1(t) \equiv \int dx dy |\tilde{E}_1(x,y,t)|^2 / (4\pi)$$

and electromagnetic waves

$$W_2(t) \equiv \int dx dy |\tilde{E}_2(x,y,t)|^2 / (8\pi)$$

[which are simply related to the above spatial averages

$$W_1 = A \langle |\tilde{E}_1|^2 \rangle / (4\pi), \quad W_2 = A \langle |\tilde{E}_2|^2 \rangle / (8\pi),$$

where  $A = L_x \times L_y$  is the area of the simulation box]. The effect of the quasi-linear evolution of the distribution function can be seen by comparing the saturated level of  $\langle |\tilde{E}_1|^2 \rangle / 4\pi n_0 T_e$  with and without evolution of Eq. (6) for the spatially averaged electron-distribution function. Previously in Myatt *et al.*,<sup>26</sup> estimates of electron heating by TPD were based on the *ZAK* model using test particles; Fig. 134.37 demonstrates the importance of self-consistently evolving the electron-distribution function. The results are broadly consistent with those anticipated.<sup>26</sup> Figure 134.38 shows a contour plot of the self-consistently evolved electron-distribution function, where significant deviation from the initial Maxwellian distribution is evident.

Figure 134.39 illustrates the dependence of  $\langle |\tilde{E}_1|^2 \rangle / 4\pi n_0 T_e$  (or equivalently  $W_1$ ) on laser intensity for three values of  $Z_{\text{eff}}$  (5.3, 10, and 14) and for weak ( $\tilde{\nu}_i = 0.02$ ) and strong ( $\tilde{\nu}_i = 0.1$ ) ion-acoustic damping. It is evident that for a given ion-acoustic damping rate, the case of  $Z_{\text{eff}} = 14$  has the lowest value of  $W_1$ . Regardless of the value of  $Z_{\text{eff}}$ ,  $W_1$  is smaller if ion-acoustic waves are weakly damped. The saturated value of  $W_1$  can be connected to enhanced absorption of laser energy in the quarter-critical region in the following way: it can be shown

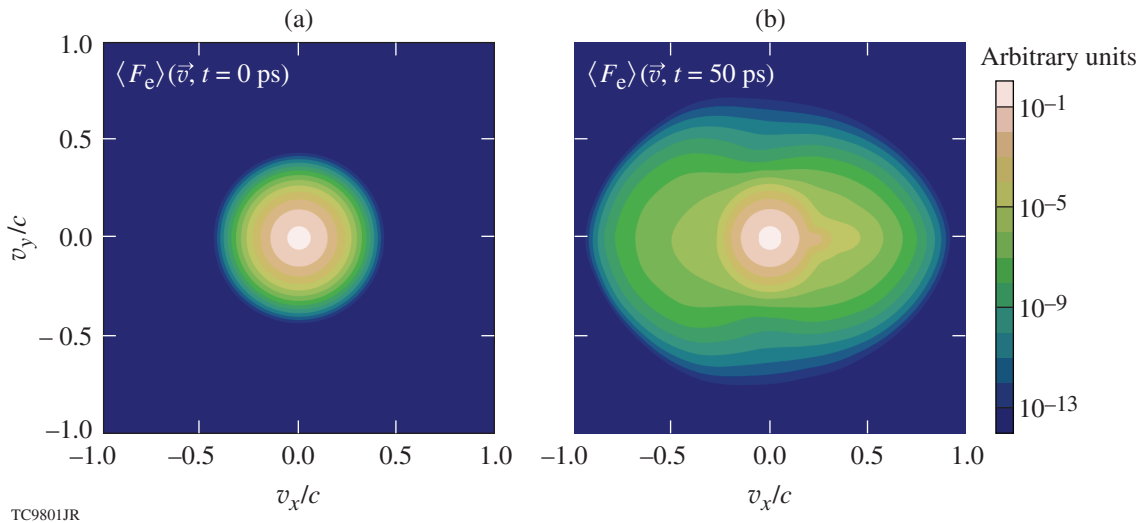
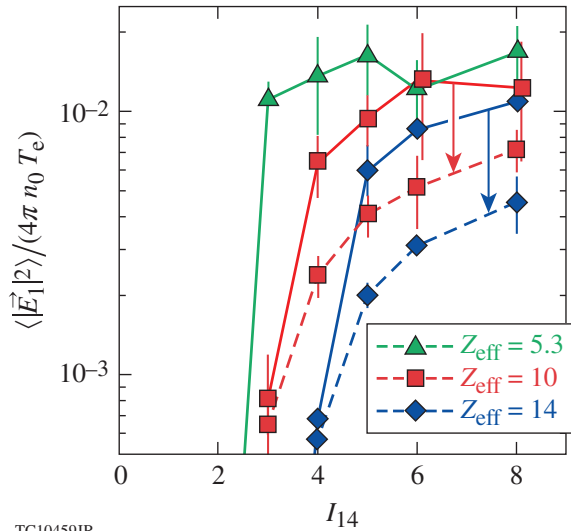


Figure 134.38

The electron distribution function  $\langle F_e \rangle(\vec{v}, t = 0)$  is shown in velocity space at (a)  $t = 0$  ps and (b) at a later time ( $t = 50$  ps) after evolving according to the self-consistent quasi-linear diffusion equation [Eq. (6)].



TC10459JR

Figure 134.39

The electrostatic field intensity  $\langle |\vec{E}_1|^2 \rangle / (4\pi n_0 T_e)$  at nonlinear saturation as a function of total laser intensity for values of  $Z_{\text{eff}} = 5.3$  (green), 10 (red), and 14 (blue), and for weak ( $\tilde{\nu}_1 = 0.02$ ) (dashed) and strong ( $\tilde{\nu}_1 = 0.1$ ) ion-acoustic wave (IAW) damping (solid curves). The error bars give the rms deviation from the mean values. The deviation can become quite significant for the most strongly driven cases.

that the field equations [Eqs. (3)–(5)] satisfy the energy conservation law

$$\partial_t [W_1 + W_2] = -2 \sum_k [\nu_{\text{coll}} + \gamma_L(\vec{k})] \frac{|\vec{E}_1(\vec{k})|^2}{4\pi} - 2\nu_{2,T} W_2 - \int d\vec{s} \cdot \vec{\mathcal{P}}_2, \quad (10)$$

where  $\vec{\mathcal{P}}_2$  is the Poynting vector

$$\vec{\mathcal{P}}_2 = (c^2 / 4\omega_p) i [\vec{E}_2^* \cdot \nabla \vec{E}_2 - \vec{E}_2 \cdot \nabla \vec{E}_2^*]$$

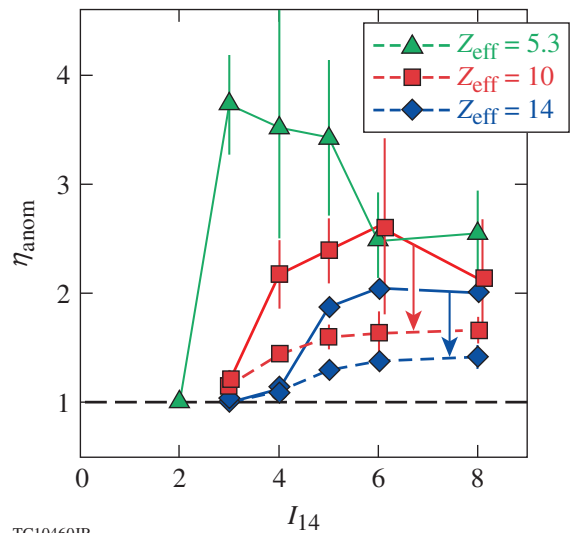
and recalling that  $\nu_{2,T} \approx (n_0 / n_c) \nu_{\text{ei}} / 2$  is the damping rate of the driving EM waves and  $\nu_{\text{coll}} \approx \nu_{\text{ei}} / 2$ . Note that the dissipation associated with ion-acoustic waves does not enter in Eq. (10) because of the smallness of the mass ratio. In statistical steady state, defined by  $\langle \partial_t [W_1 + W_2] \rangle_\tau = 0$ , where  $\langle \rangle_\tau$  implies a running time average,

$$-\langle \int d\vec{s} \cdot \vec{\mathcal{P}}_2 \rangle_\tau = \frac{\nu_{\text{ei}}}{4} \left[ 1 + 4 \frac{\langle W_1 \rangle_\tau}{\langle W_2 \rangle_\tau} \right] \langle W_2 \rangle_\tau + 2 \sum_k \left\langle \gamma_L(\vec{k}) \frac{|\vec{E}_1(\vec{k})|^2}{4\pi} \right\rangle_\tau, \quad (11)$$

which, if  $\gamma_L(\vec{k})$  is positive definite, gives the lower bound for the amount of power dissipated in the quarter-critical region, caused by electron–ion collisions, by the incident electromagnetic waves:

$$-\langle \int d\vec{s} \cdot \vec{\mathcal{P}}_2 \rangle_\tau \geq \frac{\nu_{\text{ei}}}{4} \left[ 1 + 4 \frac{\langle W_1 \rangle_\tau}{\langle W_2 \rangle_\tau} \right] \langle W_2 \rangle_\tau. \quad (12)$$

The term in the square brackets in Eq. (12) is a factor that multiplies the usual collisional energy absorption rate. This factor represents the anomalous (anom) enhancement of laser energy absorption caused by TPD  $\eta_{\text{anom}} \equiv 1 + 4 \langle W_1 \rangle_\tau / \langle W_2 \rangle_\tau$  (the assumption being that absorption is caused by electron–ion collisions and does not involve suprathermal electrons). A value of  $\eta_{\text{anom}} = 1$  would give the usual amount of power dissipated that is associated with collisional absorption of light waves and corresponds to the usual terms present in ICF direct-drive hydrodynamic design codes. This can be estimated, for small absorption, as  $(I_0 - I) / I_0 \approx (\nu_{\text{ei}} / 4) (L_x / c) \sim 0.24$  (for CH). Figure 134.40 shows Fig. 134.39 replotted to illustrate the dependence of  $\eta_{\text{anom}}$  on laser intensity for materials of different ionization  $Z_{\text{eff}}$  and IAW damping rate. These results could be used to modify hydrocode predictions in a simple way by introducing a multiplier ( $\eta_{\text{anom}}$ ) on the usual inverse bremsstrahlung term.



TC10460JR

Figure 134.40

The anomalous absorption factor  $\eta_{\text{anom}}$  [see Eq. (12)] computed as a function of total laser intensity for values of  $Z_{\text{eff}} = 5.3$  (green), 10 (red), and 14 (blue), for weak ( $\tilde{\nu}_1 = 0.02$ ) (dashed) and strong ( $\tilde{\nu}_1 = 0.1$ ) IAW damping (solid curves). The error bars show the rms deviation from the mean value computed at nonlinear saturation.

Figure 134.41 shows the dissipation spectrum

$$\langle \gamma_L(\vec{k}) |\vec{E}_1(\vec{k})|^2 / (4\pi) \rangle_\tau$$

that is associated with suprathermal electron production, i.e., the last term on the right-hand side of Eq. (11). It can be seen that features similar to the linearly unstable LW's exist, but dissipation extends to the Landau cutoff. Comparison of the size of the two terms on the right-hand side of Eq. (11) shows that the first (collisional term) is generally larger than the second, and that pump depletion is important for the more strongly driven runs presented here. It also suggests that the reference electron temperature  $T_e$  should be evolved. A future improvement of the code will be to evolve Eq. (3) self-consistently including pump depletion and collisional absorption. Evolution of the reference electron temperature  $T_e$  will also be considered.

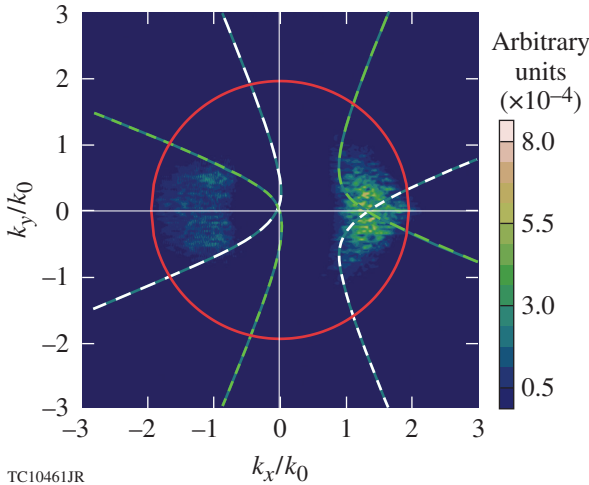


Figure 134.41

A snapshot of the dissipation spectrum  $\gamma_L(\vec{k}) |\vec{E}_1(\vec{k})|^2 / (4\pi)$  (in arbitrary units) that is associated with hot-electron generation and whose sum determines the power dissipated by collisionless processes [Eq. (11)]. As in Fig. 134.36, the green (white) curves show the spectral location of the maximum in TPD growth rate as calculated by homogeneous theory for each beam [Eq. (1)] and the red circle indicates the location of the Landau cutoff ( $|\vec{k}| \lambda_{De} = 0.25$ ).

## 2. The Production of Energetic Electrons

Velocity moments can be taken of Eq. (6) in the usual way to obtain evolution equations for the hydrodynamic variables. For example, an energy equation can be derived from Eqs. (6) and (7) for the spatially averaged electron-distribution function  $\langle F_e \rangle$  (by multiplying by  $m_e v^2/2$  and integrating over velocities) with the result

$$\begin{aligned} \partial_t W_e + A \sum_{i=1}^2 \frac{s_i}{L_i} \Delta Q_i = & \sum_k \gamma_k \frac{|\vec{E}(\vec{k})|^2}{16\pi} \\ & + \int d\vec{v} \frac{1}{2} m v^2 \hat{\sigma}_{IB} \left[ \langle F_e \rangle, |\vec{E}_1|^2 \right] \\ & + \int d\vec{v} \frac{1}{2} m v^2 \hat{\sigma}_{IB} \left[ \langle F_e \rangle, |\vec{E}_{2,T}|^2 \right], \end{aligned} \quad (13)$$

where  $W_e = (m_e/2) \int d\vec{v} v^2 \langle F_e \rangle$  is the total electron kinetic energy. The terms on the right-hand side of Eq. (13) can be identified as the dissipated power associated with the production of suprathermal electrons, the collisional absorption of Langmuir waves, and collisional absorption of the pumping laser (which is usually the only term included in radiation-hydrodynamic calculations). A statistical steady state can exist if these source terms balance the flux through the boundaries, where  $\Delta Q_i \equiv \Delta Q_i^> - \Delta Q_i^< = (q_i^> - q_{i,0}^>) - (q_i^< - q_{i,0}^<)$  and the subscript  $i$  denotes each of the coordinate directions. The heat flux has its usual definition  $\vec{q} \equiv (m_e/2) \int_0^\infty d\vec{v} v^2 \langle F_e \rangle$  with the exception that the integral is split into two parts  $q_i = q_i^< + q_i^>$ , depending on the sign of the velocity component  $v_i$  [i.e., each piece corresponds to either forward-going (>) or backward-going (<) velocities with respect to the  $i$  direction]. The subscript “0” implies that it is calculated with the initial electron-distribution function  $\langle F_e \rangle(t=0)$ . For a symmetric (e.g., Maxwellian) initial distribution,  $\vec{q}_0^> = -\vec{q}_0^<$  and the net heat flux vanishes.<sup>80</sup>

Together with Eq. (10), global energy conservation may be expressed as

$$\partial_t [W_1 + W_2 + W_e] = -A \sum_{i=1}^2 \frac{s_i}{L_i} \Delta Q_i - \int d\vec{s} \cdot \vec{\mathcal{P}}_2 \quad (14)$$

provided that

$$\int d\vec{v} (1/2) m v^2 \hat{\sigma}_{IB} \left[ \langle F_e \rangle, |\vec{E}_1|^2 \right]$$

can be reduced to  $\nu_{ei} \langle W_1 \rangle$  and

$$\int d\vec{v} (1/2) m v^2 \hat{\sigma}_{IB} \left[ \langle F_e \rangle, |\vec{E}_{2,T}|^2 \right]$$

to  $2\nu_{2,T} \langle W_2 \rangle \sim \nu_{ei} \langle W_{2,T} \rangle / 4$ . Therefore, in statistical steady state

$$-\frac{1}{A} \left\langle \int d\vec{s} \cdot \vec{\mathcal{P}}_2 \right\rangle_\tau = \sum_{i=1}^2 \frac{s_i}{L_i} \langle \Delta Q_i \rangle_\tau, \quad (15)$$

and the absorbed power of the laser is balanced by the power flowing through the boundaries carried by the kinetic energy of electrons. For the case where the velocity space diffusion is assumed periodic in the  $i$  direction (which is the  $y$  direction transverse to the density gradient in all the calculations presented here), the corresponding flux term  $\Delta Q_i/L_i$  is absent. Consequently, for doubly periodic boundaries, the only steady-state solution is the trivial one  $\langle \int d\vec{s} \cdot \vec{\mathcal{P}}_2 \rangle_\tau = 0$ . When one boundary is open (e.g., in the direction of the gradient), it corresponds to the use of “thermalizing” boundaries as is often implemented in PIC codes. The applicability of these boundary conditions has been discussed in Myatt *et al.*,<sup>26</sup> where the possibility of the reheating of electrons that pass multiple times through the quarter-critical region was evaluated.

Figure 134.42 shows the hot-electron power fraction  $f_h^{>30}$  as a function of time for two runs that correspond to overlapped laser intensities of  $I_L = 6 \times 10^{14}$  W/cm<sup>2</sup> and an effective ionization of  $Z_{\text{eff}} = 10$  for two values of the ion-acoustic damping rate ( $\tilde{\nu}_i = 0.1$  and 0.02). The fraction  $f_h^{>30}(t)$  is defined as the ratio of the heat flux  $\Delta Q_x$  to the (constant) laser intensity  $I_L$  (in W/cm<sup>2</sup>) with the restriction that the limits on the range of integration in the integral determining the heat flux  $\Delta Q_x$  are adjusted to include only electrons having

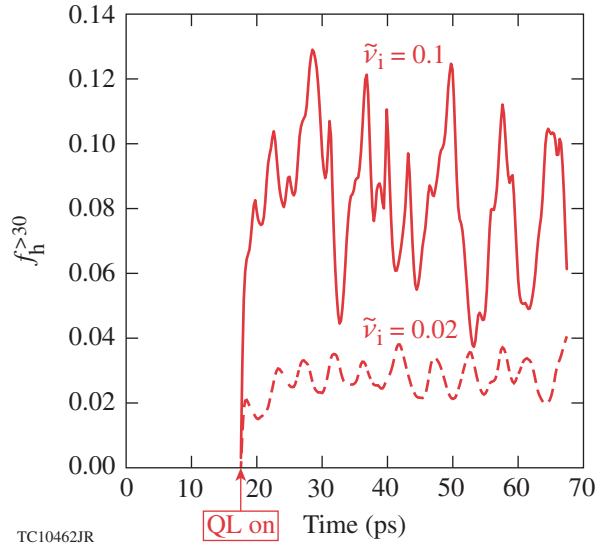


Figure 134.42 The heat flux carried by hot electrons with energies greater than 30 keV as a fraction of the incident laser power as a function of time [ $f_h^{>30}(t)$ ]. These results were obtained for a plasma with  $Z_{\text{eff}} = 10$  and a total laser intensity of  $5 \times 10^{14}$  W/cm<sup>2</sup>. The solid curve corresponds to an ion-acoustic damping rate of  $\tilde{\nu}_i = 0.1$ , while the dashed curve corresponds to  $\tilde{\nu}_i = 0.02$ . In both cases, the runs commence at  $t = 0$  but quasi-linear diffusion is not started until approximately  $t = 17$  ps (as indicated by the arrow).

energies greater than 30 keV (for this reason, the superscript). Experimentally, the fraction  $f_{h,\text{exp}} \equiv E_h/E_L$  is a time-integrated measurement often determined (for a laser pulse of energy  $E_L$ ) by inferring the energy  $E_h$  of suprathermal electrons via the strength of  $K_\alpha$  emission from a fluorescent layer buried in the target.<sup>16</sup> A model of electron–photon transport in matter is used to relate the observed energy in  $K_\alpha$  emission to the energy of hot electrons. For example, a molybdenum layer was used in Yaakobi *et al.*<sup>16</sup> having  $E_{K_\alpha} \approx 17.5$  keV [which justifies our cutoff energy of 30 keV in the definition of  $f_h^{>30}(t)$ ]. To facilitate a comparison with experiment, we define a running time average  $\langle f_h^{>30} \rangle_\tau$ . It can be seen from Fig. 134.42 that it is often possible to define a meaningful steady state so that  $\langle f_h^{>30} \rangle_\tau$  is constant (and can be crudely equated with the experimental energy fraction  $\langle f_h^{>30} \rangle_\tau \sim f_{h,\text{exp}}$ ). This steady-state time average (for  $\tau > 35$  ps) is plotted in Fig. 134.43 for materials of varying  $Z_{\text{eff}}$  and  $\tilde{\nu}_i$ .

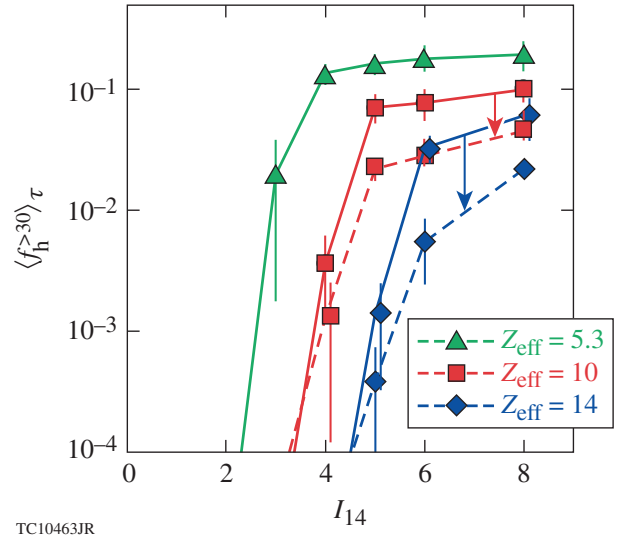


Figure 134.43 Hot-electron fraction  $\langle f_h^{>30} \rangle_\tau$ , as determined at nonlinear saturation as a function of total laser intensity for  $Z_{\text{eff}} = 5.3$  (green curve), 10 (red curve), and 14 (blue curve). The solid curves indicate runs with an IAW damping rate of  $\tilde{\nu}_i = 0.1$ , while the dashed curves correspond to  $\tilde{\nu}_i = 0.02$ . The error bars quantify the rms fluctuations about the average that is associated with the steady state.

Figure 134.43 shows the main results of this study. It can be seen that the hot-electron fraction  $\langle f_h^{>30} \rangle_\tau$  increases rapidly for  $I_L \gtrsim 3$  to  $5 \times 10^{14}$  W/cm<sup>2</sup> (with a threshold depending on  $Z_{\text{eff}}$ ) and then saturates at the level of several percent for CH targets, which is broadly consistent with PIC calculations<sup>27,68</sup> when electron–ion collisions are accounted for (in the RPIC calculations of Vu *et al.*,<sup>27</sup> grid damping plays the role of elec-

tron-ion collisions), and also experimental measurements<sup>65</sup> (the density scale length, electron temperature, and laser intensities were motivated by OMEGA EP experimental conditions using CH targets<sup>65</sup>). Calculations of SiO<sub>2</sub> targets, having weak ion-acoustic wave damping ( $\tilde{\nu}_i = 0.02$ ), show a similar intensity dependence but saturate at a level approximately half that of CH targets, while calculations of Si targets ( $Z_{\text{eff}} = 14$ ,  $\tilde{\nu}_i = 0.02$ ) had the lowest hot-electron fraction of all, which is particularly pronounced at mid-intensities ( $I_L \sim 5 \times 10^{14}$  W/cm<sup>2</sup>). In part, this is due to the effect of the increased threshold for Si associated with the Langmuir-wave damping (see Fig. 134.35).

*In general, the lowest hot-electron production was seen for materials with the highest  $Z_{\text{eff}}$  and the smallest ion-acoustic wave damping  $\tilde{\nu}_i = 0.02$ . This suggests CH ablaters might not be the best choice of ablator material from the point of view of TPD.*

### 3. Confirmation of the Sensitivity to Ion-Acoustic Damping Using RPIC Calculations

Two 2-D RPIC simulations that do not make the quasi-linear approximation or any assumption regarding the spatial uniformity of the electron distribution function were performed to independently investigate the effect of the IAW damping rate on the development and saturation of TPD.

Over 50 QZAK calculations were performed in the current analysis, most for a long density scale length ( $L_n = 330$   $\mu\text{m}$ ) and integrated out to times close to  $\sim 0.1$  ns ( $\sim 5$  ns in combined total). Because RPIC calculations are much more computationally intensive than QZAK, the RPIC calculations were performed at a shorter scale length ( $L_n = 130$   $\mu\text{m}$ ) and integrated for shorter times ( $t = 9$  ps). The ion-acoustic damping rate was modified by varying the ion Landau-damping contribution to  $\tilde{\nu}_i$  through the ion temperature [a hydrogen ( $Z = 1$ ) plasma was assumed]. All other physical parameters were the same as described earlier for the QZAK calculations.

The two RPIC simulations used identical simulation domains consisting of 4096 ( $x$  direction)  $\times$  1024 ( $y$  direction) computational cells, and the electron and proton distributions were each represented by 32 particles/computational cell. The boundary conditions were compatible with those assumed by QZAK [see **Numerical Simulation of TPD Growth and Saturation in Inhomogeneous Collisional Plasma** (p. 113) and **The Production of Energetic Electrons** (p. 120)]: the particles were recycled periodically in the  $y$  direction and absorbed at the surfaces  $x = 0$  (laser entrance boundary) and  $x = L_x$  (laser exit

boundary). At these boundaries, Maxwellian baths of electrons with temperature  $T_e$  and ions with temperature  $T_i$  were assumed, and the particles absorbed at these surfaces were replenished accordingly. Each of the two incident pump plane EM waves was given an intensity of  $I_0 = 1 \times 10^{15}$  W/cm<sup>2</sup> with polarization in the  $x$ - $y$  plane.

The so-called “low” and “high” IAW damping simulations correspond to  $T_i = 0.1$  keV ( $T_e/T_i = 20$  and  $\tilde{\nu}_i \approx 1.11 \times 10^{-3}$ ) (electron Landau damping of IAW is not present in RPIC) and  $T_i = 1$  keV ( $T_e/T_i = 2$  and  $\tilde{\nu}_i \approx 2.70 \times 10^{-1}$ ), respectively. The high-damping case has been presented elsewhere,<sup>27,28</sup> but the results are reproduced here for comparison. Figure 134.44 shows the suprathermal heat flux  $f_h$  ( $\Delta Q_x^>$  normalized to the total laser intensity) as a function of time over a period of 10 ps for both cases. In the simulations,  $\Delta Q_x^>$  is computed from the electron flux accumulated at the laser exit boundary ( $x = L_x$ ) accounting for electrons of all energies. As before [The **Production of Energetic Electrons** (p. 120)],  $\Delta Q_x^>$  represents the electron heat flux in excess of its initial (Maxwellian) value.

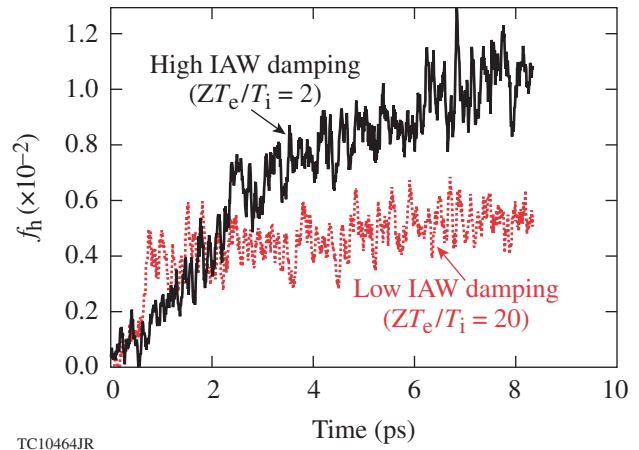


Figure 134.44

The suprathermal heat flux  $f_h$ , as computed by the code RPIC,<sup>27</sup> is shown as a function of time for cases of high ( $\tilde{\nu}_i \approx 2.70 \times 10^{-1}$ ) and low ( $\tilde{\nu}_i \approx 1.11 \times 10^{-3}$ ) IAW damping. While the low-damping case reaches saturation much more quickly, its saturation level is lower.

Figure 134.44 indicates that both the high-damping and low-damping cases reached saturation, and that the high-damping case achieved a suprathermal heat flux  $\Delta Q_x^>$  about twice as large as that of the low-damping case. Furthermore, while the high-damping case took several ( $\sim 10$ ) picoseconds to reach saturation, the low-damping case achieved saturation in about

0.5 ps. The comparison shown in Fig. 134.44 presents supporting evidence that the IAW damping rate has an important effect on the temporal development and saturation level of TPD.

The RPIC simulation corresponding to high  $\bar{v}_i$  and shown in Fig. 134.44 has been previously analyzed in some detail.<sup>27,28</sup> The nonlinear state was described in terms of cavitating LW turbulence, and it was determined that prerequisites for the quasi-linear description were met—i.e., the distribution function was well described by its spatial average and trapping effects were negligible.<sup>28</sup> A comparison between RPIC and *QZAK* is given in Vu *et al.*,<sup>81</sup> but we speculate here on the importance of the ion-acoustic damping rate in the context of cavitating LW turbulence.

#### 4. Dependence of $\langle f_h \rangle$ on the IAW Damping Rate and Nucleation Dynamics

The significant sensitivity of the saturated level of TPD excitation on the IAW damping rate is clearly a nonlinear effect since the linear theory does not involve IAW's. Such sensitivity might be anticipated since it has been observed in previous *ZAK* model studies of SRS in the weak Landau-damping regime.<sup>29</sup> Previous work<sup>30–32</sup> has also demonstrated that nucleation of cavitons is favored by strong IAW damping. The detailed manifestation of this for the simulation regime considered here is under study. A qualitative summary of our current view is based on the assumption that Langmuir cavitation and collapse are the dominant processes in the nonlinear stage of TPD for the parameters considered.<sup>28</sup>

In the cavitating turbulence scenario, the level of electrostatic fluctuations is governed by the nucleation–collapse–burnout cycle<sup>82,83</sup> and the time scale of this process is governed by the IAW damping rate.<sup>27</sup> The interference pattern of the linearly excited triad of free plane LW's (see Fig. 134.36) produces density trenches that are modulated longitudinally by the beating of the forward common LW with the backward pair of triad waves. The ponderomotive force from the peaks in  $|\tilde{E}_1|^2$  resulting from this modulation produces density depressions that can support localized (or bound) states of the Langmuir field. The backward triad waves have long wavelengths and frequencies near the local electron plasma frequency and can directly nucleate the bound state.<sup>82,83</sup> These localized states then proceed to collapse and burn out, producing a large enhancement of LW energy and electron flux. As the triad modes evolve to higher  $k$  values,<sup>28</sup> the spatial scale of the longitudinal modulation appears to produce much stronger, smaller-scale density cavities in the trenches.

These residual cavities appear to be too narrow and deep to efficiently nucleate new cavitons. The Langmuir turbulence then dies out locally until the short-scale density fluctuations dissipate by IAW Landau damping. The nucleation process can then resume with another burst of Langmuir turbulence once this has occurred.

In the nucleation–collapse–burnout cycle,<sup>82,83</sup> a source must be present that can excite the bound state. The nucleation source is essentially the overlap integral of the bound-state wave function and the source, which may be the TPD current on the right-hand side of Eq. (4). This source produces freely propagating LW's that are dominantly the triad modes discussed recently.<sup>27,28</sup> If this source has frequencies close enough to the bound-state eigenfrequency, it can cause a near-resonant excitation of the bound state and initiate a collapse. To have such frequencies, free LW's must have long wavelengths such that the bound-state wave function having the largest overlap integral with this long-wavelength source is the lowest or “ground state” with no nodes in its wave function. Our experience is that only this state is appreciably excited. A density well that is too deep may have a deeply bound ground-state wave function, which will not efficiently couple to a long-wavelength free LW. This means that for efficient nucleation, the density well should not be too deep, implying that the spatial width should be large enough to trap a weakly bound ground state. Strong IAW damping appears to produce more cavities of this type (because of this nucleation effect, the LDI cascade, where LW's decay into LW's with increasingly lower wavelengths, never progresses past a few steps before cavitons are nucleated in the ion-density fluctuations created by the LDI process itself).<sup>29</sup> For these TPD simulations, LDI appears to play a minor role, while the TPD triad<sup>25</sup> and the ion-density fluctuations arising from their beating play a similar role in the nucleation process.

It is very difficult to diagnose, in microscopic detail, a system with as many as  $10^4$  cavitons.<sup>28</sup> The scenario outlined above is consistent with our experience with simpler systems. Further microscopic details will be presented in a future publication.

#### Summary and Discussion

A two-dimensional model that further generalizes the extended Zakharov model of TPD to include quasi-linear diffusion of the electron distribution function has been described. The model addresses the nonlinear evolution of the TPD instability caused by the self-consistent coupling of TPD-generated LW's with ion-density fluctuations and quasi-linear evolution of the electron-distribution function. Quasi-linear evolution of

the electron-distribution function was shown to lead to saturation of the average LW intensity at lower values than predicted by the Zakharov model alone for parameters of interest to recent experiments.

In the linear regime of infinitesimal LW amplitude, the model allows for TPD stability to be determined in the presence of both density inhomogeneity and LW damping for a laser pump described in terms of multiple overlapping plane EM waves in two dimensions. A more-complete treatment requires the model to be solved in three dimensions. A 3-D code solving Eqs. (4) and (5) but omitting the quasi-linear diffusion terms is described in Zhang *et al.*<sup>76</sup> It was shown that collisional damping of LW's is important for directly driven ICF targets at the ignition scale. In the nonlinear stage of TPD it was shown that the energy absorbed by the target and converted into electron thermal energy by the collisional absorption of TPD LW's is comparable to, or greater than, the energy converted into hot electrons. It was suggested that maximizing the collisional damping of LW's in direct-drive designs could be beneficial in mitigating TPD absorption and preheat.

For fixed electron temperature and density scale length, the lowest hot-electron production was seen for materials with the highest  $Z_{\text{eff}}$  and the smallest IAW damping rate. The reduction in hot-electron fraction can be partly explained by the increased threshold. The nonlinear effect associated with weakly damped ion-acoustic waves was independently investigated with RPIC calculation, and a possible physical explanation for this effect was given in terms of nucleation dynamics of cavitating Langmuir turbulence. An experimental test might be to compare TPD in two materials of similar  $Z_{\text{eff}}$ , e.g., Si- and Ge-doped plastic, where the second material has a greater IAW damping rate because of the presence of light (H) ions.

Future improvements to the *QZAK* model will include implementation of terms describing the effects of pump depletion and collisional absorption for the EM pump. Self-consistent evolution of the reference electron temperature will also be investigated. Work is also underway to implement the quasi-linear diffusion equation in three dimensions.

#### ACKNOWLEDGMENT

This work was supported by the U.S. Department of Energy Office of Inertial Confinement Fusion under Cooperative Agreement No. DE-FC52-08NA28302, the University of Rochester, and the New York State Energy Research and Development Authority. The support of DOE does not constitute an endorsement by DOE of the views expressed in this article.

#### REFERENCES

1. M. V. Goldman, *Ann. Phys.* **38**, 117 (1966).
2. M. N. Rosenbluth, *Phys. Rev. Lett.* **29**, 565 (1972).
3. Y. C. Lee and P. K. Kaw, *Phys. Rev. Lett.* **32**, 135 (1974).
4. V. P. Silin and A. N. Starodub, *Sov. Phys.-JETP* **39**, 82 (1974).
5. A. B. Langdon, B. F. Lasinski, and W. L. Kruer, *Phys. Rev. Lett.* **43**, 133 (1979).
6. A. Simon, R. W. Short, E. A. Williams, and T. Dewandre, *Phys. Fluids* **26**, 3107 (1983).
7. H. Derblom *et al.*, *J. Geophys. Res., A, Space Phys.* **94**, 10111 (1989).
8. D. W. Phillion *et al.*, *Phys. Rev. Lett.* **49**, 1405 (1982).
9. W. Seka, R. E. Bahr, R. W. Short, A. Simon, R. S. Craxton, D. S. Montgomery, and A. E. Rubenchik, *Phys. Fluids B* **4**, 2232 (1992).
10. S. P. Regan, N. B. Meezan, L. J. Suter, D. J. Strozzi, W. L. Kruer, D. Meeker, S. H. Glenzer, W. Seka, C. Stoeckl, V. Yu. Glebov, T. C. Sangster, D. D. Meyerhofer, R. L. McCrory, E. A. Williams, O. S. Jones, D. A. Callahan, M. D. Rosen, O. L. Landen, C. Sorce, and B. J. MacGowan, *Phys. Plasmas* **17**, 020703 (2010).
11. W. Seka, D. H. Edgell, J. F. Myatt, A. V. Maximov, R. W. Short, V. N. Goncharov, and H. A. Baldis, *Phys. Plasmas* **16**, 052701 (2009).
12. N. A. Ebrahim *et al.*, *Phys. Rev. Lett.* **45**, 1179 (1980).
13. H. A. Baldis and C. J. Walsh, *Phys. Rev. Lett.* **47**, 1658 (1981).
14. D. M. Villeneuve, R. L. Keck, B. B. Afeyan, W. Seka, and E. A. Williams, *Phys. Fluids* **27**, 721 (1984).
15. C. Rousseaux *et al.*, *Phys. Fluids B* **4**, 2589 (1992).
16. B. Yaakobi, P.-Y. Chang, A. A. Solodov, C. Stoeckl, D. H. Edgell, R. S. Craxton, S. X. Hu, J. F. Myatt, F. J. Marshall, W. Seka, and D. H. Froula, *Phys. Plasmas* **19**, 012704 (2012).
17. C. S. Liu and M. N. Rosenbluth, *Phys. Fluids* **19**, 967 (1976).
18. B. B. Afeyan and E. A. Williams, *Phys. Rev. Lett.* **75**, 4218 (1995).
19. E. Z. Gusakov, *Sov. J. Plasma Phys.* **8**, 324 (1982).
20. G. Laval, R. Pellat, and D. Pesme, *Phys. Rev. Lett.* **36**, 192 (1976).
21. C. Stoeckl, R. E. Bahr, B. Yaakobi, W. Seka, S. P. Regan, R. S. Craxton, J. A. Delettrez, R. W. Short, J. Myatt, A. V. Maximov, and H. Baldis, *Phys. Rev. Lett.* **90**, 235002 (2003).
22. D. F. DuBois, B. Bezzeridels, and H. A. Rose, *Phys. Fluids B* **4**, 241 (1992).
23. R. W. Short, *Bull. Am. Phys. Soc.* **53**, 245 (2008).

24. D. T. Michel, A. V. Maximov, R. W. Short, S. X. Hu, J. F. Myatt, W. Seka, A. A. Solodov, B. Yaakobi, and D. H. Froula, *Phys. Rev. Lett.* **109**, 155007 (2012).
25. H. X. Vu, D. F. DuBois, D. A. Russell, and J. F. Myatt, *Phys. Plasmas* **17**, 072701 (2010).
26. J. F. Myatt, J. Zhang, J. A. Delettrez, A. V. Maximov, R. W. Short, W. Seka, D. H. Edgell, D. F. DuBois, D. A. Russell, and H. X. Vu, *Phys. Plasmas* **19**, 022707 (2012).
27. H. X. Vu, D. F. DuBois, J. F. Myatt, and D. A. Russell, *Phys. Plasmas* **19**, 102703 (2012).
28. H. X. Vu, D. F. DuBois, D. A. Russell, and J. F. Myatt, *Phys. Plasmas* **19**, 102708 (2012).
29. D. A. Russell, D. F. DuBois, and H. A. Rose, *Phys. Plasmas* **6**, 1294 (1999).
30. D. F. DuBois *et al.*, *Phys. Fluids B* **5**, 2616 (1993).
31. D. F. DuBois *et al.*, *J. Geophys. Res.* **98**, 17543 (1993).
32. D. F. DuBois, D. A. Russell, and H. A. Rose, *Phys. Rev. Lett.* **74**, 3983 (1995).
33. V. A. Smalyuk, R. Betti, J. A. Delettrez, V. Yu. Glebov, D. D. Meyerhofer, P. B. Radha, S. P. Regan, T. C. Sangster, J. Sanz, W. Seka, C. Stoeckl, B. Yaakobi, J. A. Frenje, C. K. Li, R. D. Petrasso, and F. H. Séguin, *Phys. Rev. Lett.* **104**, 165002 (2010).
34. S. X. Hu, D. T. Michel, D. H. Edgell, D. H. Froula, R. K. Follett, V. N. Goncharov, J. F. Myatt, S. Skupsky, and B. Yaakobi, *Phys. Plasmas* **20**, 032704 (2013).
35. R. Betti, R. Nora, M. Lafon, J. F. Myatt, and K. S. Anderson, *Bull. Am. Phys. Soc.* **57**, 154 (2012).
36. M. Lafon, R. Nora, and R. Betti, *Bull. Am. Phys. Soc.* **57**, 153 (2012).
37. V. N. Goncharov, T. C. Sangster, T. R. Boehly, S. X. Hu, I. V. Igumenshchev, F. J. Marshall, R. L. McCrory, D. D. Meyerhofer, P. B. Radha, W. Seka, S. Skupsky, C. Stoeckl, D. T. Casey, J. A. Frenje, and R. D. Petrasso, *Phys. Rev. Lett.* **104**, 165001 (2010).
38. V. E. Zakharov, *Sov. Phys.-JETP* **35**, 908 (1972).
39. A. Hasegawa, *Phys. Rev. A* **1**, 1746 (1970).
40. R. C. Davidson, *Methods in Nonlinear Plasma Theory* (Academic Press, New York, 1972).
41. P. A. Robinson, *Rev. Mod. Phys.* **69**, 507 (1997).
42. M. V. Goldman, *Rev. Mod. Phys.* **56**, 709 (1984).
43. P. Y. Cheung and A. Y. Wong, *Phys. Rev. Lett.* **55**, 1880 (1985).
44. A. Y. Wong and P. Y. Cheung, *Phys. Rev. Lett.* **52**, 1222 (1984).
45. B. Eliasson and B. Thidé, *J. Geophys. Res., A, Space Phys.* **113**, A02313 (2008).
46. D. A. Russell and D. F. DuBois, *Phys. Rev. Lett.* **86**, 428 (2001).
47. J. Briand *et al.*, *Phys. Fluids B* **2**, 160 (1990).
48. J. C. Weatherall, *Astrophys. J.* **506**, 341 (1998).
49. A. Hanssen *et al.*, *J. Geophys. Res., A, Space Phys.* **97**, 12,073 (1992).
50. D. F. DuBois, H. A. Rose, and D. Russell, *Phys. Rev. Lett.* **66**, 1970 (1991).
51. D. F. DuBois and M. V. Goldman, *Phys. Rev.* **164**, 207 (1967).
52. A third-harmonic envelope could be used to describe  $3/2\omega_0$  emission, as in Ref. 46.
53. A. N. Starodub and M. V. Filippov, *Sov. J. Plasma Phys.* **5**, 610 (1979).
54. V. Yu. Bychenkov, V. P. Silin, and V. T. Tikhonchuk, *Sov. J. Plasma Phys.* **3**, 730 (1977).
55. R. L. Berger and L. V. Powers, *Phys. Fluids* **28**, 2895 (1985).
56. W. Seka, B. B. Afeyan, R. Boni, L. M. Goldman, R. W. Short, K. Tanaka, and T. W. Johnston, *Phys. Fluids* **28**, 2570 (1985).
57. V. E. Zakharov, in *Handbook of Plasma Physics*, edited by M. N. Rosenbluth and R. Z. Sagdeev, Volume 2: Basic Plasma Physics II, edited by A. A. Galeev and R. N. Sudan (Elsevier Science Publishers B.V., Amsterdam, 1984), Chap. 5.3, pp. 81–121.
58. P. Mounaix *et al.*, *Phys. Fluids B* **3**, 1392 (1991).
59. J. Dawson and C. Oberman, *Phys. Fluids* **5**, 517 (1962).
60. A series of runs were performed to investigate the sensitivity of the saturated state (described in terms of LW excitation level and hot-electron flux) to the LW noise level. No significant difference was found when varying the intensity of LW noise over two orders of magnitude.
61. K. Y. Sanbonmatsu *et al.*, *Phys. Plasmas* **7**, 2824 (2000).
62. B. Fornberg, *A Practical Guide to Pseudospectral Methods*, Cambridge Monographs on Applied and Computational Mathematics, Vol. 1 (Cambridge University Press, Cambridge, England, 1998).
63. O. Skjaeraasen, P. A. Robinson, and D. L. Newman, *Phys. Plasmas* **18**, 022103 (2011).
64. D. Peaceman and H. H. Rachford, Jr., *J. Soc. Indust. Appl. Math.* **3**, 28 (1955).
65. D. H. Froula, B. Yaakobi, S. X. Hu, P.-Y. Chang, R. S. Craxton, D. H. Edgell, R. Follett, D. T. Michel, J. F. Myatt, W. Seka, R. W. Short, A. Solodov, and C. Stoeckl, *Phys. Rev. Lett.* **108**, 165003 (2012).
66. R. Yan, A. V. Maximov, C. Ren, and F. S. Tsung, *Phys. Rev. Lett.* **103**, 175002 (2009).
67. R. Yan, A. V. Maximov, and C. Ren, *Phys. Plasmas* **17**, 052701 (2010).
68. R. Yan, C. Ren, J. Li, A. V. Maximov, W. B. Mori, Z. M. Sheng, and F. S. Tsung, *Phys. Rev. Lett.* **108**, 175002 (2012).

69. C. S. Liu, in *Advances in Plasma Physics*, edited by A. Simon and W. B. Thompson (Wiley-Interscience, New York, 1976), Vol. 6, pp. 167–174.
70. B. F. Lasinski and A. B. Langdon, Lawrence Livermore National Laboratory, Livermore, CA, Report UCRL-50021-77, 4-49 (1978).
71. T. R. Boehly, D. L. Brown, R. S. Craxton, R. L. Keck, J. P. Knauer, J. H. Kelly, T. J. Kessler, S. A. Kumpan, S. J. Loucks, S. A. Letzring, F. J. Marshall, R. L. McCrory, S. F. B. Morse, W. Seka, J. M. Soures, and C. P. Verdon, *Opt. Commun.* **133**, 495 (1997).
72. L. J. Waxer, D. N. Maywar, J. H. Kelly, T. J. Kessler, B. E. Kruschwitz, S. J. Loucks, R. L. McCrory, D. D. Meyerhofer, S. F. B. Morse, C. Stoeckl, and J. D. Zuegel, *Opt. Photonics News* **16**, 30 (2005); D. N. Maywar, J. H. Kelly, L. J. Waxer, S. F. B. Morse, I. A. Begishev, J. Bromage, C. Dorrer, J. L. Edwards, L. Folsbee, M. J. Guardalben, S. D. Jacobs, R. Jungquist, T. J. Kessler, R. W. Kidder, B. E. Kruschwitz, S. J. Loucks, J. R. Marciante, R. L. McCrory, D. D. Meyerhofer, A. V. Okishev, J. B. Oliver, G. Pien, J. Qiao, J. Puth, A. L. Rigatti, A. W. Schmid, M. J. Shoup III, C. Stoeckl, K. A. Thorp, and J. D. Zuegel, *J. Phys., Conf. Ser.* **112**, 032007 (2008).
73. M. V. Goldman, *Ann. Phys.* **38**, 95 (1966).
74. W. L. Kruer, in *The Physics of Laser Plasma Interactions*, *Frontiers in Physics*, Vol. 73, edited by D. Pines (Addison-Wesley, Redwood City, CA, 1988).
75. J. Zhang, J. F. Myatt, A. V. Maximov, R. W. Short, D. F. DuBois, D. A. Russell, and H. X. Vu, *Bull. Am. Phys. Soc.* **57**, 299 (2012).
76. J. Zhang, J. F. Myatt, R. W. Short, A. V. Maximov, H. X. Vu, D. F. DuBois, and D. A. Russell, “Multibeam Two-Plasmon Decay from Linear Threshold to Nonlinear Saturation,” to be published in *Physical Review Letters*.
77. W. J. Hogan, E. I. Moses, B. E. Warner, M. S. Sorem, and J. M. Soures, *Nucl. Fusion* **41**, 567 (2001); E. I. Moses, *Fusion Sci. Technol.* **54**, 361 (2008).
78. H. X. Vu, J. M. Wallace, and B. Bezzerides, *Phys. Plasmas* **1**, 3542 (1994).
79. E. A. Williams, R. L. Berger, R. P. Drake, A. M. Rubenchik, B. S. Bauer, D. D. Meyerhofer, A. C. Gaeris, and T. W. Johnston, *Phys. Plasmas* **2**, 129 (1995).
80. The assumption that the reference distribution function is Maxwellian is not quite correct because there is expected to be a nonvanishing heat flux at the quarter-critical surface. Future work will take this into account, where it is speculated that heat-carrying electrons propagating down the density gradient may be able to couple more efficiently with TPD-generated Langmuir waves.
81. H. X. Vu, D. F. DuBois, D. A. Russell, and J. F. Myatt, *Phys. Plasmas* **19**, 102708 (2012).
82. G. D. Doolen, D. F. DuBois, and H. A. Rose, *Phys. Rev. Lett.* **54**, 804 (1985).
83. D. A. Russell, D. F. DuBois, and H. A. Rose, *Phys. Rev. Lett.* **60**, 581 (1988).

---

# Hot-Electron Generation from Laser/Pre-Plasma Interactions in Cone-Guided Fast Ignition

## Introduction

The cone-guided scheme for fast-ignition inertial confinement fusion (ICF)<sup>1,2</sup> provides the potential of higher gains at lower total driver energy than conventional central hot-spot-ignition schemes. In this scheme, a spherical target with a hollow gold cone attached is first compressed by laser beams outside the cone and then ignited by a petawatt (PW) short ignition pulse launched into the cone. The cone keeps the plasma out during the compression so that the ignition pulse can reach the cone tip and generate MeV electrons close to the assembled fuel core. Given the angular spread of laser-generated hot electrons, keeping the hot-electron source closer to the assembled core is important to the success of fast ignition. Early Gekko XII experiments with the cone-guided scheme showed good laser-core coupling.<sup>2,3</sup> Recent scaled-up integrated experiments on OMEGA/OMEGA EP showed, however, a lower coupling efficiency.<sup>4</sup>

One of the important factors affecting the laser-core coupling efficiency is the pre-plasma inside the cone.<sup>5</sup> The pre-plasma is generated by an ~1-mJ laser prepulse from amplified spontaneous emission in the PW ignition pulse. Previous experiments and simulations<sup>5-7</sup> have shown that the pre-plasma can significantly reduce the forward-going hot-electron flux. The interaction of the main ignition pulse with the pre-plasma depends on the duration of the ignition pulse, as indicated by recent particle-in-cell (PIC) simulations of laser channeling<sup>8,9</sup> for the channeling/hole-boring fast-ignition scheme. The duration of the short pulse in the early work was of the order of 1 ps (Refs. 5 and 7), and was shorter than the 10-ps pulse in the OMEGA experiment.<sup>4</sup> The required pulse duration for ignition, producing an electron beam with tens of kilojoules of energy,<sup>10</sup> would be 10 to 20 ps. PIC simulations with longer ignition-pulse durations can help answer questions such as whether a longer ignition pulse can essentially push away the pre-plasma to interact mostly with the cone tip.

Here we present recent PIC simulations using *OSIRIS*<sup>11</sup> to study hot-electron generation and their transport in plasma at densities up to  $100 n_c$ , where  $n_c = 1 \times 10^{21} \text{ cm}^{-3}$  is the critical density of 1.053- $\mu\text{m}$  laser light, as used in the cone-in-shell

integrated fast-ignition experiments at the Omega Laser Facility.<sup>4</sup> The simulations are 2-D in space and 3-D in velocity. The pulse duration in the simulations was 6.7 ps, comparable to the 10-ps OMEGA EP pulse. To achieve these simulations, we used an artificial drag force<sup>12</sup> to slow down hot electrons after they leave the laser-interaction region. This prevented the hot electrons from accumulating near the simulation box boundaries and interrupting the simulations. Combined with particle thermal boundary conditions, this also reduced the effects of a finite box size on laser-plasma interactions. The simulations showed that the generated hot electrons were dominated in number by low-energy electrons but in energy by multi-MeV electrons. The hot electrons had a mean half-angle of  $68^\circ$ . Except for differences during the early stage of the pulse, *s*- and *p*-polarizations showed similar accumulated laser-absorption rates and hot-electron characteristics. The electron transport in the density region from  $5 n_c$  to  $100 n_c$  was ballistic, which may make it possible to use the current results for further transport study.

The following sections describe the simulation setup and results, which are then discussed and summarized.

## Simulation Setup

The simulation setup is shown in Fig. 134.45(a). Three species of particles were used in the simulations: the electrons (Species 1) and ions (Species 2) initially inside the cone and the electrons initially outside the cone (Species 3). The “cone boundary” in this article refers to the  $n_c = 100 n_c$  surface. The cone boundary had a full opening angle of  $34^\circ$ . The ions outside the cone were treated as immobile. The plasma density profile inside the cone was obtained from linear interpolation of a hydrodynamics simulation using *HYDRA*,<sup>13</sup> in which the laser prepulse had an energy of ~22 mJ and a duration of 0.9 ns. The initial density scale length at  $n_c$  was ~20  $\mu\text{m}$ . Densities above  $100 n_c$  (outside the cone) were capped at  $100 n_c$ ; therefore, particle transport in plasmas above  $100 n_c$  was not studied. The temperatures of all electrons and gold ions were set at 1 keV. The ionization state of the ions was fixed at 20, estimated based on the *HYDRA* simulation.

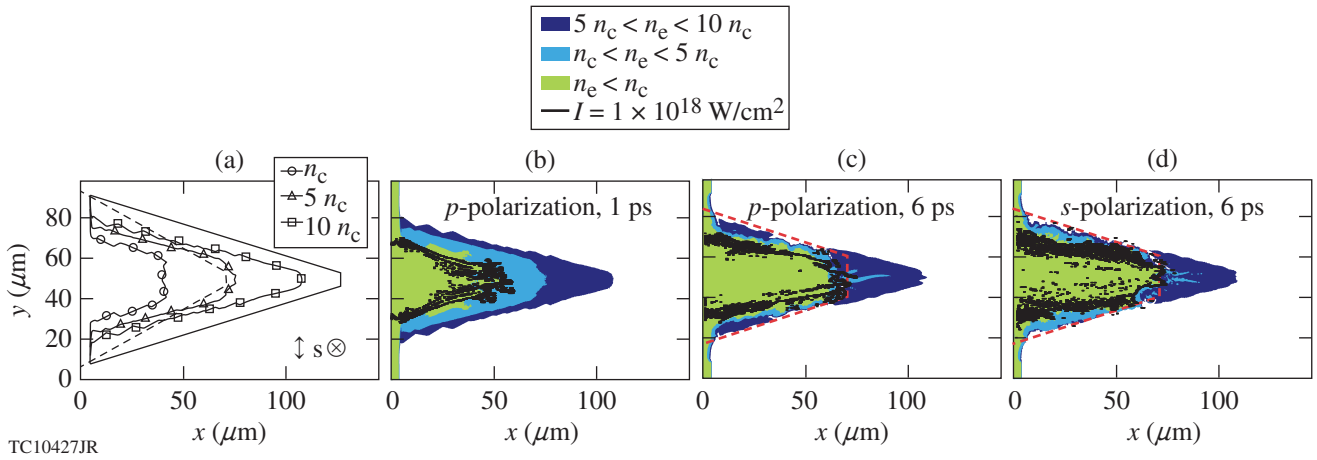


Figure 134.45

(a) Initial setup of pre-plasma inside the cone. The double arrow and the circle with a cross show the oscillation directions of the electric field for  $p$ - and  $s$ -polarizations. The solid line is the boundary ( $100 n_c$ ) and the dashed line is the first diagnostic boundary. Plasma density and magnitude of the laser Poynting vector for  $p$ -polarization at (b) 1 ps and (c) 6 ps and (d) for  $s$ -polarization at 6 ps. The white regions indicate electron density  $n_e > 10 n_c$ . The solid black lines show the laser intensity contours of  $1.0 \times 10^{18} \text{ W/cm}^2$ . In (c) and (d), the red dashed lines are the boundaries for checking charge balance.

The incident laser with wavelength  $\lambda = 1.053 \mu\text{m}$  was launched at time  $t = 0$  from the left side and focused at the cone tip with a peak intensity of  $1 \times 10^{19} \text{ W/cm}^2$  and a rise time of 0.56 fs. This short rise time was chosen to speed up the simulation. The transverse profile of the laser intensity was Gaussian with a full width at half maximum (FWHM) of  $w_0 = 21 \mu\text{m}$ . Both  $p$ - and  $s$ -polarizations were used in separate simulation runs to infer three-dimensional (3-D) effects. For comparison, the 1.053- $\mu\text{m}$ -wavelength short pulse from OMEGA EP had an energy of  $\sim 1 \text{ kJ}$  and a 10-ps duration and was focused to a spot with a diameter of  $D_{80} = 52 \pm 4 \mu\text{m}$  containing 80% of the laser energy. The peak intensity exceeded  $1 \times 10^{19} \text{ W/cm}^2$ , while the average intensity within  $D_{80}$  was several times  $10^{18} \text{ W/cm}^2$ .

The simulation box size was  $150 \times 100 \mu\text{m}$ . The Cartesian grid sizes  $dx$  and  $dy$  were set at  $0.05 c/\omega_0 = 7.96 \times 10^{-3} \mu\text{m}$  and the time step at  $dt = 0.035/\omega_0 = 1.86 \times 10^{-2} \text{ fs}$ , where  $\omega_0$  and  $c$  are the laser-pulse frequency and the speed of light, respectively. The total number of grid cells was  $17,856 \times 11,900$ . The number of particles per cell was chosen to be 10, 1, and 4 for Species 1, 2, and 3, respectively. For electromagnetic fields, we used open boundary conditions in the  $x$  (longitudinal) direction and periodic boundary conditions in the  $y$  (transverse) direction.

For particles, a thermal boundary condition was used at all four boundaries; electrons reaching the boundaries were reflected with a new Maxwellian velocity distribution at the initial temperature (1 keV). To prevent hot electrons from accumulating near the boundaries, an artificial drag<sup>12</sup> was introduced on electrons above 30 keV outside the cone

$$\frac{d\vec{v}}{dt} = -\alpha\vec{v}, \quad (1)$$

where  $\vec{v}$  is the electron velocity normalized to  $c$  and  $t$  is the time normalized to  $1/\omega_0$ . The drag coefficient  $\alpha$  was chosen to be 0.0043, which would stop a 1-MeV electron in  $17 \mu\text{m}$ .

The initial density change was represented by a change in the charge weights of the particles while the number of particles per cell was initially constant throughout the simulation box. Therefore, the particles in higher-density regions had larger charge weights than the particles in lower-density regions.

Figure 134.45(a) shows the initial setup for the PIC simulations with different contours matching the critical ( $n_c$ ),  $5n_c$ , and  $10n_c$  density lines inside the cone that were obtained from the *HYDRA* simulation. It is noted that the full-scale plasma in the cone tip was implemented in the simulation and that the target was the same as in the integrated experiments ( $34^\circ$  full inner cone angle,  $10\text{-}\mu\text{m}$  flat tip, Au cone wall, and pre-plasma). Hot-electron diagnostics were set up at two places as shown in Fig. 134.45(a). The first diagnostic boundary (dashed line) was near the initial  $n_e = 5n_c$  surface and the other was at the cone boundary, where  $n_e = 100 n_c$ . Whenever an electron passed one of these diagnostic boundaries, its position, momentum, and charge weight were recorded. The incoming and outgoing electrons were separately recorded at these two boundaries. In this article, when calculating hot-electron-related quantities such as average energy, a net distribution function of the hot electrons ( $>30 \text{ keV}$ ) was usually used:

$$f_{\text{hot}} = f_{\text{outgoing}} - f_{\text{incoming}}, \quad (2)$$

where the flux was normal to the cone boundary. This definition excluded the hot electrons trapped near the boundaries.

## Simulation Results

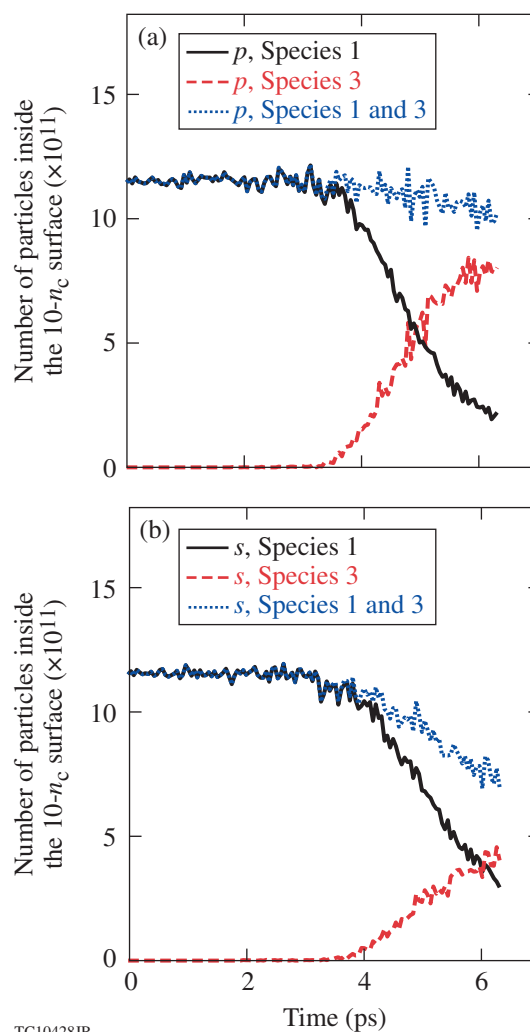
### 1. Laser Propagation Inside the Cone

To illustrate the laser and plasma evolution inside the cone, we plot the contours of plasma density and the magnitude envelope of the laser Poynting vector at time  $t = 1$  ps [Fig. 134.45(b)] and at 6 ps [Fig. 134.45(c)] for the  $p$ -polarization case, and at  $t = 6$  ps [Fig. 134.45(d)] for the  $s$ -polarization case. The initial position of  $n_c$  was  $\sim 85 \mu\text{m}$  away from the cone tip and was pushed  $\sim 25 \mu\text{m}$  forward with  $s$ -polarization ( $\sim 60 \mu\text{m}$  from cone tip) and  $\sim 30 \mu\text{m}$  with  $p$ -polarization ( $\sim 55 \mu\text{m}$  from cone tip) at 6 ps. At 1 ps, the laser intensity contour of  $1.0 \times 10^{18} \text{ W/cm}^2$  interacted with  $n_c < n < 5n_c$  plasma. At 6 ps, however, the plasma was pushed transversely to both sides so that the side  $n_c$  surface was far from the laser intensity contour of  $1.0 \times 10^{18} \text{ W/cm}^2$ . In this case hot electrons can be generated only in the underdense plasma. At the end of the simulation ( $t = 6.7$  ps), the laser had not reached the original  $10n_c$  surface, demonstrating the importance of the pre-plasma effect for hot-electron generation inside the cone.

### 2. Establishment of Return Currents

For the laser to continuously generate hot electrons from the pre-plasma inside the cone during the time considered, there must be a return current drawn from outside the laser-plasma interaction region. Any inhibition of this return current would lead to the buildup of an electrostatic field, preventing further electron acceleration. This could occur numerically as a result of the high weight of the particles in the  $100n_c$  region, preventing them from moving freely into a region with a density near  $n_c$ .

Therefore, the total charges of Species 1 and 3 inside a region defined by the red dashed line in Figs. 134.45(c) and 134.45(d) are plotted as a function of time in Fig. 134.46(a) for  $p$ -polarization and Fig. 134.46(b) for  $s$ -polarization. The total charge of Species 1 (the electrons originally inside the cone) decreased over time as a result of laser acceleration. In the meantime, Species 3 (the electrons originally outside the cone) moved into the cone to form the return currents, as shown in Figs. 134.46(a) and 134.46(b). The total charge of Species 1 and 3 inside this region was very close to the total charge of Species 2 (the ions, not shown) throughout the simulation, which decreased at later times as the ions were expelled. Similar results were obtained for other regions where  $n_c < 3n_c$  and  $n_c < 30n_c$ . Therefore, the charge was mostly balanced



TC10428JR

Figure 134.46

Total charge of the electron Species 1 and 3 inside the  $10n_c$  surface in the unit of electron charge for (a)  $p$ -polarization and (b)  $s$ -polarization.

and the return current was well established in our simulations. We note that more electrons were pushed out of the cone early for the  $p$ -polarized laser beam than for the  $s$ -polarized laser beam. We will discuss the reason for this feature in **Energy Density of Electrons** (p. 132).

### 3. Laser-to-Hot-Electron Conversion Rates and Hot-Electron Energy Spectra

To study how much laser energy was transferred into hot electrons, we define an instantaneous laser-to-hot-electron conversion rate as the total energy of the net outgoing hot electrons normalized by the incident laser energy in a short period of  $\sim 0.05$  ps. To calculate this rate, the contribution from the incoming hot electrons was subtracted, using Eq. (2). The instantaneous conversion rates of both  $p$ - and  $s$ -polarized laser

beams are shown in Fig. 134.47(a). Initially, the  $p$ -polarized laser beam had a higher conversion rate than the  $s$ -polarized laser beam, but the difference decreased at later times. The conversion rates from 3.5 to 6.7 ps for both cases were about 50%.

The mean energy of the hot electrons is shown in Fig. 134.47(b) as a function of time. The mean energies for the  $p$ - and  $s$ -polarized cases reached maximum values of 2 MeV and 1.5 MeV at 0.74 ps and 0.93 ps, respectively; they then decreased over time. This trend was the opposite from that in Ref. 14, where no significant pre-plasma was present, indicating a different hot-electron-generation mechanism in these simulations [see **Energy Density of Electrons** (p. 132)]. After 4 ps, the  $p$ - and  $s$ -polarized cases had about the same mean energies.

The energy spectra for accumulated hot electrons for both polarizations are plotted in Fig. 134.47(c). The overall spectra are similar. They can be fitted by a two-temperature function

$$f(E) = 1.06 \times 10^{11} \exp(-E/0.12) + 5.8 \times 10^8 \exp(-E/3.3), \quad (3)$$

where  $E$  is the electron energy in MeV. The temperature was  $0.12 \pm 0.03$  MeV for the “cold” component (below 500 keV) and  $3.3 \pm 0.2$  MeV for the “hot” component (above 1 MeV). The hot-component temperature was  $3.5 \times$  the ponderomotive energy (corresponding to the laser intensity of  $1 \times 10^{19}$  W/cm<sup>2</sup>) of 0.95 MeV. This again indicates a different hot-electron-generation mechanism from that in previous simulations with no significant pre-plasma.<sup>15</sup>

To describe the spectra in more detail, we define an electron energy fraction function  $g(E)$  that is the fraction of the electron energy below  $E$ :

$$g(E) = \frac{\int_{30 \text{ keV}}^E f(E') E' dE'}{\int_{30 \text{ keV}}^{E_{\max}} f(E') E' dE'}, \quad (4)$$

where  $f(E)$  is the distribution function of the hot electrons from Eq. (2) and  $E_{\max}$  is chosen to be 30 MeV, above which there were few electrons.

Figure 134.47(d) plots  $g(E)$  for the accumulated hot-electron spectra for both polarizations. While the mean hot-electron energies at the end of the simulations dropped below 0.5 MeV, the sub-1-MeV electrons contributed only 22% of the total hot-electron energy, as indicated by point A. The electron distribution was dominated by the low-energy electrons in number but by the high-energy electrons in energy. The median energy  $E_M$ , defined as  $g(E_M) = 0.5$ , was much higher than the mean energy of the distribution in Fig. 134.47(b). In Fig. 134.47(d), the median energy  $E_M$  was 4.2 MeV for the  $p$ -polarized case and 3.7 MeV for the  $s$ -polarized case. These data clearly show that the hot-electron energy is mainly carried by high-energy electrons.

#### 4. Angular Distribution of Hot Electrons

The divergence of the electrons above 1 MeV is one of the quantities critical to the ultimate energy-coupling efficiency in fast ignition. Here, we define the half spread angle of an electron as

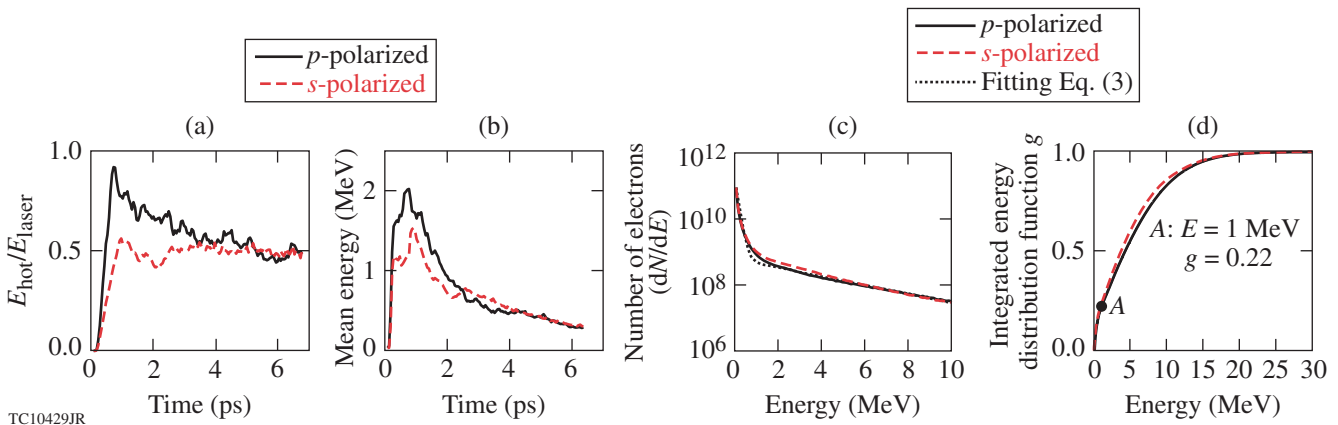


Figure 134.47

(a) Instantaneous laser-to-hot-electron conversion rate; (b) mean energy of the outgoing hot electrons; (c) accumulated hot-electron energy spectra and the fitting [Eq. (3)]; and (d) function  $g$  in Eq. (4) for accumulated hot electrons. All plots are shown for both  $p$ - and  $s$ -polarization cases.

$$\theta = \tan^{-1} \left( \frac{p_y}{p_x} \right), \quad (5)$$

$$\frac{\sum_i \theta_i q_i E_i}{\sum_i q_i E_i}$$

where  $p_x$  and  $p_y$  are the momenta of the electron in the  $x$  and  $y$  directions.

Since the hot electrons were dominated in number by low-energy electrons, we plot the normalized angular distribution of hot electrons with and without energy weighting in Fig. 134.48(a). These distributions show that a significant amount of energy was carried by electrons with a large  $\theta$ . The energy-weighted, mean half-angle

of the hot electrons is plotted in Fig. 134.48(b), where  $q_i$  and  $E_i$  are the charge weight and kinetic energy of each particle, respectively. The mean half-angle for the accumulated distribution increased slightly over time and was between  $58^\circ$  and  $68^\circ$ .

### 5. Ballistic Electron Motion Inside the Cone

A realistic electron source is vital for the transport study of hot electrons in fast ignition.<sup>10,15–17</sup> Figure 134.49 plots the energy-weighted angular spread and energy spectra from

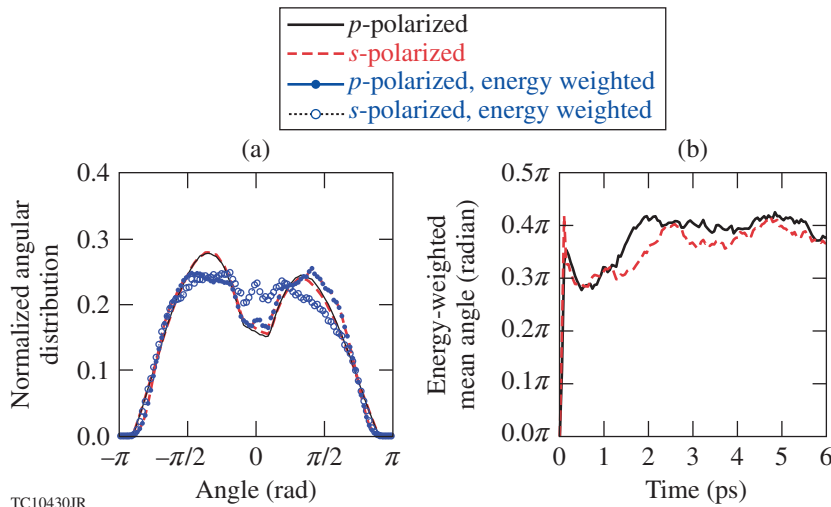


Figure 134.48

(a) Normalized angular distribution of accumulated hot electrons with and without energy weighting; (b) energy-weighted mean angle of accumulated hot electrons versus time for  $p$ - (solid) and  $s$ -polarization (dashed).

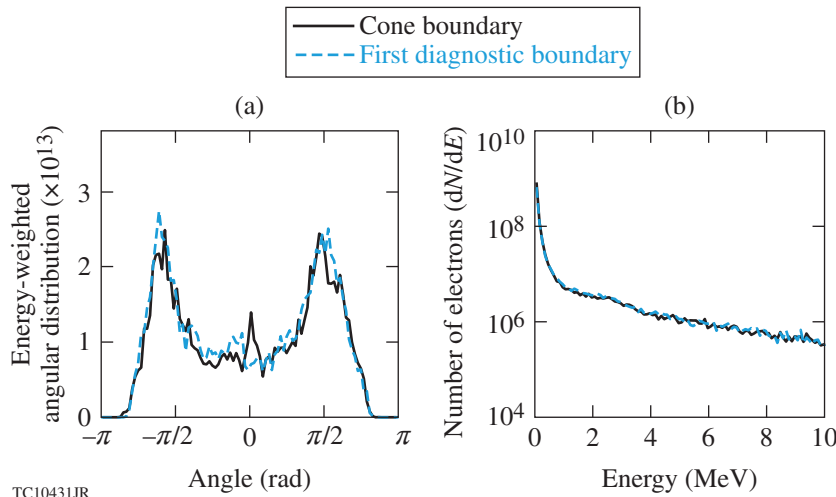


Figure 134.49

(a) Energy-weighted angular distribution at  $1.96 \text{ ps} < t < 2.01 \text{ ps}$  and (b) corresponding energy spectrum recorded at the cone boundary (solid) and the first virtual boundary (dashed).

both the first diagnostic boundary [see Fig. 134.45(a)] and the cone boundary at  $1.96 \text{ ps} < t < 2.01 \text{ ps}$ . The similarity of the electron characteristics shows that the transport between the two boundaries was mostly ballistic. This makes it possible to build an electron source from the information collected at the cone boundary for future transport study.

## 6. Energy Density of Electrons

The observed hot-electron characteristics, including the accumulated energy and angular distributions and the long-term laser-to-hot-electron conversion rates, were similar for  $p$ - and  $s$ -polarizations. Significant differences existed only early in time (Fig. 134.47), indicating that some of the known laser-heating mechanisms operating only in  $p$ -polarization, such as resonant<sup>18,19</sup> and Brunel<sup>20</sup> heating, were not dominant in these simulations. To further illustrate this, the electron energy densities at two different times for both polarizations are plotted in Fig. 134.50. The normalized electron energy density is defined as

$$h(x,y) = n_e(x,y) \bar{E}_k(x,y) / (n_c m c^2), \quad (6)$$

where  $n_e(x,y)$  is the total electron density, including both Species 1 and 3;  $\bar{E}_k(x,y)$  is the mean kinetic energy of local electrons; and  $n_c$ ,  $m$ , and  $c$  are the previously defined quantities. Initially, with the uniform electron temperature  $T_e = 1 \text{ keV}$ ,  $h(x,y)$  was in the range  $[0, 0.3]$ . When hot electrons are present,  $h(x,y)$  can increase to the range  $[1, 3]$ , as shown by the regions in black in Fig. 134.50. Therefore, Fig. 134.50 essentially plots the hot-electron energy density.

At 1 ps [Figs. 134.50(a) and 134.50(b)], both polarizations show the highest hot-electron densities in the laser region and hot-electron fluxes in the forward direction. For  $p$ -polarization, however, additional fluxes were propagating sideways. The sideways fluxes had a modulated structure with a wavelength close to the laser wavelength  $\lambda$ . They appeared to originate from the edge of the laser beam, where the electron density was approximately  $n_c$  and the density scale length was  $\sim \lambda$  [see also Fig. 134.45(b)]. This indicates that Brunel heating<sup>20</sup> was the likely generation mechanism for these sideways hot electrons and accounts for the higher conversion rate for the  $p$ -polarization in Fig. 134.47(a). The return current for the  $p$ -polarization also emerged earlier in Fig. 134.46(a).

At 6 ps, more sideways fluxes appeared for both polarizations [Figs. 134.50(c) and 134.50(d)]; however, these fluxes did not have a modulated structure, indicating that they were no longer generated by the Brunel mechanism. This is also corroborated by the fact that the  $n_c$  surface moved away from the laser region [Figs. 134.45(c) and 134.45(d)]. Most hot electrons were likely generated stochastically through interactions of the laser pulse with the underdense plasma. From particle trajectories, we observed many hot electrons passing through the laser region multiple times before crossing the cone boundary. Actual heating processes are difficult to analyze but they can be a high-intensity analog of the stochastic heating from mode coupling in parametric instabilities<sup>21</sup> and/or the stochastic heating from the laser pulse and its reflection.<sup>22,23</sup> The electrons can be heated stochastically to an energy much higher than the laser ponderomotive potential.<sup>24</sup> The sideways fluxes in

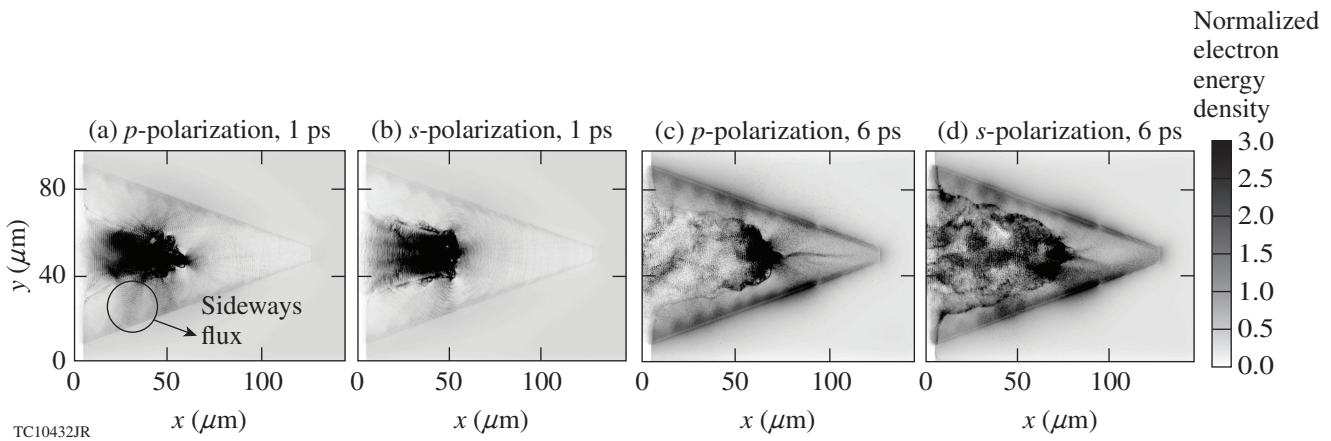


Figure 134.50

Energy density of all electrons (Species 1 and 3) for a  $p$ -polarized laser beam at (a) 1 ps and (c) 6 ps and for an  $s$ -polarized laser beam at (b) 1 ps and (d) 6 ps.

Figs. 134.50(a) and 134.50(b) explain the large spreading angles in Figs. 134.48(a) and 134.48(b). The stochastic heating is independent of the polarization direction and the hot electrons generated are relatively isotropic. The large spreading angles observed here have a different origin from the deformation of the laser/overdense-plasma interface observed in previous simulations where no significant pre-plasmas were present.<sup>14,25,26</sup>

### Discussion and Summary

Figure 134.51 compares several measured electron spectra from the integrated experiments<sup>4</sup> and the simulated spectrum of the outgoing electrons. In the experiment, fast electrons that escaped the target were recorded in two different directions: in the laser's forward direction [Fig. 134.51(a)] and sideways [Fig. 134.51(b)] at an angle of 79° to the laser-beam axis. For the

simulation, the simulated outgoing electrons with an absolute angle of less than 9° and between 70° and 88°, respectively, were considered as forward and sideways electrons. They are also plotted in Fig. 134.51 multiplied by a factor of 20 to allow for a better comparison with the experimental data. The choice of an angular range of  $\pm 9^\circ$  is arbitrary but justified by the fact that over this range, the shape of the simulated electron spectrum was uniform. Despite the shot-to-shot fluctuations in the measured spectra, the experimental and simulated spectra are remarkably similar in the high-energy region above  $\sim 10$  MeV. A quantitative comparison of the simulated and measured spectra over the entire energy range is made difficult by the fact that the escaped electrons measured in the experiments were influenced by the electron transport in the dense ( $n_e > 100 n_c$ ) plasmas, which was not simulated here. Strong self-generated electric and magnetic fields in the dense plasma region would affect the directionality of lower-energy electrons ( $\leq 1$  MeV) and were not taken into account in the simulation data. It is expected, however, that the high-energy tail of the escaped electrons was less influenced by the transport and that inferred slope temperatures should be comparable. Figure 134.52 shows the inferred slope temperatures from the electron spectra in the 10- to 20-MeV energy range of Fig. 134.51. The circles correspond to the spectra in the forward direction and the triangles correspond to the sideways spectra. The square

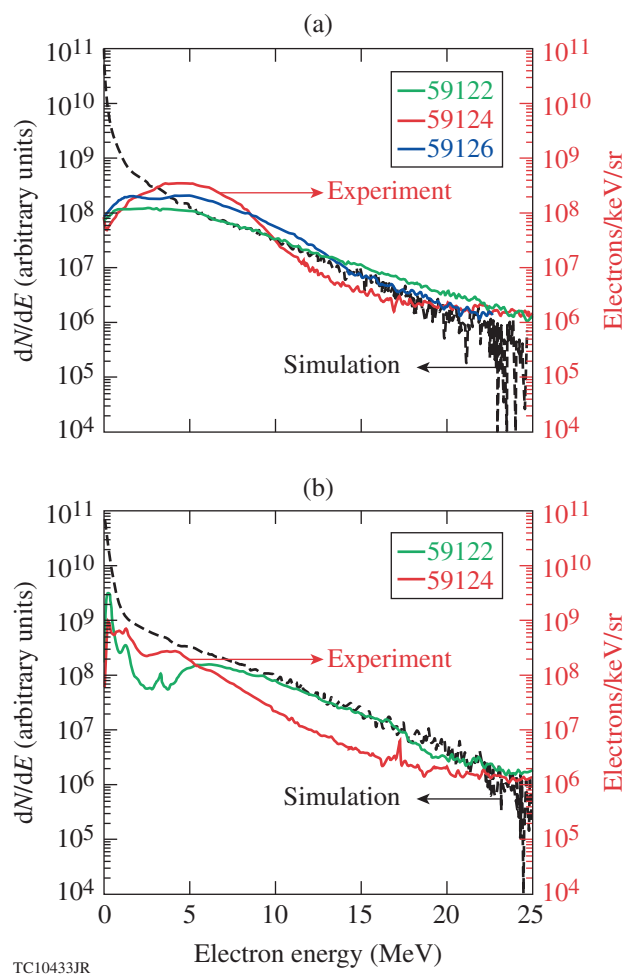


Figure 134.51  
Comparison of measured (solid) and simulated (dashed) electron spectra in (a) the laser's forward direction and (b) approximately 79° to the laser-beam direction.<sup>4</sup>

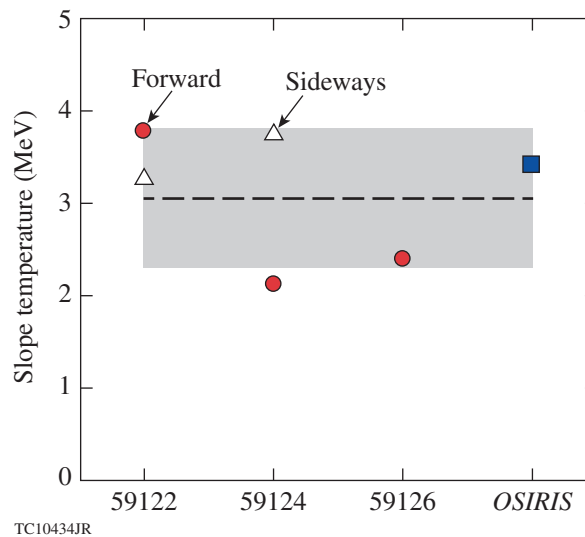


Figure 134.52  
Inferred slope temperature from the electron spectra in Fig. 134.51 in the 10- to 20-MeV energy range. The circles correspond to the spectra in the forward direction and the triangles correspond to the sideways spectra. The square represents the simulation result. The dashed line is the average of the five measurements and the gray band represents the measurement uncertainty (range equal to twice the standard deviation).

represents the simulated temperature. The dashed line is the average of the five measurements, 3.05 MeV, which is close to the simulated value of 3.4 MeV within the measurement uncertainty (gray band). This shows good agreement between the simulation and the experiment. The laser–core energy coupling rate in the simulation is estimated by assuming the compressed dense deuterated plastic core is 115  $\mu\text{m}$  away from the laser–plasma interface with an areal density of 0.1  $\text{g}/\text{cm}^2$  and a diameter of 160  $\mu\text{m}$ . These conditions were obtained from the previous hydrodynamic simulations of the implosion.<sup>27</sup> With the assumption of ballistic motion, hot electrons with a deflection angle smaller than  $35^\circ$  can reach the dense core and deposit energy there. Considering the different energy-deposition rates of hot electrons with different energies, the total energy-coupling rate from laser beam to the dense core is  $\sim 0.9\%$ , which is less than the  $3.5 \pm 1.0\%$  estimation from the integrated-experiment results. There are two possible reasons for the inconsistency. First, a self-generated magnetic field could exist that can couple the electrons with a larger deflection angle to the core.<sup>9,28</sup> Second, the neutrons might be generated by fast-electron–induced shocks in the core plasma. Such shocks can be generated either by direct heating of the core by fast electrons or by hydrodynamic expansion of the gold cone heated by fast electrons to  $\sim 1$  keV (Ref. 4). A significant number of electrons were recorded in the sideways direction, corroborating a large divergence angle of the electrons. The large hot-electron spread angles found here can qualitatively explain the low laser–core coupling in these experiments. It is worth noting that recent integrated-experiments<sup>29</sup> using Cu-doped shells and monochromatic imaging of the Cu  $K_\alpha$  fluorescence emission induced by the fast electrons also showed that a significant amount of hot electrons hit the side wall of the cone, which is again an indication of the large angular spread of the electrons consistent with the simulations. These simulations will help us gain a further understanding of the integrated experiments, and the hot-electron source from the simulations can be used in transport studies.

In summary, we have studied the properties of hot electrons generated during laser/pre-plasma interactions in cone-guided fast ignition over 6.7 ps using PIC simulations. Hot electrons were generated mainly through stochastic heating, which produced similar hot-electron characteristics for  $p$ - and  $s$ -polarizations in 2-D, indicating that this will also be the case in 3-D. The laser-to-hot-electron conversion rate approached 50%. Electrons with energy  $< 300$  keV dominated in number in the distribution but 78% of the hot-electron energy was carried by electrons with energy above 1 MeV. The hot electrons

had an energy-weighted mean half-angle of  $68^\circ$ . The electron transport in the  $5-n_c$  to  $100-n_c$  region was ballistic. These results provide further evidence of the detrimental effects of pre-plasma in the cone.

#### ACKNOWLEDGMENT

This work was supported by U.S. Department of Energy under Grant Nos. DE-FG02-06ER54879, DE-FC02-04ER54789, DE-FG52-06NA26195, and DE-FG02-03ER54271. The simulations used resources of the National Energy Research Scientific Computing Center.

#### REFERENCES

1. M. Tabak *et al.*, Phys. Plasmas **1**, 1626 (1994).
2. R. Kodama *et al.*, Nature **412**, 798 (2001).
3. R. Kodama *et al.*, Nature **418**, 933 (2002).
4. W. Theobald, A. A. Solodov, C. Stoeckl, K. S. Anderson, R. Betti, T. R. Boehly, R. S. Craxton, J. A. Delettrez, C. Dorrer, J. A. Frenje, V. Yu. Glebov, H. Habara, K. A. Tanaka, J. P. Knauer, R. Lauck, F. J. Marshall, K. L. Marshall, D. D. Meyerhofer, P. M. Nilson, P. K. Patel, H. Chen, T. C. Sangster, W. Seka, N. Sinenian, T. Ma, F. N. Beg, E. Giraldez, and R. B. Stephens, Phys. Plasmas **18**, 056305 (2011).
5. A. G. MacPhee *et al.*, Phys. Rev. Lett. **104**, 055002 (2010).
6. H. Shiraga *et al.*, Plasma Phys. Control. Fusion **53**, 124029 (2011).
7. S. D. Baton *et al.*, Phys. Plasmas **15**, 042706 (2008).
8. G. Li *et al.*, Phys. Rev. Lett. **100**, 125002 (2008).
9. G. Li *et al.*, Phys. Plasmas **18**, 042703 (2011).
10. A. A. Solodov, K. S. Anderson, R. Betti, V. Gotcheva, J. Myatt, J. A. Delettrez, S. Skupsky, W. Theobald, and C. Stoeckl, Phys. Plasmas **15**, 112702 (2008).
11. R. A. Fonseca *et al.*, Lect. Notes Comput. Sci. **2331**, 342 (2002).
12. J. Tonge *et al.*, Phys. Plasmas **16**, 056311 (2009).
13. M. M. Marinak *et al.*, Phys. Plasmas **3**, 2070 (1996).
14. A. J. Kemp and L. Divol, Phys. Rev. Lett. **109**, 195005 (2012).
15. D. J. Strozzi *et al.*, Phys. Plasmas **19**, 072711 (2012).
16. J. J. Honrubia and J. Meyer-ter-Vehn, Nucl. Fusion **46**, L25 (2006).
17. T. Johzaki, Y. Nakao, and K. Mima, Phys. Plasmas **16**, 062706 (2009).
18. D. W. Forslund *et al.*, Phys. Rev. A **11**, 679 (1975).
19. K. Estabrook and W. L. Kruer, Phys. Rev. Lett. **40**, 42 (1978).
20. F. Brunel, Phys. Rev. Lett. **59**, 52 (1987).

21. J. J. Thomson, R. J. Faehl, and W. L. Kruer, *Phys. Rev. Lett.* **31**, 918 (1973).
22. Z.-M. Sheng *et al.*, *Phys. Rev. Lett.* **88**, 055004 (2002).
23. Z.-M. Sheng *et al.*, *Phys. Rev. E* **69**, 016407 (2004).
24. S. C. Wilks *et al.*, *Phys. Rev. Lett.* **69**, 1383 (1992).
25. A. Debayle *et al.*, *Phys. Rev. E* **82**, 036405 (2010).
26. H. Schmitz, R. Lloyd, and R. G. Evans, *Plasma Phys. Control. Fusion* **54**, 085016 (2012).
27. A. A. Solodov, M. Theobald, A. S. Anderson, A. Shvydky, R. Betti, J. F. Myatt, and C. Stoeckl, *Bull. Am. Phys. Soc.* **57**, 29 (2012).
28. A. A. Solodov, K. S. Anderson, R. Betti, V. Gotcheva, J. F. Myatt, J. A. Delettrez, S. Skupsky, W. Theobald, and C. Stoeckl, *Phys. Plasmas* **16**, 056309 (2009).
29. L. C. Jarrott, M. S. Wei, A. A. Solodov, H. Sawada, R. B. Stephens, A. Greenwood, D. Hoover, N. Alfonso, H. Huang, E. Giraldez, W. Theobald, C. Stoeckl, F. J. Marshall, J. Delettrez, R. Betti, P. K. Patel, H. McLean, C. Chen, M. K. Key, H. Chen, T. Doeppner, T. Yabuuchi, H. Habara, and F. N. Beg, presented at the 2012 Stewardship Science Academic Alliances (SSAA) Symposium, Washington, D.C., 22 February 2012.

---

# Pulsed Laser Ablation of Dental Calculus in the Near-Ultraviolet

## Introduction

Selective removal of subgingival dental calculus is a preferred treatment method in nonsurgical periodontal therapy. While complete removal of calculus and disease-causing agents (i.e., oral bacteria) is of primary importance, leaving behind a hard tissue surface less prone to bacterial accumulation is also important. Grooves and craters resulting from conventional cleaning measures provide sites for future bacteria and calculus crystals to accumulate.<sup>1</sup> Healthy cementum should be preserved since attachments, via periodontal ligaments, from either the gingiva or alveolar bone with root dentin are not as strong as with root cementum.<sup>2,3</sup> A weak connection could lead to subsequent reoccurrence of periodontal problems.

Conventional methods to remove calculus typically depend on the experience of the clinician<sup>4,5</sup> and other treatment factors.<sup>1</sup> Unintentional damage can easily occur using hand instruments<sup>6</sup> and power-driven scalers (e.g., ultrasonic and air abrasion)<sup>7</sup> that cause grooves and/or excessive cementum removal. In most cases, mechanical root scaling leaves behind a smear layer containing harmful bacteria, infected cementum, and calculus debris.<sup>8,9</sup>

Currently, the Er:YAG laser ( $\lambda = 2.94 \mu\text{m}$ ) (Ref. 10) is the only commercially available laser with significant experimental and clinical studies for dental hard tissue removal.<sup>1</sup> Hard-tissue (enamel, dentin, and cementum) ablation at this wavelength relies on absorption by water,<sup>11</sup> so calculus ablation is not selective. A review of several clinical studies<sup>12</sup> and recent meta-analysis<sup>13</sup> concluded that the clinical outcome of calculus removal using the Er:YAG laser is similar to conventional mechanical debridement.

A frequency-doubled alexandrite (FDA) laser ( $\lambda \sim 380 \text{ nm}$ ) can selectively remove plaque, caries, and calculus without damaging the underlying and surrounding hard tissue.<sup>14</sup> The ablation mechanism is assumed to be based on absorption by haemins (i.e., iron-containing porphyrins) into the Soret band.<sup>15,16</sup> Iron-containing porphyrins are found in some oral bacteria in dental plaque and dental calculus.<sup>15,17</sup> However,

the inconsistent output of the FDA laser has not allowed for more-detailed studies into the calculus ablation mechanism.

Recently, a frequency-doubled Ti:sapphire laser ( $\lambda = 400 \text{ nm}$ ) was developed to allow for a more-detailed analysis of dental calculus ablation in the near-ultraviolet (NUV, 300 to 400 nm) (Ref. 18). This laser selectively removes dental calculus<sup>19,20</sup> and extrinsic enamel stains.<sup>21</sup> For incident laser fluences close to the ablation threshold (1 to 2 J/cm<sup>2</sup>), ablation stalling is frequently encountered. Stalling is not observed at fluences well above the ablation threshold (6 to 8 J/cm<sup>2</sup>).

This article describes a variety of experimental diagnostics used to study the ablation mechanism of dental calculus at 400 nm and compares the results with predictions made by heuristic ablation models. Laser profilometry measures volume and depth of calculus ablated for different irradiation conditions. Blue-light microscopy and fluorescence spectroscopy identify photobleaching during calculus ablation. Together these diagnostics allow one to identify a heuristic, modified ablation blowoff model that explains the experimental observations. Finally, the effect of tooth sterilization prior to laser irradiation is assessed by comparing removal rates of gamma-ray-sterilized and unsterilized calculus samples at the same incident fluence. This information has been used to propose a mechanism for calculus ablation at 400 nm.

## Heuristic Ablation Models

### 1. Standard Blowoff Model

In the standard blowoff model, Beer's law is assumed to govern energy deposition into calculus.<sup>22</sup> In this model, deposited energy densities  $E_d$  exceeding the ablation-threshold energy density  $E_{abl}$  cause calculus removal. The threshold energy density is typically a constant<sup>22,23</sup> related to the enthalpy of ablation for calculus. The absorption coefficient  $\mu_a$  is assumed to remain constant during irradiation, and scattering is assumed to be negligible. For the standard blowoff model,  $E_d$  is given by

$$E_d = -\frac{dF}{dz} = \mu_a F(z) = \mu_a F_0 e^{-\mu_a z}, \quad (1)$$

where  $F_0$  is the incident fluence (in  $\text{J}/\text{cm}^2$ ) and  $F(z)$  is the fluence at depth  $z$ . Ablation occurs over the etch depth  $\delta_{\text{SB}}$  if  $\mu_a F(z) > E_{\text{abl}}$ . Beyond the etch depth, tissue is not ablated but merely heated. The fluence at the etch depth is the ablation threshold fluence  $F_{\text{th}}$ , and for  $F(z) > F_{\text{th}}$  the etch depth is found from Eq. (1) to be

$$\delta_{\text{SB}} = \frac{1}{\mu_a} \ln \left( \frac{F_0}{F_{\text{th}}} \right). \quad (2)$$

## 2. Modified Blowoff Model

In the modified blowoff model, the absorption coefficient is assumed to decrease during the laser pulse. This assumption may be better suited for predicting calculus-removal rates since a photobleached surface layer is observed after 400-nm irradiation.<sup>18</sup> This model was originally proposed for photoablation of polymethyl methacrylate (PMMA) in the deep ultraviolet.<sup>23</sup> For photoablation, the number density of chromophores  $\rho_a$  decreases as the absorption of UV photons breaks chemical bonds that prevent absorption of subsequent photons.<sup>24,25</sup> Permanent photochemical damage of the chromophores (i.e., photobleaching) similarly decreases  $\rho_a$  during laser irradiation. The derivation for the modified blowoff model is

found in Ref. 23, where the approximate etch depth  $\delta_{\text{MB}}$ , for the fluences used in this article, is determined to be

$$\delta_{\text{MB}} \approx \frac{F_0 - F_{\text{th}}}{h\nu\rho_a}, \quad (3)$$

where  $h$  is Planck's constant and  $\nu$  is the laser frequency. The etch depth depends linearly on  $F_0$  as opposed to the logarithmic dependence in Eq. (2) for the standard model. The full expression for Eq. (3) is found in Ref. 23. The chromophore number density is related to the absorption coefficient by  $\mu_a = \sigma_a\rho_a$ , where  $\sigma_a$  is the absorption cross section of the chromophore. The deposited energy density is approximately constant for  $z < \delta_{\text{MB}}$  and is given by

$$E_d(z < \delta_{\text{MB}}) \approx h\nu\rho_a. \quad (4)$$

Equation (4) indicates that the deposited energy is limited by the chromophore number density of the tissue within the etch depth. The deposited energy density for both blowoff models is plotted as a function of depth in Fig. 134.53 based on the data in Table 134.VI. A layer consisting of partially photobleached chromophores is located beyond the etch depth in Fig. 134.53(b).

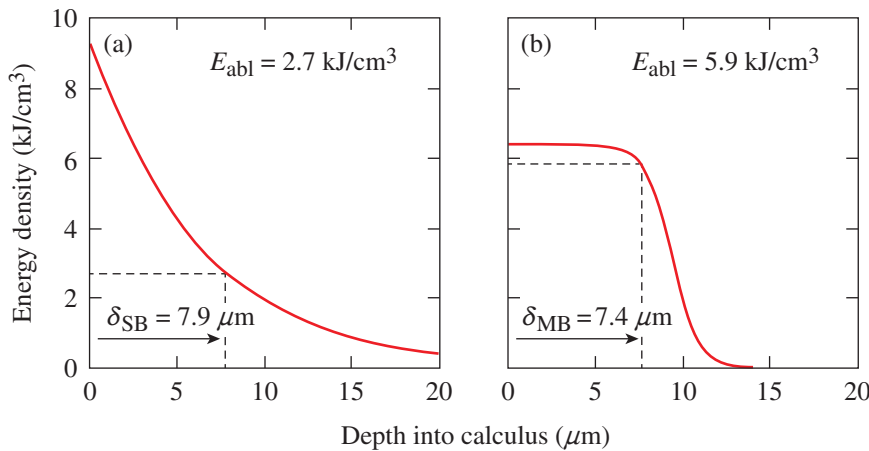


Figure 134.53  
Deposited energy density as a function of depth in calculus based on the (a) standard and (b) modified blowoff models. The incident fluence is  $6 \text{ J}/\text{cm}^2$ . The curves are based on data in Table 134.VI. In (a)  $\mu_a = 1600 \text{ cm}^{-1}$  and in (b)  $\rho_a = 1.3 \times 10^{22} \text{ cm}^{-3}$ .

E21791JR

Table 134.VI: Absorption coefficients, threshold fluences, and chromophore number densities for the standard and modified blowoff models obtained from removal rates in Fig. 134.58.

	Removal Rates		Standard Blowoff Model		Modified Blowoff Model	
	$\frac{\mu\text{m}/\text{pulse}}{\text{J}/\text{cm}^2}$	$\times 10^{14} \frac{\mu\text{m}^3/\text{pulse}}{\text{J}/\text{cm}^2}$	$\mu_a \text{ (cm}^{-1}\text{)}$	$F_{\text{th}} \text{ (J}/\text{cm}^2\text{)}$	$\rho_a \text{ } 10^{22} \text{ (cm}^{-3}\text{)}$	$F_{\text{th}} \text{ (J}/\text{cm}^2\text{)}$
Supragingival	$1.5 \pm 0.3$	$6.6 \pm 1.4$	$1618 \pm 323$	$1.7 \pm 0.4$	$1.32 \pm 0.27$	$1.2 \pm 0.4$
Subgingival	$1.6 \pm 0.3$	$7.9 \pm 1.6$	$1574 \pm 281$	$1.8 \pm 0.4$	$1.27 \pm 0.23$	$1.3 \pm 0.4$

### 3. Removal Rates

The etch depths in Eqs. (2) and (3) can be used to calculate volume removal rates for each blowoff model. Assuming an  $n$ th-order super-Gaussian fluence distribution  $F(r)$ , we find

$$F(r) = F_0 \exp\left(-r^n/w^n\right), \quad (5)$$

with peak fluence  $F_0$  and  $1/e$  beam width  $w$ . Substituting Eq. (5) into Eqs. (2) and (3), one obtains a radial distribution of the etch region. Scattering is assumed to be negligible compared to absorption. The volume removal rate is found by integrating over the entire volume irradiated at fluences  $>F_{th}$ . The volume removal rate  $V_{SB}$  per pulse for the standard blowoff model is

$$V_{SB} = \frac{2\pi w^2}{\mu_a} \left(\frac{1}{n+2}\right) \left(\ln \frac{F_0}{F_{th}}\right)^{\frac{n+2}{n}}. \quad (6)$$

The volume removal rate predicted by the modified blowoff model  $V_{MB}$  is

$$V_{MB} = \frac{2\pi^2}{\rho_a h\nu} \left[ \frac{F_0 \Gamma(2/n)}{n} \eta_E(n, F_0/F_{th}) - \frac{F_{th}}{2} \left(\ln \frac{F_0}{F_{th}}\right)^{2/n} \right], \quad (7)$$

where  $\eta_E$  is the energy efficiency for selective ablation shown in Ref. 18 and  $\Gamma$  is the gamma function. For our experimental conditions the volume removal rates in Eqs. (6) and (7) simplify to  $V_{SB}(\mu\text{m}^3) \approx (10^8/\mu_a)$  and  $V_{MB}(\mu\text{m}^3) \approx (F_0/\rho_a) \times 10^{27}$ , where the units of  $\rho_a$ ,  $\mu_a$ , and  $F_0$  are  $\text{cm}^{-3}$ ,  $\text{cm}^{-1}$ , and  $\text{J}/\text{cm}^2$ , respectively. The underlying experimental parameters are  $n = 10$ ,  $w = 150 \mu\text{m}$ ,  $F_0/F_{th} \approx 4$  to  $5$ ,  $\eta_E \approx 1$ , and  $h\nu = 3.1 \text{ eV}$ .

## Materials and Methods

### 1. Tooth Samples

Twenty extracted human teeth exhibiting calculus, equally divided between sub- and supragingival calculus, were obtained from the Department of Preventive and Restorative Dental Sciences, School of Dentistry at the University of California, San Francisco. They were sterilized with gamma radiation and stored in a 0.1% thymol solution. Ten extracted, unsterilized human teeth with subgingival calculus were obtained from the Eastman Institute for Oral Health at the University of Rochester (UR) and stored in a saline solution.

### 2. Experimental Setup

A frequency-doubled Ti:sapphire laser (400-nm wavelength, 60-ns pulse duration, 10-Hz repetition rate, and 25-mJ pulse energy) was developed for selective calculus ablation and

has been described elsewhere.<sup>18</sup> Laser radiation was coupled into a 600- $\mu\text{m}$ -core-diam optical fiber with a 1.8-mm-diam tapered input (FVPE600660710/2M, Polymicro Technologies) using a  $\Delta\theta = 0.5^\circ$  engineered diffuser (RPC Photonics) and an  $F = 7.5$ -cm lens [Fig. 134.54(a)]. The output beam was demagnified using an  $F = 2$ -cm lens objective to create an  $\sim 300$ - $\mu\text{m}$ -diam, tenth-order super-Gaussian irradiation beam on the calculus surface. This irradiation geometry was chosen to facilitate experimental observations. The peak fluence of each pulse was varied from 1.7 to  $8 \text{ J}/\text{cm}^2$  ( $\pm 0.1 \text{ J}/\text{cm}^2$ ) by varying the laser pulse energy. All tooth surfaces were irradiated at normal (perpendicular) incidence to the surface. (Similar ablation studies using oblique incidence were reported in Ref. 19.)

During laser irradiation, the tooth samples were sprayed with a water/air mixture at  $\sim 3 \text{ mL}/\text{min}$ . The effect of this water spray on the intensity distribution of the irradiation laser at the tooth surface is minimal.<sup>18</sup> After five laser pulses, excess water was gently blown off the tooth samples using an air spray to allow for the diagnostic imaging (i.e., laser profilometry and blue-light microscopy) described below.

### 3. Laser Profilometry

The depth and volume of calculus removed were measured using a laser profilometer. A HeNe laser at  $\lambda = 543 \text{ nm}$  (Model LHGR-0050, PMS Electro-Optics) was focused to a line onto the tooth surface using an  $F = 10$ -cm cylindrical lens and then scanned across the irradiated region before and after laser irradiation. The line was magnified  $3\times$  (VMZ450i, Edmund Industrial Optics) by imaging onto a charge-coupled-device (CCD) camera (TM-1020A-15CL, JAI) along a line of sight at  $45^\circ$ , resulting in an axial resolution of  $\sim 6 \mu\text{m}$ . The transverse resolution was  $60 \mu\text{m} \times 40 \mu\text{m}$ . Depth-removal maps were found by taking the difference between 3-D surface images taken before and after irradiation (as described in Ref. 19). Calculus removal rates were determined by irradiating in five-pulse increments using a remotely operated shutter in the laser cavity. The average depth and volumetric removal rate uncertainties are  $\pm 0.6 \mu\text{m}/\text{pulse}$  and  $1.4 \times 10^{-3} \mu\text{m}^3/\text{pulse}$  based on the uncertainty in the 3-D surface images resulting from laser speckle and the high  $f$  number of the imaging objective.

### 4. Blue-Light Microscopy

Images of calculus before and after laser irradiation were taken with illumination from a flashing blue light-emitting diode (LED,  $\lambda \sim 450$  to  $490 \text{ nm}$ ) using the same camera used in laser profilometry, as shown in Fig. 134.54(a). Identical images were obtained when illuminating with a 400-nm light source. Blue-light illumination provides high contrast between healthy

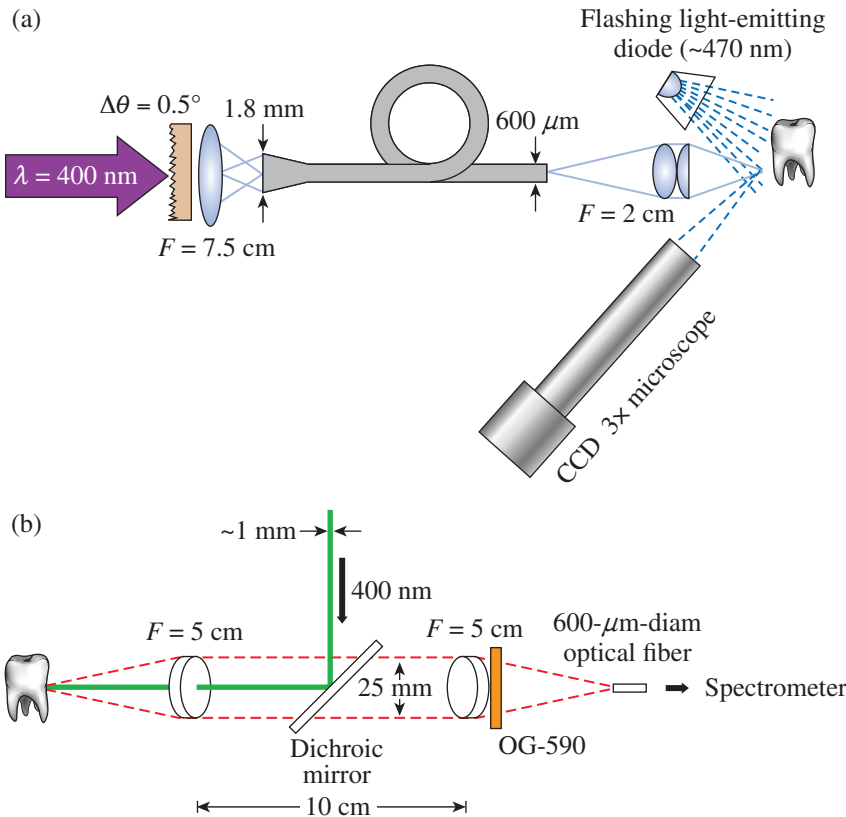


Figure 134.54

(a) Experimental setup for tooth irradiation with the 400-nm laser and for blue-light microscopy. (b) Hard tissue fluorescence between 600 and 800 nm was excited at 400 nm and coupled into an optical fiber leading to a fiber-coupled spectrometer. CCD: charge-coupled device.

hard tissue and dental calculus. It also serves to qualitatively distinguish unbleached from photobleached calculus since the latter appears brighter under blue-light microscopy because of increased scattering and decreased absorption.

### 5. Fluorescence Spectroscopy

Fluorescence spectroscopy was used to compare unbleached and photobleached calculus. As shown in Fig. 134.54(b), fluorescence was excited with low pulse energy ( $\leq 200 \mu\text{J}$  at 400 nm) over a  $50\text{-}\mu\text{m}$  beam spot. Fluorescence between 600 and 800 nm was then directed into a fiber-coupled spectrometer (HR2000CG-UVNI, Ocean Optics) using two  $F = 5\text{-cm}$  achromatic doublets, a dichroic mirror, and an OG590 filter. In this spectral range, one can discriminate between dental hard tissue and calculus caused by fluorescence from bacterial porphyrins.<sup>26</sup> At each measurement, 50 spectra were collected with a 10-s integration time, averaged, and smoothed by applying an  $\sim 5\text{-nm}$  spectral averaging filter.

### 6. Scanning Electron Microscopy

The laser-treated areas were examined using a scanning electron microscope (SEM) (Zeiss-Auriga CrossBeam FIB-SEM, Carl Zeiss NTS) at the UR's Institute of Optics. The tooth surface topology was examined using an SE2 detector and

a 10-keV electron beam with a  $30\text{-}\mu\text{m}$  aperture and  $\leq 15\text{-mm}$  working distance. The teeth were dried in a desiccator for at least 24 h. An  $\sim 5\text{-nm}$  gold layer was subsequently sputtered onto the tooth surface.

### Results

Blue-light microscope images show nonsterilized subgingival calculus removed at  $6.4 \text{ J/cm}^2$  [Figs. 134.55(a)–134.55(f)] within the irradiation beam (dashed red lines). After 30 pulses, the calculus was completely removed and the underlying cementum was reached [Fig. 134.55(f)]. No ablative stalling was observed, but irradiated calculus appears brighter compared to nonirradiated calculus, indicating a photobleached surface layer. Differential depth removal maps [Figs. 134.55(g)–134.55(k)] are shown below the microscope images. Average depth and volume removal rates for nonsterilized calculus are  $9.7 \pm 3.1 \mu\text{m/pulse}$  and  $5.3 \times 10^5 \pm 1.8 \times 10^5 \mu\text{m}^3/\text{pulse}$ , respectively. Identical results are found for ablating sterilized subgingival calculus<sup>19</sup> at the same fluence.

Blue-light microscope and fluorescence spectra of supragingival calculus irradiated at a  $3.5\text{-J/cm}^2$  fluence are shown in Figs. 134.56(a) and 134.56(b). The calculus was irradiated with a  $650\text{-}\mu\text{m}$ -diam, sixth-order super-Gaussian beam. The tooth

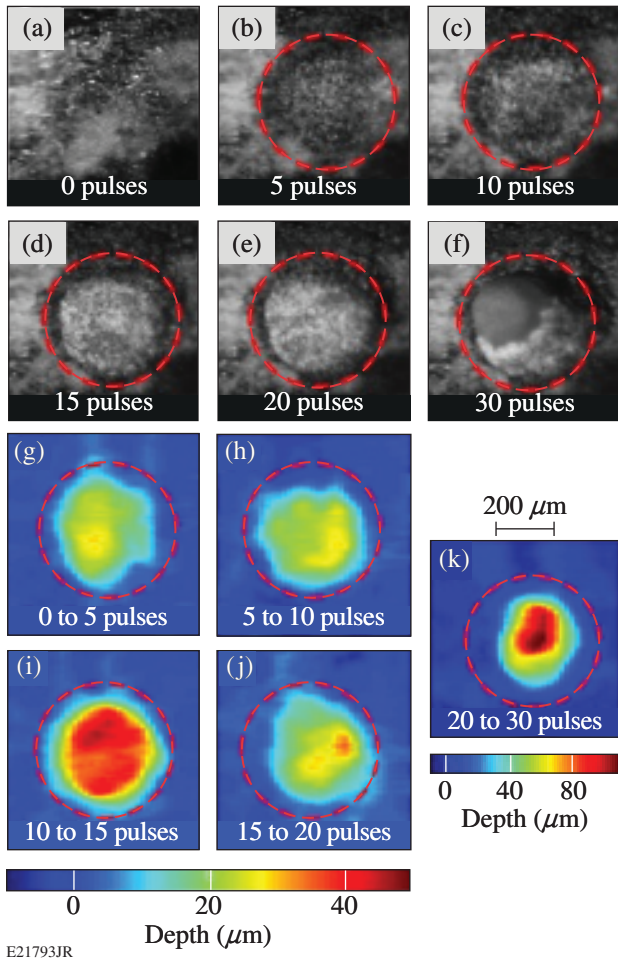


**Figure 134.55**  
Blue-light microscope images of nonsterilized subgingival calculus irradiated at  $6.4 \text{ J/cm}^2$  (a) before and after (b) 5, (c) 10, (d) 15, (e) 20, and (f) 30 irradiation pulses. Differential removal maps from (g) 0 to 5, (h) 5 to 10, (i) 10 to 15, (j) 15 to 20 and (k) 20 to 30 irradiation pulses correspond to the above microscope images. Red dashed circles outline the irradiation area.

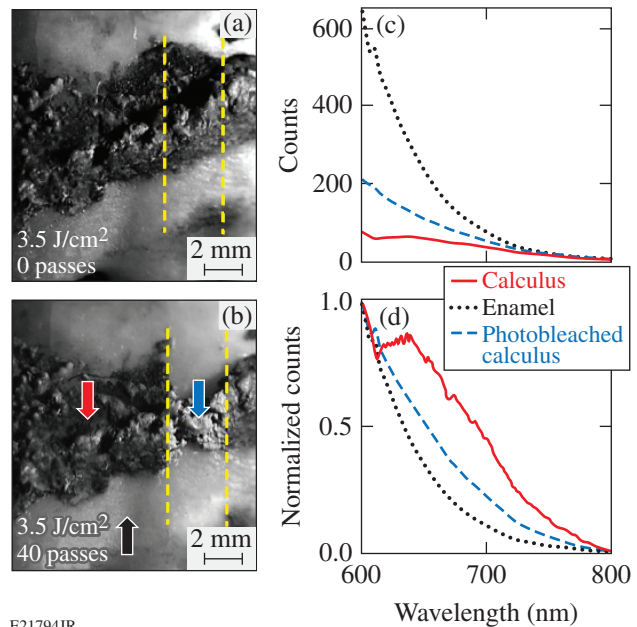
was moved back and forth for 40 passes at  $0.2 \text{ mm/s}$ , resulting in  $\sim 30$  superposed irradiation pulses per pass along the center on any given spot. The blue-light microscope images before and after irradiation [Figs. 134.56(a) and 134.56(b)] indicate that a layer of calculus was removed but a photobleached calculus surface layer remained [blue arrow in Fig. 134.56(b)]. The ablation stalled and further irradiation at this fluence removed no additional calculus.

Figure 134.56(c) shows the fluorescence spectra between 600 and 800 nm, excited at 400 nm, of the enamel (black arrow), unbleached calculus (red arrow), and photobleached calculus (blue arrow) indicated in Fig. 134.56(b). The fluorescence spectrum of photobleached calculus resembles the spectrum of enamel in shape, emitting more fluorescence photons

than unbleached calculus [Fig. 134.56(c)]. Normalizing each spectrum [Fig. 134.56(d)] reveals that unbleached calculus has a distinct structure between 615 and 725 nm caused by the Soret band of porphyrins.<sup>26–28</sup> This band is not seen for either enamel or photobleached calculus. Fluorescence from these tissues originates from the hard-tissue matrix. Remnant unbleached porphyrins within the photobleached calculus likely result in the differences observed for enamel and photobleached calculus spectra.

Removing the OG590 filter in the fluorescence setup allowed us to measure the scattered/reflected signal at 400 nm. Photobleached calculus and enamel scattered twice as much 400-nm light into the collection optics as did unbleached calculus. The exact amount of 400-nm light scattered by photobleached calculus varies from tooth to tooth and can equal that for sound enamel.

Subgingival calculus irradiated with 25 pulses at  $5 \text{ J/cm}^2$  was investigated under a SEM [Fig. 134.57(a)]. The  $\sim 100\text{-nm}$  pores on the calculus surface [arrows in Fig. 134.57(a)] act as



**Figure 134.56**  
Blue-light microscope images of supragingival calculus on enamel (a) before and (b) after 40 passes at  $3.5 \text{ J/cm}^2$  using an  $\sim 650\text{-}\mu\text{m}$ -diam, sixth-order super-Gaussian beam. The dashed yellow lines outline the irradiation path. (c) Fluorescence spectra of enamel, unbleached calculus, and photobleached calculus using a 400-nm excitation wavelength. (d) Normalized fluorescence spectra corresponding to (c). Colored arrows in (b) correspond to the spectra in (c) and (d) (i.e., red arrow: unbleached calculus; black arrow: enamel; and blue arrow: photobleached calculus).

a reservoir for oral bacteria.<sup>29–32</sup> For comparison, the porous surface of non-laser-irradiated calculus, covered with a bio-film, was also observed under a SEM [Fig. 134.57(b)]. The calculus surface was always covered by a layer of noncalcified dental plaque.<sup>1</sup> Blue-light microscope images (not shown) of the irradiated calculus surface in Fig. 134.57(a) indicate it was photobleached. The pores seen in this image were likely originally filled with oral bacteria that were removed upon NUV irradiation.

Average depth and volume removal rates for sub- and supra-gingival calculus are plotted as a function of incident fluence in Fig. 134.58. Within the error bars, both depth and volume removal rates increase linearly with increasing incident fluence and are indistinguishable between sub- and supra-gingival calculus. We have attributed the large error bars to tissue variations in absorption and/or the heterogeneity of the physical properties in calculus.<sup>19</sup> The absolute error in depth and volume removal rates increases with fluence in Fig. 134.58 but the relative error actually decreases. Depth removal rates in Figs. 134.58(a) and

134.58(b) are fitted to Eqs. (2) and (3). The results from these fits are summarized in Table 134 VI. The error bars render  $\mu_a$ ,  $\rho_a$ , and  $F_{th}$  indistinguishable for both types of calculus. The relevant tissue parameters in Table 134 VI are substituted into Eqs. (6) and (7) and plotted in Figs. 134.58(c) and 134.58(d) as predicted volume removal rates for sub- and supra-gingival calculus, respectively. The modified blowoff model overestimates the volume removal rate, whereas the standard model underestimates it.

The single-pulse (SP) depth and volume removal rates at  $\sim 6.3 \text{ J/cm}^2$  for either subgingival [Figs. 134.59(a) and 134.59(c)] or supra-gingival [Figs. 134.59(b) and 134.59(d)] calculus show similar trends with the number of incident pulses. The SP removal rate is calculated as the depth/volume removed from five laser pulses divided by the number of pulses, whereas the average removal rates in Fig. 134.58 are calculated from the total depth/volume removed. Outliers in the SP removal-rate data that skew the distribution are rejected according to Chauvenet’s criterion.<sup>33</sup> The SP removal rates of sub- and

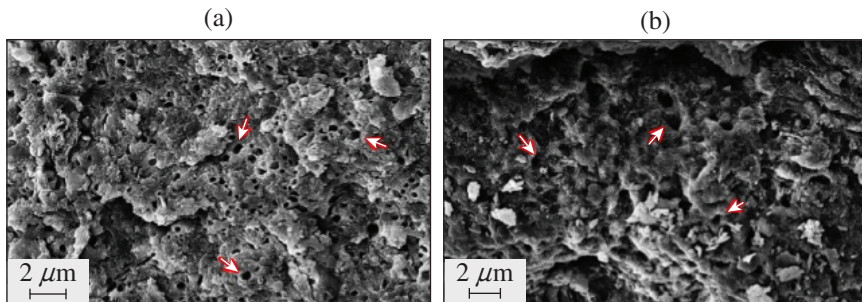
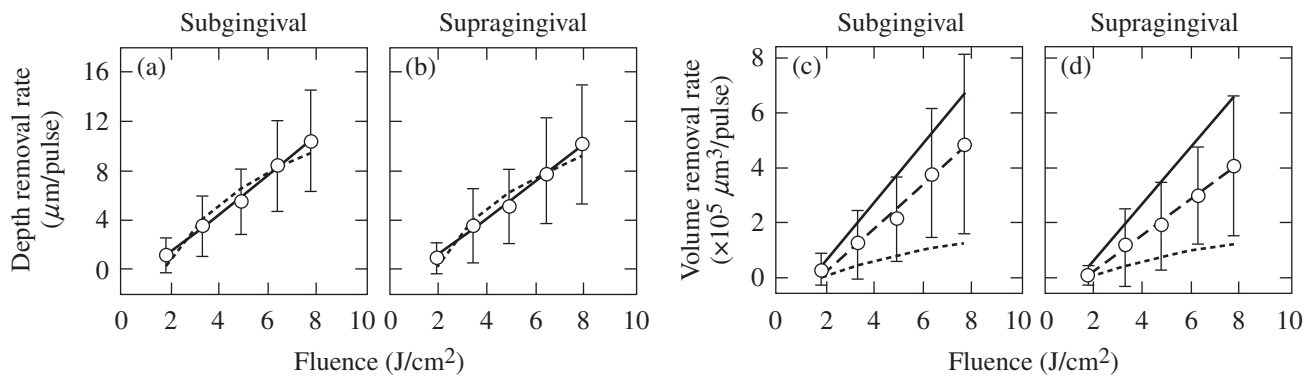


Figure 134.57 Scanning electron microscope (SEM) images of (a) laser-irradiated ( $5\text{-J/cm}^2$ ) and (b) non-laser-irradiated subgingival calculus. Arrows in (a) and (b) indicate representative  $\sim 100\text{-nm}$  craters found in the calculus surface.

E21795JR



E21796JR

Figure 134.58 Fluence-dependent depth removal rates for (a) subgingival and (b) supra-gingival calculus and corresponding volume removal rates [(c) and (d), respectively]. Solid and short-dashed lines correspond to fits using the modified and standard blowoff models, respectively. Long-dashed lines in (c) and (d) are a linear regression through the data.

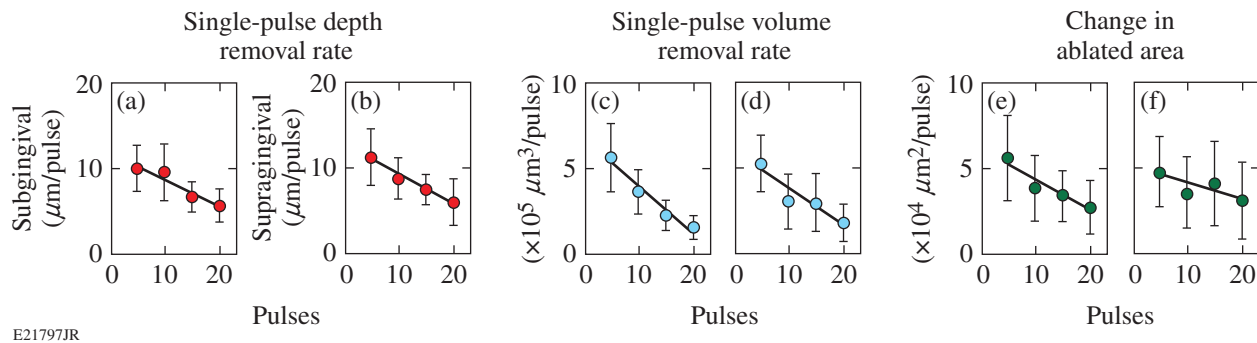


Figure 134.59

Single-pulse (SP) removal rates for all calculus samples irradiated at  $6.3 \text{ J/cm}^2$  as a function of the number of incident pulses: the SP depth removal rates for (a) subgingival and (b) supragingival calculus; the SP volume removal rates for (c) subgingival and (d) supragingival calculus; the change in ablated area for (e) subgingival and (f) supragingival calculus. Trend lines through data are from a linear regression.

supragingival calculus at fluences from  $3.5$  to  $7.7 \text{ J/cm}^2$  exhibit similar behavior. The change in the ablated area at  $6.3 \text{ J/cm}^2$  for sub- and supragingival calculus [Figs. 134.59(e) and 134.59(f)] was found by dividing the SP volume removal rates by the SP depth removal rates in Fig. 134.59. The ablated area also decreases with increasing number of incident pulses. There is no statistically significant difference between the SP removal rates for sub- and supragingival calculus.

### Discussion

The properties (i.e., pulse energy and duration) of the 400-nm laser used in this study are extremely reproducible, causing shot-to-shot variations in ablation measurements to be attributable to the material heterogeneity of calculus itself. Therefore, using the diagnostics outlined earlier allows for rather detailed inferences regarding the actual ablation mechanism. This contrasts with previous work using the 380-nm FDA laser<sup>34</sup> whose poor reproducibility and characterization rendered it unsuitable for this kind of detailed study. However, the selective removal of oral bacteria, dental caries, and calculus by the 380-nm laser (summarized in Ref. 14) was attributed to porphyrins endogenous to oral bacteria.

In this study, blue-light microscopy clearly indicates photobleaching and reduced absorption on the calculus surface after laser irradiation (Figs. 134.55 and 134.56). For thick calculus layers and laser fluences of less than  $\sim 6 \text{ J/cm}^2$ , this may lead to stalling before the entire calculus layer is removed. Therefore, photobleaching affects calculus ablation but does not necessarily prevent it.

Fluorescence spectroscopy (Fig. 134.56) supports the interpretation of the blue-light microscope images. The fluorescence spectra [Fig. 134.56(c)] of irradiated and nonirradi-

ated photobleached calculus show that endogenous porphyrins (e.g., protoporphyrin IX and coporphyrin) in oral bacteria (e.g., *P. intermedia*, *P. nigrescens*, and *P. melaninogenica*) are the primary absorbers for 400-nm ablation. This finding is further supported by the corresponding SEM images in Fig. 134.57, which show empty pores and paucity of microorganisms on the surface of irradiated calculus. These diagnostics are unable to determine, however, the depth of this photobleached layer, which, from here on, we refer to as the “depletion layer.” This depletion layer also leads to the measured increase in reflection/scattering of 400-nm radiation compared to nonirradiated calculus and clearly affects ablation by subsequent laser pulses.

The modified blowoff model appears well suited to explain calculus ablation at 400 nm, while the standard blowoff model does not. The assumption of permanent chromophore depletion agrees with the results of blue-light microscopy, fluorescence spectroscopy, and scattered-laser-light measurements. The model predicts a partially depleted layer of chromophores [Fig. 134.55(b)] with thickness  $\sim 1/\mu_a$  beyond the etch depth after each laser pulse. The linear dependence of the average depth and volume removal rates with incident fluence (Fig. 134.57) also agrees with this model.

The modified blowoff model readily agrees with most of the observations in Figs. 134.55–134.58. This model does not, however, predict the ablation stalling seen in Fig. 134.56 nor the reduction of ablation depth and volume with successive laser pulses in Fig. 134.59. This limitation probably is caused mostly by the modified blowoff model neglecting scattering of laser light within dental calculus. These losses, especially within the depletion layer, can be significant because of multiple scattering, including broadening of the spot size. In addition, calculus formation is layered,<sup>35</sup> progressing from low chromo-

phore number density (low  $\rho_a$ ), gram-positive bacteria<sup>36</sup> on the calculus/tooth interface to high  $\rho_a$ , gram-negative bacteria on the calculus surface.<sup>36–40</sup>

The gradual decrease in absorber density with depth and the concomitant increase in the depletion layer exacerbate the laser-light losses ahead of the region where it may be effectively absorbed. This naturally leads to decreasing removal rates with depth (Fig. 134.59) and potential stalling. This problem is compounded by the fact that the scattering length within dental hard tissue<sup>41</sup> is not much longer than typical measured etch depths. (For this purpose we have assumed scattering within calculus to be comparable to that in enamel.) The same reasoning also predicts that increasing the incident fluence and corresponding etch depths effectively prevents stalling before complete removal of the calculus layer. These conclusions agree with our observations that stalling occurs close to the ablation threshold (1 to 2 J/cm<sup>2</sup>) and is typically not observed for fluences >6 J/cm<sup>2</sup>.

Of significant importance is the fact that sound cementum and enamel are not ablated below 9 and 12 J/cm<sup>2</sup>, respectively.<sup>42</sup> Therefore, selective calculus ablation without stalling is assured for fluences of 6 to 8 J/cm<sup>2</sup>.

Most ablation experiments in this study were carried out with gamma-ray-sterilized teeth. However, comparison of ablation rates of sterilized and unsterilized teeth under otherwise identical conditions were essentially indistinguishable. Previous NUV ablation studies<sup>43</sup> carried out at 380 nm reported ablation fluences of 1 to 2 J/cm<sup>2</sup> for effective calculus ablation using unsterilized teeth. Our comparison study eliminates the possibility that sterilization of the teeth significantly affects calculus ablation. We therefore suspect that the complicated nature of the temporal laser pulse shape in the 380-nm experiments (two successive, irregular 100-ns pulses within ~10  $\mu$ s) may account for the different reported relevant ablation fluences.

## Conclusion

Calculus ablation at 400 nm is best described by a modified blowoff model that is based on chromophore depletion (photo-bleaching). The results presented here strongly suggest that the relevant calculus chromophores are bacterial porphyrins, endogenous to plaque and dental calculus. A thin surface layer of these chromophores becomes photobleached after each irradiation pulse. Tissue scattering within this photobleached layer exacerbated by a decreasing absorber (bacterial porphyrin) density with depth leads to decreasing removal rates with successive laser pulses and potential ablation stalling. Stalling

can be avoided, however, by irradiating at incident fluences >6 J/cm<sup>2</sup>.

## ACKNOWLEDGMENT

We thank Dr. Georgios Romanos for contributing the nonsterilized tooth samples for this study. This work was supported by the U.S. Department of Energy Office of Inertial Confinement Fusion under Cooperative Agreement No. DE-FC52-08NA28302, the University of Rochester, and the New York State Energy Research and Development Authority. The support of DOE does not constitute an endorsement by DOE of the views expressed in this article. This work was also partially financially supported through a 2010 student grant from the American Society for Laser Medicine and Surgery (ASLMS).

## REFERENCES

1. S. Jepsen *et al.*, *Periodontol.* 2000 **55**, 167 (2011).
2. S. Nyman *et al.*, *J. Clin. Periodontol.* **9**, 290 (1982).
3. P. Rechmann and T. Hennig, *Med. Laser Appl.* **16**, 223 (2001).
4. H. T. Bellini and J. R. Johansen, *Acta Odontol. Scand.* **31**, 283 (1973).
5. W. K. Brayer *et al.*, *J. Periodontol.* **60**, 67 (1989).
6. J. Eberhard *et al.*, *J. Clin. Periodontol.* **30**, 511 (2003).
7. A. Aoki *et al.*, *Periodontol.* 2000 **36**, 59 (2004).
8. A. M. Polson *et al.*, *J. Periodontol.* **55**, 443 (1984).
9. P. A. Adriaens *et al.*, *J. Periodontol.* **59**, 493 (1988).
10. L. J. Walsh, *Aust. Dent. J.* **48**, 146 (2003).
11. D. Fried, in *Photon Processing in Microelectronics and Photonics IV*, edited by J. Fieret *et al.* (SPIE, Bellingham, WA, 2005), Vol. 5713, pp. 259–269.
12. F. Schwarz *et al.*, *J. Clin. Periodontol.* **35**, 29 (2008).
13. F. Sgolastra *et al.*, *Lasers Med. Sci.* **27**, 661 (2012).
14. P. Rechmann, *Dent. Clin. North Am.* **48**, 1077 (2004).
15. P. Rechmann, T. Hennig, and B. Spengler, in *The 4th International Congress on Lasers in Dentistry*, edited by H. Loh (Monduzzi Editore, International Proceedings Division, Bologna, Italy, 1994), pp. 159–162.
16. P. Rechmann, U.S. Patent No. 5,795,153 (18 August 1998).
17. T. E. Bramanti and S. C. Holt, *J. Bacteriol.* **173**, 7330 (1991).
18. J. E. Schoenly, W. Seka, and P. Rechmann, *Lasers Surg. Med.* **42**, 51 (2010).
19. J. E. Schoenly, W. D. Seka, and P. Rechmann, *J. Biomed. Opt.* **16**, 071404 (2011).
20. J. E. Schoenly, W. Seka, and P. Rechmann, in *Lasers in Dentistry XVI*, edited by P. Rechmann and D. Fried (SPIE, Bellingham, WA, 2010), Vol. 7549, p. 754906.

21. J. E. Schoenly, W. Seka, J. D. B. Featherstone, and P. Rechmann, *Lasers Surg. Med.* **44**, 339 (2012).
22. A. Vogel and V. Venugopalan, *Chem. Rev.* **103**, 577 (2003).
23. G. H. Pettit, in *Lasers in Medicine*, edited by R. W. Waynant (CRC Press, Boca Raton, FL, 2002), pp. 109–133.
24. R. Srinivasan, *Science* **234**, 559 (1986).
25. G. H. Pettit *et al.*, *Appl. Phys. A* **58**, 573 (1994).
26. W. Buchalla, A. M. Lennon, and T. Attin, *J. Periodontal. Res.* **39**, 327 (2004).
27. Y. L. Qin *et al.*, *J. Photochem. Photobiol. B: Biol.* **87**, 88 (2007).
28. W. C. Dolowy *et al.*, *J. Vet. Dent.* **12**, 105 (1995).
29. B. T. K. Tan *et al.*, *J. Periodontal.* **75**, 23 (2004).
30. H. E. Schroeder, *Helv. Odont. Acta* **8**, 117 (1964).
31. J. Friskopp and L. Hammarström, *J. Periodontal.* **51**, 553 (1980).
32. J. Friskopp, *J. Periodontal.* **54**, 542 (1983).
33. J. R. Taylor, *An Introduction to Error Analysis: The Study of Uncertainties in Physical Measurements*, Second ed., Third print (University Science Books, Sausalito, CA, 1997), p. 327.
34. P. Rechmann and T. Hennig, in *Medical Applications of Lasers III*, edited by S. G. Bown *et al.* (SPIE, Bellingham, WA, 1996), Vol. 2623, pp. 180–188.
35. D. J. White, *Biofouling* **4**, 209 (1991).
36. P. Marsh and M. Martin, *Oral Microbiology*, 4th ed. (Oxford, Boston, MA, 1999), p. 193.
37. L. J. Walsh and F. Shakibaie, *Australas. Dent. Prac.* **18**, 56 (2007).
38. N. S. Soukos *et al.*, *Antimicrob. Agents Chemother.* **49**, 1391 (2005).
39. S. S. Socransky *et al.*, *J. Clin. Periodontol.* **25**, 134 (1998).
40. W. E. C. Moore and L. V. H. Moore, *Periodontol. 2000* **5**, 66 (1994).
41. D. Fried, R. E. Glena, J. D. B. Featherstone, and W. Seka, *Appl. Opt.* **34**, 1278 (1995).
42. J. E. Schoenly, “Selective Ablation of Dental Calculus at 400 nm,” Ph.D. thesis, University of Rochester, 2012.
43. P. Rechmann and T. Hennig, in *Lasers in Dentistry*, edited by H. A. Wigdor, J. D. Featherstone, and J. M. White (SPIE, Bellingham, WA, 1995), Vol. 2394, pp. 203–210.

---

# Improving Cryogenic DT Implosion Performance on OMEGA

## Introduction

Layered cryogenic deuterium–tritium (DT) capsules are being imploded on LLE’s 60-beam OMEGA Laser System<sup>1</sup> to demonstrate hydrodynamic performance equivalent to that of a symmetric direct-drive target designed to ignite with the laser energy available at the National Ignition Facility (NIF).<sup>2</sup> Hydrodynamic equivalence implies that the shell velocity at the end of acceleration (typically referred to as the implosion velocity or  $V_{\text{imp}}$ ), the in-flight aspect ratio (IFAR, defined as the ratio of the shell radius and the shell thickness evaluated after the shell has imploded to 2/3 of its initial radius), and the peak laser drive intensity ( $I_1$ ) are the same as those of a symmetric ignition design<sup>3</sup> for the NIF. The demonstration of direct-drive hydrodynamic equivalence is viewed as an important scientific prerequisite for a polar-drive (PD)–ignition campaign on the NIF later in this decade.<sup>4</sup>

The polar-drive concept<sup>5</sup> was developed in 2004 to provide a platform for directly driven implosions on the NIF while the facility is configured for x-ray drive. A preliminary assessment of PD hot-spot target designs has shown that direct-drive ignition might be achieved on the NIF with a laser energy as low as 1 MJ<sub>UV</sub> (Ref. 6). The experimental plan to support the PD-ignition campaign is based on the validation of symmetric direct-drive performance modeling (laser coupling,<sup>7–10</sup> shock timing<sup>11</sup> and thermal transport,<sup>12,13</sup> hot-electron generation,<sup>14</sup> and adiabat control<sup>15</sup>) using cryogenic layered DT implosions on OMEGA. Additionally, select 40-beam, ambient gas-filled PD implosions are being used to confirm drive symmetry modeling.<sup>16</sup> Therefore, PD-ignition designs for the NIF will be based on physics models embedded in the radiation–hydrodynamic design codes that have been validated against symmetric direct-drive–implosion data.

The cryogenic implosion database at the Omega Laser Facility includes over 270 layered fuel implosions [roughly half using pure deuterium (D<sub>2</sub>) fuel and half using DT]. The first cryogenic D<sub>2</sub> capsule implosions<sup>17</sup> were performed in 2000 and cryogenic DT implosions<sup>18</sup> began in late 2006. Among the highlights of these experiments was the demonstration of areal

densities in D<sub>2</sub> fuel in excess of 200 mg/cm<sup>2</sup> (Refs. 12 and 19), the demonstration of areal densities in DT fuel of 300 mg/cm<sup>2</sup> (Refs. 3 and 20) (nominally the minimum areal density needed to sustain a thermonuclear burn wave), and the demonstration of yields relative to 1-D predictions in excess of 15% (Ref. 21).

This article describes recent progress toward demonstrating ignition hydrodynamically equivalent implosion performance on OMEGA. The following sections (1) discuss the concept of hydrodynamic similarity and the requirements for OMEGA target design; (2) present and discuss the data from a series of cryogenic DT implosions spanning a design space that includes ignition, concluding that target performance on OMEGA is impacted by capsule surface perturbations leading to ablator mixing into the hot spot; (3) discuss the origin and hydrodynamic modeling of these capsule surface perturbations; and (4) plot all of the cryogenic DT data using the experimental ignition threshold factor (ITFx) formalism described in Ref. 22 scaled appropriately for the target mass and laser-energy differences between OMEGA and the NIF. The ITFx formalism is a convenient metric for comparing relative target performance across a broad design space and is related to the generalized Lawson criterion applied to inertial confinement fusion (ICF) derived by Betti *et al.*<sup>23</sup> Final concluding remarks are given in the last section.

## Hydrodynamic Similarity and Experimental Design

Hydrodynamic similarity can be used to extrapolate implosion performance from the 26-kJ<sub>UV</sub> OMEGA to the 1.8-MJ<sub>UV</sub> NIF laser. In this way, implosions can be performed on OMEGA to probe the design space for targets on the NIF. In Ref. 24, Betti *et al.* showed explicitly that an ignition design for the NIF based on a specific adiabat ( $\alpha$ , defined as the ratio of the shell pressure to the Fermi-degenerate pressure), implosion velocity, and laser intensity can be reproduced on OMEGA with the same adiabat, implosion velocity, and laser intensity. While this scaling should lead to the same peak stagnation pressure and density in the OMEGA and NIF cores, the resulting yields and fuel areal density will necessarily be lower on OMEGA because of the smaller fuel mass and laser energy. Indeed, for

hydrodynamic similarity, the target mass must scale as the laser energy  $E_L$ , the target radius as  $E_L^{1/3}$ , the laser power as  $E_L^{2/3}$ , and the laser pulse length as  $E_L^{1/3}$ .

The assumption implicit in the hydro scaling argument is that the ablation pressure and preheat sources are independent of target scale (and facility). This is unlikely to be the case, however, since the coronal plasma scale length on the NIF relative to OMEGA will scale as the radius of the capsule (approximately 4× longer) for hydrodynamically similar implosions. The longer plasma scale lengths will reduce the ablation pressure via light-scattering losses and increased cross-beam energy transfer (CBET)<sup>8</sup> and increase the production of hot electrons (and potentially fuel preheating) from the two-plasmon–decay (TPD) instability.<sup>14,25</sup> Although these laser–plasma instabilities do not *a priori* restrict the design space available on OMEGA for ignition-relevant implosions, they may limit the penultimate performance that can be achieved.

The cryogenic target design for the experiments discussed here is shown in Fig. 135.1. This design is scaled from the 1.5-MJ symmetric direct-drive–ignition design published by Goncharov *et al.* in 2010 (Ref. 3). The capsule ablator material [Fig. 135.1(a)] is pure CD (deuterated plastic) or CD doped with a few atom percent of silicon (the dopant tailors the adiabat at the ablation surface to reduce the imprint growth rate<sup>7</sup>). The peak intensity of the triple-picket drive pulse [Fig. 135.1(b)] is  $9 \times 10^{14}$  W/cm<sup>2</sup>; the total drive energy is designed to be 26 kJ. The capsule radius is nominally 430 μm, which is  $(1.5 \text{ MJ}/0.026 \text{ MJ})^{1/3} \sim 3.9\times$  smaller than the 1.5-MJ ignition design (1700 μm).

Based on the hydrodynamic similarity argument above, this target platform can be used to access a broad region of design space that includes the 1.5-MJ ignition design. With constant drive intensity and laser energy, the  $V_{\text{imp}}$  and IFAR are varied

by changing the thickness of the ablator and DT ice layer and adjusting the picket energies and temporal spacing to achieve the desired adiabat at the inner fuel surface (the picket adjustments are used to ensure the correct shock timing and radial convergence). Figure 135.2 is a scatter plot in IFAR and adiabat space of recent cryogenic DT capsule implosions on OMEGA (i.e., each point represents an implosion on OMEGA with the indicated adiabat and IFAR). These implosions were selected from a set of over 60 experiments (performed over the past 18 months) based on a set of “physics quality” criteria that include target alignment at shot time (within 15 μm of target chamber center), ice-layer quality [less than 2-μm root mean square (rms) over all modes], and pulse-shape quality (typically picket energies within 10% of the design specification). The shaded region for

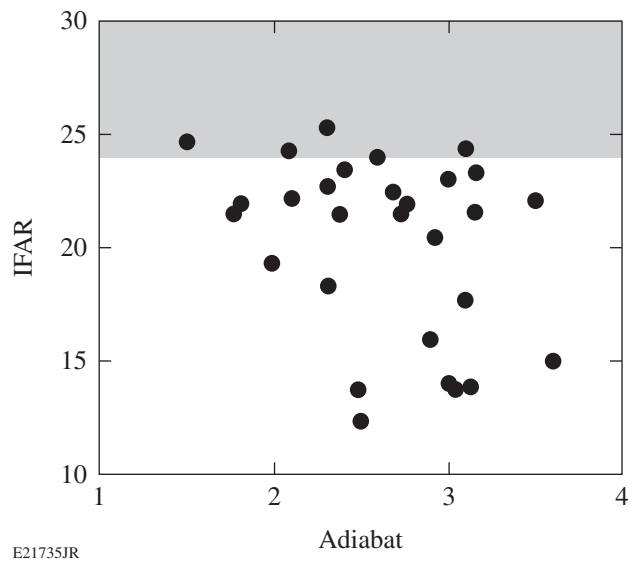


Figure 135.2  
A scatter plot in IFAR–adiabat design space of 29 cryogenic DT implosions on OMEGA. Each black circle represents an implosion with the specific post-shot calculated values of IFAR and adiabat. The shaded region represents the ignition-relevant region of this design space. IFAR: in-flight aspect ratio.

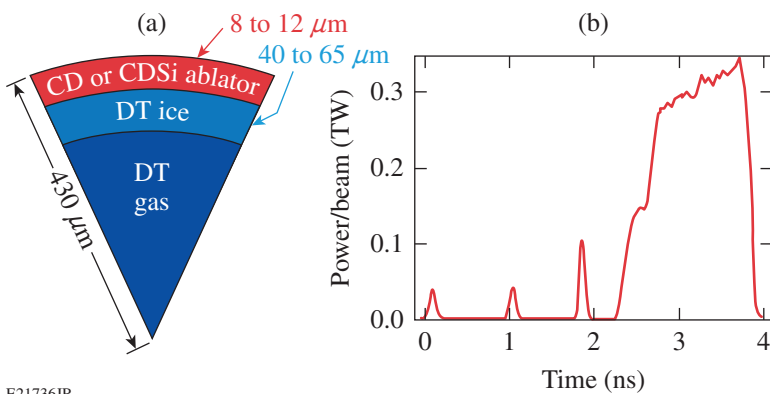


Figure 135.1  
(a) The standard cryogenic DT capsule imploded on OMEGA consists of a thin CD or doped-CD ablator fill with several hundred atm of DT gas to create a 40- to 60-μm-thick ice layer. (b) The standard 25-kJ drive pulse consists of a series of three pickets used to establish the shell adiabat and control shock coalescence and a high-intensity main drive.

E21736JR

IFAR > 23 shows the approximate design space for ignition with implosion velocities between 350 and 400 km/s.

Figure 135.1(a) shows the range of ablator and ice thickness used for the points shown in Fig. 135.2. The implosion velocities range from 250 km/s to 380 km/s (e.g., a 9.2- $\mu\text{m}$  CD ablator with an ice layer of 48  $\mu\text{m}$  is predicted to achieve a  $V_{\text{imp}}$  of 350 km/s). Although the adiabat, IFAR, and  $V_{\text{imp}}$  are calculated quantities [based on the one-dimensional (1-D) design code *LILAC*<sup>26</sup>], the  $V_{\text{imp}}$  is confirmed experimentally by measuring the implosion burn history using the neutron temporal diagnostic (NTD).<sup>27</sup> *LILAC* incorporates nonlocal thermal transport<sup>12</sup> and a stimulated Brillouin scattering (SBS) model<sup>8</sup> to account for cross-beam energy transfer. A 10% change in the predicted velocity is a timing shift of 150 ps in the NTD. The absolute temporal accuracy of the NTD is 25 ps, so the implosion velocity is known to within a few percent.

### Measurements and Discussion

The ICF Lawson criterion<sup>23</sup> can be used to connect the design parameters  $V_{\text{imp}}$ , adiabat, and IFAR to the experimentally measured observables. These observables include the primary neutron yield  $Y_n$ , the compressed fuel areal density  $\rho R$ , the hot-spot ion temperature  $T_{\text{ion}}$ , the absorbed laser energy, and the neutron burn history. The Lawson criterion is defined as  $\chi = P\tau/P\tau(T)_{\text{ign}} > 1$  (Ref. 28), where  $P$  is the plasma pressure and  $\tau$  is the energy confinement time. In Ref. 28, Betti *et al.* derived an approximate 1-D ignition parameter based on the generalized Lawson criterion

$$\chi(1\text{-D}) \sim (\rho R^{\text{no } \alpha})^{0.8} \times (T_{\text{ion}}^{\text{no } \alpha} / 4.4)^{1.8} > 1, \quad (1)$$

where  $T_{\text{ion}}$  is given in keV and  $\rho R$  in  $\text{g}/\text{cm}^2$ . The superscript “no  $\alpha$ ” indicates that alpha-particle energy deposition is turned off in the 1-D simulations used to validate the analytic scaling. Recognizing that implosion nonuniformities significantly degrade 1-D performance, the authors used a simple three-dimensional (3-D) burn model to derive a generalized Lawson criterion

$$\chi(3\text{-D}) \sim (\rho R^{\text{no } \alpha})^{0.8} \times (T_{\text{ion}}^{\text{no } \alpha} / 4.4)^{1.8} \times \text{YOC}_{3\text{-D}}^m. \quad (2)$$

$\text{YOC}_{3\text{-D}}$  is the ratio of the estimated 3-D yield to the predicted 1-D yield and  $m$  is analytically given as 0.64 but is between 0.4 and 0.5 based on fitting simulation yields with an ignition criterion of  $\chi \sim 1$ . It is difficult to use this form of  $\chi$  to evaluate absolute implosion performance given the dependence on simulations and the measured  $T_{\text{ion}}$ , which is sensitive to fuel motion. Therefore, Betti *et al.*<sup>24</sup> modified Eq. (2) to remove the

explicit dependence on the YOC and replace the  $T_{\text{ion}}$  with the absolute yield  $Y_n$ . This version of the “measurable” generalized Lawson criterion for ICF is given by

$$\chi \sim (\rho R^{\text{no } \alpha})^{0.61} \times (0.24 Y_n / M_{\text{fuel}})^{0.34}, \quad (3)$$

where  $\rho R$  is in  $\text{g}/\text{cm}^2$ ,  $Y_n$  is in units of  $10^{16}$ , and the fuel mass  $M_{\text{fuel}}$  is in mg. This form of  $\chi$  depends only on the measured fuel  $\rho R$  and the neutron yield and is roughly equivalent to the cube root of the experimental ignition threshold factor (ITFx) derived by Haan *et al.*<sup>22</sup>

It has been shown<sup>24</sup> that ignition hydrodynamically equivalent implosions on OMEGA occur for values of  $\chi \gtrsim 0.16$ . This can be satisfied for a range of areal densities and yields. Given that a  $\rho R$  of  $\sim 300 \text{ mg}/\text{cm}^2$  has already been demonstrated on OMEGA,<sup>3,20</sup> a  $\chi \sim 0.16$  corresponds to a yield of  $4 \times 10^{13}$ . These values of  $Y_n$  and  $\rho R$  provide a convenient metric for demonstrating ignition hydrodynamically equivalent implosion performance with symmetric direct drive on OMEGA and are consistent with an earlier analysis discussed in Ref. 20.

Figure 135.3 shows the dependence of the 1-D fractional measured  $\rho R$  ( $\rho R / \rho R_{1\text{-D}}$ ) as a function of the calculated fuel adiabat [Fig. 135.3(a)] and IFAR [Fig. 135.3(b)] for the database shown in Fig. 135.2. As expected, the fraction of the 1-D  $\rho R$  produced in the implosions is lower for higher-convergence, lower-adiabat implosions. The trend of lower  $\rho R$  with decreasing shell stability is also clear as a function of IFAR. The measured fraction of the 1-D  $\rho R$  approaches 80% for values of the adiabat above  $\sim 2.5$  and values of IFAR below  $\sim 20$  (note that

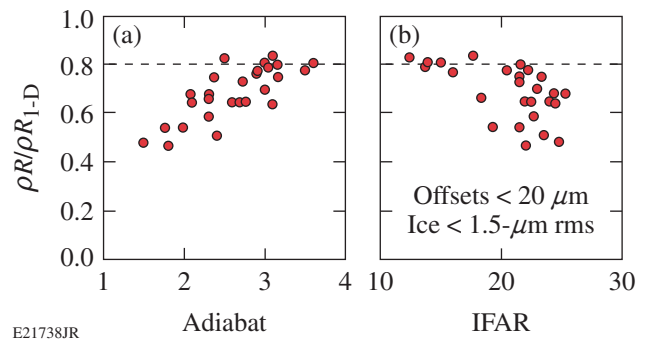


Figure 135.3

(a) The correlation between the ratio of the measured and 1-D-predicted areal density and the calculated adiabat for the implosions in Fig. 135.2 shows a drop in the measured  $\rho R$  for adiabats generally less than 2.5. (b) The correlation between the ratio of the measured and 1-D-predicted areal density and the calculated IFAR for the implosions in Fig. 135.2 shows a drop in the measured  $\rho R$  for IFAR's generally greater than 17.

the velocities for the implosions at these lower adiabats range from 280 to 320 km/s). Burn truncation<sup>29</sup> and <sup>3</sup>He buildup in the capsule caused by tritium  $\beta$ -decay can account for much of the degradation relative to the prediction. Estimates of the void pressure resulting from the buildup of <sup>3</sup>He are sufficient to cause a degradation of the predicted  $\rho R$  of 10% to 15%. The 1-D prediction for the points in Fig. 135.3 does not take into account the increased pressure in the capsule related to <sup>3</sup>He buildup as the target ages.

The  $\rho R$  measurements in Fig. 135.3 were obtained with two independent instruments: the magnetic recoil spectrometer (MRS)<sup>30</sup> and a highly collimated neutron time-of-flight (nTOF) detector.<sup>31</sup> The areal density inferred from the nTOF is based on a different part of the (n,T/D) scattering cross section<sup>32</sup> than that used in the reduction of the MRS data. While the MRS measures the fraction of the primary yield forward scattered by the compressed DT, the nTOF measures the (n,T) backscatter edge at 3.5 MeV to infer the triton density in the compressed fuel. The systematic error on the  $\rho R$  inferred from the nTOF is somewhat higher (estimated to be <15%) than that from the MRS (6%). However, where both measurements are available (a small number of the experiments did not have the nTOF available), the value of the  $\rho R$  used in Fig. 135.3 (and subsequent analyses) is the average of the two measurements.

Figure 135.4 is a duplicate of Fig. 135.2 with contours of constant  $\rho R/\rho R_{1-D}$  based on the same database of shots. In this two-dimensional (2-D) design space, a stability boundary sug-

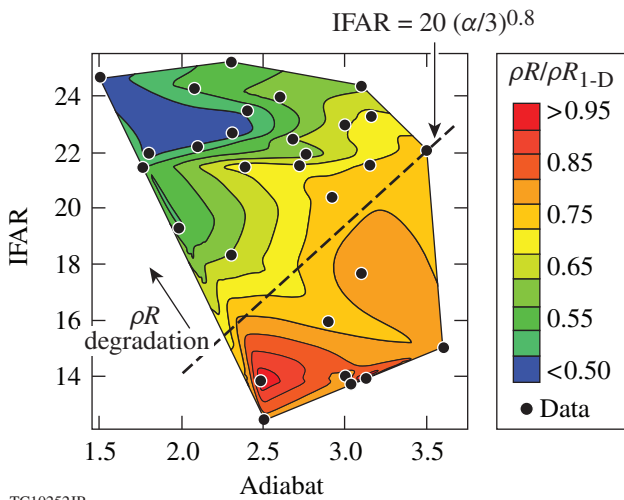


Figure 135.4  
Contours of the measured areal-density fraction relative to 1-D prediction ( $\rho R/\rho R_{1-D}$ ) show a steep drop for values of the IFAR above the line defined by  $20(\alpha/3)^{0.8}$ .

gested by Figs. 135.3(a) and 135.3(b) is clearly evident. For this set of experiments, the edge of the boundary can be roughly defined as  $IFAR = 20(\alpha/3)^{0.8}$ . While Fig. 135.3(b) suggests that the measured  $\rho R$  begins to deviate from the 1-D prediction for values of  $IFAR > 17$ , the 2-D contour plot clearly shows that the 1-D  $\rho R$  is recovered for larger  $IFAR$  as long as the adiabat is suitably large. This further confirms that the stability of these targets is sensitive to design details that can be fully accessed based on the flexibility of the target platform.

Figure 135.5 shows the measured (red circles) and 1-D-predicted (black circles)  $Y_n$  [Fig. 135.5(a)] and  $T_{ion}$  [Fig. 135.5(b)]

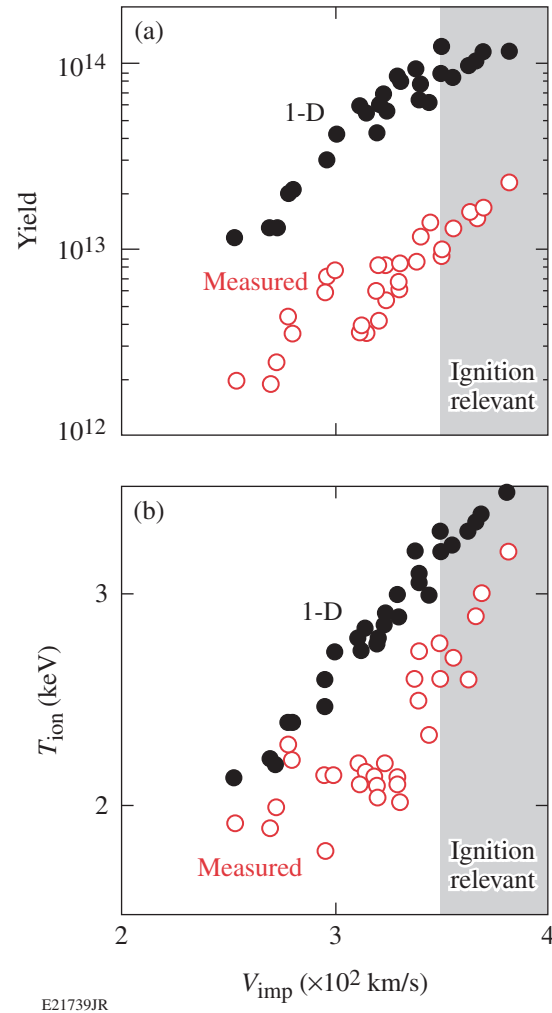


Figure 135.5  
(a) The predicted 1-D and measured yields increase with increasing implosion velocity. The adiabat was increased to reach implosion velocities above 330 km/s. (b) While the 1-D ion temperature increases linearly with the implosion velocity, the measured temperature is fairly constant until the implosion velocity exceeds 330 km/s. The shaded regions indicate ignition-relevant implosion velocities.

as functions of the calculated implosion velocity. The measured yield increases uniformly with implosion velocity from 250 km/s to 380 km/s. The larger spread in the experimental yields for  $V_{imp} \sim 300$  to 320 km/s suggests that the shell is becoming increasingly unstable as the implosion velocity is increased. The data points at higher  $V_{imp}$  were therefore acquired using a higher fuel adiabat to stabilize perturbation growth at the ablation surface and the ice–gas interface. This additional stabilization is clearly evident in Fig. 135.5(b), where there is little variation in the measured  $T_{ion}$  with increasing  $V_{imp}$  until the fuel adiabat is raised to access  $V_{imp}$  above  $\sim 320$  km/s. With the higher-adiabat implosions,  $T_{ion}$  increases rapidly with  $V_{imp}$  reaching 90% to 95% of the prediction at 380 km/s.

Figure 135.6 is a duplicate of Fig. 135.2 with contours of constant  $Y_n/Y_{n1-D}$  [this is the ratio of the measured and simulated yields from Fig. 135.5(a), commonly referred to as YOC]. The vertical contours indicate that the measured yield depends primarily on the adiabat for values of IFAR < 20 to 22. Only at the highest adiabat does the yield appear to be independent of IFAR for ignition-relevant values (a target is unlikely to ignite at these adiabats with the energy available on the NIF). The YOC for these few data points is >20%. The YOC for ignition-relevant values of the adiabat and IFAR is generally less than 10%.

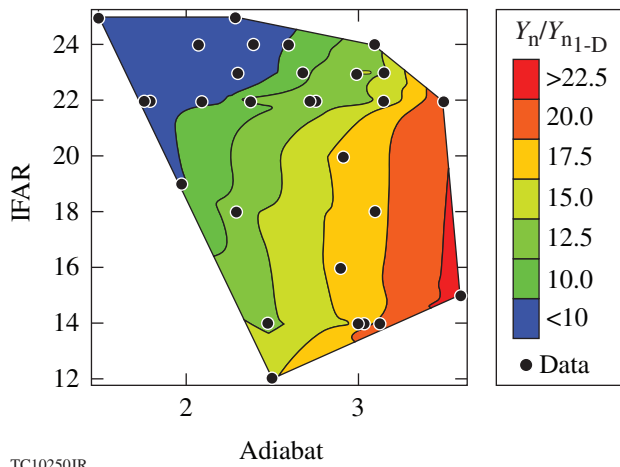


Figure 135.6  
Contours of the measured yield fraction relative to 1-D predictions [yield-over-clean (YOC)] show that the yield depends primarily on the adiabat for IFAR’s generally less than 20.

The largest value of  $\chi$  [Eq. (3)] in this data set is 0.09. For this shot (and several others in the 0.08 range), the values of the measured  $\rho R$  and  $Y_n$  are approximately half of the values needed to demonstrate ignition hydrodynamically equivalent

implosion performance. These highest-performing implosions are not associated with ignition-relevant values of IFAR and adiabat. This is seen in Fig. 135.7, where contours of constant  $\chi/\chi_{1-D}$  are plotted in the IFAR–adiabat space of Fig. 135.2. The contours clearly show that relative to 1-D prediction, target performance decreases with increasing IFAR and decreasing adiabat. Not surprisingly, this is consistent with the stability boundary identified in Fig. 135.4.

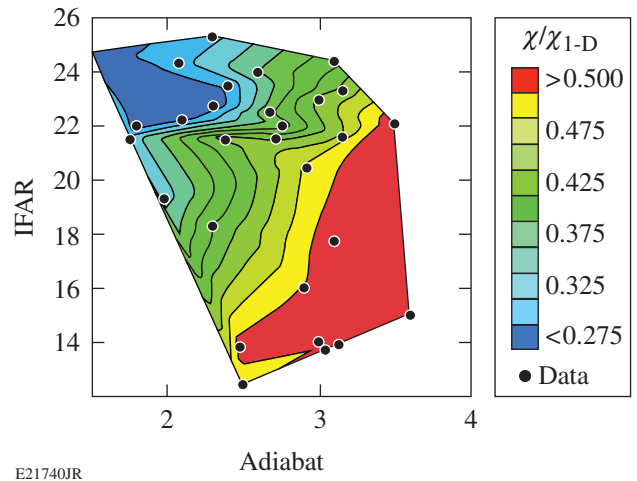
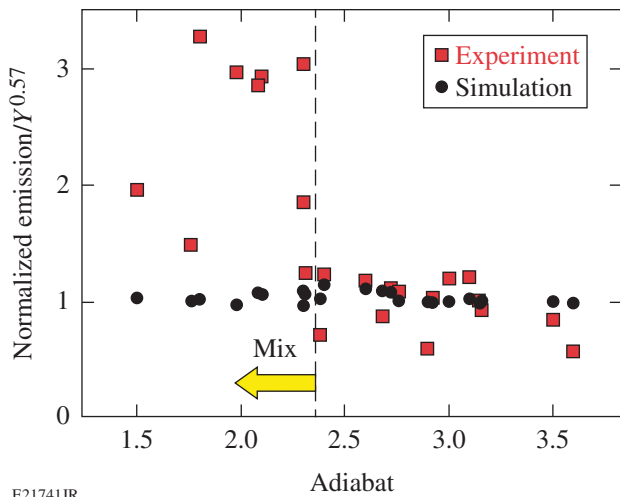


Figure 135.7  
Contours of the measured  $\chi$  fraction relative to the 1-D–predicted  $\chi$  show a steep drop with increasing IFAR for ignition-relevant adiabats (<2.5).

Together, these data suggest that as the design approaches ignition hydrodynamic equivalence, the fuel shell breaks apart during acceleration, leading to a drop in the burn-averaged fuel areal density. The subsequent loss in the hot-spot pressure and temperature leads to a drop in the primary yield. The shell breakup during acceleration suggests Rayleigh–Taylor (RT) perturbation growth from the ablation surface (as opposed to deceleration-driven growth at the ice–gas interface). Such growth would be expected to mix ablator material into the core. This mixing is confirmed in Fig. 135.8, where the yield-normalized x-ray emission from the core is plotted as a function of the adiabat. The yield normalization factor comes from a fit of the 1-D–predicted x-ray emission. When normalized to  $Y_{1-D}^{0.57}$ , simulated core x-ray emission is approximately constant for all of the experiments. This is shown by the black circles in Fig. 135.8. If carbon mixing enhances the core emission, this should be evident when the experimental x-ray emission is normalized to  $Y_{meas}^{0.57}$ . These values are plotted as the red squares. The data clearly show that when the adiabat is less than 2.5, the core x-ray emission is strongly enhanced relative to the high-adiabat experiments, whereas Figs. 135.4 and 135.6 show that the shell is likely integral through acceleration. The



E21741JR

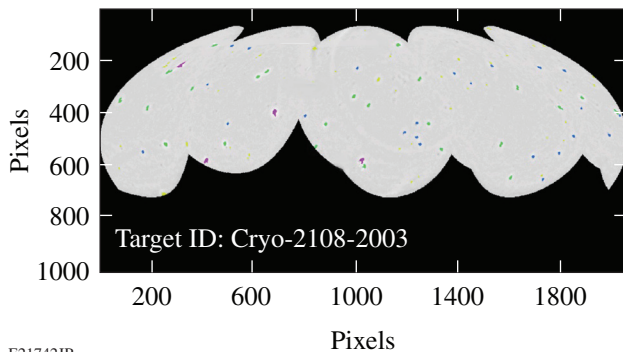
Figure 135.8

The yield-normalized x-ray emission from 1-D simulations (black circles) and cryogenic DT implosions (red squares) is plotted as a function of the implosion adiabat. The experimental points show a pronounced increase in the x-ray emission relative to 1-D prediction for adiabats generally less than 2.5, indicating that this emission may be due to higher-Z carbon mixing into the core.

normalization of the experimental and simulated points at high adiabats is arbitrary, as are the units of the normalized emission. The simulated x-ray emission used to establish the yield normalization is restricted to the sensitivity range of the gated x-ray imager used for the measurement (roughly 4 to 7 keV).

**Capsule Surface Quality and 2-D Simulations**

As discussed in **Measurements and Discussion** (p. 147), the accumulated data suggest a high level of ablator mixing into the hot spot at peak burn. This level of mix would require a significant source of perturbations on the capsule surface to drive CD into the core before stagnation. The shadowgraphy-based imaging system used to characterize the ice-layer quality was refocused to image the capsule surface. Figure 135.9 shows a stitched image in pixel space of five capsule surface images acquired at the same focal depth as the target was rotated. The stitched image contains about 2/3 of the capsule surface and



E21742JR

shows dozens of surface “defects” distributed randomly (there is no discernible pattern from one target to another) across the surface.

A detailed optical analysis of these defects confirms that most of the features reside on the outer capsule surface and originate during the high-pressure fill and cooling cycle (Ref. 18 describes the permeation filling process and the DT layering/characterization in detail), i.e., the features do not correspond with fabrication defects identified prior to the fill. A subset of the filled capsules has a small number of dendritic defects on the inner surface of the CD shell. An analysis of one of these inner surface dendritic defects following a controlled depressurization of a filled capsule showed that the radial depth is of the order of 0.1 μm or less, within the smoothness specification for the capsule.

Every target imploded on OMEGA since January 2012 has had the surface defects analyzed based on images such as the one shown in Fig. 135.9. The analysis identifies the type of defect (outer surface or inner surface) and the defect area. Figure 135.10(a) is a plot of the defect-size distribution for the targets filled in 2012 (48 total). The average defect size is ~140 μm<sup>2</sup>; the imaging system is capable of resolving features with an area as small as 20 μm<sup>2</sup>. Figure 135.10(b) shows a histogram of the target defect frequency distribution (bin size is ten defects). The defect count can exceed 100 on a single target. The total defect area for the targets discussed in this article ranged from a few thousand up to 15,000 μm<sup>2</sup> (nearly 1% of the total capsule surface area). The variation in defect count and total area from target to target and fill to fill is not understood.

Two-dimensional simulations of a single isolated surface defect suggest that the defects account for much of the observed target performance degradation relative to 1-D prediction. The implosion performance of several targets was simulated by assuming a uniform distribution of constant-size defects

Figure 135.9

A stitched set of images of a cryogenic DT capsule surface during characterization. The image shows dozens of surface defects associated with the high-pressure DT permeation fill. The defects are likely frozen gas contaminants in the DT fuel.

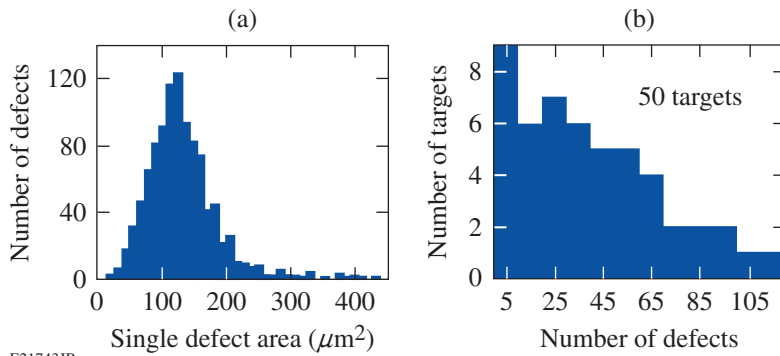


Figure 135.10  
 (a) The defect-size distribution for the targets characterized in 2012 show that the average defect size is about  $140 \mu\text{m}^2$ .  
 (b) The frequency distribution of the defects on 50 targets filled and characterized in 2012. Most targets have several dozen individual defects.

E21743JR

( $80 \mu\text{m}^2$ ) with a thickness of  $1 \mu\text{m}$ . The thickness of the defects cannot be measured with the optical imaging system used to characterize the DT ice layer (limited spatial resolution and contrast) unless they can be resolved on the limb of the images. In some cases this has been possible; however, most of the defects cannot be identified on the limb of the capsule images. A thickness of  $1 \mu\text{m}$  was used in the simulations as a compromise: some will be larger while most are smaller. A 2-D simulation with a single defect and reflecting boundary conditions was performed using a sector defined as  $4\pi/N$ , where  $N$  is the number of defects on the target. The reflecting boundaries mimic the presence of neighboring defects in this simplified 2-D simulation. Assuming that the defects are identical and uniformly distributed around a target, the predicted yield is then  $N$  times the results of the simulation. The simulated ion temperature and neutron-averaged  $\rho R$  are taken as the average for the target. Table 135.I shows the results for shot 66999 (August 2012). The first row is the 1-D prediction using *LILAC* with nonlocal (NL) thermal transport and an SBS model to account for CBET in the absorbed energy.<sup>8</sup> The second row is the 2-D simulation described above including single-beam laser imprint<sup>33</sup> but no isolated defects. The third row is the 2-D simulation including the average isolated defect with  $N = 150$ . The fourth row is the experimentally measured values. The isolated defect simulation reproduces the experimental

measurements reasonably well, while the imprint-only simulations cannot explain the observed implosion performance. The other simulated implosions show a quantitatively similar behavior with respect to measured target performance. While the number of defects simulated was larger than the average number shown in Fig. 135.10(b) and the area of each defect was less than the average shown in Fig. 135.10(a), the total defect area was similar to the average of most targets in the 2012 database. The key point is that injecting the proper amount of ablator material into the core via ablation-front RT growth reproduces the experimental performance observables.

Further progress toward the demonstration of ignition hydrodynamically equivalent implosion performance requires that these isolated defects be eliminated from the capsules. Few, if any, of these defects are particulate in nature. Steps taken in 2011 eliminated the identified sources for particulate debris. The defects are condensed non-hydrogenic gases entrained in the closed DT-fuel supply; analysis confirms that the fuel supply contains nearly 0.5% organics and hundreds of ppm of nitrogen, water, and  $\text{CO}_2$ . The organics are likely generated by the energetic tritium  $\beta$ -decay electrons that liberate carbon atoms from the CD capsule and the cryogenic epoxies used in the target mounts (the target and support structures are immersed in DT gas during the diffusion fill and the pressure is ramped up to hundreds of atmospheres at room temperature over a 24-h period). Since the DT fuel supply is operated as a closed loop, organics formed during a fill remain entrained in the fuel for subsequent fills.

Table 135.I: For shot 66999, the results of 1-D simulations including nonlocal thermal transport and cross-beam energy transfer, 2-D simulations with imprint, and 2-D simulations based on an isolated surface defect are compared with the measured yield, areal density, and ion temperature.

Shot 66999	$Y_n (\times 10^{13})$	$\rho R (\text{mg}/\text{cm}^2)$	$T_{\text{ion}} (\text{keV})$
1-D (NL + SBS)	7.9	238	3.1
2-D imprint	4.5	242	3.4
2-D defect	1.8	151	2.7
Measured	1.2	175	2.5

The gases condense on the outer surface of the capsule as it is being cooled under pressure. As the temperature of the DT approaches the triple point, the DT liquefies, immersing the capsule and effectively stopping further contaminant gas condensation from the vapor phase on the outer surface. The contaminant gases are presumably on the inside of the capsule as well since the shell is quite permeable at room temperature. The gases likely form monolayers on the inner surface as the

temperature falls below the various triple points. Based on the characterization possible to date, there is no visible evidence of crystalline or condensation-related features on the inner surface of the CD shell. Any features on the inner surface would need to first feed out to the ablation surface (where the amplitudes would be quite reduced) to be associated with carbon mixing in the core (recall Fig. 135.8).

Two facility projects are underway to eliminate these “trace” gases in the fuel supply. The first is a PdAg filter<sup>34</sup> that passes only hydrogen into the high-pressure permeation cell with the capsules. This filter will be implemented in early 2013. The second project is an isotope separation unit that will remove all contaminants from the DT-fuel supply including protium (<sup>1</sup>H). Protium forms HD, HT, and HH molecules that lower the effective triple point of the fuel, impacting layer formation and the density of the void. This system is expected to become operational in late 2013.

### Experimental Ignition Threshold Factor

The goal of the National Ignition Campaign (NIC) was to demonstrate alpha heating and ignition using indirectly driven (ID) cryogenic DT implosions on the NIF.<sup>35</sup> Using multidimensional hydrodynamic simulations, Haan *et al.*<sup>22</sup> derived a convenient metric (ITFx) for tracking the relative implosion performance as capsule and drive parameters were tuned to achieve the required implosion symmetry, fuel adiabat, and implosion velocity. The ITFx is given by

$$\text{ITFx}(\text{ID}) = \left( Y_n / 3.2 \times 10^{15} \right) \times (\text{DSR} / 0.07)^{2.3}, \quad (4)$$

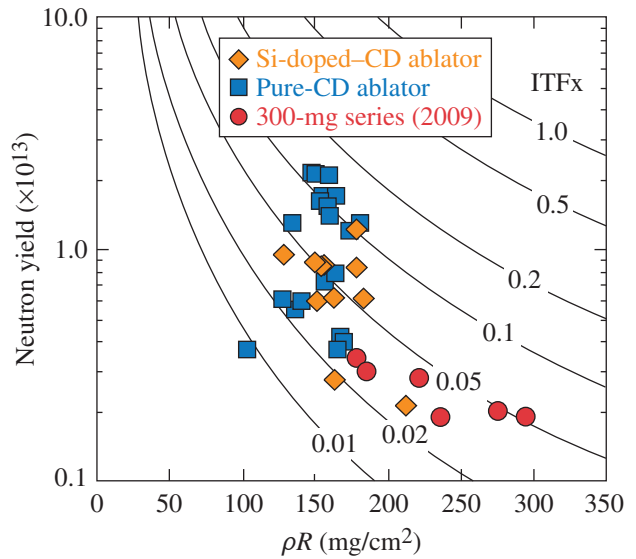
where DSR is the “down-scatter ratio”<sup>36</sup> in percent and related<sup>37</sup> to the total fuel areal density by  $\rho R \text{ (g/cm}^2\text{)} = 21 \times \text{DSR}(\%)$ , i.e., the normalization factor of 0.07 is effectively a fuel areal density of 1.5 g/cm<sup>2</sup>. The normalization factors on the yield and areal density are set so that an ITFx of unity implies a 50% probability that the target will ignite (given the spectrum of tolerances used in the simulations). Symmetric direct-drive (DD) implosions on OMEGA can be plotted using the ITFx(ID) on an equivalent performance basis by using the standard hydrodynamic relations<sup>24</sup>  $\rho R \sim E_L^{1/3}$ ,  $Y \sim T_i^{4.7} \times \rho R^{0.56} \times M_{\text{fuel}}$ , and  $T \sim E^{0.07}$ . The ignition  $Y_n$  and  $\rho R$  in Eq. (4) can be replaced by laser energy and mass-scaled quantities from OMEGA cryogenic DT implosions. The OMEGA ignition-equivalent ITFx is then

$$\text{ITFx}(\text{NIF DD}) = \text{ITFx}(\text{ID } \Omega) \times \left( E_{\text{NIF}} / E_{\Omega} \right)^{1.28} \times \left( M_{\text{NIF}} / M_{\Omega} \right) \times \left( \text{YOC}_{\text{NIF}} / \text{YOC}_{\Omega} \right), \quad (5)$$

where ITFx (ID  $\Omega$ ) is Eq. (4) with the OMEGA ( $\Omega$ ) measured quantities,  $E$  is the laser energy,  $M$  is the fuel mass, and YOC is based on an equivalent perturbation spectrum for each facility.<sup>24</sup> The assumption is that the YOC on the NIF will be higher than on OMEGA for an equivalent perturbation spectrum, given the larger capsule and consequent smaller perturbation wavelengths. For  $E_{\text{NIF}} = 1.8 \text{ MJ}$ ,  $E_{\Omega} = 25 \text{ kJ}$ ,  $M_{\text{NIF}} = 0.17 \text{ mg}$ ,  $M_{\Omega} = 0.02 \text{ mg}$ , and  $\text{YOC}_{\text{NIF}} = 50\%$  and  $\text{YOC}_{\Omega} = 25\%$  (best  $\text{YOC}_{\Omega}$  for an adiabat of  $\sim 3$  and  $V_{\text{imp}}$  of  $\sim 350 \text{ km/s}$ ),

$$\text{ITFx}(\text{NIF DD}) = 3505 \times \text{ITFx}(\text{ID } \Omega). \quad (6)$$

Figure 135.11 shows the distribution of the implosions discussed above in a plot of measured yield and  $\rho R$  (as in Fig. 135.2 each point represents an experiment). The blue squares are implosions using pure-CD ablators while the orange diamonds are Si-doped ablators (typically a few atom percent of silicon in the outer few microns of the shell). The red circles are from a high-areal-density series of experiments performed in 2009 (Refs. 3 and 20). There is no discernible difference between the doped and undoped ablators, confirming the conclusion from Table 135.I that imprint alone cannot explain the current target performance. Curves of constant ITFx (NIF DD) from Eq. (6) are superimposed. The best-performing implosions on OMEGA have achieved an equivalent NIF direct-drive ITFx



TC10124JR

Figure 135.11

The implosions represented in Fig. 135.2 are plotted according to the measured yield and areal density. Curves of constant NIF-equivalent direct-drive ITFx [Eq. (6)] are also plotted. The blue squares are pure-CD ablators while the orange diamonds are Si-doped-CD ablators. The red circles are from a high-areal-density series of experiments performed in 2009 (Refs. 3 and 20).

of nearly 0.2 (this includes the 2× multiplier from the YOC scaling). The highest  $\rho R$  to date in an OMEGA DT implosion (~295 mg/cm<sup>2</sup>) produced an ITFx (NIF DD) nearly 3× less as a result of the low yield. An ITFx (NIF DD) of unity is satisfied for an areal density of 300 mg/cm<sup>2</sup> and a yield of  $4 \times 10^{13}$ , very similar to the values derived by Betti *et al.*<sup>24</sup> from the generalized Lawson criterion for ICF and discussed above.

It is apparent from Fig. 135.11 that recent experiments have not produced areal densities above 200 mg/cm<sup>2</sup> regardless of the design adiabat and the implosion velocity. All attempts to reduce the adiabat to increase the areal density led to a decrease in both the yield and areal densities; at an adiabat of 3, the measured yields and areal densities drop to below 10% and 50% of 1-D predictions, respectively (with ITFx values well below 0.1). This suggests that ablation-front hydrodynamic instabilities remain the leading cause of the breakup of the fuel shell in-flight.

### Conclusion

The goal of the cryogenic DT implosion experiments at LLE is to demonstrate ignition hydrodynamic similarity. Recent cryogenic DT implosions on OMEGA have probed a broad region of design space that includes fuel adiabats from <2 to 4, IFAR's from <15 to more than 25, and implosion velocities from 250 to 380 km/s. Several of the targets would have demonstrated ignition hydrodynamic equivalence had the measured performance agreed with the 1-D prediction. The key to this rapid progress is the flexible symmetric direct-drive target platform on the OMEGA laser. With the peak drive intensity defined by the hydro scaling discussed in **Hydrodynamic Similarity and Experimental Design** (p. 145), the adiabat of any layered DT target can be easily changed by adjusting the laser-drive picket energies and relative timings, while the implosion velocity and IFAR are set by the mass of the ablator and ice.

The conclusion from the data and 2-D simulations is that the stability of the imploding shell is compromised by dozens of isolated outer-surface defects. These defects act as perturbation seeds that grow rapidly at the ablation surface and mix ablator material into the core. The defects that appear on the capsules following the permeation fill process are most likely caused by contaminant gases in the DT fuel supply that freeze on the surface of the capsule as it is being cooled under pressure.

High implosion velocities are achieved with higher-adiabat target designs that stabilize the hydro-instability growth at the ablation surface. At the highest adiabats (4), the measured areal

density and primary neutron yield are >80% to 90% and  $\geq 25\%$  of the 1-D prediction, respectively. Comparable performance relative to 1-D at adiabats of 2.0 to 2.5 is needed to demonstrate ignition hydrodynamic similarity.

### ACKNOWLEDGMENT

This work was supported by the U.S. Department of Energy Office of Inertial Confinement Fusion under Cooperative Agreement No. DE-FC52-08NA28302, the University of Rochester, and the New York State Energy Research and Development Authority. The support of DOE does not constitute an endorsement by DOE of the views expressed in this article.

### REFERENCES

1. T. R. Boehly, D. L. Brown, R. S. Craxton, R. L. Keck, J. P. Knauer, J. H. Kelly, T. J. Kessler, S. A. Kumpan, S. J. Loucks, S. A. Letzring, F. J. Marshall, R. L. McCrory, S. F. B. Morse, W. Seka, J. M. Soures, and C. P. Verdon, *Opt. Commun.* **133**, 495 (1997).
2. W. J. Hogan, E. I. Moses, B. E. Warner, M. S. Sorem, and J. M. Soures, *Nucl. Fusion* **41**, 567 (2001).
3. V. N. Goncharov, T. C. Sangster, T. R. Boehly, S. X. Hu, I. V. Igumenshchev, F. J. Marshall, R. L. McCrory, D. D. Meyerhofer, P. B. Radha, W. Seka, S. Skupsky, C. Stoeckl, D. T. Casey, J. A. Frenje, and R. D. Petrasso, *Phys. Rev. Lett.* **104**, 165001 (2010).
4. P. B. Radha, F. J. Marshall, J. A. Marozas, A. Shvydky, I. Gabalski, T. R. Boehly, T. J. B. Collins, R. S. Craxton, D. H. Edgell, R. Epstein, J. A. Frenje, D. H. Froula, V. N. Goncharov, M. Hohenberger, R. L. McCrory, P. W. McKenty, D. D. Meyerhofer, R. D. Petrasso, T. C. Sangster, and S. Skupsky, *Phys. Plasmas* **20**, 056306 (2013).
5. S. Skupsky, J. A. Marozas, R. S. Craxton, R. Betti, T. J. B. Collins, J. A. Delettrez, V. N. Goncharov, P. W. McKenty, P. B. Radha, T. R. Boehly, J. P. Knauer, F. J. Marshall, D. R. Harding, J. D. Kilkenny, D. D. Meyerhofer, T. C. Sangster, and R. L. McCrory, *Phys. Plasmas* **11**, 2763 (2004).
6. S. Skupsky, R. S. Craxton, F. J. Marshall, R. Betti, T. J. B. Collins, R. Epstein, V. N. Goncharov, I. V. Igumenshchev, J. A. Marozas, P. W. McKenty, P. B. Radha, J. D. Kilkenny, D. D. Meyerhofer, T. C. Sangster, and R. L. McCrory, *J. Phys. IV France* **133**, 233 (2006).
7. S. X. Hu, G. Fiksel, V. N. Goncharov, S. Skupsky, D. D. Meyerhofer, and V. A. Smalyuk, *Phys. Rev. Lett.* **108**, 195003 (2012).
8. I. V. Igumenshchev, W. Seka, D. H. Edgell, D. T. Michel, D. H. Froula, V. N. Goncharov, R. S. Craxton, L. Divol, R. Epstein, R. Follett, J. H. Kelly, T. Z. Kosc, A. V. Maximov, R. L. McCrory, D. D. Meyerhofer, P. Michel, J. F. Myatt, T. C. Sangster, A. Shvydky, S. Skupsky, and C. Stoeckl, *Phys. Plasmas* **19**, 056314 (2012).
9. S. X. Hu, V. A. Smalyuk, V. N. Goncharov, J. P. Knauer, P. B. Radha, I. V. Igumenshchev, J. A. Marozas, C. Stoeckl, B. Yaakobi, D. Shvarts, T. C. Sangster, P. W. McKenty, D. D. Meyerhofer, S. Skupsky, and R. L. McCrory, *Phys. Rev. Lett.* **100**, 185003 (2008).
10. P. B. Radha, C. Stoeckl, V. N. Goncharov, J. A. Delettrez, D. H. Edgell, J. A. Frenje, I. V. Igumenshchev, J. P. Knauer, J. A. Marozas, R. L.

- McCrory, D. D. Meyerhofer, R. D. Petrasso, S. P. Regan, T. C. Sangster, W. Seka, and S. Skupsky, *Phys. Plasmas* **18**, 012705 (2011).
11. T. R. Boehly, V. N. Goncharov, W. Seka, M. A. Barrios, P. M. Celliers, D. G. Hicks, G. W. Collins, S. X. Hu, J. A. Marozas, and D. D. Meyerhofer, *Phys. Rev. Lett.* **106**, 195005 (2011).
  12. V. N. Goncharov, T. C. Sangster, P. B. Radha, R. Betti, T. R. Boehly, T. J. B. Collins, R. S. Craxton, J. A. Delettrez, R. Epstein, V. Yu. Glebov, S. X. Hu, I. V. Igumenshchev, J. P. Knauer, S. J. Loucks, J. A. Marozas, F. J. Marshall, R. L. McCrory, P. W. McKenty, D. D. Meyerhofer, S. P. Regan, W. Seka, S. Skupsky, V. A. Smalyuk, J. M. Soures, C. Stoeckl, D. Shvarts, J. A. Frenje, R. D. Petrasso, C. K. Li, F. Séguin, W. Manheimer, and D. G. Colombant, *Phys. Plasmas* **15**, 056310 (2008).
  13. S. X. Hu, V. Smalyuk, V. N. Goncharov, S. Skupsky, T. C. Sangster, D. D. Meyerhofer, and D. Shvarts, *Phys. Rev. Lett.* **101**, 055002 (2008).
  14. B. Yaakobi, P.-Y. Chang, A. A. Solodov, C. Stoeckl, D. H. Edgell, R. S. Craxton, S. X. Hu, J. F. Myatt, F. J. Marshall, W. Seka, and D. H. Froula, *Phys. Plasmas* **19**, 012704 (2012).
  15. V. N. Goncharov, J. P. Knauer, P. W. McKenty, P. B. Radha, T. C. Sangster, S. Skupsky, R. Betti, R. L. McCrory, and D. D. Meyerhofer, *Phys. Plasmas* **10**, 1906 (2003).
  16. P. B. Radha, J. A. Marozas, F. J. Marshall, A. Shvydky, T. J. B. Collins, V. N. Goncharov, R. L. McCrory, P. W. McKenty, D. D. Meyerhofer, T. C. Sangster, and S. Skupsky, *Phys. Plasmas* **19**, 082704 (2012).
  17. C. Stoeckl, C. Chiritescu, J. A. Delettrez, R. Epstein, V. Yu. Glebov, D. R. Harding, R. L. Keck, S. J. Loucks, L. D. Lund, R. L. McCrory, P. W. McKenty, F. J. Marshall, D. D. Meyerhofer, S. F. B. Morse, S. P. Regan, P. B. Radha, S. Roberts, T. C. Sangster, W. Seka, S. Skupsky, V. A. Smalyuk, C. Sorce, J. M. Soures, R. P. J. Town, J. A. Frenje, C. K. Li, R. D. Petrasso, F. H. Séguin, K. Fletcher, S. Padalino, C. Freeman, N. Izumi, R. Lerche, and T. W. Phillips, *Phys. Plasmas* **9**, 2195 (2002).
  18. T. C. Sangster, R. Betti, R. S. Craxton, J. A. Delettrez, D. H. Edgell, L. M. Elasky, V. Yu. Glebov, V. N. Goncharov, D. R. Harding, D. Jacobs-Perkins, R. Janezic, R. L. Keck, J. P. Knauer, S. J. Loucks, L. D. Lund, F. J. Marshall, R. L. McCrory, P. W. McKenty, D. D. Meyerhofer, P. B. Radha, S. P. Regan, W. Seka, W. T. Shmayda, S. Skupsky, V. A. Smalyuk, J. M. Soures, C. Stoeckl, B. Yaakobi, J. A. Frenje, C. K. Li, R. D. Petrasso, F. H. Séguin, J. D. Moody, J. A. Atherton, B. D. MacGowan, J. D. Kilkenny, T. P. Bernat, and D. S. Montgomery, *Phys. Plasmas* **14**, 058101 (2007).
  19. T. C. Sangster, V. N. Goncharov, P. B. Radha, V. A. Smalyuk, R. Betti, R. S. Craxton, J. A. Delettrez, D. H. Edgell, V. Yu. Glebov, D. R. Harding, D. Jacobs-Perkins, J. P. Knauer, F. J. Marshall, R. L. McCrory, P. W. McKenty, D. D. Meyerhofer, S. P. Regan, W. Seka, R. W. Short, S. Skupsky, J. M. Soures, C. Stoeckl, B. Yaakobi, D. Shvarts, J. A. Frenje, C. K. Li, R. D. Petrasso, and F. H. Séguin, *Phys. Rev. Lett.* **100**, 185006 (2008).
  20. T. C. Sangster, V. N. Goncharov, R. Betti, T. R. Boehly, D. T. Casey, T. J. B. Collins, R. S. Craxton, J. A. Delettrez, D. H. Edgell, R. Epstein, K. A. Fletcher, J. A. Frenje, V. Yu. Glebov, D. R. Harding, S. X. Hu, I. V. Igumenshchev, J. P. Knauer, S. J. Loucks, C. K. Li, J. A. Marozas, F. J. Marshall, R. L. McCrory, P. W. McKenty, D. D. Meyerhofer, P. M. Nilson, S. P. Padalino, R. D. Petrasso, P. B. Radha, S. P. Regan, F. H. Seguin, W. Seka, R. W. Short, D. Shvarts, S. Skupsky, V. A. Smalyuk, J. M. Soures, C. Stoeckl, W. Theobald, and B. Yaakobi, *Phys. Plasmas* **17**, 056312 (2010).
  21. P. B. Radha, R. Betti, T. R. Boehly, J. A. Delettrez, D. H. Edgell, V. N. Goncharov, I. V. Igumenshchev, J. P. Knauer, J. A. Marozas, F. J. Marshall, R. L. McCrory, D. D. Meyerhofer, S. P. Regan, T. C. Sangster, W. Seka, S. Skupsky, A. A. Solodov, C. Stoeckl, W. Theobald, J. A. Frenje, D. T. Casey, C. K. Li, and R. D. Petrasso, *IEEE Trans. Plasma Sci.* **39**, 1007 (2011).
  22. S. W. Haan, J. D. Lindl, D. A. Callahan, D. S. Clark, J. D. Salmonson, B. A. Hammel, L. J. Atherton, R. C. Cook, M. J. Edwards, S. Glenzer, A. V. Hamza, S. P. Hatchett, M. C. Herrmann, D. E. Hinkel, D. D. Ho, H. Huang, O. S. Jones, J. Kline, G. Kyrala, O. L. Landen, B. J. MacGowan, M. M. Marinak, D. D. Meyerhofer, J. L. Milovich, K. A. Moreno, E. I. Moses, D. H. Munro, A. Nikroo, R. E. Olson, K. Peterson, S. M. Pollaine, J. E. Ralph, H. F. Robey, B. K. Spears, P. T. Springer, L. J. Suter, C. A. Thomas, R. P. Town, R. Vesey, S. V. Weber, H. L. Wilkens, and D. C. Wilson, *Phys. Plasmas* **18**, 051001 (2011).
  23. C. D. Zhou and R. Betti, *Phys. Plasmas* **15**, 102707 (2008).
  24. R. Betti, presented at the 24th IAEA Fusion Energy Conference, San Diego, CA, 8–13 October 2012.
  25. H. A. Baldis and C. J. Walsh, *Phys. Fluids* **26**, 1364 (1983).
  26. J. Delettrez, R. Epstein, M. C. Richardson, P. A. Jaanimagi, and B. L. Henke, *Phys. Rev. A* **36**, 3926 (1987).
  27. R. A. Lerche, D. W. Phillion, and G. L. Tietbohl, *Rev. Sci. Instrum.* **66**, 933 (1995).
  28. R. Betti, P. Y. Chang, B. K. Spears, K. S. Anderson, J. Edwards, M. Fatenejad, J. D. Lindl, R. L. McCrory, R. Nora, and D. Shvarts, *Phys. Plasmas* **17**, 058102 (2010).
  29. P. B. Radha, T. J. B. Collins, J. A. Delettrez, Y. Elbaz, R. Epstein, V. Yu. Glebov, V. N. Goncharov, R. L. Keck, J. P. Knauer, J. A. Marozas, F. J. Marshall, R. L. McCrory, P. W. McKenty, D. D. Meyerhofer, S. P. Regan, T. C. Sangster, W. Seka, D. Shvarts, S. Skupsky, Y. Srebro, and C. Stoeckl, *Phys. Plasmas* **12**, 056307 (2005).
  30. J. A. Frenje, K. M. Green, D. G. Hicks, C. K. Li, F. H. Séguin, R. D. Petrasso, T. C. Sangster, T. W. Phillips, V. Yu. Glebov, D. D. Meyerhofer, S. Roberts, J. M. Soures, C. Stoeckl, K. Fletcher, S. Padalino, and R. J. Leeper, *Rev. Sci. Instrum.* **72**, 854 (2001).
  31. C. J. Forrest, P. B. Radha, V. Yu. Glebov, V. N. Goncharov, J. P. Knauer, A. Pruyne, M. Romanofsky, T. C. Sangster, M. J. Shoup III, C. Stoeckl, D. T. Casey, M. Gatu-Johnson, and S. Gardner, *Rev. Sci. Instrum.* **83**, 10D919 (2012).
  32. J. A. Frenje, C. K. Li, F. H. Séguin, D. T. Casey, R. D. Petrasso, D. P. McNabb, P. Navratil, S. Quaglioni, T. C. Sangster, V. Yu. Glebov, and D. D. Meyerhofer, *Phys. Rev. Lett.* **107**, 122502 (2011).
  33. V. A. Smalyuk, V. N. Goncharov, K. S. Anderson, R. Betti, R. S. Craxton, J. A. Delettrez, D. D. Meyerhofer, S. P. Regan, and T. C. Sangster, *Phys. Plasmas* **14**, 032702 (2007).
  34. H. Amandusson, L.-G. Ekedahl, and H. Darnetun, *J. Membr. Sci.* **193**, 35 (2001).

35. J. D. Lindl and E. I. Moses, *Phys. Plasmas* **18**, 050901 (2011).
36. J. A. Frenje, D. T. Casey, C. K. Li, J. R. Rygg, F. H. Séguin, R. D. Petrasso, V. Yu. Glebov, D. D. Meyerhofer, T. C. Sangster, S. Hatchett, S. Haan, C. Cerjan, O. Landen, M. Moran, P. Song, D. C. Wilson, and R. J. Leeper, *Rev. Sci. Instrum.* **79**, 10E502 (2008).
37. A. J. Mackinnon, J. L. Kline, S. N. Dixit, S. H. Glenzer, M. J. Edwards, D. A. Callahan, N. B. Meezan, S. W. Haan, J. D. Kilkenny, T. Döppner, D. R. Farley, J. D. Moody, J. E. Ralph, B. J. MacGowan, O. L. Landen, H. F. Robey, T. R. Boehly, P. M. Celliers, J. H. Eggert, K. Krauter, G. Frieders, G. F. Ross, D. G. Hicks, R. E. Olson, S. V. Weber, B. K. Spears, J. D. Salmonsén, P. Michel, L. Divol, B. Hammel, C. A. Thomas, D. S. Clark, O. S. Jones, P. T. Springer, C. J. Cerjan, G. W. Collins, V. Y. Glebov, J. P. Knauer, C. Sangster, C. Stoeckl, P. McKenty, J. M. McNaney, R. J. Leeper, C. L. Ruiz, G. W. Cooper, A. G. Nelson, G. G. A. Chandler, K. D. Hahn, M. J. Moran, M. B. Schneider, N. E. Palmer, R. M. Bionta, E. P. Hartouni, S. LePape, P. K. Patel, N. Izumi, R. Tommasini, E. J. Bond, J. A. Caggiano, R. Hatarik, G. P. Grim, F. E. Merrill, D. N. Fittinghoff, N. Guler, O. Drury, D. C. Wilson, H. W. Herrmann, W. Stoeffl, D. T. Casey, M. G. Johnson, J. A. Frenje, R. D. Petrasso, A. Zylestra, H. Rinderknecht, D. H. Kalantar, J. M. Dzenitis, P. Di Nicola, D. C. Eder, W. H. Courdin, G. Gururangan, S. C. Burkhart, S. Friedrich, D. L. Blueuel, L. A. Bernstein, M. J. Eckart, D. H. Munro, S. P. Hatchett, A. G. Macphee, D. H. Edgell, D. K. Bradley, P. M. Bell, S. M. Glenn, N. Simanovskaia, M. A. Barrios, R. Benedetti, G. A. Kyrala, R. P. J. Town, E. L. Dewald, J. L. Milovich, K. Widmann, A. S. Moore, G. LaCaille, S. P. Regan, L. J. Suter, B. Felker, R. C. Ashabranner, M. C. Jackson, R. Prasad, M. J. Richardson, T. R. Kohut, P. S. Datte, G. W. Krauter, J. J. Klingman, R. F. Burr, T. A. Land, M. R. Hermann, D. A. Latray, R. L. Saunders, S. Weaver, S. J. Cohen, L. Berzins, S. G. Brass, E. S. Palma, R. R. Lowe-Webb, G. N. McHalle, P. A. Arnold, L. J. Lagin, C. D. Marshall, G. K. Brunton, D. G. Mathisen, R. D. Wood, J. R. Cox, R. B. Ehrlich, K. M. Knittel, M. W. Bowers, R. A. Zacharias, B. K. Young, J. P. Holder, J. R. Kimbrough, T. Ma, K. N. La Fortune, C. C. Widmayer, M. J. Shaw, G. V. Erbert, K. S. Jancaitis, J. M. DiNicola, C. Orth, G. Heestand, R. Kirkwood, C. Haynam, P. J. Wegner, P. K. Whitman, A. Hamza, E. G. Dzenitis, R. J. Wallace, S. D. Bhandarkar, T. G. Parham, R. Dylla-Spears, E. R. Mapoles, B. J. Koziolowski, J. D. Sater, C. F. Walters, B. J. Haid, J. Fair, A. Nikroo, E. Giraldez, K. Moreno, B. Vanwonderghem, R. L. Kauffman, S. Batha, D. W. Larson, R. J. Fortner, D. H. Schneider, J. D. Lindl, R. W. Patterson, L. J. Atherton, and E. I. Moses, *Phys. Rev. Lett.* **108**, 215005 (2012).

## Polar-Drive Experiments with Shimmed Targets on OMEGA

The polar-drive (PD) approach to directly driven, inertial confinement fusion<sup>1</sup> is being pursued as a means of demonstrating thermonuclear ignition at the National Ignition Facility<sup>2</sup> (NIF) with the beams of NIF in the indirect-drive configuration. Extensive experiments have been performed on the OMEGA Laser System<sup>3</sup> to evaluate this technique.<sup>4–7</sup> Ignition target designs using cryogenically cooled, DT-filled CH shells have been investigated using two-dimensional (2-D) hydrodynamic simulations.<sup>8,9</sup> These simulations suggest that gains of at least 20 to 30 can be achieved using 1.5 MJ of laser energy to irradiate a DT-ice-layer-bearing cryogenic target. In a recent simulation study by Collins *et al.*,<sup>9</sup> the drive symmetry was optimized by using a combination of beam pointing, beam shaping, pulse shaping, and target-layer shimming. Shimming uses an ideal ice-layer profile that is thinner at the target equator, where the beam illumination is the most oblique, and energy coupling to the target is reduced. The inclusion of an ice-layer shim increased the gain of the ignited plasma. Collins *et al.* also note that a shim applied to the CH capsule could equivalently be used to shape the imploding plasma.<sup>9</sup> This article presents the first results of shimmed PD experiments showing that improved implosion symmetry is obtained. The experiments were performed on the OMEGA Laser System in the PD configuration with D<sub>2</sub>-gas-filled, shimmed CH shells.

The unablated shell material in a laser-driven implosion behaves much like the payload of a rocket.<sup>10</sup> The final velocity of the unablated shell depends nonlinearly on the initial shell thickness and the intensity of the laser light being used to accelerate the shell through ablation.<sup>10</sup> For polar drive, the intensity varies as a function of both polar angle and time. Optimizing polar drive is accomplished by picking the beam shapes, beam pointing, pulse shapes, and target-shim profile that result in the most spherically shaped implosion, leading to the highest target gain. This is done experimentally and with simulations using a 2-D hydrodynamics code. If it is assumed that lateral mass flow in the imploding shell can be neglected, then the simulations can be performed with a one-dimensional (1-D) hydrocode, provided that the amount of absorbed energy can be accurately predicted. To apply this to polar drive it is

assumed that the average absorbed intensity is solely a function of polar angle. The capsule thickness as a function of polar angle needed to compensate for the angular variation of the average intensity can therefore be determined from a series of 1-D simulations. This is illustrated in Fig. 135.12, where the calculated trajectories of the fuel–shell interface  $R_{fs}$  as a function of time for two D<sub>2</sub>-filled CH shells with identical inner shell radii (412  $\mu\text{m}$ ) and fill pressure (10 atm), but with differing shell thicknesses of 24 and 27  $\mu\text{m}$ , respectively, are shown. The simulations were performed with the 1-D hydrocode *LILAC*<sup>11</sup> for nominal laser conditions of 27 kJ of UV light in a 1-ns square pulse ( $\sim 1 \times 10^{15}$  W/cm<sup>2</sup> at a radius of 430  $\mu\text{m}$ ). The 27- $\mu\text{m}$  shell implodes more slowly than the 24- $\mu\text{m}$  shell.  $R_{fs}$  is also shown for an intensity reduced to 80% of the nominal case. This trajectory (dashed line) is nearly identical to that of the 27- $\mu\text{m}$ -thick shell at the nominal intensity.

A series of such simulations were performed to determine the approximate shell thickness as a function of average intensity needed so that  $R_{fs}$  was the same as the nominal intensity case at a time close to shell stagnation. Figure 135.13 shows

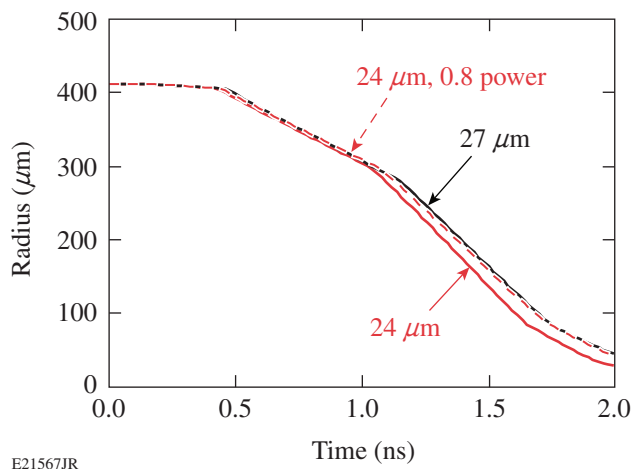
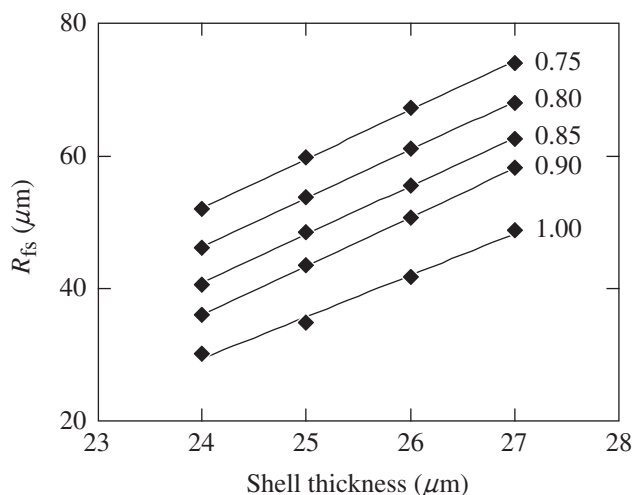


Figure 135.12  
Simulated fuel–shell interface  $R_{fs}$  trajectory for a 24- and a 27- $\mu\text{m}$ -thick shell at nominal laser conditions of 27 kJ, 1-ns square pulse, and for a 24- $\mu\text{m}$ -thick shell at 0.8 times nominal laser intensity.



E21812JR

Figure 135.13

Simulated values of  $R_{fs}$  at  $t = 2.0$  ns as a function of shell thickness for cases of 0.75, 0.80, 0.85, 0.90, and 1.00 times nominal laser intensity.

values of  $R_{fs}$  at  $t = 2.0$  ns, when the fuel-shell interface is close to a minimum, for shell thicknesses  $\Delta r$  from 24 to 27  $\mu\text{m}$ , and intensities  $I$  of 0.75 to 1.0 times nominal. A straight line was fit to each set of values of  $R_{fs}$  for a given  $I$ . The value of shell thickness  $\Delta r$  as a function of intensity that results in an  $R_{fs}$  of 49  $\mu\text{m}$  at  $t = 2.0$  ns was determined from these fits by linear regression. The resulting equation for  $\Delta r$  in microns as a function of intensity is given by

$$\Delta r = 6.4 + 29.6 I - 9.0 I^2, \quad (1)$$

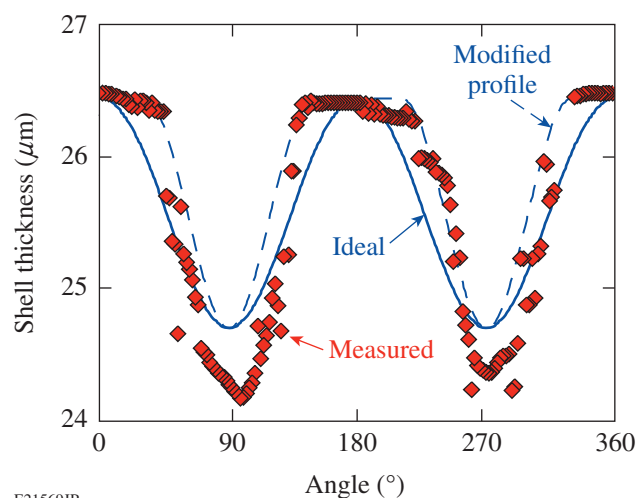
where  $I$  is in units of the nominal intensity. The lowest even mode intensity perturbation that could result from PD illumination is the second Legendre mode, i.e.  $\ell = 2$ . By restricting the perturbation to this first even Legendre mode, the intensity is given by

$$I(\theta) = I_0 \left[ 1 + \frac{i_2}{2} (3 \cos^2 \theta - 1) \right] / (1 + i_2), \quad (2)$$

where  $I_0$  is the intensity at  $\theta = 0$  and  $i_2$  is the amplitude of the  $\ell = 2$  mode. When Eq. (2) is substituted into Eq. (1), the ideal shell thickness profile is determined for this intensity profile.

The shimmed shells used in the experiments described in this article were manufactured by precision machining at the General Atomics (GA) Target Facility.<sup>12</sup> The ideal target profile was chosen by assuming that the average intensity profile was 10% prolate ( $i_2 = +0.1$ )—a magnitude and sign likely to result from PD illumination but otherwise an arbitrary choice. To

accomplish this process on a lathe using a single mounting direction, it was decided to avoid machining the shells near the poles (also the rotation axis of the lathe), avoiding errors in alignment introduced by switching the mounting direction of the target from one pole to the other. This leaves a region of constant shell thickness near the poles. Figure 135.14 shows the ideal profile, a modified profile that avoids the need to machine the poles, and an actual measured profile for one GA-machined shell. The modified profile is arrived at from the ideal profile by setting  $\Delta r$  equal to a constant from  $0^\circ$  to  $30^\circ$  and then using  $\Delta r = \Delta r(\theta')$ , where  $\theta' = (\theta - 30^\circ) \times 1.5$  for  $30^\circ \leq \theta \leq 90^\circ$ . The initial mean shell thickness for this shell was 26.5  $\mu\text{m}$ , so all values of the calculated profiles were shifted by 0.5  $\mu\text{m}$ , and the machining was performed with respect to this thinner profile. The measured profile is close to the modified profile. Machining errors were kept to  $\sim 0.5$   $\mu\text{m}$  from the desired thickness. Three such targets were used in OMEGA experiments, and the results were compared to targets that were manufactured in an identical fashion at GA but did not undergo machining.



E21569JR

Figure 135.14

Measured shimmed shell thickness as a function of polar angle compared to the ideal profile and modified profile that avoids the need to machine near the poles.

The experiments were performed on OMEGA in the polar-drive configuration, where 40 of the 60 OMEGA beams are used to illuminate the target.<sup>5</sup> The experiments were performed with 14 kJ of UV light (351 nm) using an  $\sim 3$ -ns-duration, triple-picket pulse shape,<sup>7</sup> designed to keep the target on a low adiabat, obtaining a high convergence ratio (CR, the ratio of the initial fuel-shell radius to final fuel-shell radius). CR's of  $\sim 19$  were calculated for these experiments. The OMEGA laser

beams were smoothed using 0.5-THz-bandwidth smoothing by spectral dispersion (SSD),<sup>13</sup> with polarization smoothing.<sup>14</sup> The beam profiles were shaped using distributed phase plates (DPP's), resulting in a super-Gaussian beam shape given by  $I/I_0 = \exp[-(r/r_0)^n]$  with  $r_0 = 308 \mu\text{m}$  and  $n = 3.66$  (Ref. 15). Beam pointing was chosen by using the modified capsule thickness profile as input to a series of *DRACO* 2-D hydrocode simulations<sup>16</sup> with varying beam pointing. Beam offset is used to quantify beam pointing, with the magnitude being the distance from beam center to target center, perpendicular to the beam propagation direction, and with a positive offset meaning toward the equator of the PD axis.<sup>5</sup> The pointing chosen (0-, 120-, and 140- $\mu\text{m}$  offsets for rings 1, 2, and 3, respectively) resulted in the most-symmetric implosion in the simulations. This beam offset case is less than the case previously found for spherically symmetric shells with polar drive described in Marshall *et al.*<sup>6</sup> (90-, 150-, and 150- $\mu\text{m}$  offsets for rings 1, 2, and 3, respectively). The beams were precision pointed to an accuracy of  $\sim 8 \mu\text{m}$  to these ideal offset locations using the method described in Ref. 15.

The time-dependent shapes of the imploding shells were measured with framed x-ray backlighting, using a 6- $\mu\text{m}$ -thick Ti foil illuminated by 8 of the 20 remaining OMEGA beams. The beams were overlapped onto the foil, four on each side, defocused to a diameter of 0.7 mm. The foil was thin enough (6  $\mu\text{m}$ ) to be nearly transparent to the principal Ti-emitting line at 4.75 keV ( $\text{He}\alpha$ ), effectively doubling the backlighter brightness. The backlighter was placed on the opposite side of the target from a high-speed framing camera<sup>17</sup> having four strips, each timed to capture an array of images from 10- $\mu\text{m}$ -diam pinholes, with a magnification of 6, spaced so that the separation in time of each image was 30 ps. The view of the target was  $11^\circ$  from the equator of the polar-drive axis, where the shapes of the observed radiographs were almost the same as at the equator (within  $\sim 2\%$  for pure  $\ell$  modes at this angle, see Ref. 5). Absolute frame times were determined from observation of the backlighter onset on the first strip, from the measured strip-to-strip delay, and from the image-to-image time delay on a strip. An absolute time accuracy of  $\sim 50$  ps was obtained with a frame-to-frame time accuracy of  $\sim 15$  ps. As described in Ref. 6, the recorded images were corrected for both film sensitivity and backlighter intensity variation as a function of position and are presented as the optical depth of the radiographed plasma as a function of position. Figure 135.15 shows sample radiographs of a spherical shell and two shimmed shells. The two shimmed shell cases are shown to demonstrate repeatability. The times are from the end of the laser pulse ( $\sim 3.0$  ns) to a time just before shell stagnation ( $\sim 3.5$  ns). As can be seen from the images, the

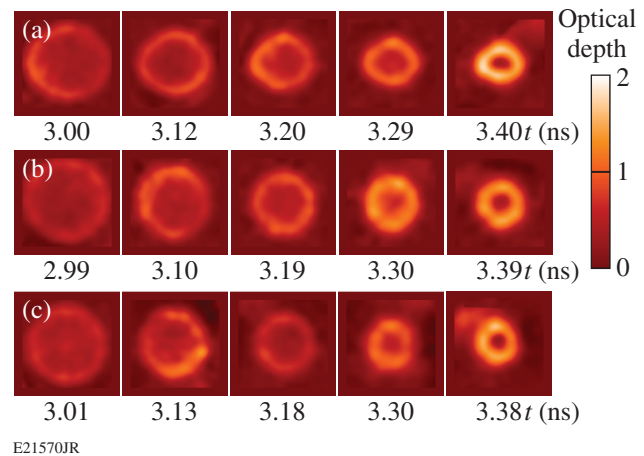


Figure 135.15

Sample radiographs of  $500 \times 500\text{-}\mu\text{m}$  regions centered on the imploding plasma shell for (a) a spherical shell and [(b,c)] two shimmed shells, all imploded with the same beam-pointing condition.

shimmed shells implode with a more spherical shape for this beam pointing.

The shapes of the imploding plasmas are quantified by fitting the positions of the observed peak optical depth as a function of angle to the PD axis to a Legendre polynomial. The shape of the plasma is well measured at times corresponding to CR's of  $\sim 7$  or less. At later times (higher CR's) self-emission obscures the backlighter. Figure 135.16 shows sample fits to both measured and simulated radiographs for a spherical shell [Figs. 135.16(a) and 135.16(b)] and a shimmed shell [Figs. 135.16(c) and 135.16(d)], both at the latest time measured. The simulated radiographs are determined from *DRACO* simulations. The shell shape is included in the shimmed-target simulations by a Legendre-mode decomposition up to mode 10 of the measured shell thickness. The simulations were post-processed by the code *Spect3D*,<sup>18</sup> which takes into account radiation transport, spatial blurring ( $\sim 15 \mu\text{m}$ ), and integration over the frame time (30 ps). Mode amplitudes (normalized to the average radius) of the fits at all measured times for the two most significant modes  $\ell = 2$  and  $\ell = 4$  modes (i.e.,  $a_2$  and  $a_4$ ) are shown for both the spherical shell [Fig. 135.16(e)] and the shimmed shell [Fig. 135.16(f)]. The spherical shell develops a significant negative  $a_2$  ( $\sim -15\%$ ) late in time indicative of an oblate shape. The  $\ell = 4$  mode is significant and positive ( $\sim +5\%$ ). The shimmed shell target obtains a more nearly spherical shape with  $a_2$  and  $a_4$  being  $\lesssim 2\%$  to  $3\%$  for all times measured. The amplitudes determined from the simulations are close to those observed. For the spherical target case [Fig. 135.16(e)], both the sign and magnitude of  $a_2$  from the simulation match the observations, whereas the magnitude of  $a_4$  is overpredicted

compared to observations. This is also true for the shimmed target [Fig. 135.16(f)], where both observations and simulations show a small  $a_2$  but the simulation predicts a positive  $a_4$  of  $\sim 5\%$  to  $10\%$ . This may indicate a difference in the actual and predicted distribution of material in the plasma at that time. Nevertheless, the shimmed target obtains the most symmetric shape in both experiment and simulation for these cases.

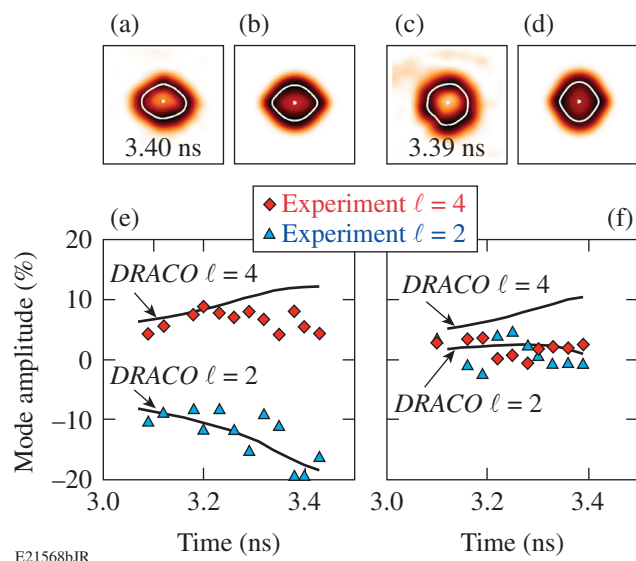


Figure 135.16

Fits to (a) measured and (b) simulated radiographs for a spherical shell, and fits to (c) measured and (d) simulated radiographs for a shimmed shell, at the indicated times. All regions are  $500 \times 500 \mu\text{m}$ . The  $\ell = 2$  and  $\ell = 4$  components of the fits to the measured radiographs are shown in (e) and (f) along with values determined from the simulations.

These results show that a shimmed target can improve the symmetry of a polar-driven imploding shell but taken alone do not demonstrate the benefit of using shimmed shells over just beam repointing to control this shape. The combined benefit is more aptly demonstrated by comparing the symmetry of spherical targets imploded by polar-drive beam pointing, chosen to give the best low-mode symmetry ( $a_2 \approx 0$ ), with the shimmed target result of Fig. 135.16. Figure 135.17 shows the modal fit to a radiograph of a spherical shell imploded with a beam repointing of 90-, 133-, and 133- $\mu\text{m}$  offsets for Rings 1, 2, and 3, respectively, (all other conditions the same) compared to the shimmed shell with the beam pointing given above at  $\sim 100$  ps before stagnation (3.4 ns) and with nearly equal average radii ( $\sim 70 \mu\text{m}$ ). Note that for the spherical target  $a_2 \approx 0$ , while  $a_4 \approx +16\%$ . The plasma exhibits a “diamond-like” shape from this significant positive  $\ell = 4$  mode. In contrast,  $a_2$  and  $a_4$  are both small ( $\leq 2\%$ ) for the shimmed target, demonstrating the

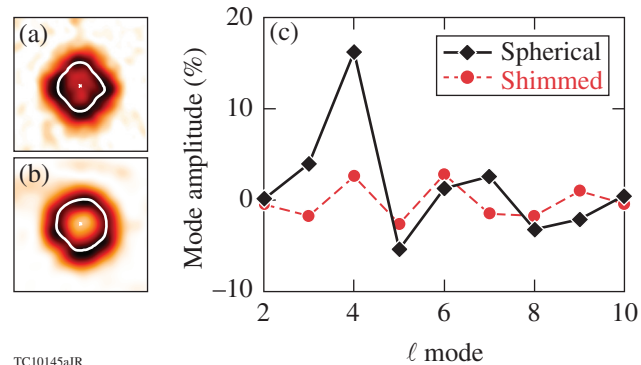


Figure 135.17

Fits to radiographs of (a) a spherical target with optimum pointing for the spherical target (see text), and (b) a shimmed target with the pointing used for the shimmed target experiments (see text). Both radiographs are of  $400 \times 400\text{-}\mu\text{m}$  regions just before stagnation of the shell. (c) Mode amplitudes from Legendre polynomial fits to these shapes

combined benefit of beam repointing and target shimming in controlling the shape of the polar-driven implosion.

As demonstrated by these experiments, target shimming can increase the low-mode symmetry over beam repointing alone. Given the need to control the shape of PD implosions on the NIF, and the anticipated benefit of shimming to increase the ignition margin, these results indicate that further research into methods to shape the DT encapsulating shell, and/or the DT layer itself should be undertaken. Indirectly driven implosions may also benefit from using a shimmed target, emphasizing the importance of this method.

## ACKNOWLEDGMENT

The authors acknowledge the support of the staff at the University of Rochester's Laboratory for Laser Energetics. This work was supported by the U.S. Department of Energy, Office of Inertial Confinement Fusion under Cooperative Agreement No. DE-FC52-08NA28302, the University of Rochester, and the New York State Energy Research and Development Authority.

## REFERENCES

1. S. Skupsky, J. A. Marozas, R. S. Craxton, R. Betti, T. J. B. Collins, J. A. Delettrez, V. N. Goncharov, P. W. McKenty, P. B. Radha, T. R. Boehly, J. P. Knauer, F. J. Marshall, D. R. Harding, J. D. Kilkenny, D. D. Meyerhofer, T. C. Sangster, and R. L. McCrory, *Phys. Plasmas* **11**, 2763 (2004).
2. G. H. Miller, E. I. Moses, and C. R. Wuest, *Opt. Eng.* **43**, 2841 (2004).
3. T. R. Boehly, D. L. Brown, R. S. Craxton, R. L. Keck, J. P. Knauer, J. H. Kelly, T. J. Kessler, S. A. Kumpan, S. J. Loucks, S. A. Letzring, F. J. Marshall, R. L. McCrory, S. F. B. Morse, W. Seka, J. M. Soares, and C. P. Verdon, *Opt. Commun.* **133**, 495 (1997).

4. R. S. Craxton, F. J. Marshall, M. J. Bonino, R. Epstein, P. W. McKenty, S. Skupsky, J. A. Delettrez, I. V. Igumenshchev, D. W. Jacobs-Perkins, J. P. Knauer, J. A. Marozas, P. B. Radha, and W. Seka, *Phys. Plasmas* **12**, 056304 (2005).
5. F. J. Marshall, R. S. Craxton, M. J. Bonino, R. Epstein, V. Yu. Glebov, D. Jacobs-Perkins, J. P. Knauer, J. A. Marozas, P. W. McKenty, S. G. Noyes, P. B. Radha, W. Seka, S. Skupsky, and V. A. Smalyuk, *J. Phys. IV France* **133**, 153 (2006).
6. F. J. Marshall, P. W. McKenty, J. A. Delettrez, R. Epstein, J. P. Knauer, V. A. Smalyuk, J. A. Frenje, C. K. Li, R. D. Petrasso, F. H. Séguin, and R. C. Mancini, *Phys. Rev. Lett.* **102**, 185004 (2009).
7. P. B. Radha, J. A. Marozas, F. J. Marshall, A. Shvydky, T. J. B. Collins, V. N. Goncharov, R. L. McCrory, P. W. McKenty, D. D. Meyerhofer, T. C. Sangster, and S. Skupsky, *Phys. Plasmas* **19**, 082704 (2012).
8. J. A. Marozas, F. J. Marshall, R. S. Craxton, I. V. Igumenshchev, S. Skupsky, M. J. Bonino, T. J. B. Collins, R. Epstein, V. Yu. Glebov, D. Jacobs-Perkins, J. P. Knauer, R. L. McCrory, P. W. McKenty, D. D. Meyerhofer, S. G. Noyes, P. B. Radha, T. C. Sangster, W. Seka, and V. A. Smalyuk, *Phys. Plasmas* **13**, 056311 (2006).
9. T. J. B. Collins, J. A. Marozas, K. S. Anderson, R. Betti, R. S. Craxton, J. A. Delettrez, V. N. Goncharov, D. R. Harding, F. J. Marshall, R. L. McCrory, D. D. Meyerhofer, P. W. McKenty, P. B. Radha, A. Shvydky, S. Skupsky, and J. D. Zuegel, *Phys. Plasmas* **19**, 056308 (2012).
10. J. D. Lindl *et al.*, *Phys. Plasmas* **11**, 339 (2004).
11. J. Delettrez, R. Epstein, M. C. Richardson, P. A. Jaanimagi, and B. L. Henke, *Phys. Rev. A* **36**, 3926 (1987).
12. General Atomics, San Diego, CA 92121-1122.
13. S. Skupsky, R. W. Short, T. Kessler, R. S. Craxton, S. Letzring, and J. M. Soures, *J. Appl. Phys.* **66**, 3456 (1989).
14. T. R. Boehly, V. A. Smalyuk, D. D. Meyerhofer, J. P. Knauer, D. K. Bradley, R. S. Craxton, M. J. Guardalben, S. Skupsky, and T. J. Kessler, *J. Appl. Phys.* **85**, 3444 (1999).
15. R. A. Forties and F. J. Marshall, *Rev. Sci. Instrum.* **76**, 073505 (2005).
16. P. B. Radha, V. N. Goncharov, T. J. B. Collins, J. A. Delettrez, Y. Elbaz, V. Yu. Glebov, R. L. Keck, D. E. Keller, J. P. Knauer, J. A. Marozas, F. J. Marshall, P. W. McKenty, D. D. Meyerhofer, S. P. Regan, T. C. Sangster, D. Shvarts, S. Skupsky, Y. Srebro, R. P. J. Town, and C. Stoeckl, *Phys. Plasmas* **12**, 032702 (2005).
17. D. K. Bradley *et al.*, *Rev. Sci. Instrum.* **66**, 716 (1995).
18. J. J. MacFarlane *et al.*, *High Energy Density Phys.* **3**, 181 (2007).

---

# Localized Time-Resolved Electron-Temperature Measurements Indicate Nonuniformly Driven Two-Plasmon–Decay Instability in Direct-Drive Implosions

The two-plasmon–decay (TPD) instability is the decay of an incident laser photon into two plasmons<sup>1,2</sup> that can generate energetic electrons, thereby preheating direct-drive inertial confinement fusion (ICF)<sup>3,4</sup> implosions and degrading their performance. The phase-matching conditions for this instability restrict it to electron densities of  $n_e \leq n_c/4$ , where  $n_c$  is the critical density at which the plasma frequency equals the laser frequency. This instability is generally accompanied by optical emission near  $\omega_0/2$  and  $3\omega_0/2$ , where  $\omega_0$  is the laser frequency. Above the TPD threshold, energetic electron production is frequently observed as evidenced by hard x-ray emission.

Various aspects of the half-harmonic emission from laser-produced plasmas were analyzed in 1985 (Ref. 5). In particular, a sharp red-shifted spectral feature was identified as a result of the absolute TPD instability<sup>6</sup> in inhomogeneous plasmas<sup>6–9</sup> that occurs very close to the  $n_c/4$  density. This feature is most likely caused by inverse resonance absorption that can efficiently convert the low-frequency TPD plasmons to photons. Since the frequencies of these plasmons depend only on the local electron temperature, this spectral feature also provides a powerful electron-temperature diagnostic<sup>5</sup> in close proximity of the  $n_c/4$  surface. Absorption of this feature on the way out of the plasma is significant (80% to 90%), but its intensity is generally sufficient to make it readily observable.

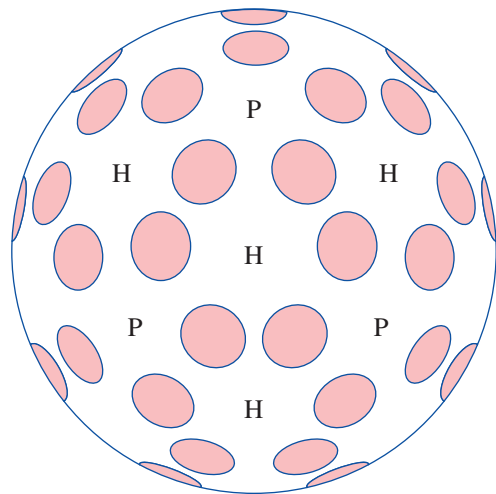
The TPD instability was originally thought to involve only a single laser beam. In 2003, planar-interaction experiments and spherical implosion experiments<sup>10</sup> at LLE demonstrated that the TPD instability was a multibeam instability.<sup>11</sup> At that time there was no theory to explain the multibeam interaction, energetic electron generation, or different onsets for the half-integer harmonics and hard x-ray emission. The spectral extent of the  $\omega/2$  and  $3\omega/2$  emission indicated that this instability extended well into the convective TPD regime<sup>12–14</sup> to densities limited by Landau damping near  $n_e \leq n_c/5$  (Ref. 11), where  $k_p \lambda_{De} \sim 0.25$  ( $k_p$  and  $\lambda_{De}$  are the longer of the two TPD plasmon  $\underline{k}$ -vectors and the Debye length). Over the past decade, significant progress has been made on multibeam TPD theories and simulations using kinetic particle-in-cell (PIC),<sup>14–16</sup> reduced

PIC (RPIC),<sup>17–20</sup> and fluid-type Zakharov simulations.<sup>20–23</sup> These simulations have shown that both absolute and convective TPD instabilities can be driven by multiple beams and that beam configurations (number of beams, angles of incidence, and polarization) determine the outcome. They also showed that within  $\sim 10$  ps or less, the TPD instability is dominated by nonlinear effects and saturation. This implies that the linear regime of this instability is not observable experimentally.

Recent work at LLE showed the effect of beam configurations, polarization, threshold, and intensity scaling of hot-electron production resulting from TPD<sup>24,25</sup> based on experiments and linear gain calculations.

In this article we present the first precision ( $\sim 5\%$ ), time-resolved electron-temperature measurements in different areas of an imploding target and located in density space between  $0.24 < n_e/n_c < 0.25$ . These measurements indicate that close to the TPD threshold, the measured temperatures agree well with those predicted by hydrodynamic simulations, while above the threshold, they typically exceed the simulations by up to 20%. The exact amount of the excess temperature depends on the number of overlapping beams that drive the instability in any particular area.

Experiments were carried out on LLE's 60-beam OMEGA Laser System<sup>26</sup> using spherical targets. Each beam illuminates the entire hemisphere of the target using distributed phase plates (DPP's)<sup>27</sup> and smoothing by spectral dispersion (SSD).<sup>28</sup> Time-resolved  $\omega/2$  spectra were recorded in three locations: one through one of the beam ports (backscattering) and two centered within a hex or pent port (see Fig. 135.18). The signals from beam and hex ports were collected near the target chamber and fiber optically relayed to a time-multiplexed, 1/3-m spectrometer. The signal from the pent port was optically relayed to a similar spectrometer. Both spectrometers were proximity coupled to ROSS streak cameras.<sup>29</sup> Typical spectral and temporal resolutions were  $\sim 1$  nm and  $\sim 100$  ps, respectively. All streak records were routinely corrected for geometric and sweep-speed nonlinearities to near 1% residual



E22224JR

Figure 135.18

Schematic of the OMEGA target chamber with beam ports (shaded) and the locations of hex (H) and pent (P) ports.  $\omega/2$  spectra were recorded through one of the beam ports and centered on one of the H and P ports.

nonlinearity. The two multiplexed spectra viewed the entire target sphere, while the spectra recorded in the pent location viewed an  $\sim 50\text{-}\mu\text{m} \times 50\text{-}\mu\text{m}$  area on the target sphere.

Half-harmonic images were recorded on a charge-coupled-device (CCD) camera at the center of another hex port. Colored glass and an interference filter at the camera input integrated over either the entire  $\omega/2$  spectrum (680 nm and 720 nm) or

only the blue part of the spectrum (680 nm to 700 nm). (The central  $\omega_0/2$  wavelength lies at 702 nm.)

Representative  $\omega/2$  spectra recorded at the center of the pent port are shown in Fig. 135.19 for two viewing directions: one viewing an imploding target along the target normal [Fig. 135.19(a)]; the other one displaced by  $\sim 100\ \mu\text{m}$  and inclined by  $\sim 10^\circ$  relative to the target normal [Fig. 135.19(d)]. The sharp red-shifted spectral feature [Fig. 135.19(a)] is the same as that previously identified with the absolute TPD instability.<sup>5,6</sup> This spectral feature results from plasmon-to-photon conversion<sup>30</sup> via inverse resonance absorption of the lower-frequency TPD plasmons whose  $\mathbf{k}$ -vectors nearly vanish. The multibeam nature of the instability is inferred from threshold calculations. The absolute TPD threshold<sup>6,23</sup> can be defined as  $\eta = 1$ , where  $\eta = I_{14}L_n/\mu\text{m}/(233T_e/\text{keV})$  and  $I_{14}$ ,  $L_n$ , and  $T_e$  are the intensity, density scale length, and electron temperature at  $n_c/4$  in units of  $10^{14}\ \text{W}/\text{cm}^2$ ,  $\mu\text{m}$ , and keV, respectively. For the multibeam geometries prevalent on OMEGA,  $I_{14}$  represents the sum of all the beam intensities that can contribute to the absolute TPD instability at the point of interest.<sup>23</sup> For the shots shown in Fig. 135.19, the single-beam peak intensity toward the end of the laser pulse was  $I_{14} \sim 2.35$ ,  $L_n \sim 100\ \mu\text{m}$ , and  $T_e \sim 1.8\ \text{keV}$ , resulting in  $\eta \sim 0.2$ , i.e., far below the absolute TPD threshold. Using hydrodynamic predictions for these quantities where  $I_{14}$  is the total intensity at quarter critical summed over all angles of incidence, we note that  $\eta$  shown in Fig. 135.19(c) is close to 1, i.e., the threshold. In fact, this average intensity

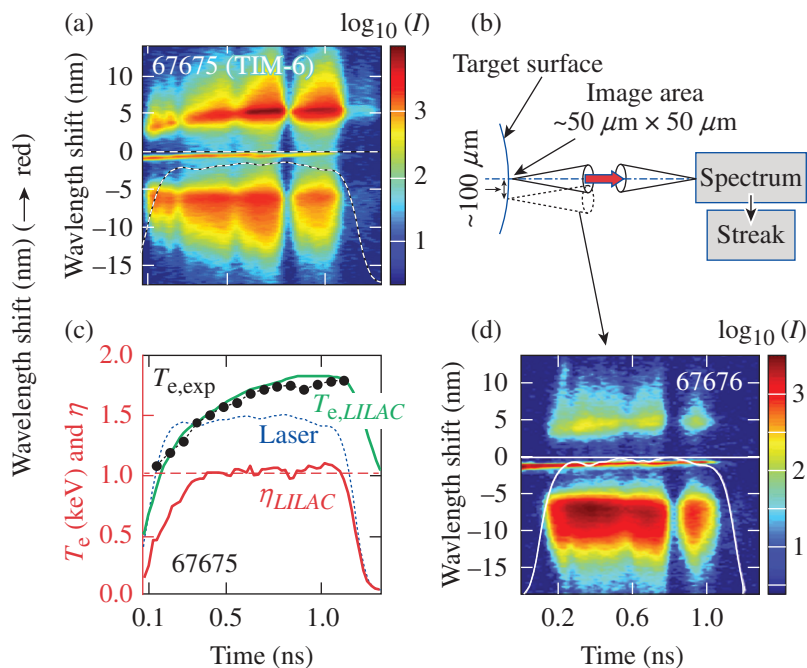


Figure 135.19

Time-resolved  $\omega/2$  spectra viewing a small area on the target surface. (a) Spectrum taken along the target normal; (b) schematic setup for time-resolved  $\omega/2$  spectroscopy; (c) measured electron temperatures (black dots), LILAC predictions (green line), laser power (blue dashed line), and threshold parameter  $\eta$  obtained from LILAC (red line); (d) equivalent  $\omega/2$  spectrum taken  $\sim 10^\circ$  off the target normal.

E22225JR

is an overestimate of the relevant overlapped intensity that can drive the TPD instability, particularly if polarization smoothing is included, which presumably halves the TPD drive intensity. The discrepancy may be related to the speckle nature of the focal spot for which peak intensities can easily be  $3\times$  to  $5\times$  larger. The influence of speckles on driving the TPD instability is presently being investigated using the Zakharov simulations.

Figure 135.19(d) shows the off-axis  $\omega/2$  spectrum, which is dominated by the broad blue-shifted spectral feature corresponding to TPD decays well below  $n_c/4$ . These features cannot be generated by mode conversion but require Thomson scattering using one of the irradiation beams as the Thomson probe. For the OMEGA geometry, the phase-matching conditions for generating  $\omega/2$  radiation via Thomson scattering are not satisfied for Thomson scattering off primary TPD plasmons using any of the OMEGA beams as the Thomson probe. These conditions can be satisfied, however, if the TPD plasma waves roughly fill  $k$  space up to the Landau cutoff density as predicted in the nonlinear evolution of the instability by PIC,<sup>16</sup> RPIC,<sup>18,31</sup> and Zakharov<sup>20,32,33</sup> simulations. In principle, inverse parametric decay could generate some of these spectral features. This process is not very likely since it is a higher-order process involving TPD plasmons and ion waves with appropriate  $\mathbf{k}$ -vectors.

The broad  $\omega/2$  spectral features do not reveal the generation processes but indicate the range of densities involved in the TPD instability. The two TPD plasmons have frequencies  $\omega_{1,2} = \omega_0/2 \pm \Delta\omega$ . Along the maximum TPD growth-rate curve<sup>5,6,11</sup>  $\Delta\omega/\omega_0 = 4.4 \times 10^{-3} \kappa T_{e,\text{keV}}$ , where  $\kappa = \mathbf{k}_1 \cdot \mathbf{k}_0 / k_0^2 - 1/2$  (Ref. 5), and  $k_0$  and  $k_1$  are the  $\mathbf{k}$ -vectors of the incident photons and the larger- $k$  plasmon of the two TPD waves. The absolute TPD instability near  $n_c/4$  has the lowest single and multibeam thresholds,<sup>6,23,33</sup> corresponding to  $\kappa \approx 0.5$  and  $T_{e,\text{keV}} \approx \Delta\lambda_{\text{nm}}/3.1$  for  $\lambda_L = 351$  nm. The wavelength shift  $\Delta\lambda_{\text{nm}}$  of the sharp red-shifted spectra in Fig. 135.19, therefore, indicates an electron temperature at  $n_c/4$  of  $T_e \approx 1.66$  keV, in good agreement with 1-D hydrodynamic LILAC<sup>34</sup> predictions [green line in Fig. 135.19(c)]. Near the Landau cutoff, the frequency shifts are  $2\times$  to  $3\times$  larger but are of limited diagnostic value since they depend sensitively on the wave vectors probed.

Images of the  $\omega/2$  emission provide significant information regarding localization of the TPD instability (Fig. 135.20). Figure 135.20(a) was filtered for the entire  $\omega/2$  spectrum (680 nm to 740 nm) for an imploding target at  $I_{\text{max}} \sim 10^{15}$  W/cm<sup>2</sup>, while in Fig. 135.20(b) only the blue  $\omega/2$  component was recorded.

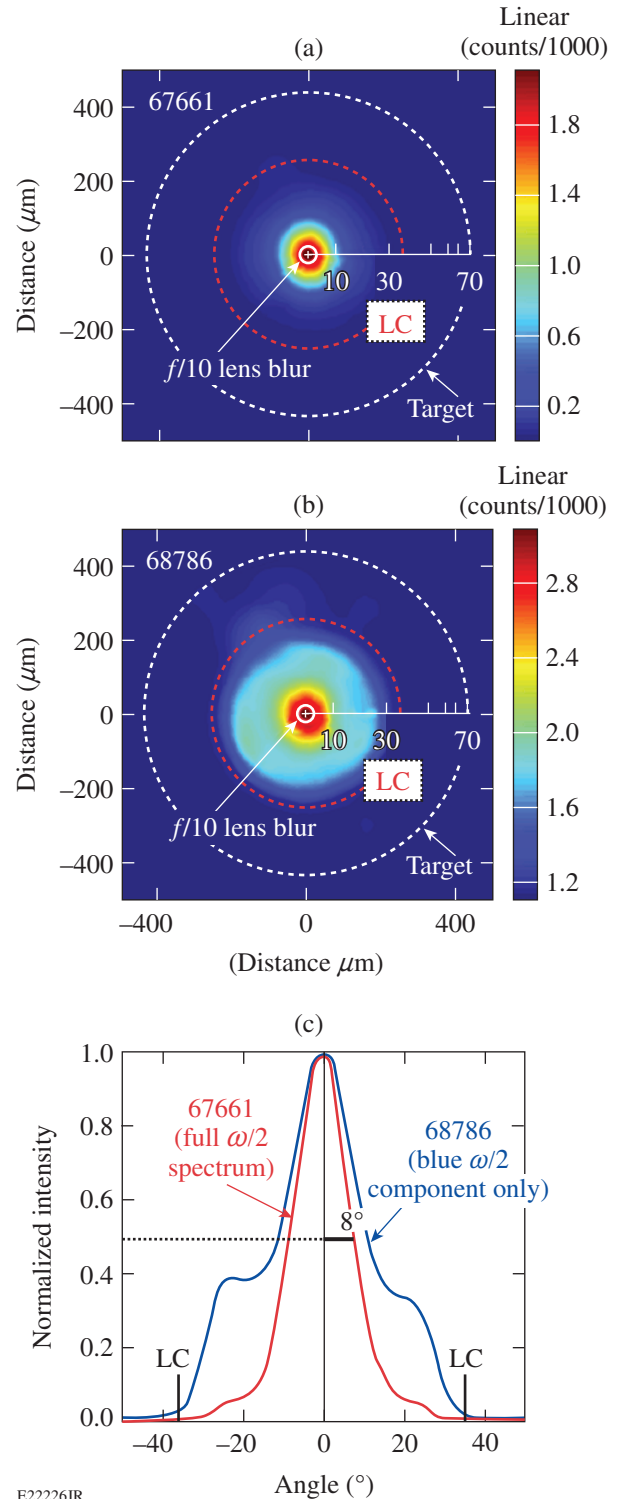


Figure 135.20

The  $\omega/2$  images taken through a hex port (surrounded by six beams). (a) Image of an imploding target for  $680 \text{ nm} < \lambda < 740 \text{ nm}$ ; (b) same as in (a) but  $680 \text{ nm} < \lambda < 700 \text{ nm}$ ; (c) cross-sectional lineouts through the center of the target for (a) and (b). LC: Landau cutoff.

A scale is superposed in Figs. 135.20(a) and 135.20(b) translating the spatial information in the images into emission angles in degrees. Figure 135.20(c) shows two lineouts through the centers of Figs. 135.20(a) and 135.20(b). Figure 135.20(a) is dominated by the sharp red feature that originates very near its critical density. This emission is guided along the density gradient because of the conservation of the wave vector perpendicular to the density gradient in the near-planar density profile. This also explains the narrow emission cone angle in Fig. 135.20(c), which is  $\sim 6^\circ$  after correction for the  $f/10$  imaging optics. Assuming planar geometry (valid considering the dimensions and angles involved relative to the curvature of the  $n_c/4$  surface), this narrow cone angle can be used to estimate the maximum density from which the sharp red feature may be emitted. This maximum density is  $n_e/n_c \approx 0.247$  and includes the density region for the absolute instability,  $0.247 < n_e/n_c \leq 0.25$ , depending on  $T_e$ .

The  $\omega/2$  image in Fig. 135.20(b) is consistent with the spectra shown in Fig. 135.19. Since the sharp red feature is not recorded, this image sees only emission from lower densities (larger  $\Delta\lambda$ ) corresponding to larger emission angles. If this source were isotropic over the entire quarter-critical surface, this image intensity would drop off at the polar angle  $\theta_{LC} \sim 37^\circ$ , determined by refraction of  $\omega/2$  light generated at the Landau cutoff. The location of the Landau cutoff is indicated in Fig. 135.20 by LC and the red dashed circles. There is only scant emission at or beyond the Landau cutoff consistent with past Thomson-scattering results.<sup>11</sup> A halo of blue  $\omega/2$  emission extends to the Landau cutoff with three areas of increased emission near the 12, 5, and 7 o'clock positions. The former is likely caused by the six beams surrounding the hex port, while the

latter correspond to the positions of the three neighboring pent ports (Fig. 135.18) located at  $\theta \sim 37.5^\circ$  or right at the Landau cutoff. (The three neighboring hex ports are located  $4^\circ$  farther out and emission from these port locations is not identifiable in these images.) The angular resolution of these images is severely limited by refraction and the large angle emission of the broad  $\omega/2$  features. It is therefore impossible to resolve individual beams separated by  $\sim 23^\circ$ .

The relatively narrow central spike in Fig. 135.20(b) ( $\sim 11^\circ$  half-cone angle) is consistent with a small TPD interaction area centered on the hex ports. Analogous arguments hold for the pent ports where the thresholds are  $\sim 20\%$  higher than in the hex ports (five versus six beams as primary contributors to the instability). In the 60 beam-port locations, four beams can effectively drive the absolute TPD instability, albeit at another 20% increased threshold intensity. The interaction area estimates are very rough since they depend on the nonlinear TPD plasma wave spectrum and the possible experimental Thomson-scattering scenarios on OMEGA.

The onset of  $\omega/2$  emission in Fig. 135.21 is consistent with the TPD thresholds<sup>6</sup> if the intensity includes the total number of overlapping beams that can drive the absolute instability at a particular location. At the center of a hex port, six beams overlap but their intensities are reduced by absorption ( $\sim 10\%$ ) on the way to  $n_c/4$  and the intensity profile ( $\sim 10\%$ ) for a total intensity of  $\sim 4.8\times$  the single-beam peak intensity. Near the center of each beam, four beams can drive the TPD instability (Fig. 135.18). After accounting for absorption and beam profile, the total intensity is  $\sim 3.4\times$  the single-beam intensity at this location. (Higher-angle beams contribute insignificantly

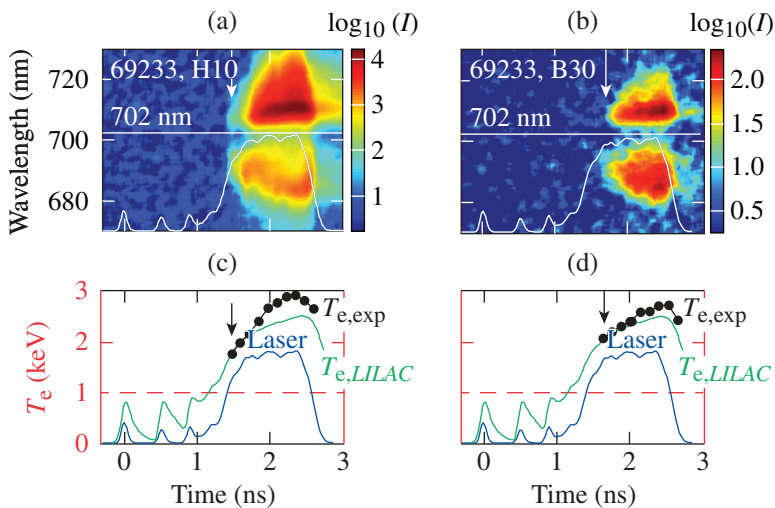


Figure 135.21

The  $\omega/2$  spectra taken for an imploding room-temperature target at  $9.3 \times 10^{14} \text{ W/cm}^2$  through (a) a beam port and (b) a hex port. The laser pulse shape is shown in each panel. The sharp red-shifted features in (a) and (b) were used to measure  $T_e$  in (c) and (d). Random error bars are equal to the symbol sizes. Hydrodynamic predictions for  $T_e$  are shown in green. Arrows indicate the onset of  $\omega/2$  emission and estimated TPD thresholds.

E22227JR

because of the intensity profiles.) Different onset times for the TPD instability (white and black arrows in Fig. 135.21) are evident in the spectra taken at the beam port and hex port locations. The onsets the  $T_e$  increase and corresponding maximum electron temperatures [Fig. 135.21(c)] in the two locations reflect the different absolute TPD thresholds  $I_{th} \sim IL_n/T_e$ , where  $I$  is the overlapped intensity and  $L_n$  is density gradient length. Both  $I$  and  $L_n$  increase with time past  $t = 1.5$  ns in Fig. 135.21. The maximum temperatures vary over the quarter-critical surface and locally exceed the average temperatures predicted by hydrodynamic simulations by 10% to 20%. (At the onset of the spectra, the measured temperatures agree well with the hydrodynamic simulations.) The measured temperature excursions beyond the hydrodynamic predictions entail  $n_c/4$  surface perturbations caused by pressure uniformity in the corona. Such perturbations have been reproduced in two-dimensional (2-D) hydrodynamic simulations.

In conclusion, spatially and temporally resolved half-harmonic spectra and images of laser-driven implosions show clear evidence for the multibeam nature of the TPD instability, its rapid nonlinear evolution, and its spatially limited extent. The thresholds correspond to the multibeam-driven absolute instability and are identified via a sharp red-shifted spectral feature. These thresholds agree with published absolute thresholds after adjusting the intensity for multibeam effects. The broad  $\omega/2$  spectral features that develop essentially simultaneously with the sharp red-shifted feature are identified as the nonlinear phase of the TPD instability that extends rapidly all the way to the Landau cutoff covering the conventionally called convective regime. There is no experimental evidence for a linear convective regime. These results are in good agreement with recent fluid and kinetic TPD simulations. Localized  $T_e$  measurements and  $\omega/2$  images point toward localized temperature islands near  $n_c/4$ , where temperatures exceed the average by 10% to 20% and entail localized surface perturbations.

#### ACKNOWLEDGMENT

This work was supported by the U.S. Department of Energy Office of Inertial Confinement Fusion under Cooperative Agreement No. DE-FC52-08NA28302, the University of Rochester, and the New York State Energy Research and Development Authority. The support of DOE does not constitute an endorsement by DOE of the views expressed in this article.

#### REFERENCES

1. M. V. Goldman, *Ann. Phys.* **38**, 95 (1966).
2. M. V. Goldman, *Ann. Phys.* **38**, 117 (1966).
3. J. D. Lindl, *Inertial Confinement Fusion: The Quest for Ignition and Energy Gain Using Indirect Drive* (Springer-Verlag, New York, 1998).
4. D. W. Phillion *et al.*, *Phys. Rev. Lett.* **49**, 1405 (1982).
5. W. Seka, B. B. Afeyan, R. Boni, L. M. Goldman, R. W. Short, K. Tanaka, and T. W. Johnston, *Phys. Fluids* **28**, 2570 (1985).
6. A. Simon, R. W. Short, E. A. Williams, and T. Dewandre, *Phys. Fluids* **26**, 3107 (1983).
7. C. S. Liu, M. N. Rosenbluth, and R. B. White, *Phys. Rev. Lett.* **31**, 697 (1973).
8. M. N. Rosenbluth, R. B. White, and C. S. Liu, *Phys. Rev. Lett.* **31**, 1190 (1973).
9. B. B. Afeyan and E. A. Williams, *Phys. Rev. Lett.* **75**, 4218 (1995).
10. C. Stoeckl, R. E. Bahr, B. Yaakobi, W. Seka, S. P. Regan, R. S. Craxton, J. A. Delettrez, R. W. Short, J. Myatt, A. V. Maximov, and H. Baldis, *Phys. Rev. Lett.* **90**, 235002 (2003).
11. W. Seka, D. H. Edgell, J. F. Myatt, A. V. Maximov, R. W. Short, V. N. Goncharov, and H. A. Baldis, *Phys. Plasmas* **16**, 052701 (2009).
12. M. N. Rosenbluth, *Phys. Rev. Lett.* **29**, 565 (1972).
13. L. V. Powers and R. L. Berger, *Phys. Fluids* **28**, 2419 (1985).
14. R. Yan, A. V. Maximov, and C. Ren, *Phys. Plasmas* **17**, 052701 (2010).
15. R. Yan, A. V. Maximov, C. Ren, and F. S. Tsung, *Phys. Rev. Lett.* **103**, 175002 (2009).
16. R. Yan, C. Ren, J. Li, A. V. Maximov, W. B. Mori, Z. M. Sheng, and F. S. Tsung, *Phys. Rev. Lett.* **108**, 175002 (2012).
17. H. X. Vu, D. F. DuBois, D. A. Russell, and J. F. Myatt, *Phys. Plasmas* **17**, 072701 (2010).
18. H. X. Vu, D. F. DuBois, J. F. Myatt, and D. A. Russell, *Phys. Plasmas* **19**, 102703 (2012).
19. H. X. Vu, D. F. DuBois, D. A. Russell, and J. F. Myatt, *Phys. Plasmas* **19**, 102708 (2012).
20. J. F. Myatt, J. Zhang, J. A. Delettrez, A. V. Maximov, R. W. Short, W. Seka, D. H. Edgell, D. F. DuBois, D. A. Russell, and H. X. Vu, *Phys. Plasmas* **19**, 022707 (2012).
21. D. A. Russell and D. F. DuBois, *Phys. Rev. Lett.* **86**, 428 (2001).
22. J. F. Myatt, H. X. Vu, D. F. DuBois, D. A. Russell, J. Zhang, R. W. Short, and A. V. Maximov, *Phys. Plasmas* **20**, 052705 (2013).
23. J. Zhang, J. F. Myatt, R. W. Short, A. V. Maximov, H. X. Vu, D. F. DuBois, and D. A. Russell, "Multibeam Two-Plasmon Decay from Linear Threshold to Nonlinear Saturations," to be submitted to *Physical Review Letters*.
24. D. T. Michel, A. V. Maximov, R. W. Short, J. A. Delettrez, D. Edgell, S. X. Hu, I. V. Igumenshchev, J. F. Myatt, A. A. Solodov, C. Stoeckl, B. Yaakobi, and D. H. Froula, *Phys. Plasmas* **20**, 055703 (2013).

25. D. T. Michel, A. V. Maximov, R. W. Short, S. X. Hu, J. F. Myatt, W. Seka, A. A. Solodov, B. Yaakobi, and D. H. Froula, *Phys. Rev. Lett.* **109**, 155007 (2012).
26. T. R. Boehly, D. L. Brown, R. S. Craxton, R. L. Keck, J. P. Knauer, J. H. Kelly, T. J. Kessler, S. A. Kumpan, S. J. Loucks, S. A. Letzring, F. J. Marshall, R. L. McCrory, S. F. B. Morse, W. Seka, J. M. Soures, and C. P. Verdon, *Opt. Commun.* **133**, 495 (1997).
27. Y. Lin, T. J. Kessler, and G. N. Lawrence, *Opt. Lett.* **20**, 764 (1995).
28. S. Skupsky, R. W. Short, T. Kessler, R. S. Craxton, S. Letzring, and J. M. Soures, *J. Appl. Phys.* **66**, 3456 (1989).
29. W. R. Donaldson, R. Boni, R. L. Keck, and P. A. Jaanimagi, *Rev. Sci. Instrum.* **73**, 2606 (2002).
30. R. E. Turner *et al.*, *Phys. Fluids* **27**, 511 (1984).
31. H. X. Vu, D. F. DuBois, J. F. Myatt, and D. A. Russell, presented at the 41st Annual Anomalous Absorption Conference, San Diego, CA, 19–24 June 2011.
32. J. F. Myatt, J. Zhang, A. V. Maximov, R. W. Short, D. F. DuBois, D. A. Russell, and H. X. Vu, *Bull. Am. Phys. Soc.* **56**, 328 (2011).
33. J. Zhang, J. F. Myatt, A. V. Maximov, R. W. Short, D. F. DuBois, D. A. Russell, and H. X. Vu, *Bull. Am. Phys. Soc.* **57**, 299 (2012).
34. J. Delettrez, R. Epstein, M. C. Richardson, P. A. Jaanimagi, and B. L. Henke, *Phys. Rev. A* **36**, 3926 (1987).

---

## Measurements of the Divergence of Fast Electrons in Laser-Irradiated Spherical Targets

Fast electrons produced by the two-plasmon-decay (TPD) instability<sup>1–4</sup> in direct-drive fusion can deposit their energy into the nuclear fuel (preheat), leading to a reduction in the maximum compression and target performance.<sup>5–8</sup> Typical direct-drive-ignition designs can withstand of the order of  $\sim 0.1\%$  of the laser energy converted to preheat<sup>6</sup> before significant degradation occurs. In recent experiments (both planar<sup>9,10</sup> and spherical<sup>11,12</sup>), a Mo layer was used to determine the energy in fast electrons as a fraction of laser energy, using the Mo– $K_\alpha$  line. The energy in fast electrons was found to increase rapidly with laser intensity. At the maximum laser irradiance for spherical targets of  $\sim 1.1 \times 10^{15}$  W/cm<sup>2</sup>, the energy in fast electrons was  $\sim 1\%$  of the laser energy. This is about  $10\times$  higher than the maximum that can be tolerated for ignition, and if effectively coupled to the fuel, the effects would be prohibitive. The fast-electron divergence established in this experiment, however, limits the fraction of fast electrons that contribute to preheat. The electrons in the recent experiments were nearly completely absorbed by the Mo layer, providing a measure of the total energy in fast electrons. However, in typical cryogenic direct-drive experiments,<sup>13</sup> the fraction of the fast-electron energy deposited as preheat can be significantly less; only preheat of the compressed fuel shell can be detrimental to target performance. Fast electrons are generated near the end of the laser pulse<sup>4</sup> when the density scale length reaches a maximum. At that time the compressed fuel shell has converged to about half the original target size.<sup>13</sup> Fast electrons produced by TPD are generated near the quarter-critical density layer, and if they have a wide angular divergence, only  $\sim 1/4$  of the fast electrons will be intercepted by the compressed fuel.

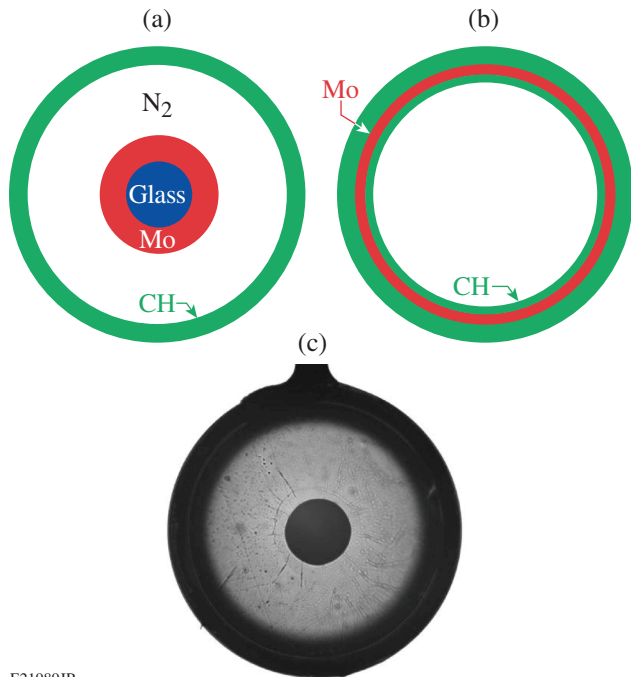
Knowledge of the fast-electron divergence is crucial in assessing their effect on direct-drive experiments and ignition designs. The total energy in fast electrons (as well as the fast-electron temperature) in fusion target implosions is studied using the emitted hard x rays (HXR's).<sup>7,14–16</sup> Without a knowledge of the divergence, the preheat in the compressed fuel cannot readily be determined. This is because the relationship between the measured HXR and the number of fast electrons depends on the atomic number  $Z$ ; therefore (in  $D_2$ - or

DT-filled CH shells) this relationship depends on the partition of the HXR produced by the nuclear fuel and by the outer CH layer. This partition depends on the divergence of fast electrons: the higher the divergence, the larger the fraction of the HXR coming from the CH (since more electrons miss the central fuel shell and travel within the CH). Therefore, an understanding of the fast-electron divergence in laser-fusion experiments is critical for (a) determining the total number of fast electrons, and (b) determining the fraction of the total that is absorbed in the compressed fuel shell.

The fraction  $1/4$  stated above stems from the fact<sup>13</sup> that at the time of peak fast-electron production, most of HXR-emitting CH mass is comprised within the original target volume. Therefore the relevant fraction of fast electrons is stated with respect to the total number of fast electrons intercepted by the area of the original target surface. Electrons outside this solid angle are not detected and are of no interest.

The divergence of fast electrons was studied with targets [Fig. 135.22(a)] in which Mo-coated solid glass spheres were placed at the center of nitrogen-filled CH shells. A series of targets were irradiated with a 1-ns square pulse while varying the Mo outer diameter  $D$  ( $\sim 200$  to  $600$   $\mu\text{m}$ ). The Mo– $K_\alpha$  line as well as the HXR were measured; both are signatures of fast electrons.<sup>9</sup> To extend the measurements to larger-diameter Mo shells ( $\sim 800$   $\mu\text{m}$ ), a Mo-coated CH shell target overcoated with CH was used [Fig. 135.22(b)]. Figure 135.22(c) is a photograph of the target type illustrated in Fig. 135.22(a), before being shot.

To ensure the same production of fast electrons in all the shots, the outer target diameter was the same ( $860 \pm 1\%$   $\mu\text{m}$ ), as was the laser energy (26 kJ, to within  $\pm 1\%$ ). To minimize target motion, the outer CH thickness was  $50$   $\mu\text{m}$ . This maintained similar underdense hydrodynamic conditions by ensuring a reproducible hot-electron source and limiting instabilities that could result from the acceleration of the shell, therefore decoupling the fast-electron transport from the hydrodynamics. The Mo layer in all targets was  $\sim 30$   $\mu\text{m}$  thick, which absorbed most of the fast electrons. This prevented refluxing (the re-entry



E21989JR

Figure 135.22

Target geometries: (a) Mo-coated solid glass sphere was placed at the center of a nitrogen-filled CH shell. A series of targets with varying Mo outer diameters was used to study the divergence. (b) To extend the divergence measurements to a larger-diameter Mo shell, a Mo-coated CH shell target was used (overcoated with CH). (c) A photograph of a target of type (a) before being shot.

of fast electrons after reflection from the electrostatic sheath around the target) and isolated the effect of divergence. The space between the CH shell and the Mo ball was filled with N<sub>2</sub> at ~1 atm to minimize electric-field effects. The 60-beam OMEGA Laser System<sup>17</sup> was used for these experiments and was smoothed by distributed phase plates,<sup>18</sup> 2-D spectral dispersion,<sup>19</sup> and polarization rotators.<sup>20</sup>

The Mo-K<sub>α</sub> line was measured by two identical planar LiF crystal spectrometers (XRS's), as well as a Cauchois-type quartz crystal spectrometer (TCS).<sup>21</sup> The high-energy continuum spectrum (HXR) was measured by the four-channel hard x-ray detector (HXRD) spectrometer<sup>22</sup> from which the fast-electron temperature was determined. The relative energy in x rays above ~50 keV, measured by one of these channels, is reported in this article.

Figure 135.23 shows the intensity of the Mo-K<sub>α</sub> line measured by the XRS and TCS, as well as the HXR radiation measured by the HXRD spectrometer. The *EGSnrc* Monte Carlo (MC) code<sup>23</sup> was used to simulate the transport of fast electrons and the emission of the Mo K<sub>α</sub> and the HXR; these results, assuming a wide divergence of the fast electrons, are

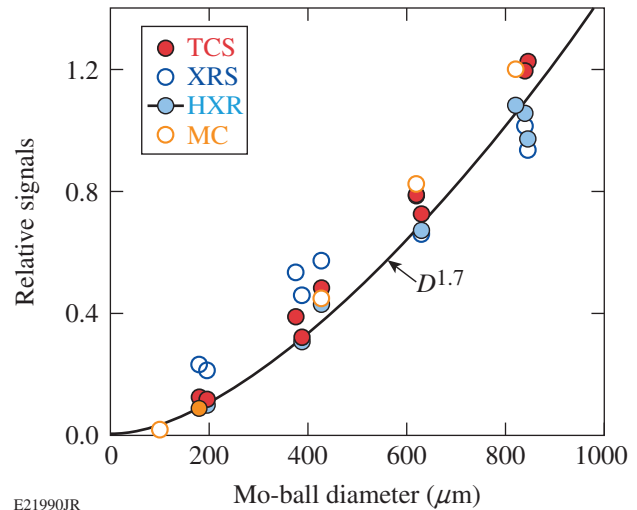
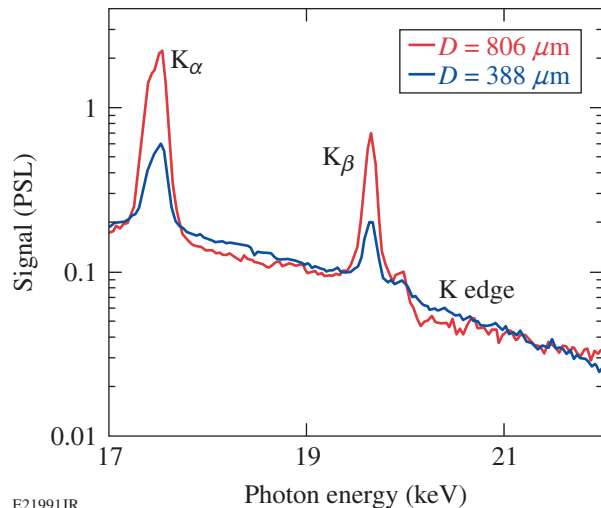


Figure 135.23

The intensity of the Mo-K<sub>α</sub> line measured by the XRS and TCS, as well as the hard x-ray radiation measured by HXRD. The Monte Carlo (MC) simulation results for a divergent fast-electron beam are also shown. The curve is the best fit to the HXR data. The increase of the signals with the Mo-shell diameter indicates a wide-angle divergence of fast electrons.

shown in Fig. 135.23. The incident fast electrons in the simulations are assumed to start from a point on the outer surface of the target and move isotropically within a half space. Unlike the Mo-K<sub>α</sub> line, hard x rays are also emitted by the outer CH shell (not just the Mo layer), but the emission from the CH is independent of the Mo diameter (see Fig. 135.24); therefore, it



E21991JR

Figure 135.24

The measured x-ray spectrum for two Mo-shell diameters, used to assess the pumping of the Mo-K<sub>α</sub> line by continuum radiation (above the Mo K edge). The continuum is emitted mostly by the outer CH shell; therefore it is about the same for all Mo diameters. PSL: photostimulated luminescence.<sup>24</sup>

must be a fraction of the total HXR emission for the smallest-diameter Mo target. That fraction was determined by running the MC code for an empty CH shell and was then subtracted from the HXR signals of all targets. The spread of the points can be related to the high sensitivity of fast-electron production to the laser intensity. A  $\pm 1\%$  variation in both the laser energy and the outer target diameter ( $\pm 3\%$  in the overlapped intensity) corresponds to about  $\pm 10\%$  variation in the  $K_\alpha$  and the HXR signals.<sup>11</sup> The curve is the best fit to the HXR data.

The results of Fig. 135.23 show that fast electrons have a divergence extending at least to the original target diameter. As explained above, this is the relevant measure in assessing fast-electron preheat in cryogenic direct-drive implosions. The x-ray signals are not exactly proportional to the area of the Mo ball. MC simulations show that for the largest-diameter Mo ball, electrons are significantly slowed down because they traverse the CH shell diagonally and are significantly scattered out of the Mo layer because of the large angle of incidence on that layer. Without these effects the signals for  $D \sim 800 \mu\text{m}$  would align closer to a  $D^2$  scaling. The most-obvious explanation for the close to  $\sim D^2$  rise in Fig. 135.23 is the wide-angle divergence of the fast electrons. The exact shape of the rise is unimportant; the very fact that the curve rises is an indication of divergence since a radially directed electron beam would result in constant signals, independent of  $D$ . The indicated minimum fast-electron divergence is given by the solid angle of the largest Mo ball at a point on the quarter-critical layer. Three alternative explanations to the rise in signals were investigated: electron scattering in the outer CH shell, radiation excitation of the Mo- $K_\alpha$  line, and a radial electric field related to the return current within the ionized  $\text{N}_2$  fill gas.

Electron scattering in the CH was shown to be relatively unimportant by MC simulations using a narrow ( $< 1\text{-}\mu\text{m}$ ) radial electron beam for various Mo diameters. For a non-scattered beam, the energy in the Mo- $K_\alpha$  line should be independent of  $D$ . Instead, the MC simulations showed that the energy rises with  $D$  and reaches a plateau below  $D \sim 300 \mu\text{m}$ . Scattering broadens the electron beam to an extent consistent with the early rise in Fig. 135.23 but not with the rest of the curve.

The  $K_\alpha$  line is excited by fast electrons but could also be pumped by the plasma radiation from the laser absorption region in the CH. Unless this contribution is small, the rise of  $K_\alpha$  yield with  $D$  may not reflect fast-electron divergence (particularly since the radiation is isotropic). To examine this contribution to the measured  $K_\alpha$  energy, the spectra for targets of two Mo diameters,  $\sim 400$  and  $\sim 800 \mu\text{m}$ , are shown

in Fig. 135.24. The ratio of the  $K_\alpha$  line intensities for the two shots is, as expected, about equal to the ratio in areas of the Mo balls. The continuum, which is emitted by the outer CH shell, is about the same for the two targets. The radiation contribution to the  $K_\alpha$  line can be calculated through the integral  $E_R = \int I_c(E) \omega_K [(K_\alpha)/E] dE$ , where  $I_c(E)$  is the continuum spectrum,  $\omega_K = 0.76$  is the  $K_\alpha$  fluorescence yield of Mo, and the integral extends upward from the K edge (at  $\sim 20 \text{ keV}$ ). Only the relative intensity of the spectrum is required for calculating  $E_R$ . For the larger diameter,  $E_R$  is less than  $\sim 10\%$  of the total energy of the  $K_\alpha$  line. For the smaller diameter, the relevant continuum intensity is smaller than that shown in Fig. 135.24 because the Mo shell intercepts only a fraction ( $\sim 1/4$ ) of the CH continuum. The relative contribution of the radiation is the same for all Mo diameters (but can best be determined from the larger diameter). Therefore, radiation pumping of the Mo- $K_\alpha$  line is unimportant. Additionally, it should be emphasized that the HXR measurements, shown to track the  $K_\alpha$  measurements in Fig. 135.23, are related only to the fast electrons, thereby confirming the conclusions on fast-electron divergence.

The rise in the signals with  $D$  shown in Fig. 135.23 could be related to a retarding radial electric field caused by a return current that will reduce the values of the measured signals. For a radially directed fast-electron beam, the effect would increase with decreasing  $D^2$  because of the increase in the fast-electron current density at decreasing radii. This possibility was addressed in two ways: First, the experiment was repeated using a lower laser energy (18 kJ instead of 26 kJ). This reduced the energy in fast electrons and consequently the electric field by a factor of  $\sim 80$  (Ref. 11). Figure 135.25 shows the HXR signals for the two cases (the radiation contribution to the Mo- $K_\alpha$  line is larger for the low-power shots; therefore, the  $K_\alpha$  data were omitted in Fig. 135.25). The shape of the two curves is approximately the same. If the rise in Fig. 135.23 resulted from electric-field effects, rather than fast-electron divergence, we would expect the lower-power curve to tend toward a constant value with increasing  $D$ .

Additionally, the electric field resulting from a return current in the  $\text{N}_2$  gas between the Mo and CH shells has been estimated (no space charges can build up because they will lead to extremely high retarding fields). The total fast-electron current density at the quarter-critical surface was calculated as  $J_{\text{hot}}(r_{1/4}) = f_{\text{hot}} e I_L / E_{\text{hot}}$ , where  $f_{\text{hot}}$  is the fraction of instantaneous laser power that is converted to fast-electron power,  $I_L$  is the laser irradiance, and  $E_{\text{hot}}$  is a typical fast-electron energy. For the shots reported in Fig. 135.23,  $I_L = 1.1 \times 10^{15} \text{ W/cm}^2$  and the HXR-measured hot-electron temperature is  $\sim 50 \text{ keV}$ ;

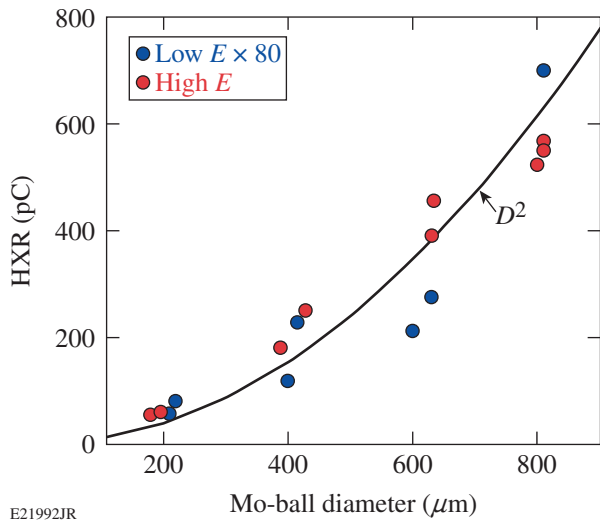
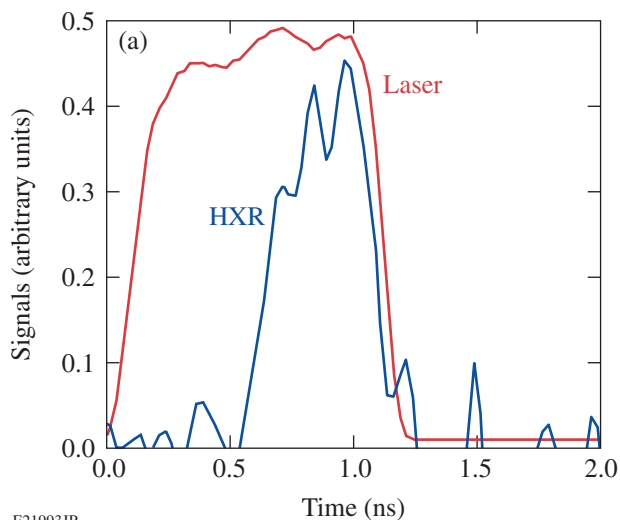


Figure 135.25

The hard x-ray measurements for 18- and 26-kJ laser energies, indicating a reduction by a factor  $\sim 80$  in the production of fast electrons, consequently in the electric field. The  $D^2$  curve serves merely to guide the eye. The similarity of the two sets of data sharply reduces the likelihood of electric-field effect on the results shown in Fig. 135.23.

therefore, for a three-dimensional Maxwellian distribution,  $E_{\text{hot}} \sim 75$  keV. Figure 135.26(a) shows the time histories of the laser power and the HXR for one of the shots shown in Fig. 135.23. Note that most of the fast electrons are produced in the latter part of the laser pulse. For a laser irradiance of  $1.1 \times 10^{15}$  W/cm<sup>2</sup>, the time-integrated value of  $f_{\text{hot}}$  is  $\sim 0.01$



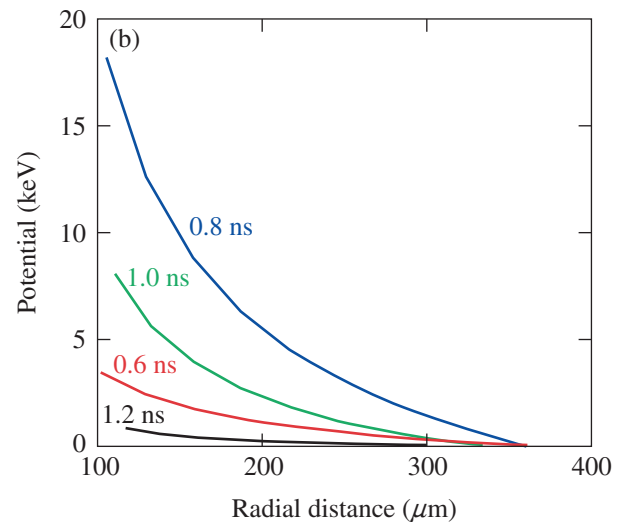
E21993JR

Figure 135.26

(a) The measured pulse shapes of the laser and hard x-ray (HXR) radiation. (b) The electric potential across the N<sub>2</sub> fill gas resulting from the return current produced by the radial fast-electron current is estimated at several times. The electric potential drop is much smaller than a typical fast-electron energy ( $\sim 75$  keV), thereby eliminating electric fields as a possible cause for the signal's rise shown in Fig. 135.23.

(Refs. 11 and 12). Using Fig. 135.26(a), the instantaneous  $f_{\text{hot}}$  was determined and used to calculate the time history of  $J_{\text{hot}}(r_{1/4})$ . The calculated total current is of the order of a few megaamperes, which is much above the Alfvén limiting current,<sup>25</sup> forcing a return current density equal to  $J_{\text{hot}}(r)$ . The return current gives rise to a resistive radial electric field given by  $E(r) = J_{\text{hot}}(r) / \sigma(r)$ , where  $\sigma(r)$  is the parallel Braginskii conductivity:<sup>26</sup>  $\sigma = 1.96 Ne^2 \tau_e / m_e$  in terms of the electron collision time  $\tau_e$ . We estimate  $\sigma(r)$  using the temperature and ionization of the N<sub>2</sub> gas (no density dependence), simulated by the hydrodynamic code *LILAC*<sup>27</sup> for the case of a 200- $\mu$ m-diam Mo ball. The fill gas was ionized by shock and radiation heating. Figure 135.26(b) shows the estimated electric potential drop across the N<sub>2</sub> gas for several times during the laser pulse. The time history of the field follows that of the HXR curve; the outer surface of the Mo layer is seen to expand in time as a result of heating by absorbed radiation; this is an additional source of ionization of the fill gas. The maximum electric potential is much smaller than typical fast-electron energy ( $\sim 75$  keV); therefore, the generated electric field has a negligible effect on the fast-electron current and the results shown in Fig. 135.23.

In conclusion, we have described a new technique for studying the divergence of fast electrons in laser fusion using Mo-coated balls embedded within CH shell targets. We have shown that the fast electrons generated on the OMEGA laser at an irradiance of  $\sim 1.1 \times 10^{15}$  W/cm<sup>2</sup> are widely divergent. This result greatly improves the outlook for direct-drive



laser fusion by reducing the expected preheat. It also enables one to precisely determine the preheat in any given direct-drive laser-fusion experiment by using an electron-transport calculation in conjunction with a hydrodynamic code and a single observable: the emitted HXR. For imploding cryogenic targets on OMEGA, the maximum laser irradiance is  $\sim 8 \times 10^{14}$  W/cm<sup>2</sup> and the total energy in fast electrons is  $\sim 0.2\%$  of the laser energy,<sup>11</sup> but the results reported here show that only  $\sim 1/4$  of the fast electrons will intersect the cold fuel and potentially preheat it. This reduces the fraction of fast-electron energy converted to preheat to less than  $\sim 0.05\%$ , well below the maximum tolerated. Therefore, preheat by fast electrons in current OMEGA cryogenic experiments is negligible. Polar-drive-ignition designs<sup>28</sup> for the National Ignition Facility (NIF)<sup>29</sup> with peak intensities of  $1.1 \times 10^{15}$  W/cm<sup>2</sup> show<sup>28</sup> that the cold fuel shell has converged by about a factor 2 around the time of maximum density scale length; therefore, the same reduction in preheat caused by fast-electron divergence is expected for polar-drive-ignition experiments on the NIF.

#### ACKNOWLEDGMENT

We acknowledge the efforts of J. Fooks and the General Atomics team for producing the complicated targets used in this study. This material is based upon work supported by the Department of Energy National Nuclear Security Administration under Award Number DE-NA0001944, the University of Rochester, and the New York State Energy Research and Development Authority. The support of DOE does not constitute an endorsement by DOE of the views expressed in this article.

#### REFERENCES

1. M. N. Rosenbluth, R. B. White, and C. S. Liu, *Phys. Rev. Lett.* **31**, 1190 (1973).
2. H. A. Baldis and C. J. Walsh, *Phys. Fluids* **26**, 1364 (1983).
3. B. B. Afeyan and E. A. Williams, *Phys. Plasmas* **4**, 3827 (1997).
4. C. Stoeckl, R. E. Bahr, B. Yaakobi, W. Seka, S. P. Regan, R. S. Craxton, J. A. Delettrez, R. W. Short, J. Myatt, A. V. Maximov, and H. Baldis, *Phys. Rev. Lett.* **90**, 235002 (2003).
5. J. D. Lindl, *Inertial Confinement Fusion: The Quest for Ignition and Energy Gain Using Indirect Drive* (Springer-Verlag, New York, 1998), Chap. 11.
6. *LLE Review Quarterly Report* **79**, 121, Laboratory for Laser Energetics, University of Rochester, Rochester, NY, LLE Document No. DOE/SF/19460-317, NTIS Order No. DE2002762802 (1999). Copies may be obtained from the National Technical Information Service, Springfield, VA 22161.
7. R. L. McCrory, D. D. Meyerhofer, R. Betti, R. S. Craxton, J. A. Delettrez, D. H. Edgell, V. Yu. Glebov, V. N. Goncharov, D. R. Harding, D. W. Jacobs-Perkins, J. P. Knauer, F. J. Marshall, P. W. McKenty, P. B. Radha, S. P. Regan, T. C. Sangster, W. Seka, R. W. Short, S. Skupsky, V. A. Smalyuk, J. M. Soures, C. Stoeckl, B. Yaakobi, D. Shvarts, J. A. Frenje, C. K. Li, R. D. Petrasso, and F. H. Séguin, *Phys. Plasmas* **15**, 055503 (2008).
8. V. A. Smalyuk, D. Shvarts, R. Betti, J. A. Delettrez, D. H. Edgell, V. Yu. Glebov, V. N. Goncharov, R. L. McCrory, D. D. Meyerhofer, P. B. Radha, S. P. Regan, T. C. Sangster, W. Seka, S. Skupsky, C. Stoeckl, B. Yaakobi, J. A. Frenje, C. K. Li, R. D. Petrasso, and F. H. Séguin, *Phys. Rev. Lett.* **100**, 185005 (2008).
9. B. Yaakobi, P.-Y. Chang, A. A. Solodov, C. Stoeckl, D. H. Edgell, R. S. Craxton, S. X. Hu, J. F. Myatt, F. J. Marshall, W. Seka, and D. H. Froula, *Phys. Plasmas* **19**, 012704 (2012).
10. D. H. Froula, B. Yaakobi, S. X. Hu, P.-Y. Chang, R. S. Craxton, D. H. Edgell, R. Follett, D. T. Michel, J. F. Myatt, W. Seka, R. W. Short, A. Solodov, and C. Stoeckl, *Phys. Rev. Lett.* **108**, 165003 (2012).
11. D. H. Froula, D. T. Michel, I. V. Igumenshchev, S. X. Hu, B. Yaakobi, J. F. Myatt, D. H. Edgell, R. Follett, V. Yu. Glebov, V. N. Goncharov, T. J. Kessler, A. V. Maximov, P. B. Radha, T. C. Sangster, W. Seka, R. W. Short, A. A. Solodov, C. Sorce, and C. Stoeckl, *Plasma Phys. Control. Fusion* **54**, 124016 (2012).
12. D. T. Michel, A. V. Maximov, R. W. Short, J. A. Delettrez, D. Edgell, S. X. Hu, I. V. Igumenshchev, J. F. Myatt, A. A. Solodov, C. Stoeckl, B. Yaakobi, and D. H. Froula, *Phys. Plasmas* **20**, 055703 (2013).
13. V. N. Goncharov, T. C. Sangster, T. R. Boehly, S. X. Hu, I. V. Igumenshchev, F. J. Marshall, R. L. McCrory, D. D. Meyerhofer, P. B. Radha, W. Seka, S. Skupsky, C. Stoeckl, D. T. Casey, J. A. Frenje, and R. D. Petrasso, *Phys. Rev. Lett.* **104**, 165001 (2010).
14. S. P. Regan, N. B. Meezan, L. J. Suter, D. J. Strozzi, W. L. Kruer, D. Meeker, S. H. Glenzer, W. Seka, C. Stoeckl, V. Yu. Glebov, T. C. Sangster, D. D. Meyerhofer, R. L. McCrory, E. A. Williams, O. S. Jones, D. A. Callahan, M. D. Rosen, O. L. Landen, C. Sorce, and B. J. MacGowan, *Phys. Plasmas* **17**, 020703 (2010).
15. B. Yaakobi, T. R. Boehly, T. C. Sangster, D. D. Meyerhofer, B. A. Remington, P. G. Allen, S. M. Pollaine, H. E. Lorenzana, K. T. Lorenz, and J. A. Hawreliak, *Phys. Plasmas* **15**, 062703 (2008).
16. T. Döppner *et al.*, *Phys. Rev. Lett.* **108**, 135006 (2012).
17. T. R. Boehly, D. L. Brown, R. S. Craxton, R. L. Keck, J. P. Knauer, J. H. Kelly, T. J. Kessler, S. A. Kumpan, S. J. Loucks, S. A. Letzring, F. J. Marshall, R. L. McCrory, S. F. B. Morse, W. Seka, J. M. Soures, and C. P. Verdon, *Opt. Commun.* **133**, 495 (1997).
18. Y. Lin, T. J. Kessler, and G. N. Lawrence, *Opt. Lett.* **20**, 764 (1995).
19. S. Skupsky, R. W. Short, T. Kessler, R. S. Craxton, S. Letzring, and J. M. Soures, *J. Appl. Phys.* **66**, 3456 (1989).
20. T. R. Boehly, V. A. Smalyuk, D. D. Meyerhofer, J. P. Knauer, D. K. Bradley, R. S. Craxton, M. J. Guardalben, S. Skupsky, and T. J. Kessler, *J. Appl. Phys.* **85**, 3444 (1999).
21. J. F. Seely *et al.*, *Rev. Sci. Instrum.* **81**, 10E301 (2010).
22. C. Stoeckl, V. Yu. Glebov, D. D. Meyerhofer, W. Seka, B. Yaakobi, R. P. J. Town, and J. D. Zuegel, *Rev. Sci. Instrum.* **72**, 1197 (2001).

23. I. Kawrakow *et al.*, NRC, Ottawa, Canada, NRCC Report PIRS-701 (May 2011); I. Kawrakow, *Med. Phys.* **27**, 485 (2000).
24. A. L. Meadowcroft, C. D. Bentley, and E. N. Stott, *Rev. Sci. Instrum.* **79**, 113102 (2008).
25. S. Atzeni and J. Meyer-ter-Vehn, *The Physics of Inertial Fusion: Beam Plasma Interaction, Hydrodynamics, Hot Dense Matter*, International Series of Monographs on Physics (Clarendon Press, Oxford, 2004), p. 423.
26. S. I. Braginskii, in *Reviews of Plasma Physics*, edited by Acad. M. A. Leontovich (Consultants Bureau, New York, 1965), Vol. 1, p. 205.
27. R. Epstein, S. Skupsky, and J. Delettrez, *J. Quant. Spectrosc. Radiat. Transf.* **35**, 131 (1986).
28. T. J. B. Collins, J. A. Marozas, K. S. Anderson, R. Betti, R. S. Craxton, J. A. Delettrez, V. N. Goncharov, D. R. Harding, F. J. Marshall, R. L. McCrory, D. D. Meyerhofer, P. W. McKenty, P. B. Radha, A. Shvydky, S. Skupsky, and J. D. Zuegel, *Phys. Plasmas* **19**, 056308 (2012).
29. G. H. Miller, E. I. Moses, and C. R. Wuest, *Opt. Eng.* **43**, 2841 (2004).

---

# Copper K-Shell Emission Cross Sections for Laser–Solid Experiments

## Introduction

Fast-electron generation in laser–plasma interactions has long been of interest for a variety of reasons, such as avoiding pre-heat during compression in inertial confinement fusion (ICF), heating the compressed core of an ICF target for fast ignition,<sup>1</sup> generating a shock in an ICF target for shock ignition,<sup>2</sup> and as a means to produce energetic secondary particles,<sup>3</sup> such as protons<sup>4</sup> and gamma rays.<sup>5,6</sup>

K-shell emission<sup>7,8</sup> is a widely used fast-electron diagnostic in laser–solid experiments; it has also been used to provide a source of x rays at a specific energy. The most commonly used emitter in these experiments is copper. K-shell emission is produced when a fast electron knocks out a K-shell electron from an atom in the solid target, which is then replaced by an electron from an outer shell—a transition that leads to the emission of a photon with a characteristic energy in the x-ray band. If the outer shell involved is the L shell, the emission is called  $K_\alpha$ ; if it is the M shell, it is called  $K_\beta$ .  $K_\alpha$  emission is more probable than  $K_\beta$  emission, so the majority of K-shell diagnostics used in laser–solid experiments rely entirely on  $K_\alpha$  emission. It is assumed that the fraction of atoms with missing K-shell electrons, as a result of fast electrons or target heating, is always negligible. A fundamental parameter required when analyzing such measurements is the cross section for K-shell emission by fast electrons. The objective of this article is to identify a simple and accurate published expression for the K-shell emission cross section of copper. The principal motivation for this study was the analysis of  $K_\alpha$ -emission diagnostics in laser–solid experiments at peak intensities above  $10^{18}$  W/cm<sup>2</sup>, where the fast-electron energy range of interest is roughly 0.1 to 10 MeV.

This work began with an analysis of time-resolved measurements of total  $K_\alpha$  emission in laser–solid experiments;<sup>7</sup> 20- $\mu$ m-thick copper foils were irradiated at normal incidence by  $\sim$ 1-ps laser pulses at intensities from  $10^{18}$  to  $10^{19}$  W/cm<sup>2</sup>, and the x-ray emission was recorded using a streaked spectrometer. While looking for a simple expression for the K-shell emission cross section, a confusingly large selection of expressions was found, some of which differed significantly from one another.

A number of nonrelativistic expressions that use  $1/E$  in place of  $2/m_e v^2$ , where  $E$  is the kinetic energy,  $m_e$  is the electron mass, and  $v$  is the velocity, could be immediately discarded as inaccurate at all energies of interest. Closer analysis of the remaining expressions showed that a number of these differences were caused by typing errors, which were identified by comparing the curves given with those in the respective papers, by comparing similar terms used in multiple papers, and by simple physical arguments. The only significant difference that remained was whether the cross section varied as  $\ln E$  or  $\ln(p^2/2m_e)$ , where  $p$  is the momentum, which made a difference at relativistic energies. Comparison with the standard expression for electron stopping power suggested a third form, not used in any of the expressions. Furthermore, it suggested a reduction in the cross section at strongly relativistic energies, known as the density-effect correction, which had not been adequately considered. We then turned to measurements of K-shell emission from copper made with electron beams to select the most-accurate expression. Very few measurements in the 0.1- to 10-MeV region were found, so it was not possible to significantly narrow the number of apparently adequate expressions. Too few measurements were found with differences between them that were too large to clearly determine the correct limiting form at relativistic energies. Fortunately, for analyzing our measurements to determine a mean fast-electron energy, where only the relative  $K_\alpha$ -emission rate as a function of electron energy was important, these differences were found to be irrelevant. They would be significant if absolute  $K_\alpha$  yields were important, for example, to determine the number of fast electrons. To complete our study of K-shell emission, attention was turned to other possible sources of emission in laser–solid experiments, namely keV photons and MeV protons. A brief analysis of K-shell yields for photons and protons showed that the contribution from these sources may not always be entirely negligible, as originally assumed.

Although this work concentrates on copper, which is the most widely used in high-intensity laser–solid experiments and in electron-beam experiments, the basic considerations apply to any material and most of the expressions considered apply

to any material. We have also included some discussion on the variation with atomic number ( $Z$ ).

In the following sections, the measurements and expressions are presented, followed by a brief discussion of the divergence in the expressions at relativistic energies. Next, the implications of the results for the interpretation of laser–solid experiments are considered, calculating emission rates and yields per electron as a function of electron energy. K-shell yields from other sources in laser–solid experiments that could be confounding factors for fast-electron diagnostics are then considered, namely photons and protons. Finally, our conclusions are presented, followed by the full expressions for the K-shell ionization cross sections in the appendix, with a number of typing errors corrected, and a simple fit for the K-shell emission cross section of copper is proposed.

### Electron K-Shell Emission Cross Sections for Copper

K-shell emission cross sections  $\sigma_K$  have been measured using electron beams passing through thin copper films, down to a few nanometers in thickness, to a typical quoted accuracy of better than  $\pm 10\%$ . The results, however, are always expressed in terms of K-shell ionization cross section  $\sigma_{\text{ion}}$ , given by

$$\sigma_K = f_K \sigma_{\text{ion}}, \quad (1)$$

where  $f_K$  is fluorescence yield, for which different values have been used; it represents the fact that not all ionization events lead to emission of a photon. To obtain the K-shell emission cross section, it is important to correctly undo this step. Liu *et al.*<sup>9</sup> give a table of values from papers published before 2000, all modified to a fluorescence yield of 0.441, which simplifies the task. Since then, Llovet *et al.*<sup>10</sup> have published measurements, also using a fluorescence yield of 0.441, and Zhou *et al.*<sup>11</sup> have published measurements with an unstated fluorescence yield, but since this publication is from the same group as Liu *et al.*<sup>9</sup> it seems reasonable to assume that they also used 0.441. We are unaware of any other measurements published before 2013. These values, plotted in Fig. 135.27, are multiplied by the atomic number density of solid copper  $n_a$  ( $8.49 \times 10^{28} \text{ m}^{-3}$ ; copper will always refer to solid-density, un-ionized copper), giving what is known as the macroscopic cross section: the mean number of photons emitted per fast electron per meter.

Clearly the differences between various sets of measurements (individual experiments) are far greater than the quoted errors. Llovet *et al.*<sup>10</sup> give a clear explanation of the difference

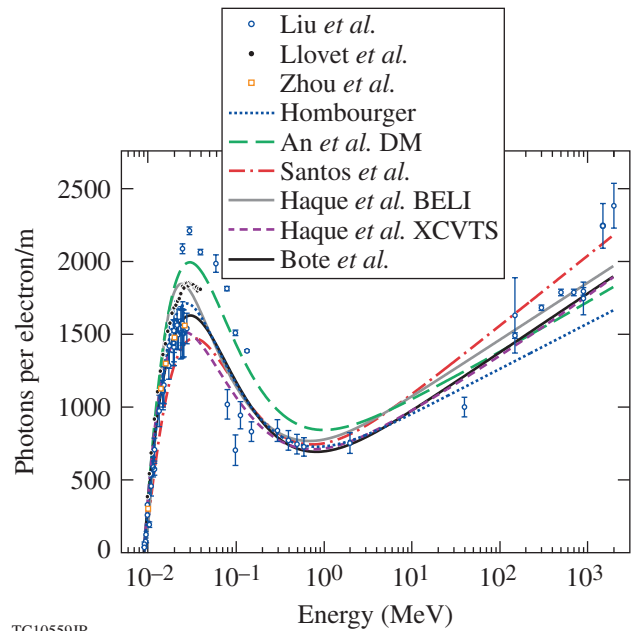


Figure 135.27

Macroscopic K-shell emission cross sections for solid copper. Points are from measurements given by Liu *et al.*,<sup>9</sup> Llovet *et al.*,<sup>10</sup> and Zhou *et al.*<sup>11</sup> Curves are from expressions given by Hombourger,<sup>17</sup> An *et al.*,<sup>22</sup> Santos *et al.*,<sup>25</sup> Haque *et al.*'s BELI model,<sup>19</sup> Haque *et al.*'s XCVTS model,<sup>24</sup> and Bote *et al.*<sup>14</sup> using a fluorescence yield of 0.45. DM: Deutsch–Märk.

between relative and absolute errors in such experiments and estimate theirs to be 2% and 10%, respectively (error bars not shown). We therefore conclude that the quoted errors are, in most cases, representative of the relative errors in the experiments. The uncertainty in the absolute values in Fig. 135.27 would have to be  $\sim 20\%$  to make all but a few outlying points consistent with one another, but some of the measurements may have significant systematic errors.

The remainder of this section briefly discusses the general features of these measurements and how they vary with atomic number.

The threshold for K-shell emission is the K-shell binding energy  $B$ , or K edge, which is known from measurements and numerical calculations to be 8.98 keV for copper to a precision far greater than any of the other results considered here. K-shell binding energy scales approximately as  $Z^2$ .<sup>17</sup> Above this threshold, the cross section rises sharply, peaks at  $\sim 3\times$  the binding energy, then starts to fall. The large number of measurements in this region is in good agreement on the position and shape of the peak, if not on the absolute values. Above  $\sim 1$  MeV, the cross section starts to increase continually from a minimum

that is roughly a factor of 2 below the initial peak for copper. The position of this minimum does not vary significantly with atomic number, and its depth decreases with increasing atomic number as the peak moves up toward it. Eventually it vanishes; for example, gold shows no clear local maximum or minimum in the cross section, showing what could be better described as a point of inflexion. Unfortunately, there are very few measurements in this region, which is the region of particular interest for high-intensity laser–solid experiments; there is only one point between 0.6 and 40 MeV. Therefore, all of the measurements, up to 2 GeV, have been included to see how well expressions interpolate over this region; however, a rigorous analysis of the correlation of the expressions with the measurements has not been carried out since it would be almost meaningless for our purposes.

The expressions—numerical, theoretical, and empirical—all consider the ionization cross section, so a fluorescence yield is required to give the emission cross section. Kahoul *et al.*<sup>12</sup> give a convenient compilation of measurements published before 2011. From these we chose to use 0.45 for three reasons: (1) it is the value from the most-recent measurement given ( $0.452 \pm 0.036$ ); (2) it is the value from the measurement given with the smallest quoted error ( $0.452 \pm 0.003$ ); and (3) it is the highest value since we noted a general tendency for the expressions to lie below the measurements. It should be noted that expressions with parameters obtained by fitting measurements all used fluorescence yields for copper from 0.4 to just under 0.45, so we may slightly overestimate the original fit in some cases. Kahoul *et al.* give five different fits for the fluorescence yield, all of which give adequate agreement with the measurements. The simplest is

$$f_K = 0.985 \frac{(Z/30.896)^{3.847}}{1 + (Z/30.896)^{3.847}}, \quad (2)$$

which gives 0.433 for copper.

K-shell ionization cross sections have been calculated numerically (for example, see Bote *et al.*<sup>13</sup>), but all of these calculations are approximate since an exact model for copper would require solving the full Dirac equation for 30 electrons (one incident electron and 29 electrons in the atom) and this would still neglect collective effects from many atoms. Therefore, these results are not necessarily a better reference than measured values. Also, we have not found a convenient set of tabulated numerical results. We will show Bote *et al.*'s<sup>14</sup> fit to

their numerical results, which has ten fitting parameters determined individually for every element, giving a stated accuracy better than 1% up to the maximum energy considered of 1 GeV.

A plethora of theoretical and empirical expressions exists for the K-shell ionization cross section. To limit the universe of expressions, we did not consider the many nonrelativistic ones that write a factor of  $2/m_e v^2$  as  $1/E$ , leading to a cross section that falls continually with energy above the peak. Such expressions have been used in modeling laser–solid experiments, which would have led to significant errors;  $2E/m_e v^2$  exceeds 1.1 at only 34 keV and exceeds 2 at 0.32 MeV. We then considered 12 relativistic expressions,<sup>14–25</sup> and there are almost certainly more out there. Since this time, a minor modification of Santos *et al.*'s expression<sup>25</sup> has been published by Guerra *et al.*<sup>26</sup> Only four expressions clearly failed to reproduce the measurements: Jakoby *et al.*'s<sup>16</sup> expression, Tang *et al.*'s<sup>18</sup> expression, Haque *et al.*'s Kolbenstvedt model,<sup>20</sup> and Haque *et al.*'s modified Deutsch–Märk model.<sup>23</sup> In the case of Jakoby *et al.*'s expression and Haque *et al.*'s Kolbenstvedt model, this failure appears to be caused, at least in part, by typing errors that we could not resolve. We identified and corrected typing errors in Grynski's relativistic factor<sup>27</sup> in Casnati *et al.*'s,<sup>15</sup> Hombourger's,<sup>17</sup> and Gstir *et al.*'s<sup>21</sup> expressions. Eight models are too many to show conveniently in Fig. 135.27, so we have chosen to plot only six that envelope the range of values given by all eight expressions. The highest values are given by An *et al.*'s<sup>22</sup> version of the Deutsch–Märk model,<sup>21</sup> up to just beyond the dip, and by Santos *et al.*'s<sup>25</sup> expression at higher energies. The lowest values are given by Haque *et al.*'s BELI model<sup>19</sup> just above threshold, by Santos *et al.*'s<sup>25</sup> expression from there up to the peak, by Haque *et al.*'s XCVTS model<sup>24</sup> just beyond the peak, by Bote *et al.*'s<sup>14</sup> expression around the dip, and by Hombourger's<sup>17</sup> expression at higher energies.

The expression of Santos *et al.*<sup>25</sup> was used to model our experiments<sup>7</sup> because it was the first relativistic result we found and they had compared it to measurements for copper, showing adequate agreement; in hindsight we cannot give a rigorous justification for the choice of this expression.

The measurements of Llovet *et al.*<sup>10</sup> represent the most-extensive and accurate single set of measurements of emission cross section from just beyond threshold up to the peak (32 points, roughly a third of all the measurements, from 9.5 keV to 40 keV with a quoted relative error of  $\pm 2\%$ ), so it seems reasonable to use them to determine the most-accurate

expression for ionization cross section in this region, which may be of interest to others. To determine which expression was the most accurate without assuming a value for the fluorescence yield and without being influenced by possible systematic errors in the absolute values of the measurements, we used the gradient of a linear fit to expression versus measurement, the gradient closest to one indicating the most accurate. The expression of Hombourger was the most accurate, with that of Casnati *et al.* coming close. We then found the value of fluorescence yield for these two expressions that gave the best fit to the measurements, obtaining  $f_K = 0.488$  for Hombourger and  $f_K = 0.455$  for Casnati *et al.*, with Hombourger giving the best fit, as expected. This means that Casnati *et al.* gave the best fit using the fluorescence yield we chose of 0.45. A fluorescence yield of 0.488 is clearly higher than any measured value,<sup>12</sup> indicating that either Hombourger's expression is too low by a factor of  $0.488/0.45 = 1.084$ , at least for copper, or that Llovet *et al.*'s<sup>10</sup> measurements are systematically high, which would be within their absolute error estimate of  $\pm 10\%$ . Llovet *et al.*'s measurements are systematically higher than the measurements of Zhou *et al.*,<sup>11</sup> but it is not possible to tell whose measurements are more precise. On the other hand, such an increase in Hombourger's expression gives a result at relativistic energies that is closer to all of the other expressions.

Because of the large number and length of the expressions, we have placed them in an appendix, including our corrections to what appear to be typing errors. It is possible, however, to give a simple expression that summarizes them for electron energies  $E$  somewhat greater than threshold  $B$  (for nonrelativistic  $B$ ), introducing only three dimensionless parameters  $f$ ,  $g$ , and  $n$  that have a limited range of values:

$$\sigma_{\text{ion}} \sim \frac{N_K 100 (1+f)}{\beta^2 B_{\text{keV}}^{1+g}} \ln \left[ \left( \frac{\gamma+1}{2} \right)^n \frac{E}{B} \right] \text{ barns}, \quad (3)$$

where  $N_K$  is the number of K-shell electrons;  $\beta$  is  $v/c$ , where  $v$  is the average relative velocity of the fast and K-shell electrons and  $c$  is the speed of light;  $\gamma$  is the Lorentz factor of the fast electron;  $f$  is between 0 and 1;  $g$  is typically 0 or close to 0; and  $n$  is 0 or 1. Most models use  $n = 0$ , while Santos *et al.*,<sup>25</sup> Guerra *et al.*<sup>26</sup> (not shown), and Bote *et al.*<sup>14</sup> [all based on the results of Scofield<sup>28</sup> (not considered)] along with Kolbenstvedt<sup>29</sup> (not considered) use  $n = 1$ . Scofield's expression was not considered because he gave no fitting parameters for copper; Kolbenstvedt's two expressions [his Eq. (11) and the sum of his Eqs. (14) and (15)] were not considered because

they are valid only well above threshold. [Haque *et al.*'s Kolbenstvedt model<sup>20</sup> does not have this form, which appears to be a typing error;  $T(T+2)$  should replace  $(T+2)$  in the log term.] The limited number of measurements above 1 MeV and the significant variations between them mean that a value of  $n$  cannot be determined with meaningful accuracy.

In most laser–solid experiments, only the  $K_\alpha$  emission is considered, not the  $K_\beta$  emission, so if absolute numbers are required, the K-shell emission cross section must be multiplied by the fraction of  $K_\alpha$  emission. Published measurements and numerical calculations of this fraction agree to within a few percent,<sup>30</sup> giving 0.880 for copper. Values can also be obtained from the code *FLYCHK*.<sup>31</sup> This fraction is roughly constant for atomic numbers from 20 to 30, then decreases slowly with atomic number, reaching 0.784 for gold. The copper  $K_\alpha$  imagers used in laser–solid experiments image only the  $K_{\alpha 1}$  line.<sup>8</sup> The fraction of K-shell emission in this line has not been as widely considered but can be obtained from *FLYCHK*, which gives 0.591 for copper. It should be noted that these ratios could be higher for many cases of interest as a result of ionization of outer shells caused by target heating.

Before moving on to consider the implication of these results for the interpretation of laser–solid experiments, we will briefly consider the bifurcation in the expressions at relativistic energies ( $n = 0$  or 1) out of academic interest.

### K-Shell Ionization Cross Section in the Relativistic Limit

The origin of  $n = 1$  is a relativistic result for energy transfer to excitation of bound electrons caused by the electric field of a charged particle moving at constant velocity, often called the Bethe term. The origin for  $n = 0$  could be the use of the nonrelativistic result  $E = p^2/2m_e$  in the Bethe term or the use of the binary collision cross section. Surprisingly, both of these choices differ from the standard expression for fast-electron stopping power<sup>32,33</sup>

$$\frac{dE}{ds} = -\frac{Zn_a e^4}{4\pi\epsilon_0^2 m_e v^2} \times \left[ \ln \left( \sqrt{\frac{\gamma+1}{2}} \frac{E}{I_{\text{ex}}} \right) - \frac{\delta}{2} + \frac{0.909}{\gamma^2} - \frac{0.818}{\gamma} - 0.284 \right], \quad (4)$$

where  $s$  is the path length,  $n_a$  is the atom number density,  $e$  is the electron charge,  $\epsilon_0$  is the permittivity of free space,  $I_{\text{ex}}$  is the mean excitation potential (322 eV for copper), which is usually

determined by fitting measurements, and  $\delta$  is the density-effect correction, which we will return to later. Bremsstrahlung is not included in this expression. It applies to fast electrons with energy much greater than the binding energy of the electrons contributing to the stopping because they are assumed to be stationary. The connection to K-shell ionization cross section is more obvious if we consider the magnitude of the stopping power caused by only K-shell electrons:

$$\left| \frac{dE}{ds} \right| = -\frac{N_K n_a e^4}{4\pi\epsilon_0^2 m_e v^2} \times \left[ \ln \left( \sqrt{\frac{\gamma+1}{2}} \frac{E}{I_K} \right) - \frac{\delta}{2} + \frac{0.909}{\gamma^2} - \frac{0.818}{\gamma} - 0.284 \right] > n_a B \sigma_{\text{ion}}, \quad (5)$$

where  $I_K$  is the mean excitation potential for K-shell electrons, which exceeds their binding energy;<sup>32</sup> for example, for hydrogen the mean excitation potential is 19.2 eV, whereas the binding energy is 13.6 eV. The magnitude of the stopping power must be greater than  $n_a B \sigma_{\text{ion}}$  because  $B$  is the minimum energy exchange in a K-shell ionization event and energy can be lost to K-shell electrons without ionizing them. This indicates that  $n$  should be  $1/2$ , not 0 or 1—a value that has not been used in any expression we have encountered. The origin of this  $n = 1/2$  is a combination of binary collisions for large energy transfers and the Bethe term for small energy transfers.

The density-effect correction represents a reduction in stopping power caused by shielding of the fast electron's charge by surrounding electrons, which is not considered in the Bethe term. It increases with density of the surrounding electrons and with fast-electron energy, occurring only above a threshold energy in insulators. It has not been included in any of the expressions considered here, although Santos *et al.* state that it should be included at energies greater than a GeV and Scofield,<sup>28</sup> who did not consider copper, did include it. In copper, the reduction in total stopping power exceeds 10% above roughly 10 MeV (Refs. 32 and 33), indicating that the density effect should be considered at energies considerably less than a GeV, and this energy will decrease with increasing atomic number. The general expression is complex, but it has a simple limiting form for strongly relativistic electrons:

$$\frac{\delta}{2} \rightarrow \ln \left( \frac{\gamma \hbar \omega_p}{I_{\text{ex}}} \right) - \frac{\beta^2}{2}, \quad \beta \rightarrow 1, \quad (6)$$

where  $\hbar \omega_p$  is the plasmon energy calculated from total electron density (58.3 eV for copper). Equation (6) is within 10% of a more-accurate calculation for copper<sup>32,33</sup> above roughly 30 MeV; at lower energies it is an underestimate.

This implies that the rate of increase in the K-shell ionization cross section with energy should noticeably decrease at strongly relativistic energies. If the density-effect correction is not included in the expressions of Santos *et al.*<sup>25</sup> and Guerra *et al.*,<sup>26</sup> the inequality in Eq. (5) will not hold in the strongly relativistic limit (to this extent they are correct to state that the density effect should be included above 1 GeV). For expressions using  $n = 0$ , including the density effect will give a cross section that becomes independent of energy at strongly relativistic values, indicating that  $n = 0$  is not a physically correct choice. Scofield<sup>28</sup> did find that the density effect led to the cross section becoming independent of energy, but this appears to be a mistake in using  $\delta$  in place of  $\delta/2$  combined with his use of  $n = 1$ . The maximum cross section he gives is lower than values that have been measured at high energies and no saturation in any  $K_\alpha$  cross section has yet been reported.

Calculations and fitting formulas of the density-effect correction are readily available.<sup>32–34</sup> We found that the total stopping power of copper<sup>32,33</sup> was reproduced to within 1% by using

$$\frac{\delta}{2} = \ln \left[ 1 + (\gamma - 1) \frac{\hbar \omega_p}{I_{\text{ex}}} \exp(-0.5) \right], \quad (7)$$

which is zero at zero energy and tends to Eq. (6) in the relativistic limit, but does not fit at intermediate energies; however, here the density-effect correction makes a negligible contribution to the stopping power and the same would be expected for the K-shell ionization cross section. This will also work well for higher- $Z$  metals; we have found that it works better for molybdenum, but not insulators, where there is a threshold energy for the density effect to occur.

There is a potential complication when considering the inclusion of the density effect: the nanometer-thick films used in many of the measurements could suppress it because it is a collective effect that requires a minimum amount of material. For a strongly relativistic electron, the relevant length scale should be  $c/\omega_p$ , which is 3.4 nm for copper, so this is a concern. Evaluating the density effect in this case will require numerical calculations. We therefore conclude that the correct value of  $n$

appears to be 1/2 and that the density-effect correction should be included for copper at fast-electron energies above 10 MeV and at lower energies for higher atomic numbers.

Finally, it should be noted that these considerations as to which value of  $n$  is physically correct and the need to include the density-effect correction strictly apply only to physics-based expressions, such as those of Santos *et al.*<sup>25</sup> and Guerra *et al.*<sup>26</sup> Expressions with free parameters used to fit measurements could still give adequate fits over any energy range of interest, whatever value of  $n$  is assumed and without including the density effect, although a better physical basis for a fitting function should allow one to obtain a better fit. If an expression with free parameters is modified, the free parameters should be redetermined.

### K-Shell Emission as a Fast-Electron Diagnostic in Laser–Solid Experiments

Some of the implications of these results for K-shell emission diagnostics in laser–solid experiments will now be considered, the first being the choice of a K-shell emitter based on K-shell yield.

Using  $\sigma_{\text{ion}} \propto Z^{-2}$ <sup>17</sup> and Eq. (2) for the fluorescence yield, we find that there is a maximum in the K-shell emission cross section at an atomic number close to 21, which is scandium. Considering the atomic number density of solids in this region, the maximum macroscopic cross section should belong to titanium (22), which has been used in high-intensity laser–solid experiments almost as frequently as copper. Considering that the K-shell emission self-absorption depth is roughly proportional to the atomic number, increasing the thickness of the layer from which emission can be obtained and consequently total yield, we find that maximum yield occurs near 29, which is copper. This provides a further motivation for concentrating on copper, although, given the approximations made, nickel or zinc could give a higher yield. The available measurements do not allow one to more precisely determine the maximum emission cross section and maximum yield.

For time-resolved measurements, the key parameter is an emission rate of  $n_a \sigma v$ ; the results given in Fig. 135.27 multiplied by velocity are shown in Fig. 135.28. The emission rate has no initial peak and is almost independent of energy over the range of interest. This means that the  $K_\alpha$ -emission rate is, to a good approximation, proportional to the number of fast electrons, provided that the mean energy is much greater than the binding energy. Our results,<sup>7</sup> which did not depend on

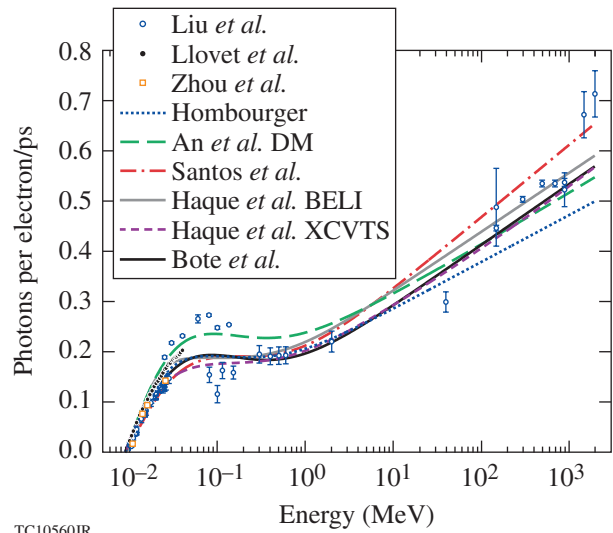


Figure 135.28

Same as Fig. 135.27 but multiplied by the electron velocity to give the emission rate in copper.

absolute values, were found to be insensitive to the expression used and to some accidental variations of individual terms in the expression of Santos *et al.*<sup>25</sup> by a factor of 2 because all of these expressions give an approximately constant emission rate at the relevant energies. This would not have been the case if the mean fast-electron energy was not much greater than the binding energy; just above the binding energy, the emission rate increases significantly with energy and the different expressions would give noticeably different results.

The most important parameter in determining the sensitivity of K-shell emission diagnostics to electron energy is the yield per electron  $Y$ , so we will now calculate this for two cases of particular interest to laser–solid experiments.

For an isolated copper foil, the vast majority of the electrons will be confined to the foil by the electrostatic field they generate, so K-shell emission yield will be determined by the emission rate times the stopping time. Considering only stopping resulting from collisions given by Eq. (4), the yield is

$$Y = \int_B^E \frac{n_a \sigma_K}{|dE/ds|} dE. \quad (8)$$

To illustrate this result for copper, we used only the BELI model of Haque *et al.*<sup>19</sup> since it lies roughly in the middle of the others over the energy range of interest. This yield is given by the

upper line in Fig. 135.29; it increases continually with energy, tending to a linear increase at high energies. Bremsstrahlung would lead to the yield flattening out by about 60 MeV, when it becomes the dominate energy-loss mechanism in copper.<sup>32</sup>

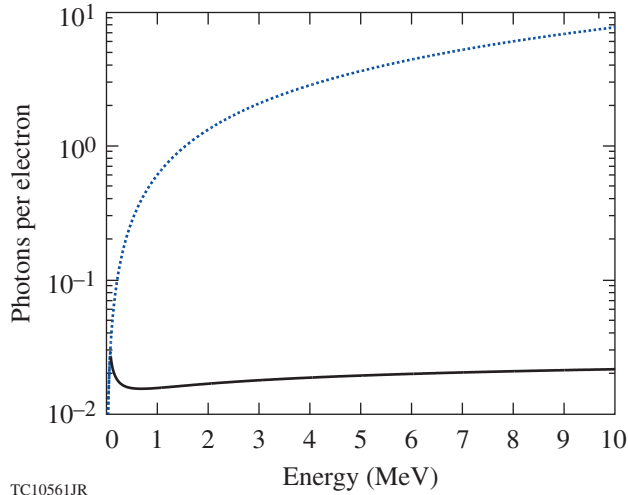


Figure 135.29  
K-shell yield per electron including collisional stopping in solid, un-ionized copper for electrons that stop in the copper (dotted blue line) and electrons that travel a maximum distance of 20  $\mu\text{m}$  (solid black line).

Equations (3) and (8) indicate that  $ZBY/f_K$  as a function of  $E/B$  should be weakly dependent on material, while bremsstrahlung is negligible, so this result can be readily scaled to any material of interest. Bremsstrahlung will lead to the yield flattening out at lower energies for higher atomic numbers.

Most K-shell emission experiments use a thin layer buried within a thick target. For electrons that maintain a constant velocity and travel a distance  $s$ , the yield is simply  $n_a \sigma_K s$ ; therefore, its variation with energy is the same as that for the macroscopic cross section given in Fig. 135.27. The lower line in Fig. 135.29 gives the yield for electrons traveling a maximum distance of 20  $\mu\text{m}$ , a typical upper value for the thickness of a copper fluor layer since it is roughly the attenuation depth of the K-shell emission. This gives a yield that is practically independent of energy from 0.7 to 10 MeV. Below this there is a narrow peak, where the yield increases by a factor of 1.9; then below 60 keV, the yield rapidly becomes negligible. In practice, the yield per electron from a 20- $\mu\text{m}$  copper layer would lie between the two curves in Fig. 135.29 because the distance traveled by an electron going through the layer at an angle  $\theta$  to the normal will be  $20/\cos\theta$   $\mu\text{m}$  and angular scattering will increase the average path length,<sup>35</sup> more so for

lower-energy electrons. Therefore, to a first approximation, copper K-shell emission from a thin layer in a thick target is proportional to the number of electrons above roughly 60 keV that reach it, provided that the majority of electrons reaching it exceed this energy.

An important general feature to note from Fig. 135.29 is that collisions significantly suppress the K-shell emission yield of electrons with an energy up to roughly  $6\times$  the threshold energy; therefore, the effective detection threshold is significantly higher than might be expected. The physical reason for this is that electrons just above threshold are far more likely to lose their energy colliding with one of the other electrons in the material than to cause K-shell emission. Another important feature is that the local maximum in the K-shell emission cross section does not lead to the emission being particularly sensitive to a narrow range of fast-electron energies, as is often assumed. For mean energies well above the effective threshold, K-shell emission, either time resolved from an isolated thin foil or time integrated from a thin foil buried in a thick target, is most sensitive to the number of fast electrons and not sensitive to their energy. The energy distribution can be inferred from the variation in signal with time or depth, provided the energy dependence of stopping time or distance is known. The only significant difference between the expressions we have considered will be in determining the absolute number of fast electrons. For mean energies that are not much greater than threshold, K-shell emission will be dominated by the higher-energy electrons in the distribution and interpretation of the results will be sensitive to the shape of the cross section near threshold, where the expressions we have considered are noticeably different.

Another important factor when evaluating absolute yields in experiments is the opacity of the target, which can change significantly as it ionizes, but this will not be considered here.

We will next examine how accurate it is to assume that K-shell emission measurements in laser–solid experiments are due entirely to fast electrons.

### Other Sources of K-Shell Emission

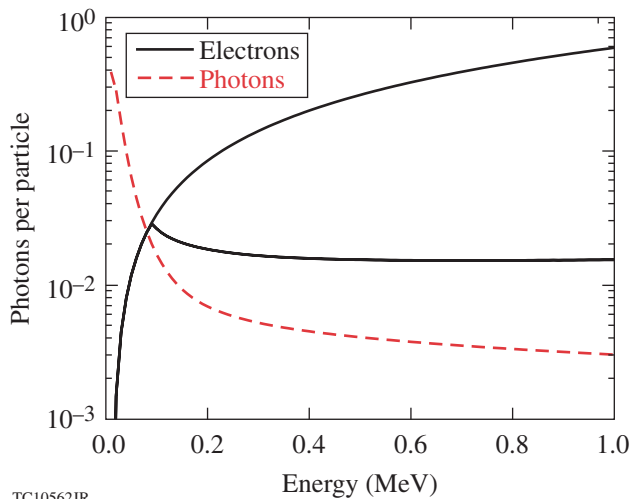
An essential requirement when using K-shell emission as a fast-electron diagnostic is that fast electrons be the primary source of the emission, but photons and ions can also cause K-shell emission and are also produced in laser–solid interactions, so we will briefly consider the yields from these other potential sources of K-shell emission.

## 1. Photons

To estimate the yield from photons, we considered only photons below the threshold for pair production (1.022 MeV) where absorption is caused only by photoionization. For the fraction of K-shell photoionizations in copper, we used 0.8796, as used in the EGS Monte Carlo code;<sup>36</sup> therefore, we need to calculate only  $0.8796 \times$  the number of photons absorbed in the copper. To do this, we assumed an isotropic photon source and averaged exponential attenuation over all straight-line trajectories through a sheet of thickness  $s$ , obtaining

$$Y = 0.396 \left[ 1 - \exp\left(-\frac{s}{l_{\text{ph}}}\right) + \frac{s}{l_{\text{ph}}} E_1\left(\frac{s}{l_{\text{ph}}}\right) \right], \quad (9)$$

where  $E_1$  is the exponential integral and  $l_{\text{ph}}$  is photon attenuation depth, obtained from XCOM,<sup>37</sup> excluding photon scattering, which makes only a small contribution to photon attenuation. This result for a 20- $\mu\text{m}$  copper layer is plotted in Fig. 135.30 along with the previous results for electron yields.



TC10562JR

Figure 135.30  
K-shell yield per photon for an isotropic distribution of photons incident on a 20- $\mu\text{m}$  copper layer and the yields per electron from Fig. 135.29.

The yield for photons has a maximum at threshold and decays continually with energy, whereas the yield for electrons is zero at threshold and increases continually with energy. This indicates that, for copper, photons less than 70 keV are of particular concern because they could cause more K-shell emission than electrons with only a fraction of the energy of the electrons. This justifies the neglect of photons above 1 MeV, although the pairs produced by higher-energy photons would contribute to K-shell emission (not considered here).

Three principle sources of photons in laser-solid experiments could cause K-shell emission: bremsstrahlung from fast electrons in the target, emission from the laser-heated plasma on the front surface, and line emission from higher- $Z$  elements, if present.

Bremsstrahlung will turn a fraction of the fast-electron energy into photons with a comparable energy distribution. This fraction, the radiation yield, increases with electron energy and the atomic number of the target.<sup>32</sup> Radiation yield becomes significant only for electron energies greater than 1 MeV, where electrons always have a far greater K-shell yield than photons, so in most cases bremsstrahlung will not make a significant contribution to the total yield, with the possible exception of very high- $Z$  targets. Even though the *total* yield from bremsstrahlung photons should be negligible, the K-shell emission from a layer at a large-enough depth may be dominated by bremsstrahlung photons because the attenuation depth of photons is larger than the mean free path of electrons at the same energy. In other words, the fraction of the fast-electron energy distribution converted into photons would be expected to propagate farther into a target than the fast electrons.

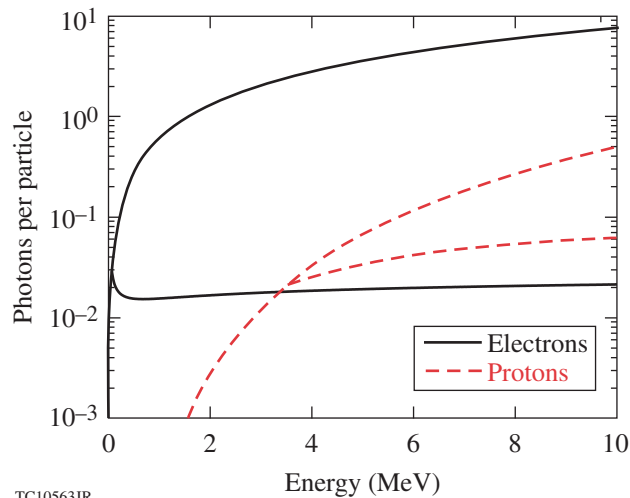
The laser-driven plasma could emit a significant number of photons just above the K edge. Unfortunately, it is not straightforward to estimate this emission since the systems of interest are usually far from equilibrium; therefore we cannot, in general, easily rule out a significant contribution to K-shell emission from this source. A good means of quantifying this in experiments would be to measure the x-ray emission in the relevant range from the front of the target.

If elements with a higher  $Z$  than the K-shell emitting layer are used in targets (for example, to give two emitters in one target), the line emission must be carefully considered; a non-negligible fraction of the emission from the higher- $Z$  layer could cause emission from the lower- $Z$  layer. This must be considered for each individual target design.

## 2. Protons

For ions we will consider only protons since they are always present; because of impurities, protons are the ions that are most efficiently accelerated in laser-plasma interactions and they have, by far, the lowest stopping power of all ions.

To estimate the yield from protons in copper, we used the K-shell ionization cross section from Kahoul *et al.*<sup>38</sup> (given in the appendix), who fitted a compilation of experimental results between 80 keV and 13 MeV, and we used the proton-stopping



TC10563JR

Figure 135.31

Same as Fig. 135.29 but for protons as well as electrons.

power given by PSTAR.<sup>39</sup> The result, seen in Fig. 135.31, is combined with our previous results for the yield from electrons.

Proton and electron energies have been found to be strongly correlated to one another in laser–solid interactions,<sup>3</sup> so it is reasonable to compare the yields at the same energies. For a thin, isolated target where the majority of the electrons are expected to recirculate and any protons are expected to go through the target, K-shell emission yield per proton will always be lower than that per electron. For a thin layer in a thick target, the yield per proton can exceed the yield per electron; for a 20- $\mu\text{m}$  copper layer this occurs above 3.4 MeV because the cross section for protons then exceeds that for electrons. Despite this, the total yield from protons would be expected to be lower than that from electrons because the fraction of laser energy transferred to protons entering the target has been found to be lower than that for electrons, for parameters of interest. Emission from protons accelerated into the target may not be entirely negligible, however, particularly at the higher intensities used, and there could be regions in the target where the number of protons equals or exceeds the number of electrons, so it would be worth considering in a more-detailed analysis.

## Conclusions

Nine expressions for K-shell ionization cross sections<sup>14,15,17,19,21,22,24–26</sup> have been identified that, based on published measurements for copper,<sup>9–11</sup> appear to be adequate for modeling copper K-shell emission diagnostics used in high-intensity laser–solid experiments. For the fluorescence yield required to convert the K-shell ionization cross section to the K-shell emission cross section, a useful summary of measure-

ments and fitting formulas has been given by Kahoul *et al.*<sup>12</sup> For copper we chose 0.45 and, if required, we would consider the uncertainty in this value to be  $\pm 0.01$ . For the fraction of K-shell emission in the  $K_{\alpha}$  line, published measurements and numerical calculations<sup>30,31</sup> are in good agreement, giving 0.880; a reasonable estimate of the uncertainty in this value would be  $\pm 0.01$ . We were unable to narrow down the field because very little attention has been paid to energies from 0.1 to 10 MeV. Instead, past attention has concentrated on the behavior of ionization cross sections near threshold. In this region, the expression given by Hombourger<sup>18</sup> with a fluorescence yield of 0.488 gave the best fit to measurements. The only models that are clearly inadequate are the nonrelativistic ones that use a factor of  $1/E$  in place of  $2/m_e v^2$ .

Should an estimate of the uncertainty in the K-shell emission cross section be required, we suggest a conservative value of  $\pm 20\%$ . Alternatively, a number of these expressions that give upper and lower bounds on the cross section could be used. We found that six expressions were required to give upper and lower bounds over the full range of energies, at least for copper, but for most applications four expressions should be sufficient: Santos *et al.*<sup>25</sup> (or Guerra *et al.*<sup>26</sup>), An *et al.*,<sup>22</sup> Hombourger,<sup>18</sup> and Bote *et al.*<sup>14</sup>

In examining these models we identified an unresolved issue regarding the energy dependence of the ionization cross section at relativistic energies: the factor  $n$  in Eq. (3), where either 0 or 1 is used. By comparison with the standard result for fast-electron stopping power,<sup>32</sup> we found that  $n = 1/2$  appears to be the correct choice. Furthermore, we found for copper that the density-effect correction should be considered above 10 MeV, and this energy will decrease with an increasing atomic number. The available measurements at strongly relativistic energies are insufficient to indicate which form is correct and how the density-effect correction should be included. In order to provide an adequate fit to cross sections for energies of current interest, these are not important issues but are interesting physics issues for future work in this area.

Using these results and the standard expression for electron stopping power, it was found that the effective detection threshold of K-shell emission diagnostics is roughly  $6\times$  higher than the threshold energy for causing K-shell emission. Both the  $K_{\alpha}$ -emission rate, as used in our experiments,<sup>7</sup> and the total  $K_{\alpha}$  emission from typical buried layer experiments are approximately proportional to the number of electrons above this threshold and are not sensitive to the electron energy, provided that the majority of fast electrons are above the

effective detection threshold. Near the detection threshold,  $K_{\alpha}$  emission is far more sensitive to electrons with higher energies, and current uncertainties in the cross section will lead to significant uncertainties in interpreting measurements. The local maximum in the  $K_{\alpha}$ -emission cross section does not lead to  $K_{\alpha}$  emission being particularly sensitive to a narrow range of electron energies, as is often assumed.

K-shell emission caused by photons and protons was briefly considered. Photons from the laser-heated plasma and higher-Z layers could make a significant contribution in some experiments and deserves careful consideration. Protons accelerated into the target should not make a significant contribution because of their smaller number, but if significant numbers of protons above 3 MeV are accelerated into the target, they should be considered in a more-detailed modeling.

### Appendix A: Expressions for K-Shell Ionization Cross Sections

For the incident electron we use  $E$  for kinetic energy,  $v$  for velocity,  $\beta$  for  $v/c$ , where  $c$  is the speed of light, and  $\gamma$  for the Lorentz factor ( $1 + E/m_e c^2$ ), where  $m_e$  is the electron mass. For the K-shell electrons we use  $B$  for binding energy,  $B_{\text{keV}}$  when it is expressed in keV (SI units are used unless specified), and  $N_K$  for number (2 for all cases of interest). The material is indicated by its atomic number  $Z$ . Three expressions use Rydberg energy  $R$  (13.606 eV). Two dimensionless parameters are used in most expressions:

$$U = \frac{E}{B}, \quad (\text{A1})$$

often called the overpotential, and

$$J = \frac{m_e c^2}{B} \quad (\text{A2})$$

(56.9 for copper), which appears naturally when writing relativistic expressions in terms of  $U$ . A number of the expressions use Grysinski's relativistic factor<sup>27</sup> written as

$$G = \frac{1+2J}{U+2J} \left( \frac{U+J}{1+J} \right)^2 \times \left[ \frac{(1+U)(U+2J)(1+J)^2}{J^2(1+2J)+U(U+2J)(1+J)^2} \right]^{1.5}, \quad (\text{A3})$$

which is intended to convert a nonrelativistic expression for energy exchange in a binary collision between electrons with kinetic energies  $E$  and  $B$  to a relativistically correct expression. This always appears as  $G/E$ , so we introduce the parameter

$$G' = \frac{G}{2(\gamma-1)} = \frac{JG}{2U}. \quad (\text{A4})$$

The reason for this choice, and the effect of this complex-looking term, can be easily illustrated by considering a nonrelativistic binding energy  $J \gg 1$ , valid for most cases of interest,

$$G' \approx \frac{1}{\beta^2}, \quad B \ll m_e c^2, \quad (\text{A5})$$

so Grysinski's relativistic factor essentially replaces the  $1/E$  in nonrelativistic expressions with  $2/m_e v^2$ . We believe that a number of the expressions have typing errors in this factor.<sup>15,17,21</sup>

Casnati *et al.*'s<sup>15</sup> expression for any element is

$$\begin{aligned} \sigma_0 &= \frac{N_K 187}{B_{\text{keV}}^{1.0318}} \text{ barns}, \\ f &= -\frac{0.316}{U} + \frac{0.1135}{U^2}, \\ \sigma_{\text{ion}} &= \sigma_0 G' \left( \frac{R}{B} \right)^f \exp \left( -\frac{1.736}{U} + \frac{0.317}{U^2} \right) \ln U. \end{aligned} \quad (\text{A6})$$

Tang *et al.*<sup>18</sup> used this expression and obtained different fitting parameters: 137 and 1.0514 in  $\sigma_0$ ,  $-0.4935$  and  $0.3529$  in  $f$ , and  $-1.227$  and  $-0.2791$  in the exponential. Note that  $a_0$  in their expression should be  $a_0^2$  and that their coefficients  $C_{1-3}$  have the wrong sign, or, equivalently, it should be  $-C_u$  or  $(E_k/R_y)$  in place of  $(R_y/E_k)$ .

Jakoby *et al.*'s<sup>16</sup> expression and Haque *et al.*'s<sup>20</sup> Kolbenstvedt expression, as printed, do not reproduce the published figures. Even after correcting a number of obvious typing errors and experimenting with likely looking variants, we could not obtain sensible results; therefore we have not reproduced them here.

Hombourger's<sup>17</sup> expression for any element is

$$\begin{aligned}\sigma_0 &= \frac{N_K 175}{B_{\text{keV}}^{1.0305}} \text{ barns}, \\ f &= -\frac{0.316}{U} + \frac{0.1545}{U^2}, \\ \sigma_{\text{ion}} &= \sigma_0 G' \left( \frac{R}{B} \right)^f \left( 1 - \frac{1.335}{U} + \frac{0.6006}{U^2} \right) \ln U.\end{aligned}\quad (\text{A7})$$

We suggest using  $N_K 190 / B_{\text{keV}}^{1.0305}$  for  $\sigma_0$  based on fitting this expression to the measurements of Llovet *et al.*<sup>10</sup> and measurements of the fluorescence yield for copper<sup>12</sup> that indicate a value of 0.45.

Haque *et al.*'s<sup>19</sup> BELI expression for any element is

$$\begin{aligned}\sigma_0 &= \frac{N_K 205}{B_{\text{keV}}} \text{ barns}, \\ \sigma_{\text{ion}} &= \sigma_0 G' \left[ 1 + 3 \left( \frac{1 - N_K / Z}{U} \right)^{1.27} \right] \\ &\quad \times \left[ \ln(U) + \sum_{n=1}^5 b_n \left( 1 - \frac{1}{U} \right)^n \right],\end{aligned}\quad (\text{A8})$$

where  $b_n$  is  $-0.971, 0.381, 0.0952, -0.0476,$  and  $-0.190$ . The term in brackets following Grynski's relativistic factor represents shielding of the K-shell electrons by the remaining electrons in the atom.

A number of expressions have been based on the Deutsch-Märk model. For these we use

$$\sigma_0 = 1.72 \times 10^{-3} f_H r_K^2, \quad (\text{A9})$$

where  $f_H = 0.553$  for hydrogen and  $= 1$  otherwise and  $r_K$  is the radius of maximum areal density, tabulated (in units of the Bohr radius  $5.2918 \times 10^{-11}$  m) by Desclaux,<sup>40</sup> which is  $1.807 \times 10^{-12}$  m for copper. The most-recent version we found from the originators of the model is Gstir *et al.*:<sup>21</sup>

$$\begin{aligned}\sigma_{\text{ion}} &= \sigma_0 \left( 1 + \frac{2U^{0.25}}{J^2} \right) G' \left( \frac{U-1}{U+1} \right)^{1.06} \\ &\quad \times \left( 1.353 - \frac{0.55}{U} \right) \ln(2.7 + \sqrt{U-1}).\end{aligned}\quad (\text{A10})$$

The first term in parentheses is a modification to Grynski's relativistic factor. An *et al.*<sup>22</sup> have since determined the fitting parameters including subsequent measurements:

$$\begin{aligned}\sigma_{\text{ion}} &= \sigma_0 \left( 1 + \frac{2U^{0.25}}{J^2} \right) G' \left( \frac{U-1}{U+1} \right)^{0.95} \\ &\quad \times \left( 1.4 - \frac{0.475}{U} \right) \ln(2.7 + \sqrt{U-1}).\end{aligned}\quad (\text{A11})$$

Haque *et al.*<sup>23</sup> give a significantly modified version

$$\begin{aligned}\sigma_{\text{ion}} &= \sigma_0 \frac{1 + 1.5J}{1.2J} \left( 1 + \frac{1.5U^{0.055}}{J} \right) \\ &\quad \times G' \left( 1 + 6.75 \frac{1 - N_K / Z}{Z^{0.5} U} \right)^{0.85} \\ &\quad \times \left[ 0.86 - \frac{0.63}{1 + (U/3.76)^{2.08}} \right] \ln(1.01U).\end{aligned}\quad (\text{A12})$$

The first two terms are modifications to Grynski's relativistic factor, and the term following it represents shielding of the K-shell electrons by the remaining electrons in the atom. We believe there may be typing errors in this expression.

Haque *et al.*'s<sup>24</sup> XCVTS expression is

$$\begin{aligned}\sigma_0 &= \frac{N_K 4.5 \times 10^6 B_{\text{keV}}}{Z^{4.35}} \text{ barns}, \\ \sigma_{\text{ion}} &= \sigma_0 \left( \frac{U+J}{1+J} \right)^{0.02} \left( 1 - \frac{0.22U^{0.27}}{J^2} \right) \\ &\quad \times G' \left( 1 + 0.01 \frac{Z - N_K}{U} \right) \ln U.\end{aligned}\quad (\text{A13})$$

The first term is a modification to Grynski's relativistic factor. The next term in parentheses, introduced to prevent the expression from increasing without limit, cannot be correct for strongly relativistic energies since it will eventually lead to a negative cross section; there is also nothing to indicate that the cross section does not increase continually with energy. The term after Grynski's relativistic factor represents shielding of the K-shell electrons by the remaining electrons in the atom.

Bote *et al.*'s<sup>14</sup> fit to their numerical results for copper is

$$U \leq 16,$$

$$\sigma_0 = 351.9 \text{ barns},$$

$$\sigma_{\text{ion}} = \sigma_0 \frac{U-1}{U^2} \times \left[ 3 + 0.05003U - \frac{3.48}{1+U} + \frac{3.339}{(1+U)^3} - \frac{3.683}{(1+U)^5} \right]^2, \quad (\text{A14})$$

$$U > 16,$$

$$\sigma_0 = \frac{22.84U}{U+0.765} \frac{1}{\beta^2} \text{ barns},$$

$$x = \sqrt{\gamma^2 - 1},$$

$$\sigma_{\text{ion}} = \sigma_0 \left\{ \left[ \ln(x^2) - \beta^2 \right] \left( 1 + \frac{0.3024}{x} \right) + 6.261 - \frac{1.024}{\sqrt{\gamma}} + \frac{0.4543}{x} \right\}.$$

The fitting parameters for other elements can be found in Bote *et al.*'s paper. Note that they calculate the binding energy of copper to be 8.95 keV, not 8.98 keV.

For Santos *et al.*'s<sup>25</sup> and Guerra *et al.*'s<sup>26</sup> expressions, we use

$$\sigma_0 = \frac{N_K 255}{B_{\text{keV}}} \text{ barns}, \quad (\text{A15})$$

$$\sigma_B = \sigma_0 \left\{ \frac{1}{2} \left[ \ln \left( \frac{\gamma+1}{2} U \right) - \beta^2 \right] \left( 1 - \frac{1}{U^2} \right) + 1 - \frac{1}{U} + \left( \frac{2}{\gamma+1} \right)^2 \left[ \frac{U-1}{2J^2} - (2\gamma-1) \frac{\ln U}{1+U} \right] \right\}.$$

We believe that the density-effect correction  $(-\delta/2)$  should be inserted in the first set of square brackets. This is divided by a term of the form  $\beta^2$ , which could be interpreted as the mean-

squared relative velocity of the incident and K-shell electrons. Santos *et al.*'s<sup>25</sup> give

$$\sigma_{\text{ion}} = \frac{\sigma_B}{2} \left( \frac{1}{\beta^2} + \frac{1}{\beta^2 + \beta_B^2 + \beta_K^2} \right), \quad (\text{A16})$$

where

$$\beta_x^2 = 1 - \frac{1}{(1 + x/m_e c^2)^2}, \quad (\text{A17})$$

where  $x$  is an energy and  $K$  is the mean kinetic energy of the K-shell electrons, tabulated in Santo *et al.*'s paper (11.32 keV for copper). Guerra *et al.* give

$$\sigma_{\text{ion}} = \frac{\sigma_B}{\beta^2 + (0.126 - 0.213Z + 0.195Z^2)(2R/B)\beta_B^2}. \quad (\text{A18})$$

Kahoul *et al.*'s<sup>38</sup> expression for copper K-shell ionization by protons is

$$x = \ln \left( \frac{E_{\text{MeV}}}{16.489} \right), \quad (\text{A19})$$

$$\sigma_{\text{ion}} = \frac{\exp(11.292 + 0.192x - 0.371x^2 + 0.028x^3)}{80.6404} \text{ barns}.$$

The fitting parameters for other elements can be found in Kahoul *et al.*'s paper.

## Appendix B: A Proposed Fit to the K-Shell Emission Cross Section of Copper

Our objective was never to develop our own expression for the K-shell emission cross section but to find a simple expression that we could plug into our calculations; this is most likely the reader's objective, so it appears to be something of a disservice to end with a long list of complex expressions and no clear recommendation. Therefore, we will propose a simple expression for the K-shell emission cross section of copper that gives the best fit to the measurements and that in the limit of strongly relativistic energies has the form indicated by the fast-electron stopping power. Since 77% of the measurements are in the region from threshold to peak, the best fit to them is largely determined by the form of the expression in this region.

A simple expression that reproduces all of the general features and has the desired limiting form is

$$f_0 = \frac{\sigma_0}{\beta^2} \left\{ \ln \left[ \left( \frac{\gamma + 1}{\gamma_B + 1} \right)^{1/2} U \right] - \frac{\delta - \delta_B}{2} \right\}, \quad (\text{B1})$$

where the subscript  $B$  indicates quantities evaluated at the binding energy  $B$ , rather than the fast-electron kinetic energy  $E$ , to give an expression that is identically zero at threshold. An equally valid approach would be to multiply by a function that is zero at threshold and tends to a constant at large energies.

The density-effect correction  $\delta$  could be calculated either numerically, from tabulated values, or from a fitting formula. An approach that may provide the best means to fit data would be to use a fitting formula and redetermine its parameters by fitting the data. For a number of applications it could be ignored. For simplicity we used Eq. (7), which is intended to have the right form in the strongly relativistic limit and not to cause significant errors at lower energies; it is not a fitting formula. At energies of the order of 1 MeV, it is an underestimate. It will not work for nonconductors and will not work well for lower  $Z$  than copper.

Equation (B1) does not give a good fit to the measurements. Since Hombourger's expression gave the best fit to Llovet *et al.*'s data, we tried multiplying  $f_0$  by

$$f_1 = 1 + \sum_{n=1}^N \frac{a_n}{U^n}. \quad (\text{B2})$$

$N = 1$  gave a good fit to Llovet *et al.*'s data and the fit did not improve significantly until  $N = 4$ , which gave a value of  $\sigma_0$  that appeared too low (16.95 barns). We also used  $N = 1$  to fit all of the measurements and obtained very similar results. The resulting expression for the K-shell emission cross section of copper is

$$\sigma_K = \left( 1 - \frac{0.2824}{U} \right) \frac{20.95}{\beta^2} \times \ln \left[ \left( \frac{U + 113.8}{114.8} \right)^{1/2} \frac{57.0098U}{56.9 + 0.1098U} \right] \text{ barns}. \quad (\text{B3})$$

The resulting macroscopic cross section is plotted along with the measurements in Fig. 135.32, where we have included the  $\pm 10\%$  absolute error quoted by Llovet *et al.*,<sup>10</sup> imposed a minimum error of  $\pm 10\%$  on the measurements given by Liu *et al.*,<sup>9</sup> and plotted our fit at the  $\pm 10\%$  levels. We have not plotted the other expressions in order to emphasize a comparison with the

measurements and avoid too many lines. Our proposed fit is in good agreement with the measurements up to and just beyond the peak but agrees only with subsets of the measurements compiled by Liu *et al.*<sup>9</sup> at higher energies, even considering variations of  $\pm 10\%$ , which is also true of all the other expressions. Compared to the other expressions, it lies roughly in the middle of them up to just above the peak, where it clearly gives the best fit to the measurements, gives the highest values near the dip, lies within their range of values between roughly 50 MeV and 2 GeV, and gives the lowest values at higher energies.

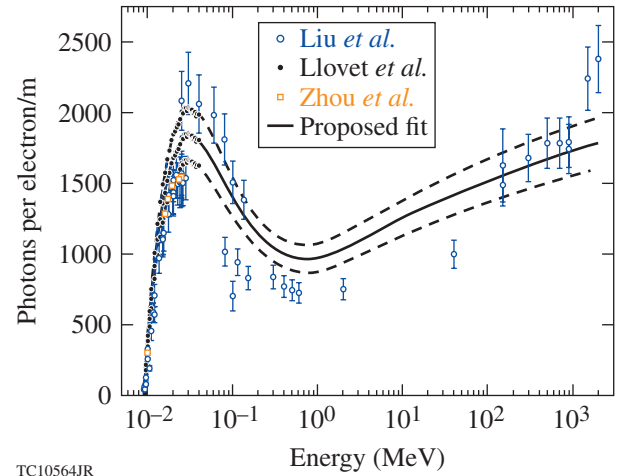


Figure 135.32

Macroscopic K-shell emission cross sections for solid copper. Circles are measurements compiled by Liu *et al.*<sup>9</sup> with a minimum error of  $\pm 10\%$  imposed. Dots joined by a solid line are the measurements of Llovet *et al.*,<sup>10</sup> the dots on the dashed lines are these values at  $\pm 10\%$ —their quoted absolute error. Squares are the measurements of Zhou *et al.*<sup>11</sup> The solid line is our proposed fit; dashed lines are the fit at  $\pm 10\%$ .

This approach is good only for fitting data from threshold to peak;  $f_1$  in all the fits was close to one beyond the peak. Further factors should be added that can adjust the depth of the dip and the value of  $\sigma_0$  in the strongly relativistic limit; it does appear that the dip should be lowered. We have not considered this further because there are only a limited number of measurements with significant differences between them in this region.

#### ACKNOWLEDGMENT

This work has been supported by the U.S. Department of Energy under Cooperative Agreement Nos. DE-FC02-04ER54789, Fusion Science Center supported by the Office of Fusion Energy Sciences, and DE-FC52-08NA28302 Office of Inertial Confinement Fusion, the New York State Energy Research Development Authority, and the University of Rochester. The support of DOE does not constitute an endorsement by DOE of the views expressed in this article.

## REFERENCES

1. M. Tabak *et al.*, Phys. Plasmas **1**, 1626 (1994).
2. S. Gus'kov *et al.*, Phys. Rev. Lett. **109**, 255004 (2012).
3. J. T. Mendonça, J. R. Davies, and M. Eloy, Meas. Sci. Technol. **12**, 1801 (2001).
4. J. R. Davies, Laser Part. Beams **20**, 243 (2002).
5. S. P. Hatchett, C. G. Brown, T. E. Cowan, E. A. Henry, J. S. Johnson, M. H. Key, J. A. Koch, A. B. Langdon, B. F. Lasinski, R. W. Lee, A. J. MacKinnon, D. M. Pennington, M. D. Perry, T. W. Phillips, M. Roth, T. C. Sangster, M. S. Singh, R. A. Snavely, M. A. Stoyer, S. C. Wilks, and K. Yasuike, Phys. Plasmas **7**, 2076 (2000).
6. M. I. K. Santala *et al.*, Phys. Rev. Lett. **84**, 1459 (2000).
7. P. M. Nilson, J. R. Davies, W. Theobald, P. A. Jaanimagi, C. Mileham, R. K. Jungquist, C. Stoeckl, I. A. Begishev, A. A. Solodov, J. F. Myatt, J. D. Zuegel, T. C. Sangster, R. Betti, and D. D. Meyerhofer, Phys. Rev. Lett. **108**, 085002 (2012).
8. K. B. Wharton *et al.*, Phys. Rev. Lett. **81**, 822 (1998); R. B. Stephens *et al.*, Phys. Rev. E **69**, 066414 (2004); K. L. Lancaster, J. S. Green, D. S. Hey, K. U. Akli, J. R. Davies, R. J. Clarke, R. R. Freeman, H. Habara, M. H. Key, R. Kodama, K. Krushelnick, C. D. Murphy, M. Nakatsutsumi, P. Simpson, R. Stephens, C. Stoeckl, T. Yabuuchi, M. Zepf, and P. A. Norreys, Phys. Rev. Lett. **98**, 125002 (2007); J. S. Green *et al.*, Phys. Rev. Lett. **100**, 015003 (2008).
9. M. Liu *et al.*, At. Data Nucl. Data Tables **76**, 213 (2000).
10. X. Llovet, C. Merlet, and F. Salvat, J. Phys. B **33**, 3761 (2000).
11. C.-G. Zhou, Z. An, and Z.-M. Luo, Chin. Phys. Lett. **18**, 759 (2001).
12. A. Kahoul *et al.*, Radiat. Phys. Chem. **80**, 369 (2011).
13. D. Bote and F. Salvat, Phys. Rev. A **77**, 042701 (2008).
14. D. Bote *et al.*, At. Data Nucl. Data Tables **95**, 871 (2009); D. Bote *et al.*, At. Data Nucl. Data Tables **97**, 186 (2011).
15. E. Casnati, A. Tartari, and C. Baraldi, J. Phys. B **15**, 155 (1982).
16. C. Jakoby, H. Genz, and A. Richter, J. Phys. Colloq. **48**, 487 (1987).
17. C. Hombourger, J. Phys. B, At. Mol. Opt. Phys. **31**, 3693 (1998).
18. C.-H. Tang *et al.*, Chin. Phys. Lett. **18**, 1053 (2001).
19. A. K. F. Haque *et al.*, Phys. Rev. A **73**, 012708 (2006).
20. A. K. F. Haque *et al.*, Eur. Phys. J. D **42**, 203 (2007).
21. B. Gstir *et al.*, J. Phys. B **34**, 3377 (2001).
22. Z. An, Z. M. Luo, and C. Tang, Nucl. Instrum. Methods Phys. Res. B **179**, 334 (2001).
23. A. K. F. Haque *et al.*, Int. J. Quantum Chem. **109**, 1442 (2009).
24. A. K. F. Haque *et al.*, J. Phys. B **43**, 115201 (2010).
25. J. P. Santos, F. Parente, and Y.-K. Kim, J. Phys. B: At. Mol. Opt. Phys. **36**, 4211 (2003).
26. M. Guerra *et al.*, Int. J. Mass Spectrom. **313**, 1 (2012).
27. M. Gryziński, Phys. Rev. **138**, A322 (1965).
28. J. H. Scofield, Phys. Rev. A **18**, 963 (1978).
29. H. Kolbenstvedt, J. Appl. Phys. **46**, 2771 (1975).
30. Md. R. Khan and M. Karimi, X-Ray Spectrom. **9**, 32 (1980); M. Ertuğrul *et al.*, J. Phys. B **34**, 909 (2001); J. P. Marques, F. Parente, and P. Indelicato, J. Phys. B **34**, 3487 (2001).
31. H. K. Chung *et al.*, High Energy Density Phys. **1**, 3 (2005).
32. H. O. Wyckoff, *ICRU Report*, International Commission on Radiation Units and Measurements, Inc., Bethesda, MD (1984).
33. ESTAR, accessed 16 May 2013, <http://physics.nist.gov/PhysRefData/Star/Text/ESTAR.html>.
34. R. M. Sternheimer, M. J. Berger, and S. M. Seltzer, At. Data Nucl. Data Tables **30**, 261 (1984).
35. S. Atzeni, A. Schiavi, and J. R. Davies, Plasma Phys. Control. Fusion **51**, 015016 (2009).
36. EGSnrc Monte Carlo code, accessed 17 May 2013, <http://www.nrc-cnrc.gc.ca/eng/rd/mss/index.html>.
37. XCOM, accessed 16 May 2013, <http://physics.nist.gov/PhysRefData/Xcom/html/xcom1.html>.
38. A. Kahoul *et al.*, Radiat. Phys. Chem. **80**, 369 (2011).
39. PSTAR, accessed 16 May 2013, <http://physics.nist.gov/PhysRefData/Star/Text/PSTAR.html>.
40. J. P. Desclaux, At. Data Nucl. Data Tables **12**, 311 (1973).

---

# Fracture Mechanics of Delamination Defects in Multilayer Dielectric Coatings

## Introduction

Multilayer-dielectric (MLD) thin-film coatings are widely used to produce high-quality optical components, having diverse applications ranging from Bragg mirrors to polarizer optics. Hafnia ( $\text{HfO}_2$ )–silica ( $\text{SiO}_2$ ) multilayers are frequently used to fabricate MLD diffraction gratings for high-intensity laser systems because of the inherently high laser-damage resistance of this material combination.<sup>1,2</sup> The laser-damage thresholds of MLD gratings are typically well below those of the constituent dielectric materials themselves, however, because surface texture, contamination, and microscopic defects can dramatically affect laser-damage resistance.<sup>3–9</sup>

Multilayer-dielectric coatings are susceptible to a variety of unique defects and phenomena arising from fabrication and storage, including nodules,<sup>5,6</sup> pits,<sup>4,7</sup> absorption of volatilized contaminants from vacuum,<sup>10</sup> and optical instabilities resulting from moisture penetration into porous oxide layers from humid air.<sup>11,12</sup> Patterned optical components such as MLD diffraction gratings require aggressive cleaning operations to remove photoresist and other lithographic residues. Unfortunately, some of the most-effective cleaning methods—usually involving high temperatures and strong acids or bases—can themselves induce chemical degradation and thermal stresses in the coating, leading to delamination and defects.<sup>9,13</sup>

Micron-scale delamination defects have been observed on MLD coatings after exposure to a hot acid piranha solution—a mixture of hydrogen peroxide and sulfuric acid that is commonly used to clean MLD gratings.<sup>9,14–16</sup> Delamination defects are distinguished by a characteristic pattern of crescent-shaped fractures in the coating, with the layers uplifted at the defect site. Because these features interrupt the continuity of the MLD surface, they may cause electric-field enhancement and reduced laser-damage thresholds. While we have been able to largely avoid the production of cleaning defects by reducing piranha solution temperatures to 40°C (Ref. 9), a thorough understanding of the causes and formation mechanism of delamination defects will be important in the continued development of cleaning technologies.

We investigate the causes of delamination defects and describe a mechanism for the deformation and failure of the MLD coating in response to hydrogen peroxide in the cleaning solution. In the proposed mechanism, we assume a localized pressure buildup in a small volume of acid piranha trapped in the coating that drives the propagation of an interface crack in the multilayer. The associated fracture mechanics problem is that of a pressure-loaded blister in a multilayer material—an extension of the pressurized circular blister treated by Jensen.<sup>17</sup> The appropriate length scale for the multilayer blister problem is explored. Finally, the predicted path of a crack propagating through the MLD coating layers is compared with the observed cross-sectional geometry of a defect.

## Materials and Methodology

The MLD samples used in this study were 3-mm-thick, 100-mm-diam BK7 substrates coated by electron-beam evaporation in a high reflector design (a modified quarter-wave stack of high- and low-index layers) with an extra-thick top layer.<sup>18</sup> The coating comprised 28 layers of alternating hafnia ( $\text{HfO}_2$ ) and silica ( $\text{SiO}_2$ ) with a bottom layer of  $\text{HfO}_2$  and top layer of  $\text{SiO}_2$ . The total coating thickness was 5.0  $\mu\text{m}$ , with typical layer thicknesses of 190 nm for the silica layers and 142 nm for the hafnia layers. Samples were not patterned or etched. For cleaning experiments, each sample was broken into eight wedges.

Defects were generated by submerging the samples in the acid piranha solution. For each test, a 400-mL acid piranha solution was prepared and cooled to room temperature. The ratio of sulfuric acid to hydrogen peroxide was either two parts  $\text{H}_2\text{SO}_4$  to one part  $\text{H}_2\text{O}_2$  (2:1 piranha) or five parts  $\text{H}_2\text{SO}_4$  to one part  $\text{H}_2\text{O}_2$  (5:1 piranha), depending on the test. After preparation, the piranha solution was used within 24 h to limit degradation. Except as noted, samples were submerged into the piranha solution at room temperature, heated to the prescribed soak temperature over a ramp period of 30 min, held at the soak temperature for the specified duration, and then cooled to room temperature over 30 min using an ice bath. After the MLD samples were removed from the solution, they were rinsed with de-ionized water and dried using a filtered nitrogen

gun. Samples were inspected by a Leica Nomarski microscope after the piranha treatment and evaluated for defect formation.

## Characterization of the Delamination Defect

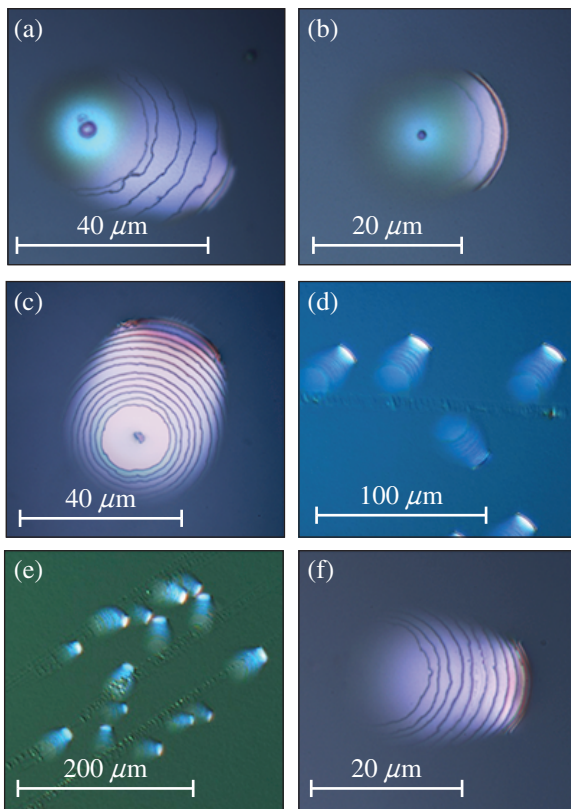
### 1. Microscopy

Nomarski micrographs of representative delamination defects are shown in Fig. 135.33. The piranha treatments for the samples shown are specified in the captions. Delamination defects had typical dimensions of 20 to 50  $\mu\text{m}$  and featured a characteristic array of circular- and crescent-shaped cracks radiating out from an initiating point, typically an existing surface feature. Some defects were associated with nodules, as shown in Figs. 135.33(a) and 135.33(b), while other defects were paired with pieces of debris, as in Fig. 135.33(c), or formed

in groups along scratches, as in Figs. 135.33(d) and 135.33(e). Occasionally, delamination defects were identified that seemed not to be linked to any other artifact, as shown in Fig. 135.33(f). Because we have only rarely observed defects in this final category, they may be connected with small features that simply could not be resolved in the light microscope. Defects sometimes involved many coating layers, as in Figs. 135.33(a) and 135.33(c), or just a few coating layers, as in Fig. 135.33(b).

Because the oxide layers of the coating are transparent to white light, cracks in each layer are visible in the optical micrographs of Fig. 135.33. The approximate depths of cracks in the multilayer were determined by recording the  $z$  position of best focus and, in all cases, the crack nearest to the “initiating” artifact was located in the deepest coating layer involved in the defect. The crack front farthest from this central artifact was at the surface layer, suggesting that delamination defects nucleate within the coating, not at the surface.

Defects were examined in a scanning electron microscope (SEM) to further probe their geometries. Because the SEM “sees” only the sample’s surface, a top-down SEM image [Fig. 135.34(a)] revealed only the arc-shaped crack in the uppermost coating layer. To examine the defect’s cross section, focused-ion-beam (FIB) milling was used to cut a trench in the MLD coating, bisecting a delamination defect. A thin layer of platinum was locally deposited immediately prior to milling to enable the beam to cut a clean cross section instead of gradually eroding the multilayer. The resulting cross-sectional view, shown in Fig. 135.34(b), reveals a zigzagging crack in the upper 24 layers of the coating (the bottom two layer pairs were apparently unaffected in this particular case). The uplifting of the coating at the defect site and the separation between crack faces explain the “bright” appearance of delamination defects in the optical microscope images of Fig. 135.33. The uplifting of the coating also explains previous nanoindentation results showing that delamination defects are more compliant than the surrounding coating.<sup>19</sup> The crack path revealed by FIB will be treated in detail in **Fracture Mechanics** (p. 192).



G9912JR

Figure 135.33

Nomarski micrographs of representative delamination defects: [(a,b)] defects associated with nodules; (c) a defect associated with a piece of surface debris; [(d,e)] defects that formed along scratches; and (f) a defect that was not observed with any apparent surface feature. Defects were generated by submerging the samples in 2:1 piranha, with the following temperature treatments: [(a,b)] 90°C soak for 2 h with 30-min heating and cooling ramps; (c) sample submerged at 70°C and cooled to room temperature over 2 h; [(d,e)] samples submerged at 90°C and cooled over 30 min; and (f) sample submerged at 70°C and cooled over 30 min.

### 2. Causes of Delamination Defects

A screening experiment was carried out to investigate the factors contributing to defect formation during piranha cleaning. The experiment was designed using JMP<sup>®</sup> statistical software and design-of-experiments (DOE) methodology to randomize trial order and to choose appropriate factor levels. The effects of five parameters were studied: (1) the age of the MLD coating at the time of cleaning (because the intrinsic coating stress level has been shown to vary with time);<sup>20–23</sup> (2) the

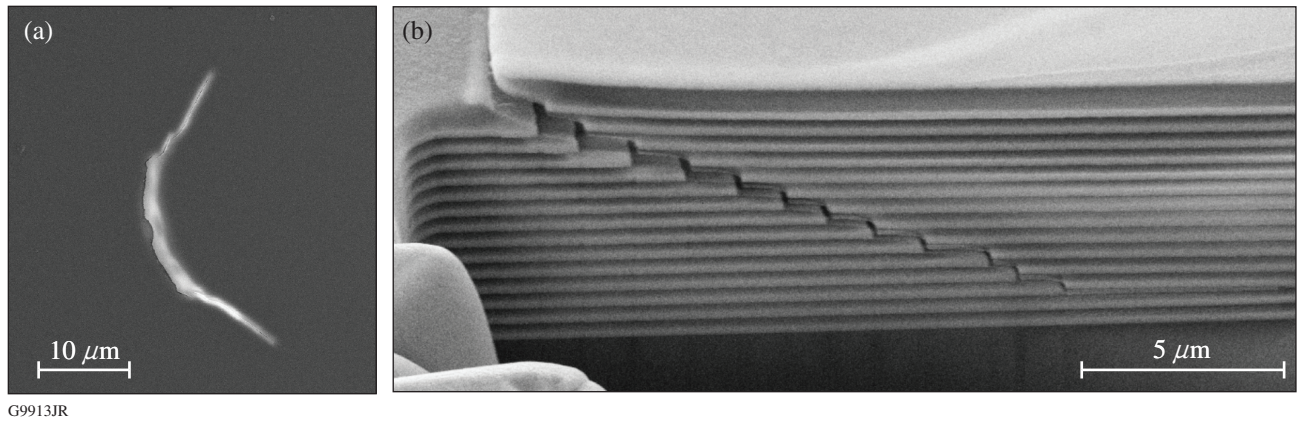


Figure 135.34 Scanning electron microscope (SEM) images showing (a) a delamination defect observed from a bird's eye view, showing its surface structure and (b) a defect bisected by focused-ion-beam (FIB) milling and viewed in cross section.

ratio of sulfuric acid to hydrogen peroxide (piranha ratio) in the acid piranha solution; (3) the solution temperature during the soak period; (4) the soak duration, not including time spent ramping up to the soak temperature or cooling to room temperature; and (5) whether or not the sample was heat shocked by submerging it directly into hot piranha at the soak temperature (rather than slowly heated to the soak temperature over 30 min). Defect density on the MLD sample after cleaning (number of delamination defects per unit surface area) was used as the response for the experiment. Analysis-of-variances (ANOVA) results from the experiment are presented in Table 135.II.

Assigning a confidence limit of 95%, the piranha ratio was the only factor judged statistically significant in this experiment (denoted by asterisks in Table 135.II). The samples treated with 2:1 piranha had defect densities that were, on average, an order-of-magnitude higher than the samples cleaned with 5:1 piranha, indicating that hydrogen peroxide plays an important role in cleaning-induced defect formation. Anecdotally, this result is supported by the fact that we have regularly observed delamination defects on MLD samples exposed to acid piranha (and on samples exposed to 30% hydrogen peroxide) but never on samples exposed to non-peroxide-containing chemicals that

Table 135.II: ANOVA results for the delamination defect screening experiment.

Factor	Level	Mean Defect Density (defects/cm <sup>2</sup> )	Sum of Squares (SS)	Mean Square (MS)	Degrees of Freedom (dof)	F Ratio	Prob > F (p value)
Coating age	2 weeks	1.92	9.57	4.78	2	0.96	0.39
	6 weeks	1.47					
	12 weeks	0.95					
Piranha ratio (H <sub>2</sub> SO <sub>4</sub> :H <sub>2</sub> O <sub>2</sub> )	5:1	0.24	68.57	68.57	1	13.74	0.001***
	2:1	2.76					
Soak temperature	50°C	1.18	2.09	1.05	2	0.21	0.81
	70°C	1.44					
	90°C	1.69					
Soak time	0 min	0.98	13.31	6.66	2	1.33	0.28
	30 min	1.23					
	60 min	2.12					
Heat shock	Shocked	1.06	7.56	7.56	1	1.52	0.23
	Not shocked	1.82					
Error estimate	–	–	154.59	4.99	31	–	–

\*\*\*Significance at the  $p \leq 0.001$  level.

we have tested, including sulfuric acid and a variety of solvents and commercial photoresist strippers. Trends in the data that warrant further investigation also suggest connections between increased defect formation and high piranha temperatures, long soak duration, and freshly deposited MLD coatings.

### 3. The Process of Defect Formation

Typically, delamination defects are observed immediately after piranha cleaning: by the time a sample can be rinsed, dried, and transferred to the microscope, all cleaning-induced defects have already formed. In one experiment, however, the real-time formation of delamination defects was witnessed firsthand during a routine inspection of an MLD sample approximately 45 min after removal from piranha solution.

Frames captured from a video of defect formation, showing a  $75 \times 75\text{-}\mu\text{m}$  area as viewed in Nomarski, are shown in Fig. 135.35. The formation process took about 20 s. The defect grew with a round shape at first, shown in Figs. 135.35(a)–135.35(c), then expanded to an oblong shape as it broke through the layers of the MLD [Figs. 135.35(d) and 135.35(e)]. The defect had nearly reached its final size about 3 s after it began to form and reached a stable geometry [Fig. 135.35(h)] after about 20 s. The bright spot in the lower part of Figs. 135.35(a)–135.35(d) is another smaller artifact. At the 3-s mark [Fig. 135.35(e)], the newly formed defect merged with this small artifact.

Figure 135.36 shows the evolution of a  $160 \times 140\text{-}\mu\text{m}$  area surrounding the defect of Fig. 135.35. Two new defects formed in this region: one appearing in Fig. 135.36(b) and another in Fig. 135.36(c). The just-formed defects “flickered” distinctly and appeared to be liquid filled, with a pulsating effect pos-

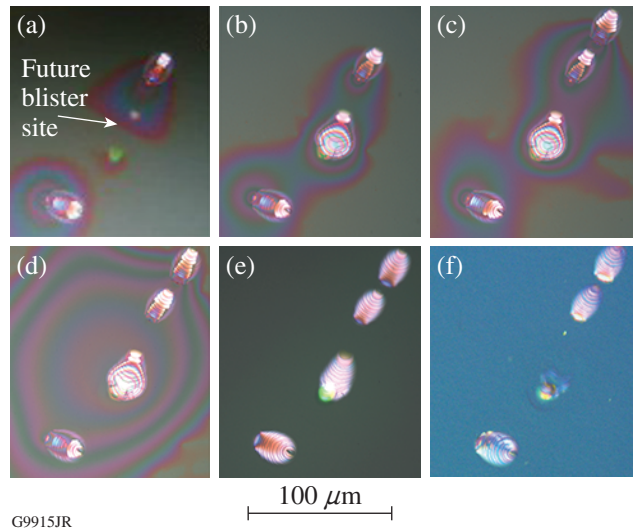


Figure 135.36  
Nomarski micrographs of a  $160 \times 140\text{-}\mu\text{m}$  region containing the defect seen in Fig. 135.35. Images were captured (a) 45 min, (b) 60 min, (c) 61 min, (d) 100 min, (e) 48 h, and (f) 6 months after the sample was removed from the piranha solution.

sibly caused by rapid evaporation. The defects were initially surrounded by regions of trapped fluid, which moved about and agglomerated into larger areas over time [see Figs. 135.36(a)–135.36(d)]. These features may be similar to the “moisture penetration patterns” described by Macleod *et al.*,<sup>11</sup> involving the incorporation of fluid into the porous structure of oxide layers.

Several hours after piranha cleaning, the trapped liquid had escaped from the MLD coating and the flickering had stopped. A difference in optical thickness remained, leading to the bright appearance of mature delamination defects in Nomarski microscopy [Fig. 135.36(e)]. Interestingly, when the MLD

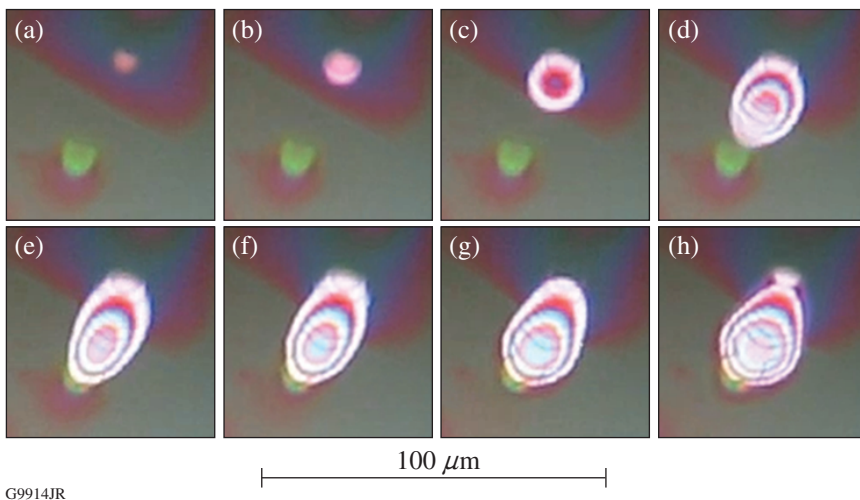


Figure 135.35  
A series of  $75 \times 75\text{-}\mu\text{m}$  frames captured from a Nomarski microscope video of an individual delamination defect’s formation approximately 45 min after a 2-h submersion in 2:1 piranha at  $90^\circ\text{C}$ . Images of the defect’s development were captured (a) 0 s, (b) 2.0 s, (c) 2.6 s, (d) 2.7 s, (e) 3.0 s, (f) 6.0 s, (g) 11.0 s, and (h) 20.0 s after it began to form.

sample was re-inspected several months later [Fig. 135.36(f)], the defect of Fig. 135.35 had nearly disappeared, possibly after collapsing into optical contact. The smaller, overlapping defect was still apparent.

**A Mechanism for Delamination Defect Formation**

We propose a mechanism to explain the primary features of delamination defects presumed from experimental observations; namely, that (1) hydrogen peroxide is essential to defect formation; (2) delamination defects are typically associated with an existing flaw that interrupts the coating; (3) defects are initially filled with liquid; (4) the crack in the multilayer advances in a zigzagging fashion upward toward the surface; (5) separation of crack faces leads to a permanent uplifting of the coating and a change in optical thickness at the defect site; but (6) delamination defects can “heal” by collapsing into optical contact.

A proposed mechanism for defect formation that satisfies all of the above requirements is shown schematically in Fig. 135.37. First, acid piranha penetrates into the MLD coating [Fig. 135.37(a)] through a large pore, small scratch, or defect (not shown), and a small volume of piranha becomes trapped in the coating at an interface where adhesion has locally failed (between layers or between substrate and coating). Pressure builds up at this location because of the evolution of oxygen

gas from hydrogen peroxide in the trapped piranha, and the MLD layers deform into a circular blister to accommodate the increasing pressure [Fig. 135.37(b)]. Once the critical stress for fracture is reached in the deforming MLD, crack propagation occurs. The crack may initially propagate along the interface (increasing the debond area), but to explain the characteristic fracture pattern, the crack must eventually kink upward into the multilayer [Fig. 135.37(c)]. The crack propagates through the MLD coating to the surface, where accumulated oxygen gas escapes, relieving built-up pressure and collapsing the inflated blister structure. The final defect geometry includes a gap between crack faces [Fig. 135.37(d)], but if the layers later collapse into contact, eliminating air gaps, the defect may appear to have “healed.”

Figure 135.38 shows hypothesized cross-sectional geometries of two observed delamination defects. Twelve arc-shaped cracks, labeled A–L, were counted in the Nomarski micrograph of defect (a). This defect likely initiated between layers 4 (silica) and 5 (hafnia), and each observed arc-shaped crack involved one hafnia/silica layer pair. In defect (b), 14 cracks (A–N) were identified, consistent with a substrate-initiated blister with fracture through all 28 layers. At least five of the 14 cracks (A–E) were circular. Cracks in the upper layer pairs (F–N) were arc shaped with successively shorter arc lengths. The hypothesized geometry in this case is similar to (a), but with complete circular

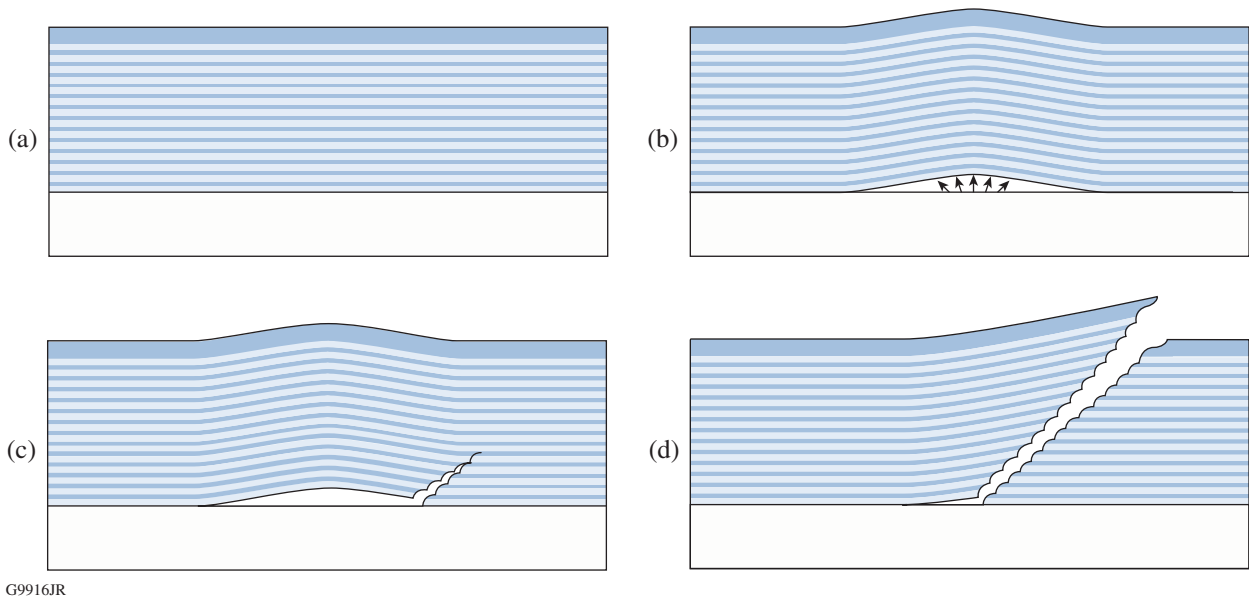


Figure 135.37 Schematic illustrating the hypothesized delamination defect formation mechanism: (a) undisturbed MLD coating, (b) initial pressure development in coating and deformation, (c) kinked fracture at edge of pressurized blister, and finally (d) propagation of the crack to MLD surface. Light bands represent hafnia layers in the coating, while dark bands represent silica layers.

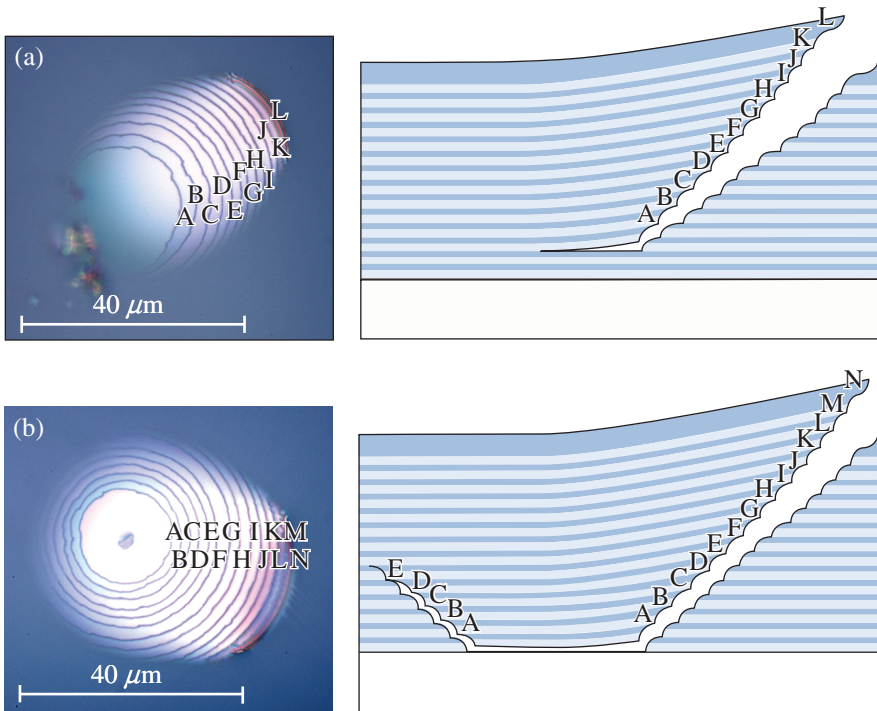


Figure 135.38  
Nomarski micrographs of two delamination defects with schematics showing hypothesized cross-sectional geometries: (a) defect initiated between the second and third MLD layer pairs, with arc-shaped cracks; (b) substrate-initiated defect with fracture through all 14 layer pairs. Fracture in the bottom few layers occurred as circular cracks at the blister's perimeter, while cracks in upper layers were arc shaped.

G9917JR

cracks in the initial few layers with an asymmetrical geometry developing as the crack propagated upward.

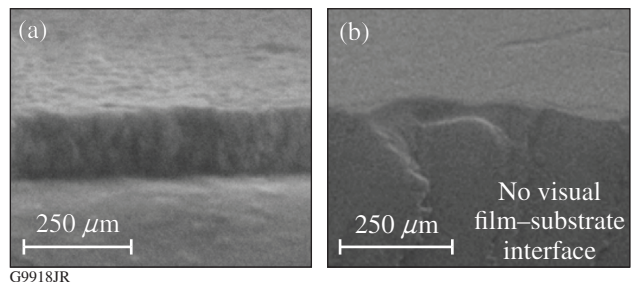
The proposed mechanism requires that a small volume of liquid becomes trapped between layers of the MLD coating. The original entry path must not be a viable path for the escape of gas or liquid; otherwise, high pressures could not develop in the cavity because the oxygen gas evolved from the decomposition of acid piranha could simply travel out of the volume to relieve pressure. Considering the multilayer structure of the thin-film coating, we suggest the coefficient-of-thermal-expansion mismatch between hafnia and silica layers as an explanation: if the MLD layers deform or shift with respect to each other during elevated temperature cleaning, a path to the surface through adjacent layers could become blocked, and pressure could develop freely in a void containing trapped acid piranha.

**Fracture Mechanics**

**1. Material Properties of Dielectric Layers and MLD Coating**

The properties of thin films can be sensitive to the deposition technique,<sup>24,25</sup> and therefore it can be unwise to assume thin-film properties for one coating based on data from a different coating, unless it is known that the deposition method was the same. Nanoindentation of single-layer hafnia and silica films was carried out to accurately estimate the elastic moduli of the

MLD layers. Cross sections of the films tested are shown in Fig. 135.39. The thicknesses of the single-layer films (135 nm for hafnia and 180 nm for silica) were similar to the thicknesses of those layers in the multilayer coating, and the deposition technique was the same as that used for the MLD coating layers. To avoid substrate effects in the nanoindentation measurements, mechanical properties were assessed using data from indenter penetration into only the top 10% to 20% of the total film thickness. The average Young's moduli calculated for the films were  $E_{\text{haf}} = 128 \pm 12.5$  GPa (average  $\pm$  standard deviation of four measurements) for hafnia and  $E_{\text{sil}} = 92 \pm 5$  GPa for silica. These measurements were within  $\sim 25\%$  of moduli reported by Thielsch *et al.*<sup>24</sup> for thin-film hafnia (deposited by reac-



G9918JR

Figure 135.39  
SEM images showing cross sections of oxide monolayers used in nanoindentation experiments: (a) a 160-nm layer of hafnia and (b) a 180-nm layer of silica. There was no visible interface between the substrate and the amorphous silica film.

tive evaporation) and silica (deposited by plasma ion-assisted deposition). Poisson ratio  $\nu$  for the films was estimated from reported values,<sup>26,27</sup> and shear and bulk moduli  $\mu$  and  $B$  were calculated from  $E$  and  $\nu$  using the relations  $\mu = E/2(1 + \nu)$  and  $B = E/3(1-2\nu)$ , respectively.

MLD coating properties were estimated from the single-layer properties determined by nanoindentation experiments. Upper and lower limits on shear modulus and bulk modulus were calculated by the rule of mixtures,

$$\begin{aligned}\mu_{\text{MLD}}^{\text{upper}} &= \mu_{\text{haf}} V_{\text{haf}} + \mu_{\text{sil}} V_{\text{sil}}, \\ B_{\text{MLD}}^{\text{upper}} &= B_{\text{haf}} V_{\text{haf}} + B_{\text{sil}} V_{\text{sil}},\end{aligned}\quad (1)$$

and

$$\begin{aligned}\frac{1}{\mu_{\text{MLD}}^{\text{lower}}} &= \frac{V_{\text{haf}}}{\mu_{\text{haf}}} + \frac{V_{\text{sil}}}{\mu_{\text{sil}}}, \\ \frac{1}{B_{\text{MLD}}^{\text{lower}}} &= \frac{V_{\text{haf}}}{B_{\text{haf}}} + \frac{V_{\text{sil}}}{B_{\text{sil}}},\end{aligned}\quad (2)$$

where  $V_{\text{haf}}$  and  $V_{\text{sil}}$  are the volume fractions of hafnia and silica ( $V_{\text{haf}} = 0.39$  and  $V_{\text{sil}} = 0.61$  for the MLD used in this work). The calculated lower and upper limits on bulk modulus were 58.4 GPa and 63.4 GPa, respectively, and the limits on shear modulus were 44.5 GPa and 45.2 GPa, respectively. These bounds were averaged to estimate the bulk and shear moduli for the multilayer. Poisson ratio and Young's modulus for the MLD were calculated from these moduli using the relations

$$\nu = \frac{3B-2\mu}{6B+2\mu}, \quad E = 2\mu(1+\nu).\quad (3)$$

Bulk properties for the BK7 substrate came from Schott product literature.<sup>28</sup> Material properties are summarized in Table 135.III.

## 2. Contributions of Pressure and Intrinsic Stress to Blister Deformation

In **A Mechanism for Delamination Defect Formation** (p. 191), it was hypothesized that the delamination defect is initiated by pressure developed in a small, disk-shaped volume of acid piranha trapped in the coating. We therefore modeled the blister (prior to fracture) as a circular plate of thickness  $h$  and radius  $R$ , subjected to an internal pressure  $p_c$  and an equibiaxial intrinsic stress  $\sigma$ , and fixed to a thick substrate at its edges ( $r = R$ , where  $r$  is the radial coordinate), as shown in Fig. 135.40. The residual stresses in an evaporated MLD coating can be significant, and the pressure  $p_c$  evolved from piranha decomposition might not be large, so the effects of both loadings are considered in this analysis. The normal displacements of the plate are given by  $w(r)$ .

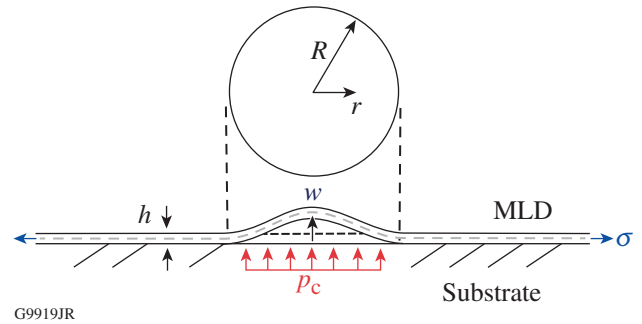


Figure 135.40  
Schematic of a pressurized blister in an MLD film with a residual film stress.

Jensen<sup>17</sup> showed that, in nondimensional form, the von Kármán plate equations for the situation shown in Fig. 135.40 can be written as

$$\begin{aligned}\frac{1}{12(1-\nu^2)} \rho \frac{d}{d\rho} \left[ \frac{1}{\rho} \frac{d}{d\rho} (\rho \xi) \right] - \bar{\varphi} \xi + \frac{p_c R^4}{2Eh^4} \rho^2 &= \frac{\sigma R^2}{Eh^4} \xi, \\ \rho \frac{d}{d\rho} \left[ \frac{1}{\rho} \frac{d}{d\rho} (\rho \bar{\varphi}) \right] + \frac{1}{2} \xi^2 &= 0, \\ \xi(\rho) = -\frac{dw}{d\rho}, \quad \bar{\varphi}(\rho) = \frac{R\varphi}{Eh^3}, \quad \varphi = \frac{d\Phi}{dr},\end{aligned}\quad (4)$$

Table 135.III: Material properties used in the fracture mechanics analysis.

Material	Young's Modulus $E$ (GPa)	Poisson Ratio $\nu$	Shear Modulus $\mu$ (GPa)	Bulk Modulus $B$ (GPa)
BK7 (bulk)	82	0.21	33.9	47.1
SiO <sub>2</sub> (thin film)	95	0.17	40.6	48.0
HfO <sub>2</sub> (thin film)	130	0.25	52.0	86.7
MLD coating	108	0.20	44.7	60.6

where  $\nu$  and  $E$  are the Poisson ratio and Young's modulus of the thin-film coating,  $\Phi$  is the Airy stress function, and  $\rho$  and  $\bar{w}$  are nondimensional quantities defined by  $\rho = r/R$  and  $\bar{w} = w/h$ . For plate behavior, the appropriate boundary conditions are zero slope at the center of the blister, no rotations or displacements at the fixed edges, and  $\bar{w}$  bounded everywhere.

If the nonlinear  $\bar{\varphi}\xi$  term in Eq. (4) can be neglected, the first equation can be uncoupled from the second, and the resulting ordinary differential equation can be written as

$$\rho^2 \xi'' + \rho \xi' - (S\rho + 1)\xi = -P\rho^3, \quad (5)$$

where prime indicates differentiation with respect to  $\rho$ . Two new nondimensional quantities,  $S = 12(1-\nu^2)\sigma R^2/Eh^2$  (residual stress term) and  $P = 6(1-\nu^2)p_c R^4/Eh^4$  (pressure term), were introduced for convenience. In the special case of negligible residual stresses,  $S = 0$  and Eq. (5) reduces to an equidimensional Euler–Cauchy equation. Applying the boundary conditions, the solution for the  $\sigma = 0$  case is

$$\xi(\rho) = -\frac{P}{8}(\rho^3 - \rho) \quad (6)$$

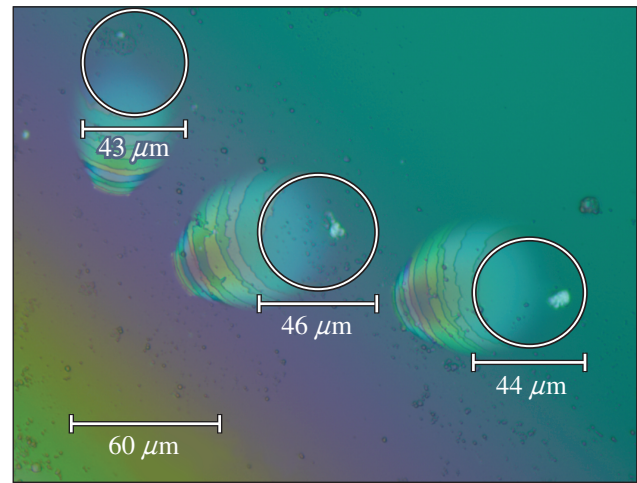
and

$$\bar{w}(\rho) = -\int \xi d\rho = \frac{P}{32}(\rho^4 - 2\rho^2 + 1). \quad (7)$$

Returning to the general case [Eq. (5)], it can be shown that the solution for  $\xi(\rho)$  can be given in terms of modified Bessel functions of the first and second kinds and the Meijer G function. The solution  $\xi(\rho)$  could not be readily integrated to find the blister deflections  $\bar{w}(\rho)$  in closed form. An approximate solution was found by expanding all products in the expression for  $\xi(\rho)$  and integrating term by term. The integrals of all but one term in the expanded form of  $\xi(\rho)$  could be expressed in standard mathematical functions, and the remaining term was approximated by a five-term power series and integrated. The resulting approximation for  $\bar{w}(\rho)$  agreed with the closed-form solution [Eq. (7)] for  $\sigma \rightarrow 0$ . A few specific cases are now considered.

Geometrical and material properties were selected as follows:  $E = 108$  GPa and  $\nu = 0.20$  (see Table 135.III),  $h = 5$   $\mu\text{m}$  (the thickness of the MLD coating), and  $R = 20$   $\mu\text{m}$  (estimated by measuring the diameter of the first fracture ring in micrographs of typical delamination defects, as shown in Fig. 135.41).

It was difficult to accurately determine the residual stress  $\sigma$  in the coating because intrinsic stresses vary with deposition parameters, coating age, storage environment, and other factors. Based on measurements of similar coatings,<sup>21–23</sup> the residual stress was expected to be tensile and in the range of  $\sigma = 0$  to 150 MPa. We have not considered compressive coatings (typical of energetic-deposition methods). The pressure developed in the blister  $p_c$  was also unknown, but we estimated that the upper limit on  $p_c$  (for the case of the irreversible decomposition reaction  $2\text{H}_2\text{O}_2 \rightarrow 2\text{H}_2\text{O} + \text{O}_2$  going to completion in a closed volume) is 254 MPa for a reaction temperature of 60°C, assuming ideal gas behavior for the evolved oxygen gas and incompressibility for water and peroxide; therefore, we consider blister pressures in the range of  $p_c = 3$  MPa to 200 MPa.



G9920JR

Figure 135.41  
Measurement of blister diameter.

Figure 135.42 shows blister deformations resulting from several values of internal pressure  $p_c$ . The solid curves show the deformations for an intrinsic stress level of 150 MPa, while the dashed curves show the zero-intrinsic stress case [that is, the simple solution in Eq. (7)]. The inset plot shows the 3-MPa case, which is difficult to resolve in the larger plot, with the axis limits reset to fit the data. Blister pressure had a profound effect on the magnitude of deformations. Blister pressures in the range of 3 to 200 MPa resulted in maximum blister displacements differing by two orders of magnitude: 6-nm maximum displacement for  $p_c = 3$  MPa and 400 nm for  $p_c = 200$  MPa. In contrast, the effect of residual stress was small, with the difference in displacements for the  $\sigma = 0$  and the  $\sigma = 150$ -MPa cases never more than 4%. This is not surprising given that the stress parameter is  $S = 0.26$  for the  $\sigma = 150$ -MPa case, i.e.,

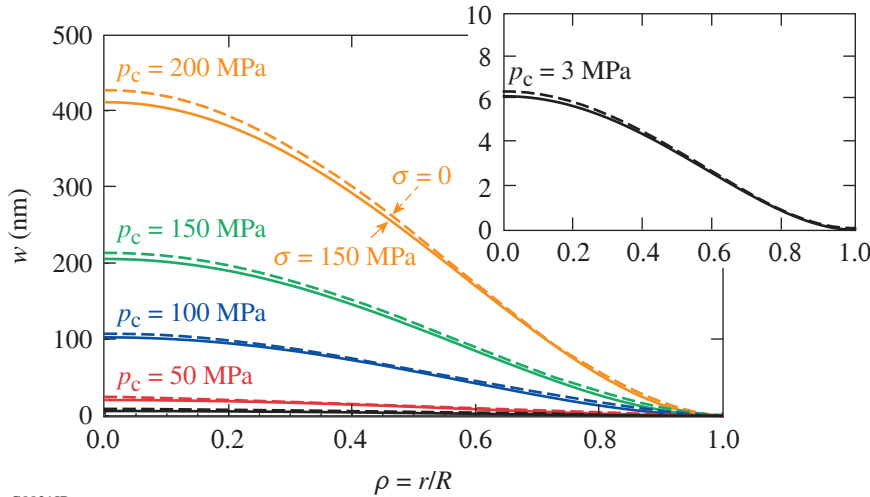


Figure 135.42  
Dependence of blister deformations on internal blister pressure for intrinsic coating stresses of zero (dashed curves) and 150 MPa (solid curves). Inset plot shows a larger view of the  $p_c = 3$ -MPa curves.

G9921JR

small. Note from Eq. (7) that the blister deformation is linear in the pressure  $p_c$ .

### 3. Prediction of Crack Path in Multilayer Coating and Length-Scale Considerations

In the previous section, we considered a pre-existing circular debond (interface crack)—that is, we assumed that the MLD coating was not adhered to the substrate at the blister site, and the coating was free to deflect in response to pressure. To explain the characteristic fracture pattern, the interfacial crack must propagate in response to the pressure loading. If energetically favorable, it is possible for the crack to propagate at first along the interface, growing the blister to a larger diameter, but eventually the interface crack must propagate to the surface by kinking upward into the multilayer.

For an interface crack between two dissimilar materials, the ratio of the energy release rates for the kinked crack  $\mathcal{G}$  and the crack advancing in the interface  $\mathcal{G}_0$  is given by<sup>30</sup>

$$\frac{\mathcal{G}}{\mathcal{G}_0} = \frac{|c|^2 + |d|^2 + 2\text{Re}[cd \exp(2i\bar{\psi})]}{q^2}, \tag{8}$$

$$q = \sqrt{\frac{1-\beta^2}{1+\alpha^2}}, \quad \bar{\psi} = \psi + \varepsilon \ln(al/h),$$

where  $\text{Re}(x)$  gives the real part of  $x$ . The mode mixity angle  $\psi = \tan^{-1}(K_1/K_2)$  describes the crack loading, where  $K_1$  and  $K_2$  are the mode-1 (opening) and mode-2 (shearing) stress-intensity factors, respectively. The corrected  $\bar{\psi}$  includes a term that depends on the problem length scale  $al/h$  and the bimaterial constant  $\varepsilon$ . The quantities  $c$ ,  $d$ , and  $q$  are dimensionless quanti-

ties that depend on the material combination and crack kink angle. The Dundurs material moduli parameters  $\alpha$  and  $\beta$  and bimaterial constant  $\varepsilon$  are defined by<sup>31,32</sup>

$$\alpha = \frac{\mu_1(1-\nu_2) - \mu_2(1-\nu_1)}{\mu_1(1-\nu_2) + \mu_2(1-\nu_1)},$$

$$\beta = \frac{1}{2} \left[ \frac{\mu_1(1-2\nu_2) - \mu_2(1-2\nu_1)}{\mu_1(1-\nu_2) - \mu_2(1-\nu_1)} \right], \tag{9}$$

$$\varepsilon = \frac{1}{2\pi} \ln \left( \frac{1-\beta}{1+\beta} \right),$$

where  $\mu_1$ ,  $\nu_1$ , and  $\mu_2$ ,  $\nu_2$  are the shear moduli and Poisson ratios of materials 1 and 2, respectively. Note that the material mismatch parameters  $\alpha$ ,  $\beta$ , and  $\varepsilon$  vanish in the homogeneous case (material 1 = material 2). We take material 1 to be the substrate and material 2 to be the coating, such that the interface crack either continues along the material 1/material 2 interface or kinks upward into material 2 with crack length  $a$  at kink angle  $\omega$ , as illustrated in Fig. 135.43. If the interface crack is located between MLD layers rather than between the substrate and the coating, the layers beneath the crack are grouped with the substrate as a single material, and the partial multilayer

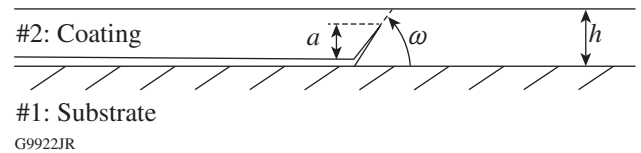


Figure 135.43  
Geometry of kinked crack.

G9922JR

above the crack is treated as material 2. Mismatch parameters  $\alpha$ ,  $\beta$ , and  $\varepsilon$  for relevant material combinations are shown in Table 135.IV.

Table 135.IV: Values for the Dundurs parameters  $\alpha$  and  $\beta$  and bimaterial modulus  $\varepsilon$ .

Material 1	Material 2	$\alpha$	$\beta$	$\varepsilon$
BK7	MLD coating	-0.13	-0.04	0.01
BK7	HfO <sub>2</sub>	-0.23	-0.09	0.03
HfO <sub>2</sub>	SiO <sub>2</sub>	0.17	0.10	-0.03
SiO <sub>2</sub>	HfO <sub>2</sub>	-0.17	-0.10	0.03

The ratio of the energy release rates for the kinked crack and crack advancing in the interface  $\mathcal{G}/\mathcal{G}_0$  is plotted versus kink angle for several values of  $\bar{\psi}$  in Fig. 135.44 for the case of a BK7 substrate with a hafnia/silica MLD coating. Parameters  $c$  and  $d$  were estimated from the tabulated numerical data of He and Hutchinson<sup>33</sup> using linear interpolation. Note that, excepting the case of  $\bar{\psi} = 0$  (corresponding to a pure mode-I crack), a local maximum of  $\mathcal{G}/\mathcal{G}_0$  exists for a nonzero value of  $\omega$ , interpreted as an energetically preferred kink angle. The preferred kink angle  $\omega_p$  increases with increasingly negative  $\bar{\psi}$ , corresponding to a greater mode-II loading contribution. The specific value of  $\omega_p$  can be determined if  $\bar{\psi}$  is known.

For the case of a pressure-loaded blister with small  $p_c$ , the uncorrected mode mixity angle  $\psi$  can be expressed as the

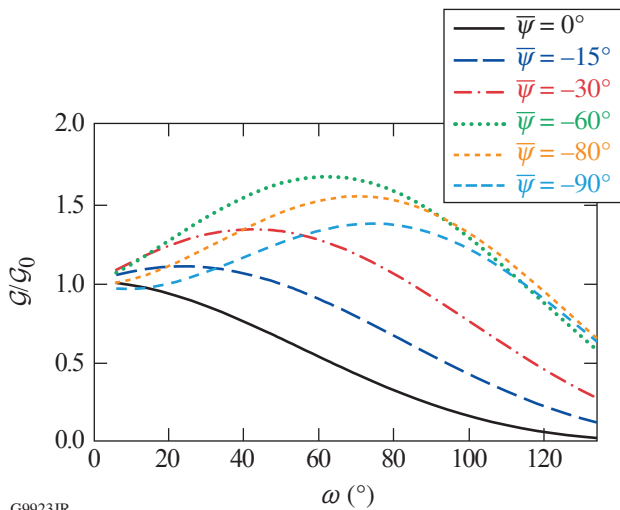


Figure 135.44 Relationship between energy-release rate ratio  $\mathcal{G}/\mathcal{G}_0$  and kink angle for several mode mixity angles for the BK7/MLD coating material combination.

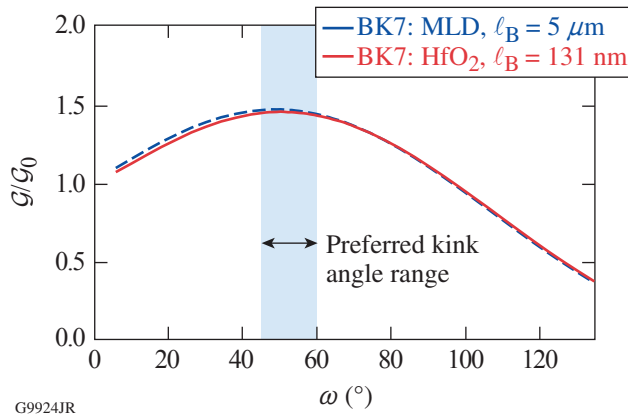
solution to  $\tan(\psi) = -\cot(\gamma)$ , where  $\gamma = \gamma(\alpha, \beta, \eta)$  is a function of the Dundurs parameters and a geometrical parameter  $\eta = h/H$  (Ref. 32). When the substrate thickness  $H$  is much larger than the coating thickness  $h$  (as in the case of an MLD thin-film coating on a thick glass substrate),  $\eta \approx 0$  and  $\gamma(\alpha, \beta, 0)$  can be drawn from the tabulated numerical data of Suo and Hutchinson<sup>34</sup> to calculate  $\psi$ . Small  $p_c$  is considered a good assumption when  $p_c \ll p_0$ , where  $p_0$  is given by<sup>32</sup>

$$p_0 = \frac{16E}{3(1-\nu^2)} \left( \frac{h}{R} \right)^4. \quad (10)$$

For the 40- $\mu\text{m}$ -diam blister considered here,  $p_0 = 7.4$  GPa, and the assumption is quite reasonable for a blister pressure of a few megapascals. To determine the corrected mode mixity  $\bar{\psi}$ , one must know the relevant length scale at which fracture occurs. To analyze the effect of fracture length scale, we write  $\psi_B = \psi_A + \varepsilon \ln(\ell_B/\ell_A)$ , where the mode mixity  $\psi_A$  is associated with fracture at the length scale  $\ell_A$ , and  $\psi_B$  with fracture at the length scale  $\ell_B$ . Notice that, since the bimaterial parameter  $\varepsilon$  is small, this effect will be rather small.

We assume that the mode mixity  $\psi_A$  is associated with the length scale  $\ell_A$  comparable to the MLD coating thickness of  $h = 5 \mu\text{m}$ , and we consider two extreme cases for the effects of the length scale  $\ell_B$ . When fracture processes occur at the length scale  $\ell_B$  comparable to the MLD thickness (i.e.,  $\ell_B = \ell_A$ ), the correction term  $\varepsilon \ln(\ell_B/\ell_A)$  vanishes, and we use the BK7/MLD mismatch parameters from Table 135.IV to find that  $\bar{\psi} = -37.4^\circ$ . On the other hand, when fracture processes are at the length scale  $\ell_B$  comparable to the first layer thickness ( $t_1 = 131 \text{ nm}$ ), we select the BK7/hafnia mismatch parameters because the first layer of the MLD coating adjacent to the BK7 substrate is HfO<sub>2</sub>. In this case,  $\psi_A = -35.9^\circ$  and  $\varepsilon \ln(\ell_B/\ell_A) = -5.8^\circ$ , yielding a corrected mode mixity of  $\bar{\psi} = -41.7^\circ$ . The  $\mathcal{G}/\mathcal{G}_0$  curves for these two extreme cases are plotted in Fig. 135.45. Both cases have a broad maximum in the range of  $\omega_p = 45^\circ$  to  $60^\circ$ .

Measurements of the crack propagation angles in the SEM cross-sectional view of a delamination defect are shown in Fig. 135.46(a), and a closer view in Fig. 135.46(b) shows the crack's path through each MLD layer. The crack kinked sharply upward at the first hafnia layer and whenever it reached an interface with a new hafnia/silica layer pair. Within the silica layers (dark bands), the crack curved to a shallower angle, advancing along a trajectory nearly parallel to the layers as it approached the next hafnia layer. The kink angles in the hafnia



G9924JR

Figure 135.45 Energy-release-rate ratio versus kink angle for two problem length scales: fracture involving the full MLD coating and fracture involving only the first MLD layer. The blue band shows the broad range of energetically preferred kink angles between  $\omega = 45^\circ$  and  $60^\circ$ .

layers (light bands) ranged from  $\omega = 52^\circ$  to  $66^\circ$ : comparable to the preferred angle  $\omega_p$  calculated in the fracture mechanics analysis, especially considering that measurements could be overestimated if the defect were not perfectly bisected during FIB milling.

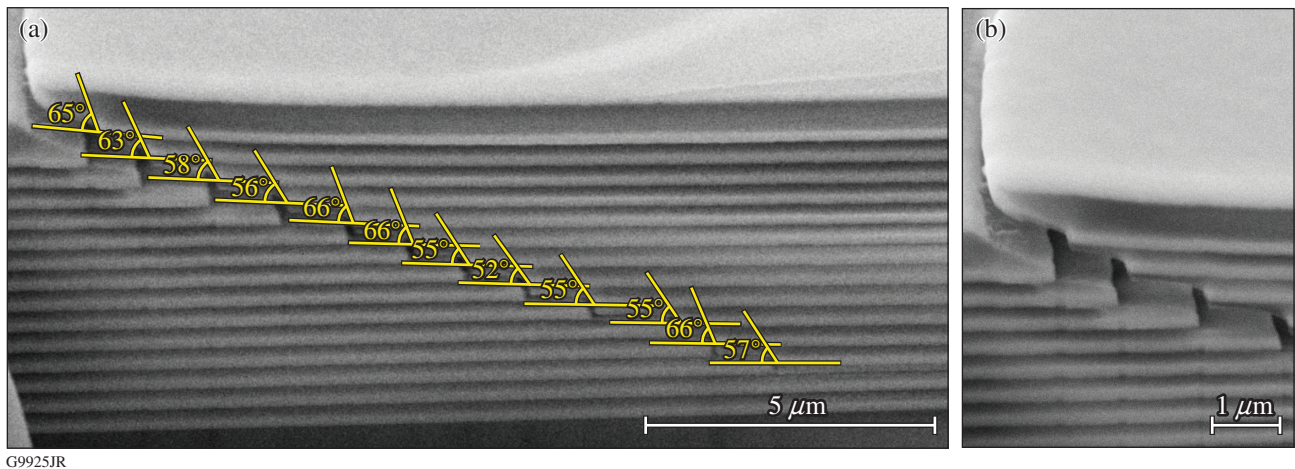
Within the multilayer, the jagged crack trajectory can be explained by the relative stiffness of the layers in the MLD coating. When a crack propagating in a stiffer layer approaches an interface with a more-compliant layer, the crack tends to veer toward the interface, shortening its path through the stiff material. When a crack approaches an interface with a stiffer

material, the crack veers away from the interface, assuming an increasingly horizontal trajectory through the compliant layer, as the energy release rate approaches zero near the interface with the stiffer material.<sup>35</sup> Hafnia is significantly stiffer than silica, so the fracture pattern in the defect is consistent with this behavior.

In our fracture mechanics model, we have used the literature on the interfacial or kinking cracks in a single layer bonded to a substrate. Although this analysis gives a fair representation of the kink angle, it does not take into account the full presence of the multilayer in the crack kinking mechanism: the multilayer is viewed as an equivalent single-layer coating with isotropic elastic properties. Of course, the actual multilayer is anisotropic, with different elastic properties parallel to and normal to the interface with the substrate. A full fracture mechanics analysis would include the presence of the individual single layers and, given the pressure in the interfacial crack, determine the traction variation with distance away from the crack tip, and therefore find the mode mixity directly. We are initiating this work.

**Conclusion**

A mechanism has been proposed for the formation of peroxide-induced delamination defects in multilayer coatings. The mechanism, involving pressure development in a small cavity in the coating, is supported by experimental results and microscopic observation of defects. A fracture mechanics model was developed to explain the deformation and failure of the MLD. The characteristic fracture pattern of the defect



G9925JR

Figure 135.46 (a) Kink angles measured from an observed crack path in a delamination defect; (b) close-up of the defect cross section near the surface, illustrating crack trajectories through the layers of hafnia (light bands) and silica (dark bands).

is found to be consistent with the crack path that maximizes energy release rate.

#### ACKNOWLEDGMENT

The authors thank Dr. J. B. Oliver for helpful discussions. Two of the authors (H. P. Howard-Liddell and K. Marshall) acknowledge support through Horton Fellowships at the Laboratory for Laser Energetics. This material is based upon work supported by the U.S. Department of Energy under Award DE-EE0006033.000 and by the Department of Energy National Nuclear Security Administration under Award DE-NA0001944.

#### REFERENCES

1. M. Alvisi *et al.*, *Thin Solid Films* **358**, 250 (2000).
2. X. Cheng *et al.*, *Appl. Opt.* **50**, C357 (2011).
3. J. Neauport *et al.*, *Opt. Express* **15**, 12508 (2007).
4. Y. G. Shan *et al.*, *Opt. Commun.* **284**, 625 (2011).
5. Y. Shan *et al.*, *Appl. Opt.* **49**, 4290 (2010).
6. J. F. DeFord and M. R. Kozlowski, in *Laser-Induced Damage in Optical Materials: 1992*, edited by H. Bennett *et al.* (SPIE, Bellingham, WA, 1993), Vol. 1848, pp. 455–472.
7. M. D. Feit *et al.*, in *Laser-Induced Damage in Optical Materials: 2000*, edited by G. J. Exarho *et al.* (SPIE, Bellingham, WA, 2001), Vol. 4347, pp. 316–323.
8. W. Kong *et al.*, *Microelectron. Eng.* **83**, 1426 (2006).
9. H. P. Howard, A. F. Aiello, J. G. Dressler, N. R. Edwards, T. J. Kessler, A. A. Kozlov, I. R. T. Manwaring, K. L. Marshall, J. B. Oliver, S. Papernov, A. L. Rigatti, A. N. Roux, A. W. Schmid, N. P. Slaney, C. C. Smith, B. N. Taylor, and S. D. Jacobs, *Appl. Opt.* **52**, 1682 (2013).
10. K. L. Marshall, Z. Culkova, B. Ashe, C. Giacomini, A. L. Rigatti, T. J. Kessler, A. W. Schmid, J. B. Oliver, and A. Kozlov, in *Thin-Film Coatings for Optical Applications IV*, edited by M. J. Ellison (SPIE, Bellingham, WA, 2007), Vol. 6674, Paper 667407.
11. H. A. Macleod and D. Richmond, *Thin Solid Films* **37**, 163 (1976).
12. H. K. Pulker, *Appl. Opt.* **18**, 1969 (1979).
13. H. Howard, J. C. Lambropoulos, and S. Jacobs, in *Optical Fabrication and Testing*, OSA Technical Digest (online) (Optical Society of America, Washington, DC, 2012), Paper OW3D.3.
14. B. Ashe, K. L. Marshall, C. Giacomini, A. L. Rigatti, T. J. Kessler, A. W. Schmid, J. B. Oliver, J. Keck, and A. Kozlov, in *Laser-Induced Damage in Optical Materials: 2006*, edited by G. J. Exarhos *et al.* (SPIE, Bellingham, WA, 2007), Vol. 6403, Paper 640300.
15. B. Ashe, C. Giacomini, G. Myhre, and A. W. Schmid, in *Laser-Induced Damage in Optical Materials: 2007*, edited by G. J. Exarhos *et al.* (SPIE, Bellingham, WA, 2007), Vol. 6720, Paper 67200N.
16. S. Chen *et al.*, in *5th International Symposium on Advanced Optical Manufacturing and Testing Technologies: Advanced Optical Manufacturing Technologies*, edited by L. Yang *et al.* (SPIE, Bellingham, WA, 2010), Vol. 7655, Paper 765522.
17. H. M. Jensen, *Int. J. Fract.* **94**, 79 (1998).
18. J. B. Oliver, T. J. Kessler, H. Huang, J. Keck, A. L. Rigatti, A. W. Schmid, A. Kozlov, and T. Z. Kosc, in *Laser-Induced Damage in Optical Materials: 2005*, edited by G. J. Exarhos *et al.* (SPIE, Bellingham, WA, 2005), Vol. 5991, Paper 59911A.
19. K. Mehrotra, H. P. Howard, S. D. Jacobs, and J. C. Lambropoulos, in *Nanocomposites, Nanostructures and Heterostructures of Correlated Oxide Systems*, edited by T. Endo *et al.*, *Mat. Res. Soc. Symp. Proc.* Vol. 1454 (Cambridge University Press, Cambridge, England, 2012), pp. 215–220.
20. H. Leplan *et al.*, *J. Appl. Phys.* **78**, 962 (1995).
21. J. B. Oliver, P. Kupinski, A. L. Rigatti, A. W. Schmid, J. C. Lambropoulos, S. Papernov, A. Kozlov, C. Smith, and R. D. Hand, *Opt. Express* **20**, 16,596 (2012).
22. J. F. Anzellotti, D. J. Smith, R. J. Sczupak, and Z. R. Chrzan, in *Laser-Induced Damage in Optical Materials: 1996*, edited by H. E. Bennett *et al.* (SPIE, Bellingham, WA, 1997), Vol. 2966, pp. 258–264.
23. J. B. Oliver, P. Kupinski, A. L. Rigatti, A. W. Schmid, J. C. Lambropoulos, S. Papernov, A. Kozlov, and R. D. Hand, in *Optical Interference Coatings*, OSA Technical Digest (Optical Society of America, Washington, DC, 2010), Paper WD6.
24. R. Thielsch, A. Gatto, and N. Kaiser, *Appl. Opt.* **41**, 3211 (2002).
25. R. Thielsch *et al.*, *Thin Solid Films* **410**, 86 (2002).
26. S. L. Dole, O. Hunter, and C. J. Wooge, *J. Am. Ceram. Soc.* **60**, 488 (1977).
27. M. J. Bamber *et al.*, *Thin Solid Films* **398–399**, 299 (2001).
28. Optical Glass Data Sheets, available online at [http://www.schott.com/advanced\\_optics/us/abbe\\_datasheets/schott\\_datasheet\\_all\\_us.pdf](http://www.schott.com/advanced_optics/us/abbe_datasheets/schott_datasheet_all_us.pdf), Schott North America.
29. L.-K. Wu *et al.*, *J. Therm. Anal. Calorim.* **93**, 115 (2008).
30. M.-Y. He and J. W. Hutchinson, *J. Appl. Mech.* **56**, 270 (1989).
31. J. Dundurs, *J. Appl. Mech.* **36**, 650 (1969).
32. J. W. Hutchinson and Z. Suo, in *Advances in Applied Mechanics*, edited by J. W. Hutchinson and T. Y. Wu (Academic Press, Boston, 1992), Vol. 29, pp. 63–191.
33. M.-Y. He and J. W. Hutchinson, Harvard University, Division of Applied Sciences, Cambridge, MA, Report MECH-113A (February 1989).
34. Z. Suo and J. W. Hutchinson, *Int. J. Fract.* **43**, 1 (1990).
35. M.-Y. He and J. W. Hutchinson, *Int. J. Solids Struct.* **25**, 1053 (1989).

---

# Demonstration of the Improved Rocket Efficiency in Direct-Drive Implosions by Using Different Ablator Materials

In direct-drive inertial confinement fusion (ICF), laser beams directly illuminate a fusion capsule.<sup>1</sup> The laser beams ablate the target surface and, through the rocket effect,<sup>2</sup> drive the capsule to velocities required for thermonuclear ignition. To achieve ignition conditions, the imploding shell must reach kinetic energy larger than a threshold value ( $E_{\min}$ ) that depends strongly on the implosion velocity (maximum mass-averaged shell velocity),  $E_{\min} \propto V_{\text{imp}}^{-6}$  (Ref. 3). To maximize the implosion velocity, the conversion of laser energy into kinetic energy of the shell (hydrodynamic efficiency) can be optimized by an appropriate choice of ablator material. By changing the ablator material, the rocket efficiency can be optimized (conversion of absorbed laser energy into kinetic energy of the shell). This article reports on the experimental investigation of the material dependence of the rocket efficiency in direct-drive implosions using the OMEGA laser.<sup>4</sup>

The rocket efficiency of ICF implosions depends on the drive pressure and mass ablation rate. To gain physical insight into the material dependence of these quantities, a stationary laser ablation model was used.<sup>5-7</sup> The sound speed at the ablation region  $[c_s \sim (I_L/\rho_A)^{1/3}]$  is given by balancing the energy flux of the laser (laser intensity  $I_L$ ) with the energy flux of the plasma flow  $\rho_A c_s^3$ , where  $\rho_A$  is the mass density at the maximum laser absorption and  $c_s$  is the sound speed. Since the laser deposition region is given by the critical electron density, the mass density at the deposition region is given by  $\rho_c = (\langle A \rangle / \langle Z \rangle) n_c m_p$ , where  $\rho_c$  is the mass density at the critical density,  $n_c$  is the electron critical density,  $m_p$  is the mass of a proton, and  $\langle A \rangle / \langle Z \rangle$  is the average atomic number over the average atomic mass. This shows that both the ablation pressure ( $p_a \sim \rho_c c_s^2 \sim \rho_c^{1/3}$ ) and mass ablation rate ( $m_a \sim \rho_c c_s \sim \rho_c^{2/3}$ ) increase with the ratio of  $\langle A \rangle / \langle Z \rangle$ . Although the model does not take into account some key physics of laser coupling, including the temperature dependence of laser deposition or cross-beam energy transfer (CBET),<sup>8,9</sup> it predicts an increased rocket efficiency with increasing  $\langle A \rangle / \langle Z \rangle$  in the ablator material.

Experimentally, the rocket efficiency is typically inferred by measuring the velocity of the target and using numerical

simulations to obtain the unablated target mass. Different techniques have been employed to measure the velocity of the shell in ICF experiments. Early planar experiments investigated the rocket efficiency using shadowgraphy and the peak x-ray emission from the coronal plasma.<sup>10-12</sup> In more-recent studies, time-averaged velocities were inferred from neutron bang-time measurements<sup>13,14</sup> and time-resolved velocities have been determined using x-ray backlighting.<sup>15-18</sup> In the direct-drive experiments, the absorbed energy has been varied by changing the intensity of the laser, the wavelength of the laser, the aspect ratio (thickness over the diameter of the shell) of the target, and the diameter of the laser beams relative to the target diameter.<sup>8,12-15</sup> An extensive indirect-drive study of the implosion velocity was conducted at the National Ignition Facility, where the dopant material and dopant concentration were varied while maintaining a nearly constant  $\langle A \rangle / \langle Z \rangle$  (Ref. 18).

This article describes the first demonstration of the effects of  $\langle A \rangle / \langle Z \rangle$  on the hydrodynamic efficiency by measuring the implosion velocities for Be ( $\langle A \rangle / \langle Z \rangle = 2.25$ ), C ( $\langle A \rangle / \langle Z \rangle = 2$ ), and CH ( $\langle A \rangle / \langle Z \rangle = 1.85$ ) ablators. A 20% increase in the velocity of the shell is measured for a Be ablator compared to CH and C ablators when maintaining a constant initial target mass. The hydrodynamic simulations of the time-resolved radius, velocity of the shell, and unabsorbed laser energy are in good agreement with the measurements. These results show an increase in hydrodynamic efficiency of 7% for C and 18% for Be over the CH ablator.

The experiments employed 60 OMEGA ultraviolet ( $\lambda_0 = 351$  nm) laser beams that uniformly illuminated the target and were smoothed by polarization smoothing,<sup>19</sup> smoothing by spectral dispersion,<sup>20</sup> and distributed phase plates [fourth-order super-Gaussian with a 650- $\mu\text{m}$  full width at half maximum (FWHM)].<sup>21</sup> Three 100-ps-long pickets were used to set the target implosion onto a low adiabat<sup>22</sup> followed by a 1.2-ns square pulse that drove the target to its final velocity. The laser energy during the main drive was  $22.9 \pm 0.2$  kJ, which resulted in an on-target overlapped intensity of  $7 \times 10^{14}$  W/cm<sup>2</sup>. Three ablators (CH, C, and Be) were used with various mass densities

of  $1.03 \text{ mg/cm}^3$ ,  $3.35 \text{ mg/cm}^3$ , and  $1.83 \text{ mg/cm}^3$  corresponding to CH, C, and Be, respectively. Their thicknesses were varied to maintain the total ablator mass to be equivalent to 27- $\mu\text{m}$ -thick CH. The outer radius was  $447 \pm 10 \mu\text{m}$  and the total mass was  $64 \pm 2 \mu\text{g}$ .

The total unabsorbed laser energy was measured with an uncertainty of 5% using several calorimeters located around the target chamber. The scattered light was time resolved at four locations by multiplexing the signal into a 1.5-m spectrometer using a high-dynamic-range streak camera.<sup>23</sup> The system had a 100-ps (FWHM) temporal resolution.

The soft x rays (1 keV) emitted by the imploding target were imaged with a pinhole array (10- $\mu\text{m}$ -diam holes) onto a four-strip x-ray framing camera (XRFC) with a magnification of 12 (Ref. 24). This resulted in 16 time-resolved images (four per strip). Each image was time integrated over 40 ps. The relative timing between images ( $\Delta t$ ) was known to  $\sigma(\Delta t) \sim 5 \text{ ps}$  after off-line calibration using 10-ps x-ray bursts produced by the Multi-Terawatt laser.<sup>25</sup> The relative timing of the XRFC between shots was determined by measuring the electric pulse at the output of the microchannel plate relative to the laser fiducial. The absolute timing was determined by measuring the rise in x-ray emission relative to the laser fiducial. A 4-mm-diam gold target was irradiated with five

spatially distinct square laser beam pulses that rose over 100 ps to a 1-ns-long flattop [Fig. 136.1(a)]. An accuracy of 30 ps was determined from the standard deviation of several absolute timing measurements.

An accurate measurement of the position of the ablation surface was made using the steep inner edge [Fig. 136.1(b)] observed in the self-emission images [Fig. 136.1(c)]. This edge is created by the combination of the limb effect from the coronal soft x-ray emission and the absorption of the x rays, from the opposite side of the target, in the cold dense shell.<sup>24</sup> The absorption steepens the gradient by reducing the emission by a factor of 2 over a few microns in its direction. The position of the half-intensity point of this edge follows the radius, where the plasma temperature approaches zero (ablation surface) and provides an accurate measure of the radius of the shell. Since the peak-to-valley intensity is much larger than the noise, the position of the half-intensity point is not sensitive to it. The measurement accuracy of the position of the half-intensity point in the inner emission gradient for a single lineout is given by  $(\text{MTF}/2) \times [1/(\text{S}/\text{N})] \approx 1 \mu\text{m}$ , where  $\text{MTF} = 10 \mu\text{m}$  is the modulation transfer function of the diagnostic and  $\text{S}/\text{N} \sim 5$  is the signal-to-noise ratio, where the signal is given by the difference in the peak-to-valley. This accuracy is supported by the 3- $\mu\text{m}$  standard deviation of the radius from the best-fit circle using a  $\chi^2$  analysis [insert in Fig. 136.1(b)]. The radius of

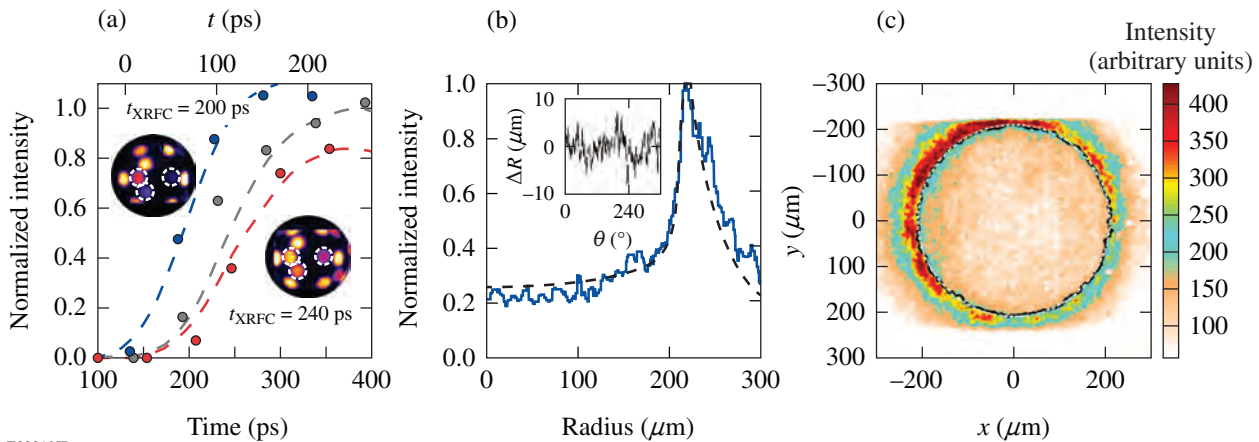


Figure 136.1

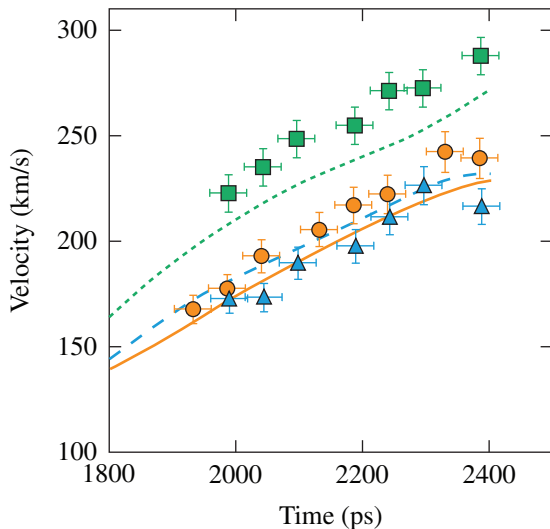
(a) A gold sphere is illuminated by several laser beams that are delayed with successive 50-ps intervals. To absolutely calibrate the timing of the x-ray framing camera (XRFC) to the laser, the x-ray emission measured by the XRFC, in the time reference (bottom axis) of the XRFC (symbols), is compared to the measured laser pulse, in the time reference (top axis) of the laser (curves). The two images (insets) correspond to the XRFC measurements at  $t_{\text{XRFC}} = 200 \text{ ps}$  and  $t_{\text{XRFC}} = 240 \text{ ps}$ . The dashed white circles correspond to the three beams used in the plot. (b) A single radial lineout (solid curve) of the self-emission image is compared with a lineout obtained from post-processing the hydrodynamic simulation (dashed curve). The variation of the difference between the half-intensity point and the radius of the best circle is plotted (inset). (c) The self-emission image at  $t = 2.5 \text{ ns}$  was obtained from a CH target. The black curve corresponds to the location of the half-intensity point; the dashed white circle corresponds to the best-fit circle.

the shell, at each time, was obtained by averaging the position of the inner gradient over angle. This improved the accuracy by a factor of  $\sqrt{N} \approx 10$ , where  $N = 2\pi R/\text{MTF}$  is the number of independent measurements and  $R$  is the radius from the  $\chi^2$  analysis. This results in a radial measurement accuracy of  $\sigma(R) < 0.4 \mu\text{m}$ . The accuracy in the measurement of the averaged ( $\Delta t = 200$  ps) velocity is given by

$$\frac{\sigma(V)}{V} = \sqrt{\left[\frac{\sigma(\Delta t)}{\Delta t}\right]^2 + \left[\frac{\sigma(\Delta R)}{\Delta R}\right]^2} \approx 4\%, \quad (1)$$

where, for a velocity of 200 km/s,  $\Delta R = 40 \mu\text{m}$  and  $\sigma(\Delta R) = \sqrt{2}\sigma(R) = 0.6 \mu\text{m}$ .

Figure 136.2 shows that, for all times, the velocity of the shell is higher in the Be ablator than in the CH and C ablaters. The velocity increases in time to  $\sim 240$  km/s for the CH,  $\sim 230$  km/s for the C, and  $\sim 290$  km/s for the Be ablator. A 20% increase in the velocity of the shell was measured at the end of the laser pulse when a Be ablator was used rather than the standard CH or C ablator. This increase is a result of the increase in  $\langle A \rangle / \langle Z \rangle$  for Be compared to C and CH.



E22220JR

Figure 136.2

Comparison of the calculated (curves) and measured velocities of the shells averaged over 200 ps (symbols) in CH (orange solid line and circles), C (blue dashed line and triangles), and Be (green dotted line and squares) ablaters. Timing error bars correspond to the absolute timing; the relative timing between points is smaller (5 ps).

Figures 136.3(a)–136.3(c) show the time-resolved radii of the imploding shell for the three ablaters. An excellent reproduc-

ibility in trajectory measurements was observed by repeating the shots (two times for C and three times for Be). A decoupling between the position of the shell and the measured radius from the self-emission images occurred at the end of the laser pulse when the plasma was no longer being heated. This reduced the plasma expansion velocity, increasing the plasma density on the outside of the shell.

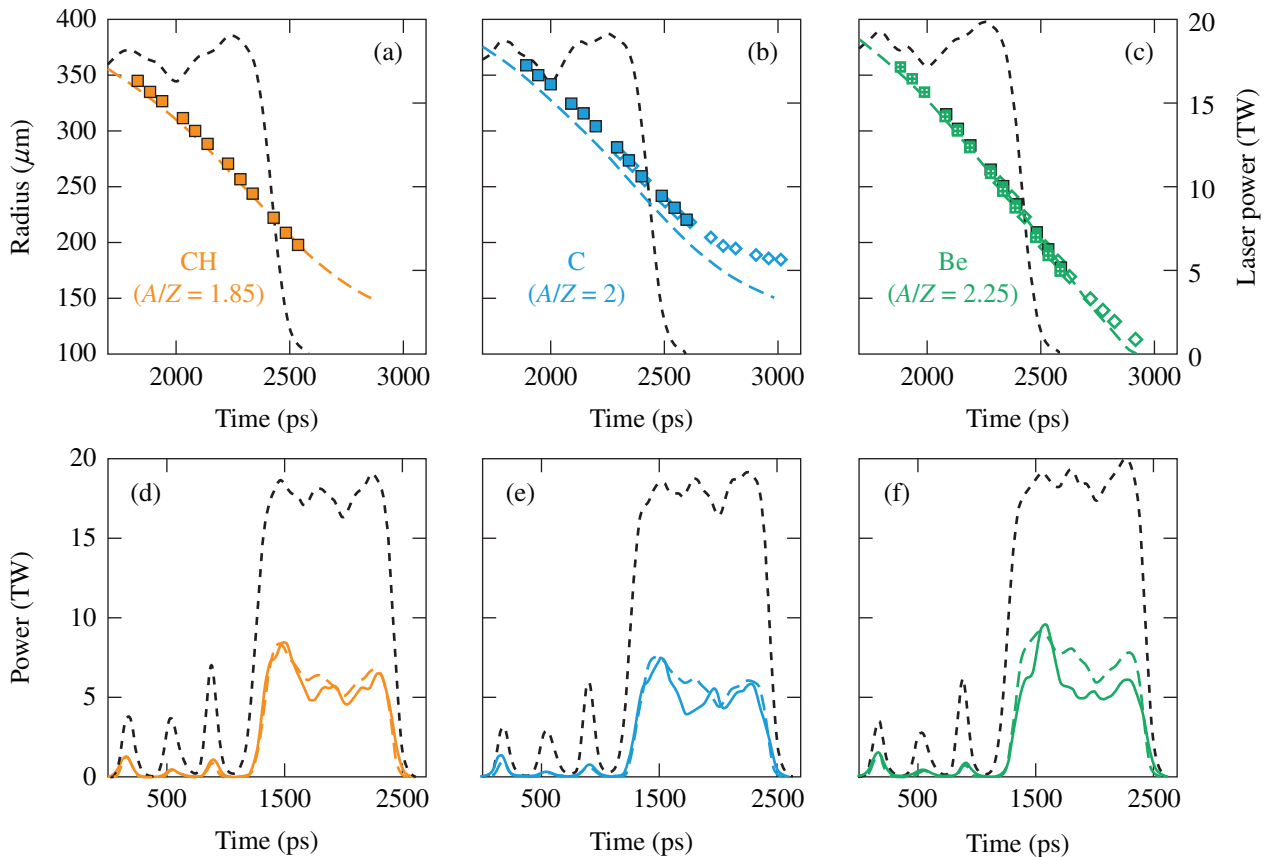
Simulations of the trajectories [Figs. 136.3(a)–136.3(c)] and velocities (Fig. 136.2) of the shells are in good agreement with measurements, indicating that the ablation pressure  $P_a$  and the mass  $M$  of the shell are well modeled:

$$\left(\frac{P_a}{M} = \frac{1}{4\pi R^2} \frac{dV}{dt}\right). \quad (2)$$

This suggests that the coupling of the absorbed laser energy to the shell motion is well modeled. The 80-ps delay observed in the C trajectories [Fig. 136.3(b)] and velocities (Fig. 136.2) may be caused by a delay in the arrival of the shock at the inner interface of the shell, leading to a delay in the initial target motion and indicating an error in the equation of state for C.

The measured shell trajectories were compared with hydrodynamic simulations by post-processing simulations with *Spect3D*<sup>26</sup> and extracting the position of the half-intensity point at each time in the calculated self-emission profile. Simulations included both nonlocal heat transport<sup>27</sup> and CBET models<sup>9</sup> developed in the 1-D hydrodynamic code *LILAC*.<sup>28</sup> Simulated images were integrated over 40 ps and convolved by the MTF of the diagnostic. The comparison of the measured and calculated emission profiles displayed in Fig. 136.1(b) shows that the gradients of the inner edge are in excellent agreement. The position of the inner surface is insensitive to the models used since it is dominated by the point where the temperature approaches zero (a well-defined point in the simulations) and does not require Abel inversion for comparison with the simulations. The half-intensity point follows the ablation front with a constant difference of  $3.5 \mu\text{m}$  caused by the widening of the inner edge by the convolution with the MTF of the diagnostic.

Figures 136.3(d)–136.3(f) show the time-resolved unabsorbed laser light measurements for the three ablaters. The total absorption was measured to be 69% for Be and CH, increasing to 72% for C. This indicates that the increase in implosion velocity for the Be ablator is a result of increased conversion efficiency of the absorbed energy into kinetic energy, not an increase in the absorption. There is excellent agree-



E22221JR

Figure 136.3

[(a)–(c)] Comparison of the calculated (curves) and measured (symbols) shell trajectories (the different symbols represent different shots). [(d)–(f)] Comparison of the measured (solid curve) and calculated (dashed curve) unabsorbed scattered light. The results are presented for [(a) and (d)] CH, [(b) and (e)] C, and [(c) and (f)] Be ablaters. The laser power is plotted on each figure (dashed black curve) and corresponds to an on-target overlapped intensity of  $7 \times 10^{14}$  W/cm<sup>2</sup>.

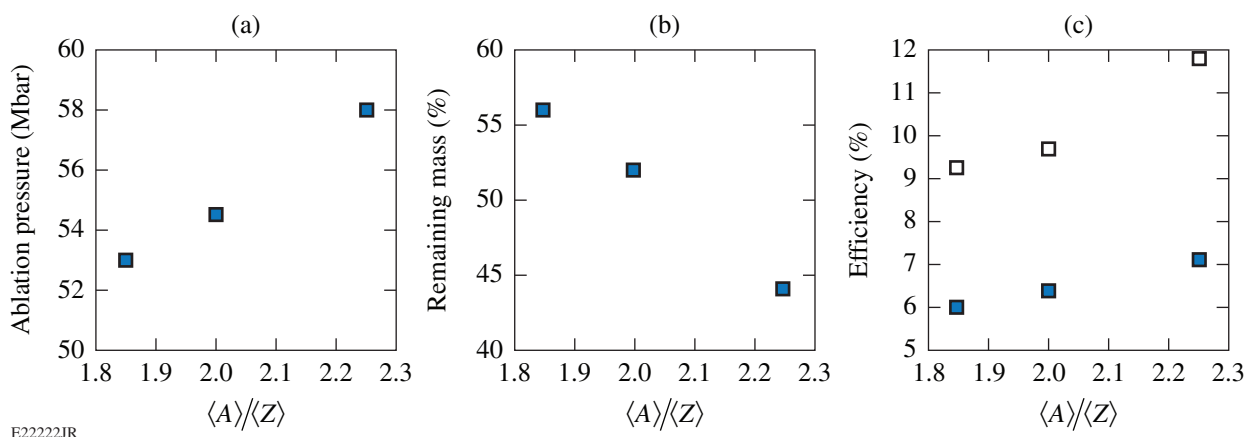
ment between the simulated and measured unabsorbed laser powers for C and CH ablaters, which is consistent with the good agreement in shell velocities (Fig. 136.2). This indicates that when both nonlocal heat transport and CBET are included, the simulations correctly account for the absorption of the laser energy. For the Be ablator, the calculated total absorption is slightly smaller (60%) than in the experiments, which is consistent with the slightly lower (6% lower) calculated velocities.

Figure 136.4 shows the results from simulations where the ablation pressure increases and the percentage of remaining mass decreases with increasing  $\langle A \rangle / \langle Z \rangle$ . This produces a higher acceleration of the shell, at a given radius, leading to a higher implosion velocity for Be. In higher-energy designs, the longer acceleration phase will likely increase the velocity of the shell in Be more than what is measured in these experiments.

The increased ablation pressure, combined with the higher mass ablation rate, leads to a higher kinetic energy and hydro-

dynamic efficiency [Fig. 136.4(c)]. The hydrodynamic efficiency was calculated to be increased by 18% for Be and 7% for C compared to the CH ablator. In these experiments, the simulation slightly underestimates the hydrodynamic efficiency for Be since the laser absorption [Fig. 136.3(f)] and the shell velocity (Fig. 136.2) were measured to be slightly higher than calculated by the simulations. The transfer of absorbed laser energy into the kinetic energy (rocket efficiency) of the shell was calculated to increase by 28% for Be and 5% for C ablaters compared to the CH ablator.

In summary, a 20%-higher implosion velocity was obtained when using a Be ablator compared to a C or CH ablator. Simulations that include nonlocal heat transport and CBET models accurately reproduce shell trajectories, velocities, and unabsorbed laser power for the three materials. They show that the increase in velocity is a result of increasing  $\langle A \rangle / \langle Z \rangle$  and that the hydrodynamic efficiency is increased by 18% for Be and 7% for C ablaters over a CH ablator.



E22222JR

Figure 136.4

Comparison of the calculated (a) ablation pressure and (b) percentage of remaining mass at  $t = 2.3$  ns for the CH ablator ( $\langle A \rangle / \langle Z \rangle = 1.85$ ), C ablator ( $\langle A \rangle / \langle Z \rangle = 2$ ), and Be ablator ( $\langle A \rangle / \langle Z \rangle = 2.25$ ). (c) Comparison of the hydrodynamic efficiency (solid squares) and the efficiency of the transfer of the absorbed laser into the kinetic energy of the shell (open squares) for the three ablators.

## ACKNOWLEDGMENT

This work was supported by the U.S. Department of Energy Office of Inertial Confinement Fusion under Cooperative Agreement No. DE-FC52-08NA28302, the University of Rochester, and the New York State Energy Research and Development Authority. The support of DOE does not constitute an endorsement by DOE of the views expressed in this article.

## REFERENCES

1. J. Nuckolls *et al.*, *Nature* **239**, 139 (1972).
2. M. Murakami and K. Nishihara, *Jpn. J. Appl. Phys.* **26**, 1132 (1987).
3. M. C. Herrmann, M. Tabak, and J. D. Lindl, *Nucl. Fusion* **41**, 99 (2001).
4. T. R. Boehly, D. L. Brown, R. S. Craxton, R. L. Keck, J. P. Knauer, J. H. Kelly, T. J. Kessler, S. A. Kumpan, S. J. Loucks, S. A. Letzring, F. J. Marshall, R. L. McCrory, S. F. B. Morse, W. Seka, J. M. Soures, and C. P. Verdon, *Opt. Commun.* **133**, 495 (1997).
5. W. M. Manheimer, D. G. Colombant, and J. H. Gardner, *Phys. Fluids* **25**, 1644 (1982).
6. P. Mora, *Phys. Fluids* **25**, 1051 (1982).
7. C. E. Max, C. F. McKee, and W. C. Mead, *Phys. Fluids* **23**, 1620 (1980).
8. D. H. Froula, I. V. Igumenshchev, D. T. Michel, D. H. Edgell, R. Follett, V. Yu. Glebov, V. N. Goncharov, J. Kwiatkowski, F. J. Marshall, P. B. Radha, W. Seka, C. Sorce, S. Stagnitto, C. Stoeckl, and T. C. Sangster, *Phys. Rev. Lett.* **108**, 125003 (2012).
9. I. V. Igumenshchev, W. Seka, D. H. Edgell, D. T. Michel, D. H. Froula, V. N. Goncharov, R. S. Craxton, L. Divol, R. Epstein, R. Follett, J. H. Kelly, T. Z. Kosc, A. V. Maximov, R. L. McCrory, D. D. Meyerhofer, P. Michel, J. F. Myatt, T. C. Sangster, A. Shvydky, S. Skupsky, and C. Stoeckl, *Phys. Plasmas* **19**, 056314 (2012).
10. R. Decoste *et al.*, *Phys. Rev. Lett.* **42**, 1673 (1979).
11. B. H. Ripin *et al.*, *Phys. Plasmas* **23**, 1012 (1980).
12. D. T. Attwood *et al.*, *Phys. Rev. Lett.* **38**, 282 (1977).
13. T. H. Tan *et al.*, *Phys. Fluids* **24**, 754 (1981).
14. P. B. Radha, C. Stoeckl, V. N. Goncharov, J. A. Delettrez, D. H. Edgell, J. A. Frenje, I. V. Igumenshchev, J. P. Knauer, J. A. Marozas, R. L. McCrory, D. D. Meyerhofer, R. D. Petrasso, S. P. Regan, T. C. Sangster, W. Seka, and S. Skupsky, *Phys. Plasmas* **18**, 012705 (2011).
15. M. H. Key *et al.*, *Opt. Commun.* **44**, 343 (1983).
16. B. A. Hammel *et al.*, *Phys. Fluids B* **5**, 2259 (1993).
17. D. G. Hicks, B. K. Spears, D. G. Braun, R. E. Olson, C. M. Sorce, P. M. Celliers, G. W. Collins, and O. L. Landen, *Phys. Plasmas* **17**, 102703 (2010).
18. D. G. Hicks *et al.*, *Phys. Plasmas* **19**, 122702 (2012).
19. T. R. Boehly, V. A. Smalyuk, D. D. Meyerhofer, J. P. Knauer, D. K. Bradley, R. S. Craxton, M. J. Guardalben, S. Skupsky, and T. J. Kessler, *J. Appl. Phys.* **85**, 3444 (1999).
20. S. Skupsky, R. W. Short, T. Kessler, R. S. Craxton, S. Letzring, and J. M. Soures, *J. Appl. Phys.* **66**, 3456 (1989).
21. T. J. Kessler, Y. Lin, J. J. Armstrong, and B. Velazquez, in *Laser Coherence Control: Technology and Applications*, edited by H. T. Powell and T. J. Kessler (SPIE, Bellingham, WA, 1993), Vol. 1870, pp. 95–104.
22. V. N. Goncharov, T. C. Sangster, T. R. Boehly, S. X. Hu, I. V. Igumenshchev, F. J. Marshall, R. L. McCrory, D. D. Meyerhofer, P. B. Radha, W. Seka, S. Skupsky, C. Stoeckl, D. T. Casey, J. A. Frenje, and R. D. Petrasso, *Phys. Rev. Lett.* **104**, 165001 (2010).

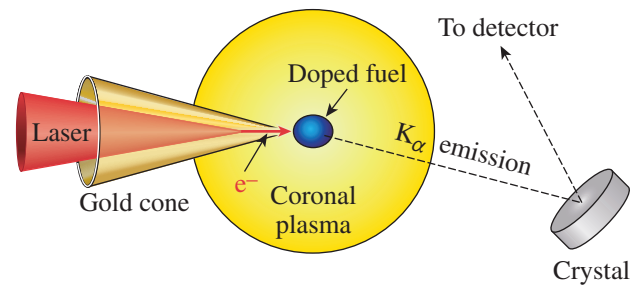
23. W. R. Donaldson, R. Boni, R. L. Keck, and P. A. Jaanimagi, *Rev. Sci. Instrum.* **73**, 2606 (2002).
24. D. T. Michel, C. Sorce, R. Epstein, N. Whiting, I. V. Igumenshchev, R. Jungquist, and D. H. Froula, *Rev. Sci. Instrum.* **83**, 10E530 (2012).
25. V. Bagnoud, I. A. Begishev, M. J. Guardalben, J. Puth, and J. D. Zuegel, *Opt. Lett.* **30**, 1843 (2005).
26. J. J. MacFarlane *et al.*, *High Energy Density Phys.* **3**, 181 (2007).
27. V. N. Goncharov, T. C. Sangster, P. B. Radha, R. Betti, T. R. Boehly, T. J. B. Collins, R. S. Craxton, J. A. Delettrez, R. Epstein, V. Yu. Glebov, S. X. Hu, I. V. Igumenshchev, J. P. Knauer, S. J. Loucks, J. A. Marozas, F. J. Marshall, R. L. McCrory, P. W. McKenty, D. D. Meyerhofer, S. P. Regan, W. Seka, S. Skupsky, V. A. Smalyuk, J. M. Soures, C. Stoeckl, D. Shvarts, J. A. Frenje, R. D. Petrasso, C. K. Li, F. Ségui, W. Manheimer, and D. G. Colombant, *Phys. Plasmas* **15**, 056310 (2008).
28. J. Delettrez, *Can. J. Phys.* **64**, 932 (1986).

# Characterization of a High-Photon-Energy X-Ray Imager

## Introduction

In the *fast-ignition* (FI) approach to inertial confinement fusion (ICF), a compressed deuterium–tritium (DT) fuel capsule is ignited by injecting high-energy particles just prior to peak compression.<sup>1</sup> In the cone-in-shell concept, the particles are energetic (*fast*) electrons that are accelerated from the tip of a cone by a high-energy, short-pulse laser with a power of several petawatts. The hollow cone is embedded in a capsule that is imploded by a high-energy nanosecond laser with energies of several hundred kilojoules. The cone-in-shell concept reduces the distance over which the electrons must propagate to reach the compressed part of the fuel while maintaining a plasma-free path for the short-pulse ignitor laser. Experiments that determine the fast-electron penetration efficiency into FI fuel capsules are essential. Surrogate integrated experiments<sup>2</sup> were performed on the 60-beam OMEGA Laser System<sup>3</sup> to assess the fast-electron coupling from a measurement of the neutron-yield enhancement from compressed deuterated plastic shells. Those experiments allow only a global coupling efficiency to be inferred. They did not show where the fast electrons deposited their energy in the compressed plastic. Imaging  $K_\alpha$  emission generated by fast electrons while propagating through a buried fluorescent layer is a powerful technique to determine local energy deposition.<sup>4</sup> In integrated experiments, this technique has been further developed by imaging the  $K_\alpha$  x rays emitted from fluorescent materials that are doped into the fuel.<sup>5,6</sup> Figure 136.5 illustrates this concept. Electrons accelerated from the cone tip propagate into the compressed capsule where they stimulate the emission of  $K_\alpha$ , which propagates out of the capsule. A spherically bent crystal, oriented at the Bragg angle, collects and focuses the  $K_\alpha$  photons to an x-ray detector [charge-coupled device (CCD) or imaging plate]. The resulting image shows the spatial distribution of the  $K_\alpha$  photons from which the spatial distribution of the fast electrons can be inferred.

The use of  $K_\alpha$  emission in ICF studies is well established, with most applications employing the  $K_{\alpha 1}$  of Cu at  $\sim 8.048$  keV. The fast-electron spreading angle in flat-foil targets, irradiated with a high-intensity laser, is routinely inferred by imaging the



E21813JR

Figure 136.5

Fast electrons, originating from the tip of a gold cone inserted into an ICF capsule, propagate into the doped fuel, where they stimulate the emission of  $K_\alpha$  x rays. The x rays, which are imaged to a detector using a spherically bent crystal, are used to infer the fast-electron spatial distribution.

$K_{\alpha 1}$  emitted from Cu layers buried at different depths inside the foil.<sup>4</sup> Another application involves backlighting the ICF fuel assembly with Cu  $K_{\alpha 1}$  to generate radiographic information about the fuel density.<sup>7</sup> The use of Cu  $K_{\alpha 1}$  to diagnose the penetration efficiency of fast electrons in hot dense ICF fuel capsules is limited, however, by the  $K_\alpha$  line shift that accompanies high-temperature–induced ionization in the background fuel.<sup>5</sup> As the  $K_\alpha$  lines shift in energy, they move outside the acceptance bandwidth of the imaging crystals; consequently, the detection efficiency drops. For Cu  $K_{\alpha 1}$ , a background temperature of  $\sim 35$  eV is sufficient for the center wavelength to shift beyond the acceptance bandwidth of a typical quartz crystal reflector cut with Miller indices (211) (Ref. 8). One-dimensional hydrodynamic calculations performed to estimate the temperature of a  $870\text{-}\mu\text{m}$ -diam fuel capsule with a  $40\text{-}\mu\text{m}$ -thick shell, imploded using 20 kJ from the OMEGA laser, indicated a shell temperature in excess of 200 eV (Ref. 9).

The issue of line shifting may be mitigated by using  $K_\alpha$  radiation from higher-Z materials, such as Zr, that are more robust against temperature-induced shifts. Promising results with a novel quartz-crystal imager working at a photon energy of 15.6909 keV, corresponding to the Zr  $K_{\alpha 2}$  line, were recently reported.<sup>10</sup> Calculations described in Ref. 10 suggest that the center wavelength of the Zr  $K_{\alpha 2}$  line remains inside

the acceptance band of a quartz reflector up to a temperature of at least 200 eV. There is very little experimental work reporting on crystal imaging systems at such high photon energies. This article reports on the performance of a spherically curved quartz-crystal imager designed to reflect photons with an energy of 15.6909 keV. Since the design of the imaging system relies on an accurate knowledge of the crystal, which is cut with Miller indices (234), measurements were taken to determine the Bragg angle, rocking curve, peak reflectivity, and integrated reflectivity. Several curved crystals and a flat sample were characterized using a narrow-bandwidth x-ray source tuned to 15.6909 keV. The imager was successfully tested using a Zr plasma source generated with a 10-J, 1-ps laser system. The measured peak reflectivity from the laser experiment is in agreement with the results from a synchrotron facility.

### Quartz-Crystal Imager

Figure 136.6 shows the configuration in which the  $K_{\alpha}$  imager is aligned for use in laser–solid experiments. In the first stage of alignment, a continuous-wave (cw) alignment laser is propagated through target chamber center (TCC), indicated by the position of the imaging fiducial in Fig. 136.6, and onto the center of the crystal. To enhance its reflectivity in the visible, the crystal is coated with 30 nm of Al. The crystal is oriented to reflect the laser light back along its own path. This arrangement defines the origin of the angular coordinate system. The crystal is then rotated through an angle  $\theta_{1/2}$ , where  $\theta_{1/2}$  is  $90^{\circ} - \theta_B$  and  $\theta_B$  is the Bragg angle for the  $K_{\alpha}$  diffraction. The laser light is then reflected through a full angle  $\theta_F = 2\theta_{1/2}$ .

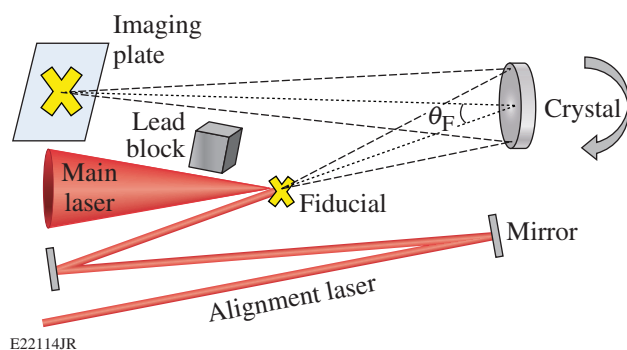


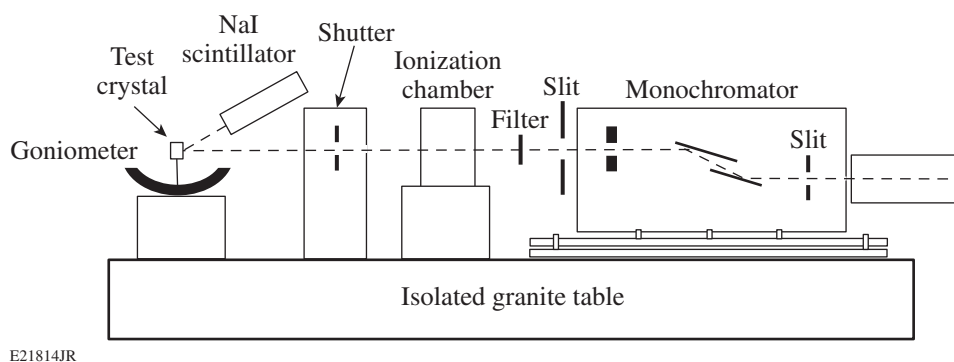
Figure 136.6  
Schematic representation of a  $K_{\alpha}$  x-ray imager simultaneously demonstrating the alignment and experimental configurations. For the experiment with the main laser, the curved crystal is rotated to satisfy the Bragg condition for  $K_{\alpha}$  x rays that are diffracted and focused onto the imaging plate.

The fiducial is then positioned at TCC and imaged to an imaging plate (or CCD camera) with a magnification  $m$  that is determined by the crystal focal length  $f$  and the fiducial–crystal

separation distance  $s_0$  by  $m = f/(s_0 - f)$ . The position of the visible image is recorded. In the experiment, with the fiducial and alignment laser removed, the main laser irradiates a target placed at TCC and the  $K_{\alpha}$  emission is imaged onto the imaging plate with the same magnification. The imaging plate is wrapped in Al foil to prevent exposure to room and laser light. A lead block placed between the target and the imaging plate prevents the direct line-of-sight x-ray irradiation of the imaging plate. The alignment technique relies on the visible and  $K_{\alpha}$  images being close to coincident. If the visible image forms at an angle that is outside the crystal's rocking-curve range of angles, the Bragg condition will not be satisfied for the  $K_{\alpha}$  emission and no  $K_{\alpha}$  image will form. Such a discrepancy arises from misalignment of the crystal planes and the crystal surface. In the laser–solid experiments described below, a fiducial was imaged by the crystal designated Sph3 using visible light from the alignment laser before being rotated to the correct position for  $K_{\alpha}$  diffraction with an accuracy of  $0.01^{\circ}$ . The displacement between the visible and the  $K_{\alpha}$  images along the dispersion direction 1.85 m away at the imaging plate was  $\sim 2$  mm, corresponding to an angular offset of  $\sim 0.06^{\circ}$ . In this case, the offset was within the measured rocking-curve width of  $0.12^{\circ}$  full width at half maximum (FWHM) of this crystal. In general, the visible image can be offset by a predetermined angle to ensure the Bragg condition is satisfied for the  $K_{\alpha}$  emission.

### Determination of the Crystal Bragg Angle, Rocking Curve, and Reflectivity

Measurements were made to determine the Bragg angle, rocking curve, and reflection efficiency of three curved (25-cm focal length) and one flat sample of a quartz crystal (Miller indices 234) for a photon energy of 15.6909 keV corresponding to the  $K_{\alpha 2}$  line of Zr. The measurements were made with the X15A x-ray beamline at the National Synchrotron Light Source at Brookhaven National Laboratory. Figure 136.7 shows the experimental configuration. The X15A beamline provides x rays from around  $E_{\nu} = 5$  keV to  $E_{\nu} = 28$  keV. A slit ensures that the x rays are collimated. A quartz-crystal monochromator selects the energy, providing a beam with a bandwidth  $\Delta E/E \sim 10^{-4}$ . The monochromator crystals are cut perpendicular to the axis with Miller indices (111) corresponding to a lattice spacing of  $3.136 \text{ \AA}$ . The crystal surfaces are set to be parallel and are rotated together to select a specific energy. The monochromator was first calibrated using the K edge of Zr at  $E = 17.998$  keV, corresponding to an x-ray angle of incidence from the storage ring of  $6.3057^{\circ}$ . The monochromator crystals were then rotated to select the desired x-ray energy of  $E = 15.6909$  keV corresponding to Zr  $K_{\alpha 2}$ . In addition to the selected energy, the monochromator passes x rays whose energy corresponds



E21814JR

Figure 136.7

Experimental configuration. A monochromator selects x rays with a bandwidth of  $\Delta E/E = 10^{-4}$ . The beam is apertured to 1.6 mm (horizontally) by  $100 \mu\text{m}$  (vertically). An ionization chamber measures the flux. The crystal is mounted on a motorized goniometer that rotates the crystal in the vertical direction. A shutter, synchronized with the goniometer, releases the beam when the crystal is stationary. Photons reflected from the crystal are detected using a NaI scintillator.

to the third, fourth, and fifth higher harmonic orders.<sup>11</sup> The flux of these x rays is sequentially weaker. At 15.6909 keV, the fundamental carries 99.7% of the x-ray energy while the third, fourth, and fifth orders contribute 0.28%, 0.013%, and 0.0003% of the energy, respectively. Filtering of the x-ray beam, a necessity for the experiment described here, increases the relative amount of higher-order x rays through differential attenuation. To suppress the propagation of higher orders of the fundamental x-ray energy, the monochromator was slightly detuned from the peak transmission angle of its rocking curve to the 50% transmission angle. With such a configuration, the third-order component is reduced by a factor of  $\sim 100$ , while the higher-order components are suppressed even more.

To limit the overall flux, a second lead slit apertured the x-ray beam to  $1.6 \text{ mm} \times 100 \mu\text{m}$  in the horizontal and vertical directions, respectively. Mo filter foils can be placed in front of the slit to further attenuate the beam where necessary. An ionization chamber measures the x-ray flux after the slit. The x-ray flux at the ionization chamber is directly proportional to the electron current in the main storage ring. A computer-controlled shutter sets the x-ray exposure time. Typical exposure times were 1 s with an absolute error of  $\sim 20$  ms. The test crystal is mounted on a computer-controlled goniometer with a  $90^\circ$  full range of motion. X rays reflected from the crystal were measured using a NaI scintillator positioned to intercept the x rays at the focus of the curved crystal. The test crystal was positioned to intercept the x-ray beam at its center. To obtain the rocking curve, the goniometer rotated the test crystal about its center in  $0.0025^\circ$  steps in the vertical direction. For each step, the rotation paused and the shutter opened for 1.0 s. The large NaI detector with a radius of 2.54 cm ensured that all the reflected x-ray photons were collected over the entire angular

range. The same procedure was used for all four samples. Three crystals (flat, Sph1, and Sph2) were provided by Inrad Optics and were fabricated from the same batch, while the curved crystal Sph3 was provided by Eco Pulse. The Inrad crystals had a thickness of  $71 \pm 1 \mu\text{m}$  and a diameter of 30 mm, while the Eco Pulse crystal had a thickness of  $125 \mu\text{m}$  and a diameter of 25 mm. To determine the energy incident on the crystal, the scintillator was placed in front of the crystal to directly intercept the x-ray beam at normal incidence. To reduce the x-ray signal below the scintillator saturation level, a  $225\text{-}\mu\text{m}$ -thick Mo filter was placed (as indicated in Fig. 136.7) to attenuate the beam.

Prior to obtaining its efficiency with the NaI scintillator, the Bragg angle of Sph3 was measured using a Fuji SR imaging-plate detector. The imaging plate was oriented in the vertical direction and positioned in place of the scintillator. To prevent room-light illumination of the imaging plates, they were wrapped in a  $25\text{-}\mu\text{m}$ -thick sheet of Al foil. The crystal was first aligned in its mount on an optical table and oriented such that a horizontally propagating cw laser, with normal incidence on the crystal, was back-reflected along its own path. The crystal and mount were then transferred to the goniometer and swept through an angular range of  $4^\circ$ . The Bragg angle is computed by determining the vertical position of the peak of the rocking curve, recorded on the imaging plate, relative to the x-ray beam and the distance of the peak position to the center of the crystal. Averaging over four sweeps, the peak was observed to occur at an incidence angle of  $\theta_{1/2} = 2.80^\circ$  with a standard deviation of  $0.06^\circ$ . The variation arises from the finite repeatability of repositioning the imaging plate between measurements. A further error associated with the finite precision with which the relevant distances could be measured was evaluated to be

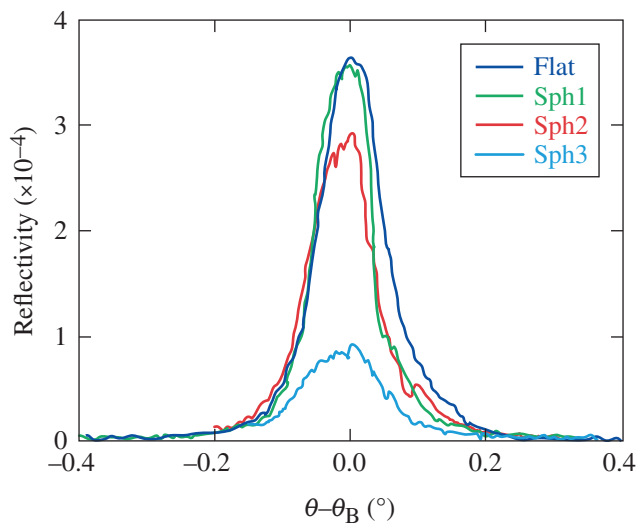
$\sim\pm 0.25^\circ$ . The Bragg angle was therefore measured to be  $\theta_B = 87.2\pm 0.3^\circ$  for the Zr  $K_{\alpha 2}$  line (15.6909 keV), which results in an inferred crystal  $2d$  spacing of  $2d = 1.5822(4)$  Å using Bragg's law ( $n\lambda = 2d\sin\theta_B$ ) in the second order. In addition, Inrad provided rocking-curve measurements for their samples using the Cu  $K_{\alpha 1}$  line at 8.0478 keV and measured a Bragg peak at  $(76.75\pm 0.10)^\circ$  in the first order, from which  $2d = 1.5827(7)$  Å is inferred. The corresponding Bragg angle in the second order for the Zr  $K_{\alpha 2}$  line is  $(86.8\pm 0.5)^\circ$ . Both inferred  $2d$  values agree within the measurement uncertainty and are close to the calculated value of  $2d_{\text{cal}} = 1.5825$  Å (Ref. 6).

The rocking curves and reflection efficiencies for all four crystals are shown in Fig. 136.8. The results show that the spherical crystal Sph1 had the highest reflectivity of the curved crystals at around  $(3.6\pm 0.7) \times 10^{-4}$  with a curve FWHM of  $\sim 0.09^\circ$ . The primary errors in the reflectivity measurement arise from jitter in the scintillator exposure time as a result of the shutter response and from the uncertainty in the thickness of the Mo stack used to filter the direct beam. For the exposure time employed, the shutter error is estimated to be  $\sim 2\%$ . The stack thickness was calculated from the total weight, measured using a Scientech analytical balance, and the stack transverse size, measured with digital calipers. The associated error in the transmission was determined to be around  $\sim 17\%$ . Errors associated with uncertainties in the storage ring current, the

free-space x-ray propagation distances, and photon-counting statistics in the scintillator are negligible. A flat crystal from the same production batch produced a very similar result, showing that the crystal bending had a minor effect on the rocking curve. A lower reflectivity was measured for Sph2 from the same production batch, while the sample Sph3 had an  $\sim 4\times$ -lower peak reflectivity. The results are summarized in Table 136.I. As a check, the measurements were repeated with Fujifilm SR imaging-plate detectors, instead of the NaI scintillator, producing similar results, albeit with larger errors. The SR imaging-plate detectors were also used to determine the homogeneity of the reflectivity of crystal Sph3 over a region of its surface. The crystal was translated to positions  $\pm 5$  mm above, below, and to the side of the center position, and the measurements were repeated with no significant variation in the performance at the different sites.

Table 136.I: Rocking-curve width, peak reflectivity, and integrated reflectivity of a flat and various curved quartz (234) crystals at the Zr  $K_{\alpha 2}$  line (15.6909 keV).

Crystal	FWHM ( $\theta^\circ$ )	Peak reflectivity	Integrated reflectivity (mrad)
Flat	0.11	$(3.7\pm 0.7) \times 10^{-4}$	$(8.8\pm 1.8) \times 10^{-4}$
Sph1	0.09	$(3.6\pm 0.7) \times 10^{-4}$	$(7.7\pm 1.8) \times 10^{-4}$
Sph2	0.14	$(2.9\pm 0.6) \times 10^{-4}$	$(7.0\pm 1.4) \times 10^{-4}$
Sph3	0.12	$(9.0\pm 1.8) \times 10^{-5}$	$(2.5\pm 0.6) \times 10^{-4}$



E21815JR

Figure 136.8 Measured rocking curves of four quartz crystals (234) at 15.6909 keV. The spherical crystal Sph1 had a peak reflectivity of  $(3.6\pm 0.7) \times 10^{-4}$  and a rocking-curve full width at half maximum of  $0.09^\circ$ . Also shown are the rocking curves for another spherical crystal (Sph2) and a flat crystal, all from the same production batch, and a third spherical crystal (Sph3) obtained from a different vendor.

The theoretical value of reflectivity for each crystal was calculated using the x-ray oriented programs (*XOP*) code.<sup>12</sup> The *XOP* code uses the *DEBAX* database of atomic and molecular properties and photon-interaction cross sections and scattering factors for a wide range of crystal materials. The crystal type was selected to be  $\alpha$  quartz with the Miller indices set to (468), indicating that the calculation was performed for the second-order diffraction. The photon energy was set to 15.69 keV, the Poisson ratio to 0.17, and the polarization to sigma. The asymmetry angle was set to  $0^\circ$ , signifying perfect parallelism between the diffracting planes and the crystal surface. The diffraction geometry was set to Bragg and, to account for the crystal curvature, the calculation theory was set to Multilamellar. The final input parameter was the Debye–Waller temperature parameter that took into account the thermal motion of the crystal lattice. The precise value of the temperature parameter is difficult to determine for trigonal crystalline structures such as quartz. Approximate formulas exist in *XOP* for cubic crystal structures such as pure silicon. In that case, the temperature parameter is close to unity for the lowest-order diffraction but is reduced for higher orders. In the current calculation, the tem-

perature factor was a free parameter that was adjusted until the calculated width of the rocking curve matched the experimentally observed value. The corresponding reflectivity values were then recorded. The temperature parameter and the calculated peak and integrated reflectivity for spherical crystals Sph1 and Sph3 are displayed in Table 136.II. The calculated values of the integrated reflectivity for the two crystals are a factor of  $\sim 3$  and  $\sim 8$  higher than the measured values, respectively.

It is not clear why the measured reflectivity is lower than the predicted values. Measurements of the crystal thickness of Sph1 indicated that the thickness was within 2% of the stated value. The calculations include x-ray absorption in quartz, which for a 71- $\mu\text{m}$  thickness decreases the calculated reflectivity by  $\sim 9\%$  compared to the case where absorption is not included. Absorption by impurities is not accounted for but is an unlikely explanation; although moderate- to high- $Z$  impurities could have a significant effect on absorption, the most-common impurities in quartz crystals are low- $Z$  materials such as Li and Al, and since the crystal is visibly transparent, we can assume that the crystal is reasonably pure. Another possibility is that the reflectivity was suppressed by defects introduced in the crystal during the manufacturing process. We also cannot eliminate the possibility that imperfections on the substrate surface might have been transferred to the crystal or that the bonding mechanism introduced stress and dislocations to the diffracting structures. There is no indication that the additional bending of the crystal led to any further degradation since the reflectivity of the flat sample was similar in magnitude to the curved crystals. Finally, the application of models that are strictly derived for cubic crystal geometry provides uncertainty and another potential source of disagreement between the measured and calculated values.

### Imaging Capability and Reflectivity Using a Plasma-Based Source

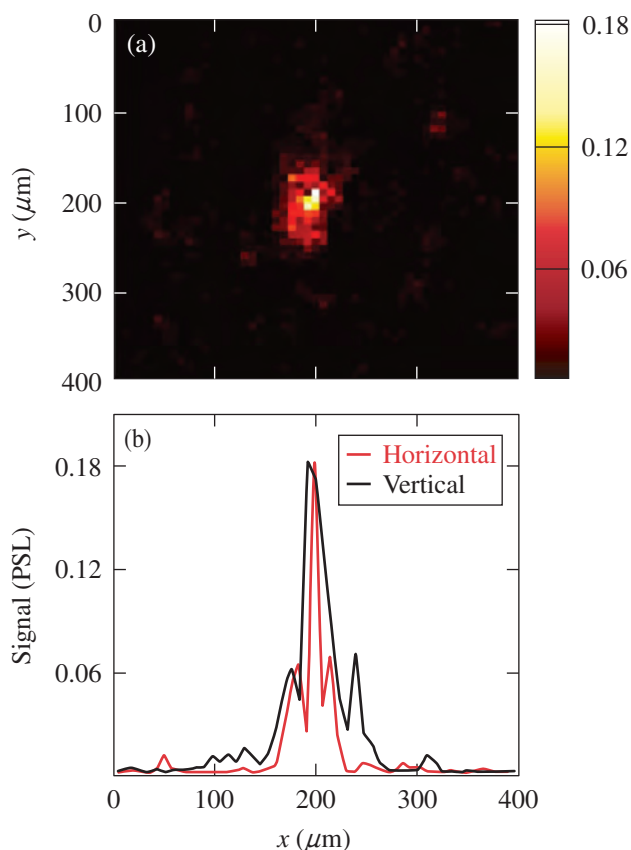
Laser experiments were performed with LLE's Multi-Terawatt (MTW) laser<sup>13</sup> to test the imaging capability of a spherical crystal using Zr  $K_{\alpha 2}$  x rays. This test was performed with the sample Sph3. The crystal imaged the emission from

the rear surface of a Zr foil target irradiated with a  $p$ -polarized laser pulse with a 10-J energy incident at a  $45^\circ$  angle. The laser energy is absorbed by electrons at the critical-density surface of a plasma that forms in front of the target at the beginning of the laser interaction. The electrons are driven into the target where they stimulate the emission of  $K_{\alpha}$  radiation. The  $K_{\alpha}$  yield from such a target is proportional to the laser energy, while background noise caused by bremsstrahlung as the electrons lose energy in collisions is proportional to the laser intensity. To reduce the background, the pulse duration was lengthened to 10 ps and the laser spot was defocused to  $\sim 30 \mu\text{m}$  (FWHM) corresponding to a mean intensity of  $\sim 1 \times 10^{17} \text{ W/cm}^2$ . The crystal was oriented to reflect the  $K_{\alpha 2}$  emission on a Fujifilm TR imaging plate. To further reduce the background signal and enhance the signal-to-background ratio, a 17- $\mu\text{m}$ -thick Zr filter and a 25- $\mu\text{m}$ -thick Al filter were placed in front of the imaging plate while a 3-mm-thick lead collimator obstructed the direct line of sight to the target. The target dimensions were 1 mm  $\times$  1 mm  $\times$  17  $\mu\text{m}$ . The distance from the target to the center of the crystal was 28.9 cm, providing a magnification of 6.6. The crystal diameter was 2.5 cm, corresponding to a solid angle from the target of  $5.9 \times 10^{-3}$  sr. The extreme rays that diffract at the edge range of the crystal subtend angles of  $2.2^\circ$  and  $4.4^\circ$ . The corresponding energies were 15.679 keV and 15.711 keV, respectively, giving an energy acceptance bandwidth for the crystal of 32 eV. The  $K_{\alpha 2}$  line broadening and shifting that accompany target heating are not expected to be significant for the current case of moderate laser energy and a large-mass target, and the  $K_{\alpha 2}$  line is expected to remain fully within the bandwidth.

Figure 136.9 shows an image corrected for magnification along with a horizontal and a vertical lineout through the peak intensity pixel. The FWHM of the horizontal and vertical lineouts is 32 and 38  $\mu\text{m}$ , respectively. The image exhibits a signal-to-background ratio of better than 40:1 with an x-ray signal that peaks at around 0.18 PSL. A single-photon-counting spectrometer<sup>14</sup> determined the total number of radiated  $K_{\alpha}$  photons to be  $(10^{+7/-2}) \times 10^{10}$  corresponding to a laser-to- $K_{\alpha}$  energy conversion efficiency of  $\sim 3 \times 10^{-5}$ . Taking into

Table 136.II: The peak and integrated reflectivity for each crystal calculated using the x-ray oriented programs (XOP) software.<sup>12</sup>

Crystal	Radius of curvature (cm)	Thickness ( $\mu\text{m}$ )	Temperature parameter	Peak reflectivity	Integrated reflectivity (mrad)
Sph1	50	71	0.45	$1.4 \times 10^{-3}$	$2.2 \times 10^{-3}$
Sph3	50	125	0.35	$1.0 \times 10^{-3}$	$2.1 \times 10^{-3}$



E21816JR

Figure 136.9

(a) An image of the Zr  $K_{\alpha 2}$  emission through the rear surface of a 17- $\mu\text{m}$ -thick laser-irradiated Zr foil (the color scheme refers to the measured signal in PSL) and (b) horizontal and vertical lineouts through the peak of the emission.

account the relative solid angle between the single-photon-counting spectrometer and the crystal, the total number of  $K_{\alpha}$  photons incident on the quartz crystal was  $\sim 5 \times 10^7$ . The quartz crystal reflects only the  $K_{\alpha 2}$  line on the detector, which contains one third ( $\sim 1.6 \times 10^7$ ) of the total number of  $K_{\alpha}$  photons. Accounting for the 17- $\mu\text{m}$ -thick Zr filter and the 25- $\mu\text{m}$ -thick Al filter ( $\sim 77\%$  total transmission) and assuming an imaging plate sensitivity of  $(2.5 \pm 0.5)$  mPSL/photon at 15.7 keV (Ref. 15), a perfectly reflecting crystal is estimated to produce a total signal of  $(3.0 + 3.4/-1.1) \times 10^4$  PSL. Comparing this with the experimentally measured value of  $(5.5 \pm 1.1)$  PSL, which is the spatially integrated value from Fig. 136.9, implies a peak reflectivity of  $(1.8 + 1.4/-1.0) \times 10^{-4}$  at 15.7 keV. The peak reflectivity inferred from the laser experiment is a factor of  $\sim 2$  higher, but it is within the experimental uncertainties in reasonable agreement with the peak reflectivity obtained from the rocking curve measurement of Sph3 (see Table 136.I).

## Conclusion

A high-energy x-ray-photon imager has been developed to image the x-ray emission from laser-generated Zr plasmas. The imager's optic consists of a spherically bent quartz crystal with Miller indices (234) and a focal length of 25 cm. The Bragg angle, rocking curve, and reflectivity were determined for three spherically bent samples. A flat crystal was tested as a control to determine the impact of the bending procedure. The experiments were carried out at The National Synchrotron Light Source using photons with an energy of 15.6909 keV, corresponding to the Zr  $K_{\alpha 2}$  line. The lattice  $2d$  spacing for two of the curved samples was determined by the supplier to be  $2d = 1.5827(7)$  Å, corresponding to Bragg and incidence angles, for Zr  $K_{\alpha 2}$  x rays of  $(86.8 \pm 0.5)^\circ$  and  $(3.2 \pm 0.5)^\circ$ , respectively. The incident angle of the third curved sample was directly measured to be  $(2.8 \pm 0.3)^\circ$ , resulting in a Bragg angle of  $(87.2 \pm 0.3)^\circ$  and inferred  $2d = 1.5822(4)$  Å. The peak reflectivity and rocking curve width for the best-performing sample were determined to be  $\sim 4 \times 10^{-4}$  and  $\sim 0.1^\circ$ , respectively. An image of the Zr line emission was obtained using a laser-generated Zr plasma produced by the 10-J Multi-Terawatt laser. The measurement confirmed the peak reflectivity of the crystal for the Zr  $K_{\alpha 2}$  line by using the emitted  $K_{\alpha}$  photon number measured with an absolutely calibrated single-photon-counting spectrometer.<sup>14</sup>

## ACKNOWLEDGMENT

This work was supported by the U.S. Department of Energy Office of Inertial Confinement Fusion under Cooperative Agreement No. DE-FC52-08NA28302, the University of Rochester, and the New York State Energy Research and Development Authority. This work was also supported by the U.S. Department of Energy Office of Fusion Energy Sciences (OFES), Fusion Science Center grant No. DE-FC02-04ER54789, the OFES ACE Fast Ignition grant No. DE-FG02-05ER54839, the Office of Basic Energy Sciences under contract No. DE-AC02-98CH10886, and Brookhaven National Laboratory under LDRD 05-057. The support of DOE does not constitute an endorsement by DOE of the views expressed in this article.

## REFERENCES

1. M. Tabak *et al.*, Phys. Plasmas **1**, 1626 (1994).
2. W. Theobald, A. A. Solodov, C. Stoeckl, K. S. Anderson, R. Betti, T. R. Boehly, R. S. Craxton, J. A. Delettrez, C. Dorrer, J. A. Frenje, V. Yu. Glebov, H. Habara, K. A. Tanaka, J. P. Knauer, R. Lauck, F. J. Marshall, K. L. Marshall, D. D. Meyerhofer, P. M. Nilson, P. K. Patel, H. Chen, T. C. Sangster, W. Seka, N. Sinenian, T. Ma, F. N. Beg, E. Giraldez, and R. B. Stephens, Phys. Plasmas **18**, 056305 (2011).
3. T. R. Boehly, D. L. Brown, R. S. Craxton, R. L. Keck, J. P. Knauer, J. H. Kelly, T. J. Kessler, S. A. Kumpan, S. J. Loucks, S. A. Letzring, F. J. Marshall, R. L. McCrory, S. F. B. Morse, W. Seka, J. M. Soures, and C. P. Verdon, Opt. Commun. **133**, 495 (1997).

4. R. B. Stephens *et al.*, Phys. Rev. E **69**, 066414 (2004).
5. M. H. Key, J. C. Adam, K. U. Akli, M. Borghesi, M. H. Chen, R. G. Evans, R. R. Freeman, H. Habara, S. P. Hatchett, J. M. Hill, A. Heron, J. A. King, R. Kodama, K. L. Lancaster, A. J. MacKinnon, P. Patel, T. Phillips, L. Romagnani, R. A. Snavely, R. Stephens, C. Stoeckl, R. Town, Y. Toyama, B. Zhang, M. Zepf, and P. A. Norreys, Phys. Plasmas **15**, 022701 (2008).
6. L. Jarrott, M. S. Wei, H. Sawada, W. Theobald, A. A. Solodov, C. McGuffey, R. B. Stephens, C. Stoeckl, C. Mileham, F. Marshall, J. Delettrez, R. Betti, P. K. Patel, H. McLean, C. Chen, M. H. Key, T. Doeppner, T. Yabuuchi, T. Iwawaki, H. Habara, A. Greenwood, N. Alfonso, D. Hoover, E. Giraldez, and F. N. Beg, Bull. Am. Phys. Soc. **57**, 115 (2012).
7. W. Theobald, A. A. Solodov, C. Stoeckl, V. Yu. Glebov, S. Ivancic, F. J. Marshall, G. McKiernan, C. Mileham, T. C. Sangster, F. N. Beg, C. Jarrott, E. Giraldez, R. B. Stephens, M. S. Wei, M. H. Key, H. McLean, and J. Santos, Bull. Am. Phys. Soc. **57**, 115 (2012).
8. U. K. Akli, "Fast Ignition Experimental and Theoretical Studies," Ph.D. thesis, University of California at Davis, 2006.
9. J. Delettrez, R. Epstein, M. C. Richardson, P. A. Jaanimagi, and B. L. Henke, Phys. Rev. A **36**, 3926 (1987).
10. K. U. Akli, M. S. del Rio, S. Jiang, M. S. Storm, A. Krygier, R. B. Stephens, N. R. Pereira, E. O. Baronova, W. Theobald, Y. Ping, H. S. McLean, P. K. Patel, M. H. Key, and R. R. Freeman, Rev. Sci. Instrum. **82**, 123503 (2011).
11. Z. Zhong *et al.*, Nucl. Instrum. Methods Phys. Res. A **450**, 556 (2000).
12. M. Sanchez del Rio and R. J. Dejus, in *Advances in Computational Methods for X-Ray and Neutron Optics*, edited by M. Sanchez del Rio (SPIE, Bellingham, WA, 2004), Vol. 5536, pp. 171–174.
13. V. Bagnoud, I. A. Begishev, M. J. Guardalben, J. Puth, and J. D. Zuegel, Opt. Lett. **30**, 1843 (2005).
14. B. R. Maddox *et al.*, Rev. Sci. Instrum. **79**, 10E924 (2008).
15. A. L. Meadowcroft, C. D. Bentley, and E. N. Stott, Rev. Sci. Instrum. **79**, 113102 (2008).

---

# Plasma-Ion-Assisted Coatings for 15-fs Laser Systems

## Introduction

Interest in femtosecond (fs)-pulsed, high-intensity laser facilities continues to grow as evidenced by numerous large laser projects, including the Astra Gemini and Vulcan 10PW lasers at the Rutherford Appleton Laboratory, the Scarlet laser at Ohio State, the planned construction of the Apollon Laser Facility, the Extreme Light Infrastructure (ELI) project, and the planned construction of the Multi-Terawatt Optical Parametric Amplifier Line (MTW-OPAL) laser at the University of Rochester.<sup>1–5</sup> These laser facilities are designed to explore matter interactions with ultra-intense laser sources, necessitating the construction of high-energy, short-pulse lasers with ever-higher peak powers. Optical coatings capable of withstanding such high incident laser intensity must be developed and deposited on substrates at the beam size of these lasers, making it possible to create such laser facilities and achieve the desired laser intensities.

Electron-beam evaporation remains the primary optical coating technology for large-scale lasers, such as those used for inertial confinement fusion (ICF), although most coatings have been used for nanosecond (ns)- and picosecond (ps)-pulse durations.<sup>6–11</sup> The addition of plasma-ion-assisted deposition (PIAD) has also been successfully demonstrated for fabricating coatings for high-power lasers.<sup>12,13</sup> Since these technologies are readily available and have been proven successful in the production of meter-scale, high-laser-damage-threshold coatings, plasma-assisted evaporation has been selected for this development effort of large-aperture optical coatings for 15-fs applications.

Coatings for laser systems that must deliver compressed pulses of less-than-1-ps duration require more-stringent performance criteria than those for longer pulses, based on the wavelength-dependent group delay (GD), the group-delay dispersion (GDD), and higher-order dispersion terms resulting from the reflected phase from the coated surface. Spatial variations in the reflected phase over the optic aperture are particularly challenging since such variations cannot generally be compensated by other components in the laser system. Optical coatings for femtosecond applications require not only a controlled, smooth

GDD over the required bandwidth to maintain the temporal profile of the pulse but also a smooth phase across the optic aperture to provide consistent performance over the beam, so any coating technology pursued must be able to provide such performance over the desired substrate aperture.

This work describes the development of high-laser-damage-threshold coatings for a 15-fs optical parametric chirped-pulse-amplification (OPCPA) laser system having a spectral bandwidth of 810 to 1010 nm using plasma-ion-assisted electron-beam evaporation.<sup>5</sup> The high degree of sensitivity of controlled-phase coating designs requires that the coating performance be independent of relative humidity, thereby creating a need for a densified coating process producing low-porosity films. The use of optical coatings with high-peak-power laser systems necessitates high laser-damage thresholds, limiting potential coating materials and electric-field distributions within the coating structure. In addition, spatial control of phase on reflection for the entire bandwidth is critical to preserving pulse length; coating deposition must be quite uniform, without high-spatial-frequency changes in the reflected phase of the coating. Coating requirements are demonstrated on 10-in. substrates, although the deposition process was designed to be scalable for use on meter-class laser system components, such as those in use at the National Ignition Facility, the Laser MégaJoule Facility, the OMEGA EP Laser System, and other fusion-class lasers.<sup>6–11</sup>

## Background

The primary challenge when depositing coatings for femtosecond pulses is to preserve the compressibility of the temporal pulse. The consequence of a 15-fs temporal pulse is that its physical length is of the order of the thickness of an optical interference coating; in this case, the physical length of a 15-fs pulse would be 4.5  $\mu\text{m}$ , or approximately five wavelengths of light. Each wavelength in the spectral bandwidth has a relative GD when reflecting from a multilayer optical coating, corresponding to the time that particular spectral region remains in the coating, since the interference effects of the coating may occur at different depths in the multilayer for

different wavelengths. In the case of a 15-fs pulse, differences in the delay will lead to a temporal broadening of the pulse since some wavelengths will be reflected from the outer layers of the coating while others will be reflected from farther within the mirror. Through proper design of the coating, adjustments to the delay for different wavelengths may be made, for example, by the use of Gires–Tournois interferometer structure(s), resulting in coatings with positive, negative, or neutral dispersion.<sup>14</sup> Any significant delays incorporated in the optical coating, however, are typically the result of resonant cavities, leading to the amplification of the electric field intensity and likely resulting in a significant reduction in the laser-damage threshold of the coating.<sup>15–18</sup> By properly selecting the coating materials and minimizing the electric-field intensity in the lower-bandgap layers, one can achieve significant improvements in the laser-damage threshold of the coating.<sup>15–20</sup>

The shape of the wavelength-dependent GDD is also an important consideration for pulse compression since low-order phase profiles may be able to be compensated by tuning the combination of the stretcher and compressor in an OPCPA system.<sup>21</sup> Furthermore, GDD ripple of one mirror may be reduced by using another compensating mirror with the inverse ripple in the GDD.<sup>22–24</sup> This requires a systems-level approach for optical coating design since a given GDD magnitude or profile may or may not be acceptable, depending on the other components in the system, and whether the dispersion is purely additive or if there are coatings that cancel accumulated dispersion. Such components, if they contain higher electric-field intensities as a result of resonant cavities, may be placed in positions of low electric-field intensity prior to pulse amplification to offset the dispersive properties of coatings in high-fluence regions of the system.

A primary challenge for the production of coatings for femtosecond applications remains the deposition of such coatings for large-aperture applications, given that most femtosecond coatings are produced by ion-beam or magnetron sputtering.<sup>16,25–27</sup> Precision deposition for large-area coatings is generally performed by electron-beam evaporation as a result of the relative ease of scaling the coating process; while some femtosecond coatings have been demonstrated using evaporation processes, low-dispersion, high-damage-threshold coatings suitable for use in a meter-class laser system have not been thoroughly investigated.<sup>28,29</sup> To maintain acceptable wavefront performance and dispersion characteristics of the coatings, thickness uniformity and thin-film stress must be controlled over the aperture of interest while limiting film defects that may lead to reduced laser-damage thresholds.<sup>13,30–32</sup>

To meet the spectral bandwidth of a coating, a quarter-wave reflector is typically constructed of alternating high- and low-index materials; the width of the reflector at normal incidence is given by

$$\Delta g = \frac{2}{\pi} \sin^{-1} \left( \frac{n_H - n_L}{n_H + n_L} \right), \quad (1)$$

where  $\Delta g$  is the half-width of the reflector in normalized frequency,  $n_H$  is the refractive index of the high-index material, and  $n_L$  is the refractive index of the low-index material.<sup>33</sup> The upper and lower normalized frequency bounds of the reflector are then given by

$$g_{\text{edge}} = 1 \pm \Delta g \quad (2)$$

with the corresponding wavelengths of the reflector edges given by

$$\lambda_{\text{edge}} = \lambda_0 / g_{\text{edge}}. \quad (3)$$

Using coating materials suitable for the visible spectrum and a center wavelength of 910 nm, the width of a reflector using  $n_H = 2.2$  and  $n_L = 1.45$  is insufficient to maintain high reflectance and low GDD for the spectral extent of a 15-fs pulse. At near-normal incidence, the design complexity must become much greater by using multiple reflectors or a geometric stack in order to achieve the desired bandwidth, leading to greater difficulties in obtaining the desired group delay for one spectral region relative to another. To achieve the desired bandwidth, a larger difference in refractive index (which is not available) must be used or the coating must be used in *s*-polarization at oblique incidence since the width of the reflector increases as the incidence angle increases. The use of a greater  $\Delta n$  for the layers of the reflector coating, where  $\Delta n$  is defined as  $n_H - n_L$ , leads to a broader reflectance band for a quarter-wave reflector as does the use of *s*-polarization at higher angles of incidence. As shown in Fig. 136.10, the use of a niobia ( $n_H = 2.20$ )/silica ( $n_L = 1.45$ ) reflector provides a significantly broader reflectance band than if hafnia ( $n = 2.05$ ) is used as the high-index material, although based on the work of Mangote *et al.*, the expected laser-damage resistance is less than half that of hafnia.<sup>20,33</sup>

## Experiment

An initial series of dielectric coatings were prepared in a cryo-pumped, 54-in. coating chamber equipped with quartz heater lamps, dual electron-beam guns, multipoint quartz crystal monitoring, and planetary substrate rotation. Granular

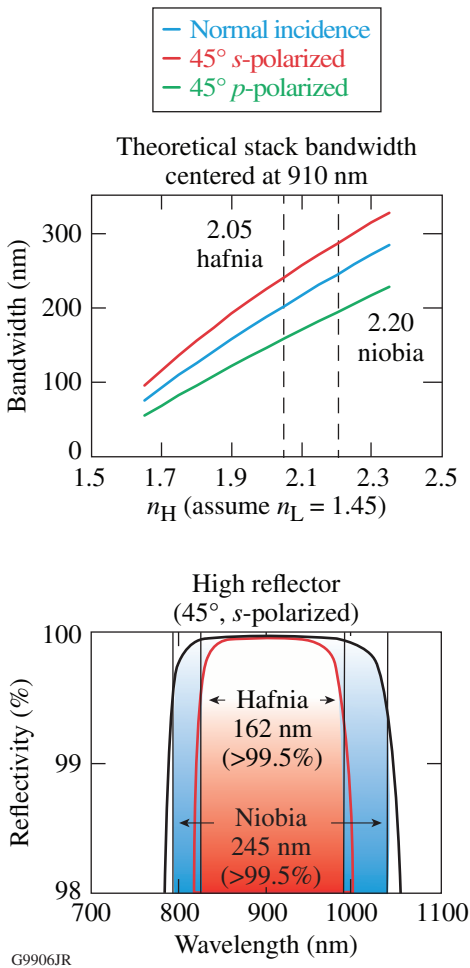


Figure 136.10 (a) Dependence of a high-reflector stack width on  $n_H$ , assuming  $n_L = 1.45$ , for normal and 45°-incidence use. (b) Theoretical width of an  $s$ -polarized reflector at 45° incidence is significantly broader for a niobia/silica coating than for a hafnia/silica coating. Using the reflector in  $s$ -polarization at high incidence angles broadens the reflectance band, while using  $p$ -polarization narrows the usable spectral bandwidth.

silicon dioxide was evaporated from a continuously rotating pan, while niobium, hafnium, silver, copper, and aluminum oxide were deposited from a six-pocket electron-beam gun. A Thin Film Solutions plasma source was installed in the chamber to provide densification and more-complete oxidation of the niobium and hafnium. The plasma source was operated with a beam voltage of 160 V with a 35-A discharge current for deposition of dielectric coatings with an oxygen flow of 55 sccm introduced through the process gas ring above the plasma source. The plasma source was reduced to a 5-A discharge current with no oxygen flow for deposition of metal layers as well as the first 15 nm of alumina deposited over the silver to minimize oxidation of the silver surface.

To meet the required spectral bandwidth using a traditional quarter-wave reflector, different material combinations, angles of incidence, and polarizations were evaluated. For an all-dielectric solution, it was determined that a 45°-incidence,  $s$ -polarized quarter-wave reflector fabricated with refractive indices of 2.20 ( $\text{Nb}_2\text{O}_5$ ) and 1.45 ( $\text{SiO}_2$ ) would be sufficient to meet the 810- to 1010-nm bandwidth with relatively low dispersion effects. Using a high-index material with a refractive index of less than 2.20 would require a greater angle of incidence with a corresponding larger substrate or a more-complex design to broaden the reflectivity while controlling the dispersion properties, typically resulting in higher electric-field intensities and an associated reduction in damage thresholds. To provide broader bandwidths,  $p$ -polarized reflectors, and lower-incidence angles, more-complex dielectric coatings with potentially higher GD, GDD, and electric-field intensity may be considered, or it will become necessary to use coatings based on a metal reflector.

Coating deposition for the all-dielectric coatings was performed at a substrate temperature of 120°C to stabilize the deposition temperature in the presence of heating from the electron-beam guns and plasma source. Niobia and hafnia were deposited at a deposition rate of 0.12 nm/s, silica at 0.4 nm/s, and alumina at 0.2 nm/s. Metal coatings were deposited at ambient temperature, with the only substrate heating resulting from the deposition and plasma sources. Copper was deposited at 1 nm/s, while silver was deposited as quickly as possible for maximum reflectance without ejection of defects from the source, which was determined to be  $\sim 1.8$  nm/s.

The positions of the electron-beam guns and planetary rotation geometry were configured for uniform deposition over the substrate aperture without the use of uniformity masks; the goal was to limit phase discontinuities in the coating resulting from disruptions in the vapor plume caused by uniformity masking.<sup>30,34</sup> A custom planetary rotation was designed and fabricated with three 13-in. planets alternating with three 4-in. planets designed for through-planet optical monitoring as shown in Fig. 136.11. All components were fabricated with precise manufacturing tolerances to ensure minimal thickness errors from differences in planet height or angular tilt with respect to the planet axis of rotation. The smaller-diameter rotation system makes higher revolution speeds possible, ensuring greater averaging of the deposition and a more-uniform coating. Comparable performance could also be achieved by reducing the deposition rate of the dielectric materials if it became necessary to coat larger substrates that could not practically be rotated at such high speeds.

Coating designs of alternating niobia and silica layers were selected to flatten GDD, minimize the standing-wave electric-field intensity, and achieve a compromise between the two goals. The influence of film nonuniformity was also evaluated by theoretically propagating a pulse through a system

containing 25 identical mirrors with 1% uniformity errors. The theoretical performance of the coating designs is shown in Figs. 136.12(a)–136.12(c). Adjustments to the stretcher/compressor angles and distances provide for up to third-order phase-error compensation; consequently, coating designs that

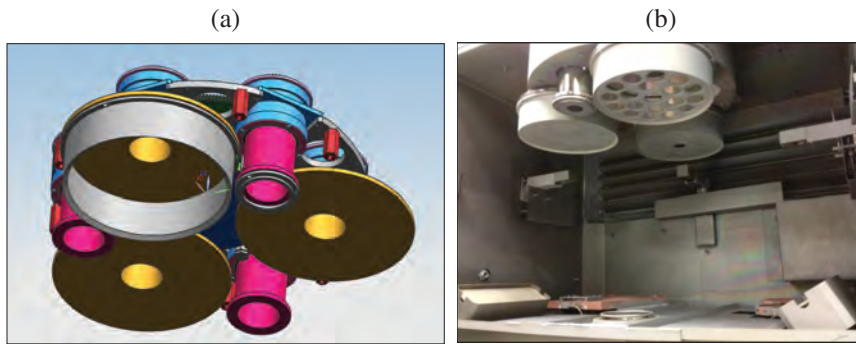
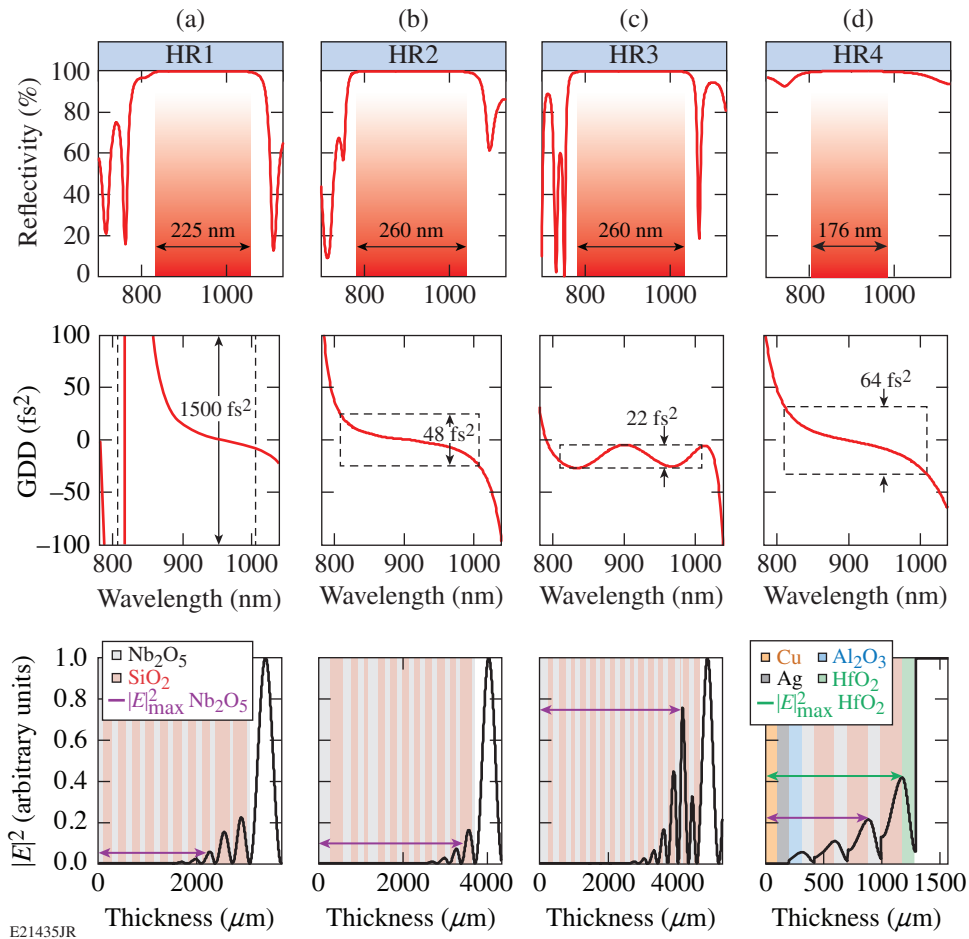


Figure 136.11

(a) Design of a precision planetary rotation system for high-speed rotation of substrates up to 310 mm in diameter, as well as the (b) fabricated rotation installed in a 54-in. coating diameter. Substrate planets alternate with 100-mm planets, making through-planet optical monitoring possible. System geometry is configured for uniform deposition over the substrate aperture without the use of shadow masks.

G9899JR



E21435JR

Figure 136.12

Theoretical reflectance, group-delay dispersion, and standing-wave electric-field intensity within the coating structure for HR1–HR4. Note that HR1–HR3 are for *s*-polarization, while HR4 is for *p*-polarized usage. Reflectance bandwidth is indicated for  $R > 99.5\%$ .

provide a phase-on reflection that closely fits a third-order polynomial are preferred to designs with less dispersion containing higher-order phase terms.<sup>21</sup>

While the all-dielectric design meets the specifications for an *s*-polarized reflector, a *p*-polarized reflector is also required. No low-GDD, all-dielectric design has been identified that is expected to maintain high laser-damage thresholds, owing to the enhanced electric-field intensities within the coating structure required for dispersion control. Instead, an enhanced silver coating was developed, as shown in Fig. 136.12(d). A copper underlayer was incorporated between the substrate and the silver layer to improve environmental durability; the dielectric enhancement layers consist of alumina (adhesion to the silver), niobia/silica (maximum  $\Delta n$  for reflectivity and spectral bandwidth), and hafnia (laser-damage resistance in the highest electric-field intensity).<sup>35</sup> The design for this coating can be expressed as

$$\text{substrate/Cu Ag A (NS)}^3\text{H/air}, \quad (4)$$

where A, N, S, and H represent nominally one quarter-wave optical thickness of alumina, niobia, silica, and hafnia, respectively, and the superscript “3” denotes a repetition of the included layers. The theoretical performance of such a coating meets reflectivity and dispersion requirements, with laser-damage thresholds remaining as the primary concern. For comparison, a protected silver mirror with a nominal half-wave optical thickness of alumina as well as an enhanced silver mirror with two hafnia/silica pairs of enhancement layers were also deposited.

These coatings are being developed for use with a 15-fs pulse having a spectral bandwidth of 810 to 1010 nm; however, a laser-damage test facility with this capability has not been identified. As a result, laser-damage thresholds have been evaluated with a number of different systems, with different center wavelengths, temporal pulse lengths, use environment, and evaluation criteria. The primary testing for femtosecond-coating performance was performed by Lidaris (formerly VULRC, Vilnius University) with an 800-nm laser and a 59-fs pulse. Damage testing was also performed at LLE by systems at 1053 nm with 1-ns, 10-ps, and 0.6-ps pulse durations, with testing at the nanosecond- and picosecond-pulse durations in accordance with the protocols described by Papernov and Howard, respectively.<sup>36,37</sup> In all cases, coating designs were adjusted from a nominal 910-nm center wavelength to center the coating performance at the wavelength being tested. All laser-damage thresholds are reported as the fluence of the inci-

dent beam; i.e., as the coating surface is adjusted to a greater angle of incidence relative to the incident laser, the beam fluence remains constant while the fluence on the surface is decreased by the cosine of the angle of incidence.

Accurate dispersion measurement was also not available at LLE. Sample coatings were evaluated with a beta version of a KMLabs *Chromatis* white-light interferometer for characterizing GDD. Measurements were compared to expected theoretical performance using this system, and further characterization will be pursued as possible. Initial results showed that HR2 and HR3 performed consistent with the theoretical GDD shown in Fig. 136.12, with an estimated measurement accuracy of  $\pm 10 \text{ fs}^2$ .

## Results

Source positions for niobium and silicon dioxide were optimized individually to provide uniform deposition over the substrate aperture by adjusting the radial distance from the chamber center and the source height, with multilayer uniformity evaluated based on the performance of a modified Grezes–Besset stack as described by Baumeister.<sup>38</sup> Optimal source positions were found to be 520 mm from center for niobium with a source-to-substrate distance of 606 mm, while the silica source was located 509 mm from chamber center with a source-to-substrate distance of 584 mm. The slight difference in optimal source position can be attributed to differences in the vapor plume shape of the two materials, as well as the extended size of the silica source relative to the small spot evaporation of the niobium. The multilayer thickness uniformity based on measurements of five samples distributed over a 254-mm aperture was determined to be  $\pm 0.04\%$  by characterizing a best fit of the spectral data in OptiRE shown in Fig. 136.13 (Ref. 39). The uniformity was found to be sensitive to changes in source height of the order of 1 to 2 mm, requiring significant care in the loading of sources particularly for silicon dioxide granules, which were  $\sim 3$  mm in size.

Samples of HR1–HR4 as described in Fig. 136.12 were deposited on 50.8-mm-diam fused-silica substrates. Analysis of the coating performance included simulations of the effects of the coating on a theoretical system containing 25 mirrors, assuming second- and third-order dispersion effects could be compensated by tuning the stretcher/compressor combination. Figure 136.14 shows the impact on the temporal pulse shape assuming a system of 25 identical mirrors for each of the coating designs. HR2 has a moderate amplitude with a low-order dispersion that can be compensated through stretcher/compressor adjustments.

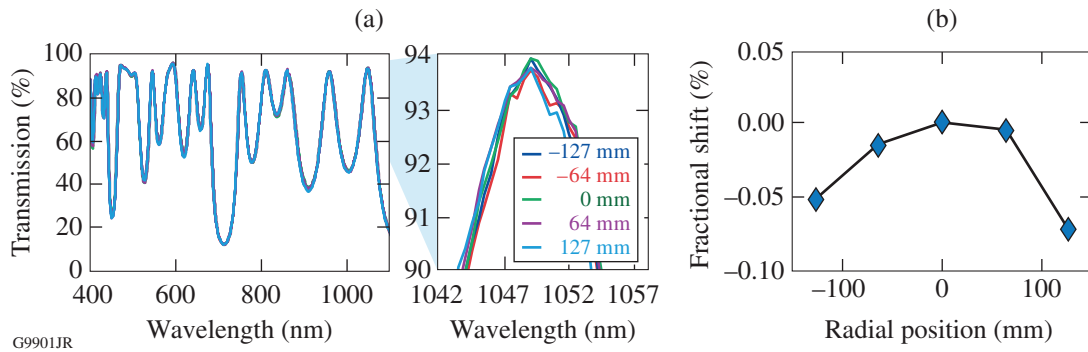


Figure 136.13 Measured thin-film uniformity over a 254-mm aperture based on system geometry. (a) Overlay of the spectral transmittance shows a negligible variation in coating performance among the samples. (b) Curve fitting and normalization of film thickness indicate film nonuniformity is of the order of  $\pm 0.04\%$ . Thickness variations are slowly varying, with minimal phase errors since the film deposition is continuous with no shadow masks between the source and substrate.

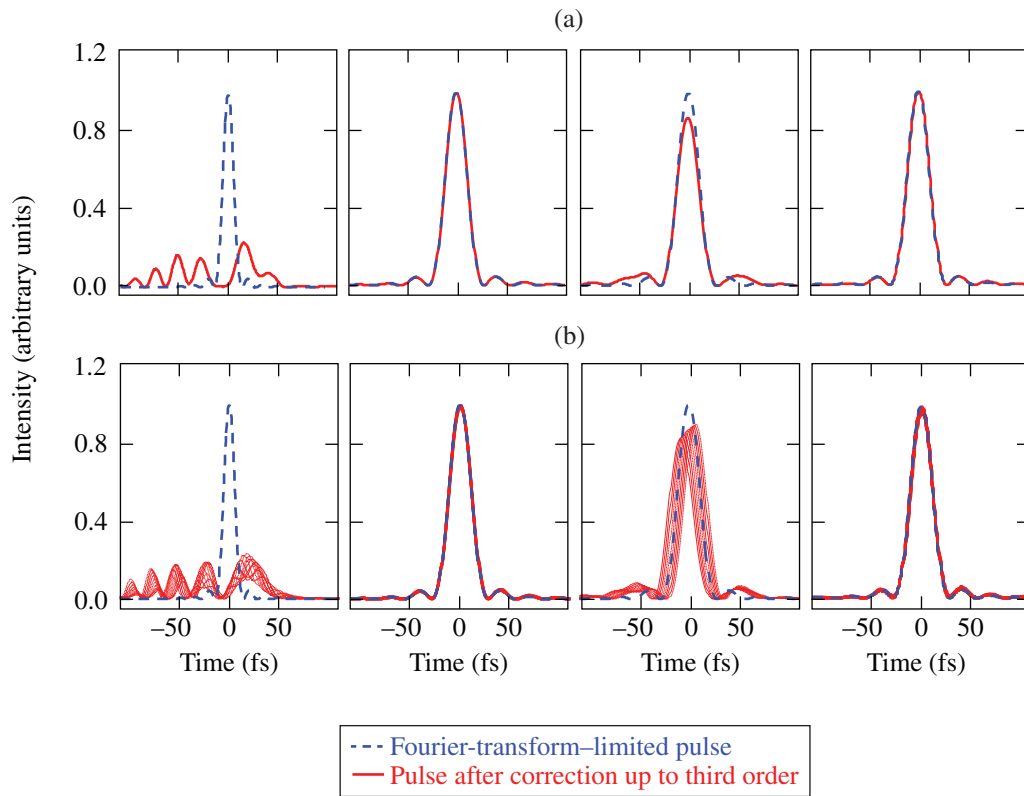


Figure 13.14 Impact on the temporal pulse shape for a theoretical system containing 25 mirrors of HR1, HR2, HR3, and HR4. The second- and third-order phase error resulting from dispersion is removed, based on the assumption that such error can be compensated by stretcher/compressor tuning. The performance in (a) is based strictly on the dispersion of the mirrors, while (b) assesses the impact of 1% film thickness nonuniformity over the mirror aperture.

Laser-damage testing by Lidaris at 59 fs required deposited coatings that were spectrally centered at an 800-nm wavelength to align with the test capability. The nominal  $S:1$  laser-damage thresholds (beam fluence) of HR1, HR2, and HR3 were measured to be  $1.64 \text{ J/cm}^2$ ,  $1.16 \text{ J/cm}^2$ , and  $0.12 \text{ J/cm}^2$ , respectively,

indicating a strong correlation with the maximum electric-field intensity in the niobia layers, as shown in Fig. 136.15. Based on the work of Mero *et al.*, it is expected that use with a 15-fs pulse will result in a reduction of the damage threshold of approximately  $1/3$ , using a  $\tau^{0.3}$  scaling law.<sup>40</sup>

The laser-damage threshold of the enhanced silver coating HR4 is also shown in Fig. 136.15, with its performance at  $0.69 \text{ J/cm}^2$  remaining consistent with that of HR1–HR3 based on the electric-field intensity in the outer high-index layers. Note that the damage threshold of HR4 is higher than expected [above the dashed line in Fig. 136.15(b)] based on the electric-field intensity in the outermost layer, which is hafnia, but this would correspond to the larger bandgap of hafnia relative to that of niobia in HR1–HR3, in agreement with the findings of Mangote *et al.*<sup>20</sup>

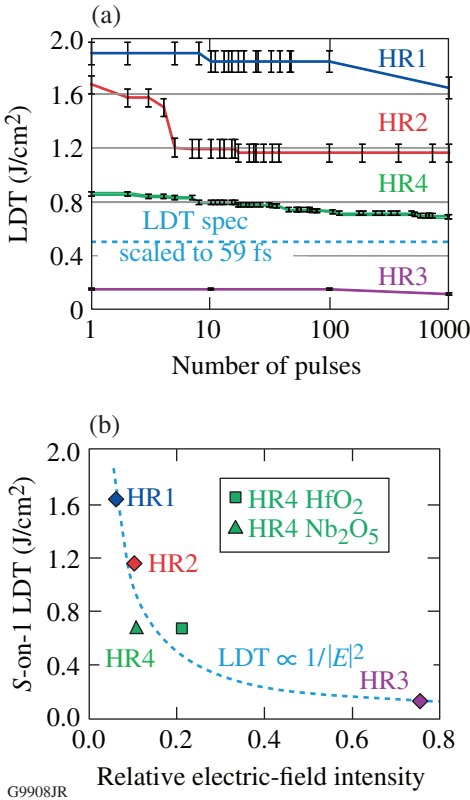


Figure 136.15 (a) Laser-damage thresholds (LDT's) of HR1–HR4 as tested by Lidaris using a 59-fs pulse with a center wavelength of 800 nm. (b) The performance of each coating is consistent with its relative electric-field intensity in the air-side high-index layer, indicating the damage is driven by the low electronic bandgap of the high-index material. Manipulation of the relative intensity of the electric field provides higher damage thresholds in HR1 and HR2.

Based on the performance of HR4 as a *p*-polarized reflector and the inherent broad reflectance and low GDD, two additional silver-based coatings were evaluated. Evaporated Cu/Ag metallic coatings were overcoated with a half-wave optical thickness of alumina (substrate/Cu Ag 2A/air) as well as enhanced with two dielectric pairs of layers (substrate/Cu Ag AHSH/air),

where A, H, and S are as defined previously. As the number of layer pairs in the dielectric overcoat is reduced, the reflectivity, in general, is decreased but the GDD is improved, approaching  $0 \text{ fs}^2$  for a layer of bare silver. As shown in Fig. 136.16, the laser-damage performance of the silver mirrors remains similar, with HR4 shown to have the lowest average damage threshold of the three mirror designs. As additional dielectric enhancement layers are added, the electric-field intensity at the silver layer is reduced, with an expected improvement in laser-damage threshold; since the hafnia-overcoated metal mirrors consistently have the highest laser-damage threshold, it appears the damage threshold remains a function of the bandgap of the high-index dielectric layer and not the metallic layers beneath.

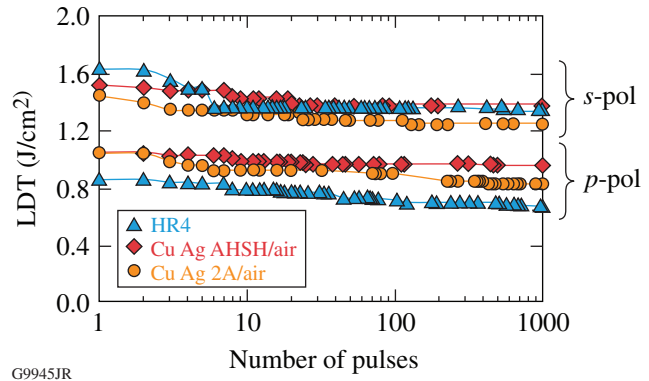


Figure 136.16 Laser-damage thresholds of silver-based mirrors as tested by Lidaris using a 59-fs pulse with a center wavelength of 800 nm. Damage thresholds for *s*-polarization remain consistently higher than those for *p*-polarization.

This work is intended for use over large apertures, with initial coating requirements for a 254-mm aperture, and ultimate potential needs of the order of a 1-m aperture. Based on the results above concerning temporal pulse shape and laser-damage threshold, HR2 was selected for demonstration on a larger-aperture substrate. The coating was deposited on a 310-mm-diam by 14-mm-thick fused-silica substrate, with a surface deviation of less than  $\lambda/10$  from flat. The primary concerns for scale-up include spatial irregularities in the reflected phase leading to variations in GDD and surface flatness, with minimal variation in reflectivity assured, given the measured film-thickness nonuniformity. The HR2 coating was deposited and the reflected wavefront performance was measured on an 18-in. phase-shifting Zygo interferometer operating at 1064 nm. The wavefront performance is shown in Fig. 136.17.

The optical power of 1.76 waves at 1064 nm, as measured in Fig. 136.17(b), corresponds to a thin-film stress of the order of 150 MPa based on Stoney's equation. A flatter coated surface

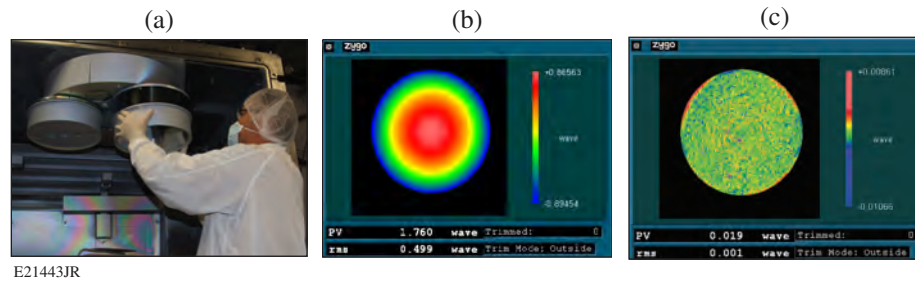


Figure 136.17

(a) The deposition process was demonstrated on a 310-mm-diam substrate, with (b) the flatness of the coated substrate in  $\sim 150$  MPa of thin-film stress. (c) Removal of the stress-induced surface deformation results in a remaining spatial phase error of a random speckle pattern below the resolution of the interferometer.

may be realized by increasing the substrate thickness or depositing a compensating coating on the rear surface of the optic. As shown in Fig. 136.17(c), removing the stress-induced power and astigmatism from the wavefront map leads to a wavefront error indistinguishable from the noise of the interferometer resolution, with no discernible pattern indicative of spatial phase error from the substrate rotation, shadows, or other irregularities in the coating process. This shows that the deposition process provides a smooth optical phase-on reflection suitable for use with femtosecond optical pulses.

**Future Work**

Development of improved high-reflector coating designs is continuing, based on minimizing the electric-field intensity in high-refractive-index layers, maximizing the electronic bandgap of all coating materials in regions of high electric-field intensity, and controlling GDD as possible with metallic layers. Magnetron sputtering of metallic coatings will be evaluated as a means of limiting film defects for silver and copper deposition.

Remaining optical-coating challenges to be demonstrated for construction of the MTW-OPAL laser include a beam combiner/separator for the pump and signal beams as they enter and exit the nonlinear crystals for amplification of the signal pulse. To minimize the impact on GDD, a configuration transmitting the signal and reflecting the 527-nm pump laser has been selected for this dichroic filter. Operating at Brewster’s angle for a *p*-polarized signal beam and an *s*-polarized pump beam eliminates the need for a second-surface antireflection coating. In addition, a filter is also required to reject the idler beam (1100 to 1505 nm) resulting from the parametric amplification process. Since the signal must again be propagated without negatively impacting the spectral phase, a transmissive coating design was selected for this application, with the idler being reflected at  $56^\circ$  incidence in *s*-polarization, in order to provide a sufficiently broad spectral width of the reflectance

band and to reject the full spectrum of the idler beam. Measured performance of current demonstrations of these coatings is shown in Fig. 136.18, with both coating designs having a

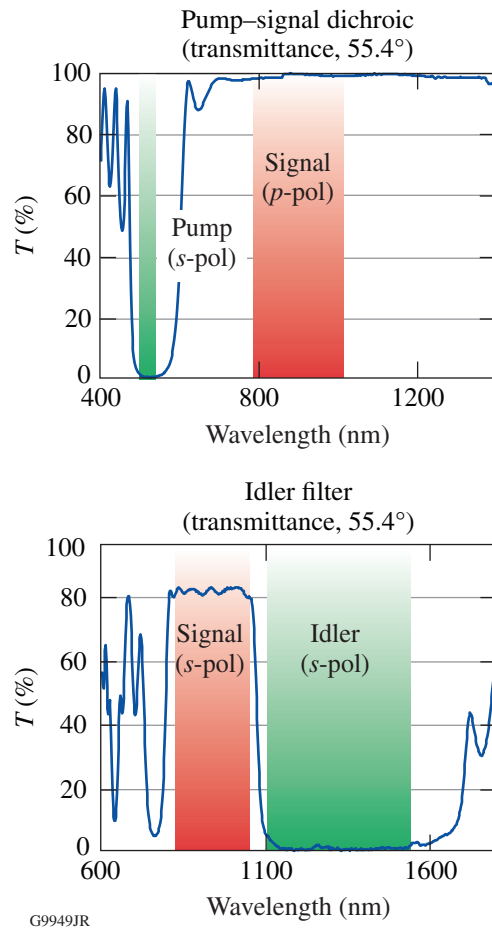


Figure 136.18

(a) Filters for the pump-signal combiner/seperator and (b) removal of the idler from the co-propagating signal beam. Performance of both filter types has been successfully demonstrated for small apertures.

negligible impact on the theoretical GDD of the signal beam in transmission.

A final challenge is the deposition of a reflective coating for the final focusing optic. As the pulse is focused onto target, the beam will be full fluence with a compressed, 15-fs pulse. Dispersion and nonlinear refractive index of optical glasses necessitates the use of a reflective focusing optic, although a radially dependent GD and GDD resulting from coating nonuniformity over the curved substrate surface may lead to broadening of the temporal pulse at the focus if a dielectric interference coating is used. Metallic coatings may not possess a sufficiently high laser-damage threshold for the highest-fluence region of the optical system. At this time, modifying the radial source position within the overall system geometry is being pursued to match the coating-thickness distribution over the curvature of the substrate surface. Current models indicate adjustments in source position relative to chamber center are sufficient to compensate expected film nonuniformity caused by substrate curvature. This will be pursued further once an optical system design has been completed for MTW-OPAL, specifying the dimensions and curvature of the final focusing optic.

### Conclusions

A process for producing plasma-assisted evaporated coatings with high reflectivity, high laser-damage thresholds, and controlled dispersion over large apertures has been developed. Demonstrated performance of an all-dielectric solution for a 45°-incidence, *s*-polarized reflector over a range of 810 to 1010 nm includes  $R > 99.5\%$ , a laser-damage threshold of  $>1.1 \text{ J/cm}^2$  (coating design shifted to be centered at 800 nm and tested with a 59-fs pulse), and a low-order (correctable) GDD  $< 50 \text{ fs}^2$ . It has been shown that laser-damage performance depends on the maximum electric-field intensity in the high-refractive-index layers, with improved performance for larger-bandgap high-index materials, such as hafnia. Film-thickness nonuniformity is less than 0.1% over a 254-mm aperture, with spatial phase errors remaining well controlled, successfully limiting the spatial-dependent mirror dispersion. Such a coating is suitable for the propagation of 15-fs pulses with negligible degradation of the transform-limited pulse shape, based on temporal modeling with stretcher/compressor compensation.

Near-normal incidence and 45°-incidence, *p*-polarized reflectors have been demonstrated using protected and enhanced silver coatings. The dispersion performance of an enhanced silver coating is much better than that of the all-dielectric solution, with comparable reflectivity; while *p*-polarized damage thresholds are lower, *s*-polarized performance of

the metallic coatings is comparable or better than that shown by the all-dielectric films. The performance achieved is readily scaled from the 254-mm aperture demonstrated to larger optics, using plasma-assisted evaporation coating systems.

### ACKNOWLEDGMENT

This material is based upon work supported by the Department of Energy National Nuclear Security Administration under Award Number DE-NA0001944, the University of Rochester, and the New York State Energy Research and Development Authority. The support of DOE does not constitute an endorsement by DOE of the views expressed in this article.

### REFERENCES

1. O. Chekhlov *et al.*, in *High Power Lasers for Fusion Research II*, edited by A. A. S. Awwal (SPIE, Bellingham, WA, 2007), Vol. 6735, Paper 67350J.
2. J. P. Chambaret *et al.*, in *Solid State Lasers and Amplifiers IV, and High-Power Lasers*, edited by T. Graf *et al.* (SPIE, Bellingham, WA, 2010), Vol. 7721, Paper 77211D.
3. G. Overton, *Laser Focus World* **48**, 15 (2012).
4. G. A. Mourou *et al.*, *Plasma Phys. Control. Fusion* **49**, B667 (2007).
5. J. Bromage, C. Dorrer, M. Millecchia, J. Bunkenburg, R. Jungquist, and J. D. Zuegel, in *Conference on Lasers and Electro-Optics 2012*, OSA Technical Digest (online) (Optical Society of America, 2012), Paper CTh1N.7.
6. J. H. Campbell *et al.*, in *Optical Engineering at the Lawrence Livermore National Laboratory II: The National Ignition Facility*, edited by M. A. Lane and C. R. Wuest (SPIE, Bellingham, WA, 2004), Vol. 5341, pp. 84–101.
7. J. B. Oliver, J. Howe, A. Rigatti, D. J. Smith, and C. Stolz, in *Optical Interference Coatings*, OSA Technical Digest Series (Optical Society of America, Washington, DC, 2001), Paper ThD2.
8. B. Pinot *et al.*, in *Laser-Induced Damage in Optical Materials 2001*, edited by G. J. Exarhos *et al.* (SPIE, Bellingham, WA, 2002), Vol. 4679, pp. 234–241.
9. E. Lavastre *et al.*, in *Optical Interference Coatings*, OSA Technical Digest Series (Optical Society of America, Washington, DC, 2004), Paper TuF3.
10. J. B. Oliver, T. J. Kessler, H. Huang, J. Keck, A. L. Rigatti, A. W. Schmid, A. Kozlov, and T. Z. Kosc, in *Laser-Induced Damage in Optical Materials: 2005*, edited by G. J. Exarhos *et al.* (SPIE, Bellingham, WA, 2005), Vol. 5991, Paper 59911A.
11. J. Bellum *et al.*, in *Laser-Induced Damage in Optical Materials: 2009*, edited by G. J. Exarhos *et al.* (SPIE, Bellingham, WA, 2009), Vol. 7504, Paper 75040C.
12. R. Thielsch *et al.*, *Thin Solid Films* **410**, 86 (2002).
13. J. B. Oliver, P. Kupinski, A. L. Rigatti, A. W. Schmid, J. C. Lambropoulos, S. Papernov, A. Kozlov, J. Spaulding, D. Sadowski,

- Z. R. Chrzan, R. D. Hand, D. R. Gibson, I. Brinkley, and F. Placido, *Appl. Opt.* **50**, C19 (2011).
14. R. Szipöcs *et al.*, *Opt. Lett.* **19**, 201 (1994).
  15. C. K. Carniglia *et al.*, in *Laser Induced Damage in Optical Materials: 1983*, edited by H. E. Bennett *et al.*, Natl. Bur. Stand. (U.S.), Spec. Publ. 688 (U.S. Government Printing Office, Washington, DC, 1985), pp. 347–353.
  16. K. Starke, T. Groß, and D. Ristau, in *Laser-Induced Damage in Optical Materials: 2000*, edited by G. J. Exarhos *et al.* (SPIE, Bellingham, WA, 2001), Vol. 4347, pp. 528–534.
  17. S. Chen *et al.*, *Appl. Opt.* **51**, 6188 (2012).
  18. J. H. Apfel, *Appl. Opt.* **16**, 1880 (1977).
  19. J. B. Oliver, S. Papernov, A. W. Schmid, and J. C. Lambropoulos, in *Laser-Induced Damage in Optical Materials: 2008*, edited by G. J. Exarhos *et al.* (SPIE, Bellingham, WA, 2008), Vol. 7132, Paper 71320J.
  20. B. Mangote *et al.*, *Rev. Sci. Instrum.* **83**, 013109 (2012).
  21. S. Kane and J. Squier, *J. Opt. Soc. Am. B* **14**, 1237 (1997).
  22. F. X. Kärtner *et al.*, *J. Opt. Soc. Am. B* **18**, 882 (2001).
  23. F. X. Kärtner *et al.*, U.S. Patent No. US6,590,925 B1 (8 July 2003).
  24. V. Pervak *et al.*, *Opt. Express* **17**, 7943 (2009).
  25. F. X. Kärtner *et al.*, *Opt. Lett.* **22**, 831 (1997).
  26. V. Pervak *et al.*, *Opt. Express* **16**, 10220 (2008).
  27. V. Pervak *et al.*, in *Advances in Optical Thin Films II*, edited by C. Amra, N. Kaiser, and H. A. Macleod (SPIE, Bellingham, WA, 2005), Vol. 5963, Paper 59631P.
  28. M. Bischoff *et al.*, in *Advances in Optical Thin Films II*, edited by C. Amra, N. Kaiser, and H. A. Macleod (SPIE, Bellingham, WA, 2005), Vol. 5963, Paper 59631N.
  29. Z. Jinlong *et al.*, *Appl. Opt.* **50**, C388 (2011).
  30. J. B. Oliver and D. Talbot, *Appl. Opt.* **45**, 3097 (2006).
  31. C. J. Stolz *et al.*, in *27th Annual Boulder Damage Symposium: Laser-Induced Damage in Optical Materials: 1995*, edited by H. E. Bennett *et al.* (SPIE, Bellingham, WA, 1996), Vol. 2714, pp. 374–382.
  32. C. J. Stolz, M. D. Feit, and T. V. Pistor, *Appl. Opt.* **45**, 1594 (2006).
  33. H. A. Macleod, *Thin-Film Optical Filters*, 4th ed., Series in Optics and Optoelectronics, edited by E. R. Pike and R. G. W. Brown (CRC Press, Boca Raton, FL, 2010), pp. 222–223.
  34. S. K. Yao, *J. Appl. Phys.* **50**, 3390 (1979).
  35. D.-Y. Song *et al.*, *Appl. Opt.* **24**, 1164 (1985).
  36. S. Papernov and A. W. Schmid, *J. Appl. Phys.* **82**, 5422 (1997).
  37. H. P. Howard, A. F. Aiello, J. G. Dressler, N. R. Edwards, T. J. Kessler, A. A. Kozlov, I. R. T. Manwaring, K. L. Marshall, J. B. Oliver, S. Papernov, A. L. Rigatti, A. N. Roux, A. W. Schmid, N. P. Slaney, C. C. Smith, B. N. Taylor, and S. D. Jacobs, *Appl. Opt.* **52**, 1682 (2013).
  38. P. Baumeister, *Optical Coating Technology* (SPIE Optical Engineering Press, Bellingham, WA, 2004), pp. 9-56–9-57.
  39. A. V. Tikhonravov and M. K. Trubetskov, OptiLayer Thin Film Software, Optilayer Ltd., <http://www.optilayer.com> (9 June 2005).
  40. M. Mero *et al.*, *Phys. Rev. B* **71**, 115109 (2005).

---

# Spectral and Temporal Properties of Optical Signals with Multiple Sinusoidal Phase Modulations

## Introduction

High-energy laser systems have been developed for exploring regimes of high-intensity interaction of light with matter, e.g., plasma physics, astrophysics, and the generation of particles. One application of these lasers is inertial confinement fusion (ICF)—a strategy for producing energy by compressing and heating capsules filled with hydrogen isotopes and igniting fusion reactions that release a large number of energetic neutrons.<sup>1,2</sup> Laser systems developed for ICF are large-scale complex optical systems that must produce temporally shaped optical pulses containing megajoules of energy in the ultraviolet (UV).<sup>3,4</sup> The laser–target interaction is an intensity-dependent process that requires the time-dependent power of the optical pulses to be precisely shaped. Temporal phase modulation must be added to prevent damage to the laser system and smooth out intensity variations at the surface of the target. High-intensity narrowband optical waves lead to stimulated Brillouin scattering (SBS) in optical components with potentially catastrophic consequences.<sup>5</sup> The growth of SBS waves is inhibited by increasing the bandwidth of the optical wave, typically by phase modulation in the low-energy front end to generate multiple sidebands. Phase modulation at a few GHz's with index modulation sufficient to create approximately ten sidebands is used on systems like the National Ignition Facility (NIF) and the Laser Mégajoule Facility (LMJ).<sup>5–7</sup> Uniform compression of the target is required to reach the conditions for fusion in the target core, but such compression is hindered by instabilities.<sup>8</sup> Smoothing by spectral dispersion (SSD) reduces the fluence variations of individual beams to produce a target irradiation that is spatially uniform on a time-averaged basis.<sup>9–11</sup> SSD uses temporal phase modulation to induce a time-dependent instantaneous frequency on the optical pulse. A phase plate placed before the focusing component at the end of the laser system creates a highly modulated far field composed of speckles.<sup>12</sup> A diffractive component in the laser system ensures that the far-field position depends on the optical frequency. The combination of time-varying instantaneous frequency, frequency-dependent far-field position, and highly modulated far field is used to obtain a uniform target illumination when averaged over the duration of the optical pulse. The NIF and the LMJ were built for indirect

drive—an approach to ICF where the target is compressed by x rays generated when the optical pulses interact with the walls of a hohlraum.<sup>1</sup> In this approach, phase modulation at a single frequency with a modulation index of a few radians is sufficient for SSD when implemented with angular dispersion in only one direction. In the direct-drive approach to ICF, the optical pulses directly compress the target.<sup>2</sup> If SSD is implemented in only one direction, modulation at multiple frequencies is required, at least during the low-energy portion of the pulse shape.<sup>11,13</sup> Theoretical studies and experimental demonstration of a system combining pulses with three high-frequency phase modulations and pulses with SBSS (SBS suppression) and single-frequency SSD have been performed.<sup>14–16</sup> Optical pulses with multiple temporal phase modulations are routinely used on these high-energy laser facilities for reducing the threat of SBS and optimizing the target illumination by SSD.

A known issue when using phase-modulated optical pulses is the conversion of frequency modulation to amplitude modulation (FM-to-AM conversion).<sup>7,17–19</sup> A pulse of constant power with a single sinusoidal temporal phase modulation at frequency  $f$  has spectral sidebands at frequencies separated by  $f$  with spectral density given by Bessel functions of the first kind and precise phase relations.<sup>20</sup> When the spectral amplitude and/or phase of these sidebands are modified, the power becomes time dependent, e.g., it has a sinusoidal modulation at frequency  $f$ . A modification of the time-varying power of the shaped pulse might be detrimental to the interaction of the pulse with the target. It can also lead to optical damage in the laser system by increasing the peak power beyond the damage threshold of optical components. Sources of FM-to-AM conversion include chromatic dispersion, wavelength-dependent gain of laser amplifiers, generation of low-energy replicas interfering with the main signal, and spectral clipping. Studies of FM-to-AM conversion in pulses with a single phase modulation are available in the literature. Examples of FM-to-AM conversion of signals with SBSS at 2 GHz and SSD at 14.25 GHz have been presented in the context of the LMJ,<sup>7</sup> but no general study for pulses with multiple phase modulation (multi-FM) has been published. This study is highly relevant to the operation of cur-

rent systems and engineering of future systems because these systems typically use phase modulation at multiple frequencies.

This article first presents a statistical study of the optical spectrum of multi-FM signals. The optical spectrum of these signals is shown to converge to a normal distribution using an analogy with the statistical properties of the probability density function of the sum of independently distributed variables, which allows one to use the central limit theorem. Convergence of the frequency integral of the spectral density to the cumulative density function of the normal distribution makes it possible to predict the frequency range containing a given fraction of the total energy. The statistical study is followed by general derivations of FM-to-AM conversion in optical signals with multiple phase modulations from linear and quadratic spectral amplitude modulation, for example, resulting from spectral filters and optical amplifiers and from quadratic and cubic spectral phase modulations, for example, caused by chromatic dispersion in optical fibers in the front end. These impairments are inherently present in high-energy laser systems because of their architecture and component availability. Compensation subsystems must be developed so that the transfer function of the entire laser system does not lead to FM-to-AM conversion. These compensators are, for example, Lyot-type filters that compensate for the gain narrowing in a Nd:glass amplifier and a grating compressor that compensates for chromatic dispersion.<sup>6,16</sup> The design and performance of these subsystems are intrinsically linked to understanding the modulation magnitude in critical parts of the system where optical damage might occur. FM-to-AM conversion caused by the nonlinear frequency conversion from the infrared to the ultraviolet is not treated but could be the subject of further studies based on what is already known for single-frequency modulation.<sup>7,18,19,21</sup> FM-to-AM conversion from free-space propagation close to image planes of the diffraction grating used for SSD is described by a quadratic spectral phase<sup>7,14</sup> and can be treated with the same formalism. Another source of FM-to-AM conversion in high-energy laser systems is the interference of multiple replicas of the main pulse generated during amplification in the fiber front end.<sup>17,22</sup> This is inherent to the propagation of polarized signals in polarization-maintaining optical fibers having a finite extinction ratio, but the associated AM can be significantly reduced via engineering, in particular using optical fibers that transmit light along only one well-defined polarization<sup>17</sup> or alternating the orientation of the fast and slow axes of the optical fibers.<sup>22</sup>

For the impairments considered in this article, the amplitude modulation is evaluated by two metrics without frequency

resolution: peak-to-valley (PV) and root-mean-square (rms) modulation on the temporal pulse, and by the PV modulation at specific frequencies. The specific frequencies are the individual modulation frequencies  $f_n$  in the case of linear amplitude modulation and quadratic phase modulation. They are the sums and differences of modulation frequencies  $f_i \pm f_j$  for quadratic amplitude modulation and cubic phase modulation. Evaluating the amplitude modulation on the temporal pulse is crucial to setting allowable limits for individual impairments. Evaluating the modulation at specific frequencies helps to interpret time-resolved measurements provided by high-bandwidth diagnostics. Bandwidth-limited measurements of the instantaneous power can be interpolated at high frequencies not measured by the diagnostic. It is conceivable that limiting impairments can be identified from the spectral signature of the measured relative modulations at different frequencies.

The following sections (1) present general notations and definitions; (2) present a statistical approach to predicting the spectrum of signals with multiple sinusoidal phase modulations and frequency intervals containing a given fraction of the total energy; (3) describe FM-to-AM conversion in the presence of linear amplitude modulation and quadratic phase modulation, which leads to amplitude modulation at the phase-modulation frequencies; (4) detail FM-to-AM conversion in the presence of quadratic amplitude modulation and cubic phase modulation, which leads to amplitude modulation at combinations of the phase-modulation frequencies; and (5) present additional considerations and conclusions.

## General Considerations

### 1. Definitions

An initially monochromatic field at the frequency  $\omega_0$  is modulated at multiple microwave frequencies  $f_j = \Omega_j / 2\pi$  with respective modulation index  $m_j$ . For simplification, the oscillating term resulting from  $\omega_0$ , present in all the temporal fields, is not written, and spectral fields are consistently plotted after translation by  $\omega_0$ ; i.e., with a zero carrier frequency. The phase modulations are co-phased at  $t = 0$  for the derivation of FM-to-AM conversion. One reason for doing so is that for a small number of modulation frequencies, one can identify a time around which the sinusoidal modulations are co-phased, i.e., reach a maximum. This is justified by the absence of correlation for the values of sinusoidal modulations at non-commensurate frequencies. As such, the probability that one reaches a maximum around a given time is uncorrelated to the probability that the others reach a maximum around the same time, and the probability that they are all within some range of their maximal value at a given time is the product of the

individual probability, which is nonzero. Various simulations with co-phasing and with random relative phases on monochromatic fields have led to similar results, and the relative phase of the uncorrelated sinusoidal modulations generally does not play a significant role when calculating the overall amplitude modulation in a PV and rms sense. When using a pulse of finite duration, the relative phases of the temporal phase modulations and their timing relative to the power of the pulse play a role, e.g., the maximum PV modulation might not be reached over the finite time interval where the pulse power is nonzero. The derivations presented here correspond to a worst-case scenario, where the amplitude modulations are considered over a very large temporal range. With these conventions, the temporal field is simply written as

$$E(t) = \exp \left[ i \sum_j m_j \cos(\Omega_j t) \right]. \quad (1)$$

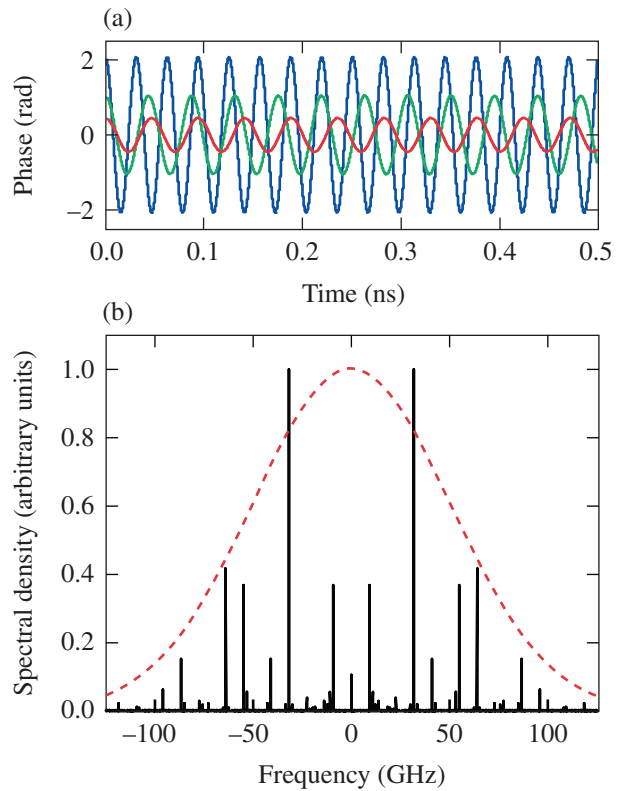
## 2. Parameters for Derivations and Simulations

The analytical derivations are performed for an arbitrary number of noncommensurate microwave frequencies of arbitrary modulation index with impairments leading to a small change in the electric field of the optical pulse, i.e., inducing a small amplitude modulation. This is the useful range for application to high-energy lasers since the impairments and amplitude modulation must be minimized. Signals with commensurate frequencies have been studied in the context of providing a uniform spectral density over a given bandwidth, but the resulting on-target smoothing might be impacted by resonances.<sup>23</sup> These signals should be the subject of a separate study if they find an application for beam smoothing. Simulations have been performed with the parameters defined in Ref. 16 for the so-called picket channel. The corresponding frequencies and modulation indices are given in Table 136.III and a detail of the phase modulations is shown in Fig. 136.19(a). The optical signal obtained by phase modulation with these parameters is called the “test signal” for the remainder of this

Table 136.III: Characteristics of the phase modulations used for simulations. All frequencies are multiples of the reference frequency  $f_{\text{ref}} = 37.998935$  MHz.

Modulation	Frequency (GHz)	Multiple of $f_{\text{ref}}$	Modulation index (rad)
Multi-FM-1	$f_1 = 21.165$	557	0.45
Multi-FM-2	$f_2 = 22.837$	601	1.04
Multi-FM-3	$f_3 = 31.881$	839	2.07

article. These parameters were determined by simulations to optimize the on-target smoothing, including the engineering constraints related to potential implementation on the NIF.<sup>13</sup> Small relative changes to these frequencies would not affect the smoothing, but they have been chosen as multiples of a reference clock available at the Omega Laser Facility because this allows them to be temporally synchronized to the optical pulse. The microwave frequencies are commensurate, but the integer multiples linking them are so large that no effect of commensurability has been observed in simulations. The resulting optical spectrum is shown in Fig. 136.19(b). A Gaussian spectral density with an identical rms bandwidth (50 GHz) has been plotted, as discussed in the next section.



E22665JR

Figure 136.19

(a) Phase modulations used for simulations with parameters given in Table 136.III ( $f_1$ ,  $f_2$ , and  $f_3$  plotted in red, green, and blue, respectively). (b) Optical spectrum resulting from these phase modulations applied to a monochromatic field (black solid line) and Gaussian spectrum with identical root mean square (rms) bandwidth (red dashed line).

The considered spectral impairments are linear amplitude modulation (parameter  $l$ ), quadratic amplitude modulation (parameter  $q$ ), quadratic phase modulation (parameter  $\varphi_2$ ), and cubic phase modulation (parameter  $\varphi_3$ ), with transfer function given, respectively, by

$$\tau(\omega) = \sqrt{1 + l\omega}, \quad (2)$$

$$\tau(\omega) = \sqrt{1 + q\omega^2}, \quad (3)$$

$$\tau(\omega) = \exp(i\varphi_2\omega^2/2), \quad (4)$$

$$\tau(\omega) = \exp(i\varphi_3\omega^3/6). \quad (5)$$

The range of impairment parameters for simulations was arbitrarily chosen between 0 and a maximal value calculated so that for amplitude impairments, the magnitude of the transfer function reaches the value 1.2 at  $f = 100$  GHz and for phase impairments, the phase of the transfer function reaches the value 0.2 rad at  $f = 100$  GHz. The parameters  $l$ ,  $q$ ,  $\varphi_2$ , and  $\varphi_3$  are chosen positive to simplify the equations.

### Spectrum and Bandwidth of Signals with Multiple Phase Modulations

#### 1. Spectrum and Bandwidth of Signal with Single Phase Modulation

Signals with a single temporal phase modulation are widely used in telecommunications and their spectral properties are well documented.<sup>20</sup> The optical spectrum of a signal with phase modulation at frequency  $\Omega$  with index  $m$  is composed of discrete sidebands at the frequencies  $n\Omega$  and power given by the Bessel function of the first kind  $|J_n(m)|^2$ . According to Carson's rule, 98% of the energy is contained in the bandwidth

$$BW_{98\%} = 2(m + 1)\Omega. \quad (6)$$

Knowledge of the spectral properties of signals with multiple phase modulations can be obtained using statistical arguments, as shown in this section. One approach for obtaining an operational definition of the bandwidth of these signals is to use the bandwidth of the spectrum  $S(\omega, m, \Omega) = |\tilde{E}(\omega, m, \Omega)|^2$  in the rms sense,

$$BW_{\text{rms}}(m, \Omega) = \sqrt{\int \omega^2 S(\omega, m, \Omega) d\omega / \int S(\omega, m, \Omega) d\omega}, \quad (7)$$

which can be expressed using the properties of the Fourier transform as

$$BW_{\text{rms}}(m, \Omega) = \sqrt{\int \left| \frac{\partial E}{\partial t}(t) \right|^2 dt / \int |E(t)|^2 dt}. \quad (8)$$

Equation (8) is straightforward to calculate, resulting in

$$BW_{\text{rms}}(m, \Omega) = m\Omega / \sqrt{2}. \quad (9)$$

#### 2. Bandwidth of Signals with Multiple Phase Modulations

Equation (8) can be extended to a signal with multiple phase modulations given by Eq. (1):

$$BW_{\text{rms}}(\{m_j, \Omega_j\}) = \sqrt{\int \left[ \sum_j m_j \Omega_j \sin(\Omega_j t) \right]^2 dt}, \quad (10)$$

where the square can be expanded to give

$$BW_{\text{rms}}(\{m_j, \Omega_j\}) = \sqrt{\sum_{j,k} m_j m_k \Omega_j \Omega_k \int \sin(\Omega_j t) \sin(\Omega_k t) dt}. \quad (11)$$

For noncommensurate frequencies  $(\Omega_j, \Omega_k)$ , the integral in Eq. (11) is 0, while for  $j = k$ , the integral is equal to 1/2, leading to the expression

$$BW_{\text{rms}}(\{m_j, \Omega_j\}) = \sqrt{\sum_j m_j^2 \Omega_j^2 / 2}. \quad (12)$$

The rms bandwidth of a signal with multiple noncommensurate phase modulations is the root mean square of the individual rms bandwidths.

An alternate way to obtain this result is to consider that the temporal electric field of a signal with multiple phase modulations is the product of the fields corresponding to individual phase modulations. In the spectral domain, this implies that the resulting field is the convolution of the individual fields. Because the modulation frequencies are not commensurate, the optical frequency of each sideband in the resulting spectrum is obtained by a unique linear combination of the optical frequencies of the sidebands of the individual fields. The amplitude of that sideband in the convolved field is given by a product of the amplitudes in each individual field. As a result, the power of that sideband is given by a product of the corresponding powers. The optical spectrum of the signal with multiple phase modulations is the convolution of the spectra corresponding to the individual modulations only when the modulation frequencies are non-commensurate. This general result was used in Ref. 7 for the two particular frequencies corresponding to SBSS and

SSD on the LMJ. From the general properties of the Fourier transform, it is known that the rms width of a convolution of multiple functions is equal to the rms of the individual rms widths, which confirms Eq. (12).

### 3. Spectrum of Signals with Multiple Phase Modulations

Obtaining an approximation of the spectrum of a signal with multiple phase modulations is important to quantify the energy present in a particular frequency interval. A comparison of Eqs. (6) and (9) indicates that the rms width and the Carson's rule bandwidth are loosely connected for arbitrary values of the modulation index. The rms width is computationally easy to use but it is not a precise indicator of the energy fraction present in a given frequency interval. One possible strategy to obtain useful information about the spectral density of a signal given by Eq. (1) is to formally reconsider the property that the resulting spectrum is the convolution of the individual spectra for modulation parameters  $(m_j, \Omega_j)$  in light of the probability theory.

One considers  $N$  independent random variables  $\{\omega_j\}$ , where each random variable  $\omega_j$  has a probability density function (pdf) given by  $S(\omega, m_j, \Omega_j)$ . Since the modulation frequencies are different, the probability density functions are different and the variables are not identically distributed. The convolution of these spectra,  $S(\omega, \{m_j, \Omega_j\})$  is the pdf of the sum of the  $N$  random variables

$$S_N = \sum_j \omega_j$$

because of the probabilistic independence. The sum of a large number of independent and identically distributed variables with zero mean is probabilistically described by the central limit theorem, which states that the probability density function of the sum converges to a normal distribution with variance equal to  $N$  times the individual variance. This result is true in some conditions for the sum of  $N$  random variables that are independent but not identically distributed: the probability density function of the sum also converges to a normal distribution with variance given by the sum of the individual variances.<sup>24</sup> The sum cumulative distribution function (cdf) converges to the cdf of that normal distribution. A sufficient condition for convergence is that the third-order moment of the absolute value of each individual variable is finite. It is straightforward to simulate this quantity for Bessel spectra and conclude that this is the case. This makes it possible to conclude that the spectrum of the field given by Eq. (1) converges to a Gaussian function with standard deviation given by Eq. (12) for a large

number of modulation frequencies. The normal distribution and its cdf are well documented. For a normally distributed random variable  $x$  with unity standard deviation, the probit function, i.e., the quantile function (inverse of the cdf) of the normal distribution, yields the quantity  $x_p$ , defining the interval  $[-\infty, x_p]$ , corresponding to a statistical probability  $p$  (Ref. 25). For a Gaussian spectral density of standard deviation  $\sigma$ , the probit function gives the multiple  $x_p$ , defining the interval  $[-\infty, \sigma x_p]$ , containing the fraction  $p$  of the signal energy. Symmetric intervals  $[-f_p, f_p]$  containing 98% of the energy, are considered in this article to be consistent with Carson's rule for a single modulation frequency. Considering the symmetry of the normal distribution, the frequency  $f_p$  is the product of the standard deviation by the probit function applied to  $p = 0.99$ , i.e.,  $f_p = 2.326 \sigma$ .

### 4. Simulations

The optical spectrum of signals with multiple phase modulations has been simulated for a variety of situations. The cumulative distribution function for the test-signal spectrum shown in Fig. 136.19(b) is displayed in Fig. 136.20. The cdf of a normal distribution with identical rms bandwidth (50 GHz) is also plotted for comparison. The agreement between these two curves is good. The cdf calculated from the spectrum reaches 99% at ~99 GHz, indicating that 98% of the energy is contained in the frequency interval  $2 \times 99 \text{ GHz} = 198 \text{ GHz}$  (note that the cdf is by definition an integral starting at  $-\infty$ , while the bandwidth of interest is defined as a symmetric interval centered at the

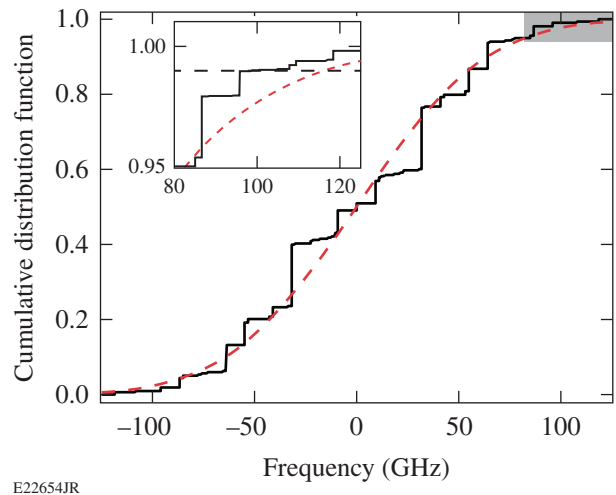


Figure 136.20

Cumulative density function of the spectrum shown in Fig. 136.19(b) (black solid line) and the Gaussian function with identical rms bandwidth (red dashed line). The inset is a close-up of the tail of the cumulative density functions at high frequencies, where a horizontal dashed line has been added to show the frequency values at which the two functions reach 0.99.

zero frequency). The 98% bandwidth of the Gaussian spectral density with rms bandwidth equal to 50 GHz is  $2 \times 2.326 \times 50 \text{ GHz} = 233 \text{ GHz}$ . The ratio of the actual 98% bandwidth to the 98% bandwidth predicted by the normal distribution is  $\rho = 0.85$ . The inset in Fig. 136.20 displays a close-up of the two cumulative density functions at high frequencies, confirming the discrepancy for the predicted 98% bandwidth. It is clear from this inset that the spectrum of the test signal is more concentrated and expands less toward high frequencies. The 17% overestimate predicted by the normal distribution is consistent with the more-general results obtained below.

Statistical simulations were performed to quantify the convergence of the spectrum of a multi-FM signal to its Gaussian approximation and of the corresponding cdf's. Figure 136.21 shows simulation results for the ratio  $\rho$  of the bandwidth containing 98% of the energy calculated from the spectral density to the bandwidth containing 98% of the energy assuming that the spectrum is Gaussian with standard deviation given by Eq. (12). For each number of modulation frequencies  $N$  (horizontal axis, from 1 to 10 on the left plots and 10 to 100 on the right plots) the standard deviation of the modulation index  $\sigma_m$  was allowed to vary between 1 and 5 (vertical axis). For each combination of  $N$  and  $\sigma_m$ , 1000 random draws of the modulation indices and modulation frequencies were made. For each draw, the modulation index is normally distributed with standard deviation  $\sigma_m$  and the modulation frequencies are initially normally distributed with standard deviation equal to 1 but are rescaled so that the rms bandwidth of the resulting signal is 100 GHz, following Eq. (12). This rescaling allows one to standardize the simulation results and necessary sampling in the time and frequency domain. Because it would be, in practice, difficult to co-phase a large number of sinusoidal modulations, the relative phase of the  $N$  modulations was chosen as a random variable uniformly distributed between 0 and  $2\pi$ . This procedure allows one to map a wide range of multi-FM signals. The results displayed in the first row of Fig. 136.21 are the average values of the ratio  $\rho$  as a function of  $\sigma_m$  and  $N$ . For example,  $\langle \rho \rangle = 1$  means that the 98% bandwidth of the calculated spectrum and Gaussian approximation are on average the same; values lower than 1 indicate that the Gaussian function overestimates the 98% bandwidth. The second row of Fig. 136.21 represents the standard deviation of the ratio  $\rho$  calculated over the 1000 random draws performed for the  $N$  modulation frequencies and modulation indices of standard deviation  $\sigma_m$ .

The optical spectrum of the phase-modulated fields effectively converged to a Gaussian distribution, and the cumulative

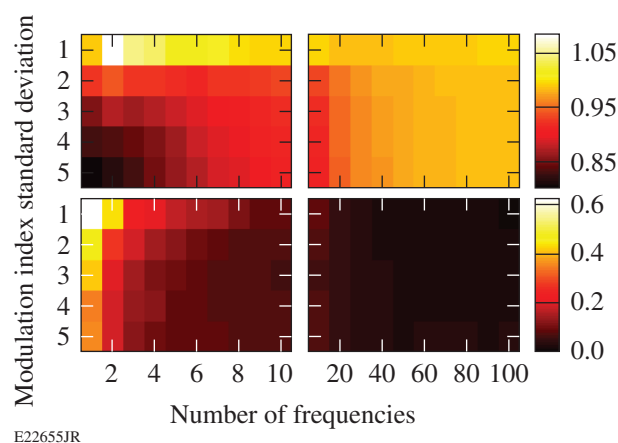


Figure 136.21

Statistics for the ratio  $\rho$  of the bandwidths containing 98% of the energy calculated from the spectral density of a multi-FM spectrum and directly calculated from the modulation parameters (frequencies and indices) assuming a normal spectral density. The upper and lower rows correspond to the average value and standard deviation, respectively, determined as a function of the number of modulation frequencies and standard deviation of the modulation index. The statistics are calculated over 1000 random draws of the modulation parameters.

distribution function of the spectrum converged to the corresponding cdf as the number of frequencies was increased. A strong correlation between the convergence of the cdf and the convergence of  $\langle \rho \rangle$  toward 1 was observed, making it possible to discuss the following general spectral properties in light of the bandwidth results presented in Fig. 136.21:

- The spectrum approximation by a normal distribution gets better as the number of modulation frequencies increases. The average value of the ratio  $\rho$  converges to 1 and the standard deviation around the average value decreases as  $N$  increases. This is expected because the central limit theorem applies to the sum of a large number of independent variables.
- The ratio  $\rho$  is in most cases smaller than 1, meaning that the calculated spectrum is more concentrated toward lower frequencies than its normal approximation. This can be explained by the squarish shape of the spectrum of phase-modulated signals, which leads to more energy concentration for a given standard deviation. Predicting the spectral extent of a multi-FM signal using its rms bandwidth and the normal approximation leads to an overestimate.
- Small phase-modulation indices lead to a better approximation than large modulation indices; in particular for  $\sigma_m = 1$ , the normal approximation is good in an average sense even

for a small number of modulation frequencies. This is caused by the general shape of the spectrum of sinusoidally modulated signals: for a single phase modulation with low modulation index, the spectrum is close to a bell-shaped curve multiplied by a frequency comb at the modulation frequencies. Since the individual probability density functions are closer to normal distribution, the convergence of the probability density function of the sum of the variables to a normal distribution is faster.

- The spread of the simulated  $\rho$  relative to the average value is smaller as the number of frequencies increases (consequence of the central limit theorem) and as the modulation index increases for a given number of frequencies. The latter is attributed to the larger number of spectral modes resulting from larger modulation indices, leading to a smoother cdf because the spectral density of individual modes is on average smaller.

### Impairments Leading to FM-to-AM Conversion at the Modulation Frequencies

#### 1. Linear Spectral Amplitude

A linear spectral modulation corresponds, for example, to amplification at a frequency detuned from the maximum of an amplifier gain. The corresponding transfer function over the bandwidth of the pulse is

$$\tau(\omega) = \sqrt{1 + l\omega} \approx 1 + \frac{l}{2}\omega. \quad (13)$$

The temporal field after this transfer function is

$$E' = E + \frac{il}{2} \frac{\partial E}{\partial t}. \quad (14)$$

With the expression of the initial electric field given by Eq. (1), the modulated field is

$$E'(t) = E(t) \left[ 1 + \frac{l}{2} \sum_j m_j \Omega_j \sin(\Omega_j t) \right], \quad (15)$$

and the modulated power at first order in  $l$  is

$$P'(t) = 1 + l \sum_j m_j \Omega_j \sin(\Omega_j t). \quad (16)$$

Equation (16) shows that the modulation on the output pulse is at the modulation frequencies  $\Omega_j$  with PV amplitude

$$\text{PV}(\Omega_j) = 2lm_j \Omega_j. \quad (17)$$

The highest modulation is observed at the frequency for which the associated bandwidth  $m_j \Omega_j$  is maximal. With noncommensurate modulation frequencies, there are times when the modulations in Eq. (16) are simultaneously close to a maximum and other times at which they are simultaneously close to a minimum. The PV modulation is given by

$$\text{PV} = 2l \sum_j m_j \Omega_j, \quad (18)$$

and the rms modulation for these uncorrelated sinusoidal modulations is given by

$$\text{rms} = l \sqrt{\sum_j m_j^2 \Omega_j^2 / 2}. \quad (19)$$

Simulation results for the test signal are shown in Figs. 136.22 and 136.23. Figure 136.22 displays the modulated temporal power corresponding to a linear spectral amplitude modulation  $l = 0.44/(100 \text{ GHz})$ : it is dominated by the modulation at the highest frequency  $f_3$  but the influence of other frequencies can be seen as the slight modulation of the local power extrema. Figure 136.23 compares simulated and analytical results for the modulations determined without frequency resolution (PV and rms AM) [Eqs. (18) and (19)] and at the three modulation frequencies [Eq. (17)]. An excellent agreement is obtained. The highest modulation is observed at the frequency  $f_3$  since that frequency corresponds to the highest product  $m_j \Omega_j$ .

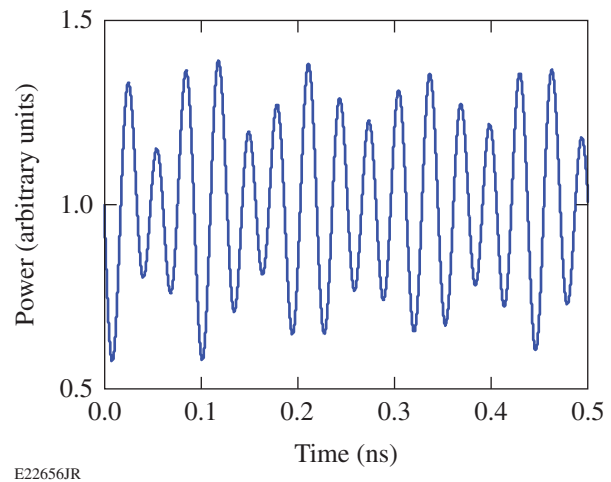
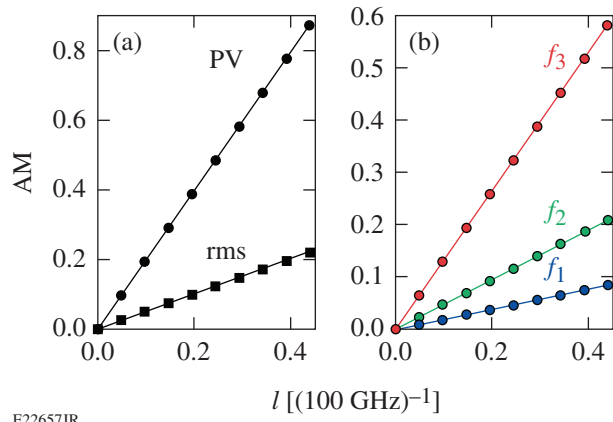


Figure 136.22  
Temporal power after linear spectral amplitude modulation corresponding to  $l = 0.44/(100 \text{ GHz})$ .



E22657JR

Figure 136.23

(a) Peak-to-valley and rms amplitude modulation (AM) versus magnitude of the linear spectral amplitude modulation. (b) Peak-to-valley AM at the frequencies  $f_j$  versus magnitude of the linear spectral amplitude modulation. The lines correspond to the simulations and the markers correspond to the analytical derivation.

## 2. Quadratic Spectral Phase

A quadratic spectral phase is the dominant phase term due to the chromatic dispersion of materials, e.g., laser glass and optical fibers, as well as the dominant term when propagating in a grating compressor. This impairment is represented in the spectral domain by the transfer function

$$\tau(\omega) = \exp\left(i\varphi_2 \omega^2 / 2\right) \approx 1 + i\varphi_2 \omega^2 / 2, \quad (20)$$

which leads to the temporal field

$$E' = E - i \frac{\varphi_2}{2} \frac{\partial^2 E}{\partial t^2}. \quad (21)$$

With the expression of the initial field given by Eq. (1), the resulting field is

$$E'(t) = E(t) \left\{ 1 - \frac{\varphi_2}{2} \sum_j m_j \Omega_j^2 \cos(\Omega_j t) + i \frac{\varphi_2}{2} \left[ \sum_j m_j \Omega_j \sin(\Omega_j t) \right]^2 \right\}. \quad (22)$$

When calculating the power (i.e., the modulus squared of the field), the imaginary component in Eq. (22) leads to a second-order term in  $\varphi_2$ . The power is given at first order by

$$P'(t) = 1 - \varphi_2 \sum_j m_j \Omega_j^2 \cos(\Omega_j t). \quad (23)$$

A quadratic spectral phase leads to amplitude modulation at the frequencies  $\Omega_j$  with respective peak-to-valley amplitude

$$\text{PV}(\Omega_j) = 2\varphi_2 m_j \Omega_j^2. \quad (24)$$

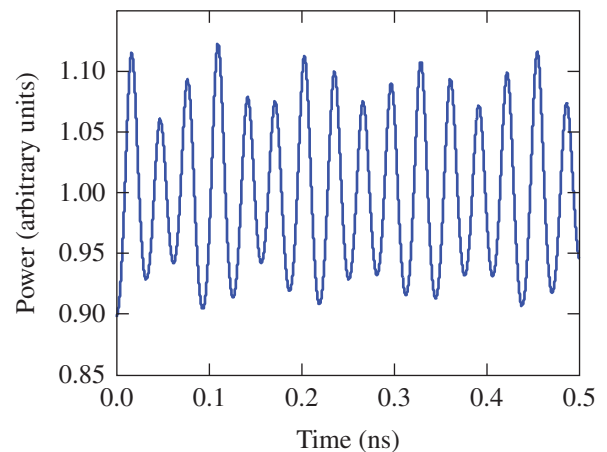
Temporal modulations are observed at the modulation frequencies  $\Omega_j$ , as for linear amplitude modulation, but the largest modulation corresponds to the frequency having the largest product  $m_j \Omega_j^2$ . An argument similar to that made about Eq. (16) shows that the overall peak-to-valley AM is

$$\text{PV} = 2\varphi_2 \sum_j m_j \Omega_j^2, \quad (25)$$

while the rms AM is given by

$$\text{rms} = \varphi_2 \sqrt{\sum_j m_j^2 \Omega_j^4 / 2}. \quad (26)$$

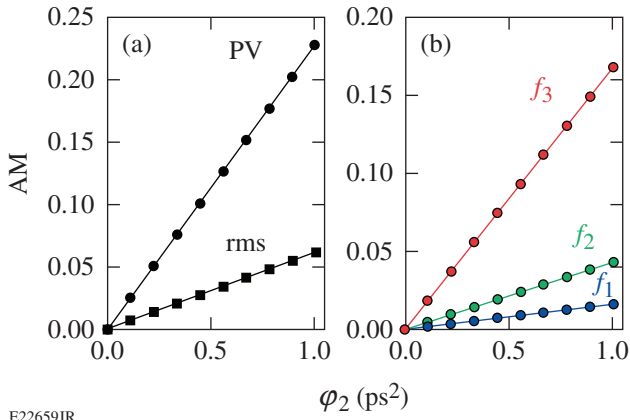
Simulation results for quadratic spectral phase modulation are shown in Figs. 136.24 and 136.25. Figure 136.24 shows the modulated power after second-order dispersion  $\varphi_2 = 1.01 \text{ ps}^2$ . Features similar to those of Fig. 136.22 are observed. Figure 136.25 shows the excellent agreement between the simulated and analytical results [Eqs. (25) and (26) for the peak-to-valley and rms AM, and Eq. (24) for the peak-to-valley AM at



E22658JR

Figure 136.24

Temporal power after quadratic spectral phase corresponding to  $\varphi_2 = 1.01 \text{ ps}^2$ .



E22659JR

Figure 136.25

(a) Peak-to-valley and rms AM versus magnitude of the quadratic spectral phase modulation. (b) Peak-to-valley AM at the frequencies  $f_j$  versus magnitude of the quadratic spectral phase modulation. The lines correspond to the simulations and the markers correspond to the analytical derivation.

each frequency  $f_j$ ] when the magnitude of the phase modulation is modified. The highest temporal modulation is observed at the frequency  $f_3$  because that frequency corresponds to the largest quantity  $m_j \Omega_j^2$ , considering the parameters in Table 136.III.

### 3. Combination of Linear Spectral Amplitude and Quadratic Spectral Phase

Linear amplitude modulation and quadratic temporal phase modulation lead to temporal modulation at the frequencies  $\Omega_j$ . Inspection of Eqs. (16) and (23) shows that the corresponding modulations occur in quadrature, each of them being either a sine or a cosine of the argument  $\Omega_j t$ . It is straightforward to show that the peak-to-valley AM at frequency  $\Omega_j$  resulting from the in-quadrature modulations with respective PV amplitudes  $2lm_j \Omega_j$  and  $2\phi_2 m_j \Omega_j^2$  is

$$\sqrt{(2\phi_2 m_j \Omega_j^2)^2 + (2lm_j \Omega_j)^2},$$

i.e.,

$$\text{PV}(\Omega_j) = 2m_j \Omega_j \sqrt{(\phi_2 \Omega_j)^2 + l^2}. \quad (27)$$

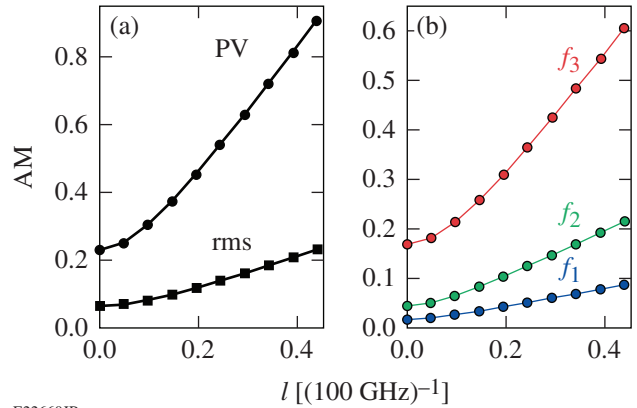
Since the modulation frequencies are not commensurate, there are times at which the extrema of the individual modulations are simultaneously reached, leading to the peak-to-valley AM

$$\text{PV} = 2 \sum_j m_j \Omega_j \sqrt{(\phi_2 \Omega_j)^2 + l^2}. \quad (28)$$

The rms AM is obtained by considering that the resulting temporal power is the sum of uncorrelated sinusoidal functions oscillating at  $\Omega_j$  with amplitude given by half the PV modulation expressed by Eq. (27). This leads to

$$\text{rms} = \sqrt{\sum_j m_j^2 \Omega_j^2 [(\phi_2 \Omega_j)^2 + l^2]} / 2. \quad (29)$$

Figure 136.26 compares simulated and analytical results when the second-order dispersion is  $\phi_2 = 1.01 \text{ ps}^2$  and the linear spectral amplitude modulation is modified. Excellent agreement is obtained, confirming the fact that Eqs. (27)–(29) accurately predict the influence of the combined phase and amplitude modulations. Similar agreement was observed when scanning the magnitude of the phase modulation for a given amplitude modulation.



E22660JR

Figure 136.26

(a) Peak-to-valley and rms AM versus magnitude of the linear spectral amplitude for  $\phi_2 = 1.01 \text{ ps}^2$ . (b) Peak-to-valley AM at the frequencies  $f_j$  versus magnitude of the linear spectral amplitude for  $\phi_2 = 1.01 \text{ ps}^2$ . The lines correspond to the simulations and the markers correspond to the analytical derivation.

### Impairments Leading to FM-to-AM Conversion at Intermodulation Frequencies

#### 1. Quadratic Spectral Amplitude

Quadratic amplitude modulation occurs after propagation in a component at a frequency corresponding to an amplitude extremum of the component's transfer function; for example, amplification at the peak of the gain of an amplifier. The corresponding transfer function is

$$\tau(\omega) = \sqrt{1 + q\omega^2} \approx 1 + \frac{q}{2} \omega^2, \quad (30)$$

leading to the temporal field

$$E' = E - \frac{q}{2} \frac{\partial^2 E}{\partial t^2}. \quad (31)$$

The resulting field is

$$E'(t) = E(t) \left\{ 1 + \frac{q}{2} \left[ \sum_j m_j \Omega_j \sin(\Omega_j t) \right]^2 + i \frac{q}{2} \sum_j m_j \Omega_j^2 \cos(\Omega_j t) \right\}, \quad (32)$$

where the real component proportional to  $q$  between the curled brackets will be the main modulation source since the complex quantity in the same brackets is squared when calculating the optical power. The resulting power, at first order in  $q$ , is

$$P'(t) = 1 + q \left[ \sum_j m_j \Omega_j \sin(\Omega_j t) \right]^2. \quad (33)$$

When  $q > 0$ , the modulated power in Eq. (33) is higher than the average power of the signal in the absence of impairment at all times. This is explained by the fact that the transfer function [Eq. (30)] does not conserve the signal energy. Since one is interested in the temporal modulation of the power around its average value, and not around its value without impairment, AM determinations are scaled by the average power of the signal of Eq. (33),

$$1 + \frac{q}{2} \sum_j m_j^2 \Omega_j^2.$$

The minimum value of Eq. (33) is 1. The maximum value is obtained when all the modulations reach an extremum, and the resulting peak-to-valley AM is

$$PV = q \left( \sum_j m_j \Omega_j \right)^2 / \left( 1 + \frac{q}{2} \sum_j m_j^2 \Omega_j^2 \right). \quad (34)$$

The rms AM on the resulting power is calculated from Eq. (33), leading to

$$\text{rms} = \frac{q \sqrt{\sum_j m_j^4 \Omega_j^4 / 8 + \sum_{j,k} m_j^2 m_k^2 \Omega_j^2 \Omega_k^2}}{\left( 1 + \frac{q}{2} \sum_j m_j^2 \Omega_j^2 \right)}. \quad (35)$$

Equation (33) can be developed into a sum of terms proportional to  $\sin(\Omega_j t) \sin(\Omega_k t)$ . The choice of  $j = k$  leads to a term oscillating at the frequency  $2\Omega_j$  with PV amplitude  $qm_j^2 \Omega_j^2$ . The two terms corresponding to the choice  $(j,k)$  and  $(k,j)$  with  $j \neq k$  lead to modulations at  $\Omega_j + \Omega_k$  and  $\Omega_j - \Omega_k$ , each of them with a PV amplitude  $2qm_j m_k \Omega_j \Omega_k$ . The resulting AM's at these frequencies are

$$PV(2\Omega_j) = qm_j^2 \Omega_j^2 / \left( 1 + \frac{q}{2} \sum_j m_j^2 \Omega_j^2 \right) \quad (36)$$

and

$$PV(\Omega_j \pm \Omega_k) = 2qm_j m_k \Omega_j \Omega_k / \left( 1 + \frac{q}{2} \sum_j m_j^2 \Omega_j^2 \right). \quad (37)$$

The modulation amplitudes at the frequencies  $\Omega_j + \Omega_k$  and  $\Omega_j - \Omega_k$  are identical. Simulation and analytical results for quadratic spectral amplitude modulation are displayed in Figs. 136.27 and 136.28. Figure 136.27 shows the complex behavior of the amplitude modulation, in particular the clear presence of modulations at multiple frequencies. Figure 136.28

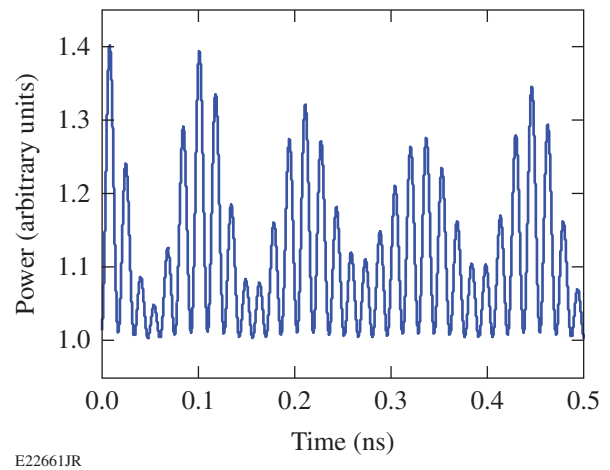
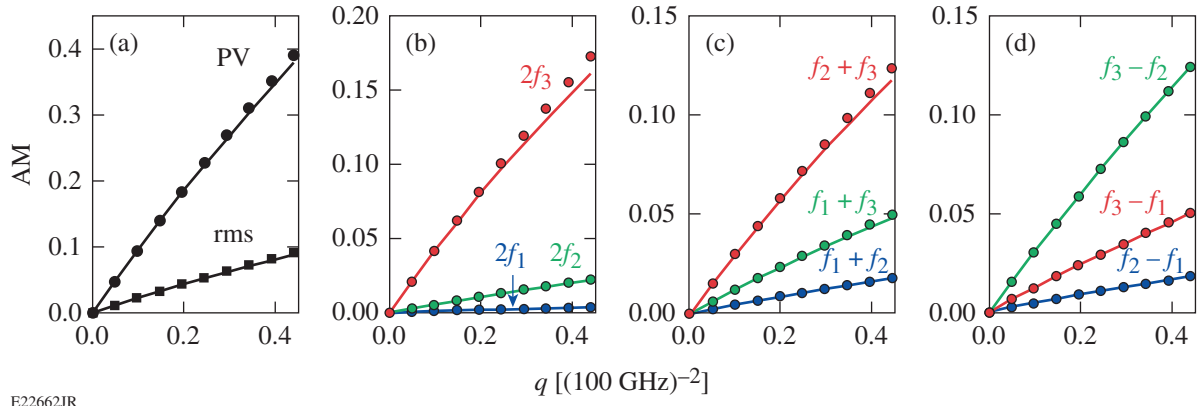


Figure 136.27  
Temporal power after quadratic spectral amplitude modulation corresponding to  $q = 0.44/(100 \text{ GHz})^2$ .



E22662JR

Figure 136.28

(a) Peak-to-valley and rms AM versus magnitude of the quadratic spectral amplitude modulation. [(b)–(d)] Peak-to-valley AM at the frequencies  $2f_j$ ,  $f_j + f_k$ , and  $f_j - f_k$  versus magnitude of the quadratic spectral amplitude modulation. The lines correspond to the simulations and the markers correspond to the analytical derivation.

details the PV and rms AM for the temporal power as well as the frequency-resolved peak-to-valley AM. The simulation results are in excellent agreement with the analytical results from Eqs. (34)–(37). The highest modulations are observed at the frequencies  $2f_3$ ,  $f_2 + f_3$ , and  $f_3 - f_2$ , which contribute most of the PV modulation observed in the time domain. The first two of these frequencies are larger than 50 GHz, while the third is approximately 10 GHz. Bandwidth limitation in a temporal diagnostic might hinder the ability to accurately characterize the temporal modulation. Detection of a modulation at a low frequency (e.g.,  $\Omega_j - \Omega_k$ ) indicates the presence of modulation at a higher frequency (e.g.,  $\Omega_j + \Omega_k$ ) with identical amplitude.

## 2. Cubic Spectral Phase

A cubic spectral phase is typically the leading phase impairment once the quadratic spectral phase has been compensated over the bandwidth of the source. Because the relative signs of the second-order and third-order dispersions for propagation in materials and in a grating compressor are different, a cubic spectral phase is induced when a grating compressor is used to compensate the chromatic dispersion of optical fibers. The transfer function is represented by

$$\tau(\omega) = \exp\left(i\varphi_3\omega^3/6\right) \approx 1 + i\varphi_3\omega^3/6. \quad (38)$$

This leads to the output temporal field

$$E' = E + \frac{\varphi_3}{6} \frac{\partial^3 E}{\partial t^3}. \quad (39)$$

The expression for the third-order derivative of Eq. (1) is lengthy, but only the real terms should be kept since they are the ones leading to an approximation of the modulated power at first order in  $\varphi_3$  when inserted into Eq. (39). The modulated power is given by

$$P'(t) = 1 - \varphi_3 \sum_j m_j \Omega_j \sin(\Omega_j t) \sum_j m_j \Omega_j^2 \cos(\Omega_j t). \quad (40)$$

For this impairment, the spectrally resolved amplitude modulation is calculated first. The product of the two summation terms in Eq. (40) gives modulations at the frequencies  $2\Omega_j$  and at the intermodulation frequencies  $\Omega_j \pm \Omega_k$ . The term at  $2\Omega_j$  corresponds to

$$\begin{aligned} &\varphi_3 m_j \Omega_j \sin(\Omega_j t) m_j \Omega_j^2 \cos(\Omega_j t) = \\ &\varphi_3 m_j^2 \Omega_j^3 \sin(2\Omega_j t)/2. \end{aligned} \quad (41)$$

The peak-to-valley AM at  $2\Omega_j$  is

$$\text{PV}(2\Omega_j) = \varphi_3 m_j^2 \Omega_j^3. \quad (42)$$

The terms corresponding to  $j \neq k$  are

$$\begin{aligned} &\varphi_3 m_j m_k \Omega_j \Omega_k \left[ \Omega_k \sin(\Omega_j t) \cos(\Omega_k t) \right. \\ &\left. + \Omega_j \sin(\Omega_k t) \cos(\Omega_j t) \right], \end{aligned} \quad (43)$$

which can be expressed using a trigonometric identity for the product of a sine and cosine as

$$\begin{aligned} & \varphi_3 m_j m_k \Omega_j \Omega_k \left\{ \left( \Omega_j + \Omega_k \right) \sin \left[ \left( \Omega_j + \Omega_k \right) t \right] \right. \\ & \left. + \left( \Omega_k - \Omega_j \right) \sin \left[ \left( \Omega_j - \Omega_k \right) t \right] \right\} / 2. \end{aligned} \quad (44)$$

The peak-to-valley AM for these sum/difference frequencies is therefore

$$PV(\Omega_j \pm \Omega_k) = \varphi_3 m_j m_k \Omega_j \Omega_k (\Omega_j \pm \Omega_k), \quad (45)$$

where it has been assumed that  $\Omega_j > \Omega_k$ .

The rms AM is obtained by noting that the average temporal value of Eq. (40) is equal to 1 because the spectral field is phase modulated but not amplitude modulated. One can then write

$$\begin{aligned} \text{rms}^2 &= \varphi_3^2 \int \left[ \sum_j m_j \Omega_j \sin(\Omega_j t) \right]^2 \\ &\quad \times \left[ \sum_j m_j \Omega_j^2 \cos(\Omega_j t) \right]^2 dt. \end{aligned} \quad (46)$$

Each square in the previous equation can be developed, and considering that the integral of a product of sinusoidal functions with noncommensurate frequencies is zero if it contains odd powers of a sinusoidal function (either sine or cosine) at a particular frequency, Eq. (46) can be rewritten as

$$\text{rms}^2 = \varphi_3^2 \int \sum_j m_j^2 \Omega_j^2 \sin^2(\Omega_j t) \sum_j m_j^2 \Omega_j^4 \cos^2(\Omega_j t) dt \quad (47)$$

and as

$$\begin{aligned} \text{rms}^2 &= \varphi_3^2 \int \left[ \sum_j m_j^4 \Omega_j^6 \sin^2(\Omega_j t) \cos^2(\Omega_j t) \right. \\ &\quad \left. + \sum_{j \neq k} m_j^2 m_k^2 \Omega_j^2 \Omega_k^4 \sin^2(\Omega_j t) \cos^2(\Omega_k t) \right] dt. \end{aligned} \quad (48)$$

Equation (48) can be calculated to obtain the rms AM in the presence of third-order dispersion,

$$\text{rms} = \frac{\varphi_3}{2} \sqrt{\sum_j m_j^4 \Omega_j^6 / 2 + \sum_{j \neq k} m_j^2 m_k^2 \Omega_j^2 \Omega_k^4}. \quad (49)$$

The peak-to-valley AM is difficult to obtain in the general case because the different sinusoidal components in Eq. (40) have different frequencies and reach their maxima at different times, but a minimal and maximal bound for that quantity can be obtained. A minimal bound  $PV_{\min}$  is obtained by considering that the peak-to-valley modulation must be larger than the modulation amplitude obtained considering any two different temporal arguments in Eq. (40). One can consider a time value for which each sine and cosine in that equation is equal to  $\pm 1/\sqrt{2}$ , leading to the inequality

$$PV \geq PV_{\min} = \varphi_3 \sum_j m_j \Omega_j \sum_j m_j \Omega_j^2. \quad (50)$$

A maximal bound  $PV_{\max}$  is obtained by considering that, at this approximation order, only the modulations at all the frequencies  $2\Omega_j$  and  $\Omega_j + \Omega_k$  contribute to the temporal modulation. The resulting peak-to-valley AM is smaller than the sum of individual peak-to-valley AM (the equality is reached only if a time exists when all the individual modulations reach their maximum and another time when they all reach their minimum). The maximal bound is the sum of Eqs. (42) and (45), leading to the inequality

$$PV \leq PV_{\max} = PV_{\min} + \varphi_3 \sum_{j>k} m_j m_k \Omega_j \Omega_k (\Omega_j - \Omega_k). \quad (51)$$

The span of the interval  $PV_{\max} - PV_{\min}$  is small compared to the predicted range of peak-to-valley modulation values since the summation in Eq. (51) contains terms that are small, because either some of the modulation indices are small or the frequency differences are smaller than the frequency sums. In particular, one has  $PV_{\min} = PV_{\max} = \varphi_3 m_1^2 \Omega_1^3$  for a single modulation frequency.

Figures 136.29 and 136.30 display results pertaining to temporal AM in the presence of a cubic spectral phase. The existence of multiple modulation frequencies is clearly visible in Fig. 136.29. Figure 136.30(a) shows the analytical and simulation results for the peak-to-valley and rms modulation on the test signal as a function of the cubic spectral modulation magnitude. Excellent agreement is obtained for the rms AM. The peak-to-valley AM obtained by simulation is correctly bracketed by the AM calculated with Eqs. (50) and (51). The frequency-resolved peak-to-valley AM reveals that the AM is dominated by contributions at the frequencies  $2f_3$  and  $f_2 + f_3$ . Contrary to the case of quadratic gain modulation, AM at

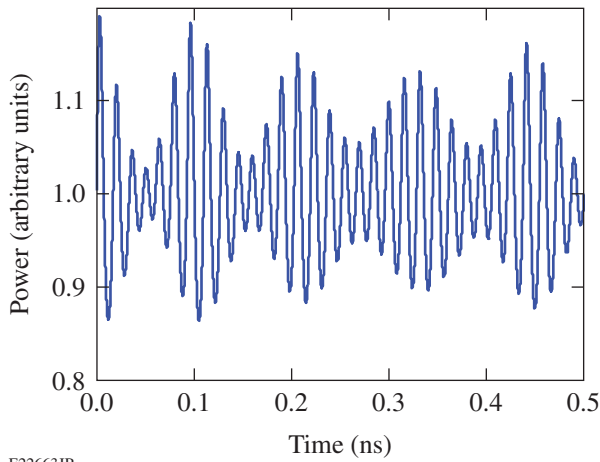


Figure 136.29  
Temporal power after cubic spectral phase modulation corresponding to  $\varphi_3 = 4.8 \text{ ps}^3$ .

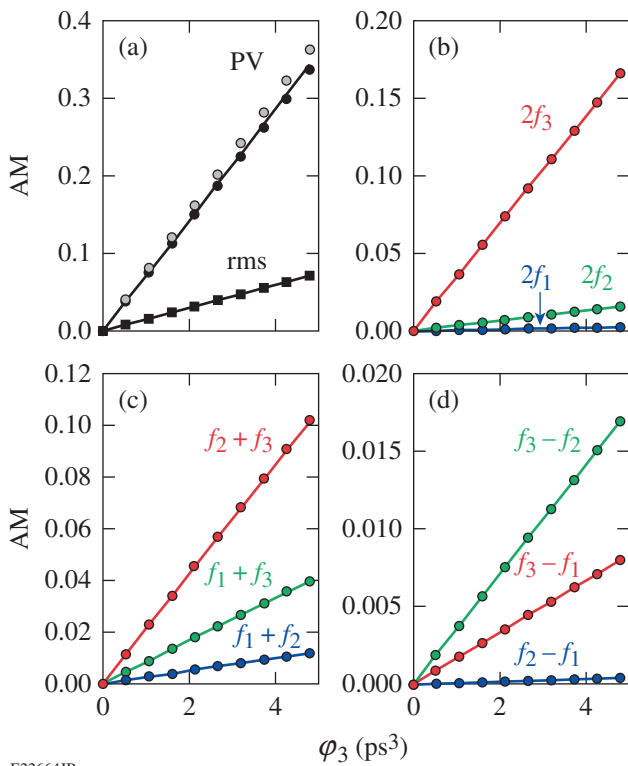


Figure 136.30  
(a) Peak-to-valley and rms AM versus magnitude of the cubic spectral phase modulation. The lower and higher bounds for the peak-to-valley AM are shown with black and gray markers, respectively. [(b)–(d)] Peak-to-valley AM at the frequencies  $2f_j$ ,  $f_j + f_k$ , and  $f_j - f_k$  versus magnitude of the cubic spectral phase modulation. The lines correspond to the simulations and the markers correspond to the analytical derivation.

the low frequency  $f_3 - f_2$  is much smaller than the AM at  $f_2 + f_3$ . A signal impaired by third-order dispersion detected by a low-bandwidth temporal diagnostic might seem of much better quality than it actually is.

### Additional Considerations

At first order in the modulation resulting from each impairment, the power of an impaired signal is

$$\begin{aligned}
 P'(t) = & 1 + l \sum_j m_j \Omega_j \sin(\Omega_j t) - \varphi_2 \sum_j m_j \Omega_j^2 \cos(\Omega_j t) \\
 & + q \left[ \sum_j m_j \Omega_j \sin(\Omega_j t) \right]^2 - \varphi_3 \sum_j m_j \Omega_j \sin(\Omega_j t) \\
 & \times \sum_j m_j \Omega_j^2 \cos(\Omega_j t), \quad (52)
 \end{aligned}$$

where the summations correspond to linear amplitude modulation, quadratic phase modulation, quadratic amplitude modulation, and cubic phase modulation. Because the Fourier transform is a linear operator, the frequency signature of the modulated power can partially reveal the origin of the impairments: temporal modulations at some of the phase-modulation frequencies indicate that the signal is impaired by a linear amplitude modulation or quadratic phase modulation, while temporal modulations at some of the sum or difference frequencies indicate that the signal is impaired by a quadratic amplitude modulation or cubic phase modulation.

The ratio of the AM at different frequencies can be used in some cases to identify the source of impairment. For example, this ratio for frequencies  $f_j$  and  $f_k$  is  $m_j f_j / m_k f_k$  when the main impairment is linear amplitude modulation [Eq. (17)] and  $m_j f_j^2 / m_k f_k^2$  when the main impairment is quadratic phase modulation [Eq. (24)]. Since the modulation indices and frequencies are known, such quantitative analysis can reveal the origin of the temporal modulation. When these two impairments are present, a more-precise study of the ratio of the AM at different frequencies is likely to reveal their respective contributions—Eq. (27) contains only two unknowns: the coefficient for linear amplitude modulation  $l$  and the coefficient for quadratic phase modulation  $\varphi_2$ . These unknowns can be determined if at least two modulation frequencies are present in the signal. With more than two frequencies, the best set of coefficients can be determined in the least-squares sense. Similar considerations can be applied to modulations observed

at intermodulation frequencies when quadratic amplitude modulation and cubic phase modulation are present.

Analytical expressions for the amplitude modulation resulting from impairments of a phase-modulated signal are the necessary starting points for understanding the requirements of temporal diagnostics used to characterize the resulting signals. In practical situations, a diagnostic with a flat response up to a frequency as high as twice the highest phase-modulation frequency in the system is necessary and sufficient to capture the time-domain signal, provided that the impairments are limited to those treated in this article. Insufficient bandwidth leads to an underestimate of the amplitude modulation present on the signal. For signals corresponding to the parameters in Table 136.III, intermodulation frequencies can be at frequencies difficult to reach with the current state-of-the-art single-shot oscilloscopes and photodetector (e.g.,  $2f_3 \sim 64$  GHz). In general, AM is also generated at lower frequencies (e.g.,  $f_3 - f_2 \sim 10$  GHz), but a photodetection system with insufficient bandwidth might lead to a significant underestimate of the physical modulation, particularly in the presence of cubic phase.

### Conclusions

The spectral and temporal properties of optical signals generated by multiple sinusoidal phase modulations of a monochromatic source have been studied. A formalism for the statistical prediction of the optical spectrum of these signals has been developed based on the central limit theorem, showing the convergence of the spectrum of a signal with multiple phase modulations to a Gaussian spectrum with identical rms bandwidth, which can be calculated analytically from the modulation parameters, and the associated convergence of their cumulative density functions. The comparison between the directly simulated spectrum and predicted Gaussian spectrum for a finite number of frequencies confirmed the asymptotic result and showed that in most conditions, the frequency interval containing 98% of the energy can be predicted from the modulation parameters, although there is significant variation when the number of frequencies is low. FM-to-AM conversion on signals with multiple phase modulations has been analytically described for typical spectral impairments to extend the results known for signals modulated at a single frequency. An excellent agreement with direct simulations has been observed. These results are useful in understanding the current limitations of the laser systems using phase modulation along with the associated subsystems and diagnostics, and in optimizing the engineering of existing and future systems.

### ACKNOWLEDGMENT

This work was supported by the U.S. Department of Energy Office of Inertial Confinement Fusion under Cooperative Agreement No. DE-FC52-08NA28302, the University of Rochester, and the New York State Energy Research and Development Authority. The support of DOE does not constitute an endorsement by DOE of the views expressed in this article.

### REFERENCES

1. J. D. Lindl *et al.*, *Phys. Plasmas* **11**, 339 (2004).
2. R. L. McCrory, D. D. Meyerhofer, R. Betti, R. S. Craxton, J. A. Delettrez, D. H. Edgell, V. Yu Glebov, V. N. Goncharov, D. R. Harding, D. W. Jacobs-Perkins, J. P. Knauer, F. J. Marshall, P. W. McKenty, P. B. Radha, S. P. Regan, T. C. Sangster, W. Seka, R. W. Short, S. Skupsky, V. A. Smalyuk, J. M. Soures, C. Stoeckl, B. Yaakobi, D. Shvarts, J. A. Frenje, C. K. Li, R. D. Petrasso, and F. H. Séguin, *Phys. Plasmas* **15**, 055503 (2008).
3. C. A. Haynam *et al.*, *Appl. Opt.* **46**, 3276 (2007).
4. N. Fleurot, C. Cavailler, and J. L. Bourgade, *Fusion Eng. Des.* **74**, 147 (2005).
5. J. R. Murray *et al.*, *J. Opt. Soc. Am. B* **6**, 2402 (1989).
6. P. J. Wisoff *et al.*, in *Optical Engineering at the Lawrence Livermore National Laboratory II: The National Ignition Facility*, edited by M. A. Lane and C. R. Wuest (SPIE, Bellingham, WA, 2004), Vol. 5341, pp. 146–155.
7. S. Hocquet *et al.*, *Appl. Opt.* **47**, 3338 (2008).
8. J. D. Kilkenny, S. G. Glendinning, S. W. Haan, B. A. Hammel, J. D. Lindl, D. Munro, B. A. Remington, S. V. Weber, J. P. Knauer, and C. P. Verdon, *Phys. Plasmas* **1**, 1379 (1994).
9. S. Skupsky, R. W. Short, T. Kessler, R. S. Craxton, S. Letzring, and J. M. Soures, *J. Appl. Phys.* **66**, 3456 (1989).
10. J. E. Rothenberg, *J. Opt. Soc. Am. B* **14**, 1664 (1997).
11. *LLE Review Quarterly Report* **114**, 73, Laboratory for Laser Energetics, University of Rochester, Rochester, NY, LLE Document No. DOE/NA/28302-826, OSTI ID 935224 (2008).
12. Y. Lin, T. J. Kessler, and G. N. Lawrence, *Opt. Lett.* **20**, 764 (1995).
13. T. J. B. Collins, J. A. Marozas, K. S. Anderson, R. Betti, R. S. Craxton, J. A. Delettrez, V. N. Goncharov, D. R. Harding, F. J. Marshall, R. L. McCrory, D. D. Meyerhofer, P. W. McKenty, P. B. Radha, A. Shvydky, S. Skupsky, and J. D. Zuegel, *Phys. Plasmas* **19**, 056308 (2012).
14. J. H. Kelly, A. Shvydky, J. A. Marozas, M. J. Guardalben, B. E. Kruschwitz, L. J. Waxer, C. Dorrer, E. Hill, A. V. Okishev, and J.-M. Di Nicola, in *High Power Lasers for Fusion Research II*, edited by A. A. S. Awwal (SPIE, Bellingham, WA, 2013), Vol. 8602, Paper 86020D.
15. B. E. Kruschwitz, J. H. Kelly, C. Dorrer, A. V. Okishev, L. J. Waxer, G. Balonek, I. A. Begishev, W. Bittle, A. Consentino, R. Cuffney,

- E. Hill, J. A. Marozas, M. Moore, R. G. Roides, and J. D. Zuegel, in *High Power Lasers for Fusion Research II*, edited by A. A. S. Awwal (SPIE, Bellingham, WA, 2013), Vol. 8602, Paper 86020E.
16. C. Dorrer, R. Roides, R. Cuffney, A. V. Okishev, W. A. Bittle, G. Balonek, A. Consentino, E. Hill, and J. D. Zuegel, *IEEE J. Sel. Top. Quantum Electron.* **19**, 3500112 (2013).
17. J. E. Rothenberg, D. F. Browning, and R. B. Wilcox, in *Third International Conference on Solid State Lasers for Application to Inertial Confinement Fusion*, edited by W. H. Lowdermilk (SPIE, Bellingham, WA, 1999), Vol. 3492, pp. 51–61.
18. H. Cao *et al.*, *Appl. Opt.* **50**, 3609 (2011).
19. S. Hocquet, G. Lacroix, and D. Penninckx, *Appl. Opt.* **48**, 2515 (2009).
20. L. W. Couch III, *Digital and Analog Communication Systems*, 3rd ed. (Macmillan Publishing Company, New York, 1990).
21. S. Vidal, J. Luce, and D. Penninckx, *Opt. Lett.* **36**, 3494 (2011).
22. D. Penninckx *et al.*, *J. Lightwave Technol.* **24**, 4197 (2006).
23. S. Hocquet *et al.*, *Appl. Opt.* **49**, 1104 (2010).
24. J. W. Goodman, *Statistical Optics* (Wiley, New York, 2000).
25. D. Collett, *Modelling Binary Data*, 2nd ed. (Chapman & Hall/CRC, Boca Raton, FL, 2003).

---

# The Fifth Omega Laser Facility Users Group Workshop

## Introduction

A capacity gathering of over 100 researchers from 25 universities and laboratories met at the Laboratory for Laser Energetics (LLE) for the Fifth Omega Laser Facility Users Group (OLUG) workshop. The purpose of the 2.5-day workshop was to facilitate communications and exchanges among individual Omega users and between users and the LLE management; to present ongoing and proposed research; to encourage research opportunities and collaborations that could be undertaken at the Omega Laser Facility and in a complementary fashion at other facilities [such as the National Ignition Facility (NIF) or the Laboratoire pour l'Utilisation des Lasers Intenses (LULI)]; to provide an opportunity for students, postdoctoral fellows, and young researchers to present their research in an informal setting; and to provide feedback to LLE management from the users about ways to improve the facility and future experimental campaigns. The interactions were wide-ranging and lively, as illustrated in the accompanying photographs.

OLUG consists of over 300 members from 35 universities and many centers and national laboratories. Names and affiliations can be found at <http://www.lle.rochester.edu/media/about/documents/OLUGMEMBERS.pdf>. OLUG is by far the largest users group in the world in the field of high-energy-density physics and is also one of the most active.

The first two mornings of the workshop were comprised of seven science and facility presentations. The facility talks proved especially useful for those unfamiliar with the art and complexities of performing experiments at the Omega Laser Facility. But since the facility is constantly evolving and improving, even experienced users benefited significantly from these updates. The overview science talks, given by leading world authorities, described the breadth and excitement of high-energy-density (HED) science either being undertaken at the Omega Laser Facility or well within the reach of the facility with improvements or upgrades.



U1627JR

Figure 136.31

A capacity gathering of 100 researchers from 25 universities and laboratories around the world participated in this year's workshop. The users group itself has well over 300 members from 35 universities and 25 laboratories, making it by far the largest users group in the world in high-energy-density physics. The next annual OLUG Workshop will occur 23–25 April 2014.

Forty students and postdoctoral fellows participated in the workshop, and 36 were supported by travel grants from the National Nuclear Security Administration (NNSA). The content of their presentations encompassed the spectrum from target fabrication to simulating aspects of supernovae; the presentations generated spirited discussions, probing questions, and friendly suggestions. In total, there were 68 contributed posters, including eight that focused on the Omega Laser Facility.



U1606JR

Figure 136.32

Nearly all the 40 students and postdoctoral fellows who attended made poster presentations; 36 received travel assistance from an NNSA grant. The workshop emphasized the participation and involvement of young researchers.

An important function of the workshop was to develop a set of **Findings and Recommendations** to help set and define future priorities for the Omega Laser Facility. These were grouped into three areas: 60-beam OMEGA, OMEGA EP, and general facility improvements and accessibility of OMEGA operational information. LLE management uses these recommendations as a guide for making decisions about Omega Laser Facility operations, priorities, and future changes. In addition, the status of these OLUG **Findings and Recommendations** will be updated and reviewed at a satellite evening meeting during the 2013 APS-DPP Conference. They will also form the grist for the forthcoming workshop. The widely discussed **Findings and Recommendations** are listed below.

One highlight of the workshop, as in past workshops, was a panel of students and postdoctoral fellows who discussed their experiences at the Omega Laser Facility and their thoughts and recommendations on facility improvements. Engaging discussions were sparked by this forum, which resulted in the student/postdoctoral recommendations for the facility.

For the first time, three posters were presented by students in LLE's Summer High School Research Program. We plan to expand the number of these excellent presentations in the 2014 April Workshop.



U1607JR

Figure 136.33

A total of 68 posters, the majority by young researchers, were presented during three poster sessions.

Another important event at the end of the workshop was a panel of experts who gave an overview of the HED opportunities at national laboratories. These discussions are very useful for young researchers who may not know all the capabilities and HED research occurring at these various institutions.

Finally, it was decided to hold the next workshop on 23–25 April 2014. Plans are already well underway for this event.

### Principal Findings and Recommendations of the 2013 Workshop

#### 1. Wednesday Evening Session for Young Researchers

The young researchers would like to have a Wednesday evening session (on the first day of the workshop), where they could discuss topics and concerns that most directly impact their research, especially as it relates to the Omega Laser Facility. From their discussions, this would be used as important input to the Findings and Recommendations for the 2014 workshop.

#### 2. Tritium-Filling Capability

While notable and important capabilities have occurred in tritium filling of capsules with different gas mixtures (such as with  $^3\text{He}$  for  $\text{D}^3\text{He}$  shots), and as well with reasonable high-T purity (for TT shots, where an  $\sim 1.5\%$  D contamination level was achieved), we look forward, with implementation of the isotope separator, to even higher-purity-T experiments (0.2% D).

This will lead to very important advances in plasma nuclear science (D. McNabb, M. Gatu Johnson, D. Casey, J. Caggiano, H. Herrmann, L. Bernstein, and J. Frenje).

### 3. OMEGA EP to Full Specifications

While very significant improvements in the last year have occurred in bringing OMEGA EP closer to full performance specifications, for which we applaud the Omega Laser Facility, we look forward to continued improvement in its capabilities (L. Willingale, M.-S. Wei, R. Mancini, P. Norreys, and P. Drake).

### 4. OMEGA EP Long-UV-Pulse Operations

Long-pulse operation, in the 10- to 100-ns interval, would enable new and unique science to be performed. These include shock, photoionization-relaxation and nonequilibrium, late-time instabilities, and, in general, larger time-scale laboratory astrophysical experiments (R. Mancini, C. Kuranz, R. Heeter, D. Martinez, J. Kave, P. Drake, P. Keiter, M.-S. Wei, and H.-S. Park).

### 5. Opposing UV Beams on OMEGA EP

While OLUG recognizes this is a long-term, substantial project requiring considerable resources, it also felt that such a project would be an important new capability of the facility (M.-S. Wei, L. Willingale, C. Kuranz, H. Chen, P. Drake, C. Huntington, and H.-S. Park).

### 6. Independent, or Semi-Independent, Legs for OMEGA-60's Three Legs

While OLUG recognizes this as a major undertaking, this would bring with it significant new capabilities for exciting frontier science (C. Kuranz, R. Mancini, L. Willingale, R. Rygg, and P. Norreys). Related to this is the possible decoupling of Beam 25 for Thomson scattering (C. Huntington).

### 7. Foreground Target Illumination on OMEGA-60

Improvement in the foreground target illumination is recommended (J. Cobble and C. Kuranz).

### 8. Updating the Omega Users' Guide

This document is extremely useful to all users and would benefit from being updated (many users).

### 9. Low-Energy Neutron Spectroscopy.

Extending spectroscopy in the  $\sim 1$ - to  $\sim 2$ -MeV regime, as well as from  $\sim 0.1$  to  $\sim 1$  MeV, would be an outstanding new diagnostic to add to the existing OMEGA 60-beam neutron diagnostics. In addition to giving a new window for basic

capsule-implosion performance, it would almost certainly significantly advance the frontier field of plasma nuclear science, which has been pioneered at the Omega Laser Facility. It is important to note that very significant work has taken place in the past year in this regard (C. Forrest, M. Gatu Johnson, D. McNabb, C. Sangster, J. Frenje, L. Bernstein, J. Caggiano, H. Herrmann, and Y. Kim).

### 10. High-Resolution X-Ray Imaging Spectrometer

This current project, initiated in 2013 by colleagues from Princeton and the University of Rochester, is an outstanding diagnostic that we applaud, bringing additional unique capabilities to the OMEGA 60-beam laser (K. Hill, P. Nilson, H.-S. Park, N. Landen, and J. Frenje).

### 11. Super GCD-3 Gamma Spectrometer

Extending gamma spectroscopy to study low-probability reactions would be highly desirable from both the point of view of implosions physics and for enabling innovative plasma nuclear science/nucleosynthesis such as the H-D fusion line at 5.5 MeV (Y. Kim, H. Herrmann, D. McNabb, A. Zylstra, J. Frenje, and L. Bernstein).

### 12. Differential Burn-Time Diagnostic of D-D and D<sup>3</sup>He

There is a very strong likelihood that for capsules filled with D<sup>3</sup>He, the bang times of D-D and D<sup>3</sup>He may differ by an order of  $\sim 30$  ps or more. Such a differential could be an indication of either two-ion-fluid effects or kinetic effects, neither of which have been deeply explored, although there is strong evidence that such effects should be present. This is a project that was initiated in 2013 and is well underway, with the first system tests and experiments to be conducted on 20 November 2013 (H. Sio, C. Bellei, R. Mancini, P. Amendt, P. Norreys, N. Hoffmann, S. Wilks, S. Atzeni, J. Frenje, C. Stoeckl, V. Glebov, R. Betti, and D. Shvarts).

### 13. Implementing a Two-Ion Fluid Capability in LILAC

LILAC and all other standard hydrocodes in existence—LASNEX, HYDRA, DUED, HYADES—are all single-ion-fluid codes. Having a capability to probe differences in bang time for the two-ion species would be a timely development, as noted above for the differential burn-time diagnostic (H. Sio, C. Bellei, J. Frenje, S. Wilks, P. Amendt, N. Hoffmann, G. Kagan, R. Betti, S. Atzeni, K. Molvig, and D. Shvarts).

### 14. Improvement in SOP/ASBO

Several recommendations were made in this regard. For the active shock breakout (ASBO): a faster comb (4 GHz) is needed along with the ability to image spatial-distortion data

at full sweep speed; alignment and  $Q$ -switching procedures should be updated; new etalons should be acquired. For the streaked optical pyrometer (SOP): improvements are needed in background and noise mitigation along with absolute calibration and imaging spatial-distortion data at full sweep speed (M. Millot, P. Celliers, and T. Boehley).

15. Compact High-Resolution, 14.1-MeV Neutron Spectrometers

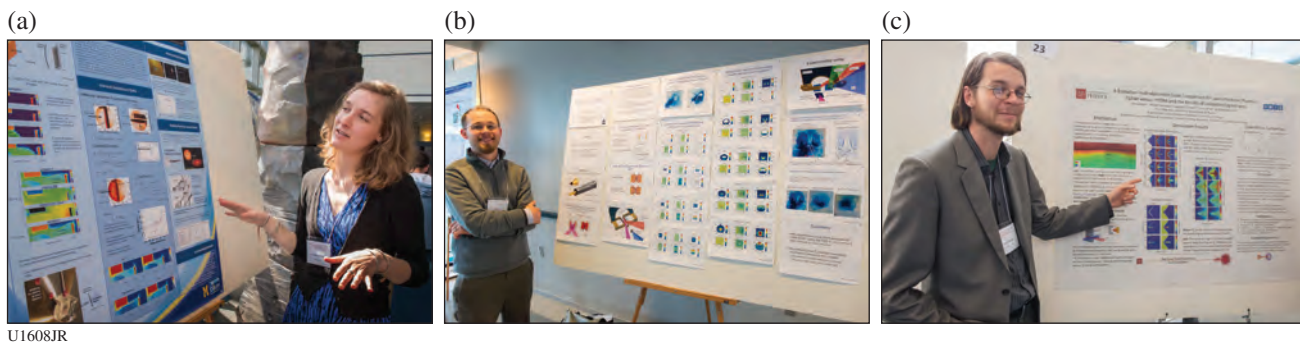
Since kinetic-flow effects are very likely to have a significant impact on furthering our fundamental understanding of cryo and non-cryo capsule implosions, this new diagnostic would extend and nicely complement OMEGA-60's present capabilities. The compactness of the design would allow, for the first time, comprehensive views of the implosions, therefore

enabling blue and red shifts to be simultaneously observed. This project is well underway, with some excellent preliminary data already obtained (A. Zylstra, J. Frenje, V. Glebov, V. Goncharov, J. Caggiano, and J. Kilkenny).

16.  $4\omega$  Thomson Scattering on OMEGA EP

This would be an extremely valuable capability and may not be too resource intensive (W. Fox, C. Kuranz, L. Willingale, H.-S. Park, and C. Huntington).

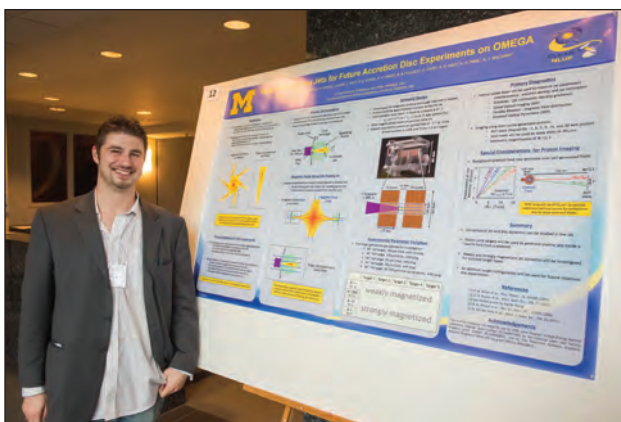
The photographs on the following pages provide a representative sampling of the workshop's talks, interactions, and ambience.



U1608JR

Figure 136.34

The posters ran the gamut from (a) laboratory astrophysics (Christine Krauland from the University of Michigan), to (b) reconnection in high- $\beta$  plasmas (Will Fox, from the University of New Hampshire), to (c) high-end simulations utilizing FLASH (Chris Orban from Ohio State University).



U1609JR

Figure 13.35

NASA's Einstein postdoctoral fellow Mario Manuel presented his continuing OMEGA research plans. Mario, now at the University of Michigan, is the first NLUF/NNSA-sponsored Ph.D. to receive this prestigious Einstein Fellowship. Congratulations to Mario and the Omega Laser Facility, where Mario's Ph.D. research was conducted.



U1610JR

Figure 136.36

Presentations included superb posters given by three researchers in LLE's 2012 Summer High School Research Program. Shown from left are Emily Armstrong, Christa Caggiano, and Raz Rivlis. We plan to expand the number of these high school LLE summer participants in the 2014 workshop.



Figure 136.37

(a) Engineers Mark Labuzeta and Chuck Sorce and (b) engineer Steve Stagnitto. The eight “Facility” posters, many addressing Findings and Recommendations of OLUG, were widely lauded by the users; “tremendously useful and informative” was the universal sentiment for this session. The 2014 workshop will continue this tradition since it has proved so valuable to the workshop attendees.



Figure 136.38

The young researcher’s panel and town meeting is one of OLUG’s most important sessions, highlighting many of the challenges faced by young researchers at the Omega Laser Facility and elsewhere. Next year’s chair of the young researcher’s panel is MIT’s Alex Zylstra (far left).



Figure 136.39

Tours of the facility are a critical part of the workshop and bring home the complexity, coordination, and long-range planning needed for implementing a successful campaign. Here OMEGA EP Senior Engineer and Laser Facility Manager Dave Canning describes OMEGA EP’s hardware, layout of the principal components in the Laser Bay, and the planning needed for a successful OMEGA EP campaign.



U1617JR

Figure 136.40

One of the Finding and Recommendations, discussed here by MIT Ph.D. student Hong Sio, was to use a novel diagnostic to measure, with high accuracy, the differential nuclear bang time of D–D and D<sup>3</sup>He in D<sup>3</sup>He-filled implosions. Such work should illuminate two-fluid-ion effects and/or kinetic plasma effects. The first full-on test of this diagnostic will take place 20 November 2013.

(a)

(c)



(b)



Figure 136.41

World-class physicists described cutting-edge research either ongoing at the Omega Laser Facility, or those tantalizing possibilities “just around the corner:” (a) Don Lamb from the University of Chicago, (b) Mark Koeperle from West Virginia University, and (c) Valeri Goncharov from LLE.



U1612JR



U1620JR

Figure 136.42

The workshop banquet at the Meliora, on the University of Rochester’s campus, offered a wonderful time for old and new friends to mingle in a congenial ambiance.

---

## LLE's Summer High School Research Program

During the summer of 2013, 15 students from Rochester-area high schools participated in the Laboratory for Laser Energetics' Summer High School Research Program. The goal of this program is to excite a group of high school students about careers in the areas of science and technology by exposing them to research in a state-of-the-art environment. Too often, students are exposed to "research" only through classroom laboratories, which have prescribed procedures and predictable results. In LLE's summer program, the students experience many of the trials, tribulations, and rewards of scientific research. By participating in research in a real environment, the students often become more excited about careers in science and technology. In addition, LLE gains from the contributions of the many highly talented students who are attracted to the program.

The students spent most of their time working on their individual research projects with members of LLE's technical staff. The projects were related to current research activities at LLE and covered a broad range of areas of interest including laser physics, computational modeling of implosion physics, experimental diagnostic development, spectroscopy, cryogenic deuterium properties, liquid crystal devices, tritium detection and capture, ballistic deflection transistors, positioning systems, and 3-D virtual modeling (see Table 136.IV).

The students attended weekly seminars on technical topics associated with LLE's research. Topics this year included laser physics, fusion, holography, nonlinear optics, atomic force microscopy, electronic paper, and scientific ethics. The students also received safety training, learned how to give scientific presentations, and were introduced to LLE's resources, especially the computational facilities.

The program culminated on 28 August with the "High School Student Summer Research Symposium," at which the students presented the results of their research to an audience including parents, teachers, and LLE staff. The students' written reports will be made available on the LLE Website and

bound into a permanent record of their work that can be cited in scientific publications.

Three hundred and twelve high school students have now participated in the program since it began in 1989. This year's students were selected from nearly 80 applicants.

At the symposium LLE presented its 17th annual William D. Ryan Inspirational Teacher Award. The recipient this year was Mrs. Eugenie Foster, a mathematics teacher from Brighton High School. This award is presented to a teacher who motivated one of the participants in LLE's Summer High School Research Program to study science, mathematics, or technology and includes a \$1000 cash prize. Teachers are nominated by alumni of the summer program. Mrs. Foster was nominated by Mitch Perry, Julia Tucker, and Jack Valinsky, participants in the 2012 program. They wrote, "Not only is Mrs. Foster a smart and capable teacher, she also has a knack for making math fun and cares about her students ... She allows her students to develop an intuition for the material on their own and encourages them to further their exploration of math outside of the classroom." They credit Mrs. Foster with developing a discrete math course to showcase mathematical topics outside of the core curriculum for students who "have that extra thirst which only mathematics can quench." They also credit Mrs. Foster with developing an Intro to College Math course "to reach out to students who do not perceive themselves pursuing math-related fields in college or those to whom math does not come easily." They go on to say, "Her popularity among her students is due not only to her superb teaching and love of math, but also the personal connections she makes with her students... Past students still come into her classes years after they have graduated to say hello, showing her lasting impact on each and every one of her students." Mrs. Foster also received strong support from Dr. Thomas Hall, principal of Brighton High School, who described her as "a phenomenal teacher, dedicated and passionate, someone who makes herself available to students 24/7."

Table 136.IV: High School Students and Projects—Summer 2013.

Name	High School	Supervisor	Project Title
Aaron Appelle	Brighton	R. Sobolewski and Y. Akbas	Drift-to-Ballistic Electron Transport in Conducting Nanochannels for the Operation of Ballistic Deflection Transistors
Alexander Frenett	Allendale Columbia	F. J. Marshall	Integration of X-Ray Microscope Elements to a High-Speed Framing Camera Format
Sara Gnolek	Webster Thomas	W. T. Shmayda	Catalytic Oxidation of Hydrogen in Air Streams
Samuel Goodman	Pittsford Mendon	W. T. Shmayda	Detecting Hydrogen in Helium Streams
Michael Hartman	Pittsford Sutherland	R. Kidder	Creating a Virtual Research Environment Through Collaborative Networking
Eric Hwang	Penfield	R. Boni and W. R. Donaldson	The Development and Testing of a Signal Processing Algorithm to Improve OMEGA Beam Timing
Katherine James	Honeoye Falls-Lima	K. L. Marshall	Rewriteable Photoalignment of Liquid Crystals as a Route to High-Laser-Damage-Threshold Active Beam Shapers
John Jamieson	Allendale Columbia	M. J. Guardalben	Modeling the Effects of Deformable Mirror Location in the OMEGA EP Pulse Compression System
Yifan Kong	Webster Schroeder	R. S. Craxton	Beam-Pointing Optimization for Proton Backlighting on the National Ignition Facility
Nathaniel Rogalskyj	McQuaid	G. Brent and D. Lonobile	A Cryogenic and Radiation Tolerant Encoder
Benjamin Saltzman	Brighton	P. M. Nilson	Understanding K-Line Shifts in Rapidly Heated Matter
Adeeb Sheikh	Pittsford Sutherland	R. Epstein	Controlling Laser Beam Speckle with Optimized Illumination of Zooming Phase Plates
Logan Toops	Webster Thomas	R. Sobolewski and Y. Akbas	Modeling and Controlling Electron Movement in a Ballistic Deflection Transistor
Erin Wang	Brighton	D. R. Harding	Thermodynamics of the Solid-Liquid Phase Boundary of Deuterium
Cameron Ziegler	Canandaigua Academy	S.-W. Bahk	Alignment of an Offner Triplet Radial Group Delay Compensator

## FY13 Laser Facility Report

During FY13, the Omega Laser Facility conducted 1408 target shots on the 60-beam OMEGA laser and 576 target shots on the four-beam OMEGA EP laser for a total of 1984 target shots (see Tables 136.V and 136.VI). OMEGA averaged 11.5 target shots per operating day with Availability and Experimental Effectiveness averages of 93.9% and 96.6%, respectively.

OMEGA EP was operated extensively in FY13 for a variety of internal and external users. Of the 576 total shots, 507 target shots were taken into the OMEGA EP target chamber and 69 joint target shots were delivered to the OMEGA target

chamber. OMEGA EP averaged 6.7 target shots per operating day with Availability and Experimental Effectiveness averages of 93.8% and 93.7%, respectively.

### Highlights of Achievements in FY13

#### 1. Joint Cryo Backlighting

A new platform has been developed for backlighting 60-beam cryogenic target implosions on OMEGA using the OMEGA EP beam. A ten-inch manipulator (TIM)-based fast positioner has been developed that can place a backlighter target 10 mm from the cryogenic target after the cryogenic shroud

Table 136.V: OMEGA Laser Facility Target Shot Summary for FY13.

Laboratory/ Program	Planned Number of Target Shots	Actual Number of Target Shots	ICF	Shots in Support of ICF	Non- ICF
CEA	40	53	0	0	53
LANL	170	206	21	0	185
LBS	155	163	0	0	163
LLE	390	428	0	416	12
LLNL	295	350	108	0	242
NLUF	150	183	0	0	183
UMich	10	10	0	0	10
Other	0	15	0	15	0
Total	1210	1408	129	431	848

Table 136.VI: OMEGA EP Laser Facility Target Shot Summary for FY13.

Laboratory/ Program	Planned Number of Target Shots	Actual Number of Target Shots	ICF	Shots in Support of ICF	Non- ICF
LANL	0	0	0	0	0
LBS	65	106	0	0	106
LLE	110	165	0	129	36
LLNL	110	158	58	0	100
NLUF	65	91	0	0	91
Other	0	56	0	56	0
Total	350	576	58	185	333

has been retracted. The target is inserted 80 mm in 70 ms with a position accuracy of 25  $\mu\text{m}$ . This fast positioner is being utilized in concert with the spherical crystal imager to capture stop-action images of the cryogenic target during implosions.

## 2. $4\omega$ Probe Diagnostics

Following the successful installation of the  $4\omega$  probe laser in the OMEGA EP Target Bay, the optical diagnostic infrastructure was commissioned in FY13. The first diagnostic leg that was activated can capture shadowgraphs or schlieren images of the laser–plasma interaction. A novel improvement to the schlieren diagnostic placed an angular filter at the Fourier plane to map the refraction of the beam at the target plane to contours in the image plane. The diagnostic also has additional ports available; a polarimetry diagnostic has been designed and will be completed in early FY14.

## 3. Neutron Temporal Diagnostic Replaced

The neutron temporal diagnostic (NTD) is the primary diagnostic for characterization of the reaction rate history of neutron emission for a DT or D<sub>2</sub> target experiment. The original NTD, in use for 15 years on OMEGA and ~10 years prior to that on NOVA at LLNL was decommissioned after the controls and mechanics became obsolete. The improved design increases the service access, shielding, and operability and modernizes the control electronics and streak camera.

## 4. Tritium Fill Station Cryo Permeator

The yield on cryogenic target shots has been improved by a factor of ~2 following the addition of a permeator. A Pd/Ag permeator removes organic impurities and decay helium from the DT fuel as the tritium is transported from the storage beds to the high-pressure fill system. This additional fuel purification step was added to the fill procedures and has been in use on all fills since 1 January 2013.

## 5. Sydor Framing Camera

In a joint development venture with Sydor Instruments LLC, a new gated x-ray detector has been fielded on OMEGA. The Sydor framing cameras can be paired with all unimount-compatible front ends including pinhole imagers and crystal spectrometers. It is compatible with film packs and also with a Sydor vacuum charge-coupled-device (CCD) camera design. Two units have been deployed, one “fast” and one “slow” camera.

## 6. Solid-State Pockels Cell Drivers

LLE has developed a custom solid-state Pockels cell driver to replace discontinued commercially available high-voltage power supplies. The large-aperture ring amplifiers in OMEGA utilize a pulsed Pockels cell in a configuration where thyatron high-voltage switching electronics were used reliably for the past 20+ years. These supplies were the only available technology that could achieve the required long-duration pulse and failsafe requirements to prevent laser damage. The replacement LLE device uses readily available metal–oxide–semiconductor field-effect transistor (MOSFET) solid-state electronics in an inductive–adder configuration to reliably produce pulses with improved rise times, fall times, and uniformity. Five of the LLE-designed power supplies were fabricated in FY13.

## Experimental Operations and Diagnostics

Twenty-five new target diagnostics were commissioned in FY13 on OMEGA and seven on OMEGA EP. The OMEGA additions included the neutron temporal diagnostic (NTD) and framing camera projects described above. The two new Sydor x-ray framing cameras (SFC’s) were commissioned on both OMEGA and OMEGA EP. Updates to the diagnostic inventory on OMEGA EP included the commissioning of the  $4\omega$  probe laser and diagnostic table, the slit imager for the ultrafast x-ray streak camera (UFXRSC), and the LLNL specular frequency-resolved optical gating (SpecFROG) diagnostic. Also on OMEGA, reflective spectrometer channels were added to the TIM-based  $\mu\text{DMX}$  x-ray diode array. As in previous years, many of the new instruments were developed by or in collaboration with other laboratories, including LLNL, LANL, and CEA.

Facility improvements on OMEGA included the Sydor CCD x-ray framing camera readout system, the FASTPOS target positioning system for cryogenic target backlighting, and the Port-2 neutron diagnostic inserter (NDI) system. Two additional OMEGA TIM’s were retrofitted with new electromagnetic interference (EMI)–resistant control systems; four are now complete and the remaining two will be completed in FY14. Minor changes to the OMEGA target chamber and diagnostics improved the typical operating vacuum pressure by nearly an order of magnitude. On OMEGA EP, Target Viewing System (TVS) distortion correction was implemented.

---

## National Laser Users' Facility and External Users' Programs

Under the facility governance plan that was implemented in FY08 to formalize the scheduling of the Omega Laser Facility as a National Nuclear Security Administration (NNSA) User Facility, Omega Facility shots are allocated by campaign. The majority (68.3%) of the FY13 target shots were allocated to the Inertial Confinement Fusion (ICF) campaign conducted by integrated teams from the national laboratories and LLE and the high-energy-density campaigns conducted by teams led by scientists from the national laboratories.

The fundamental science campaigns were allocated 28.3% of the shots taken in FY13. Half of these were dedicated to university fundamental science under the National Laser Users' Facility (NLUF) Program, and the remaining shots were allotted to the Laboratory Basic Science (LBS) Program, comprising peer-reviewed fundamental science experiments conducted by the national laboratories and by LLE, including the Fusion Science Center (FSC).

The Omega Laser Facility is also being used for several campaigns by teams from the Commissariat à l'Énergie Atomique (CEA) of France and the Atomic Weapons Establishment (AWE) of the United Kingdom. These programs are conducted at the facility on the basis of special agreements put in place by DOE/NNSA and participating institutions.

The facility users during this year included 11 collaborative teams participating in the NLUF Program; 16 teams led by Lawrence Livermore National Laboratory (LLNL) and LLE scientists participating in the LBS Program; many collaborative teams from the national laboratories conducting ICF experiments; investigators from LLNL and Los Alamos National Laboratory (LANL) conducting experiments for high-energy-density-physics programs; and scientists and engineers from CEA, AWE, and the Center for Radiative Shock Hydrodynamics (CRASH) of the University of Michigan.

In this section, we briefly review all the external user activity on OMEGA during FY13.

### **FY13 NLUF Program**

FY13 was the first of a two-year period of performance for the NLUF projects approved for the FY13–FY14 funding and OMEGA shots. Eleven NLUF projects (see Table 136.VII) were allotted Omega Laser Facility shot time and conducted a total of 274 target shots at the facility. This NLUF work is summarized in this section.

#### ***Systematic Study of Fast-Electron Energy Deposition in Imploded Plasmas with Enhanced OMEGA EP Laser Contrast and Intensity***

Principal Investigators: F. N. Beg (University of California, San Diego) and M.S. Wei (General Atomics)

Co-investigators: C. McGuffey and B. Qiao (University of California, San Diego); R. B. Stephens (General Atomics); A. A. Solodov, W. Theobald, C. Stoeckl, J. A. Delettrez, and R. Betti (LLE); C. D. Chen, M. H. Key, P. Patel, and H. McLean (LLNL); and T. Yabuuchi and H. Habara (Institute of Laser Engineering, Japan)

Lead Graduate Student: L.C. Jarrott (University of California, San Diego)

Understanding fast-electron transport and spatial energy deposition in high-density plasmas is extremely important for fast-ignition (FI) inertial confinement fusion. The goal of the University of California San Diego NLUF project is to characterize fast-electron spatial energy deposition in integrated cone-guided FI experiments by measuring fast-electron-induced Cu K-shell fluorescence emission using Cu-doped CD shells attached to a Au cone. This target design facilitates the knowledge of the crucial parameters that can affect the coupling, so that coupling to the core can be improved. In this FY13 experiment, the laser energy contrast on the OMEGA EP laser had been improved by nearly two orders of magnitude compared with the FY12 NLUF campaign (from ~80 mJ to <1 mJ in the nanosecond prepulse). With this, a comparison of fast-electron coupling efficiency and spatial distribution as a function of laser contrast was made.

Table 136.VII: NLUF proposals approved for shots at the Omega Laser Facility for FY13–FY14.

Principal Investigator	Institution	Project Title
F. N. Beg	University of California, San Diego	Systematic Study of Fast-Electron Energy Deposition in Imploded Plasmas with Enhanced OMEGA EP Laser Contrast and Intensity
R. P. Drake	University of Michigan	Experimental Astrophysics on the OMEGA Laser
T. Duffy	Princeton University	Dynamic Compression of Earth and Planetary Materials Using OMEGA
W. Fox	University of New Hampshire	Dynamics and Instabilities of Magnetic Reconnection Current Sheets in High-Energy-Density Plasmas
P. Hartigan	Rice University	Astrophysical Dynamics in the Laboratory: Mach Stems and Magnetized Shocks
R. Jeanloz	University of California, Berkeley	Journey to the Center of Jupiter, Recreating Jupiter's Core on OMEGA
H. Ji	Princeton University	Study of Particle Acceleration and Fine-Scale Structures of Collisionless Magnetic Reconnection Driven by High-Energy Petawatt Lasers
R. D. Petrasso	Massachusetts Institute of Technology	Studies of Laboratory Astrophysics, Inertial Confinement Fusion, and High-Energy-Density Physics with Nuclear Diagnostics
B. Qiao	University of California, San Diego	Dynamics of High-Energy Proton Beam Focusing and Transition into Solid Targets of Different Materials
A. Spitkovsky	Princeton University	Generation of Collisionless Shocks in Laser-Produced Plasmas
R. B. Stephens	General Atomics	Investigation of the Dependence of Fast-Electron Generation and Transport on Laser Pulse Length and Plasma Materials

This work used the OMEGA laser for fuel assembly and an OMEGA EP beam focused onto the inner cone tip to produce fast electrons. A spherical crystal imager (SCI) was used to image the  $K_{\alpha}$  radiation from the Cu dopant atoms. Emission was observed in the imploding plasma initiated by suprathermal electrons from the OMEGA beams as well as the fast electrons produced from the OMEGA EP beam. A calibrated zinc Von Hamos (ZVH) x-ray spectrometer, tuned to measure Cu K-shell and ionic line emission, recorded yield measurements. Several other diagnostics, including broadband x-ray imaging pinhole cameras and Kirkpatrick–Baez (KB) microscopes, neutron time-of-flight detectors, and magnetic electron spectrometers (one multichannel spectrometer along the OMEGA EP beam axis and one single-channel spectrometer at the side), were employed.

With improvements to our FY12 demonstration experiment, the dopant level in the CD shells was increased from 0.9% to 1.3% as a means to increase Cu  $K_{\alpha}$  photon statistics, and the SCI beam block was modified to reduce background. The filtration level on the neutron detectors was also adjusted from previous campaigns, resulting in observed neutron yields for the first time in this series of experiments.

Figure 136.43 compares integrated Cu  $K_{\alpha}$  yield for FY12 and FY13 NLUF campaigns measured with the ZVH spectrometer. Differences in dopant level have been taken into account. With the improved OMEGA EP contrast, up to ~50% enhancement in fast-electron–produced Cu  $K_{\alpha}$  was measured. Further, the scaling of Cu  $K_{\alpha}$  with OMEGA EP energy was steeper, indicating better coupling of laser energy into fast electrons at high (kJ) laser energies. Fusion neutron yield was also found to increase by roughly a factor of 3 when increasing the OMEGA EP energy from 0 J (OMEGA-only implosion) to full energy (1.2 kJ) as seen in Fig. 134.44.

A major component of the project has been the development and benchmarking of our modeling capabilities through experimental results. Three parallel studies are underway using three different codes to model the experimental results. In each study, simulations of the implosion using the radiation–hydrodynamic code *DRACO* are used as input to model the fast-electron transport through the imploded plasma. In addition the laser–plasma interaction from the OMEGA EP beam with the inner Au cone is simulated using the particle-in-cell code *LSP*. With this, a more-accurate electron source can be used while simultaneously validating the electron source simulations via

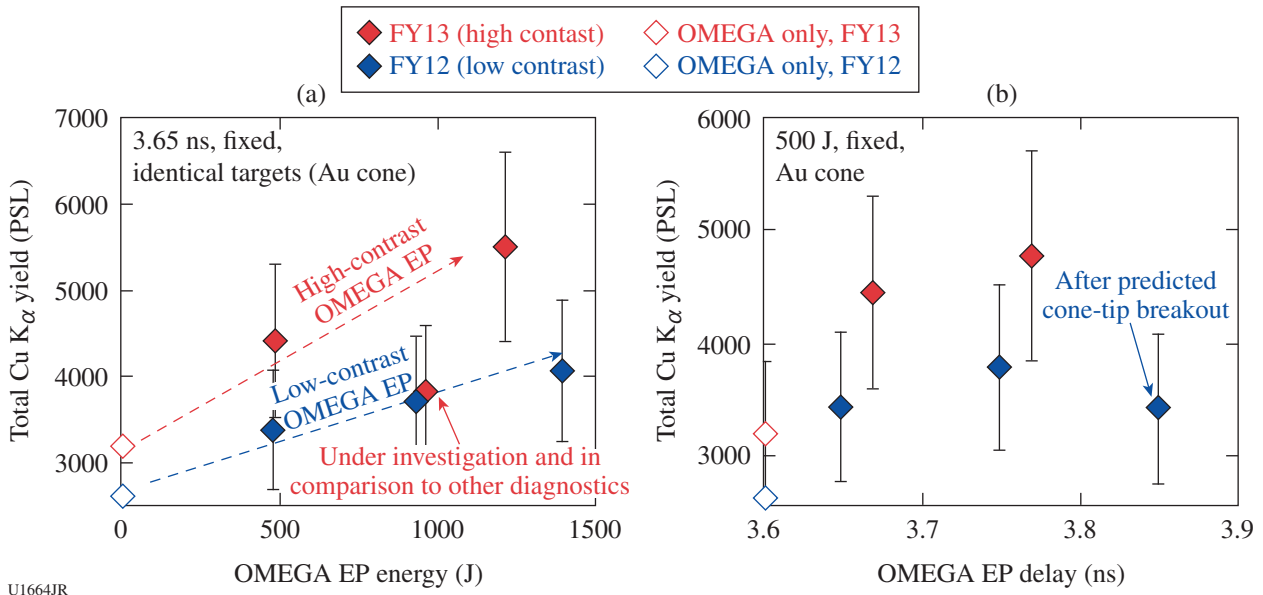


Figure 136.43

Comparison of Cu K $\alpha$  yield enhancement caused by fast electrons measured by zinc Von Hamos (ZVH) as a function of (a) OMEGA EP beam energy and (b) OMEGA EP timing delay using high- and low-contrast OMEGA EP pulses. The 1-kJ shot had anomalously low K $\alpha$  and continuum on the ZVH diagnostic only, which is under further scrutiny.

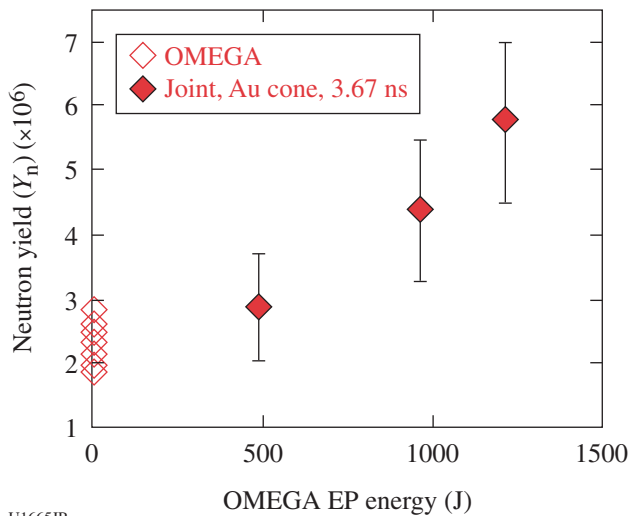


Figure 136.44

FY13 data set showing D–D neutron yield for the first time from the Cu-doped targets. Yield increased as a function of laser energy.

a backward analysis of the transport codes. Diagnostics have been implemented in the codes to emulate the projected Cu K $\alpha$  profile for direct comparison to the experimental images.

In summary, the NLUF fast-electron transport experiment using a cone-in-shell (with Cu doping) target has been success-

fully performed on the OMEGA laser with a comprehensive suite of x-ray, particle, and, for the first time, neutron diagnostics. The platform for complex electron-transport physics experiments has been established and will be pursued for >kJ short-pulse laser energies.

**Richtmyer–Meshkov Mode Coupling on OMEGA EP**

Principal Investigators: R. P. Drake, P. Keiter, and C. Kuranz (University of Michigan)

Co-investigators: S. Lebedev (Imperial College); D. Shvarts and Y. Elbaz (Negev Research Center); G. Gregori (Oxford); M. Koenig (École Polytechnique); B. van der Holst, B. Torralva, and M. Grosskopf (University of Michigan); E. Blackman (University of Rochester); J. P. Knauer, T. R. Boehly, G. Fiksel, and D. H. Froula (LLE); C. Michaut (Observatoire de Paris); and B. Loupias (CEA)

Shock-wave–related interface phenomena play important roles in many diverse high-energy-density (HED) processes, such as the cooling of fusion fuel capsules or mixing of layers in supernova remnants. Recently, the unique laser and diagnostic capabilities of OMEGA EP has enabled us to develop a novel series of experiments exploring HED hydrodynamics driven by steady shock waves. Here, we describe an experiment observing, for the first time, well-characterized multimode Richtmyer–Meshkov (RM) physics under these conditions.

RM occurs when a shock wave crosses the interface between two materials of differing densities. If a region of such an interface is not perfectly smooth, the shock will cross the interface at different times in adjacent locations and will briefly have different velocities in the two locations. This results in the deposition of vorticity at this interface perturbation, and the vorticity in turn causes the perturbation to grow in time. This experiment seeks to study RM behavior at late times, when the growth has become nonlinear, and in particular to observe the interaction between perturbation modes.

The initial conditions for this experiment involve a layer of carbon foam of  $0.4\text{-g/cm}^3$  density pressed against a layer of plastic of  $1.4\text{-g/cm}^3$  density. On the surface of the plastic, at its interface with the foam, a two-mode (wavelengths of 50 and  $100\ \mu\text{m}$ ) sinusoidal seed perturbation has been machined. The materials are ordered such that the shock passes from the lower-density foam into the higher-density plastic, making the configuration Rayleigh–Taylor stable. A plastic ablator, of  $1.2\text{-g/cm}^3$  density, is placed before the foam in order to avoid direct irradiation of the foam by the laser. A sketch of this system is shown in Fig. 136.45. Two (a third can also be used) OMEGA EP beams, operating in UV mode with 10-ns pulse durations and fired sequentially to create an effective 20-ns-long pulse, are used to drive a shock wave into this system. The beams have an energy of roughly 4 kJ each and are smoothed by  $1100\text{-}\mu\text{m}$ -diam phase plates, resulting in an irradiance of roughly  $4 \times 10^{13}\ \text{W/cm}^2$ . Following passage of the shock wave, a RM structure develops over time at the foam/plastic interface. The interface is then diagnosed using the OMEGA EP spherical crystal imager to perform side-on radiography. Examples of data are shown in Fig. 136.46.

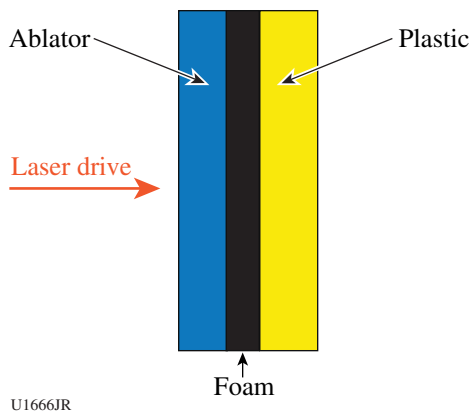
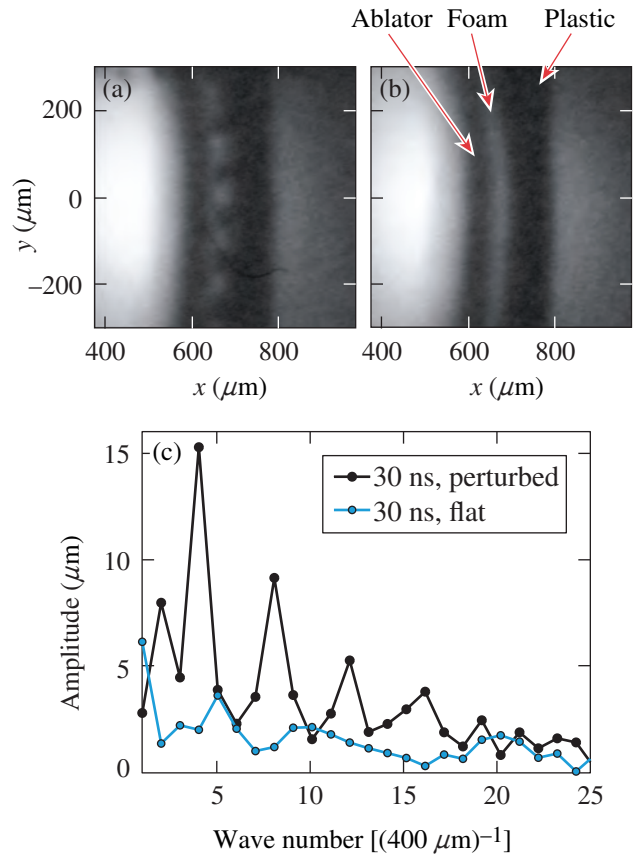


Figure 136.45  
Experimental schematic. The laser irradiates the left edge of the ablator, driving a rightward-propagating shock into the system.



U1667JR

Figure 136.46

Examples of radiographs from shots (a) with and (b) without the machined seed perturbation, respectively. Both images were taken roughly 13 ns after the shock crossed the foam/plastic interface. (c) The Fourier transform of the foam/plastic interface contour, demonstrating the growth of the initial modes of wave number  $k = 4$  and  $k = 8$ , corresponding to  $100\text{-}\mu\text{m}$  and  $50\text{-}\mu\text{m}$  wavelengths, respectively, as well as the appearance of harmonic modes  $k = 4 + 8 = 12$  and  $k = 12 + 4 = 16$ , corresponding to  $33\text{-}\mu\text{m}$  and  $25\text{-}\mu\text{m}$  wavelengths, respectively.

### X-Ray Diffraction Study of the Structure and Equation of State of Molybdenum to 9 Mbar

Principal Investigator: T. Duffy (Princeton)

The goal of this campaign was to study the structure of solid molybdenum (Mo) using x-ray diffraction under both ramp and shock-wave loading. Experiments were performed using the powder x-ray diffraction image plate (PXRDIIP) diagnostic (Fig. 136.47). Four OMEGA beams were focused on the main target to drive and compress the Mo powder (sandwiched between two diamonds) and up to ten beams were focused on a Cu backlighter to generate quasi-monochromatic x-ray emission for diffraction measurements. We used a 3.5-ns ramp (rm3501) followed by a 1-ns square pulse (sg1018) to drive

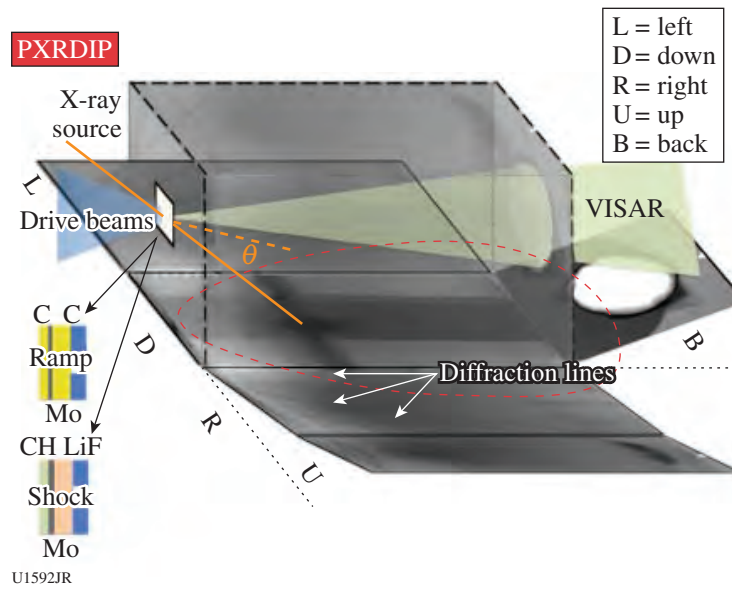


Figure 136.47

Powder x-ray diffraction image plate (PXRDIIP) experimental setup. Thin Mo pellets ( $\sim 4 \mu\text{m}$ ) or foils ( $\sim 10 \mu\text{m}$ ) were placed between two diamond plates (ramp) or a CH ablator and LiF window (shock) and attached to a  $300\text{-}\mu\text{m}$ -diam Ta pinhole. The target package was ramp compressed or shock compressed by the OMEGA laser drive. The pressure was determined from the velocity interferometer system for any reflector (VISAR) record of the interface of Mo and window material. X rays generated from a Cu foil were collimated through the pinhole and produced diffraction from the sample. The unfolded image plates show the diffraction lines of the sample and pinhole material.

the main target and a 1-ns square to drive the backlighter. The active shock breakout (ASBO) [velocity interferometer system for any reflector (VISAR)] was used to measure the free-surface velocity of the diamond, and backward integration was used to determine the pressure at the interface of the diamond and sample.

The Mo was ramp and shock compressed to approximately 900 GPa and 350 GPa, respectively. The x-ray diffraction patterns were recorded on image plates attached to the inner wall of the PXRDIIP diagnostic. Diffraction peaks obtained from ramp-compressed Mo are consistent with the body-centered-cubic (bcc) structure up to 900 GPa, and we found no evidence of solid–solid phase transition as predicted by theoretical studies using the density functional theory. Under shock loading, the bcc phase of Mo also remained stable along the Hugoniot to at least 350 GPa, and no evidence was observed for the solid–solid phase transformation around 210 GPa as reported in previous gas-gun experiments. Figure 136.48 shows the pressure–density relationship obtained from the diffraction data combined with applied stress from the VISAR record. Since ramp compression avoids large heating compared with shock loading, our data are intermediate between previous shock (gray triangles) and static (red symbols) compression data (Fig. 136.48).

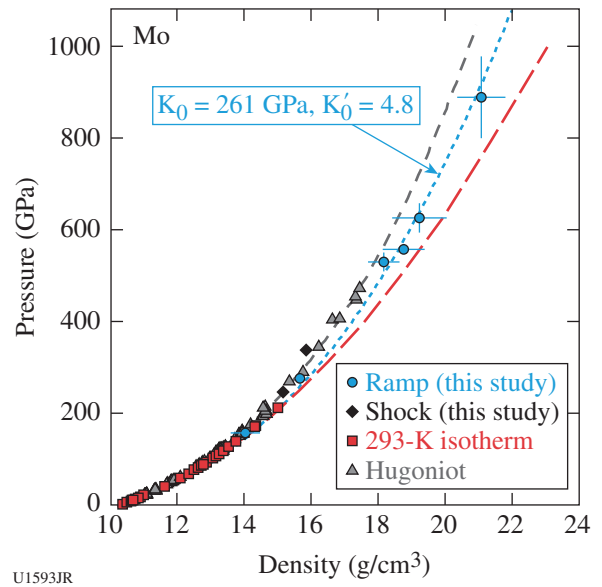


Figure 136.48

Compression behavior of molybdenum under both ramp and shock loading up to 900 GPa. The blue circles represent the data from ramp compression fit with the body-centered-cubic (bcc) structure. The black diamonds show the data along Hugoniot curve also fit with the bcc structure. The blue dashed line is an equation-of-state fit to the ramp-compression data with the bulk modulus  $K_0$  fixed to 261 GPa and a fit pressure derivative of the bulk modulus  $K'_0 = 4.8$ . Also plotted in this figure for comparison are the results of previous shock and static compression studies.

**Dynamics of Magnetic Reconnection Current Sheet in High-Energy-Density Plasmas**

Principal Investigator: W. Fox (University of New Hampshire)  
 Co-investigators: A. Bhattacharjee (Princeton); and G. Fiksel, P. M. Nilson, and S. X. Hu (LLE)

We have developed and conducted experiments on OMEGA EP to study the phenomenon of magnetic reconnection. Magnetic reconnection occurs when regions of opposite directed magnetic fields in a plasma can interact and relax to a lower-energy state; it is an essential plasma physics process in many systems that governs the storage and explosive release of magnetic energy in systems such as the earth's magnetosphere, the solar corona, and magnetic fusion devices. The energy thereby liberated can produce heat and flows and can enable the acceleration of a large number of particles to high energies.

These experiments on OMEGA EP used an externally applied magnetic field of the order of 12 T as the seed field for reconnection. With an externally applied field, the fields undergoing reconnection are under experimental control, so it is possible to conduct experiments with variable fields and topologies; for example, we have already conducted the "zero field" null experiment. We have successfully magnetized and collided the counterpropagating plasmas. Figure 136.49 shows

a sequence of proton radiography images of the collision and interaction of the magnetized plasmas. The results are qualitatively different than the unmagnetized case and show the formation of a pair of magnetized "ribbons" propagating toward one another. These ribbons are regions of a deficit of protons to the film and indicate regions of strong magnetic field—magnetized plasma—that have steered the diagnostic proton beam off-film. The successful formation of these pairs of ribbons is non-trivial—it was found that it was essential to add a third "background" plasma source, triggered before the blowoff plasma forms the two primary targets, to fill the experimental volume with a diffuse low-density plasma. The image sequence shows the ribbons propagating toward one another and colliding at the midplane, generating bubble-like structures as the regions of oppositely magnetized plasmas interact and drive reconnection of the magnetic fields. The results are presently being analyzed and compared with particle-in-cell simulations.

**Shock Waves and Clumpy Environments in Astrophysical Flows**

Principal Investigator: P. Hartigan (Rice University)  
 Co-investigators: A. Liao (Rice University); J. Foster, P. Graham, and P. Rosen (AWE); G. Fiksel (LLE); G. Gregori and J. Cross (Oxford); K. Yirak and B. Wilde (LANL); A. Frank and S. Li (University of Rochester); and B. Blue (General Atomics)

During FY13, we continued our investigation of irregular (Mach) shock-reflection phenomena that was partly reported last year; we have tested a laser-driven gas-cell target for the study of shock-interaction phenomena in radiative shocks; and we have begun a new series of experiments by developing a platform to study hydrodynamic flow in clumpy media in the presence of an imposed magnetic field. The now-complete set of data from our Mach-reflection experiment (Mach-stem growth rate and hysteresis for various angles of incidence of a warm-dense-plasma shock at a reflecting boundary) was reported at the most-recent High-Energy-Density Laboratory Astrophysics (HEDLA) meeting.<sup>1</sup> In the present report, we concentrate on our work to develop a platform for a magnetized-plasma laboratory analogue of the wind–cloud interaction.

Magnetic fields are ubiquitous in astrophysical environments, and yet the hydrodynamics of magnetized plasmas has been largely neglected in many laser-driven laboratory astrophysics studies. This omission arises from the difficulty of establishing an environment in which the magnetic pressure is sufficiently large, compared to the thermodynamic and

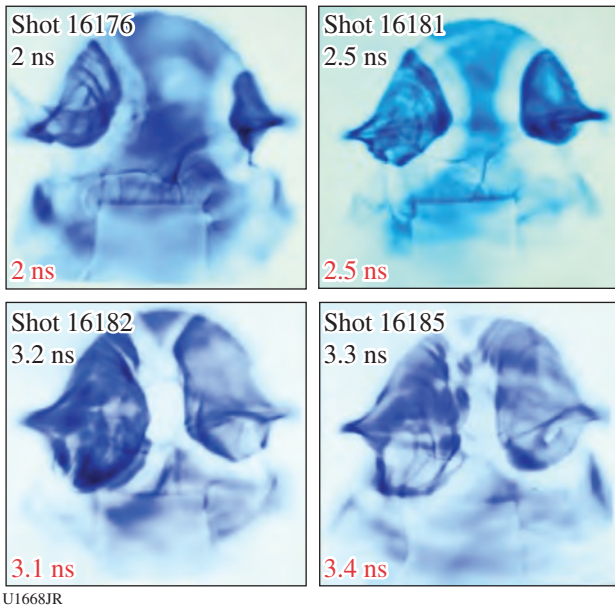
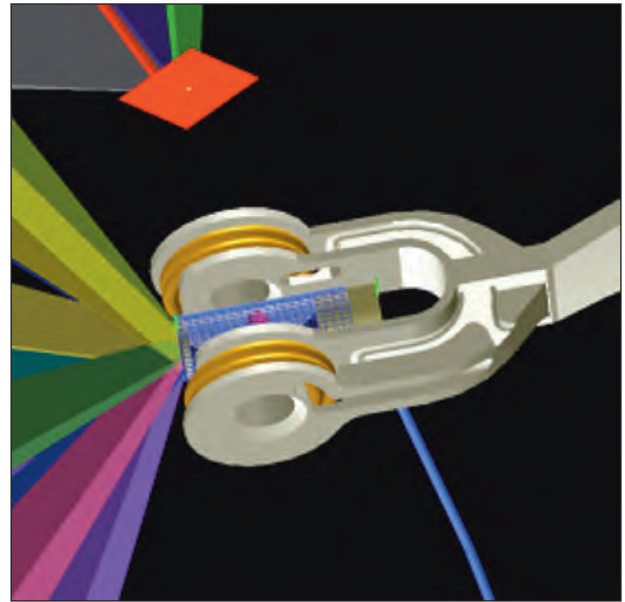


Figure 136.49 Time-sequenced proton radiography images of the collision and interaction of two counter-propagating plasmas (left and right, respectively, on each shot). The two white zones (magnetized ribbons) propagating toward each other represent a reduction in proton flux.

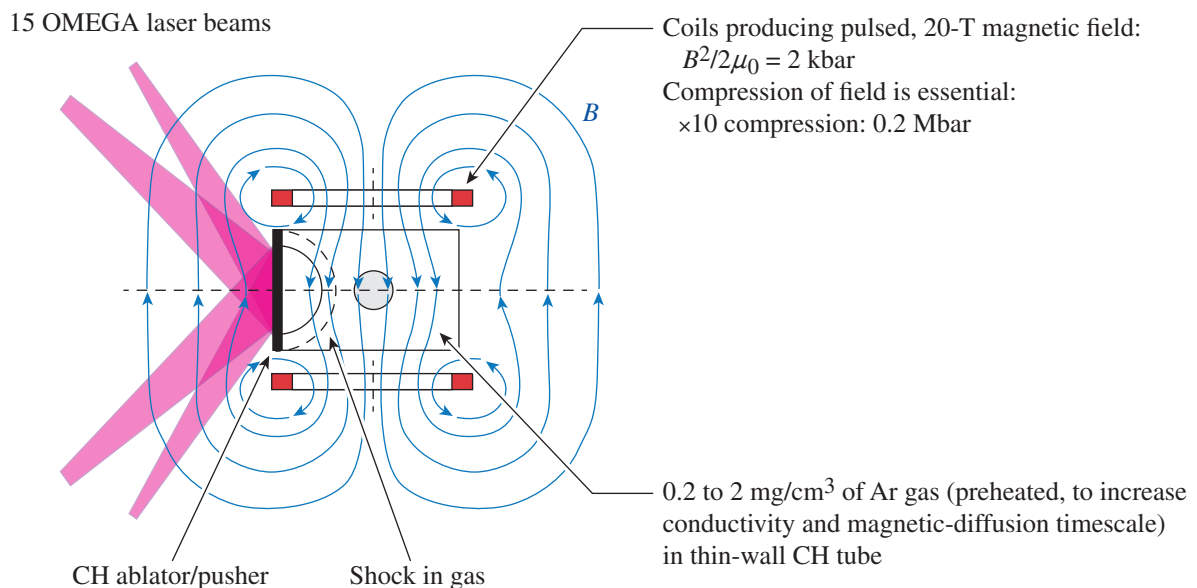
ram pressures, to affect some measurable quantity such as the overall hydrodynamic flow or the growth of instabilities. The recent availability on OMEGA of the magneto-inertial fusion electrical discharge system (MIFEDS) compact magnetic-field generator has led us to attempt a laboratory analogue of the interaction between a magnetized wind and embedded denser cloud in relative supersonic motion. Gregori *et al.*<sup>2,3</sup> present results from three-dimensional magnetohydrodynamic (MHD) simulations investigating such wind–cloud interactions. In their model, the cloud is treated as initially spherical, while the magnetic field is uniform and transverse to the direction of relative motion of the cloud and ambient, magnetized medium. Stretching the magnetic field lines leads to a strong enhancement of the field at the leading edge of the cloud and a significant modification of the hydrodynamics. Even for a surprisingly large initial ratio of the ram and magnetic pressures ( $\beta = 100$ ), a clear difference is found from a simulation without magnetic field ( $\beta = \infty$ ) because of compression enhancement of the magnetic field at the pole of the cloud. A laboratory analogue of Gregori's model astrophysical simulation seems to be accessible only on OMEGA—given an imposed magnetic field from MIFEDS of the order of 20 T, supersonic flow in a low-density ( $\ll 1\text{-mg/cm}^3$ ) gas, and an adequately long magnetic diffusion time scale ( $>200$  ns) in the (radiatively preheated and therefore conducting) ambient gas.

Figures 136.50 and 136.51 show our experimental setup. Fifteen OMEGA laser beams directly drive ( $2 \times 10^{14}$  W/cm<sup>2</sup> incident intensity) a thin (few- $\mu\text{m}$ -thickness) CH ablator that



U1670JR

Figure 136.51  
VISRAD rendering of the experiment, showing the MIFEDS magnetic-field coils and x-ray backlighting target.



U1669JR

Figure 136.50  
Schematic of an OMEGA experiment to study the flow of a low-density, magnetized plasma over an embedded particle—a laboratory analogue of the astrophysical wind–cloud interaction.

closes one end of a cylindrical gas-cell laser target (typically 3 mm in diameter, several mm in length). The gas cell is filled with, for example, argon gas at atmospheric or subatmospheric pressure (0.2- to 2-mg/cm<sup>3</sup> density) and contains a low-density aerogel sphere or cylinder, or a gas-filled, thin-wall capsule. This assembly is placed at the center of the MIFEDS pulsed magnetic-field generator that provides an initial magnetic field transverse to the axis of the experiment of 10 to 20 T. Direct laser drive at the thin end wall of the gas cell results in an ablatively driven shock that reaches and sweeps over the embedded object in a time scale of 20 to 50 ns, and radiative preheat ahead of the shock results in a radiation precursor, raising the ambient gas temperature to 20 to 50 eV over a distance of the order of 1 mm. This radiative preheat results in sufficient electrical conductivity for the magnetic-diffusion time (~200 ns) to adequately exceed the hydrodynamic time scale of the experiment, allowing (at least in principle) significant enhancement of the field. The hydrodynamic flow of the embedded particle is diagnosed by x-ray point-projection backlighting radiography, and comparison is made of experiments with and without magnetization of the ambient-gas plasma.

We concluded our FY13 NLUF allocated time on OMEGA by starting this experiment. In developing the experimental

platform, we used a relatively simple (although not ideal) laser target (1 atm-pressure argon gas, 50-mg/cm<sup>3</sup> embedded silica-aerogel cylinder) and modest magnetic-field strength (7 T), resulting in conditions that fall somewhat short of our required plasma  $\beta = 100$ . Nevertheless, the excellent experimental data that we obtained have been used to verify pre-shot, 2-D, non-MHD simulations of the hydrodynamics. Our pre-shot calculations of shock positions in the gas and embedded particle (spherical particle in the case of the 2-D simulation) agree well with those observed experimentally and provide confidence in modeling our design of a lower gas density,  $\beta = 100$ , experiment planned for FY14.

Figure 136.52 shows typical radiographic data from the experiment, at the time of approximately half-crushing the embedded aerogel cylinder. Further modeling of the experiment, including both ideal- and resistive-MHD simulations, is in progress.

In addition to our experimental work on OMEGA, one of the authors (P. Hartigan) has acted as editor of the proceedings of the recent HEDLA laboratory-astrophysics meeting and has published a paper<sup>4</sup> on irradiated interfaces that is also of direct relevance to our experiments on OMEGA.

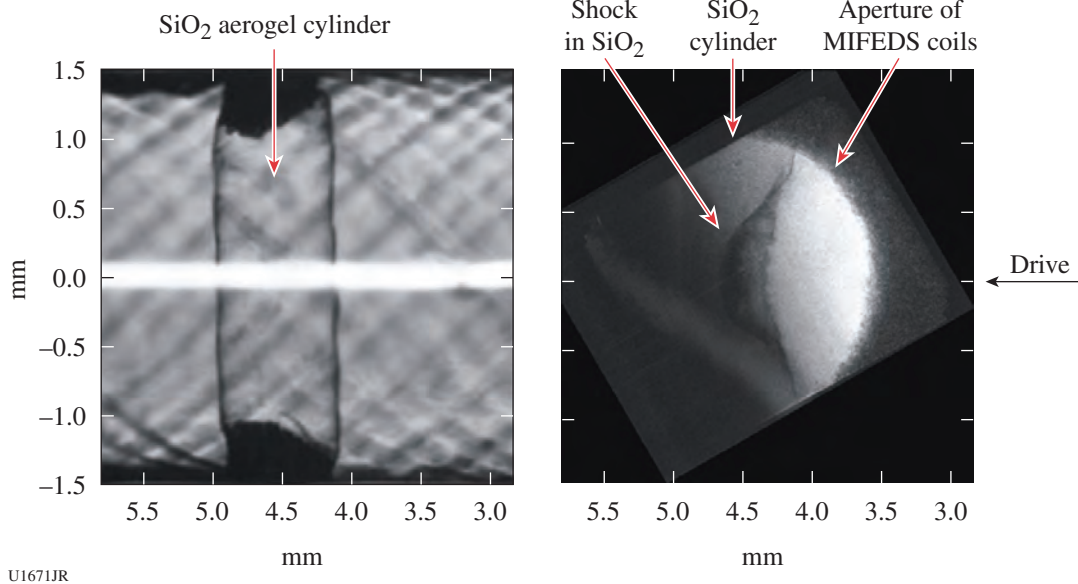


Figure 136.52

(a) Pre-shot optical image of the silica-aerogel cylinder within the gas-cell target and (b) experimental radiograph of the shock in the aerogel cylinder, observed at approximately one-half crushing time and 50 ns after the onset of the laser drive. The dimensions of the space scale are in millimeters, and the spatial resolution is 15  $\mu$ m. MIFEDS imposed a magnetic field of 7 T.

**Journey to the Center of Jupiter: Recreating Jupiter's Core at Omega**

Principal Investigator: R. Jeanloz (University of California, Berkeley)

Co-investigators: S. Brygoo and P. Loubeyre (CEA); M. Millot (University of California, Berkeley); P. M. Celliers, J. H. Eggert, S. Hamel, J. R. Rygg, and G. W. Collins (LLNL); and T. R. Boehly (LLE)

During FY13, the PlanetCore University of California, Berkeley/CEA/LLNL/LLE collaboration conducted four very successful campaigns at the Omega facility with 28 shots. We continued our long-term effort to document the physics of warm dense hydrogen and helium under the extreme conditions of pressure and temperature that exist deep within giant planets like Jupiter, Saturn, and extra-solar objects. We used ultrafast Doppler velocimetry (VISAR) and streaked optical pyrometry (SOP) to measure the equation of state and optical properties of H<sub>2</sub> and He along the Hugoniot, starting from highly precompressed states.

We recently managed (see Fig. 136.53) to significantly extend the precompression domain in hydrogen and helium

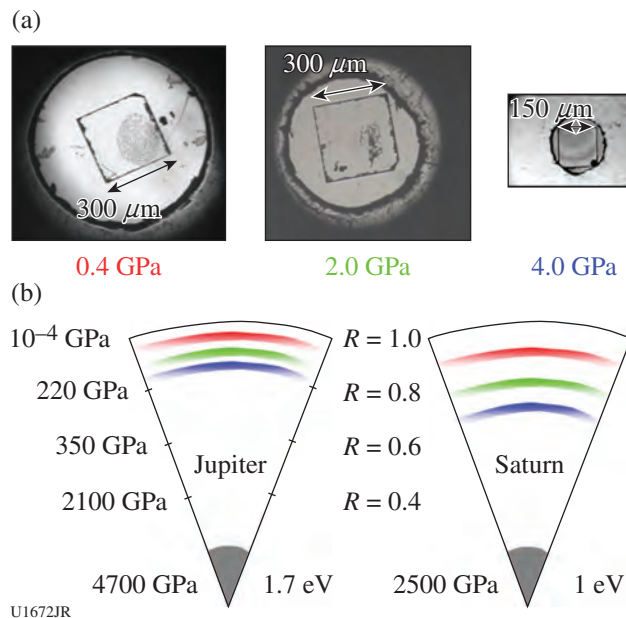


Figure 136.53 (a) Change in pressure-chamber dimensions within the diamond-anvil cell targets, documenting how design improvements over the past years have allowed the PlanetCore team to achieve higher precompressions than ever. (b) Achieving higher precompression allowed us to study hydrogen, helium, and hydrogen–helium mixtures at pressure–density–temperature conditions relevant for deeper regions inside Jupiter and Saturn: the color scale links the initial pressure and the depth within the planets that we were able to *recreate* at the Omega Laser Facility.

samples to an initial pressure larger than 5 GPa. The new equation-of-state data in very dense plasmas of hydrogen (Fig. 136.54) now approach the degeneracy and correlation conditions of the DT plasma along the ICF compression path. Preliminary analysis provides new constraints on the temperature–pressure–density localization of the metallization of warm dense fluid hydrogen. However, no density discontinuity was found along the Hugoniot, in contrast with previous explosive-driven compression radiographic measurements in a cylindrical geometry.<sup>5</sup> The nature and magnitude of a density jump on metallization are of particular importance for comparisons with theory.

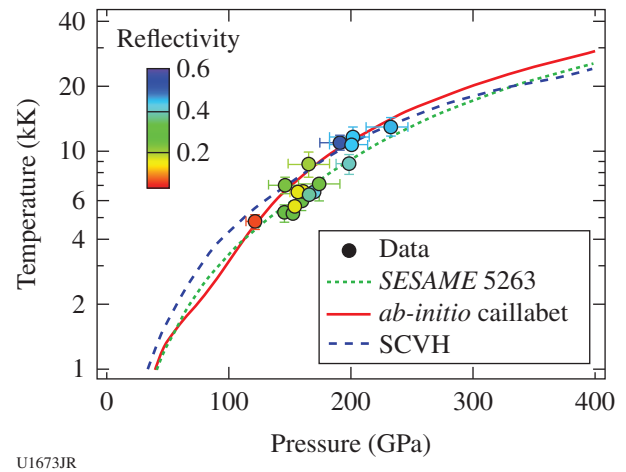


Figure 136.54 During FY13 the PlanetCore team measured the equation of state and optical reflectivity of shock-compressed deuterium, starting from solid D<sub>2</sub> precompressed to 6 GPa and reaching final pressures above 250 GPa. The initial density is 1.7× the highest initial density previously reported [precompression of 1.5 GPa (Ref. 7)]. Preliminary analysis suggests that the new data provide an important benchmark in temperature–pressure–density space for characterizing the metallization of warm dense fluid hydrogen. No density discontinuity is found along the Hugoniot, in contrast with previous explosive-driven compression radiographic measurements in a cylindrical geometry.<sup>5</sup> Shock temperatures are in good agreement with recent *ab-initio* simulations (solid red line). SCVH: Saumon–Chabrier–Van Horn EOS model.

In our previous measurement of the He Hugoniot with precompressed data to 1.5 GPa, the reflectivity was measured versus density and temperature. A fit to the data suggested that (1) the electronic mobility gap closes with density and (2) hot dense helium should become metallic around 1.9 g/cm<sup>3</sup>, i.e., at much lower density than predicted by first-principles calculations. We have now measured the reflectivity of shock-compressed helium up to a final density of 2 g/cm<sup>3</sup> along the Hugoniot starting at 5 GPa (Fig. 136.55). Preliminary analysis of the new data set suggests that the metallization density,

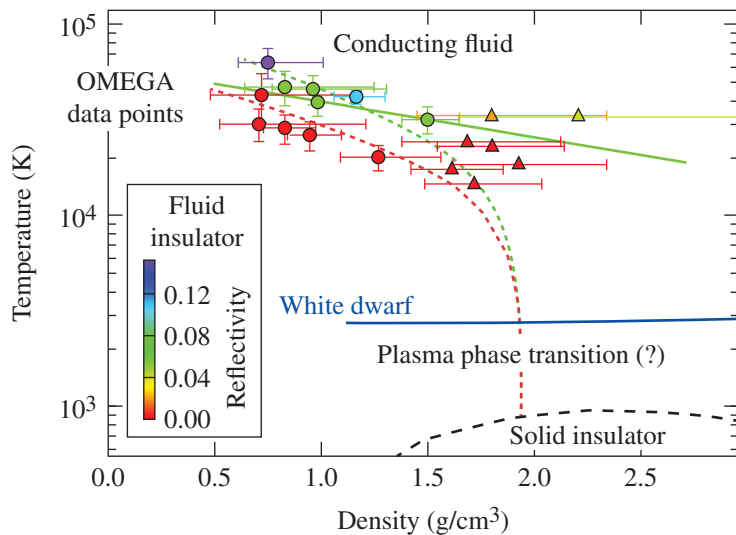


Figure 136.55

Evolution of the optical reflectivity (representative of metallization, color scale) of warm dense helium as a function of temperature and density. During FY13, the PlanetCore team measured the reflectivity of shock-compressed helium up to a final density of  $2 \text{ g/cm}^3$  along the Hugoniot, starting at 5 GPa (solid triangles). In 2008, a set of helium data points (solid circles) were obtained on OMEGA with a maximum precompression of 1.1 GPa, covering a density from  $0.7 \text{ g/cm}^3$  to  $1.5 \text{ g/cm}^3$  (Ref. 8). A Drude model fit of the 2008 data predicted metallization (closure of the band gap)  $\sim 2 \text{ g/cm}^3$  at moderate temperature (dotted lines). The new data set indicates that the metallization density was previously underestimated. The new determination of gap closure as a function of density and temperature (solid green line, preliminary analysis) is in fair agreement with a recent *ab-initio* prediction of gap closure above  $5 \text{ g/cm}^3$  (Ref. 6).

U1674JR

obtained by extrapolation over a more-limited density range, was previously underestimated. The new experimental estimate for the gap closure as a function of density and temperature is found to be in fair agreement with the recent *ab-initio* prediction of a gap closure above  $5 \text{ g/cm}^3$  (Ref. 6).

**Particle Acceleration from Collisionless Magnetic Reconnection Using the Short-Pulse OMEGA EP Laser**  
Principal Investigator: H. Ji (Princeton)

Magnetic reconnection is a ubiquitous astrophysical phenomenon in which magnetic-field energy is rapidly converted into plasma kinetic energy, in the form of flow energy and thermal energy, as well as nonthermal energetic particles. Despite its long history, little laboratory work in this area has focused on the particle acceleration. The experiments performed on OMEGA EP were the first of this kind using short-pulse (10-ps), high-energy petawatt ( $10^{18}\text{-W/cm}^2$ ) lasers, in contrast to many previous experiments using long-pulse (1-ns) and low-energy ( $10^{15}\text{-W/cm}^2$ ) lasers.

Experiments during the first shot day were performed using two short-pulse OMEGA EP lasers, successfully demonstrating the timing and pointing capabilities necessary for the proposed studies; an initial assessment of particle acceleration and jet formation was also made. Cu foils were used as the target with two laser foci separated by about  $100 \mu\text{m}$ . Each laser was 20 ps long in duration, but timing of these two lasers was controlled to also about 20 ps in accuracy, resulting in only about half of the shots being useful for this study. Three radiochromic film detector packs were used to measure high-energy particles in different angles with respect to the target plane, and an

energetic beam was detected in one of the co-timed shots in the direction consistent with the expectations from the reconnection processes. The next step will be to perform relevant numerical simulations to guide the choices of experimental parameters and to develop new magnetic and particle diagnostics for the proposed shot day in FY14.

**Studies of High-Energy-Density Plasmas, Inertial Confinement Fusion Implosions, and Nuclear Science for Astrophysics**

Principal Investigators: R. D. Petrasso and C. K. Li (MIT)  
Co-investigators: F. H. Séguin and J. A. Frenje (MIT); T. C. Sangster, V. Yu. Glebov, D. D. Meyerhofer, and R. Betti (LLE); and O. L. Landen (LLNL)

MIT work in FY13 included a wide range of experiments that applied proton radiography, charged-particle spectrometry, and neutron spectrometry methods developed by MIT and collaborators to the study of high-energy-density physics (HEDP) and inertial confinement fusion (ICF) plasmas. Seven papers<sup>9-15</sup> and two MIT Ph.D. theses<sup>16,17</sup> about NLUF-related research were published in FY13; also many invited and contributed talks were presented at conferences. Our NLUF experiments provided unique research opportunities in HEDP for seven MIT graduate students, and much of the current NLUF data will appear in major parts of upcoming theses. Several MIT undergraduates also participated.

The success and relevance of MIT's NLUF work during the last decade are reflected in the fact that Principal Investigator R. D. Petrasso received this year's Edward Teller Medal (see Fig. 136.56) for his MIT Division's work in ICF and HEDP.



U1675JR

Figure 136.56  
Principal Investigator R. D. Petrasso accepting the Edward Teller Medal at the International Inertial Fusion Science and Applications Conference (IFSA) in Nara, Japan, in September 2013. The medal was awarded by the Fusion Energy Division of the American Nuclear Society “for pioneering the use of nuclear diagnostics for understanding inertial confinement fusion implosions and high-energy-density physics.” Much of his work and that of his MIT Division was supported by the NLUF Program.

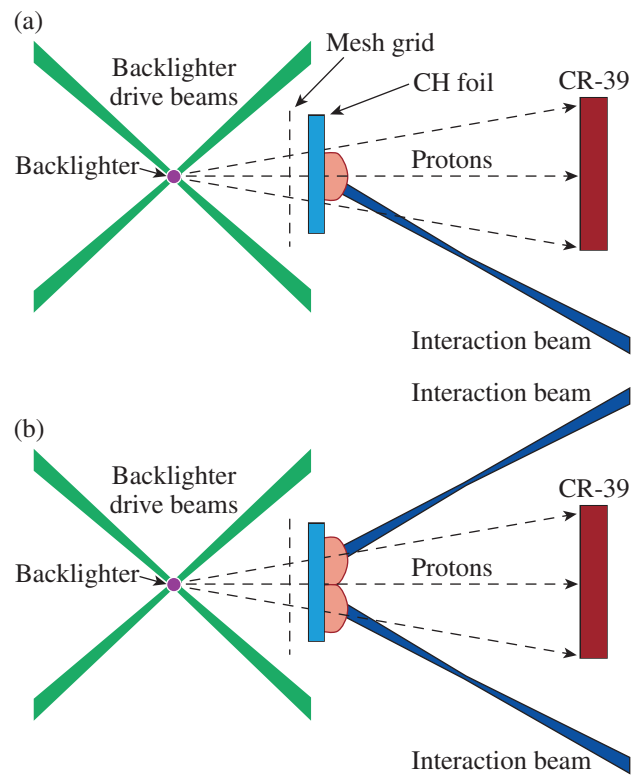
A large fraction of that work was done at the Omega Laser Facility, and much of that was directly sponsored by NLUF.

Topics studied this year on the OMEGA<sup>18</sup> and OMEGA EP<sup>19</sup> Laser Systems and already published include imaging, identifying, and measuring electric and magnetic fields generated in direct- and indirect-drive ICF plasmas<sup>9–12,14,17</sup> and other laser-generated plasmas,<sup>15–17</sup> and measuring ICF performance and fusion products.<sup>13</sup> Data acquired in FY13 and currently under analysis bear on a range of topics including magnetic reconnection, plasma kinetic effects in ICF implosions, the behavior of plasma jets, the stopping of ions in plasmas, cross sections of nuclear reactions relevant to stellar nucleosynthesis, and developing new diagnostics. This work successfully addresses basic physics issues and issues directly relevant to the future success of ignition experiments at the National Ignition Facility (NIF) as well as general issues of importance to HEDP and the physics of fields generated by laser–plasma interactions. A few highlights are discussed below.

Previous MIT NLUF work developed the tool of proton radiography<sup>20</sup> and then used it to provide the first images of coronal filamentation in direct-drive ICF implosions.<sup>21,22</sup> New NLUF work utilized proton imaging of self-generated electric and magnetic-field structures on laser-driven planar foils to investigate the possible roles of different instabilities in generating the filamentation seen in ICF experiments. Planar foils were used because they allow for direct observation in a direction perpen-

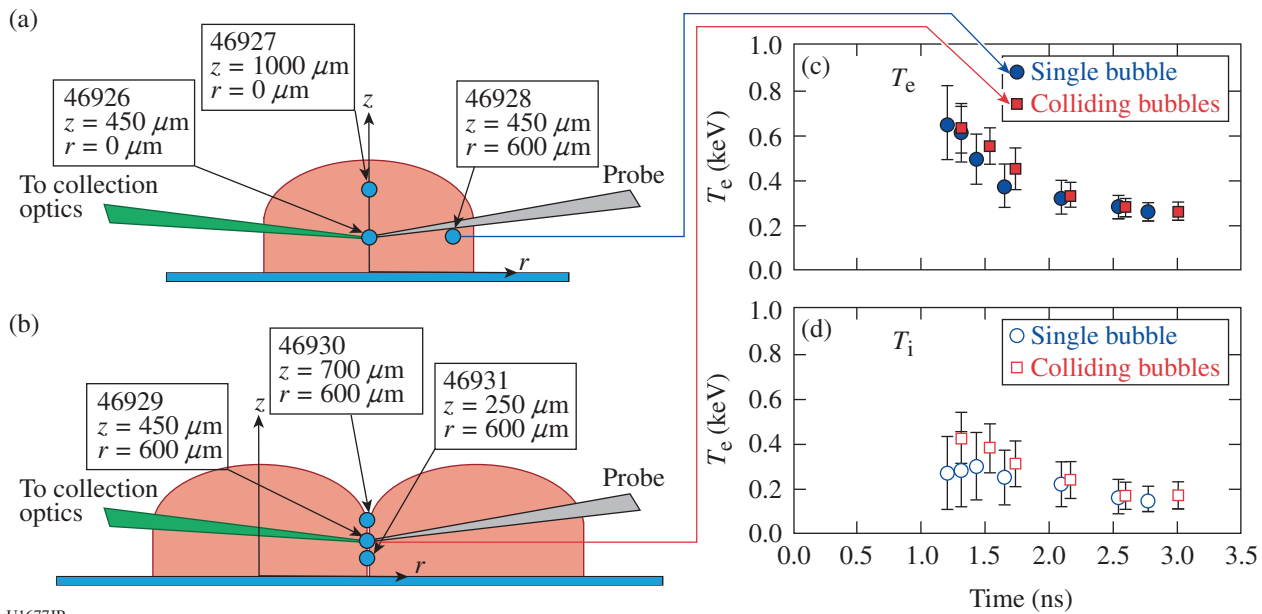
dicular to the laser-driven surface, which cannot be accomplished when studying ICF capsules with thick shells; x-ray images were used to study areal-density perturbations in the foil so their effects on proton radiographs could be separated from the effects of fields. The radiographic data were compared with the mathematical characteristics of a wide range of plasma instabilities (including collisionless Weibel, magnetothermal, laser–plasma, collisional Weibel, electrothermal, and Rayleigh–Taylor), and it was determined that the instability most likely to be causing the observed filamentation was the magnetothermal instability.<sup>23</sup>

Other recent NLUF work<sup>15</sup> utilized local, time-resolved Thomson-scattering measurements of electron and ion temperatures in combination with proton radiography measurements of magnetic fields to comprehensively characterize experiments with a single laser beam incident on a foil and with two laser beams incident on a foil (see Figs. 136.57 and 136.58). Each laser beam generated a plasma bubble and, in the



U1676JR

Figure 136.57  
Proton radiography setups for imaging (a) one plasma bubble, generated on a CH foil by a single laser interaction beam, and for imaging (b) a pair of plasma bubbles, generated by two beams that collide and produce magnetic reconnection. The backlighter<sup>20</sup> is an imploding pusher implosion of a capsule with D<sup>3</sup>He fill, which produces 14.7-MeV protons, and the imaging detector is CR-39.



U1677JR

Figure 136.58

[(a) and (b)] Thomson-scattering setup for experiments shown in Fig. 136.57. In different experiments, measurements were made in three different locations in each type of experiment. (c) Electron temperatures and (d) ion temperatures were found to be approximately equal in single-bubble and colliding-bubbles experiments, suggesting that thermal enhancement caused by magnetic reconnection is minimal in these experiments. This experimental conclusion is consistent with the fact that the  $\beta$  of the plasma is high. (For details, see Ref. 15.)

case with two bubbles, their collision produced reconnection of  $\sim 0.5$ -MG magnetic fields. The temperature evolution in a single laser-produced plasma bubble was well captured by 2-D radiation-hydrodynamics models, predicting a gradual decay after laser shutoff. It was found that there is minimal difference in either the electron or ion temperature between the perimeter of a single plasma bubble and in the interaction region of two colliding bubbles. This result confirms the expectation of negligible enhancement of thermal energy caused by the annihilation of magnetic fields in the two-bubble reconnection experiments since the plasma  $\beta$  (ratio of thermal to magnetic energy) is  $\sim 8$  and the initial magnetic energy is comparably small.

### ***Dynamics of High-Energy Proton-Beam Focusing and Transition into Solid Targets of Different Materials***

Principal Investigators: B. Qiao (University of California, San Diego)

Co-investigators: C. McGuffey (University of California, San Diego); M. E. Foord (LLNL); J. Fuchs and S. N. Chen (LULI); R. B. Stephens and M. S. Wei (General Atomics); and P. M. Nilson (LLE)

Intense, focused proton beams have applications ranging from isochoric heating of plasma to imaging shock wave and magnetic fields. Beam production and use involve a constantly

evolving target/plasma topology and hot-electron flow as the protons are accelerated from a shaped surface into vacuum and then transition into target plasmas for heating or probing. The dynamics involved are expected to become more complex as the laser energy and resulting beam current increase, and as a beam's pulse length increases. The goal of this project is to extend our physics understanding of the phenomena into this range, facilitating optimal source designs for various applications and eventually experiments like NIF-integrated proton fast-ignition experiments with the advanced radiographic capability (ARC) beam. Data from this study will be used to benchmark simulation codes including 3-D explicit particle-in-cell (PIC) and hybrid PIC codes. The results will have a significant impact in the field of HED physics.

In this FY13 experiment, we used the OMEGA EP dual short-pulse configuration to study focusing of the proton beam created by the interaction of the OMEGA EP backlighter (BL) beam (1250 J in 10 ps) with a spherically curved ( $R_c = 300 \mu\text{m}$ ) diamond (C) target. Three target-mounting configurations were investigated: (1) on a stalk, (2) with an open-sided wedge structure surrounding the focusing beam, and (3) with a conical structure [see Fig. 136.59(a)]. A  $10\text{-}\mu\text{m}$  Cu foil was placed at the expected beam focus position (on the back of the structures or stalk mounted at the same distance). Cu K-shell

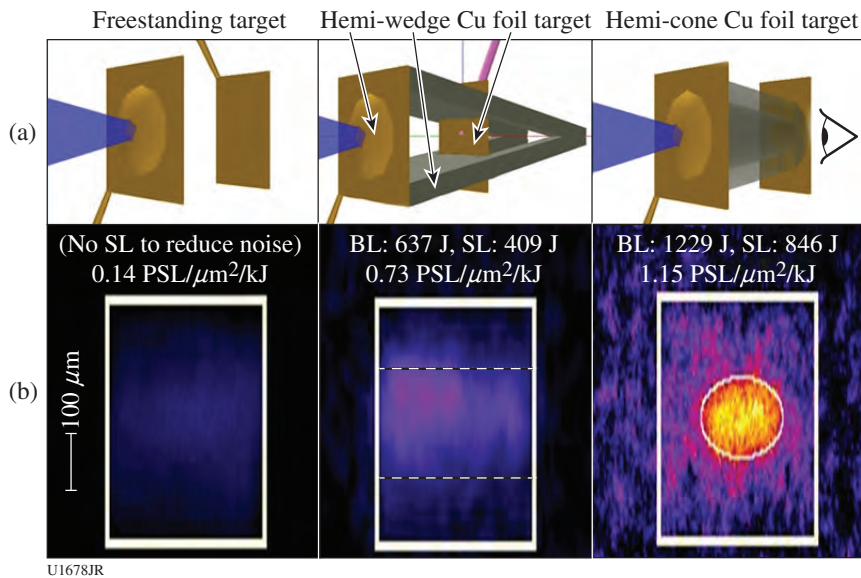


Figure 136.59

(a) Schematic of the three target configurations used in the experiment. (b) Cu  $K_{\alpha}$  images were obtained with the spherical crystal imager for the corresponding target configuration. BL: back-lighter; SL: sidelighter.

x-ray fluorescence was caused by collisions of the beam protons and electrons (to a lesser extent) with Cu atoms. The emission profile was imaged with the spherical crystal imager (SCI) giving an indication of the beam profile and total energy. The spectrum of transmitted protons was measured in the forward direction using a stack of radiochromic films.

The OMEGA EP sidelighter (SL) (850 J in 10 ps) was used to sidelight the target, structure, and Cu foil via proton radiography. The SL irradiated a Au foil, producing protons with a broad spectrum. The protons probed the interaction and were recorded on a stack of radiochromic films.

This was the first measurement of a proton-induced copper K profile on OMEGA EP and high-quality data were obtained, as shown in Fig. 136.59 (b). The white overlays show the foil dimensions and approximate positions of the structure edges. For the stalk-mounted target, the beam was not obscured by any structure and emission was observed from the majority of the foil. For the targets with wedge and cone structures, the emission from the unblocked region was brighter than the stalk-mounted case by factors of 5 and 8, respectively. In the cone structure case, smooth, bright emission is observed in a circle with the exact size of the cone bore. The enhanced emission is presumably due to focusing caused by charging of the structures as hot electrons from the diamond target escape into the structure, forming an electrostatic sheath along the structure walls. This effect has been documented in our previous experimental<sup>24</sup> and PIC simulation<sup>25</sup> work at much lower laser energy.

Forty-four proton radiograph frames were captured on a single shot, showing the evolution of the target and surrounding plasma features throughout a span of 163 ps. Example radiographs are shown in Fig. 136.60, displaying some of the interesting features observed near the time of BL laser arrival from the right side of the images [Figs. 136.60(a)–136.60(c)] and a closeup at later times [Fig. 136.60(d)]. Of particular interest is

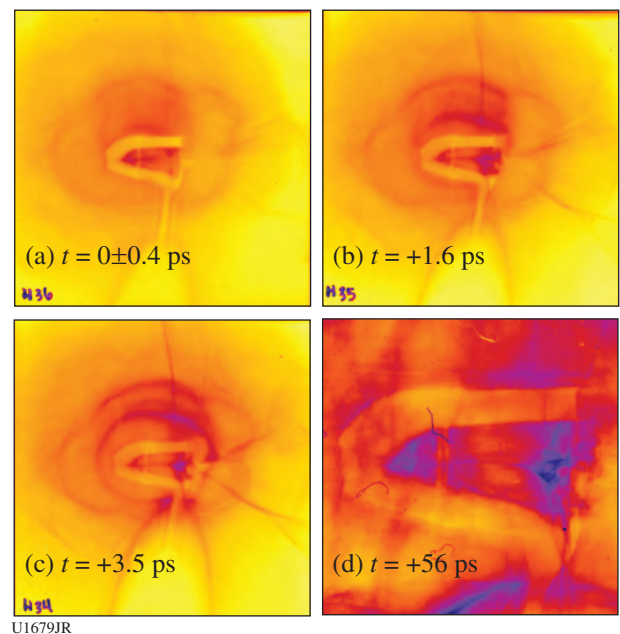


Figure 136.60

Time-sequenced proton radiographs showing the evolution of the target and surrounding plasma features throughout a span of ~52 ps.

the horizontal dark feature on the wedge structure axis of symmetry during the interaction. Darkness indicates an additional dose, i.e., focusing of probe electrons toward the axis. This may be a measurement of the electrostatic structure charging field implicated in the discussion above. At late time a dark line is observed centered on the Cu foil [Fig. 136.60(d), left vertical feature], suggesting opposing fields on the foil surfaces.

In the upcoming FY14 experiment, we will use the stalk-mounted and conical structure targets to focus protons into various transport materials coated in front of the Cu foil to study material-dependent transport effects that were observed in an experiment with lower beam current using the Trident laser.

**Generation of Collisionless Shocks in Laser-Produced Plasmas**

Principal Investigator: A. Spitkovsky (Princeton, for the ACSEL Collaboration)

This NLUF program studies the creation of collisionless shocks in counter-propagating laser-produced plasmas. Collisionless shocks are of great importance in astrophysical and space plasmas and occur when the mean free path to Coulomb collisions is large compared to the size of the shock transition. The shock is then mediated by collective plasma effects related to the interaction between plasma particles and the self-generated electromagnetic fields. Collisionless plasma conditions can now be created on OMEGA and OMEGA EP, where the laser-driven plasmas propagate at speeds of  $\sim 1000$  km/s and densities of  $\sim 10^{18}$  to  $10^{19}$  cm<sup>-3</sup>. The experiments in this program collide two streams of high-speed plasma and study the formation of shocks as a function of externally applied magnetic field that is generated by a set of Helmholtz coils at the interaction region (Fig. 136.61). The theoretical expectation is that at low external fields, the shock is mediated by the filamentation (Weibel) instability, while at higher fields, magnetic reflection of ions will form the shock. These regimes are representative of the conditions encountered in a range of astrophysical environments, including supernova remnant shocks and solar wind shocks. The experiments on OMEGA and OMEGA EP are testing these shock-formation mechanisms and addressing the open questions of astrophysical collisionless shock physics such as the presence of particle acceleration and the mechanisms of magnetic-field amplification in shocks.

In FY13, we had two shot days: an OMEGA EP-only experiment, EP-MagShock-13a, on 28 February 2013, and a joint shot day, MagShock-J-13a, on 21 May 2013. In these experiments the lasers (OMEGA and/or OMEGA EP) were used to initiate

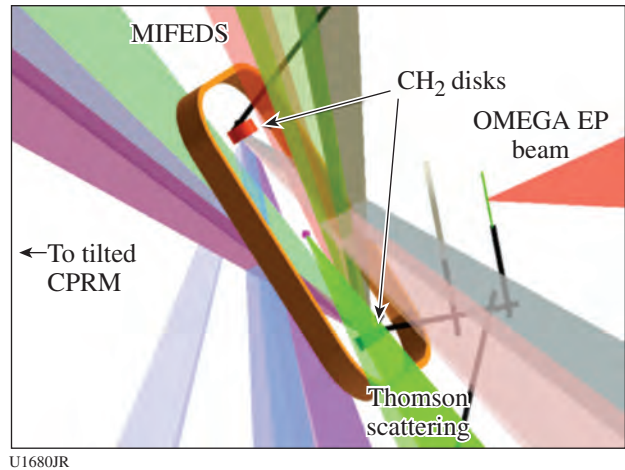


Figure 136.61  
Diagram of the experimental setup for NLUF MagShock-12a. CPRM: tilted circular proton radiography module.

two ablated plasma flows from CH or Be foils. An OMEGA EP short pulse was then used to provide proton radiography of the interaction region. On the joint shot day, the Thomson-scattering diagnostic was also used. A new design of a magnetic coil together with upgraded the magneto-inertial fusion electrical discharge system (MIFEDS) energy resulted in higher B fields of 6.5 T at target chamber center (TCC). For the first time we used MIFEDS on both OMEGA EP and joint days. We monitored the interaction of the flows with and without magnetic fields. One of the main goals was to reconcile the features seen in radiography on OMEGA EP and in previous joint shots. Prominent “line” features orthogonal to the flow direction were previously observed on OMEGA EP shots,<sup>26</sup> yet in our previous joint campaign in 2011–2012, they were not clearly seen.

We now understand that these features are due to advected Biermann battery fields that were created during target ablation. When we changed the proton radiography impact angle to be 90° to the flow as on OMEGA EP (previously it was 60° on joint shots because of experimental constraints), we recovered the Biermann features, as illustrated in Fig. 136.62. Now that it has been confirmed that the results on the two laser systems are consistent, we can proceed with more confidence to study the collisionless physics of the interaction. In particular, on joint shots we begin to see the filamentation instability of the two counter-streaming flows [vertical striations on Fig 136.62(b)]. This major result, recently confirmed in the ACSEL July experiment using D<sup>3</sup>He probing, has recently been submitted to Nature by the ASCEL collaboration.

We continued to model the experiment using particle-in-cell (PIC) simulations and simulated proton radiography, where

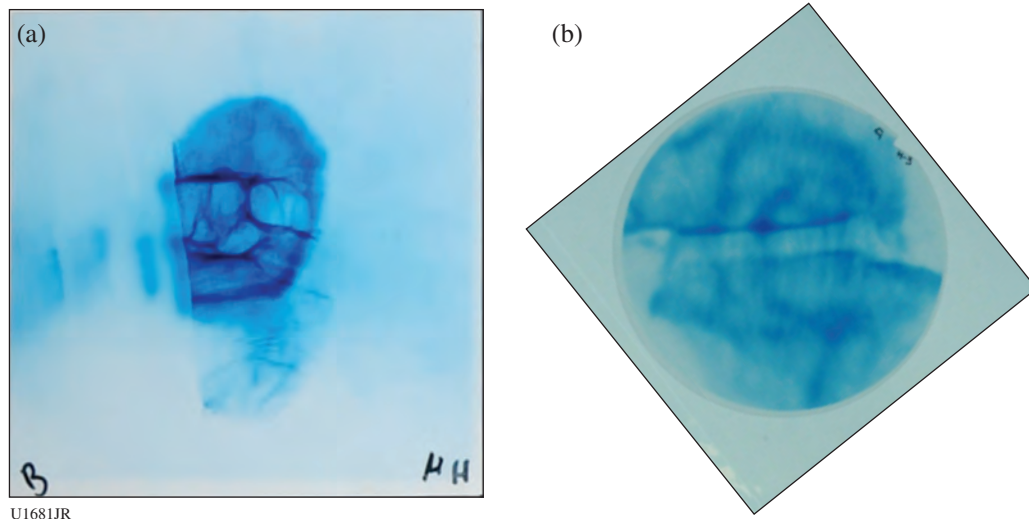


Figure 136.62

Proton images 3 ns after the lasers were fired. (a) Example of “horizontal line” features in proton radiography of counter-streaming flows on OMEGA EP. (b) The same features appear on joint shots with an appropriate radiography angle. Flows collide along the vertical direction.

test protons are traced through the output of a PIC simulation. We are now including Biermann fields and multitemperature species (hot electrons, cold ions) to self-consistently model the creation and advection of the magnetic fields and their interaction with the superimposed fields. We also produced a number of 3-D simulations with predictions for NIF conditions. On the NIF, larger effective separation of the targets will result in the creation of a full shock.

***Study of Fast-Electron–Beam Dynamics and Resistive Magnetic Collimation Using the High-Contrast OMEGA EP Laser at a 10-ps Pulse Duration***

Principal Investigators: M. S. Wei and R. B. Stephens (General Atomics)

Co-investigators: F. N. Beg, C. McGuffey, and B. Qiao (University of California, San Diego); H. McLean and P. Patel (LLNL); W. Theobald (LLE); and R. Mishra and Y. Sentoku (University of Nevada, Reno)

Lead graduate students: A. Sorokovikova and J. Peebles (University of California, San Diego)

Efficient conversion of high-intensity laser energy to fast electrons and their subsequent transport is fundamental to high-energy-density (HED) science, which has many potential applications such as initiating fusion using the fast-ignition (FI) technique, producing warm dense matter by isochoric heating, and creating x-ray emission for use as a backlighter source. The energy coupling is controlled by laser–plasma interaction (LPI) dynamics, which strongly depends on laser-

intensity distribution and the plasma density scale length at the LPI interface, as well as the dynamic response of the transport material. Using the high-intensity, high-energy (up to 1.5 kJ) OMEGA EP laser with low-contrast pulses in our previous experiments, we observed that electron beams dynamically evolve from a single diffuse spot in a subpicosecond interaction into multiple angularly separated electron filaments over a 10-ps interaction.<sup>27</sup> Collisional particle-in-cell simulations suggest that the high-intensity laser beam undergoes filamentation, hole-boring, and hosing instabilities, which have time to grow during the multiple-picosecond interaction in the preformed plasma created by the intrinsic nanosecond pedestal prepulse, leading to the observed electron filaments. The objectives of this General Atomics NLUF project are to further investigate the LPI dynamics and fast-electron transport dependence on pre-plasma, pulse duration, and target material using the OMEGA EP laser with the newly available high-contrast pulse.

In the FY13 NLUF experiment, we first studied the LPI-produced electron-beam characteristics using the high-contrast laser pulse to understand time evolution of the LPI dynamics from 0.7 ps to 10 ps and the role of pre-plasma (by comparing with previous data taken with the low-contrast pulse). For this study, we used identical multilayered planar-foil targets consisting of an Al substrate with a Cu x-ray tracer layer (20  $\mu\text{m}$  thick) buried  $\sim 100 \mu\text{m}$  below the front surface and a large (5-mm  $\times$  5-mm, 1-mm-thick) conductive carbon layer at the back to minimize refluxing, similar to that used in previous experiments with the low-contrast pulse. The high-contrast OMEGA EP backlighter

beam (0.7- and 10-ps pulse durations with energies of 150 J and 1500 J, respectively) was normally incident onto the front target surface. The beam was tightly focused with a spot radius of  $\sim 15 \mu\text{m}$  that contained 80% of the laser energy, resulting in a peak laser intensity of  $4 \times 10^{19} \text{ W/cm}^2$ . The measured nanosecond prepulse energy was  $\leq 1 \text{ mJ}$ , which is  $100\times$  smaller than in the case of the low-contrast pulse. Fast electrons were characterized by measuring their induced Cu  $K_\alpha$  fluorescence spot using a spherical crystal imager (SCI), and the total  $K_\alpha$  yield was characterized by a calibrated x-ray spectrometer using a curved highly oriented pyrolytic graphite (HOPG) crystal [zinc von Hamos (ZVH) spectrometer]. A fast-electron-induced high-energy bremsstrahlung spectrum was monitored at two angles behind the targets with two fixed-port bremsstrahlung MeV x-ray spectrometers (BMXS's). The measured bremsstrahlung data showed that fast electrons produced from the 10-ps LPI have a hotter spectrum than in the subpicosecond case, consistent with particle-in-cell (PIC) simulation results.<sup>28,29</sup> Detailed bremsstrahlung data analysis including field effects via the hybrid transport modeling is underway.

As shown in Fig. 136.63,  $K_\alpha$  image data showed a more-confined electron beam produced from the clean interaction with a steep density gradient in the 10-ps LPI case using the high-contrast OMEGA EP pulse. Also noted is the higher signal level in the  $K_\alpha$  intensity in the confined electron beam, compared to that in the spreading multiple electron filaments in the

LPI in the low-contrast case [Fig. 136.63(c)]. This verified that the multiple angularly separated electron filaments observed in the low-contrast pulse experiment were indeed caused by nonlinear instabilities during LPI over multiple picoseconds with the presence of a large pre-plasma. These new findings emphasize the requirement of a high-contrast capability of the high-energy, high-intensity laser pulse needed to avoid the unnecessary LPI instability for efficient energy coupling.

Using the high-contrast OMEGA EP pulse, we have also extended our previous work on resistive collimation with laser pulses at subpicosecond<sup>27,30</sup> to a 10-ps pulse duration using a high-Z transport target that has a thin (a few- $\mu\text{m}$ ) Au layer embedded about  $10 \mu\text{m}$  beneath the Al substrate [Fig. 136.64(a)]. Two-dimensional  $K_\alpha$  images [Figs. 136.64(b) and 136.64(c)] clearly show a better confined and stable electron beam compared to that with the pure Al transport target [Fig. 136.64(b)]. A remarkably collimated electron beam, with a spot size as small as  $50 \mu\text{m}$  after a  $>100\text{-}\mu\text{m}$  propagation distance, has been demonstrated for the first time for fast-ignition-relevant 10-ps pulses. The achieved electron-beam size is comparable to the required spot size ( $\sim 40 \mu\text{m}$ ) for FI. In addition, the sensitivity of magnetic collimation of fast-electron transport on the Z-layer thickness has also been examined. As shown in Figs. 136.64(c) and 136.64(d), both  $9\text{-}\mu\text{m}$  and  $3\text{-}\mu\text{m}$  Au layers showed collimation effects compared to the Al transport target case.

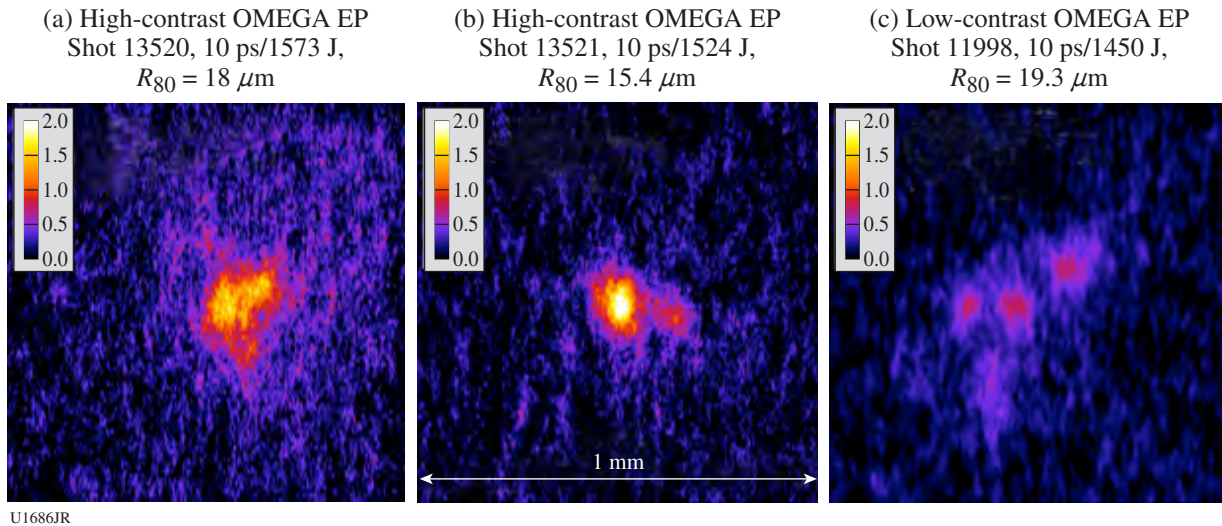


Figure 136.63 Two-dimensional  $K_\alpha$  images observed in a 10-ps laser-plasma interaction (LPI) with identical Al transport targets [(a) and (b)] using the high-contrast OMEGA EP pulse (nanosecond prepulse energy  $\sim 1 \text{ mJ}$ ) and (c) with the low-contrast (prepulse energy  $\sim 110 \text{ mJ}$ ) OMEGA EP laser beam. Images (view angle corrected) are on the same spatial and color scale. Although shape varied shot-to-shot, high-contrast, laser-produced electron beams are more confined with brighter peak signals compared to the spreading filaments in the low-contrast case.

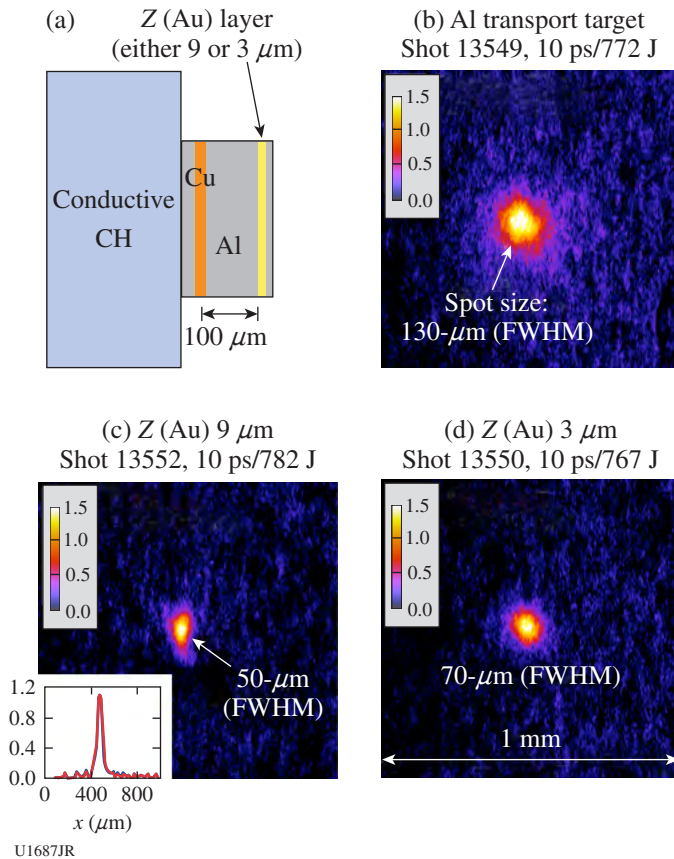


Figure 136.64 (a) Multilayered planar-foil target with a Z (Au) transport layer and the measured  $K_{\alpha}$  images (view angle corrected) from the 10-ps interactions using the high-contrast OMEGA EP pulse; (b) from the Al transport target without the high-Z Au layer and [(c) and (d)] from the Z (Au) transport targets with a 9- $\mu\text{m}$  and 3- $\mu\text{m}$  Au layer, respectively. Inset in (c) is the horizontal lineout of the image data (blue) and the Lorentzian fit (red) showing the spot size of 50  $\mu\text{m}$  [full width at half maximum (FWHM)].

In summary, the FY13 GA-led NLUF experiment was successfully performed and demonstrated that high-contrast pulses improve energy coupling and facilitate strong electron-beam collimation in high-Z transport targets by self-generated resistive magnetic fields in a 10-ps interaction. The experimental data will be used to benchmark various PIC and hybrid PIC codes for developing a predictive modeling capability.

### FY13 Laboratory Basic Science (LBS) Program

In FY13, LLE issued a solicitation for LBS proposals to be conducted in FY14. A total of 38 proposals were submitted. An independent review committee reviewed the proposals and recommended that 17 proposals receive 28 shot days at the Omega Laser Facility in FY14. Table 136.VIII lists the successful LBS proposals.

Sixteen LBS projects were allotted Omega Facility shot time and conducted a total of 269 target shots at the facility in FY13 (see Table 136.IX). This work is summarized in this section.

### Equation of State and Optical Properties of Dense Silica: Shock Study of Stishovite

Principal Investigator: P. Celliers (LLNL)  
 Co-investigators: M. Millot and R. Jeanloz (University of California, Berkeley); N. Dubrovinskaia, A. Cernok, S. Blaha, and L. Dubrovinsky (Bayreuth University, Germany); S. Hamel, J. H. Eggert, and G. W. Collins (LLNL); and T. R. Boehly (LLE)

The equation of state and optical properties of silica ( $\text{SiO}_2$ ) were investigated in an unexplored regime of warm dense matter, with pressure above 20 Mbar (2 TPa) and density in excess of 10  $\text{g/cm}^3$ . Such conditions were achieved by laser-induced shock loading of stishovite, a high-pressure polymorph of  $\text{SiO}_2$ . Because of its high initial density ( $\rho_0 = 4.3 \text{ g/cm}^3$ ), the Hugoniot of stishovite explores a much denser and cooler path than the shock Hugoniot of  $\alpha$  quartz ( $\rho_0 = 2.65 \text{ g/cm}^3$ ) and fused silica ( $\rho_0 = 2.2 \text{ g/cm}^3$ ) (see Fig. 136.65).

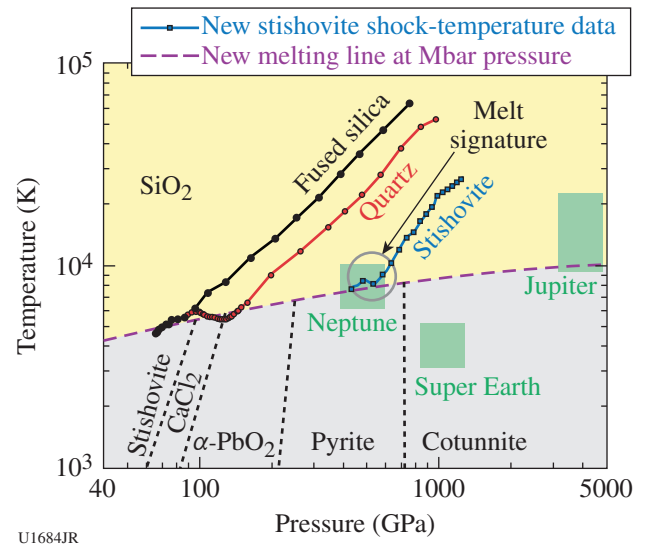


Figure 136.65 Phase diagram for warm dense  $\text{SiO}_2$ , including previous shock-temperature data for fused silica (black) and  $\alpha$  quartz (red) as well as representative new data for stishovite (blue, preliminary analysis). We interpret a temperature anomaly along the stishovite Hugoniot, indicated by the gray circle, as a signature of melting similar to that observed for the fused silica and  $\alpha$  quartz at lower pressures. This allows us to pinpoint the melting line for  $\text{SiO}_2$  at 5 Mbar and 8000 K. This measurement is directly relevant to models of planetary formation (e.g., late-stage giant impacts) and interior evolution (green squares show typical planetary core conditions).

Knowledge of the physical properties of highly compressed silica is critical for astrophysical applications, particularly for modeling the origins and interior structures of terrestrial (“rocky”) planets, as well as the cores of giant and supergiant gaseous planets. Silica is a prototypical constituent of rock and

abundant in the planet Earth and many exoplanets because it is a strongly bonded form of oxygen, the most-abundant chemical element after the light elements hydrogen and helium. The behavior of silica at high pressures is vastly different from its well-known properties at ambient conditions, and, as a rela-

Table 136.VIII: LBS proposals approved for shots in FY14.

Principal Investigator	Title	Institution	Facility required	OMEGA shot days allocated	OMEGA EP shot days allocated
A. Bernstein	Nuclear Excitation by Electron Capture in a Reduced-Scale Hohraum	LLNL	OMEGA	1	0
P. M. Celliers	Measurement of the Viscosity of Shock-Compressed Fluids of Water and Silica	LLNL	OMEGA	2	0
H. Chen	Exploring Pair Plasmas and Their Applications Using the OMEGA EP and OMEGA Lasers	LLNL	OMEGA EP	0	2
G. Fiksel	Magnetized ICF Implosions on OMEGA	LLE	OMEGA (1) and joint (1)	2	1
R. F. Heeter	Gatling Gun Long-Duration Radiation Sources on OMEGA EP for Sustained-Drive Hydrodynamics and Low Density at Atomic Physics Applications on OMEGA EP and the NIF	LLNL	OMEGA EP	0	1
S. Ivancic	Channeling Through Long-Scale-Length Plasmas	LLE	OMEGA EP	0	1
M. Lafon	Gigabar Shocks for Shock-Ignition and High-Energy-Density-Physics Studies	LLE	OMEGA	1	0
T. Ma	Creation and Measurements of Novel High-Pressure Electrude States of Matter	LLNL	OMEGA	1	0
D. Martinez	Imprint-Driven Richtmyer–Meshkov Instability in Thick Planar Targets	LLNL	OMEGA	2	0
D. McNabb	Thermonuclear Reactions in Stellar Plasmas	LLNL	OMEGA (2 half days, 1 full day)	2	0
S. Nagel	Measuring Charged-Particle Stopping Powers Using Short-Pulse Lasers	LLNL	OMEGA EP	0	1
P. M. Nilson	Radiation Hydrodynamics of Double-Ablation Fronts	LLE	OMEGA EP	0	1
H.-S. Park	Astrophysical Collisionless Shocks and Magnetic Fields in Laser-Produced Plasmas	LLNL	OMEGA EP	0	2
P. K. Patel	Fast-Electron Focusing Using Ellipsoidal-Tip Cone Targets for Fast Ignition	LLNL	OMEGA (1) and joint (1)	1	2
J. R. Rygg	Structure and Equation of State of Solid and Super-Ionic Warm Dense Matter	LLNL	OMEGA	2	0
R. Smith	Understanding Strength Effects in Diamond Ablators Used for Ramp Compression	LLNL	OMEGA EP	0	1
C. Stoeckl	Spectroscopy of Neutrons Generated Through Nuclear Reactions with Light Ions in Short-Pulse Laser Interaction Experiments	LLE	OMEGA EP	0	2

tively simple covalent material, it is an excellent test case for understanding changes in bonding and electronic properties in the warm-dense-matter regime.

Multiple synthesis runs led by the Bayreuth University team produced optically transparent stishovite, including large single crystals, using large-volume press techniques at high-pressure/temperature conditions (see Fig. 136.66). The samples were characterized by powder and single-crystal x-ray diffraction, Raman spectroscopy, scanning electron microscopy, and wavelength-dispersive x-ray spectroscopy. Their phase and chemical purity was confirmed by appropriate analytical methods. Finally the crystals were oriented and polished into thin plates suitable for the envisioned laser-shock experiments.

We collected ultrafast Doppler velocity interferometry (VISAR) and streaked optical pyrometry (SOP) data during direct-drive shock compression of stishovite single and poly-

crystals using up to 6 kJ of UV light at the Omega Laser Facility (see Fig. 136.67). This provided pressure/density/temperature equation-of-state (EOS) data, as well as information on the optical reflectivity (therefore electron conductivity) of warm dense SiO<sub>2</sub> along the stishovite Hugoniot.

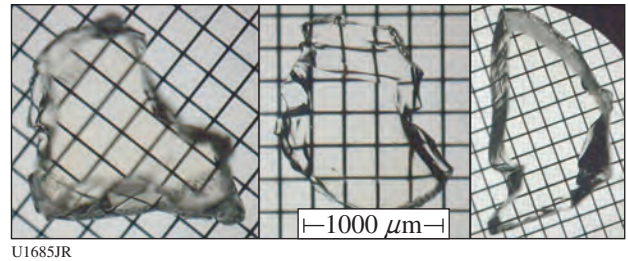


Figure 136.66 Representative single crystals of stishovite as polished into thin plates. Lateral dimensions in excess of 1 mm allow planar laser-shock compression studies.

Table 136.IX: Approved FY13 LBS proposals.

Principal Investigator	Affiliation	Project Title
P. M. Celliers	LLNL	Equation of State and Optical Properties of Dense Silica: Shock Study of Coesite and Stishovite
H. Chen	LLNL	Exploring Pair Plasmas and Their Applications Using OMEGA EP
J. R. Davies	LLE	Fast-Electron Control with a Magnetic Field in a Hohlraum
J. H. Eggert	LLNL	HED Condensed Matter: Magnesium and Aluminum
G. Fiksel	LLE	Magnetized ICF Implosions in OMEGA
G. Fiksel	LLE	Magnetic Reconnection and Particle Energization in High-Energy-Density Plasmas and the Presence of an External Magnetic Field
R. F. Heeter	LLNL	“Gatling Gun” Long-Duration Radiation Sources on OMEGA EP for Sustained-Drive Hydrodynamics and Low-Density Atomic Physics Applications on OMEGA EP and the NIF
B. R. Maddox	LLNL	Direct Measurements of Dislocation-Based Plastic Flow in Quasi-Isentropically Compressed bcc Metals
H.-S. Park	LLNL	Astrophysical Collisionless Shock Generation by Laser-Driven Experiments
P. K. Patel	LLNL	Areal-Density Measurements of Cone-in-Shell Implosions Using Compton Radiography for Fast Ignition
Y. Ping	LLNL	Long-Term Dynamics of Hole Boring and Target Heating at Fast-Ignition-Relevant Conditions
S. P. Regan	LLE	Collective X-Ray Scattering from Shocked Liquid Deuterium
J. R. Rygg	LLNL	Extreme Chemistry, Equation of State, and Optical Properties of Dense Water at Terapascal Pressure
A. A. Solodov	LLE	Fast-Ignition Integrated Experiments with Low-Z Cone-Tip Targets
C. Stoeckl	LLE	Spectroscopy of Neutrons Generated Through Nuclear Reactions with Light Ions in Short-Pulse Laser-Interaction Experiments
W. Theobald	LLE	Laser Channeling in Long-Scale-Length, Overdense Plasmas

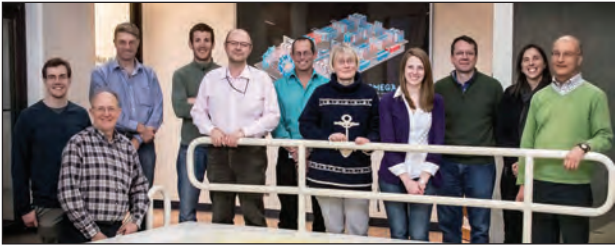


Figure 136.67  
LLNL/University of California, Berkeley/Bayreuth University/LLE experimental team at the Omega Laser Facility for the first laser-shock campaign on stishovite.

Preliminary analysis suggests that we were not only able to document the onset of metallic reflectivity but also to pinpoint melting along the Hugoniot of stishovite, near 5 Mbar and 8000 K. This is the first experimental measurement of the melting temperature for silica above 2 Mbar.

These data serve as a valuable complement to existing shock studies on  $\alpha$  quartz and fused silica, and we plan to include our data in an updated EOS table. This fundamental study will serve as an important experimental benchmark for advanced condensed matter theories, planetary modeling, and a more-complete understanding of the evolution of chemical bonding at extreme pressure and temperature conditions.

**Exploring Pair Plasmas and Their Applications Using OMEGA EP**

Principal Investigator: H. Chen (LLNL)

In FY13, three successful Laboratory Basic Science (LBS) experiments on OMEGA EP were performed by an LLNL/LLE team on the subject of “exploring pair plasmas and their applications.” The experiments focused on the pair-jet collimation using both an electrical and a magnetic field. Very effective pair-jet collimation was observed using an externally applied magnetic field.

Previous LBS experiments by this team have shown that quasi-monoenergetic relativistic positron jets are formed during high-intensity interactions with thick gold targets.<sup>31</sup> The beam divergence was 30° (Ref. 32). The current experiments were designed to collimate the positron jet with an external magnetic lens. Using the new magneto-inertial fusion electrical discharge system (MIFEDS),<sup>33</sup> strong collimation of both positrons and electrons was observed. This resulted in a near pencil beam with an equivalent beam divergence angle of 5°.

The charge imbalance was reduced from ~100 (no collimation) to ~2.5 (with collimation)—a significant step toward making a charge-neutral electron–positron pair plasma in the laboratory.

The experiments were performed using the OMEGA EP short-pulse beams at ~1 kJ at 10 ps. The targets were made of 1-mm-thick gold. A jet of positrons and electrons was emitted from the rear side of the target. Between the target and the detector, MIFEDS coils produced a peak magnetic field of about 7 T (Fig. 136.68). The collimated beams were measured with a magnetic electron–positron spectrometer. Without the external magnetic field, the peak densities were about  $10^{13}$  and  $10^{15}$  cm<sup>-3</sup> for positrons and electrons, respectively.<sup>32</sup> With the external B field applied, a factor of ~40 increase in the peak positron and electron signal was observed.

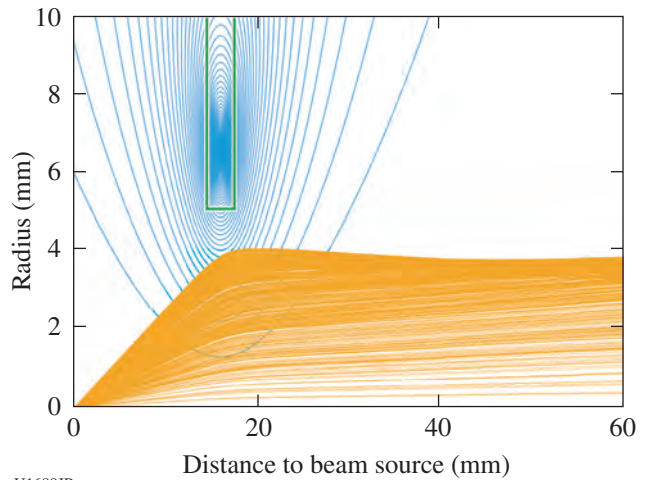


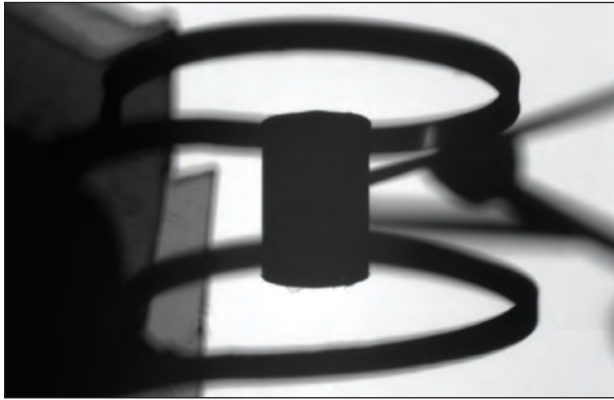
Figure 136.68  
Simulation of the B fields (blue) from the MIFEDS coil (green box) and their effect on the positron jets (golden).

The next step is to confine the particles to make a pair plasma.<sup>34</sup> The ultimate goal will be to confine the particles to make a relativistic charge neutral electron–positron pair plasma. If successfully confined, an electron–positron plasma would offer a novel system that would enable us to conduct a detailed study of some of the most-exotic and energetic systems in the universe.<sup>35</sup>

**Fast-Electron Control with Magnetic Field in Hohlräume**  
Principal Investigator: J. R. Davies (LLE)

The objectives of this experiment were to demonstrate control of fast-electron transport and suppression of stimulated

Raman scattering (SRS) in gas-filled hohlraums using a magnetic field, generated by MIFEDS—two potential benefits of magnetized inertial confinement fusion (ICF) specific to indirect drive that had not been studied before. The experimental setup is shown in Fig. 136.69.



TC11059JR

Figure 136.69

View of a hohlraum and MIFEDS coils in the target chamber. In this setup a peak magnetic field of 10 T is generated along the hohlraum axis to inhibit electron transport into the walls. The hohlraum is filled with gas but does not contain a capsule.

The basic mechanism is quite simple: the magnetic field prevents charged particles from moving across field lines. Fast electrons, generated by SRS, can therefore be prevented from reaching the walls, where they would produce hard x rays, and the capsule, where they would cause preheat. Similarly, electron thermal transport across the field is reduced, leading to a higher gas temperature, thereby reducing the SRS growth rate. A further benefit is a lower gas density sufficient enough to prevent hohlraum wall expansion from affecting the capsule, further reducing SRS growth rate.

Unfortunately, leakage of the hohlraums led to a wide range of gas densities with no repeat shots; therefore, only tentative conclusions can be drawn from these initial experiments. The results indicate that (1) SRS was negligible at fill densities of  $0.03 n_c$  or less, where  $n_c$  is critical density; (2) at densities around  $0.04 n_c$ —the density in a National Ignition Campaign (NIC) hohlraum—a 10-T axial magnetic field reduced SRS light and hard x-ray emission by a factor of 10; and (3) at densities of  $0.09 n_c$  and greater, the magnetic field had no significant effect since, as expected, the collision frequency exceeded the electron cyclotron frequency. These results provide a strong

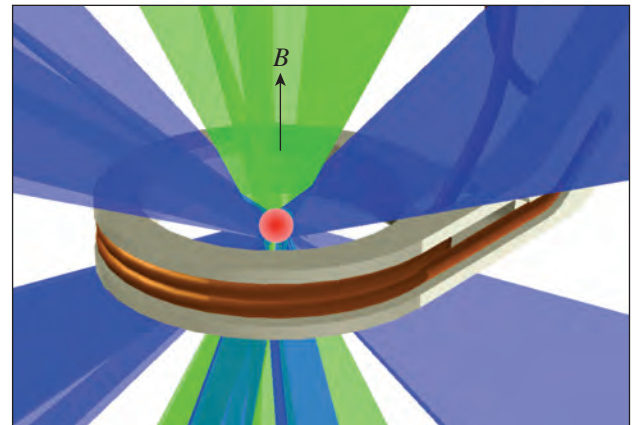
motivation to further study magnetic-field suppression of SRS in gas-filled hohlraums.

### Magnetized ICF Implosions on OMEGA

Principal Investigators: G. Fiksel, P.-Y. Chang, J. R. Davies, D. Barnak, and R. Betti (LLE)

The objective of this OMEGA experiment was to measure fusion enhancement (increase in neutron yield and ion temperature) in spherically imploded targets embedded in an externally generated seed field. The experiment was conducted in April 2013.

The experimental setup is shown in Fig. 136.70. A spherical CH plastic shell with a diameter of  $860 \mu\text{m}$  and a thickness of  $22 \mu\text{m}$  was irradiated by 40 OMEGA laser beams with a beam energy of 450 J. The beams were arranged in the polar-drive (PD) configuration. The targets were filled with  $\text{D}_2$  gas at a pressure of 10 atm. A seed magnetic field of 7 T was created by a four-turn coil with an internal diameter of 4.5 mm powered by MIFEDS.

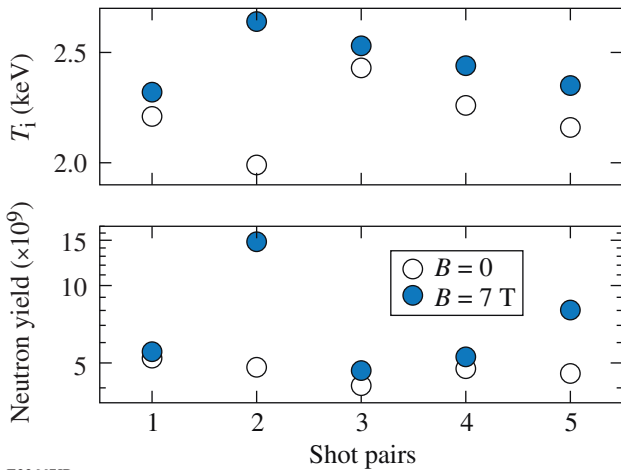


E22666JR

Figure 136.70

Setup for the fusion enhancement experiment.

The neutron yield and ion temperature for shots with and without a magnetic field are compared in Fig. 136.71. For this plot, the shots were grouped in pairs with target and laser parameters as similar as possible. On average, we observed a 23% increase in the neutron yield and an 11% increase in the ion temperature. The results are close to that obtained with *LILAC* simulations (20% and 10%, respectively). A surprisingly high jump in both neutron yield and ion temperature for shot pair #2 is not understood at this time.



E22667JR

Figure 136.71  
Comparison of neutron yield and ion temperature for shots with and without a magnetic field.

The objective of the joint experiment was to measure the compressed magnetic field in spherically imploded targets embedded in an externally generated seed field. To improve the quality and the accuracy of that measurement we (a) significantly increased the proton fluency by using OMEGA EP-generated fast protons and (b) used radiochromic film (RCF) as a proton detector for prompt image visualization. The experiment was conducted in February 2013.

The experimental setup is shown in Fig. 136.72. A spherical CH plastic shell with a diameter of 860  $\mu\text{m}$  and a thickness of 22  $\mu\text{m}$  was irradiated by 40 OMEGA laser beams with a 1-ns square pulse and beam energy of 450 J. The beams were arranged in the polar-drive-like configuration and laser-beam rings 1 and 1\*, 2 and 2\*, and 4 and 4\* (top and bottom) were used. Rings 3 and 3\* were blocked by the magnetic-field coils

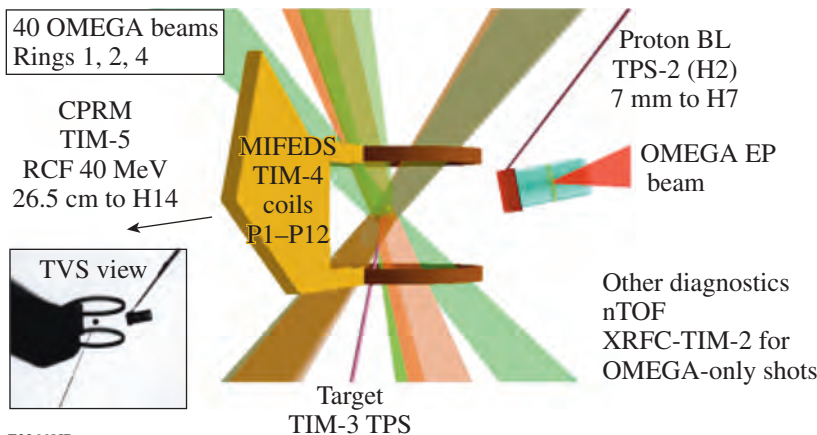
and were not used in this experiment. In addition, the energy in the polar-most Rings 1 and 1\* was reduced by 25% to improve the compression symmetry [as indicated by the DRACO-magnetohydrodynamic (MHD) code]. The targets were filled with  $\text{D}_2$  gas at a pressure of 20 atm. The seed magnetic field was created by a pair of Helmholtz coils powered by MIFEDS.

To diagnose the field compression, the imploding plasma was imaged by fast protons generated with a short-pulse IR beam (1.053  $\mu\text{m}$ , 800 J, 10 ps) irradiating a thin Cu disk with a focal spot of about 25  $\mu\text{m}$ . The protons were imaged with a stack of radiographic film interleaved with Al filters of varying thickness, with proton energies resolved by their varying Bragg peak. The Cu proton source disk was located 7 mm from target chamber center (TCC), while the film pack was placed  $\sim 26.5$  cm from TCC. A collimating Ta slit with a thickness of 0.5 mm and a width of 0.35 mm was placed in front of the proton source to prevent the background protons from striking the RCF area, where protons deflected by the compressed magnetic field are expected to land. The magnetic field was evaluated from

$$\int Bdr = (d/eL)(2m_p E_p)^{1/2},$$

where  $d$  is the proton linear deflection,  $L$  is the distance to the detector, and  $m_p$  and  $E_p$  are the proton mass and energy.

The proton radiography image (shot 68758) for a proton energy of  $E_p = 16.7$  MeV and a corresponding synthetic ion-tracing simulation are shown in Fig. 136.73. For this shot, a magnetic seed field of 6 T was applied and the OMEGA EP beam was fired at a “bang time” of 2.2 ns after the drive beams



E22668JR

Figure 136.72  
The experimental setup for the magnetic compression experiment.

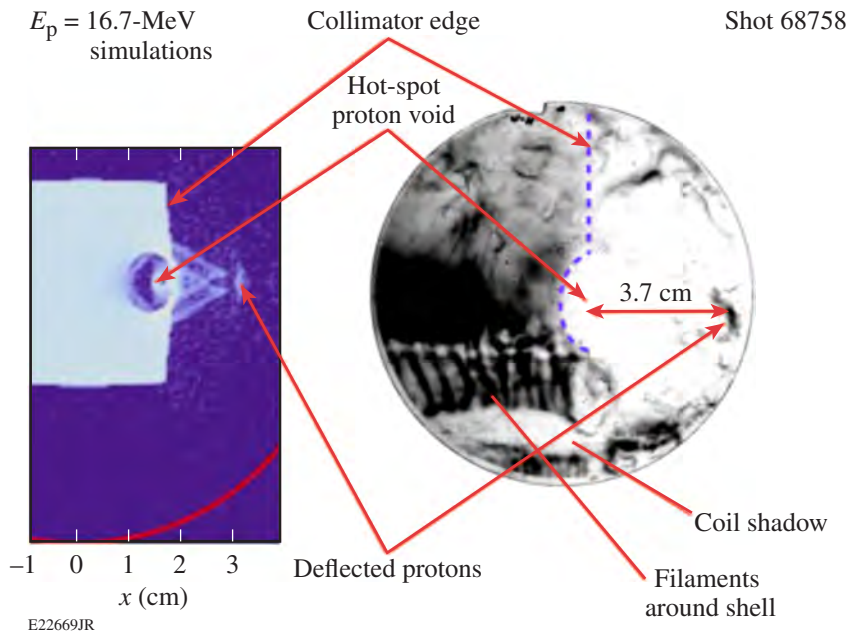


Figure 136.73  
Comparison of a proton deflectometry image (right) for 16.7-MeV protons and simulation results (left). For this shot, the target was magnetized with a seed magnetic field of 6 T.  $E_p$ : proton energy.

were turned on. The most-notable features of the image are the following:

- A boundary separates the left part (where undeflected protons strike the RCF) from the right, “clean” part (where the protons deflected by the compressed magnetic field are expected to land).
- A half-circle-shaped proton void at the center of the film could be an indication of a strong magnetic field deflecting the protons away from the area.
- A dark spot at 3.7 cm from the hot-spot center could be an imprint of the deflected fast protons. The direction of the deflection agrees with the polarity of the applied seed magnetic field, and the amount of deflection corresponds to the field integral of 0.08 Tm, which is close to a value of 0.06 Tm expected from DRACO–MHD simulations.

***Magnetic Reconnection and Particle Energization in High-Energy-Density Plasmas in the Presence of an External Magnetic Field***

Principal Investigators: G. Fiksel, P. M. Nilson, and S. X. Hu (LLE); W. Fox (University of New Hampshire); and A. Bhattacharjee (Princeton)

We have been developing and conducting counter-propagating plasma interaction experiments on the OMEGA EP laser, including experiments with and without magnetic fields. Experiments with applied magnetic fields can study the inter-

action and collision of magnetized plasmas and phenomena such as magnetic reconnection. We first conducted a simpler experiment with zero applied field, leading to collision and interaction of unmagnetized plasmas. A pair of opposing CH targets separated by 4.5 mm were irradiated by 1.8-kJ laser pulses on OMEGA EP, driving a pair of ablative flows toward the collision region at the midplane between the two foils. As a result of the long mean free path between ions in opposing streams, the streams are initially free to interpenetrate, establishing supersonic counter-streaming conditions in the ion populations.

These first unmagnetized experiments found an unexpected and very interesting result: observation of the growth of an ion-driven Weibel instability generated as the two plumes interpenetrate. This instability is interesting because it has been predicted to be a key ingredient in astrophysical collisionless shocks. These astrophysical shocks must be mediated by collective electromagnetic fields since coulomb collisions alone are too weak to sustain shocks in such high-temperature astrophysical plasmas. The Weibel instability has been proposed to generate a turbulent magnetic field in the shock front and thereby mediate shock formation in cosmological shocks and blast-wave shocks in gamma ray bursts and supernova remnants. This is the first experimental observation of this instability in the shock-relevant case of interpenetrating supersonic flows.

Figure 136.74 shows radiochromic film images of the development of a striated instability as the two plumes interact. Qualitatively, the observations bear many expected features

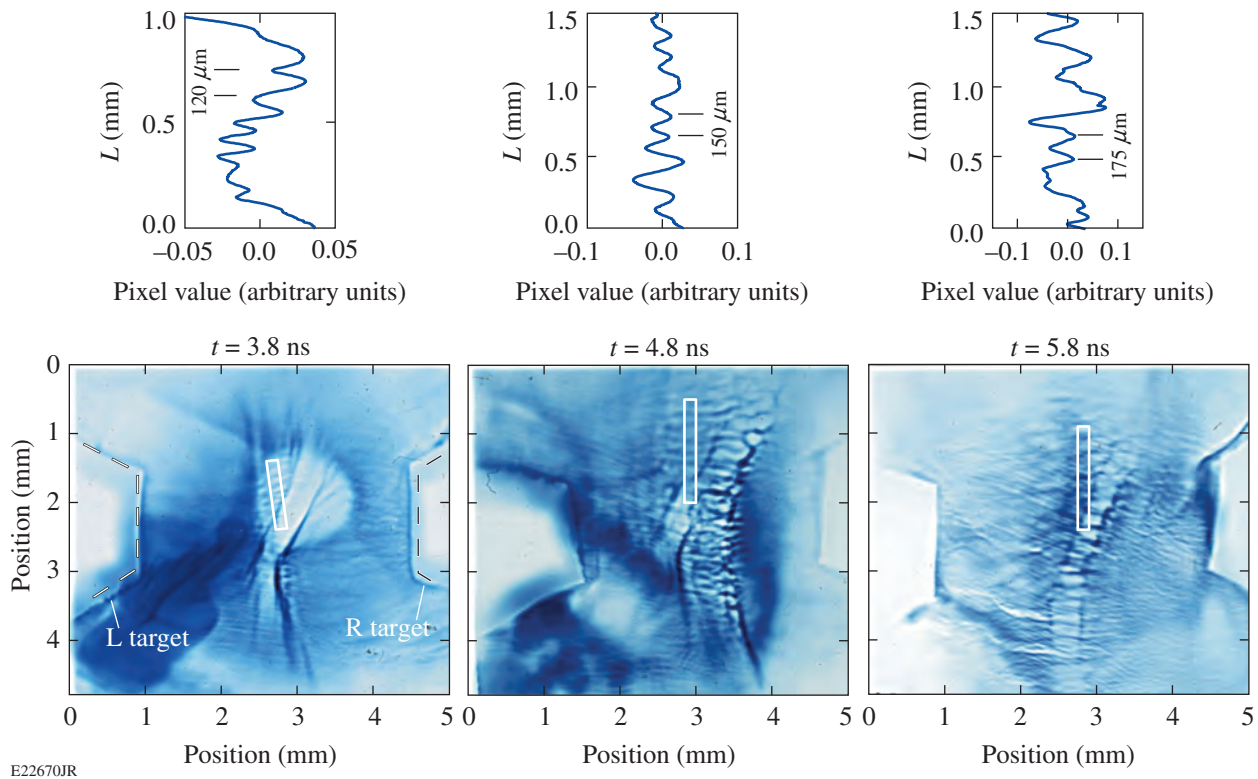


Figure 136.74

Sequence of proton radiography images taken on radiochromic film of the interaction of two plasma plumes. The insets show 1-D traces of the proton intensity along the long axis of the regions denoted in the film. L: left; R: right.

of this instability, including localization to the overlap region and formation of elongated filaments parallel to the ablation flows. The insets show 1-D traces of proton intensity along the long axis of the regions denoted in the film. Typical filament wavelengths of 100 to 150  $\mu\text{m}$  at 3.8 and 4.8 ns expand to wavelengths near 250  $\mu\text{m}$  at 5.8 ns. The growth rate and typical filament size compare favorably to predictions from the Weibel-instability linear theory and to particle-in-cell simulations. These results are presently under review at Physical Review Letters.

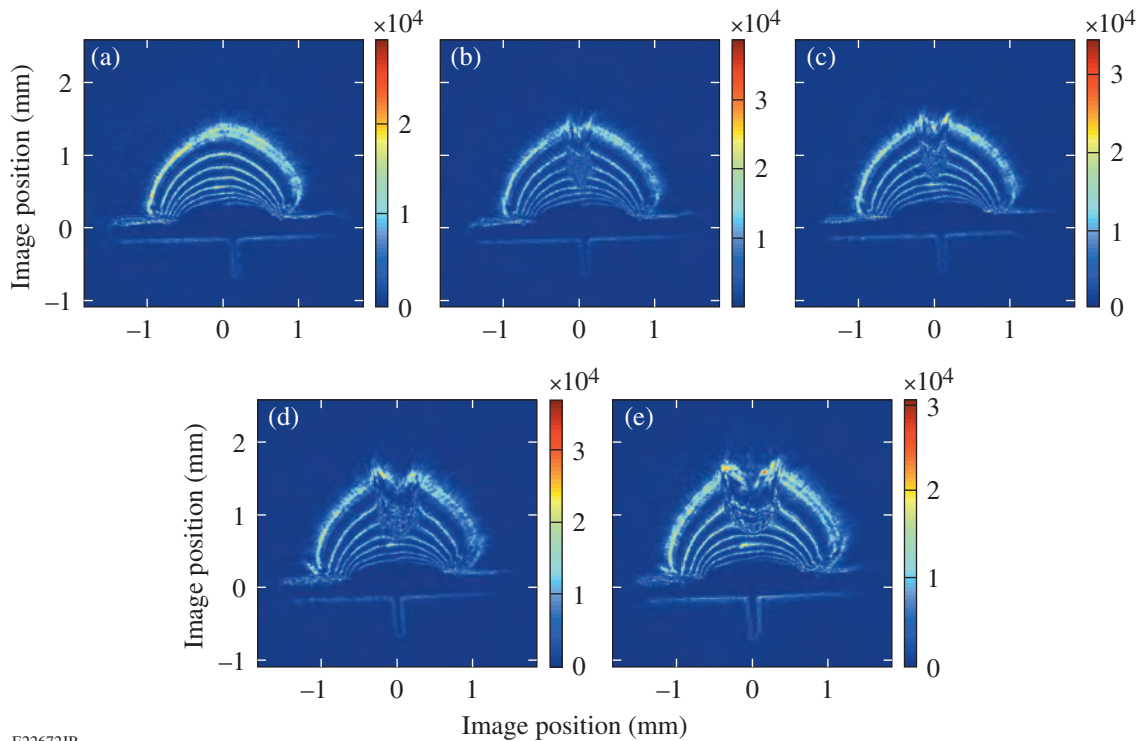
### ***Laser Channeling in Long-Scale-Length, Overdense Plasmas***

Principal Investigators: S. Ivancic and W. Theobald (LLE)  
 Co-investigators: D. Haberberger, D. D. Meyerhofer, D. H. Froula, S. X. Hu, K. S. Anderson, C. Stoeckl, and J. R. Davies (LLE); and H. Habara, T. Iwawaki, and K. A. Tanaka (Osaka University, Japan)

Laser-beam propagation at relativistic intensities ( $>10^{18} \text{ W/cm}^2$ ) is important for the field of highly nonlinear laser-plasma interactions in both under- and overdense plasmas with a long

density scale length. The purpose of this LBS experiment was to study the physics of guiding a high-intensity IR laser pulse along the density gradient of large surrounding plasma to the vicinity of high densities. This study has potential applications for the fast-ignition scheme<sup>36</sup> without using a re-entrant cone target. The experiment was performed with the OMEGA EP laser using one of the short-pulse IR beams (1.2 kJ, 10 ps) to form a channel in a large blowoff plasma with an electron temperature of  $\sim 1.8$  keV that was generated by 2-ns, 1-kJ UV laser beams. The plasma was diagnosed using a 10-ps, 263-nm probe laser<sup>37</sup> to simultaneously measure the background plasma density and image the channel. The phase gradients were discriminated by a novel technique using an angular spectral filter that is placed in a Fourier plane behind the collection optics of the probe beam. The details of the technique are described in Ref. 38.

Figure 136.75 shows measured images of the plasma at various delay times of the probe beam with respect to the channeling beam. Figure 136.75(a) shows an image of the unperturbed plasma taken 45 ps prior to the channeling pulse. The expanding plume is made visible by the alternating light and dark



E22672JR

Figure 136.75

Probe image of the plasma taken at various delay times of the probe beam ( $-45$  ps,  $6$  ps,  $15$  ps,  $78$  ps, and  $200$  ps) with respect to the channeling beam. Image (a) was taken prior to the channeling beam while images (b)–(e) show the channel formation in the plasma and the subsequent hydrodynamic evolution. The edge of the channel steepens to a shock wave moving at a velocity of  $\sim 1$   $\mu\text{m}/\text{ps}$  measured by the radial expansion of the outer limb as a function of time. The lower sharp contour shows the back surface of the foil target and the alignment fiber.

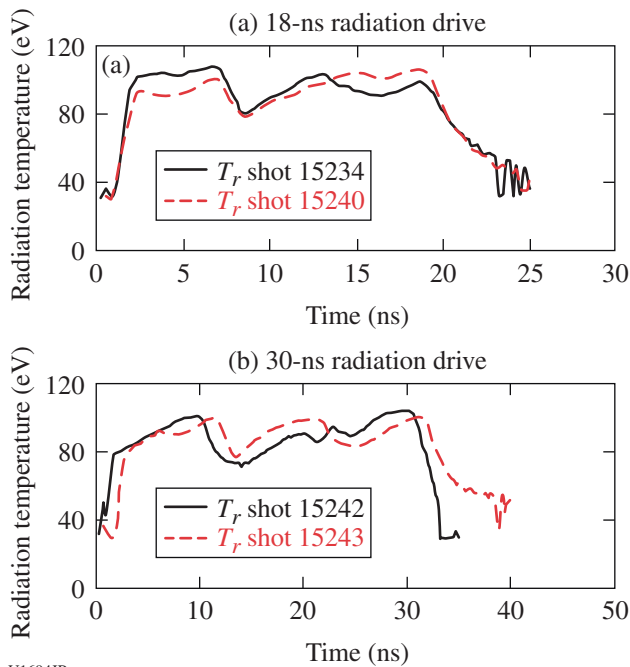
bands. Counting from the outside toward the initial target surface, the plasma density increases, as does the refracted angle of the probe beam. The band structures correspond to contours of constant refracted angle through the plasma. By relating the angle of refraction to density scale length in the plasma, a quantitative measure of plasma density and scale length is obtained. The outermost contour corresponds to roughly  $2 \times 10^{19} \text{ cm}^{-3}$  and the innermost corresponds to the critical density for IR light. An average density scale length of  $275 \mu\text{m}$  is inferred from the image. Two-dimensional hydrodynamic simulations are in good agreement with the measured plasma density profile. Figure 136.75(b) was taken during the interaction of the channeling beam showing that a channel was formed that reached up to half the IR critical density with a channel width of  $\sim 200 \mu\text{m}$ . Individual filaments were observed at the critical surfaces, indicating that the laser became unstable and broke up into multiple filaments. Images taken at later times in Figs. 136.75(c)–136.75(e) show the radial evolution of a strong blast wave from the channel walls.

**“Gatling Gun” Long-Duration Radiation Sources on OMEGA EP for Sustained-Drive Hydrodynamics and Low-Density Atomic Physics Applications on OMEGA EP and the NIF**

Principal Investigators: D. Martinez, J. O. Kane, and R. Heeter (LLNL); A. Casner (CEA); and R. C. Mancini (University of Nevada, Reno)

The High Energy Density Laboratory Physics (HEDLP)–funded Eagle nebula project, in collaboration with the LLNL/University of Nevada Photoionization/Black Hole Physics effort, has successfully executed the first day of Laboratory Basic Science (LBS) long-duration radiator shots, performed on OMEGA EP. This experiment employed a novel technique using a copper multihohlraum target with three hohlraums filled with a  $4\text{-mg}/\text{cm}^3$  poly(4-methyl-1-pentene) (TPX) foam fill to act as a gas surrogate. Each hohlraum was driven with an OMEGA EP UV beam with either a 6-ns pulse with  $3.3$  kJ of energy or a 10-ns pulse with  $4.3$  kJ. Each hohlraum was

heated in succession to generate an 18-ns or 30-ns, 100-eV x-ray source for future laboratory astrophysics studies. The x-ray source was characterized with the CEA  $\mu$ DMX diagnostic and velocity interferometer system for any reflector (VISAR) using a quartz shock sample with a CH ablator over a single hohlraum. The shot day was successful with six hohlraum shots on OMEGA EP with two 30-ns x-ray drive shots. The data indicated that the novel foam-filled multihohlraum ("Gatling gun"), long-duration source performed as designed with all three hohlraums lighting up without significant interhohlraum interference (Fig. 136.76). In addition, the x-ray drive source was able to illuminate a Ti photoionization demonstration physics package with a 90- to 100-eV x-ray drive, generating Ti L-shell band radiation as expected. This source will next be applied to study ablation-driven hydrodynamic experiments relevant to the Eagle nebula and to further develop the photoionization studies with a controlled 30-ns x-ray source.



U1694JR  
 Figure 136.76  
 Radiation temperature generated from the Gatling gun target measured with  $\mu$ DMX.

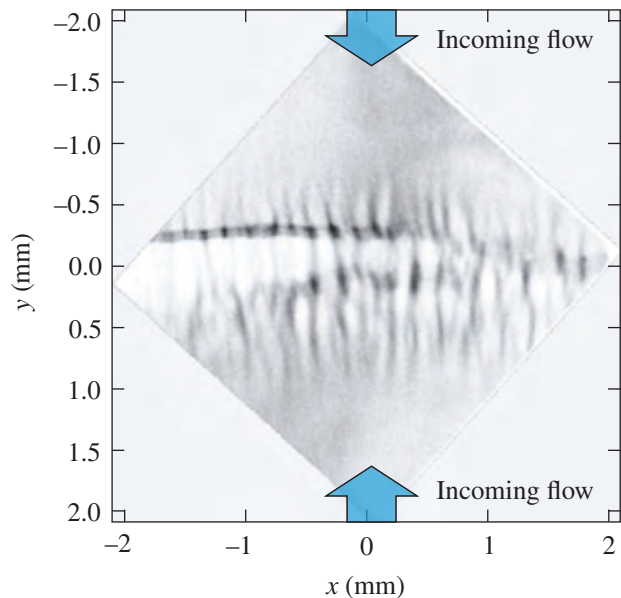
**Astrophysical Collisionless Shock Experiments with Lasers (ACSEL)**

Principal Investigator: H.-S. Park, S. Ross, and C. Huntington (LLNL)

The ACSEL collaboration had three shot days in FY13, with two shot days on OMEGA EP and one on OMEGA. These

experiments expanded on the collisionless shock platform common to ACSEL (LBS) and MagShock (NLUF), the former concentrating exclusively on nonmagnetized (no external applied magnetic field) plasmas. Irradiating a pair of opposing planar targets with 2.2 kJ (OMEGA EP) or 4 kJ (OMEGA) of laser light, counter-propagating flows are created, each with bulk velocity near 1000 km/s (Ref. 39). The flows interact near the midplane between the targets, where the interpenetrating plasma is susceptible to a range of instabilities, including the two-stream and Weibel instabilities. Study of these phenomena is essential to understanding a range of astrophysical systems, including gamma-ray bursts, supernovae remnants, and young stellar objects.

Experiments conducted this year included several new diagnostics, including x-ray spectroscopy (MSPEC on OMEGA EP),  $4\omega$  imaging (optical suite on OMEGA EP), neutronics (wedge-range filters on OMEGA), and proton probing at 14.7 MeV using  $D^3He$  (OMEGA). In the  $D^3He$  experiments, filamentation of the plasma was observed along the direction of the flow, consistent in size and growth rate with Weibel instability (see Fig. 136.77).<sup>40</sup> Weibel is notoriously difficult to diagnose in an experiment, making this an important laboratory astrophysics result. In addition to ongoing efforts to analyze data from the many new diagnostics, ACSEL experiments in FY13 also employed various single- and multispecies targets



U1695JR  
 Figure 136.77  
 Proton radiography image of the interaction of two counter-streaming plasmas showing filaments produced by the Weibel instability.

to create plasma flows. Observations from a range of target material increase our understanding of the stabilizing effect of light ions (H in CH targets versus pure C or Be targets) in the instabilities that shape these counter-streaming plasmas.

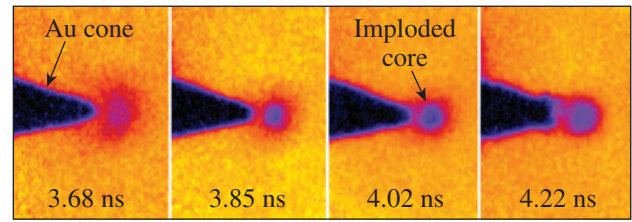
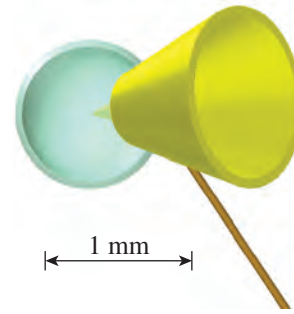
Protons from a  $D^3He$  capsule are detected using a CR-39 detector at an  $\sim 30\times$  magnification. Incoming plasma flows from the top and bottom of the frame interact, coalescing into filaments along the plasma-flow direction. Additionally, horizontal magnetic plate structures are observed, consistent with previous experiments in similar geometries.<sup>41</sup> These are the result of Biermann battery fields produced at the target surface that are entrained in the flow and lead to large-scale features at the midplane.

### Areal-Density Measurement of Fast-Ignition Targets

Principal Investigators: F. Pérez (LLNL) and H. Sawada (University of California, San Diego)

Co-investigators: W. Theobald, A. A. Solodov, J. A. Delettrez, V. Yu. Glebov, and C. Stoeckl (LLE); L. C. Jarrott and F. N. Beg (University of California, San Diego); M. S. Wei and R. B. Stephens (General Atomics); and H. S. McLean, M. H. Key, and P. Patel (LLNL)

The fast-ignition (FI) approach to inertial fusion has a potential to achieve a higher energy gain compared to a central-hot-spot-ignition scheme. It requires a moderate fuel assembly and an injection of a high-energy, short laser pulse near the peak compression to locally heat the fuel core, initiating thermonuclear ignition and burn wave. In the cone-guided FI scheme, a re-entrant Au cone embedded in a capsule clears the path of the ignition laser. Since the presence of the cone in the shell breaks symmetry, it is important to measure an evolution of the fuel assembly of the cone-in-shell target and to benchmark the 2-D radiation-hydrodynamics code with the experimental result. Based on the results of our FY12 Compton radiograph campaign and the success of the recent  $K_\alpha$  radiograph campaign by W. Theobald *et al.* for cone in shell with Al disk targets, a joint experiment to measure areal density of a cone-in-shell target was conducted using 54 18-kJ OMEGA beams for implosion and a 10-ps, 1.25-kJ OMEGA EP laser beam to generate Cu  $K_\alpha$  backlighter x rays. The radiograph images were recorded using the OMEGA spherical crystal imager (SCI). Figure 136.78 shows a schematic of a cone-in-shell target and four snapshots of the radiograph images at 3.68, 3.85, 4.02, and 4.22 ns after the beginning of the implosion drive. Each image clearly shows the shadow of the cone as well as the formation of the dense core. Preliminary comparisons of the experimental optical depth and post-processed 2-D *DRACO* simulations show a



U1689JR

Figure 136.78

Schematic of the cone-in-shell target and four sequential snapshots of the  $K_\alpha$  x-ray radiography of the implosion.

very good agreement ( $<5\%$  discrepancy of areal density) for early times; i.e., when the knowledge of the implosion is most important for future FI studies such as integrated FI simulations for core heating. For later times, the comparison shows a deviation of up to 30%. These high-quality, radiograph images will provide a solid basis for benchmarking the 2-D *DRACO* code and advancing integrated FI core-heating simulations to compare OMEGA integrated FI experiments.

### Simultaneous X-Ray Diffraction and EXAFS Measurements of Al and Mg

Principal Investigators: Y. Ping, F. Coppari, J. Hawreliak, J. Emig, R. Heeter, J. H. Eggert, and G. W. Collins (LLNL); and B. Yaakobi (LLE)

Our paper on extended x-ray absorption fine structure (EXAFS) measurements of dynamically compressed iron up to 560 GPa has been published in *Physical Review Letters*.<sup>42</sup> During FY13 we extended this platform to study Al and Mg. Both materials have new phases at high pressures that have been predicted but not previously observed. In addition to EXAFS, the setup on OMEGA with an implosion backlighter allowed us to perform simultaneous diffraction measurements, providing complimentary phase information to EXAFS on the compressed material. We have obtained undriven EXAFS data of Al [Fig. 136.79(a)] that is in good agreement with calculations. A few issues have been identified from the two half-day campaigns. First, because of the low x-ray energy of Al and

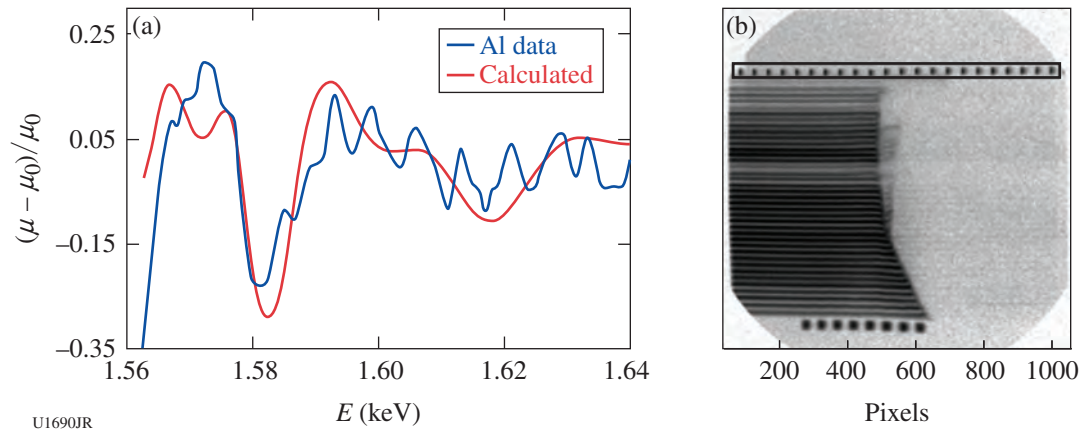


Figure 136.79

(a) Measured EXAFS spectrum of undriven Al, showing good agreement with calculations. (b) ABSO data during multishock compression. The loss of reflectivity of Be causes the signal to diminish when the shock breaks out.

Mg K edges, the blast shield of the x-ray spectrometer must be minimized, resulting in some damage to the crystal during shots. Second, the target material was sandwiched in Be foils and the active shock breakout (ASBO) beam was reflected from a polished Be surface. The ASBO signal was blanked out when the shock broke out because of loss of reflectivity of Be, as shown in Fig. 136.79(b). Third, the diffraction angle and dispersion angle were coupled in the diffraction geometry, making it difficult to exactly match for any diffraction peaks. We are working on potential improvements to mitigate these issues.

#### **Hole-Boring Dynamics and Electron Focusing Under Fast-Ignition-Relevant Conditions**

Principal Investigators: Y. Ping, T. Link, E. Kemp, N. Whiting, M. S. Wei, and P. Patel (LLNL)

During FY13 we designed and installed SpecFROG—a new diagnostic for OMEGA EP. This diagnostic, based on a scheme of frequency-resolved optical gating (FROG), measures time-resolved spectral shift with a high temporal resolution of  $\sim 200$  fs. We used it to measure the Doppler shift induced by the competition between the light pressure and the plasma thermal pressure at the laser–plasma interface. Initial testing of SpecFROG was complicated by electromagnetic interference (EMI) noise that prevented the data-acquisition system from operating properly. This issue was finally resolved after the seventh shot. The  $2\omega$  light reaching SpecFROG was lower than expected, so we plan to operate SpecFROG at  $1\omega$  for FY14 LBS shots that have been awarded. The second goal of this OMEGA EP campaign was to focus relativistic electrons by an ellipsoidal magnetic field using a novel target with buried ellipsoids or wires. The target geometry and results are shown

in Fig. 136.80. Three types of targets have been used: flat foil, buried ellipsoid, and buried wire. The Cu layer at the back serves as a fluor layer to show the distribution of hot electrons. The spot size in ellipsoid/wire targets is clearly reduced in comparison to the flat target, indicating focusing or collimation of relativistic electrons. These promising results provide a pathway to eventually solving the electron divergence problem, which is the current bottleneck for the fast-ignition scheme.

#### **Collective X-Ray Scattering from Shocked Liquid Deuterium**

Principal Investigators: S. P. Regan, T. R. Boehly, S. X. Hu, and P. B. Radha (LLE)

Co-investigators: G. Gregori and P. Kozlowski (Oxford)

The experimental platform to measure inelastic x-ray scattering from shocked liquid deuterium on OMEGA was extended from the noncollective regime<sup>43</sup> to the collective regime by changing the scattering angle from  $90^\circ$  to  $40^\circ$ . Two shot days on OMEGA for Laboratory Basic Science were used to demonstrate the planar cryogenic target having a  $40^\circ$  scattering geometry. A photograph of the new target is shown in Fig. 136.81. On the first shot day, a weak signature of elastic scattering was observed; however, the target produced too much debris, which punctured the blast shield of the primary diagnostic that recorded the scattered spectra. The target was redesigned for the second shot date to mitigate the target debris problem and to increase the amount of x rays incident on the shocked liquid deuterium. The debris mitigation strategy was successful on the second shot date at the end of FY13. Increasing the photon throughput from the backlighter to the scattering sight was also successful. Preliminary analysis of the measured spectra

indicates evidence of elastic scattering from the shocked liquid deuterium as well as plasmon features. A flat fielding shot to calibrate the Bragg crystal spectrometer used to record the spec-

trum will be taken as a ride-along experimental objective for an upcoming diagnostic development day on OMEGA. Once the flat-field response is determined, the collective x-ray scat-

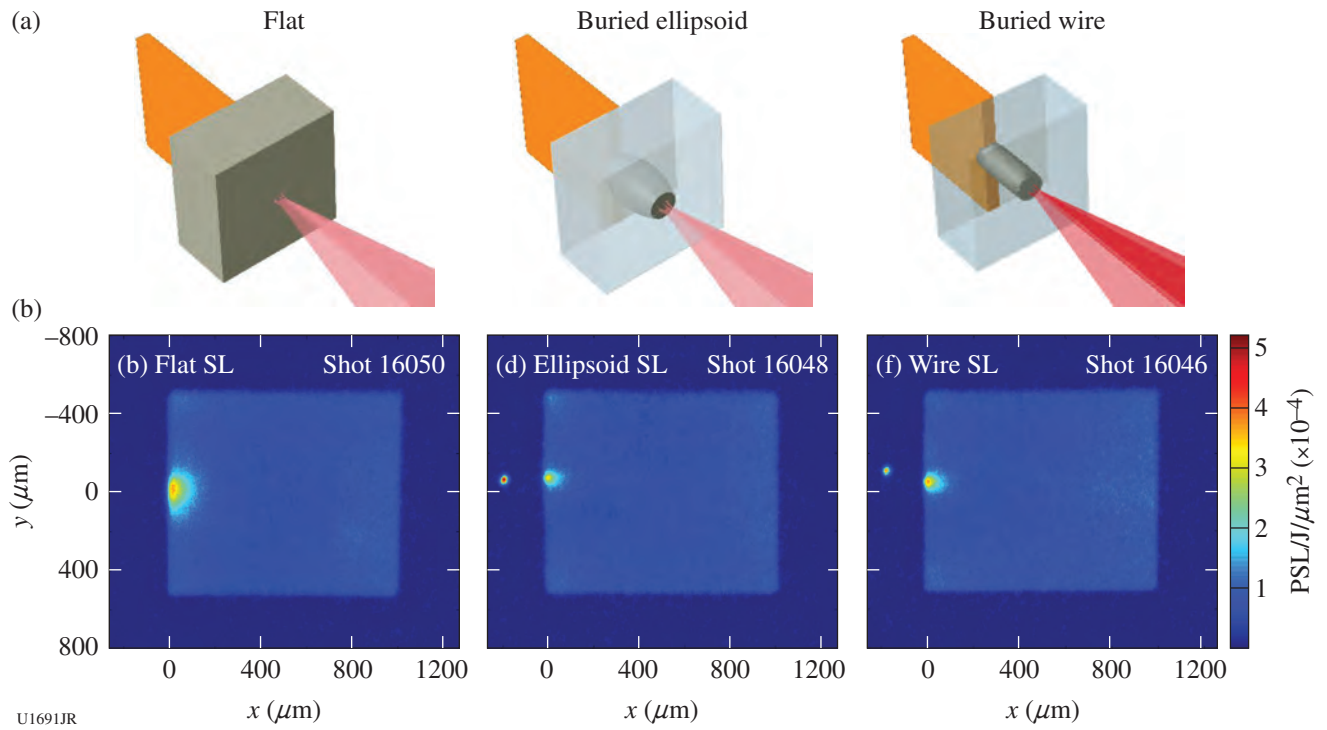
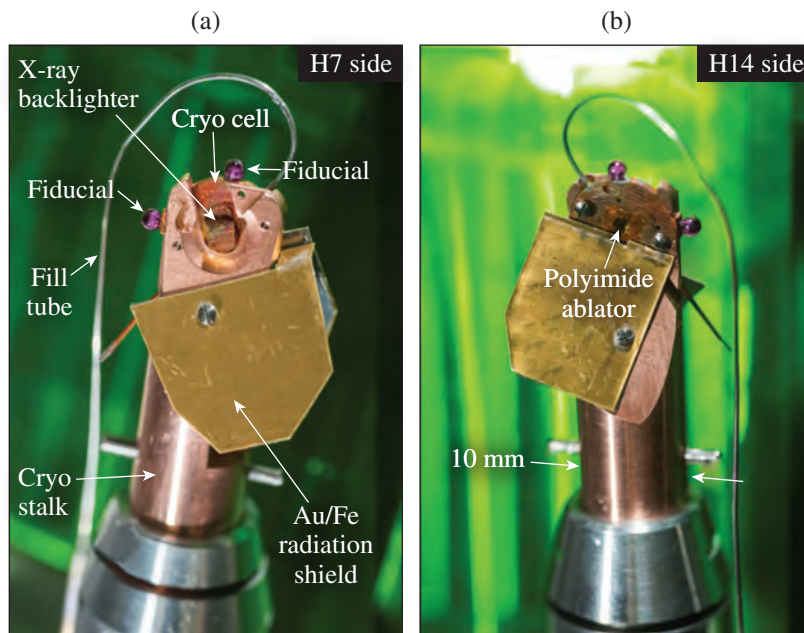


Figure 136.80

(a) Schematic of three types of targets: flat foil, buried ellipsoid, and buried wire. The Cu layer at the back serves as a fluor layer to show the distribution of hot electrons. (b) Cu  $K_{\alpha}$  images from the three targets. The spot size in the ellipsoid/wire targets is clearly reduced in comparison to the flat target.



E22671JR

Figure 136.81

Photographs of the planar cryogenic liquid deuterium target for a  $40^\circ$  x-ray scattering experiment. Deuterium is delivered to the cryo cell via the fill tube. The cryo cell, containing  $\sim 5 \text{ mm}^3$  of liquid deuterium, is aligned using the mechanical fiducials. The Au/Fe radiation shields block a direct line of sight between the x-ray emission sources and the detector (not shown). (a) The H7 side of the target highlights the x-ray backlighter and (b) the H14 side of the target highlights the  $8\text{-}\mu\text{m}$ -thick polyimide ablator.

tering spectrum will be analyzed to infer the electron density of the shocked liquid deuterium from the downshifted photon energy of the plasmon feature. To lowest order, the position of the energy-downshifted plasmon feature is related to the electron plasma frequency  $\omega_{pe} = (e^2 n_e / 4\pi\epsilon_0 m_e)^{1/2}$ , providing an electron density diagnostic.

### Extreme Chemistry, Equation of State, and Optical Properties of Dense Water at Terapascal Pressure

Principal Investigator: J. R. Rygg (LLNL)

Co-investigators: M. Millot and R. Jeanloz (University of California, Berkeley); and S. Hamel and G. W. Collins (LLNL)

We investigated the bonding of dense water at extreme conditions, achieving terapascal (TPa) pressures by shock loading precompressed samples. Our LLNL/UC Berkeley team conducted four half-day campaigns, obtaining 27 shots on the OMEGA Laser System.

Improving our knowledge of dense water is of paramount importance for modeling icy planets, such as Neptune and Uranus, and numerous exoplanets. However, our knowledge of the physical and chemical properties of water at the conditions existing in the deep interiors of these objects is limited. A better understanding of the equation of state of hot dense water is needed to constrain the mass distribution within the planets, model their internal energy fluxes, and determine how the planets formed and evolved. In addition, improving our knowledge of the transport coefficients, such as the electrical conductivity,

is crucial for correlating the gravitational and particular magnetic properties of these planets. A unique superionic phase with a solid lattice of oxygen ions and mobile protons could play a key role in the thermal and electric-charge fluxes.

Using diamond anvil cells to precompress water up to  $1.6 \text{ g/cm}^3$  and ultrafast Doppler velocity interferometry (VISAR) coupled with streaked optical pyrometry (SOP), we obtained a set of equation-of-state (EOS) and optical conductivity data for warm dense water (see Fig. 136.82). These measurements were taken at unprecedented conditions of pressure and temperature, so they provide an important experimental benchmark for advanced condensed matter theories and planetary modeling and for a more-complete understanding of chemical bonding at extreme pressure and temperature conditions. Preliminary analysis suggests that the most-recent first-principle-based molecular dynamics simulations capture most of the behavior of water at these conditions.

Furthermore, we obtained clear experimental evidence of a sharp transition in the optical properties of dense water around 2 Mbar and 4000 K along the Hugoniot of solid ice VII (initial pressure and density of  $p_0 \sim 2.4 \text{ GPa}$  and  $\rho_0 \sim 1.6 \text{ g/cm}^3$ , respectively) (see Fig. 136.83). In this region, SOP data exhibit a dramatic change from a semiconducting, absorbing state to a metallic, reflecting state, while shock pressure is only slightly increased (see Fig. 136.83). We interpret this transition as the *melting* of the superionic solid into the dense plasma fluid state that has been predicted. Further analysis will allow us to pre-

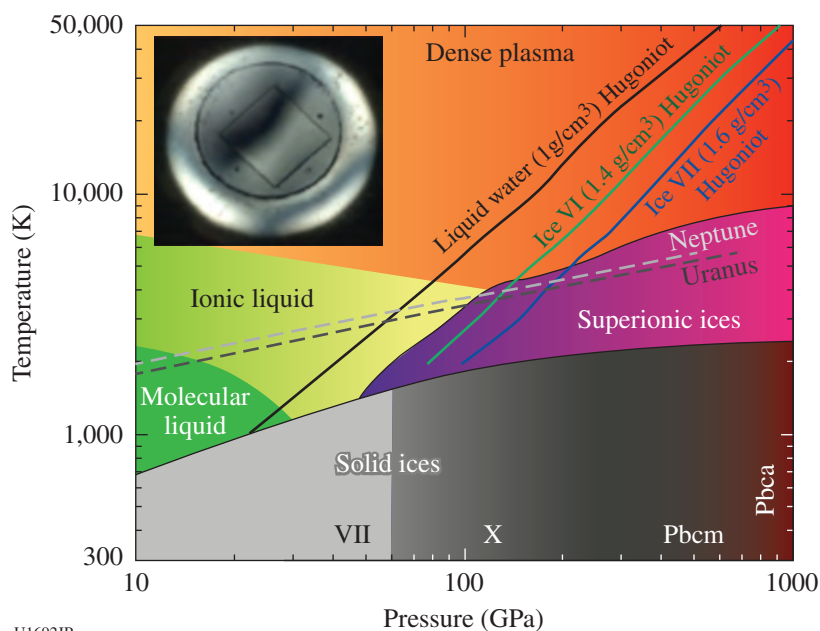


Figure 136.82

Theoretical water pressure/temperature phase diagram including the molecular liquid, the ionic liquid, the solid and superionic high-pressure ices, and warm dense metallic plasma. State-of-the-art theoretical interior isentropes for Neptune and Uranus (dashed lines) suggest that superionic ices may exist deep within these planets. The shock Hugoniot from water ice VI (green) and ice VII (light blue) were investigated during this campaign, from the vicinity of the predicted transition from superionic to metallic plasma around 1 to 2 Mbar up to pressure in excess of 7 Mbar (0.7 TPa). Inset: Microscope image of the diamond-anvil cell pressure chamber at 2.5 GPa containing ice VII water and a  $400\text{-}\mu\text{m}$ -sq quartz witness plate ready for a laser-shock compression experiment on the OMEGA laser.

U1692JR

cisely locate the pressure–density–temperature conditions of this transition, as well as the first experimental measurements of the electronic conductivity in the superionic phase.

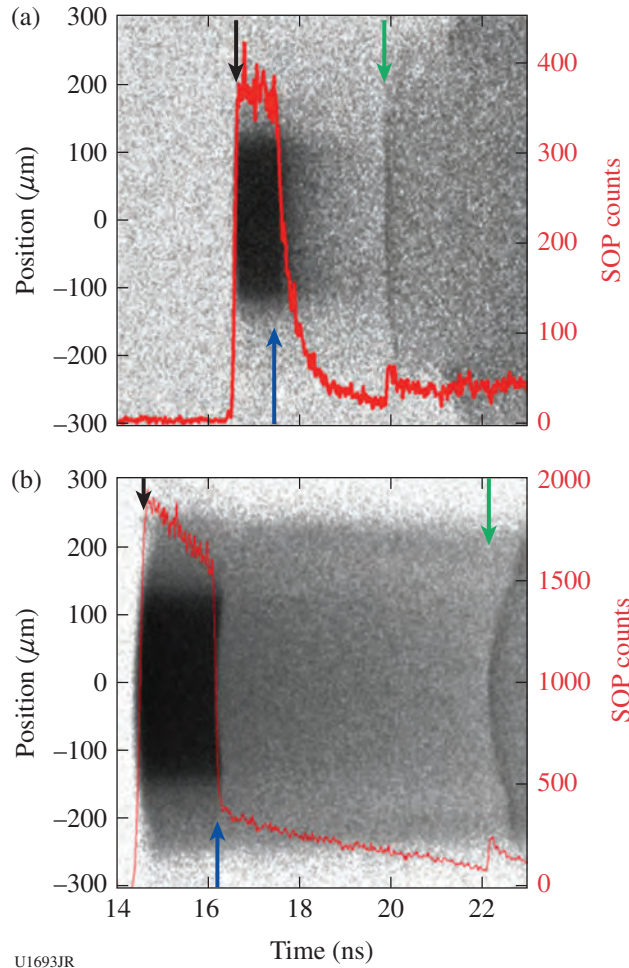


Figure 136.83  
Representative raw streaked optical pyrometry (SOP) images acquired during laser-shock compression of water ice VII in the vicinity of the predicted transition from superionic to metallic plasma around 2 Mbar. Lineouts (red) are overlaid. Strong optical emission is recorded as the shock travels through the quartz plate (from the black to the blue arrows), but a striking difference in the temporal behavior of the SOP signal as the shock transits the water layer (from the blue to the green arrows) is indicative of a qualitative difference in the optical properties of water at these different pressures. (a) At lower pressures, the SOP intensity exhibits an exponential decay with time, interpreted as the quartz emission transmitted through an increasing thickness of semiconducting, partially optically absorbing water as the shock transits the water layer. (b) At slightly higher pressure, the SOP intensity drops sharply upon breakout from the quartz into the water (blue arrow) and decays nearly linearly as the slightly decaying shock transits the water layer. This, together with the VISAR data (not shown), provides a clear signature of the metallic-like reflecting state.

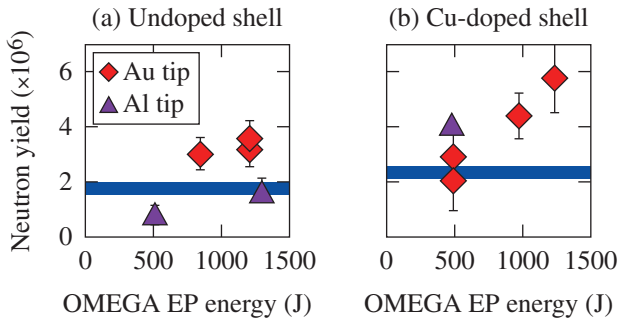
### Fast-Ignition Integrated Experiments with Low-Z Cone-Tip Targets

Principal Investigators: A. A. Solodov and W. Theobald (LLE)  
Co-investigators: C. Stoeckl (LLE); F. N. Beg (University of California, San Diego); E. Giraldez, R. B. Stephens, and M. S. Wei (General Atomics); H. McLean (LLNL); H. Sawada (University of Nevada, Reno); and H. Habara (Institute of Laser Engineering, Japan)

Integrated fast-ignition experiments on OMEGA with cone-in-shell targets have demonstrated  $\sim 3.5\%$  coupling efficiency of short-pulse laser energy into the compressed target.<sup>44</sup> The goal of this LBS experiment was to study the short-pulse–laser/fast-electron coupling efficiency using an improved OMEGA EP laser and to compare the coupling of a new aluminum cone tip target to the previous Au cone-tip design.<sup>44</sup> The hydrodynamics of the new target design has been modeled with simulations using the code *DRACO*.<sup>45</sup> The modeling predictions were validated in an FY12 LBS backlighter experiment<sup>46</sup> that showed excellent agreement between measured and simulated fuel assemblies. The radiographs showed how the implosion destroys and pushes back the cone tip. The measured time of peak compression ( $\sim 4.10 \pm 0.05$  ns) compared well to the predicted time (4.06 ns), and the measured peak areal density of  $270 \pm 50$  mg/cm<sup>3</sup> was close to the predicted peak value of 320 mg/cm<sup>3</sup>.

The fast-electron coupling was studied for the two target types. The OMEGA EP laser was significantly improved with a smaller focus ( $R_{80} = 15$   $\mu\text{m}$ ), a higher energy (1.2 kJ), and a higher contrast ( $\sim 0.5$  mJ of prepulse energy). Compared to the previous experiment,<sup>44</sup> the average intensity increased about  $4\times$  to  $\sim 2 \times 10^{19}$  W/cm<sup>2</sup>. The laser contrast was sufficiently high so that no significant pre-plasma formation was expected. Figure 136.84 shows the measured neutron yield versus OMEGA EP laser energy for (a) the LBS experiment using the two cone types with regular plastic shells and (b) the same cone designs with Cu-doped plastic shells. The later data were obtained in an FY13 NLUF experiment led by F. Beg from the University of California, San Diego. The blue lines mark the neutron yield from the implosion alone without OMEGA EP. The measured neutron yield increase in (a) is marginal and smaller than in (b) with Cu-doped shell targets. The neutron yield from the target with the Al tip was similar to the implosion yield in (a) and a factor of  $\sim 2$  higher in (b) for 500-J short-pulse energy. A clear trend of an increased yield with laser energy is observed in (b) for the standard targets with Au tips. The data show that the  $\sim 1\%$  atomic Cu doping in the plastic shell increased the energy deposition

of the fast electrons in the compressed shell. Compared to previous measurements with higher prepulse and a lower OMEGA EP laser intensity, the neutron yield was lower and the fast-electron coupling did not improve. This was probably due to the higher laser intensity, which resulted in a more-energetic fast-electron population that did not couple as well in the compressed plasma as a colder distribution. This was supported by the measured slope temperature of the distribution of escaped fast electrons, which increased from ~2.5 to ~5 MeV with higher intensity.



TC11060JR

Figure 136.84 Measured neutron yield from integrated experiments using standard Au tip targets (red diamonds) and Al tip targets (purple triangles) using (a) regular plastic shells and (b) Cu-doped plastic shells. The series in (b) was obtained from an NLUF experiment in FY13 led by F. Beg from the University of California, San Diego.

**Spectroscopy of Neutrons Generated Through Nuclear Reactions with Light Ions in Short-Pulse Laser Interaction Experiments**

Principal Investigators: C. Stoeckl, V. Yu. Glebov, and U. Schroeder (LLE)

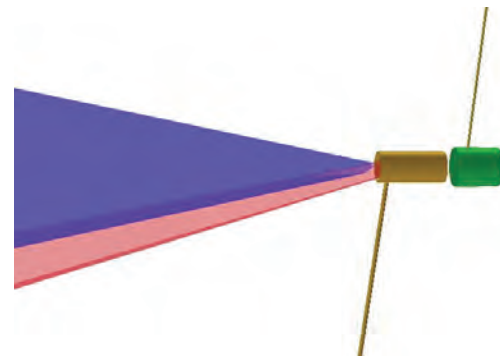
The experimental objective of this project is to study nuclear reactions in light ions by measuring the spectrum of neutrons generated in short-pulse laser interaction experiments and comparing it with simulated spectra based on the published cross sections.

Planar targets are irradiated with one short-pulse beam focused at the target's front surface. Charged particles from the back side of the target create neutrons and charged particles through nuclear reactions in a second converter target placed closely behind the primary interaction target. The spectrum of the neutrons generated in the converter target is measured using a three-channel scintillator photomultiplier-based neutron

time-of-flight detector system. Charged-particle detectors are used to measure the spectra of the primary particles.

The previous experiments in FY12 with copper primary and LiD secondary targets resulted in neutron spectra dominated by background from p–n reactions in the targets and the target chamber. No specific spectral features like DT fusion neutrons were visible in the recorded data.

Two shot days were available for experiments in FY13. On the first shot day a larger LiD container with 10× more LiD compared to the FY12 experiments was used to increase the expected signal. Even with the increased mass of the LiD in the secondary target, no DT fusion neutrons were observed; the neutron spectrum was still dominated by background. Two different strategies were used on the second shot day in an effort to reduce the background. A CH shield tube was placed around the primary target (see Fig. 136.85), which stops or slows protons below the threshold of (p,n) reactions. Since carbon has a high threshold for (p,n) reactions of >20 MeV, placing a CH shield to intercept all protons that would not interact with the secondary target could significantly reduce the background, provided that the proton spectrum not contain a large number of protons above 20 MeV. Additionally a pre-plasma was created on the front side of the primary target using a 100-J, 100-ps UV laser pulse, which was fired 1 ns before the main IR short pulse. Previous experiments have shown that the presence of plasma can significantly reduce the number of charged particles generated on a surface. The



E22673JR

Figure 136.85 Schematic of the target setup for the background-reduction experiments. The primary target (not visible) is contained in a CH shield tube (brown). It is irradiated by a 100-J, 100-ps UV laser pulse (purple), 1 ns before the main IR short pulse (red) arrives, to create a pre-plasma. The secondary converter target (green) is placed as close as possible to the end of the shield tube.

UV laser energy and timing were chosen such that a plasma was generated only on the front side of the primary target and not on the back side of the target from the laser-generated shock reaching the back surface at the time the short-pulse laser was fired.

CD foils were used for primary and secondary targets in the background reduction study since the D–D fusion cross section is higher (of the order of 1 barn) than the Li breakup cross section (<100 mb) and very well known.

Figure 136.86 shows two neutron time-of-flight signals from the background reduction experiments, (a) with UV prepulse and (b) without prepulse. The neutron background is reduced substantially with the prepulse, and a clean D–D fusion neutron peak can be seen at the expected time of 750 ns. Without a prepulse, the background signal is very high and masks any D–D peak that might be present. A detailed analysis of the experimental data is in progress.

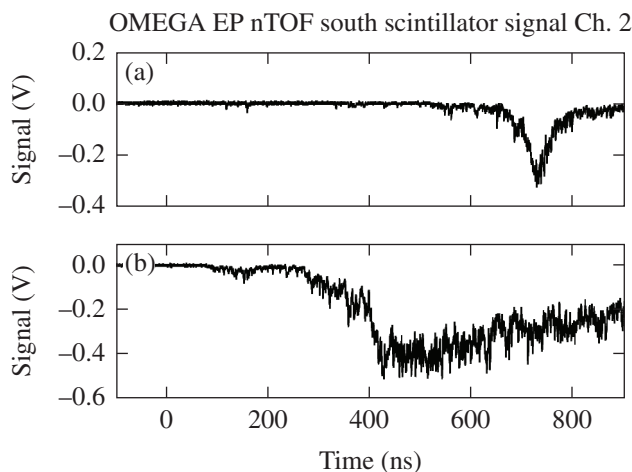


Figure 136.86 Neutron time-of-flight (nTOF) signals from the background-reduction experiments. (a) When the UV prepulse is used, the background is reduced substantially and a clean D–D fusion neutron peak is visible at the expected time of 750 ns. (b) Without a prepulse, the data are dominated by background and no D–D peak is seen.

### ***Direct Measurement of Dislocation-Based Plastic Flows in Quasi-Isentropically Compressed bcc Metals***

Principal Investigator: C. Wehrenberg (LLNL)

Our goal was to record a time series of Laue diffraction patterns in shock-compressed single-crystal Ta at a range of

shock pressures near the expected homogeneous nucleation threshold. With these results we would be able to study the strain relaxation process in Ta. For these shots, an imploding CH capsule driven by 29 beams provided a broadband x-ray source, and a Ta sample with a high-density–carbon (HDC) ablator was driven by a single beam. High-quality diffraction data were recorded for shock pressures of 0.4 to 0.8 Mbar. Data at 0.4 Mbar show the strain at first extending out to a maximum that matches theoretical predictions for uniaxial compression and then relaxes to a final strain state over the course of  $\sim 1$  ns. Above 0.7 Mbar, the Ta relaxes to a final strain state faster than the resolution of the experiment ( $\sim 0.2$  ns). This behavior is consistent with the predicted homogenous nucleation threshold occurring at 0.65 Mbar.

In addition, simultaneous recovery experiments designed to measure the average dislocation velocity during shock loading of Ta were performed. In these experiments a high dislocation density region was seeded by nano-indenting single-crystal Ta samples and grown by driving a shock wave with a single beam. Movement of the dislocation region was measured pre- and post-mortem by transmission electron microscopy (TEM). Several samples with a range of single crystal orientations and indents were recovered and the TEM analysis is ongoing.

### **FY13 LLNL OMEGA Experimental Programs**

Principal Investigators: R. Heeter, K. Fournier, K. Baker, G. V. Brown, D. T. Casey, P. M. Celliers, L. Fletcher, D. E. Fratanduono, J. Hawreliak, C. Huntington, A. Lazicki, T. Ma, D. Martinez, M. May, A. Moore, A. Pak, H.-S. Park, R. Patterson, F. Perez, Y. Ping, C. Plechaty, J. S. Ross, J. R. Rygg, M. Schneider, V. A. Smalyuk, R. Tommasini, C. Wehrenberg, G. W. Collins, O. L. Landen, A. Wan, and W. Hsing (LLNL); H. Rinderknecht and A. Zylstra (MIT)

In FY13, LLNL's high-energy-density (HED) physics and indirect-drive inertial confinement fusion (ICF-ID) programs conducted several campaigns on the OMEGA and OMEGA EP Laser Systems, as well as campaigns that jointly used the OMEGA and OMEGA EP beams. Overall LLNL led 448 target shots (290 target shots involving OMEGA and 158 target shots involving OMEGA EP). (These shots do not include the target shots taken under the LBS program.) Approximately 34% of the total number of shots (93 OMEGA shots, 58 OMEGA EP shots) supported the ICF-ID Program. The remaining 66% (197 OMEGA shots and 100 OMEGA EP shots) were dedicated to experiments for HED physics.

### Indirect-Drive Inertial Confinement Fusion Experiments

#### A New Platform for Absolute Equation-of-State Measurements

Principal Investigator: D. E. Fratanduono

Using OMEGA EP, a radiographic equation-of-state (EOS) platform was developed for use at the National Ignition Facility (NIF). The concern regarding traditional velocity interferometer system for any reflector (VISAR)-based EOS platforms is that at high pressures (>5000 GPa), optical windows (i.e., quartz and LiF) would become opaque because of x-ray pre-heat or radiative shock fronts. As a result, at such extreme pressures, the VISAR diagnostic would no longer be useful in performing EOS measurements. In addition, VISAR EOS measurements at the NIF and OMEGA are not absolute since they rely on a standard reference. Therefore, a new experimental platform is required to perform high-pressure absolute Hugoniot measurements.

Radiography experiments have been conducted to measure the shock density and shock velocity at high pressure. The purpose of these experiments was to radiograph a shock front in a low-Z sample (CH) as shown in Fig. 136.87. The radiographs were used to determine the shock velocity and the shock density of the compressed materials. ABSEOS-13A-EP was successful in demonstrating the platform. We were able to determine the EOS of the CH sample. Measurements are in agreement with previous experiments performed by M. A. Barrios using VISAR as shown in Fig. 136.88. The platform design was improved for a second campaign, ABSEOS-13B-EP, to reduce high background levels in the emission and to resolve parallax issues. Both issues were resolved in ABSEOS-13B-EP, producing better-quality data. Future platform development would be to conduct experiments on OMEGA using halfraun drives since the OMEGA EP experiments use direct drive.

#### VISAR Measurements of the EOS of Boron Carbide

Principal Investigator: D. E. Fratanduono

The ICF campaign has begun to investigate alternate ablaters (i.e., diamond, B<sub>4</sub>C, and SiC). As a result, a campaign to measure the Hugoniot of B<sub>4</sub>C was conducted. Previous Hugoniot measurements of B<sub>4</sub>C were limited to ~200 GPa because of the limiting pressure range using a two-stage gas

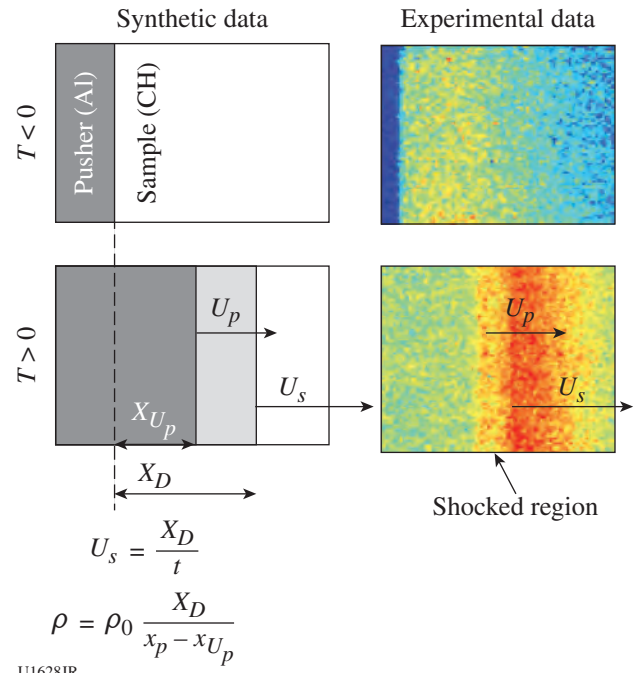


Figure 136.87 Synthetic and experimental data illustrating the radiography technique to perform Hugoniot experiments.

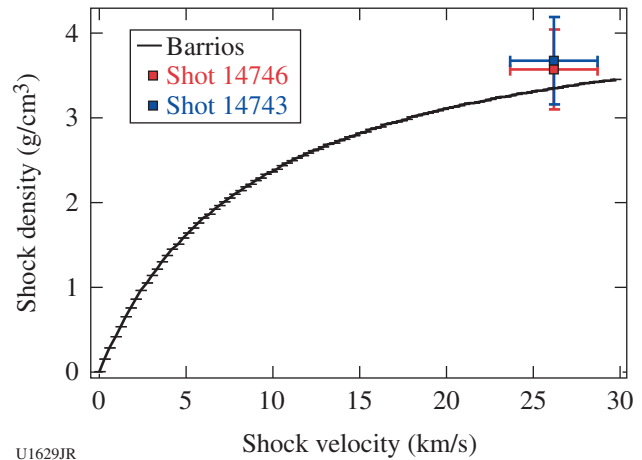


Figure 136.88 Comparison of radiography measurements with experimental fit to CH data from the thesis of M. A. Barrios.

gun. Experiments were conducted on OMEGA to extend the pressure range to 800 GPa; 12 experiments measured the Hugoniot from ~250 GPa to ~800 GPa. Experimental data are shown in Fig. 136.89. Measurements are consistent with lower-pressure data. A slight disagreement with LEOS table

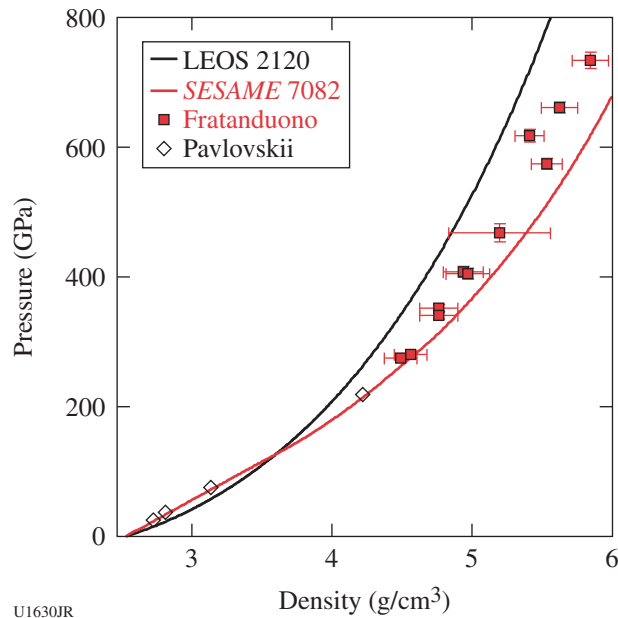


Figure 136.89  
 $B_4C$  Hugoniot measurements (red squares) from the B4C-EOS-13A campaign. Measurements are compared with low-pressure Pavlovskii data, LEOS table 2120, and *SESAME* table 7082.

2120 and *SESAME* table 7082 is observed. These data will be used to generate a new EOS model that will assist in hydrocode simulations and future experimental design for ICF.

**Shock Release Isentrope Measurements of ICF-Relevant Materials**

Principal Investigator: D. E. Fratanduono

The goal of this campaign was to demonstrate the feasibility of previous experimental designs using thin silicon-nitride films (150 nm) with a low-density methane gas ( $0.6 \text{ mg/cm}^3$ ) present on both sides of the film simulating the  $D_2$  vapor that would be present on a NIF capsule experiment. Previously, the thin films acted as a boundary between methane and vacuum. The concern was that the methane gas behind the silicon nitride would become opaque to the VISAR when the shock passed through the silicon-nitride film. Experimental results indicated that the methane gas is transparent to the VISAR probe and the silicon-nitride velocity was observed. Results also indicated that the presence of gas on both sides of the film helped to tamp the nitride and prevent it from breaking during the experiment. Results continue to indicate that the LEOS tables overpredict the velocity of the release isentropes (see Fig. 136.90).

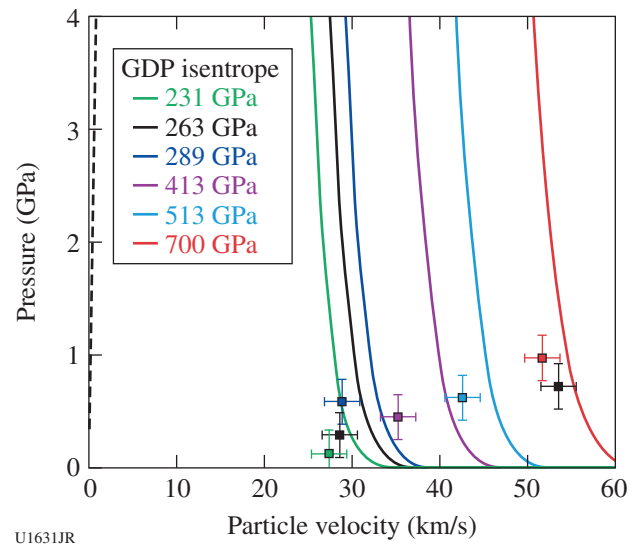


Figure 136.90  
 Experimental measurements are shown as squares and are color coded with release isentropes from the LEOS table for CH. Measurements indicate that the LEOS models overpredict the release velocity.

**Thomson-Scattering Measurements from Au Spheres**

Principal Investigator: J. S. Ross

Co-investigators: E. L. Dewald and M. D. Rosen (LLNL); and D. H. Froula (LLE)

During the AuSphere-13A campaign we performed high-Z sphere experiments illuminated in direct-drive geometry to investigate atomic physics models and radiative properties of the laser-spot plasma relevant to ICF indirect-drive-ignition hohlraum plasmas. Using SG4 laser phase plates, 1-mm Au spheres were uniformly irradiated with 3 to 30 kJ of laser energy at intensities of 0.1, 0.5, and  $1 \times 10^{15} \text{ W/cm}^2$ , similar to the intensities found in National Ignition Campaign (NIC) hohlraums. The  $4\omega$  Thomson-scattering probe beam was aligned at various radial locations ranging from 100 to 300  $\mu\text{m}$  from the target surface and used to characterize the low-density plasma blowoff. All of the laser beams used a 1-ns square laser pulse. An example of the Thomson-scattering ion feature data is shown in Fig. 136.91, taken 200  $\mu\text{m}$  from the target surface.

The electron temperature and density, the plasma-flow velocity, and the average ionization state were measured by fitting the theoretical Thomson-scattering form factor to the observed data. The measured data were then compared to post-shot simulations with different atomic physics and elec-

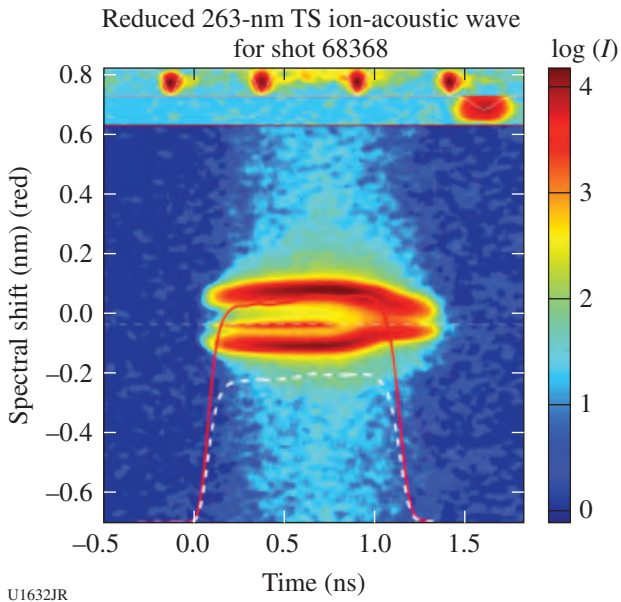


Figure 136.91 Thomson-scattering (TS) data from 200  $\mu\text{m}$  off the surface of the Au sphere irradiated at an intensity of  $5 \times 10^{14} \text{ W/cm}^2$ .

tron transport models. The different models predict different electron temperatures for the experimental conditions (see Fig. 136.92).

The simulation with the detailed-configuration accounting (DCA) nonlocal model most closely reproduces the tempera-

tures measured during the experiment. The LLNL atomic physics model XSN with a flux-limited transport model using a flux limiter of 0.05, previously used to simulate high-Z hohlraums, predicts an electron temperature significantly higher than measured. Additional measurements at different radial locations and different intensities appear most consistent with an intermediate model with a temperature between that predicted by the XSN and DCA models. Further data analysis is underway to compare Thomson-scattering data, Dante absolute x-ray flux measurements, and x-ray spectroscopy to simulations in our effort to validate atomic physics models employed in simulations.

**Measuring the Adiabatic Index of Polystyrene Using Counter-Propagating Shocks and X-Ray Thomson Scattering**

Principal Investigator: A. Pak  
 Co-investigators: T. Ma, L. Fletcher, T. Döppner, S. H. Glenzer, and O. L. Landen

Understanding the EOS and opacity of polystyrene—a material similar to the NIF ablator—at densities of a few  $\text{g/cm}^3$  and temperatures of several eV is of interest since it can inform the design and performance of current implosion experiments. In the CH-HeatCap campaign on OMEGA EP, the electron density, temperature, and charge state of shocked polystyrene (CH) were directly measured with x-ray Thomson scattering (XRTS). The goal of these campaigns was to test the hypothesis

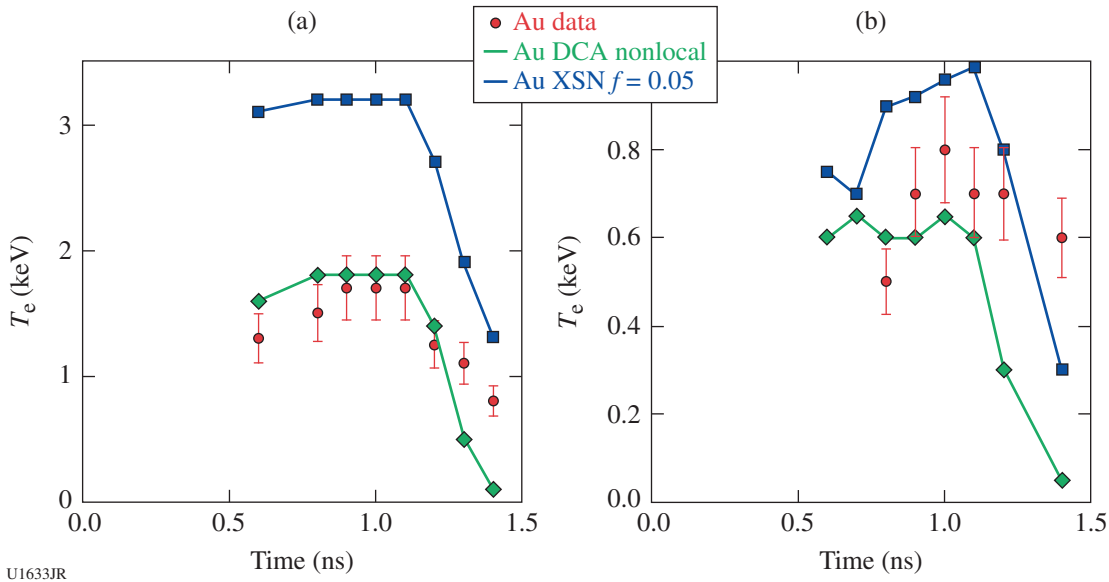


Figure 136.92 The measured electron temperature (red dots) compared to post-shot simulations using the detailed-configuration accounting (DCA) nonlocal model (green line) and the XSN flux-limited model (blue line) for intensities of (a)  $5 \times 10^{14} \text{ W/cm}^2$  and (b)  $1 \times 10^{14} \text{ W/cm}^2$  at a radial location of 200  $\mu\text{m}$ .

that the continuum lowering effect would increase the charge state of CH as the compression of the material was increased. Understanding in detail the charge state of CH could improve opacity models that are used to calculate the ablation dynamics of NIF implosions.

In the experimental setup [Fig. 136.93(a)], Beams 2 and 3 were used to drive a shock in the CH sample. The strength of the shock, and therefore the expected post-shock density, was varied from shot to shot by using three different drive intensities of  $5 \times 10^{12}$ ,  $1.5 \times 10^{13}$ , and  $2 \times 10^{14}$  W/cm<sup>2</sup>. The shocked state was probed using the zinc He<sub>α</sub> line at an energy of 9 keV. This line was produced by irradiating a zinc foil placed 1.6 mm away from the CH sample with Beams 1 and 4 at an intensity of  $\sim 1 \times 10^{15}$  W/cm<sup>2</sup>. X rays that were scattered at an angle of 154° with respect to the incident angle were collected by a curved highly oriented pyrolytic graphite (HOPG) crystal placed in the ZSPEC spectrometer. The HOPG crystal spectrally dispersed the transversely focused scattered signal onto a framing camera that has a integration time of 250 to 300 ps.

Figure 136.93(b) compares the measured spectral intensity for three different shots: undriven, driven at  $I = 5 \times 10^{12}$  W/cm<sup>2</sup>, and driven at  $I = 2 \times 10^{14}$  W/cm<sup>2</sup>. Detailed fits of the scattered spectrum using the current description of the bound-free scattering component have been unable to accurately model the data. A revised code that incorporates a more-accurate model of the bound-free spectrum has been developed and will be applied to this data in the future. Qualitatively, the increase in charge state as the density of the shock state is increased is believed to have been

observed. This is shown in Fig. 136.93(c), where the inelastic components of the three spectra have been overlaid. As the drive intensity is increased, the spectral width of the inelastic feature is observed to increase on the higher-energy side, while decreasing on the lower-energy side. It is believed that the decrease in spectral width on the low-energy side is due to the decreased L-shell contribution in the bound-free spectra, while the broadening on the high-energy side is due to an increase in the electron density.

The initial results of the heat capacity campaign appear of sufficient quality to determine if continuum lowering is occurring and how the final charge state, density, and temperature vary with the magnitude of the drive intensity.

#### Angularly Resolved X-Ray Thomson-Scattering Measurements of Shock-Compressed Aluminum

Principal Investigator: L. Fletcher (University of California, Berkeley)

Co-investigators: T. Ma, A. Pak, H. J. Lee, T. Döppner, C. Fortmann, O. L. Landen, and S. H. Glenzer (LLNL); and R. Falcone (University of California, Berkeley)

We have directly demonstrated the ability to measure the ion-ion correlation peak using simultaneous angularly, temporally, and spectrally resolved x-ray scattering measurements in laser-driven shock-compressed aluminum. Molybdenum He<sub>α</sub> (17.9-keV) x rays have been used to probe Al foils that are compressed using both single and double (counter-propagating) shocks in a forward, small-angle scattering platform with very high angular precision (Fig. 136.94).

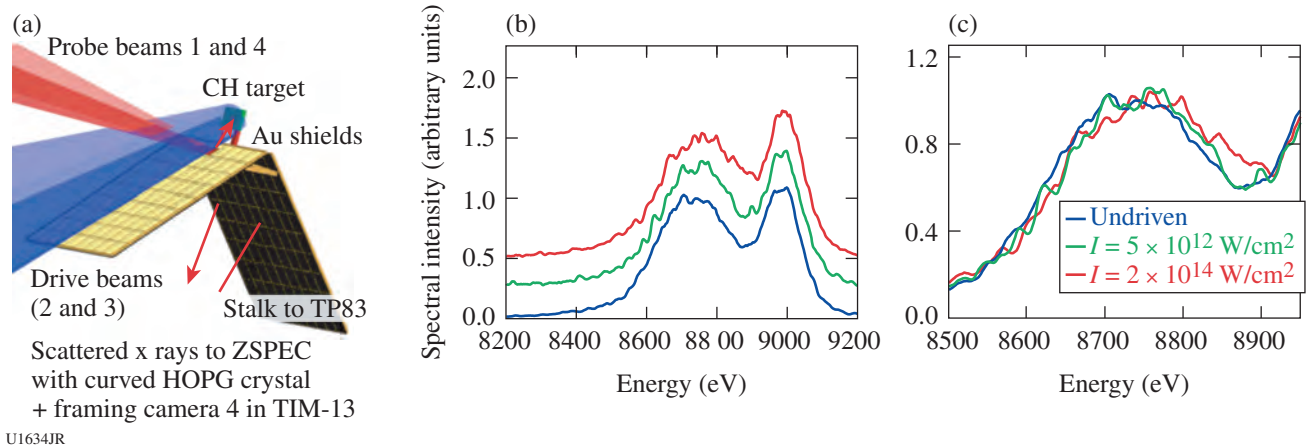


Figure 136.93

(a) Experimental setup. (b) Scattered spectrum observed at three different drive conditions. Here the signals have been normalized and offset from each other. (c) Overlay of the normalized inelastic scattered feature where the decrease in the width on the low-energy side as the drive intensity is increased may be an indication of continuum lowering.

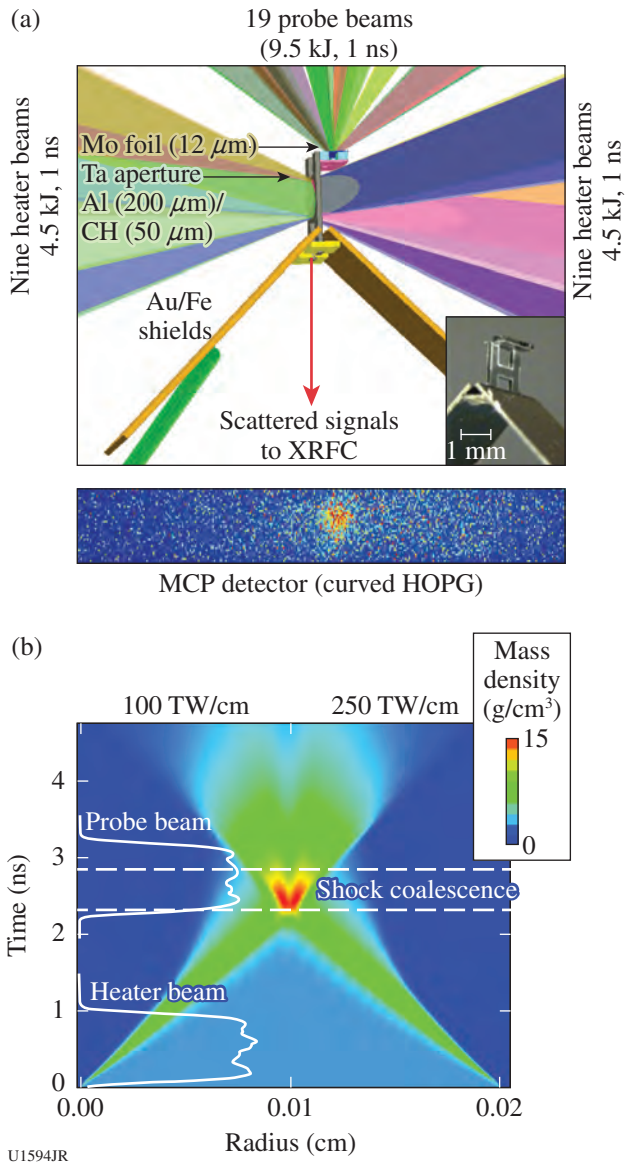


Figure 136.94  
 The experimental setup for HiZShk-13A: (a) 200- $\mu\text{m}$ -thick Al target (double-shock configuration) and beam configuration, along with a photo of the Al scattering target, and gated x-ray framing-camera–multichannel plate (XRFC–MCP) detector data; (b) 2-D Helios simulation of the mass density as a function of Al foil radius, and input pulse shape dimensions (TW and time duration).

In our study, 125- $\mu\text{m}$ -thick and 200- $\mu\text{m}$ -thick Al targets were compressed 3 $\times$  and 6 $\times$  the solid density using 1-ns pulses with a total laser energy of 4.5 kJ and 9 kJ, respectively. A total drive intensity of  $3 \times 10^{14}$  W/cm<sup>2</sup> on each irradiated aluminum surface was used to drive shocks into the sample, while  $7 \times 10^{14}$  W/cm<sup>2</sup>, incident on a thin Mo foil, was used to generate Mo He $_{\alpha}$  x rays at 17.9 keV, in order to probe the compressed targets. Figure 136.95(b) demonstrates a shift in

a well-pronounced peak in the static structure factor at wave numbers of  $k = 3.5 \text{ \AA}^{-1}$  and  $4.5 \text{ \AA}^{-1}$ , corresponding to higher-compression material states.

The magnitude of this correlation peak is in good agreement with calculations that use a potential with strong short-range

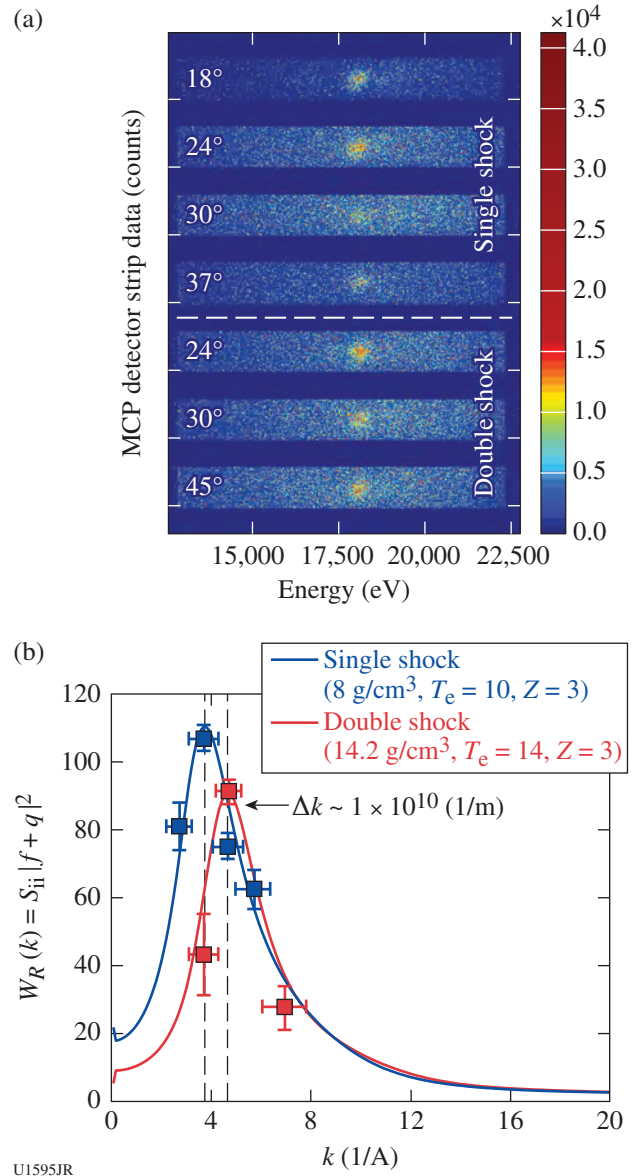


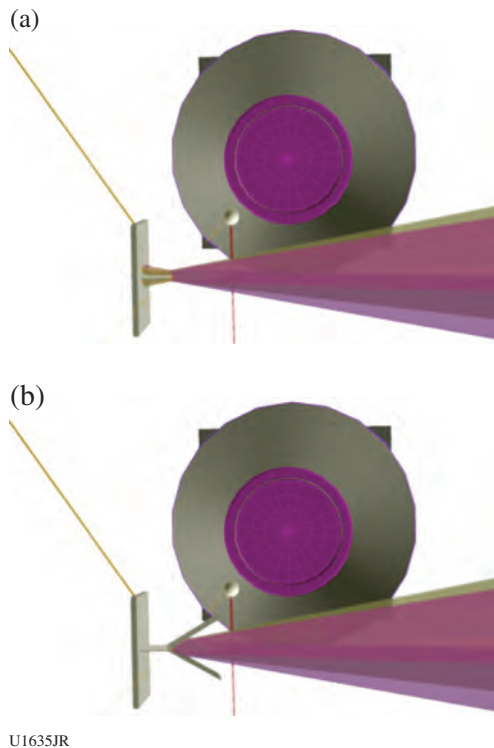
Figure 136.95  
 (a) Raw data of scattered spectrally resolved x-ray Thomson-scattering (XRTS) signals for single- and double-shock configurations. (b) Preliminary data analysis shows the total integrated signal (corrected for experimental geometry) of the scattering data as a function of  $k$  follows the trends predicted by the split-ring resonator (SRR) models using the frequency-integrated, quasi-elastic contribution to the dynamic structure factor of single-shocked ( $\rho = 8 \text{ g/cm}^3$ ) and double-shocked ( $\rho = 14 \text{ g/cm}^3$ ) aluminum.

repulsion (SRR). The results will show that the elastic x-ray scattering amplitude, angularly resolved, shifts to a higher wave number of approximately  $\Delta k = 1 \times 10^{-10} \text{ m}^{-1}$  with increasing density. This presents a new scattering diagnostic to fully characterize states of matter at densities and temperatures that have not been previously accessible.

### Enhanced Bremsstrahlung Backlighters

Principal Investigator: R. Tommasini

The motivation of the UV-CR-BL-13A campaign was to test and characterize enhanced broadband x-ray sources emitting around and above 75 keV, to be used in the Compton radiography of ICF targets on the NIF. In FY09 we characterized Au microwire backlighters irradiated by 10-ps-long OMEGA EP pulses. In FY10 we characterized Au microwire backlighters irradiated by 100-ps-long OMEGA EP pulses ( $1\omega$ ) and OMEGA pulses ( $3\omega$ ), with the primary goal of measuring the effect of a longer-pulse-generated backlighter with respect to the source size. In FY13 we characterized Au microwire backlighters irradiated by 1-ns OMEGA pulses ( $3\omega$ ) and compared the performance of wires with and without CH wedges (see Fig. 136.96).



U1635JR

Figure 136.96  
Backlighter geometry used for the experiments: (a) bare Au wire; (b) Au wire inside a CH wedge.

The 30- $\mu\text{m}$  Au microwires were arranged in a point-projection end-on geometry and were  $\sim 500 \mu\text{m}$  long. They were mounted on a CH slab, and, in about half of the performed shots, they were sitting inside a CH wedge with a  $30^\circ$  half-angle. The bremsstrahlung radiation was generated by irradiating the Au wires with 1-ns square pulses. The energy on target was changed between 500 J and 2500 J by changing the number of incident beams from one to five. Solid W spheres with diameters of 200  $\mu\text{m}$  located at a distance of 10 mm from the backlighters were used as radiography samples.

A Compton radiography snout (CRS) was used to record the radiographs and measure the time-integrated backlighter spectra. A combination of high- and low-Z filters inside the snout restricted the backlit photon energies to about and above 75 keV. A Fuji BAS imaging plate was used as a detector 400 mm from the backlighter. The neutron temporal diagnostic (NTD) recorded the time-resolved emission from the backlighter. The data show an increase in the peak of the time-resolved backlighter signal by  $\sim 4\times$  and in the total time-integrated signal by  $\sim 2\times$  when using wire in the CH wedge. These values are very close to those predicted by simulations. The analysis of the radiographs of the W sphere allowed us to reconstruct the source size of the backlighters. We measured  $\sim 30 \mu\text{m}$  for the Au wire in the CH wedge versus  $\sim 45 \mu\text{m}$  for the bare Au wire, which we ascribe to plasma confinement generated by the CH wedge.

### Hohlraum Drive Spectroscopy

Principal Investigator: G. V. Brown and M. Schneider

Co-investigators: K. Widmann, R. Heeter, and J. Emig

The objective of the DriveSpec-13A campaign was three-fold: (1) to assess what is necessary to field on the NIF a fully calibrated, high-resolution crystal spectrometer whose spectra can be used to refine data from the Dante diode array drive diagnostic; (2) to assess the atomic physics taking place in a hohlraum's non-LTE (local thermodynamic equilibrium) drive radiation field; and (3) to use the high-resolution spectra to aid in the deconvolution of the Dante spectra.

To provide benchmark high-resolution spectra for models of the drive radiation for ICF, three target types were fielded. The first was a 2.25-mm-long, 1.2-mm-diam, 100%-open laser entrance holes (LEH's), 25- $\mu\text{m}$ -wall gold hohlraum; the second was a gold hohlraum of the same dimensions but with interior surfaces coated with 4 to 11  $\mu\text{m}$  of uranium; and the third was a gold halfraum with a single 0.8-mm, 100%-open LEH, a length of 0.75 mm, and closed on the side opposite the

LEH. Eight of the 1.2-mm LEH gold targets, one 1.2-mm LEH uranium target, and two 0.8-mm LEH gold targets were shot.

Radiation from each shot was detected with several spectrometers. The main diagnostics were three high-resolution "MSpec" elliptical spectrometers, each covering a continuous bandwidth form of  $\sim 1.7$  to 3 keV. Two of the MSpecs recorded time-integrated spectra using an image plate and were on nearly the same sightline at the Dante temperature diagnostic: one at  $42^\circ$  relative to the LEH on the H10 side of the hohlraum, i.e., on the opposite side as Dante, and one at  $37^\circ$  on the H11 side of the hohlraum, i.e., on the opposite side of Dante. A third MSpec recorded time-resolved spectra. A variable line spaced grating spectrometer (VSG) covering the  $\sim 0.2$  to 1.5 keV band was also used to record time-resolved spectra.

Spectra from this campaign have already provided new insight as to the deconvolution of the Dante spectra, especially regarding the distribution of the M-band emission from highly charged gold ions. High-resolution spectra of the gold M-band emission is also being compared to models used to predict the drive radiation field in NIF ICF hohlraums. Calibration measurements of the full instrument response, including filter x-ray transmission efficiencies and Bragg crystal reflectivities, have been completed. These results demonstrate technical readiness to field a fully calibrated drive spectrometer on the central channel of the NIF Dante.

**Ablator Opacity Measurements**

Principal Investigator: R. Heeter

Co-investigators: A. Graf, G. V. Brown, C. Mauche, R. E. Marrs, and B. Wilson

In a follow-up to earlier ablator opacity measurements, improved experiments were performed to measure the transmission opacity of hot Si-doped glow-discharge polymer (GDP) (using OMEGA 60) and pure Si (using OMEGA EP) at  $T \approx 100$  eV,  $\rho \approx 0.1$  g/cm<sup>3</sup>. The OMEGA platform used a Be-tamped, Si-doped GDP sample heated indirectly in a hohlraum. The OMEGA EP platform used a CH-tamped, embedded Si dot heated by 100-ps UV impulses. Both platforms used dual-axis backlighting, both face-on and edge-on, simultaneously to obtain density via sample expansion radiography, Si ionization balance data, and GDP and/or Si transmission opacities via absorption spectroscopy. The GDP measurements used a high-Z backlighter to record the transmission spectrum for x rays rang-

ing from 250 to 1600 eV, as well as from 1600 to 3000 eV. The Si measurements span the x-ray band from 1600 to 3000 eV.

Compared to prior measurements using similar opacity platforms on OMEGA, the sample density was increased about fourfold, and the sample uniformity was also improved, particularly for the Si on OMEGA EP by using a thicker tamper on the laser-heated side. In addition, backlighter and spectrometer performances were also improved on both platforms, yielding  $2\times$  to  $3\times$  improvements in signal-to-noise of absorption and transmission measurements. The resulting data can provide constraints on opacities in conditions approaching those where capsule performance (via the Atwood number) may depend strongly on the Si and C opacities (Fig. 136.97).

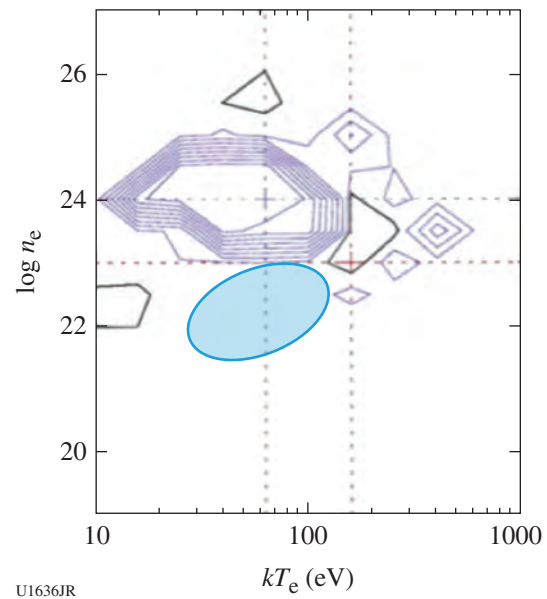


Figure 136.97 Using 1-D ignition capsule simulations, and varying the assumed opacity of the Si dopant in localized regions of density/temperature space by 30%, it was found that the Atwood number varies by up to 37%. The sensitivity is localized for near-solid density plasmas at temperatures from 30 to 100 eV. The Atwood number is also sensitive to the opacity of carbon, although the specific processes and region in parameter space are different.

The Si measurements illustrated in Fig. 136.98 can be brought into agreement with simulations for the  $n = 1$  to  $n = 2$  absorption features, but they require a wider charge-state distribution than expected in LTE, suggesting non-LTE physics or sample nonuniformities. Data for the higher- $n$  transitions

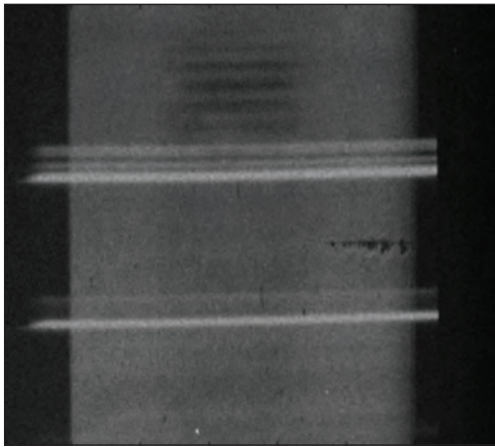


Figure 136.98  
X-ray absorption spectrum of silicon from ~1.7 to ~2.1 keV, from a plasma at  $T \approx 70$  eV,  $\rho \approx 0.2$  g/cm<sup>3</sup>. Photon energy runs from top to bottom; the horizontal direction includes regions of background, sample self-emission, backlighter-only and backlit sample transmission spectra. Absorption features including  $n = 1$  to  $n = 2$  transitions, higher- $n$  features, and continuum absorption appear as a dark band running down the center of the image from top to bottom. The absorption features from multiple L-shell ion stages of Si (Be, B, C-like...) are seen as dark horizontal bands in the top center. Emission features from H-like and He-like ions of the hotter, denser Si produced prior to the short-pulse absorption measurement are also observed (horizontal white features).

are not in especially good agreement with the opacity models. Additional Si measurements are planned for FY14.

**Hohlraum Wall-Plasma Emissivity Measurements**

Principal Investigator: R. Heeter  
Co-investigators: A. Graf, G. V. Brown, M. E. Foord, C. Mauche, R. E. Marrs, J. S. Ross, and B. Wilson

Motivated by discrepancies observed in NIF hohlraum experiments, new benchmark data for the x-ray emissivity of hot gold plasmas were sought. Of particular interest were the inferred “drive deficits” on ignition capsule implosions and observed differences in drive spectra and x-ray emission images on ViewFactor shots. The NIF data indicate a substantially different distribution of mass and temperature in the ablated gold “wall plasma” than predicted by simulations. One concern that arises is that the complex modeling of the gold itself may need better validation. This requires precision spectroscopy of uniform, near-steady-state plasmas at the relevant conditions. Prior benchmark data<sup>47</sup> were obtained at  $n_e = 10^{21}$ /cm<sup>3</sup>, but on the NIF the gas- and capsule-plasma filling holds back the expanding gold plasma ablated off the walls, such that the

density of interest is an order of magnitude greater. In addition, alternate NIF ICF hohlraum designs incorporate a mid-Z coating (Ni or Cu) to suppress the Au M-band emission, so measurements of Ni or Cu are timely as well.

In the experiment fielded late in Q4 FY13, Be-tamped samples of Au, Ni, or co-mixed Au:Ni were directly heated for 3 ns using a train of OMEGA beams. To obtain the sample density and temperature, a combination of expansion imaging, Ni K-shell spectroscopy, and  $4\omega$  Thomson-scattering diagnostics were applied. A sample of the Thomson data is shown in Fig. 136.99. Using thicker tampers and lower laser drive, and

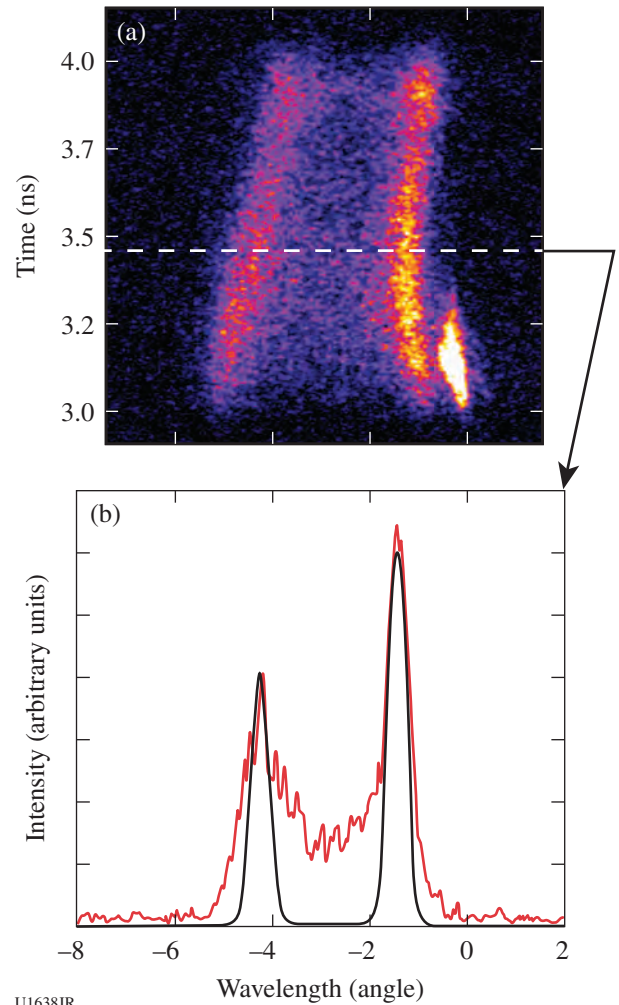


Figure 136.99  
Ion feature data from fourth-harmonic Thomson-scattering diagnostic, with fit by J. S. Ross for nickel plasma at  $T_e = 850$  eV.

imaging the sample expansion with 15- to 20- $\mu\text{m}$  resolution, plasmas with  $n_e > 2 \times 10^{22}/\text{cm}^3$  were studied. Samples at two temperatures were produced by varying the laser intensity on different shots. Benchmark-quality, absolute- and relatively calibrated sample emission spectra were obtained from 250 to 3000 eV using gated, space-resolved grating and crystal spectrometers and the Dante multichannel filtered diode array.

***D–D and D–<sup>3</sup>He Yield Anomalies Versus D:<sup>3</sup>He Fuel Ratio in Indirect-Drive Exploding Pushers***

Principal Investigator: H. Rinderknecht (MIT)

Co-investigators: C. K. Li (MIT) and P. A. Amendt (LLNL)

Anomalous nuclear yield reduction as a function of D:<sup>3</sup>He fuel ratio was observed in a study of D<sup>3</sup>He-filled indirect-drive implosions performed on 7 May 2013 using the OMEGA laser. Previous experiments in directly driven implosions of CH capsules demonstrated anomalous reduction of the compression yield in D<sup>3</sup>He mixtures, relative to implosions filled with hydroequivalent fills of D<sub>2</sub> (Ref. 48). A similar yield anomaly has also been observed in shock yield from directly driven thin glass targets.<sup>49</sup> This study was designed to investigate whether these yield trends were also observed in indirectly driven SiO<sub>2</sub> shells filled with D<sup>3</sup>He mixtures.

Targets were 600- $\mu\text{m}$ -diam SiO<sub>2</sub> shells with 24.4- $\mu\text{m}$ -thick walls, fielded inside 2-mm-long vacuum hohlraums with a 1.6-mm outer diameter (OD) and a 50% LEH. These targets were filled with mixtures of D<sub>2</sub> and <sup>3</sup>He with an initial mass density of 4.6 mg/cm<sup>3</sup>, with a deuterium ion fraction of 0.2, 0.5, 0.8, and 1. Resulting compression yields demonstrated a trend of reduction in the DD-neutron and D<sup>3</sup>He-proton yield-over-clean (YOC) as the deuterium ion fraction was decreased from pure D<sub>2</sub> fill (see Fig. 136.100) [simulations were performed by P. A. Amendt (LLNL)]. The observed trend is comparable with direct-drive studies between the deuterium fractions of 0.5 and 1; however, unlike previous studies, the observed yield continues to decrease relative to hydro-equivalent D<sub>2</sub> as the deuterium fraction drops below 0.5. A similar trend is also observed in D<sup>3</sup>He proton yields for targets with initial gas fill between the deuterium fractions of 0.2 and 0.8 (see Fig. 136.101). Implosions of targets with 50:50 mixtures of D<sup>3</sup>He and mass density of 2.9 and 1.5 mg/cm<sup>3</sup> demonstrated a reduction in the observed DD-neutron YOC as pressure was reduced. These results confirm the anomalous reduction of compression yield in indirect-drive implosions of D<sup>3</sup>He fuel mixtures, supporting the hypothesis that multiple-ion plasma effects are significantly perturbing the evolution of indirect-drive implosions.

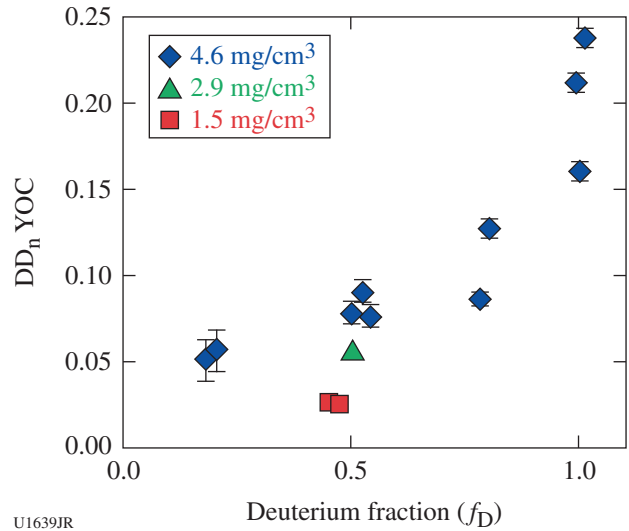


Figure 136.100 DD-neutron YOC versus deuterium fraction in indirect-drive hydro-equivalent D<sup>3</sup>He fuel mixtures. Initial mass density is given for each set of implosions.

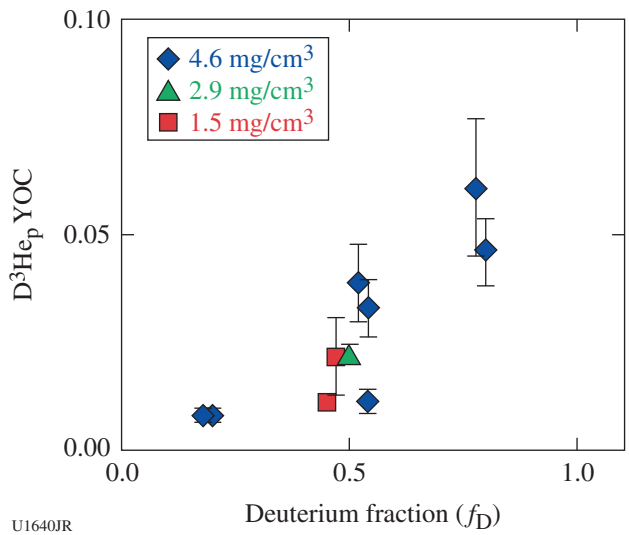


Figure 136.101 D<sup>3</sup>He-proton YOC versus deuterium fraction in indirect-drive hydro-equivalent D<sup>3</sup>He fuel mixtures.

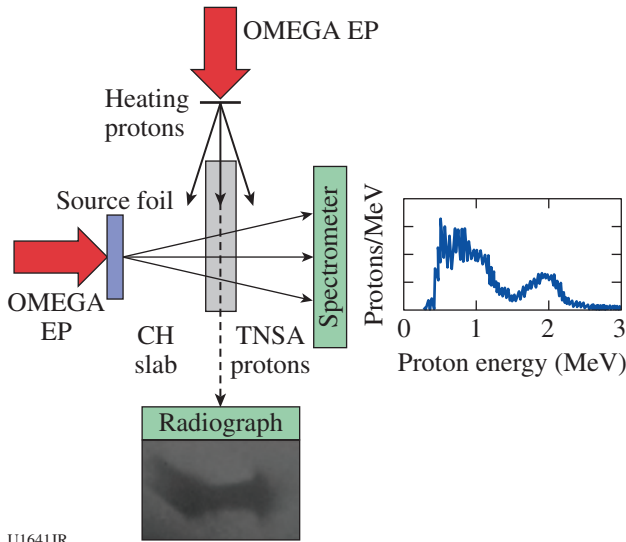
***Platform Development for Measuring Charged-Particle Stopping in Warm Dense Plasmas***

Principal Investigator: A. Zylstra (MIT)

Co-investigator: J. R. Rygg (LLNL)

Charged-particle stopping power is a critical transport process for ignition and burn, and calculating DT- $\alpha$  stopping in relevant plasma conditions depends on untested theories. To address the need to validate these theories, a platform is being developed on OMEGA EP to measure charged-particle energy

loss. The experimental schematic is shown in Fig. 136.102, where the two short-pulse beams are used to generate energetic protons via the target normal sheath acceleration (TNSA) mechanism that heats and then probes a sample plasma. The FY13 experiments characterized the heating and probing protons separately via x-ray radiography and charged-particle spectroscopy (shown in Fig. 136.102). Future experiments will combine these techniques to measure the stopping power.



U1641JR

Figure 136.102  
Experimental schematic. One OMEGA EP short-pulse laser beam is used to heat a sample via proton isochoric heating; the second beam creates probing protons. The FY13 campaign characterized the isochoric heating with x-ray radiography (bottom) and studied proton source candidates for the stopping experiment (right).

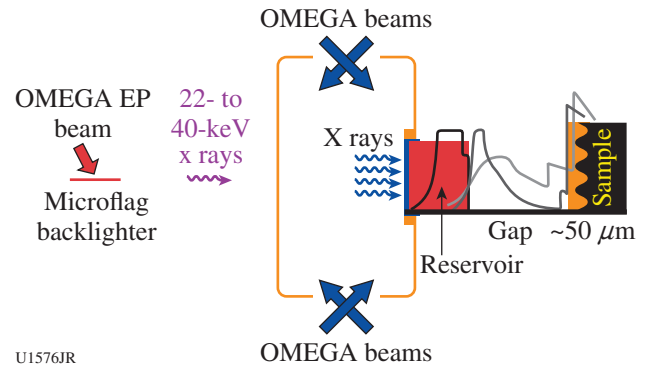
## High-Energy-Density Experiments

### 1. Material Dynamics and Strength

#### Tantalum Rayleigh–Taylor Experiments

Principal Investigator: C. Plechaty

The focus of the ICETaRT campaign was to study Ta material strength at high pressure ( $>1$  Mbar) and high strain rates ( $10^6$  to  $10^8$   $s^{-1}$ ). To achieve these conditions in an experiment while keeping the temperature of the Ta sample well below melting, a reservoir and vacuum gap<sup>50</sup> configuration was employed to produce a quasi-isentropic pressure drive (Fig. 136.103). In the experiment, the plasma drive was produced by using 40 OMEGA beams to deposit 20 kJ of laser energy into a hohlraum. The x rays produced in this process interact with the reservoir to produce a plasma. The plasma then crosses the gap and stagnates onto the physics package.



U1576JR

Figure 136.103  
Experimental configuration employed for OMEGA EP joint shots. OMEGA beams deposited energy into the hohlraum, producing a plasma drive. Face-on, high-energy radiography was employed on the rippled Ta sample by using a short-pulse OMEGA EP beam to ablate an Ag backlighter. For OMEGA shots, the rippled Ta sample was replaced by a VISAR witness sample to characterize the plasma drive.

The physics package employed for these experiments consisted of a Ta sample, coated with a polyethylene (CH) heat shield (to protect the Ta sample from the hot plasma). Imposed on the surface of the Ta were sinusoidal perturbations with a  $50\text{-}\mu\text{m}$  wavelength and an amplitude of  $1.7\ \mu\text{m}$  or  $2.0\ \mu\text{m}$ . In the experiment, as the plasma from the reservoir crosses the gap and stagnates on the sample package, the Ta ripples undergo an effective acceleration from the stagnating plasma drive. This acceleration actuates Rayleigh–Taylor (RT) growth of the pre-imposed sinusoidal pattern. Since the Ta material strength acts to suppress the amount of RT growth, measuring the RT ripple amplitude gives a measure of the material strength.<sup>50–52</sup> To measure the perturbation amplitude, face-on, high-energy x-ray radiography (22-keV Ag  $K_{\alpha}$ ) was employed using the OMEGA EP short-pulse beam. The OMEGA EP beam was required in order to employ a high-energy backlighter (22 keV) to probe the high-Z tantalum material. To characterize the plasma drive, separate shots were taken using VISAR, where the physics package was replaced with a witness package.

The FY13 ICETaRT campaign (ICETaRT-13A) focused on studying the effect of crystal orientation on the material strength. In the multiscale model,<sup>53</sup> crystal orientation can affect material strength via a parameter known as the “Taylor factor.” To understand the effect of crystal orientation on the material strength, we placed [100] and [111] oriented samples side by side and compared the ripple growth between these samples for the same shot and under the same drive conditions. Initial results from these shots suggest that the difference in the growth factor between these two crystal orientations is

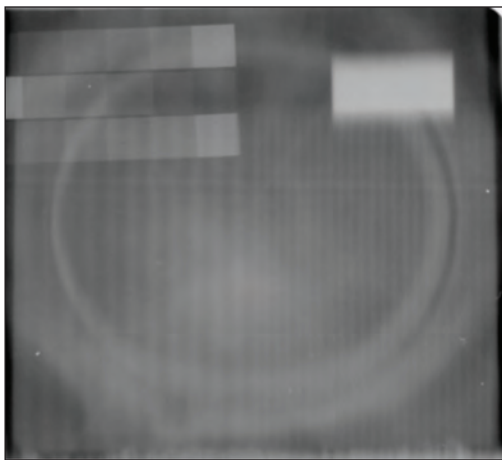
too small to be measured within our error bars of  $\sim 25\%$ . The implications of this are currently under investigation.

### **Iron Rayleigh–Taylor Experiments**

Principal Investigator: C. Huntington

The solid–solid phase transition between the bcc ( $\alpha$ ) and hcp ( $\epsilon$ ) lattice structures in iron is known to occur as the material is compressed. When kept below its melting point, an effective increase in the macroscopic strength of the material accompanies this phase transition. Understanding the material strength of iron throughout the deformation process presents a significant computational challenge, but it is important for improving models of planetary structure, including interpretation of seismic measurements taken through Earth's core.

The IronRT OMEGA campaign used an indirect-drive platform to produce pressures of  $\sim 1$  Mbar on a thin Fe disk with a sinusoidal ripple pattern machined on its face. These ripples seed the growth of the Rayleigh–Taylor (RT) instability, the magnitude of which is suppressed by the material strength of the sample. The amplitude of the ripples was diagnosed with high-energy x-ray radiography, using Ag micro-flags as the x-ray source (see Fig. 136.104). In addition to radiography, the VISAR diagnostic was essential to characterizing the drive profile on the iron sample. On this IronRT shot day, five radiography shots measured the Fe growth factors between 1 and 2.



U1642JR

Figure 136.104

Example radiography data from the IronRT-13A campaign. The step features in the upper left allow for calibration of the detected x-ray signal with the material areal density ( $\rho R$ ) traversed by the x rays. The opaque region in the upper right is a gold knife edge for calculating the modulation transfer function (MTF), with the remainder of the sample dedicated to the ripple measurement at two wavelengths (side-by-side 100- and 50- $\mu\text{m}$  wavelengths).

Comparison of these measured iron growth factors to a range of models for material strength in iron is ongoing. More important, the ability to reach  $\sim 1$  Mbar on OMEGA extends the accessible parameter space for this work, when combined with previous experiments conducted at 0.1- to 0.3-Mbar pressures.<sup>54</sup>

### **Long-Pulse Silver Backlighter Development**

Principal Investigator: C. Huntington

The LPAgBL campaign was a half-day effort to quantify the spatial resolution achievable from a range of micro-flag x-ray source (backlighter) designs. Crucial for experiments in the material strength campaigns on the NIF and OMEGA, the small ( $300 \times 300\text{-}\mu\text{m}$ ) silver foils produce a quasi-1-D x-ray source when heated by the laser and viewed edge on, allowing for radiography of ripple growth in the strength experiments. On this shot day, each of the five designs was irradiated with 18 beams, producing a total on-target intensity of  $8 \times 10^{16}$  W/cm<sup>2</sup> and generating Ag  $K_{\alpha}$  x rays (near  $\sim 22\text{-keV}$  photon energy). From knife-edge radiography, the modulation transfer function (MTF) of each backlighter was measured. From this work it was determined that the MTF at a spatial frequency of 100  $\mu\text{m}$  from a 3- $\mu\text{m}$ -thick foil was twice that from a 10- $\mu\text{m}$ -thick foil. The results of this experiment have been incorporated into several recent NIF target designs exploring the material strength of Ta.

### **Material Recovery Experiment**

Principal Investigator: M. May

The FY13 material recovery shots tested a prototype target recovery system that enables us to perform post-shot target analysis of material samples (see Fig. 136.105). A new recovery tube platform was qualified for use on OMEGA for these experiments. Five hohlraum target shots were performed. OMEGA was used to deliver 20 kJ of energy with 40 beams in a 1-ns pulse to heat these targets. Four hohlraum targets were used to drive samples into the recovery tubes. Two of the samples were driven into recovery tubes at a lower pressure ( $\sim 1$  Mbar) and two were driven at a higher pressure ( $\sim 2$  Mbar). One drive characterization target was shot to measure the high-pressure drive using the VISAR. Analysis of the VISAR indicated that this pressure was  $\sim 1.8$  Mbar. Platinum was used as the driven sample material since it is uncommon in laser-produced plasma experiments and can be easily extracted chemically from the recovery tubes. To catch and hold the driven Pt, the recovery tubes were filled with two layers of increasing-density (50- and 500-mg/cm<sup>3</sup>) dicyclopentadiene with a final layer of solid-density CH. The photographs show (a) the pre-shot target mounted to the

recovery tube and (b) the post-shot recovery tube. The post-shot photo shows material residue on the recovery tube and a small gap between the target mount and the recovery tube. Post-shot analysis of the recovered samples indicated that <10% of the Pt from the targets was collected in the recovery tubes. Valuable insight was gained regarding the participating physics and changes needed for future catcher designs involving a hohlraum.

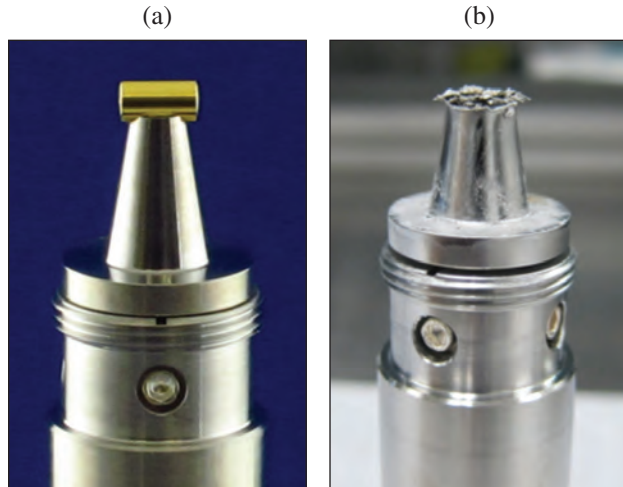


Figure 136.105  
Photographs of (a) the pre-shot target and recovery tube and (b) the post-shot recovery tube.

### Diffraction Studies on Shocked Tantalum

Principal Investigator: C. Wehrenberg

Two distinct diffraction experiments were conducted to study the behavior of shocked tantalum. The first experiment sought to make strength measurements of single-crystal Ta samples that were shock compressed in the low-pressure (<0.6-Mbar) regime. Previous campaigns (FY11, FY12) have explored up-to-2-Mbar shocks in Ta and successfully matched multiscale model predictions; however, ~0.6 Mbar is expected to be a threshold for homogeneous nucleation of dislocations, which should alter the material's behavior. In two half-day campaigns on OMEGA, 12 shots were performed in which an imploding CH capsule driven by 29 beams provided a broadband x-ray source. A single beam drove a thick CH ablator, with the shock wave attenuating as it propagated through the ablator to lower the shock pressure into the desired range. A time series of Laue patterns were recorded in the 0.2- to 0.8-Mbar range. Figure 136.106 shows a series of Laue patterns for a 0.4-Mbar shock pressure. This series shows the strain evolving from uniaxial compression to an ultimate flow stress. These lattice level measurements are directly comparable to multiscale model predictions.

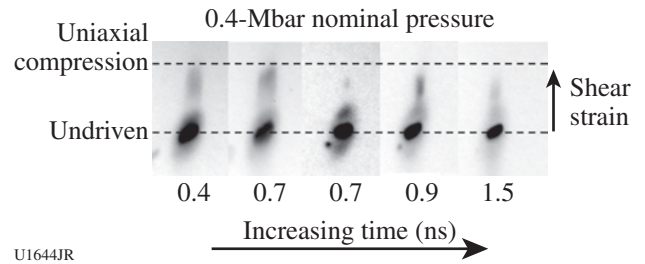


Figure 136.106  
A time series of Laue images of single-crystal Ta loaded along the (001) direction by a 0.4-Mbar shock wave. Shear strain is indicated by a shift in the diffraction spot from the undriven position. The time series shows the strain relaxing with time.

In parallel, a second class of experiments developed methods for recording diffraction patterns from polycrystalline samples using high-energy backlighters. In one shot day, a single short-pulse (100-ps) beam drove the Zr backlighter foil. In a second shot day, three UV beams were used to drive a Zr foil backlighter with a 2-ns pulse. A separate UV beam was used to drive a target consisting of a high-density-carbon (HDC) ablator, a Ta foil sample, and a HDC window attached to a heavymet pinhole mounted on the broadband x-ray diffraction (BBXRD) diagnostic. No diffraction lines were recorded with the short-pulse beam because of a very high background. The long-pulse shot day recorded up to seven diffraction lines from the Ta sample, using backlighter laser intensities of  $3$  to  $9 \times 10^{15}$  W/cm<sup>2</sup>. Figure 136.107 shows a static shot (no Ta drive

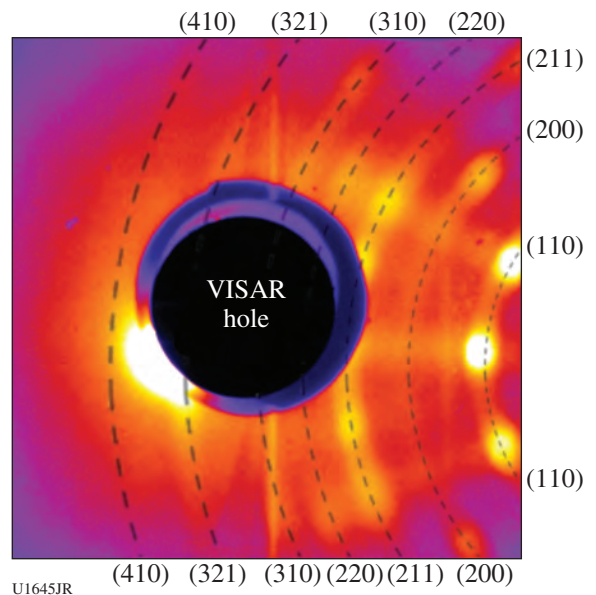


Figure 136.107  
Static diffraction image from a Ta foil sample using a Zr backlighter (2-ns pulse) and a 1-mm pinhole.

beam) using a 1-mm pinhole. Additional shots used a 0.5-mm pinhole to achieve greater angular resolution, but with a lower signal-to-noise ratio. These shots represent the first high-quality diffraction data recorded using high-energy, laser-driven x-ray sources. Driven diffraction data were recorded at  $\sim 2$  Mbar; however, due to difficulties in timing the arrival of the shock wave, the diffraction was taken while the Ta was in the process of releasing to ambient pressure. Despite essentially splitting the signal between two strain states, two driven diffraction lines and four ambient lines were recorded.

**Classical Rayleigh–Taylor Experiments**

Principal Investigator: H.-S. Park

The classical Rayleigh–Taylor campaign is part of a continuing effort aimed at assessing the strength of various metals (primarily Ta and Fe) at high strain rates. Central to all of these experiments is a planar sample with a pre-imposed sinusoidal ripple on one surface (Fig. 136.108). Under load

generated by the laser drive, the rippled surface is unstable to Rayleigh–Taylor (RT) instability and will grow in time to a perturbation that can be measured using face-on radiography. In the metal samples, strength of the material resists deformation and suppresses RT. To properly characterize the degree of resistance in metals, however, the classical RT platform was developed to measure purely plastic RT evolution (that is, instability growth in the absence of material strength). On this shot day the rippled sample was made of brominated plastic (BrCH), which is able to deform without any resistance from an underlying lattice structure. The VISAR and face-on x-ray radiography were the primary diagnostics, and the laser drive was generated via direct irradiation of a plastic ablator. Good data were collected using both primary diagnostics, and growth factors of  $\sim 10$  have been calculated for the plastic sample. This experiment provided important “no-strength” data for the materials strength effort, and the remainder of the plastic dispersion curve will be measured in an upcoming FY14 shot day.

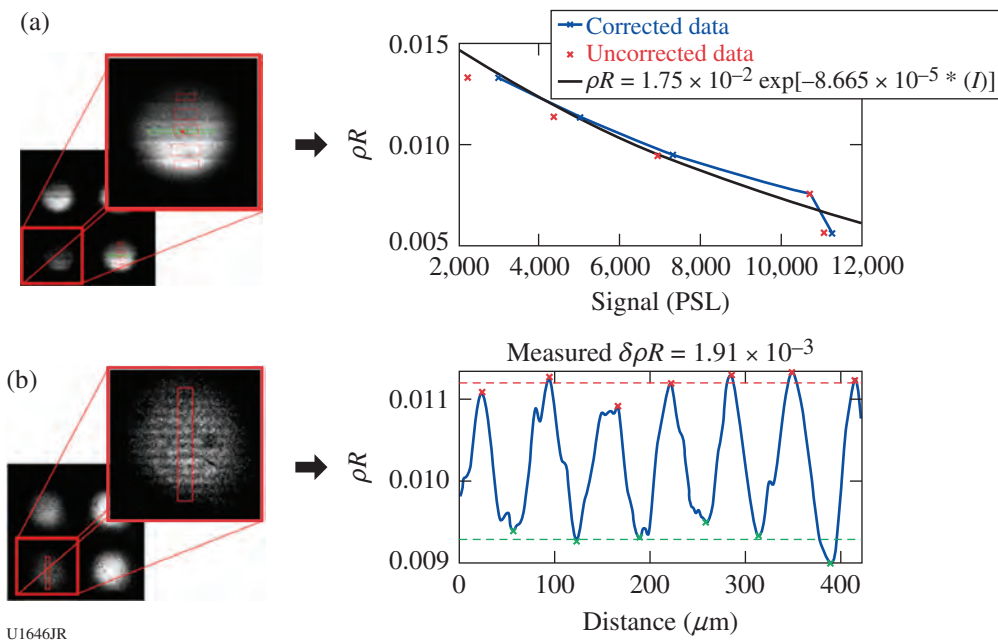


Figure 136.108

Classical RT is an experimental campaign that evaluates the Rayleigh–Taylor (RT) strength platform on a material without strength. Our test material for this campaign was brominated plastic (12.5% BrCH). (a) An x-ray framing-camera (XRFC) image of BrCH steps (left panel) for radiometric calibration. The right panel shows the raw data points (red  $\times$ 's) and the background corrected data points (blue  $\times$ 's). The data are fitted to an exponential function (black line) that converts the raw gray values of the XRFC image into the areal density in  $\text{g}/\text{cm}^2$ . This calibration is used to derive the growth factor from the ripple images. (b) A face-on BrCH ripple growth radiography (left panel) driven by  $\sim 1$  Mbar ramped pressure at 45 ns after the laser. The initial ripple amplitude was  $0.6 \mu\text{m}$  and the wavelength was  $60 \mu\text{m}$ . The ripple growth is clearly visible as shown in the lineouts on the right panel. The measured growth factor is  $\sim 10$ , which agrees with the post-shot simulation results, demonstrating that the RT platform works for the materials without strength.

## 2. Material Equation of State

**Demonstration of Single-Shot EXAFS Measurements on Ramp-Compressed Ta**

Principal Investigator: Y. Ping

Co-investigators: F. Coppari, J. H. Eggert, and G. W. Collins (LLNL); and B. Yaakobi (LLE)

Experiments in FY13 advanced a recently published extended x-ray absorption fine structure (EXAFS) technique for dynamically compressed materials. The prior work on EXAFS measurements of dynamically compressed iron up to 560 GPa (Ref. 42) has been extended to study ramp-compressed Ta. EXAFS at the Ta L<sub>3</sub> edge is challenging because the signal is very small (of the order of 1% modulation in intensity). We have improved the backlighter brightness by 2× and the spectrometer efficiency by 5×, so that one shot is now equivalent to ten previous shots. A specially designed quintuple-crystal spectrometer [Fig. 136.109(a)] acquires five spectra in a single shot [Fig. 136.109(b)], which can be averaged to improve the signal-to-noise ratio. EXAFS of both undriven and ramp-compressed Ta at 1 to 3 Mbar has been observed in single-shot measurements. A typical EXAFS spectrum is shown in Fig. 136.109(c). The data indicate that Ta undergoes a phase transition above 1 Mbar. A paper summarizing these results has been submitted.<sup>55</sup>

**Tin Melting and Recrystallization**

Principal Investigator: A. Lazicki

The TinMelt campaign is an effort to detect and map out a recrystallization transition by shock melting a sample and then ramp-compressing it across the solid–liquid phase boundary. The metrics for recrystallization are (1) features in the profile of the ramped velocity history, measured using VISAR, that could indicate a phase transition, and (2) the presence of a solid x-ray diffraction signature after the recrystallization. Two half-day campaigns in FY13 searched for evidence of this transition in tin and also in lead. Lead is isovalent with tin, has a similarly low melting temperature, and is a much-stronger x-ray scatterer. These shots also experimented with new methods for optimizing the signal-to-noise ratio on the image plates in our diffraction diagnostic. Efforts were made to increase the x-ray flux from the backlighter foil by (1) ablating it from both sides, (2) increasing the laser-to-x-ray conversion efficiency by adding a prepulse to the laser drive, and (3) increasing the laser-to-x-ray conversion efficiency by using a new converging cylinder geometry.

The targets for these shots were composed of tin or lead foils placed next to foils of high-melting-temperature tantalum. The two regions were subjected to the same shock-ramp pulse shape to determine if the wave profile features could be associated

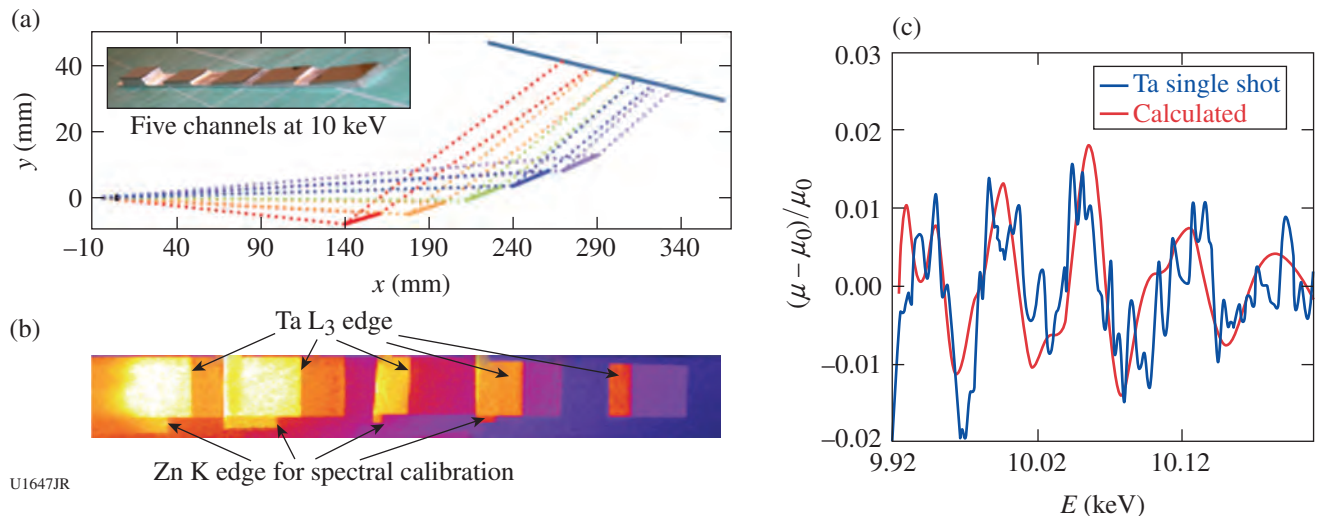


Figure 136.109

(a) Design of the quintuple-crystal spectrometer to record five spectra in one shot. The ray-tracing results of the five channels are represented by different colors. A photo of the actual crystal is displayed at the upper-left corner. (b) A raw image of the detected spectra shows the five channels with Ta L<sub>3</sub> edges and Zn K edges as a spectral fiducial. (c) EXAFS data at Ta L<sub>3</sub> edge taken by the quintuple-crystal spectrometer in a single shot and averaged over the five channels.

with a solid–liquid transition (expected in the Sn/Pb but not in Ta). Diffraction from the shock-melted, ramp-compressed samples shows a crystalline solid (see Fig. 136.110), indicating that recrystallization occurs over the time scale of the experiment. However, the wave profile results do not definitively show a unique feature that could be associated with this transition.

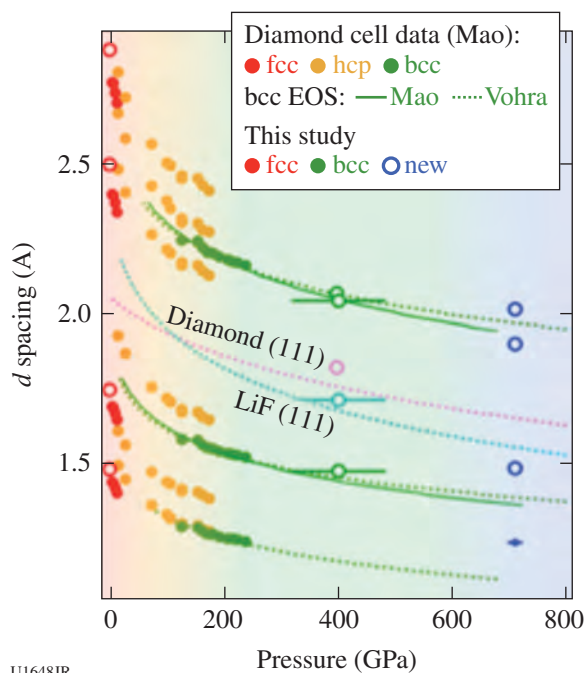


Figure 136.110

X-ray diffraction results from lead ramp compressed from a shock-melted state bcc (body-centered cubic) EOS from Refs. 56 and 57. fcc: face-centered cubic; hcp: hexagonal close packed.

### Ta X-Ray Diffraction with Ramp Compression

Principal Investigator: A. Lazicki

The TaDiff-13A/13B campaigns were designed to study a high-pressure phase transition and equation of state in tantalum and to improve methods for performing the diffraction measurements above 10 Mbar. During these campaigns, targets were ramp compressed to pressures as high as 14 Mbar and x-ray diffraction measurements were made using the powder x-ray diffraction image plate (PXRDIIP) diagnostic with a copper foil x-ray source. Pressure was determined from VISAR measurements. The 13 successful shots consisted of eight tantalum targets, two tin targets, two lead targets, and one iron target, all sandwiched between diamond plates, with indium or sputter-deposited gold heat shields. The tantalum shots were interspersed with tin, iron, and low-pressure lead shots to

produce information needed to tune the ramp pulse shape and properly time the x-ray source. Diffraction data were obtained from tin between 11 to 13 Mbar (see Fig. 136.111), from lead at 7 Mbar, and from tantalum at 2 Mbar and 7 to 12 Mbar. Successfully tested were a new black kapton filter material, an x-ray preheat shield, and a new x-ray source configuration, all of which contributed to diffraction data that were much improved over previous campaigns. The data on Pb indicate a new high-pressure phase transition, and the results on Sn further support a previously observed transition.

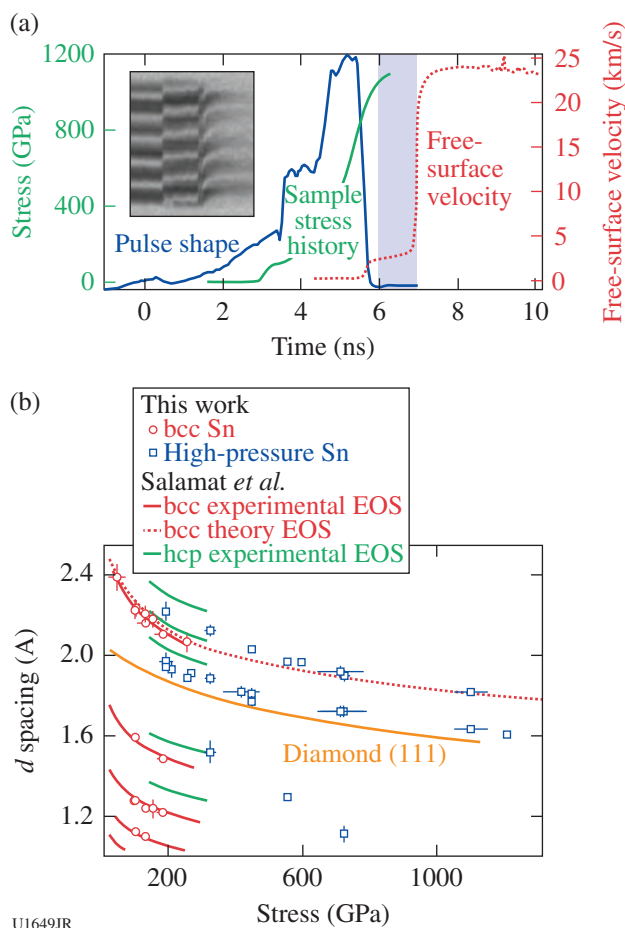


Figure 136.111

(a) VISAR and (b) diffraction data from tin above 10 Mbar collected during the TaDiff-13B campaign.

### Development of a Soller-Slit Diagnostic for Dynamic Diffraction Studies

Principal Investigator: J. Hawreliak

The bulk of high-pressure research over the past century has been conducted in a diamond anvil cell (DAC), where pressure

is applied by two opposing anvils. This technique is ultimately limited by the strength of the anvils, and for diamond—the strongest material—it is extremely difficult to achieve and sustain pressures above 300 GPa. Studying material states at higher pressures requires the use of dynamic compression techniques, which are not limited by the ability of an anvil to sustain the pressure, but instead rely on inertial confinement of the material to sustain great pressures temporarily. Dynamic compression is ultimately limited by the energy density, which can be imparted to the sample before it disassembles or the pressure is released. *In-situ* x-ray diffraction has become an important tool for probing the atomic structure of these materials at ultrahigh-pressure states. The most-extreme environments associated with laser-driven dynamic compression experiments require unique diagnostic capabilities, and in FY13 the ADVXRD campaign tested a Soller-slit diffraction diagnostic.

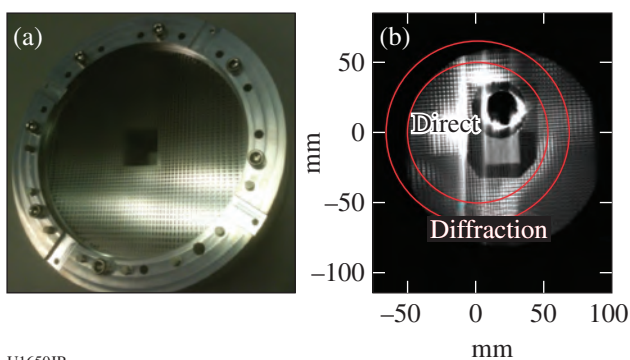
A conventional Soller slit on a synchrotron is a single pair of thin high-Z metal plates (typically tantalum) used to isolate a single line of sight. The direction of the slit is adjusted over a range of angles, and a measurement is made of a static sample. This reduces noise by allowing only the signal that follows a particular path to fall on the detector. For laser-based experiments, one can use an array of Soller collimators to provide a range of angles for a single experimental event. Figure 136.112(a) shows the array of Soller collimators used over the detector, giving an effective pixel size of  $400\ \mu\text{m}$ . This reduces the background and makes it possible to record diffraction from a dynamically driven sample without collimating the beam at the target. There are two experimental advantages to this technique over collimating at the target: (1) The target can be simplified because it does not need to include a collima-

tor. (2) Drive noise is reduced because the collimation occurs farther from the x-ray sources, i.e., not at the sample, but at the detector. Figure 136.112(b) shows the diffracted signal from an undriven tantalum sample. The alignment was such that some pixels had direct line of sight of the backlighter and are saturated, but the diffraction ring is visible. These data will be used to benchmark the diagnostic and drive further development to improve the signal-to-noise ratio and angular resolution. Future experiments are envisioned to use this Soller-slit collimator with a hohlraum-driven sample.

### **Radiographic Equation-of-State Measurements of Shocked Foams**

Principal Investigator: J. Hawreliak

Materials in extreme conditions generated by shock compression of aerogel foams are an important area of HED science. LLNL and its partners have developed the capability to engineer low-density foams with the desired properties for a range of programmatic and scientific experiments. The initial density of the foam is used to set the thermodynamic path of the shock Hugoniot. For laboratory astrophysics and other HED experiments, where low-density aerogels are used to model interstellar matter, a detailed understanding of the EOS is important. However, continuum EOS theories make assumptions about bulk behavior of these foams that ignore the underlying fact that foams are fundamentally a heterogeneous material at small scale lengths. Continuum EOS models cannot be scaled simply by density scaling, therefore requiring foam EOS Hugoniot measurements. Furthermore, many low-density carbon and CH-based foams of interest are not transparent, making impedance-matching experiments difficult and less accurate. To avoid these issues, a platform has been developed for *in-situ* radiography of shocked foams, from which the shock speed and density can be measured.



U1650JR

Figure 136.112

(a) The Soller collimators and (b) sample data.

Figure 136.113(a) shows a VISRAD model of the experimental configuration. Two or three beams are used to generate a K-shell area backlighter from a material chosen to deliver sufficient photon flux to the detector with an x-ray energy low enough for the foam sample's absorption cross section to yield good contrast at the shock front. For  $50\text{-mg/cm}^3$  carbon resorcinol formaldehyde (CRF), the  $\text{Cl He}_\alpha$  x rays from Saran are used as the backlighter. A second set of beams aimed onto a quartz drive plate generates an expanding spherical shock front. The spherical shock front removes parallax issues associated with the different viewing directions of different strips on the framing camera. Figure 136.113(b) shows a single frame from

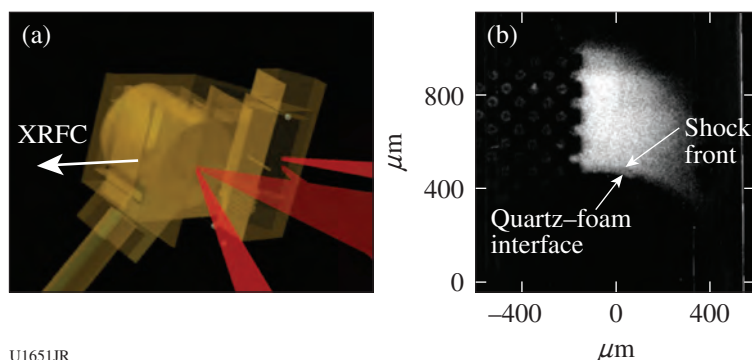


Figure 136.113

(a) VISRAD model of the experiment; (b) single frame from a two-strip framing camera.

U1651JR

the x-ray framing camera identifying the shock front and the opaque quartz pusher.

### High-Energy X-Ray Diffraction Development

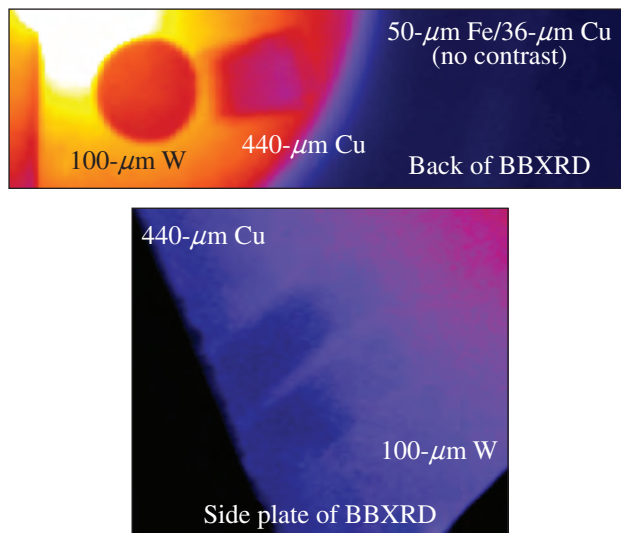
Principal Investigator: J. Hawreliak

*In-situ* x-ray diffraction is a powerful diagnostic technique for probing atomic structure at high pressures. Cutting-edge molecular dynamic simulations show that structure becomes more complex at higher pressures, requiring shorter-wavelength x-ray sources to uniquely determine the phase. K-shell emission short-pulse lasers such as OMEGA EP is a technique for generating high-energy x rays, but it also produces a high-energy bremsstrahlung spectrum that generates background. Although techniques have been developed that use short-pulse x-ray backlighters for radiography, the use of similar backlighters for x-ray line diffraction, in the HighE-Xdiff Campaign, was not successful. To identify the failure mode, one set of Ross-pair filters was used to isolate tungsten L-shell fluorescence, while a second pair isolated  $>50$ -keV x rays. The data showed that the predominant source of strong background is from x rays with energies  $>50$  keV. Tungsten was the primary material used for x-ray shielding, and its K-shell fluorescence at 59 keV appears to be the dominant source of background in the BBXRD diffraction diagnostic, rather than direct  $>50$ -keV x rays from the backlighter. Figure 136.114 shows the Ross-pair images on the image plate.

### Lithium Hydride Equation of State

Principal Investigator: A. Lazicki

The LiHEOS campaigns represent an effort to measure the shock Hugoniot of LiH, for the purpose of constraining theoretical models. Two methods were pursued in FY13: The first used the VISAR velocity diagnostic to track reflecting shock waves in targets composed of single-crystal quartz and LiH, relying upon impedance matching to the quartz standard to determine the Hugoniot data points. The other method used



U1652JR

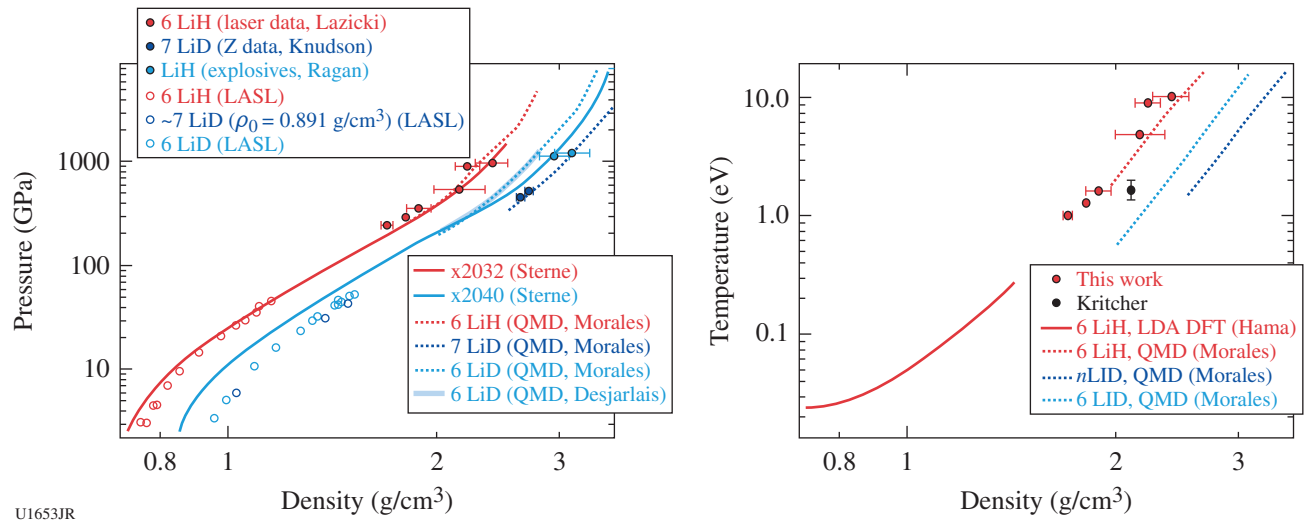
Figure 136.114

Images of the Ross pairs used to study the background spectrum and discriminate between direct x rays from the backlighter and fluorescence from the diagnostic hardware.

radiographic imaging to capture the motion of the shock front in LiH using a framing camera. Several radiography geometries were investigated: imaging through pinholes or slits with an area backlighter and a point-projection configuration.

The VISAR measurements were demonstrated to be successful, and highly valuable data were acquired (see Fig. 136.115), in spite of challenging issues with sample contamination (resulting from LiH's reactivity with moisture) and also with the VISAR technique (because of the large index-of-refraction mismatch between the two materials, which can create spurious reflections off of LiH-quartz interfaces).

Furthermore, after addressing debris, signal strength, and target alignment issues, successful radiographic measurements were demonstrated, using an area backlighter and imaging the shock front through narrow slits.



U1653JR

Figure 136.115  
Pressure and temperature of LiH along the Hugoniot measured using VISAR and SOP. Previous data from Refs. 58–60.

### Ta Equation of State

Principal Investigator: D. E. Fratanduono

Six experimental shots were conducted on OMEGA to measure the shock Hugoniot of Ta. VISAR data were collected.

### 3. Radiation Transport and Opacity

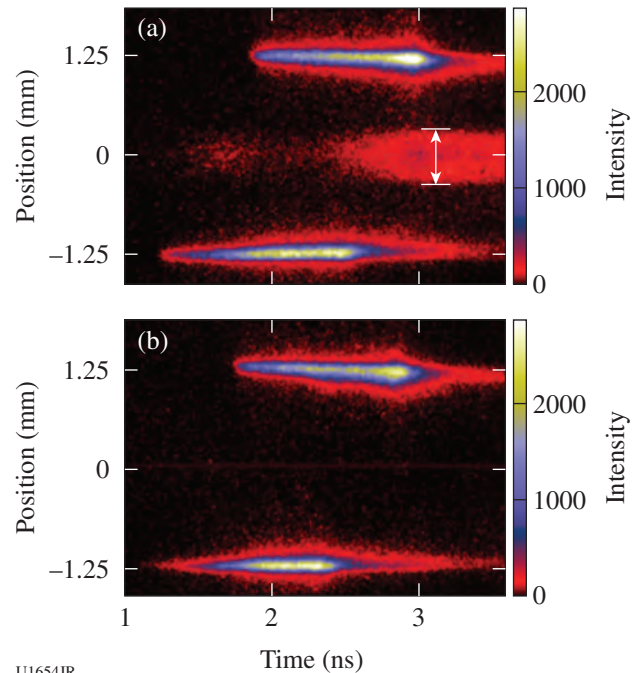
#### Heated Wall Radiation Transport

Principal Investigator: K. Baker

A campaign of six shots was carried out on the OMEGA laser to measure radiation transport in a geometry that minimizes wall loss. In these experiments a heat wave was propagated axially down a 30-mg/cm<sup>3</sup> SiO<sub>2</sub> foam, 700  $\mu\text{m}$  in diameter  $\times$  1.7 mm in length, whose outer diameter was enclosed by a 70- $\mu\text{m}$ -thick Ta<sub>2</sub>O<sub>5</sub> annular foam. This foam structure was then placed inside a 1.6-mm-diam, 2.9-mm-long hohlraum and radiatively heated by the x-ray flux driven by laser interaction with the hohlraum walls. A supersonic heat wave was driven axially down the length of the SiO<sub>2</sub> foam, and a transonic heat wave was driven radially inward through the Ta<sub>2</sub>O<sub>5</sub> foam. The radially propagating transonic heat wave minimized the wall loss for the axially propagating supersonic heat wave, enabling it to propagate over longer distances.

A heat wave was successfully propagated over a distance greater than twice the Rosseland mean free path and more than twice the diameter of the foam cylinder in which the

heat wave propagated, as shown in Fig. 136.116(a). A control target was also employed, consisting of an inner SiO<sub>2</sub> foam surrounded by 25- $\mu\text{m}$ -thick gold annular walls to prevent a



U1654JR

Figure 136.116  
Heat-wave signature measured at the end of the SiO<sub>2</sub> foam for the case of (a) Ta<sub>2</sub>O<sub>5</sub> and (b) gold walls. The features at the 1.25-mm and -1.25-mm positions represent the two timing lasers, which were incident at 1.75 and 1.25 ns, respectively.

radially propagating heat wave from reaching the inner SiO<sub>2</sub> foam. As seen in Fig. 136.116(b), no heat wave was observed for this control target.

4. Hydrodynamics

**Toto—Radiography Development for NIF Hydrodynamics Experiments**

Principal Investigator: V. A. Smalyuk

Backlighting experiments were performed on the OMEGA Laser System to study symmetry of foam balls illuminated with hohlraum x rays. Backlighter targets were driven with the OMEGA EP short-pulse IR beam in joint experiments. In the joint configuration, 10- $\mu\text{m}$ -thick Ag wires, mounted on  $300 \times 300\text{-}\mu\text{m}$ -sq, 10- $\mu\text{m}$ -thick polyimide foils were irradiated with an  $\sim 1.2\text{-kJ}$  short-pulse ( $\sim 100\text{-ps}$ ) IR beam at a laser intensity of  $\sim 1 \times 10^{17} \text{ W/cm}^2$ . X-ray radiographs of targets were measured on image plates using the HERIE diagnostic placed  $\sim 50 \text{ cm}$  from the sample, yielding a magnification of  $\sim 50$ . In addition, tests were performed using the short-pulse backlighting parameters that will be used on future NIF experiments backlit by the short-pulse advanced radiographic capability (ARC) beam. This latter configuration adjusted the OMEGA EP short-pulse beam to deliver 1.0 kJ of IR light with a 50-ps pulse shape and an intensity of  $\sim 2 \times 10^{17} \text{ W/cm}^2$ . The radiograph signal and contrast with the ARC-like beam parameters were consistent with previous experiments and showed increased resolution (13  $\mu\text{m}$ ) compared to experiments with the nominal backlighter parameters (19- $\mu\text{m}$  resolution), as shown in Fig. 136.117. These

experiments were very successful, producing high-quality radiographs that created a baseline for future complex hydrodynamics experiments on the NIF.

**Copper Foam Shock-Breakout Measurements**

Principal Investigator: A. Moore

High-Z metal foams made via a copper ceramic casting process, and with approximately one-tenth solid density ( $\sim 1 \text{ g/cm}^3$ ), have been developed at LLNL and are being produced routinely at AWE. These provide a novel target material for use in high-energy-density-physics experiments on the NIF, Orion, and OMEGA, but they must be well characterized with a good understanding of the material opacity and EOS in order for experimental results to be constraining to radiation-hydrodynamics simulation codes. With advances in the manufacturing techniques, it has been possible to produce foam material with an average pore diameter of 1  $\mu\text{m}$  and less. In the five experiments conducted in the CuFmDrive-13A campaign described here, comparisons were made of the shock propagation in two materials, 1.0- $\mu\text{m}$  and 0.5- $\mu\text{m}$  pore foams, as a means to qualify the 0.5- $\mu\text{m}$  foam for use in future experiments.

The Rankine-Hugoniot relations for a single shock demonstrate the simple dependence of the shock velocity on the pressure achieved in the shocked foam, which is in turn dependent on the internal energy of the foam. Given this dependence, measuring the propagation of a single shock through a material sample has been developed as a reliable method to quantitatively validate the EOS model for a given material.

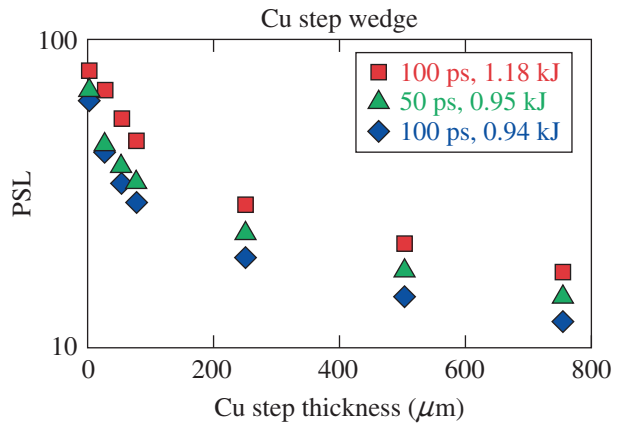
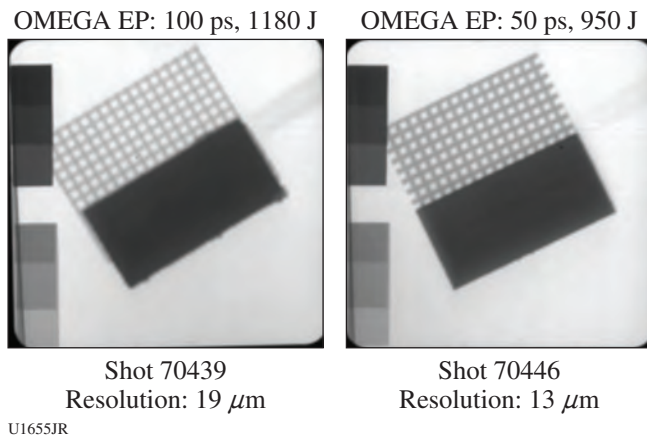


Figure 136.117 Backlighter performance data using a gold foil-grid radiography target and a Cu step wedge.

The platform to measure the shock transit time in Cu foams was developed using a 5.5-kJ laser drive from 15 beams of the 60-beam, 30-kJ, 351-nm OMEGA Laser System. In these experiments the target package consists of a washer containing two foam samples, with a polystyrene ablator and aluminum flashing to improve the VISAR laser reflection. The ablator side faces the drive hohlraum. The copper foam samples are 0.7 mm in diameter and nominally 0.25 mm in thickness with a nominal density of  $0.9 \text{ g/cm}^3$ . The hohlraum used is 1.6 mm in diameter and 1.0 mm long, with 1.2-mm-diam holes at each end (one for laser-beam entry and one to drive the ablator), and reaches a peak temperature of  $208 \pm 5 \text{ eV}$ . Data using the streaked optical pyrometer (SOP) were obtained on five shots, an example of which is shown in Fig. 136.118(b). The average shock velocity for the  $1.0\text{-}\mu\text{m}$  Cu foam was  $51.0 \pm 3.2 \text{ km/s}$ , which is compared to  $50.3 \pm 3.0 \text{ km/s}$  measured with the  $0.5\text{-}\mu\text{m}$  foam, indicating

that a reduction in the pore size does not significantly alter the material EOS of the Cu foam.

In general, comparing the results with post-shot simulations are favorable, again indicating that there are no significant differences in EOS. That said, limitations in the pre-shot characterization of the sample led to a large uncertainty in the sample thickness, allowing for a wide range of possible breakout times. A follow-on campaign in FY14 will extend the measurement to include shock velocity using VISAR and will repeat some shots following better characterization of the sample thickness.

**Short-Pulse, UV Backlighting Development for the NIF**

Principal Investigator: D. Martinez

A series of eight shots were performed on OMEGA EP to optimize, for NIF experiments, a point-projection backlighter technique using a Zn backlighter foil, apertured with a  $20\text{-}\mu\text{m}$  pinhole tilted  $30^\circ$  from the normal of a  $50\text{-}\mu\text{m}$ -thick,  $5\text{-mm} \times 5\text{-mm}$ -sq Ta plate (see Fig. 136.119). The Zn foil was suspended from the Ta pinhole, with either a  $15^\circ$  or  $37^\circ$  angle between the Zn foil normal and the laser axis, to recreate the designed angle of incidence for the backlighter targets on the NIF. The CH-Zn foil was positioned to create a  $500\text{-}\mu\text{m}$  separation distance between the surface of the Zn foil and the pinhole. The intensity was varied between  $1 \times 10^{15}$  and  $5 \times 10^{15} \text{ W/cm}^2$  on the Zn foil and was controlled by changing the number of beams on target. The backlighter performance was characterized using a gold foil/grid target and imaged onto a single-strip x-ray framing camera with a magnification of  $M = 23$ . The Zn spectrum was recorded using the SSC-A SXS streaked spectrometer with a photon energy range of 7.76 to 12.87 keV. The resolution of the system was measured to be  $20\text{-}\mu\text{m}$  mode, which corresponds to a 20% transmission in the modulation transfer function (MTF) for all shots. From the spectrometer, the x-ray signal was primarily monochromatic in the observed photon-energy range for all tested intensities; however, there was reduced contrast in the x-ray framing camera (XRFC) images for intensities above  $4 \times 10^{15} \text{ W/cm}^2$ . Peak contrast recorded for the experiment was at intensities around  $2.5 \times 10^{15} \text{ W/cm}^2$ . From the streaked spectrometer, the  $\text{He}_\alpha$  lines scaled well with the intensity of the beam. The angle of incidence did not have a noticeable effect on the peak Zn  $\text{He}_\alpha$  signal or the resolution of the backlighter. The results from this data were used to confirm the backlighter design for NIF experiments and have led to high-quality images on the NIF.

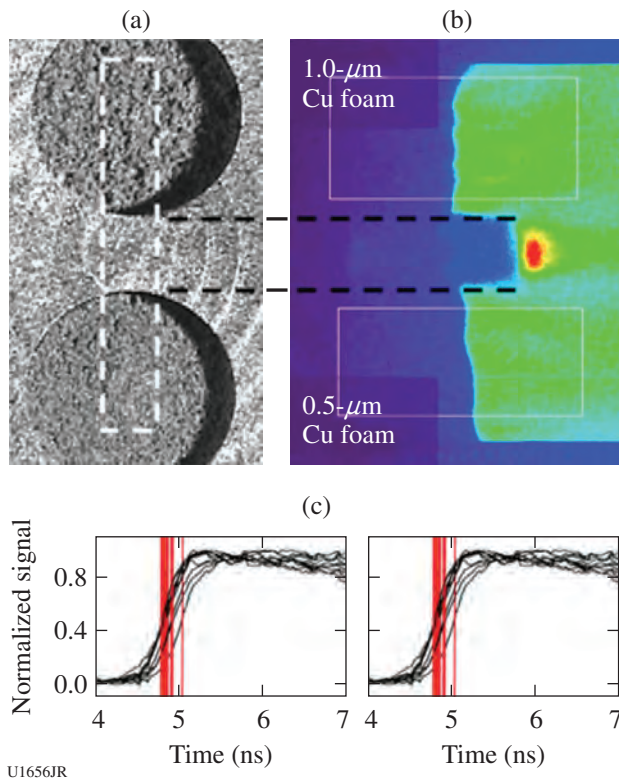


Figure 136.118 Streaked optical pyrometer (SOP) data from shot 68018. (a) Pre-shot images of the Cu foam surface viewed by the SOP. The thickness of the  $1.0\text{-}\mu\text{m}$  foam sample was  $248 \mu\text{m}$  and the  $0.5\text{-}\mu\text{m}$  foam was  $276 \mu\text{m}$ . (b) Raw SOP image data and (c) optical emission caused by shock breakout show that the shock in the  $1.0\text{-}\mu\text{m}$  Cu foam arrived at  $4.86 \pm 0.06 \text{ ns}$ ; in the  $0.5\text{-}\mu\text{m}$  foam the shock arrived at  $5.49 \pm 0.14 \text{ ns}$ .

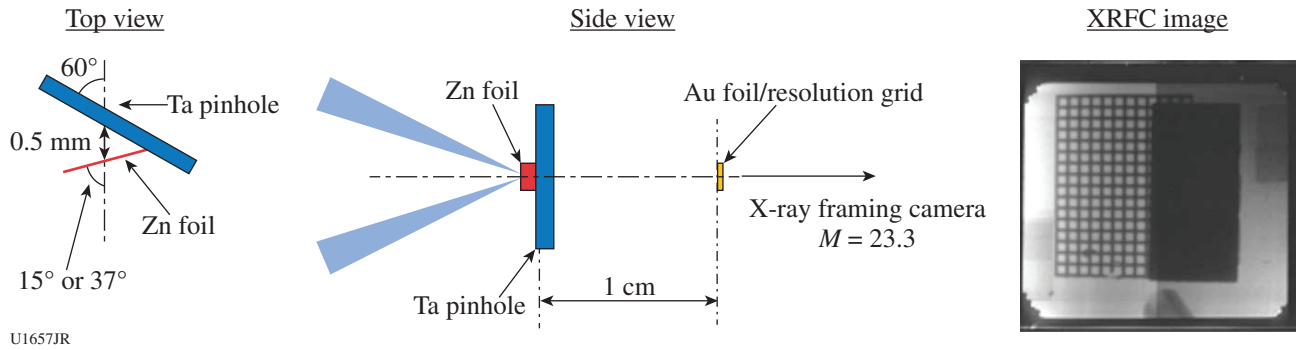


Figure 136.119

The experimental setup, showing angles of the Ta pinhole substrate and Zn foil with respect to the laser/imaging axis. Shown on the right is a sample x-ray framing camera (XRFC) image of the Au Grid and Au foil. A Zn filter covered half the image and two sets of 4- and 8-Cu filter steps are also present in the corners.

**X-Ray Area Backlighter Development**

Principal Investigator: K. Baker

A campaign of six shots was carried out on the OMEGA laser to measure the conversion efficiency and uniformity of zinc backlighters. A common platform was used to evaluate the conversion efficiency from Zn foils with and without a 2.8-ns prepulse, ZnO-coated aerogels, and ZnO foams. The common platform consisted of a 2-mm-diam, 2-mm-long tube that was filled with either a low-density foam or had two foils glued on the ends of an empty tube. As shown in Fig. 136.120, the highest overall conversion efficiency came from a 5- $\mu$ m-thick Zn foil target driven with a 2.8-ns prepulse that was  $\sim 3\times$  brighter than the same Zn foil without a prepulse. The second-most-efficient target was a pure ZnO foam, followed by ZnO-coated SiO<sub>2</sub> aerogels. The foam targets, which underwent volume ionization, exhibited more-uniform radial emission above 1 keV than the foil targets, with or without prepulse (see Fig. 136.121).

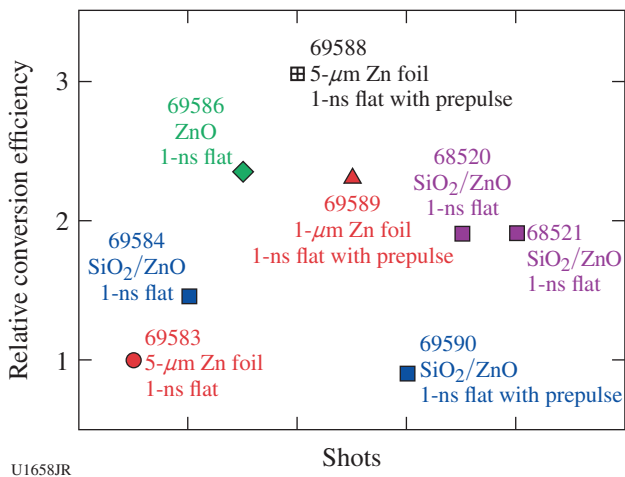


Figure 136.120

Relative energy conversion efficiency for the various zinc targets.

The thinnest Zn exploding foil target, which was 1  $\mu$ m thick, stagnated in the middle of the tube, producing a temporally longer He $_{\alpha}$  emission than the other targets.

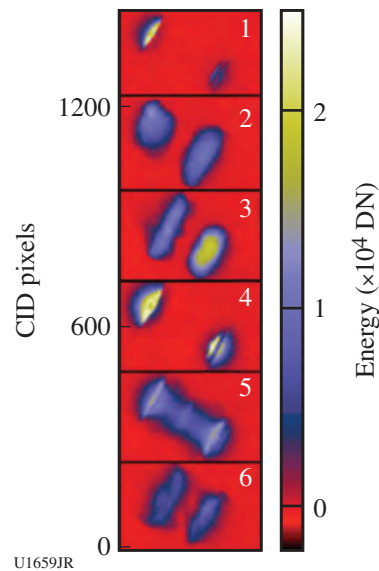


Figure 136.121

Time-integrated x-ray pinhole images of the various targets showing the increased fluence from the foil targets with prepulse (4) and the greatly increased uniformity with the low-density foams (2, 3, and 6).

**5. Burn Physics**

**High-Resolution Measurements of Velocity Nonuniformities in an Alternative Ignition Capsule Ablator Material, Boron Carbide**

Principal Investigator: P. M. Celliers

Two days of CAPSEED campaigns took place in FY13. These campaigns began our initial evaluations of boron carbide

(B<sub>4</sub>C) as an alternate ablator material for NIF ignition target designs. The large fraction of boron in this material makes it a particularly efficient ablator, similar to others such as CH and C. B<sub>4</sub>C undergoes brittle failure, however, when stresses exceed the yield stress; therefore, it is anticipated that it may have a complicated shock response, similar to diamond. Two CAPSEED campaigns this year provided the initial evaluations of ablator nonuniformities produced in B<sub>4</sub>C under shock.

For the CAPSEED-13A campaign, the B<sub>4</sub>C samples were obtained from a commercial source using a sintering process. Characterization of the sample revealed carbon inclusions and voids, and the polished samples incurred large (micron-sized) defects on the surfaces owing to these issues. Attempts to mitigate these problems were made, but the resulting shock quality was severely compromised. The second campaign, CAPSEED-13B, investigated samples that were also created through a sintering process developed at LLNL, but with much lower levels of nonuniformity and voids. Results from the later samples showed a clear improvement; however, the shock-front nonuniformities in these samples were still clearly evident in the data as shown in Fig. 136.122. The velocity spectra of the current B<sub>4</sub>C samples (Fig. 136.123), when compared with high-quality Be and GDP ablator samples, are too nonuniform for use

in a NIF capsule. Improvements in the fabrication processes to control these nonuniformities are required for further progress with this material.

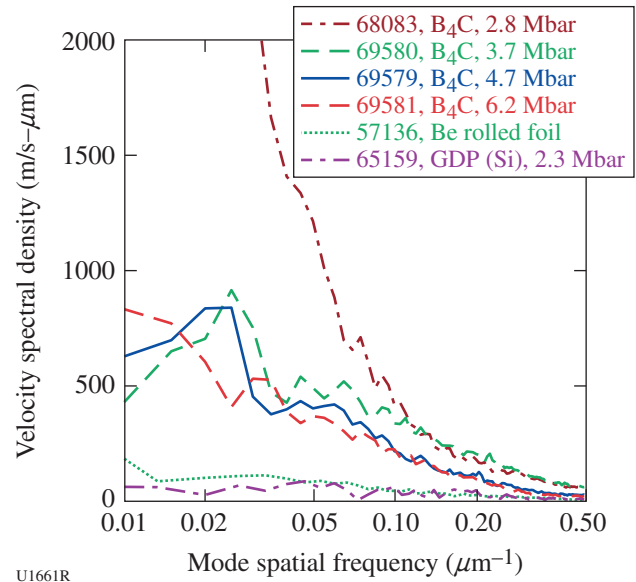


Figure 136.123 Velocity fluctuation spectra measured for B<sub>4</sub>C from CAPSEED-13A (low-quality sample, shot 68083) and with improved samples CAPSEED-13B (shots 69580, 69579, 69581). Fluctuation levels are still a factor of 5× to 10× too high for use as a NIF ablator. For comparison, results from a NIF-quality Be foil (57136) and silicon-doped glow discharge polymer (GDP) sample (65159) show much lower fluctuation levels.

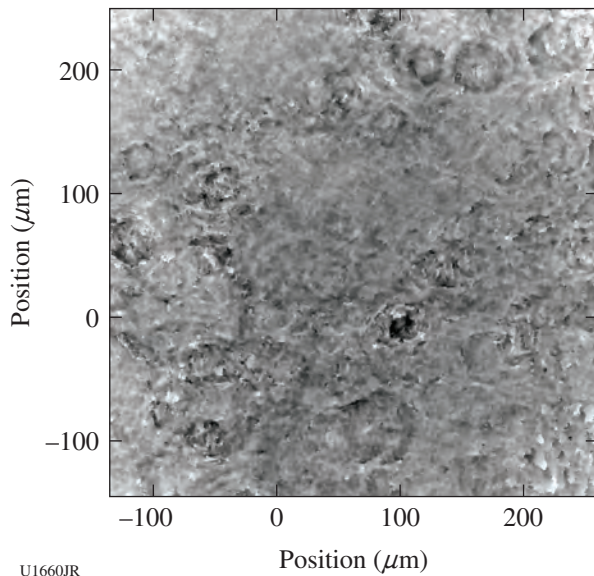


Figure 136.122 Gray-scale representation of the shock-front velocity as measured on shot 69581, a B<sub>4</sub>C sample shocked to 6.2 Mbar. The presence of voids and carbon inclusions distributed throughout the sample resulted in the circular ripple-like disturbances in the velocity pattern. These disturbances produce most of the spectral power in the 10- to 100- $\mu$ m-wavelength range (0.01- to 0.1- $\mu$ m<sup>-1</sup> spatial frequency range).

### Ablator Physics: Tests of Beryllium Capsules

Principal Investigator: D. T. Casey

The goal of the AblatPhys-J-13A OMEGA/OMEGA EP joint shot day was to demonstrate Be as a high-performance ablator for indirect-drive-ignition experiments on the NIF. These experiments were diagnosed with the OMEGA neutronics suite and also used OMEGA EP-driven Cu K $\alpha$  backlighting observed with the spherical crystal imager. This was the first use of the spherical crystal imager in indirect drive at the Omega Laser Facility; the excellent data we obtained resulted in high-quality radiographs and neutronics data. The capsules were 600  $\mu$ m in diameter with 30- $\mu$ m-thick Be walls (where the inner 7.5  $\mu$ m was doped with 4% Cu) and were filled with deuterium gas. General Atomics, who manufactured the capsules, tackled a number of complex target fabrication issues, including deuterium gas retention, Be polishing, Cu diffusion, and residual glue from the gas-fill hole. Several targets also included thin 0.1- $\mu$ m W layers on the inner capsule surface to provide radiographic contrast. The capsules were driven using

1.6-mm-diam, 2.1-mm-long, 50- $\mu\text{m}$ -thick Au hohlraums irradiated by 40 OMEGA laser beams. These targets performed exceptionally well, providing around 80% of the neutron yield expected based on simulations. Figure 136.124 shows (a) the radiograph geometry, (b) a sample radiograph, and (c) the Be target performance (without the W layer) as indicated by the yield divided by the simulated yield (YOS).

6. X-Ray Source Development and Application

**Solar Cell Electrostatic Discharge**

Principal Investigator: R. Patterson

The solar cell electrostatic discharge campaign is a joint effort of the Naval Research Laboratory, the Defense Threat Reduction Agency, and the X-Ray Source Development team at LLNL. The goal of this campaign is to establish a platform capable of performing x-ray exposure testing on arrays of solar cells,<sup>61</sup> specifically to demonstrate that a sustained arc can be formed between individual cells.

On 11 July 2013, the team successfully fielded the time-of-flight Langmuir probe (XLPD)<sup>62</sup> and active solar cell array (XLPDAC) diagnostics on ten shots, obtaining excellent data indicative of electrostatic discharge over a range of source-to-cassette distances between 60 cm and 96 cm. The improvements in robustness and reproducibility of acquired

data resulted from modifications to the XLPDAC hardware (Fig. 136.125), including electrical insulation of the solar cells from the aluminum cassette and improved shielding of previously exposed contacts.

XLPD measurements confirmed the arrival of the source plasma a few  $\mu\text{s}$  after x-ray loading,<sup>63</sup> consistent with prior measurements of plasma velocities,  $\sim 15 \text{ cm}/\mu\text{s}$ . Figure 136.126 shows the solar cell output signals for several shots. The data

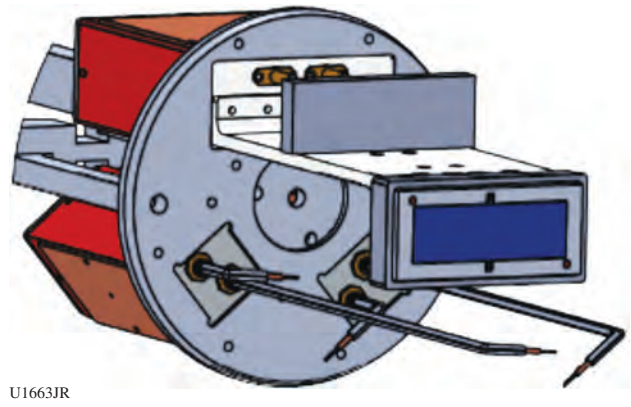


Figure 136.125  
A CAD model including the modifications made to the XLPDAC. Mounted from the circular aluminum cassette face are the solar cell support bracket (light gray) with cells (blue) and two pairs of Langmuir probes beneath. The bias and power circuitry housing (red) is attached to the rear of the cassette.

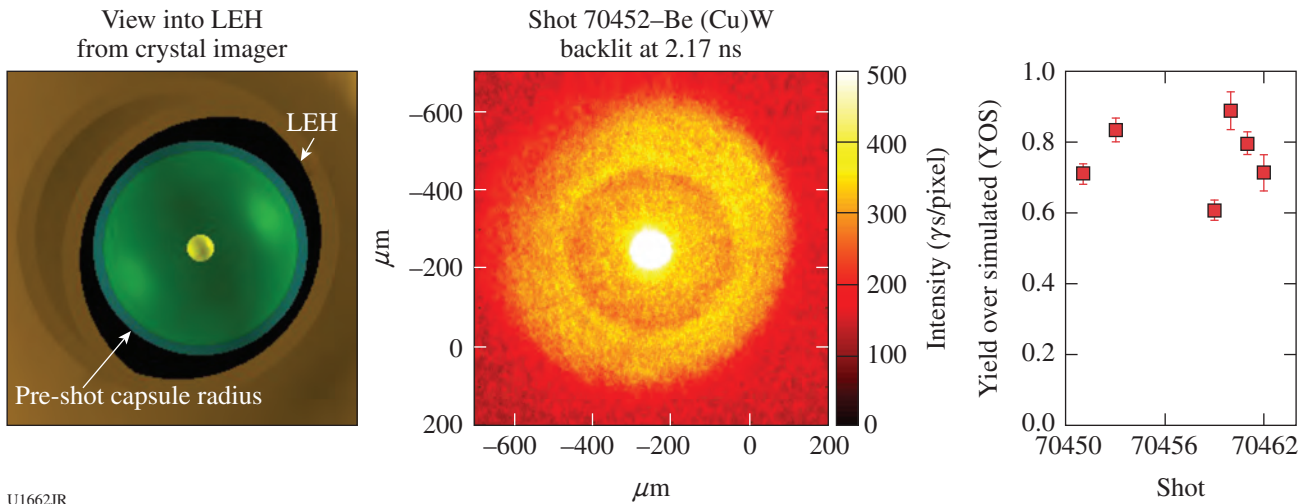


Figure 136.124  
(a) A view of the capsule into the hohlraum, as seen by the spherical crystal imager. (b) OMEGA EP-driven  $\text{Cu K}\alpha$  backlit radiograph of the imploding shell 2.17 ns after the start of the main OMEGA drive. The radiograph was obtained by the spherical crystal imager. (c) Performance of the Be capsule implosions as indicated by the yield-over-simulated (YOS) neutron yield.

suggest that the arc formation is not between the cells themselves. The cell biased at +100 V and limited to 4-A maximum current behaves similarly to an area Langmuir probe, drawing current from the surrounding plasma. The other cell was grounded and not current limited, showing signals consistent with initial photoionization of the cover glass and a subsequent decrease in amplitude resulting from neutralization with the plasma. Future experiments will include different or no current limits on the cells and cell geometry variations that allow discrimination between arcing and photoionization effects (geometry independent versus scaling with area).

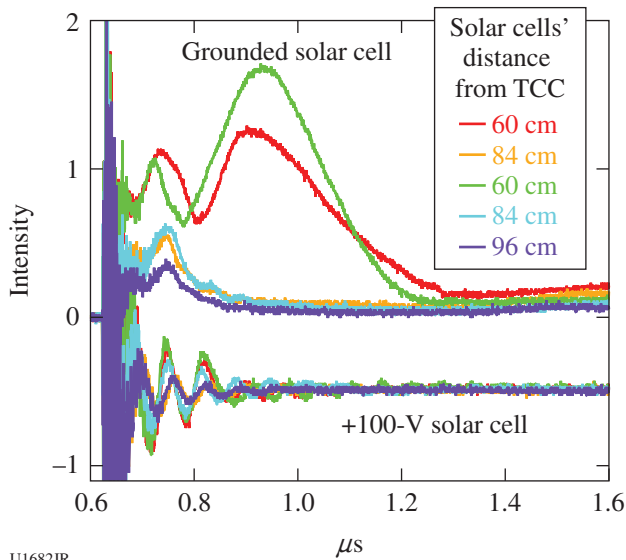


Figure 136.126  
 Voltages recorded from grounded (upper) and +100 V biased (lower) solar cells. Signals are from shots with Ge-doped SiO<sub>2</sub> aerogel x-ray sources, irradiated with ~20 kJ in a 1-ns square pulse.

**X-Ray Source Development  
 with Nanostructured Materials**

Principal Investigator: F. Perez

In FY13 the X-Ray Source Development team, funded by the Defense Threat Reduction Agency, created the most-efficient Ti-doped foam for generating bright, ns-class x-ray pulses to date. Two new fabrication techniques achieved record concentrations of Ti emitters (up to 33 at. %) by coating TiO<sub>2</sub> on an aerogel or nano-porous scaffold. These foams now demonstrate laser-to-x-ray conversion efficiencies above 5%, comparable to other types of x-ray-source targets such as metallic cavities and pre-exploded foils. The x rays are generated when 40 beams of the OMEGA laser irradiate a foam sample (see Fig. 136.127).

This year, after obtaining x-ray flux and laser-heating propagation measurements in the targets, the team found that the dynamics of the foam heating were not well reproduced by state-of-the-art computer simulations. This discrepancy, under investigation, could be explained by an unexpected role of foam structure, metal-dopant content, or the presence of absorbed water, or by effects not included in the simulations. Understanding and mitigating these effects may lead to new designs and even-higher x-ray efficiencies.

In parallel, new types of foams are being investigated. The present limitation is that most of the foam is made of elements lighter than Ti (Si and O), which channel energy out of the system. Cu-based foams, containing only trace amounts of light elements, were tested this year for the first time. Being still at an early stage of development, the current results will serve as a reference point for next year's ultralow-density (<10-mg/cm<sup>3</sup>), almost-pure Cu foams.

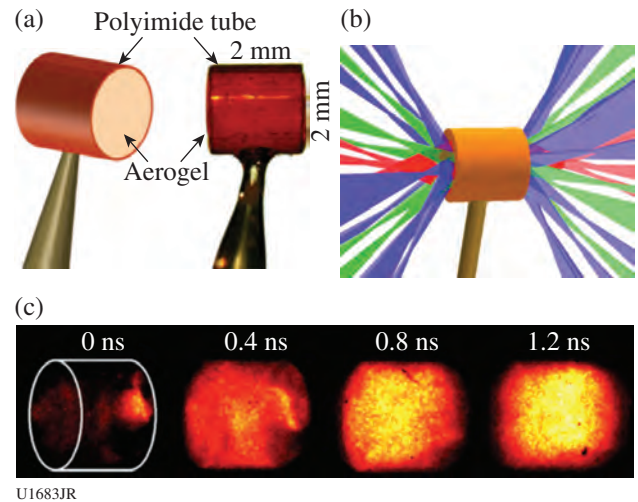


Figure 136.127  
 (a) Foam sample held in a plastic tube; (b) laser irradiation pattern of the OMEGA laser; (c) x-ray emission images at different times relative to the beginning of the interaction.

**ACKNOWLEDGMENT**

This work was performed under the auspices of the U.S. Department of Energy by Lawrence Livermore National Laboratory under Contract DE-AC52-07NA27344.

**FY13 LANL Experimental Campaigns—Overview**

In FY13, Los Alamos National Laboratory (LANL) executed 207 total shots on OMEGA. LANL experiments contributed to the National Ignition Campaign (NIC) in the following ways:

- Measured the x-ray ablative Richtmyer–Meshkov growth of isolated defects on beryllium ablators
- Studied branching ratios and species separation (plasma kinetic effects) in DT fusion plasmas
- Continued neutron imaging and gamma-ray scintillator development for the National Ignition Facility (NIF)
- Studied the suppression of hohlraum laser–plasma interaction (LPI) with magnetic fields

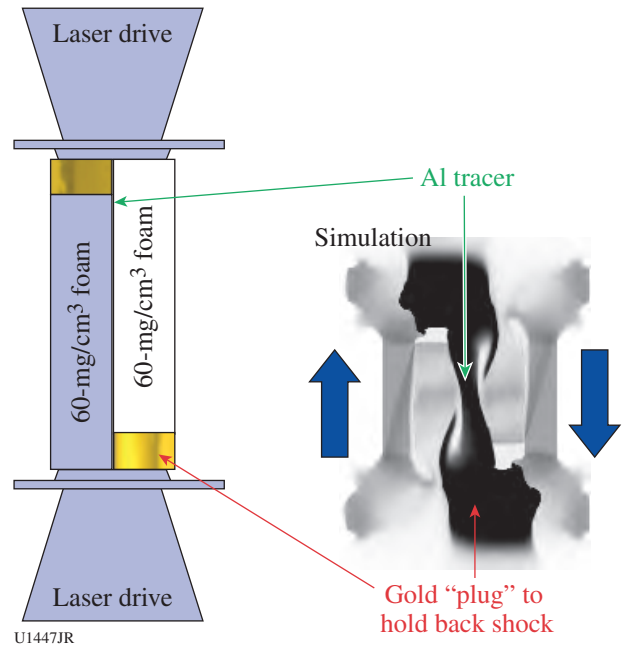
High-energy-density (HED) campaigns included

- Study of shear in a counter-propagating flow geometry driving turbulent mixing
- Backlit defect implosion experiments to study polar-drive symmetry control
- Measurement of spatial distribution of mix in gas-filled capsules
- Imaging x-ray Thomson-scattering platform development for dense plasmas and warm-dense-matter equation of state (EOS)
- Measurement of a supersonic radiation wave and foam aerogel EOS

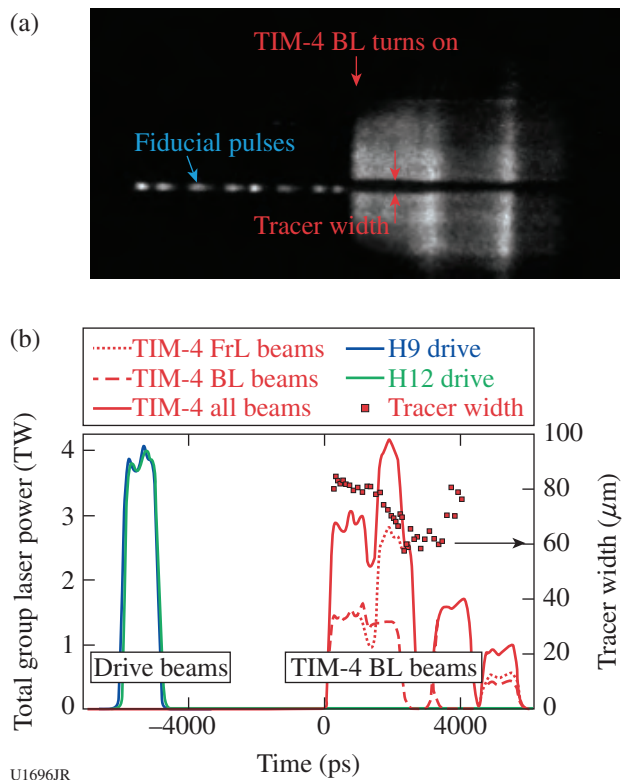
**Shear**

In FY13 the Shear campaign focused on extending our counter-propagating flow platform for studying shear-driven turbulent mixing to include long-duration streaked imaging of the mix layer. These experiments used beryllium tubes containing low-density polystyrene-foam half-cylinders separated by aluminum tracer layers. The counter-propagating flow is created by inserting gold “plugs” in front of each foam semi-cylinder at opposite ends to hold back the shock in each foam at one end (see Fig. 136.128). With the plugs in place, the beryllium tube ends are irradiated with  $10^{15}$ -W/cm<sup>2</sup> laser intensity to initiate counter-propagating shocks. When the shocks cross, they establish a shear layer in the aluminum, which then grows as a result of Kelvin–Helmoltz followed by turbulent mixing.

During our November 2013 shot day we switched from x-ray-framing-camera (XRFC)–based radiography of the mix layer to a long-duration streaked imager. This required an area backlighter designed to emit x rays over 5 ns or longer that would be recorded with an OMEGA streak camera (20× magnification). Thin scandium foils sandwiching a thicker beryllium foil allowed us to irradiate both sides of the backlighter with grouped beams staggered in time. The central beryllium foil prevented burnthrough but still allowed a significant number of x rays to transmit from the back scandium foil. Figure 136.129 shows an example of a streaked image, indicating where the laser is turned on along with the mix layer (aluminum tracer foil), which shows the absence of a signal as a result of x-ray



U1447JR  
Figure 136.128 Target geometry and simulated radiographs for counter-propagating shear experiments.



U1696JR  
Figure 136.129 (a) Raw and (b) analyzed streak data of mix width from shear experiments. FR: front lit; BL: backlit.

absorption in the aluminum. Figure 136.130 summarizes mix-width data and compares simulations using the Los Alamos Bernard–Harlow–Rauenzahn (BHR) turbulent mix model, streaked imaging, and x-ray-framing-camera data.

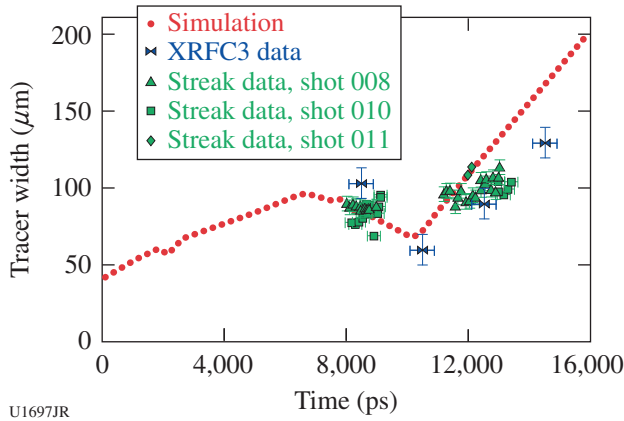


Figure 136.130 Comparison between framing camera, streak camera, and simulated mix-width evolution.

**BeARM**

The Be ablative Richtmyer–Meshkov (BeARM) campaign had one shot day in January 2013. The overall goal of these experiments was to measure the oscillation frequency of small perturbations on CH and Be ablators driven by the x-ray ablation Richtmyer–Meshkov (RM) effect. This knowledge would provide a better understanding of how isolated defects behave during the first shock transit stage of a NIF ignition attempt, which would then provide methods for minimizing perturbations at the onset of Rayleigh–Taylor instability.

Our experiments used 15 beams inside large Au half-hohlraums, which were staggered in time to produce a 7.5-ns radiation drive with a radiation temperature of 80 eV (see Fig. 136.131). Targets with 2-D arrays of 5- $\mu\text{m}$ -tall, 17- $\mu\text{m}$ -FWHM Gaussian bumps and 25- $\mu\text{m}$ -wavelength Be sinusoids were attached over the opposite laser entrance hole with the defects facing inside the halfraum. During the experiment the bump arrays were backlit with Y and Ta backlighters ( $\sim 2.2\text{-keV}$  emission) and imaged at  $37\times$  magnification onto an x-ray framing camera. Radiation–hydrodynamics simulations running with equation-of-state (EOS) tables for Be predict these small-amplitude (2.5- $\mu\text{m}$ ) sinusoids undergo damped oscillations for our experimental conditions as shown in Fig. 136.132. We measured the ablative RM of the Be sinusoids with four data points extending out to 7 ns as shown in Fig. 136.133. At the

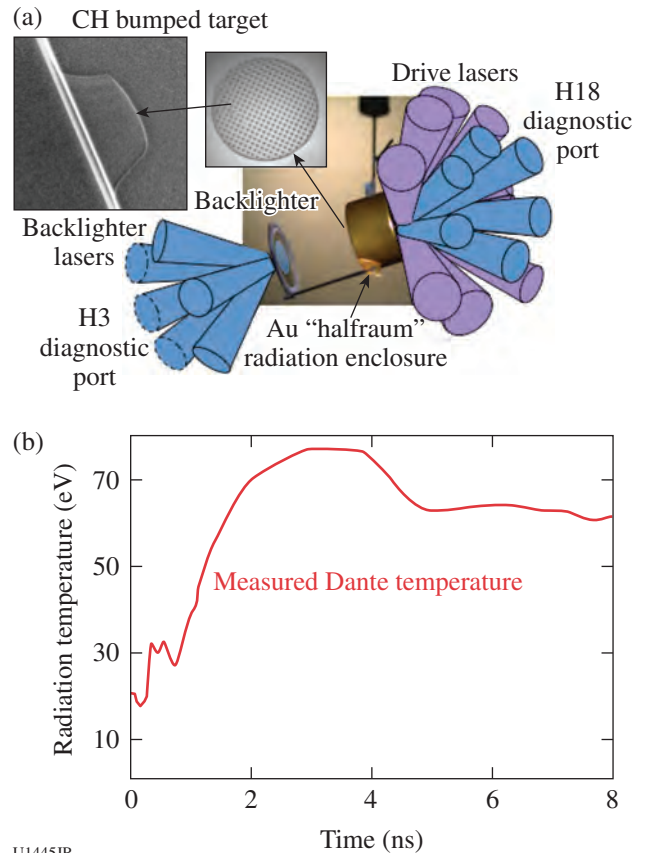


Figure 136.131 Overview of indirect-drive ablative Richtmyer–Meshkov (RM) experiments.

two data points around 3.5 ns, the sinusoids appeared to go through an inversion and then reappear by 7 ns. This appears to be consistent with the 20- $\mu\text{m}$  simulation of Fig. 136.132, where

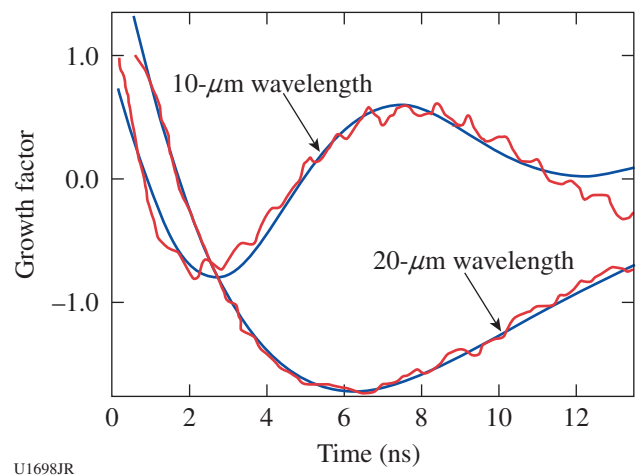


Figure 136.132 Simulated oscillations of ablative RM sinusoids in Be.

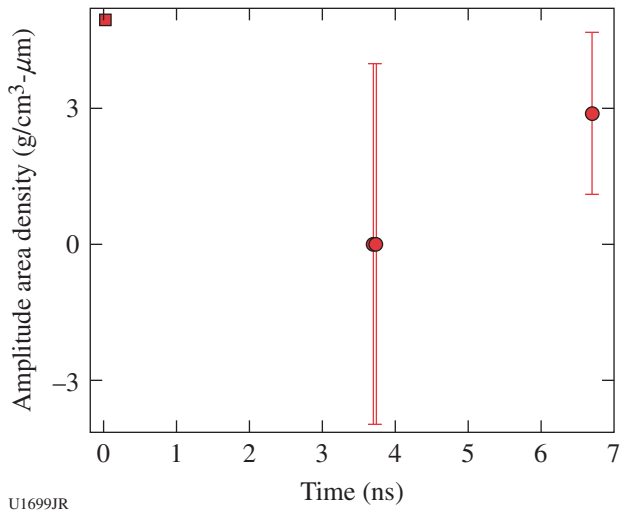


Figure 136.133  
Measured areal density of Be sinusoids. An apparent inversion is reached near 4 ns. The point at 7 ns is likely an inverted feature (local minimum), which was not apparent directly from the data.

the inversion occurs around 2 ns and then the inverted sinusoid reaches a minimum by 6 ns. With the slightly longer wavelength of our targets (25 μm), the inversion would be delayed slightly along with the time of the minimum of the inverted sinusoid.

**Gamma-Ray History**

The ICF gamma-ray physics team, led by H. Herrmann and Y. Kim of P-24, completed 24 inertial confinement fusion (ICF) implosions on OMEGA over two days to investigate plasma kinetic effects and turbulent mix. Plastic capsules of four different shell thicknesses were shot at two different fill pressures for each thickness in order to vary the ion temperature and density and, consequently, the ion mean free path. Performance predictions were provided by N. Hoffman and M. Schmitt of XCP-6 prior to the shot day. Hoffman is in the process of developing a reduced ion kinetic transport model for fluid simulations of high-Knudsen-number capsule implosions, where the Knudsen number is simply the ratio of the thermal-ion mean free path to the characteristic system dimension (i.e., approximately the distance from the center of the compressed core to the cold shell). The plasma kinetic terms of ion diffusion, viscosity, and thermal conduction (i.e., conservation of mass, momentum, and energy) as well as reactivity reduction by free-streaming ion loss near the Gamow peak are incorporated into the reduced model. Turbulent mix is also allowed to play a role, although it did not appear to be a dominant factor in these implosions. By employing an extensive suite of diagnostics, we were able to acquire the most highly constrained simulations to date. Measured attributes include laser energy coupling, D–T and

D–D neutron yields and ion temperatures, fusion reaction histories, x-ray imaging, and areal densities of fuel and shell. Preliminary experimental results in terms of yield and ion temperature are reasonably close to predictions from the new model (Fig. 136.134), but there are some remaining discrepancies (by comparison, yield-over-clean was typically in the 5% to 25% range). In particular, simulations tended to slightly overpredict yields at low ion temperature (while remaining within the uncertainty of the prediction) and underpredict at high ion temperature for the 5-atm fills. Notably, the ~7-μm-thick capsules at 2-atm fill pressure did not achieve the high predicted ion temperatures (~12 versus 16 keV) but still achieved the predicted yields. Detailed experimental analysis and post-shot simulations accounting for “as-shot” parameters are in progress.

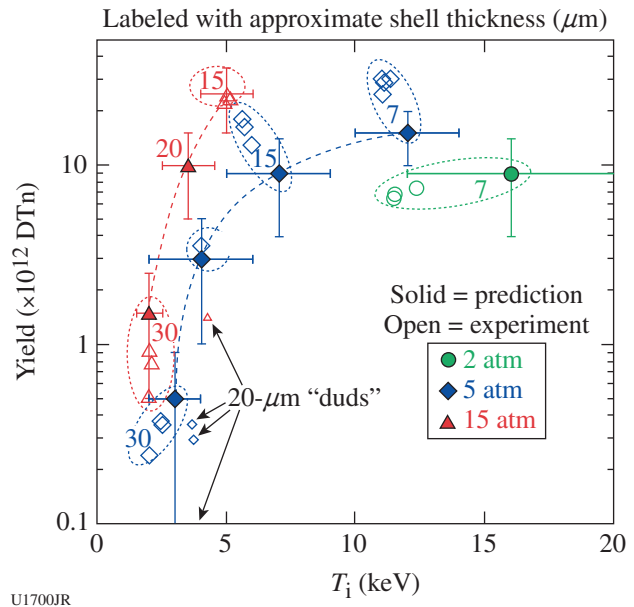


Figure 136.134  
Measured and predicted yield at varying fill pressures. Simulations include new models of plasma kinetic effects that better fit the measured yields and ion temperatures.

**HED–MMI**

1. Spatially Resolving Mix Brings with It Difficulties in Interpretation

An exciting possible method to measure the spatial information of mixing has been doping the inner wall of a plastic shell in conjunction with a relatively new diagnostic that allows one to spectroscopically image the atomic emission. The spectroscopic imager [multiple-monochromatic imager (MMI)] consists of a pinhole array in front of an x-ray crystal. This

produces many dispersed images that can be parsed to provide images over a narrow bandwidth. Alternatively, one may obtain the spectrum emitted from particular zones of the image.

In June 2012 OMEGA experiments, LANL researchers R. Shah and J. Benage (both of P-24), in collaboration with Prof. R. Mancini's University of Nevada-Reno group, obtained images with the MMI imaging spectrometer of such doped targets. To be differentiated from experiments described below, these targets were doped uniformly around the entirety of the spherical shell. Since small-scale features were expected to dominate the mix and create symmetric annular emission, the team was surprised to instead find strongly asymmetric images. Most important, the features cast doubt on the ability to interpret if dopant emission came from central regions or was localized along the shell–fuel interface as predicted.

## 2. Specialized Targets Provide Insight into Spatial Features of the Mixing

To address the difficulty in interpretation, researchers worked with target fabrication teams at both LANL (Materials Science and Technology) and General Atomics. This collaborative effort resulted in fabricated targets in which only a small patch of the capsule shell was doped. Such a localized doping along the equator of the implosion coupled with imaging down the capsule pole could avoid obfuscation of interior information by surface emission. In February 2013 Shah and Benage, along with a student from the university collaboration,

returned to LLE to test this approach and its relevance to the longstanding absence of images, revealing just how deeply a shell mixes into the imploding cavity. Figure 136.135 shows images obtained at the  $\text{He}_\beta$  emission line with such a target using two separate spectral imagers. The two instruments were operated simultaneously and on the same shot but oriented so as to provide different views (as illustrated in the insets). In Fig. 136.135(a) the quasi-polar view very clearly shows that the brightest emission, which in the previous experiment could not be clearly identified as interior or surface, remains near the outside of the capsule. One also notes that a signal—originating from the dopant that was initially in the shell—is present across the image. The more face-on view of Fig. 136.135(b) indicates substantial transverse migration of the dopant.

### DIME

For the January 2013 defect-induced mix experiment (DIME) on OMEGA, the primary objective was to demonstrate the ability to manipulate spherical implosion symmetry with 40 beams in the polar-drive (PD) configuration. Typically, with equal-power PD beams and preferred LLE pointing, our capsules compressed with an oblate (pancake) configuration—a major/minor axis ratio increasing in time to  $>2:1$ . We explored two modifications of PD: (1) The energy balance was changed for the three sets of PD beam cones as a function of polar angle,  $E(\theta)$ . We reduced the nominal polar cone power and increased equatorial power to mitigate the oblate effect. As we cooled the poles and provided enhanced heating to the equator, models

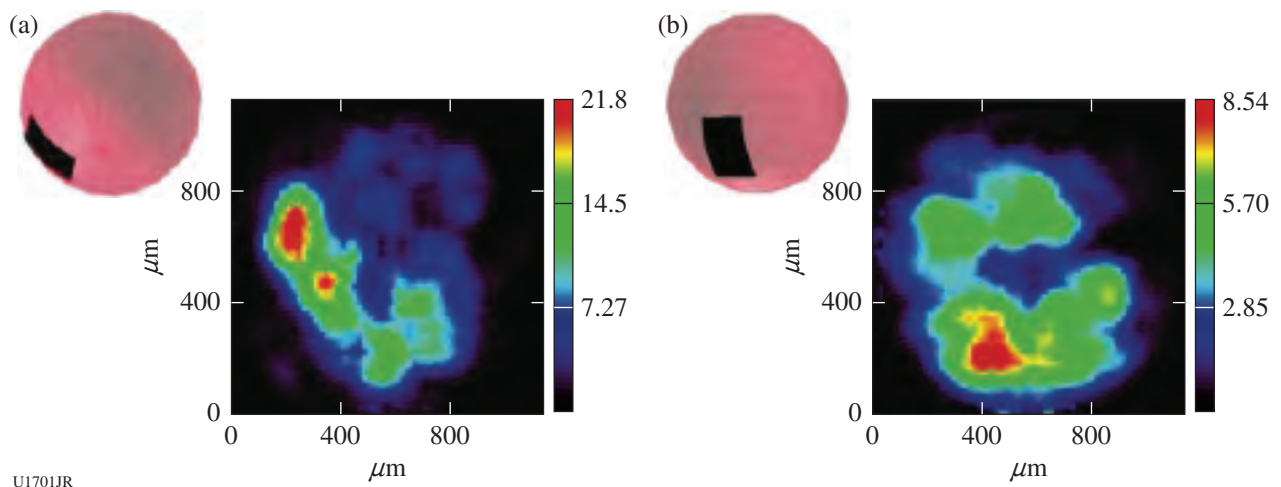


Figure 136.135

Images obtained with modified targets having localized doping of the shell. Spectral images formed at the  $\text{He}_\beta$  emission line of dopant for both (a) quasi-polar and (b) quasi-face-on views. Images were obtained using two separate multiple-monochromator imager (MMI) instruments operating simultaneously on the same shot. Diagrams in each inset show the orientation of the patch.

and experiments showed a capsule transformation away from the oblate shape (Fig. 136.136). (2) The beam pointing was changed on the second shot day with a second  $E(\theta)$  scan (see Tables 136.X and 136.XI). As predicted by simulations, the second-order Legendre mode  $P_2$  was reduced (Fig. 136.137),

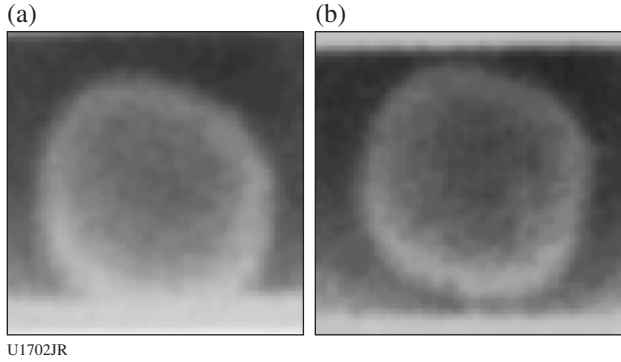


Figure 136.136  
Images taken at time when  $R \sim 0.5 R_0$ : (a) shot 68467 and (b) shot 68469.

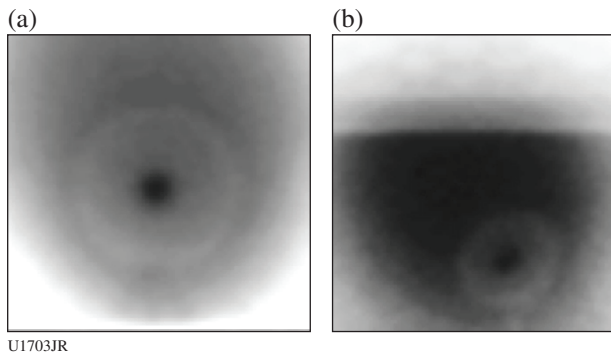


Figure 136.137  
(a) Shot 68489 taken at time when  $R \sim 0.6 R_0$ ; (b) shot 68486 taken at time when  $R \sim 0.4 R_0$ .

but a fourth-order mode  $P_4$  left the capsules with a “rounded diamond”-like shape. This campaign proved that control of independent PD cone power and pointing can impact capsule symmetry.

**DPEOS**

The major goal for the dense plasma equation of state (DPEOS) project on OMEGA was to successfully obtain a complete set of EOS measurements on carbon. The technique we are using—laser-driven shock and release combined with imaging x-ray Thomson scattering—should enable us to obtain, for the first time, measurements of density, temperature, and pressure for materials at warm-dense-matter (WDM) conditions. To this end, two experimental days were carried out in FY13: the first on 13 December 2012, where we obtained 13 shots and a near-100% data return, and the second on 29 May 2013, where we completed 15 shots and also obtained a very high data return rate. The emphasis on the first day was to obtain x-ray radiographs for our targets along with improving the Thomson-scattering measurements. The results from that shot day indicated that the WDM conditions in the target were being produced too long after the laser drive was turned off, negating the effectiveness of the pressure measurement. The experimental target and laser drives were reconfigured for the second experimental day with a dramatic improvement in the results.

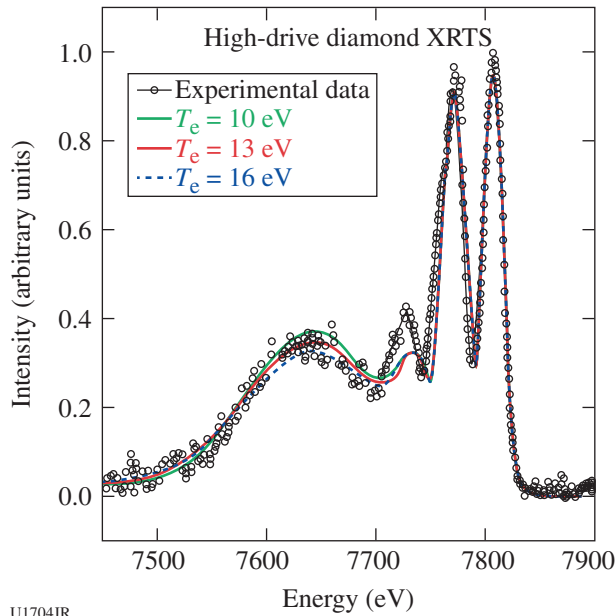
Our results for the second day have been analyzed, and we can now state with confidence that we have demonstrated that this technique can be used to obtain accurate measurements of density, temperature, and pressure for materials in the WDM regime. An example of our Thomson-scattering results in Fig. 136.138 shows our analyzed scattering results from shot 69918 and fits to these results at various temperatures. These

Table 136.X: DIME cone-energy variation with the usual pointings, 850- $\mu\text{m}$ , 17- $\mu\text{m}$ -thick CH capsule.

Shot	Cone beam energy (J)	Neutron yield	Ti (keV)	Bang time (ns)	$P_2$ (experiment)	$P_2$ (simulated)
68467	400/400/400	$1.51 \times 10^{10}$	3.25	1.85	-11.1%	-16.6%
68469	333/400/433	$2.45 \times 10^{10}$	3.66	1.88	-3.6%	-8.0%

Table 136.XI: DIME cone-energy variation with new pointings, similar capsules.

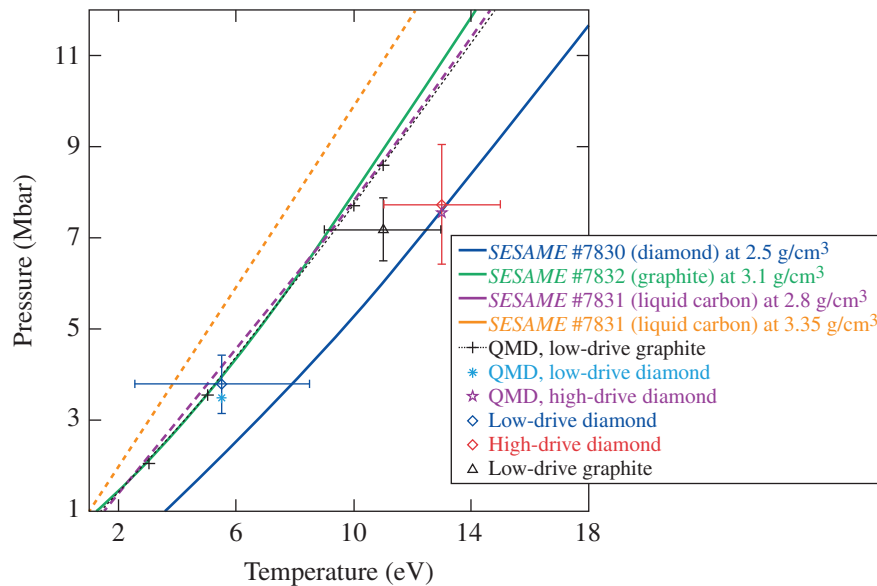
Shot	Cone beam energy (J)	Neutron yield	Ti (keV)	Bang time (ns)	$P_2$ (experiment)	$P_2$ (simulated)
68486	333/400/433	$1.28 \times 10^{10}$	3.08	1.88	-7.5%	-6.1%
68489	400/400/400	$2.01 \times 10^{10}$	3.57	1.87	-3.1%	-7.5%



U1704JR

Figure 136.138  
X-ray Thomson-scattering data analyzed from OMEGA shot 69918. The fits to the data utilize the known x-ray source spectrum from the Ni backlighter, the scattering angle of 100°, and the density of 2.3 g/cm<sup>3</sup> obtained from the radiograph of this shot.

data, combined with results from the x-ray radiography and the velocity interferometer system for any reflector (VISAR) and streaked optical pyrometer (SOP) measurements, have been used to determine density, temperature, and pressure for carbon at three distinct conditions. We find that our results compare favorably to quantum molecular dynamics (QMD) calculations at these conditions. This is shown in Fig. 136.139 where the



U1705JR

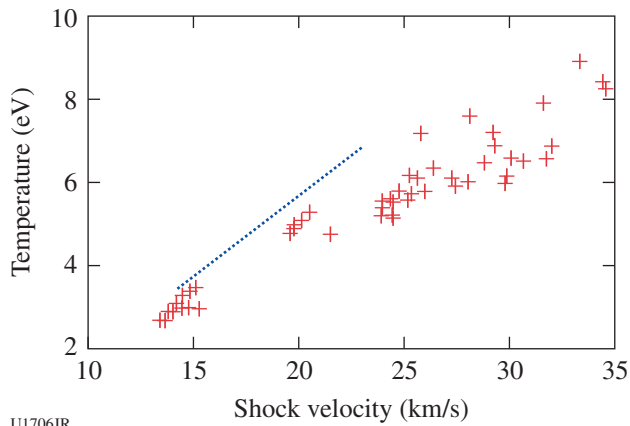
Figure 136.139  
Comparison of warm-dense-matter (WDM) carbon measurements to various isochors of equation-of-state (EOS) models of carbon. The data points (marked by inclusion of error bars) represent carbon at 2.8 g/cm<sup>3</sup> and 5.5 eV, 3.1 g/cm<sup>3</sup> and 11 eV, and 2.3 g/cm<sup>3</sup> and 13 eV. The corresponding quantum molecular dynamics (QMD) calculations are color matched and compare very well with the data except for the 11-eV point. For this case we have plotted the QMD results for 3.0 g/cm<sup>3</sup> and several temperatures that fall within the uncertainty of the measurements.

data are compared to QMD and several *SESAME* EOS models. There is also reasonable agreement with several EOS models for carbon, although some models compare better than others.

### NIF-5

The major goal for the NIF-5 Project on OMEGA was to successfully obtain temperature measurements from shocked aerogel foams and shocked CH foams using the SOP diagnostic. To accomplish this goal, two experimental days were carried out in FY13: the first on 7 November 2012, where we obtained 15 shots and a high rate of data return, and the second on 1 May 2013, where we also completed 15 shots and obtained a high data-return rate. The emphasis on the first day was to obtain temperature data from our aerogel foam targets at a range of conditions. The second experimental day focused on the CH foams, which had an initial density of 0.15 g/cm<sup>3</sup>.

The results for the two days indicate two important things: First, the temperatures measured for the silicon aerogel foams agree with EOS models at low pressures but drop below the models as the pressure is increased. We also find that it is below temperature values obtained using QMD calculations, which we expect to be quite accurate at these low temperatures. This is shown by the graph in Fig. 136.140. We are currently performing highly resolved simulations of the shock process to better understand the physics mechanisms behind this difference. Similar experiments on CH were conducted on the second day. The results were a little surprising because the effective temperatures were quite a bit lower than the aerogel temperatures for a given pressure drive. This is likely because of the higher bond and ionization energies for CH. Further data analysis is ongoing.



U1706JR

Figure 136.140

Streaked optical pyrometer (SOP) temperature measurements for shocked aerogel foam. The red crosses represent individual data points and the green curve is from QMD calculations for the EOS of the shocked foam.

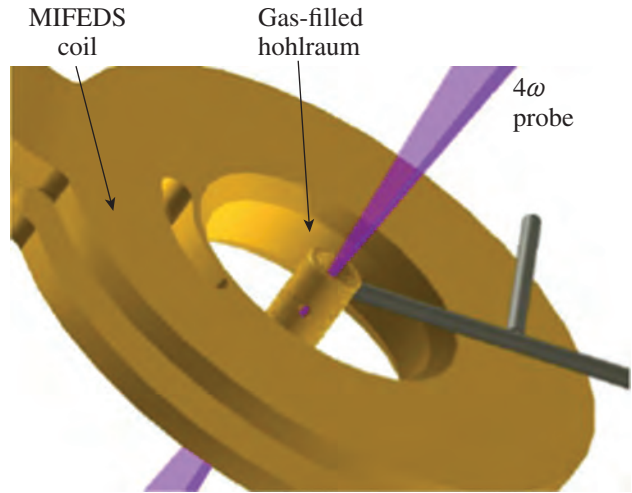
**MagLPI**

The goal of the MagLPI campaign at the Omega Laser Facility is to demonstrate laser-plasma instability (LPI) mitigation using magnetic fields. Using a sufficiently strong external magnetic field, thermal heat transport is expected to be reduced across a magnetic field since the transport step size is determined by the electron Larmor radius instead of the electron-ion collisional mean free path. In this regime of “magnetic insulation,” the plasma electron temperature is expected to increase compared to the case with no external field. The ability to increase the underdense plasma temperature in a NIF ignition hohlraum is highly desirable since it would reduce inverse bremsstrahlung losses of the NIF inner beams as they propagate through the long-scale-length low-Z plasma. In addition, increasing the plasma temperature would significantly increase Landau damping and help mitigate stimulated Raman scattering (SRS).

Using a magneto-inertial fusion electrical discharge system (MIFEDS)-pulsed magnetic coil, an external field up to  $B_z = 8$  T was applied with the field aligned along the axis of a gas-filled hohlraum on OMEGA (Fig. 136.141). The hohlraum axis was aligned along the P9-P4 ports and 39 beams irradiated the hohlraum in three beam cones. The  $4\omega$  Thomson-scattering beam probed the plasma at the center of the hohlraum, as viewed through a diagnostic hole at the hohlraum midplane. The specific deliverables for this campaign were to measure the electron temperature, SRS backscatter, and hard x rays versus B-field strength.

A total of nine target shots were performed on 20 August 2013. Preliminary results indicate an increase in plasma temperature with external B field, and the correlation with LPI and

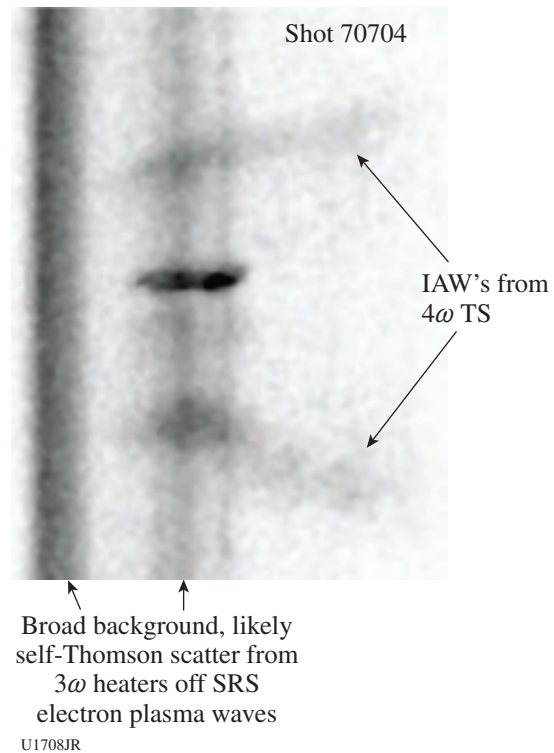
B-field strength is currently being analyzed as seen by data in Fig. 136.142.



U1707JR

Figure 136.141

Schematic of experimental layout with a magneto-inertial fusion electrical discharge system (MIFEDS) coil, which generates an external magnetic field, and the hohlraum axis aligned along the  $4\times$  Thomson probe-beam axis.



U1708JR

Figure 136.142

Thomson-scattering (TS) measurement from thermal levels of ion-acoustic waves (IAW's). Wavelength is in the vertical axis and time increases to the right. The separation between the IAW's increases with increasing plasma temperature.

**Gamma-Ray Imaging**

On 6 August 2013, LANL successfully executed a full day of shots on OMEGA in support of two experimental science campaigns. Characterization data of a novel gamma-ray imaging camera were collected, as well as hard x-ray aperture images of bremsstrahlung radiation produced by hot electrons traversing the remnant shell material from implosions of plastic capsules. The gamma-ray imaging diagnostic is being developed by LANL in collaboration with the University of Arizona's Center for Gamma Ray Imaging. Additionally, LANL collected data in support of its Turbulent MIX DR project, shooting a variety of separated reactant targets comprised of <sup>3</sup>He-filled plastic capsules constructed with 1- $\mu$ m-thick deuterated layers within the inner regions of a CH shell. In these experiments D-<sup>3</sup>He fusion reactions are used as the direct signature for atomic mix. Good neutron and proton yield data were collected, as well as gamma images of the implosions, as illustrated in Fig. 136.143.

**Neutron Imaging System**

Imaging technologies are typically benchmarked with a known system to determine the residual distortions. In radiography a standard static object is imaged in transmission, the analysis techniques are applied, and the result of the analysis is

compared to the known object. This allows one to characterize the performance of the image formation and reconstruction algorithms. One of the difficult aspects of neutron imaging has been that no "standard" neutron source is available to perform this type of test. This has resulted in a strong reliance on modeling and simulation to characterize the performance of the image formation and reconstruction algorithms. No neutron source is suitable because the system is designed to image sources that are very bright ( $\sim 10^{17}$  neutrons/cm<sup>2</sup> at the source surface) and very small ( $\sim 100$   $\mu$ m in diameter). The system was designed and tested through measurements on OMEGA, but these dynamic sources are not well enough characterized and reproducible to be used as a standard neutron source for benchmarking the full system performance.

A series of experiments have been performed on OMEGA in the last year to overcome this limitation. In the design of these experiments, simulations were used to determine the neutron flux at the detector, which results from a known neutron source after passing through the aperture array. A copper object was designed to generate this same neutron flux at the image plane when located just in front of the image collection system. These known static objects were then placed in front

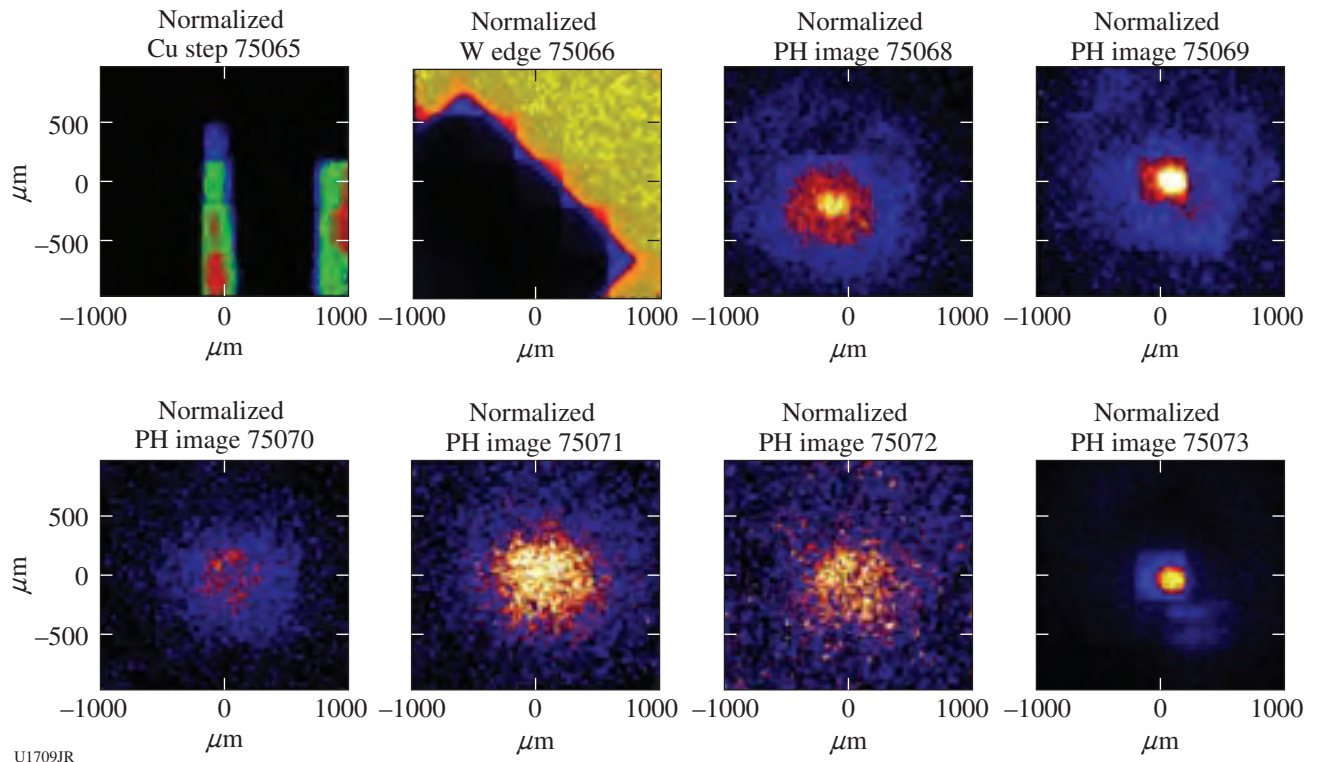


Figure 136.143  
Several images taken using the gamma-ray imaging diagnostic.

of the image collection system on OMEGA, and the neutron flux passing through these objects was measured. The standard analysis techniques were used to extract the source information from these images, and this information was compared to the simulated neutron source. These experimental data have allowed us to determine the system performance, including the detector and reconstruction algorithms, and to partially overcome the limitation of not having a standard neutron source for benchmarking our detection and reconstruction algorithms.

Figure 136.144 shows the two images collected from two test objects. Figure 136.144(a) shows the neutron flux after passing through an object designed to simulate a point source of neutrons, while Fig. 136.144(b) shows the flux from a 20- $\mu\text{m}$ -diam neutron source. These test objects were designed to generate the neutron flux that would be expected from the NIF geometry through the mini-penumbra presently being used on the NIF.

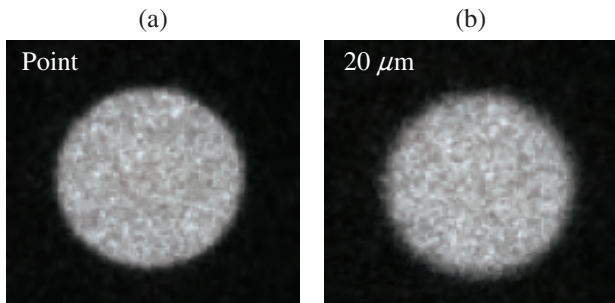


Figure 136.144  
 (a) Mini-penumbra image expected from a point source of neutrons through the NIF mini-penumbra; (b) mini-penumbra image expected from a neutron source with a  $P_0$  of 20  $\mu\text{m}$ .

The standard set of reconstruction algorithms, which were developed for NIF data analysis, was used to process and reconstruct these images. The results are shown in Fig. 136.145.

Over the past year a significant effort has been devoted to determining error bars in the reconstructed parameters. These estimates have come directly from simulations. One would expect that these measurements should be consistent, however, with these error bars. To check this, simulations have been performed to determine the error bars in  $P_0$  and  $P_2$  for the extended source shown above to be  $\pm 1 \mu\text{m} \pm 5\%$ , respectively. This is in good agreement with the observed reconstruction values.

These measurements have provided a test of our imaging system and analysis scheme using simulation through the aperture array combined with experimental measurements at each

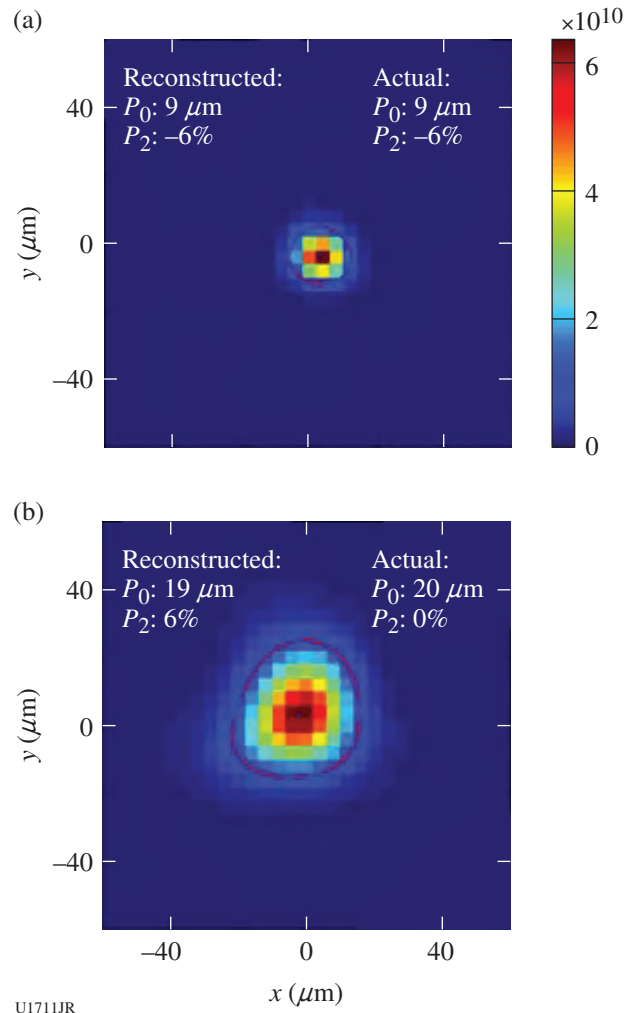


Figure 136.145  
 Reconstruction of the images in Fig. 136.144. (a) The point source reconstructed to have a radius or  $P_0$  of 9  $\mu\text{m}$  and the source with a  $P_0$  of 20  $\mu\text{m}$  resulted in a reconstructed  $P_0$  of 19  $\mu\text{m}$ . The reconstruction of the point source provides a measure of the reconstructed resolution of this system. The good agreement between the actual and reconstructed  $P_0$  of the extended source demonstrates the performance of the reconstruction algorithms.

level. It has been demonstrated that the reconstructed resolution of the mini-penumbra apertures is  $\sim 10 \mu\text{m}$  and has provided confidence in our determination of error bars.

The DIME series of experiments, which are planned on the NIF in the coming years, will rely on the neutron imaging system for a measure of the extent of mixing in the implosion of separated reactant capsules. This requires the measurement and reconstruction of the neutron source in the shape of a spherical shell. The thickness of this spherical shell provides a measure of the extent of mixing in these experiments. A series of measurements on OMEGA have been performed to test the mini-penumbra aperture being proposed for this

measurement. A test object was constructed, similar to the objects described above, that can generate the flux of neutrons expected in these DIME experiments on the NIF. These measurements were made to test the measurement and reconstruction methods to determine how well these mini-penumbra could be used to reconstruct a spherical shell neutron source. These measurements were collected in August 2013 so the analysis is not complete, but the results are encouraging. The reconstruction of this neutron source (Fig. 136.146) shows that the general characteristics of the spherical shell are recovered in these reconstructions.

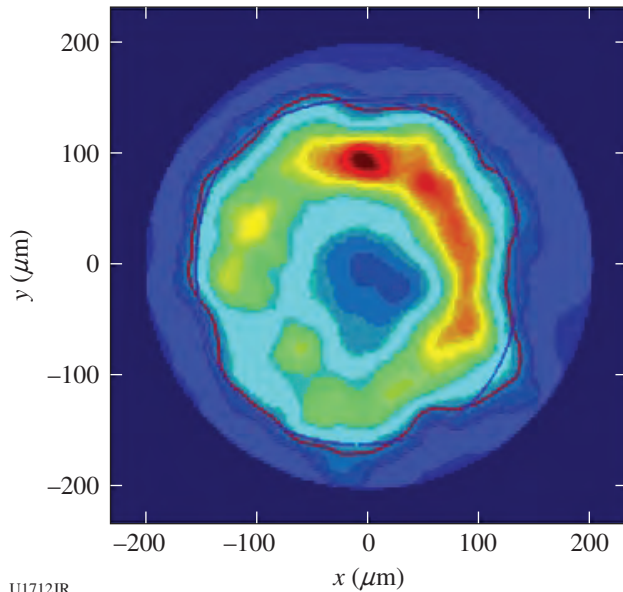


Figure 136.146  
 Reconstruction of the measured neutron flux from the test object that generates the flux of neutrons expected from the DIME experiments on the NIF (150-mm radius with 50-mm width). This shows a clear spherical source. These data provide an opportunity for comparisons to simulation, ultimately characterizing the error bars associated with this type of measurement.

Neutron-generating experiments on OMEGA continue to provide important data to fully characterize the neutron imaging system at the NIF. These measurements provide a stringent test of our simulations and models as well as providing known sources for the testing of our reconstruction algorithms.

**FY13 CEA Experiments at the Omega Laser Facility**

**CEA Vulnerability Diagnostics on OMEGA**

Typical high-yield DT shots at the Omega Laser Facility can deliver up to  $10^{14}$  14-MeV neutrons. These shots generate an integrated dose in the range of 1 to 10 mrad at 5 m from target chamber center (TCC).

Simulations of  $10^{16}$  neutron-DT shots on megajoule-class facilities such as the National Ignition Facility (NIF) or Laser Mégajoule (LMJ) show that the integrated dose in the immediate surroundings of a diagnostic inserter and in the first 100 ns of the experiment (i.e., time of flight of 14-MeV neutrons from TCC to the target chamber wall) is  $\sim 10$  mrad. The Omega Laser Facility is therefore an appropriate facility at which to reproduce the dose rates expected during the first 100 ns on megajoule-class laser facilities and can be used to study the survivability of diagnostic elements such as optical relays or optical analyzers.

Continuing FY12 studies, a standard optical-relay system consisting of two Maksutov objectives, a field lens, a light amplifier, and a cooled charge-coupled-device (CCD) camera, has been exposed to high-neutron-yield shots at a distance of 6 m from TCC (see Fig. 136.147). The level of nuclear background generated on OMEGA leads to visible effects on the recorded image using the CCD camera (see Fig. 136.148), which has been quantified by using masks positioned along the optical path,

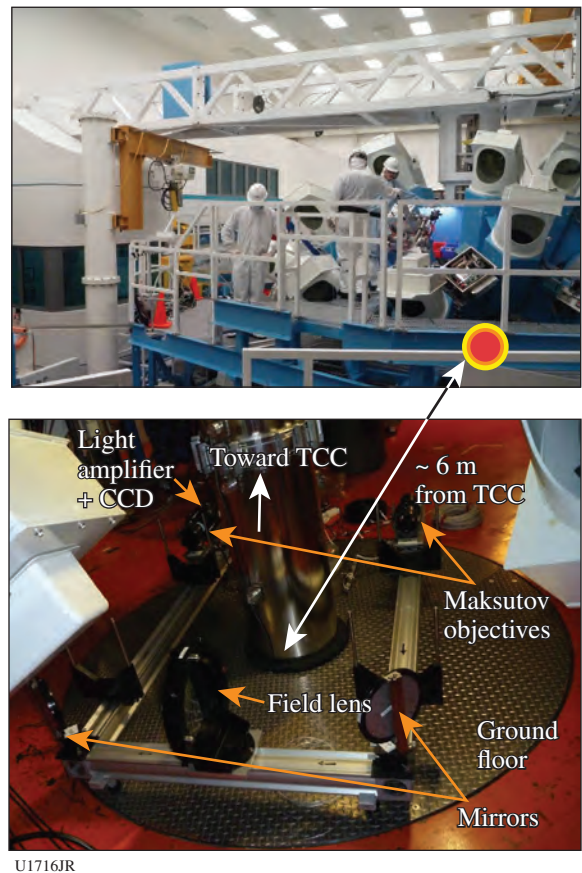


Figure 136.147  
 Optical-relay benchmark experimental setup.

isolating the contributions of the main components of this optical system. As a result (see Fig. 136.149), the increasing background level of the recording device was clearly proportional to the neutron fluence. In addition, the dynamic loss induced by the optical relay is very low compared to a fiber-optic bundle. The robustness has been checked and extrapolation to NIF or LMJ radiative constraints leads us to expect the diagnostic will be successful. Therefore, such an optical relay presents a hardened architecture and could be used as a diagnostic.

Radiation-tolerance studies of a complementary metal-oxide-semiconductor (CMOS) image sensor used in plasma diagnostics have been performed in a collaboration with CEA, the Institut Supérieur de l'Aéronautique et de l'Espace (ISAE, Toulouse), and the University of Saint-Etienne. Previous experiments performed in April 2012 demonstrated the relevance of the global reset functionality. The CMOS sensor is now part of a basic x-ray imaging diagnostic composed of a pinhole array and a thin layer of P43 (a long-decay-time scintillator) layered on the sensor surface (see Fig. 136.150). This diagnostic was inserted via a ten-inch manipulator (TIM) into the chamber and exposed to neutron yields produced by OMEGA DT shots in an attempt to record an x-ray self-emission image of the imploding target. As expected, the global reset mode significantly reduced the transient perturbation (parasitic white pixels) without degrading the image quality (see Fig. 136.151), but the

x-ray image resolution was very poor due to the bad quality of the scintillator deposition on the sensor.

Nevertheless, this first attempt was successful and improvements in the experiment design will be completed for the next neutron campaign in 2014.

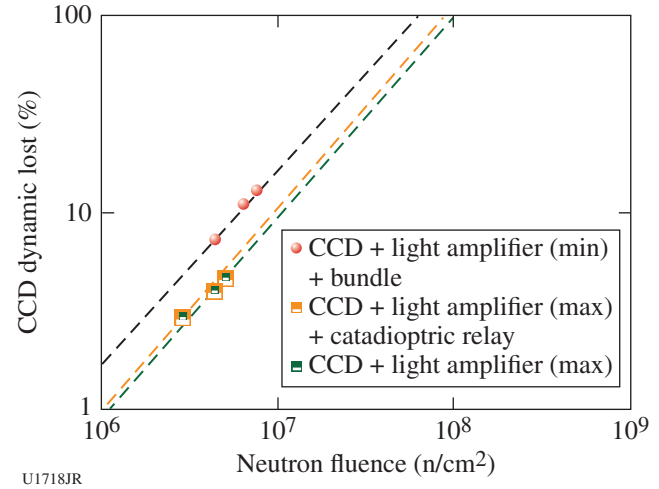


Figure 136.149 Parasitic signal intensity converted into a charge-coupled-device (CCD) dynamic-range loss.

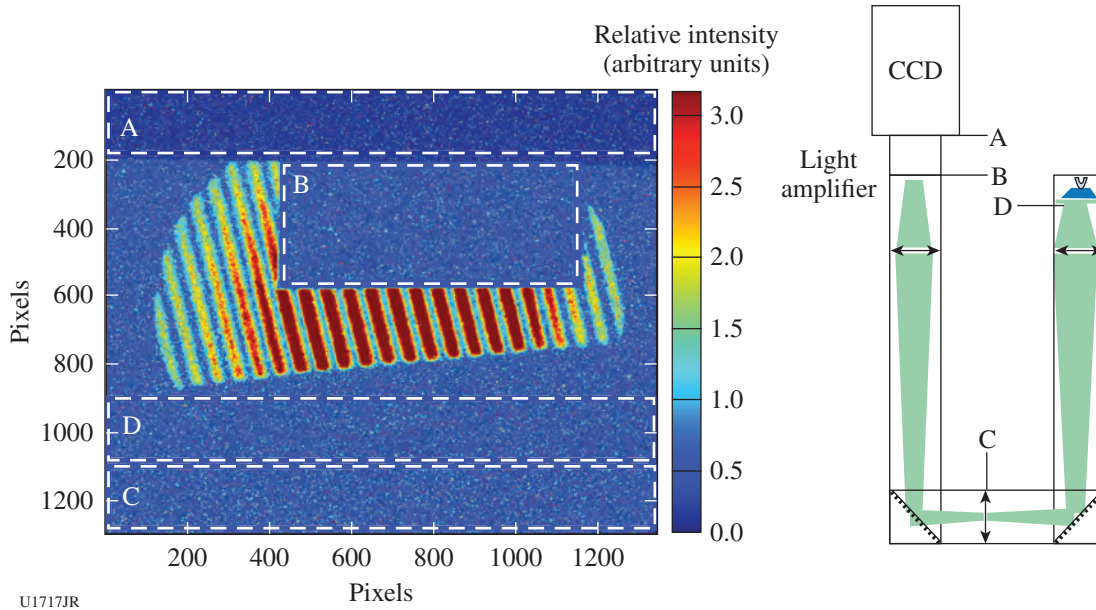


Figure 136.148 Typical image recording on the optical-relay benchmark for neutron yield of  $10^{13}$ . Four masks distributed along the optical path isolate four zones into the image.

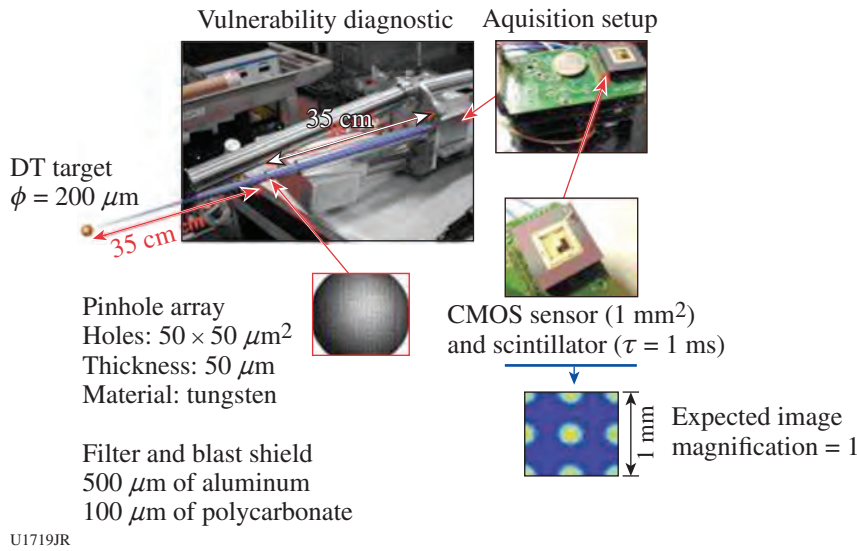


Figure 136.150  
Basic x-ray imaging diagnostic experimental setup.

### Diagnostic Development

The DEMIN (detector Micromegas for neutrons) neutron spectrometer<sup>64</sup> designed by CEA was successfully qualified and tested on OMEGA in FY13. DEMIN is based on a neutron-to-proton converter (CH foil, 2 mm thick) followed by a thin Micromegas chamber (600  $\mu\text{m}$  thick) (Ref. 65). Neutrons are detected individually on the striped Micromegas anode and neutron energy is measured by the time-of-flight technique. Because of the thin Micromegas chamber dimensions, the signals exhibit good timing properties [ $\sim 2$ -ns rise time for a good energy resolution and  $\sim 3$ -ns full width at half maximum (FWHM) to record more than one neutron per strip, important for obtaining enough statistics in the final spectrum]. This original setup makes the diagnostic rather insensitive to gamma rays since the gas-ionization probability for an electron is low, compared to recoil protons (see Fig. 136.152). DEMIN is, therefore, designed to measure the areal density  $\langle \rho R \rangle$  in high-neutron-yield implosions by detecting tertiary or secondary neutrons in DT or DD implosions, respectively.

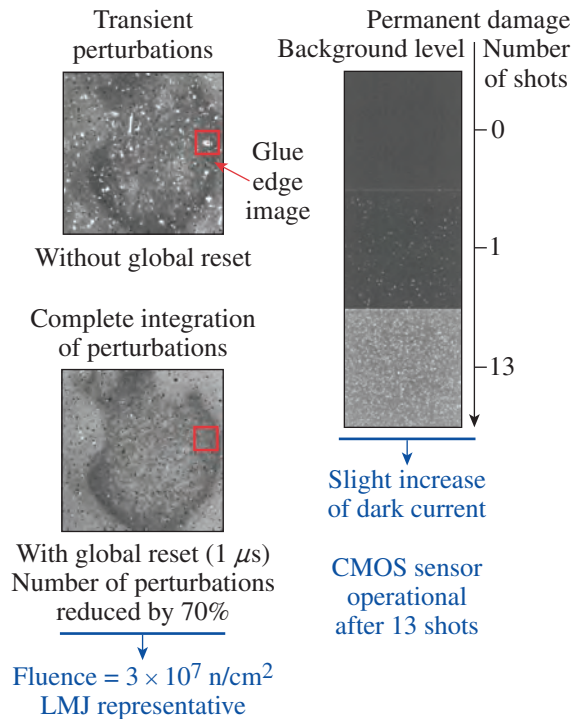
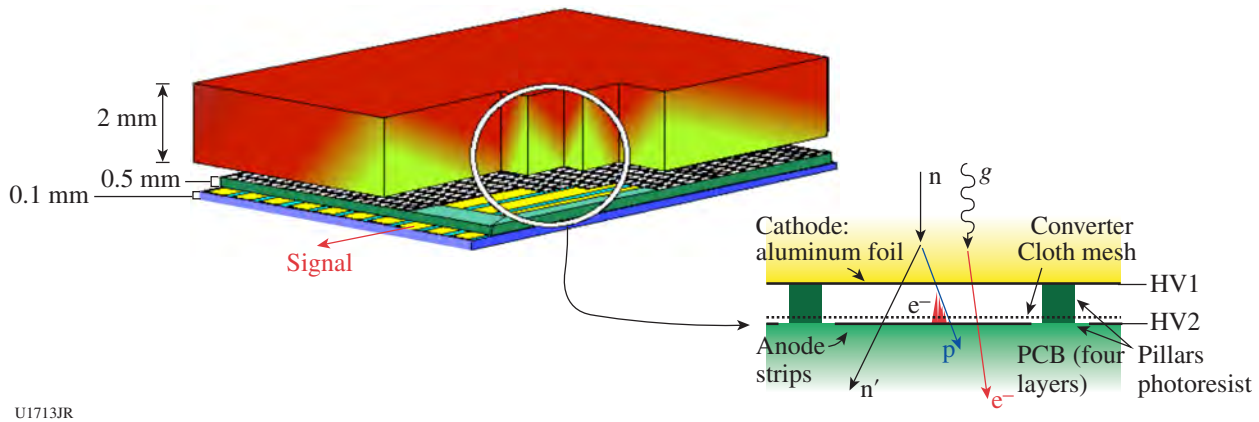


Figure 136.151  
Typical image recording for a  $10^{13}$  neutron yield. The global-reset mode proved its efficiency and the CMOS sensor was still operational after 13 shots, even though a slight increase of dark current was observed.

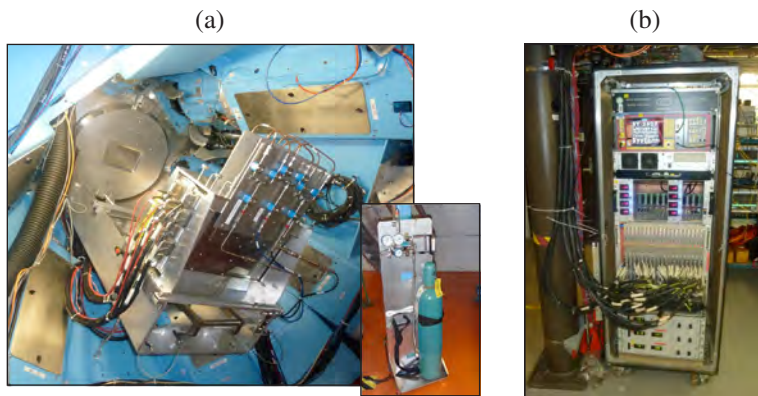
In November 2012 and March 2013, DEMIN was tested on TT (11 shots) and DT (13 shots) gas implosions. Its first use in November was made possible only with the help and involvement of all LLE teams. The aim of these experiments was to test the diagnostic in a harsh environment, to show the capability to measure individual neutrons after the intense 14-MeV peak, and to verify the insensitivity to gamma rays. Prior to the experiments, DEMIN was fully qualified on OMEGA. DEMIN is positioned on the personnel access port (H20), at 2.84 m from TCC (see Fig. 136.153). The aluminum



U1713JR

Figure 136.152

Schematic view of the DEMIN concept. Ionization electrons are produced along the path of scattered protons. They drift and are amplified due to the polarizations and are finally detected on the strips. Conversely, electrons produced by  $\gamma$  rays go through the gaps with a low-ionization probability.



U1714JR

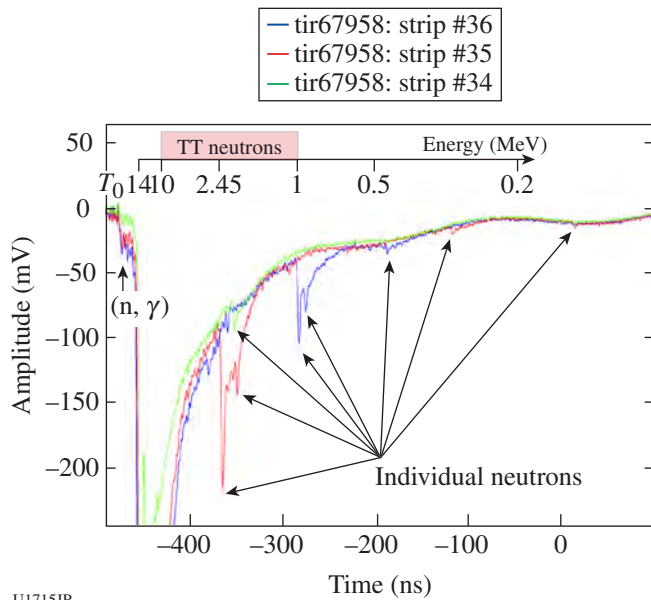
Figure 136.153

DEMIN experimental setup. (a) DEMIN 160-channel prototype positioned on the ManHatch port, viewing the thinned aluminum window. Inset: Part of the gas-distribution system, designed by LLE teams. (b) Electronic bay (acquisition system, HV and LV power supply, etc.) located in La Cave.

window was reduced to a 5-mm thickness by LLE staff to take into account DEMIN constraints. The gas-distribution system (gas bottle, tubing, manifold, pressure gauges, etc.), was designed by LLE's Mechanical Design Group and is fully operational. A gas mixture consisting of He (89%), isobutan (5%), and  $\text{CF}_4$  (6%) was used to achieve correct signal shapes. For these experiments, a 160-channel prototype was tested. The data-acquisition system, composed of 20 eight-channel digitizer boards,<sup>66</sup> was located in La Cave. Data-acquisition and Micromegas high voltages were remotely controlled to avoid manual intervention between shots.

Raw DEMIN signals, recorded on a TT implosion (shot 67958,  $Y_{14 \text{ MeV}} = 3.5 \times 10^{12}$ ,  $Y_{\text{TT}} \sim 1.5 \times 10^{12}$ ) are presented

for three adjacent strips in Fig. 136.154. After a saturated 14-MeV peak, individual neutrons were clearly identified, with decreasing energy according to their time of flight. TT neutrons and sub-MeV neutrons are also detected. The intensity of an individual neutron signal is not proportional to neutron energy, since it depends on the recoil proton-deposited energy in the gas. Therefore, neutron energy can be retrieved only by the neutron arrival time. Before the arrival of 14-MeV neutrons, we observed small signals caused by gamma rays produced by the interaction of 14-MeV neutrons on the aluminum chamber, showing good insensitivity to gamma rays. Nevertheless, a 5-mm lead shielding is necessary to avoid direct gas ionization by an intense x-ray flux. Signals exhibit a good signal-to-noise ratio and no cross-talk between strips was observed.



U1715JR

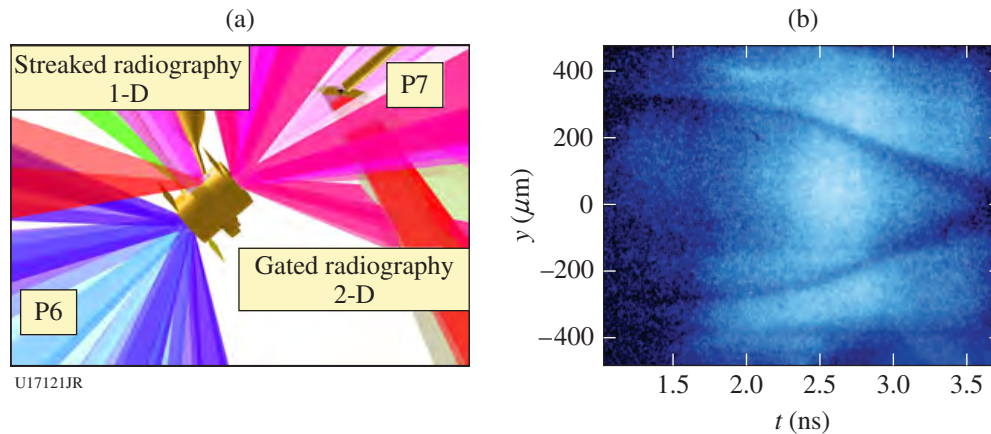
Figure 136.154  
Raw DEMIN signals recorded on three adjacent DEMIN strips for a TT implosion (shot 67958,  $Y_{14 \text{ MeV}} = 3.5 \times 10^{12}$ ).

### Convergent Ablation Measurements Using a Gas-Filled Rugby Hohraum on OMEGA

The baseline design for implosion experiments on the LMJ relies on a rugby-shaped hohlraum, which presents significant advantages in terms of laser-plasma interaction (LPI) mitigation,<sup>67</sup> coupling efficiency, and symmetry control with energy

balance.<sup>68</sup> The increased x-ray flux on capsules in the rugby hohlraum compared to a classical cylindrical hohlraum was subsequently confirmed at the OMEGA scale by enhanced fusion performances.<sup>69</sup> It is, nevertheless, important to acquire convergent ablation measurements<sup>70</sup> to assess the implosion velocity, a key metric for implosion performance. Convergent-ablation experiments with a gas-filled rugby hohlraum were, therefore, performed at the Omega Laser Facility.

A time-resolved 1-D streaked radiography of the capsule implosion [see Fig. 136.155(a)] was acquired in the direction perpendicular to the hohlraum axis, whereas a 2-D gated radiography was acquired on an x-ray framing camera at the same time along the hohlraum axis. The implosion trajectory was measured for various kinds of uniformly doped ablaters, including germanium-doped and silicon-doped polymers (CH), at two different doping fractions (2% and 4% by atom). It has, in fact, been demonstrated that Si-doped ablaters are more efficient than Ge-doped ones at the NIF scale.<sup>70</sup> A typical backlight implosion is shown in Fig. 136.155(b) for the case of a silicon-doped polymer (4% atomic fraction) with an initial ablator thickness of 55  $\mu\text{m}$ . The position of the external limb of the capsule could easily be extracted by an automatic edge-detection algorithm. The experimental implosion trajectory is compared with an FCI2 post-processed radiograph [see Fig. 136.156(a)]. One should notice that fully integrated 2-D simulations (including hohlraum and capsule) are necessary to describe the dynamics of the implosion. Preliminary post-shot



U17121JR

Figure 136.155

(a) Experimental configuration along P6/P7. The streaked implosion radiography was performed toward H14, perpendicular to the hohlraum axis. (b) Typical streaked radiography on a capsule implosion in a gas-filled rugby hohlraum.

simulations are shown in Fig. 136.156. The general tendency is that the simulated trajectories converge slightly earlier than the experimental radiographs, which is consistent with the late bang times (~200 to 300 ps) measured in rugby implosion experiments on OMEGA.

Figure 136.156(b), however, shows that the final limb velocity does not show an important velocity deficit as observed in NIF implosions. In that case, the final limb velocity is close to  $200 \mu\text{m/ns}^1$  ( $\pm 20 \mu\text{m/ns}^1$ ) and FCI2 simulations remain in the error bars of the measurements. Final implosion velocities in excess of  $300 \mu\text{m/ns}^1$  were achieved even in the case of thinner ablaters. This rich implosion database will be used to benchmark FCI2 simulations of germanium and silicon-doped ablaters and to test the rocket model in the high-ablation regime limit.<sup>71</sup>

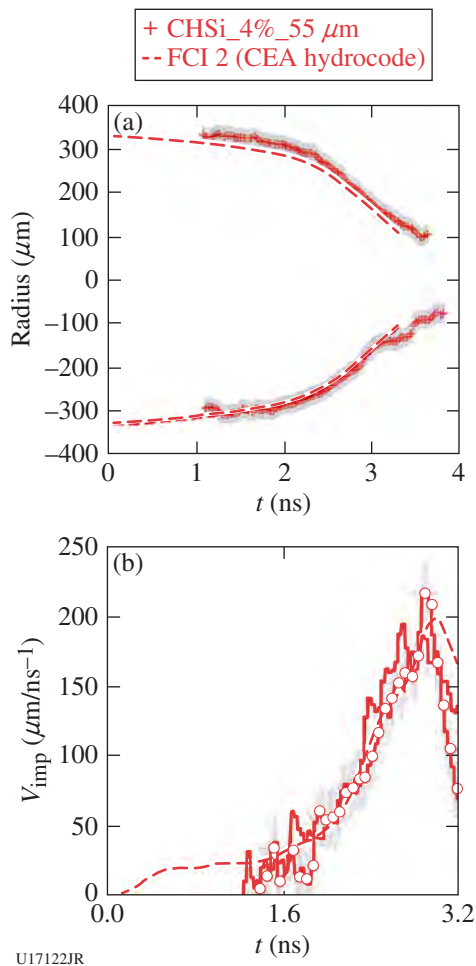


Figure 136.156  
 (a) Comparison of experimental limb trajectory with FCI2 post-processed simulations. (b) Comparison of experimental and simulated implosion velocities.

### Laser-Imprint Mitigation Using Underdense Foams

Laser-beam smoothing by parametric instabilities in low-density foams has been observed in previous experiments.<sup>72</sup> During the ImprintMit-13A campaign on OMEGA, we investigated for the first time the effects of low-density foams on the subsequent Rayleigh–Taylor growth.

The foams used in this campaign—manufactured at Lebedev Institute—were low-density  $\text{C}_{15}\text{H}_{20}\text{O}_6$  aerogels with an  $\sim 1\text{-}\mu\text{m}$  pore size. They were formed in the center of a Cu washer that was glued to a  $15\text{-}\mu\text{m}$ -thick CH foil. A 1-mm-wide slit in the washer side allowed us to measure the self-emission from the ionization wave propagating through the foam and from the accelerated CH foil. The foam was used to mitigate the laser imprint. Indeed, during its propagation through the foam plasma, the laser drive's parametric instabilities, such as forward stimulated Brillouin scattering and filamentation, led to an effective smoothing of the hot-spot pattern. Because of the low density of the foam, the ionization was supersonic and no shock wave was created.

Figure 136.157 shows the experimental configuration. Specific phase plates (M30 and M60) that created 2-D intensity modulations were mounted on one of the drive beams. Imprint conditions were therefore well known and reproducible from shot to shot. The target was either a CH foil alone (to make a reference imprint measurement) or a foil glued to a washer

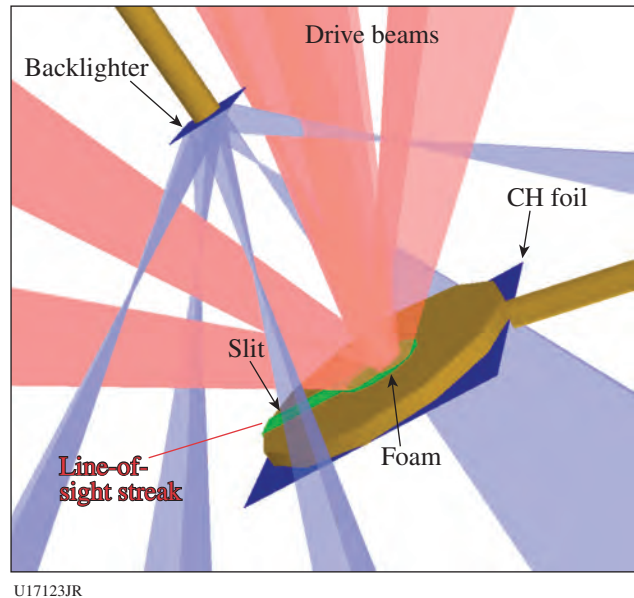


Figure 136.157  
 Experimental configuration for the ImprintMit-13A campaign. Drive beams (red) illuminating the underdense foam and backlighter beams (blue) are represented.

containing the foam of various densities: 5, 7, or 10 mg/cm<sup>3</sup>. The drive pulse was either a 2-ns square pulse at  $3 \times 10^{14}$  W/cm<sup>2</sup> (CH foil alone) or a 2-ns step pulse with a higher intensity during the first nanosecond (target with foam) to balance the energy absorbed in the foam and maintain the laser drive on the CH foil. The growth of target modulations has been measured with x-ray face-on radiography using a uranium backlighter (~1.3 keV) on an x-ray framing camera (XRFC) with 10- $\mu$ m spatial resolution and 80-ps temporal resolution. The side view self-emission was measured through the slit with a streak camera and showed that trajectories of the foil with and without foam were equivalent [as shown in Figs. 136.158(a) and 136.158(b)].

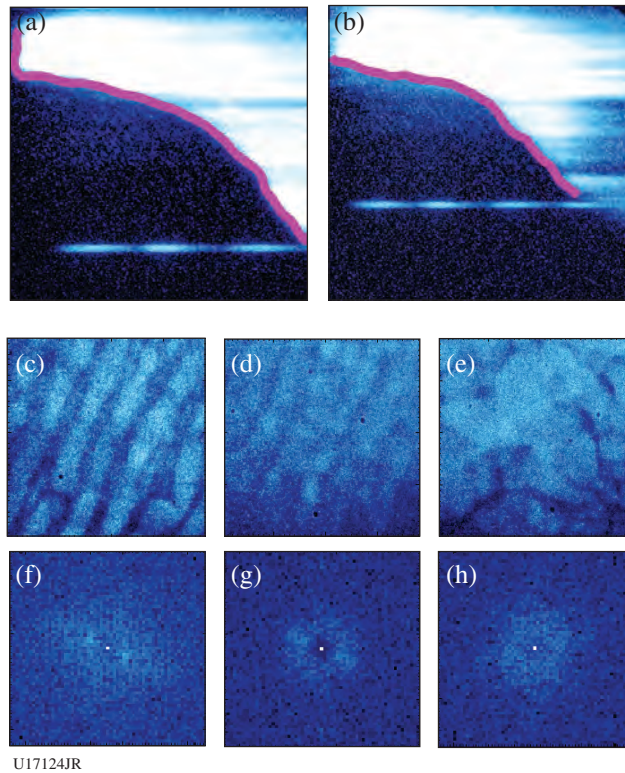


Figure 136.158  
Self-emission streak-camera measurements for a foil (a) without and (b) with foam; [(c)–(e)] x-ray framing-camera (XRFC) radiographies and [(f)–(h)] corresponding 2-D Fourier spectra [(c),(f)] imprinted by the M60 phase plate on a CH foil, [(d),(g)] CH foils with 7-mg/cm<sup>3</sup> foam, and [(e),(h)] 5-mg/cm<sup>3</sup> foam 1.41 ns, 1.35 ns, and 1.19 ns, respectively, after the beginning of the acceleration of the ablation front.

Figure 136.158 shows typical experimental XRFC radiographies and the corresponding 2-D Fourier spectra. The imprinting phase plate was the M60, which means that the initial perturbations are 2-D 60- $\mu$ m-wavelength modulations. These modulations were observed on the first radiography of a

target without foam. To summarize the analysis of the images in Fig. 136.158, the initial 2-D pattern imprinted without foam was smoothed in the case of the 7-mg/cm<sup>3</sup> foam and completely disappeared with the 5-mg/cm<sup>3</sup> foam. On the other hand, 3-D modulations appeared with the foams, especially with the one at 5 mg/cm<sup>3</sup>. The mechanisms that created those modulations are not completely understood but different options are being investigated: the nonuniformities imprinted by the SG4 beams, the roughness of the CH foil, or an effect of the foam during early laser propagation.

During the experimental campaign ImprintMit-13A on OMEGA, we demonstrated for the first time the effect of low-density foams on the hydrodynamic instability mitigation. A smoothing of the initial pre-imposed perturbation is clearly shown. Several observed features must be investigated further, however, and the interpretation of the experiments is still in progress.

## REFERENCES

1. K. Yirak *et al.*, *High Energy Density Phys.* **9**, 251 (2013).
2. G. Gregori *et al.*, *Astrophys. J.* **527**, L113 (1999).
3. G. Gregori *et al.*, *Astrophys. J. Lett.* **543**, 775 (2000).
4. P. Hartigan, J. Palmer, and L. I. Cleeves, *High Energy Density Phys.* **8**, 313 (2012).
5. V. E. Fortov *et al.*, *Phys. Rev. Lett.* **99**, 185001 (2007).
6. F. Soubiran *et al.*, *Phys. Rev. B* **86**, 115102 (2012).
7. P. Loubeyre, S. Brygoo, J. Eggert, P. M. Celliers, D. K. Spaulding, J. R. Rygg, T. R. Boehly, G. W. Collins, and R. Jeanloz, *Phys. Rev. B* **86**, 144115 (2012).
8. P. M. Celliers, P. Loubeyre, J. H. Eggert, S. Brygoo, R. S. McWilliams, D. G. Hicks, T. R. Boehly, R. Jeanloz, and G. W. Collins, *Phys. Rev. Lett.* **104**, 184503 (2010).
9. M. J.-E. Manuel, C. K. Li, F. H. Séguin, N. Sinenian, J. A. Frenje, D. T. Casey, R. D. Petrasso, J. D. Hager, R. Betti, S. X. Hu, J. Delettrez, and D. D. Meyerhofer, *Phys. Plasmas* **20**, 056301 (2013).
10. C. K. Li *et al.*, *New J. Phys.* **15**, 025040 (2013).
11. C. K. Li, F. H. Séguin, J. A. Frenje, N. Sinenian, M. J. Rosenberg, M. J.-E. Manuel, H. G. Rinderknecht, A. B. Zylstra, R. D. Petrasso, P. A. Amendt, O. L. Landen, A. J. Mackinnon, R. P. J. Town, S. C. Wilks, R. Betti, D. D. Meyerhofer, J. M. Soures, J. Hund, J. D. Kilkenny, and A. Nikroo, *Nucl. Fusion* **53**, 073022 (2013).
12. N. Sinenian *et al.*, *Plasma Phys. Control. Fusion* **55**, 045001 (2013).
13. D. T. Casey, J. A. Frenje, M. Gatu Johnson, F. H. Séguin, C. K. Li, R. D. Petrasso, V. Yu Glebov, J. Katz, J. Magoon, D. D. Meyerhofer, T. C.

- Sangster, M. Shoup, J. Ulreich, R. C. Ashabranner, R. M. Bionta, A. C. Carpenter, B. Felker, H. Y. Khater, S. LePape, A. MacKinnon, M. A. McKernan, M. Moran, J. R. Rygg, M. F. Yeoman, R. Zacharias, R. J. Leeper, K. Fletcher, M. Farrell, D. Jasion, J. Kilkenny, and R. Paguio, *Rev. Sci. Instrum.* **84**, 043506 (2013).
14. N. Sinenian, W. Theobald, J. A. Frenje, C. Stoeckl, F. H. Séguin, C. K. Li, R. D. Petrasso, and R. B. Stephens, *Phys. Plasmas* **19**, 112708 (2012).
  15. M. J. Rosenberg, J. S. Ross, C. K. Li, R. P. J. Town, F. H. Séguin, J. A. Frenje, D. H. Froula, and R. D. Petrasso, *Phys. Rev. E* **86**, 056407 (2012).
  16. M. J.-E. Manuel, "Rayleigh-Taylor-Induced Electromagnetic Fields in Laser-Produced Plasmas," Ph.D. thesis, Massachusetts Institute of Technology, 2013.
  17. N. Sinenian, "Fast-Ion Spectrometry of ICF Implosions and Laser-Foil Experiments at the Omega and MTW Laser Facilities," Ph.D. thesis, Massachusetts Institute of Technology, 2013.
  18. T. R. Boehly, D. L. Brown, R. S. Craxton, R. L. Keck, J. P. Knauer, J. H. Kelly, T. J. Kessler, S. A. Kumpan, S. J. Loucks, S. A. Letzring, F. J. Marshall, R. L. McCrory, S. F. B. Morse, W. Seka, J. M. Soures, and C. P. Verdon, *Opt. Commun.* **133**, 495 (1997).
  19. L. J. Waxer, D. N. Maywar, J. H. Kelly, T. J. Kessler, B. E. Kruschwitz, S. J. Loucks, R. L. McCrory, D. D. Meyerhofer, S. F. B. Morse, C. Stoeckl, and J. D. Zuegel, *Opt. Photonics News* **16**, 30 (2005).
  20. C. K. Li, F. H. Séguin, J. A. Frenje, J. R. Rygg, R. D. Petrasso, R. P. J. Town, P. A. Amendt, S. P. Hatchett, O. L. Landen, A. J. Mackinnon, P. K. Patel, V. Smalyuk, J. P. Knauer, T. C. Sangster, and C. Stoeckl, *Rev. Sci. Instrum.* **77**, 10E725 (2006).
  21. J. R. Rygg, F. H. Séguin, C. K. Li, J. A. Frenje, M. J.-E. Manuel, R. D. Petrasso, R. Betti, J. A. Delettrez, O. V. Gotchev, J. P. Knauer, D. D. Meyerhofer, F. J. Marshall, C. Stoeckl, and W. Theobald, *Science* **319**, 1223 (2008).
  22. F. H. Séguin, C. K. Li, M. J.-E. Manuel, H. G. Rinderknecht, N. Sinenian, J. A. Frenje, J. R. Rygg, D. G. Hicks, R. D. Petrasso, J. Delettrez, R. Betti, F. J. Marshall, and V. A. Smalyuk, *Phys. Plasmas* **19**, 012701 (2012).
  23. D. A. Tidman and R. A. Shanny, *Phys. Fluids* **17**, 1207 (1974).
  24. T. Bartal *et al.*, *Nat. Phys.* **8**, 139 (2012).
  25. B. Qiao *et al.*, *Phys. Rev. E* **87**, 013108 (2013).
  26. N. L. Kugland, D. D. Ryutov, P. Y. Chang, R. P. Drake, G. Fiksel, D. H. Froula, S. H. Glenzer, G. Gregori, M. Grosskopf, M. Koenig, Y. Kuramitsu, C. Kuranz, M. C. Levy, E. Liang, J. Meinecke, F. Miniati, T. Morita, A. Pelka, C. Plechaty, R. Presura, A. Ravasio, B. A. Remington, B. Reville, J. S. Ross, Y. Sakawa, A. Spitkovsky, H. Takabe, and H. S. Park, *Nat. Phys.* **8**, 809 (2012).
  27. M. Wei, R. Mishra, S. Chawla, A. Sorokovikova, F. N. Beg, C. Chen, H. Chen, R. Fedosejevs, J. Jaquez, L. C. Jarrott, G. Kemp, M. Key, J. Kim, A. Link, H. McLean, A. Morace, V. M. Ovchinnikov, P. K. Patel, Y. Ping, B. Qiao, H. Sawada, Y. Sentoku, C. Stoeckl, W. Theobald, and R. B. Stephens, in *24th Fusion Energy Conference on CD-ROM (IAEA, Vienna, 2013)*, Paper IFE/P6-06.
  28. A. Sorokovikova *et al.*, "Intense Laser-Plasma Interaction and Fast Electron Generation in Multi-Picosecond Time Scales," to be submitted to *Physical Review Letters*.
  29. A. J. Kemp and L. Divol, *Phys. Rev. Lett.* **109**, 195005 (2012).
  30. S. Chawla *et al.*, *Phys. Rev. Lett.* **110**, 025001 (2013).
  31. H. Chen, S. C. Wilks, J. D. Bonlie, E. P. Liang, J. Myatt, D. F. Price, D. D. Meyerhofer, and P. Beiersdorfer, *Phys. Rev. Lett.* **102**, 105001 (2009).
  32. H. Chen, S. C. Wilks, D. D. Meyerhofer, J. Bonlie, C. D. Chen, S. N. Chen, C. Courtois, L. Elbersson, G. Gregori, W. Krueer, O. Landoas, J. Mithen, J. Myatt, C. D. Murphy, P. Nilson, D. Price, M. Schneider, R. Shepherd, C. Stoeckl, M. Tabak, R. Tommasini, and P. Beiersdorfer, *Phys. Rev. Lett.* **105**, 015003 (2010).
  33. O. V. Gotchev, J. P. Knauer, P. Y. Chang, N. W. Jang, M. J. Shoup III, D. D. Meyerhofer, and R. Betti, *Rev. Sci. Instrum.* **80**, 043504 (2009).
  34. J. Myatt, A. V. Maximov, R. W. Short, and D. D. Meyerhofer, *Bull. Am. Phys. Soc.* **52**, 66 (2007).
  35. H. Chen, D. D. Meyerhofer, S. C. Wilks, R. Cauble, F. Dollar, K. Falk, G. Gregori, A. Hazi, E. I. Moses, C. D. Murphy, J. Myatt, J. Park, J. Seely, R. Shepherd, A. Spitkovsky, C. Stoeckl, C. I. Szabo, R. Tommasini, C. Zулlick, and P. Beiersdorfer, *High Energy Density Phys.* **7**, 225 (2011).
  36. M. Tabak *et al.*, *Phys. Plasmas* **1**, 1626 (1994).
  37. D. H. Froula, R. Boni, M. Bedzyk, R. S. Craxton, F. Ehrne, S. Ivancic, R. Jungquist, M. J. Shoup, W. Theobald, D. Weiner, N. L. Kugland, and M. C. Rushford, *Rev. Sci. Instrum.* **83**, 10E523 (2012).
  38. D. Haberberger, presented at the Omega Laser Facility Users Group Workshop, Rochester, NY, 24–26 April 2013.
  39. J. S. Ross, S. H. Glenzer, P. Amendt, R. Berger, L. Divol, N. L. Kugland, O. L. Landen, C. Plechaty, B. Remington, D. Ryutov, W. Rozmus, D. H. Froula, G. Fiksel, C. Sorce, Y. Kuramitsu, T. Morita, Y. Sakawa, H. Takabe, R. P. Drake, M. Grosskopf, C. Kuranz, G. Gregori, J. Meinecke, C. D. Murphy, M. Koenig, A. Pelka, A. Ravasio, T. Vinci, E. Liang, R. Presura, A. Spitkovsky, F. Miniati, and H.-S. Park, *Phys. Plasmas* **19**, 056501 (2012).
  40. C. M. Huntington *et al.*, "Direct Observation of Electromagnetic Weibel Filamentation in Counter-Streaming Plasma Flows," to be published in *Nature*.
  41. N. L. Kugland, D. D. Ryutov, P. Y. Chang, R. P. Drake, G. Fiksel, D. H. Froula, S. H. Glenzer, G. Gregori, M. Grosskopf, M. Koenig, Y. Kuramitsu, C. Kuranz, M. C. Levy, E. Liang, J. Meinecke, F. Miniati, T. Morita, A. Pelka, C. Plechaty, R. Presura, A. Ravasio, B. A. Remington, B. Reville, J. S. Ross, Y. Sakawa, A. Spitkovsky, H. Takabe, and H. S. Park, *Nat. Phys.* **8**, 809 (2012).
  42. Y. Ping, D. G. Hicks, B. Yaakobi, F. Coppari, D. Fratanduono, S. Hamel, J. H. Eggert, J. R. Rygg, R. F. Smith, T. R. Boehly, and G. W. Collins, *Phys. Rev. Lett.* **111**, 065501 (2013).
  43. S. P. Regan, K. Falk, G. Gregori, P. B. Radha, S. X. Hu, T. R. Boehly, B. J. B. Crowley, S. H. Glenzer, O. L. Landen, D. O. Gericke,

- T. Döppner, D. D. Meyerhofer, C. D. Murphy, T. C. Sangster, and J. Vorberger, *Phys. Rev. Lett.* **109**, 265003 (2012).
44. W. Theobald, A. A. Solodov, C. Stoeckl, K. S. Anderson, R. Betti, T. R. Boehly, R. S. Craxton, J. A. Delettrez, C. Dorrer, J. A. Frenje, V. Yu. Glebov, H. Habara, K. A. Tanaka, J. P. Knauer, R. Lauck, F. J. Marshall, K. L. Marshall, D. D. Meyerhofer, P. M. Nilson, P. K. Patel, H. Chen, T. C. Sangster, W. Seka, N. Sinenian, T. Ma, F. N. Beg, E. Giraldez, and R. B. Stephens, *Phys. Plasmas* **18**, 056305 (2011).
  45. P. B. Radha, T. J. B. Collins, J. A. Delettrez, Y. Elbaz, R. Epstein, V. Yu. Glebov, V. N. Goncharov, R. L. Keck, J. P. Knauer, J. A. Marozas, F. J. Marshall, R. L. McCrory, P. W. McKenty, D. D. Meyerhofer, S. P. Regan, T. C. Sangster, W. Seka, D. Shvarts, S. Skupsky, Y. Srebro, and C. Stoeckl, *Phys. Plasmas* **12**, 056307 (2005).
  46. W. Theobald, A. A. Solodov, C. Stoeckl, V. Yu. Glebov, S. Ivancic, F. J. Marshall, G. McKiernan, C. Mileham, T. C. Sangster, F. N. Beg, C. Jarrott, E. Giraldez, R. B. Stephens, M. S. Wei, M. H. Key, H. McLean, and J. Santos, *Bull. Am. Phys. Soc.* **57**, 115 (2012).
  47. R. F. Heeter, S. B. Hansen, K. B. Fournier, M. E. Foord, D. H. Froula, A. J. Mackinnon, M. J. May, M. B. Schneider, and B. K. F. Young, *Phys. Rev. Lett.* **99**, 195001 (2007).
  48. J. R. Rygg, J. A. Frenje, C. K. Li, F. H. Séguin, R. D. Petrasso, J. A. Delettrez, V. Yu. Glebov, V. N. Goncharov, D. D. Meyerhofer, S. P. Regan, T. C. Sangster, and C. Stoeckl, *Phys. Plasmas* **13**, 052702 (2006).
  49. H. G. Rinderknecht, H. Sio, C. K. Li, A. B. Zylstra, M. J. Rosenberg, M. Gatu Johnson, J. A. Frenje, F. H. Séguin, R. D. Petrasso, J. Delettrez, V. Yu. Glebov, C. Stoeckl, T. C. Sangster, C. Bellei, P. Amendt, and S. Wilks, "Anomalous Reduction in the Shock Yield of Shock-Driven D<sup>3</sup>He Implosions at Omega," to be submitted to *Physical Review Letters*.
  50. H.-S. Park *et al.*, *Phys. Rev. Lett.* **104**, 135504 (2010).
  51. J. F. Barnes *et al.*, *J. Appl. Phys.* **45**, 727 (1974).
  52. H.-S. Park *et al.*, *Phys. Plasmas* **17**, 056314 (2010).
  53. N. R. Barton *et al.*, *J. Appl. Phys.* **109**, 073501 (2011).
  54. J. L. Belof *et al.*, *AIP Conf. Proc.* **1426**, 1521 (2012).
  55. Y. Ping, D. G. Hicks, B. Yaakobi, F. Coppari, J. Eggert, and G. W. Collins, "A Platform for XAFS Study of Dynamically Compressed Materials Above 1 Mbar," to be published in *Review of Scientific Instruments*.
  56. Y. K. Vohra and A. L. Ruoff, *Phys. Rev. B* **42**, 8651 (1990).
  57. H. K. Mao *et al.*, *Solid State Commun.* **74**, 1027 (1990).
  58. C. E. Ragan III *et al.*, Los Alamos National Laboratory, Los Alamos, NM, LA-UR-83-2081 (1983).
  59. J. Hama, K. Suito, and N. Kawakami, *Phys. Rev. B* **39**, 3351 (1989).
  60. A. L. Kritcher *et al.*, *Phys. Plasmas* **16**, 056308 (2009).
  61. P. P. Jenkins *et al.*, in *35th IEEE Photovoltaic Specialists Conference (PVSC), 2010* (IEEE, New York, 2010), pp. 002550–002553.
  62. J. R. Patterson *et al.*, *Rev. Sci. Instrum.* **83**, 10D725 (2012).
  63. K. B. Fournier, J. H. Satcher, M. J. May, J. F. Poco, C. M. Sorce, J. D. Colvin, S. B. Hansen, S. A. MacLaren, S. J. Moon, J. F. Davis, F. Girard, B. Villette, M. Primout, D. Babonneau, C. A. Coverdale, and D. E. Beutler, *Phys. Plasmas* **16**, 052703 (2009).
  64. M. Houry, E. Delagnes, D. Riz, B. Canaud, L. Disdier, F. Garaude, Y. Giomataris, V. Yu. Glebov, Ph. Legou, Ph. Rebourgeard, and C. Sangster, *Nucl. Instrum. Methods Phys. Res. A* **557**, 648 (2006).
  65. Y. Giomataris *et al.*, *Nucl. Instrum. Methods Phys. Res. A* **376**, 29 (1996).
  66. D. Breton, E. Delagnes, and M. Houry, *IEEE Trans. Nucl. Sci.* **52**, 2853 (2005).
  67. S. Laffite and P. Loiseau, *Phys. Plasmas* **17**, 102704 (2010).
  68. M. Vandenboomgaerde *et al.*, *Phys. Rev. Lett.* **99**, 065004 (2007).
  69. F. Philippe, A. Casner, T. Caillaud, O. Landoas, M. C. Monteil, S. Liberatore, H. S. Park, P. Amendt, H. Robey, C. Sorce, C. K. Li, F. Seguin, M. Rosenberg, R. Petrasso, V. Glebov, and C. Stoeckl, *Phys. Rev. Lett.* **104**, 035004 (2010).
  70. D. G. Hicks *et al.*, *Phys. Plasmas* **19**, 122702 (2012).
  71. Y. Saillard, *Nucl. Fusion* **46**, 1017 (2006).
  72. S. Depierreux, C. Labaune, D. T. Michel, C. Stenz, P. Nicholaï, M. Grech, G. Riazuelo, S. Weber, C. Riconda, V. T. Tikhonchuk, P. Loiseau, N. G. Borisenko, W. Nazarov, S. Hüller, D. Pesme, M. Casanova, J. Limpouch, C. Meyer, P. Di-Nicola, R. Wrobel, E. Alozy, P. Romary, G. Thiell, G. Soullié, C. Reverdin, and B. Villette, *Phys. Rev. Lett.* **102**, 195005 (2009).

---

## Publications and Conference Presentations

---

### Publications

---

- K. S. Anderson, R. Betti, P. W. McKenty, T. J. B. Collins, M. Hohenberger, W. Theobald, R. S. Craxton, J. A. Delettrez, M. Lafon, J. A. Marozas, R. Nora, S. Skupsky, and A. Shvydky, “A Polar-Drive Shock-Ignition Design for the National Ignition Facility,” *Phys. Plasmas* **20**, 056312 (2013).
- M. Barczys, S.-W. Bahk, M. Spilatro, D. Coppenger, E. Hill, T. H. Hinterman, R. W. Kidder, J. Puth, T. Touris, and J. D. Zuegel, “Deployment of a Spatial Light Modulator–Based Beam-Shaping System on the OMEGA EP Laser,” in *High Power Lasers for Fusion Research II*, edited by A. A. S. Awwal (SPIE, Bellingham, WA, 2013), Vol. 8602, Paper 86020F.
- B. Beeman, A. G. MacPhee, J. R. Kimbrough, G. A. Lacaille, M. A. Barrios, J. Emig, J. R. Hunter, E. K. Miller, and W. R. Donaldson, “Mach-Zehnder Modulator Performance Using the Comet Laser Facility and Implications for Use on NIF,” in *Target Diagnostics Physics and Engineering for Inertial Confinement Fusion*, edited by P. Bell and G. P. Grim (SPIE, Bellingham, WA, 2012), Vol. 8505, Paper 850507.
- J. R. Davies, R. Betti, P. M. Nilson, and A. A. Solodov, “Copper K-Shell Emission Cross Sections for Laser–Solid Experiments,” *Phys. Plasmas* **20**, 083118 (2013).
- C. Dorrer, “Analysis of Pulse Replicators for High-Bandwidth, High-Dynamic-Range, Single-Shot Optical Characterization,” *J. Lightwave Technol.* **31**, 1374 (2013).
- C. Dorrer, “Analysis of the Chromaticity of Near-Field Binary Beam Shapers,” *Appl. Opt.* **52**, 3368 (2013).
- D. H. Froula, T. J. Kessler, I. V. Igumenshchev, R. Betti, V. N. Goncharov, H. Huang, S. X. Hu, E. Hill, J. H. Kelly, D. D. Meyerhofer, A. Shvydky, and J. D. Zuegel, “Mitigation of Cross-Beam Energy Transfer: Implication of Two-State Focal Zooming on OMEGA,” *Phys. Plasmas* **20**, 082704 (2013).
- D. H. Froula, D. T. Michel, I. V. Igumenshchev, S. X. Hu, B. Yaakobi, J. F. Myatt, D. H. Edgell, R. Follett, V. Yu. Glebov, V. N. Goncharov, T. J. Kessler, A. V. Maximov, P. B. Radha, T. C. Sangster, W. Seka, R. W. Short, A. A. Solodov, C. Sorce, and C. Stoeckl, “Laser–Plasma Interactions in Direct-Drive Ignition Plasmas,” *Plasma Phys. Control. Fusion* **54**, 124016 (2012).
- L. Gao, P. M. Nilson, I. V. Igumenshchev, G. Fiksel, R. Yan, J. R. Davies, D. Martinez, V. Smalyuk, M. G. Haines, E. G. Blackman, D. H. Froula, R. Betti, and D. D. Meyerhofer, “Observation of Self-Similarity in the Magnetic Fields Generated by the Ablative Nonlinear Rayleigh–Taylor Instability,” *Phys. Rev. Lett.* **110**, 185003 (2013).
- V. N. Goncharov, “Cryogenic Deuterium and Deuterium–Tritium Direct–Drive Implosions on Omega,” in *Laser-Plasma Interactions and Applications*, edited by P. McKenna, D. Neely, R. Bingham, and D. A. Jaroszynski, Scottish Graduate Series (Springer, Switzerland, 2013), Chap. 7, pp. 135–183.
- D. R. Harding and W. T. Shmayda, “Stress- and Radiation-Induced Swelling in Plastic Capsules,” *Fusion Sci. Technol.* **63**, 125 (2013).
- D. R. Harding, M. D. Wittman, and D. H. Edgell, “Considerations and Requirements for Providing Cryogenic Targets for Direct-Drive Inertial Fusion Implosions at the National Ignition Facility,” *Fusion Sci. Technol.* **63**, 95 (2013).
- H. P. Howard, A. F. Aiello, J. G. Dressler, N. R. Edwards, T. J. Kessler, A. A. Kozlov, I. R. T. Manwaring, K. L. Marshall, J. B. Oliver, S. Papernov, A. L. Rigatti, A. N. Roux, A. W. Schmid, N. P. Slaney, C. C. Smith, B. N. Taylor, and S. D. Jacobs, “Improving the Performance of High-Laser-Damage-Threshold, Multilayer Dielectric Pulse-Compression Gratings Through Low-Temperature Chemical Cleaning,” *Appl. Opt.* **52**, 1682 (2013).
- S. X. Hu, “Boosting Photoabsorption by Attosecond Control of Electron Correlation,” *Phys. Rev. Lett.* **111**, 123003 (2013).
- S. X. Hu, D. T. Michel, D. H. Edgell, D. H. Froula, R. K. Follett, V. N. Goncharov, J. F. Myatt, S. Skupsky, and B. Yaakobi,

“Hydrodynamic Simulations of Long-Scale-Length Two-Plasma–Decay Experiments at the Omega Laser Facility,” *Phys. Plasmas* **20**, 032704 (2013).

I. V. Igumenshchev, D. H. Froula, D. H. Edgell, V. N. Goncharov, T. J. Kessler, F. J. Marshall, R. L. McCrory, P. W. McKenty, D. D. Meyerhofer, D. T. Michel, T. C. Sangster, W. Seka, and S. Skupsky, “Laser-Beam Zooming to Mitigate Crossed-Beam Energy Losses in Direct-Drive Implosions,” *Phys. Rev. Lett.* **110**, 145001 (2013).

I. V. Igumenshchev, V. N. Goncharov, W. T. Shmayda, D. R. Harding, T. C. Sangster, and D. D. Meyerhofer, “Effects of Local Defect Growth in Direct-Drive Cryogenic Implosions on OMEGA,” *Phys. Plasmas* **20**, 082703 (2013).

J. H. Kelly, A. Shvydky, J. A. Marozas, M. J. Guardalben, B. E. Kruschwitz, L. J. Waxer, C. Dorrer, E. Hill, A. V. Okishev, and J.-M. Di Nicola, “Simulations of the Propagation of Multiple-FM Smoothing by Spectral Dispersion on OMEGA EP,” in *High Power Lasers for Fusion Research II*, edited by A. A. S. Awwal (SPIE, Bellingham, WA, 2013), Vol. 8602, Paper 86020D.

B. E. Kruschwitz, J. H. Kelly, C. Dorrer, A. V. Okishev, L. J. Waxer, G. Balonek, I. A. Begishev, W. Bittle, A. Consentino, R. Cuffney, E. Hill, J. A. Marozas, M. Moore, R. G. Roides, and J. D. Zuegel, “Commissioning of a Multiple-Frequency Modulation Smoothing by Spectral Dispersion Demonstration System on OMEGA EP,” in *High Power Lasers for Fusion Research II*, edited by A. A. S. Awwal (SPIE, Bellingham, WA, 2013), Vol. 8602, Paper 86020E.

M. Lafon, X. Ribeyre, and G. Schurtz, “Optimal Conditions for Shock Ignition of Scaled Cryogenic Deuterium-Tritium Targets,” *Phys. Plasmas* **20**, 022708 (2013).

J. Li, J. R. Davies, T. Ma, W. B. Mori, C. Ren, A. A. Solodov, W. Theobald, and J. Tonge, “Hot-Electron Generation from Laser–Pre-Plasma Interactions in Cone-Guided Fast Ignition,” *Phys. Plasmas* **20**, 052706 (2013).

K. L. Marshall, C. Dorrer, M. Vargas, A. Gnolek, M. Statt, and S.-H. Chen, “Photoaligned Liquid Crystal Devices for High-Peak-Power Laser Applications,” in *Liquid Crystals XVI*, edited by I. C. Khoo (SPIE, Bellingham, WA, 2012), Vol. 8475, Paper 84750U (invited).

R. L. McCrory, R. Betti, T. R. Boehly, D. T. Casey, T. J. B. Collins, R. S. Craxton, J. A. Delettrez, D. H. Edgell, R. Epstein,

J. A. Frenje, D. H. Froula, M. Gatu-Johnson, V. Yu. Glebov, V. N. Goncharov, D. R. Harding, M. Hohenberger, S. X. Hu, I. V. Igumenshchev, T. J. Kessler, J. P. Knauer, C. K. Li, J. A. Marozas, F. J. Marshall, P. W. McKenty, D. D. Meyerhofer, D. T. Michel, J. F. Myatt, P. M. Nilson, S. J. Padalino, R. D. Petrasso, P. B. Radha, S. P. Regan, T. C. Sangster, F. H. Séguin, W. Seka, R. W. Short, A. Shvydky, S. Skupsky, J. M. Soures, C. Stoeckl, W. Theobald, B. Yaakobi, and J. D. Zuegel, “Progress Toward Polar-Drive Ignition for the NIF,” *Nucl. Fusion* **53**, 113021 (2013).

K. Mehrotra, H. P. Howard, S. D. Jacobs, and J. C. Lambropoulos, “Mechanical Characterization of ‘Blister’ Defects on Optical Oxide Multilayers Using Nanoindentation,” in *Nanocomposites, Nanostructures and Heterostructures of Correlated Oxide Systems*, edited by T. Endo, H. Nishikawa, N. Iwata, A. Bhattacharya, and L. W. Martin, *Mat. Res. Soc. Symp. Proc. Vol. 1454* (Cambridge University Press, Cambridge, England, 2012), pp. 215–220.

K. Mehrotra, H. P. Howard, S. D. Jacobs, and J. C. Lambropoulos, “Nanoindentation Probing of High-Aspect Ratio Pillar Structures on Optical Multilayer Dielectric Diffraction Gratings,” in *Local Probing Techniques and In-Situ Measurements in Materials Science*, edited by N. Balke, H. Wang, J. Rijssenbeek, and T. Glatzel, *Mater. Res. Soc. Symp. Proc. Vol. 1474* (Materials Research Society, Pittsburgh, PA, 2012).

D. T. Michel, A. V. Maximov, R. W. Short, J. A. Delettrez, D. Edgell, S. X. Hu, I. V. Igumenshchev, J. F. Myatt, A. A. Solodov, C. Stoeckl, B. Yaakobi, and D. H. Froula, “Measured Hot-Electron Intensity Thresholds Quantified by a Two-Plasmon-Decay Resonant Common-Wave Gain in Various Experimental Configurations,” *Phys. Plasmas* **20**, 055703 (2013).

D. T. Michel, A. V. Maximov, R. W. Short, S. X. Hu, J. F. Myatt, W. Seka, A. A. Solodov, B. Yaakobi, and D. H. Froula, “Experimental Validation of the Two-Plasmon-Decay Common-Wave Process,” *Phys. Rev. Lett.* **109**, 155007 (2012).

C. Mileham, C. Stoeckl, W. Theobald, G. Fiksel, D. Guy, R. K. Junquist, P. M. Nilson, T. C. Sangster, and M. J. Shoup III, “Crystal Imager Development at the Laboratory for Laser Energetics,” in *Target Diagnostics Physics and Engineering for Inertial Confinement Fusion*, edited by P. Bell and G. P. Grim (SPIE, Bellingham, WA, 2012), Vol. 8505, Paper 85050L.

- J. F. Myatt, H. X. Vu, D. F. DuBois, D. A. Russell, J. Zhang, R. W. Short, and A. V. Maximov, "Mitigation of Two-Plasmon Decay in Direct-Drive Inertial Confinement Fusion Through the Manipulation of Ion-Acoustic and Langmuir Wave Damping," *Phys. Plasmas* **20**, 052705 (2013).
- A. V. Okishev, I. A. Begishev, R. Cuffney, S. Papernov, and J. D. Zuegel, "A Highly Energetic, Multiwavelength, Diode-Pumped Nanosecond Laser System with Flexible Pulse-Shaping Capability," in *Solid State Lasers XXII: Technology and Devices*, edited by W. A. Clarkson, and R. K. Shori (SPIE, Bellingham, WA, 2013), Vol. 8599, Paper 85990Q.
- S. Papernov, "Mechanisms of Near-Ultraviolet, Nanosecond-Pulse-Laser Damage in  $\text{HfO}_2/\text{SiO}_2$ -Based Multilayer Coatings," *Chin. Opt. Lett.* **11**, S10703 (2013).
- S. Papernov, E. Shin, T. Murray, A. W. Schmid, and J. B. Oliver, "355-nm Absorption in  $\text{HfO}_2$  and  $\text{SiO}_2$  Monolayers with Embedded Hf Nanoclusters Studied Using Photothermal Heterodyne Imaging," in *Laser-Induced Damage in Optical Materials: 2012*, edited by G. J. Exarhos, V. E. Gruzdev, J. A. Menapace, D. Ristau, and M. J. Soileau (SPIE, Bellingham, WA, 2012), Vol. 8530, Paper 85301H.
- L. Parlato, R. Arpaia, C. De Lisio, F. Miletto Granozio, G. P. Pepe, P. Perna, V. Pagliarulo, C. Bonavolontà, M. Radovic, Y. Wang, R. Sobolewski, and U. Scotti di Uccio, "Time-Resolved Optical Response of All-Oxide  $\text{YBa}_2\text{Cu}_3\text{O}_7/\text{La}_{0.7}\text{Sr}_{0.3}\text{MnO}_3$  Proximitized Bilayers," *Phys. Rev. B* **87**, 134514 (2013).
- J. Qiao, P. A. Jaanimagi, R. Boni, J. Bromage, and E. Hill, "Measuring 8–250 ps Short Pulses Using a High-Speed Streak Camera on Kilojoule, Petawatt-Class Laser System," *Rev. Sci. Instrum.* **84**, 073104 (2013).
- P. B. Radha, F. J. Marshall, J. A. Marozas, A. Shvydky, I. Gabalski, T. R. Boehly, T. J. B. Collins, R. S. Craxton, D. H. Edgell, R. Epstein, J. A. Frenje, D. H. Froula, V. N. Goncharov, M. Hohenberger, R. L. McCrory, P. W. McKenty, D. D. Meyerhofer, R. D. Petrasso, T. C. Sangster, and S. Skupsky, "Polar-Drive Implosions on OMEGA and the National Ignition Facility," *Phys. Plasmas* **20**, 056306 (2013).
- S. P. Regan, R. Epstein, B. A. Hammel, L. J. Suter, H. A. Scott, M. A. Barrios, D. K. Bradley, D. A. Callahan, C. Cerjan, G. W. Collins, S. N. Dixit, T. Döppner, M. J. Edwards, D. R. Farley, K. B. Fournier, S. Glenn, S. H. Glenzer, I. E. Golovkin, S. W. Haan, A. Hamza, D. G. Hicks, N. Izumi, O. S. Jones, J. D. Kilkenny, J. L. Kline, G. A. Kyrala, O. L. Landen, T. Ma, J. J. MacFarlane, A. J. MacKinnon, R. C. Mancini, R. L. McCrory, N. B. Meezan, D. D. Meyerhofer, A. Nikroo, H.-S. Park, J. Ralph, B. A. Remington, T. C. Sangster, V. A. Smalyuk, P. T. Springer, and R. P. J. Town, "Hot-Spot Mix in Ignition-Scale Inertial Confinement Fusion Targets," *Phys. Rev. Lett.* **111**, 045001 (2013).
- S. P. Regan, K. Falk, G. Gregori, P. B. Radha, S. X. Hu, T. R. Boehly, B. J. B. Crowley, S. H. Glenzer, O. L. Landen, D. O. Gericke, T. Döppner, D. D. Meyerhofer, C. D. Murphy, T. C. Sangster, and J. Vorberger, "Inelastic X-Ray Scattering from Shocked Liquid Deuterium," *Phys. Rev. Lett.* **109**, 265003 (2012).
- T. C. Sangster, V. N. Goncharov, R. Betti, P. B. Radha, T. R. Boehly, D. T. Casey, T. J. B. Collins, R. S. Craxton, J. A. Delettrez, D. H. Edgell, R. Epstein, C. J. Forrest, J. A. Frenje, D. H. Froula, M. Gatu-Johnson, V. Yu. Glebov, D. R. Harding, M. Hohenberger, S. X. Hu, I. V. Igumenshchev, R. T. Janezic, J. H. Kelly, T. J. Kessler, C. Kingsley, T. Z. Kosc, J. P. Knauer, S. J. Loucks, J. A. Marozas, F. J. Marshall, A. V. Maximov, R. L. McCrory, P. W. McKenty, D. D. Meyerhofer, D. T. Michel, J. F. Myatt, R. D. Petrasso, S. P. Regan, W. Seka, W. T. Shmayda, R. W. Short, A. Shvydky, S. Skupsky, J. M. Soares, C. Stoeckl, W. Theobald, V. Versteeg, B. Yaakobi, and J. D. Zuegel, "Improving Cryogenic Deuterium-Tritium Implosion Performance on OMEGA," *Phys. Plasmas* **20**, 056317 (2013).
- J. E. Schoenly, W. Seka, G. Romanos, and P. Rechmann, "The Efficacy of Selective Calculus Ablation at 400 nm: Comparison to Conventional Calculus Removal Methods," in *Lasers in Dentistry XIX*, edited by P. Rechmann and D. Fried (SPIE, Bellingham, WA, 2013), Vol. 8566, Paper 85660E.
- S.-J. Scott and D. R. Harding, "Accelerated Evaporative Drying of RF Foam for ICF Target Fabrication," in *2013 IEEE 25th Symposium on Fusion Engineering (SOFE)* (IEEE, Piscataway, NJ, 2013).
- W. T. Shmayda, D. R. Harding, V. Versteeg, C. Kingsley, M. Hallgren, and S. J. Loucks, "Micron-Scaled Defects on Cryogenic Targets: An Assessment of Condensate Sources," *Fusion Sci. Technol.* **63**, 87 (2013).
- W. Theobald, R. Nora, M. Lafon, A. Casner, X. Ribeyre, K. S. Anderson, R. Betti, J. A. Delettrez, J. A. Frenje, V. Yu. Glebov, O. V. Gotchev, M. Hohenberger, S. X. Hu, F. J. Marshall, D. D. Meyerhofer, T. C. Sangster, G. Schurtz, W. Seka, V. A. Smalyuk, C. Stoeckl, and B. Yaakobi, "Spherical Shock-

Ignition Experiments with the 40 + 20-Beam Configuration on OMEGA,” *Phys. Plasmas* **19**, 102706 (2012).

H. X. Vu, D. F. DuBois, J. F. Myatt, and D. A. Russell, “Hot-Electron Production and Suprathermal Heat Flux Scaling with Laser Intensity from the Two-Plasmon–Decay Instability,” *Phys. Plasmas* **19**, 102703 (2012).

H. X. Vu, D. F. DuBois, D. A. Russell, and J. F. Myatt, “Hot-Electron Generation by ‘Cavitating’ Langmuir Turbulence in the Nonlinear Stage of the Two-Plasmon–Decay Instability,” *Phys. Plasmas* **19**, 102708 (2012).

Q. Wang, J. U. Wallace, T. Y.-H. Lee, J. J. Ou, Y.-T. Tsai, Y.-H. Huang, C.-C. Wu, L. J. Rothberg, and S. H. Chen, “Evaluation

of Propylene-, *Meta*-, and *Para*-Linked Triazine and *Tert*-Butyltriphenylamine as Bipolar Hosts for Phosphorescent Organic Light-Emitting Diodes,” *J. Mater. Chem. C* **1**, 2224 (2013).

Q. Wang, J. U. Wallace, T. Y.-H. Lee, L. Zeng, J. J. Ou, and S. H. Chen, “Charge Carrier Mobility Through Vacuum–Sublimed Glassy Films of *s*-Triazine- and Carbazole-Based Bipolar Hybrid and Unipolar Compounds,” *Org. Electron.* **14**, 2925 (2013).

B. Yaakobi, A. A. Solodov, J. F. Myatt, J. A. Delettrez, C. Stoeckl, and D. H. Froula, “Measurements of the Divergence of Fast Electrons in Laser-Irradiated Spherical Targets,” *Phys. Plasmas* **20**, 092706 (2013).

### OMEGA External Users’ Publications

M. A. Barrios, A. MacPhee, S. P. Regan, J. Kimbrough, S. R. Nagel, L. R. Benedetti, S. F. Khan, D. Bradley, P. Bell, D. Edgell, and G. W. Collins, “X-Ray Bang-Time Measurements at the National Ignition Facility Using a Diamond Detector,” *Rev. Sci. Instrum.* **83**, 10E105 (2012).

P. A. Bradley, J. A. Cobble, I. L. Tregillis, M. J. Schmitt, K. D. Obrey, V. Glebov, S. H. Batha, G. R. Magelssen, J. R. Fincke, S. C. Hsu, N. S. Krashennikova, T. J. Murphy, and F. J. Wysocki, “Role of Shocks and Mix Caused by Capsule Defects,” *Phys. Plasmas* **19**, 092703 (2012).

T. Caillaud, O. Landoas, M. Briat, B. Rossé, I. Thfoin, F. Philippe, A. Casner, J. L. Bourgade, L. Disdier, V. Yu. Glebov, F. J. Marshall, T. C. Sangster, H. S. Park, H. F. Robey, and P. Amendt, “A New Compact, High Sensitivity Neutron Imaging System,” *Rev. Sci. Instrum.* **83**, 10E131 (2012).

D. T. Casey, J. A. Frenje, M. Gatu Johnson, F. H. Séguin, C. K. Li, R. D. Petrasso, V. Yu. Glebov, J. Katz, J. P. Knauer, D. D. Meyerhofer, T. C. Sangster, R. M. Bionta, D. L. Bleuel, T. Döppner, S. Glenzer, E. Hartouni, S. P. Hatchett, S. Le Pape, T. Ma, A. MacKinnon, M. A. McKernan, M. Moran, E. Moses, H.-S. Park, J. Ralph, B. A. Remington, V. Smalyuk, C. B. Yeaman, J. Kline, G. Kyrala, G. A. Chandler, R. J. Leeper, C. L. Ruiz, G. W. Cooper, A. J. Nelson, K. Fletcher, J. Kilkenny, M. Farrell, D. Jasion, and R. Paguio, “Measuring the Absolute Deuterium–Tritium Neutron Yield Using the Magnetic Recoil Spectrometer at OMEGA and the NIF,” *Rev. Sci. Instrum.* **83**, 10D912 (2012).

D. T. Casey, J. A. Frenje, M. Gatu Johnson, F. H. Séguin, C. K. Li, R. D. Petrasso, V. Yu. Glebov, J. Katz, J. Magoon, D. D. Meyerhofer, T. C. Sangster, M. Shoup, J. Ulreich, R. C. Ashabranner, R. M. Bionta, A. C. Carpenter, B. Felker, H. Y. Khater, S. LePape, A. MacKinnon, M. A. McKernan, M. Moran, J. R. Rygg, M. F. Yeoman, R. Zacharias, R. J. Leeper, K. Fletcher, M. Farrell, D. Jasion, J. Kilkenny, and R. Paguio, “The Magnetic Recoil Spectrometer for Measurements of the Absolute Neutron Spectrum at OMEGA and the NIF,” *Rev. Sci. Instrum.* **84**, 043506 (2013).

S. Demmler, J. Rothhardt, S. Hädrich, J. Bromage, J. Limpert, and A. Tünnermann, “Control of Nonlinear Spectral Phase Induced by Ultra-Broadband Optical Parametric Amplification,” *Opt. Lett.* **37**, 3933 (2012).

S. Depierreux, P. Loiseau, D. T. Michel, V. Tassin, C. Stenz, P.-E. Masson-Laborde, C. Goyon, V. Yahia, and C. Labaune, “Experimental Investigation of the Stimulated Brillouin Scattering Growth and Saturation at 526 and 351 nm for Direct Drive and Shock Ignition,” *Phys. Plasmas* **19**, 012705 (2012).

K. B. Fournier, M. J. May, J. D. Colvin, M. A. Barrios, J. R. Patterson, and S. P. Regan, “Demonstration of a 13-keV Kr *K*-Shell X-Ray Source at the National Ignition Facility,” *Phys. Rev. E* **88**, 033104 (2013).

J. A. Frenje, R. Bionta, E. J. Bond, J. A. Caggiano, D. T. Casey, C. Cerjan, J. Edwards, M. Eckart, D. N. Fittinghoff, S. Friedrich, V. Yu. Glebov, S. Glenzer, G. Grim, S. Haan,

- R. Hatarik, S. Hatchett, M. Gatu Johnson, O. S. Jones, J. D. Kilkenny, J. P. Knauer, O. Landen, R. Leeper, S. Le Pape, R. Lerche, C. K. Li, A. Mackinnon, J. McNaney, F. E. Merrill, M. Moran, D. H. Munro, T. J. Murphy, R. D. Petrasso, R. Rygg, T. C. Sangster, F. H. Séguin, S. Sepke, B. Spears, P. Springer, C. Stoeckl, and D. C. Wilson, “Diagnosing Implosion Performance at the National Ignition Facility (NIF) by Means of Neutron Spectrometry,” *Nucl. Fusion* **53**, 043014 (2013).
- M. Gatu Johnson, J. A. Frenje, D. T. Casey, C. K. Li, F. H. Séguin, R. Petrasso, R. Ashabranner, R. M. Bionta, D. L. Bleuel, E. J. Bond, J. A. Caggiano, A. Carpenter, C. J. Cerjan, T. J. Clancy, T. Doepfner, M. J. Eckart, M. J. Edwards, S. Friedrich, S. H. Glenzer, S. W. Haan, E. P. Hartouni, R. Hatarik, S. P. Hatchett, O. S. Jones, G. Kyrala, S. Le Pape, R. A. Lerche, O. L. Landen, T. Ma, A. J. MacKinnon, M. A. McKernan, M. J. Moran, E. Moses, D. H. Munro, J. McNaney, H. S. Park, J. Ralph, B. Remington, J. R. Rygg, S. M. Sepke, V. Smalyuk, B. Spears, P. T. Springer, C. B. Yeamans, M. Farrell, D. Jasion, J. D. Kilkenny, A. Nikroo, R. Paguio, J. P. Knauer, V. Yu Glebov, T. C. Sangster, R. Betti, C. Stoeckl, J. Magoon, M. J. Shoup III, G. P. Grim, J. Kline, G. L. Morgan, T. J. Murphy, R. J. Leeper, C. L. Ruiz, G. W. Cooper, and A. J. Nelson, “Neutron Spectrometry—An Essential Tool for Diagnosing Implosions at the National Ignition Facility,” *Rev. Sci. Instrum.* **83**, 10D308 (2012) (invited).
- G. P. Grim, N. Guler, F. E. Merrill, G. L. Morgan, C. R. Danly, P. L. Volegov, C. H. Wilde, D. C. Wilson, D. S. Clark, D. E. Hinkel, O. S. Jones, K. S. Raman, N. Izumi, D. N. Fittinghoff, O. B. Drury, E. T. Alger, P. A. Arnold, R. C. Ashabranner, L. J. Atherton, M. A. Barrios, S. Batha, P. M. Bell, L. R. Benedetti, R. L. Berger, L. A. Bernstein, L. V. Berzins, R. Betti, S. D. Bhandarkar, R. M. Bionta, D. L. Bleuel, T. R. Boehly, E. J. Bond, M. W. Bowers, D. K. Bradley, G. K. Brunton, R. A. Buckles, S. C. Burkhart, R. F. Burr, J. A. Caggiano, D. A. Callahan, D. T. Casey, C. Castro, P. M. Celliers, C. J. Cerjan, G. A. Chandler, C. Choate, S. J. Cohen, G. W. Collins, G. W. Cooper, J. R. Cox, J. R. Cradick, P. S. Datte, E. L. Dewald, P. Di Nicola, J. M. Di Nicola, L. Divol, S. N. Dixit, R. Dylla-Spears, E. G. Dzenitis, M. J. Eckart, D. C. Eder, D. H. Edgell, M. J. Edwards, J. H. Eggert, R. B. Ehrlich, G. V. Erbert, J. Fair, D. R. Farley, B. Felker, R. J. Fortner, J. A. Frenje, G. Frieders, S. Friedrich, M. Gatu-Johnson, C. R. Gibson, E. Giraldez, V. Y. Glebov, S. M. Glenn, S. H. Glenzer, G. Gururangan, S. W. Haan, K. D. Hahn, B. A. Hammel, A. V. Hamza, E. P. Hartouni, R. Hatarik, S. P. Hatchett, C. Haynam, M. R. Hermann, H. W. Herrmann, D. G. Hicks, J. P. Holder, D. M. Holunga, J. B. Horner, W. W. Hsing, H. Huang, M. C. Jackson, K. S. Jancaitis, D. H. Kalantar, R. L. Kauffman, M. I. Kauffman, S. F. Khan, J. D. Kilkenny, J. R. Kimbrough, R. Kirkwood, J. L. Kline, J. P. Knauer, K. M. Knittel, J. A. Koch, T. R. Kohut, B. J. Koziolowski, K. Krauter, G. W. Krauter, A. L. Kritcher, J. Kroll, G. A. Kyrala, K. N. La Fortune, G. LaCaille, L. J. Lagin, T. A. Land, O. L. Landen, D. W. Larson, D. A. Latray, R. J. Leeper, T. L. Lewis, S. LePape, J. D. Lindl, R. R. Lowe-Webb, T. Ma, B. J. MacGowan, A. J. MacKinnon, A. G. MacPhee, R. M. Malone, T. N. Malsbury, E. Mapoles, C. D. Marshall, D. G. Mathisen, P. McKenty, J. M. McNaney, N. B. Meezan, P. Michel, J. L. Milovich, J. D. Moody, A. S. Moore, M. J. Moran, K. Moreno, E. I. Moses, D. H. Munro, B. R. Nathan, A. J. Nelson, A. Nikroo, R. E. Olson, C. Orth, A. E. Pak, E. S. Palma, T. G. Parham, P. K. Patel, R. W. Patterson, R. D. Petrasso, R. Prasad, J. E. Ralph, S. P. Regan, H. Rinderknecht, H. F. Robey, G. F. Ross, C. L. Ruiz, F. H. Séguin, J. D. Salmonson, T. C. Sangster, J. D. Sater, R. L. Saunders, M. B. Schneider, D. H. Schneider, M. J. Shaw, N. Simanovskaia, B. K. Spears, P. T. Springer, C. Stoeckl, W. Stoeffl, L. J. Suter, C. A. Thomas, R. Tommasini, R. P. Town, A. J. Traille, B. Van Wonterghem, R. J. Wallace, S. Weaver, S. V. Weber, P. J. Wegner, P. K. Whitman, K. Widmann, C. C. Widmayer, R. D. Wood, B. K. Young, R. A. Zacharias, and A. Zylstra, “Nuclear Imaging of the Fuel Assembly in Ignition Experiments,” *Phys. Plasmas* **20**, 056320 (2013).
- S. Hamel, L. X. Benedict, P. M. Celliers, M. A. Barrios, T. R. Boehly, G. W. Collins, T. Döppner, J. H. Eggert, D. R. Farley, D. G. Hicks, J. L. Kline, A. Lazicki, S. LePape, A. J. Mackinnon, J. D. Moody, H. F. Robey, E. Schwegler, and P. A. Sterne, “Equation of State of CH<sub>1.36</sub>: First-Principles Molecular Dynamics Simulations and Shock-and-Release Wave Speed Measurements,” *Phys. Rev. B* **86**, 094113 (2012).
- M. J. Haugh, S. P. Regan, K. D. Jacoby, P. W. Ross, J. Magoon, M. A. Barrios, J. A. Emig, M. J. Shoup III, and K. B. Fournier, “Integrated X-Ray Reflectivity Measurements of Elliptically Curved Pentaerythritol Crystals,” *Rev. Sci. Instrum.* **83**, 10E122 (2012).
- N. M. Hoffman, H. W. Herrmann, Y. H. Kim, H. H. Hsu, C. J. Horsfield, M. S. Rubery, E. K. Miller, E. Grafil, W. Stoeffl, J. A. Church, C. S. Young, J. M. Mack, D. C. Wilson, J. R. Langenbrunner, S. C. Evans, T. J. Sedillo, V. Yu. Glebov, and T. Duffy, “Measurement of Areal Density in the Ablators of Inertial-Confinement-Fusion Capsules *via* Detection of Ablator ( $n, n'\gamma$ ) Gamma-Ray Emission,” *Phys. Plasmas* **20**, 042705 (2013).
- N. Krasheninnikova, M. Schmitt, I. Tregillis, P. Bradley, J. Cobble, G. Kyrala, T. Murphy, K. Obrey, S. Hsu, R. Shah,

S. Batha, S. Craxton, and P. McKenty, “Symmetry Tuning for DIME Campaign,” *Bull. Am. Phys. Soc.* **57**, 297 (2012).

N. L. Kugland, D. D. Ryutov, P.-Y. Chang, R. P. Drake, G. Fiksel, D. H. Froula, S. H. Glenzer, G. Gregori, M. Grosskopf, M. Koenig, Y. Kuramitsu, C. Kuranz, M. C. Levy, E. Liang, J. Meinecke, F. Miniati, T. Morita, A. Pelka, C. Plechaty, R. Presura, A. Ravasio, B. A. Remington, B. Reville, J. S. Ross, Y. Sakawa, A. Spitkovsky, H. Takabe, and H.-S. Park, “Self-Organized Electromagnetic Field Structures in Laser-Produced Counter-Streaming Plasmas,” *Nat. Phys.* **8**, 809 (2012).

O. L. Landen, R. Benedetti, D. Bleuel, T. R. Boehly, D. K. Bradley, J. A. Caggiano, D. A. Callahan, P. M. Celliers, C. J. Cerjan, D. Clark, G. W. Collins, E. L. Dewald, S. N. Dixit, T. Doeppner, D. Edgell, J. Eggert, D. Farley, J. A. Frenje, V. Glebov, S. M. Glenn, S. H. Glenzer, S. W. Haan, A. Hamza, B. A. Hammel, C. A. Haynam, J. H. Hammer, R. F. Heeter, H. W. Herrmann, D. G. Hicks, D. E. Hinkel, N. Izumi, M. Gatu Johnson, O. S. Jones, D. H. Kalantar, R. L. Kauffman, J. D. Kirkenny, J. L. Kline, J. P. Knauer, J. A. Koch, G. A. Kyrala, K. LaFortune, T. Ma, A. J. Mackinnon, A. J. MacPhee, E. Mapoles, J. L. Milovich, J. D. Moody, N. B. Meezan, P. Michel, A. S. Moore, D. H. Munro, A. Nikroo, R. E. Olson, K. Opachich, A. Pak, T. Parham, P. Patel, H.-S. Park, R. P. Petrasso, J. Ralph, S. P. Regan, B. A. Remington, H. G. Rinderknecht, H. F. Robey, M. D. Rosen, J. S. Ross, J. D. Salmonson, T. C. Sangster, M. B. Schneider, V. Smalyuk, B. K. Spears, P. T. Springer, L. J. Suter, C. A. Thomas, R. P. J. Town, S. V. Weber, P. J. Wegner, D. C. Wilson, K. Widmann, C. Yeaman, A. Zylstra, M. J. Edwards, J. D. Lindl, L. J. Atherton, W. W. Hsing, B. J. MacGowan, B. M. Van Wonterghem, and E. I. Moses, “Progress in the Indirect-Drive National Ignition Campaign,” *Plasma Phys. Control. Fusion* **54**, 124026 (2012).

P. Loubeyre, S. Brygoo, J. Eggert, P. M. Celliers, D. K. Spaulding, J. R. Rygg, T. R. Boehly, G. W. Collins, and R. Jeanloz, “Extended Data Set for the Equation of State of Warm Dense Hydrogen Isotopes,” *Phys. Rev. B* **86**, 144115 (2012).

T. Ma, P. K. Patel, N. Izumi, P. T. Springer, M. H. Key, L. J. Atherton, L. R. Benedetti, D. K. Bradley, D. A. Callahan, P. M. Celliers, C. J. Cerjan, D. S. Clark, E. L. Dewald, S. N. Dixit, T. Döppner, D. H. Edgell, R. Epstein, S. Glenn, G. Grim, S. W. Haan, B. A. Hammel, D. Hicks, W. W. Hsing, O. S. Jones, S. F. Khan, J. D. Kirkenny, J. L. Kline, G. A. Kyrala, O. L. Landen,

S. Le Pape, B. J. MacGowan, A. J. Mackinnon, A. G. MacPhee, N. B. Meezan, J. D. Moody, A. Pak, T. Parham, H.-S. Park, J. E. Ralph, S. P. Regan, B. A. Remington, H. F. Robey, J. S. Ross, B. K. Spears, V. Smalyuk, L. J. Suter, R. Tommasini, R. P. Town, S. V. Weber, J. D. Lindl, M. J. Edwards, S. H. Glenzer, and E. I. Moses, “Onset of Hydrodynamic Mix in High-Velocity, Highly Compressed Inertial Confinement Fusion Implosions,” *Phys. Rev. Lett.* **111**, 085004 (2013).

R. C. Mancini, C. A. Iglesias, S. Ferri, A. Calisti, and R. Florido, “The Effect of Improved Satellite Line Shapes on the Argon He $\beta$  Spectral Feature,” *High Energy Density Phys.* **9**, 731 (2013).

A. R. Miles, H.-K. Chung, R. Heeter, W. Hsing, J. A. Koch, H.-S. Park, H. F. Robey, H. A. Scott, R. Tommasini, J. Frenje, C. K. Li, R. Petrasso, V. Glebov, and R. W. Lee, “Numerical Simulation of Thin-Shell Direct Drive DHe3-Filled Capsules Fielded at OMEGA,” *Phys. Plasmas* **19**, 072702 (2012).

J. S. Milnes, C. J. Horsfield, M. S. Rubery, V. Yu. Glebov, and H. W. Herrmann, “Ultra-High Speed Photomultiplier Tubes with Nanosecond Gating for Fusion Diagnostics,” *Rev. Sci. Instrum.* **83**, 10D301 (2012).

M. J. Moran, E. J. Bond, T. J. Clancy, M. J. Eckart, H. Y. Khater, and V. Yu. Glebov, “Deuterium–Tritium Neutron Yield Measurements with the 4.5 m Neutron-Time-of-Flight Detectors at NIF,” *Rev. Sci. Instrum.* **83**, 10D312 (2012).

M. J. Rosenberg, J. S. Ross, C. K. Li, R. P. J. Town, F. H. Séguin, J. A. Frenje, D. H. Froula, and R. D. Petrasso, “Characterization of Single and Colliding Laser-Produced Plasma Bubbles Using Thomson Scattering and Proton Radiography,” *Phys. Rev. E* **86**, 056407 (2012).

J. R. Rygg, J. H. Eggert, A. E. Lazicki, F. Coppari, J. A. Hawreliak, D. G. Hicks, R. F. Smith, C. M. Sorce, T. M. Uphaus, B. Yaakobi, and G. W. Collins, “Powder Diffraction from Solids in the Terapascal Regime,” *Rev. Sci. Instrum.* **83**, 113904 (2012).

M. J. Schmitt, P. A. Bradley, J. A. Cobble, J. R. Fincke, P. Hakel, S. C. Hsu, N. S. Krashennikova, G. A. Kyrala, G. R. Magelssen, D. S. Montgomery, T. J. Murphy, K. A. Obrey, R. C. Shah, I. L. Tregillis, J. A. Baumgaertel, F. J. Wysocki, S. H. Batha, R. S. Craxton, P. W. McKenty, P. Fitzsimmons, A. Nikroo, and R. Wallace, “Development of a Polar Direct-Drive Platform for Studying Inertial Confinement Fusion

Implosion Mix on the National Ignition Facility,” *Phys. Plasmas* **20**, 056310 (2013).

M. J. Schmitt, P. A. Bradley, J. A. Cobble, P. Hakel, S. C. Hsu, N. S. Krasheninnikova, G. A. Kyrala, T. J. Murphy, K. A. Obrey, R. C. Shah, I. L. Tregillis, S. C. Craxton, P. W. McKenty, R. C. Mancini, H. M. Johns, T. Joshi, and D. Mayes, “Recent Results of the Defect-Induced Mix Experiments (DIME) on NIF,” *Bull. Am. Phys. Soc.* **57**, 296 (2012).

R. H. H. Scott, E. L. Clark, F. Pérez, M. J. V. Streeter, J. R. Davies, H.-P. Schlenvoigt, J. J. Santos, S. Hulin, K. L. Lancaster, S. D. Baton, S. J. Rose, and P. A. Norreys, “Measuring Fast Electron Spectra and Laser Absorption in Relativistic Laser-Solid Interactions Using Differential Bremsstrahlung Photon Detectors,” *Rev. Sci. Instrum.* **84**, 083505 (2013).

N. Sinenian, W. Theobald, J. A. Frenje, C. Stoeckl, F. H. Séguin, C. K. Li, R. D. Petrasso, and R. B. Stephens, “Proton Emission from Cone-in-Shell Fast-Ignition Experiments at Omega,” *Phys. Plasmas* **19**, 112708 (2012).

L. Willingale, K. Krushelnick, A. G. R. Thomas, F. J. Dollar, A. Maksimchuk, C. Zulick, H. Chen, A. U. Hazi, G. J. Williams, P. M. Nilson, R. S. Craxton, T. C. Sangster, V. Glebov, C. Stoeckl, W. Nazarov, J. Cobble, and P. A. Norreys,

“Relativistic Laser Interactions with Near-Critical Density Plasmas,” *Bull. Am. Phys. Soc.* **57**, 210 (2012).

L. Willingale, A. G. R. Thomas, P. M. Nilson, H. Chen, J. Cobble, R. S. Craxton, A. Maksimchuk, P. A. Norreys, T. C. Sangster, R. H. H. Scott, C. Stoeckl, C. Zulick, and K. Krushelnick, “Surface Waves and Electron Acceleration from High-Power, Kilojoule-Class Laser Interactions with Underdense Plasma,” *New J. Phys.* **15**, 025023 (2013).

T. Yabuuchi, R. Mishra, C. McGuffey, B. Qiao, M. S. Wei, H. Sawada, Y. Sentoku, T. Ma, D. P. Higginson, K. U. Akli, D. Batani, H. Chen, L. A. Gizzi, M. H. Key, A. J. Mackinnon, H. S. McLean, P. A. Norreys, P. K. Patel, R. B. Stephens, Y. Ping, W. Theobald, C. Stoeckl, and F. N. Beg, “Impact of Extended Preplasma on Energy Coupling in Kilojoule Energy Relativistic Laser Interaction with Cone Wire Targets Relevant to Fast Ignition,” *New J. Phys.* **15**, 015020 (2013).

C. Zulick, F. Dollar, L. Willingale, V. Chvykov, G. Kalintchenko, A. Maksimchuk, A. G. R. Thomas, V. Yanovsky, K. Krushelnick, J. Davis, G. M. Petrov, V. Glebov, P. M. Nilson, T. C. Sangster, C. Stoeckl, R. S. Craxton, P. A. Norreys, J. Cobble, and H. Chen, “Neutron Generation through Ultra-Intense Laser Plasma Interactions,” *Bull. Am. Phys. Soc.* **57**, 216 (2012).

### Conference Presentations

The following presentations were made at the 24th IAEA Fusion Energy Conference, San Diego, CA, 8–13 October 2012:

R. Betti, “Theory of Ignition and Hydro-Equivalence for Inertial Confinement Fusion.”

R. L. McCrory, D. D. Meyerhofer, R. Betti, T. R. Boehly, D. T. Casey, T. J. B. Collins, R. S. Craxton, J. A. Delettrez, D. H. Edgell, R. Epstein, J. A. Frenje, D. H. Froula, M. Gatu-Johnson, V. Yu. Glebov, V. N. Goncharov, D. R. Harding, M. Hohenberger, S. X. Hu, I. V. Igumenshchev, T. J. Kessler, J. P. Knauer, C. K. Li, J. A. Marozas, F. J. Marshall, P. W. McKenty, D. T. Michel, J. F. Myatt, P. M. Nilson, S. J. Padalino, R. D. Petrasso, P. B. Radha, S. P. Regan, T. C. Sangster, F. H. Séguin, W. Seka, R. W. Short, O. Shvydyk, S. Skupsky, J. M. Soures, C. Stoeckl, W. Theobald, B. Yaakobi, and J. D. Zuegel, “Progress Toward Polar-Drive Ignition for the NIF.”

The following presentations were made at Frontiers in Optics 2012, Rochester, NY, 14–18 October 2012:

C. Dorrer, V. Bagnoud, I. A. Begishev, J. Bromage, A. Consentino, M. J. Guardalben, A. V. Okishev, J. Qiao, R. G. Roides, and J. D. Zuegel, “OPCPA Front End and Contrast Optimization for the OMEGA EP Kilojoule, Picosecond Laser.”

C. Dorrer, K. L. Marshall, S. H. Chen, M. Vargas, M. Statt, C. Caggiano, S. K.-H. Wei, J. B. Oliver, P. Leung, K. Wegman, J. Boulé, Z. Zhao, S. Papernov, A. Rakhmann, and I. Jovanovic, “High-Damage-Threshold Beam Shaping Using Optically Patterned Liquid Crystal Devices.”

T. Petersen and J. Bromage, “Intracavity Chirped-Pulse Amplification for High-Energy, Ultrafast Optical Parametric Oscillators.”

J. P. Knauer, P.-Y. Chang, M. Hohenberger, G. Fiksel, F. J. Marshall, D. D. Meyerhofer, R. Betti, F. H. Séguin, and R. D. Petrasso, “Compressing Magnetic Fields with High-Energy Lasers,” 14th International Conference on Megagauss Magnetic Field Generation and Related Topics, Maui, HI, 14–19 October 2012.

S. Papernov, “Mechanisms of Near-Ultraviolet, Nanosecond-Pulse Laser Damage in  $\text{HfO}_2/\text{SiO}_2$ -Based Multilayer Coatings,” Frontiers of Optical Coatings, Hangzhou, China, 15–18 October 2012.

The following presentations were made at the 54th Annual Meeting of the APS Division of Plasma Physics, Providence, RI, 29 October–2 November 2012:

K. S. Anderson, R. Betti, P. W. McKenty, T. J. B. Collins, M. Hohenberger, W. Theobald, R. S. Craxton, J. A. Delettrez, M. Lafon, J. A. Marozas, R. Nora, S. Skupsky, and A. Shvydky, “A Polar-Drive Shock-Ignition Design for the National Ignition Facility” (invited).

R. Betti, R. Nora, M. Lafon, J. F. Myatt, C. Ren, R. Yan, J. Li, A. V. Maximov, D. H. Froula, W. Seka, K. S. Anderson, R. Epstein, J. A. Delettrez, S. X. Hu, P. M. Nilson, V. A. Smalyuk, and W. Theobald, “High-Z Ablator Targets for Direct-Drive ICF.”

T. R. Boehly, V. N. Goncharov, S. X. Hu, J. A. Marozas, T. C. Sangster, and D. D. Meyerhofer, “The Growth of Surface Defects Driven by Shock Waves.”

A. Bose, R. Betti, P.-Y. Chang, and J. R. Davies, “Non-Inertial Eulerian Hydrodynamic Code for ICF Implosion Simulations.”

P.-Y. Chang, A. Agliata, D. H. Barnak, W. Bittle, G. Fiksel, D. Hassett, M. Hohenberger, D. Lonobile, M. J. Shoup III, C. Taylor, and R. Betti, “Experimental Platform for Magnetized HEDP Science at OMEGA.”

T. J. B. Collins, J. A. Marozas, K. S. Anderson, V. N. Goncharov, P. W. McKenty, R. Betti, and S. Skupsky, “Optimization with *Telios* of the Polar-Drive Point Design for the National Ignition Facility.”

R. S. Craxton, P. W. McKenty, P. A. Olson, D. H. Froula, D. T. Michel, S. Le Pape, and A. J. MacKinnon, “Optimization of

Drive Uniformity in NIF Polar-Drive Implosions Using Gated X-Ray Self-Emission Images.”

J. A. Delettrez, T. J. B. Collins, A. Shvydky, G. Moses, D. Cao, and M. M. Marinak, “Effect of Nonlocal Electron Transport in Two Dimensions on the Symmetry of Polar-Drive-Ignition Targets.”

D. H. Edgell, P. B. Radha, V. N. Goncharov, I. V. Igumenshchev, J. Marozas, J. F. Myatt, W. Seka, and D. H. Froula, “Modeling Cross-Beam Energy Transfer for Polar-Drive Experiments.”

B. Eichman, W. Theobald, C. Stoeckl, C. Mileham, and T. C. Sangster, “Time-Resolved X-Ray Brightness Measurements from Short-Pulse Laser-Irradiated Thin Foils.”

R. Epstein, S. P. Regan, R. L. McCrory, D. D. Meyerhofer, T. C. Sangster, J. L. Tucker, B. A. Hammel, L. J. Suter, H. Scott, D. A. Callahan, C. Cerjan, N. Izumi, M. H. Key, O. L. Landen, N. B. Meezan, B. A. Remington, I. E. Golovkin, J. J. MacFarlane, R. C. Mancini, and K. J. Peterson, “Spectroscopy of Mid-Z Shell Additives in Implosions at the National Ignition Facility.”

G. Fiksel, V. A. Goncharov, D. D. Meyerhofer, T. C. Sangster, B. Yaakobi, M. J. Bonino, and V. A. Smalyuk, “Experimental Reduction of Laser Imprinting and Rayleigh–Taylor Growth in Spherically Compressed, Medium-Z–Doped Plastic Targets.”

R. K. Follett, D. T. Michel, J. F. Myatt, S. X. Hu, B. Yaakobi, and D. H. Froula, “Thomson-Scattering Measurements of Ion-Acoustic Wave Amplitudes Driven by the Two-Plasmon–Decay Instability.”

C. J. Forrest, V. Yu. Glebov, J. P. Knauer, T. C. Sangster, C. Stoeckl, S. Gardner, K. S. Anderson, P. B. Radha, V. N. Goncharov, D. D. Meyerhofer, C. Morrison, D. Baldwin, and S. Padalino, “Modeling Cold Fusion Distributions Inferred from Elastically Scattered Neutrons in Layered Cryogenic DT Direct-Drive Implosions.”

J. A. Frenje, D. T. Casey, M. Gatu-Johnson, C. K. Li, F. H. Séguin, R. D. Petrasso, R. Bionta, M. J. Edwards, S. H. Glenzer, O. L. Landen, A. J. MacKinnon, D. H. Munro, P. J. Springer, J. D. Kilkenny, V. Yu. Glebov, T. C. Sangster, and C. Stoeckl, “A Streak-Camera–Based Magnetic Recoil Spectrometer (SCMRS) for Measurements of  $T_i(t)$ ,  $Y_n(t)$ ,  $d_{sr}(t)$  on OMEGA and the NIF.”

D. H. Froula, B. Yaakobi, D. T. Michel, D. H. Edgell, R. K. Follett, W. Seka, C. Stoeckl, T. C. Sangster, A. A. Solodov,

- S. X. Hu, I. V. Igumenshchev, P. B. Radha, J. A. Delettrez, J. F. Myatt, R. W. Short, and V. N. Goncharov, “Two-Plasmon–Decay Electron-Divergence Measurements in Direct-Drive Implosions on OMEGA.”
- L. Gao, P. M. Nilson, I. V. Igumenshchev, S. X. Hu, J. R. Davies, C. Stoeckl, D. H. Froula, R. Betti, D. D. Meyerhofer, and M. G. Haines, “Magnetic-Field Generation by the Rayleigh–Taylor Instability in Planar Targets on OMEGA EP.”
- M. Gatu-Johnson, D. T. Casey, J. A. Frenje, C. K. Li, F. H. Séguin, R. D. Petrasso, V. Yu. Glebov, J. P. Knauer, T. C. Sangster, R. Bionta, M. J. Edwards, S. H. Glenzer, S. P. Hatchett, O. L. Landen, A. J. MacKinnon, D. McNabb, D. H. Munro, J. Pino, S. Sepke, P. J. Springer, and J. D. Kilkenny, “Measurements and Interpretation of TT and Down-Scattered DT Neutron Spectra on OMEGA and the NIF.”
- V. Yu. Glebov, C. Stoeckl, T. C. Sangster, C. Forrest, and R. A. Lerche, “Absolute Ion-Temperature Measurements in DD and DT Implosions on OMEGA.”
- V. N. Goncharov, T. C. Sangster, R. Epstein, S. X. Hu, I. V. Igumenshchev, D. H. Froula, R. L. McCrory, D. D. Meyerhofer, D. T. Michel, P. B. Radha, W. Seka, S. Skupsky, C. Stoeckl, D. T. Casey, J. A. Frenje, and M. Gatu-Johnson, “Improving Implosion Velocity in Cryogenic Deuterium–Tritium Implosions on OMEGA.”
- D. Haberberger, D. H. Froula, S. X. Hu, C. Joshi, S. Tochitsky, C. Gong, F. Fiuza, and L. Silva, “Collisionless Shock Wave Acceleration of Ions on OMEGA EP.”
- M. Hohenberger, W. Theobald, S. X. Hu, R. Betti, K. S. Anderson, T. R. Boehly, A. Casner, D. D. Meyerhofer, X. Ribeyre, T. C. Sangster, G. Schurtz, W. Seka, C. Stoeckl, and B. Yaakobi, “Shock-Ignition Studies in Planar Geometry on OMEGA.”
- S. X. Hu, V. N. Goncharov, and S. Skupsky, “Burning DT Plasmas with Ultrafast Soft X-Ray Pulses.”
- I. V. Igumenshchev, V. N. Goncharov, T. R. Boehly, T. C. Sangster, and S. Skupsky, “Fuel–Ablator Mix from Surface Nonuniformities in Directly Driven Implosions.”
- S. Ivancic, W. Theobald, R. Boni, D. H. Froula, S. X. Hu, and D. D. Meyerhofer, “Ray-Trace Simulations for the Optical  $4\omega$  Probe Diagnostic on OMEGA EP.”
- J. P. Knauer, “Neutron Spectroscopy at the National Ignition Facility” (invited).
- M. Lafon, R. Nora, K. S. Anderson, and R. Betti, “Hydrodynamic Simulations of Direct-Drive Targets with Moderate-Z Ablators.”
- J. Li, R. Yan, C. Ren, A. V. Maximov, W. B. Mori, and F. S. Tsung, “Collisional Effects on Hot-Electron Generation in Two-Plasmon–Decay Instability in Inertial Confinement Fusion.”
- M. J.-E. Manuel, C. K. Li, F. H. Séguin, D. T. Casey, R. D. Petrasso, S. X. Hu, R. Betti, J. D. Hager, D. D. Meyerhofer, and V. A. Smalyuk, “Measurements of Rayleigh–Taylor-Induced Magnetic Fields During Linear and Nonlinear Growth Phases.”
- J. A. Marozas, T. J. B. Collins, D. H. Edgell, I. V. Igumenshchev, and J. F. Myatt, “Cross-Beam Energy Transfer with Additional Ion Heating Integrated into the 2-D Hydrodynamics Code *DRACO*.”
- F. J. Marshall, P. B. Radha, M. J. Bonino, J. A. Delettrez, R. Epstein, S. Skupsky, and E. Giraldez, “Polar-Drive Experiments with Shimmied Targets on OMEGA.”
- A. V. Maximov, J. F. Myatt, R. W. Short, I. V. Igumenshchev, D. H. Edgell, and W. Seka, “Scattering of Multiple Crossing Laser Beams in Direct-Drive ICF Plasmas.”
- C. McCoy, T. R. Boehly, P. M. Nilson, T. J. B. Collins, T. C. Sangster, D. D. Meyerhofer, D. E. Fratanduono, P. M. Celliers, and D. G. Hicks, “The Release of Shocked Materials.”
- P. W. McKenty, R. S. Craxton, A. Shvydky, D. H. Froula, D. T. Michel, J. A. Marozas, T. C. Sangster, D. D. Meyerhofer, R. L. McCrory, J. D. Kilkenny, A. Nikroo, M. L. Hoppe, S. Le Pape, A. J. MacKinnon, and D. H. Munro, “Drive-Symmetry Studies of NIF Exploding-Pusher Experiments.”
- D. D. Meyerhofer, D. H. Froula, V. N. Goncharov, I. V. Igumenshchev, S. J. Loucks, P. W. McKenty, R. L. McCrory, P. B. Radha, and T. C. Sangster, “Polar-Drive–Ignition Experimental Plan on the NIF.”
- D. T. Michel, A. V. Maximov, R. W. Short, J. A. Delettrez, D. Edgell, S. X. Hu, I. V. Igumenshchev, J. F. Myatt, A. A. Solodov, C. Stoeckl, B. Yaakobi, and D. H. Froula, “Measured Hot-Electron Intensity Thresholds Quantified by a Two-Plasmon–Decay Gain in Various Experimental Configurations” (invited).

J. F. Myatt, J. Zhang, R. W. Short, A. V. Maximov, A. A. Solodov, W. Seka, D. H. Froula, B. Yaakobi, D. T. Michel, D. H. Edgell, D. F. DuBois, D. A. Russell, and H. X. Vu, “Mitigating Two-Plasmon–Decay Hot-Electron Generation Through the Modification of Langmuir and Ion-Acoustic Dissipation in Directly Driven Targets.”

P. M. Nilson, G. Fiksel, C. Stoeckl, P. A. Jaanimagi, C. Mileham, W. Theobald, J. R. Davies, J. F. Myatt, A. A. Solodov, D. H. Froula, R. Betti, and D. D. Meyerhofer, “Tracking Intense Flows of Energy Inside OMEGA EP Laser-Irradiated Metal Targets.”

R. Nora, W. Theobald, R. Betti, J. A. Delettrez, A. A. Solodov, K. S. Anderson, W. Seka, and M. Lafon, “Analysis of Fast Electrons in Shock-Ignition Implosions on OMEGA.”

S. Padalino, M. Krieger, M. Russ, D. Polsin, M. Bienstock, D. Ellison, and A. Simone, “Design and Characterization of a Collimated Neutron Beam User Facility at SUNY Geneseo.”

S. Padalino, D. Polsin, M. Russ, M. Krieger, M. Bienstock, D. Ellison, A. Simone, C. Stillman, M. Yuly, K. Mann, T. Reynolds, and T. C. Sangster, “Cross Section of the  $(n, 2n)$  Reaction in  $^{12}\text{C}$  in the Energy Interval 20-30 MeV.”

S. Padalino, D. Polsin, M. Russ, M. Krieger, M. Bienstock, D. Ellison, A. Simone, C. Stillman, M. Yuly, K. Mann, T. Reynolds, and T. C. Sangster, “In Situ Calibration for Proton Particle Telescope.”

S. Padalino, M. Russ, D. Polsin, M. Krieger, C. Stillman, M. Bienstock, D. Ellison, A. Simone, M. Yuly, K. Mann, T. Reynolds, and T. C. Sangster, “Coincidence Efficiency Measurement Using  $^{11}\text{B}(p,n)^{11}\text{C}$ .”

J. Park, C. Ren, J. C. Workman, and E. G. Blackman, “Particle-in-Cell Simulations of Particle Energization via Shock Drift Acceleration from Low Mach Number Quasi-Perpendicular Shocks in Solar Flares.”

P. B. Radha, F. J. Marshall, J. A. Marozas, A. Shvydky, I. Gabalski, T. R. Boehly, T. J. B. Collins, R. S. Craxton, D. H. Edgell, R. Epstein, J. Frenje, D. H. Froula, V. N. Goncharov, M. Hohenberger, R. L. McCrory, P. W. McKenty, D. D. Meyerhofer, R. D. Petrasso, T. C. Sangster, and S. Skupsky, “Polar-Drive Implosions on OMEGA and the National Ignition Facility” (invited).

S. P. Regan, “X-Ray Thomson Scattering: Incisive Probe for Warm, Dense Matter.”

S. P. Regan, R. Epstein, B. A. Hammel, L. J. Suter, J. Ralph, H. Scott, M. A. Barrios, D. K. Bradley, C. Cerjan, T. Doepfner, S. H. Glenzer, I. E. Golovkin, S. W. Haan, O. Jones, J. D. Kilkenny, J. L. Kline, and O. L. Landen, J. J. MacFarlane, R. C. Mancini, H.-S. Park, B. A. Remington, V. A. Smalyuk, and J. Springer, “Hot-Spot Mix and Compressed Ablator  $\rho R$  Measurements in Ignition-Scale Implosions.”

H. G. Rinderknecht, C. K. Li, M. Gatu-Johnson, A. Zylstra, M. Rosenberg, J. A. Frenje, F. H. Séguin, R. D. Petrasso, P. A. Amendt, A. Miles, J. R. Rygg, V. Yu. Glebov, C. Stoeckl, and T. C. Sangster, “Anomalous Shock Yields in Direct- and Indirect-Drive  $\text{D}^3\text{He}$  Exploding Pushers.”

T. C. Sangster, V. N. Goncharov, R. Betti, P. B. Radha, T. R. Boehly, D. T. Casey, T. J. B. Collins, R. S. Craxton, J. A. Delettrez, D. H. Edgell, R. Epstein, C. J. Forrest, J. A. Frenje, D. H. Froula, M. Gatu-Johnson, V. Yu. Glebov, D. R. Harding, M. Hohenberger, S. X. Hu, I. V. Igumenshchev, R. T. Janezic, J. H. Kelly, T. J. Kessler, C. Kingsley, T. Z. Kosc, J. P. Knauer, S. J. Loucks, J. A. Marozas, F. J. Marshall, A. V. Maximov, R. L. McCrory, P. W. McKenty, D. D. Meyerhofer, D. T. Michel, J. F. Myatt, R. D. Petrasso, S. P. Regan, W. Seka, W. T. Shmayda, R. W. Short, A. Shvydky, S. Skupsky, J. M. Soures, C. Stoeckl, W. Theobald, V. Versteeg, B. Yaakobi, and J. D. Zuegel, “Improving Cryogenic DT Implosion Performance on OMEGA” (invited).

W. Seka, D. H. Edgell, D. H. Froula, J. Katz, J. F. Myatt, J. Zhang, R. W. Short, D. T. Michel, A. V. Maximov, and V. N. Goncharov, “Multibeam Two-Plasmon Decay: Experimental Signatures and Diagnostic Applications.”

R. W. Short, J. F. Myatt, A. V. Maximov, D. T. Michel, D. H. Froula, and J. Zhang, “The Effects of Beam Polarization and Orientation on Convective and Absolute Two-Plasmon Decay by Multiple Laser Beams.”

A. Shvydky, M. Hohenberger, J. A. Marozas, M. J. Bonino, D. Canning, T. J. B. Collins, T. J. Kessler, P. W. McKenty, T. C. Sangster, and J. D. Zuegel, “Two-Dimensional Numerical Evaluation of 1-D Multi-FM SSD Experiments.”

N. Sinenian, M. J.-E. Manuel, J. A. Frenje, F. H. Séguin, C. K. Li, R. D. Petrasso, V. N. Goncharov, J. A. Delettrez, C. Stoeckl,

T. C. Sangster, and J. Cobble, “An Empirical Target-Discharging Model for Direct-Drive Implosions on OMEGA.”

H. Sio, M. Rosenberg, H. G. Rinderknecht, D. T. Casey, A. Zylstra, C. Waugh, M. Gatu-Johnson, F. H. Séguin, C. K. Li, J. A. Frenje, R. D. Petrasso, J. A. Delettrez, V. Yu. Glebov, T. C. Sangster, C. Stoeckl, V. N. Goncharov, P. A. Amendt, C. Bellei, and S. C. Wilks, “Developing a D<sup>3</sup>He Exploding-Pusher Platform to Study Kinetic Effects.”

A. A. Solodov, W. Theobald, K. S. Anderson, A. Shvydky, R. Betti, J. F. Myatt, C. Stoeckl, and R. B. Stephens, “Simulations of Cone-in-Shell Targets for Integrated Fast-Ignition Experiments on OMEGA.”

C. Stoeckl, J. A. Delettrez, G. Fiksel, D. Guy, R. K. Jungquist, C. Mileham, P. M. Nilson, T. C. Sangster, M. J. Shoup III, and W. Theobald, “Soft X-Ray Backlighting of Direct-Drive Implosions Using a Narrowband Crystal Imaging System.”

W. Theobald, A. A. Solodov, C. Stoeckl, R. Epstein, V. Yu. Glebov, G. Fiksel, S. Ivancic, F. J. Marshall, G. McKiernan, C. Mileham, P. M. Nilson, T. C. Sangster, C. Jarrott, F. N. Beg, E. Giraldez, R. B. Stephens, M. S. Wei, H. McLean, H. Sawada, and J. Santos, “Monochromatic 8.05-keV Flash Radiography of Imploded Cone-in-Shell Targets.”

C. Waugh, M. Rosenberg, J. A. Frenje, F. H. Séguin, R. D. Petrasso, V. Yu. Glebov, T. C. Sangster, and C. Stoeckl, “A New Platform for Calibrating nTOF Detectors at ICF Facilities Using CR-39-Based Proton Detectors.”

J. Zhang, J. F. Myatt, R. W. Short, A. V. Maximov, H. X. Vu, D. A. Russell, and D. F. DuBois, “A Three-Dimensional Zakharov Model of the Two-Plasmon-Decay Instability in Inhomogeneous Plasmas Driven by Multiple Laser Beams.”

The following presentations were made at the 12th International Workshop on Fast Ignition of Fusion Targets, Napa Valley, CA, 4–8 November 2012:

J. R. Davies, “Scaling of Ignition Laser Parameters with Fast-Electron Parameters.”

A. A. Solodov, W. Theobald, K. S. Anderson, A. Shvydky, R. Betti, J. F. Myatt, and R. B. Stephens, “Integrated Fast-Ignition Experiments on OMEGA.”

S. P. Regan, R. Epstein, B. A. Hammel, L. J. Suter, C. A. Iglesias, B. G. Wilson, M. A. Barrios, D. K. Bradley, D. A. Callahan, C. Cerjan, T. Doeppner, M. J. Edwards, S. H. Glenzer, I. E. Golovkin, S. W. Haan, N. Izumi, O. S. Jones, J. D. Kilkenny, J. L. Kline, G. A. Kyrala, O. L. Landen, T. Ma, J. J. MacFarlane, R. C. Mancini, R. L. McCrory, N. B. Meezan, D. D. Meyerhofer, H.-S. Park, K. J. Peterson, J. Ralph, B. A. Remington, T. C. Sangster, V. A. Smalyuk, P. Springer, and R. P. J. Town, “X-Ray Spectroscopy of Ignition-Scale Implosions on the National Ignition Facility,” 15th Workshop on Radiative Properties of Hot Dense Matter, Santa Barbara, CA, 5–9 November 2012.

W. T. Shmayda, D. R. Harding, and T. B. Jones, “Tritium Fuel Cycle for Direct-Drive Inertial Fusion Reactors Using Microfluidics,” 2012 American Nuclear Society Winter Meeting and Nuclear Technology Expo, San Diego, CA, 11–15 November 2012.

D. R. Harding, W. Wang, and T. B. Jones, “Textured Silicon Surfaces for Moving Oil Droplets in ‘Lab-on-Chip’ Devices,” Material Research Society Fall Meeting, Boston, MA, 25–30 November 2012.

The following presentations were made at the Fusion Power Associates Meeting, Washington, DC, 5–6 December 2012:

R. Betti, “Fusion Science Center Activities on Advanced ICF Ignition.”

R. L. McCrory, “Progress Toward Polar-Drive Ignition for the NIF.”

R. L. McCrory, “LLE FY13–FY15 Plans,” 2013 ICF Executives Meeting, Washington, DC, 10 January 2013.

J. E. Schoenly, W. Seka, G. Romanos, and P. Rechmann, “The Efficacy of Selective Calculus Ablation at 400 nm: Comparison

to Conventional Calculus Removal Methods,” Lasers in Dentistry XIX, San Francisco, CA, 2–7 February 2013.

The following presentations were made at LASE Photonics West, San Francisco, CA, 2–7 February 2013:

M. Barczys, S.-W. Bahk, M. Spilatro, D. Coppenbarger, E. Hill, T. Hinterman, R. W. Kidder, J. Puth, T. Touris, and J. D. Zuegel, “Deployment of a Spatial Light Modulator-Based Beam-Shaping System on the OMEGA EP Laser.”

J. H. Kelly, A. Shvydky, J. A. Marozas, M. J. Guardalben, B. E. Kruschwitz, L. J. Waxer, C. Dorrer, E. Hill, and A. V. Okishev, “Simulations of the Propagation of Multiple-FM Smoothing by Spectral Dispersion on OMEGA EP.”

B. E. Kruschwitz, J. H. Kelly, C. Dorrer, A. V. Okishev, L. J. Waxer, G. Balonek, I. A. Begishev, W. A. Bittle, A. Consentino, R. Cuffney, E. Hill, J. A. Marozas, M. Moore, R. G. Roides, and J. D. Zuegel, “Commissioning of a Multiple-FM Smoothing by Spectral Dispersion Demonstration System on OMEGA EP.”

A. V. Okishev, I. A. Begishev, R. Cuffney, S. Papernov, and J. D. Zuegel, “A Highly Energetic Multiwavelength Diode-Pumped Nanosecond Laser System with Flexible Pulse-Shaping Capability.”

L. Gao, P. M. Nilson, I. V. Igumenshchev, G. Fiksel, R. Yan, J. R. Davies, D. Froula, R. Betti, D. D. Meyerhofer, M. G. Haines, D. Martinez, V. A. Smalyuk, and E. Blackman, “Observation of Self-Similarity in the Magnetic Fields Generated by the Nonlinear Rayleigh–Taylor Instability,” Workshop on Exploratory Topics in Plasma and Fusion Research, Fort Worth, TX, 12–15 February 2013.

R. L. McCrory, “Direct-Drive and Alternate Approaches for Laser Inertial Confinement Fusion,” 2013 AAAS Annual Meeting, Boston, MA, 14–18 February 2013.

D. H. Froula, J. Bromage, D. Haberberger, P. M. Nilson, J. D. Zuegel, and D. D. Meyerhofer, “Ultrahigh-Intensity Research

Plans at the Laboratory for Laser Energetics,” Workshop on Frontiers in Extreme Relativistic Optics, Columbus, OH, 20–21 February 2013.

M. M. Mayton, Z. Hobbs, and S. D. Jacobs, “Reclamation of Slurries Used in Optics Manufacturing,” The Center for Emerging and Innovative Sciences, University Technology Showcase, Rochester, NY, 26 March 2013.

D. D. Meyerhofer, “Observation of Self-Similarity in the Magnetic Fields Generated by the Nonlinear Rayleigh–Taylor Instability,” Reconnection Workshop, Princeton, NJ, 4 April 2013.

W. T. Shmayda, “Overview of Tritium Activities of the Laboratory for Laser Energetics,” Tritium Focus Group Workshop, Germantown, MD, 23–25 April 2013.

The following presentations were made at the Omega Laser Facility Users Group Workshop, Rochester, NY, 24–26 April 2013:

A. T. Agliata, “How to Ensure Successful Diagnostic Qualification at the OMEGA Laser Facility.”

E. F. Armstrong, M. Barczys, B. E. Kruschwitz, and S.-W. Bahk, “Wavefront Measurements of High-Power UV Lasers with a Hartmann Sensor.”

M. Barczys, S.-W. Bahk, M. Spilatro, D. Coppenbarger, E. Hill, T. H. Hinterman, R. W. Kidder, J. Puth, T. Touris, and J. D. Zuegel, “Deployment of a Spatial Light Modulator-Based Beam-Shaping System on the OMEGA EP Laser.”

C. M. Caggiano, “Fabrication and Characterization of Radial and Azimuthal Polarization Converters with Photoaligned Liquid Crystals.”

D. Canning, S. Householder, M. Labuzeta, J. Puth, S. F. B. Morse, B. E. Kruschwitz, M. Barczys, E. Hill, J. Kwiatowski, and R. W. Kidder, “OMEGA EP Shot Performance and Facility Enhancement Status.”

J. A. Fooks, M. J. Bonino, A. L. Greenwood, J. S. Jaquez, and M. L. Hoppe, Jr., “Assembly Techniques and Challenges of Two-Plasmon–Decay (TPD) Double-Shell Targets.”

V. N. Goncharov, “Recent Progress in Omega Cryogenic Implosions.”

D. Haberberger, R. Boni, M. Barczys, J. Brown, R. G. Roides, R. Huff, S. Ivancic, M. Bedzyk, R. S. Craxton, F. Ehrne, E. Hill, R. K. Jungquist, J. Magoon, D. Mastrosimone, J. Puth, W. Seka, M. J. Shoup III, W. Theobald, D. Weiner, C. Stoeckl, J. D. Zuegel, and D. H. Froula, “OMEGA EP 4 $\omega$  Diagnostic: System Description and Recent Results.”

E. Hill and J. Puth, “Omega Laser Facility Timing Management.”

R. W. Kidder, M. Miller, C. Kingsley, and A. Zeller, “LLE Resources Are Established to Provide Access to Information for External Users.”

R. L. McCrory, “Welcoming Remarks: Omega Laser Users’ Group 5th Annual Meeting.”

S. F. B. Morse, “Omega Laser Facility Update: 2013 Progress on OLUG Recommendations.”

P. M. Nilson, R. Jungquist, C. Stoeckl, C. Mileham, P. A. Jaanimagi, I. A. Begishev, W. Theobald, J. R. Davies, J. F. Myatt, A. A. Solodov, J. D. Zuegel, D. H. Froula, R. Betti, D. D. Meyerhofer, K. Hill, M. Bitter, P. Efthmion, and B. Stratton, “High-Resolving-Power, Ultrafast Streaked X-Ray Spectrometer for OMEGA EP.”

G. Pien, “Diagnostic Performance on OMEGA.”

P. B. Radha, F. J. Marshall, M. Hohenberger, T. R. Boehly, T. J. B. Collins, R. S. Craxton, D. H. Edgell, D. H. Froula, V. N. Goncharov, J. A. Marozas, R. L. McCrory, P. W. McKenty, D. D. Meyerhofer, D. T. Michel, T. C. Sangster, S. Skupsky, J. A. Frenje, and R. D. Petrasso, “Recent Results from Polar-Drive–Implosions on OMEGA and the NIF.”

R. Q. Rivlis, R. Boni, and S. Ivancic, “Optical Modeling and Analysis of a High-Throughput and High-Temporal-Resolution Spectrometer.”

C. Sorce and M. Labuzeta, “Exploring the Capabilities of the Omega Laser Facility Web Pages.”

S. Stagnitto, M. Labuzeta, and C. Sorce, “Qualifying as an External Instrument Specialist/Technician at LLE.”

The following presentations were made at the 9th International Laser Operations Workshop, Livermore, CA, 13–16 May 2013:

D. Canning, G. Balonek, A. Consentino, C. Dorrer, E. Hill, S. Householder, B. E. Kruschwitz, S. F. B. Morse, J. Puth, and J. D. Zuegel, “Multi-FM and NIF PAM Operation on OMEGA EP.”

S. F. B. Morse, R. E. Bahr, S. J. Loucks, J. Ulreich, B. Rice, M. J. Shoup III, D. W. Jacobs–Perkins, C. Stoeckl, and C. Mileham, “Cryogenic DT System Improvements for Enhanced ICF Platforms.”

J. Puth, S. F. B. Morse, D. Canning, S. Stagnitto, S. Householder, M. Labuzeta, M. Barczys, E. Hill, M. Spilatro, D. Haberberger, J. Kwiatkowski, R. W. Kidder, B. E. Kruschwitz, G. Pien, and G. Fiksel, “Omega Laser Facility Status and Performance.”

T. C. Sangster, “Migrating Polar Drive from OMEGA to the NIF.”

C. Sorce, R. E. Bahr, J. Katz, D. Mastrosimone, M. McCluskey, C. Mileham, A. Sorce, N. Whiting, and D. H. Froula, “The Experimental Support Group’s Role at the OMEGA Facility.”

L. J. Waxer, J. H. Kelly, B. E. Kruschwitz, C. Dorrer, M. J. Guardalben, A. V. Okishev, and J. D. Zuegel, “Considerations for Successful Operation of the OMEGA EP Multi-FM SSD System.”

P. M. Nilson, “High-Resolving Power, Ultrafast Streaked X-Ray Spectrometer for OMEGA EP,” NIF Diagnostic Workshop, Livermore, CA, 21 May 2013.

The following presentations were made at Photonics North, Ottawa, Canada, 3–5 June 2013:

C. Chakraborty, J. Serafini, J. Zhang, R. Sobolewski, L. Q. Zhang, Y. Alimi, A. M. Song, I. Iñiguez-de-la-Torre, J. Mateos, and T. González, “Self-Switching Diodes as Optical Photodectors.”

J. Serafini, Y. Wang, and R. Sobolewski, "Time Resolved Carrier Dynamics in Si-on-Glass Absorbers for Photovoltaic Cells."

J. Serafini, J. Zhang, Y. Akbas, R. Sobolewski, M. Mikulics, and R. Adam, "Time-Resolved Relaxation Dynamics of Non-equilibrium Carriers in Free-Standing GaAs Films."

The following presentations were made at CLEO 2013, San Jose, CA, 9–14 June 2013:

K. S. Anderson, R. Betti, P. W. McKenty, T. J. B. Collins, M. Hohenberger, W. Theobald, T. R. Boehly, R. S. Craxton, J. A. Delettrez, D. H. Edgell, S. X. Hu, M. Lafon, J. A. Marozas, D. D. Meyerhofer, R. Nora, T. C. Sangster, W. Seka, S. Skupsky, C. Stoeckl, A. Shvydkiy, B. Yaakobi, X. Ribeyre, G. Schurtz, A. Casner, L. J. Perkins, M. R. Terry, and D. E. Fratanduono, "Shock-Ignition OMEGA Experiments and Target Design for the NIF."

S.-W. Bahk, J. Bromage, J. D. Zuegel, and R. K. Jungquist, "An Off-Axis, Single-Pass Radial-Group-Delay Compensator Design Using an Offner Triplet for a Broadband OPCPA Laser."

C. Dorrer, "Characterization of Highly Dispersive Components Using Direct Instantaneous Frequency Measurements."

D. Haberberger, S. Ivancic, M. Barczys, R. Boni, and D. H. Froula, "Plasma Refractometry Using Angular Spectral Filters on OMEGA EP."

T. Z. Kosc, A. Owens, A. L. Rigatti, S. D. Jacobs, and J. H. Kelly, "Long-Term Performance of Liquid Crystal Optics on Large Fusion Lasers."

J. Qiao, J. Papa, and A. Kalb, "Design and Analysis of Meter-Size Deformable Gratings for Compressing Kilojoule, Petawatt Laser Pulses."

T. C. Sangster, "Polar-Direct-Drive Ignition on the NIF."

The following presentations were made at the 25th Symposium on Fusion Engineering, San Francisco, CA, 10–14 June 2013:

D. R. Harding, T. B. Jones, W. Weiqiang, and Z. Bei, "Status and Challenges for Mass Producing Inertial Fusion Energy Targets Using an Automated Electromechanical Microfluidic Process."

S.-J. Scott and D. R. Harding, "Accelerated Evaporative Drying of RF Foam for ICF Target Fabrication."

W. T. Shmayda, "Evaluation of Tritium Capture Systems."

T. C. Sangster, "Polar-Drive ICF," NIF Management Advisory Committee, Livermore, CA, 11–12 June 2013.

J. B. Oliver, J. Bromage, C. Smith, D. Sadowski, C. Dorrer, and A. L. Rigatti, "Plasma-Ion-Assisted Coatings for 15-fs Laser Systems," Optical Interference Coatings 2013, Whistler, Canada, 16–21 June 2013.

S. D. Jacobs, T. Jacobs, D. Saulnier, M. M. Mayton, T. DePorter, J. Sydor, and Z. Hobbs, "Reclamation of Rare-Earth Oxides from Spent Optical Polishing Slurries: Expanding the Technology," Rochester Regional Optics/Photonics/Imaging Business Connections Symposium, Rochester, NY, 20 June 2013.

S.-W. Bahk and C. Dorrer, "Wavefront Sensing Improvements Using a Checkerboard Amplitude Mask," Computational Optical Sensing and Imaging, Arlington, VA, 23–27 June 2013.

R. Nora, W. Theobald, K. S. Anderson, M. Hohenberger, M. Lafon, J. A. Delettrez, A. A. Solodov, P. W. McKenty, W. Seka, T. R. Boehly, S. X. Hu, C. Stoeckl, B. Yaakobi, R. Yan, X. Ribeyre, G. Schurtz, A. Casner, and R. Betti, "Shock Ignition: Past, Present, and Future," 4th International Conference on High Energy Density Physics, Saint-Malo, France, 25–28 June 2013.

J. M. Soures, "The Omega Laser Facility Provides Unique High-Energy-Density Science Capabilities to University, National Laboratory, and Industry Researchers," 2013 User Science Exhibition, Washington, DC, 26 June 2013.

The following presentations were made at the 43rd Anomalous Absorption Conference, Stevenson, WA, 7–12 July 2013:

D. H. Edgell, T. J. B. Collins, V. N. Goncharov, I. V. Igumenshchev, J. A. Marozas, D. T. Michel, J. F. Myatt, P. B. Radha, W. Seka, and D. H. Froula, “Cross-Beam Energy Transfer in Polar-Drive Implosions on OMEGA and the NIF.”

R. K. Follett, D. H. Froula, J. Katz, D. T. Michel, S. X. Hu, J. F. Myatt, and R. J. Henchen, “Observation of Two-Plasmon Decay Produced Electron Plasma Waves Using UV Thomson Scattering.”

D. H. Froula, T. J. Kessler, I. V. Igumenshchev, V. N. Goncharov, H. Huang, S. X. Hu, E. Hill, J. H. Kelly, D. D. Meyerhofer, A. Shvydky, and J. D. Zuegel, “Implications of Two-State Focal Zooming on OMEGA to Mitigate Cross-Beam Energy Transfer.”

D. Haberberger, D. H. Edgell, S. X. Hu, S. Ivancic, B. Yaakobi, R. Boni, and D. H. Froula, “Measurement of Long-Scale-Length Plasma Density Profiles for Two-Plasmon Decay Studies.”

S. X. Hu, D. H. Edgell, D. H. Froula, V. N. Goncharov, D. T. Michel, J. F. Myatt, S. Skupsky, and B. Yaakobi, “Understanding the Creation of NIF-Scale Plasmas on OMEGA EP for Laser–Plasma Instability Studies.”

J. A. Marozas, T. J. B. Collins, P. B. Radha, D. H. Edgell, D. H. Froula, M. Hohenberger, F. J. Marshall, D. T. Michel, and W. Seka, “Comparison of the 2-D *DRACO* Cross-Beam Energy Transfer (CBET) Simulations with OMEGA and NIF Experiments.”

A. V. Maximov, J. F. Myatt, R. W. Short, I. V. Igumenshchev, and W. Seka, “Nonlinear Interaction Between Multiple Incoherent Laser Beams in the Plasmas of Direct-Drive ICF.”

D. T. Michel, V. N. Goncharov, I. V. Igumenshchev, P. B. Radha, S. X. Hu, W. Seka, and D. H. Froula, “Comparison of Implosion Velocities for Be, C, and CH Ablators Measured in Direct-Drive Implosions.”

W. Seka, J. F. Myatt, R. W. Short, D. H. Froula, J. Katz, V. N. Goncharov, and I. V. Igumenshchev, “Time-Resolved Electron Temperature Measurements Near  $n_c/4$  Reveal Temperature Islands on Imploding Targets.”

W. Seka, J. F. Myatt, J. Zhang, R. W. Short, D. H. Froula, D. T. Michel, A. V. Maximov, V. N. Goncharov, I. V. Igumenshchev,

D. F. DuBois, D. A. Russell, and H. X. Vu, “The Nonlinear Behavior of the Two-Plasmon–Decay Instability.”

R. W. Short, J. F. Myatt, and J. Zhang, “The Effects of Beam Geometry and Polarization on Two-Plasmon Decay Driven by Multiple Laser Beams.”

A. A. Solodov, B. Yaakobi, J. F. Myatt, J. A. Delettrez, F. J. Marshall, C. Stoeckl, and D. H. Froula, “Measurements of the Divergence of Fast Electrons in Laser-Irradiated Spherical Targets.”

J. Zhang, J. F. Myatt, A. V. Maximov, R. W. Short, D. F. DuBois, D. A. Russell, and H. X. Vu, “Linear Growth and Nonlinear Saturation of Two-Plasmon Decay Driven by Multiple Laser Beams.”

The following presentations were made at the High-Energy-Density Physics Summer School, Columbus, OH, 15–19 July 2013:

D. D. Meyerhofer, “Diagnostics for High-Energy-Density Physics.”

P. B. Radha, “Hydrodynamic Simulations of HED Plasmas.”

J. D. Zuegel, J. Bromage, S.-W. Bahk, I. A. Begishev, J. Bunkenburg, T. Conley, C. Dorrer, H. Huang, R. K. Jungquist, C. Kellogg, T. J. Kessler, E. Kowaluk, J. R. Marciante, S. F. B. Morse, A. V. Okishev, J. B. Oliver, T. Petersen, C. Stoeckl, D. Haberberger, P. M. Nilson, G. Fiksel, J. F. Myatt, and D. D. Meyerhofer, “Technology Development and Prospects for Exawatt-Class OPCPA Pumped by OMEGA EP,” 3rd IZEST Meeting, Livermore, CA, 17–18 July 2013.

D. H. Froula, “Direct-Drive Inertial Confinement Fusion: Where We Started (60 kJ), Where We Stand Today (1.5 MJ), and Where We Will be in 50 Years (100 kJ),” Intense Laser and Beam Plasma Interactions Workshop, Los Angeles, CA, 19–20 July 2013.

J. Bromage, R. G. Roides, S.-W. Bahk, J. B. Oliver, C. Mileham, C. Dorrer, and J. D. Zuegel, “Noncollinear Optical Parametric

Amplifiers for Ultra-Intense Lasers,” *Nonlinear Optics 2013*, Kamuela, HI, 21–26 July 2013.

The following presentations were made at Optics and Photonics, San Diego, CA, 25–29 August 2013:

M. Hohenberger, N. E. Palmer, G. LaCaille, E. L. Dewald, L. Divol, E. J. Bond, T. Döppner, J. J. Lee, J. D. Salmonson, C. A. Thomas, D. K. Bradley, C. Stoeckl, and T. C. Sangster, “Measuring the Hot-Electron Population Using Time-Resolved, Hard X-Ray Detectors on the NIF.”

K. L. Marshall, D. Saulnier, H. Xianyu, S. Serak, N. Tabiryan, and C. Dorrer, “Liquid Crystal Near-IR Beam Shapers Employing Photoaddressable Alignment Layers for High-Peak-Power Applications.”

D. Saulnier, B. Taylor, K. L. Marshall, T. J. Kessler, and S. D. Jacobs, “Liquid Crystal Chiroptical Polarization Rotators for the Near UV Region: Theory, Materials, and Device Applications.”

The following presentations were made at the University of Alberta ICF Committee, Rochester, NY, 28 August 2013:

K. S. Anderson, R. Betti, P. W. McKenty, T. J. B. Collins, M. Hohenberger, W. Theobald, T. R. Boehly, R. S. Craxton, J. A. Delettrez, D. H. Edgell, S. X. Hu, M. Lafon, J. A. Marozas, D. D. Meyerhofer, R. Nora, T. C. Sangster, W. Seka, S. Skupsky, C. Stoeckl, A. Shvydky, B. Yaakobi, R. Yan, X. Ribeyre, G. Schurtz, A. Casner, L. J. Perkins, M. R. Terry, and D. E. Fratanduono, “Shock-Ignition OMEGA Experiments and Target Design for the NIF.”

D. H. Froula, “Experimental Plasma Physics Program.”

D. R. Harding, T. B. Jones, D. D. Meyerhofer, S. H. Chen, R. Q. Gram, M. Bobeica, Z. Bei, M. Moynihan, W. Wang, W. T. Shmayda, S.-J. Scott, A. Nikroo, J. Hund, R. Paguio, G. Randall, J. Fooks, D. Goodin, R. Garrell, and A. Tucker-Schwartz, “Mass Production of Targets for Inertial Fusion Energy.”

J. F. Myatt, R. W. Short, A. V. Maximov, A. A. Solodov, J. Zhang, C. Ren, R. Yan, I. V. Igumenshchev, S. X. Hu, V. N. Goncharov, W. Seka, D. H. Edgell, D. H. Froula, B. Yaakobi, D. T. Michel, D. F. DuBois, D. A. Russell, and H. X. Vu, “The Theoretical Plasma Physics Program at LLE.”

T. C. Sangster, “The Polar-Drive–Ignition Campaign Plan Through FY15.”

P. B. Radha, “Overview of Direct-Drive–Implosion Physics: Results from OMEGA and the NIF,” 8th International Conference on Inertial Fusion Sciences and Applications, Nara, Japan, 8–13 September 2013.

S. Papernov, A. A. Kozlov, J. B. Oliver, and B. Marozas, “Near-Ultraviolet Absorption Annealing Effects in HfO<sub>2</sub> Thin Films Subjected to Continuous-Wave Laser Irradiation at 355 nm,” *Laser Damage 2013*, Boulder, CO, 22–25 September 2013.

J. Katz, N. Fillion, R. J. Henchen, C. Sorce, D. H. Froula, and J. S. Ross, “A Reflective Image Rotating Periscope of Spatially Resolved Thomson-Scattering Experiments on OMEGA,” 16th International Symposium on Laser Aided Plasma Diagnostics, Madison, WI, 22–26 September 2013.

